Evolution géodynamique du craton Ouest Africain au nord du Ghana

Sylvain Block

▶ **To cite this version:**

Sylvain Block. Evolution géodynamique du craton Ouest Africain au nord du Ghana. Géologie appliquée. Universite Toulouse III Paul Sabatier, 2015. Français. NNT : . tel-01170855

HAL Id: tel-01170855
https://theses.hal.science/tel-01170855

Submitted on 2 Jul 2015

HAL is a multi-disciplinary open access archive for the deposit and dissemination of scientific research documents, whether they are published or not. The documents may come from teaching and research institutions in France or abroad, or from public or private research centers.

L'archive ouverte pluridisciplinaire **HAL**, est destinée au dépôt et à la diffusion de documents scientifiques de niveau recherche, publiés ou non, émanant des établissements d'enseignement et de recherche français ou étrangers, des laboratoires publics ou privés.

Université de Toulouse

THÈSE

En vue de l'obtention du

DOCTORAT DE L'UNIVERSITÉ DE TOULOUSE

Délivré par : *l'Université Toulouse 3 Paul Sabatier (UT3 Paul Sabatier)*

Présentée et soutenue le *01/04/2015* **par :**

Sylvain BLOCK

Évolution géodynamique du craton Ouest Africain au nord du Ghana

---

JURY

Philippe GONCALVES	Rapporteur	Membre du Jury
Kurt STÜWE	Rapporteur	Membre du Jury
Mark JESSELL	Directeur de thèse	Membre du Jury
Lenka BARATOUX	Directrice de thèse	Membre du Jury
Laurent AILLERES	Co-directeur de thèse	Membre du Jury
Jean-François MOYEN	Examinateur	Membre du Jury
Olivier VANDERHAEGHE	Examinateur	Président du Jury

École doctorale et spécialité :
SDU2E : Astrophysique, Sciences de l'Espace, Planétologie
Unité de Recherche :
Géosciences Environnement Toulouse
Directeur(s) de Thèse :
Mark JESSELL, Lenka BARATOUX et *Laurent AILLERES*
Rapporteurs :
Philippe GONCALVES et *Kurt STÜWE*

Résumé

Cette thèse porte sur l'histoire géologique Paléoprotérozoïque du Craton Ouest Africain au nord du Ghana. La géologie régionale est présentée à l'aide de nouvelles cartes lithologique, métamorphique et structurale, produites à partir de l'interprétation de données géophysiques et de terrain. Le nord du Ghana est constitué de domaines granito-gneissiques, de ceintures de roches vertes de bas degré métamorphique, et d'ortho- et paragneiss de haut grade, intrudés par plusieurs générations de granitoïdes. Ces domaines sont séparés par des chevauchements, des détachements et des décrochements formés pendant l'orogenèse Éburnéenne (2.15-2.07 Ga).

Les roches magmatiques sont issues de la série calco-alcaline ou sont analogues aux TTG archéens. La géochronologie U-Pb sur zircon indique un magmatisme continu entre 2.21 et 2.11 Ga, et livre des âges hérités jusqu'à 2.30 Ga. L'isotopie Lu-Hf indique que l'ensemble des magmas est juvénile, avec des temps de résidence crustaux de 2.45-2.30 Ga. Les caractéristiques géochimiques des roches magmatiques sont indépendantes de leurs âges. Elles suggèrent que les magmas sont issus de l'interaction et de la fusion simultanée de deux soucres : l'une mantellique, enrichie en éléments incompatibles, l'autre constituée d'une croûte basique.

Le métamorphisme Éburnéen au nord du Ghana se caractérise par une diversité des régimes thermiques. De rares reliques métamorphiques enregistrant des conditions à la transition entre les faciès schiste-bleu et amphibolite témoignent d'un géotherme apparent froid (HP-BT, $\sim 15\,^{\circ}$C/km). Elles sont surimprimées par un épisode métamorphique à la transition entre les faciès amphibolite et granulite HP ($20\,^{\circ}$C/km) synchrone d'une phase de raccourcissement N-S (D1). Cette déformation produit des chevauchements, un épaississement crustal et l'enfouissement de roches superficielles en base de croûte. Son âge est contraint entre 2145 et 2125 Ma par la datation de monazites métamorphiques et de zircons. La formation de détachements entre les migmatites et les ceintures de roches vertes témoigne d'un régime d'extension orientée N-S (D2). Il est interprété comme la conséquence de l'effondrement gravitaire de la pile orogénique. Les roches partiellement fondues sont exhumées au sein d'un dôme anatectique et mises en contact avec des unités de faible degré métamorphique. Ensuite, une compression orientée E-O génère une déformation initialement distribuée (D3) entre 2125 et 2105 Ma, synchrone d'un métamorphisme en faciès amphibolite (25-30 $^{\circ}$C/km) ; puis localisante (D4-D6), qui ré-active en décrochement les accidents structuraux antérieurs.

Peu après le paroxysme métamorphique vers 2130 Ma, l'évolution géodynamique se termine au nord du Ghana, alors que le magmatisme se propage et s'intensifie dans les régions plus au sud et à l'ouest. Ce diachronisme révèle l'existence de fragments continentaux distincts par leur histoire, mis en contact et stabilisés séquentiellement lors de l'orogenèse.

Il est proposé qu'un événement magmatique produise, à partir de 2.45 Ga et loin de toute marge active, des fragments d'une croute juvénile basique précoce, précurseur du Craton Ouest Africain. Ce protolithe a subi une différenciation intense jusqu'à ce que l'orogenèse Éburnéenne entraîne l'amalgamation et la stabilisation de ses différents sous-ensembles. Le nord du Ghana pourrait représenter une suture entre deux compartiments cratoniques entrés en collision. L'enregistrement structural et métamorphique est similaire en certains points aux orogènes modernes, sans

être strictement identique. Cette étude montre qu'au lendemain de la transition Archéen - Paléoprotérozoïque, un épisode majeur de croissance crustale a lieu en dehors des périodes supposées de formation des super-continents. La géodynamique paléoprotérozoique semble unique dans l'histoire de la Terre et représente un état transitoire de son évolution séculaire, entre un régime "archaïque" et la tectonique des plaques moderne.

Abstract

This thesis focuses on the Paleoproterozoic geological evolution of the West African Craton in northern Ghana. New lithological, metamorphic and structural regional maps are built from fieldwork and the interpretation of airborne geophysical data. The crust in northern Ghana comprises granite-gneiss terranes, low-grade metamorphic greenstone belts and high-grade ortho- and paragneissic terranes, which are intruded by successive generations of granitoids. The different litho-tectonic domains are separated by thrusts, detachments and strike-slip shear zones formed during the Eburnean orogeny (2.15-2.07 Ga).

The magmatic rocks belong to the calc-alkaline suite, or are analogue to Archean TTGs. U–Pb zircon dating reveals that magmatic activity was uninterrupted between 2.21 and 2.11 Ga, and yields inherited ages back to *ca.* 2.30 Ga. Lu–Hf isotope analyses show that the magmas are juvenile and derived from a source extracted from the mantle at 2.45-2.30 Ga. Their geochemical signatures do not change significantly through time, and suggest that they were generated from the interaction and coeval melting of a mafic crustal source and an incompatible element-enriched mantle source.

The Eburnean metamorphic record of northern Ghana reflects a diversity of thermal regimes. Rare metamorphic relics record conditions at the transition between blueschist and amphibolite facies that correspond to a cold apparent geothermal gradient (HP-LT, $\sim 15\,^{\circ}$C/km). They are overprinted by amphibolite- to high-P granulite-facies metamorphism ($20\,^{\circ}$C/km) which developed during a phase of N-S directed shortening (D1). Contractional deformation formed thrusts, caused crustal thickening and burial of supracrustal rocks into the lower-crust. Its timing is constrained between 2145 and 2125 Ma by the dating of metamorphic monazite and zircon. Detachment faults separate migmatites from greenstone belts. They formed during N-S directed extension (D2), which is interpreted to reflect the gravitational collapse of the over-thickened crust. The partially molten lower crust is exhumed in an anatectic migmatite dome and juxtaposed to rock units of lower metamorphic grade. Subsequently, E-W directed shortening (D3) produced distributed contractional strain between 2125 and 2105 Ma which is coeval with an amphibolite-facies metamorphic overprint. Strain is gradually localised (D4-D6) and older shear-zones are re-activated in a strike-slip regime.

Following the metamorphic paroxysm at ca. 2130 Ma, the geodynamic evolution terminates in northern Ghana, while magmatism propagates and intensifies in the regions to the south and west. This diachronism suggests that different crustal fragments with distinct histories were assembled and stabilised sequentially during the orogeny.

We suggest that a major magmatic event started at 2.45 Ga and produced fragments of juvenile, dominantly mafic crust, away from active continental margins. They formed the protolith of the West African Craton's crust. The proto-crust underwent intense magmatic differentiation, until the Eburnean orogeny amalgamated and stabilised the different crustal blocs. Northern Ghana may represent a suture zone between two distinct cratonic domains that collided. Its structural and metamorphic record shares some similarities with modern orogenic belts, although it is not strictly identical. This work confirms that an episode of crustal growth took

place after the Archean-Proterozoic transition, in between two periods of inferred super-continent assembly. The Paleoproterozoic geodynamic settings are probably unique in the history of the Earth, as they represent a transitional regime in its secular evolution, between archaic geodynamics and modern plate tectonics.

Remerciements

Les quelques années passées à Toulouse et ponctuées de séjours en Afrique de l'Ouest pour mener à bien ces travaux de recherche ont été pour moi un réel plaisir et une source de satisfaction personnelle. Bien évidemment, rien de tout ceci n'aurait été possible sans les nombreuses personnes qui y ont pris part et y ont contribué à leur façon, et je voudrais ici les remercier chaleureusement.

Tout d'abord, merci à toi Mark de m'avoir fait confiance aussi rapidement, à l'issue d'une brève discussion, le temps de regarder quelques données géophysiques provenant d'un coin du nord du Ghana qui avait l'air fort sympathique. J'ai pris le train du projet en marche et tu m'as permis d'y trouver ma place facilement. Merci de m'avoir donné l'opportunité de mener à bien ce travail et de voyager de conférence en mission de terrain au fil de son avancement. À propos de terrain, ces séjours laissent une quantité d'anecdotes qui sont autant de chouettes souvenirs. Promis Mark, des passages de frontières clandestins et des contre-coups des randos par 40 ˚C, rien ne filtrera !

Merci à Lenka pour ta disponibilité et ton enthousiasme qui explique que j'avais déjà quelques cailloux avec lesquels m'amuser avant même de rentrer dans le vif du sujet. Heureusement que tu étais là pour mes premiers pas dans l'univers IRD à Ouaga. Merci à vous deux pour toutes les discussions géologiques passionnantes et pour la confiance que j'ai ressenti dans votre encadrement, qui m'a permis de prendre beaucoup d'initiatives librement, autant pour établir des collaborations que sur le terrain...

Merci également à Laurent, la French Connexion en Australie, pour tes nombreuses questions sur le terrain qui m'ont forcé à préciser mes idées et à étayer mes modèles, et pour toutes ces discussions sur nos sujets de prédilection : les plis en fourreaux et la sagduction. L'escapade à Broken Hill a été une belle expérience... le *sheath fold* s'en souvient !

Cette thèse ne serait pas ce qu'elle est sans la participation de personnes qui m'ont permis d'acquérir des données et qui ont contribué à faire mûrir mes idées. Je remercie :

- Olivier Bruguier, pour avoir cassé du caillou avec nous sous un soleil de plomb, de m'avoir accueilli à Montpellier pour analyser des échantillons au laser, et de m'avoir permis de co-publier tes données acquises un peu plus tôt. Merci !
- Armin Zeh, de m'avoir acueilli à Frankfort pour des sessions de laser. *Viele danke für deine Geduld !*,
- Luis Parra, à Perth, pour avoir bien voulu passer certains de mes échantillons au SHRIMP. *Thank you for your help !*,
- Oscar Laurent, ami de l'époque stephano - clermonto - sud-africaine. Merci pour ton aide à l'interprétation des données géochimiques !
- Jérôme Ganne pour nos nombreux échanges et réflexions communes. Ta dextérité à la microsonde et ta profusion d'idées sur la thermicité du "WAC" ont été très appréciées et ont contribué à nourrir ces travaux.

Merci aux autres collègues du GET avec qui j'ai eu la chance de tâter du Craton Ouest Africain, Marieke van Lichtervelde, Luc Siebenaller et Mathieu Benoît. À ces

deux derniers, j'ai beaucoup apprécié d'en refaire la géologie autour d'une bière ou d'un plat de foufou trop pimenté. Qu'on se le dise, l'accoutumance à la gastronomie Ghanéenne nécessite patience et longueur de temps !

Je tiens à exprimer ma reconnaissance à ceux dont le travail m'a permis d'avancer dans mes propres chantiers, et qui m'ont transmis une part de leur connaissance ou de leur savoir-faire. Je pense en particulier à Jean-François Mena, Ludovic Menjot et Fabienne de Parseval, fins artisans de la lame mince toujours prets à donner un coup de main, Sophy Gouy et Philippe de Parseval pour leur disponibilité et leur aide à la microsonde et à Thierry Aigouy pour son accompagnement au MEB.

Pour poursuivre, je suis pleinement redevable pour le bon déroulement du travail de terrain à Kwasi Duah, chauffeur du Service Géologique du Ghana, mais également à ses heures traducteur, rafistoleur de pistes cabossées, mécano, négociant en bière de mil, vin de palme ou leurs équivalents distillés, logisticien, marchandeur de droits de passage, et recueil de bons tuyaux. Sa bienveillance m'a fait chaud au coeur et je lui en remercie. Je salue également le travail des chauffeurs de l'IRD de Ouagadougou avec qui j'ai eu l'occasion de travailler, Salifou Yougbaré, Boukary Ouedraogo et Matthieu Kaboré, qui ont apporté une joyeuse coloration à nos séjours, et remercie Koné Moumouni, le logisticien du projet WAXI à Ouaga, pour ses précieux coups de main. Ma reconnaissance admirative va également aux paysannes et paysans habitant les régions que j'ai parcouru, qui sont riches d'une grande hospitalité.

Je souhaite remercier les nombreuses personnes avec lesquelles j'ai pu avoir des discussions de géologie, à qui j'ai pu demander des avis et des informations en tout genre, en particulier les collègues du GET, Dominique Chardon, Stéphanie Duchêne, Michèle de Saint-Blanquat, Julien Berger, Joseph Martinod, Yohan Denèle, mais aussi Max Vidal, Alain Kouamelan et les collègues jeunes géologues africains : Saga Sawadogo, Pascal Ouiya, Hamidou Waongo, Prince Amponsah, Abigail Ayikwei et Raymond Sagna. Merci également à Stephane Perrouty, mon prédécesseur toulousain dans la région ghanéenne d'Ashanti, pour ses conseils en début de thèse, et à Helen McFarlane, qui reprend le flambeau dans la ceinture de Sefwi et qui m'a permis de m'y rendre pour avoir un aperçu de la géologie de cette région.

Enfin, je n'oublie pas Anais Brethes, Suzelle Sigo et Julie Carcone qui ont apporté leurs pierres à l'édifice au cours de leurs stages respectifs, ni Sabine Mélézan, qui fut d'une aide administrative précieuse.

Je remercie également les membres du jury, Philippe Goncalves, Kurt Süwe, Jean-François Moyen, Pavel Pitra et Olivier Vanderhaeghe, d'avoir bien voulu se déplacer à Toulouse pour évaluer mon travail et pour en discuter avec tant d'intérêt.

Je voudrais exprimer ma gratitude envers les enseignantes et les enseignants qui ont façonné mon goût de la géologie et ma curiosité au cours de ma scolarité, aux premiers rangs desquels François Rosé, mon prof de prépa à Marcellin Berthelot, puis Pierre Thomas, Hervé Bertrand et Éva Chamorro-Perez à l'ENS Lyon. Enfin, j'adresse un remerciement tout particulier à Jean-François Moyen pour m'avoir donné l'opportunité dès le début de master de m'attaquer aux problématiques de l'Archéen en Afrique du Sud, et d'explorer des thématiques qui se retrouvent à

présent au centre de cette thèse. C'est avec toi que mon parcours dans la recherche débute et que je creuse mes thèmes de prédilection. Tu m'as transmis une partie de ta passion pour la géologie dans le Lowveld, lors des battues aux hyènes, mais aussi sur les pentes du Pilat et dans les gorges ardèchoises. Ceci m'amène à saluer toute la "bande à Jeff" rencontrée de Stellenbosch à Saint-Etienne. Merci à Arnaud, Oscar (encore là !), Justine, Antoine, LSD, grand Simon, ptit' Simon, Gautier et les autres pour les discussions et les bons moments de rigolade.

Je suis tout autant redevable pour la richesse de ces années de thèse aux personnes rencontrées pendant cette période, aussi bien au labo qu'en dehors. En premier lieu, je tiens à remercier l'équipe de choc des jeunes du GET, camarades doctorants et post-docs, pour l'environnement qu'ils ont participé à créer au labo. Un environnement souvent marqué par une atmosphère chargée d'épais nuages de gras de canard et autres effluves cullinaires, de fumées de tupperwears cramés, de vapeurs de café ou autres vins chauds. Et puis, entre ces moments de légèreté, trève de rigolade lors de nos réunions "au sommet" pour animer tout ce microcosme laborantin ! Merci à Alex, le roi du gras et des acronymes, pour les gueuletons et tout le reste, Sylvaine ma "marraine" *de facto*, Léandre, pour avoir partagé les ambiances "reggae" dans le bureau, Maria, pour nous avoir supportés tout ce temps, mais aussi JLG, Guillaume, Caro, Adrien, Damien, Arnaud, Jean, Laetitia, Thomas, Antonin, Sylvain, Brian, Cori, Van Bai, Vincent, les Fabrices, Quentin, Pierre et les autres d'avoir fait du GET bien d'avantage qu'un lieu de travail. D'autre part, la coloc' de la Cousquille a constitué un sorte de monde parallèle, anti-thèse rafraichissant au monde du labo. J'ai une pensée affectueuse pour toutes celles et ceux qui ont fait et font vivre ce lieu, Thibaud, Laurence, Anabelle, Louis, Maeva, Lidia, Erwan, Jean, Taleb, Anne, Julie, etc. Et une pensée tendre pour Camille, que notre parcours commun se poursuive et nous amène sur des terres propices, dans les contrées africaines comme ici.

Enfin, je tiens à remercier ma famille, du côté de laquelle mes éveils naturalistes s'enracinent. Merci à Eugène Raguin, qui m'a sans doute transmis une part de son intérêt pour la géologie, et à mes grands parents maternels qui ont assidument relayé cet héritage. Merci à mes parents pour leur soutien avant et pendant la thèse, également à mes frères et soeurs pour leur curiosité et l' intérêt qu'ils y ont porté.

Table des matières

Introduction

Introduction générale

Les sciences de la Terre s'intéressent à la formation et à l'évolution de la planète Terre, aux processus qui façonnent ses surfaces et aux interactions entre ses différents réservoirs (asthénosphère, lithosphère, hydrosphère, biosphère,...). Elles visent à développer une meilleure compréhension de la Terre, de son fonctionnement et de son histoire. Comme dans toutes les sciences, l'accumulation de données et de connaissances, au moyen de dispositifs techniques en mutation constante, s'accompagne de la construction de cadres théoriques servant à les interpréter. Il me semble possible d'identifier deux principaux déterminants scientifiques du cadre d'interprétation en vigueur actuellement au sein de la communauté des Sciences de la Terre. Le premier est l'émergence de la datation radiochronologique absolue, qui rendit possible la reconstruction, avec une confiance nouvelle, de l'histoire de la Terre. Le second est l'acceptation progressive, au début du siècle dernier, de la théorie de la dérive des continents, et l'avènement de son héritière en tant que paradigme : la tectonique des plaques.

La théorie de la tectonique des plaques permet de décrire de façon satisfaisante la dynamique de la Terre moderne. Son acceptation est telle que le terme désigne aujourd'hui non plus une théorie, mais bien le mode de fonctionnement de la Terre. La production de chaleur tellurique induit la convection du manteau. Celui-ci se différencie pour former la lithosphère, qui constitue la couche limite thermique du système convectif. La lithosphère océanique se forme en surface des courants convectifs ascendants, elle finit par entrer en subduction et plonger au niveau de courants convectifs descendants. La lithosphère continentale, elle même produite par la différentiation progressive du manteau, se déplace et se déforme en réaction à la dynamique induite par le système convectif. La tectonique des plaques désigne le mode de convection actuel du manteau terrestre, où la couche limite thermique (la lithosphère) est couplée aux cellules de convection.

Les méthodes géochronologiques ont apporté la démonstration que la lithosphère continentale s'est formée en continu au cours de l'histoire de la Terre. Certains fragments de continents anciens on échappé à un recyclage total et nous sont parvenus. La croûte continentale constitue donc le registre fossile observable de l'histoire de la Terre. Elle témoigne des processus géologiques et de leurs évolutions à travers les temps. Or la théorie de la tectonique des plaques a été historiquement construite en intégrant une multitude de données issues de l'observation d'objets géologiques actifs, ou du moins récents, c'est à dire essentiellement formés à l'ère Phanérozoïque (550–0 Ma), dont nous savons qu'il représente environ 13% de l'histoire de la Terre. La tectonique des plaques (en tant que cadre d'interprétation) est donc "calibrée" pour la Terre moderne.

Des décennies de recherche en sciences de la Terre ont permis de mettre en évidence d'importantes différences entre l'enregistrement géologique récent et la géologie des continents anciens. En particulier, le registre géologique des cratons datant de l'Archéen (4.0–2.5 Ga) et du Paléoprotérozoïque (2.5–1.6 Ga) suggère qu'ils se sont formés dans des contextes géodynamiques qui ne sont plus en vigueur sur la Terre actuelle, ou du moins dont nous n'observons plus d'analogues stricts. La géodynamique de la Terre primitive constitue donc un problème scientifique majeur en sciences de la Terre. La théorie de la tectonique des plaques fournit-elle

un cadre théorique transposable à l'identique à la Terre primitive ? Le mode de convection terrestre était-il le même il y a 2.5 ou 3.5 Ga ? Un certain nombre de considérations théoriques sur la thermicité de la Terre primitive nous permettent d'en douter. Dans ce cas, comment interpréter les données tirées de l'étude des cratons ? Il est sans doute nécessaire d'identifier et de caractériser les processus géologiques (pétrologie, magmatisme, tectonique) dans un premier temps, puis de conserver une liberté d'interprétation lorsqu'il s'agit de reconstituer la gamme des contextes géodynamiques dans laquelle ces processus ont pu avoir lieu.

La géologie Archéenne a fait l'objet d'études prolifiques. Les roches magmatiques, volcaniques, métamorphiques et sédimentaires qui s'y trouvent, les ressources minérales, les grands traits architecturaux des domaines continentaux les distinguent des continents actuels. De nombreux modèles géodynamiques ont été proposés pour expliquer leurs spécificités. Un consensus semble s'établir sur l'idée que le manteau Archéen était plus chaud qu'à l'actuel, et qu'il en découlait logiquement un mode de convection différent, distinct de la tectonique des plaques (Chapitre 1). Le passage d'un régime Archéen à une géodynamique moderne est situé entre 3.0 et 2.5 Ga, selon les objets d'étude. Cette transition, dont on peut discuter du caractère abrupt ou graduel, est interprétée comme étant la conséquence du refroidissement séculaire de la Terre, et de la transformation du mode de convection terrestre. Elle ouvre sur le Protérozoïque, une ère géologique longue de près de 2.0 Ga dont la communauté des sciences de la Terre considère qu'elle était façonnée par la tectonique des plaques, ou du moins une sorte de tectonique des plaques similaire à la géodynamique actuelle sans être strictement identique. En effet, le registre géologique du Protérozoïque présente une systématique qui rappelle la Terre moderne, bien que dans le détail les objets géologiques des deux époques puissent être différents (Chapitre 1).

Cette thèse s'inscrit dans la problématique de l'évolution séculaire de la géodynamique terrestre, et se propose d'étudier un objet géologique formé au lendemain de la transition Archéen-Protérozoïque. Celle-ci est censée correspondre à la généralisation, à échelle globale, d'un fonctionnement "moderne" de la Terre. L'étude se porte sur une portion du Craton Ouest Africain datant du Paléoprotérozoïque (2.25-2.10 Ga), située dans la partie septentrionale du Ghana. Elle a pour objectif d'explorer les mécanismes de formation du craton Ouest Africain, et des masses continentales en général, à cette époque de la Terre. Elle cherche à reconstituer l'histoire géologique de cette région afin de formuler des hypothèses sur la géodynamique en vigueur à une période clé de l'évolution de la planète. Il est donc fréquemment fait référence aux registres géologiques de l'Archéen et du Phanérozoïque, deux périodes qui servent de modèles comparatifs pour qualifier le Paléoprotérozoïque. L'étude de cette portion du craton Ouest-Africain est traitée en prenant en compte une grande diversité de données petrologiques, métamorphiques, cartographiques, géochronologiques,... C'est pourquoi le qualificatif de "géologie générale" me semble convenir à ces travaux de thèse. Chacun des chapitres présentant les résultats de la thèse développe préférentiellement une approche et une méthode d'étude. Les chapitres sont rédigés en anglais, ceux qui sont présentés sous forme de publications scientifiques sont introduits par un résumé en français.

A l'échelle globale, l'évolution séculaire de la dynamique terrestre se caractérise par une métamorphose progressive des modes de déformation et des conditions mé-

tamorphiques dans les orogènes, de la composition de la croûte continentale et du type de roches qui s'y trouve, ou encore de l'architecture générale de la croûte continentale. La présentation de l'évolution séculaire de la Terre est l'objet du chapitre 1. Les controverses scientifiques autour de la transition Archéen - Paléoprotoérozoïque sont présentées dans le chapitre 2. La géologie du craton Ouest Africain, qui fournit un précieux enregistrement du fonctionnement de la Terre à cette période charnière, et les controverses sur sa formation, sont détaillées dans ce même chapitre.

Le refroidissement de la Terre a permis la formation de lithosphères plus froides et mécaniquement plus résistantes, répondant aux contraintes par une déformation cassante, un épaississement ou un amincissement localisés, plutôt que par un fluage distribué. Le chapitre 3 est consacré à l'étude du mode de déformation de la croûte du Craton Ouest Africain pendant l'orogenèse Éburnéenne (2.15-2.10 Ga). Il fournit des données permettant de discuter de la rhéologie de la croûte juvénile Paléoprotérozoïque du nord du Ghana.

Les types de déformation, la capacité de la croûte à s'épaissir ou à fluer sous la contrainte et le régime thermique de la croûte déterminent la nature des roches métamorphiques qui s'y forment et y sont préservées pendant une orogenèse. L'histoire de la Terre témoigne de l'apparition d'une dualité de régimes thermiques à partir du Paléoprotérozoïque, et d'un refroidissement progressif des géothermes fossiles. Le chapitre 4 présente une étude complète de l'évolution métamorphique des unités géologiques du nord du Ghana, et compare les associations métamorphiques qui s'y trouvent à celles des orogènes plus anciens et plus récents.

La modélisation numérique permet de tester des hypothèses concernant le mode de déformation et le régime thermique d'une croûte ou d'une lithosphère théorique. Le chapitre 5 présente une étude de modélisation thermo-mécanique et thermodynamique qui teste la capacité d'un régime tectonique donné (raccourcissement 2D) à reproduire l'enregistrement métamorphique du Craton Ouest Africain, en particulier à exhumer des roches métamorphisées dans la croûte moyenne ou inférieure.

La croûte Archéenne est essentiellement constituée de "gneiss gris", dont la plus grande proportion est dérivée de roches magmatiques appartenant à la série des TTGs (tonalites, trondhjemites, granodiorites). Ces roches sont quasiment absentes des continents plus récents, dont les granites représentent la lithologie la plus fréquente. La transformation du magmatisme continental au cours de l'histoire de la Terre reflète un changement dans les sources des magmas crustaux et dans les processus pétrogénétiques qui les produisent. Le chapitre 6 s'intéresse à la géochimie des roches magmatiques paléoprotérozoïques présentes au nord du Ghana, pour tenter d'identifier la source du magmatisme et les processus qui le contrôlent. L'étude géochimique est couplée à une étude géochronologique, afin de reconstituer l'histoire de la production, de la maturation et de la stabilisation de la croûte juvénile. Ces informations sont ensuite utilisées pour envisager les contextes géodynamiques potentiels dans lesquels la croute continentale du nord du Ghana, et à plus grande échelle, du craton paléoprotérozoïque, s'est formée.

Le chapitre 7 synthétise les principaux résultats et aborde quelques perspectives de recherche ouvertes par ces travaux.

Déroulement de la thèse

Cette thèse se déroule dans le cadre de l'Initiative d'Exploration en Afrique de l'Ouest (IXAO/WAXI). Il s'agit d'un projet de recherche qui développe une collaboration entre des universités et des services géologiques de pays d'Afrique de l'Ouest, des instituts de recherche de pays occidentaux (principalement l'Australie, la France et la République Tchèque) et de l'Afrique du Sud, et des compagnies de l'industrie minière actives en Afrique de l'Ouest. Le projet WAXI a pour objectifs de stimuler la recherche scientifique en Afrique de l'Ouest afin d'accroître les connaissances géologiques générales sur le Craton Ouest Africain, de former et transmettre des compétences aux étudiants, universitaires, personnels administratifs et employés du secteur minier ouest-africains, et de répondre aux demandes de compagnies minières en matière scientifique. Les zones d'études du projet sont choisies en fonction des collaborations scientifiques établies, de la situation politique et de la disponibilité de données géologiques gouvernementales ou industrielles.

La thèse a été financée par une bourse du Ministère de l'Enseignement Supérieur et de la Reecherche français. Les frais de recherche ont été pris en charge par le projet WAXI, dans son second cycle (WAXI II), à partir de septembre 2011. A cette époque, l'équipe WAXI a déjà entrepris des travaux de recherche au sud du Mali, sud du Ghana, sud-ouest et nord du Burkina Faso, qui sont en cours ou sont achevés. Le nord du Ghana se situe alors entre différentes régions ayant déjà fait l'objet d'une étude géologique et cartographique. De plus, l'équipe WAXI a construit un réseau de collaborations performant avec des collègues ghanéens et burkinabés. Enfin, depuis la fin des années 2000, le gouvernement ghanéen dispose de données géophysiques aéroportées de bonne qualité sur son territoire, et quelques publications récentes suggèrent que la géologie du nord du Ghana a un potentiel scientifique important. Dans ces circonstances, un nouveau projet de recherche y est lancé.

Initialement, la formulation du sujet de la thèse laisse volontairement une liberté dans le choix des aspects à explorer en détail : "L'évolution géodynamique de la ceinture paléoprotérozoïque de Bolé-Nangodi, nord du Ghana, Craton Ouest Africain". L'objectif étant de contraindre l'histoire géologique générale de la zone d'étude. Dans un premier temps, la priorité est de produire une nouvelle carte géologique du nord du Ghana à partir de l'interprétation des données géophysiques et de données cartographiques de terrain, en suivant les méthodes utilisées lors d'autres travaux de l'équipe WAXI. L'état des connaissances disponibles sur le craton semble souffrir d'une carence de données métamorphiques couplées à des contraintes géochronologiques et structurales. Compte-tenu de la présence reconnue de roches métamorphiques qui se prêtent aux études thermo-barométriques dans la région, il est pertinent de développer le volet métamorphique pour étudier la géologie régionale. Pendant le travail de terrain, l'échantillonnage porte sur tous types de roches, afin d'avoir la possibilité d'étudier d'autres aspects de l'histoire géologique. Ainsi, à un stade plus avancé de la thèse, l'étude géochimique et géochronologique des roches magmatiques est intégrée aux travaux, en collaboration avec de nombreux collègues.

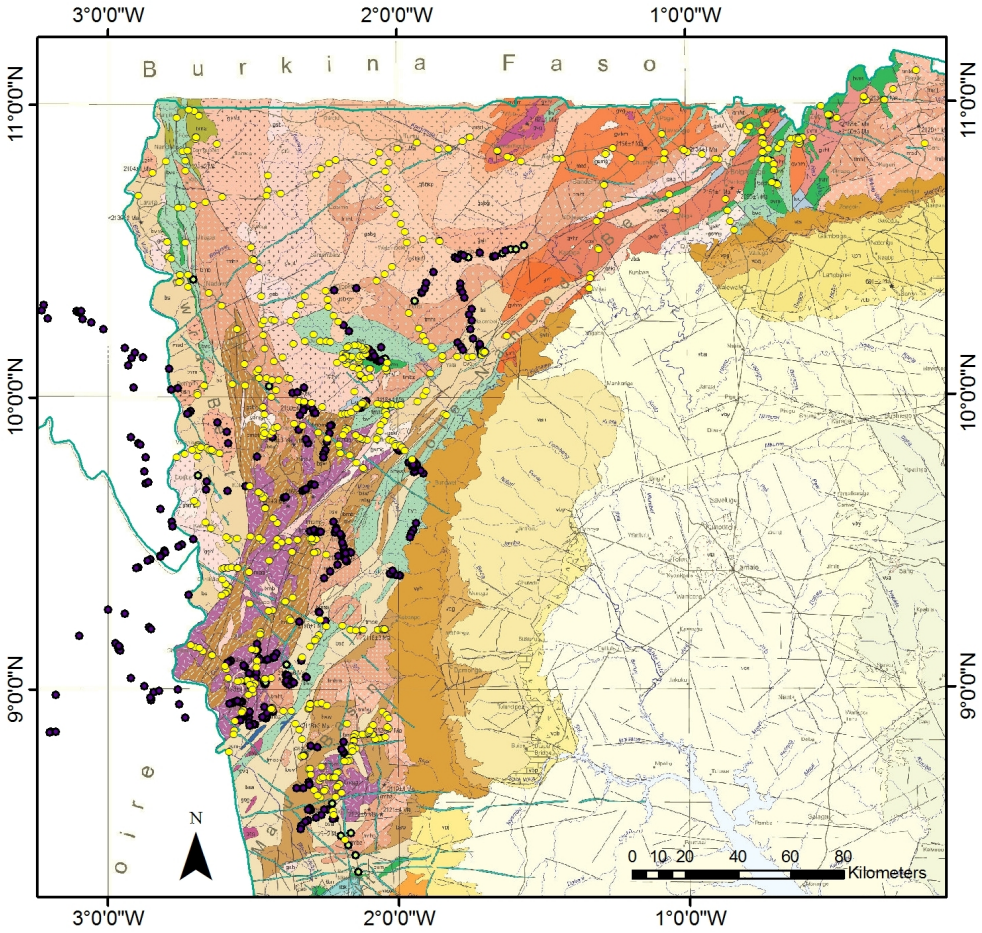

Sites d'affleurements étudiés en 2012 (jaune) et 2013 (bleu). / Localisation of outcrop sites visited in 2012 (yellow) and 2013 (blue). Carte / Map 1 :1 000 000 Duodu (2009)

Travail de terrain

Le nord du Ghana - informations utiles

La zone d'étude s'étend depuis la frontière entre le Togo et le Ghana à l'est, le long de la frontière septentrionale du Ghana, jusqu'au centre-ouest du pays, dans la région frontalière de la Côte d'Ivoire à l'ouest. Elle inclut les régions ghanéennes "Upper East" et "Upper West", ainsi que le tiers occidental de la "Northern region". Cette aire géographique correspond à l'ensemble du socle paléoprotérozoïque au nord de la ville de Banda-Nkwanta. Quelques observations de terrain sont également effectuées dans les zones limitrophes au sud du Burkina Faso, dans la région de Gaoua et Batié, ainsi qu'au au nord-est de la Côte d'Ivoire.

Ces régions se trouvent dans la zone climatique Soudano-Guinéenne. Celle-ci se caractérise par un régime de mousson entre avril et septembre, une saison sèche le reste de l'année, et un fort gradient S-N de pluviométrie. Le couvert végétal naturel consiste en une savanne arborée ou une forêt sèche, dont les kaicedras, les karités et, au nord, les baobabs sont emblématiques. Les hautes herbes sèches sont mises à

feu dès novembre, ce qui facilite la progression dans la savanne entre décembre et avril. Les températures sont maximales en mars-avril.

La topographie du nord du Ghana est faible et l'altitude de 200-400m environ. Les points hauts topographiques correspondent à des buttes témoin d'un plateau latéritique dont les fragments sont distribués sur l'ensemble de la région. Les collines latéritiques dominent des plaines alluviales et des coteaux à la topographie très douce. Le socle paléoprotérozoïque y affleure de manière discontinue. Les affleurements sont principalement situés dans le lit des cours d'eau ou sur les coteaux, au niveau de changements de pente à l'approche d'un cours d'eau ou de la limite du plateau latéritique. Des granitoïdes forment d'occasionels inselbergs. Les quartzites et les conglomérats du bassin de la Volta, datant du Néoprotérozoïque et déposé en discordance sur le craton, forment des crêtes qui culminent jusqu'à une centaine de mètres au dessus de la plaine.

L'agriculture est la principale activité économique de la région. L'igname, le maïs, le manioc, le pois et le sorgho sont cultivés de façon extensive sur brûlis. Les collines latéritiques sont relativement densément boisées car elles ne sont pas arables. L'activité agricole se concentre en saison humide. En Côte d'Ivoire, et dans une moindre mesure au Ghana, de grandes surfaces sont utilisées pour la culture de mangue et de noix de cajou, mais elles sont ouvertes d'accès. Au Ghana, l'abattage d'arbres pour la production de bois d'œuvre ou de charbon de bois a grandement endommagé la forêt. Récemment, l'extraction artisanale d'or ("Galamsey") a pris d'importantes proportions. Des campements temporaires regroupant des milliers de personnes s'installent sur ces sites. L'orpaillage est officiellement illégal au Ghana, mais il est apparemment lucratif. De ce fait, il est préférable de se présenter à l'entrée des sites d'extraction. La densité de population est faible, les rencontres avec les cultivateurs, chasseurs et éleveurs semi nomades sont fréquentes sur le terrain. De nombreuses langues différentes sont parlées dans le nord du Ghana, parmi lesquelles le Gonja (région de Bolé) et le Dagaari (région de Wa).

Les modes d'usage des terres impactent la façon d'organiser le travail de terrain. La période la plus appropriée est entre décembre et mars. La savanne est parcourue par de nombreux chemins, en particulier le long des cours d'eau. Des pistes carrossables sont régulièrement ouvertes par les orpailleurs, les cultivateurs et les charbonniers.

Campagnes de terrain

La majorité du travail de terrain a lieu lors des saisons 2012 et 2013, entre janvier et mars. En 2012, un première mission de terrain de 3 mois a pour objectif d'acquérir une vision d'ensemble de la géologie et de l'organisation des différents domaines structuraux. Tous les principaux types de roches sont échantillonnés. Des données structurales préliminaires permettent de formuler des hypothèses sur l'histoire géologique de la région. L'année suivante (3 mois), l'étude se concentre sur les domaines poly-déformés les plus complexes situés au nord-ouest du Ghana, afin de tester les hypothèses issues du travail de l'année précédente. Les relations de terrain sont étudiées en détail, en particulier à pied le long de profils pour établir des coupes géologiques. Des travaux de reconnaissance ont également lieu au sud du Burkina Faso et au nord-est de la Côte d'Ivoire, de part et d'autre du Mou-Houn. En 2014 une formation de terrain axée sur la géologie métamorphique et structurale

est organisée pendant 7 jours dans la zone d'étude. Le livret guide bilingue rédigé à cette occasion est fourni en annexe de la thèse. La formation est déstinée aux étudiants d'université et de personnels des services géologiques et de l'industrie (voir le document en annexe). Elle réunit une douzaine de participants, plus une dizaines de collaborateurs (chauffeurs, aides logistique,...). Le séjour sur place dure environ deux mois et permet également d'effectuer des observations complémentaires sur la zone d'étude et dans les régions avoisinantes.

Au total, 963 sites d'affleurements sont décrits et référencés dans une base de donnée. Les informations collectées à chaque affleurement comprennent des données lithologiques, pétrologiques et structurales, ainsi que des photographies et des mesures de susceptibilité magnétique. Environ 330 échantillons ont été collectés sur 250 sites.

Thesis development

Scientific context of the thesis

The work presented in this thesis was carried out in the framework of the West African Exploration Initiative (WAXI) project. This project is a collaboration between West African universities and geological surveys, research institutions from a few western countries (mainly Australia, France and the Czech Republic) and South Africa, and companies of the mining industry that are active in West Africa. It is mainly funded by industry participants. Its objectives are to enhance research in West Africa to increase the general geological knowledge of the West African Craton, to train and transfer capacities to the West African students and university staff, administrations and companies, and to adress some of the scientific demands of exploration and mining companies working in West Africa. Target study areas of the project are selected depending on the working collaborations, political situation, government and industry data availability at a given time.

This thesis was funded by scholarship of the French research ministry, while research costs were partially covered by the WAXI project. It started in the sixth year of the WAXI project, in september 2011. At this time, significant research work was carried out by the WAXI team and its collaborators in southern Mali, southern Ghana, south-western and northern Burkina Faso. Northern Ghana is located in between a few previously studied areas. Furthermore, the WAXI team had build high-quality collaborations with Ghanean and Burkinabe collaborators. Finally, good quality geophysical data was available for northern Ghana, and previous work suggested that this area held interesting geological, architectural and metamorphic features. All these reasons incited the beginning of a new research project in northern Ghana.

The initial objectives of this thesis were voluntarily loosely formulated : “The geodynamic evolution of the Paleoproterozoic Bole-Nangodi belt, northern Ghana, West African Craton”. This wide definition allowed the possibility to carry out investigations in various directions in order to produce a general geological framework of the study area. Two objectives were specifically envisaged. The first one was to produce a geological map of northern Ghana based on the interpretation of airborne geophysical datasets and on field mapping, similar to what had been produced by other members of the WAXI team. Secondly, there was a strong incentive to carry out an in-depth metamorphic study, because the use of metamorphism to constrain the evolution of the West African was limited compared to other cratonic provinces. Launching a field study in northern Ghana was also an occasion to enrich the geochronological and geochemical database that the WAXI project was progressively building.

Field work

Useful information on northern Ghana

The study area extends from the vicinity of the junction between the Togo-Ghana and Burkina Faso - Ghana international borders to the northeast, along the northern border with Burkina Faso, and down to central-western Ghana, in the region bordering Côte d’Ivoire. It includes all of the Upper East and Upper West

Savanne arborée du nord du Ghana. / Wooded savannah of northern Ghana.

regions, along with the western third of the Northern region. This corresponds to all of the exposed Paleoproterozoic basement to the north of Banda-Nkwanta town. Reconnaissance field work was also carried out in the border region of southern Burkina Faso, near to Gaoua and Batie towns, and in north-eastern Côte d'Ivoire, in the area of Bouna town. The investigated area corresponds to the south-central part of the Sudano-Guinean climate zone. It is characterised by a monsoon rainfall regime between April and September, a dry climate for the rest of the year, and a strong S-N annual rainfall gradient. The area is naturally covered by an open dry forest savannah. Kaicedras, shea butter trees and, to the north, baobabs are emblematic specimens of the region flora. The biomass burning seasons starts in November, and large land surfaces are clear of the seasonal vegetation cover between December and April. Temperatures are at their highest in March and April.

Northern Ghana has very little topography, and lies on average at 200-400 m altitude. Topographic highs are formed by a dismembered laterite ("duricrust") plateau. It forms hills that dominate over vast plains, stream beds and floodplains, where the Paleoproterozoic basement crops out discontinuously. Basement outcrops are mostly found in riverbeds, at a change of slope when approaching riverbeds or laterite hills, or as granitic inselbergs. The quartzites and conglomerates of the Neoproterozoic Volta basin form ridges up to a hundred meters high above the plain.

Traditional human activities are mostly agricultural. The dominant agricultural practice consist of "slash and burn" extensive farming. Farmers mainly grow beans, maize, sorghum, cassava and yam. Duricrust hills are most thickly wooded because of the absence of soil which renders them unsuitable for farming. Farming is mostly restricted to the wet season. In Côte d'Ivoire and to a lesser extent, in Ghana, large

land surfaces are used for cashew nut and mango plantations, and they are open to fieldwork. In Ghana, logging and charcoal export have greatly damaged the forest. Recently, artisanal gold mining ("Galamsey") has boomed to an impressive scale. Temporary towns of a few thousand people settle on the sites of mineable gold deposits. Officially, Galamsey is illegal in Ghana, but it is apparently highly profitable. This reality always makes it a bit delicate to enter a Galamsey site without any warning. Population density is low and grassland is extensive, which makes it a favourable land for cattle herding by semi-nomadic peoples (Furanis). Northern Ghana has multiple languages, among which Gonja (Bole area) and Dagaari (Wa area).

The land use impacts the way fieldwork is organised. The most appropriate period for fieldwork is between December and March. Footpaths and cattle paths are plentiful, especially parallel to river beds. Vehicle tracks in the savannah are regularly cleared by artisanal miners, farmers and charcoal traders.

Field campaigns

Most of the field work was carried out during the 2012 and 2013 field seasons, between January and March. In 2012, reconnaissance field work aimed at providing a large-scale view of the geology and the spatial organisation of the various tectonic domains. All of the principal rock-types were sampled. Preliminary structural data allowed to formulate hypotheses on the geological history. The 2013 field season focused on the most complex, poly-deformed geological units found in the north-western part of Ghana, where the hypotheses drawn from the previous field season were tested. Field relationships were studied in detail, mainly on foot along cross-sections. Reconnaissance field work was done in southern Burkina Faso and north-eastern Côte d'Ivoire, across the Black Volta river from north-western Ghana. In 2014, a field training course on structural and metamorphic geology was organised in the study area. The field guidebook is presented in the appendix of the thesis. The training course was run with a dozen participants, including university students and lecturers, staff from geological surveys and from mining companies, and about ten aides (drivers, etc). During the two-months stay in 2014, complementary field observations were carried out in the study area and in the neighbouring regions.

A total of 963 outcrop localities were described and referenced in a database. Data collected at each outcrop site systematically included lithological, petrological and structural information, and occasionally comprised photographs, magnetic susceptibility readings. About 330 rock samples were collected from 250 outcrop localities.

Chapitre 1

The secular evolution of the Earth

1.1 Introduction

1.1.1 Historical perspective

Alfred Wegener formulates the theory of contiental drift in 1912 (Wegener, 1912). His theory is based on the shape complementarity of continents (particularly on either sides of the Atlantic ocean) and on geological and paleontological correlations from one continent to another. Additionally, his work stems from multiple earlier scientific findings and from advances in geophysics during the XVIII and XIXth centuries. Indeed, in 1749 Bouguer reports measures of gravity anomalies in the vicinity of topographic relief in the Andes which he interprets as originating from spatial variations in continental mass distribution (Bouguer, 1749). Decades later, Boscovich, followed by Airy (Airy, 1855), interpret these findings as the result of a "compensation" between masses in an upper compartment, the "sial", and in a lower, denser viscous layer, the "sima". This compensation of lateral density gradients is termed isostasy. In 1915, Barrell identifies the lower viscous fluid layer as the asthenosphere, and distinguishes it from the superficial and rigid lithosphere (Barrell, 1915). At the end of the XIXth century, the pioneer work of Bertrand in the Alps describes large-scale thrusts ("nappes de charriage") which provide evidence for major lateral bulk contraction and for horizontal stresses in orogens (Bertrand, 1892). Finally, Haug notices in 1900 that deformation on the Earth surface is localised in "belts" delineating contiental domains (Haug, 1900). In this scientific environment, Wegener claims that the theory of "continental bridges", supposedly linking continents together in the past and presently submerged below sea level, cannot be reconciled with the concept of isostatic equilibrium, and is therefore invalid. His intuition probably arises from the study of glaciology and ice caps. Continents behave like icebergs colliding and fragmenting while drifting in a denser viscous fluid. His theory is derived from empirical observations, but it bears some approximations and it lacks a convincing theoretical demonstration. The distinction between continents and lithosphere is unclear, and the causal relationships are obscur. Although the forces driving continental drift are unknown, his understanding of the rheological behaviour of the Earth is sufficient for him to formulate accurately the problem.

All that can be asserted is that the Earth behaves, relative to short-period forces such as seismic waves, as a solid, elastic body ; and fluidity does not intervene in this case. However, when long-period forces are concerned and exerted over geological times, the Earth behaves as a fluid, as shown, for example, by its flattening which matches exactly its rotation period. Anyhow, if we were to determine the period over which deformation becomes fluid after being elastic, we would need to know the viscosity (Translated from french) (Wegener, 2012).

Wegener's theory challenges the dominant intellectual framework which served to interpret geological observations at his time, and fuels intense debate. Meanwhile, the community's understanding of the thermal structure of the Earth is improving. Radioactive decay is identified as a heat source, and questions are raised on the mechanisms of planetary heat transfer and dissipation. Convection is envisaged as a plausible mechanism. In 1921, Bull postulates a link between heat loss and continental drift. He suggests that convective flow may drive continental drift and provoke continent dislocation.

Another hypothesis claims that sufficient strength to cause the displacement of large parts of the crust may be provided by convective movements in the material directly underlying the crust. If, for any reason, movements occurred below the crust and exerted a sufficient friction, many things would be explained. The dislocation of permo-carboniferous Gondwanaland, leaving Africa in the center, India drifting to the north east, Australia to the east, Antarctica to the south east and South America to the west, suggests the rise of a convective flow below Africa, and its horizontal displacement below the crust of the Pacific. The circulation of such a flow below the thin oceanic crust would push on continental masses with deeper keels and displace them away (Translated from french) (Bull, 1927).

At the beginning of the 1930's, Holmes supports the theories of Wegener and Bull, as they seem to lay a fertile basis to explore heat loss processes (Holmes, 1931). He contributes to understanding the interactions between geology and the thermal structure of a convective Earth, and focuses his attention on geological processes behind heat and density gradients, such as phase transitions, metamorphism and magmatism. The scientific debate shifts on possible mechanical coupling between sial and sima, and crystallises on the rheological properties of the asthenosphere. One school of thought, represented by Jeffreys, considers that horizontal forces applied to continents are too weak to cause displacements, and that the asthenosphere is too strong to deform plastically (Jeffreys, 1926). Supporters of Wegener's theory argue that the asthenosphere may have a plastic behaviour whatever the intensity of boundary forces. This period also witnesses an increase in analytical and analogue modelling studies. The result of analogue modelling performed by Griggs suggest that there is a possible interaction between convection and orogenesis (Griggs, 1939). The idea of a mechanical coupling between different planetary envelopes is a subject of growing attention. Meinesz recognises a cyclicity in the planetary tectonic activity and, based on the wavelength of measured gravity anomalies, proposes the existence of two superimposed and intermittent convective systems with distinct wavelengths.

The acceptability of the emerging plate tectonics theory remains a challenge because of the lack of knowledge on the rheology of the Earth, or on the implications of mantle heterogeneities on convection. Many consider this theory with suspicion because of the difficulty to test it accurately, as stated by Goguel in 1952 : *Because of its flexibility, the convection hypothesis does not seem prone to establish precise rules on the position of orogenic zones or on their time distribution. On the contrary, geological analysis ought to provide us with information on the history of convection flows* (Translated from french) (Goguel, 1965).

The exploration of sea-floor geology one decade later finally provides new determining scientific facts. The demonstration of the existence of sea-floor spreading and mid-oceanic ridges provides, for the first time, a visible result of convection. Hess argues for a mechanical coupling between lithosphere and asthenosphere, and suggests that mid-oceanic ridges mark the emplacement of upwelling convective flows accounting for surface heat loss, while trenches represent downwards flows (Hess, 1962). In the following years, the plate tectonics theory becomes widely accepted by the Earth Sciences community. Nevertheless, it gains precision as the understanding of the Earth dynamics improves. In this sense, the role of subduction in maintaining convection, and the viability of plate tectonics on the early Earth remain matters

of research today.

1.1.2 Plate tectonics today

The plate tectonics theory postulates that the Earth lithosphere is divided into independent rigid mobile plates. Mantle convection and asthenosphere - lithosphere interactions are responsible for plate motion. Lithospheric plates deform along their active margins, which may be convergent or divergent. Plate dynamics control continental Wilson cycles, collision and rifting. The plate tectonics paradigm is an efficient theoretical framework to interpret general geological observations. Its present acceptance is such that the term "plate tectonics" does not strictly designate the scientific theory any more, it is also used to refer to the thermal regime and to the geodynamic setting of the modern-day Earth. The plate tectonics theory benefits from constant refinement due to improvements in our understanding of the Earth dynamics, particularly as a result of ever-growing technological and analytical capacities. It remains an active research topic today. The initiation of subduction is a process which is debated. Deviations to the plate tectonics framework (e.g. intraplate deformation) are topical. The evolution of plate tectonics through the Earth history, and its viability on the early Earth, generated a prolific literature.

The brief historical perspective recalled above shows that the plate tectonics theory rose from multiple convergent data collected from modern geological objects. The Phanerozoic geological record (0–550 Ma) played a historical role in building most ideas and defining processes in Earth Sciences. It is therefore unsurprising that the older (Precambrian) Earth is less well understood. Interpreting geological data from old domains is a long running scientific problem. Firstly, ancient geological provinces are tectonically inactive, so geologists are left to study objects "frozen" in their final evolutionary states. Secondly, the applicability of the plate tectonics framework raises questions. Has the thermal regime of the Earth changed since the formation of the planet ? Did the Earth follow a linear evolution, or stepwise transitions ? Are geological processes time-invariant ? The reliability of an uniformitarian reasoning, which postulates that the plate tectonics paradigm is valid for the interpretation of past geological record (Windley, 1993), is a matter of debate.

Exploring this scientific question requires a holistic approach of Earth Sciences, taking into account the many interactions and causal links between the geological phenomena which together form "geodynamics". In this chapter, I aim to give a broad coverage of the diversity of complementary methods which are used to investigate the geodynamic evolution of the Earth in its early days. Thermo-mechanical numerical modelling provides a tool to study possible convection modes for hotter thermal conditions, as inferred for the early Earth. Some important results are presented in part 1.2. The continental crust is the fossil record of the Earth. Secular evolution trends of the composition of the continental crust, along with continent growth models calibrated on isotopic studies, are discussed in part 1.3. Part 1.4 focuses on the implications of hotter thermal regimes on the rheology, strain patterns and tectonic styles of the lithosphere. The rock record of Phanerozoic and Precambrian orogens are compared in part 1.5. They represent field evidence for secular changes in orogenic belt, which may be related to general geodynamic transitions during the Earth history.

1.2 The Earth : a thermal machine

1.2.1 The envelopes of the Earth

Planet Earth is made of concentric envelopes with decreasing density outwards. The kernel is made of siderophile elements, essentially iron and nickel. It comprises an inner solid core and an outer liquid envelope. The kernel is separated from the mantle by a transition zone (D"). The mantle is made of lithophile elements (dominantly Si, Al, Mg, Fe and O) and its principal mineral phase is olivine. Mantle density decreases with depth across pressure-dependant phase transitions (at about 660 and 440 km depth). The crust - oceanic or continental - overlies the mantle. Mantle magmatism and differentiation continuously produced crust through geological times. The outer fluid envelopes of the Earth are the hydrosphere and the atmosphere, which host the biosphere. The various envelopes of the Planet are linked by heat and mass transfers, in such a way that the secular evolution of the Earth is recorded by physical and chemical changes within each of them.

The lithosphere is the outer envelope of the solid Earth. It is made of the crust and the lithospheric mantle, which are separated by a petrological limit : the Mohorovicic discontinuity (MOHO). The continental lithosphere has an average thickness of 100–200 km and is mostly emerged above sea level. It comprises a continental crust, andesitic in composition, about 40 km thick. The oceanic lithosphere is 0–80 km thick, including a 0–10 km crust. The asthenosphere is the mantle layer underlying the lithosphere. The boundary between lithosphere and asthenosphere is a rheological transition occurring at around 1300 $^\circ$C, at conditions where asthenosphere peridotites are mechanically weak, due to the presence of a small proportion of interstitial melt.

1.2.2 Mantle convection

The internal heat of the Earth emanates from two sources : heat production from radioactive isotope disintegration, and heat inherited from the formation of the Planet by accretion of chondritic material (e.g. latent heat of crystallisation of the kernel). Heat is lost through the asthenosphere *via* convective flow, and through the lithosphere *via* conduction and magmatism. The lithosphere represents the thermal boundary layer of the mantle-scale convective system. Surface heat loss is materialised by a measurable heat flux. Mantle convection impacts and controls lithospheric geodynamic processes. "Plate tectonics" represents a convection style where the thermal boundary layer (the lithosphere) is chemically and rheologically heterogeneous and distinct from the convective mantle. The thermal boundary layer is extracted from the asthenosphere through magmatic processes. The oceanic lithosphere, formed at mid-oceanic ridges, cools down with time, getting thicker and denser, until it becomes negatively buoyant relative to the underlying asthenosphere. The density inversion causes the lithosphere to sink, forming subduction zones. Therefore, the plate tectonics regime is characterised by a thermal boundary layer which is actively advected into the asthenosphere, and which provides the driving force of horizontal plate motion and deformation (Fig. 1.1).

Consequently, the lithosphere has some retro-control on the convection style and the efficiency of heat dissipation. Most heat loss occurs at mid-oceanic ridges, where

convective flows rise, hence the Earth cooling rate is dependent on ridge distribution, ocean spreading and subduction velocities. Subduction velocity in turns is determined by the physico-chemical properties of the lithosphere, themselves dependent on lithosphere formation processes and mantle temperatures. Understanding the Earth geodynamics and its secular evolution requires considering the causal links and feedbacks between thermo-mechanical, chemical and petrological processes in the lithosphere and at the interface with the asthenosphere.

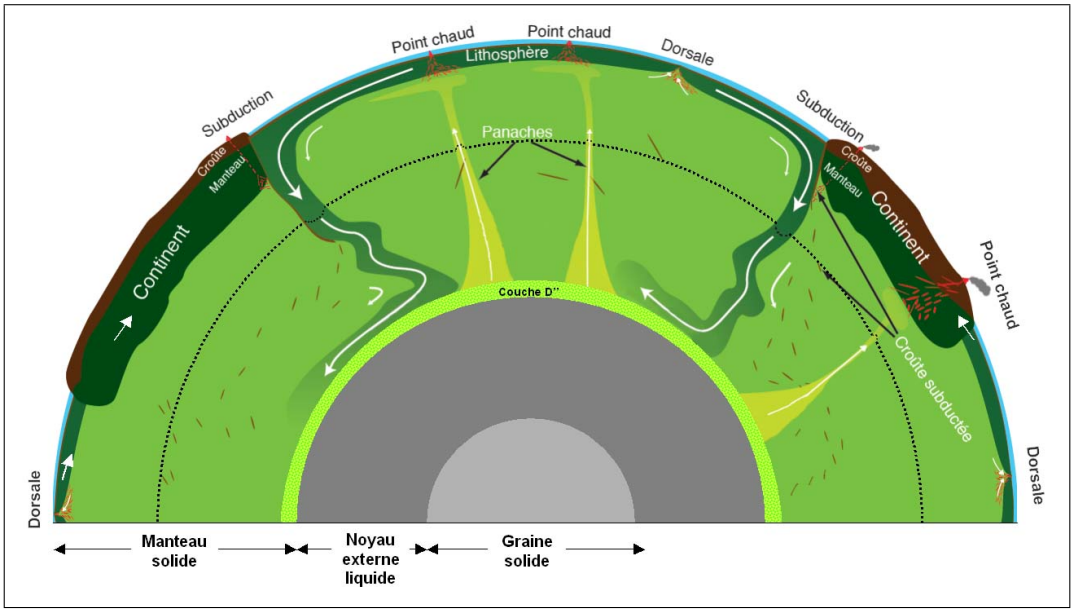

FIGURE 1.1: Simplified sketch of mantle convection on the modern Earth (http ://planet-terre.ens-lyon.fr).

1.2.3 Thermo-mechanical numerical modelling of mantle convection

The Earth formed by the accretion of chondritic material in a proto-planetary nebula, which evolved from a supernova at the origin of the solar system. Nucleosynthesis in the supernova formed radioactive isotopes. The isotopes responsible for most of the radiogenic heat produced presently are ^{235}U, ^{238}U, ^{40}K, ^{232}Th (Fig. 1.2), and their concentrations have decreased significantly since the formation of the Earth. This implies that the average mantle temperature of the primitive Earth must have been higher in the past, and that the planet gradually cooled down throughout geological time (Abbott et al., 1994; Labrosse and Jaupart, 2007). Numerical modelling has been widely used to explore the possible consequences of higher mantle temperatures on terrestrial geodynamics.

Parametrised convection models have been used to model the mantle dynamics through time (Richter, 1985; Schubert et al., 1980; Turcotte, 1980). They served as a theoretical basis for numerous geodynamic scenarios proposed for the early Earth. These models consider the convective mantle as a "classical" convective system (as water in a saucepan heated from below), for which the heat loss flux $Q(t)$ is proportional to internal temperature. Integration in time of the heat balance equation of

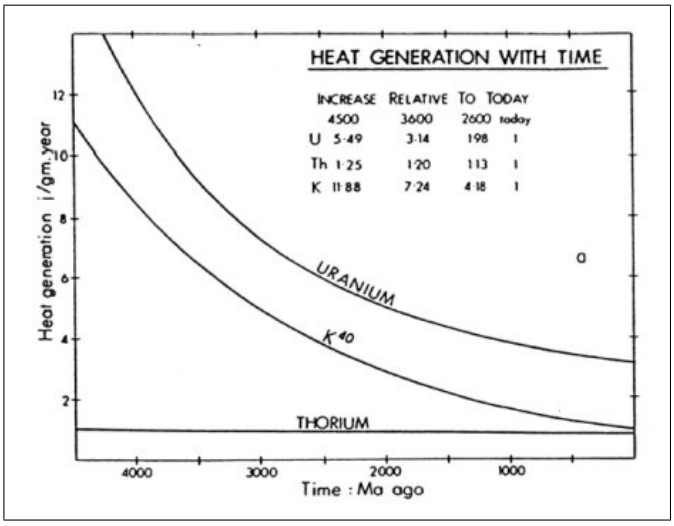

FIGURE 1.2: Evolution of the radiogenic heat production of the Earth with time. The decrease follows the desintegration curve of the main radioactive isotopes in the Earth mantle and crust (Lambert, 1976).

the Earth with a classical parametrisation of $Q(t)$ leads to a "thermal catastrophe" : the mantle potential temperature (T_{pot}) reaches unrealistically high temperatures. Indeed, an increased mantle temperature means increased heat loss, which requires even higher primitive mantle temperature in order to fit present day temperature conditions. Reconciling the results of these models with petrological constrains requires invoking stratified convection, or enhanced radiogenic heat production on the early Earth, both of which are not supported by complementary datasets. In any case, results from this type of model suggest a more vigorous convection for hotter mantle temperatures, and inspired geodynamic models with multiple small lithospheric plates and high total ocean ridge lengths to evacuate an elevated heat flux (Abbott and Menke, 1990; Hargraves, 1986; Nisbet and Fowler, 1983).

Korenaga (2006) models mantle convection for the early Earth using a different parametrisation method. The lithosphere thickness is controlled by dehydration and partial melting processes, and by thermal erosion, all of which are dependant on mantle temperature. Figure 1.3 shows the relationship between the thickness of the thermal boundary layer and mantle temperature. The thickness is minimal for thermal conditions which are similar to the modern-day thermal regime, while it increases with increasing mantle temperature as a consequence of enhanced chemical differentiation of the lithosphere. The heat flux Q is calculated from the energy balance of the thermal boundary layer (i.e. the oceanic crust), which depends on its thickness and its composition. Q is proportional to the plate velocity U. The model of Korenaga (2006) is therefore based on the energetics of plate tectonics. It predicts a less vigorous convection and a reduced heat evacuation "efficiency" for higher mantle temperatures. The maximal plate velocity is obtained for a minimal lithosphere thickness, i.e. in conditions similar to those prevailing on the modern Earth. This setting allows a more efficient heat evacuation, which is expressed as the Urey ratio :

$$Ur = H(t)/Q(t)$$

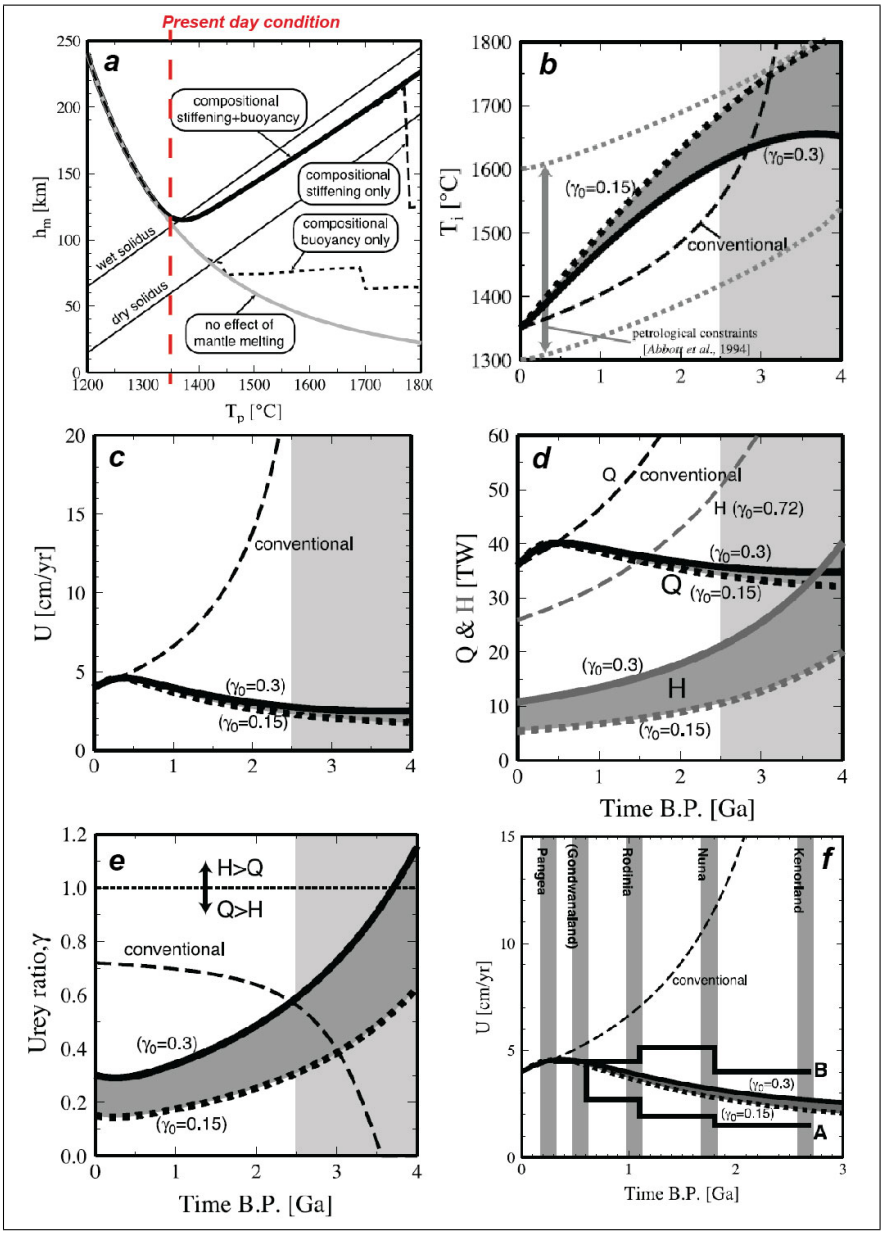

FIGURE 1.3: Modified from Korenaga (2006). (**a**) Oceanic lithosphere thickness as a function of the mantle potential temperature. The black curve is the net result of different processes with opposing effects on lithospheric thickness. Decreasing rock viscosity with increasing temperature implies a thinner lithosphere (grey curve). The effect of higher temperatures on viscosity is counter-balanced. A hotter mantle implies higher partial melting rates and melting in a thicker mantle layer. This in turns causes enhanced dehydration and chemical differentiation of the lithosphere, and an increase in the lithospheric strength (dashed curve).

FIGURE 1.3: (**b-e**) Results presented by Korenaga (2006) are obtained for different values for Ur (= γ). γ is constrained by different methods, which produce a range of values represented by the shaded zone between bold black curves. The results are compared with those of conventional parametrised convection modelling. (**b**) Mantle temperature as a functon of time. Values are within the range constrained by petrology. (**c**) Average plate kinematics *vs* time, showing decreasing velocities back through time, and a maximal velocity in the Phanerozoic. (**d**) Internal heat production (H) and outwards heat flux (Q) *vs* time (**e**) Corresponding Urey ratio showing an increasing cooling efficiency with time. (**f**) Average plate velocity compared to the episodic assembly of super-continents, which is considered to reflect the characteristic period of ocean closing.

with H and Q respectively mantle heat production and mantle heat flux across the thermal boundary layer. The Urey ratio increases back in time as mantle temperature rises, suggesting less efficient cooling and more sluggish plate tectonics in the Paleoproterozoic and Neoarchean.

Additionally, Labrosse and Jaupart (2007) take into account the changing structure of the lithosphere with age, which requires to model the age distribution of the oceanic lithosphere in order to calculate the thermal regime of the Earth. On the modern Earth, the probability for a fragment of oceanic lithosphere to be subducted is independent from its age due to the spatial competition between different ridge-subduction systems, and its maximum age is about 180 Ma. On the early Earth, the authors suggest - based on theoretical arguments - that the maximal age of the oceanic lithosphere may be smaller. They use an average age distribution integrated over the course of a Wilson cycle, and take into account a model for the growth of the continental lithosphere, and its impact on the thermal budget of the mantle. Modelling results (Fig. 1.4) indicate culminating mantle temperatures at *ca.* 3.0 Ga, which is the age limiting the applicability of the model, because subuction is not assumed to be a viable cooling mechanism before that time. Mantle cooling by 150 $^\circ$C since 3 Ga is predicted, in agreement with petrological constraints drawn from mantle-derived magmas. The latter demonstrate that mantle temperature decreased by less than 200 $^\circ$C since 4.5 Ga (Green, 1975; Herzberg et al., 2010; Nisbet et al., 1993; Sleep, 1979).
Thermo-mechanical models of the thermal state of the Earth integrated through time and which take the actual plate tectonics setting as initial conditions (e.g. Korenaga (2006); Labrosse and Jaupart (2007)) provide geologically realistic results up to *ca.* 3.0 Ga, which argues for the viability of some sort of geodynamic analogue of plate tectonics since the Neoarchean.

1.2.4 The viability of subduction

Knowing that subduction drives modern plate tectonics, understanding the geodynamic settings of the early Earth requires exploring the following question : Is subduction a viable process for higher Earth mantle temperatures ?

van Hunen and van den Berg (2008) contribute to shed light on this problem by modelling the thermo-mechanical evolution of a subducting lithosphere (subduction is under way initially) for different mantle temperatures. A range of models is

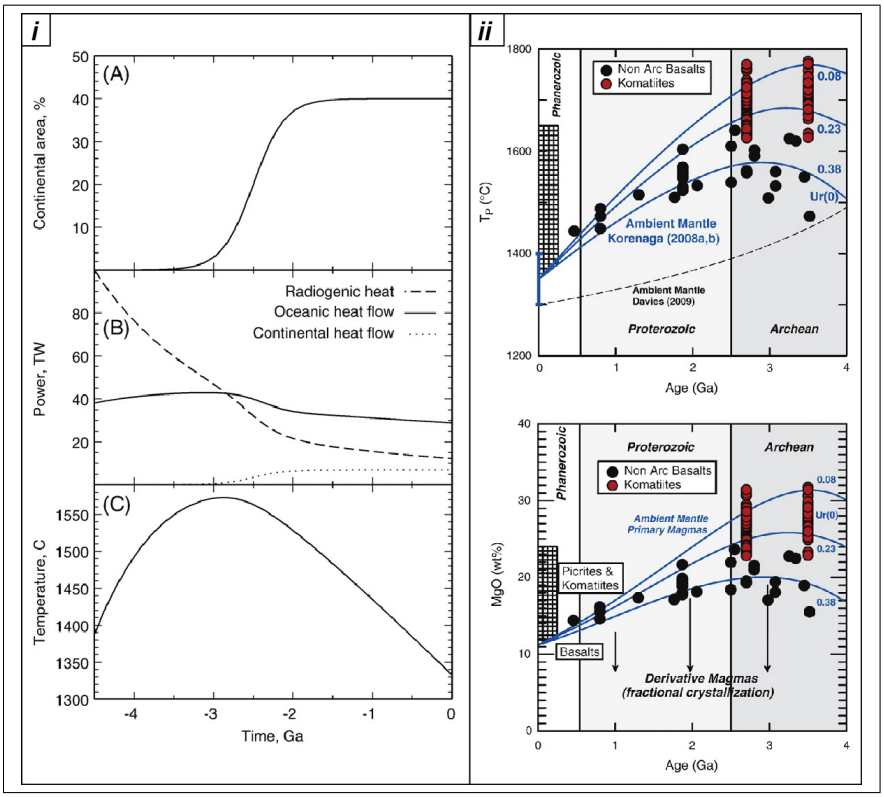

FIGURE 1.4: (i) : Numerical modelling of the Earth thermal regime, modified from (Labrosse and Jaupart, 2007). (**A**) Crustal growth model input to the thermal model, (**B**) oceanic and continental heat flux, (**C**) mantle potential temperature *vs* time. (ii) Top : mantle temperature through time, calculated for different modern-day Urey ratios (Korenaga, 2008) compared to temperatures obtained from measured MgO content of tholeitic basalts (see Herzberg et al. (2007) for the geothermometre calibration). Bottom : basalt MgO content through time, calculated from the temperature evolution curves and compared to geochemical data (Herzberg et al., 2010). Both methods yield similar results.

produced for various values of key parameters in order to identify the determining factors of subduction viability (Fig. 1.5). The viscosity of asthenosphere is a major control on subduction. Decreasing viscosity for increasing temperature increases subducted plate velocity (second column starting right, Fig.1.5, $\Delta T_{pot} = 100$ K). Above a T threshold, the subducting lithosphere becomes weak enough to break off (columns 3 et 4, $\Delta T_{pot} = 200$ and 300 K). In the absence of a deep, negatively buoyant eclogitic oceanic crust, subduction slows down or is interrupted. The authors conclude that subduction may be vigorous for moderately higher-than-actual mantle temperatures, but that slab break-off compromises subduction viability for temperatures in excess of 100-200 ° C above actual conditions. Even though subduction may be viable for higher T conditions, its initiation remains problematic. Indeed, a lithosphere derived from a relatively hotter asthenosphere would have a lower density, which prevents a rapid subduction (Davies, 1992).

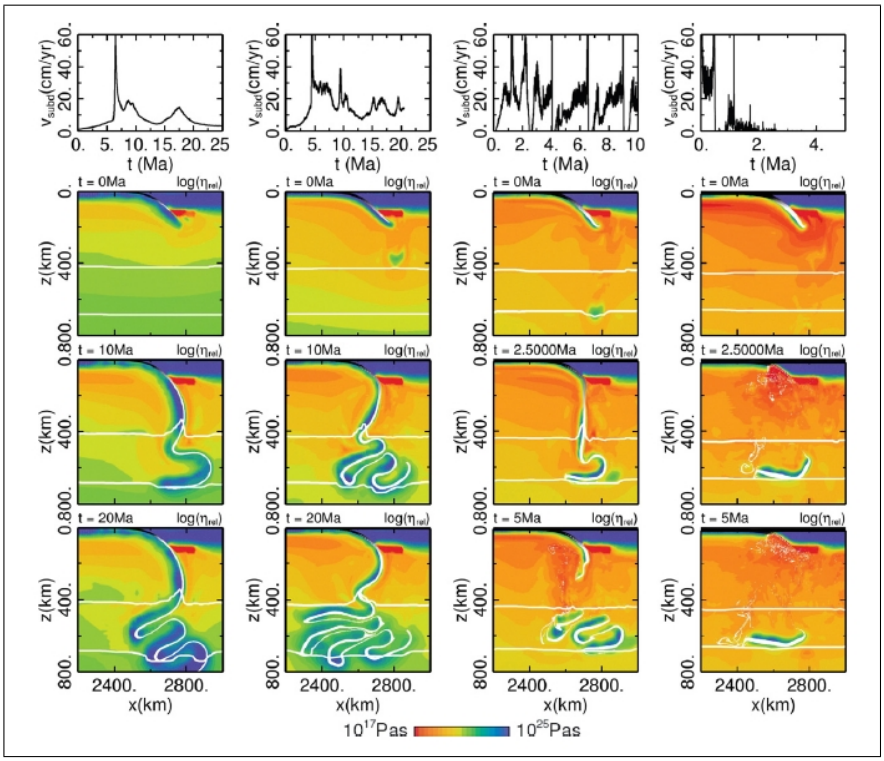

FIGURE 1.5: Modified from (van Hunen and van den Berg, 2008). Numerical modelling of the impact of mantle temperature on subduction dynamics. Results are shown for different values of mantle potential temperatures (ΔT_{pot} = 0, 100 K, 200 K, 300 K from left to right), and using average values for input rheological parameters. Top : subduction velocity. Bottom : viscosity at different run times. The white domain represents an eclogitic crust. The model suggests subduction dynamics similar to modern-day subduction for ΔT_{pot} = 0 K and 100 K. For higher temperatures, frequent slab break-off and delamination of the eclogitic oceanic crust diminish subduction driving-forces and lead to an unstable, slow subduction or to its interruption.

Sizova et al. (2010) explore the effect of mantle temperature on the initiation of subduction, by using a numerical model which integrates thermodynamic phase equilibria, partial melting and fluid transfers. Increasing mantle temperatures result in the formation of a thick, partially molten lithospheric mantle layer. This setting does not allow lithosphere-scale downwards advection, and the system does not trend towards an analogue of modern subduction. Magmatic fluids are transferred up from the partially molten layer and weaken the overlying lithosphere. This affects the lithosphere rheology and the general tectonic style. Oceanic and continental lithospheres develop large-scale buckling, and deformation is homogeneously distributed across the thickened lithosphere. Such results are compared to field observations in part 1.5.

Based on results of numerical models and on theoretical considerations, the viability of some type of subduction cannot be postulated for the entire history of the

early Earth. Therefore, alternative geodynamic models are evaluated (van Hunen et al., 2008). A first hypothesis suggests the absence of plate tectonics : the thermal boundary layer is decoupled from the convective mantle and forms a "stagnant lid" (Moresi and Solomatov, 1998). Numerical modelling studies indicate that a "stagnant lid" regime may exist transitionally, and be interrupted by brief episodes of massive crustal recycling (O'Neill et al., 2007; Van Thienen et al., 2004b). At this point, the Earth lithosphere evolves into a "mobile lid" which may be subducted, causing a large scale lithosphere overturn associated with cataclysmic magmatic episodes. This geodynamic evolution could be triggered by an inversion of the density profile across a lithosphere which underwent limited chemical differentiation. The record of episodic continental crust growth episodes is presented as an argument supporting lithosphere-scale recycling and mantle overturn models (Condie (2004) ; part 1.3). They contrast with ideas that subduction zones are the sites of continental growth in the way that the proposed growth mechanism is not continuous in space and time. Another vision considers intermittent, short-lived subduction zones, interrupted by frequent slab break-off (Halla et al., 2009; Moyen and Van Hunen, 2012), resulting in a geodynamic setting different from modern-day plate tectonics.

A second hypothesis, which may be qualified as uniformitarian (Windley, 1993), states that some sort of plate tectonics was at work on the early Earth, although it did not produce the geological markers of modern-day subduction. Evaluating this hypothesis depends on the interpretation of field observation and of objects for which no modern analogue is available. This field of research generated a voluminous scientific production, which is synthetically presented throughout this chapter. In the following parts, different datasets (isotopic, tectonic, metamorphic,...) are discussed and confronted to geodynamic models proposed for the Paleoproterozoic and Precambrian Earth.

1.3 The genesis of the continents

1.3.1 The growth and recycling of the continental crust

Our understanding of how the continental crust grows and differentiates has made huge progress in the last fifty years. The episodicity of crustal growth, first evidenced by Gastil (1960), is confirmed by the increasing availability of accurate geochronological data on all of the Earth's continental masses (Condie, 1998; Condie et al., 2009). Hurley and Rand (1969) proposed the first crustal growth curve, which has since then been significantly refined by the use of new isotopic techniques. U-Pb isotopy is used to date the crystallisation of zircons, which record magmatic episodes and resist geological resetting. Zircon oxygen, Lu-Hf and whole rock Sm-Nd isotopy provide information on the sources (mantellic, crustal or hybrid) of magmatism. Lu-Hf and Sm-Nd isotopy additionally provide information on the juvenile or recycled character of continental material by calculating model ages of magma extraction from a mantle source (Fig. 1.10). These model ages are equivalent to a crustal residence time of the source rocks of magmatism. Such data has the potential to shed some light on the timing of juvenile crust formation and of crustal recycling, on magma sources and hybridisation. Isotopic studies on zircon (O, U-Pb and Lu-Hf) are a tool to trace the souces of magmatism, to build crustal evolution models and to reveal general trends in the history of continental crust formation (Allègre and Rousseau, 1984; Condie et al., 2005; Hawkesworth et al., 2010).

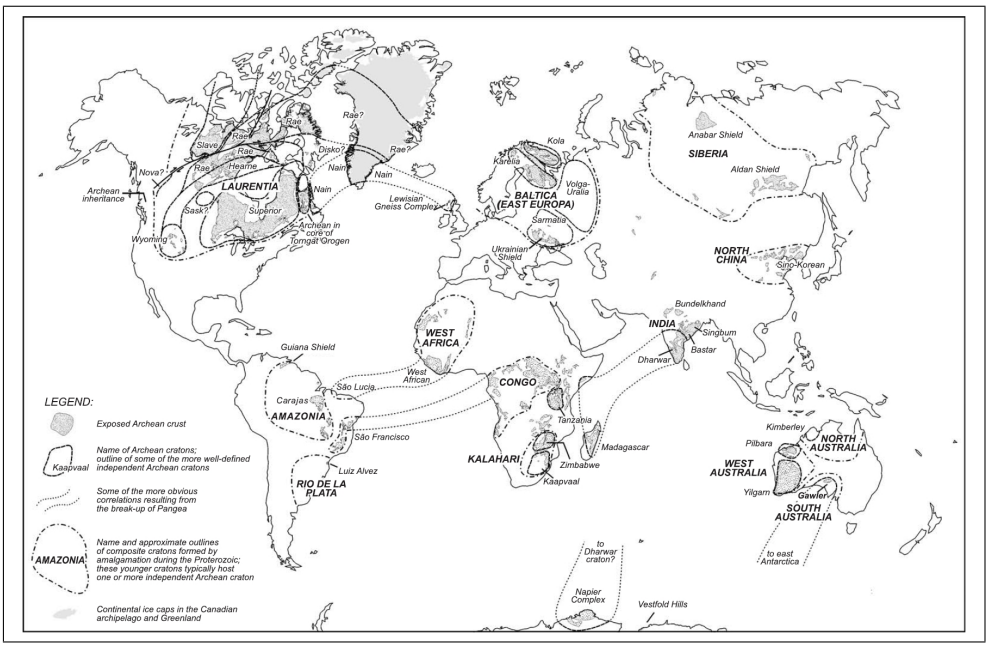

FIGURE 1.6: Present day distribution of exposed Archean crust and inferred boundaries of cratons amalgamated during the Proterozoic (Bleeker, 2003).

The extraction of the continental crust from the mantle started early in the Earth history (Harrison, 2009; Valley et al., 2005), as shown by the Hadean ages (4.0-4.4 Ga) of the Acasta gneisses (Bowring and Williams, 1999; Iizuka et al., 2006) (Canada) and of detrital zircons in the Jack Hills quartzites (Australia) (Wilde

et al., 2001). Continental crust formation has been continuous since then. Most of the continental crust preserved to date is thought to have been extracted from the mantle in the Archean (65% before 2.5 Ga, Belousova et al. (2010); Dhuime et al. (2012), Fig.1.7). This eon is characterised by a high net crustal growth rate (3.0 km3.an-1 according to Dhuime et al. (2012)). However, the Archean crust only represents a relatively small proportion of the total volume of the continental crust (Fig. 1.6), while rocks older than 4 Ga are volumetrically insignificant. This paradox requires that destructive processes affected large proportions of the old continental crust. It reflects very low preservation rates at the Hadean and Paleoarchean, and intense recycling of juvenile crust during subsequent periods.

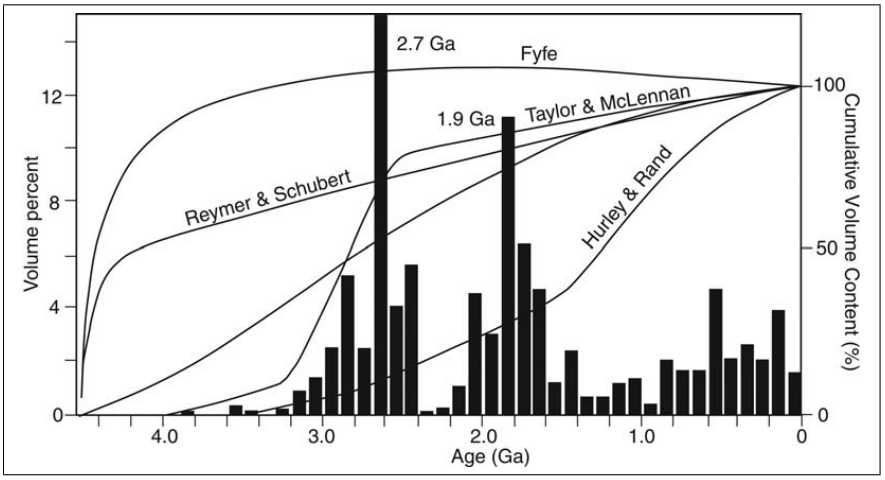

FIGURE 1.7: (Cawood et al., 2009). Histogram representing the volumetric age distribution of juvenile continental crust, based on U-Pb ages and Sm-Nd model ages (modified from Condie (1998)). Crustal growth models are super-imposed on the histogram. Hurley and Rand (1969) proposed a model based on isotopic techniques which are now considered to be vulnerable to secondary perturbation. More recent models agree on the early formation of most of the continent volume, during the Archean, albeit some variability in the shape of evolution cuves. These models are dependent on assumptions underlying the interpretation of isotopic data, and on evolution models of magmatic sources (e.g. the depleted mantle) required for model age calculations (refer to Hawkesworth et al. (2010), for a review).

The age distribution of igneous rocks and detrital zircons displays a cyclicity, with successive troughs and peaks, e.g. (Cawood et al., 2013). This is thought to reflect the different preservation potential of rocks generated in different tectonic settings. Two discrete peaks in juvenile crust production and preservation rates are recorded in the Neoarchean and the Paleoproterozoic (Fig. 1.7). These periods must correspond to the development of tectonic settings favourable to crust preservation. The formation of super-continents at that time is proposed as a mechanism to preserve juvenile continental crust from destructive tectonic processes (Condie, 1998). Juvenile crust extraction carries on in the Proterozoic, and Condie (1998) estimates that 75% of the volume of the actual continents formed before 1.65 Ga. However, the net crustal growth rate decreases at that time (0.8 $km^3.yr^{-1}$ according to Dhuime et al. (2012)),and so does the contribution of juvenile sources to magmatism Be-

lousova et al. (2010). Studies of zircon O and Hf isotopic compositions suggest an increasing reworking rate for the continental crust after the Archean (Fig. 1.8, Valley et al. (2005)). Finally, the Phanerozoic eon is characterised by a crustal growth rate close to 0 (Clift and Vannucchi, 2004), and by a weak contribution of juvenile material to magmatism (Belousova et al., 2010).

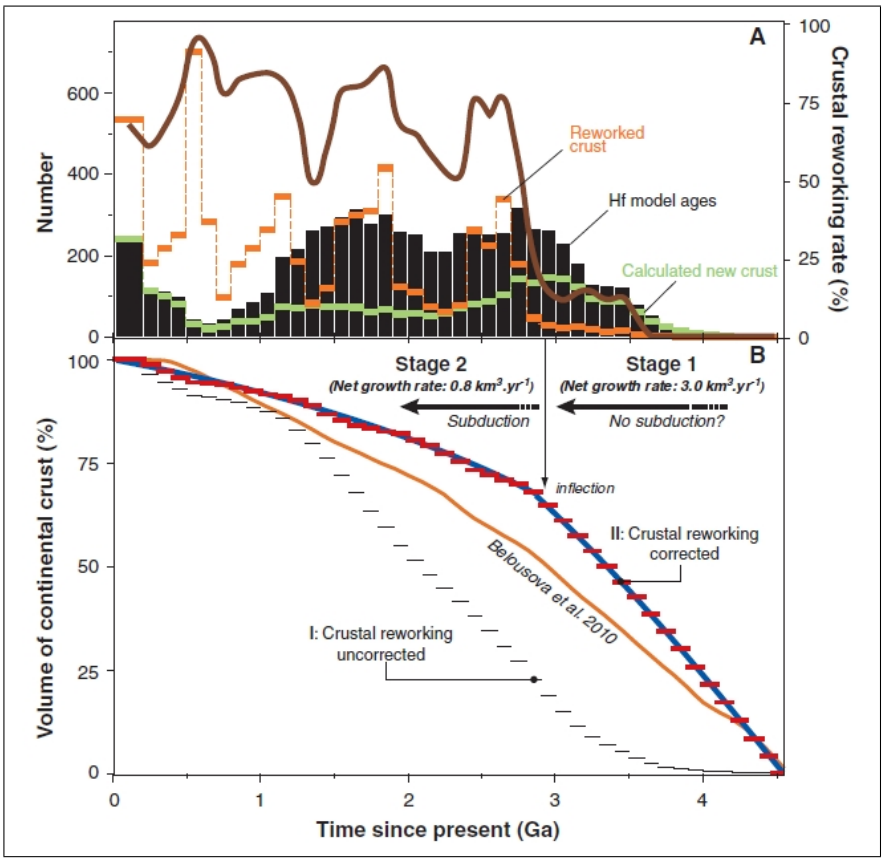

FIGURE 1.8: (Dhuime et al., 2012). (**A**) Hafnium isotopes provide model ages for the extraction of crustal rocks from the depleted mantle. Model age distribution is represented by the black bars in the histogram. Oxygen isotopes allow to discriminate between zircon derived from mantellic and crustal sources, so as to distinguish model ages representing "real" events of juvenile crust production (green bars) from hybrid ages reflecting mixed contributions of different sources or crustal reworking. This method helps evaluate the relative significance of crustal reworking *vs* juvenile magmatism (black curve). (**B**) The constraint on the reworking rate of the crust allows to build a model for the evolution of continental crust volume through the Earth history.

1.3.2 The geodynamic sites of crustal growth

On the modern Earth, the hydrated oceanic lithosphere is buried into the mantle at subduction zones. The subducted lithosphere dehydrates as it warms in contact with the asthenosphere. The aqueous fluid input to the mantle lowers the solidus of peridotite, and causes partial melting of the metasomatised mantle. Melting

produces juvenile calc-alkaline magmas which contribute to the build-up of magmatic arcs along active convergent plate margins (Arculus, 1994). Magmatic arcs have been proposed as being the principal sites of crustal growth on Earth, on the basis of similarities between the bulk continental crust composition and that of arc-derived igneous rocks (Taylor, 1967; Taylor and McLennan, 1985). Accretionary orogens develop at plate margins characterised by active subduction zones (Cawood et al., 2009; Windley, 1992). They include the magmatic arcs and may contain heterogeneous and exotic crustal fragments, ancient arcs, accretionary prisms, back-arc domains, etc. They may be active for tens of millions of years, as long as subduction is uninterrupted, and they have been proposed as sites of major juvenile crust production and preservation throughout the history of the Earth (Cawood et al., 2009; Windley, 1992).

However, some evidence conflict with the "andesite model" supporting juvenile crust production at subduction-driven accretionary orogens. Crust production and preservation was shown to be episodic, which is dissimilar to continuous calc-alkaline arc magmatism. The vast extent and absence of reworked older material in juvenile provinces which represent typical witnesses of crustal growth, such as the Abitibi and Birimian provinces, requires that they formed in the oceanic domain, away from active continental margins. The bulk composition of magmatic arcs is more mafic than the average continental crust (Holbrook et al., 1999), and may comprise thick piles of non orogenic basalts. The latter arguments are inconsistent with modern subduction analogues.

Alternative models suggest that the juvenile protolith of the continental crust is formed in the oceanic realm, before being substantially reworked along an active plate margin. Albarède (1998) proposes that mantle-plume activity may be determining for the discrete production of large continental protoliths. Upon reaching the lithosphere, mantle plumes trigger intense short-lived intra-plate volcanism. It leads to the accumulation of thick (20–40 km) piles of (predominantly mafic) eruptive rocks and associated intrusives, termed Large Igneous Provinces (Coffin and Eldholm, 1994; Ernst et al., 2005), or oceanic plateaus, when they lay in the ocean. Once the oceanic plateau is emplaced, it drifts with the oceanic lithosphere towards a convergent plate margin. The thick crust, underlain by depleted, buoyant mantle, is bound to resist subduction, and to be laterally accreted against a continent in an accretionary orogen (Abbott and Mooney, 1995; Abbott et al., 1997; Abouchami et al., 1990; Ben-Avraham et al., 1981; Puchtel et al., 1998; Stein and Hofmann, 1994).

In the specific case of an immobile "loose" lithospheric plate, an impacting mantle plume may produce a more mature continental protolith (Albarède, 1998). The oceanic plateau remains at the vertical of the hotspot and grows vertically due to prolonged volcanism and magma underplating. The high heat flow which is maintained in the thickened crust may eventually cause partial melting and internal differentiation of the plateau, until the "loose plate" geodynamic setting is interrupted and the plateau is accreted to a continental margin. Such a geodynamic setting is suggested for the development of the Kerguelen oceanic plateau (Grégoire et al., 1998)

1.3.3 Centripetal growth and terrane accretion

The worldwide space- and time-distributions of radiogenic ages show a centripetal growth pattern for the continental crust (Gastil, 1960; Hoffman, 1988; Hurley et al., 1962). Recent analytical and isotopic techniques reveal the existence of crystallisation and model age gradients oriented from cratonic nuclei towards younger mobile belts or continental margins (e.g. Czarnota et al. (2010); Percival et al. (2006); Snyder (2002), Figs. 1.9, 1.10). These evidence suggest that the lateral accretion of younger juvenile continental fragments against older craton nuclei represents one of the principal continental growth mechanisms (Zeh et al., 2009). According to the lateral accretion model, the continental protoliths (e.g. oceanic plateaus) reach subduction zones thus disruping the subduction dynamics and the geometry of the accretionary front (Moresi et al., 2014). They are assembled against older continents in accretionary orogens. The continental crust undergoes further maturation and differentiation within the collisional orogen, until it is finally stabilised.

This growth model requires that the continental domains are submitted to horizontal tectonic forces, which trigger the displacement and the collision of continental lithospheres. On the modern Earth, subduction provides the driving force of the lateral displacement of continents responsible for accretion-collision. Therefore, the applicability of the model for the early Earth may be dependent on the viability of subduction on a hotter Earth.

Nevertheless, some authors propose alternative forces for the lateral accretion of oceanic plateaus onto continents, which would originate from asthenospheric convective flow ; and argue that such tectonic regimes may adequately reproduce the centripetal age patterns observed on continents in the absence of modern subduction analogues (e.g. Bédard et al. (2013)). Aditionally, the suitability of an uniformitarian approach may be questioned because of the dissimilarities between the continental volume balance on the Phanerozoic and on the early Earth. As seen in the previous section, the volume balance of the continental crust is close to null on the modern Earth(Clift and Vannucchi, 2004), while it was clearly positive on the early Earth. This implies that continental masses did not grow from a modern plate tectonics regime, but from a general geodynamic setting for which no strict modern equivalent exists.

1.3.4 Continental architecture

Ancient continental domains are known as cratons (Fig. 1.6). They comprise a relatively thin continental crust (Keller and Schoene, 2012; Turner et al., 1992) set above a thickened lithospheric mantle, and have been geologically stable for long periods of time. Craton surface architecture is characterised by alternating granite-greenstone terranes across hundreds of km. The alternations between granite-gneiss and greenstone terranes are periodic, with sets of parallel elongated greenstone belts defining craton-scale structural trends. Granitoid gneisses and greenstone belts are affected by distributed strain and metamorphism. They are frequently transect or limited by craton-scale shear zones, suggesting that terrane alternations and crustal architecture are the result of deformation and crustal adjustment.

The greenstone belts (Condie, 1981) are made of supracrustal rocks which include intercalated komatiites, as tholeiitic or calc-alkaline lavas, ultramafic rocks

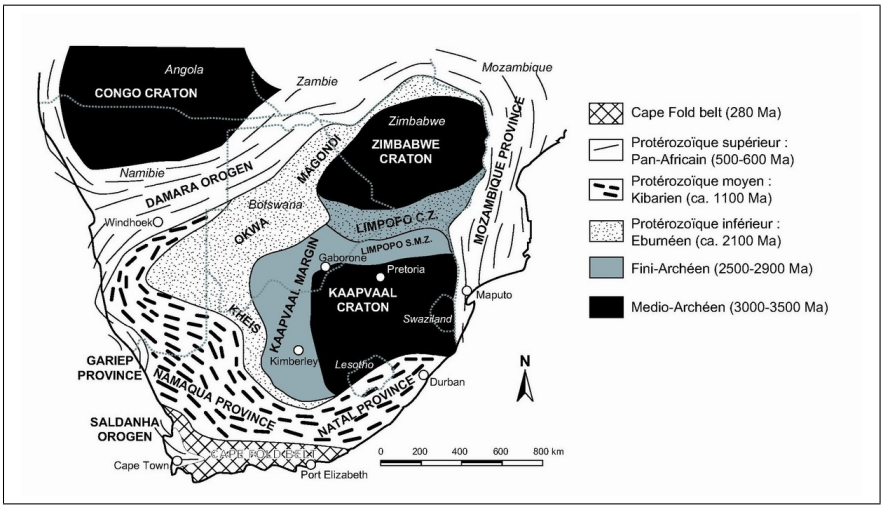

FIGURE 1.9: The lithosphere in southern Africa is built of a cratonic "nucleus" of Archean age, which is bounded by younger "mobile belts". Juvenile crust addition occured along linear active margins along the craton boundaries. This distribution supports a model of radial continental crust growth driven by lateral accretion (source : http ://jfmoyen.free.fr/spip.php ?article220).

and chemical sediments (e.g. Banded Iron Formations - BIFs). The stratigraphic sequence of greenstone belts also comprises abundant sedimentary rocks. They are dominated by volcanogenic sedimentary rocks and greywackes (Anhaeusser, 2014). Arkoses and immature quartzites occasionally form fault-bounded basins of limited extents.

Geochemical and chronological arguments suggest that greenstone belts are coeval with granitoids and contain lavas which represent the supracrustal equivalents of granites and gneisses formed at deeper crustal levels. In other provinces, greenstone belts are discordant on the orthogneisses and may represent tectonically reworked volcano-sedimentary basins deposited diachronously on an older basement (e.g. Condie (1981, 1984)).

The crustal architecture of younger continental fragments differs by numerous aspects. Greenstone belts give way to vast (over 100 x 100 km) sedimentary basins. Sedimentary rocks are deposited on continental shelfs along passive margins, as intra-continental basins on subsident continental crusts, or in flexural basins. In contrast, the structural setting of cratonic volcano-sedimentary basins suggests that they are syn-orogenic. The proportion of carbonates and mature sediments, such as shales and quartzites, increases across the Archean-Proterozoic transition, while that of greywacke and volcanogenic sediments decreases (Ernst, 2009; Veizer and Mackenzie, 2003).

Modern orogenic belts belong to planetary linear or arcuate orogenic systems, such as the Alpine-Himalayan orogen, which spans from western Europe to southeast Asia. At convergent plate margins, allochtonous terranes are transported laterally along large-scale thrusts and are stacked onto autochtonous domains. As a result, rock units with different provenances and origins are tectonically mingled. Allochtonous rocks may be sediments, gneisses, ophiolites or accretionary complexes.

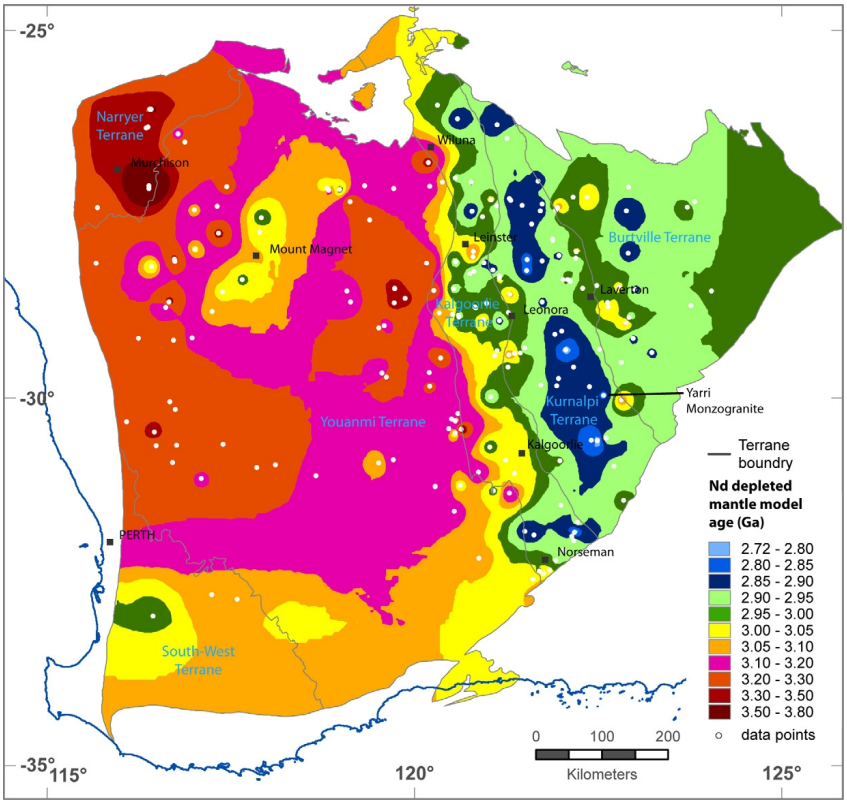

FIGURE 1.10: The Yilgarn craton is made of juxtaposed cratonic domains of Archean age, which are separated by craton-scale shear zones and are characterised by distinct (Nd) model ages. The latter display a younging trend from west to east, revealing that the craton grew of lateral addition of juvenile material extracted from the mantle during discrete magmatic events (Czarnota et al., 2010).

Ophiolites are fragments of oceanic lithosphere tectonically accreted to the continental crust around suture zones in modern orogenic belts. They display a characteristic succession of crustal and mantellic lithologies (Moores, 1982). Ophiolites are interpreted as oceanic relics amalgamated into the orogen at the closure of oceans. They are described from orogens whose ages range from actual to the Paleoproterozoic, although their occurrence is much less frequent in the Proterozoic than in the Phanerozoic (Helmstaedt and Scott, 1992). Rock sequences which resemble ophiolites but differ from Phanerozoic examples have been reported from Archean and Paleoproterozoic cratons. The interpretation that some greenstone belts represent ancient oceanic crusts is heavily debated. Some authors consider them as equivalent to modern ophiolites and evidence for the existence of plate tectonic geodynamics (de Wit, 2004; Kusky, 2004; Kusky and Li, 2003), while others challenge this view (Bédard et al., 2013; Bickle et al., 1994; Friend and Nutman, 2010).

A similar debate concerns the recognition of relics of accretionary prisms in ancient orogens (Kröner, 1981). Accretionary prisms are tectonic wedges that form in compressive environments at the front of accretionary orogens, on the overriding plate at the contact with the subducting lithosphere (e.g. Cawood et al. (2009)). They incorporate dismembered rock units from different origins (platform or abys-

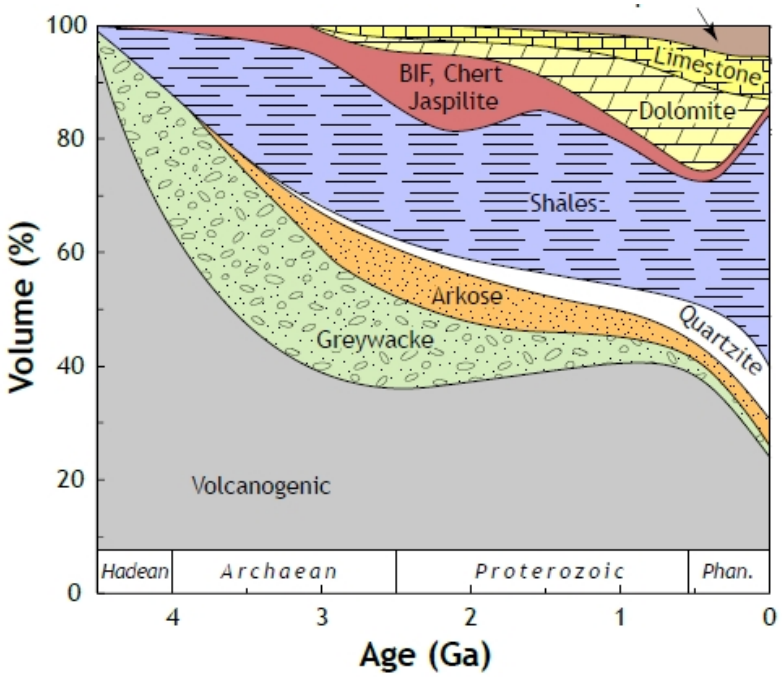

FIGURE 1.11: Secular changes in the proportion of rock-types found in sedimentary basins throughout the Earth history. From Laurent (2012), modified after Ernst (2009); Veizer and Mackenzie (2003).

sal sediments, turbidites, oceanic plate fragments, etc) that form tectonic melanges in the wedge. The accreted units are thrust or underplated against one another and are buried in the prism during compression. Some ancient terranes have been proposed to represent accretionary prisms (Komiya et al., 1999; Kusky, 1989). However, they do not necessarily display the sets of thrusts and décollements, nor the HP-LT metamorphic rocks that characterise modern accretionary prisms. Hence the geodynamic significance of proposed accretionary prisms remains ambiguous.

1.3.5 Secular changes in the composition of the lithosphere

1.3.5.1 Lithospheric mantle

The pioneer work of DePaolo (1980) and Hofmann and White (1982) provided evidence that the crust grows from the upper mantle, and that crustal material is recycled into the mantle sources of crustal magmas. The chemical composition of the sub-continental lithospheric mantle (SCLM) varies with the age of overlying continents (e.g. Griffin et al. (2003, 1999b) and references therein). Archean SCLM is essentially made of depleted harzburgite. Between the Archean and the Phanerozoic, the thickness of the SCLM decreases while its density increases. It becomes increasingly fertile, has higher Si/Mg ratios and comprises an increasing proportion of lherzolite (Fig. 1.12). The SCLM underlying Proterozoic continental crust has intermediate characteristics between Archean and Phanerozoic mantle.

The composition of the Archean SCLM is interpreted to reflect a high melting rate relative to present, high-pressure anhydrous melting which forms an olivine-

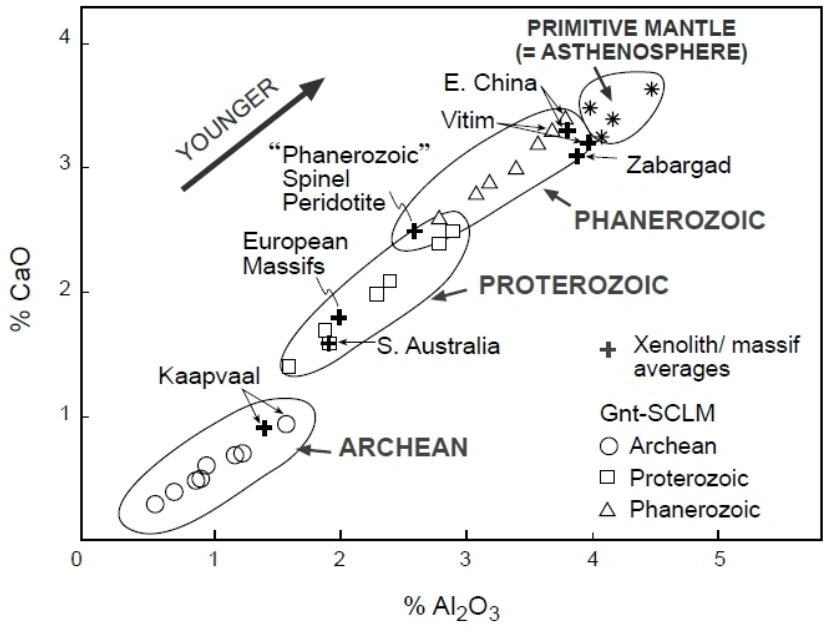

FIGURE 1.12: Secular evolution of the lithospheric mantle composition, determined from mantle xenoliths (crosses) or calculated from garnet phenocrysts (empty symbols) in lavas. The data defines a trend towards increasingly refractory compositions back in time (Griffin et al., 2003).

orthopyroxene residuum (Suzuki and Akaogi, 1995), while the modern-day SCLM composition is consistent with lower pressure melting of a hydrous mantle, in equilibrium with spinel (Kushiro, 2001). Although magma percolation and metasomatism in an ancient lithospheric mantle during subsequent re-activation may produce more fertile, "younger"s signatures, the lithospheric mantle below cratons is markedly different from the mantle in Phanerozoic active margins. The secular evolution of the SCLM composition suggests that processes responsible for the construction of the lithosphere evolved through geological time periods. Furthermore, the changes in mantle compositions mirror changes in crustal compositions. This evolution reflects changing crust - lithospheric mantle interactions through time and suggests that crust and mantle formation and differentiation were contemporaneous.

Based on petrological constraints (Herzberg, 1999), Griffin et al. (2003) propose that the Archean SCLM formed as a result of anhydrous melting of asthenospheric plumes at depths greater than 150km. The authors suggest that major magmatic events caused by mantle plumes are associated with lithospheric resurfacing event and mantle-scale convective overturn, while the contribution of processes analogue to subduction cannot be excluded (e.g. Griffin et al. (1999a)). The gradual cooling of the SCLM causes an increase in its buoyancy, which may have allowed for the preservation of continental crust and the stabilisation of cratons.

1.3.5.2 Igneous crustal rocks

The chemical composition of crustal rocks carries information on the magmatic processes which produce continental crust, and on crust-mantle interactions. As seen

earlier in this chapter, the continental crust is extracted from the mantle since the Hadean and some ancient continental domains escaped recycling and are preserved to date. In this sense, the continental crust represents the fossil record of the Earth.

Evaluating potential global secular changes in the composition of the continental crust is challenging. This difficulty is caused by the strong chemical variability between synchronous rocks belonging to a given province, or may come from possible sample biases. The bias may be geographical, with strong variations in sample density from one region to another ; or it may rise from the over-sampling of specific lithologies. To avoid these pitfalls, Keller and Schoene (2012) performed a statistical analysis of about 70 000 geo-referenced geochemical data points. Sample and preservation bias were mitigated by weighted bootstrap resampling and were corrected for sample density. A Monte Carlo analysis was performed to estimate geochemical variables for bins of 100 Ma. The results, which are presented in Fig. 1.13, show marked secular trends in the geochemical composition of igneous rocks.

Archean mafic rocks ($43 - 51\%$ SiO_2) differ from their Proterozoic and Phanerozoic equivalents (Condie, 1989; Keller and Schoene, 2012) by displaying high concentrations of compatible elements (such as Ni and Cr), and lower concentrations of incompatible elements (such as Na and K). The MgO content of rocks is also higher in the Archean than in younger eons. Komatiite lavas are among the most MgO rich igneous rocks and are mostly restricted to the Archean. Between 3.8 and 3.3 Ga, the average concentration of compatible elements increases and that of incompatible element decreases. After 3.3 Ga, the opposite trend is observed. The rising Na and K content correlates with dropping MgO content. The analysis of the database reveals a systematic decrease in compatible element and increase in incompatible element concentrations up to present day (Fig. 1.13). Incompatible element concentrations in mafic magmas are expected to increase with decreasing mantle melting rates, while the concentrations of compatible elements will decrease. In particular, komatiites are considered to be the product of high mantle melting rates under extreme temperature conditions, possibly at the apex of mantle plumes (Arndt et al., 2008; Kerrich and Xie, 2002; Wyman and Kerrich, 2002). Consequently, the secular chemical evolution of mafic rocks demonstrates that the rate of mantle partial melting rises in the Paleoarchean, before progressively decreasing down to a minimal value at present. This trend is consistent with the thermal evolution models presented in part 1.2.

Felsic rock ($62 - 74\%$ SiO_2) compositions display a strong variation across the Archean - Proterozoic transition. The Archean continental crust is dominated by "grey gneisses". This general term designates composite gneisses, sometimes migmatitic, derived from plutonic rocks, with minor amphibolites and paragneisses. The plutonic rocks are mostly represented by Tonalites, Trondjheimites and Granodiorite suites (TTGs, Jahn et al. (1981)) or by potassic granites (Moyen, 2011).

TTG suites are characterised by high Na/K ratios, strong enrichement in light rare earth elements (LREE) relative to heavy rare earth elements (HREE), i.e. high La/Yb, and by the absence of Eu and Sr anomalies (Moyen and Martin, 2012) (Fig. 1.14). They are derived from the partial melting of hydrous metabasalts. Experimental data additionally shows that Na/K and La/Yb in the magma increase with increasing pressure (Atherton and Petford, 1993), and indicate that the REE patterns of TTGs can be reproduced if melting takes place in the amphibolite

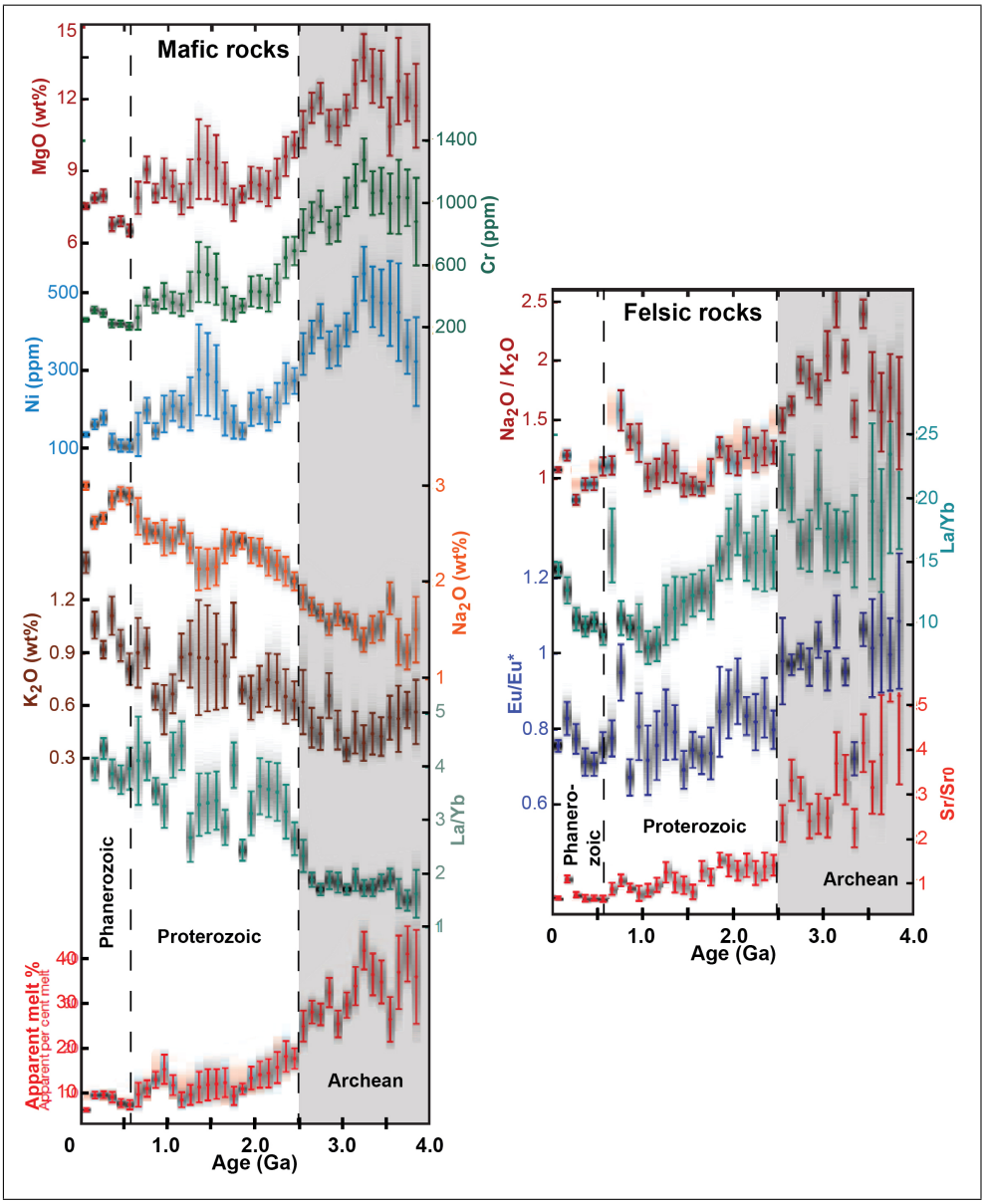

FIGURE 1.13: Secular changes in the chemical composition of mafic (left) and felsic (right) magmatic rocks. Modified from Keller and Schoene (2012).

and eclogite metamorphic facies, under conditions where garnet is stable in the residuum (Moyen and Stevens, 2006; Rapp et al., 1991). Similarly, the absence of Eu and Sr anomalies in felsic magmas is considered to reflect melting at pressures exceeding the stability of plagioclase feldspar in the source, when these elements behave as incompatible elements. Recently, Martin et al. (2014) demonstrated that the geochemical signature of TTGs is best reproduced by experimental melts derived from basaltic sources enriched in Large Ion Litophie Elements (LILE) and LREE, such as oceanic plateau basalts, rather than MORB-type basalts.

Geochemical data compilation from the least differentiated TTG plutons, emplaced across various cratons between 4.0 and 2.5 Ga, provide evidence for a gradual evolution towards higher Ni, Cr and Mg# (Mg/(Mg+Fe)) compositions, as well as

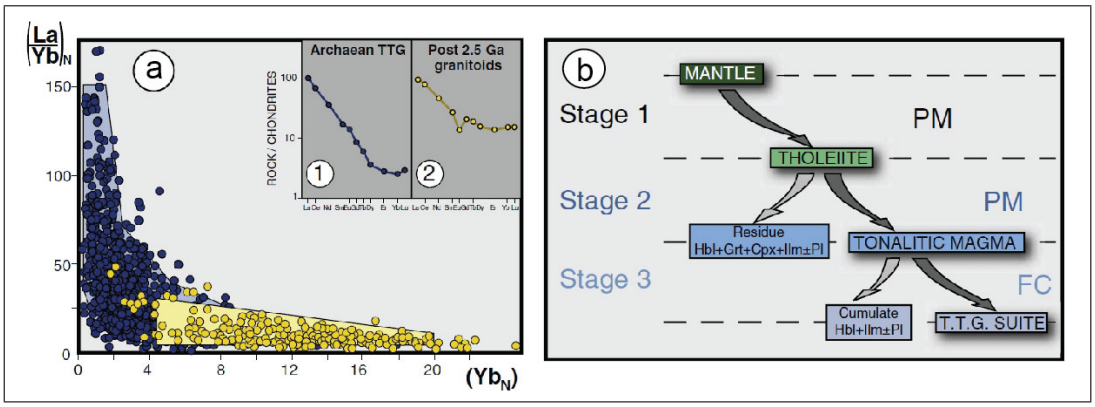

FIGURE 1.14: (**a**) The rare earth elements spectrum of TTGs (1, blue points and areas) differs from that of other potassic granitoids (2, yellow points and areas) by a strong enrichment in LREE relative to HREE. (**b**) The geochemical signature of TTGs can be reproduced by a three-step petrogenetic model : (1) mantle partial melting forming tholeiitic basalts, (2) partial melting of the metabasalt under conditions of garnet stability (in the amphibolite or eclogite facies) to form a tonalitic magma, (3) limited fractional crystallisation to form a variety of magmatic rocks (tonalites, trondjheimites, granodiorites). Modified from Moyen and Martin (2012).

for a marked increase in Sr content throughout the Archean (Martin and Moyen, 2002). The former variables are taken to reflect increasing interactions of TTG melt with mantle peridotite, while the latter is interpreted as evidence for a declining role of residual plagioclase in the source of TTG magma during the Archean. This suggests an increase of the average depth of the source of TTG magmas during the Archean. Fractional crystallisation in the crust is inferred to play a limited role in TTG petrogenesis (Fig. 1.14).

The chronology of granitoid emplacement follows a two-stage history across most cratons on Earth. TTG magmatism typically characterises the first evolutionary stage, which may last some few hundred million years (Laurent et al., 2013; Zeh et al., 2009). Subsequently, in almost every craton worldwide, TTG plutons are complemented by a large diversity of high-K granitoid plutons, which intrude grey gneisses and greenstone belts within a short timespan (Heilimo et al., 2011; Jahn et al., 1988; Laurent et al., 2014; Martin and Querré, 1984; Moyen et al., 2003; Sylvester, 1994). Although this petrological transition is diachronous from one craton to another, its timing corresponds at a global scale to the Neoarchean and the Archean - Proterozoic transition (3.0-2.5 Ga). As a consequence, this lithological group is sometimes called “late Archean” granitoids. It includes sanukitoids and potassic biotite or two-mica granites. Sanukitoids encompass a wide diversity of rocks which have a large range of SiO_2 content (Heilimo et al., 2010; Martin et al., 2009, 2005; Shirey and Hanson, 1984; Stern et al., 1989). They are ubiquitous on many cratons although they represent small proportions of the exposed crust. Rocks belonging to the sanukitoid suite share key geochemical characteristics, such as potassic calc-alkaline to alkali-calcic metaluminous compositions, and high contents of ferromagnesian oxydes. They are enriched in incompatible elements (particularly Ba and Sr) but also have elevated Ni and Cr concentrations. This dual enrichment

in "crustal" and "mantellic" elements suggests that the source of the sanukitoids formed from the interaction between mantle peridotite and an enriched component. Authors propose that the source peridotite of sanukitoids was metasomatised in contact with TTG melt, in addition to hydrous and carbonated fluids, or melt derived from recycled sediments (Heilimo et al., 2010; Laurent et al., 2011; Moyen et al., 2003; Stern et al., 1989). In any case, sanukitoid petrogenesis is consistent with the recycling of enriched crustal material into the mantle.

Potassic biotite or two mica granites are widespread on every craton, where they form late-stage intrusions. They are peraluminous leucogranites, with high concentrations in incompatible elements, and have higher HREE contents than TTGs, with negative Ba and Sr anomalies. Their chemical compositions suggests that they are derived from the low-pressure partial melting of an older felsic crust, which may include variable proportions of TTGs and paragneisses (Almeida et al., 2010; Frost et al., 2006; Laurent et al., 2014; Moyen, 2011; Moyen et al., 2003; Sylvester, 1994). Many granitoids display intermediate characteristics between the different groups presented above, and are the likely result of a mixing between magma sources.

The petrogenesis of late-Archean granitoids testifies of an increasing contribution of continental crust to the source of magmatism. The continental crust is either reworked during anatexis or during burial into the mantle, when potassic granites and sanukitoids are concerned respectively. This shift in the source of magmatism is clearly illustrated by zircon Lu/Hf or whole rock Sm/Nd isotope data. In the first period, TTG magmas have a juvenile, supra-chondritic Nd isotopic signatures, consistent with a short crustal residence time (Fig. 1.15, yellow area). This is interpreted to indicate that TTG plutons are derived from a depleted mantle source which melted shortly prior to TTG crystallisation. In contrast, late-Archean granitoids have on average less radiogenic Nd compositions and show a wide scatter in crustal residence times (Fig. 1.15, grey area). These isotopic signatures reveal that the granitoids are derived from older crust or from hybrid crustal and mantellic sources, which is consistent with a diversification of magmatic sources at the end of craton evolution.

K-rich late-Archean granitoids share genetic similarities with modern granitoids. Indeed, after the Archean - Proterozoic transition (at about 2.5 Ga), felsic igneous rocks display decreasing Na/K and LREE/HREE ratios, along with marked Eu and Sr anomalies (Condie, 1989; Keller and Schoene, 2012; Taylor and McLennan, 1985). These features are in sharp contrast with Archean TTGs and indicate that partial melting occurred at shallower depths relative to TTG magmas. Peraluminous and potassic calc-alkaline granites replace TTGs as the dominant crustal lithologies. The petrogenesis and diversity of late-Archean granitoids recalls that of Proterozoic and Phanerozoic plutons produced in continent-continent collisional orogenic belts. The latter have isotope and chemical compositions which suggest that they are also derived from either older continental crustal source rocks, or from mixed mantellic and crustal sources ((Barbarin, 1999; Bonin, 2004; Frost et al., 2001; Harris et al., 1986; Liégeois et al., 1998; Turner et al., 1992)).

1.3.6 Geodynamic implications

The secular changes presented above testify of changes in the dominant geodynamic settings of magma production. They may relate to shifting sources for

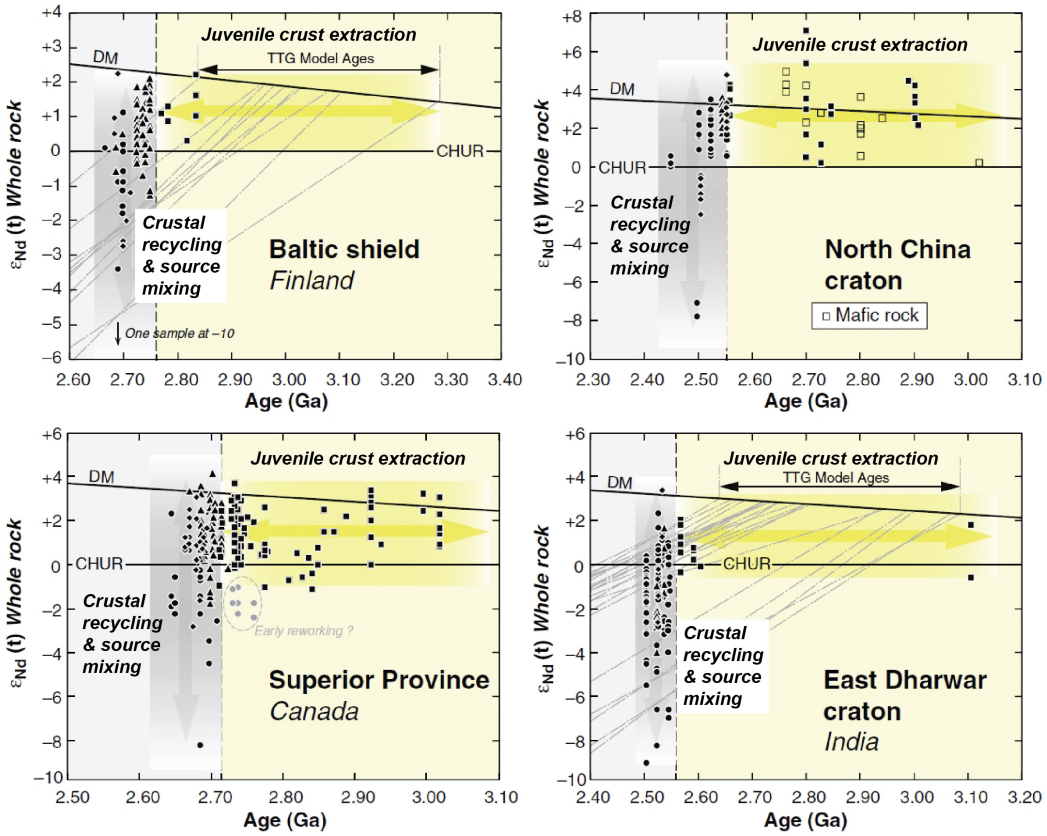

FIGURE 1.15: Whole rock ε_{Nd} *vs* age diagram of Neoarchean granitoids from four different cratons. Samples are labelled corresponding to their lithological group : TTG : square, sanukitoid : triangle, biotite and two-mica granite : circle, hybrid granite : diamond. Grey dashed lines represent the isotopic evolution trend of samples for which no absolute age is available. During the first stage of magmatic evolution, (yellow array), juvenile TTGs are produced. They have supra-chondritic ε_{Nd} values which indicates that the source was extracted from the depleted mantle shortly prior to magma generation. In the second stage of magmatic evolution (grey array), rocks show much more scattered sub- and supra-chondritic ε_{Nd} values, pointing to the combined recycling of older crust and juvenile magma input. Modified after Laurent et al. (2014).

magmatism, and to evolving thermal conditions.

1.3.6.1 Magmatogenesis

TTGs show important compositional variabilities, particularly in terms of REE patterns. This implies that their source rocks melted across a wide pressure range (Moyen, 2011). The observed chemical compositions of TTGs are consistent with melting at pressures of 10–15 and up to 25 kbar, which converts to a 50–60 km depth (Moyen and Martin, 2012). Knowing that metabasalts melt at 700–1000 ° C, TTG genesis requires the burial of basalts along 10–30 ° C/km geothermal gradients. This wide range of thermal environments suggests that TTGs may have formed in

various geodynamic settings (Moyen, 2011).

Subduction is a convenient way to bury hydrated basalts, belonging to the oceanic crust or to an oceanic plateau, into the mantle. Medium- to high-pressure, low-HREE TTGs (Halla et al., 2009; Moyen, 2011) were generated at depths exceeding crustal thickness, along cold apparent geotherms of <10–15 °C/km, which are slightly more elevated than those of modern-day subduction zones (5–10 °C, Syracuse et al. (2010)). The thermal regime of a subduction zone depends on the subduction velocity of the cold slab and on the age of the subducted plate. In the thermal and geodynamic conditions predicted for the early Earth (discussed in part 1.2), a 10–15 °C/km seems realistic for a ancient subduction. Therefore, one school of thought considers that TTGs were generated in a "hot" subduction zone, where buried basalts reached the solidus at great depths (Drummond and Defant, 1990; Foley et al., 2002; Laurent et al., 2014; Martin, 1986; Rapp et al., 2003; Smithies et al., 2003). Additionally, producing the adequate source rocks for sanukitoids also requires burying hydrous enriched material, which possibly include sediments (Halla, 2005; King et al., 1998; Laurent et al., 2011), which is easily fulfilled by a subduction.

High-P TTGs are sometimes coeval with low-pressure, high-HREE TTGs. The latter formed in higher geotherms (15–30 °C/km) that are less consistent with subduction models. They may instead reflect other mechanisms for the burial of mafic rocks. Another school of thought suggests that TTG genesis is coeval or subsequent to the delamination of the basal layers of an over-thickened (gravitationally unstable) proto-crust (Albarède, 1998; Atherton and Petford, 1993; Bédard, 2006; Bédard et al., 2013; Johnson et al., 2013; Smithies, 2000; Zegers and van Keken, 2001). Frequent delamination of the lower crust is supported by evidence of thin preserved crustal thickness across many cratons (Keller and Schoene, 2012). Crustal thickening beyond gravitational stability may be the result of the vertical growth and progressive maturation of an oceanic plateau set above a long-lived mantle plume. However, a model postulating the delamination of the eclogitic or cumulate root of an over-thickened oceanic plateau cannot directly account for TTG generation. Hydrous fluid transfers to the mantle is limited because the sinking refractory cumulates are predicted to be anhydrous, and may solely produce basalts upon melting (Johnson et al., 2013).

Van Thienen et al. (2004a) presents a numerical model coupled to thermodynamic calculation of phase equilibria, which allows to model magma production in a thickened oceanic crust, i.e. an oceanic plateau (30km basaltic crust). Different plausible geodynamic settings are tested for the possibility to melt (1) peridotites and (2) basalts, and to generate large volumes of felsic magma. Three distinct settings, defined by the choice of initial parameters, are modelled.

- Firstly, the basal eclogitic crust undergoes small-scale delamination. The mantle melts in upwelling flows within small-scale convective cells, while eclogites melt as they are advected downwards, between 2 and 3 GPa. The author considers that this pressure range is too great to fit the optimal conditions of TTG formations. Furthermore, the proportion of produced felsic magma remains minor.
- In a second run, part of the crust is thickened heterogeneously, and its base turns into negatively buoyant eclogites. The lower crust sinks into the mantle

and drags much of the lithosphere with it. This lithospheric overturn triggers generalised melting of basalts in the eclogite and amphibolite facies. Both melting conditions and magma production rates are considered appropriate to account for the petrological characteristics of TTGs and for their abundance in cratonic domains.

– Thirdly, a locally thickened crust melts at its base, in the eclogite facies, although it does not delaminate. Melting pressures are considered to be too high to fit the TTG field. The opportunistic upwelling of a mantle plume does not affect the conclusions of the study, because it increases basalt production while felsic magmas remain minor in proportion.

The results suggest that TTGs can be produced in a geodynamic setting which differs from modern subduction zone analogues. In the most satisfying model, episodic recycling of the lithosphere produces large volumes of felsic magma across vast domains, at 100 km scale. This is in agreement with evidence of the episodic nature of crustal growth.

Alternatively, the burial of mafic rocks may be the result of tectonically-driven crustal thickening during orogenesis (Bédard et al., 2003; Martin et al., 2014; Moyen, 2011) which, in specific tectono-thermal conditions, is also adequate to bury hydrous basalts. The 15–30 °C/km geothermal gradients are similar to those recorded by barrovian metamorphism in modern collisional orogens and by most metamorphic rocks on Archean and Paleoproterozoic cratons (see part 1.4). On the modern Earth, slab break-off, slab retreat or lithosphere delamination are invoked to interpret the late-orogenic evolution. These geodynamic processes provide heat to the lithosphere, reworks metasomatised mantle and cause crustal anatexis. By analogy, similar processes have been invoked for the late-Archean magmatism. Indeed, the orogenic model provides a suitable mechanism to associate geometrically two end-member sources, i.e. old crustal rocks and a metasomatised mantle.

To sum up, geochemical data reveals the coexistence of distinct magmatic suites on cratons, which therefore require that different magmatogenetic processes are active simultaneously and are geometrically associated during craton evolution (e.g. Laurent et al. (2014); Wyman et al. (2002)). However, identifying the geodynamic settings which, on the early Earth, most likely mobilise the sources recognised on geochemical grounds is uncertain. One difficulty stems from semantics. A "subduction zone" geodynamic setting, when referring to the Archean or early Proterozoic, does not need to be an analogue of modern subduction. It may more broadly designate a tectonic setting where portions of an oceanic lithosphere are advected downwards into the mantle, independently from the nature of the driving forces (Bédard, 2003), from the timing and duration of tectonic processes (Moyen and Van Hunen, 2012), or from the specific conditions required for its initiation (e.g. intra-oceanic or not). Similarly, collisional orogens are inferred from numerous field studies throughout cratons worldwide, although the thermal regime of the early Earth implies significant differences with Phanerozoic orogens, precluding strictly equivalent geodynamic evolutions. For these reasons, additional field controls are required to better constrain the under-constrained problem of geodynamics.

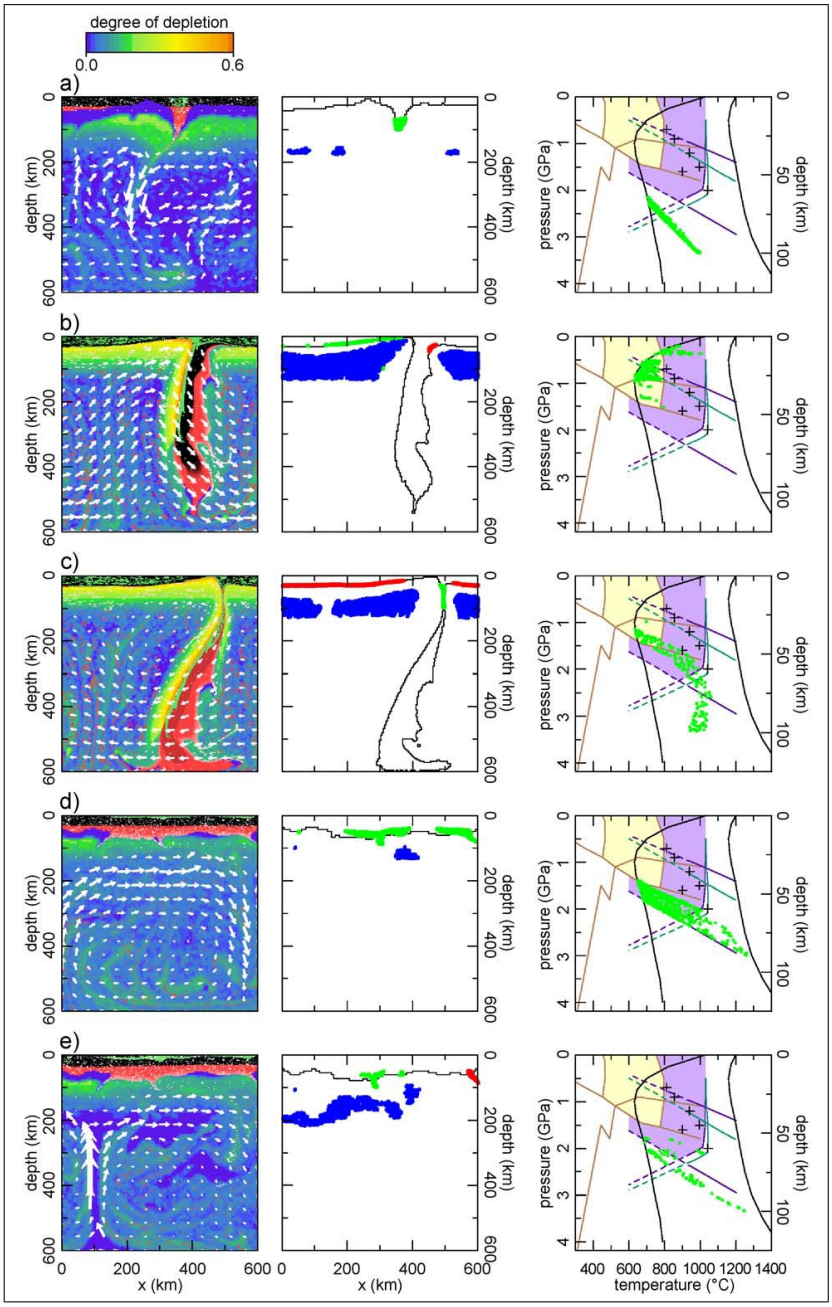

FIGURE 1.16: Figure from (Van Thienen et al., 2004a). *Left column* : lithologies and instantaneous velocity field. Black : basalt, red : eclogite, green : felsic magma. Colour scale : fertile *vs* refractory peridotite. *Central column* : black : contour of the crust, blue : melting peridotite, green and blue : melting of eclogite. *Right column* : P-T diagram showing the P-T conditions of TTG production derived from the melting of a tholeiite and a gabbro (yellow and purple respectively). Green crosses : calculated melting conditions. Black crosses : experimental results. a) : Small-scale delamination. b), c) Episodic lithospheric recycling. d) Thickened crust. e) Mantle plume under a thickened crust.

1.4 The rheology of the lithosphere

The results of numerical modelling presented in part 1.2 are strongly dependent on hypotheses concerning the rheological parameters of the lithosphere. In part 1.3, the debate on the geodynamic setting of crustal growth on the early Earth is presented. This question arguably requires additional calibration from complementary field data. Field geological and strain markers provide information on the rheological structure of the crust. The latter controls the tectonic styles and deformation modes in an orogenic belt. Therefore, the interpretation of field strain markers at multiple scales is fundamental to constrain geodynamic models. This part presents theoretical aspects on rock mechanical properties and lithosphere rheology. It discusses lithospheric-scale deformation and tectonic styles based on the shape of rheological envelopes. This knowledge is then used in part 1.5 to discuss the thermo-mechanical evolution of ancient and modern orogens in light of their respective geological records.

1.4.1 Rock rheology

Laboratory experiments on different rock types provide constraints on the mechanical behaviour (rheology) of rocks in response to forces that act upon them (e.g. Byerlee (1978); Hirth and Kohlstedt (2003); Kohlstedt et al. (1995)). Rock rheology is controlled by the rock composition, strain rate, fluid and confinement pressure, as well as by temperature.

Brittle behaviour A rock has a brittle behaviour when it breaks in response to increasing stress (discontinuous strain). The rock breaks if stress becomes too important to be accommodated by elastic deformation alone. In an ideal material with no pre-existing fractures, the conditions of rock failure were determined empirically by Byerlee (1978). Byerlee's law (also referred to as Mohr-Coulomb's failure criterion) provides a linear relationship between the shear stress and the normal stress applied on the plane in which failure occurs (Fig. 1.17, a) :

$$\tau = (\sigma_n - P_f).tan\Phi + C$$

τ and σ_n are the shear and normal stresses on the failure plane respectively. They are a function of the principal stresses σ_1 and σ_3. P_f is the pore fluid pressure, Φ the angle of internal friction, and C the cohesion of the material. This relationship gives the force required to overcome the resistance of the material. In a $\tau = f(\sigma_n)$ diagram, the equation delineates a stability "envelope" from a failure domain, where the rock breaks or where displacement occurs along the fault plane.

In most natural geological settings, the rock has local heterogeneities and fractures. Brittle deformation takes place when a pre-existing discontinuity is re-activated. The differential strain σ is proportional to lithostatic pressure (and therefore to depth z). The failure criterion can then be written as (Sibson, 1974) :

$$\sigma = \beta.\rho.g.z.(1 - \lambda)$$

with ρ being the material density, g the gravitational acceleration, β a parameter which is function of the principal stresses, of material friction Φ, and of $\lambda = P/P_f$.

σ can be represented as a function of z for a given strain rate. This relationship is valid for any rock-type and it does not depend on temperature (Fig. 1.17.b). At constant pressure, the failure criterion along a normal fault is lower than that along a strike-slip fault, and to a greater extent along a reverse fault.

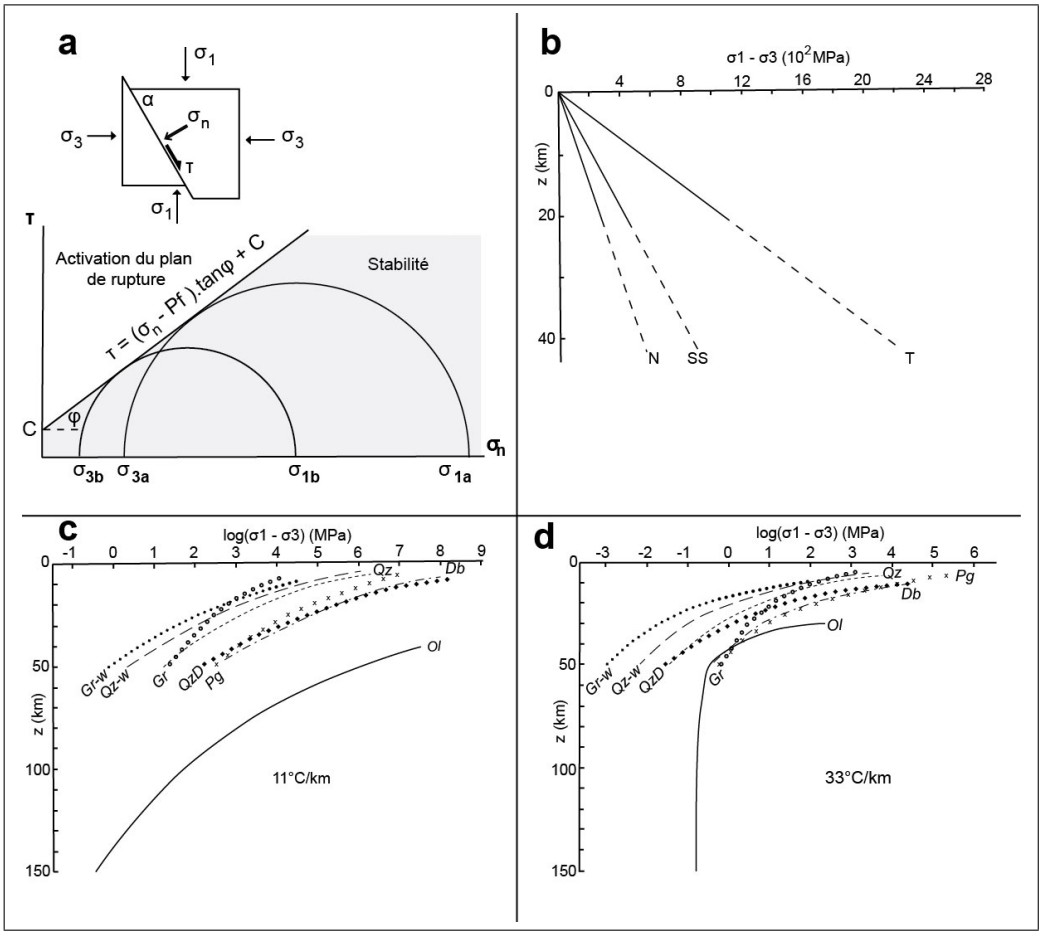

FIGURE 1.17: (**a**) Mohr-Coulomb envelope separating the strain field into two subsets : a failure domain where the rock breaks and displacements occurs along the fault planes, and a stability domain where the rock does not fail but deforms elastically. **b** Depth *vs* differential stress diagram representing Byerlee's law for various fault types. T : thrust, SS : strike-slip fault, N : normal fault. Dashed lines represent portions of the curve at depths where brittle behaviour is not observed. Modified from Sibson (1974). (**c, d**) Depth *vs* differential stress diagram representing the flow power law for different rock-types and for a strain rate of $10^{-14}.s^{-1}$. Gr : granite, Gr-w hydrated granite, Qz : quartzite, Qz-w : hydrated quartzite, Pg : Plagioclase-rich rock, QzD : Quartz-diorite, Db : diabase, Ol : Olivine-rich rock. **c** : Geotherm of 11 ° C / km, **d** : geotherm of 33 ° C / km. Modified from Ranalli and Murphy (1987).

Ductile behaviour A rock has a ductile behaviour when it flows to accommodate strain (continuous deformation) in response to stress. Ductile deformation is dominant for elevated temperatures and high confinement pressures. The deformation mechanisms responsible for ductile behaviour include dislocation creep and diffusion within grains and at grain boundaries. Ductile behaviour is described by a power law which relates strain rate ε to differential stress σ :

$$\varepsilon = A.\sigma^n.exp(-Q/RT)$$

with Q the activation energy, A a constant, n an exponential term, and R the Boltzmann constant. A, Q and n are specific for each rock-type (Kirby, 1983; Ranall, 1995; Ranalli and Murphy, 1987).

This equation allows to represent the magnitude of the force (the differential stress) required for the material to flow at a given strain rate (Fig. 1.17, c, d). For a fixed strain rate ε, the magnitude decreases sharply at higher temperature. The material softens with increasing temperature. The flow power law is valid for most materials, but olivine is an exception. The rheology of olivine is best described by the Dorn law (Stocker and Ashby, 1973) :

$$\sigma = \sigma_c.\left(1 - \sqrt{\frac{RT}{Q}.ln(\frac{\varepsilon_c}{\varepsilon})}\right)$$

with σ_c and ε_c being the critical stress and strain rates, respectively.

1.4.2 Rheological profiles

In the lithosphere, if the force necessary to cause ductile flow of the rock is smaller than the threshold required to cause brittle failure, then the rock will have a ductile behaviour. Conversely, if the rock fails before the differential stress value required for ductile flow is reached, brittle deformation is dominant. In a natural geological setting, brittle behaviour controls the rheology of rocks in the upper crust, at low temperature and low confinement pressure. In some cases, brittle deformation may also dominate in the upper part of the lithospheric mantle. Ductile behaviour is predominant at higher P and T, in the lower crust and the lower part of the lithospheric mantle. Figures 1.17.c, d show the influence of the geotherm on the rheology of the lithosphere. At a fixed strain rate, the differential stress necessary for a rock to flow decreases of 2 to 3 orders of magnitude when the geothermal gradient increases from 11 to 33 $^\circ$C/km. This implies that some lithospheric levels which have a brittle behaviour under a cold thermal regime become ductile along more elevated geotherms. Therefore, ductile behaviour may affect most of a hot lithosphere, including all of the lithospheric mantle.

In further detail, the rheology of the lithosphere is also a function of its composition and its stratification or architecture (e.g. Burov et al. (2006); Ranalli and Murphy (1987)). The rheological structure of the lithosphere can be represented by a rheological profile, which shows the differential stress needed to deform each rock type as a function of depth. The integration of stress over depth yields the " integrated strength" of the lithosphere. A lithosphere may be referred to as strong or weak depending on the magnitude of the integrated strength along a rheological profile.

Figure 1.18 represents the rheological profiles of different model lithospheres, for cold (11 ˚ C/km) or warm (33 ˚ C/km) geothermal gradients. "Hot" lithospheres have a significantly lower integrated strenght compared to "cold" lithospheres. Furthermore, the lithological layering implies rheological stratification. A model lithosphere with a granitic upper crust and a mafic lower crust displays two alternations of brittle-ductile layers, which theoretically allows for mechanical decoupling during deformation between (1) upper and lower crust, and (2) crust and mantle.

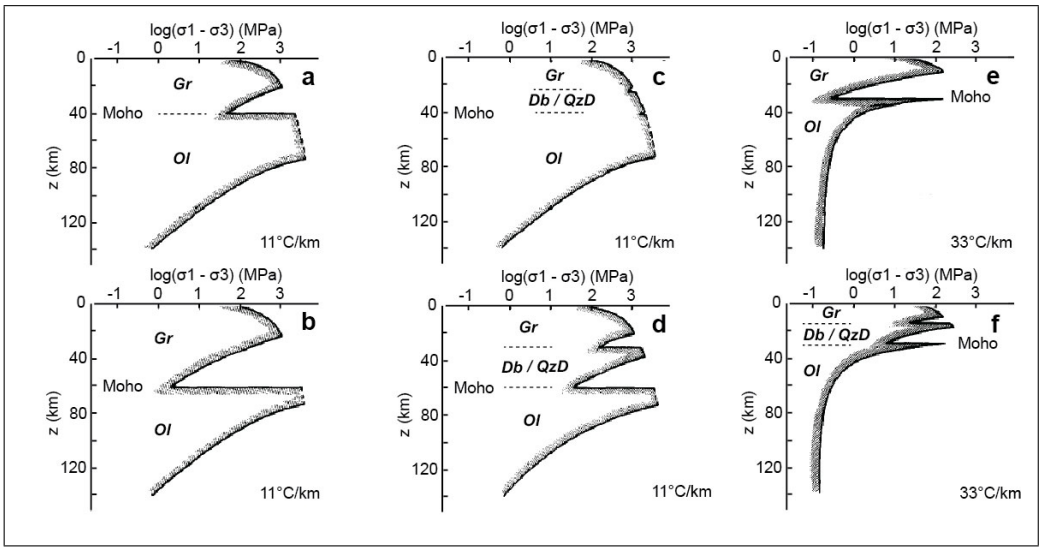

FIGURE 1.18: Modified from Ranalli and Murphy (1987). Rheological profiles of cold (**a, b, c, d**) and hot (**e, f**) lithospheres. Rheological profile of a lithosphere composed of a 40 km thick (**a**) or 60 km thick (**b**) granitic crust with a geothermal gradient of 11 ˚ C/km. The ductile lower crust separates the brittle upper crust and upper mantle. a lithosphere composed of a 40 km (**c**) or 60 km (**d**) thick lithosphere comprising a more resistant mafic lower crust, and with a geothermal gradient of 11 ˚ C/km. This causes an extra rheological stratification, with an additional alternation between ductile and brittle zones in the lower crust. Rheological profile of a thin lithosphere with a hot geothermal gradient, comprising a 30 km thick crust, with a granitic composition (**e**) or with a mafic basal crust (**f**). The latter induces an additional alternation of brittle and ductile layers. Abbreviations for lithologies are similar to figure 1.17.

1.4.3 Tectonic implications

1.4.3.1 Strain markers

The geological markers of deformation provide information on the rheological behaviour of the rocks during deformation. First order observations reveal that the brittle portions of the lithosphere are affected by discontinuous deformation and localised strain. Large-scale tectonic structures such as normal faults, thrusts and strike-slip faults localise deformation within a narrow high-strain zone in the brittle upper-crust, and at the interface between rock-units which have contrasting rheological behaviours (e.g. at the brittle-ductile transition, or between sub-solidus

and partially molten rocks). The ductile portions of the lithosphere are marked by continuous deformation and strain is distributed at a large scale. Rocks flow in response to stress, and flow may take place within an entire ductile level in the lithosphere. Consequently, a mechanical decoupling between brittle and ductile lithosphere-scale slices at different depths is plausible Vanderhaeghe and Teyssier (2001a).

1.4.3.2 Rheology and deformation styles

The lithosphere deforms in response to two main types of forces :

- Tectonic boundary forces may trigger horizontal displacements, contraction or stretching, which can cause local thickness variations (thinning or thickening) of the lithosphere. In turns, heterogeneous thickness variations within an initally stable lithosphere generate horizontal gravitational potential energy (= density) gradients across the deformation zone.
- Gravitational forces (or volume forces) gain amplitude when gravitational potential energy gradients build up. They oppose further heterogeneous thickness variations in the lithosphere and trigger deformation which tends to attenuate them.

The evolution of crustal and lithospheric thickness in areas of active tectonics is the result of the competition between boundary and volume forces (Fleitout and Froidevaux, 1982; Molnar and Lyon-Caen, 1988; Rey and Houseman, 2006). For instance, when the lithosphere is subject to horizontal shortening, deformation may be accommodated by heterogeneous thickening, thrusting and nappe-stacking in the upper crust, and by convergent crustal flow in the ductile layers of the lithosphere. This causes the buildup of lateral gravitational potential energy gradients, which oppose further thickening. The thickening rate eventually reaches a threshold, when the magnitude of gravitational forces equals or exceeds the integrated strength of the lithosphere. At this point, a change in tectonic style is expected, and shortening is accommodated by the lateral growth of the thickened zone outwards from the orogen. Deformation becomes distributed across a wider area. A similar evolution is expected if lateral gravitational potential energy gradients are caused by localised lithosphere thinning.

The threshold at which gravitational forces counter-balance tectonic stresses and become dominant in the orogen depends on the rheological profile of the lithosphere. A weak lithosphere is not able to resist strong gravitational forces produced by high lateral density gradients. In this case, relatively weak gravitational forces are sufficient to deform the lithosphere and to limit the thickening rate. The shift in tectonic style from thickening to gravitational flow intervenes earlier (for smaller thickeness variations) in a weak lithosphere compared to a strong lithosphere. The corollary is that a weak lithosphere is unable to sustain high-amplitude relief, nor thick continental and lithospheric roots. As a consequence, orogens will develop contrasting strain markers and architectures depending on their rheological structure and their thermal regimes.

The control of the rheological profile on the deformation style, and the role of volume *vs* boundary forces are investigated by Rey and Houseman (2006) for two end-member model lithospheres :

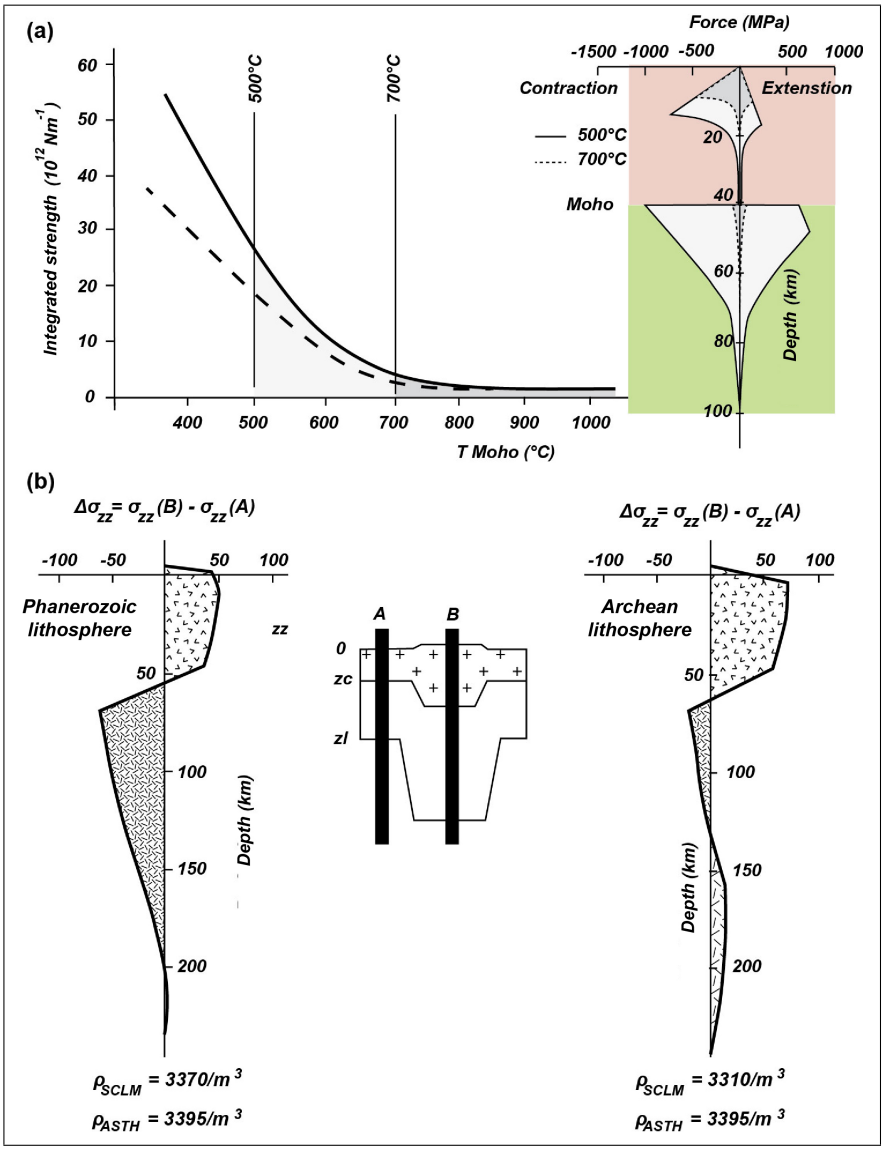

FIGURE 1.19: Modifid from Rey and Houseman (2006). (**a**) Integrated strength of the lithosphere *vs* Moho temperature, under compressional (bold curve) or tensile (dashed curve) stress. The lithospheric strength is the integral of the rheological profile (left). For a Moho temperature of 700 ° C, the integrated strength (dark grey surface) is much weaker than for a Moho temperature of 500 ° C (light + dark grey surfaces). (**b**) Horizontal density gradients formed in a thickened Phanerozoic (left) and Archean (right) lithosphere, for a given geothermal gradient . ρ_{SCLM} : Sub-continental lithospheric mantle density. ρ_{ASTH} : Asthenosphere density. The gravitational force is obtained by the depth-integration of $\Delta\sigma_{zz}$. (see text for explanations)

– The first case models a cold and strong "Phanerozoic" lithosphere, with a dense (moderately depleted) lithosperic mantle ($\rho = 3370 kg.m^3$) and with an initial Moho temperature of 500 ° C.
– The second case represents a hot and weak Archean lithosphere, with a deple-

ted, buoyant lithospheric mantle ($\rho = 3310kg.m^3$) (Griffin et al., 1998), and an initial Moho temperature of 700 ° C.

Figure 1.19.a illustrates the control of the geotherm on the integrated strength of the lithosphere. An increase of the Moho temperature from 500 to 700 ° C causes a decrease of the integrated strength by one order of magnitude. The thickness of the brittle crust is reduced at the expense of the ductile middle and lower-crust (see the rheological profile to the right). The contribution of the lithospheric mantle to the strength of the lithosphere becomes negligible. As a consequence, volume forces are expected to play an important role in the deformation and the evolution of an orogen. Figure 1.19.b shows density gradients between normal (A) and thickened (B) lithospheric sections. At a given depth z, the horizontal density gradient is expressed as $\Delta\sigma_{zz}$, the difference between the vertical stress in the thickened section $\sigma_{zz}(B)$ and in the normal section $\sigma_{zz}(A)$. The magnitude of the gradient varies with depth. It is represented along a vertical profile for typical Phanerozoic (left) and an Archean (right) lithospheres. The gravitational force caused by the thickening is the integral of $\Delta\sigma_{zz}$ along the whole vertical section :

$$F_g = \int_{bottom}^{top} \Delta\sigma_{zz}.dz = \int_{bottom}^{top} (\sigma_{zz}(B) - \sigma_{zz}(A)).dz$$

.

The gravitational force F_g is weak for a Phanerozoic lithosphere, because the excess mass represented by the thickened crust ($\Delta\sigma_{zz} > 0$) is compensated by the mass deficit due to the crustal root replacing dense lithospheric mantle ($\Delta\sigma_{zz} < 0$). Contrastingly, in an Archean lithosphere, the lithospheric mantle has a lower density, so the crustal root does not generate an important mass deficit. The gravitational force is higher and gravitational potential energy is stored into the crust.

The relative importance of the lithospheric strength and of volume forces during deformation may be evaluated by using the Argand ratio (England and McKenzie, 1982) :

$$AR = \frac{F_g}{zl.(\sigma_{zz} - \sigma_{xx})} = \frac{\text{Gravitational force}}{\text{Lithosphere strength}} = \frac{\sigma_{zz} - \sigma_{yy}}{|\sigma_{zz} - \sigma_{xx}|}$$

The model chosen by the authors imposes a tectonic boundary force which produces a constant shortening rate. Both Phanerozoic and Archean lithospheres are initially at mechanical equilibrium. Three geothermal gradients are considered, they correspond to three lithospheric thicknesses of 80, 120 and 180 km. The Argand ratio is calculated iteratively during the model run as deformation goes on.

- If $Ar < 1$, the magnitude of the gravitational force is not sufficient to cause deformation and to attenuate density gradients. The thickening rate is bound to increase.
- If $Ar \geq 1$, the gravitational force forbids any further increase in the lateral density gradients and thickening is limited.

In an Archean setting, the Argand ratio increases and converges to 1 during the model run. The increase in the ratio reflects an increasing lithospheric thickening rate, which develops in a transpressive tectonic regime, in response to horizontal shortening. When AR reaches 1, the gravitational forces prevent further thickening,

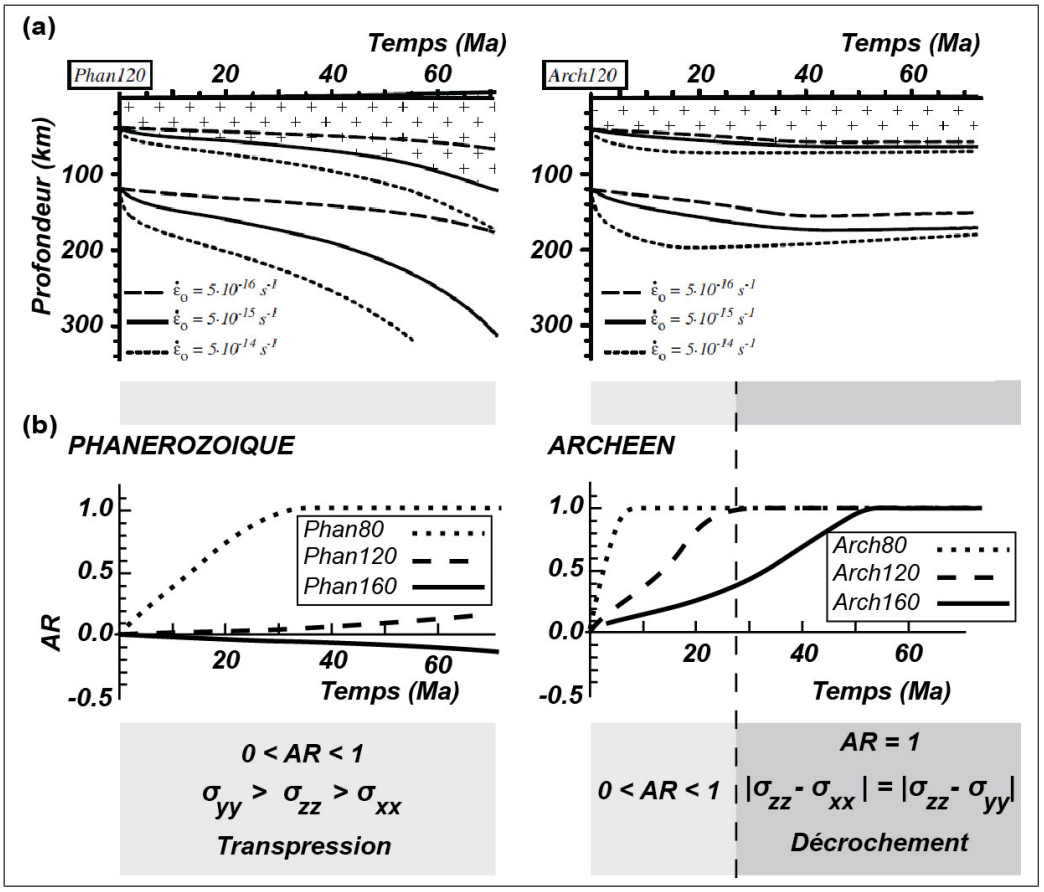

FIGURE 1.20: Modified from Rey and Houseman (2006). (**a**) Crustal and lithospheric thickness evolution through time for different shortening rates in a Phanerozoic (right) and in an Archean (left) setting. (**b**) Evolution of the Argand ratio through time for a Phanerozoic (right) and an Archean (left) lithosphere. The dominant tectonic style is labelled for a 120 km thick lithosphere in both settings (Phan120 and Arch120). For $0 < AR < 1$, transpressive tectonics dominate, while $AR = 1$ is characterised by strike-slip faults and transcurrent tectonics.

and shortening is accommodated by lateral flow of the thickened pile, in a transcurrent tectonic regime. The higher the geothermal gradient and the thinner the lithosphere, the shorter the time period required for the ratio to reach 1. The maximum thickening rate decreases with an increasing geothermal gradient (and decreasing lithospheric strength). A hot and weak Phanerozoic lithosphere (Phan80) follows an evolution that is similar to Archean lithospheres. However, for colder thermal regimes in a Phanerozoic setting (Phan 120 and Phan160), the transpressive tectonic regime associated to thickening is viable for over 60 Ma.

This study demonstrates the first-order links between the composition of the lithosphere, its thermal regime and the evolution of tectonic styles in a maturing orogen. It shows that hot and weak continental lithospheres with buoyant mantle keels are mechanically unable to sustain high-amplitude reliefs, to develop high thickening rates, and to maintain localised thickened zones, compared to colder and stronger Phanerozoic lithospheres. In the former, strain is expected to be distributed

and characterised by the lateral flow of the ductile crust, in a transcurrent regime, while in the latter, strain may be localised and cause heterogeneous thickening.

1.5 The secular evolution of orogens

Numerous cratonic domains display contractional tectonic patterns which are consistent with global horizontal shortening (Chardon et al., 2011; Kusky and Polat, 1999; Windley and Garde, 2009). These pieces of evidence suggest that horizontal tectonic forces drove the convergence and the tectonic assembly of geologic terranes within orogens back into the Paleoarchean. Part 1.3 reviewed the information on the processes driving the differentiation and the stabilisation of the continental crust which is preserved in orogens. Part 1.4 showed that the dominant tectonic regime in an orogen is controlled by the heat budget and by the lithological composition of the lithosphere. In the present section, the thermal and structural characteristics of orogens formed at different periods of the Earth history are presented. The secular changes of orogens through geological eons and their geodynamical implications are discussed.

1.5.1 Metamorphism : investigating the thermal regime of orogens

The thermal state of an orogen and its evolution through time is documented (although incompletely) by metamorphic rocks. Metamorphic rocks record petrological transformations in response to changing pressure, temperature, and other intensive parameters (fO2, aH_2O,...). These transformations affect mineral assemblages, phase compositions and textures. Metamorphism is concerned with the interpretation of metamorphic rocks in order to constrain past thermal regimes of orogens, to document their evolution through time, and to discuss their significance in terms of geodynamic processes. Metamorphic conditions are classically characterised by a facies (Eskola, 1915). A metamorphic facies represents a range of P-T conditions defined by the stability of a characteristic mineral assemblage in a given rock type. The different metamorphic facies are represented in P–T space in figure 1.21.

1.5.2 Phanerozoic orogens

Each orogen is unique by its geometry, by the association of amalgamated terranes it is made of, or by the timing, duration and type of orogenic processes it records. However, there is a consistency in the successive steps followed by an evolving orogen, which are classically described as an orogenic cycle.

1.5.2.1 Accretion

For most orogenic belts, orogenesis starts with a phase of accretion. The subduction of an oceanic lithosphere drives the convergence between lithospheric plates. Terranes with different geological histories and contrasting thermo-mechanical properties are brought in contact at convergent plate margins. These may include portions of an initially stable continental crust characterised by an “average” 8–15 °C/km geothermal gradient. The magmatic arc and the back-arc domains form

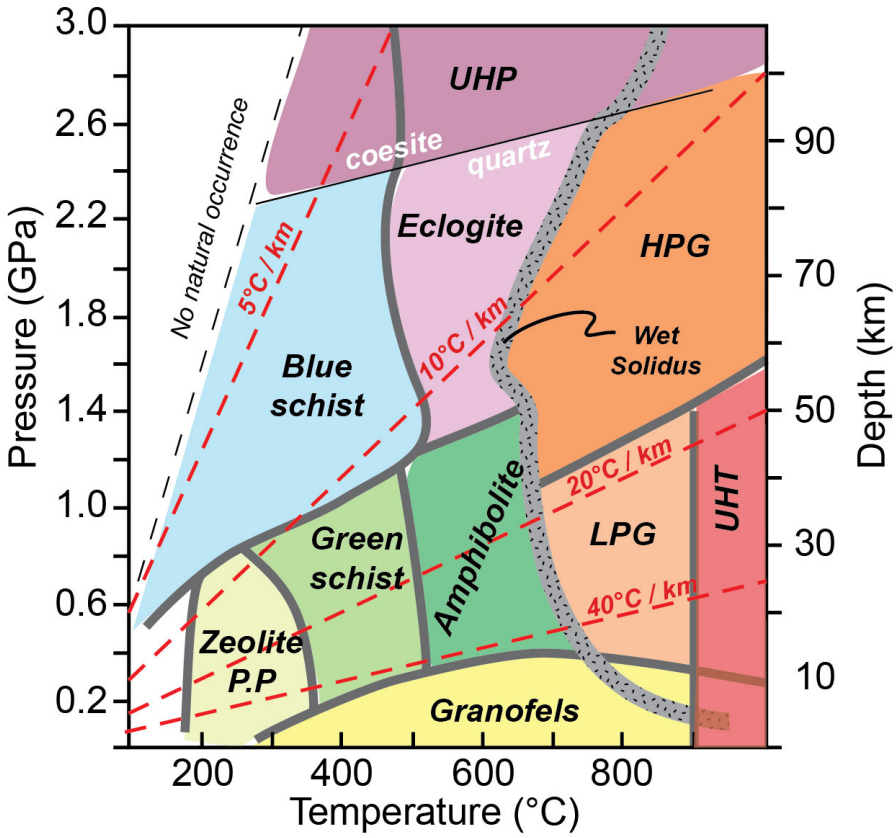

FIGURE 1.21: P–T diagram representing metamorphic facies and geothermal gradients. HPG : High Pressure Granulite, LPG : Low Pressure Granulite, UHT : Ultra High Temperature, UHP : Ultra-High Pressure, PP : Prehnite Pumpellyite. Geothermal gradients are plotted for an average crust density of 2800 kg/m^3.

hot lithospheric fragments with high geothermal gradients between 20 and 40 ° C/km. At the subduction trench, the downwards advection of a cold lithosphere induces a low geothermal gradient of 5–10 ° C/km. Therefore, the accretionary orogen is characterised by a thermal asymmetry (e.g. Hyndman et al. (2005); Johnson and Strachan (2006)). Figure 1.22.a illustrates the thermal asymmetry by representing the surface heat flow along a profile normal to the accretionary orogen. The lateral variations in the thermal regime can be converted into mechanical heterogeneities. The magmatic arc and back-arc domains comprise juvenile or remobilised continental fragments which are rheologically weak, and may act as a "mobile belt" which localises deformation at the scale of the orogen. The stable continent on the overriding plate has a more elevated integrated strength, and may act as a rigid indenter (Fig. 1.22.b). The diagram in figure 1.22.c represents the P-T conditions at the base of the crust in different parts of the orogen. Rocks buried in the accretionary prism undergo blueschist- or eclogite-faces metamorphic conditions, and record a low apparent geotherm. Simultaneously, rocks buried in the arc - back-arc domain witness amphibolite- to low-pressure granulite-facies conditions, which correspond to elevated apparent geotherms. The duality of thermal regimes is a consequence of the temporal co-existence of these two contrasted tectono-metamorphic settings

within the same orogen. It is considered to be the hallmark of accretionary orogens and modern-day plate tectonics (Brown, 2006).

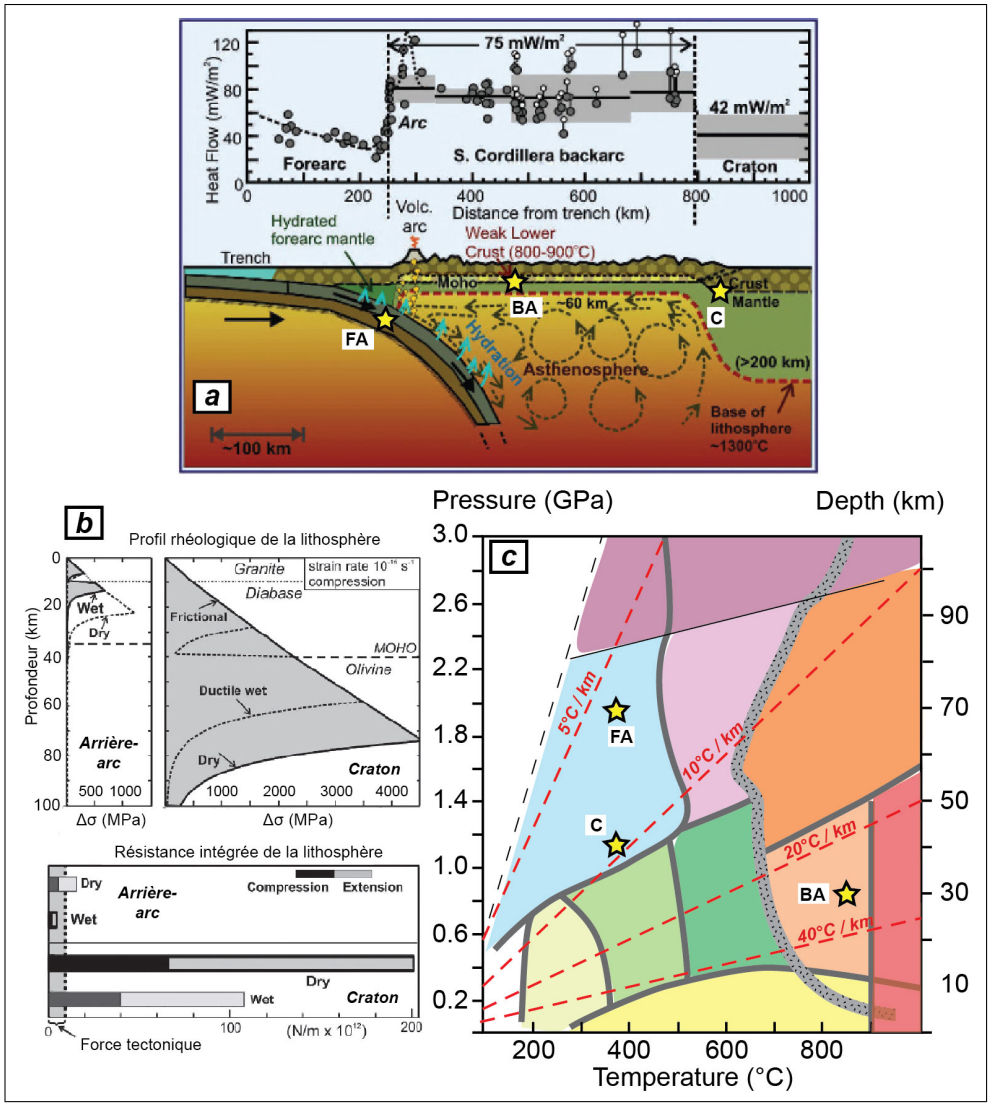

FIGURE 1.22: Modified from Hyndman et al. (2005). (**a**) Measured surface heat flow along a profile normal to the orogen. The heat flow is low in the fore-arc and decreases towards the subduction trench. It is maximal at the magmatic arc, and is elevated in the mobile belt forming the back-arc domain. The lithosphere thickness in the back arc is limited by the "thermal erosion" linked to convection in the asthenosphere. The heat flow decreases again in the stable continental lithosphere. (**b**) Lateral variations of the lithospheric strength between the back-arc domain and the stable craton. (**c**) P-T conditions at the base of the continental crust in the accretionary prism (FA : Fore-arc), in the back-arc (BA) and in the craton (C).

1.5.2.2 Collision

Crustal thickening The closure of the oceanic domain between two continents on either side of the subduction zone marks the end of the accretion stage and the

onset of continental collision. Variations from this general scheme include "intra-contiental collision", when convergence is propagated within the continental masses along inherited weakness zones. In this case, the orogen does not include any oceanic domain. In most cases however, the geological domains which evolved in different sites of the accretionary orogen are tectonically amalgamated into the collisional orogen. At the beginning of the collision, the subducting oceanic lithosphere provides the forces responsible for horizontal contraction and stacking of the various crustal fragments. Large-scale thrusts localise strain in the upper crust, cause heterogeneous crustal thickening and transport allochtonous crustal fragments (e.g. Matte and Burg (1981); Srivastava and Mitra (1994)). The rock units piled up in a stack of nappes may have contrasting provenances and evolution histories. At the scale of the orogen, thrusting and crustal thickening gradually propagates outwards from the center of the orogenic belts, to form a foreland belt. In a sedimentary cover, it develops fold-and-thrust strain patterns, with typical flat and ramp geometries (Fig. 1.23). These characteristic geological features played an important role in the construction of some concepts of the plate tectonics theory. Seismic studies reveal that thrusts in orogens may affect the whole crustal section down to the Moho discontinuity (Choukroune et al., 1990; Le Gall, 1992). The evolution of a collisional orogen is the result of multiple interacting processes such as tectonic stresses, relief formation and erosion. In cold and strong lithospheres, the gradual buildup of topography due to heterogeneous thickening amounts to the long-term application of a geological load onto the lithosphere, which causes it to flexure (Watts and Burov, 2003). Lithospheric flexure allows for the development of syn-tectonic fore-land basins, coeval with the growth of relief (DeCelles and Giles, 1996). Fore-land basins are filled by the products of relief erosion in the orogens. Relief evolution is the result of combined tectonic and erosional processes, which are particularly intense when topography is sharp and elevated. In turns, erosion plays an important role to remove the overburden of deeply buried rocks.

Continental subduction and exhumation The discovery of coesite, a high-pressure silica polymorph stable at depths greater than 90km, included within metamorphic silicates (Chopin, 1984; Smith, 1984; Wang et al., 1989) provides evidence for the burial of continental crustal rocks at UHP metamorphic conditions. This is confirmed by the finding of diamond inclusions in crustal metamorphic rocks (Dobrzhinetskaya et al., 1995; Shutong et al., 1992; Sobolev and Shatsky, 1990), which requires that the rocks reached depths of 100–150 km. Such conditions are not met in an accretionary prism, they rather require that fragments of continental crust are subducted in the trail of the sinking oceanic lithosphere. Isotopic studies carried out on UHP rocks demonstrate that they witnessed rapid exhumation and cooling during orogeny (Chavagnac and Jahn, 1996; Li et al., 2003; Shatsky et al., 1999). Peak cooling rates are shown to reach up to 90 $^\circ$C/Ma and exhumation rates up to 20km/Ma (Gebauer et al., 1997). Exhumation takes place in a period of 10–30 Ma.

The exhumation mechanisms of UHP rocks are debated (Burov et al., 2001). The break-off of crustal fragments from the subducted lithosphere may facilitate exhumation, because of their buoyancy relative to the mantle (Ernst et al., 1997). Exhumation would then take place in a "subduction channel" above the subducting lithosphere (Chemenda et al., 1996; Gerya et al., 2002). Extensional tectonics in the

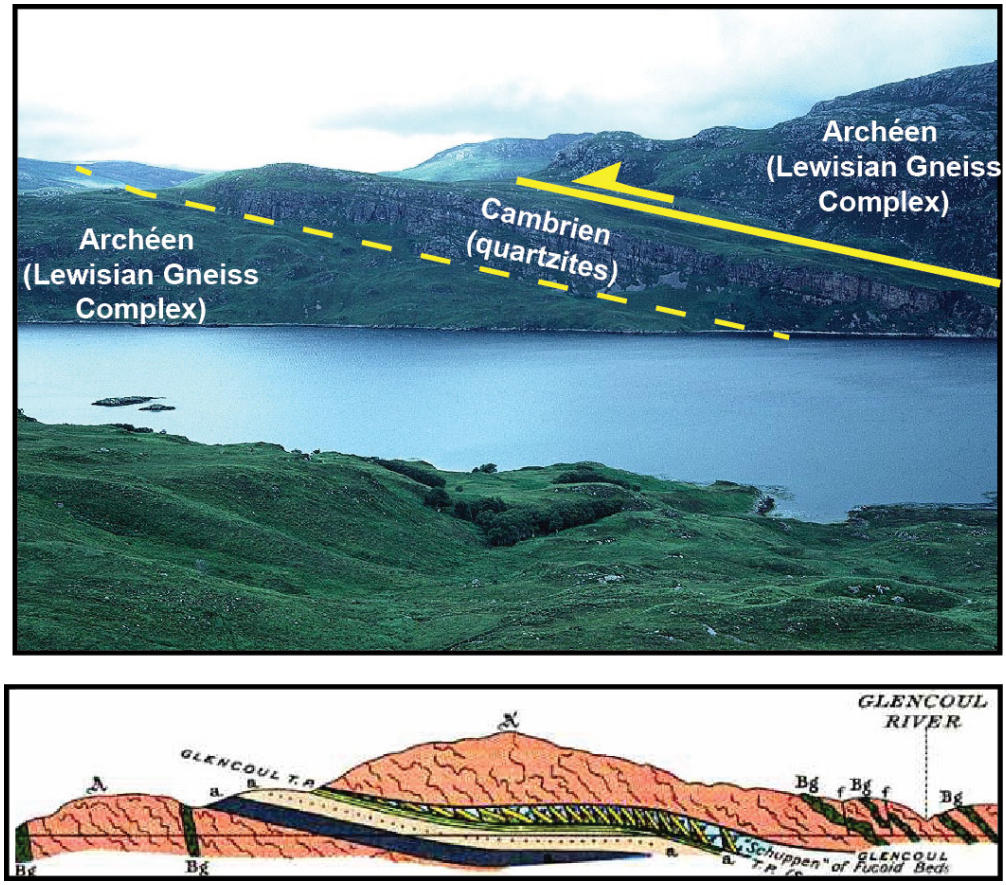

FIGURE 1.23: The Glencoul thrust in the fore-land belt of the Caledonian orogen of Scotland (e.g. Coward (1982)). Archean gneisses belonging to the Lewisian complex are found in the hanging-wall of the thrust, structurally above quartzites deposited in the Cambrian. In the footwall, the cambrian quartzites are discordant on the Lewisian complex gneisses. The thrust, which is revealed by a repetition in the stratigraphy, is interpreted to have formed as a result of bulk horizontal contraction, to accommodate horizontal displacement and crustal thickening.

orogenic crust enhances exhumation as it thins the upper crust and removes the overburden above UHP rocks (Andersen, 1998; Ballevre et al., 1990; Selverstone, 1988). However, this mechanism may not be sufficient to account for the exhumation of UHP rocks, unless extensional structures affect the whole lithospheric section down to the mantle, as it is suggested in an extensional setting induced by "slab rollback" (e.g. Brun and Faccenna (2008)). The thermo-mechanical modelling proposed by Burov et al. (2001) suggest that multiple mechanisms intervene at different depths. At mantle depths, small scale convection causes the upwards flow of the buoyant crustal rocks metamorphosed at UHP conditions. These rocks rise up through a subduction channel under the effect of buoyancy forces and reach the base of the crust. Corner flow produced by tectonic forces in the accretionary prism is coupled to extensional tectonics to achieve the exhumation of UHP rocks in the upper crust.

Transient geotherms The continental crust is enriched in incompatible radioactive elements. When it is thickened, the heat production rate per surface area increases and causes a significant rise of the geothermal gradients within a few million years. England and Thompson (1984) model the evolution of the thermal gradient following the instantaneous doubling of the thickness of the continental crust, until it reaches a new state of thermal equilibrium. This model postulates that crustal thickening is rapid compared to the thermal relaxation time of the crust. The changing thermal regime with time is referred to as a transient geotherm. Once the thickened crust reaches the state of thermal equilibrium, the geotherm is significantly higher than initially. A rock particle buried at mid-depth in the thickened crust and exhumed at a constant rate is predicted to follow a path forming a clockwise loop in P–T space, i.e. T increases during exhumation. The geometry of the P–T path depends on the exhumation rate, which is influenced by erosion and strain rates (Fig.1.24). If the rate of tectonic processes is low compared to the thermal relaxation rate of the crust, the P–T conditions recorded by rock particles may trend towards the conditions of thermal equilibrium. In the case of high burial or exhumation rates, the thermal relaxation time of the crust is low compared to the time it takes for a rock particle to be advected through the crust. Metamorphic rocks record conditions which greatly depart from the equilibrium geotherm. For example, a P–T path which includes a segment of near isothermal decompression may reflect a rapid exhumation at a rate too high for thermal re-equilibration to be effective.

Two consequences may be drawn from these results :

- Metamorphic rocks recording discrete P–T conditions reflect an "apparent" geothermal gradient. This apparent geotherm may be interpreted as the thermal conditions at a given time during the transient thermal evolution of the orogen.
- Extreme metamorphic gradients illustrate a strong departure of the lithosphere from its state of thermo-mechanical conditions, and imply geotectonic processes which are capable of generating and sustaining thermal perturbations.

The typical regional metamorphism during the collisional phase of an orogen is termed Barrovian (Barrow, 1893). It corresponds to moderate pressure - moderate temperature (MP–MT, about 20 °C/km) apparent geothermal gradients, and produces greenschist, amphibolite and granulite-facies metamorphic rocks. Barrovian metamorphism is generally characterised by clockwise P–T paths with gradual heating during and following thickening. The increasing temperature in the orogen may exceed the solidus temperature of crustal rocks and cause partial melting in some crustal layers. The development of a partially molten lower crust causes a significant drop in the integrated strength of the crust (e.g. Vanderhaeghe and Teyssier (2001a)). Consequently, the geometry of the rheological profile changes, and the integrated strength of the lithosphere decreases. This marks a shift in the deformation mode and the tectonic style of the orogen (Fig. 1.20).

1.5.2.3 Flow of the ductile crust

The formation of relief creates horizontal gravitational potential energy gradients oriented towards the margins of the orogen. As discussed in part 1.4 the

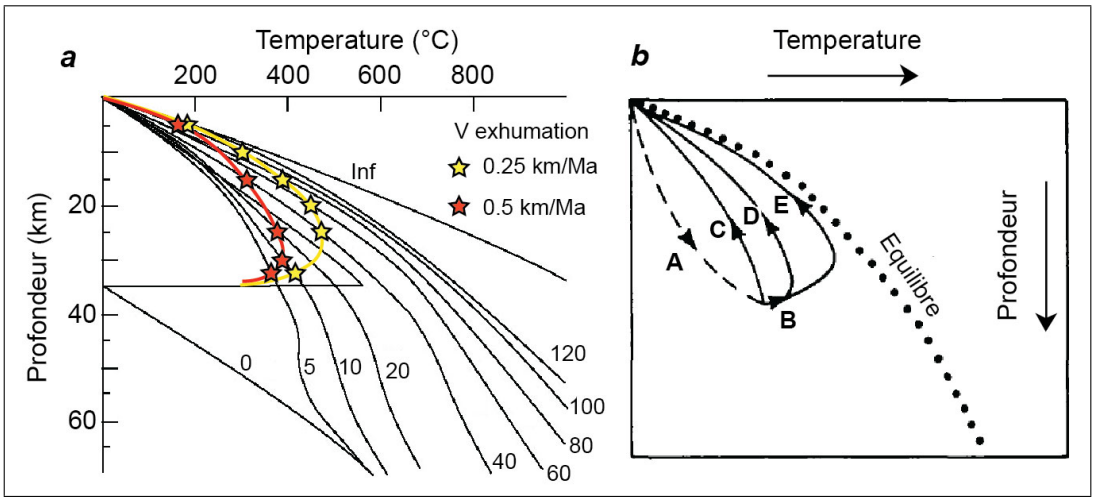

FIGURE 1.24: Modified from England and Thompson (1984). (**a**) Transient geotherm after instantaneous two-fold thickening of the crust. Yellow and red stars show the position, in P–T space, of rock particles buried in the middle crust and exhumed following 0.25 and 0.5 km/Ma exhumation rates, respectively. (**b**) The shape of the P–T–time path depends on parameters such as exhumation and erosion rates. Path ABC represents a case with a high erosion rate as soon as the particle reaches peak P at point B. Path ABD is for a low erosion rate after peak pressure is reached, which produces a heating phase at conditions close to peak P, followed by a high erosion rate, which is responsible for a decompression phase. Path ABE reflects the case where the erosion rate remains low. Peak T is then reached for $P < P_{max}$.

growth of gravitational potential energy in the orogen limits the amplitude of relief. The threshold over which gravitational potential energy triggers deformation is determined by the rheological profile of the lithosphere, which changes and decreases during the thermal re-equilibration of a thickened crust. As a consequence of the heating of the crust, the integrated strength of the lithosphere diminishes and the amplitude of gravitational forces becomes sufficient to cause deformation. Shortening is compensated by the flow of the ductile crust, away from the thickened zone, at the scale of the orogen (Vanderhaeghe and Teyssier, 2001b). Thickening propagates laterally under the effect of gravity. Partial melting of the crust, i.e. anatexis, decreases the rock viscosity by a few orders of magnitude as soon as the melting rate exceeds a few %, and that melt connectivity is achieved (Arzi, 1978; Van der Molen and Paterson, 1979; Vanderhaeghe and Teyssier, 2001a). This enhances gravitational flow in the partially molten layers of the crust. The brittle upper crust may become mechanically decoupled from the ductile lower crust and lithospheric mantle Burov et al. (2006), with strain being controlled by gravitational processes rather than by plate kinematics alone.

The Tibetan plateau is a modern example of an orogenic crust interpreted to be subject to gravitational flow. Geophysical studies reveal that the thickened crust is partially molten (e.g. Chen et al. (1996); Le Pichon et al. (1992); Nelson et al. (1996); Unsworth et al. (2005)). The plateau, which is limited to the south by the Himalaya mountain belt, to the north by large scale thrusts and strike-slip faults, and to

the east by a topographic front, does not display any sign of active contractional strain nor thickening. N-S striking normal fault systems with horst and graben successions on the plateau are indicative of E-W directed horizontal extension. The eastern topographic front does not bear any thrusts, and is interpreted as the front of the flowing partially molten-lower crust (Clark and Royden, 2000; Royden et al., 1997). Convergence between the Indian and Eurasian plates is compensated by the eastwards flow of the ductile crust below the brittle upper-crust, and fuels the extrusion of high-grade rocks at the footwall of detachment faults in the himalayan front (Beaumont et al., 2001; Harris, 2007).

1.5.2.4 Late-orogenic collapse

Crustal thickening forms a deep continental root below the orogen, and causes the burial of the lithospheric mantle into the hotter and more buoyant asthenosphere, thus creating horizontal density gradients in the mantle. As a result, convective flow in the mantle may initiate. It is predicted to cause the delamination of the lithospheric mantle and its replacement by asthenosphere. In terms of isostatic compensation, the convective erosion of the lithospheric mantle induces an elevation of the topography and enhances gravitational forces in the crust. This dynamic process is suggested to explain the 10 Ma old elevation of the Tibetan plateau to its present altitude (Molnar et al., 1993). The modern Himalayas is an example of an intermediate stage in the evolution of orogens. Both gravitational and boundary tectonic forces exert major controls on the dynamics of the orogen. However, this balance is bound to change with time. The subduction of the buoyant continental crust beneath the overriding plate is expected to oppose the forces driving convergence, and to reduce tectonic forces responsible for maintaining relief.

To sum up, the late stages of the evolution of orogens are marked by a decrease in the boundary forces and a dominance of gravitational forces. This is the consequence of combined phenomena : 1) rheological weakening of the lithosphere due to increasing geothermal gradients and partial melting, 2), decreasing tectonic boundary forces and 3) a possible thermal erosion and delamination of the lithospheric mantle. All these processes contribute to the attenuation of lateral density gradients and to the destruction of relief under the effect of gravitational forces. This is referred to as the gravitational collapse of the orogen (Dewey, 1988; Rey et al., 2001).

The late-orogenic gravitational collapse is evidenced by orogen-scale bulk extensional kinematics in over-thickened zones. The upper crust develops normal faults or detachments which initiate in the lower crust. Extension along the detachments accommodates exhumation of the partially molten lower crust in anatectic / metamorphic domes (Fig. 1.25) (Teyssier and Whitney, 2002; Whitney et al., 2004). Doming produces the conditions favourable for the rapid exhumation of metamorphic rocks. The latter frequently record a near-isothermal decompression path, followed by cooling along hot apparent geotherms of 40–70 $^\circ$C/km) (Duchêne et al., 2006; Norlander et al., 2002; Rey et al., 2009). Decompression may also be accompanied by heating in the case of lithosphere-scale thinning and upwelling of the asthenosphere. Anatectic domes are frequent in Phanerozoic orogens where they characterise the late-stage evoluton (e.g. Ledru et al. (2001); Malavieille et al. (1990); Vanderhaeghe and Teyssier (2001b)).

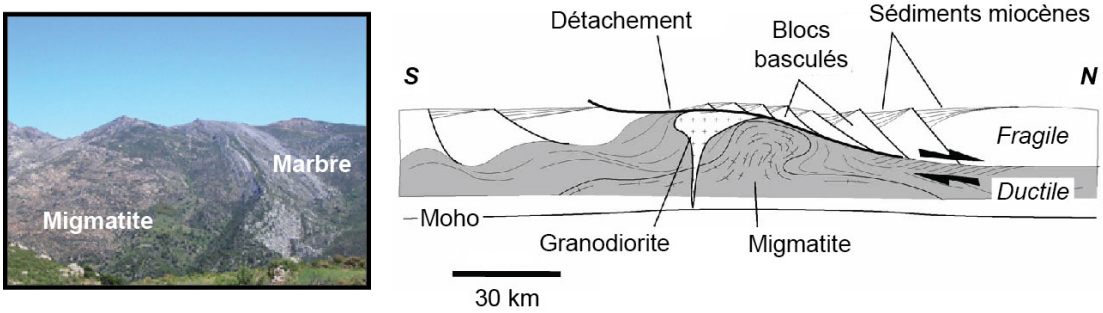

FIGURE 1.25: Right : panoramic view on the Naxos metamorphic dome. Left : cross section along a profile across the Naxos dome (Gautier et al., 1993). The migmatitic lower crust is exhumed and brought in contact with supracrustal sediments along a detachment. Metamorphic grade decreases from the dome core to its edges.

1.5.2.5 Cold orogen models

The main characteristics of orogens formed in the Phanerozoic are summarised here.

- Heterogeneous crustal thickening by thrusting and nappe stacking,
- Development of fold and thrust fore-land belts and fore-land basins,
- Syn-convergence exhumation of HP or UHP rocks,
- Gravitational flow and collapse of over-thickened crust, formation of anatectic domes,
- Increasing transient geotherm with time and record of dual HP-LT and LP-HT metamorphism (Fig. 1.26),
- Tectonic juxtaposition of terranes originating from oceanic, marginal and continental environments.

As discussed previously, and albeit multiple variations, these general geological features require that some of the lithospheric segments involved in the Phanerozoic orogenic belts are strong and characterised by cold geotherms, at least during the early stages of the orogenic cycle. In this sense, Phanerozoic orogens correspond to a "cold orogen" end member model.

1.5.3 Precambrian orogens

Major tectonic differences between orogens formed in the Archean, Proterozoic and Phanerozoic have long been recognised. The geodynamic significance of such differences is the focus of a voluminous literature (Cawood et al., 2009; Condie and Benn, 2006; Condie and Kröner, 2008; De Wit and Ashwal, 1997; Ernst, 2009; Pease et al., 2008; Stern, 2005; Windley, 1992, 1981). Cratons and granite-gneiss-greenstone domains are interpreted by one school of thought as products of subduction-driven horizontal tectonics analogue to modern plate tectonics (e.g. Cawood et al. (2006); Condie and Kröner (2008); de Wit (1998)). On the other hand, based on similar field observations, other authors invoke different geodynamic settings for crustal evolution (e.g. Hamilton (1998, 2003)) such as mantle plume-driven geodynamics (Abouchami et al., 1990; Smithies et al., 2005), convergent craton mar-

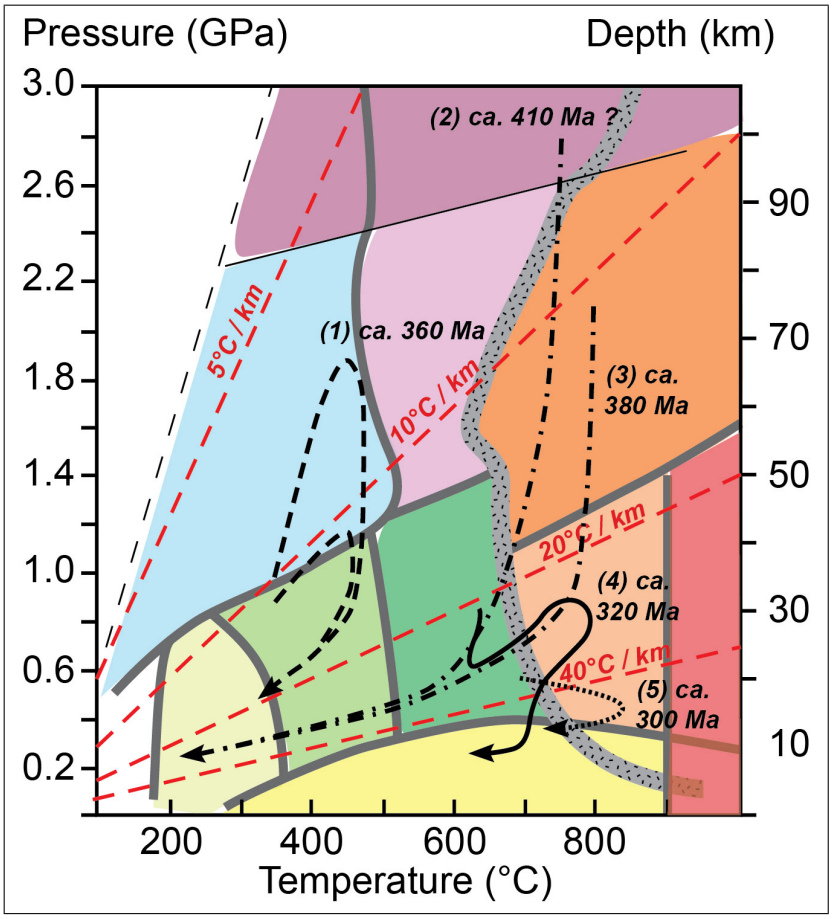

FIGURE 1.26: Synthesis of metamorphic P–T paths from the french Variscan belt illustrating the duality of thermal regimes and the increase of geothermal gradients with time which typify accretion-continental collision orogens. Dashed line : Groix blueschists (1) (Ballevre et al., 2003; Bosse et al., 2000). Dashed and dotted line : UHP metamorphism (2) and HP granulite facies melting (3) (Berger et al., 2010; Faure et al., 2008) Full line : LP granulites, southern Britanny (4) (Brown and Dallmeyer, 1996; Johnson and Brown, 2004). Dotted line : Velay dome granulites (5) (Montel et al., 1986; Mougeot et al., 1997).

gins lacking "typical" subduction zones (Bédard et al., 2013; Smithies et al., 2003), or "vertical tectonics" in hot and weak crusts deformed by gravitational forces (Bédard et al., 2003; Chardon et al., 1998; Collins et al., 1998; Van Kranendonk et al., 2004, 2007). We review some of the principal characteristics of Precambrian orogens and discuss of their interpretations.

1.5.3.1 Strain patterns

Both accretionary and collisional orogens are described in the Proterozoic and Archean geologic records. These orogens are made of amalgamated crustal domains that can be distinguished on deep crustal seismic reflection profiles (Calvert et al., 1995; De Wit and Tinker, 2004; Goleby et al., 2004) and that record different geological histories. The crustal domains are separated by shear zones that are

often interpreted as thrusts or transpressive suture zones, possibly formed after the closure of an oceanic domain. The different domains are frequently interpreted to represent a stack of accreted slivers or crustal dupleixes, for example in the Archean Kaapvaal or Paleoproterozoic North China cratons ; and some field strain patterns support thrusting models for the assembly of these orogens (De Wit and Tinker, 2004; Santosh, 2010). The deep crustal structure was alternatively interpreted to represent ductile extensional shear zones that accommodated divergent flow of a weak lower crust (Bédard et al., 2013; Calvert et al., 2004).

The crustal-scale shear zones delimit continental domains with different geological histories. However, strain is sometimes also homogeneously distributed within the crustal blocs across hundreds of km wide (Chardon et al., 2008).. This is particularly the case of granite-greenstone terranes on many Archean and Paleoproterozoic cratons. Their structure is typified by regional-scale transcurrent, often sub-vertical shear zones (Fig. 1.28C, D) that show a near-periodic spacing across the craton.

Some granite-gneiss terranes are characterised by an archetypal dome-and-keel architecture (Anhaeusser et al., 1969; Marshak, 1999). They are found both in Archean and Paleoproterozoic domains Bouhallier et al. (1995); Cagnard et al. (2007); Trap et al. (2008); Vidal et al. (2009). Dome-and-keel domains form broad and non linear metamorphic units compared to those found in modern orogenic belts. They show homogeneous distributed deformation across wide surfaces, and a typical strain partitioning between high-viscosity syn-tectonic granitoid plutons and rheologically weaker meta-supracrustal rocks (Chen et al., 2001). Greenstone belts form anastomosing synforms around domal granitoid bodies (Fig. 1.28A, B). This strain pattern is interpreted as a result of "vertical tectonics", that is the diapiric rise of hot buoyant plutons compensated by the passive downwards advection of denser greenstone supractustal sequences (Bédard et al., 2003; Bouhallier et al., 1993; Chardon et al., 2002; Van Kranendonk et al., 2007). This strain pattern is interpreted to reflect the flow of a hot and weak crust in response to bulk horizontal contraction (Chardon et al., 2009), and characterises "hot" orogens.

1.5.3.2 The metamorphic record and its secular evolution

As opposed to what is seen in modern orogens, metamorphism across cratons is frequently described as being monotonous. Metamorphic rocks on Archean cratons exhibit ordinary metamorphic P-T conditions which correspond to "average" Barrovian apparent geothermal gradients (e.g. Goscombe et al. (2009); Komiya et al. (2002); Percival (1991)), and which range from sub-greenschist to amphibolite and granulite-facies (Harley, 1989; Zhao et al., 1998). Large metamorphic domains record homogenenous metamorphic conditions and lack strong lateral baric metamorphic gradients (Percival and Skulski, 2000; Raase et al., 1986). The crustal-scale transcurrent shear zones on the cratons do not necessarily form strong metamorphic breaks. The transition from granitoid gneisses to supracrustal rocks often corresponds to metamorphic temperature gradients, with greenstone belts having lower metamorphic grades. The monotony of metamorphic conditions at terrane-scale is interpreted as a result of homogeneous uplift and denudation of the continental crust, as opposed to tectonically-driven exhumation of deeply buried slivers (Gapais et al., 2009). Metamorphic temperature variations are often interpreted as due to contact metamorphism, mantle-derived magma input in the crust,

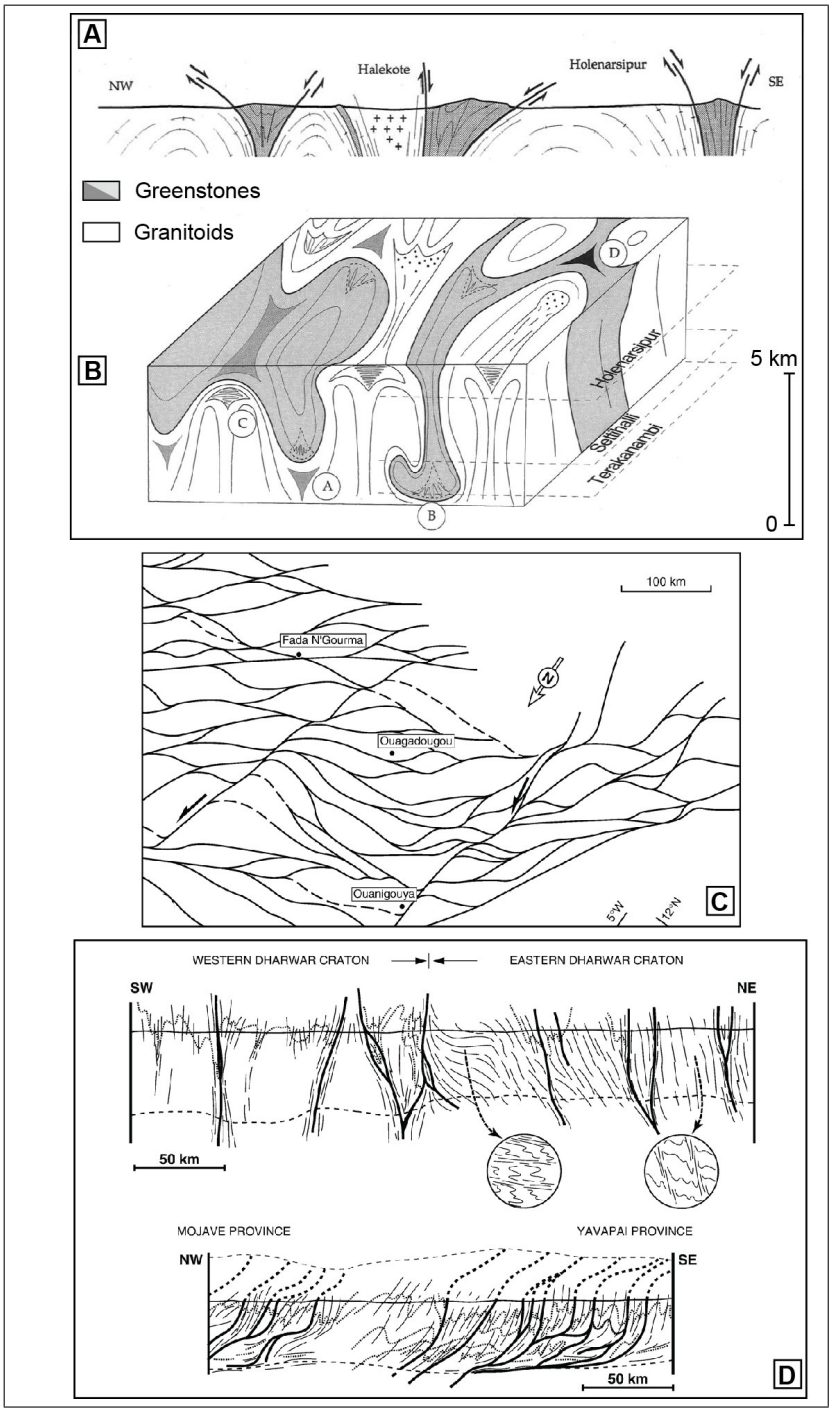

FIGURE 1.27:

or as a consequence of doming and deflexion of isotherms in the crust (Bédard, 2003; Collins et al., 1998). However, in detail some cratonic provinces show more complex metamorphic patterns. They contain slivers or rock units which exhibit contrasting metamorphic conditions and correspond to a range of different transient geothermal gradients (e.g. Block et al. (2013); Stevens and Moyen (2007)).

The Archean metamorphic record does not preserve any of the extreme geo-

FIGURE 1.27: Cross section (**A**) and sketch bloc diagram (**B**) illustrating the dome-and-basin structural relationship between supracrustal greenstone belts and its granite-gneiss basement in the Archean Dharwar craton, India (Bouhallier et al., 1995). (**C**) Map representation of the shear zone network on the south-eastern Paleoproterozoic West African Craton. (**D**) Cross sections across province boundaries in the Dharwar craton, India (top), and in the Paleoproterozoic south-western United States (Chardon et al., 2009). Strain is homogeneously distributed across crustal blocs delimited by sub-vertical shear zones.

thermal gradients found in modern orogens. Except for one Mesoarchean example (Fonarev et al., 2006), the UHT metamorphic record dates back to the Neoarchean - Paleoproterozoic transition, and is mostly a Proterozoic phenomenon. It has a tight temporal correlation with super-continent assembly (Brown, 2007). Eclogite and high-pressure granulite facies (E-HPG) metamorphism are absent before the Neoarchean (Volodichev et al., 2004), and become increasingly widespread in the Proterozoic and Phanerozoic eons (Brown, 2007). Blueschist and UHP metamorphism are first recorded in the Neoproterozoic and their frequency culminates in modern orogenic belts (Maruyama and Liou, 1998; Maruyama et al., 1996). These rocks are considered to be typical of modern-day plate tectonics and characterise cold subduction (Stern, 2005).

Based on a synthesis of worldwide metamorphic data, Brown (2007) demonstrates the existence of dual thermal regimes back to the Neoarchean. The combined occurrence of Blueschist facies - UHP metamorphism, and of granulite facies metamorphism in the Phanerozoic is interpreted as the hallmark of modern plate tectonics and subduction-driven orogenic systems (Tsujimori et al., 2006). In the Proterozoic, HP granulites and eclogite facies metamorphism coexist with UHT metamorphism. This association may be characteristic of Proterozoic plate tectonics. Therefore the metamorphic record would suggest the onset of some sort of plate tectonics back to the Neoarchean. Contrastingly, the monotonous Meso-Paleoarchean metamorphism could be representative of a distinctive geodynamic setting. Geodynamic processes before the Neoarchean may not have produce signficant transient thermal anomalies in the lithosphere, or may not have allowed to preserve rocks metamorphosed in extreme conditions.

1.5.3.3 Hot orogen model

Despite the uniqueness of each orogenic province, many Precambrian orogens display common tectonic and metamorphic patterns, and share lithological and architectural similarities, as described in the previous paragraphs. These characteristics serve as a basis for a "hot orogen" end-member model (Cagnard et al., 2006; Chardon et al., 2009; Gapais et al., 2009). This model describes the behaviour of hot, thin and weak continental lithospheres. During bulk horizontal shortening or extension, hot orogens are predicted to accommodate deformation through distributed strain, homogeneous crustal thickness variations, and three-dimensional flow of the low-viscosity lower-crust. They are unable to sustain horizontal density gradients induced by localised deformation (Rey and Houseman, 2006). As a result, they produce limited topography, low relief, and small topographic gradients (Fla-

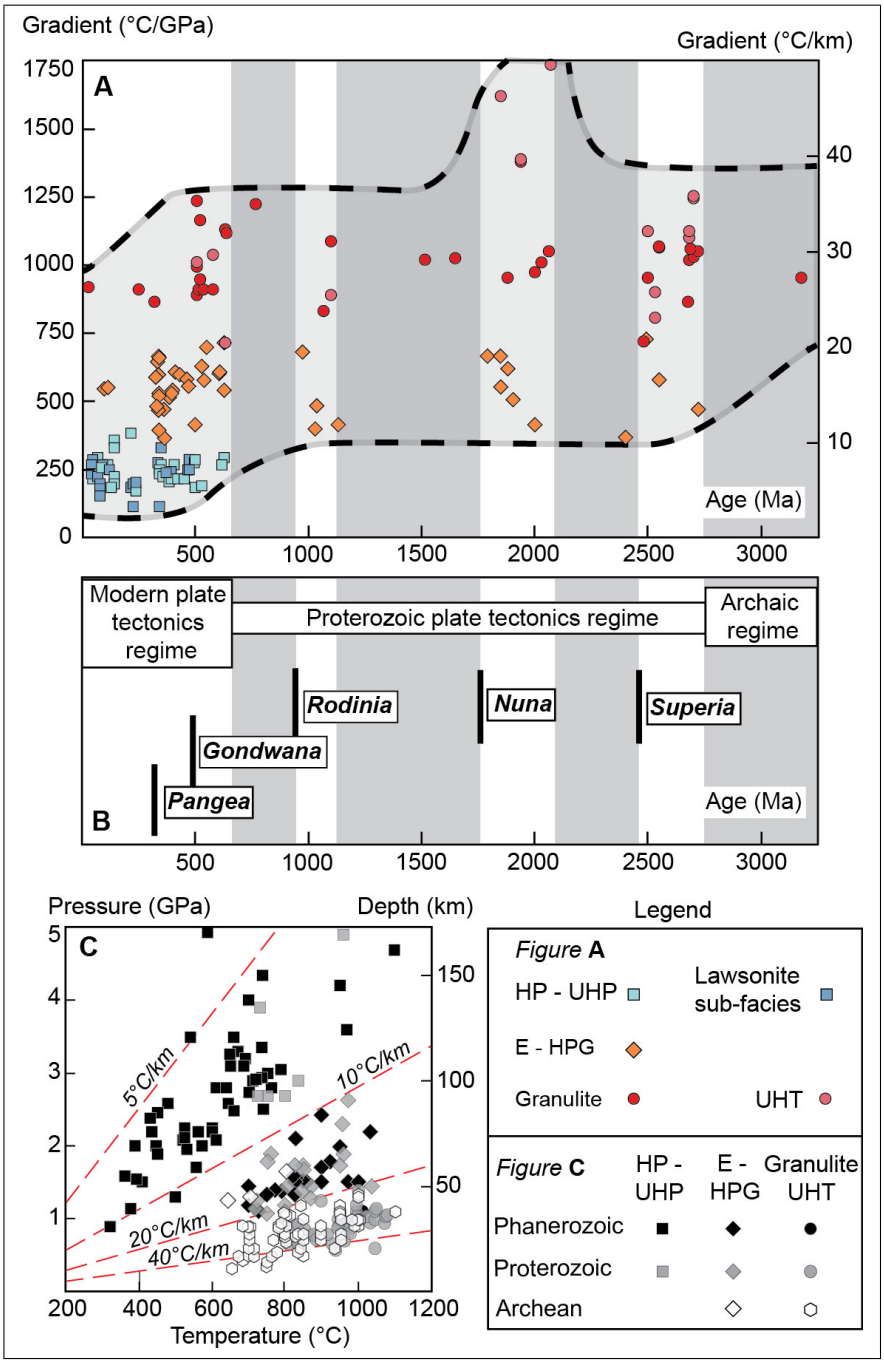

FIGURE 1.28: Modified from Brown (2007). **A** Plot of apparent geothermal gradients recorded by peak metamorphic assemblages from different types of extreme metamorphic belts *vs* age. Squares = Blueschist and UHP metamorphism, dark blue = lawsonite-bearing blueschists and eclogites. Diamonds = eclogites and high-pressure granulites. Circles = HT (red) and UHT (pink) metamorphism.

ment et al., 2008). This model has been proposed for Precambrian orogens (e.g. Cagnard et al. (2007); Chardon et al. (2011); Vidal et al. (2009)), as well as for mature Phanerozoic orogens (Beaumont et al., 2010; Clark and Royden, 2000; Royden

FIGURE 1.28: **B** The timing of metamorphism correlates with the Wilson cycles and precede the assembly of super-continents. Phanerozoic plate tectonics is characterised by the coexistence of HP-UHP and granulite-facies metamorphism. Proterozoic plate tectonics are inferred from the record of dual thermal regimes associated with coexisting E-HPG and HT-UHT metamorphism. In the Archean, more "ordinary" geotherms predominate and extreme metamorphic belts are lacking. It is interpreted to reflect archaic "non-plate" geodynamic processes. **C** Peak metamorphic P-T conditions retrieved from Phanerozoic, Proterozoic (Brown, 2007) and Archean (Komiya et al., 2002) metamorphic belts, showing a transition towards lower geothermal gradients with time.

et al., 1997; Schulmann et al., 2008; Vanderhaeghe and Teyssier, 2001b).

1.5.4 Key parameters

The modern-day thermal heat flow across the continental lithosphere shows strong spatial variations, and the thermal regime in an orogenic belt is known to change during its maturation (Artemieva and Mooney, 2001). Furthermore, the "hot" orogen model might be suitable for the late evolution of large Phanerozoic orogens. Finally, the metamorphic rock record of the early Earth does not show particularly high geothermal gradients. For all these reasons, investigating the thermal conditions of ancient crusts does not alone provide sufficient information on past geodynamic settings. Key information may rather lie in sequence of events which constitute ancient orogenic cycles, and on the spatial and temporal distribution of thermal anomalies with respect to major architectural features across cratons.

1.6 Synthesis

Multiple datasets confirm that the early Earth was profoundly dissimilar to the modern Earth. From the Hadean to the beginning of the Neoarchean, mantle temperatures were up to 200 °C higher than presently. Under such conditions, mantle convection and lithospheric geodynamics probably did not resemble much to the modern-day plate tectonics regime. Higher mantle temperatures also had fundamental impacts on the crust-mantle interactions. Melting conditions were such that the early Earth produced a range of magmatic rocks which are not formed on the modern Earth. Lithosphere differentiation and maturation processes produced continental crusts whose composition and architecture contrast with younger continents. The overall rheological behaviour of the lithosphere also changed through time. As a result, many features of the modern rock record do not seem to have ancient equivalents, and *vice versa*.

The Earth witnessed major global geodynamic changes through geological times. However, the timing and the duration of the transition from the archaic to the modern Earth is ambiguous. The appearance in the geological record of geological features which are considered to be proxies for a modern plate tectonics regime is diachronous from one craton to another. While some variables point to an early Neoarchean age for the beginning of plate tectonics on Earth, other indicators may favour a Paleoproterozoic age for the onset of modern geodynamics. Was this transi-

tion a smooth transformation or a brutal adjustment to gradually changing thermal conditions ?

In the following chapter, we focus on the nature and on the timing of the Archean - Proterozoic transition. This period is thought to mark the gradual onset of a plate tectonics regime on Earth. However, the Proterozoic geodynamic setting was not necessarily strictly similar to the modern plate tectonics. In order to further investigate this period, we examine some of the Paleoproterozoic rock record, with particular attention for the West African Craton, which may represent the youngest "Archean type" craton preserved on Earth.

Chapitre 2

The Paleoproterozoic : a transitional period ? Insights from the West African Craton.

2.1 The Archean - Proterozoic Transition

2.1.1 Definition and problems

The Archean - Proterozoic Transition (APT) is a *ca.* 500 Ma long period ranging approximately from 3.00 to 2.50 Ga, which corresponds to a major shift in crustal evolution (Reddy and Evans, 2009; Windley, 1984).

In the field, the APT is interpreted to be defined by a stratigraphic discontinuity. Vast, weakly deformed sedimentary basins are deposited onto the granite-gneiss-greenstone metamorphic domains affected by ubiquitous deformation (Windley, 1984). This discordance is one of many indicators of the progressive stabilisation and stiffening of the continental lithosphere (Chapter 1). Based on stratigraphic relationships, the boundary between the Archean and Paleoproterozoic eons was proposed to be at 2600 Ma in North America and in the USSR, by the USGS and by their soviet counterparts respectively (Semikhatov et al., 1991), in the 70s. The International Commission on Precambrian Stratigraphy finally defined the boundary at 2500 Ma (James, 1978; Plumb and James, 1986).

However, the stratigraphic definition of the APT is ambiguous. The age of discordant sedimentary basins varies from one craton to another, and some provinces comprise multiple diachronous sedimentary basins which are eligible to represent the APT. For instance, in the Kaapvaal craton of South Africa, coarse clastic sediments of the *ca.* 3.00 Ga old Pongola supergroup, the base of the Ventersdorp supergroup, or the base of the Transvaal supergroup, have all been proposed to mark the APT.

The major changes in magmatism, metamorphism, strain patterns and craton architecture documented around *ca.* 2.50 Ga in chapter 1 equally represent the Archean - Proterozoic transition. They are also diachronous from one craton to the other. Their earliest developments apparently started at *ca.* 3.0 Ga (e.g. Brown (2007); Laurent et al. (2014)), while archaic geodynamic processes seem to have dominated the evolution of the Paleoproterozoic West African Craton until *ca.* 2.20 Ga (e.g. Abouchami et al. (1990)). Therefore, the geological record suggests that the APT has a long protracted transitional character at a global scale.

Most rocks formed before the APT cannot be *easily* presented as analogues of a plate tectonics regime. After the APT, the nature and the cyclicity of the geologic record suggests the onset of Wilson cycles and of some sort of plate tectonics (Cawood et al., 2013). The geodynamic changes across the APT are inferred to be the result of the secular cooling of the Earth. However, the diachronism of these geodynamic changes implies that its timing was controlled at regional-scale by spatial heterogeneities in the thermal regime of the lithosphere. In this sense, the APT would represent the gradual shift towards a "new", plate tectonics-like thermal regime and mantle convection system ; and the Paleoproterozoic eon may correspond to the earliest time period for the global-scale predominance of plate tectonics on Earth.

2.1.2 Some insights into Paleoproterozoic orogens

The early Paleoproterozoic Siderian period (2.50-2.30 Ga) is characterised by a relative quiescence in geological activity, and by apparent minima in the juvenile

magmatic record (Condie, 1998; Condie et al., 2005; Pehrsson et al., 2014). The relative lull of tectono-magmatic activity follows the inferred assembly of one or a few Neoarchean supercratons (Bleeker, 2003) at 2.60–2.50 Ga, and is similar in amplitude to other intervals of geological quiescence after continent amalgamation events (Pehrsson et al., 2014).

Nevertheless, a number of cratonic fragments are affected by Siderian orogenesis, including the North China craton, the Gawler craton in south Australia, the Dharwar craton in India, the Rae craton in Canada and Greenland (Pehrsson et al., 2013). Low apparent juvenile crust preservation rates are recorded for this period, although juvenile crust addition is locally important, e.g. in Brazil's São Francisco craton (Seixas et al., 2012). Large volumes of juvenile crust were produced and stabilised during the Rhyacian, between 2.30 and 2.10 Ga in the São-Luis - West African Craton, which is presented in detail below.

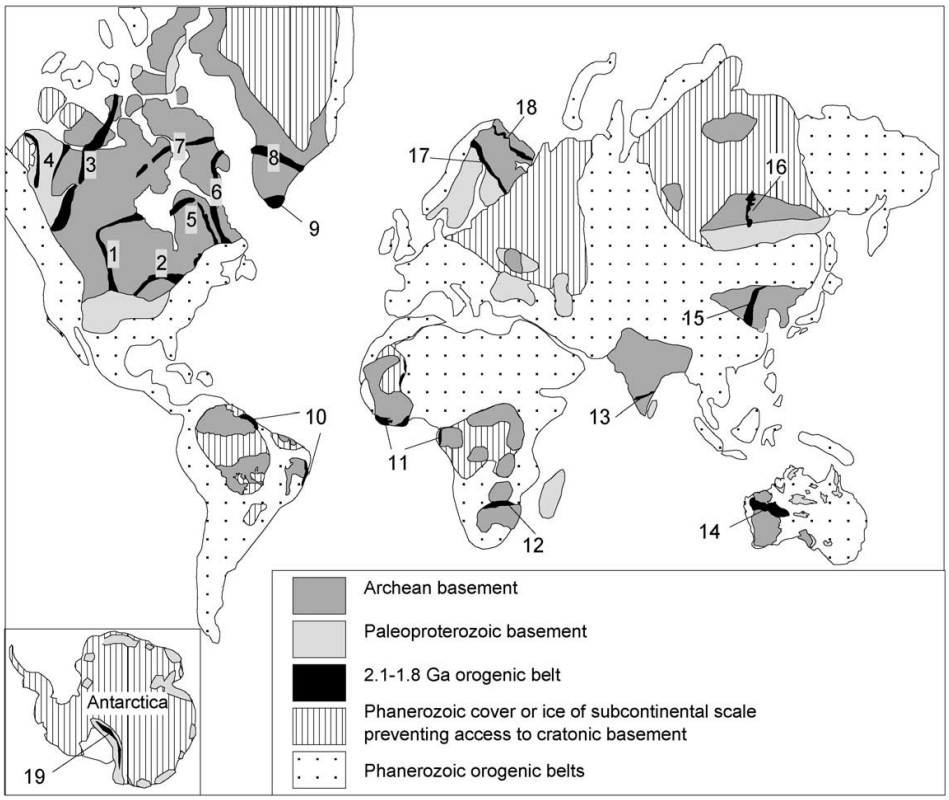

FIGURE 2.1: Sketch world map showing the spatial distribution of some of the 2.10–1.80 Ga orogens and associated cratons (Zhao et al., 2002). The orogens are inferred to have been active during the inferred assembly of super-continent Columbia. 1 : Trans-Hudson Orogen ; 2 : Penokean Orogen ; 3 : Taltson - Thelon Orogen ; 4 : Wopmay Orogen ; 5 : Cape Smith -New Quebec Orogen ; 6 : Torngat Orogen ; 7 : Foxe Orogen ; 8 : Nagssugtoqidian Orogen ; 9 : Makkovikian-Ketilidian Orogen ; 10 : Transamazonian Orogen ; 11 : Eburnian Orogen ; 12 : Limpopo Belt ; 13 : Moyar Belt ; 14 : Capricorn Orogen ; 15 : Trans-North China Orogen ; 16 : Central Aldan Belt ; 17 : Svecofennian Orogen ; 18 : Kola-Karelian Orogen ; 19 : Transantarctic Orogen.

The subsequent Paleoproterozoic evolution is marked by the global distribution of 2.10–1.80 Ga accretionary and collisional orogens (Fig. 2.1). The latter are present on almost all cratons. They comprise both juvenile crustal domains and remobilised older rocks. They form linear or arcuate "mobile belts" suturing dis-

tinct Archean cratonic fragments (Zhao et al., 2002), and they are interpreted to reflect the Paleo- to Mesoproterozoic assembly of super-continent Columbia (Rogers and Santosh, 2002). This time period corresponds to a peak in the juvenile magmatic record, suggesting that crust preservation was favoured by the amalgamation of juvenile crust into the super-continent. The 2.10–1.80 Ga orogens include the Transamazonian orogen, which coincides with the main crustal growth episode on the South American platform (Almeida et al., 2000; Cordani and Sato, 1999; Sato and Siga Junior, 2002), the Trans-Hudson orogen in North America (Lewry et al., 1994; of Canada et al., 1990), the Svecofennian and Kola-Karelian orogens of northern Europe (Gorbatschev and Bogdanova, 1993; Nironen, 1997; Patchett et al., 1987), the Trans-North China orogen (Kusky and Li, 2003; Santosh, 2010; Trap et al., 2012; Zhao et al., 2005, 1998), the Akitkan and Aldan orogens of Siberia (Rosen, 2002), the Ubendian-Usagaran belts of eastern Africa (Kazimoto et al., 2014; Lenoir et al., 1994), that preserve some of the oldest large eclogite-facies rock units on Earth (Collins et al., 2004), etc. Orogenesis is associated to the recycling of crustal material of Archean and Siderian ages in magmatic sources (Pehrsson et al., 2013). Dome and keel "archaic" strain patterns are reported from some Paleoproterozoic "hot" orogens (Cagnard et al., 2007; Trap et al., 2008; Vidal et al., 2009), while in other belts the deformation mode is described as "transitional" between Archean- and modern-type tectonics (Cagnard et al., 2011). The role of subduction in the evolution of Paleoproterozoic orogens is supported by the presence of eclogites and high-pressure granulites which match relatively cold apparent geotherms. The high-P metamorphic rocks coexist with low pressure granulite - UHT metamorphic rocks, and this dual metamorphic record is similar to what is seen in Proterozoic belts in general.

The peak in geological activity during the inferred assembly of Columbia is then followed by another period of relative quiescence until *ca.* 1.2 Ga. This is thought to reflect a period of super-continent stability before it disagregated. At *ca.* 1.2 Ga, a new cycle of super-continent destruction and assembly initiated and led to the formation of Rodinia (Li et al., 2008). This specific, cyclic, geological record is interpreted by a large body of research to be representative of Proterozoic plate tectonics, i.e. a geodynamic regime which is similar, but not strictly equivalent, to modern plate tectonics.

2.2 The West African Craton : Archaic geodynamics extending into the Paleoproterozic ?

The Paleoproterozoic West African Craton is a unique feature of the Paleoproterozoic Earth. It forms a vast and wide continental domain (about $3.10^6 km^2$) which accounts for significant juvenile crust addition after the Archean - Proterozoic boundary, and before the stabilisation of the the first Paleoproterozoic super-continent. The timing of its formation suggests that it may hold key information on the geodynamic changes of the Archean-Proterozoic transition.

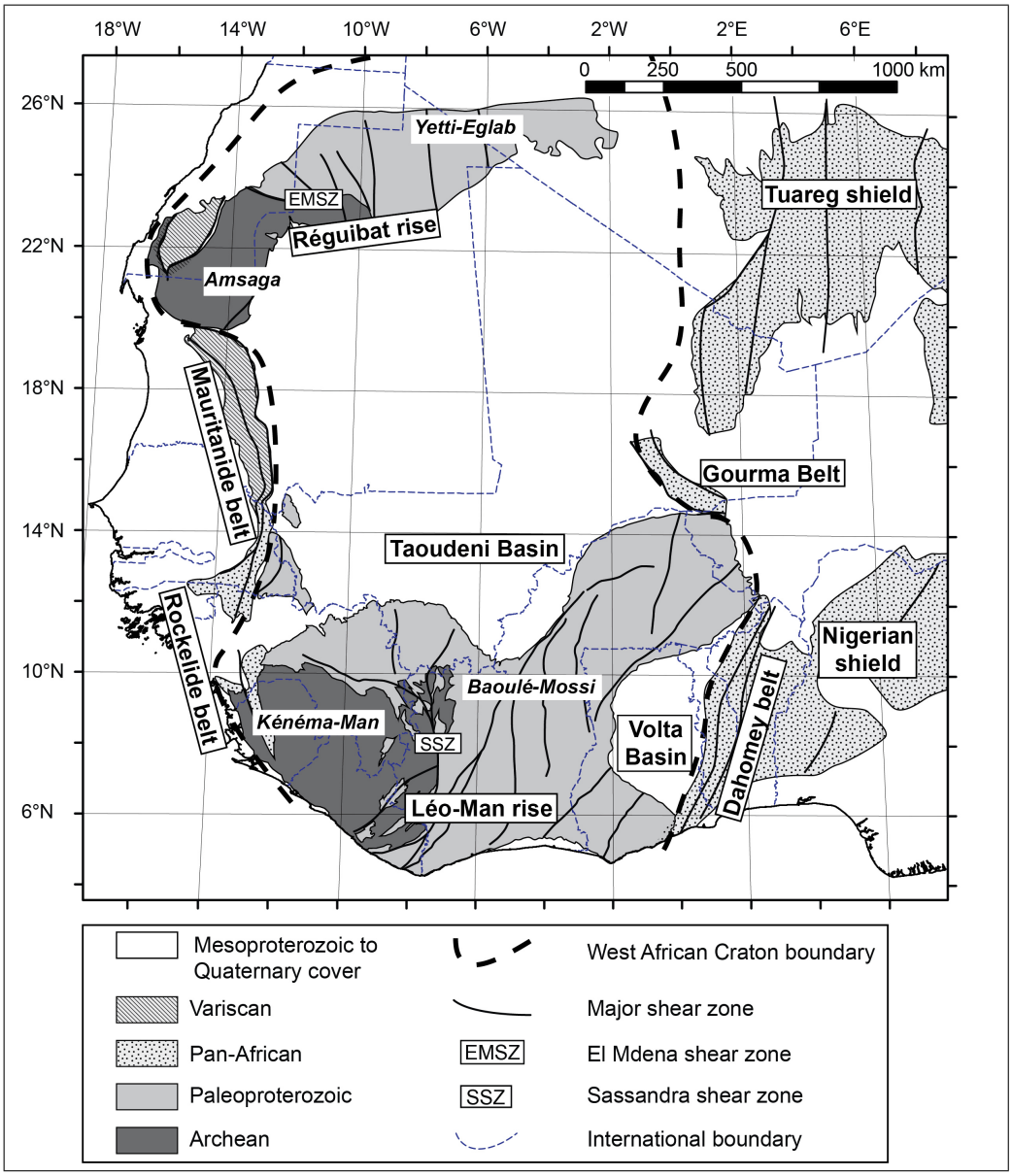

FIGURE 2.2: Simplified geological map of the West African Craton and of surrounding geological provinces

2.2.1 Geological setting

The West African Craton forms the basement of western and north-western Africa (Bessoles, 1977; Rocci et al., 1991). It crops out in the Reguibat rise, across southern Morocco - Western Sahara, Mauritania and southern Algeria. It extends to the south below the Neoproterozoic sedimentary cover of the Taoudeni basin. It is also exposed in the Kayes and Kedougou-Kenieba inliers of eastern Senegal and Mali, and in the Leo-Man rise, from the Sahelian regions of Niger, Togo, Burkina Faso, Guinea and Mali down to the Atlantic coast of Sierra Leone, Liberia, Côte d'Ivoire and Ghana. To the south-east, the craton is covered by the Neoproterozoic sedimentary rocks of the Volta basin. The São-Luis craton of north-eastern Brazil

and the North Guyana trough of French Guyana are considered to form fragments of the West African Craton, which were rifted apart during the opening of the Atlantic ocean in the Jurassic (Klein and Moura, 2008; Ledru et al., 1994; Vanderhaeghe et al., 1998). The West African Craton is bounded to the north by the Pan-African anti-Atlas mountain belt. To the west, it is limited by the N-S trending Rockelide and Mauritanide belts, which formed in the Neoproterozoic during the Pan-African orogenic event, and which were variably re-activated during the Variscan orogeny. The eastern margin of the craton is overprinted by the Pan-African Dahomeyan belt in equatorial and sahelian Africa, which forms the transition with the Nigerian shield. In saharan Africa, the West African Craton is reworked during the Pan-African orogeny in the Hoggar province of the Tuareg shield and in the Gourma belt. The São-Luis craton is bounded to the south by the Gurupi belt, which also contains reworked cratonic rocks and which belongs to the Pan-African / Braziliano orogenic system.

The West African Craton comprises both Archean and Paleoproterozoic domains. The Archean nuclei are represented by the Amsaga domain in the western Reguibat rise (Barrere, 1967), and by the Kénéma-Man domain (Camil, 1984), in the western Leo-Man rise. They are made of migmatitic grey gneisses, TTG suites, charnokite and granite plutons, greenstone belts and banded iron formations (BIFs). A 3.60–3.40 Ga crustal growth event is shown by the crystallisation ages of ancient gneisses and inherited zircons, and is confirmed by 3.60–3.20 Ga Nd model ages from magmatic zircons (Auvray et al., 1992; Chardon, 1996; Kouamelan et al., 1997; Potrel et al., 1998, 1996; Thiéblemont et al., 2001). Thiéblemont et al. (2004) argue that the ancient crust of the Kénema-Man domain was reworked by two successive orogenic cycles, i.e. the 3.25–3.05 Ga Leonian cycle and the *ca.* 2.90–2.80 Ga Liberian cycle. The Leonian event is coincident with abundant juvenile TTG plutonism, greenstone belt emplacement, and with the deposition of quartzites and banded iron formations. The Liberian cycle is responsible for a tectono-metamorphic overprint under granulite-facies metamorphic conditions, coeval with charnokite and granite intrusions (Kouamelan et al., 1997; Thiéblemont et al., 2001). It is followed by the development of late-stage basins comprising volcano-sedimentary rocks and quartzites (Thiéblemont et al., 2001). The Amsaga domain followed a similar evolution, with juvenile crust addition documented until *ca.* 3.00 Ga (Potrel et al., 1998). However, unlike in the Kénéma-Man domain, the available isotopic data does not allow to identify two discrete cycles. Juvenile TTG suites formed between 3.05 and 2.80 Ga, charnokite plutons and granulite-facies metamorphism are dated between 3.00 and 2.95 Ga, while late-stage granites intrude both Archean domains at *ca.* 2.70 Ga (Key et al., 2008; Montero et al., 2014; Schofield et al., 2012). In terms of metallogeny, the Archean craton contains abundant BIF-hosted iron ore reserves along with Ni-Co, Cr and minor PGE mineralisations in mafic to ultramafic units. Gold deposits (stratabound or hydrothermal) are relatively scarce (Milési et al. (1992) and refs. therein).

The Paleoproterozoic rocks of the West African Craton are found in the Yetti and Eglab domains, in the central and eastern portions of the Reguibat rise ; in the Baoulé-Mossi domain, which forms the eastern portion of the Leo-Man rises, and in the Kayes and Kenieba inlyers (Bessoles, 1977). They are made of granite-gneiss terranes, dominated by grey gneisses and TTG plutons, which alternate with nar-

row greenstone belts, wide volcano-sedimentary "basins" and younger fluvio-deltaic sedimentary basins. The supracrustal rocks of greenstone belts and of the volcano-sedimentary basins belong to the Birimian Supergroup (Attoh and Ekwueme, 1997; Junner, 1940; Kitson, 1928; Sylvester and Attoh, 1992). The greenstone belts comprise bimodal metamorphosed lavas and volcanoclastic rocks, i.e. tholeiitic basalts along with calc-alkaline lavas ranging from basalts to rhyolites (e.g Baratoux et al. (2011); Leube et al. (1990); Lompo (2009); Pouclet et al. (2006)). They also include small proportions of volcanogenic sediments, greywacke and manganese-rich cherts (Melcher, 1995). Volcano-sedimentary basins are dominated by shales and greywacke that are in some places intercalated with stratiform Mn deposits (e.g. Nsuta and Tambao in Ghana and Burkina Faso respectively), Zn-Ag sulfide deposits (Perkoa in Burkina Faso, Schwartz and Melcher (2003)) and porphyry Cu deposits (Gaoua, Burkina Faso). Carbonates are rare and limited to the Daléma basin of Sénégal, where diorite intrusions formed skarns hosting iron mineralisations (Schwartz and Melcher, 2004). The top of the Paleoproterozoic stratigraphic pile is made of fluvio-deltaic formations : polymict immature sediments, arkoses, quartzites and conglomerates which mostly occur in strongly-deformed, fault-bounded syn-tectonic basins of limited extent (Ledru et al., 1994). They are not necessarily correlated and may be diachronous from one belt to the other. In the Baoulé-Mossi domain, and specifically in southern Ghana, the late-stage Tarkwa basin served as a reference for the Tarkwaian stratotype (Bossière et al., 1996; Junner, 1940). It is folded and tectonically juxtaposed against Birimian rocks of the Ashanti greenstone belt (Perrouty et al., 2012). Contrastingly, in the Eglab domain of the Reguibat rise, the immature sediments of the Guelb el Hadid formation are found in a wide undeformed, post-tectonic basin and lay discordantly on the igneous and metamorphic basement (Bessoles, 1977).

Whole rock Nd isotopy carried out on magmatic rocks across the craton, and Hf isotopy of detrital zircon collected in adjacent basins all point to a juvenile source for the Paleoproterozoic continental crust (Abati et al., 2010; Abouchami et al., 1990; Boher et al., 1992; Doumbia et al., 1998; Gasquet et al., 2003; Klein et al., 2005; Klein and Veloso Moura, 2001; Peucat et al., 2005; Tapsoba et al., 2013). This suggests that the TTG suites and granites forming most of the crust were generated shortly after their mafic source-rock was extracted from the depleted mantle, between 2.50 and 2.25 Ga. Across the craton, crystallisation ages of inherited zircon grains in magmatic and sedimentary rocks provide evidence for crustal growth as early as *ca.* 2.30 Ga (e.g. Gasquet et al. (2003)), while the oldest volcanic and plutonic rocks recognised thus far have ages of 2.25 Ga (Tshibubudze et al., 2013) (Fig. 2.3). Most greenstone belts contain lavas and volcanoclastic rocks which erupted between 2.25 and 2.18 Ga (Fig. 2.3 ; Duodu (2009); Feybesse et al. (2006); Hirdes et al. (1996); Hirdes and Davis (1998), in Ghana ; Schwartz and Melcher (2003) in Burkina Faso ; Delor and d'Ivoire (1995) in Côte d'Ivoire ; Lahondère et al. (2002) in Guinea). Volcanic activity is coeval with the formation of early TTG suites (Fig. 2.3, Dia et al. (1997); Gueye et al. (2008), in Senegal ; De Kock et al. (2011); Feybesse et al. (2006), in Ghana ; (Tshibubudze et al., 2013), in Burkina Faso, (Peucat et al., 2005), in Algeria). Subsequently, TTGs and lavas are emplaced continuously until *ca.* 2.10 Ga, although volcanism is apparently less widespread and diachronous from one belt to another. Significant magmatism younger than 2.10 Ga is spatially

restricted to the western portions of the Baoulé-Mossi domain, to the Eglab massif of the Reguibat rise, and to the contact zones with the Archean craton (Davis et al. (1994); De Kock et al. (2011); Doumbia et al. (1998); Duodu (2009); Gasquet et al. (2003); Hirdes et al. (1992, 1996); Kouamelan (1996); Oberthür et al. (1998); Peucat et al. (2005); Tapsoba et al. (2013). The latter is overprinted and recycled during a 2.10–2.06 Ga thermal event, as evidenced by the resetting of geochronometres and the intrusion of Paleoproterozoic granites along the margins of the Kénéma and Amsaga domains (Egal et al., 2002; Kouamelan et al., 1997; Schofield et al., 2006; Thiéblemont et al., 2004).

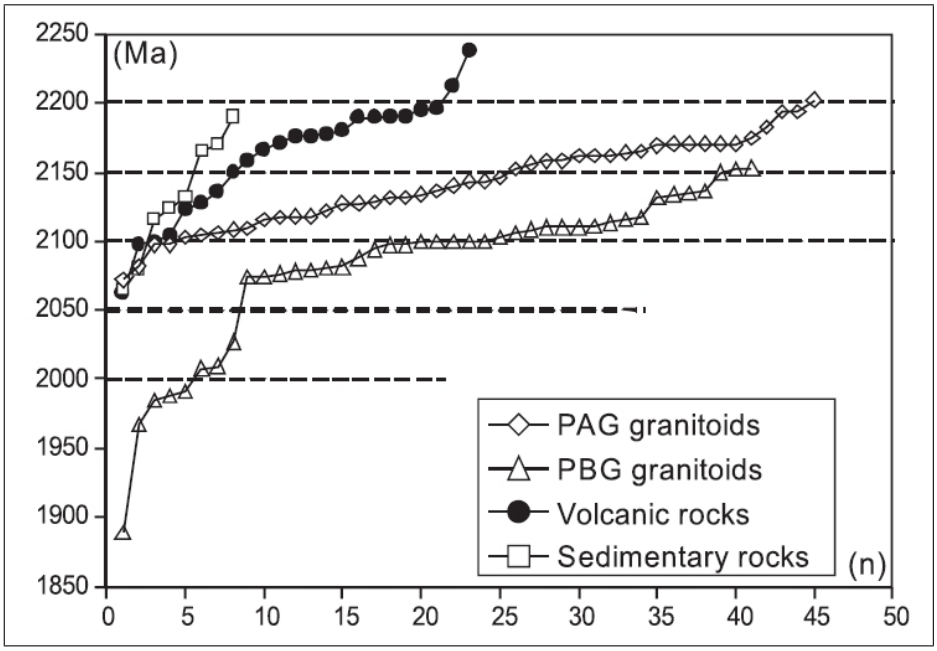

FIGURE 2.3: Timeframe showing the crystallisation or deposition ages of magmatic and sedimentary rocks on the Paleoproterozoic West African Craton (Lompo, 2009). PAG and PBG respectively designate granitoids where the dominant ferromagnesian mineral phase is amphibole or biotite. PAG and PBG loosely correlate with TTG suites and monzograintes/granites respectively. The magmatic evolution of the craton apparently lasted less than 200 Ma. The youngest ages (<2050 Ma) were obtained with isotopic techniques which are now considered to be imprecise (e.g. whole rock Rb-Sr ages).

The Paleoproterozoic domains underwent distributed deformation and were assembled together during the Eburnean orogeny (Bonhomme, 1962). The Eburnean orogeny approximately lasts from 2.15 to 2.07 Ga. It causes craton-wide metamorphism, shapes the main architectural features of the Paleoproterozoic domains, such as craton-scale shear zones, and it is responsible for the juxtaposition of various litho-tectonic terranes (Baratoux et al., 2011; Eisenlohr and Hirdes, 1992; Feybesse et al., 2006; Milési et al., 1989, 1992; Perrouty et al., 2012; Tagini, 1971; Vidal et al., 2009). The Eburnean orogeny is classically described as consisting of a first episode of transpressive tectonics, crustal thickening and greenschist- to granulite-facies metamorphism ; followed by a second phase of transcurrent to transtensive tectonics,

exhumation and retrogression (Caby et al., 2000; Debat et al., 2003; Galipp et al., 2003; Ganne et al., 2012; Jessell et al., 2012; Ledru et al., 1994, 1991; Liégeois et al., 1991; Pitra et al., 2010). During the Eburnean orogeny, the Paleoproterozoic craton was eventually juxtaposed against the Archean nucleus to form a large stable landmass by *ca.* 2.10 Ga. The contact zone between both age domains is marked by the transitional Sfariat migmatite belt and by the El Mdena shear zone in the Reguibat rise, and is marked by a plutonic belt along the Sassandra shear zone at the margin of the Kénéma-Man domain (Egal et al., 2002; Schofield and Gillespie, 2007).

During the late-stages of the Eburnean orogeny, the ubiquitous TTG magmatism locally gives way to smaller volumes of low-strain monzogranites, peraluminous and potassic granites, and to rare syenites (Dioh et al., 2006; Doumbia et al., 1998; Egal et al., 2002; Lompo, 2009; Naba et al., 2004). This evolution trend suggests an increasing involvment of metamorphosed igneous sialic or sedimentary rocks into magmatic sources as the crust gradually matured. The latest granitoid intrusions are thought to be coeval with syn- to late-orogenic epigenetic gold mineralisations hosted in Birimian and Tarkwaian rocks, and distributed in most provinces (e.g. Béziat et al. (2008); Milési et al. (1991, 1989)). In particular, southern Ghana is a major auriferous province, with the Obuasi and Tarkwa deposits of the Ashanti belt representing giant gold deposits. Most mineralisations hosted in Birimian rocks or at the contact with the overlying Tarkwaian sediments has a hydrothermal origin. They were formed during the late-stage reactivation of shear zones after the Eburnean orogenic paroxysm, and age constraints in southern Ghana indicate that they are younger than *ca.* 2105 Ma (White et al., 2014). The Tarkwaian sediments also bear placer gold deposits which were variably remobilised during subsequent hydrothermalism and deformation (Milési et al., 1991, 1992; Oberthür et al., 1998; Perrouty et al., 2012; Pigois et al., 2003; Tunks et al., 2004; White et al., 2014).

The West African Craton does not show any evidence of significant geodynamic evolution between 2.05 and 1.80 Ga, which corresponds to a period global orogenesis worldwide. The Eburnean orogeny rather represents a preliminary development of the geodynamic setting which led to the inferred assembly of super-continent Columbia. This suggests that the craton was stabilised earlier, and may have acted as a rigid block set at distance from Transamazonian mobile belts. However, the craton is reworked along all of its margins into Pan-African/Braziliano belts. The latter commonly expose vast granulitic domains of Eburnean age exhumed in the Neoproterozoic, which now form polycyclic domains within younger belts (Bendaoud et al., 2008; Bertrand and Caby, 1978; Bertrand and Jardim de Sá, 1990).

2.2.2 Controversies

2.2.2.1 Stratigraphic and tectonic correlations

The Paleoproterozoic West African Craton is vast and comprises juxtaposed domains of contrasting metamorphic conditions, that are sometimes poly-deformed. Questions that need to be adressed include : Is the Eburnean deformation coeval across the whole craton ? Did the craton undergo a monocyclic or a polycyclic evolution ? Can stratigraphic and tectonic correlations be established at the scale of the craton ?

One long running issue concerns litho-stratigraphic and tectonic correlations. Originally, Junner (1940) identified a lower Birimian group, mainly made of shales, greywacke and volcanoclastic rocks, overlain by an Upper Birimian group, dominated by lavas. Arnould (1961) and Tagini (1971) proposed a stratigraphic sequence that is the reverse of the former one. Bessoles (1977) acknowledged that lateral facies variations may cause confusions, and preferred to distinguish between narrow elongated volcano-sedimentary "troughs" and wider "basins". More recently, Milési et al. (1989) argued in favour of a discordance in the Birimian series : the lower Birimian rocks record an early deformation event that is not recognised in the "Bandaman" sediments (Hirdes et al., 1996), higher in the stratigraphic pile, which suggests a polycyclic tectonic evolution. This was also suggested in the Reguibat rise (Barbey, 1975) and further supported by Feybesse et al. (1990) in Burkina Faso, Ledru et al. (1991) in Mali, and De Kock et al. (2012); Perrouty et al. (2012) in Ghana, who proposed that rifting took place between two episodes of contractional to transcurrent deformation, and allowed for the deposition of upper Birimian sediments onto deformed lower Birimian rocks.

The polycyclic model presented above suggests that the Birimian rocks of greenstone belts were affected by two discrete deformation episodes. Other authors also recognised a polycyclic geological evolution, but that does not clearly match the former one : they claimed that an early orogenic cycle occurred *before* the emplacement of Birimian formations. This model was initially inspired from field relationships reflecting poly-phased structural-metamorphic fabrics in high-grade gneisses of Côte d'Ivoire and Burkina-Faso (Arnould, 1961; Bard and Lemoine, 1976). Historically, the high-grade composite gneisses were interpreted as the basement below the Birimain volcano-sedimentary rocks, and were thought to be of Liberian age. When it became evident that they were of Paleoproterozoic age, the gneisses were termed "Antebirimian" (Arnould, 1961; Bard and Lemoine, 1976; Roques, 1948; Sagatzky, 1954) or "Dabakalian" (Lemoine et al., 1990; Vidal et al., 1992). Dabakalian and Birimian formations are considered to be separated in time by an early deformation event affecting the basement, which is given various local names, such as "Tangaean" (Hein, 2010; Tshibubudze et al., 2009) or "Burkinian" (Lemoine et al., 1990; Tempier, 1986). They eventually were grouped under the general term of Eoeburnean (Baratoux et al., 2011; De Kock et al., 2011, 2012; Perrouty et al., 2012), designating the early tectonic evolution between 2.2 and 2.15 Ga, which is interpreted to take place before the Eburnean orogeny *s.s.*

Alternatively, another school of thought only recognises a single orogenic cycle. Leube et al. (1990) questions the validity of the Upper/Lower Birimian or belt/basin subdivisions, and suggests that the Birimian sedimentary, volcanoclastic and volcanic rocks are coeval and represent lateral facies variations controlled by the distance from volcanic centers. Geochronological and structural constraints led authors to discard the "Dabakalian" cycle and to suggest that strain patterns on the craton are the result of long-lived progressive deformation (Eisenlohr and Hirdes, 1992; Gasquet et al., 2003; Hirdes et al., 1996).

This controversy illustrates the difficulties of building tectonic and stratigraphic correlations across the craton. This task is most likely complicated by spatial variations and diachronism in geological processes, and requires detailed geochronological investigations.

2.2.2.2 Recognition and analysis of the tectonic and metamorphic records

The granite-greenstone domains of the craton are almost all metamorphosed to some extent. Metamorphic grade ranges from sub-greenschist to the granulite facies. Volcano-sedimentary sequences in greenstone belts generally reveal relatively low-grade metamorphic conditions, in the greenschist and amphibolite facies (Galipp et al., 2003; John et al., 1999; Klemd et al., 2002; Kříbek et al., 2008). Ortho- and paragneisses in belts or in granite-gneiss domains are frequently migmatitic. They underwent high-grade metamorphism in the amphibolite facies or at the transition with the granulite facies (Arnould, 1961; Bessoles, 1977; De Kock et al., 2011; Feybesse et al., 2006; Opare-Addo et al., 1993). Eburnean granulites (both high and low pressure) are described from the margins of the Paleoproterozoic craton, in the Hoggar shield and in the Kénéma-Man domain. This metamorphic diversity testifies of a wide range of apparent geothermal gradients, from cold, ~ 15 °C/km to hot > 40 °C/km geotherms (Ganne et al., 2012). U-Pb dating of the crystallisation of metamorphic monazite, zircon and titanite (mostly in Ghana) define a 2105-2080 Ma period (De Kock et al., 2011; Hirdes et al., 1996; Kouamelan et al., 1997; Oberthür et al., 1998), while a Sm-Nd garnet - whole rock isochron yields a *ca.* 2150 metamorphic age (Boher et al., 1992).

Nevertheless, comparatively few studies have used metamorphism as a constraint to explore the geodynamic mechanisms and tectonic processes controlling crustal evolution. Ganne et al. (2012) argue that low geothermal gradients recorded by rocks metamorphosed at the greenschist-blueschist facies transition are evidence for the development of modern-style subduction during craton formation. However, most studies interpret "above average" amphibolite-facies metamorphism in metasedimentary rocks as the result of contact metamorphism (Debat et al., 2003; Gasquet et al., 2003; Ndiaye et al., 1989; Vidal and Alric, 1994), or of doming due to the ascent of granitoid diapirs (Pons et al., 1995; Soumaila and Garba, 2006).

The author of this thesis feels that the metamorphic record of the West African Craton has not been sufficiently explored, and that this topic lacks a comprehensive approach, except for a few isolated studies (e.g. Ganne et al. (2012)). Metamorphic studies have the potential to provide new information which may help to discriminate between the monocyclic and polycyclic orogenic models presented above. If greenstone belts are discordant on older gneisses, then the high-grade metamorphic rocks should be older than the volcano-sedimentary protolith of the low-grade Birimian sequences. Conversely, if high-grade metamorphism is younger than the emplacement of Birimian supracrustals, then the latter may represent upper-crustal equivalents of exhumed lower-crustal gneissic layers. Furthermore, most of the metamorphic data obtained on the craton has not been interpreted within a larger tectonic and architectural framework. The distribution of metamorphic grades is not mapped, while arguments in favour of "subduction" or "collision" would need to be confronted with the spatial and temporal evolution of metamorphism.

A number of factors may have caused the current gaps in our knowledge. Until the 1980s, migmatitic rocks were accurately described in granite-gneiss terranes, but much less so in the recent years, when attention shifted to (gold bearing ?) greenstone belts and mineralising systems. This is clear in many regional or national maps presenting "locally migmatitic" granite-gneiss domains, sometimes "undiffe-

rentiated", e.g. Castaing et al. (2003). The lack of interest in lower-crustal rocks, and maybe to some extent, the development of common beliefs on craton metamorphism, have led to the erroneous interpretation of field observations. Gneisses displaying migmatitic textures presented in photographs are interpreted as *"syntectonic to late-tectonic granites [...] (no reworked gneisses or migmatites)"* (Gasquet et al., 2003).

In addition, the contact metamorphism model is frequently invoked without sufficient care or criticism. Vast portions of the central Sefwi belt display upper-amphibolite to granulite facies assemblages. Hirdes et al. (1993) describe them as being in the "upper greenschist to amphibolite facies range", with a minimum metamorphic temperature of 420 °C, based on the presence of garnet + biotite. In order to explain the relatively high metamorphic grade and the "granitised" gneissic texture, the authors suggest that the whole metamorphic terrane is *"underlain at shallow depth by a K-feldspar-rich granitoid pluton that pierces the metamorphic assemblage in areas of updoming. The roof of this pluton probably lies only a few tens of meters below the present land surface and influence of the intrusion is ubiquitous in the field"*. Similarly, Caby et al. (2000) suggest that granulites are formed due to magma intrusions, while they more likely represent the source rocks of granitoid magmas. In most cases, the hypothesis of regional anatexis is not envisaged despite abundant evidence.

Similarly to what is seen on Archean cratons, many studies interpret the tectonic pattern of the Paleoproterozoic West African Craton as the result of doming, diapirism and homogeneous thickening of the crust in a "weak-type" orogen (Caby et al., 2000; Lompo, 2009; Pons et al., 1995; Pouclet et al., 2006; Soumaila and Garba, 2006; Vidal et al., 2009). This view conflicts with another interpretation, according to which the Paleoproterozoic domains were assembled during thrusting and nappe stacking (Feybesse et al., 2006; Milési et al., 1989, 1992). In particular, it is suggested that Paleoproterozoic rocks were thrust onto the foreland of an Archean indenter during the Eburnean orogeny (Billa et al., 1999; Feybesse and Milési, 1994). The Paleoproterozoic Kediat Idjil and El Mahaoudat outliers of the Amsaga domain (Schofield and Gillespie, 2007), and the Ity-Toulepleu unit of the Kénéma-Man domain (Triboulet and Feybesse, 1998), are interpreted to represent allochtonous units transported by nappes over the Archean autochtonous (Schofield and Gillespie, 2007). However, the latter is considered to be an Eburnean complex intrusive in Archean country rock by Kouamelan et al. (1997). The metamorphic overprint along the margin of the Archean craton is consistent with crustal thickening, but it may be accounted for by homogeneous thickening rather than by nappe stacking (Pitra et al., 2010).

The diversity of the metamorphic record suggests that the thermal regime of the crust varied, possibly both in space and time. This means that the mechanical properties of the crust may also have changed in space and time. Therefore, analyses of the tectonic style should be coupled to metamorphic and geochronological constraints.

2.2.2.3 Continental growth : where is the subduction ?

The available isotopic data consistently demonstrates the juvenile character of the Paleoproterozoic craton, suggesting that the source of the magmatic rocks did

not include any older recycled continental crust. However, the magmatic processes responsible for the extraction of the crust from the mantle are still debated. Geodynamic scenarios invoked for its formation range from magmatic accretion in an oceanic plateau setting (Abouchami et al., 1990; Boher et al., 1992; Lompo, 2009) to lateral accretion in volcanic island arcs (Ama Salah et al., 1996; Attoh and Ekwueme, 1997; Dampare et al., 2008; Sylvester and Attoh, 1992), and to continental rifting of a volcanogenic "proto-crust" (Leube et al., 1990). The craton "protolith" was then reworked during orogeny.

Both tholeiitic and calc-alkaline volcanic rocks and associated intrusives of various ages coexist in greenstone belts across the craton (Baratoux et al., 2011; Hirdes et al., 1996; Pouclet et al., 2006). Basalts frequently form the lower portions of greenstone belt stratigraphy and show evidence of subaqueous emplacement (Abouchami et al., 1990; Béziat et al., 2000; Pouclet et al., 2006). They have diverse geochemical characteristics that are similar to a wide range of modern rocks formed in oceanic island arcs or oceanic plateaus (Lompo, 2009). Dampare et al. (2008) describe basalts displaying subduction-related trace element characteristics, and claim that the compositions of calc-alkaline lavas are consistent with generation in volcanic island arc, back-arc and fore-arc environments. To reconcile both end-member models (intra-oceanic island arc *vs.* oceanic plateau), some authors suggest that multiple processes intervened in the genesis of the craton, which may be derived from the combined accretion of volcanic arcs and of an oceanic plateau that underwent differentiation during orogenesis (Béziat et al., 2000; Lompo, 2009). In any case, geochemical arguments alone apparently do not provide sufficient constraints to confidently identify the geodynamic sites of Paleoproterozoic crust production.

The role played by subduction in the accretion and orogenesis is also ambiguous. Most of the literature interprets the ubiquitous TTGs and associated lavas as products of hydrous slab melting in a subduction setting (e.g. Baratoux et al. (2011); Egal et al. (2002); Peucat et al. (2005); Pouclet et al. (2006); Sylvester and Attoh (1992)). Cold apparent geothermal gradients are recorded in metamorphic rocks from a greenstone belt in Burkina Faso (Ganne et al., 2012), and ultramafic-mafic formations in the Dixcove belt of Ghana described by Attoh et al. (2006) are thought to represent ophiolite fragments. All these interpretations suggest that litho-tectonic domains that form the craton were accreted in a geodynamic setting controlled by subduction (e.g. Baratoux et al. (2011); Ndiaye et al. (1997)). However, many field and architectural characteristics of the craton cannot easily be reconciled with a model of subduction-driven tectonic accretion. First and foremost, there are no clear age gradients across sets of parallel elongated greenstone belts. The 2.25-2.18 Ga rocks forming the oldest age group on the craton are found scattered everywhere from Senegal to Ghana and Algeria. The age of the latest magmatic rocks youngs from east to west on the Baoulé-Mossi domain (Hirdes and Davis, 2002), but no such trend can be found in the Yetti-Eglab domain (Peucat et al., 2005; Schofield et al., 2006), while the litho-tectonic units are oriented N-S to NE-SW in both areas. Therefore, no clear age pattern seems to emerge from available geochronological studies, and the age distribution does not support a model of lateral juvenile terrane accretion. Proposed suture zones are ambiguous, as is the significance of major crustal discontinuities (Hirdes et al., 1996). Furthermore, no metamorphic zoning (Hyndman et al., 2005) similar to that found in modern

subduction-related orogenic belts has been recognised thus far.

2.3 Synthesis & aims of the present thesis

The Paleoproterozoic West African Craton displays many lithological and architectural similarities with Archean cratons. These similarities include the abundance of TTGs, the typical granite-gneiss - greenstone alternations, the occurrence of bimodal tholeiitic and calc-alkaline volcanism, the orogenic gold endowment, the VMS and porphyry copper deposits, the high proportion of volcanogenic sediments in syn-tectonic sedimentary basins, the apparent wide-scale homogeneity in metamorphic grades, strain, and deformation styles. This suggests that the geodynamic processes which generated the West African Craton shared some similarities with those at work during the Archean. Therefore, the scientific controversies concerning the West African Craton recall the debates on Archean geodynamics. Was the continental crust formed in a plate-tectonics setting ? How did it differ from modern-day geodynamics ? What were the sites of crustal growth ? What processes controlled the evolution of orogens ? Etc.

However, the geological record of the Paleoproterozoic West African Craton is not strictly similar to that of Archean cratons. Komatiites and banded iron formations are absent from the Birimian greenstone belts. Supracrustal formations comprising abundant shales and greywacke occur in "basins" that cover most of the southern Baoulé-Mossi domain. They represent higher surface proportions than on most Archean cratons. The metamorphic record comprises high-pressure granulites and preserves rocks that record relatively low geothermal gradients. This raises the question as to what are the secular evolutions in Earth dynamics responsible for the changing rock record between the Archean and Paleoproterozoic ?

Finally, the Paleoproterozoic West African Craton represents a major juvenile crust input to the continental masses, that lies in between two major crust preservation events, at 2.70-2.60 Ga, and 2.10-1.80 Ga. If the cyclicity of crust production and preservation is due to plate tectonics, as suggested by many authors, then what is the significance of a discrete crustal growth event at 2.30-2.10 Ga ? Does it testify of the local perpetuation of "archaic" geodynamic phenomena, on a planet otherwise dominated by some sort of plate tectonics ? Did non-plate geodynamics coexist or alternate with a Proterozoic plate tectonics regime ?

As seen in the previous section, the reconstruction of ancient geodynamic regimes is an under-constrained problem. For this reason, bringing some new information to these questions requires acquiring and synthesising multiple complementary datasets. In order to do so, this thesis combines evidence obtained from field mapping with information retrieved from regional metamorphic, structural, geochronological and geochemical data. My interest focuses on the geodynamic evolution of the Paleoproterozoic terranes located in northern Ghana.

Chapitre 3

The geology and tectonic evolution of northern Ghana

Introduction (en français)

Le chapitre 3 est consacré à l'étude de la géologie régionale paléoprotérozoïque du nord-ouest du Ghana. Il se présente sous la forme d'une publication soumise à la revue scientifique internationale *Precambrian Research* le 03/12/2014. L'étude propose une reconstruction de la séquence des événements de déformation et de l'histoire tectonique du nord du Ghana. Les critères de chronologie relative observés sur le terrain permettent de dater la formation de certaines roches magmatiques et métamorphiques par rapport aux épisodes de déformation. La datation U–Pb de monazites et de zircons crystallisés dans ces roches est utilisée pour en déduire l'âge et la durée absolus des différentes déformations. Certaines données métamorphiques présentées dans le chapitre 4 sont également utilisées pour contraindre l'évolution tectonique. Les différents jeux de données sont analysés pour discuter un modèle d'évolution tectono-métamorphique du nord du Ghana, et pour étudier la nature des processus géologiques ayant dominé l'orogenèse Éburnéenne dans la région. La tectonique éburnéenne est comparée aux caractéristiques tectonique des orogènes plus anciens (archéens) et plus récents (phanérozoïques), afin de situer la géodynamique en vigueur sur le Craton Ouest Africain dans l'évolution séculaire de la Terre.

Résumé

Cet article présente une nouvelle carte lithologique, métamorphique et structurale des domaines Paléoprotérozoiques (2.25-2.00 Ga) du Craton Ouest Africain au nord du Ghana. Elle est issue de l'interprétation de relevés géophysiques aéroportés, incluant des données de susceptibilité magnétique, de radiométrie et électromagnétiques (disponibles en annexe), ainsi que de données lithologiques et structurales de terrain. L'étude révèle que le nord du Ghana comprend des domaines métamorphiques contrastés. Des gneisses de haut grade et des ceintures volcano-sédimentaires de bas grade, séparés par des zones de cisaillement, ont été amalgamés lors de l'orogenèse Eburnéenne (2.15-2.07 Ga). Des roches volcano-sédimentaires ou intrusives ont subi un enfouissement et un métamorphisme à des conditions correspondant à la transition entre les faciès amphibolite et granulite. Cet épisode métamorphique coïncide avec une phase de déformation D1, qui correspond à un raccourcissement orienté N-S, et qui a produit des chevauchements. Par la suite, des détachements se sont formés dans un contexte d'extension N-S (D2) et ont mis en contact de part et d'autre des unités de haut et de bas degré métamporphique. Les structures formées pendant D1 et D2 ont ensuite été déformées au cours d'un raccourcissemsnt E-O, couplé à un étirement dans une direction N-NNE (D3), et synchrone d'un métamorphisme en faciès amphibolite. Les contractions D1 et D3 se traduisent par une déformation pénétrative et distribuée à l'échelle régionale. Par la suite, le raccourcissement E-O se poursuit et la déformation se localise progressivement dans plusieurs générations de zones de cisaillement décrochantes (D4-D7), qui réactivent parfois des accidents tectoniques hérités. Des datations U-Pb sur zircon et sur monazite de roches magmatiques et métamorphiques démontrent que les événements D1 à D3 forment un continuum de déformation qui s'étend entre 2140 et 2110 Ma.

Le changement du style tectonique dans la croûte entre D1 et D3 est interprété

comme reflétant la transition d'un mode de déformation déterminé par des forces tectoniques compressives aux limites, à un régime où forces tectoniques et forces gravitaires interagissent et se compensent. La prédominance croissante des forces gravitaires entraîne l'exhumation de portions de la croûte inférieure migmatitique au sein d'un dôme anatectique. La croissance du dôme est accommodée par le glissement latéral des unités de la croûte supérieure le long de détachements, dans un contexte localement extensif ; et est amplifiée par un raccourcissement synchrone orthogonal à la direction d'étirement. La rotation soudaine des directions de raccourcissement entre D1 et D3 traduit un changement des conditions mécaniques et des forces exercées aux limites de l'orogène. L'hypothèse d'une collision entre le compartiment crustal formant le nord du Ghana et celui qui constitue le sud du Burkina Faso est envisagée pour expliquer la mutation du régime tectonique dans l'orogène. Cette hypothèse est soutenue par des arguments cartographiques. Le nord-ouest du Ghana se situe à l'interface d'un domaine occidental (sud-ouest du Burkina Faso) et un domaine oriental (nord du Ghana et est du Burkina Faso), qui diffèrent par leurs caractéristiques métamorphiques, leurs évolutions tectoniques et par l'orientation des grandes failles et des ceintures de roches vertes structurant la croûte. Celles-ci se rejoignent au niveau d'une zone d'interférence où les gneisses de haut grade sont exhumés.

L'orogenèse Éburnéenne au nord du Ghana présente des enregistrements métamorphiques et structuraux qui ne ressemblent pas strictement au registre des cratons archéens. Le comportement rhéologique et le régime thermique déduits de cette étude rappellent en certains aspects les chaînes de montagnes du Protérozoique ou du Phanérozoique. L'évolution géodynamique éburnéenne ne semble pas correspondre à un modèle de croûte "chaude" et rhéologiquement faible. Ces conclusions suggèrent que la géodynamique paléoprotérozoique en Afrique de l'Ouest revêt un caractère transitoire entre un régime "archaïque" et la géodynamique moderne ; reflètant probablement le mode de fonctionnement d'une forme précoce de tectonique des plaques.

3.1 Introduction

Chapter 3 focuses on the regional Paleoproterozoic geology of northern Ghana. It presents and interprets airborne geophysical data (that are available in the appendix 3.2.9.2 at the end of the chapter), along with field lithological and structural information collected during the successive field campaigns. It also presents a new lithological map. The production of this map represented one of the main initial objectives of the PhD thesis.

The regional geological study presented here is a version that was submitted for publication to *Precambrian Research* on 03/12/2014. This publication aims to explore the deformation sequence and the tectonic evolution of northern Ghana. In order to constrain the timing and duration of deformation, U-Pb dating was performed on zircon and monazite grains from rocks whose formation ages relative to the deformation sequence could be established, on the basis of cross-cutting relationships. Some of the metamorphic constraints that are presented in Chapter 4 are also mentioned. The various datasets are combined to discuss the nature, the duration and the evolution of the tectonic processes that dominated the Eburnean orogeny in northern Ghana. The tectonic development of the Eburnean orogeny is compared to both older - Archean - and younger - Phanerozoic orogenic belts, so as to tentatively identify some tectonic characteristics of the Archean-Proterozoic transition.

3.2 Lower crust exhumation during Paleoproterozoic (Eburnean) orogeny, NW Ghana, West African Craton : interplay of coeval contractional deformation and extensional gravitational collapse.

Sylvain Block[1], Mark Jessell[2], Laurent Ailleres[3], Lenka Baratoux[3,5], Olivier Bruguier[4], Armin Zeh[6], Delphine Bosch[4], Renaud Caby[4], Emmanuel Mensah[7]

[1] *Géosciences Environnement Toulouse, Observatoire Midi Pyrénées, 14 ave E. Belin, 31400, Toulouse, France*
[2] *Center for Exploration Targeting, The University of Western Australia, 35 Stirling Highway, Crawley, Perth, Western Australia 6009*
[3] *Monash University, School of Geosciences, Wellington Road, Clayton, Vic 3800, Australia*
[4] *Géosciences Montpellier, Université Montpellier 2-CNRS, cc 066, Place Eugène Bataillon,34095 Montpellier Cedex 5, France*
[5] *IFAN, Cheikh Anta Diop, Dakar, Senegal*
[62] *Institut für Geowissenschaften, Altenhöfer Allee 1, D-60438 Frankfurt am Main, Germany*
[7] *Geological Survey Department of Ghana*

Abstract

We present a new litho-structural and metamorphic map of the Paleoproterozoic (2.25-2.00 Ga) West African Craton in northern Ghana, based on the interpretation of field observations and airborne geophysical datasets. It reveals contrasting metamorphic domains consisting of high-grade gneisses and low-grade volcano-sedimentary belts, separated by shear zones and assembled during the Paleoproterozoic Eburnean orogeny (2.15-2.07 Ga). Supracrustal rocks and intrusives were buried and metamorphosed at conditions corresponding to the amphibolite-granulite facies transition, during a (D1) deformation event consistent with N-S horizontal shortening that generated reverse shear zones. High and low metamorphic grade rocks were brought in contact along extensional shear zones formed during N-S extension (D2). These structures are overprinted by contractional deformation associated with E-W shortening and N to NNE stretching (D3), coeval with amphibolite-facies metamorphism. Late-stage tectonic evolution (D4-D7) consists of strain localisation in successive generations of narrow shear zones, and re-activation of inherited structures in a dominantly transcurrent regime. U-Pb dating of zircon and monazite from magmatic and metamorphic rocks reveals that D1-D3 deformations form a continuous and overlapping time sequence between *ca.* 2140 and 2110 Ma. The change in deformation style from D1 to D3 is interpreted to reflect a shift from dominant horizontal tectonic forces to an interplay between tectonic and gravitational forces, which allowed for the exhumation of the lower crust in anatectic migmatite

domes. We suggest that doming is accommodated by lateral extensional sliding of the upper crust and amplified by coeval orthogonal shortening. The abrupt rotation of shortening directions points to a change in boundary conditions applied to the orogen. We hypothesise that it is due to the collision of northern Ghana with the Paleoproterozoic province in modern-day south-western Burkina Faso, which shows contrasting litho-tectonic features. The results reveal that the Eburnean orogeny in NW Ghana shared some thermo-mechanical similarities with modern orogenic belts. The findings bring new insight in Paleoprotezozoic plate tectonics, at the transition between archaic and modern geodynamics.

Keywords : Paleoproterozoic, West African Craton, Anatectic dome, Collision, Archean-Proterozoic transition

3.2.1 Introduction

The applicability of the plate-tectonics paradigm to the early Earth is subject to much controversy, due to divergent interpretations derived from observations carried out on Archean cratons (Cawood et al., 2009; Condie and Kröner, 2008; De Wit and Ashwal, 1997; Pease et al., 2008; Windley, 1992). Granite-greenstone terranes, made of TTG (tonalite, trondhjemite, granodiorite) suites, alternating with elongated volcano-sedimentary belts, exposing large surfaces affected by homogeneous, distributed strain, and transect by craton-scale strike-slip shear zones, have in turns been described as the result of "modern-style" subduction-driven plate tectonics, dominated by lateral displacements (Cawood et al., 2006; Condie and Benn, 2006; Condie and Kröner, 2008; de Wit, 1998; Kusky and Polat, 1999) ; or as a consequence of "archaic" geodynamic processes, dominated by body forces and vertical displacements (Hamilton, 1998, 2003; Stern, 2005; Van Kranendonk et al., 2004, 2007). The literature contains abundant descriptions of features from Archean and Paleoproterozoic provinces interpreted as being subduction-related (e.g. ophiolites or accretionary prisms, de Wit (2004); Komiya et al. (1999); Kusky et al. (2001)). However, evidence for fold-and-thrust belts, blueschist and Ultra-High Pressure metamorphism, extensional gravitational collapse-related structures, which characterise Phanerozoic orogenic belts (e.g. Brown (2009); Chopin (2003); Dewey (1988); Miyashiro (1961)) are lacking or ambiguous. The contrasted geological record between Archean and Phanerozoic provinces has led a growing body of research to point out the limits of a strictly uniformitarian approach to geodynamics of the early Earth. Theoretical considerations on the secular thermal evolution of the Earth and numerical modelling results suggest that plate-tectonics would have operated differently relative to modern geodynamics on a hotter Earth, with strong implications on subduction viability (e.g. Korenaga (2006); van Hunen and van den Berg (2008)), deformation styles (e.g. Rey and Houseman (2006)) and metamorphic patterns (e.g. Brown (2007, 2009); Sizova et al. (2014)). Furthermore, other authors have emphasised that the interpretation of geological data in terms of geodynamics is non-unique, and alternative frameworks to plate tectonics have been proposed. They include models of juvenile crust formation by mantle plume activity (e.g. Abouchami et al. (1990); Albarède (1998); Smithies et al. (2005)), of convergent settings lacking "typical" subduction zones (e.g. Bédard et al. (2013)), and of crustal evolution controlled by crustal- or lithosphere-scale gravitational instabilities (e.g. Bédard (2006); Hamilton (1998); Harris and Bédard (2014)).

Although much of the debate has focussed on the Archean, the controversy lives on in the Paleoproterozoic. Indeed, monotonous distributed regional strain and homogeneous LP-HT metamorphic patterns are reported in Proterozoic accretionary "hot" orogens, while they lack some structural and metamorphic characteristics of modern orogenic belts (Cagnard et al., 2006; Chardon et al., 2009; Vidal et al., 2009). However, despite geochemical, lithological and structural similarities with Archean provinces, Proterozoic accretionary orogens have a specific metamorphic record, characterized by a duality of thermal regimes, inferred from rocks metamorphosed along distinct apparent geothermal gradients (Brown, 2009). The geological record of Proterozoic accretionary orogens may therefore reflect geodynamic contexts which differ both from Archean and Phanerozoic settings, and which represent a distinct, transitional phase in the secular evolution of the Earth.

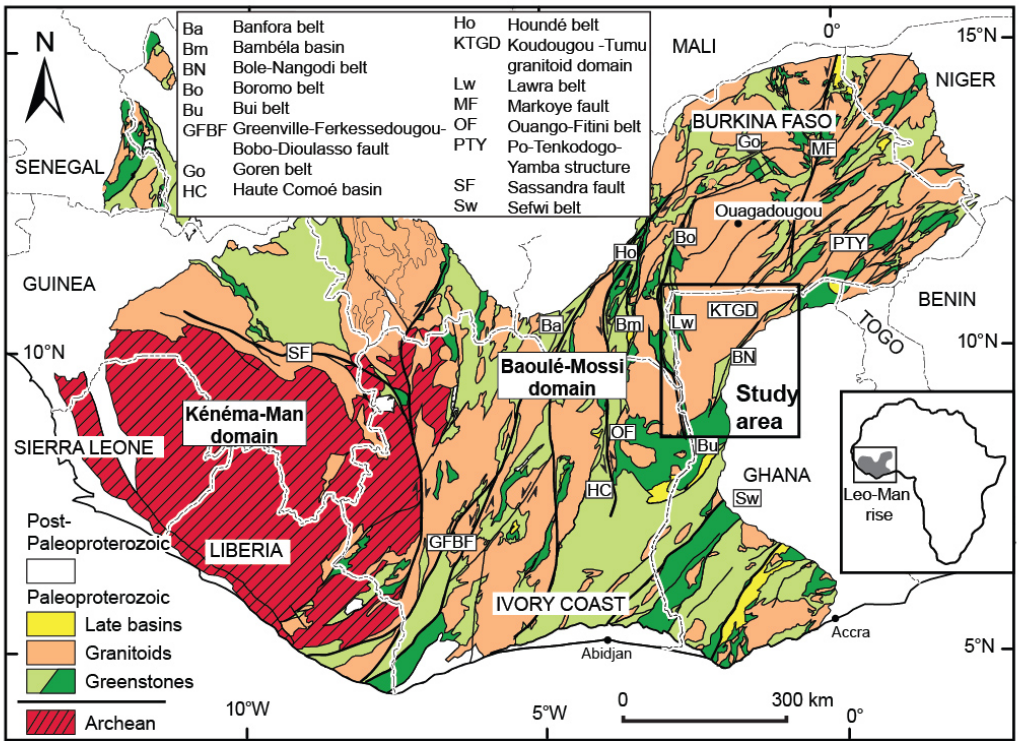

FIGURE 3.1: Simplified geological map of the Leo-Man rise (modified after the BRGM SIGAfrique map, Milési et al. (2004)). Light green areas are made of intermediate to acidic volcano-sedimentary or volcano-clastic rocks, and the dark green areas represent mafic volcanic rocks.

In order to explore the geodynamic processes at work in the Proterozoic, we draw our attention to the Paleoproterozoic (2.25-2.00 Ga) West African Craton (Abouchami et al., 1990; Boher et al., 1992). It is one of the youngest large ($\sim 3.10{-}^{6}km^{2}$) juvenile continental domains produced during a major crustal growth episode. The craton mainly consists of TTG suites (e.g. Gasquet et al. (2003)), granites and "Birimian" (Junner, 1940) greenstone belts. It is a key study area for the understanding of geodynamic processes in juvenile accretionary orogens after the Archean-Paleoproterozoic transition. This study focuses on north-western Ghana,

where large surfaces of exhumed high-grade metamorphic rocks are juxtaposed to coeval low-grade metamorphic rocks. Detailed lithological, structural and metamorphic maps are produced from the interpretation of field and geophysical data. A structural analysis is carried out and coupled to geochronological constraints, in order to describe the deformation sequence during the orogenic cycle. The new dataset helps to characterise the tectonic style of the Eburnean orogeny, constrain exhumation processes, and evaluate the suitability of a collisional orogenic model for the evolution of the Paleoproterozoic craton in north-western Ghana.

3.2.2 Geological setting

The Leo-Man rise (Fig. 3.1) forms the southern exposure of the West African Craton. It comprises an Archean nucleus, the 3.00-2.50 Ga Kénéma-Man domain, flanked to the east by the juvenile Paleoproterozoic Baoulé-Mossi domain. The Birimian greenstone belts comprise elongated sequences of volcanic and volcano-sedimentary rocks, shales and greywackes, and occasional chemical sedimentary rocks. The volcanic rocks range from basalts to rhyolites and have bimodal tholeiitic and calc-alkaline affinities (e.g. Baratoux et al. (2011); Kitson (1928); Leube et al. (1990)). Across the craton, large volumes of volcanic rocks were emplaced between 2.40 and 2.20 Ga and volcanic activity locally lasted on until ca. 2.10 Ga (Doumbia et al., 1998; Feybesse et al., 2006; Hirdes et al., 1996; Kouamelan, 1996). The greenstone belts are bounded by shear zones and alternate with granite-gneiss terranes. Intense plutonic activity generated juvenile TTG suites between 2.25 and 2.10 Ga, while magmatism gradually evolved towards more differentiated terms (potassic granites and alkaline syenites) until ca. 2.07 Ga (e.g. Arnould (1961); Egal et al. (2002); Lompo (2009)). Following magmatic accretion of the juvenile crust between 2.25 and 2.15 Ga, the Eburnean orogenic cycle led to the tectonic assembly of the Archean nucleus and the various Paleoproterozoic domains between 2.15 and 2.07 Ga (Allibone et al., 2002; Bessoles, 1977; Bonhomme, 1962; Feybesse et al., 2006; Hirdes et al., 1996; Ledru et al., 1991; Lemoine et al., 1990; Milési et al., 1989, 1992; Pouclet et al., 2006; Tagini, 1971; Vidal et al., 2009). Tarkwaian sedimentary rocks (conglomerates, phyllites and quartzites) form discordant basins on Birimian formations, and are interpreted to represent syn-orogenic to late-stage basins (Davis et al., 1994; Perrouty et al., 2012). The Eburnean orogeny caused craton-wide metamorphism, recording both low-pressure, high-temperature (LP-HT) and high-pressure, low-temperature (HT-LP) apparent geothermal gradients, between 15 and 40 °C/km (Block et al., 2015; Caby et al., 2000; Feybesse et al., 2006; Galipp et al., 2003; John et al., 1999; Klemd et al., 2002; Opare-Addo et al., 1993; Pitra et al., 2010; Triboulet and Feybesse, 1998). Two discrete tectono-metamorphic events, possibly separated by a rifting phase, are proposed for the Eburnean orogeny in some provinces (Arnould, 1961; De Kock et al., 2011, 2012; Feybesse et al., 1990; Hein, 2010; Lemoine et al., 1990; Perrouty et al., 2012; Pouclet et al., 2006; Roques, 1948; Sagatzky, 1954; Tempier, 1986; Tshibubudze et al., 2009), while a monocyclic orogenic model is proposed for other areas (Block et al., 2015; Eisenlohr and Hirdes, 1992; Gasquet et al., 2003; Hirdes et al., 1996; Leube et al., 1990). Across the craton, proposed suture zones between distinct domains (Hirdes et al., 1996) remain ambiguous, and the lack of evidence for clear lateral age gradients (Castaing et al., 2003; Delor and d'Ivoire, 1995; Doumbia et al., 1998; Hirdes et al., 1992; Lahondère

et al., 2002; Tapsoba et al., 2013; Théveniaut et al., 2010) raises questions on the applicability of lateral accretion crustal-growth models.

The debate on the tectonic regimes dominating the Eburnean orogeny echoes the controversy on Archean geodynamics. Some authors report dome and basin structural patterns, and invoke diapirism or gravity-driven tectonics to account for field observations, e.g. in Ivory Coast and Niger (Caby et al., 2000; Hirdes et al., 1992; Pons et al., 1995; Pouclet et al., 2006; Soumaila and Garba, 2006; Vidal et al., 2009). Another school of thought interprets the Eburnean orogenic record as a product of nappe-style tectonics (Billa et al., 1999; Feybesse et al., 2006; Milési et al., 1989, 1992). The late-stage evolution of the Eburnean orogeny is characterised by the activation of transcurrent shear zones (e.g. Feybesse et al. (1990); Jessell et al. (2012); Ledru et al. (1991); Lompo (2009); Nikiéma et al. (1993)) localised at the interface between greenstone belts and granite-gneiss domains.

3.2.3 Study area

The geology of north-western Ghana is characterised by low- to high-grade tectono-metamorphic domains which are transect or limited by high-strain shear zones (SZ), and are intruded by successive pulses of plutonic rocks.

3.2.3.1 Low-grade volcano-sedimentary belts

Low-grade shales, volcano-sedimentary rocks, lavas such as dacites, andesites and basalts are found in the N-S **Wa-Lawra belt** (Fig. 3.2), which is the south-eastern continuation of the Boromo greenstone belt exposed in Burkina Faso (Baratoux et al., 2011; Metelka et al., 2011). Similar low-grade lithologies are found in the E-W trending **Julie belt** (Fig. 3.2), which also comprises a unit of cross-bedded silicic volcano-sedimentary rocks, quartzites, arkoses and conglomerates. The **Maluwe domain** is a low-grade tectono-metamorphic domain elongated SW-NE along ∼250 km, which tapers off towards the NE to a thin sliver, although it may extend below the Volta Basin. It is dominated by greywackes and shales which are intercalated with volcanoclastic rocks and felsic to intermediate lavas, deposited between 2197 and 2125 Ma (De Kock et al., 2009; Thomas et al., 2009). It also comprises chemical sedimentary rocks such as Mn-rich cherts, along with mafic intrusives such as gabbros and pyroxenites. The **Nangodi belt** (Melcher and Stumpfl, 1994), in the north-eastern part of the study area (Fig. 3.2), is formed by a succession of shales, greywackes and Mn-rich cherts alternating with MORB-type basalts, overlain by calc-alkaline andesitic to rhyolitic lava flows.

3.2.3.2 High-grade metamorphic domains and granitoid domains

The **Bole-Bulenga domain** is ∼150 by 20-80 km long and elongated along a NNE direction (Fig. 3.2). It is made of high-grade orthogneisses, paragneisses and minor metabasites. The paragneisses are derived from pelites, greywackes and volcano-sedimentary rocks. They are intruded by TTG gneisses with crystallisation ages between 2195 and 2135 Ma. The lithologies of the Bole-Bulenga domain are frequently migmatitic. The **Abulembire domain** shares many lithological and metamorphic similarities with the Bole-Bulenga domain. It is essentially made of

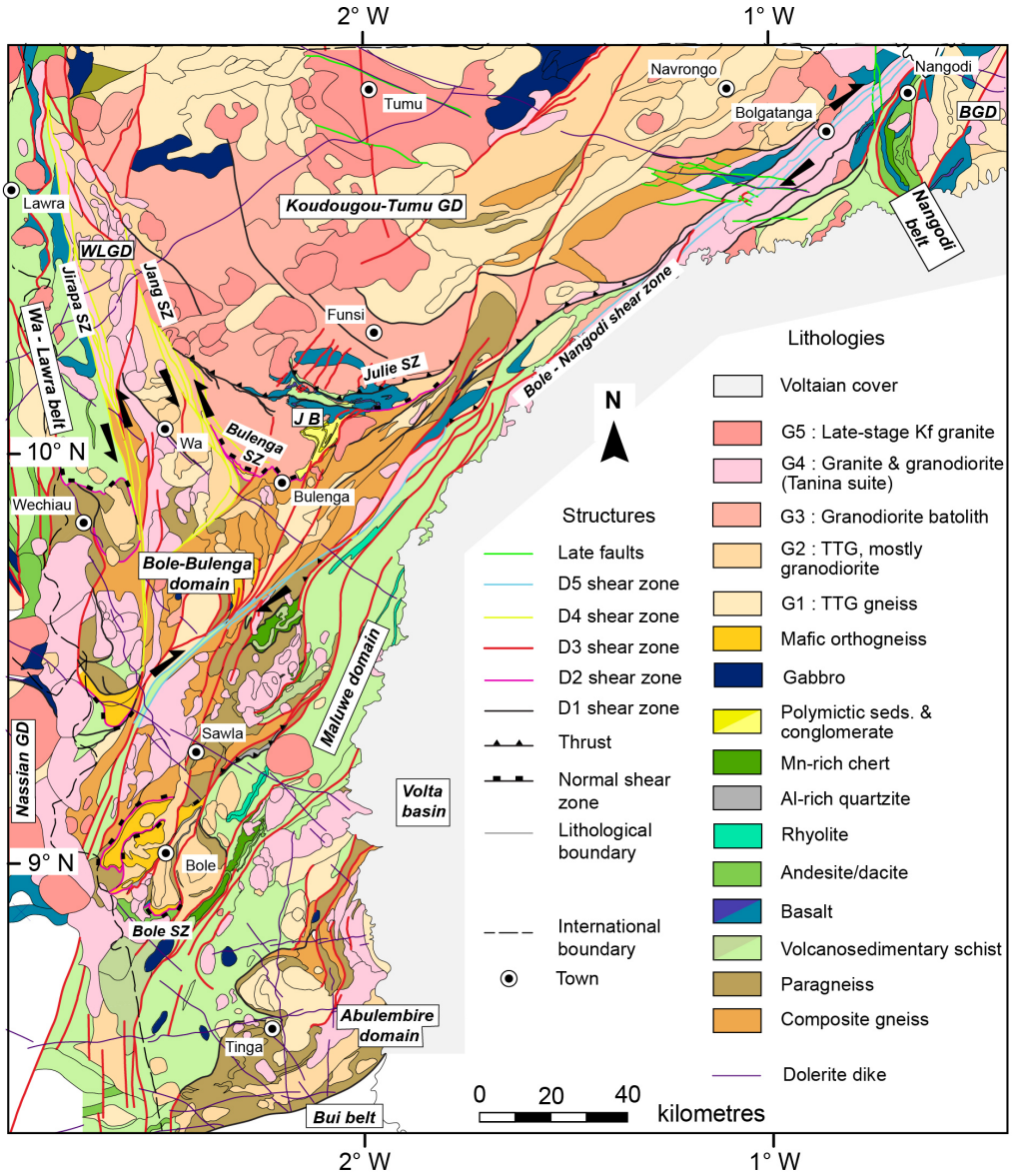

FIGURE 3.2: Lithological map of the Paleoproterozoic of northern Ghana, built from the interpretation of airborne geophysical and field data. BGD : Bawku granitoid domain. JB : Julie Belt ; WLGD : Wa - Lawra granitoid domain. GD = granitoid domain, SZ = shear zone. Shear zones are colour-coded in correspondence to the deformation event under which they were last active, i.e. D3 shear zone was formed or last re-activated during deformation D3 (see text). Darker colours used to represent the same lithology designate rocks with distinctively high magnetic response.

paragneisses, sometimes migmatitic, intruded by TTG and granite gneisses, which were emplaced between ca. 2200 and 2125 Ma (De Kock et al., 2009; Duodu, 2009). The Abulembire domain is limited to the south by the **Bui belt** (Zitsmann et al., 1997).

The Koudougou-Tumu granitoid domain (KTGD), extending north into Bur-

kina Faso, comprises abundant migmatitic TTG orthogneisses, and small volumes of mafic orthogneisses and paragneisses. The protolith of some orthogneisses crystallised between 2163 and 2154 Ma (Duodu, 2009). The **Wa-Lawra granitoid domain** (WLGD) stretches along the eastern margin of the Wa-Lawra belt. It is dominated by granite and granodiorite plutons intrusive in high grade para- and orthogneisses, which are predominant to the south of the domain. The **Bawku granitoid domain** (BGD) is flanked along the eastern margin of the Nangodi belt. It mostly consists of deformed granodiorite and granite plutons emplaced between 2170 and 2127 Ma (Duodu, 2009). This domain also comprises small volumes of volcanic rocks, dacites and basalts, which underwent metamorphism around or below the greenschist-amphibolite facies transition. The Nassian granitoid domain (Delor and d'Ivoire, 1995; Vidal et al., 2009) is found in north-eastern Côte d'Ivoire, along the western margin of the Bole-Bulenga domain. It comprises ca. 2150 Ma orthogneisses and a suite of intrusive granites.

The litho-tectonic units presented above area are extensively intruded by biotite granites (G4 ; Fig. 3.2) between 2134 and 2118 Ma (De Kock et al., 2011). Late-stage potassic porphyric granites (G5 in Fig. 3.2) with crystallization ages ranging between 2128 and 2086 Ma (Duodu, 2009; Taylor et al., 1992) intrude large swathes of the Koudougou-Tumu granitoid domain. Weakly deformed elliptical gabbro bodies are found in the Maluwe domain.

3.2.3.3 Major shear zones

The metamorphic terranes of north-western Ghana are limited by high-strain zones. The Julie shear zone, oriented E-W, bounds the Koudougou-Tumu granitoid domain to the south and forms the transition zone with the Julie belt to the south. The Bulenga shear zone separates the low-grade Julie belt to the north from the Bole-Bulenga domain to the south. The Bole shear zone forms the contact between the Bole-Bulenga domain to the north, and the Maluwe domain to the south. These structures are folded and transposed parallel to two younger major N-S and NE-SW structural trends, which characterize the architecture of the craton in NW Ghana (Fig. 3.2). N-S structures include the Jang and Jirapa shear zones. The Jang SZ separates the Koudougou-Tumu and Wa-Lawra granitoid domains. At its northern termination, it merges with the Jirapa SZ, which extends north into Burkina Faso along most of the length of the Boromo belt. The Jirapa SZ separates low-grade sedimentary and volcano-sedimentary rocks to the west from the Wa-Lawra granitoid domain to the east. The Bole-Nangodi shear zone represents a major structure oriented NE-SW. It transects the Bole-Bulenga domain and forms the northern margin of the Maluwe domain, before extending along the western margin of the Nangodi belt and into Burkina Faso (Ganne et al., 2012; Naba et al., 2004). Both structural trends merge into an interference zone within the Bole-Bulenga domain.

3.2.4 Mapping methodology

3.2.4.1 Field and geophysical data

Lithological, petrological and structural data were collected on a total of 947 observation points, and magnetic susceptibility values were measured for most of

the principal rock types in the study area. They were combined with pre-existing observation points acquired during a 1 :100 000 mapping campaign carried out in the framework of European-funded Mining Sector Support Project (MSSP) and presented in De Kock et al. (2009); Siegfried et al. (2009); Thomas et al. (2009). The field data was used to constrain the interpretation of the following geophysical dataset.

- Regional airborne magnetics provided by the Geological Survey Department of Ghana, with a gridded resolution of 100m and 200m, with a flight height of 70-80m.
- Regional airborne radiometrics provided by the Geological Survey Department of Ghana, with a gridded resolution of 100m and 200m, with a flight height of 70-80m.
- Regional airborne electromagnetics provided by the Geological Survey Department of Ghana, with a gridded resolution of 100m, with a flight height of 70-80m.
- High resolution airborne magnetics provided by Azumah resources, with a gridded resolution of 25m, with a flight height of 40m.
- High resolution airborne radiometrics provided by Azumah resources, with a gridded resolution of 25m, with a flight height of 40m.

Images of the regional geophysical datasets are provided as supplementary data.

3.2.4.2 Main lithologies

The geological map in Fig. 3.2 shows the representative lithologies of the study area. They are presented below and in Table1, along with their respective magnetic susceptibilities, radiometric and electromagnetic signals.

Granitoids Five major types of granitoids are distinguished in the study area based on their petrography, geophysical properties, and the relative chronology of their emplacement. In a chronological order, they are :

1. G1. Calc-alkaline TTG plutons and gneisses, equivalent to ME1 in Baratoux et al. (2011) and Metelka et al. (2011). They are generally amphibole- biotite-bearing, and K-feldspar is absent. Their magnetic susceptibility is variable and covers a large range of values (0.05-10x10^{-3} SI; Table 1). The TTGs generally show a penetrative gneissic metamorphic banding and are frequently migmatitic.
2. G2. Calc-alkaline TTGs, mostly granodiorites. They contain biotite and/or amphibole, as well as K-feldspar. They are usually melanocratic due to high proportions of ferro-magnesian minerals. Magnetic susceptibility is moderate to low (0.10-0.30x10^{-3} SI) and gamma ray emissions are dominated by K (Table1). Deformation in sigmoidal or elongated plutons has a variable intensity.
3. G3. Calc-alkaline granodiorite plutons bearing biotite-, amphibole- titanite- and small proportions of K-feldspar, characterised by a coarse (centimetric) grain size, a high magnetic susceptibility (1-55x10^{-3} SI) and depletion in U-Th-K reflected by a dark radiometric signal (Table1). Strain is generally low and increases towards shear zones or pluton margins.

4. G4. Leucocratic K-feldspar- biotite-granites and granodiorites, possibly equivalent to ME2 of Baratoux et al. (2011) and Metelka et al. (2011). They form alignments of elongated plutons parallel to the major N-S and NE-SW shear zones and belonged to the so-called "Tanina suite". Their magnetic susceptibility is very low (<0.01-0.15x10^{-3} SI), and they have high K and Th emissions.
5. G5. Potassic porphyric granites, sometimes metaluminous, equivalent of ME3 of Baratoux et al. (2011) and Metelka et al. (2011), form circular plutons. Amphibole is scarce or absent. They are generally undeformed. The magnetic susceptibility range is bimodal, and gamma ray emissions reveal a strong enrichment in all incompatible elements.

Table 1

Lithology	G1: TTG gneiss	G2: TTG	Mafic orthogneiss	G3 : granodiorite	G4: Biotite granite & granodiorite	G5: Potassic granite	Andesite/dacite	Basalt/metabasalt
Mineralogy	qz, pl, hbl, bt	qz, pl, kf, hbl (±ep)	qz, pl, hbl, ilm (± gt)	qz, pl, hbl, bt	qz, pl, kf, bt	qz, kf, pl, bt (±ep)	qz, pl, hbl, sph,	act, chl, qz, ep, cal
Magnetic susceptibility (10-3 SI)	0.05, 0.30-0.40, 4-10, multimodal	0.10-0.30	0.10-0.5, 1.0-10 (bimodal)	1.0-55	0.005-0.15	0.10-8.0, bimodal	0.30-0.40	*no data*
Sample	BN261	BN092	BN506	BN380	BN112	BN083	BN02	BN101
U (ppm)	0.29	2.15	0.81	0.46	1.55	4.45	0.810	0.075
Th (ppm)	3.79	3.49	2.26	1.16	12.85	13.9	2.2	0.2
K2O (%)	0.92	3.07	0.56	1.48	2.03	5.16	0.51	0.14
Map					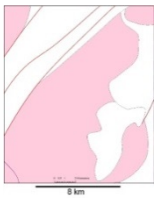	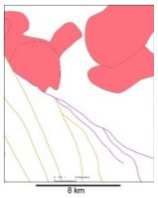	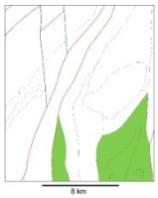	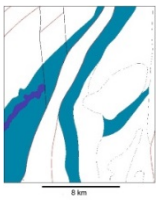
Airborne magnetic response	Moderate to high intensity, marked magnetic fabric	Low to moderate, homogeneous.	Low to high , heterogeneous, strong magnetic fabric	Very high, heterogeneous, strong magnetic fabric	Low intensity, homogeneous interlocked bodies	Low to high intensity.	Low to moderate intensity, variable	High intensity layers
Magnetic image	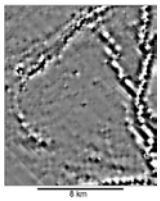	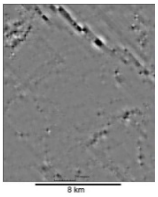		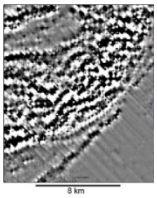	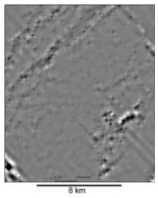		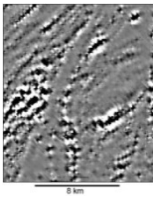	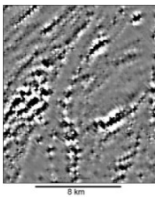
Airborne radiometric response	K, Th, U poor (dark)	Moderate to high K, moderate U, low Th (red)	Moderate K, moderate U, low Th (red to blue) *??*	Low to moderate K Th, U poor (dark to red)	Moderate K, high Th, low U (green, yellow, orange)	Very high K, high Th, moderate U (red-yellow)	moderate U (blue), low Th, K.	K, Th, U poor (dark)
Radiometric + shaded DTM					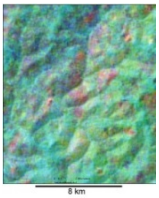	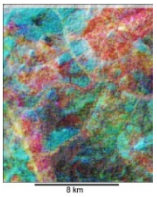	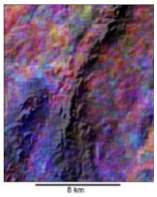	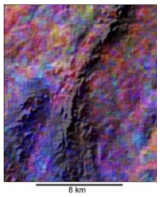
Airborne electro-magnetic signal	Heterogenous	Low intensity, homogeneous	Heterogeneous	Heterogeneous	Low intensity, homogeneous	*no data*	Low intensity, homogeneous	Moderate to high intensity
Electro-magnetic image	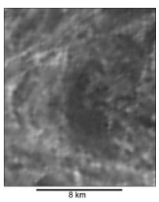	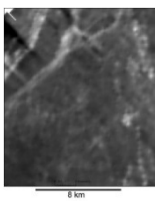	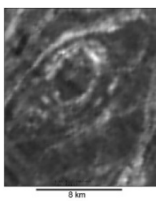	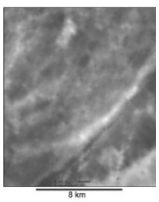	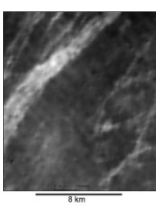	*no data*	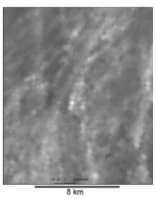	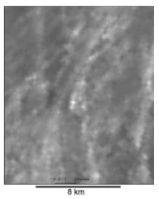

Synthesis of the petrophysical properties and geophysical signatures of the lithologies represented on the geological map. Pictures represent subsets of geophysical datasets of 12x18 km. The magnetic image is an automatic gain control of the first vertical derivative of the negative Reduced to the Equator airborne magnetic signal. Grayscale contrasts reflect magnetic susceptibility contrasts. The radiometric imaged is draped over the shaded SRTM digital terrain model. Colours show relative enrichment in K, Th, U (red, green, blue respectively, white: enrichment in all three elements, black: depletion in all three elements). The electromagnetic image represents the in-phase (IP3125) signal. Light grayscale tones show high electromagnetic response. Whole rock geochemical analyses were conducted by A.L.S. Mineral Laboratory, Sevilla, Spain.

Table 1 - continued

Lithology	Mn-rich sediment	Gabbro & dolerite dyke	Composite gneiss	Paragneiss	Polymictic sediments & conglomerates	Volcano-sedimentary schist	Rhyolite/felsic volcanoclastite
Mineralogy	*no data*	act, chl, sph, after cpx, hbl ?	qz, bt, pl, wm (± grt, alsi)	qz, bt, pl, wm, gt, alsi/st	qz, pl, kf, wm, chl, ep, py	qz, chl, ms	qz, chl, wm (± grt)
Magnetic susceptibility (10-3 SI)	0.05-0.9, unimodal	0.2-2.0	0.01-0.35	0.10-0.35		0.05-0.55	0.04-0.20
Sample	BN006	BN104	BN392	BN047	BN110	BN411	BN400
U (ppm)		0.153	1.68	1.32	1.936	1.5	1.711
Th (ppm)		0.5	6.04	5.53	6.5	5.66	5.7
K2O (%)		0.50	3.35	2.27	3.40	1.78	0.79
Map	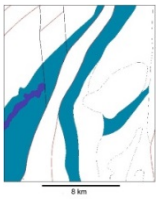	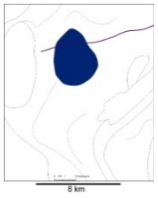	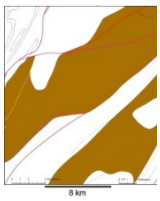		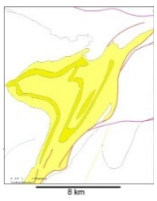	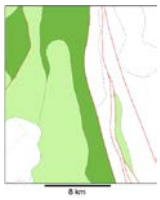	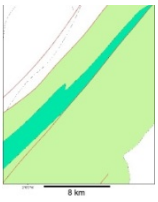
Airborne magnetic response	Low to high, marked magnetic horizons	High intensity, strong signal	Low intensity, smooth homogeneous surface	Low intensity, smooth homogeneous surface	Contrasted intensity in stratigraphic horizons	Low intensity, smooth homogeneous surface	Occasional highly magnetic lavas
Magnetic image	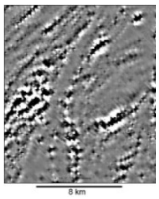	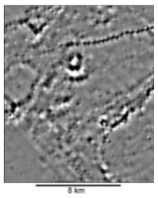	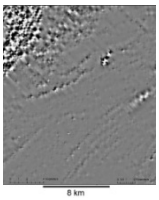		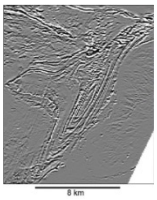	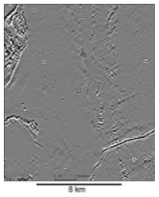	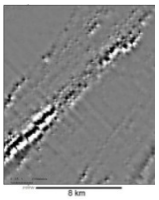
Airborne radiometric response	K, Th, U poor (dark)	K, Th, U poor (dark)	High (K+Th)/(K+Th+U) (red-orange)	Low U, moderate Th, K (green-yellow)	Low U, K, moderate to high Th (green-yellow)	Low U, moderate Th, K (orange-yellow)	Moderate U, Th, K (orange-yellow)
Radiometric + shaded DTM	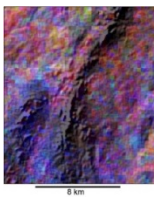	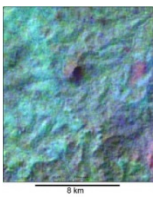			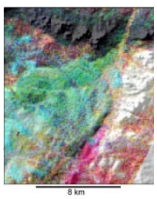		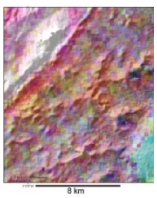
Airborne electro-magnetic signal	High intensity, heterogeneous	Low intensity	Low intensity, homogeneous	Low intensity, homogeneous	*no data*	Very high intensity	Moderate intensity
Electro-magnetic image	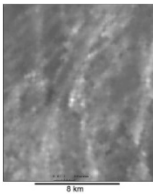	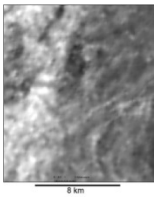	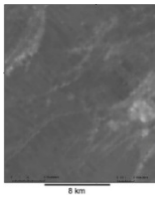	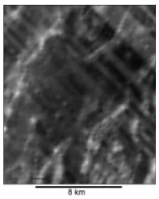	*no data*	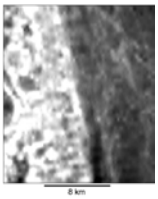	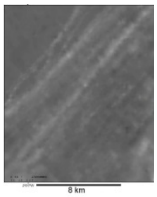

Mafic orthogneiss This rock is a high-strain melanocratic, hornblende-rich gneiss, generally migmatitic. It is found across the study area as pluri-kilometric bodies or as multiple slivers a few 100m wide, elongated along domain boundaries. It presents a variable, but generally high magnetic susceptibility (up to 10x10^{-3} SI).

Paragneiss The paragneisses are found in the Abulembire and Bole-Bulenga domains. They record regional metamorphism at conditions corresponding to the amphibolite-granulite facies transition. The rocks develop a gneissic texture defined by alternating quartz- and mica-rich beds, and sometimes display a migmatitic banding. Garnet is a common mineral, while staurolite or aluminosilicates are found in the most Al-rich layers. Magnetic susceptibility is low for this lithology (<0.35x10^{-3} SI).

Composite gneiss Large proportions of the Abulembire and Bole-Bulenga domains are formed by migmatitic ortho- and paragneisses intruded by varying proportions of granitic to granodioritic melts and pegmatite dikes. They together constitute a heterogeneous lithology termed "composite gneiss" which differs from the paragneiss based on its distinctive K+Th relative enrichment (Table 1).

Schist derived from volcano-sedimentary rocks The lithology mapped as volcano-sedimentary schist encompasses a variety of rocks including greywackes, shales and felsic to intermediate volcanic rocks. They record low-grade metamorphism under sub-greenschist to amphibolite-facies conditions. Metamorphic assemblages include quartzŮfeldspar-chlorite-white mica or quartz-feldspar-chlorite-actinolite. This group of lithologies is dominant in the Maluwe domain, the Nangodi and Wa-Lawra belts. Rocks generally displays homogeneous low magnetic susceptibility values (0.05-0.55x 10^{-3} SI), and K+Th enrichment relative to U.

Rhyolite/meta-rhyolite Rhyolites and felsic pyroclastites are found in the Maluwe domain, where they form narrow elongated units. They frequently contain flattened bombs and clasts, and show an enrichment in incompatible elements, particularly Th and K relative to U. Magnetic susceptibility is variable but mostly low (< 0.2x10^{-3} SI).

Andesite/meta-andesite Intermediate calc-alkaline lavas and pyroclastites are intercalated with phyllitic sediments and volcano-sediments in the Maluwe domain, in the Wa-Lawra and Nangodi belts. Some units are undeformed and preserve magmatic fabrics, while others are intensely sheared. They have a low (0.3-0.4x10^{-3} SI) magnetic susceptibility and their radiometric signal reveals a relative enrichment in U.

Basalt/meta-basalt Basalts metamorphosed under lower-greenschist to amphibolite-facies conditions are folded and elongated parallel to the strike of major structures in the Wa-Lawra, Julie and Nangodi belts. Airborne geophysical data reveal high-magnetic basaltic lava layers depleted in incompatible elements.

Gabbro/meta-gabbro Hornblende-bearing gabbros, gabbronorites and minor pyroxenites form elliptical bodies up to 10km long in the Maluwe and Koudougou-Tumu domains. They are characterised by a moderate magnetic susceptibility (0.2-2x10^{-3} SI) and depletion in incompatible elements.

Manganesiferous cherts Mn-rich silicic chemical sediments are found in the Nangodi belt and on the north-western margin of the Maluwe domain. They form dark, massive sediments with a low magnetic susceptibility ($<$ 1x10^{-3} SI) and depletion in incompatible elements.

Al-rich quartzite This lithology is a kyanite-bearing quartzite. It forms a discontinuous ridge which can be followed along strike for kilometres along the contact zone between the Bole-Bulenga and Maluwe domains.

Polymictic sediments and conglomerates A relatively small (20x8 km) unit of cross-bedded immature clastic sediments is located on the southeastern margin of the Julie belt, along the contact with the Bole-Bulenga domain. It comprises arkoses, quartzites and conglomerates, metamorphosed under low-grade conditions. Cross-beds are underlined by thin magnetite-rich strata. The magnetic susceptibility of the rock is therefore heterogeneous and locally very high. The radiometric signal indicates moderate K and high Th emissions. The lithology shares similarities with other clastic sedimentary units found across the craton, such as Tarkwaian sediments found in southern Ghana and Burkina Faso (Davis et al., 1994; Perrouty et al., 2012), or as Birimian sediments discordant on older Birimian volcano-sedimentary sequences in northern Burkina Faso (Hein et al., 2004). These rocks are hereafter referred to as polymictic sediments and conglomerates.

Voltaian cover Neoproterozoic sediments of the Volta basin (Affaton et al., 1980) are discordant on Paleoproterozoic formations. The basal sediments at the discordant contact generally consist of sandstone and fine grained arkoses displaying ubiquitous cross-beds.

3.2.5 Tectono-metamorphic history

3.2.5.1 Deformation sequence

D1-e : Relics of early deformation The observation of oriented inclusion trails preserved in metamorphic porphyroblasts in high-grade gneisses suggests the existence of an early deformation D1-e. The S1-e relic foliation is oblique to any regional tectonic fabric and is not visible at outcrop-scale.

D1 : N-S directed shortening D1 is materialised by a penetrative fabric developed throughout northern Ghana. In the Julie belt, this fabric (S1) is E-W trending, parallel to km-scale folds and shear zones. In migmatitic gneisses of the KTGD, S1 defines an arcuate geometry elongated E-W, while it is consistently oblique relative to the N-S orientation of the Wa-Lawra belt in adjacent gneisses and lavas.

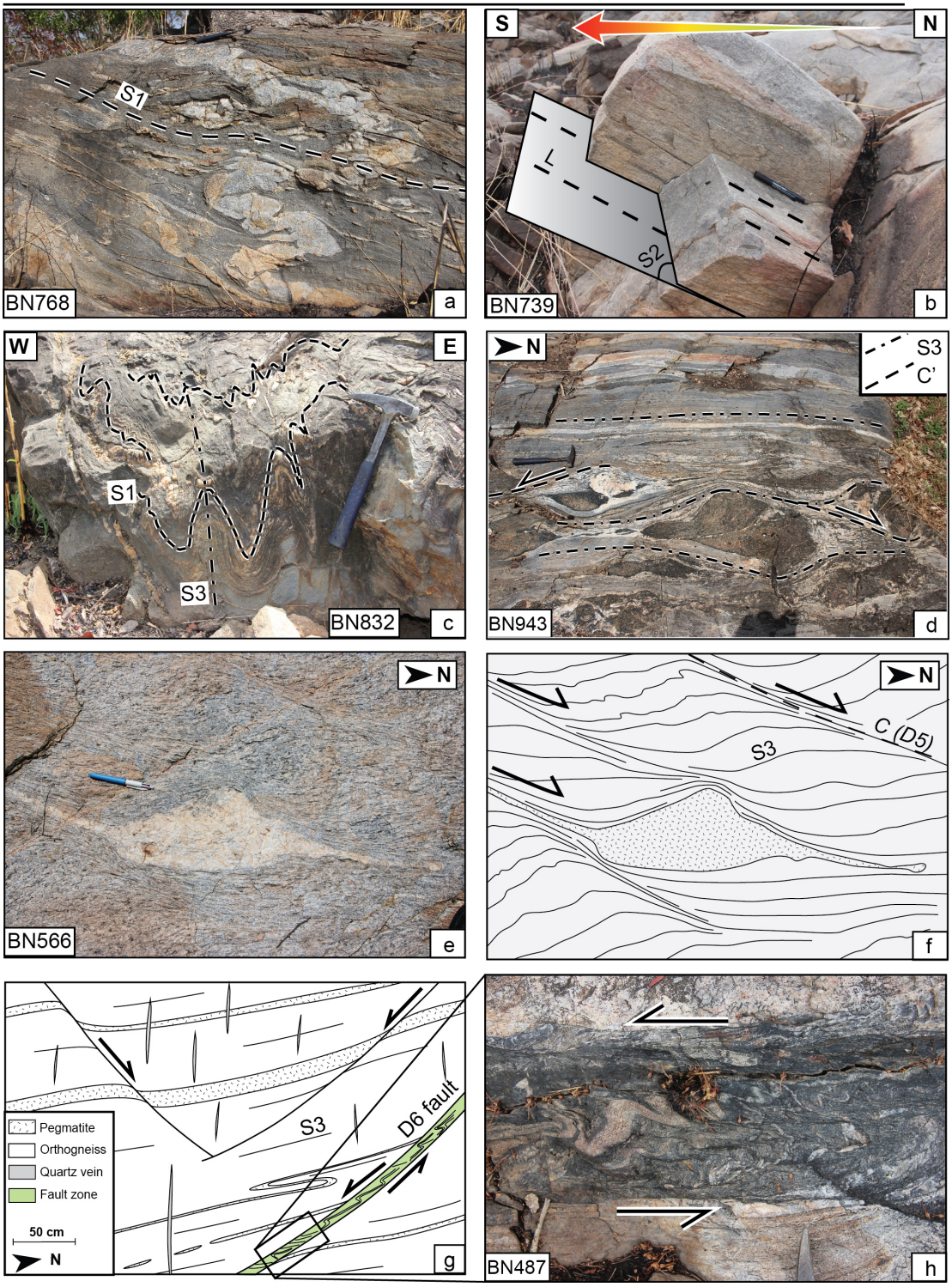

FIGURE 3.3: Representative fabrics of regional deformation. See Figs. 3.5 and 3.9 for outcrop locations.

Similarly, in the Bole-Bulenga and Abulembire domains, the early high-grade metamorphic banding is oriented approximately E-W and shows a variable transposition by later deformation. This deformation is hereafter referred to as D1.

FIGURE 3.3: (**a**) Paragneiss metatexite in the Bole-Bulenga domain displaying a shallow-dipping foliation S1, axial planar to recumbent folds. (**b**) High-strain orthogneiss in the Bulenga shear zone. The foliation dips moderately to the N and carries a stretching lineation plunging down-dip. The arrow points towards increasing metamorphic grade. (**c**) Ptygmatic folds in a migmatitic paragneiss transposing S1 parallel to a subvertical N-S cleavage S3. (**d**) Migmatitic "composite" gneiss in a D3 (N-S) shear zone, containing flattened pyroxenite boudins bounded by symmetrical "extensional" (C') shear bands. (**e**) Orthogneiss displaying a subvertical S3 fabric cross-cut by high-temperature dextral shear bands, characteristic of D5. An interpretative sketch is shown in (**f**). (**g**) Sketch of an orthogneiss outcrop showing the gneissic fabric offset by conjugate strike-slip brittle faults, and associated quartz-tension gashes. (**h**) Photograph of a detail from (**g**) showing a sinistral strike-slip fault filled by pseudotachylite. Features displayed in (**g**) and (**h**) are attributed to D6.

In the Maluwe domain and in the Julie belt, D1 is associated with a shallow- to steeply dipping S1 penetrative cleavage, parallel to the stratigraphic layering (S0) of low-grade meta-sediments. It generates km-scale folds with E-W striking vertical axial surfaces in basalts, volcano-sedimentary rocks and polymictic sediments. In the E-W Julie SZ, S1 foliation dips 50-70 ° N, bears reverse, top-to-the-south kinematic indicators and carries a stretching lineation plunging down-dip, towards higher grade rocks. The Julie SZ is interpreted as a thrust, consistent with N-S directed shortening. In high-grade rocks, S1 is a shallowly to steeply-dipping gneissic foliation. It is parallel to a transposed stratigraphic layering (S0) in meta-sediments, and is defined by alternating parallel neosomes and paleosomes in migmatitic rocks (Fig. 3.3a, c). The foliation is axial planar to F1 isoclinal and recumbent folds, and carries a strongly plunging mineral elongation lineation L1. At the contact between the Bole-Bulenga and Maluwe domains, the Bole-Nangodi SZ is NNW-dipping. It separates amphibolites, ortho- and paragneisses displaying S1-parallel leucosomes to the north, from biotite-chlorite schists to the south. The consistency in strain on either side of the shear zone suggests that low- and high-grade rocks were brought in contact during D1. This implies that the Bole-Nangodi shear zone probably acted as a reverse shear zone, before later re-activation during subsequent deformation. Therefore, field observations indicate that the N-S directed shortening event D1 causes folding and thrusting, generates metamorphic breaks across narrow high-strain zones (Fig. 3.5), and is coincident with high-grade metamorphism and partial melting of the crust.

D2 : N-S directed extension The north-dipping Bulenga shear zone represents the boundary between the low-grade Julie belt and the high-grade Bole-Bulenga domain. It contains a high-strain granitoid gneiss, which separates polymictic sediments and conglomerates in the hanging-wall from migmatitic ortho- and paragneisses in the footwall. The foliation has a moderate dip (40-50 °) to the north, and carries a stretching lineation plunging down-dip (L2, plunging to N020, Fig. 3.8c), towards lower grade lithologies of the Julie Belt (Fig. 3.3b, the arrow indicates the direction of increasing metamorphic grade). The Bulenga shear zone is interpreted as an extensional detachment. On the southern margin of the Bole-Bulenga domain,

at the contact with the Maluwe domain, the Bole shear zone dips 50-80 ° to the south. It contains a high-strain mafic orthogneiss, which sometimes displays intense retrogression. The foliation planes carry a mineral elongation lineation plunging down dip (L2, plunging to N210-220, Fig. 3.8c), towards the lower-grade volcano-sedimentary rocks of the Maluwe domain. It is also interpreted as an extensional shear zone. Therefore, the Bole-Bulenga domain is separated along its northern and southern limits from lower-grade metamorphic terranes by structures dipping in opposite directions, consistent with a N-S directed extension : D2.

In the field, D2 does not develop a strong fabric away from the above-mentioned shear zones, and no overprinting relationships could be observed between D1 and D2 structures. Within the Bole-Bulenga domain, shallow-dipping high-strain contacts between rock units may be attributed to D2.

D3 : E-W directed shortening Fabrics, structures and isograds formed during D1 and D2 are overprinted by deformation D3, which is consistent with E-W directed horizontal contraction (Fig. 3.3c). D3 generates a sub-vertical schistose cleavage S3 which strikes ∼ N020 (Fig. 3.8c). In high-grade rocks, S3 forms a penetrative foliation and is axial planar to isoclinal or ptygmatic folds F3 (Fig. 3.3c). Locally, migmatitic paragneisses display leucosomes oriented parallel to S3 and accumulated in F3 fold hinges (Fig. 3.4). D3 deformation is associated to an amphibolite-facies metamorphic overprint. In low-grade domains, S3 is defined by biotite, chlorite and white mica recrystallization and forms cleavages axial planar to isoclinal folds F3.

At a larger scale, in the Bole-Bulenga domain, D3 forms an alternation of sub-solidus amphibolite-facies rocks and of migmatitic, amphibolite- to granulite-facies gneisses, elongated parallel to a N-S structural trend and shear zones, and a repetition of lithologies is observed along E-W transects. These structures are further analysed in the discussion. D3 strain intensity gradually decreases to the south of the study area, in the south of the Maluwe domain and in the Abulembire domain. Similarly, the KTGD seems to behave as a rigid bloc unaffected by D3, except along its margins.

D4 : ENE-WSW shortening and localized sinistral strike-slip shearing The late-stage tectonic evolution of the study area is characterized by a gradual shift from distributed strain across litho-tectonic domains to localized strain at domain margins and along lithological boundaries. This shift in tectonic regime is illustrated by the activation of the Jirapa and Jang shear zones under a dominant sinistral strike-slip regime during D4. Leucosomes and competent granitic dikes in gneisses in the Jang ductile shear zone are boudinaged, indicating sub-solidus deformation conditions. The growth of chlorite, muscovite and biotite grains stretched in a sub-horizontal lineation on foliation planes in the Jirapa SZ indicates that D4 deformation occurred under greenschist-facies conditions. The observation of early microstructures (e.g. symmetrical folds, moderately-plunging stretching lineations defined by amphibolite-facies metamorphic minerals) in rocks from the Jirapa and Jang shear zones suggests that these structures are inherited and formed prior to further re-activation and re-orientation in a strike-slip setting (i.e. they formed before or during D3).

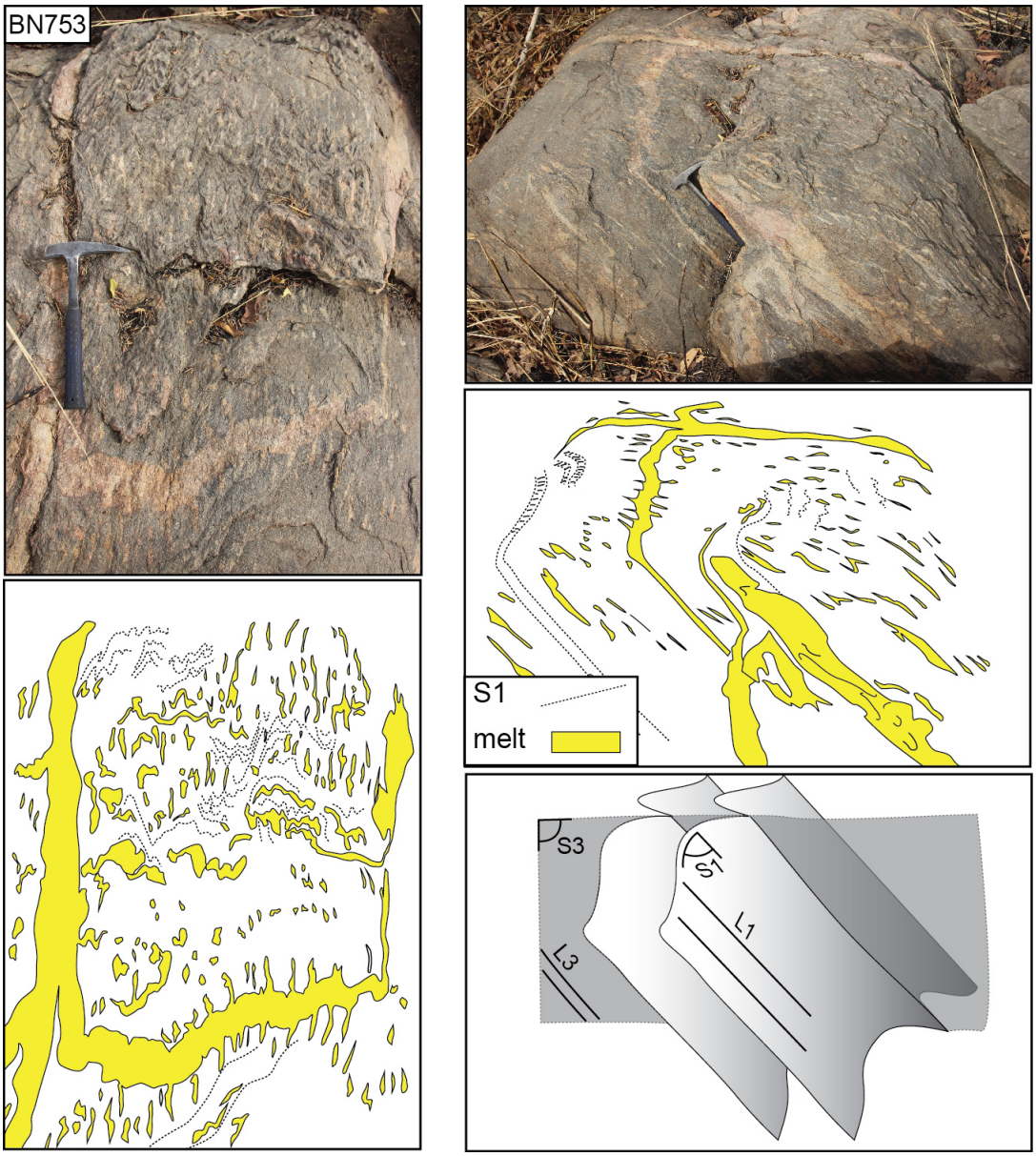

FIGURE 3.4: Photographs and interpretative sketches of a migmatitic paragneiss from the Bole-Bulenga domain. Foliation S1 is parallel to a stratigraphic layering and dips moderately to the south. It is overprinted by a sub-vertical schistose cleavage S3 that is axial-planar to tight folds and attributed to D3. Melting is evidenced by pinkish granitic leucosomes formed in more fusible (pelitic) layers. Leucosomes are parallel to axial surfaces of F3 folds, suggesting melt production and generation during D3. L1 and L3 have identical orientations.

D5 : E-W shortening and localized dextral strike-slip shearing A set of sub-vertical dextral strike slip shear zones develops in the Bole-Bulenga domain and transects lithological contacts. In the gneisses, S3 is offset by dextral shear bands (Fig. 3.3e, f). Ductile fabrics point to relatively high-T conditions for D5 deformation. The contact zone between the Maluwe and Bole-Bulenga domains is

dragged into the Bole-Nangodi shear zone, which is re-activated as a dextral shear zone (Fig. 3.5). Lower-amphibolite- to greenschist-facies retrograde metamorphic overprints develop within this shear zone.

D6 : E-W shortening, brittle deformation Brittle structures consistent with an east-west shortening, such as E-W quartz tension gashes, sometimes chlorite, white mica or epidote-bearing, and conjugate brittle strike-slip faults cross-cut the previous structures (Fig. 3.3f, g, h). These fabrics define another deformation event, D6 which takes place under brittle conditions in a strain field similar to that of D5.

D7 : NE-SW shortening, brittle deformation Incompetent and anisotropic lithologies (e.g. shales, chlorite schists, etc) occasionally develop a cross-cutting sub-vertical crenulation cleavage striking NW-SE, which represent the latest fabric observed in the study area.

3.2.5.2 Metamorphic history

A regional metamorphic study based on petrological and geochronological constraints is presented in Block et al. (2015) (see chapter 4). Relics of high-pressure, low-temperature (HP-LT) assemblages, formed at the transition between the blueschist facies and the epidote-amphibolite sub-facies, are sporadically preserved in the Bole-Bulenga and Abulembire domains . HP-LT conditions (10-14 kbar, 520-600 $^\circ$C), corresponding to a low ($\sim$15 $^\circ$C/km) apparent geothermal gradient, are deduced from the composition of the core of zoned garnet porphyroblasts. The garnet cores contain oriented Qz-Chl inclusion trails, oblique to the metamorphic banding S1 (mineral abbreviations after (Whitney and Evans, 2010) except for melt (=L)). Hence, HP-LT metamorphism is associated to deformation D1-e. The foliation S1 hosts amphibolite- to granulite-facies assemblages in high-grade rocks of the KTGD, the Bole-Bulenga and Abulembire domains. L1 is defined by the stretching of hornblende, biotite or kyanite in favourable lithologies. The high-grade metamorphic assemblages include Bt + Grt + Ky + Pl + Qz + L, and Hbl + Grt + Cpx + Pl + Ilm + Qz + L in metapelites and metabasic rocks respectively. Rocks metamorphosed at the amphibolite Ű granulite facies transition followed a clockwise pressure-temperature-time (P-T-t) path. They record melting at P above 10 kbar, at T of 700-800 $^\circ$C, followed by near isothermal decompression, or decompression-cooling along a 30 $^\circ$C/km apparent geotherm. *In-situ* U-Pb dating of monazite constrains syn-D1 melting in a migmatitic paragneiss of the Bole-Bulenga terrain (sample BN 43) at 2137 $\pm$ 8 Ma (Block et al., 2015).

The sub-vertical, overprinting cleavage S3 carries high-grade metamorphic assemblages, which include kyanite, biotite and garnet. Kyanite is hosted in both D1 and D3 microstructures. It suggests that both fabrics formed under similar high-grade conditions. In the interference zone within the Bole-Bulenga domain, a generation of leucosomes overgrows the S1 metamorphic banding. Figure 3.4 shows a migmatitic paragneiss (sample BN753) with a shallow south-dipping foliation S1, parallel to a transposed sedimentary layering S0, recognisable by the alternation of layers of fusible and refractory compositions. S1 is overprinted by the subvertical cleavage S3, which is axial-planar to tight folds F3. Melt is collected in F3 axial sur-

faces and transposed parallel to S3 (Vernon and Paterson, 2001). This observation provides evidence that conditions for partial melting were met during D3.

Late-kinematic subhedral staurolite is found partly overgrowing S3 and aligned parallel to the mineral stretching lineation L3, particularly in D3 shear zones. This suggests amphibolite-facies retrograde metamorphism at a late stage of D3. The metamorphic overprint is characterised by conditions of 7-10 kbar at 550-680 °C, which match a 20-25 °C/km apparent geotherm. The timing of amphibolite-facies metamorphism in the Abulembire and Bole-Bulenga domains was constrained by *in-situ* U-Pb dating of monazite grains at 2131 ± 6 Ma (sample BN 436) and 2127 ± 7 Ma (sample BN 47) respectively (Block et al., 2015). Replacement of garnet, biotite and aluminosilicates by chlorite, epidote and muscovite, or of hornblende by epidote and green amphibole, is observed along D4 and D5 shear structures, which must have acted as late-stage fluid pathways. Further retrograde evolution is evidenced by Qz-Chl, Qz-white mica and Qz-Ep veins, and by brittle faults in-filled by Chl.

3.2.5.3 Structural-metamorphic map

Figure 3.5 displays the trajectories of foliation S1, superimposed on the map of the distribution of metamorphic facies. S3 is also shown in lithologies when it forms the earliest fabric, i.e. in syn-D3 plutons. As in Fig. 3.2, the shear zones are colour-coded to indicate the deformation phase under which they formed or were last-activated. This map illustrates that :

- The early fabric S1 is preserved away from the prominent N-S and NE-SW high-strain zones, and outside the interference zone between the Jirapa and Bole-Nangodi shear zones. It is distributed across all tectono-metamorphic domains, and its strike varies from ENE to WNW. Isograds (e.g. *melt in* isograd = amphibolite/migmatite contact, Fig. 3.5) and metamorphic breaks are parallel to S1. They are formed by syn-D1 shear zones which terminate on younger structures. Syn-D2 structures have orientations similar to D1 faults and form domain boundaries. They may be inherited from D1.
- S1 is transposed locally due to east-west shortening, in the vicinity of younger shear zones, and in particular in the interference zone between the Jirapa and Bole-Nangodi shear zones. Syn-D3 shear zones also generate metamorphic breaks or offset pre-existing ones. Isograds and tectonic contacts formed during D1/D2 are folded parallel to a NNE direction and transposed along younger shear zones.

3.2.6 Geochronology

3.2.6.1 Method and sample description

U-Pb dating was carried out on zircon and monazite grains from magmatic and metamorphic rocks, in order to constrain the timing of deformation. A first set of analyses was performed *in-situ* on polished thin sections of samples BN118 and BN534, using laser ablation - inductively coupled plasma - sector field - mass spectrometry (LA-ICP(SF)-MS) at Goethe University Frankfurt. A second set of analyses was carried out on zircons included in epoxy mounts for samples BN110,

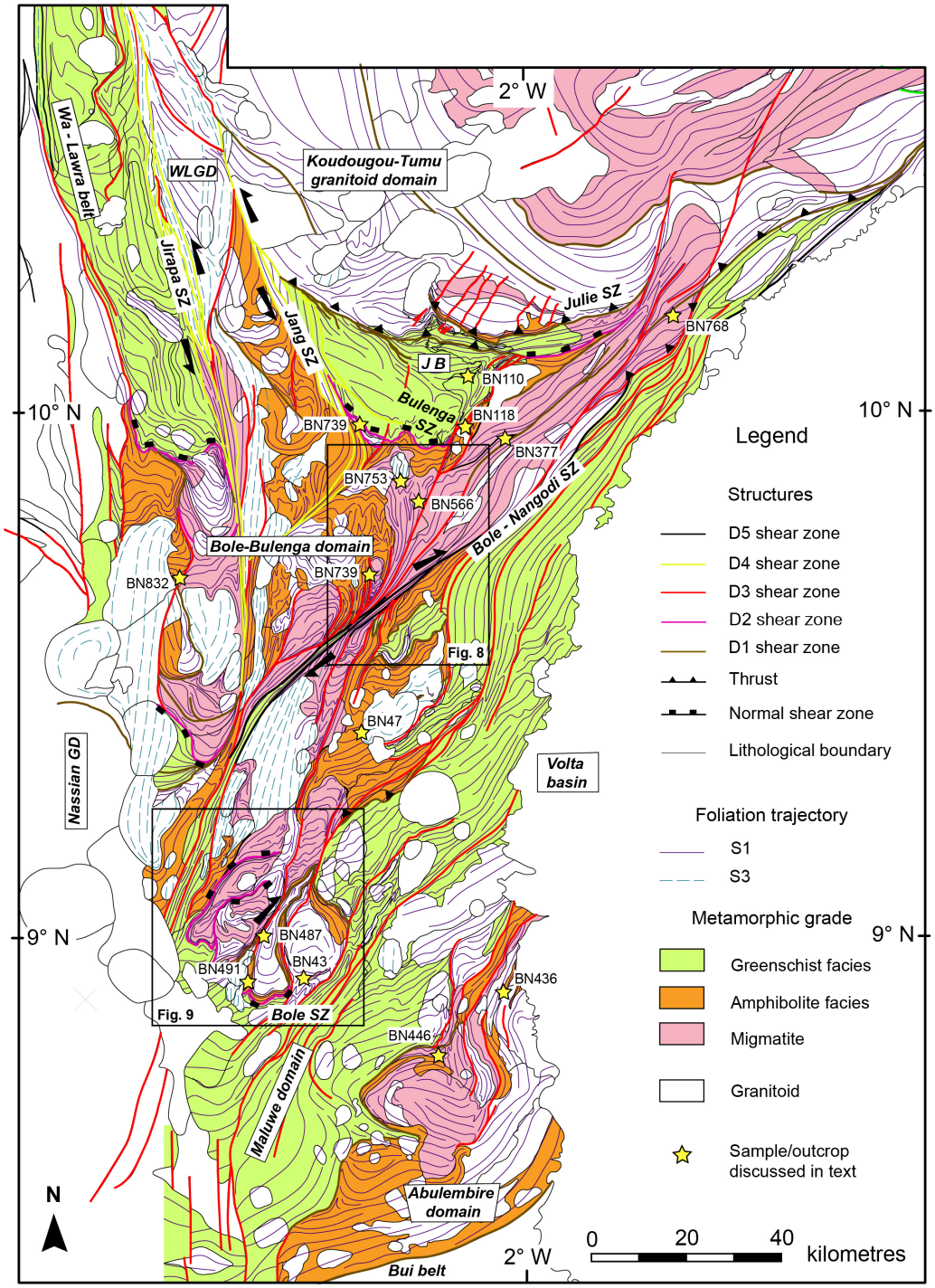

FIGURE 3.5: Structural and metamorphic map of northern Ghana. The foliation trajectory S3 is represented in lithologies where it is the earliest tectonic fabric (e.g. syn-D3 granitoids). Spacing between trajectory lines is inversely proportional to strain intensity.

BN377, BN446 and BN753 using LA-ICP-MS at Géosciences Montpellier. Methodological details are provided in the appendix 3.2.9.1.

Sample BN118 Sample BN118 is a staurolite-bearing paragneiss within a D3 shear zone, which separates the polymictic sediments and conglomerates of the Julie belt, to the west, from higher-grade paragneiss of the Bole-Bulenga domain, to the east. Fabrics in the shear zone are transposed parallel to S3, which forms a penetrative metamorphic banding. The rock has a Bt-Pl-Ilm-Qz matrix, and contains millimetric garnet and syn-kinematic staurolite porphyroblasts (Fig. 3.6a). The porphyroblasts are elongated parallel to the L3 stretching lineation. Monazite grains 15-60 ţm long and devoid of chemical zoning are deformed and aligned parallel to matrix minerals (Fig. 3.6b).

Sample BN534 Sample BN534 is from a migmatitic pelitic paragneiss, found to the west of the Jirapa shear zone, in the Bole-Bulenga domain. The rock displays alternating garnet- kyanite-bearing neosomes and biotite-rich paleosomes, oriented parallel to S1. The peak metamorphic assemblage includes Grt + Bt + Ky + Pl + Rt + L, indicating melting at P > 10 kbar Block et al. (2015). The migmatitic banding is overprinted by the S3 cleavage, defined by recrystallized secondary biotite. Late-stage (retrograde) flaky muscovite grew in leucosomes and is non oriented. Aggregates of unzoned monazite grains are found elongated parallel to S1 in neosomes and are included in muscovite (Fig. 3.6c). Their textural position suggests that monazite crystallised before sub-solidus retrogression during D1.

Sample BN 446 This sample originates from a stromatic migmatitic paragneiss in the Abulembire domain. The rock contains abundant clasts, which suggests a volcanoclastic protolith. Thin (< 1 cm) leucosomes are parallel to the S1 foliation and are transposed to S3 by axial planar ptygmatic folds. They are connected to 2-10 cm large granitic veins and dikes which cross-cut the fabrics. Zircon grains have variable shapes ; some are rounded while others are euhedral (Fig. 3.6d). They display oscillatory zoning patterns consistent with a magmatic origin. Some grains are rimmed by thin (< 10 μm) anhedral domains, which correspond to metamorphic overgrowths.

Sample BN110 Sample BN110 is a volcano-sedimentary rock from a F1 fold limb in the polymictic sediment and conglomerate basin lain in the hanging-wall of the extensional Bulenga shear zone (Fig. 3.6e). It contains quartz phenocrystals, sodic plagioclase, K-feldspar in a matrix of aligned white micas. The rock is mainly derived from reworked felsic volcanic material. The sample contains abundant zircons that form a homogeneous population in terms of size, colour and morphology. Observed in backscattered electron microscopy the grains have euhedral shapes, sharp terminations and euhedral oscillatory zoning (Fig. 3.6f). These characteristics point to a local, magmatic origin and are inconsistent with transport of sedimentary material over a long distance.

Sample BN377 Sample BN 377 originates from an outcrop of migmatitic “composite gneiss” in the north-eastern Bole-Bulenga domain. The outcrop comprises a

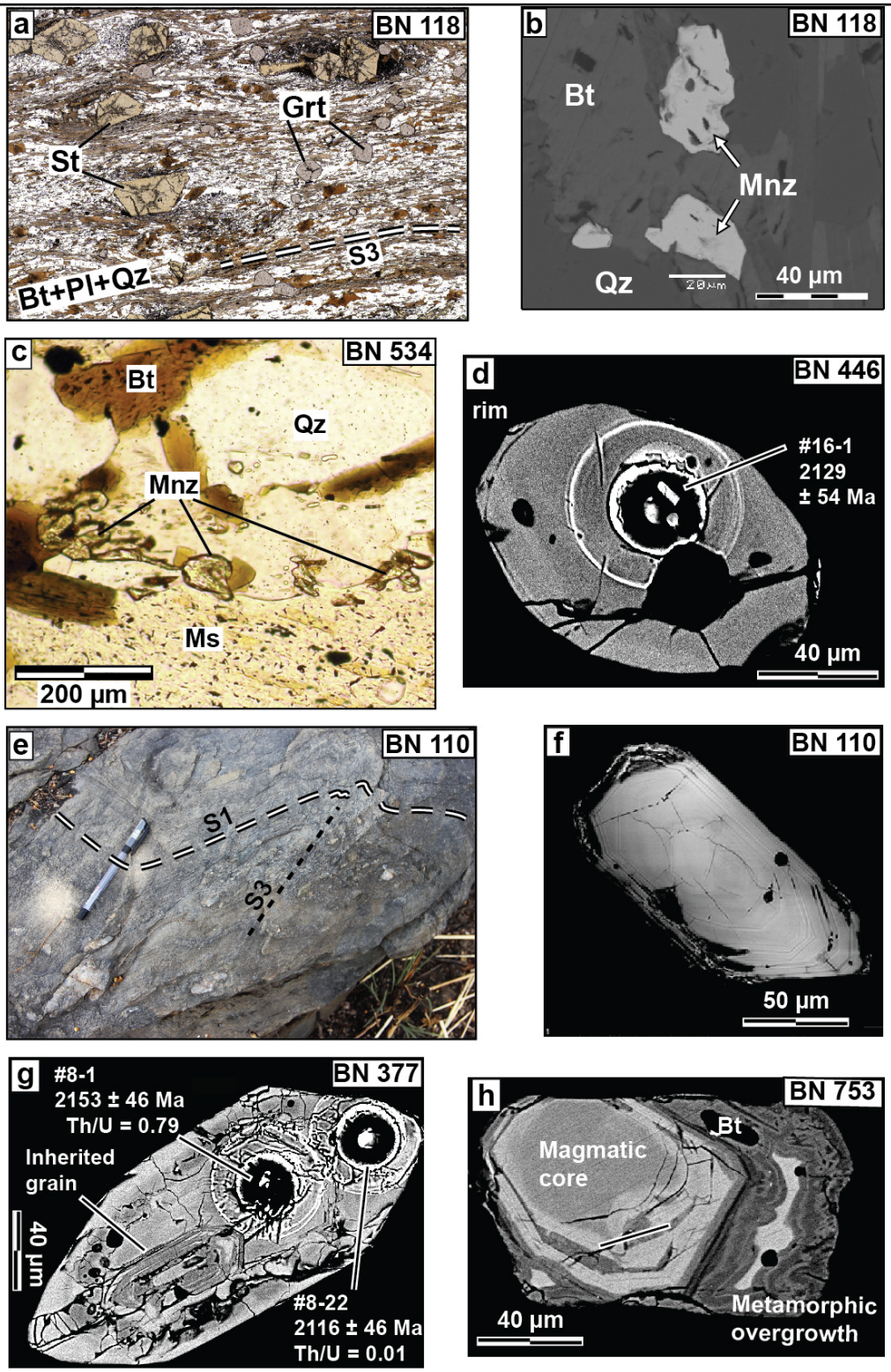

FIGURE 3.6: Photographs, photomicrographs and REM images of dated rocks.

FIGURE 3.6: (**a**). Sample BN118 displays a penetrative foliation S3 defined by aligned micas, and contains garnet and staurolite porphyroblasts. Monazite grains (**b**) are found in the matrix and are elongated parallel to the metamorphic banding. (**c**) Polymictic sedimentary rocks displaying alternating quartzite and conglomerate layers close to the site where sample BN110 was taken. The stratigraphic layering is parallel to a cleavage S1. It is folded and overprinted by S3. Quartzitic beds contain subhedral magmatic zircons (**d**). (**e**) Monazite grains in migmatitic paragneiss sample BN534. They are in contact with muscovite that grew following the crystallisation of leucosomes. (**f, g, h**) REM images of zircons from samples BN446, 377 and 753 respectively. They display zoned magmatic domains overgrown by unzoned metamorphic rims and they sometimes contain inherited grains.

granodiorite gneiss intercalated with paragneiss layers and pyroxenite lenses. Rocks display a foliation S1 parallel to the migmatitic banding. Secondary grain recrystallization defines later fabric S3. Granitic dykes and leucocratic segregates transect S1 and are localised in syn-D3 shear bands. The sample is from a leucocratic segregate 10-20 cm thick transecting S1. Zircon grains display oscillatory zoning patterns and subhedral shapes, suggesting a magmatic origin and possible resorption during metamorphism. Some grains show complex internal structures (Fig. 3.6g). They contain inherited cores rimmed by domains characterised by an oscillatory zoning. The zoning pattern is sometimes erased in outer rim domains, suggesting secondary recrystallisation of magmatic zircon.

Sample BN 753 Leucosome segregates were sampled from the outcrop of migmatitic paragneiss presented in Fig. 3.4, in the northern Bole-Bulenga domain. The leucosomes are transposed parallel to F3 fold axial surfaces. Most zircon grains are euhedral and translucent, with fine oscillatory zoning patterns, suggesting crystallisation from the magma. Inherited grains form cores in magmatic grains, or are rimmed by anhedral metamorphic overgrowths (Fig. 3.6h). The latter display a complex zoning which may represent diffusion fronts.

3.2.6.2 Results

Results are presented in Figure 3.7 and tables 3.1 to 3.3.

Sample BN 118 Seventeen U-Pb-Th spot analyses were carried out on eight elongated monazite grains located in the matrix (Fig. 3.7a). Out of these, twelve analyses from seven monazite grains yield a Concordia age of 2123 ± 8 Ma ($MSWD_{C+E}$ = 0.18, $Probability_{C+E}$ = 1.0, C+E = concordance and equivalence). This age is interpreted as the age of crystallisation of metamorphic monazite in sample BN 118, and is a maximum age for D3 deformation reflected by monazite orientation.

Sample BN534 Thirty U-Pb-Th spot analyses were performed on 4 monazite grains (Fig. 3.7b). Thirteen analyses from all grains define a Concordia age of 2128 ± 8 Ma ($MSWD_{C+E}$ = 0.14, $Probability_{C+E}$ = 1.0). Based on textural arguments, this age is interpreted to date syn-D1 supra-solidus metamorphic evolution of the rock.

Sample BN446 Twenty three U-Pb-Th spot analyses were obtained from as many zircon grains. All spots were focused on domains displaying euhedral oscillatory zoning, because the overgrowths are too thin to be analysed. Seventeen analyses yielded equivalent ^{207}Pb/ ^{206}Pb ages and define an upper intercept age of 2131 ± 12 Ma (MSWD = 0.74), which is within error of a Concordia age of 2132 ± 7 Ma ($MSWD_{C+E} = 0.56$, $Probability_{C+E} = 0.79$, n = 4, Fig. 3.7c). Other grains provide older ages, including two concordant analyses at *ca.* 2200 and 2240 Ma ages (#23-1 and 20-1 respectively). The 2132 ± 7 Ma Concordia age is interpreted to date the crystallisation of the volcanic protolith of the migmatitic paragneiss, and therefore provides a maximal age for metamorphism, while older ages date the crystallisation of inherited cores rimmed by younger domains. The 2132 Ma age is identical to the age of zircons in the volcanoclastic material from sample BN110.

Sample BN110 The twenty four spot analyses out of as many zircon grains define a cluster of sub-concordant analyses which yield a ^{207}Pb/ ^{206}Pb weighted mean age of 2129 ± 7 Ma (MSWD = 1.0, Fig. 3.7d). Since the grains have simple internal structures, and define a single age population, this age is interpreted to date the age of the volcanic material eroded and deposited to form the detrital sedimentary protolith. It is tentatively proposed that the *ca.* 2129 Ma age closely approximates the deposition age of the sedimentary material.

Sample BN377 Fifteen U-Th-Pb spot analyses were carried out on selected domains of thirteen zircon grains. Three discordant analyses from zircon cores (#3-2, 9-1 and 10-1) yield old ^{207}Pb/ ^{206}Pb ages of *ca.* 2.17 - 2.22 Ga. Three other concordant analyses (#1-1, 7-2 and 8.1) have a weighted mean age of 2160 ± 28 Ma (2σ, Fig. 3.7e). They date zircon crystallisation, possibly during emplacement of the protolith of the orthogneiss which contains the melt segregates. The nine other analyses define a limited range of overlapping ages, and data points spread along a regression line providing an upper-intercept age of 2117 ± 12 Ma (MSWD = 1.03, not shown). Out of these, six analyses are located on recrystallized zircon rims and are characterised by low Th/U ratios (<0.02) (blue ellipses in Fig. 3.7e ; e.g. #8-22 ; Table 3.2 ; Fig 3.6g). They define an upper-intercept age of 2112 ± 15 Ma (MSWD = 0.47), which is the age of zircon formed or recrystallized during high-T metamorphism, associated to the emplacement of cross-cutting granitic dikes.

Sample BN753 Seventeen U-Pb-Th LA-ICP-MS spot analyses were obtained from fifteen zircon grains (Fig. 3.7f). Out of these, fifteen analyses from thirteen euhedral (magmatic) grains have consistent ^{207}Pb/ ^{206}Pb ages and lay on a regression line yielding an upper intercept age of 2113 ± 15 Ma (MSWD = 3.0). A cluster of three concordant analyses provides an identical Concordia age of 2111 ± 7 Ma ($MSWD_{C+E} = 0.24$, $Probability_{C+E} = 0.95$). Analyses #1-1 and 8-1 respectively have concordant 2192 ± 49 Ma and discordant 2475 ± 47 Ma ^{207}Pb/ ^{206} ages (2σ) suggesting the occurrence of early Paleoproterozoic components in the source region of the detritus. The 2111 ± 7 Ma age is interpreted to date zircon crystallisation from the leucosome, while older ages reflect the ages of clastic materials which were eroded and deposited to form the paragneiss.

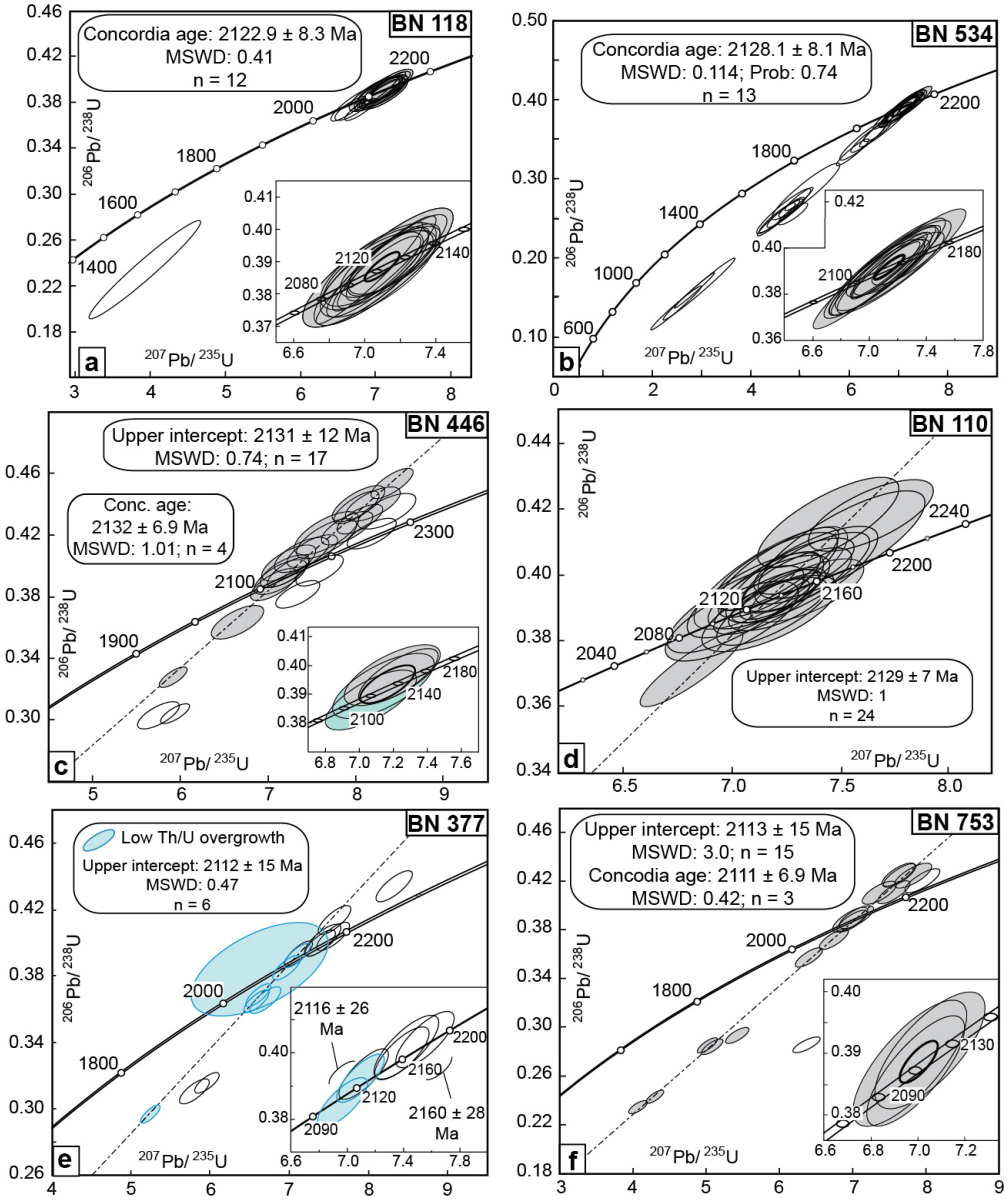

FIGURE 3.7: Results of U-Pb zircon and monazite dating. (**a**) Trail of monazite grains in a quartz-biotite-muscovite neosome, in migmatitic paragneiss BN534. **b**). Zircon grain from sample BN377 displaying an oscillatory zoning. It contains an inherited grain core and has a recrystallized rim domain that is devoid of zoning, is characterised by lower Th/U and that yields a younger Pb/Pb age. (**c**). Zircon grain from sample BN753 displaying an oscillatory zoning, overgrown by a metamorphic rim that contains biotite inclusions. (**d, e**). Results of U-Pb dating by LA-ICP-(SF)-MS of monazites from samples BN118 and BN534. (**f-i**). Results of U-Pb dating of zircon of samples BN110, BN377, BN446 and BN753, presented in Concordia diagrams. Grey shaded ellipses show analyses used for crystallisation age calculation. Blue ellipses represent analyses of metamorphic zircon overgrowths. Errors include decay constant uncertainties. Analytical uncertainties are shown as $\pm 2\sigma$.

Sample	Analysis	Pb[a] (ppm)	U (ppm)	Th (ppm)	$\frac{Th}{U}$	$\frac{^{208}Pb}{^{206}Pb}$	$\frac{^{207}Pb}{^{206}Pb}$	$\pm 2\sigma$ (%)	$\frac{^{207}Pb}{^{235}U}$	$\pm 2\sigma$ (%)	$\frac{^{206}Pb}{^{238}U}$	$\pm 2\sigma$ (%)	ρ[b]	$\frac{^{206}Pb^c}{^{238}U}$	$\pm 2\sigma$ (Ma)	$\frac{^{207}Pb}{^{235}U}$	$\pm 2\sigma$ (Ma)	$\frac{^{207}Pb}{^{206}Pb}$	$\pm 2\sigma$ (Ma)	conc.[d] (%)
BN110	**Zircon**																			
	#1-1	42.7	97.1	55.5	0.57	0.161	0.1309	2.4	7.1081	3.6	0.3939	2.7	0.74	2141	49	2125	32	2110.0	42.4	101
	#2-1	54.1	120.9	69.6	0.58	0.170	0.1306	2.4	7.0165	3.7	0.3896	2.8	0.76	2121	50	2114	32	2106.4	41.8	101
	#3-1	63.1	135.3	98.8	0.73	0.187	0.1302	2.2	7.2020	3.2	0.4011	2.4	0.75	2174	45	2137	28	2101.1	37.6	103
	#4-1	33.5	69.3	45.4	0.65	0.190	0.1298	2.4	7.4447	3.6	0.4160	2.7	0.75	2242	51	2166	32	2095.0	41.2	107
	#5-1	57.4	122.7	78.8	0.64	0.176	0.1321	1.9	7.3327	2.6	0.4027	1.7	0.67	2181	32	2153	23	2125.5	33.4	103
	#6-1	56.0	122.1	72.0	0.59	0.161	0.1327	2.5	7.3225	3.9	0.4001	3.0	0.77	2170	55	2152	34	2134.4	43.6	102
	#7-1	41.5	91.8	51.8	0.56	0.159	0.1348	2.1	7.3470	2.9	0.3953	2.0	0.68	2147	36	2155	26	2161.4	36.9	99
	#8-1	85.9	195.8	117.7	0.60	0.162	0.1315	2.5	6.9990	3.6	0.3860	2.6	0.72	2104	46	2111	31	2118.3	43.6	99
	#9-1	39.5	89.3	48.5	0.54	0.148	0.1340	2.6	7.1729	3.6	0.3883	2.4	0.68	2115	44	2133	31	2150.8	44.9	98
	#10-1	67.3	145.7	94.2	0.65	0.186	0.1328	2.0	7.3000	2.8	0.3986	2.0	0.71	2163	37	2149	25	2135.8	34.8	101
	#11-1	49.7	112.1	55.7	0.50	0.136	0.1317	2.2	7.1704	3.2	0.3948	2.3	0.72	2145	42	2133	28	2120.9	38.4	101
	#12-1	71.8	156.2	94.2	0.60	0.171	0.1328	2.2	7.3389	3.3	0.4007	2.5	0.76	2172	46	2154	29	2135.7	37.5	102
	#13-1	43.9	96.3	58.7	0.61	0.167	0.1304	2.5	7.1788	4.0	0.3991	3.2	0.79	2165	59	2134	35	2104.0	43.0	103
	#14-1	21.8	48.4	29.5	0.61	0.172	0.1340	2.0	7.1997	3.1	0.3897	2.3	0.76	2121	42	2136	27	2151.0	34.8	99
	#15-1	75.4	165.0	96.9	0.59	0.162	0.1330	2.6	7.5061	4.2	0.4092	3.3	0.78	2211	61	2174	37	2138.4	45.3	103
	#16-1	16.8	36.2	21.5	0.59	0.180	0.1337	1.9	7.2117	2.6	0.3912	1.7	0.66	2128	31	2138	23	2147.4	33.8	99
	#17-1	85.5	171.8	140.9	0.82	0.240	0.1310	1.7	7.1727	2.7	0.3971	2.1	0.76	2156	38	2133	24	2111.3	30.2	102
	#18-1	57.9	123.7	62.0	0.50	0.146	0.1302	1.9	7.2136	3.2	0.4019	2.6	0.81	2178	47	2138	28	2100.2	32.5	104
	#19-1	77.8	164.4	125.1	0.76	0.220	0.1325	1.9	7.1577	2.8	0.3918	2.1	0.74	2131	37	2131	25	2131.4	32.7	100
	#20-1	65.6	127.6	74.2	0.58	0.180	0.1326	2.2	7.6421	3.1	0.4181	2.1	0.69	2252	40	2190	27	2132.1	38.8	106
	#21-1	86.5	206.2	156.4	0.76	0.198	0.1330	1.3	6.8127	2.9	0.3714	2.5	0.88	2036	44	2087	25	2138.6	23.1	95
	#22-1	57.0	124.3	80.7	0.65	0.172	0.1329	1.4	7.2687	1.8	0.3967	1.1	0.63	2154	21	2145	16	2136.4	24.8	101
	#23-1	34.9	74.4	61.8	0.83	0.208	0.1327	1.5	7.1781	2.1	0.3922	1.4	0.68	2133	25	2134	18	2134.5	26.3	100
	#24-1	81.4	182.9	109.1	0.60	0.151	0.1329	1.4	7.2218	2.1	0.3941	1.6	0.75	2142	29	2139	19	2136.6	24.1	100
BN753	**Zircon**																			
	#1-1	35.5	95.7	59.8	0.62	0.234	0.1372	2.8	7.9523	2.5	0.4204	1.9	0.78	2262	37	2226	22	2192	49	103
	#2-1	120.7	560.9	409.5	0.73	0.149	0.12748	2.6	5.0131	2.2	0.2852	1.8	0.79	1618	25	1822	19	2064	46	78
	#3-1	102.2	243.0	58.0	0.24	0.059	0.13052	2.8	7.6415	2.4	0.4247	1.9	0.78	2282	36	2190	21	2105	48	108
	#3-2	301.8	1042.1	480.0	0.46	0.126	0.12827	2.7	4.2956	2.3	0.2430	1.8	0.78	1402	23	1693	19	2074	47	68
	#4-1	119.0	286.0	60.2	0.21	0.054	0.13353	2.8	7.5622	2.4	0.4109	1.9	0.78	2219	35	2180	22	2145	48	103
	#5-1	82.0	219.0	12.5	0.06	0.020	0.13101	2.8	6.9907	2.4	0.3872	1.9	0.77	2110	34	2110	22	2112	49	100
	#5-2	98.8	244.2	18.2	0.07	0.026	0.13013	3.2	6.9659	2.8	0.3884	2.1	0.75	2116	39	2107	25	2100	56	101
	#6-1	160.3	563.1	150.7	0.27	0.061	0.12977	2.8	5.0794	2.4	0.2840	1.8	0.77	1612	26	1833	20	2095	48	77
	#7-1	70.9	219.5	51.9	0.24	0.078	0.13139	2.8	6.7413	2.4	0.3723	1.9	0.77	2040	33	2078	21	2117	49	96
	#8-1	134.0	509.0	583.8	1.15	0.192	0.16181	2.8	6.3689	2.4	0.2856	1.8	0.77	1620	26	2028	21	2475	47	65
	#9-1	154.8	468.7	2.0	0.00	0.002	0.13	2.8	6.4016	2.4	0.3574	1.8	0.76	1970	31	2033	21	2098	49	94
	#10-1	136.4	500.3	560.5	1.12	0.126	0.13413	2.8	5.4207	2.4	0.2933	1.8	0.75	1658	27	1888	21	2153	49	77
	#11-1	261.6	639.7	4.2	0.01	0.002	0.13009	2.8	7.6261	2.4	0.4254	1.8	0.75	2285	35	2188	22	2099	49	109
	#12-1	81.0	164.6	93.9	0.57	0.163	0.13375	3.1	7.8244	2.7	0.4246	2.0	0.73	2281	38	2211	24	2148	53	106
	#13-1	137.2	578.2	382.7	0.66	0.133	0.12584	3.0	4.0649	2.6	0.2344	1.9	0.73	1358	23	1647	21	2041	53	67
	#14-1	63.5	161.0	26.9	0.17	0.054	0.13105	3.1	7.0516	2.7	0.3905	2.0	0.73	2125	36	2118	24	2112	54	101
	#15-1	219.7	607.6	44.4	0.07	0.025	0.1302	3.0	7.3648	2.6	0.4105	1.9	0.72	2217	35	2157	23	2101	53	106

TABLE 3.1: U–Pb isotopic data obtained by LA-ICP-MS analyses at Géosciences Montpellier, France.[a] Corrected for background. [b] ρ is the $^{206}Pb/^{238}U/^{207}Pb/^{235}U$ error correlation coefficient. [c] Common Pb corrected using measured ^{204}Pb. [d] degree of concordance = $^{206}Pb/^{238}U$ age / $^{207}Pb/^{206}Pb$ age x 100.

Sample	Analysis	Pb[a] (ppm)	U (ppm)	Th (ppm)	$\frac{Th}{U}$	$\frac{^{208}Pb}{^{206}Pb}$	$\frac{^{207}Pb}{^{206}Pb}$	±2σ (%)	$\frac{^{207}Pb}{^{235}U}$	±2σ (%)	$\frac{^{206}Pb}{^{238}U}$	±2σ (%)	ρ[b]	$\frac{^{206}Pb^{c}}{^{238}U}$	±2σ (Ma)	$\frac{^{207}Pb}{^{235}U}$	±2σ (Ma)	$\frac{^{207}Pb}{^{206}Pb}$	±2σ (Ma)	conc.[d] (%)
BN377	**Zircon**																			
	#1-1	74.2	166.8	37.8	0.23	0.2340	0.1341	3.0	7.4206	2.5	0.4017	2.0	0.77	2177	36	2164	23	2152	53	101
	#2-1	93.8	230.8	1.0	0.00	0.0066	0.1313	2.6	7.1174	2.0	0.3936	1.6	0.78	2140	29	2126	18	2115	45	101
	#3-1	134.3	515.0	2.3	0.00	0.0079	0.1282	2.5	5.2428	1.9	0.2968	1.5	0.78	1675	22	1860	16	2074	44	81
	#3-2	66.8	124.2	87.7	0.71	0.2139	0.1392	2.8	8.3249	2.3	0.4342	1.8	0.78	2325	34	2267	20	2217	48	105
	#4-1	209.1	727.9	25.8	0.04	0.0132	0.1302	2.5	6.6067	2.0	0.3685	1.5	0.78	2022	27	2060	17	2100	44	96
	#5-1	119.0	300.9	227.1	0.75	0.2272	0.1313	2.5	7.0953	1.9	0.3924	1.5	0.78	2134	27	2123	17	2115	44	101
	#6-1	67.1	132.7	190.6	1.44	0.3929	0.1328	2.8	7.5708	2.2	0.4139	1.7	0.77	2233	32	2181	20	2136	48	105
	#7-1	182.5	695.1	17.2	0.02	0.0148	0.1310	2.5	6.5841	2.0	0.3649	1.5	0.77	2005	26	2057	17	2112	44	95
	#7-2	76.1	150.9	111.7	0.74	0.2071	0.1358	2.8	7.5529	2.2	0.4040	1.7	0.77	2187	32	2179	20	2174	48	101
	#8-1	158.3	304.9	241.2	0.79	0.2013	0.1342	2.7	7.3895	2.1	0.3999	1.6	0.76	2169	30	2160	19	2154	46	101
	#8-2	84.9	221.0	1.8	0.01	0.0026	0.1314	2.6	6.9671	2.1	0.3851	1.6	0.76	2100	28	2107	19	2116	46	99
	#9-1	32.5	88.8	38.0	0.43	0.1403	0.1356	3.2	5.7994	2.7	0.3105	2.0	0.75	1743	30	1946	23	2172	55	80
	#10-1	78.4	208.7	189.4	0.91	0.3696	0.1371	2.7	5.9582	2.1	0.3157	1.6	0.75	1769	25	1970	19	2191	46	81
	#11-1	62.8	139.3	83.6	0.60	0.1756	0.1331	2.9	6.6963	2.4	0.3655	1.8	0.75	2008	31	2072	21	2139	51	94
	#12-1	1.6	4.4	0.1	0.02	0.0181	0.1252	11.2	6.6243	10.7	0.3841	6.0	0.56	2096	107	2063	94	2032	192	103
BN446	**Zircon**																			
	#1-1	35.1	73.3	25.2	0.34	0.109	0.13232	3.5	8.0332	3.1	0.4406	2.2	0.71	2353	43	2235	28	2129	60	111
	#2-1	33.8	81.1	27.1	0.33	0.110	0.13222	3.5	7.0682	3.1	0.3880	2.2	0.71	2113	40	2120	28	2128	61	99
	#3-1	20.2	99.4	96.9	0.98	0.234	0.1377	3.9	5.7489	3.4	0.3030	2.4	0.70	1706	36	1939	29	2199	67	78
	#4-1	14.8	31.7	15.5	0.49	0.146	0.13205	4.4	7.6681	3.9	0.4214	2.7	0.69	2267	52	2193	35	2125	76	107
	#5-1	22.7	47.3	28.7	0.61	0.183	0.13316	4.1	7.6679	3.7	0.4178	2.5	0.70	2251	48	2193	33	2140	71	105
	#6-1	25.2	58.7	22.1	0.38	0.106	0.13188	3.9	7.1413	3.4	0.3929	2.4	0.69	2136	43	2129	30	2123	67	101
	#7-1	24.8	55.3	26.1	0.47	0.131	0.13061	3.9	7.2370	3.5	0.4020	2.4	0.69	2178	44	2141	31	2106	68	103
	#8-1	60.8	121.3	114.4	0.94	0.258	0.13158	3.7	7.1939	3.2	0.3966	2.2	0.68	2153	40	2136	29	2119	64	102
	#9-1	63.0	124.9	115.0	0.92	0.249	0.1329	3.6	7.5066	3.1	0.4097	2.1	0.68	2214	40	2174	28	2137	62	104
	#10-1	121.1	275.7	102.3	0.37	0.098	0.13501	3.6	8.1973	3.1	0.4403	2.1	0.66	2352	41	2253	28	2164	62	109
	#11-1	84.8	180.0	63.7	0.35	0.111	0.13908	3.7	8.3562	3.3	0.4357	2.2	0.67	2331	42	2270	30	2216	64	105
	#12-1	17.3	44.4	15.1	0.34	0.252	0.13269	4.2	6.6514	3.7	0.3635	2.5	0.67	1999	42	2066	32	2134	72	94
	#13-1	59.7	115.6	99.2	0.86	0.243	0.13146	4.0	7.3842	3.5	0.4073	2.3	0.66	2203	43	2159	31	2118	69	104
	#14-1	25.7	52.3	35.6	0.68	0.209	0.13263	3.1	8.0113	2.6	0.4381	2.0	0.75	2342	39	2232	24	2133	54	110
	#15-1	87.0	182.6	73.3	0.40	0.107	0.13455	2.8	8.4169	2.3	0.4538	1.8	0.76	2412	36	2277	21	2158	49	112
	#16-1	36.2	79.2	46.6	0.59	0.145	0.13234	3.1	7.2296	2.6	0.3963	2.0	0.75	2152	36	2140	24	2129	54	101
	#17-1	105.2	354.5	143.4	0.40	0.152	0.14169	2.8	5.9389	2.3	0.3040	1.7	0.76	1711	26	1967	20	2248	48	76
	#18-1	105.2	372.5	141.1	0.38	0.114	0.13097	2.7	5.9177	2.2	0.3278	1.7	0.75	1828	26	1964	19	2111	47	87
	#19-1	122.8	264.8	78.7	0.30	0.084	0.13563	3.1	8.0492	2.7	0.4305	1.8	0.69	2308	35	2237	24	2172	54	106
	#20-1	62.1	134.1	57.8	0.43	0.143	0.14098	3.3	8.1848	2.8	0.4212	1.9	0.69	2266	37	2252	25	2239	56	101
	#21-1	70.7	171.1	46.4	0.27	0.096	0.13952	3.3	7.3399	2.8	0.3816	1.9	0.68	2084	34	2154	25	2221	57	94
	#22-1	62.3	143.5	18.1	0.13	0.038	0.13502	3.5	7.9044	3.0	0.4247	2.1	0.69	2282	40	2220	27	2164	61	105
	#23-1	71.1	158.6	46.0	0.29	0.097	0.13804	3.4	7.5465	2.9	0.3966	2.0	0.68	2153	36	2179	26	2203	59	98

TABLE 3.2: Continued. U–Pb isotopic data obtained by LA-ICP-MS analyses at Géosciences Montpellier, France.[a] Corrected for background. [b]ρ is the $^{206}Pb/^{238}U/^{207}Pb/^{235}U$ error correlation coefficient. [c] Common Pb corrected using measured ^{204}Pb. [d] degree of concordance = $^{206}Pb/^{238}U$ age / $^{207}Pb/^{206}Pb$ age x 100.

Sample	Analysis	location	$^{207}Pb^a$ (cps)	U[b] (ppm)	Pb[b] (ppm)	$\frac{Th}{U}^b$	$^{206}Pb^c$ (%)	$\frac{^{206}Pb^d}{^{238}U}$	$\pm 2\sigma$ (%)	$\frac{^{207}Pb^d}{^{235}U}$	$\pm 2\sigma$ (%)	$\frac{^{207}Pb^d}{^{206}Pb}$	$\pm 2\sigma$ (%)	ρ^e	$\frac{^{206}Pb}{^{238}U}$	$\pm 2\sigma$ (Ma)	$\frac{^{207}Pb}{^{235}U}$	$\pm 2\sigma$ (Ma)	$\frac{^{207}Pb}{^{206}Pb}$	$\pm 2\sigma$ (Ma)	conc.[f] (%)
BN118	**Monazite**																				
	#1-1	matrix	67350	4467	4700	4.85	0.03	0.38760	3.3	7.004	4.1	0.131	2.5	0.79	2112	59	2112	37	2112	44	100
	#1-2		40946	2843	3400	5.72	b.d.l	0.38860	2.8	7.076	3.8	0.1321	2.5	0.75	2116	51	2121	34	2126	44	100
	#2-1	matrix	73575	4930	4500	4.03	0.01	0.38910	2.3	7.081	2.7	0.132	1.3	0.87	2119	43	2122	24	2125	24	100
	#2-2		46625	3230	3000	4.29	b.d.l	0.39010	2.4	7.049	3.2	0.1311	2.2	0.74	2123	44	2118	29	2112	38	101
	#3-1		86145	5818	5400	4.23	0.04	0.38890	3.3	7.026	3.5	0.131	1.1	0.95	2118	60	2115	32	2111	20	100
	#3-2		84648	5775	5300	4.18	0.01	0.39180	3.1	7.11	3.4	0.1316	1.3	0.92	2131	56	2125	30	2120	23	101
	#3-3	matrix	80255	5753	5100	3.97	0.05	0.38910	2.9	7.074	3.3	0.1318	1.6	0.87	2119	53	2121	30	2123	29	100
	#3-4		73985	5441	4600	3.83	0.22	0.37390	2.1	6.797	2.5	0.1319	1.3	0.86	2048	37	2085	22	2123	22	96
	#4-1	matrix	55226	3946	3800	4.34	b.d.l	0.39360	2.8	7.179	3.2	0.1323	1.7	0.86	2140	51	2134	29	2128	29	101
	#5-1	matrix	89986	6577	5500	3.40	0.03	0.39160	2.2	7.123	3.0	0.1319	2.1	0.72	2130	39	2127	27	2124	37	100
	#5-2		85784	6307	5000	3.45	0.26	0.37500	2.3	6.701	2.9	0.1296	1.8	0.79	2053	41	2073	26	2093	32	98
	#6-1	matrix	25489	1676	1500	3.84	0.72	0.37810	3.1	6.693	3.5	0.1284	1.6	0.89	2067	55	2072	32	2076	29	100
	#6-2		11219	491	540	6.04	1.06	0.23400	15.0	3.929	15.5	0.1218	3.8	0.97	1355	186	1620	134	1983	68	68
	#7-1	matrix	55037	4540	4200	3.90	b.d.	0.39080	3.8	7.106	4.5	0.1319	2.4	0.84	2126	69	2125	41	2123	42	100
	#7-2		76595	6108	5600	4.29	0.01	0.39290	2.3	7.163	3.0	0.1322	1.8	0.78	2136	42	2132	27	2128	32	100
	#8-1	matrix	66922	5361	6400	6.38	0.11	0.38730	2.8	7.124	3.5	0.1334	2.1	0.81	2110	51	2127	32	2143	36	98
	#8-2		64658	5031	5100	4.86	0.24	0.39280	2.2	7.167	3.0	0.1323	2.0	0.74	2136	40	2132	27	2129	35	100
BN534	**Monazite**																				
	#1-1		85983	5672	6900	5.76	0.09	0.38070	3.5	6.944	4.0	0.1323	2.0	0.87	2079	62	2104	36	2129	34	98
	#1-2	neosome,	100664	6460	6300	3.91	b.d.	0.39160	2.5	7.155	3.1	0.1325	1.7	0.82	2130	46	2131	28	2132	30	100
	#1-3		107226	7334	6800	3.89	0.02	0.39000	4.0	7.101	4.4	0.132	1.9	0.90	2123	73	2124	40	2125	33	100
	#1-4	inclusion	82838	6909	4800	2.81	0.16	0.25740	6.1	4.71	6.6	0.1327	2.6	0.92	1477	80	1769	57	2134	45	69
	#1-5		88873	5724	4200	3.20	0.12	0.25900	9.0	4.668	9.6	0.1307	3.3	0.94	1485	121	1761	84	2108	59	70
	#1-6	in	45772	6890	4100	1.70	0.54	0.28390	10.3	5.118	11.1	0.1307	4.0	0.93	1611	148	1839	98	2108	71	76
	#1-7		62653	4790	4900	4.06	0.01	0.39030	4.1	7.115	4.4	0.1322	1.7	0.92	2124	74	2126	40	2127	30	100
	#1-8	retrograde	85405	5626	5900	4.63	0.10	0.39430	4.7	7.225	5.1	0.1329	2.1	0.91	2143	86	2140	47	2137	37	100
	#1-9		89670	5973	6100	4.49	0.14	0.39120	4.5	7.107	4.9	0.1318	1.9	0.92	2128	83	2125	45	2122	34	100
	#1-10	muscovite	61670	4897	3000	2.69	2.19	0.16050	20.0	2.95	20.3	0.1333	3.5	0.99	960	181	1395	167	2142	61	45
	#1-11		111200	7256	6600	3.51	0.10	0.39540	2.4	7.271	2.9	0.1334	1.6	0.83	2148	43	2145	26	2143	28	100
	#2-1	matrix	72519	4886	6900	7.31	0.10	0.38880	3.8	7.076	4.2	0.132	1.8	0.90	2117	69	2121	38	2125	32	100
	#3-1		142184	9894	8100	3.30	0.00	0.39030	2.6	7.112	2.8	0.1321	1.0	0.93	2124	47	2125	25	2127	18	100
	#3-2		130257	9334	7800	3.30	0.07	0.37790	3.3	6.783	3.6	0.1302	1.4	0.92	2066	58	2083	32	2100	24	98
	#3-3		215490	16152	8100	1.67	b.d.	0.26280	3.6	4.824	4.3	0.1331	2.3	0.84	1504	49	1789	37	2139	41	70
	#3-4		225381	17313	8900	1.83	0.02	0.25540	4.4	4.855	5.1	0.1379	2.5	0.87	1466	58	1794	44	2201	43	67
	#3-5	matrix	71453	17274	9700	1.15	0.11	0.39130	2.6	7.112	3.2	0.1318	1.8	0.83	2129	48	2126	29	2122	31	100
	#3-6		69120	9195	7100	2.67	0.02	0.39240	2.9	7.135	3.1	0.1319	1.1	0.94	2134	53	2128	28	2123	19	101
	#3-7		43080	6733	5000	2.91	0.13	0.34830	5.8	6.29	6.3	0.131	2.4	0.93	1927	98	2017	57	2111	41	91
	#3-8		49596	6862	6000	3.28	0.15	0.39150	2.7	7.138	2.9	0.1323	1.1	0.93	2130	50	2129	27	2128	19	100
	#3-9		48846	8238	6400	2.79	b.d.	0.36020	3.0	6.577	3.5	0.1324	1.7	0.87	1983	52	2056	31	2131	30	93
	#4-1	neosome,	114726	7411	6900	4.28	0.01	0.33340	4.2	6.07	4.4	0.1321	1.6	0.94	1855	67	1986	39	2125	27	87
	#4-2		81889	8595	6300	2.63	b.d.	0.35180	4.3	6.395	4.6	0.1319	1.8	0.93	1943	72	2032	42	2123	31	92
	#4-3	inclusion	110847	7447	6900	3.68	b.d.	0.39240	4.1	7.167	4.6	0.1325	2.2	0.88	2134	74	2132	42	2131	39	100
	#4-4		72056	14423	4300	1.05	0.01	0.13660	16.6	2.484	16.9	0.1319	3.2	0.98	826	130	1267	131	2123	56	39
	#4-5	in	152381	10906	8400	2.73	0.03	0.38740	4.7	7.035	5.0	0.1317	1.7	0.94	2111	86	2116	46	2121	30	100
	#4-6		87556	8791	5600	2.70	b.d.	0.27420	4.4	4.979	4.7	0.1317	1.7	0.93	1562	61	1816	40	2120	30	74
	#4-7	retrograde	164732	16038	5800	1.34	0.05	0.15880	11.6	2.856	11.7	0.1304	1.8	0.99	950	103	1370	92	2104	32	45
	#4-8		135848	10032	6100	2.57	b.d.	0.25020	7.4	4.564	7.7	0.1323	2.3	0.96	1440	96	1743	66	2128	40	68
	#4-9	muscovite	156766	12821	7800	2.61	0.01	0.25080	6.1	4.54	6.6	0.1313	2.4	0.93	1442	80	1738	56	2115	41	68
	#4-10		131015	9669	7300	2.80	0.00	0.36760	6.1	6.738	6.4	0.133	1.9	0.95	2018	107	2078	58	2137	34	94

TABLE 3.3: LA-ICP-MS U-Pb isotopic data of monazites from metamorphic rocks. Analyses were carried out at Goethe Universität Frankfurt

3.2.7 Discussion

3.2.7.1 Geochronological constraints on the tectonic evolution.

Relics of HP-LT, blueschist- to epidote-amphibolite-facies metamorphic assemblages suggest burial of sedimentary rocks along a cold apparent geothermal gradient before 2137 ± 8 Ma, which is the age of syn-D1 high-grade metamorphism and anatexis (Block et al., 2015). The fact that high-grade metamorphic assemblages are found aligned parallel to D1 (N-S shortening) and D3 (E-W shortening) fabrics suggests that the rocks resided at similar crustal depths during both deformations. During orogeny, changes in crustal thickness drive the lithosphere away from a state of thermo-mechanical equilibrium. Following tectonic perturbation, isostatic compensation and thermal relaxation bring the crust back towards a state of thermo-mechanical equilibrium. As a consequence, thermal conditions in orogens are transient (England and Thompson, 1984). Long-lived geological processes maintain a steady flow of rock through the orogeny (Willett and Brandon, 2002). Because of these phenomena, a given volume of rock is not expected to remain at constant P-T conditions for long periods, and significant changes in metamorphic conditions are expected over time scales of 10 Ma (e.g. Rubatto and Hermann (2001), for modern orogenic belts; Collins et al. (2004); Millonig et al. (2010), for Paleoproterozoic orogenic belts). Fabrics formed in similar metamorphic conditions are therefore likely to be nearly contemporaneous. In north-western Ghana, field observations do not provide any evidence for an interruption of tectonic activity between D1 and D3. Both deformations may have occurred within a short period of time, and may represent a continuous evolution rather than two discrete events. This hypothesis is supported by geochronological data (Fig. 3.8a). Partial melting associated to D1 fabrics in sample BN 534 is dated at 2128 ± 8 Ma. This age overlaps within errors the 2137 ± 8 Ma, 2131 ± 6 Ma and 2127 ± 7 Ma ages of monazite in samples BN 43, BN 436 and BN 47 respectively (Block et al., 2015). Furthermore, metamorphic volcano-sedimentary rocks in the Abulembire domain (sample BN 446) and polymictic sediments and conglomerates in the Julie belt (sample BN 110), both of which witnessed D1 deformation and metamorphism, contain volcanic material with crystallisation ages of 2132 ± 7 and 2129 ± 7 Ma respectively. This indicates that sediments must have been deposited in syn-tectonic basins formed during ongoing D1 shortening. As the rocks are deformed by D1, these ages provide a maximum age for the end of D1 (Fig. 3.8). Granites intrusive in the Bole-Bulenga and Maluwe domains (G4 in Fig. 3.2) with ages ranging from 2122 ± 6 Ma to 2118 ± 3 Ma (De Kock et al., 2011), are unaffected by D1 and variably develop D3 fabrics. Their crystallisation ages provide a minimum age for the end of D1 and for the beginning of D3. The 2123 ± 8 Ma age obtained from monazite in sample BN 118 provides a maximum age for the activity of a D3 shear zone and associated amphibolite-facies metamorphism. Syn-D3 melting in sample BN 753 is dated at 2111 ± 7 Ma, consistent with the 2112 ± 15 Ma metamorphic zircon overgrowths in sample BN377. An undeformed granite in the Wa-Lawra belt with a formation age of 2104 ± 1 Ma (Duodu, 2009) defines a minimum age for the end of D3. Geochronological data show that the exhumed lower crust recorded anatectic conditions maintained from 2137 ± 8 to ca. 2111 ± 7 Ma (Fig. 3.8a).

Deformations D1 and D3 are constrained by overlapping ages, pointing to a

possible continuous evolution from one strain field to the other (Fig. 3.8a). Although no overprinting relationships were found between D1 and D2 structures, we consider that extension affected a previously thickened crustal pile (see next section). This implies that extensional deformation D2 must occur in the 2129-2111 Ma bracket, between two contractional deformations. The youngest granite intrusion constrained by U-Pb ages in the study area is dated at 2095 ± 1 Ma (black diamond in Fig. 3.8a, Duodu (2009)) and provides a possible landmark for the end of magmatic activity in the Paleoproterozoic craton of north-western Ghana.

3.2.7.2 Crustal rheology, tectonic style and exhumation dynamics.

The development of a partially molten, low viscosity layer in the crust is expected to cause a significant decrease in crustal and lithospheric strength (Arzi, 1978; Vanderhaeghe and Teyssier, 2001a), with consequences on the deformation mode in the orogen. Heterogeneous crustal thickening due to thrusting and widespread melting of the lower crust provide the conditions for the development of gravity-driven flow of the orogen. The formation of extensional detachments can be interpreted as a response to the buildup of gravitational potential energy induced by crustal thickening and rheological weakening (Dewey, 1988; Rey et al., 2001). Extensional shear zones accommodate the horizontal sliding of large-scale upper crustal slices and vertical exhumation of partially molten lower crust, thus generating anatectic migmatite domes (Whitney et al., 2004). This evolution is typical of overthickened orogens and is widely documented in the Phanerozoic (e.g. Malavieille et al. (1990); Vanderhaeghe and Teyssier (2001b)) and in the Neoproterozoic (e.g. Norton (1986)). Gravity-driven flow develops as early as 20-40 Ma after the onset of collision in modern orogens (e.g. Molnar et al. (1993); Vanderhaeghe and Teyssier (2001b)) and may be maintained as long as tectonic processes form gravitational potential energy gradients in a weak, partially molten lower crust (Jamieson et al., 2011). Extension may directly follow shortening through a near-continuous transition (e.g. Ledru et al. (2001), in the French Variscan belt), or both may develop synchronously due to mechanical decoupling between crustal slices of contrasting viscosity (e.g. Vanderhaeghe and Teyssier (2001a)).

In the field, the Bulenga extensional detachment localises strain between the partially molten lower crust and mechanically stronger upper-crustal lithologies, such as the Julie belt quartzites and conglomerates. Two interpretations may be drawn. (i) The sediments were deposited and folded in an intra-orogenic basin formed during D1. Subsequently, the detachment formed along the margin of the basin. In this case, D1 and D2 are two discrete events (ii) The basin was formed by the activity of the extensional detachment. The detachment became active during D1, opened space for sediment deposition and allowed lower-crust exhumation. D1 contractional deformation further developed in the basin, which was mechanically decoupled from the partially molten lower-crust. This scenario corresponds to syn-convergent extension and exhumation, similar to tectonic models proposed for the Himalaya - Tibet orogen (Burchfiel et al., 1992; Hodges et al., 1992; Jamieson and Beaumont, 2011). In this case, the transition from D1 to D2 reflects the growing influence of gravity-driven flow during convergence.

The development of anatectic migmatite domes implies specific clockwise P-T-t paths (Norlander et al., 2002; Rey et al., 2009). Near adiabatic decompression, or

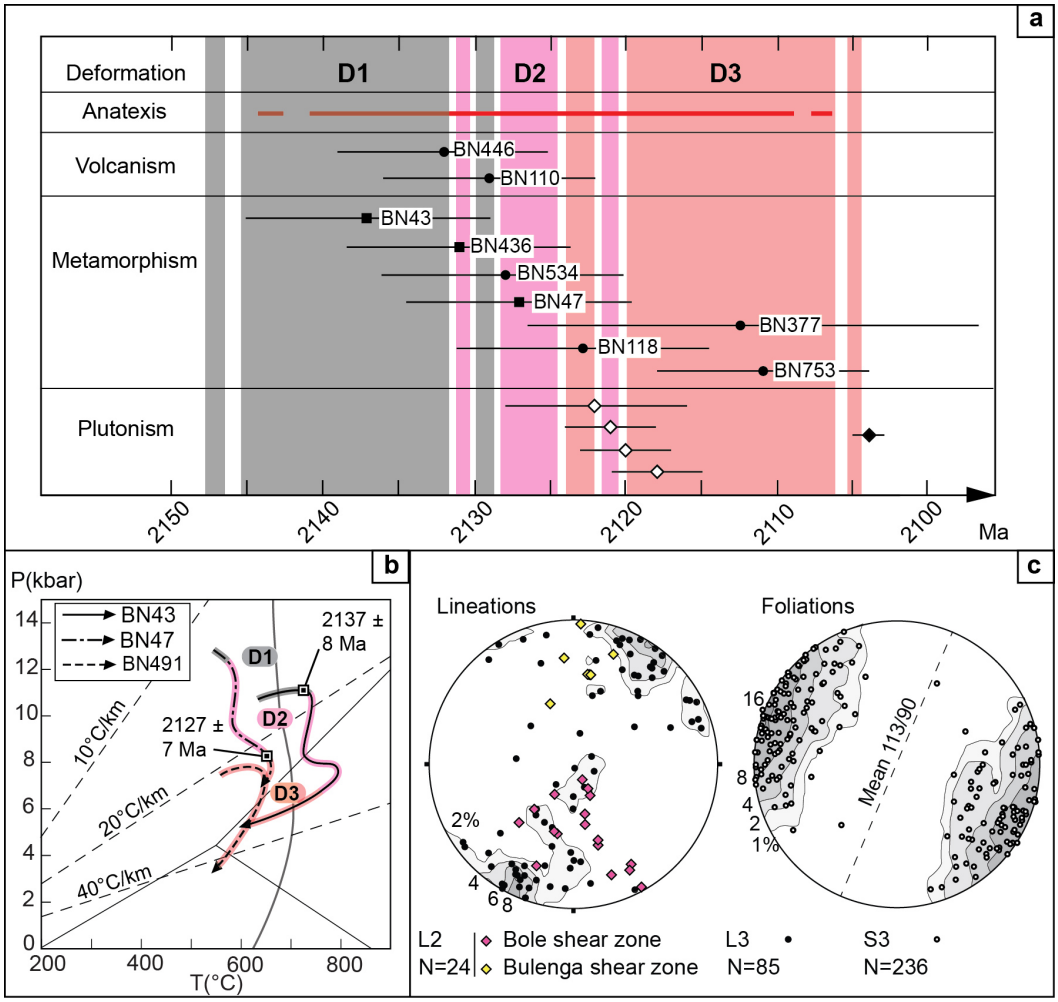

FIGURE 3.8: (**a**) Summary of geochronological constraints on the timing of deformation. Black circles : this study, black squares from Block et al. (2015) ; white diamonds : syn-D3 granite crystallisation age from De Kock et al. (2011) ; black diamond : undeformed granite (Duodu, 2009). The data provide evidence for overlapping deformation events. (**b**). Clockwise P-T-t-D paths followed by rocks of the Bole-Bulenga domain with age constraints on amphibolite- to granulite-facies metamorphic assemblages Block et al. (2015). (**c**). Stereograms built using the program Stereonet 7. Left : L2 lineations in the Bole (pink diamonds) and Bulenga (yellow diamonds) extensional shear zones, plotted with L3 lineations (black circles) and corresponding density contours. Right : S3 metamorphic foliation, density contours and mean plane.

negative dP/dT segments are expected in a context of extensional collapse. Fast exhumation is localised along high strain shear zones limiting the anatectic domes and creates thermal antiforms in the crust. Exhumed rocks record decreasing peak pressures and temperatures with distance to the core of the anatectic migmatite dome (e.g. Duchêne et al. (2006)). The P-T-t-D paths obtained from amphibolite- to granulite-facies rocks of the study area are consistent with this scenario. Migmatites testify of crustal thickening and partial melting of the lower crust at >10 kbar

during D1 (Fig. 3.8b, and Block et al. (2015)). Following peak P, P-T paths show a segment of near-isothermal decompression. The migmatitic gneisses are bounded by sub-solidus rocks that witnessed peak amphibolite-facies metamorphic conditions (Figs. 3.5) and 3.10).

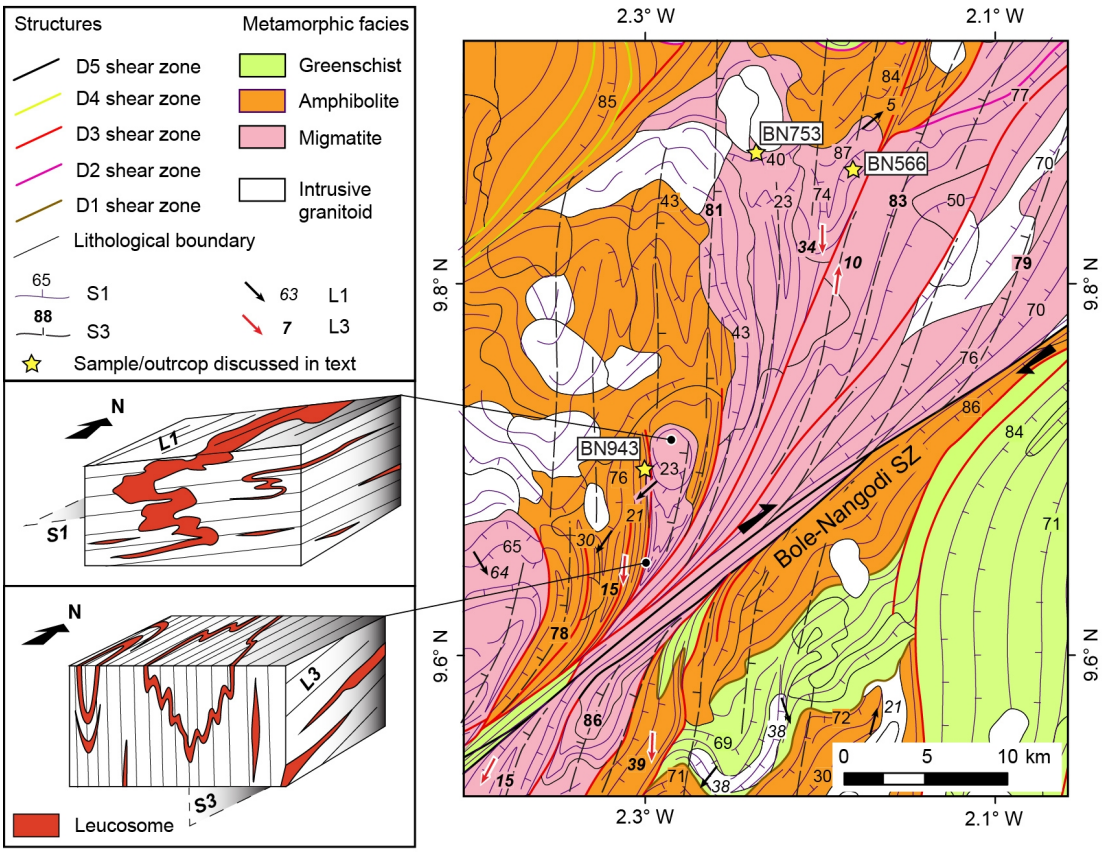

FIGURE 3.9: Detailed structural-metamorphic map of a horsetail structure along the Bole-Nangodi shear zone, in the Bole-Bulenga domain (see Fig. 3.5 for location). Block diagrams illustrate the fabrics associated to D1 and D3 in high-grade rocks.

In the Bole-Bulenga domain, some D3 fabrics are underlined by melt-bearing assemblages, while they carry greenschist- to amphibolite-facies mineral assemblages in surrounding lower-grade units. This provides evidence that high- and low-grade units were not at the same crustal level at the start of D3. On the other hand, the interface between high- and low-grade rocks is folded around F3 folds (Figs. 3.5 and 3.10), suggesting that D3 post-dates exhumation. Reconciling these antagonist field evidence requires that the exhumation and the final juxtaposition of different crustal slices occurred during D3, i.e. in a convergent setting. Fabric transposition parallel to vertical planes characterises D3, and provides evidence for a changing tectonic style (Fig. 3.9). Alternations of migmatitic and sub-solidus gneisses of ∼20 km wavelength are elongated in a N-S direction in the Bole-Bulenga domain, parallel to the D3 structural trend (Fig. 3.5). This succession of synforms and antiforms reflects the undulation of the "envelope" (i.e. a thin transitional metamorphic zone) separating low-viscosity migmatites from overlying rocks (Fig. 3.10). Such geome-

try may reflect syn-D3 amplification of gravity-driven instabilities initiated during the extensional phase D2. Melting likely played a determining role in the development of the instabilities, which contributed to the extrusion of partially molten lower-crustal lithologies (Ganne et al., 2014; Schulmann et al., 2008; Vanderhaeghe, 2009). Melt is drained from migmatites in syn-D3 low permeability or extensional structures and feeds aligned (N-S) granite plutons (G3, Fig. 3.2) which emplaced in sub-solidus rocks at a higher structural level (Fig. 3.5, Brown and Solar (1998a,b)).

S3 cleavages carry mineral stretching lineations (L3) with shallow plunges to the NNE or to the SSW, indicating a general horizontal stretching direction striking N0-N25 at the scale of the Bole-Bulenga domain (Fig. 3.8c). L2 stretching lineations respectively plunge moderately to the N and S in the Bulenga and Bole shear zones (respectively black and pink diamonds, Fig. 3.10c). They indicate local extension directions which are similar to those revealed by L3 at a broader scale. We note that N-S directed stretching is compatible with E-W directed shortening, and both may have synchronously developed within the same strain field.

3.2.7.3 A geodynamic evolution model.

The model proposed by De Kock et al. (2011, 2012) for the geodynamic evolution of north-western Ghana is not supported by our observations. Our results are inconsistent with the existence of two discrete metamorphic events (i.e. high-grade Eoeburnean and low-grade Eburnean episodes), separated by a rifting phase which allowed the deposition of the Maluwe "basin". They rather point to a continuous tectono-metamorphic evolution recorded in coeval high-grade and low-grade metamorphic terranes. According to this model, following thickening and partial melting during D1, the crust is then subject to extensional gravitational collapse and exhumation of the migmatitic lower crust. The transition from D1 to D2 is continuous. It is characterised by syn-convergent extension, exhumation and formation of intra-orogen sedimentary basins under the growing contribution of gravity forces. D2 marks the onset of gravitational flow of the orogen. In light of our complementary datasets, we propose that N-S directed stretching (D2) and E-W horizontal shortening (D3) overlap in time and develop in the same strain field during large-scale anatexis, which lasted between *ca.* 2140 and 2110 Ma. The lateral sliding of low-grade upper crustal units accommodates vertical extrusion of the partially molten lower crust, which forms the core of an anatectic migmatite dome. Horizontal contractional strain outlived extension, as illustrated by the re-folding of the envelope separating migmatites from suprasolidus rocks (Fig. 3.10). As the lower crust is exhumed and starts cooling down, the rock rheology and deformation style change. Deformation is increasingly localised in low strength zones at lithological boundaries. Inherited structures are re-activated under a transcurrent regime and focus retrogression, alteration and strain, while the crust trends towards mechanical and thermal equilibrium, and final stabilisation (D4-D6).

The study reveals a relatively short orogenic cycle, which lasted a minimum of 30 Ma. The shift from D1 to D3 represents a near instantaneous 90 ° rotation in the principal shortening direction. This requires an abrupt change in boundary stresses applied to the lithosphere. We suggest that this may be due to the tectonic juxtaposition of northern Ghana with the cratonic block found in south-western Burkina Faso, across the Wa-Lawra belt, between 2130 and 2110 Ma. This hypothesis may

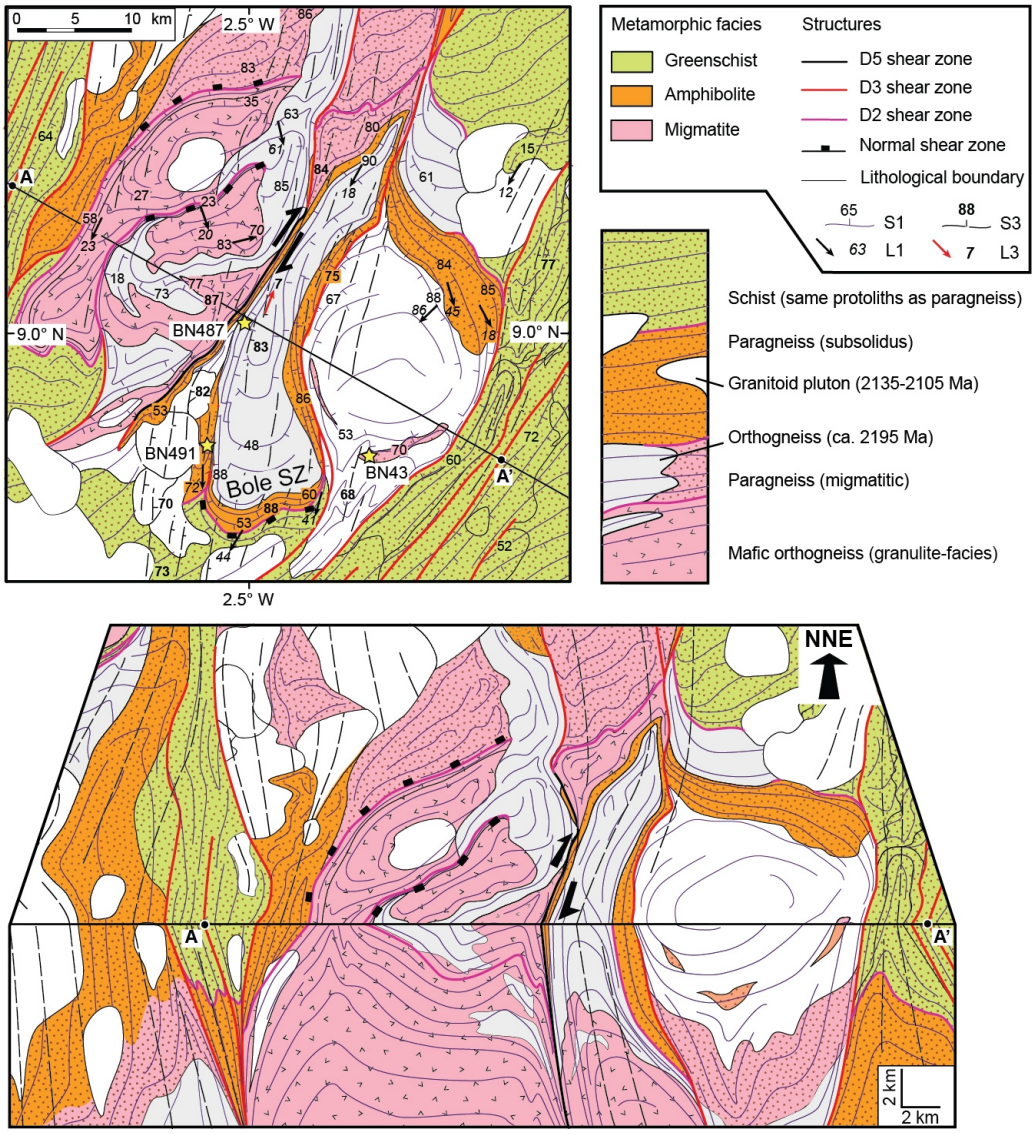

FIGURE 3.10: **Top** : Detailed structural-metamorphic map of the southern termination of the Bole-Bulenga domain (see Fig. 3.5 for location). The stratigraphic column presents the relative position of the main lithological units in the crustal pile. **Bottom** : Block-diagram illustrating the structural relationship between units. Cross-section is along a straight line through points A-A'. Lower-crustal rocks are exhumed at the core of domes bounded by shallow-dipping (D2) shear zones. Sub-vertical shear zones developed during D3 transpose earlier fabrics and form high-strain flanks of antiforms and synforms.

be tested in light of regional tectono-metamorphic correlations. Ganne et al. (2012) describe metamorphic rocks from eastern Burkina Faso which record cold apparent geothermal gradients similar to those attributed to D1-e, and which are ascribed to an early deformation event (D1 of Ganne et al. (2012)). Early (pre-Eburnean ?) deformation, sometimes associated with thrusts, is described in northern Burkina Faso (Hein, 2010; Tshibubudze et al., 2009) and Southern Ghana (Perrouty et al.,

2012). The fabrics are oblique relative to the orientation of prominent late-stage shear zones and reflect homogeneous distributed strain at regional scale. This first convergent tectonic phase may be an analogue of our D1 event. Similar fabrics are found in high-grade gneisses in north-eastern Côte d'Ivoire (Gasquet et al., 2003; Vidal et al., 2009), although their relationship with the high-grade domains of north-western Ghana are unknown. However, vast units of lower-crustal rocks have no known equivalents in south-western Burkina Faso, where the earliest deformation recognised is consistent with E-W shortening (Baratoux et al., 2011), and correlates with our D3. In the Ashanti Belt of southern Ghana, Perrouty et al. (2012) describe an extensional tectonic phase (D2) which corresponds to the deposition of the Kumasi group sediments, between 2154 and 2125 Ma. This phase follows an episode of N-S "Eoeburnean" shortening (D1) between 2187 and 2158 Ma, and precedes NW-SE "Eburnean" shortening (D3) that lasted from 2125 to 1980 Ma. In our model, extension is linked to gravitational flow of an over-thickened crust between *ca.* 2140 and 2110 Ma. Furthermore, in north-western Ghana, we do not recognise discordant Birimian basins analogue to the Kumasi basin. Age data provides evidence that rocks of the Maluwe domain were deposited before or during the orogenic cycle we describe. Therefore, we note discrepancies with the geological evolution of the Ashanti area.

To summarise, the hypothesis of a collision between the cratonic blocks of northern Ghana and south-western Burkina Faso seems supported by (1) low or non-existent D1 strain in south-western Burkina Faso ; (2) domains recording regional high-grade metamorphism at 2140-2130 Ma in NW Ghana, with no known equivalent in southern Burkina Faso or Côte d'Ivoire ; (3) N-S and NE-SW structures (the dominant structural trends in western Burkina Faso - Côte d'Ivoire, and in Ghana respectively) merging in an interference zone in the Bole-Bulenga domain ; (4) high D3 strain intensity in south-western Burkina Faso (equivalent to D1 in Baratoux et al. (2011)) and northern Ghana, while attenuating westwards with distance from the interference zone. Regional correlations reveal similarities in the metamorphic and tectonic evolution of domains in north-eastern Burkina Faso and Ghana, while rocks in south-western Burkina Faso and Côte d'Ivoire seem to have undergone a different evolution.

3.2.7.4 Implications for Paleoproterozoic geodynamics

The Paleoproterozoic craton in north-western Ghana was subject to dominantly horizontal tectonic forces during the Eburnean orogeny. They led to the juxtaposition of contrasting litho-tectonic domains and to the formation of lateral baric metamorphic gradients across thrusts or extensional shear zones. These features are at odds with the large isobaric metamorphic domains (Percival and Skulski, 2000) and dome-and-basin strain patterns described in the Archean (Bouhallier et al., 1995; Choukroune et al., 1995; Collins et al., 1998) and Paleoproterozoic (Trap et al., 2008; Vidal et al., 2009). The structural and metamorphic record illustrates a gradual increase in the apparent geothermal gradient along with a shift in tectonic style induced by rheology changes. The documented barrovian metamorphic cycle and deformation patterns are consistent with evolution models of Phanerozoic collisional orogenic belts. In particular, anatectic migmatite domes bounded by extensional shear zones are hardly reported in the Archean and Paleoproterozoic eons

(see Kisters et al. (2003); Lana et al. (2010), for a possible exception).

In ancient orogens, the apparent lack of typical extensional structures has previously been interpreted as reflecting an absence of lateral gravitational potential energy gradients (Gapais et al., 2009). This in turns was understood to result from elevated Moho temperatures, which prevent significant heterogeneous crustal thickening (Chardon et al., 2009; Rey and Houseman, 2006). Although the architecture of the West African Craton resembles that of Archean cratons, hot orogen models fail to account for the structural and metamorphic features recognized in northwestern Ghana. We consider that crustal thickening and exhumation processes of the Eburnean orogeny share some similarities with modern orogens. It confirms that the Paleoproterozoic is a transitional period representative of a specific style of plate tectonics. This conclusion is supported by complementary evidence on the onset of new processes recorded by the continental lithosphere after the Neoarchean. They include increasing crustal recycling rates (Dhuime et al., 2012; Laurent et al., 2014), changing structural patterns in orogenic belts (Cagnard et al., 2011), and a diversification of geothermal environments recorded by metamorphic rocks worldwide (Brown, 2007, 2009).

The collision model between Paleoproterozoic blocks in Ghana and Burkina Faso Ű Côte dŠIvoire is a working hypothesis which requires further testing. It has far-reaching implications for the geodynamic context of Paleoproterozoic continental crust formation and evolution. A weakness in our understanding of the Paleoproterozoic West African Craton lies in the lack of constraints required to propose a satisfying geodynamic model for the formation and stabilisation of such large volumes of juvenile continental crust in a short time span (∼200 Ma). The hypothesis of multiple juvenile continental blocs, tectonically assembled into larger masses resisting recycling, may stimulate further reflection on the stabilisation of the West African craton, and on the geodynamics of the Paleoproterozoic Earth.

3.2.8 Acknowledgements

We wish to gratefully acknowledge AMIRA International and the industry sponsors, including AusAid and the ARC Linkage Project LP110100667, for their support of the WAXI project (P934A). We recognise the logistical support and datasets provided by the Geological Survey Department of Ghana, as well as the chauffeurs from the IRD in Ouagadougou (Salifou Yougbaré, Boukary Ouedraogo and Matthieu Kaboré) and from the GSD of Ghana (Kwasi Duah).

3.2.9 Appendix

3.2.9.1 U-Pb dating

The internal structure of zircon and monazite grains were characterised by raster electron microscopy (REM) at Geosciences Environnement Toulouse using a JEOL SM-6360 OLV Scanning Electron Microscope, and at Université de Montpellier II using an Environmental Scanning Electron Microscope FEI model. Zircons were analysed at Géosciences Montpellier, Université de Montpellier II. The laser system consists in a Compex 102 (Lambda Physiks) 193nm excimer laser, coupled to Element XR sector field ICP-MS (for details on the analytical technique see Bosch

et al. (2011)). U-Th-Pb analyses were performed under helium, in a 15cm^3 circular shaped cell using an energy density of 12J cm^{-2} at a frequency of 4Hz. Laser spot sizes was 26μm. Analyses were calibrated against the zircon standard G91500 (Wiedenbeck et al., 1995) which was used to correct the collected data for mass discrimination and inter-element fractionation. The ^{202}Hg was used to monitor the ^{204}Hg interference on ^{204}Pb, but common Pb correction was not performed as this often resulted in over-correction, the 204 mass being largely dominated by ^{204}Hg. Data presented in this study thus only report analyses for which no common Pb was detected.

Monazites were analysed at Goethe University Frankfurt. Uranium, thorium and lead isotopes were analysed using a ThermoScientific Element 2 sector field ICP-MS coupled to a Resolution M-50 (Resonetics) 193 nm ArF excimer laser (ComPexPro 102F, Coherent) system, using the procedures described by Gerdes and Zeh (2006, 2009) with modifications explained in Zeh and Gerdes (2012). During this study the unknown monazite grains were analysed together with the standard zircon GJ-1 (Jackson et al., 2004), and with the standard monazites Moacir (Gasquet et al., 2010) and Manangotry (Horstwood et al., 2003). Most monazite grains (unknowns and standards) were ablated with a laser spot-size of 19 μm diameter, but for high-U monazite, a smaller spot size of 12 μm have been employed. Ablation was done with a repetition rate of 4 Hz, and ca. 2 J cm^{-2} laser energy. Particle transport was performed in a 0.63 l min^{-1} He stream, which was mixed directly after the ablation cell with 0.02 l min^{-1} N2 and 0.83 l min^{-1} Ar prior to introduction into the Ar plasma of the SF-ICP-MS. Signal was tuned for maximum sensitivity for Pb and U while keeping oxide production, monitored as ^{254}UO/^{238}U, below 0.2%. The sensitivity achieved was in the range of ca. 12900 cps/μg g^{-1} for ^{238}U with a 33 ţm spot size, at 5.0 Hz and 5 J cm^{-2} laser energy (obtained on the standard zircon GJ1). Sample surfaces were cleaned directly before each analysis by three pulses pre-ablation. Raw data were corrected offline for background signal, common Pb, laser induced elemental fractionation, instrumental mass discrimination, and time-dependent elemental fractionation of Pb/U using an in-house MS Excelľ spreadňsheet program (Gerdes and Zeh, 2006, 2009). The common-Pb correction was carried out when the common-Pb uncorrected ^{207}Pb/^{206}Pb was significantly higher than the corrected ^{207}Pb/^{206}Pb. For most analyses the common Pb level (quoted here as ^{206}Pb common of total ^{206}Pb) was below 0.2% (see Table 4.6). Common-Pb correction was carried out by using the ^{202,204}Hg interference- and background-corrected ^{204}Pb signal, and a model Pb composition (Stacey and Kramers, 1975). The interference of ^{204}Hg (ca. 250 cps; counts per second, during our sessions) on mass 204 was estimated using a ^{204}Hg/^{202}Hg ratio of 0.2299 and the measured ^{202}Hg. Laser induced elemental fractionation and instrumental mass discrimination were corrected by normalization to the reference zircon GJ-1 (primary standard). Potential matrix effects were controlled by multiple measurements of the standard monazites Moacir and Managotry (secondary standards). Prior to the normalization, the drift in inter-elemental fractionation (Pb/U) during 21s of sample ablation was corrected for the individual analysis. The correction was done by applying a linear regression through all measured ratios, excluding the outliers ($\pm 2\sigma$ standard deviation; 2 SD), and using the intercept with the y-axis as the initial ratio (=intercept method). The total offset of the measured drift-corrected

$^{206}Pb/^{238}U$ ratio from the "true" ID-TIMS value (0.0982 ± 0.0004 ; ID-TIMS GUF-value) of the analyzed GJ-1 grain was ca. 11%. Reported uncertainties (2σ) of the $^{206}Pb/^{238}U$ ratio were propagated by quadratic addition of the external reproducibility (2 SD %) obtained from standard GJ-1 (n=11 ; 2 SD∼1.23%) during the analytical session, and the within-run precision of each analysis (2 SE % ; standard error). Reproducibility of the $^{207}Pb/^{206}Pb$ ratio depends strongly on counting statistic (Gerdes and Zeh, 2009), as well as on the common-Pb content. To account for both, the uncertainty on $^{207}Pb/^{206}Pb$ signal were propagated by quadratic addition of the outlier corrected $^{207}Pb/^{206}Pb$ within-run precision (2 SE%), a 207Pb signal dependent factor, and an factor which takes the amount of common-Pb, and the uncertainties of model Pb composition into account (Gerdes and Zeh, 2009). The $^{207}Pb/^{235}U$ ratio is derived from the normalized and error propagated $^{207}Pb/^{206}Pb$ and $^{206}Pb/^{238}U$ ratios, assuming a $^{238}U/^{235}U$ natural abundance ratio of 137.88 and the uncertainties of both ratios. The standard zircon GJ1 (n=11) measured during this study yield a Concordia ages of 604.1 ± 2.7 Ma (n=11, MSWD=0.55, Probability of fit = 0.95). Multiple measurements of the standard monazite Moacir yield a Concordia age of 500.7 ± 2.5 (n=11, MSWD=1.4, Probability of fit = 0.12) and of the standard monazite Manangotry a Concordia age of 552.3 ± 2.8 (n=11, MSWD=1.18, Probability of fit = 0.26) which are within error of published data (Gasquet et al., 2010; Horstwood et al., 2003). The data were plotted using the software ISOPLOT (Ludwig, 2001).

3.2.9.2 Images of geophysical datasets

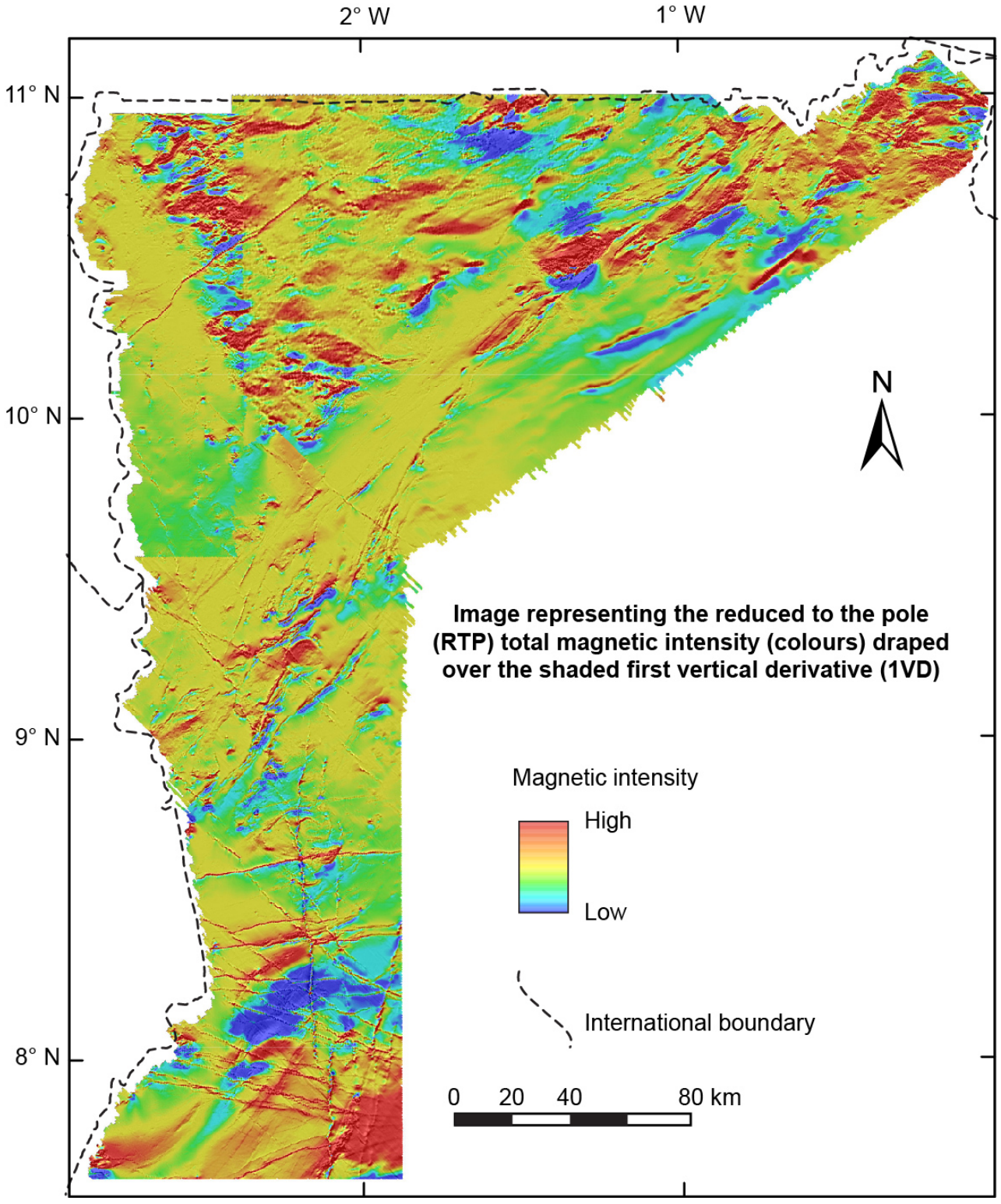
2° W
1° W
11° N
10° N
9° N
8° N
N
Image representing the reduced to the pole (RTP) total magnetic intensity (colours) draped over the shaded first vertical derivative (1VD)
Magnetic intensity
High
Low
International boundary
0 20 40 80 km

FIGURE 3.11:

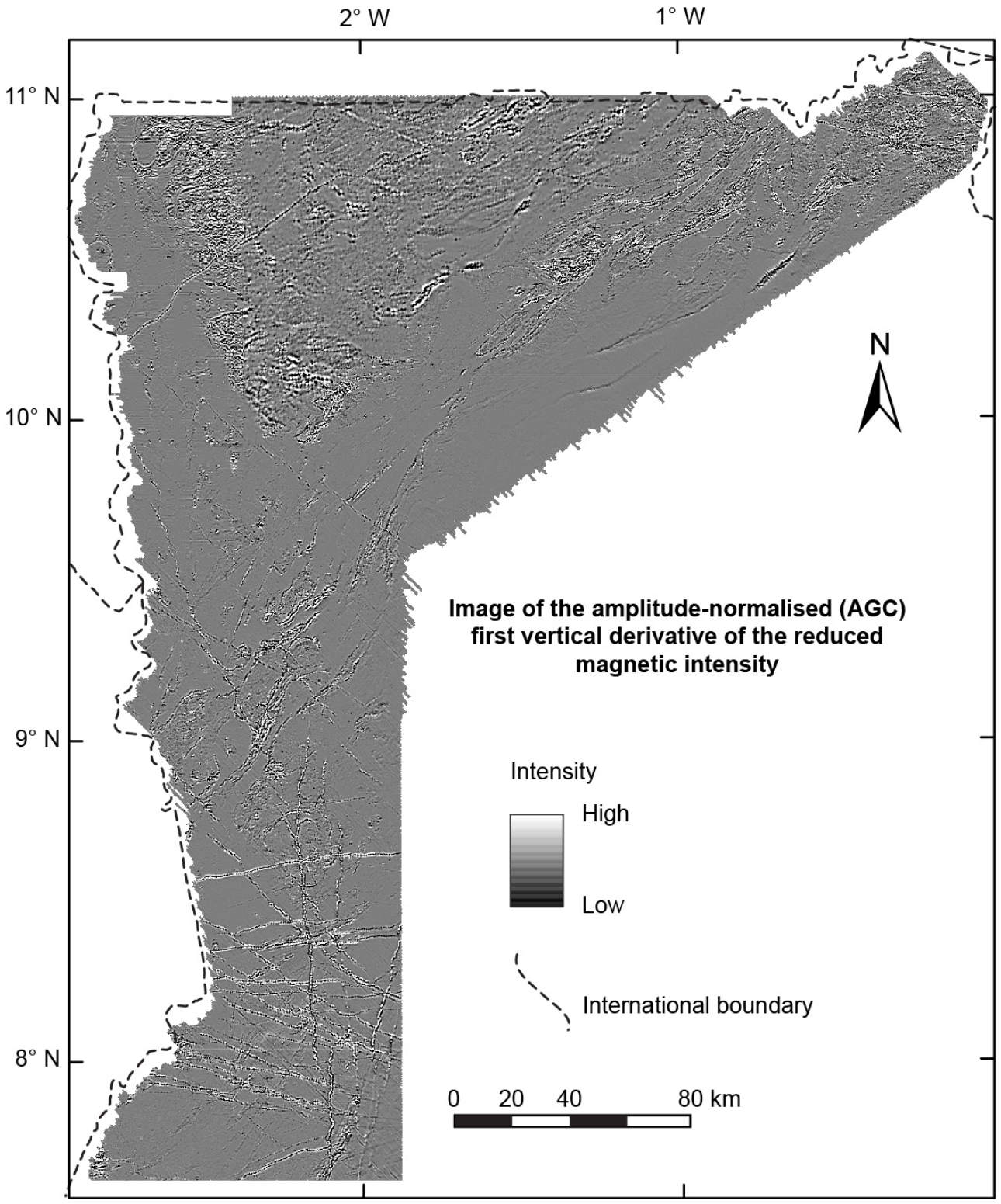
2° W
1° W
11° N
10° N
9° N
8° N
N
Image of the amplitude-normalised (AGC) first vertical derivative of the reduced magnetic intensity
Intensity
High
Low
International boundary
0 20 40 80 km

FIGURE 3.12:

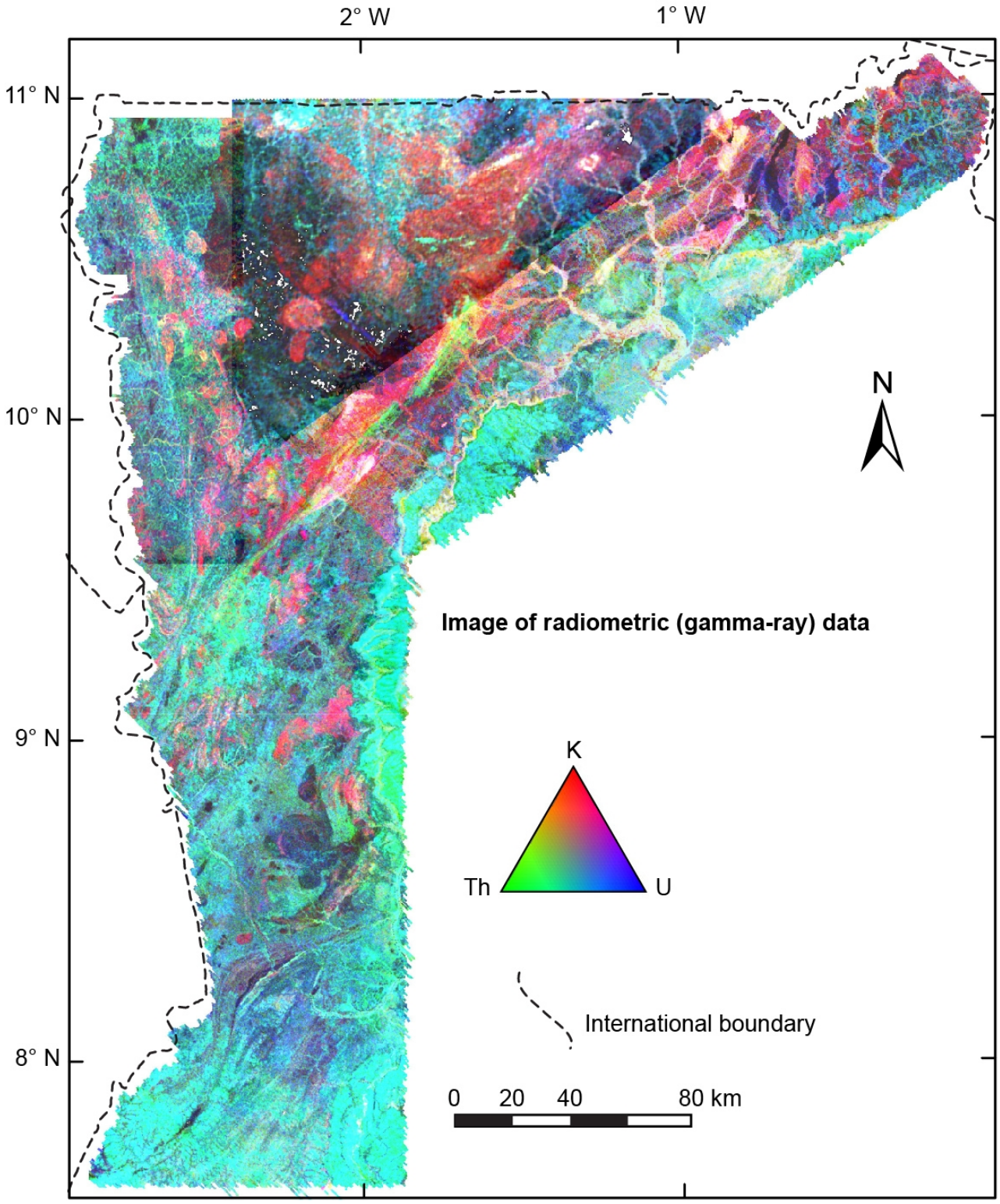
2° W
1° W
11° N
10° N
9° N
8° N
N
Image of radiometric (gamma-ray) data
K
Th
U
International boundary
0 20 40 80 km

FIGURE 3.13:

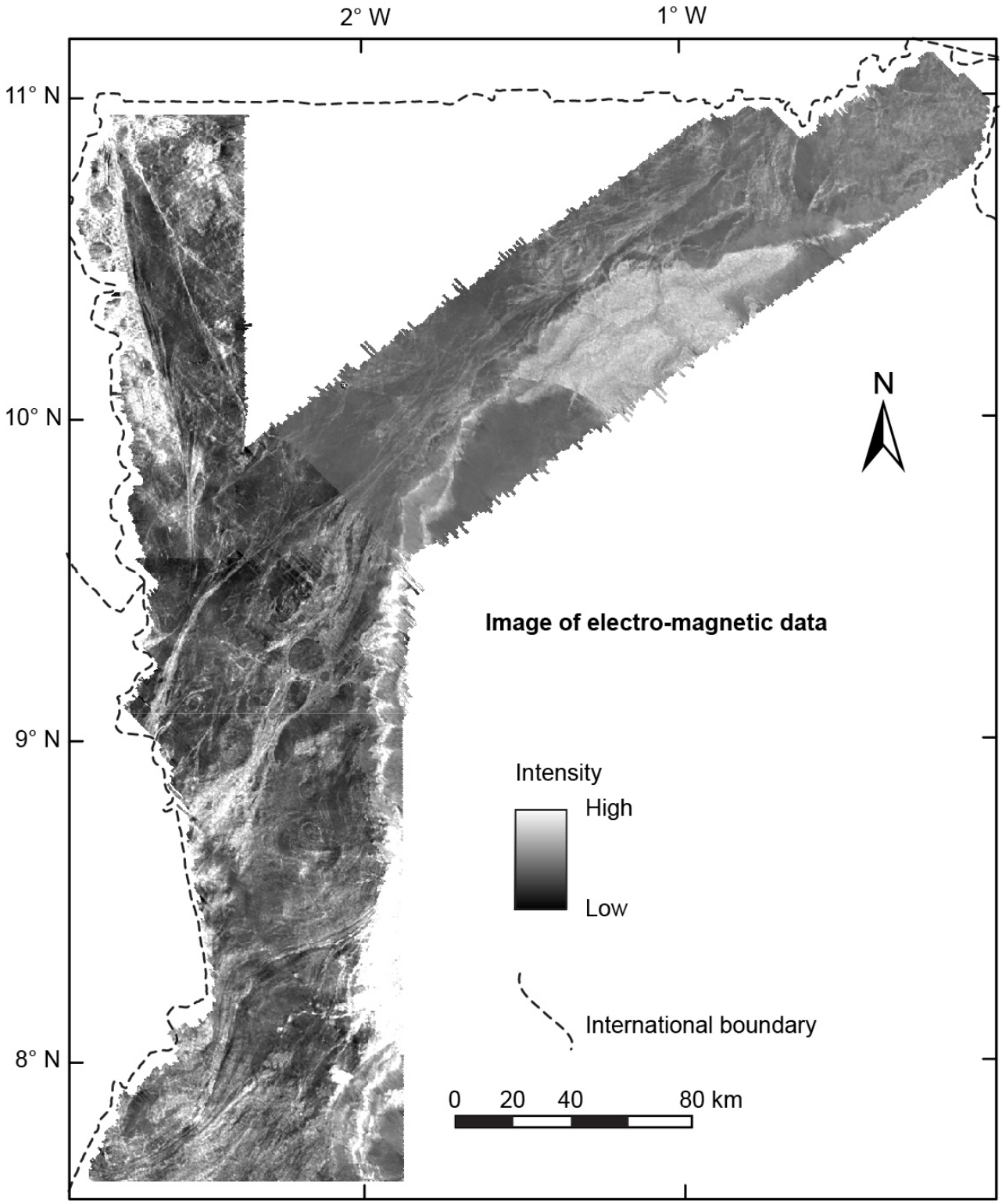
2° W
1° W
11° N
10° N
9° N
8° N
N
Image of electro-magnetic data
Intensity
High
Low
International boundary
0 20 40 80 km

FIGURE 3.14:

Chapitre 4

The metamorphic evolution of the West African Craton

Introduction (en français)

Le chapitre 3 identifie la séquence des événements tectoniques enregistrés dans les formations paléoprotérozoiques du nord du Ghana. Il conclue que les roches de haut grade métamorphique ont été exhumées au sein d'un dôme anatectique, dans un contexte de collision, lors de l'orogenèse Éburnéenne. Dans ce chapitre, le modèle tectonique est confronté aux estimations quantitatives des conditions thermobarométriques enregistrées par les roches métamorphiques du nord du Ghana. L'étude métamorphique concerne des échantillons issus de tous les principaux domaines métamorphiques de la région. La datation U-Pb de monazites métamorphiques est utilisée pour contraindre l'age du métamorphisme. Ces contraintes géochronologiques permettent de discuter la nature des relations géologiques entre les unités de haut grade et de bas grade métamorphique. Les chapitres 3 et 4 sont complémentaires et constituent deux volets d'une même étude tectono-métamorphique. Les données qu'ils présentent ont été acquises simultanément.

Ce chapitre présente également une brève synthèse du métamorphisme paléoprotérozoïque du Craton Ouest Africain, afin de présenter les connaissances disponibles à ce sujet, de donner un aperçu de la diversité des roches métamorphiques présentes et de discuter de la signification géodynamique de l'enregistrement métamorphique. La vision d'ensemble révèle l'existence de roches métamorphiques qui sont rares ou absentes des cratons archéens, sans que le registre métamorphique du craton ressemble pour autant à celui d'autres provinces datant Protérozoïque ou du Phanérozoïque.

L'étude métamorphique a été proposée pour une publication dans la revue *Journal of Metamorphic Geology*. Une première version a été soumise en juillet 2014 et corrigée en septembre puis en novembre de la même année. La version présentée ci-dessous a été acceptée le 08/12/2014. Cette version n'est toutefois pas strictement équivalente à celle envoyée à la revue, puisqu'elle présente dans le corps du texte l'étude de certains échantillons qui ne figurent qu'en annexe (pour des raisons de contraintes éditoriales) de la version sous presse.

Résumé

Cette étude présente de nouvelles données pétrologiques et géochronologiques obtenues sur des ortho- et paragneisses paléoprotérozoïques provenant du Craton Ouest Africain (2.25-2.00 Ga) au nord-ouest du Ghana. Les gneisses affleurent dans une zone d'interférence tectonique située entre deux zones de cisaillement d'échelle crustale, orientées N-S et NE-SW, qui se sont formées au cours de l'orogenèse Éburnéenne. Les domaines de haut degré et de bas degré métamorphique sont séparés par des chevauchements, des détachements ou des décrochements ductiles. De rares reliques métamorphiques préservées dans les paragneisses témoignent de conditions métamorphiques de haute-pression - basse température (HP-BT), à la transition entre les faciès des schiste bleu et des amphibolites à épidote (P = 10.0-14.0 kbar, T = 520-600 ° C). Ces conditions correspondent à un gradient géothermique apparent relativement froid (∼15 ° C/km). Les gneisses migmatitiques enregistrent des conditions métamorphiques à la transition entre les faciès amphibolite et granulite. Leur évolution métamorphique définit un chemin pression-température-temps (P-

T-t) horaire, qui débute par un franchissement du solidus à des pressions au delà de 10.0 kbar, suivi d'une décompression supra-solidus puis d'un réchauffement jusqu'à des températures maximales de 750 ° C à 5.0-8.0 kbar, le long d'un géotherme apparent d'environ 30 ° C/km. D'autre part, des gneisses enregistrent un pic de métamorphisme en faciès amphibolite, à 7.0-10.0 kbar et 550-680 ° C (ce qui correspond à un géotherme apparent de 20-25 ° C/km), qui sur-imprime l'évolution métamorphique antérieure. Certains échantillons atteignent ces conditions métamorphiques suite à un chemin prograde d'enfouissement et de réchauffement, alors que le pic de métamorphisme fait suite à une phase d'exhumation assortie d'un réchauffement pour d'autres. Des monazites ayant crystallisé durant l'anatexie, à la transition entre les faciès amphibolite et granulite, ainsi que pendant la phase métamorphique suivante, qui culmine dans le faciès amphibolite, sont datées *in-situ* par la méthode U-Pb. Les premières donnent un âge de 2138±7 Ma et les secondes de 2130±7 Ma. Ces nouvelles contraintes démontrent que les ceintures de roches vertes birimiennes ne sont pas des bassins discordants sur un socle gneissique plus ancien, puisque les âges du métamorphisme sont généralement plus jeunes que les âges de mise en place des laves (datées par ailleurs) se trouvant dans les ceintures. Les contrastes métamorphiques entre les domaines de haut grade et de bas grade ne sont donc pas liés à un quelconque diachronisme de leur mise en place. Ils seraient plutôt la conséquence de l'exhumation de la croûte inférieure le long de chevauchements, de détachements et de décrochements, qui ont permis de juxtaposer des unités crustales métamorphisées à différents niveaux de la croûte. La gamme des conditions métamorphiques enregistrée dans des unités étroitement associées de part et d'autre de zones de cisaillement ne semble pas compatible avec les modèles de croûte "chaude" et rhéologiquement faible qui sont fréquemment proposés pour représenter des provinces précambriennes. Les résultats de cette étude fournissent des contraintes sur la thermicité de la croûte éburnéenne. Les conditions métamorphiques reflètent une gamme de régimes thermiques crustaux qui rappelle la diversité du métamorphisme dans les orogènes modernes. Cependant, de nombreux faciès métamorphiques rencontrés dans les orogènes post-paléoprotérozoïques ne sont pas représentés sur le Craton Ouest Africain. Il se pourrait donc que le registre métamorphique du craton soit produit par une régime précoce de tectonique des plaques protérozoïque, et représente un état transitoire entre orogènes archéens et phanérozoiques.

4.1 Introduction

Chapter 3 detailed the successive tectono-metamorphic phases that shaped the Paleoproterozoic domains of northern Ghana, and concluded that high-grade metamorphic rocks were exhumed in an anatectic migmatite dome that developed during the Eburnean orogeny. In the present chapter, this interpretation is confronted to quantitative estimates of metamorphic conditions retrieved from rocks sampled across north-western Ghana. This study also aims at constraining the timing of metamorphism by carrying out U-Pb dating of metamorphic monazite in order to clarify the relationship between high-grade and low-grade metamorphic terranes. Therefore, both chapters 3 and 4 are complementary, and the data presented in both publications was acquired simultaneously.

A brief overview of the metamorphic record of the Paleoproterozoic West African Craton provides the framework to discuss the significance of the metamorphic rocks found in northern Ghana in terms of craton architecture and geodynamics. The metamorphic conditions obtained from this study are then analysed in light of the secular evolution of the global metamorphic record. It appears that the West African craton holds metamorphic features that are uncommon in the Archean but that do not quite match the typical Proterozoic metamorphic record either.

Chapter 4 consists of a publication submitted to *Journal of Metamorphic Geology*. The first version was submitted in July 2014. It was revised twice, in September and November 2014, and was accepted on 08/12/2014 The version presented here is equivalent to the accepted version, except that three of the eight metamorphic rock sample presented in the main text below were provided as supplementary information in the accepted version, to fit editorial length requirements.

4.2 Petrological and geochronological constraints on lower crust exhumation during Paleoproterozoic (Eburnean) orogeny, NW Ghana, West African craton.

Sylvain Block[1], Jerôme Ganne[1], Lenka Baratoux[1,2], Armin Zeh[3], Luis A. Parra-Avila[4], Mark Jessell[4], Laurent Ailleres[5]

[1] *Géosciences Environnement Toulouse, Observatoire Midi Pyrénées, 14 ave E. Belin, 31400, Toulouse, France*
[2] *IFAN, Cheikh Anta Diop, Dakar, Senegal* [3] *Institut für Geowissenschaften, Altenhöfer Allee 1, D-60438 Frankfurt am Main, Germany*
[4] *Center for Exploration Targeting, The University of Western Australia, 35 Stirling Highway, Crawley, Perth, Western Australia 6009*
[5] *Monash University, School of Geosciences, Wellington Road, Clayton, Vic 3800, Australia*

Abstract

We present new petrological and geochronological data on high-grade ortho- and paragneisses from north-western Ghana, forming part of the Paleoproterozoic (2.25-2.00 Ga) West African Craton. The study area is located in the interference zone between N-S and NE-SW trending craton-scale shear zones, formed during the Eburnean orogeny (2.15-2.00 Ga). High-grade metamorphic domains are separated from low-grade greenstone belts by high-strain zones, including early thrusts, extensional detachments and late-stage strike-slip shear zones. Paragneisses sporadically preserve high-pressure, low-temperature (HP-LT) relics, formed at the transition between the blueschist facies and the epidote-amphibolite sub-facies (P = 10.0-14.0 kbar, T = 520-600 ° C), and represent a low (∼15 ° C/km) apparent geothermal gradient. Migmatites record metamorphic conditions at the amphibolite-granulite facies transition. They reveal a clockwise pressure-temperature-time (P-T-t) path characterised by melting at pressures over 10.0 kbar, followed by decompression and heating to peak temperatures of 750 ° C at 5.0-8.0 kbar, along a 30 ° C/km apparent geotherm. A regional amphibolite-facies metamorphic overprint is recorded by rocks that followed a clockwise P-T-t path, characterised by peak metamorphic conditions of 7.0-10.0 kbar at 550-680 ° C, which match a 20-25 ° C km-1 apparent geotherm. These P-T conditions were reached after prograde burial and heating for some rock units, and after decompression and heating for others. The timing of anatexis and of the amphibolite-facies metamorphic overprint is constrained by *in-situ* U-Pb dating of monazite crystallisation at 2138±7 and 2130±7 Ma respectively. The new dataset challenges the interpretation that metamorphic breaks in the West African Craton are due to diachronous Birimian "basins" overlying a gneissic basement. It suggests that the lower crust was exhumed along reverse, normal and transcurrent shear zones and juxtaposed against shallow crustal slices during the Eburnean

orogeny. The craton in NW Ghana is made of distinct fragments with contrasting tectono-metamorphic histories. The range of metamorphic conditions and the sharp lateral metamorphic gradients are inconsistent with "hot orogen" models proposed for many Precambrian provinces. These findings shed new light on the geodynamic setting of craton assembly and stabilisation in the Paleoproterozoic. It is suggested that the metamorphic record of the West African Craton is characteristic of Paleoproterozoic plate tectonics and illustrates a transition between Archean and Phanerozoic orogens.

Keywords : Paleoproterozoic, West African Craton, Exhumation, Anatectic dome, Collision

4.2.1 Introduction

Precambrian accretionary orogens provided significant contribution to the EarthŠs crustal growth due to high juvenile crust production rates, and high degrees of preservation of the newly formed crust through assembly against older cratonic nuclei (e.g. Cawood et al. (2009); Condie (1998)). The Precambrian crust was mainly generated by successive pulses of juvenile magmas during a prolonged tectono-magmatic evolution, as is reflected by a wide range of overlapping geochronological data (e.g. Karlstrom et al. (2001); Väisänen et al. (2002); Zeh et al. (2013) and references therein). The final stages of the evolution of Precambrian accretionary orogens are characterised by tectonic accretion of various units to form stable cratons. Maturing and cratonization of the crust is reflected by changing tectonic styles (e.g.Vanderhaeghe et al. (1998)), an increasing contribution of crustal reworking during magmatic activity (e.g. Laurent et al. (2011, 2014); Martin et al. (2005)) and distinctive metamorphic overprints (e.g. Pitra et al. (2010)). Precambrian accretionary orogens commonly include large proportions of fertile juvenile crust, and show high apparent geothermal gradients. As a consequence, the lithosphere was rheologically weak and a partially molten orogenic lower crust was maintained for relatively long periods. According to some authors, the hot and weak crust accommodated regional shortening by homogeneous, distributed thickening and flow of partially molten rocks (Cagnard et al., 2006; Chardon et al., 2009; Chardon and Jayananda, 2008; Chardon et al., 2011). Precambrian accretionary orogens often comprise vast domains revealing isobaric metamorphic conditions, with isotherms running parallel to the exposed surface, except for temperature anomalies linked to pluton emplacement (e.g. Debat et al. (2003); Vidal et al. (2009)). The relative scarcity of strong lateral metamorphic gradients is assumed to result from homogeneous uplift of the entire metamorphic terrane, as opposed to a structurally controlled differential exhumation (Cagnard et al., 2007; Gapais et al., 2009, 2008; Percival et al., 1992; Percival and Skulski, 2000). However, spatial variations in geothermal gradients and contrasting metamorphic grades between domains of similar ages have been reported in some Precambrian orogens (Block et al., 2013; Ganne et al., 2012; Stevens and Moyen, 2007). These findings indicate that the thermal regime can change in space and time during the evolution of ancient orogens, that exhumation localised by high-strain zones may be viable, and suggest the existence of non-unique tectonic settings. The secular evolution of the global metamorphic record is reviewed by Brown (2007, 2009). Major changes are documented in metamorphic belts between the Neoarchean and the Paleoproterozoic

eons. Most Archean metamorphic terranes display "ordinary" metamorphic P–T conditions and geothermal gradients (Komiya et al., 2002). Contrastingly, Paleoproterozoic belts, including many collisional belts formed at 2.10-1.80 Ga during the inferred Paleoproterozoic supercontinent assembly (Zhao et al., 2002), are characterised by paired Eclogite–High-Pressure Granulite and Ultra-High Temperature metamorphism. This dual metamorphic record is interpreted as the hallmark of a "plate tectonics" geodynamic setting (Brown, 2007, 2009). The Paleoproterozoic West African Craton is considered as one of the youngest "Archean-type" continental fragments. It is a vast ($3.10^6 km^2$) juvenile continental domain extracted from the mantle between 2.50 and 2.20 Ga (Abouchami et al., 1990; Boher et al., 1992; Gasquet et al., 2003; Peucat et al., 2005), and subsequently accreted against an older Archean nucleus during the 2.15-2.07 Ga Eburnean orogeny (Allibone et al., 2002; Bonhomme, 1962; Feybesse et al., 2006, 1990; Hirdes et al., 1996; Ledru et al., 1991; Milési et al., 1989, 1992; Pouclet et al., 2006; Tagini, 1971; Vidal et al., 2009). Consequently, the Eburnean rock record is key to explore the geodynamic changes across the Archean-Proterozoic transition. The present understanding of the Eburnean metamorphism is limited by the lack of integration with geochronological and tectonic data. One of the scientific problems hampering our knowledge of the evolution of the West African Craton resides in the interpretation of the relationship between low-grade Birimian greenstone belts (Junner, 1940) and high-grade gneissic terranes dominated by TTG (tonalites-trondhjemites-granodiorites) suites. Are they coeval terranes metamorphosed in different tectonic settings before being assembled, or are greenstone belts discordant supracrustal rocks deposited on an older gneissic basement ? Answering this question has strong implications on the geodynamic processes controlling the maturation and stabilisation of cratons after the Archean-Proterozoic transition. In order to do so, we present combined field, petrological and geochronological datasets of spatially associated low-, medium- and high-grade metamorphic rocks of north-western Ghana, in the south-eastern West African Craton. The datasets are used to explore the mechanisms driving the exhumation and the tectonic assembly of the distinct metamorphic domains during the Eburnean orogeny.

4.2.2 Geological background

The Leo-Man rise forms the southern part of the West African Craton. It comprises an Archean nucleus, the Kénéma-Man domain, which is flanked to the East by the Paleoproterozoic Baoulé-Mossi domain (Fig. 4.1). The Baoulé-Mossi domain comprises Birimian greenstone belts (Junner, 1940), which are bounded by shear zones and alternate with granite-gneiss terranes. The greenstone belts comprise elongated sequences of volcanic and volcano-sedimentary rocks, shales, greywackes and chemical sedimentary rocks. The volcanic rocks range from basalts to rhyolites and have bimodal tholeiitic and calc-alkaline affinities (e.g. Baratoux et al. (2011); Kitson (1928); Leube et al. (1990)). Across the craton, large volumes of volcanic rocks were emplaced between 2.40 and 2.20 Ga and volcanic activity locally continued until c. 2.10 Ga (Doumbia et al., 1998; Feybesse et al., 2006; Hirdes et al., 1996; Kouamelan, 1996). In the granite-gneiss terranes, intense plutonic activity generated juvenile TTG suites between 2.25 and 2.10 Ga, while magmatism gradually evolved towards more differentiated terms (e.g. potassic granites) until c. 2.07 Ga

(e.g. Arnould (1961); Egal et al. (2002); Lompo (2009)). Tarkwaian sedimentary rocks (conglomerates, phyllites and quartzites) form discordant basins on Birimian formations, and are interpreted to represent syn-orogenic to late-stage basins (Davis et al., 1994; Perrouty et al., 2012).

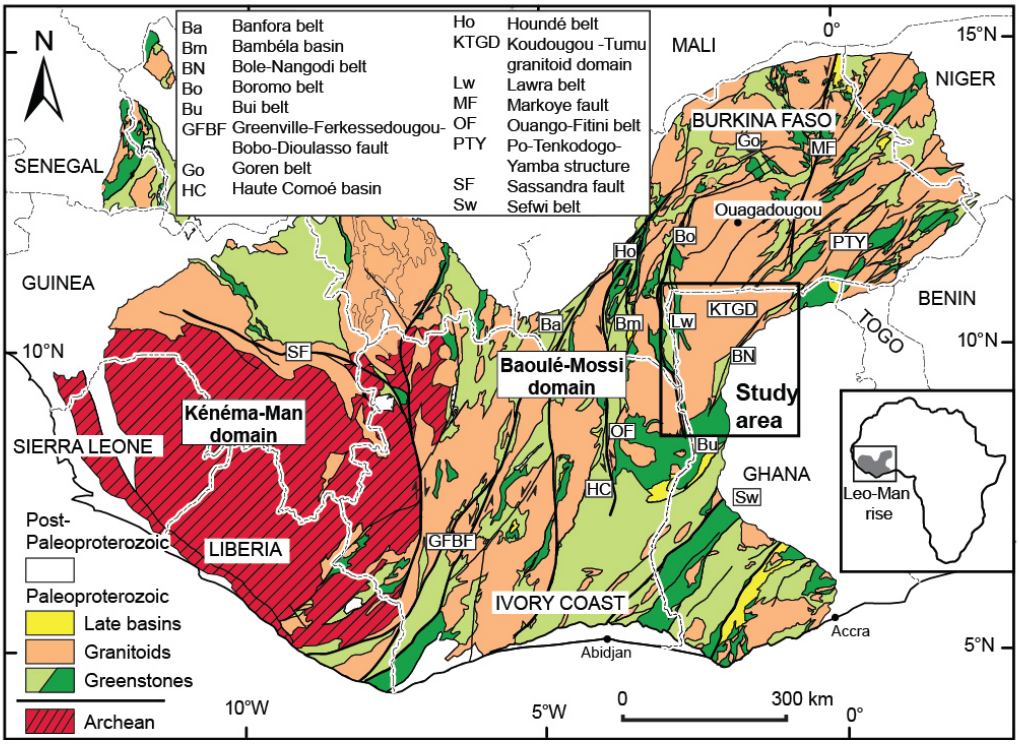

FIGURE 4.1: Simplified geological map of the Leo-Man rise (modified after the BRGM SIGAfrique map, Milési et al. (2004)). Light green areas are made of intermediate to acidic volcano-sedimentary or volcano-clastic rocks, and the dark green areas represent mafic volcanic rocks.

Based on geochemical data, some authors interpret the juvenile Paleoproterozoic West African Craton to have evolved from an oceanic plateau (Abouchami et al., 1990; Boher et al., 1992; Lompo, 2009; Pouclet et al., 1996), while others argue it formed by the accretion of several volcanic arcs (Attoh et al., 2006; Dampare et al., 2008; Vidal and Alric, 1994). Tectonic accretion is proposed to have been dominated by gravity-driven "Archean-style" vertical tectonics by one school of thought (e.g. Pons et al. (1995) in Niger ; Vidal et al. (2009) in Côte d'Ivoire), while lateral tectonics with thrust-related crustal thickening, equivalent to processes at work in modern orogens, is invoked by other authors (Milési et al. (1989, 1992) and Feybesse et al. (2006) in Ghana).

Systematic spatial variations in metamorphic conditions across the Paleoproterozoic craton were recognised by various authors as early as Roques (1948) and Arnould (1961), who described large domains of exposed migmatitic gneisses juxtaposed with low-grade volcano-sedimentary units in north-eastern Côte d'Ivoire and southern Burkina Faso. High-T supra-solidus metamorphic conditions are also reported from formations in southern Ghana (Feybesse et al., 2006; Opare-Addo

et al., 1993) and Côte d'Ivoire (Caby et al., 2000). Ganne et al. (2012) showed that rocks from greenstone belts in Senegal, Burkina Faso and Niger experienced different peak metamorphic conditions in the greenschist and amphibolite facies, and at the greenschist-blueschist facies transition. Most volcano-sedimentary sequences are metamorphosed at sub-greenschist and greenschist-facies conditions (e.g. Kříbek et al. (2008)). Amphibolite-facies metamorphic conditions are found in small volcano-sedimentary slivers within larger greenschist-facies belts. They are interpreted to result from contact metamorphic overprints (Debat et al., 2003; Gasquet et al., 2003; Ndiaye et al., 1989; Vidal and Alric, 1994) accompanied by doming due to granite emplacement (Pons et al., 1995; Soumaila and Garba, 2006). Other authors identified regional amphibolite-facies metamorphism rocks unrelated to pluton emplacement (Liégeois et al. (1991) in S Mali ; Caby et al. (2000) in NE Côte dŠIvoire ; Galipp et al. (2003); John et al. (1999); Klemd et al. (2002) in Ghana). High-P granulites (Pitra et al., 2010; Triboulet and Feybesse, 1998) and low-P granulites (Caby et al., 2000; Pitra et al., 2010) are described from the boundary between the Archean Kénéma-Man and Paleoproterozoic Baoulé Mossi domains. Most metamorphic rocks from the craton record conditions which fit a moderate to hot apparent geothermal gradient (>25 °C/km) However, metamorphic rocks recording cold (∼15 °C/km) apparent geothermal gradients (Ganne et al., 2012) are found in eastern Burkina Faso.

Historically, the high-grade metamorphic domains were interpreted as the basement below the Birimain volcano-sedimentary sequence. A polycyclic orogenic evolution was suggested on the basis of field relationships reflecting poly-phased structural-metamorphic fabrics (Arnould, 1961; Bard and Lemoine, 1976; Ledru et al., 1991). Following this model, the gneissic basement supposedly pre-dating the Birimian series underwent high-grade metamorphism during an early orogenic event (Hein, 2010; Lemoine et al., 1990; Sagatzky, 1954; Tempier, 1986; Tshibubudze et al., 2009) which is termed "Eoeburnean" (Baratoux et al., 2011; De Kock et al., 2011, 2012; Perrouty et al., 2012). After the deposition of Birimian sediments, the Paleoproterozoic domains were tectonically assembled against the Archean nucleus during the Eburnean orogeny (Kouamelan et al., 1997), in a predominantly transcurrent tectonic regime (e.g. Feybesse et al. (1990); Ledru et al. (1991). This polycyclic model is further supported by the recognition of deformed, low-grade upper Birimian volcano-sedimentary basins unconformably overlying basal Birimian rocks (Ledru et al., 1991; Milési et al., 1989; Perrouty et al., 2012; Pouclet et al., 1996; Vidal and Alric, 1994; Vidal et al., 1992). In contrast to the polycyclic model, some authors argue for a single orogenic cycle (Eisenlohr and Hirdes, 1992; Gasquet et al., 2003; Hirdes et al., 1996; Leube et al., 1990). In this view, volcano-sedimentary basins are considered to be contemporaneous equivalents of volcanic belts and to illustrate lateral facies variations. The monocyclic model implies that terranes of contrasting metamorphic grade are coeval, and that low-grade metamorphic units represent supracrustal equivalents of high-grade migmatitic gneisses. Consequently, variations in the metamorphic conditions of coeval terranes must result from differential exhumation.

A limited number of geochronological data across the West African Craton point to a prolonged period of metamorphic overprint, which lasted *ca.* 70 Ma. It spans from 2153±13 Ma given by a Sm-Nd garnet-whole rock isochron age (Boher et al.,

1992) to a 2105-2080 Ma period, defined by U-Pb and Pb-Pb crystallisation ages of zircon, monazite and titanite (De Kock et al., 2009; Feybesse et al., 2006; Hirdes et al., 1996; Kouamelan, 1996; Oberthür et al., 1998; Siegfried et al., 2009; Thomas et al., 2009). Reworking of the Archean nucleus between 2080 and 2030 Ma (Kouamelan, 1996; Kouamelan et al., 1997) is supported by geochronological data obtained by different radiometric methods, including U-Pb zircon and monazite EPMA dating. However, due to the limited number of age data from only a few outcrops throughout the West African Craton, it remains unclear whether the metamorphic overprint was continuous during ~70 Ma or occurred during several discrete events. Thus, the available age data are of little help to discriminate between the poly- and monocyclic orogenic models.

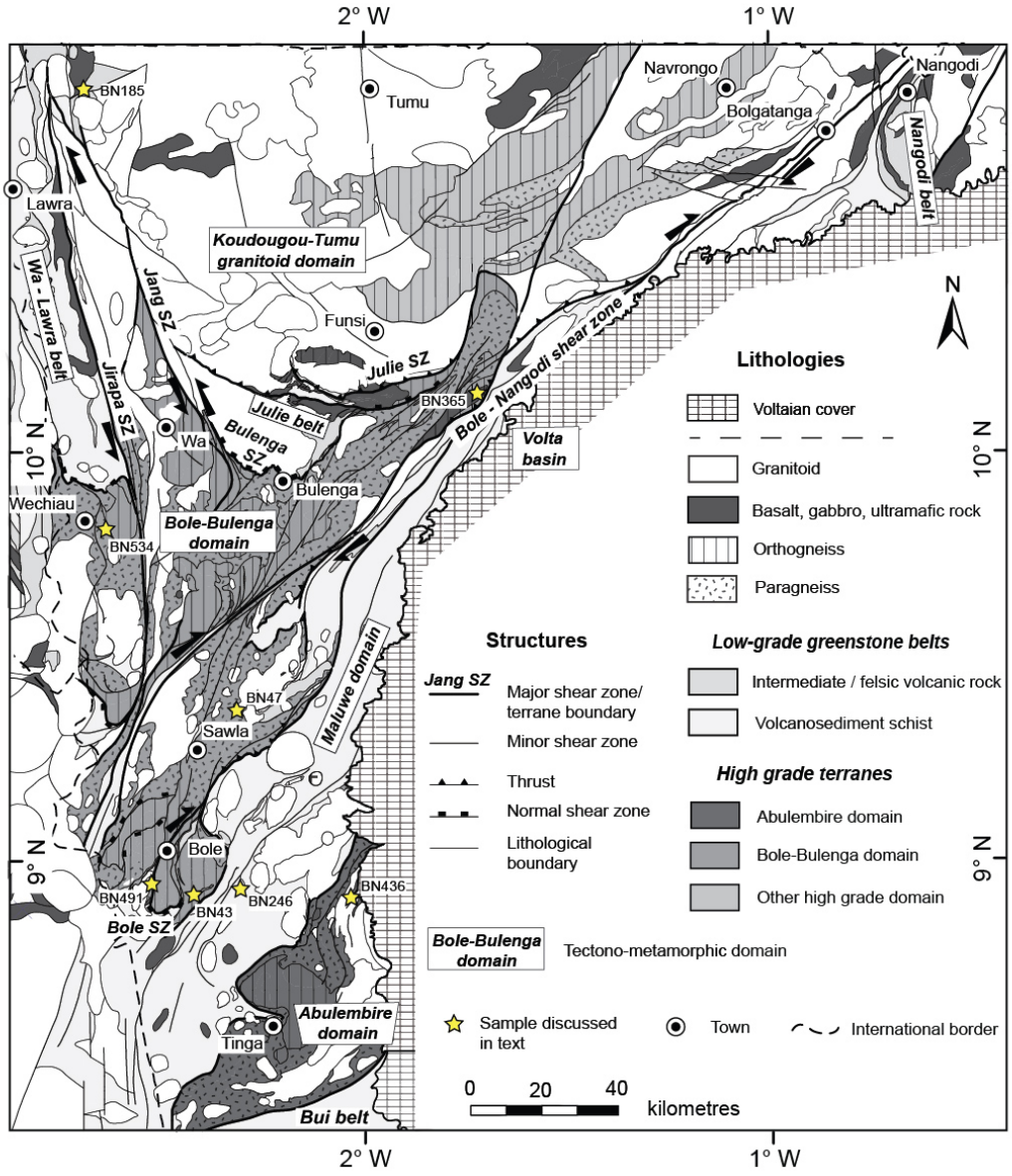

FIGURE 4.2: Simplified litho-structural map of northern Ghana. SZ = shear zone. Fault kinematics are indicated when they are unambiguous.

4.2.3 Geology of north-western Ghana

4.2.3.1 Tectono-metamorphic domains

The geology of north-western Ghana is characterised by low- to high-grade tectono-metamorphic domains which are bounded by shear zones. Low-grade shales, volcano-sedimentary rocks, lavas such as dacites, andesites and basalts are found in the N-S Wa-Lawra belt (Fig. 4.2), which is the south-eastern continuation of the Boromo greenstone belt exposed in Burkina Faso (Baratoux et al., 2011; Metelka et al., 2011). Similar low-grade lithologies are found in the E-W trending Julie belt, which also comprises silicic volcano-sedimentary rocks, quartzites and arkoses. The Maluwe domain is a low-grade tectono-metamorphic terrane elongated SW-NE along 250 km, which tapers off towards the NE to a thin sliver (Fig. 4.2). It is dominated by greywacke and shales which are intercalated with volcanoclastic rocks and felsic to intermediate lavas, deposited between 2197 and 2125 Ma (De Kock et al., 2011; Thomas et al., 2009). It also comprises chemical sedimentary rocks (Mn-rich cherts), along with gabbros and pyroxenites. The Nangodi belt (Melcher and Stumpfl, 1994), in the north-eastern part of the study area, is formed by a succession of shales, greywacke and Mn-rich cherts alternating with MORB-type basalts overlain by calc-alkaline andesitic to rhyolitic lava flows. High-grade orthogneisses, paragneisses and metabasites form most of the Bole-Bulenga domain, which is 150 by 20-80 km long and elongated in a NNE direction. The paragneisses are derived from pelites, greywacke and volcano-sedimentary rocks. They are intruded by TTG and monzogranite orthogneisses with crystallisation ages between 2195 and 2135 Ma. The lithologies of the Bole-Bulenga domain are frequently migmatitic. To the south of the study area, the Abulembire domain shares many lithological and metamorphic similarities with the Bole-Bulenga domain. It is essentially made of paragneisses, sometimes migmatitic, intruded by TTG and granite orthogneisses, which were emplaced between 2200 and 2125 Ma (De Kock et al., 2011; Duodu, 2009). The Abulembire domain is limited to the south by the Tarkwaian-type detrital sediments of the Bui belt (Zitsmann et al., 1997). The high-grade terranes and low-grade volcano-sedimentary belts are bounded by granitoid domains, such as the Koudougou-Tumu granitoid domain (Fig. 4.2). They comprise TTG orthogneisses, gabbros, granodiorite and granite plutons with crystallisation ages ranging between 2170 and 2127 Ma (Agyei Duodu et al., 2009), and late-stage intrusive potassic porphyric granites, with crystallisation ages ranging between 2128 and 2086 Ma (Duodu, 2009; Taylor et al., 1992). The Paleoproterozoic rocks are overlain in central Ghana by the Neoproterozoic sedimentary rocks of the Volta basin (Affaton et al., 1980).

4.2.3.2 Tectonic contacts separating the domains

The contacts between the low-grade and high-grade domains are tectonic, and are formed by ductile high-strain zones. The Julie shear zone (SZ) is N-dipping and forms the transition between the Koudougou-Tumu granitoid domain, to the north, and the Julie belt, to the south (Fig. 4.2). Within the shear zone, the foliation in schists and gneisses dips 50-70 ° N and carries a stretching lineation plunging down-dip, towards higher grade rocks. The Julie SZ is interpreted as a thrust, consistent with N-S directed shortening. The Bulenga SZ is a N-dipping shear zone which

separates the Julie belt, to the north, from the high-grade Bole-Bulenga domain, to the south. The transition between the two domains is formed by a high-strain migmatitic orthogneiss. The gneissic banding has a moderate dip (40-50 ˚) to the N and bears a mineral stretching lineation consistently plunging NNE, towards decreasing metamorphic grades. Similarly, the Bole SZ separates the southern Bole-Bulenga domain from the Maluwe domain (Fig. 4.2). It contains a high-strain orthogneiss. The gneissic banding dips 50-70 ˚ to the south, with the stretching lineation plunging down-dip, towards lower grade rocks. Therefore, the tectonic contacts forming the northern and southern limits of the high-grade Bole-Bulenga domains are interpreted as extensional shear zones, consistent with N-S directed extension.

These tectonic contacts are overprinted by later deformation and terminate on younger structures, which formed during NW-SE to E-W directed shortening. The Julie and Bulenga SZ both terminate to the west on the NNW-striking Jang sinistral strike-slip shear zone, along the north-eastern margin of the Bole-Bulenga domain. The Bole SZ is folded and transposed parallel to a NNE direction, where it is re-activated as a dextral strike-slip shear zone. The N-S Jirapa shear zone separates the Wa-Lawra belt from the Koudougou-Tumu granitoid domain. At its southern extension, the Jirapa SZ transects the Bole-Bulenga domain and merges with the NE-SW Bole-Nangodi SZ (Fig. 4.2), which extends for over 300 km into Burkina Faso (Naba et al., 2004). Metamorphic breaks across the Bole-Nangodi SZ suggest that it is an early thrust re-activated during later deformation as a dextral strike-slip shear zone.

Sample	Lat	Lon	Lithology	Peak metamorphic assemblage
BN043	8.9289	-2.4320	Pelitic migmatitic paragneiss	Grt + Bt + Sill + Pl + Kf + melt + Qz
BN047	9.3733	-2.3180	Pelitic paragneiss	Bt + Grt + Ky + Ms + Pl + Ilm + Qz
BN185	10.8798	-2.6954	Volcano-sedimentary schist	Chl + Ms + Pl + Cal + Qz
BN246	8.9305	-2.3082	Pelitic micaschist	Chl + Ms + Qz
BN365	10.1339	-1.7384	Migmatitic amphibolite	Hbl + Grt + Pl + Cpx + Ilm + melt + Qz
BN436	8.9090	-2.0391	Mafic granofels	Grt + Ged + Ky + Pl + Rt + Qz
BN491	8.9275	-2.5326	Pelitic paragneiss	Bt + Grt + St + Pl + Ms + Ilm +Qz
BN534	9.8166	-2.6401	Pelitic migmatitic paragneiss	Bt + Grt + Ky + Pl + Ilm + melt + Qz

TABLE 4.1: Description and location of the investigated samples.

4.2.4 Petrography and mineral chemistry

Eight rock samples from the Wa-Lawra belt, the Maluwe, Bole-Bulenga and Abulembire domains were investigated for this study (Table 4.1). Sampling of the principal metamorphic terranes of north-western Ghana aimed to establish the variability of metamorphic conditions at regional scale. Other samples were specifically picked along transects across tectonic contacts in order to evaluate metamorphic breaks. Petrographic and mineral descriptions are detailed in the main text, bulk rock and representative mineral compositions are presented in Tables 4.2 ; 4.3 and 4.4). Mineral abbreviations are after (Whitney and Evans, 2010) except for melt (=L).

4.2.4.1 High-grade rocks

Sample BN 43 (Garnet–kyanite-bearing migmatitic gneiss) Sample BN43 is a migmatitic paragneiss from the southern Bole-Bulenga domain. It was collected at the margin of a foliated granodiorite pluton that consists of a transitional zone evolving from subsolidus amphibolite-facies rocks to supra-solidus high-grade metamorphic rocks. The sample is from an outcrop of stromatic migmatites, which displays foliation-parallel leucosomes connected to granitic dykes oblique to the foliation, suggesting melt transport through the rock. Petrographic relationships are used to define a succession of five metamorphic assemblages identified here as (A) to (E) (Fig. 4.3). Paleosomes are composed of oriented biotite1, plagioclase, quartz and globular garnet1, which together belong to an early metamorphic assemblage (A) (Fig. 4.3a). Garnet1 has a modal proportion of $\sim 2-3\%$ in paleosomes (Fig. 4.4a, b). It displays a slight chemical zoning. From core to rim, composition variations are Almandine (Alm = 100 x Fe/(Fe+Mg+Ca+Mn) 72-73 => 73-75, pyrope (Prp = 100 x Mg/(Fe+Mg+Ca+Mn) 13-14 => 15-16, grossular (Grs = 100 x Ca/(Fe+Mg+Ca+Mn) 5 => 4 and spessartine (Sps = 100 x Mn/(Fe+Mg+Ca+Mn) 8 => 4 (Fig. 4.6a). The Anorthite content (An = 100 x Ca/(Ca+K+Na)) of plagioclase in contact with garnet1 in the paleosome ranges between 24 and 26. Neosomes contain kyanite porphyroblasts (Fig. 4.3b) up to 1 cm long, set in leucocratic quartz-rich domains (Fig. 4.3e). Kyanite contains inclusions of plagioclase (An21-25) and white mica (Ms1 ; Fig. 4.3b), of which two phases are found. One has a dominant muscovite fraction ((Ms = 100 x K/(Na+K+Ca)) between 63 and 79, with Si = 3.21-3.09 a.p.f.u. and Al^{vi} 1.95-1.88 a.p.f.u (based on 11 oxygens), while another has a high paragonite fraction (Pg = 100 x Na/(Na+K+Ca)) of 87-88, with Si = 2.95-3.08 a.p.f.u. and Al^{vi} = 2.00 a.p.f.u (11O).

The first assemblage (A) occurs as minerals preserved in paleosomes and included in kyanite : Grt1 + Bt1 + Pl + Ms1 + Pg + Qz. It is typical of amphibolite-facies metamorphism. Kyanite is interpreted as a peritectic phase produced by the progressive breakdown of muscovite :

$$\text{Ms1} + \text{Pl} + \text{Qz} \Rightarrow \text{Ky} + \text{melt (L)} \pm \text{Bt} \pm \text{Kfs (R1)}$$

Following Patiño Douce and Harris (1998), (R1) may be modelled as follows : 22Ms + 7Pl + 8 Qz => 25 L + 5Ky + 5Kfs + 2Bt. In this sample, (R1) illustrates the transition from assemblage (A) to (B) : Grt1 + Bt1 + Ky + Pl + Qz + L, which is transitional between the amphibolite and the high-pressure granulite facies. Corroded plagioclase in leucosomes (Fig. 4.3c) is An24-28, which partially overlaps with compositions of matrix grains. Euhedral kyanite is unresorbed and is overgrown by prismatic sillimanite (Sil1 ; Fig. 4.3b, c, e). This relationship illustrates an increase in the modal proportion of aluminosilicate (from 2.4 to 4.1%, Fig. 4.4a, b) between assemblages (B) and (C) : Grt1 + Bt1 + Sil1 + Pl + Qz + L. Garnet 2 mainly occurs in coarse-grained neosomes (Fig. 4.3a, f). It displays a minor prograde chemical zoning from centre to rim of Alm 75 => 79, Prp 17 => 19, Sps 4 => 2 and Grs 4 => 2 (Fig. 4.6a). Retrograde chemical re-equilibration on margins is documented by decreasing #Mg (Mg/(Mg+Fe)) from 0.17 to 0.10. Garnet2 is sometimes globular (subhedral) or forms atolls overgrowing garnet1 and aluminosilicate-bearing leucosomes (Figs. 4.3d and 4.4a, b). In leucocratic segregates, garnet2 growth represents a modal proportion increases from 2.3 to 7.7%

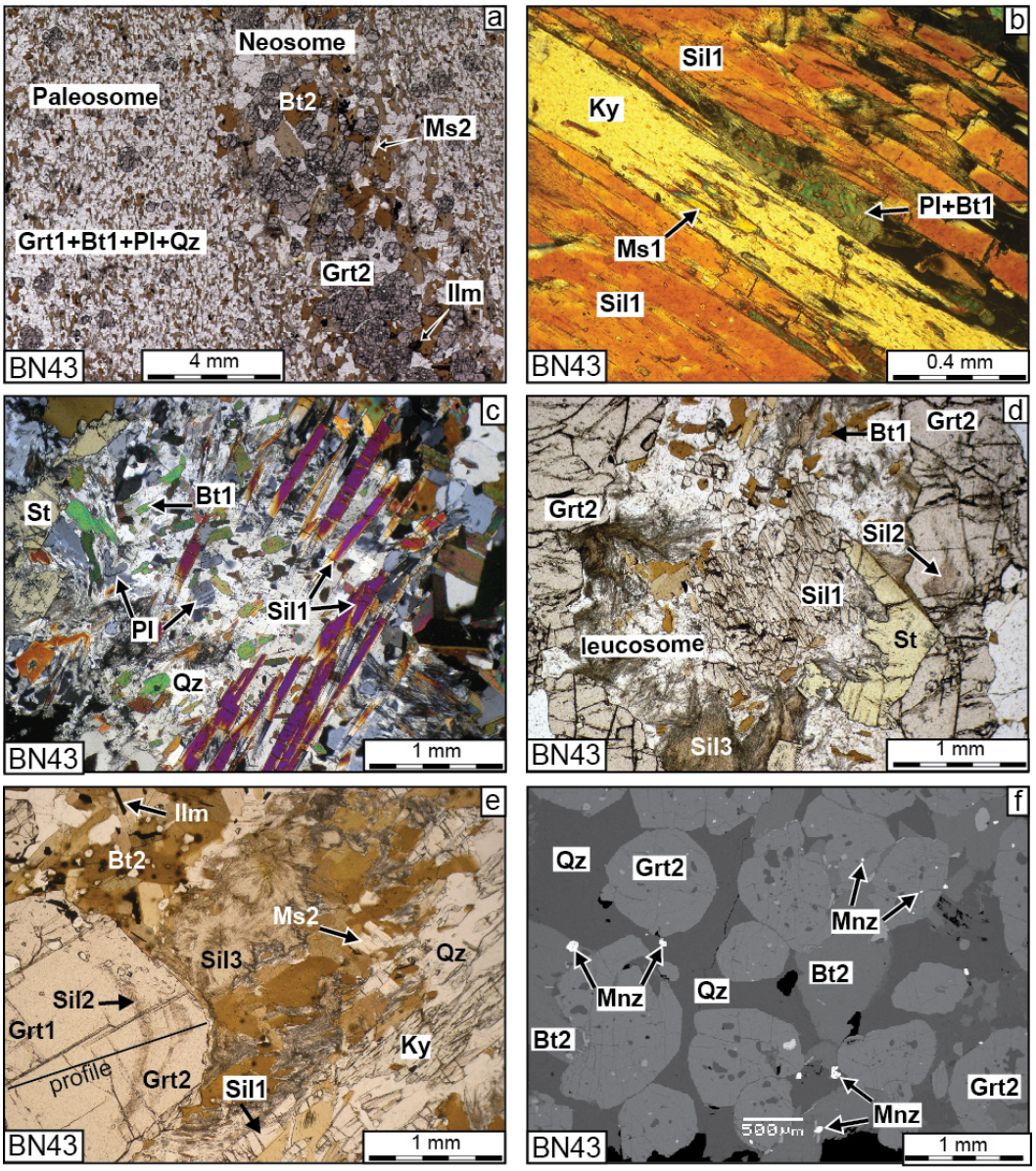

FIGURE 4.3: Photomicrographs (**a-e**) and REM image (**f**) of metapelite sample BN43. (**a**) Fine-grained paleosome comprising globular garnet1 and aligned biotite1 + plagioclase + quartz. Coarse grained neosome displays rounded garnet2 in leucocratic Qz-Pl rich domains overgrown by biotite2 and muscovite2. (**b**) Kyanite containing muscovite inclusions (Ms1) and overgrown by prismatic sillimanite porphyroblasts (Sil1) in a neosome. (**c**) Elongated crystals of prismatic sillimanite (Sil1) is a quartz-rich domain containig corroded grains of plagioclase and biotite1. (**d**) Garnet2 forms atoll-shaped aggregates around a leucocratic domain containing sillimanite1, and contains fibrolite inclusions (Sil2). Biotite1 is resorbed in the leucosome. Late-stage fibrolite (Sil3) and staurolite develop at the expense of garnet2.

(Fig 4.4a, b). Fibrolite selvedge in garnet2 and between garnet1 and 2 (Sil2 ; Fig. 4.3d, e) demonstrate that garnet2 formed in the sillimanite stability field. Corroded biotite1 within neosomes (Fig. 4.3c, d) suggests that garnet2 is a peritectic

FIGURE 4.3: (**e**) Garnet porphyroblast showing a concentric inclusion rim of fibrolite (Sil2) at the transition between garnet1 and garnet2. The profile refers to Fig. 6a. Kyanite and prismatic sillimanite1 are set in a quartz-rich leucosome. Fibrolite, ilmenite and biotite2 flakes are found at the contact between leucosome and matrix. (**f**) Back-scattered electron image taken from the coarse-grained neosome visible in (**a**). Monazite grains are restricted to the neosome, and are commonly found enclosed in garnet2 and biotite2.

phase produced by the progressive dehydration-melting of biotite (Le Breton and Thompson, 1988) :

$$\text{Bt1} + \text{Sil1} + \text{Pl} + \text{Qz} => \text{Grt2} \pm \text{Kfs} + \text{L} \quad \text{(R2)},$$

which has a pressure-dependent stoichiometry (Patiño Douce and Beard, 1995). This reaction results in the formation of the amphibolite- to granulite-facies assemblage (D) : Grt2 + Bt1 + Sil2 + Pl + Qz + L. Potassic feldspar is not observed as a product of reactions (R1) nor (R2), as is frequently the case during water-undersaturated melting of metapelites (Carrington and Watt, 1995). Monazite is restricted to neosomes and is occasionally included in garnet2 (Fig. 4.3f). This observation indicates that monazite crystallised before or simultaneously with assemblage (D).

Sample	**Oxyde (wt %)**										
	SiO2	**TiO_2**	**Al_2O_3**	**FeO**	**MnO**	**MgO**	**Na_2O**	**K_2O**	**CaO**	**H_2O**	**Total**
Average unmolten paragneiss (N=21)	63.4	0.71	18.4	6.57	0.08	2.46	2.86	2.50	1.95	1.13	100.0
BN43	50.7	1.22	23.3	10.3	0.11	4.43	2.69	3.34	1.50	exc.	97.5
BN436	43.8	2.08	26.3	15.0	0.18	5.88	1.05	0.14	3.54	exc.	98.0
BN436 (fractionated)	46.6	2.67	28.2	10.3	0.00	6.28	1.34	0.18	4.24	exc.	99.9
BN47	58.3	0.86	21.5	8.53	0.09	2.71	1.03	2.29	0.83	exc.	96.2
BN365	52.27	0.88	13.8	10.8	0.20	7.32	2.23	0.28	10.7	1.49	100.0
BN534	67.7	0.65	15.9	6.37	0.08	2.21	2.67	1.82	2.29	exc.	99.6
BN491	65.5	0.69	16.1	7.84	0.09	2.95	0.96	0.90	2.57	exc.	97.6

TABLE 4.2: Chemical compositions (oxide wt%) of samples used for P-T pseudosection calculation. Exc. = excess. Compositions with constrained water content are normalised to 100.

Large (up to 5mm long) euhedral biotite crystals (Bt2) form selvedge microstructures around leucocratic domains (Fig. 4.3a, e). They have compositions of #Mg = 0.51-0.56, Ti^{vi} = 0.11-0.07 a.p.f.u. and Al^{vi} = 0.40-0.80 a.p.f.u.), similar to biotite1. Neosomes are overgrown by fibrolite aggregates (Sil3, Fig. 4.3d, e). Biotite selvedge microstructures may be interpreted both as products of the muscovite dehydration reaction or as a retrograde phase developed at the expense of atoll-shaped garnet2 and melt (e.g. Brown (2002)). Observations of atoll-shaped garnet2 replacement by biotite selvedge at the interface between leucosomes and paleosomes suggest that this texture is due to retrogression. It reflects the following partial back-reaction :

$$\text{Grt2} + \text{L} => \text{Bt2} + \text{Sil3} + \text{Pl} + \text{Qz} \quad \text{(R-2)},$$

which also explains formation of fibrolite aggregates. White mica (Ms2) overgrows other phases in leucosomes (Fig. 4.3a, e) and has a Ms composition with a Pg content of 18-23, with Si = 3.00-3.08 a.p.f.u. and $Al^{vi} \sim 1.92 - 2.01$ a.p.f.u (11 O). It is a "late-stage" phase produced by secondary hydration, probably as hydrous fluids exsolved from the crystallising melt (Brown, 2002), when the rock crossed back over the solidus. Staurolite also is a late phase overgrowing previous microstructures (Fig. 4.3c, d). Its #Mg varies from 0.14 to 0.24. Euhedral ilmenite grains are in contact with staurolite and recrystallized biotite. These phases indicate the rock witnessed a H2O-rich fluid input at subsolidus conditions which locally formed the amphibolite-facies assemblage (E) : Grt2 + Bt2 + St + Ilm + Pl + Qz.

Sample BN47 (Garnet–kyanite - staurolite schist) Sample BN47 is from a paragneiss of the Bole-Bulenga domain. It displays a penetrative metamorphic foliation which comprises oriented white mica, biotite, plagioclase and quartz. The foliation is parallel to a transposed sedimentary layering which controls at the cm scale the distribution and modal proportion of garnet, staurolite and kyanite porphyroblasts. Petrographic relationships are used to define a succession of four metamorphic assemblages (A) to (D) (Fig. 4.4). Garnet forms millimetric euhedral grains with cores (Grt1, white dashed line in Fig. 4.4e) of composition Prp4-6, Alm70-72, Grs14-16 and Sps7-8 (Fig. 4.6a), which contain rare quartz and chlorite inclusions. The first assemblage (A) is represented by Grt1 + Chl + Qz, with modal proportion of garnet being $\sim$ 1% (Fig. 4.4c, d). Garnet rims (Grt2) display abundant small ($\sim 10\mu m$) quartz inclusions and have a composition of Prp10-13, Alm77-80, Grs4-8 and Sps1-4, and form 8-9 vol% of the rock. Core to rim zoning is characteristic of garnet growth during prograde metamorphism. Poikilitic staurolite (St1), with a #Mg of 0.15-0.17, contains quartz and ilmenite inclusion trails oblique to the metamorphic banding (Fig. 4.4e), and is in equilibrium contact with garnet2. These phases identify the amphibolite-facies assemblage (B) Grt2 + St1 + Ilm + Qz. Kyanite forms centimetric elongated porphyroblasts aligned parallel to the fabric in the matrix, or rotated due to low intensity shearing. It is in equilibrium contact with Bt + Pl + Ilm + Ms + Grt2. Matrix biotite has compositions of #Mg = 45-52 with Ti^{vi} varying from 0.09 to 0.12 a.p.f.u. Plagioclase displays significant inter-grain compositional variations, with An content ranging from 20 to 45. White mica has a muscovite composition with a paragonite fraction of 18-23, Si = 3.04-3.09 a.p.f.u and Al^{vi} =1.92 a.p.f.u (11 O). These phases define assemblage (C) Grt2 + Ky + Bt + Pl + Ilm + Qz $\pm$ Ms, which corresponds to the upper-amphibolite facies. Monazite forms elongated grains parallel to the metamorphic banding in the matrix and is also found enclosed in kyanite porphyroblasts (Fig. 4.4f). Hence it crystallised before or during the formation of assemblage (C).

Assemblage (C) is overgrown by post-kinematic inclusion-poor staurolite (St2), which has a #Mg 0.12-0.15. The modal proportion of staurolite2 is $\sim$ 17% (Fig. 4.4c, d), i.e. 10 times greater than that of the staurolite1. Garnet included in staurolite2 is sometimes partly resorbed and replaced by staurolite (black dashed line, Fig 4.4e). This reflects the transition from the stability field of kyanite to that of staurolite across the balanced reaction :

$$0.17\ \text{Grt} + 1.86\ \text{Ky} \Rightarrow 0.25\ \text{St2} + 1.00\ \text{Qz}\ \text{(R1)},$$

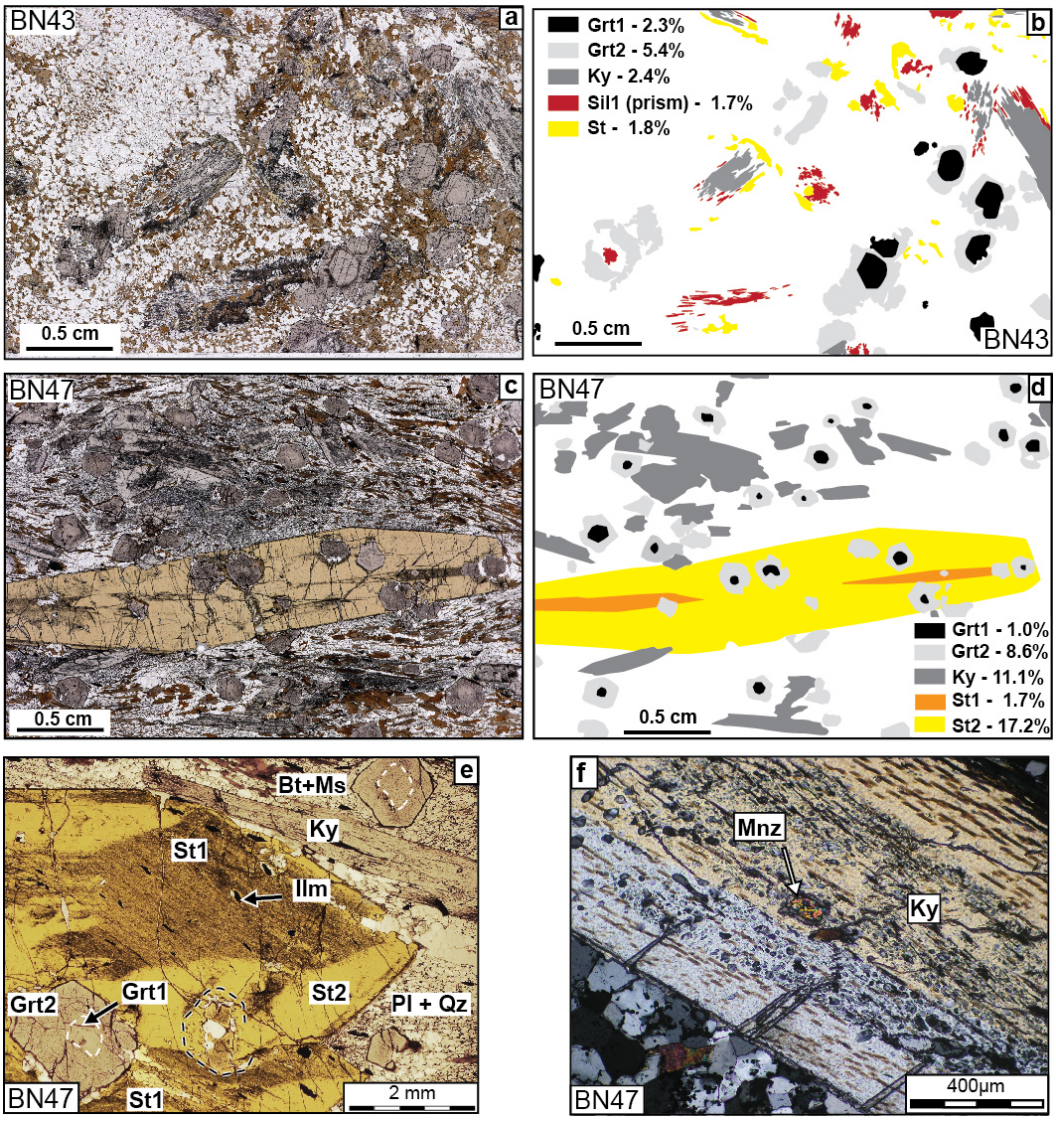

FIGURE 4.4: Modal proportion of metamorphic porphyroblasts deduced from thin section image analysis for samples BN43 (**a, e**) and BN47 (**c, d**). (**e-f**) Photomicrograph of metapelite sample BN47. (**e**) Subhedral garnet displays inclusion-poor cores (white dashed contour) and is included in staurolite. Poikiloblastic staurolite1 contains oriented quartz and ilmenite inclusions. Garnet and staurolite1 are overgrown by post-kinematic euhedral staurolite2. The latter partly replaces garnet (black dashed contour) and overprints the metamorphic banding. (**f**) Monazite grain included in kyanite in sample BN47.

resulting in the formation of lower amphibolite-facies assemblage (D) : Grt2 + St2 + Bt + Pl + Ilm + Qz.

Sample BN436 (Garnet–kyanite–gedrite granofels) Sample BN436 comes from a boudin of competent rock in high-grade meta-sedimentary rocks of the Abulembire domain. It is characterised by a low-Si, high-Al and Mg bulk rock composition (Table 4.1), and a high garnet modal proportion ($\sim$ 50%). Rock-forming

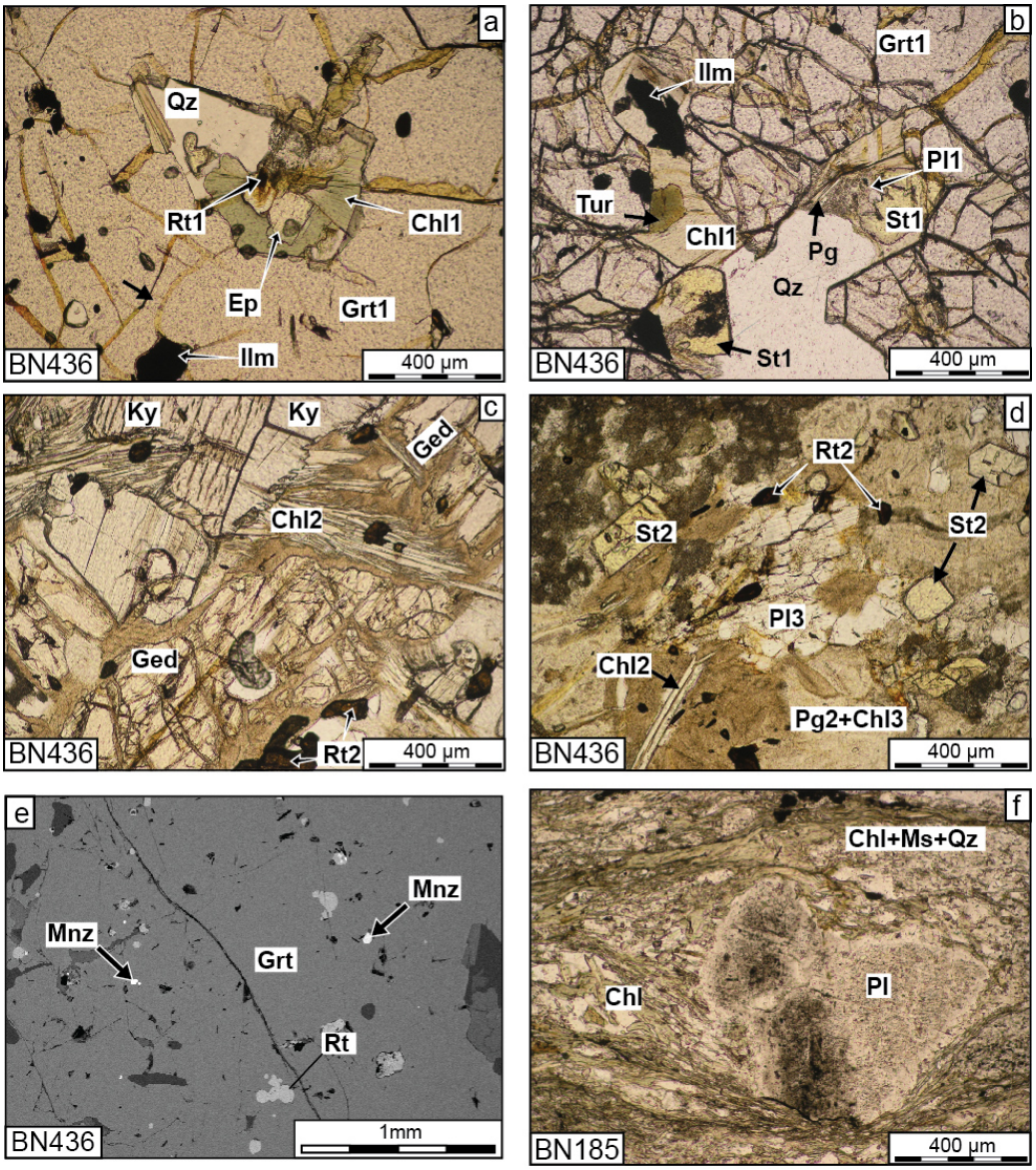

FIGURE 4.5: Photomicrographs and back-scattered electron image of samples BN436 (**a-e**) and BN185 (**f**). (**a**) Pluri-mineral inclusion in garnet porphyroblast core (Grt1), including chlorite1, epidote, rutile1 and quartz. (**b**) Pluri-mineral inclusion in garnet1 including paragonite1, plagioclase1, staurolite1, ilmenite, quartz, turmaline and chlorite with a radial growth pattern. (**c**) Kyanite, gedrite and rutile2 in contact in the matrix belong to the peak metamorphic assemblage. (**d**) Retrograde phases in the matrix include staurolite, fibrous chlorite2 and intergrown chlorite3 + paragonite2. They develop in replacement of an assemblage that includes plagioclase3, gedrite and kyanite. Note the abundance of rutile2 included in these phases and in their pseudomorphs. (e) Monazite and rutile inclusions in a garnet porpyroblast of sample in BN436. (**f**) Chlorite-muscovite-quartz alternation defines foliation and develops in pressure shadow zones of plagioclase porphyroclasts in volcano-sedimentary schist BN185.

minerals do not display any preferential orientation. The rock comprises garnet, kyanite and gedrite porphyroblasts, and a mesocratic matrix which includes staurolite, chlorite, paragonite, plagioclase, rutile and quartz (Fig. 4.5). Petrographic relationships identify four successive metamorphic assemblages (A) to (D). Garnet porphyroblasts have a radius of up to 1 cm, and display a zoning pattern typical of prograde metamorphism (Fig. 4.6a). From core (Grt1) to rim (Grt2), composition changes are Prp 17-20 => 26-32, Grs 3-6 => 6-8, Alm 76-78 => 61-65 and Sps 2 => 0.5-1. Garnet1 preserves multi-mineral inclusions belonging to early metamorphic assemblages. Rare epidote and rutile grains are found together in contact with radial chlorite aggregates (#Mg = 0.39Ů0.51) in garnet1 (Fig. 4.5a). This suggests the formation of a first greenschist- to amphibolite-facies metamorphic assemblage (A) Grt1 + Chl1 + Ep + Rt1 + Qz. Rutile inclusions are sometimes rimmed by ilmenite, suggesting a transition from the stability field of rutile to that of ilmenite. Another set of coexisting inclusions provides evidence for a second assemblage which includes Grt1 + Chl1 + St1 + Pg1 + Pl1 + Ilm + Qz (B) (Fig. 4.5b). Plagioclase1 from assemblage (B) is strongly sericitised. White mica has a muscovite composition with Pg 0.77-0.83, Si = 2.84-3.02 a.p.f.u. and Al^{vi} = 1.95 a.p.f.u (11 O), while St has #Mg of 0.07-0.10.

Garnet outer cores (Grt2) contain kyanite, biotite and plagioclase2 (An45-47) inclusions. Garnet2 is in contact with matrix kyanite, gedrite and plagioclase3 (Fig. 4.5c, d). Gedrite displays small chemical variations : the #Mg is between 0.58 and 0.61, Al^{iv} ranges from 1.3 to 1.7 a.p.f.u., and Al^{vi} is between 1.1 and 1.4 a.p.f.u. (Na+K)A is 0.21-0.31 a.p.f.u. and (Na+Ca)B is 0.12-0.17 a.p.f.u. Biotite grains have a #Mg ∼0.54, and plagioclase3 An content is 57-71. Ilmenite is absent from the matrix, suggesting that it does not belong to the peak metamorphic assemblage. Rutile2 is present in garnet outer core, in gedrite, and is common in the matrix. These relationships indicate the crossing of the following pressure-dependent reaction (Bohlen and Liotta, 1986) :

$$\text{Pl2} + \text{Ilm} + \text{Qz} \Rightarrow \text{Grt2} + \text{Rt2} \quad \text{(R1)},$$

and the formation of the peak metamorphic assemblage (C) : Grt2 + Ky + Ged + Pl3 + Rt2 + Qz ± Bt, in the upper-amphibolite-facies. Using the compositions in Table 4.3, (R1) can be balanced in the CFMASHTi system as 0.28 An + 1.16 Ilm + 1.00 Qz = 0.55 Grt2 + 2.35 Rt2. Monazite is only preserved as single grain inclusions in garnet (Fig. 4.5e), suggesting that it crystallised before the formation of assemblage (C).

The peak metamorphic assemblage is overgrown by fibrous chlorite2 (#Mg = 0.70-0.74) and euhedral staurolite2 (#Mg = 0.16-0.23), while gedrite is pseudomorphosed by intergrown paragonite2 and chlorite3 (Fig. 4.5c, d). This reflects secondary hydration and the local formation of a late metamorphic (greenschist- to amphibolite-facies) assemblage which includes Grt2 + Pg2 + Chl2 + St2 + Qz (D).

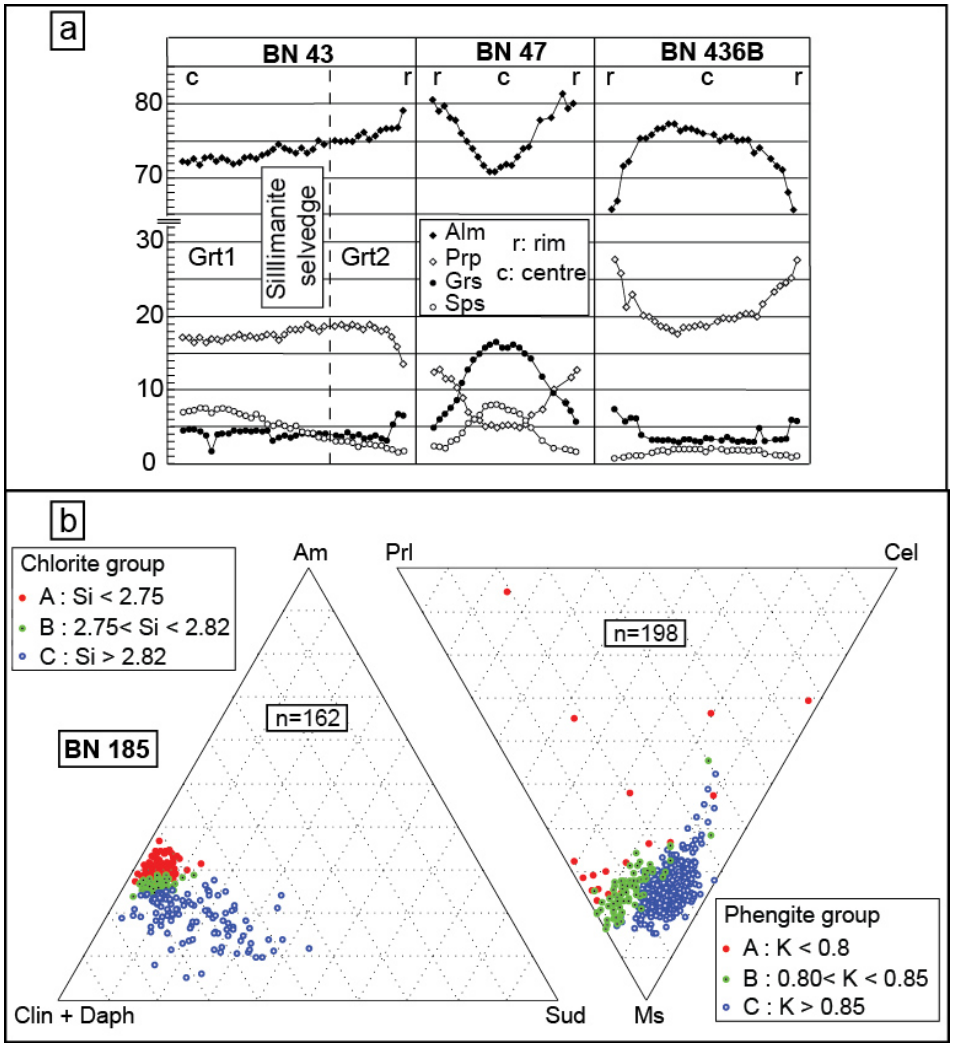

FIGURE 4.6: . (**a**) Chemical composition variations along radial profiles across garnet porphyroblasts of samples BN43, BN47 and BN436. The location of the profile for BN43 is shown in Fig. 3e. (**b**) Ternary diagrams showing the end-member proportions of chlorite and white mica from sample BN185 used for multi-equilibria calculations. Values are in a.p.f.u. Colours illustrate mineral groups defined by compositional criteria.

Sample	BN 43								BN 47							BN 436									
Mineral	Grt1	Grt2	St	Pg	Bt1	Bt2	Ms2	Pl	Grt1	Grt2	St1	St2	Bt	Ms	Pl	Grt2	Grt1	St2	St1	Pg1	Chl2	Chl1	Ged	Pl2	Pl3
position	core	rim	retrog.	Ky incl.	corroded	selvedge	retrog.	matrix	rim	core	porphyroblast		matrix	matrix	matrix	rim	core	retrogr.	Grt incl.	Grt incl.	retrog.	Grt incl.	matrix	matrix	Grt incl.
SiO_2	36.7	36.4	28.1	45.7	36.1	35.6	46.1	61.9	38.0	37.2	28.2	27.5	35.5	45.48	62.4	37.7	37.0	28.6	28.3	44.9	27.3	24.8	46.5	51.2	57.1
TiO_2	0.05	b.d.l	0.48	0.02	2.22	1.95	0.46	b.d.l	b.d.l	0.02	0.62	0.72	2.08	0.32	0.07	0.13	0.02	0.59	0.82	b.d.l	b.d.l	0.02	0.14	0.07	b.d.l
Al_2O_3	21.2	21.2	53.2	39.9	19.2	18.9	35.7	23.6	20.7	21.3	54.2	53.3	19.5	36.4	23.7	21.7	21.4	55.4	54.4	42.0	24.0	22.8	14.7	31.6	28.0
Fe_{tot} as FeO	33.3	35.8	13.8	0.25	17.4	16.8	0.93	0.10	36.0	31.6	14.0	14.4	19.0	0.95	0.08	30.9	35.0	9.99	11.9	0.77	14.5	27.9	19.0	b.d.l	0.14
MnO	3.07	1.12	0.00	0.02	b.d.l	0.01	0.09	0.05	0.99	3.46	0.02	0.05	0.00	0.05	b.d.l	0.49	0.92	0.01	0.08	0.01	0.01	0.05	0.06	b.d.l	0.04
MgO	4.22	4.65	1.22	0.05	11.2	11.5	0.56	b.d.l	2.95	1.30	1.52	0.99	9.85	0.21	b.d.l	6.70	4.74	1.35	0.49	0.00	21.9	11.7	15.9	b.d.l	b.d.l
CaO	1.28	1.10	0.03	0.68	0.04	0.05	0.03	5.04	1.61	5.86	b.d.l	0.04	0.06	0.04	4.90	2.27	1.15	0.01	0.00	2.84	0.04	b.d.l	0.50	14.2	9.72
Na_2O			b.d.l	6.60	0.28	0.09	1.67	8.76			b.d.l	0.01	0.04	1.51	9.19			0.02	0.17	6.14	b.d.l	b.d.l	1.01	3.69	6.38
K2O				0.95	9.10	8.79	8.58	0.06					8.98	8.98	0.06					0.39	0.01	b.d.l	b.d.l	0.04	0.03
Cr_2O_3	b.d.l	0.03	0.06	0.01	0.06	0.13	0.14	b.d.l	0.03	0.02	b.d.l	0.07	0.03	b.d.l	b.d.l	0.05	0.09	0.05	0.17	0.05	b.d.l	b.d.l	0.01	b.d.l	b.d.l
ZnO			0.48		b.d.l	b.d.l	b.d.l	b.d.l			0.15	0.25	b.d.l	b.d.l		b.d.l	b.d.l	0.86	1.51		b.d.l	b.d.l	0.00	b.d.l	b.d.l
Total	99.8	100.3	97.4	94.2	95.6	94.0	94.4	99.5	100.2	100.8	98.7	97.4	95.0	93.9	100.4	99.8	100.4	96.9	97.9	97.2	87.7	87.3	97.8	100.9	101.4
Oxygen	12	12	46	22	22	22	22	32	12	12	46	46	22	22	32	12	12	46	46	22	28	28	23	32	32
Si	5.91	5.85	7.84	5.92	5.41	5.41	6.15	11.0	6.10	5.96	7.75	7.71	5.39	6.10	11.0	5.93	5.91	7.87	7.83	5.68	5.39	5.31	6.66	9.25	10.1
Al^{IV}	0.09	0.15	0.16	2.08	2.59	2.59	1.85	4.96	0.00	0.04	0.25	0.29	2.61	1.90	4.93	0.07	0.09	0.13	0.17	2.32	2.61	2.69	1.34	6.72	5.85
Al^{VI}	3.93	3.86	17.3	4.00	0.80	0.80	3.76		3.90	3.99	17.3	17.3	0.87	3.84		3.94	3.94	17.8	17.6	3.93	2.97	3.06	1.15		
Fe^{3+}	0.22	0.42	0.54	0.00	0.00	0.00	0.03	0.01	0.00	0.05	0.55	0.53	0.00	0.00	0.01	0.14	0.21	0.02	0.22	0.02				0.00	0.02
Ti	0.01	0.00	0.10	0.00	0.25	0.22	0.05	0.00	0.00	0.00	0.13	0.15	0.24	0.03	0.01	0.02	0.00	0.12	0.17	0.00	b.d.l	0.00	0.02	0.01	0.00
Cr	0.00	0.00	0.01	0.00	0.01	0.02	0.01		0.00	0.00	0.00	0.02	0.00	0.00		0.01	0.01	0.01	0.04	0.01	b.d.l	b.d.l	0.00		
Mg	1.01	1.11	0.51	0.01	2.49	2.62	0.11	0.00	0.70	0.31	0.62	0.41	2.23	0.04	0.00	1.57	1.13	0.55	0.20	0.00	6.44	3.75	3.41	0.00	0.00
Fe^{2+}	4.49	4.82	2.68	0.03	2.18	2.13	0.10	0.00	4.83	4.23	2.68	2.84	2.41	0.11	0.00	4.06	4.67	2.28	2.54	0.08	2.39	5.00	2.28	0.00	0.00
Mn^{2+}	0.42	0.15	0.00	0.00	0.00	0.00	0.01	0.01	0.13	0.47	0.00	0.01	0.00	0.01	0.00	0.07	0.12	0.00	0.02	0.00	0.00	0.01	0.01	0.00	0.01
Ca	0.22	0.19	0.01	0.09	0.01	0.01	0.00	0.96	0.28	1.01	0.00	0.01	0.01	0.01	0.93	0.38	0.20	0.00	0.00	0.38	0.01	b.d.l	0.08	2.75	1.85
Na	0.00	0.00	0.00	1.65	0.08	0.03	0.43	3.02	0.00	0.00	0.00	0.00	0.01	0.39	3.15			0.01	0.09	1.51	b.d.l	b.d.l	0.28	1.29	2.19
K			0.00	0.16	1.74	1.71	1.46	0.01					1.74	1.54	0.01					0.06	0.00	0.00		0.01	0.01
Zn			0.10	0.00	0.00	0.00	0.00				0.03	0.05	0.00	0.00				0.17	0.31	0.00	0.00	0.00			
xPrp	0.17	0.19							0.12	0.05						0.26	0.18							0.32	0.54
xAlm	0.72	0.75							0.81	0.70						0.67	0.76							0.68	0.46
xSps	0.07	0.03							0.02	0.08						0.01	0.02							0.89	0.90
xGrs	0.05	0.10							0.05	0.17						0.06	0.03								
xMg	0.18	0.19	0.16	0.27	0.53	0.55			0.13	0.07	0.16	0.11	0.48			0.28	0.19	0.20	0.07		0.73	0.43	0.60		
xOr								0.00							0.00									0.00	0.00
xAb								0.75							0.77									0.32	0.54
xAn								0.24							0.23									0.68	0.46

TABLE 4.3: Representative chemical compositions of minerals forming metamorphic assemblages used to constrain P-T conditions and P-T paths from pseudosections. b.d.l. = below detection limit.

Sample BN365 (migmatitic amphibolite gneiss) Sample BN365 is from a kilometric amphibolite sliver at the base of a sequence of migmatitic ortho- and paragneisses, in the Bole-Bulenga domain. It is separated from low-grade schists of the Maluwe domain by the Bole-Nangodi shear zone (Fig. 4.2). Petrographic relationships define a succession of three metamorphic assemblages (A) to (C). The amphibolites contain small volumes of unconnected leucosomes, suggesting limited melting rate and melt loss. The rock is made of a melanocratic Hbl–Pl–Cpx–Ilm–Bt–Qz matrix, and of garnet porphyroblasts (Fig. 4.7a, b). Garnet is unzoned and has compositions of Alm50-54, Grs28-31, Prp15-18 and Sps2-4 (Fig. 4.7h). It contains inclusions of hornblende1, plagioclase1 and rutile, the latter being partly replaced by ilmenite or titanite (Fig. 4.7c). Hornblende1 is corroded and has compositions of #Mg = 0.53-0.55, Ca/Na = 3.84-4.93, with (Na+Ca)B =1.84-1.89 a.p.f.u. and (Na+K)A = 0.42-0.53 a.p.f.u. It is in contact with plagioclase1 (An35-46). In contrast, matrix hornblende2 has #Mg = 0.57-0.60, Ca/Na = 4.57-5.81, (Na+Ca)B =1.88-1.94 a.p.f.u. and (Na+K)A = 0.36-0.39 a.p.f.u. ; and is in contact with An39-45 plagioclase2. Clinopyroxene has a diopside composition with #Mg = 0.70-0.74. Biotite is a minor retrograde phase representing less than 1vol% of the rock, with a #Mg = 0.38-0.40 and Ti^{vi} = 0.07-0.09 a.p.f.u. Melting is evidenced by quartz-plagioclase-rich leucocratic domains and by "string of beads" textures between matrix grains (Fig. 4.7b). Mineral inclusions in garnet belong to assemblage (A) : Grt + Hbl1 + Pl1 + Cpx + Rt + Qz + L ± Bt. Matrix minerals in contact with garnet define the peak metamorphic assemblage (B) : Grt + Hbl2 + Pl2 + Cpx + Ilm + Qz + L ± Bt. Garnet porphyroblasts are partially replaced by leucocratic domains which are dominated by plagioclase3 and contain minor hornblende3 (Fig. 4.7a). Grains are euhedral, display 120 ° grain boundaries, and have compositions similar to matrix grains. These textural relationships suggest garnet resorption at supra-solidus conditions during reaction :

$$\text{Grt} + \text{Cpx} + \text{L} \Rightarrow \text{Pl3} + \text{Hbl3} \quad \text{(R1)}.$$

Replacement of ilmenite by titanite illustrates retrogression and the local development of assemblage (C) : Grt + Hbl3 + Pl3 + Ttn + Qz ± Bt.

Sample BN534 (Garnet–kyanite-bearing migmatitic paragneiss) Sample BN534 is a metatexite derived from a paragneiss collected in the north-western Bole-Bulenga domain, to the west of the Jirapa SZ (Fig. 4.2). At outcrop scale, it develops foliation-parallel leucosomes connected to cross-cutting granitic veins, and displays neosomes comprising aggregates of peritectic kyanite and garnet. Petrographic relationships are used to identify three successive metamorphic assemblages (A) to (C). Garnet forms centimetric aggregates in quartz-plagioclase leucocratic domains (Fig. 4.7d, e). It is unzoned and has compositions of Alm75-76, Prp17-20, Grs4-6, Sps1-3, except for margins which were re-equilibrated and have compositions of Alm77, Prp15-16, Grs6, Sps2 (Fig. 4.7h). Plagioclase in neosomes and in the matrix has similar compositions of An27-30. Neosomes additionally comprise sheared poikiloblastic kyanite with biotite1, rutile and rare muscovite1 inclusions (Fig. 4.7d, e). These phases belong to a first metamorphic assemblage (A) : Grt + Ky + Bt1 + Ms1 + Rt + Pl + Qz + L. Rutile and sheared muscovite are only present in garnet and (partly retrogressed) kyanite. This indicates that they were preserved because

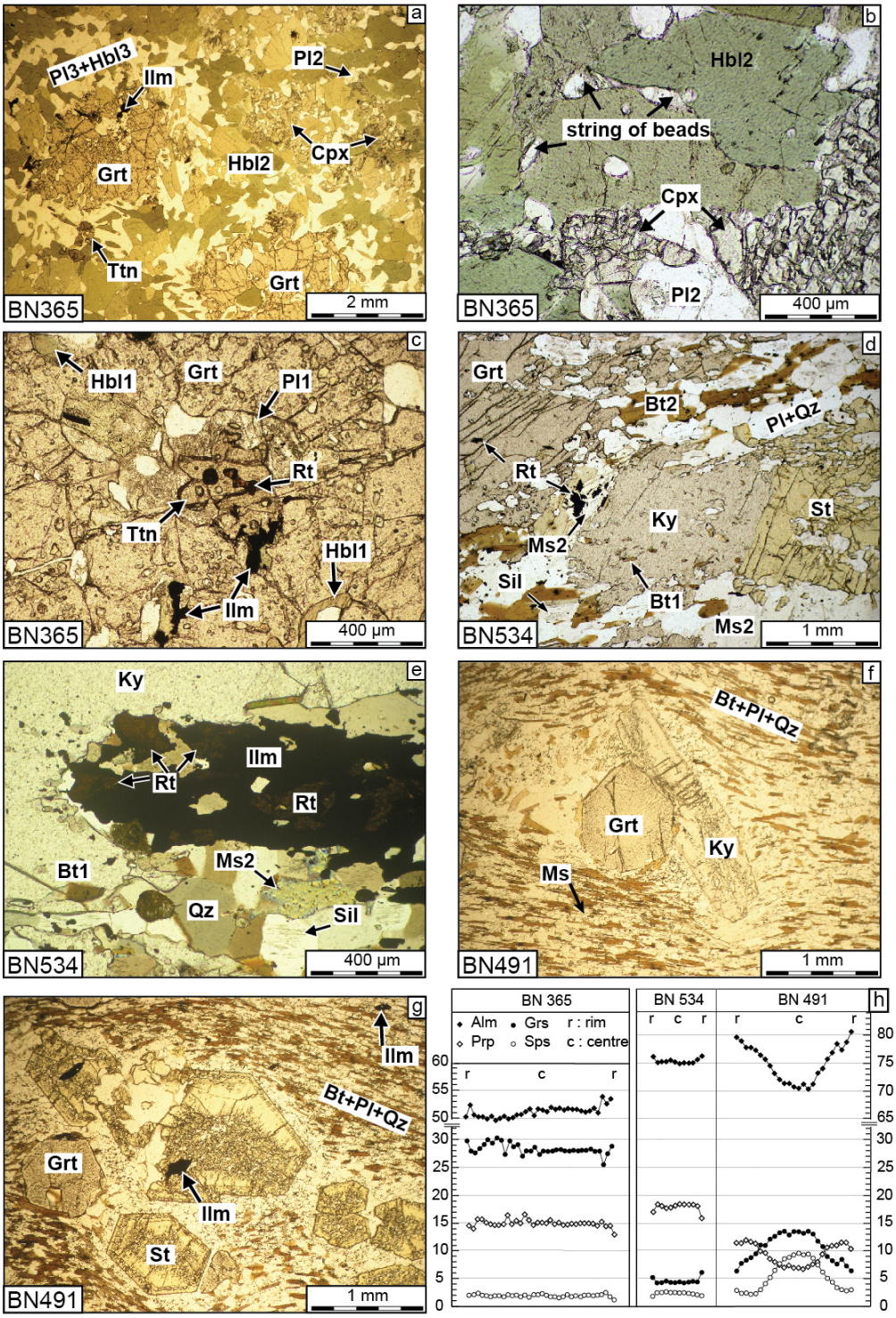

FIGURE 4.7: Photomicrographs of samples BN365 (**a-c**), BN534 (**d-e**) and BN491(**f-g**). (**a**) The rock matrix is dominated by hornblende2 and additionally contains plagioclase2, clinopyroxene, ilmenite and quartz. Garnet porphyroblasts are partially resorbed and rimmed by euhedral hornblende3 and plagioclase3 grains.

FIGURE 4.7: (**b**) Matrix hornblende2 and clinopyroxene in contact. Grain boundaries occasionally contain quartz-plagioclase "string of beads" which may represent melt relics. (**c**) Hornblende1, plagioclase1 and rutile relics included in garnet. Rutile is replaced by intergrown ilmenite-titanite. (**d**) Garnet and kyanite porphyroblasts form aggregates in quartz-plagioclase-rich neosomes. They contain inclusions of rutile, biotite1 and muscovite1 (not shown). Biotite 2 forms selvedge microstructures around neosomes. Quartz crystallised in neosome contain fibrolite. Kyanite is overgrown by staurolite and partly replaced by late-stage muscovite2. (**e**) Rutlie was initially locked in kyanite, but is sometimes found within recrystallized quartz-muscovite2 domains that develop at the expense of kyanite, where it is partly replaced by ilmenite. (**f**) Kyanite porphyroblast overgrows garnet and is rotated relative to oriented matrix biotite-plagioclase-muscovite-quartz. Retrograde muscovite develops at the expense of kyanite. (**g**) Euhedral staurolite overgrows the fabric. Quartz-ilmenite grains form concentric inclusion trails reflecting porphyroblast growth. (**h**) Chemical composition profiles across garnet porphyroblasts of samples BN365, BN534 and BN491.

they were locked in porphyroblasts. Their absence from the matrix suggests that they reacted out to form assemblage (B) : Grt + Ky + Bt1 + Pl + Qz + L. Biotite2 occurs in the matrix or forms selvedge microstructures around neosomes (Fig. 4.7d). It has compositions of #Mg = 0.54-0.59, Ti^{vi} = 0.09-0.13 a.p.f.u., that are similar to biotite1. Quartz grains crystallised in neosomes contains minor amounts of fibrolite inclusions in their centres, suggesting that the rock crossed back below the solidus under conditions of sillimanite stability (Fig. 4.7e). Large (up to 0.5cm) flakes of muscovite2 overgrow neosomes and replace kyanite . They have compositions of Ms77-82, Pg18-23, with Si = 3.05-3.14 and Al^{vi} = 1.84-1.90. Staurolite porphyroblasts develop in the matrix (Fig. 4.7e) and have Mg# = 14-22. Rutile grains are replaced by ilmenite (Fig. 4.7d, e). These phases belong to assemblage (C) : Grt + Bt2 + St + Ms2 + Pl + Ilm + Qz.

Sample BN491 (Garnet–kyanite–staurolite-bearing paragneiss) Sample BN491 originates from the southern extremity of the Bole-Bulenga domain (Fig. 4.2). It is from a sub-solidus paragneiss separated by a NNE-striking high-strain zone from diatexites and metatexites represented by sample BN43. It comprises a matrix of oriented plagioclase, biotite, ilmenite, quartz + rare muscovite, and contains garnet, staurolite and kyanite porphyroblasts (Fig. 4.7f, g). Petrological relationships identify assemblages (A) to (C). Garnet is subhedral or partially replaced by biotite or staurolite. It displays a concentric zoning pattern typical of growth during prograde metamorphism. From core (garnet1) to rim (garnet2), compositions variations are Alm70-72 => 78-81, Prp6-8 => 11-12, Grs12-14 =>6-8, Sps9-10 =>2 (Fig. 4.7h). Cation diffusion in garnet2 margins during retrogression is documented by the slight decrease of Prp content to ∼10 and an increase of Sps content to 3. Garnet1 contains small (10-100μm) ilmenite and chlorite inclusions (#Mg = 42-45), which belong to a relict metamorphic assemblage (A) : Grt1 + Chl + Ilm + Qz. Matrix biotite has #Mg = 0.45-0.49, and Ti^{vi} = 0.12-0.19 a.p.f.u., plagioclase has compositions of An24-26, white mica has a muscovite composition with Pg∼20, Si = 3.03-3.07 and Al^{vi} = 1.86-1.88. Syn-kinematic kyanite porphyroblasts

overgrow garnet and are rotated in the metamorphic fabric (Fig. 4.7f). Kyanite belongs to assemblage (B) : Grt2 + Ky + Bt + Pl + Ilm + Qz ± Ms. Staurolite forms euhedral porphyroblasts which overgrow garnet and the metamorphic banding (Fig. 4.7g). They display concentric growth patterns underlined by alternating inclusion-rich and inclusion-free domains. Staurolite #Mg is 16-18 => 8-10 from core to rim. Contact between staurolite rims, garnet2 and matrix minerals indicate the formation of assemblage (C) : Grt2 + St + Bt + Pl + Ilm + Qz.

Sample	BN 365							BN 534						BN 491						
Mineral position	Grt	Cpx matrix	Hbl1 Incl	Hbl3 rim	Pl3 rim	Pl1 Incl	Bt matrix	Grt core	Grt margin	St matrix	Ms retrog.	Bt matrix	Pl matrix	Grt core	Grt rim	St core	St rim	Pl matrix	Ms matrix	Bt matrix
SiO_2	38.9	52.2	44.1	46.6	58.0	58.3	34.4	37.5	37.5	27.3	46.2	37.1	60.9	37.2	37.6	28.6	28.7	61.7	46.4	36.8
TiO_2	0.05	0.12	1.10	0.82	b.d.l	b.d.l	1.94	0.05	b.d.l	0.56	0.59	1.49	b.d.l	b.d.l	b.d.l	0.70	0.63	0.04	0.81	2.51
Al_2O_3	21.4	2.62	11.9	10.5	26.7	27.1	16.7	21.9	21.9	53.3	36.3	19.3	24.8	21.1	21.3	53.3	54.1	24.1	36.3	19.6
Fe_{tot} as FeO	24.4	8.67	16.5	14.7	0.11	0.09	24.9	34.2	34.5	13.72	0.72	15.07	0.04	32.2	34.9	13.3	13.0	0.30	1.28	18.6
MnO	1.23	0.14	0.22	0.01	b.d.l	b.d.l	0.33	1.08	0.82	b.d.l	b.d.l	0.03	b.d.l	3.89	1.01	0.07	b.d.l	0.03	b.d.l	0.15
MgO	4.13	12.7	10.3	11.5	b.d.l	b.d.l	9.29	4.65	4.05	1.72	0.45	12.42	b.d.l	1.85	2.99	1.29	0.58	b.d.l	0.39	9.40
CaO	10.5	23.1	11.6	12.0	9.13	6.91	0.07	1.49	2.14	b.d.l	0.04	0.03	6.12	4.49	2.88	0.02	b.d.l	5.61	b.d.l	b.d.l
Na_2O	b.d.l	0.37	1.67	1.27	6.51	6.40	b.d.l	b.d.l	0.02	0.02	1.72	0.05	8.29	0.01	0.01	b.d.l	b.d.l	8.69	1.48	0.14
K_2O	b.d.l	b.d.l	0.30	0.24	0.05	1.06	7.11	0.01	b.d.l		8.84	9.34	0.06	b.d.l	b.d.l			0.03	8.85	9.30
Cr_2O_3	0.02	0.11	0.06	0.17			0.10	b.d.l	0.01	0.02	0.01	0.04		0.05	b.d.l	b.d.l	0.07		0.04	0.18
ZnO		b.d.l	b.d.l	b.d.l			b.d.l													
Total	100.6	100.0	97.7	97.8	100.5	99.9	94.9	100.8	100.9	97.0	94.9	94.8	100.2	100.8	100.7	97.6	97.3	100.5	95.5	96.8
Oxygen	12	6	23	23	32		22	12	12	46	22	22	32	12	12	46	46	32	22	22
Si	6.04	1.95	6.56	6.83	10.3	10.4	5.38	5.93	5.94	7.66	6.12	5.52	10.8	5.97	6.00	7.92	7.96	10.9	6.12	5.47
Al^{IV}	0.00	0.05	1.44	1.17	5.61	5.71	2.62	0.07	0.06	0.34	1.88	2.48	5.18	0.03	0.00	0.08	0.04	5.02	1.88	2.53
Al^{VI}	3.91	0.06	0.65	0.65			0.44	4.00	4.02	17.3	3.79	0.91		3.96	4.00	17.36	17.62		3.75	0.91
Fe^{3+}	0.00	0.01			0.02	0.00	0.00	0.09	0.07	0.59	0.02	0.00	0.01	0.09	0.00	0.50	0.23	0.04	0.03	0.00
Ti	0.01	0.00	0.12	0.09	0.00	0.00	0.23	0.01	0.00	0.12	0.06	0.17	0.00	0.00	0.00	0.15	0.13	0.01	0.08	0.28
Cr	0.00	0.00	0.01	0.02			0.01	0.00	0.00	0.00	0.00	0.01		0.01	0.00	0.00	0.01		0.00	0.02
Mg	0.96	0.70	2.28	2.52	0.00	0.00	2.16	1.10	0.96	0.72	0.09	2.76	0.00	0.44	0.71	0.53	0.24	0.00	0.08	2.08
Fe^{2+}	3.17	0.26	2.05	1.80	0.00	0.01	3.25	4.44	4.49	2.63	0.06	1.87	0.00	4.23	4.66	2.59	2.78	0.00	0.11	2.31
Mn^{2+}	0.16	0.00	0.03	0.00	0.00	0.00	0.04	0.15	0.11	0.00	0.00	0.00	0.00	0.53	0.14	0.02	0.00	0.00	0.00	0.02
Ca	1.75	0.92	1.85	1.88	1.75	1.33	0.01	0.25	0.36	0.00	0.01	0.01	1.16	0.77	0.49	0.00	0.00	1.06	0.00	0.00
Na	0.00	0.03	0.48	0.36	2.25	2.22	0.00	0.00	0.01	0.01	0.44	0.01	2.85	0.00	0.00	0.00	0.00	2.98	0.38	0.04
K	0.00	0.00	0.06	0.04	0.01	0.24	1.41	0.00	0.00		1.49	1.77	0.01	0.00	0.00			0.01	1.49	1.76
Zn		0.00								0.05	0.00	0.00				0.07	0.05		0.00	0.00
xPrp	0.16							0.18	0.16					0.07	0.12					
xAlm	0.53							0.75	0.76					0.71	0.78					
xSps	0.03							0.02	0.02					0.09	0.02					
xGrs	0.29							0.04	0.06					0.13	0.08					
xMg	0.23	0.73	0.53	0.58			0.40	0.20	0.18	0.21		0.60		0.09	0.13	0.17	0.08			0.47
xOr					0.00	0.06							0.00					0.00		
xAb					0.56	0.59							0.71					0.74		
xAn					0.44	0.35							0.29					0.26		

TABLE 4.4: Representative chemical compositions of minerals forming metamorphic assemblages used to constrain P-T conditions and P-T paths from pseudosections. b.d.l. = below detection limit.

4.2.4.2 Chlorite-mica schists

Sample BN185 (volcano-sedimentary rock) Sample BN185 is an Al-rich silicic volcano-sedimentary rock intercalated in a sequence of volcanic and volcanoclastic rocks, and originates from the north-western Wa-Lawra belt. It develops a schistosity, contains plagioclase porphyroclasts and displays alternating quartz-rich and chlorite-muscovite-rich layers. Calcite occasionally forms aggregates elongated parallel to the schistose fabric. Chlorite and white mica show strong intra-grain and inter-grain chemical variations. Chlorite #Mg varies between 0.42-0.52, although most values cluster in the range of 0.47-0.50. White mica has a strong muscovite fraction, Ms (= 100x K/(K+Na+Ca)) varies from 89 to 99 (Table 4.8). Chemical compositions of chlorite and white mica from sample BN185 are presented in Fig. 4.6b. Chlorite compositions plot near to the clinochlore + daphnite end-member. They vary from a more ferro-magnesian composition of Clin+Daph65 Am30 Sud5 to a more silicic composition of about Clin+Daph60 Am15 Sud35. Three compositional groups (A-C) are defined base on chlorite Si content (Fig. 4.6b). White micas all have compositions which are close to the muscovite end-member. They display some variations in potassium content, which is reflected in Fig. 4.6b by a scatter of data points between compositions of Ms75 Prl25 Cel0 to Ms75Prl5Cel20. Three compositional groups (A-C) are defined base on white mica K content.

Sample BN246 (Micaschist) Sample BN246 is a micaschist sampled in the southern Maluwe domain, in the vicinity of a high-strain zone mineralised in gold, at the contact between meta-sedimetary rocks and an elongated granodiorite body. It displays an assemblage of intergrown quartz-chlorite-muscovite, and a marked mineral orientation parallel to the schistosity. White mica is the least abundant of the three phases. It has variable compositions ranging from Ms74 to Ms95 (Table 4.8), Si = 3.10-3.40 a.p.f.u. and Al^{vi} =1.80-1.95 a.p.f.u (11 O). Chlorite #Mg is within 0.31-0.36, Si = 2.64-2.75 a.p.f.u., Al^{vi} = 1.46-1.52 (14 O). The sample contains abundant pyrite and is cross-cut by pyrite-calcite veins.

4.2.5 Methods

4.2.5.1 P-T conditions and P-T paths

P-T conditions and P-T paths were constrained by using the P-T pseudosection method and geothermobarometry with a multi-equilibria method. The pseudosection method is used to infer P-T conditions and P-T-t paths (e.g. Johnson et al. (2008); Millonig et al. (2010); Zeh (2001); Zeh et al. (2004)) by comparison of observed assemblages, modes, mineral compositions and zoning patterns ; with those obtained by P-T pseudosection calculations based on thermodynamic models (Connolly and Petrini, 2002; de Capitani and Brown, 1987; Powell and Holland, 2010; Powell et al., 1998). Mineral compositions were measured using a Cameca SX50 Microprobe at the GET lab in Toulouse, France. P-T pseudosections were constructed using the Perplex software (Connolly, 2005). Pseudosections used to constrain the prograde evolution of migmatite samples were constructed by using an average composition of subsolidus paragneiss (Table 4.2, Appendix 4.2.11.2). Garnet porphyroblast fractionation was taken into account when its mode was found

to be significant (> 1vol%). Methodological details relevant for individual samples are described in Appendix 4.2.11.1, along with the chosen solution models.

In addition, the multi-equilibria method (e.g. Berman (1991)) was employed to set further constraints on the P-T evolution of low-grade, greenschist- to amphibolite-facies metamorphic rocks. This method is appropriate to constain P-T conditions and P-T paths rocks characterised by high variance assemblages (e.g.Vidal et al. (2006) and references therein). Studies on natural metapelite samples have shown that minerals from different microstructural domains (foliations, shear bands, etc) of a single thin section can represent different local equilibria, and therefore reflect different P-T conditions (e.g., Ganne et al. (2012); Parra et al. (2002); Vidal et al. (2006, 2001); Yamato et al. (2007b)). The compositions of minerals used for P-T calculations are presented in Table 4.8, and calculation details are given in Appendix 4.2.11.1.

4.2.5.2 Geochronology

A first set of analyses was performed *in-situ* on polished thin sections of samples BN43, BN47 and BN436, using laser ablation–inductively coupled plasma–sector field–mass spectrometry (LA-ICP(SF)-MS) at Goethe University Frankfurt (Appendix 4.2.11.3). Prior to LA-ICP(SF)-MS, the internal structure of each monazite grain was characterised by raster electron microscopy (REM) at Géosciences Environnement Toulouse using a JEOL SM-6360 OLV Scanning Electron Microscope. A second set of analyses was carried out *in-situ* on polished thin sections of samples BN47 and BN43, using Sensitive High Resolution Ion MicroProbe (SHRIMP II) at the John de Laeter Centre for Isotope Research (JLC), Curtin University, Perth, Australia (Appendix 4.2.11.3). Monazite crystals from sample BN436 were only dated using LA-ICP-MS at GUF.

4.2.6 Results

4.2.6.1 P-T conditions and P-T paths

Sample BN43 (Garnet–kyanite-bearing migmatitic gneiss) P-T pseudosections for migmatite sample BN43 are presented in Fig. 4.8, with assemblages and reactions identified in 4.8d. Subsolidus amphibolite-facies conditions of 6.5-9.5 kbar, 600-670 ˚ C are deduced from the compositions of garnet1 (Prp13-17, Grs3-5) and plagioclase located in paleosomes (An 24-26) (Fig. 4.8b). These conditions overlap with the calculated stability conditions of the metamorphic assemblage Bt + Grt + Pl + Ms + Pg + Rt + Qz between 8.5-9.5 kbar, 650-670 ˚ C. This assemblage is identical to assemblage (A) except for rutile, which was not observed and may have totally reacted out. The composition of plagioclase preserved in kyanite (An21-25) is consistent with crossing (R1) at 10.0-11.0 kbar (Fig. 4.8c, d). The formation of assemblage (B) Grt1 + Bt1 + Ky + Pl + Qz + L requires decompression below 9.0 kbar at 680-750 ˚ C. We deduce the shape of the P-T path based on constraints drawn from the following observations :

- (1) Aluminosilicate mode increases in the stability field of sillimanite.
- (2) Garnet2 formation by reaction (R2) represents an increase in garnet mode in the stability field of sillimanite.

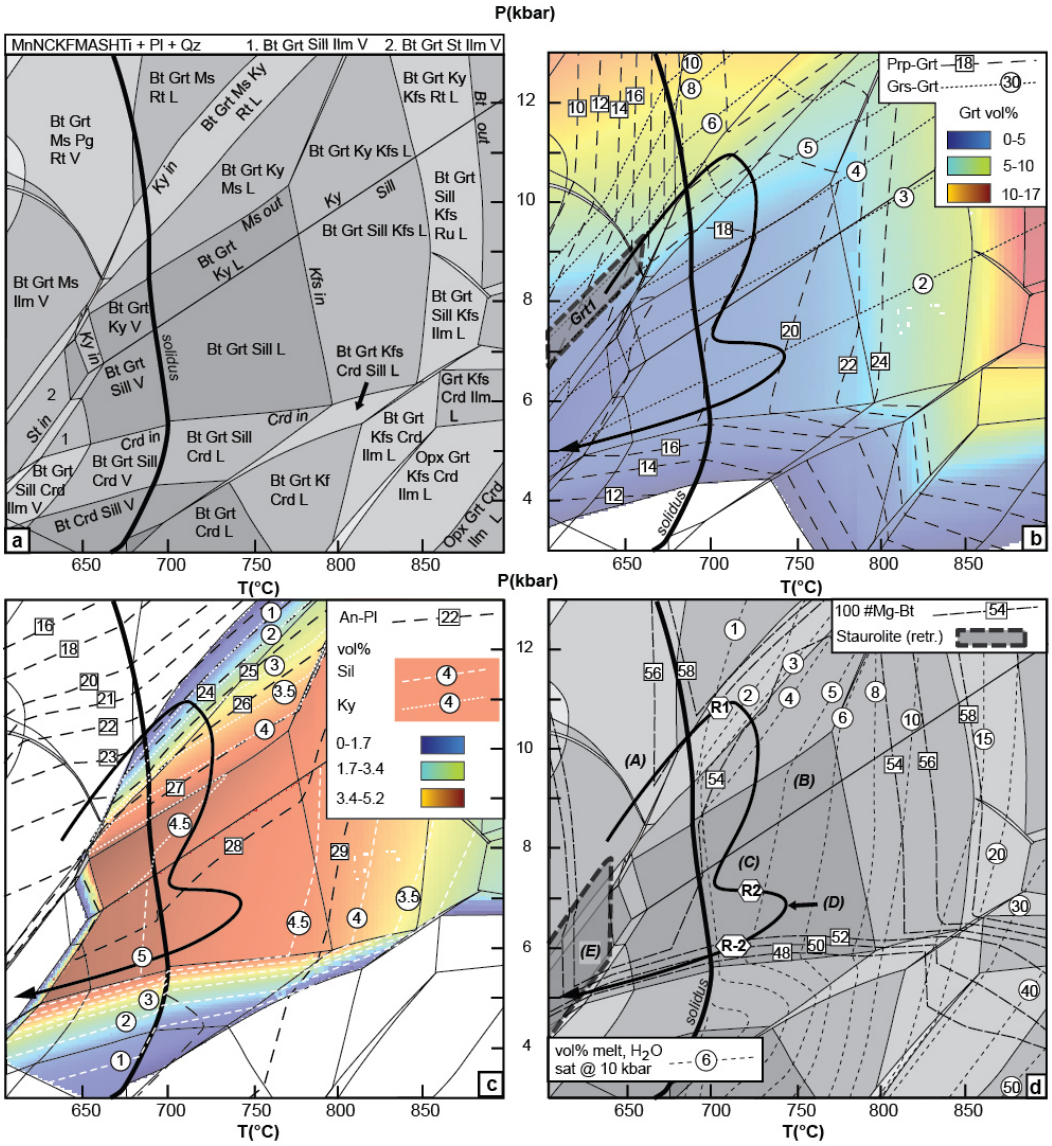

FIGURE 4.8: MnNCKFMASHTi P-T pseudosections presenting phase equilibria for sample BN43. (**a-d**) Stable assemblages calculated from an average paragneiss composition (Table 4.2, Appendix 4.2.11.1). (**b**) Calculated garnet Prp and Grs content (black dashed lines, numbers in boxes and dotted lines, numbers in circles, respectively) and garnet mode (colour gradient). (**c**) Calculated plagioclase An content (black dashed lines, numbers in boxes), and modal proportion of aluminosilicates. (**d**) Calculated melt fraction (dashed lines, numbers in circles). The shaded domain shows the stability field of retrograde staurolite in assemblage (E), calculated by using whole rock composition of sample BN43, which is suitable to study metamorphic phase relationships during the retrograde evolution of the sample (Appendix 4.2.11.1). Letters (A) to (E) refer to assemblages, and (R1) and (R2) refer to metamorphic reactions identified in the main text. A possible P-T path consistent with observed petrological relationships is shown.

Modelling results show that aluminosilicate mode decreases with increasing T (Fig. 4.8c), hence (1) requires decompression without heating from the stability field of assemblage (B) to that of assemblage (C) Grt1 + Bt1 + Sil1 + Pl + Qz + L, below 7.0-9.0 kbar. Garnet mode increases with increasing T, therefore (2) implies a temperature increase under conditions corresponding to the stability of assemblage (C) (Fig. 4.8b). Garnet2 crystallisation (which defines assemblage (D)) post-dates or is coeval with monazite crystallisation in neosomes, and corresponds to peak temperature conditions of $\sim 750\,^{\circ}$C. If H_2O saturation conditions are met on the wet solidus at 10 kbar, melt is generated in sufficient amount at peak T (>5 vol%, Fig. 4.8d) for it to segregate (e.g. Arzi (1978); Brown et al. (1995); Sawyer (1994)), inducing open system behaviour (Appendix 4.2.11.1). The absence of cordierite constrains pressure along the retrograde path to be above 5 kbar. This is consistent with the composition of biotite2 (#Mg = 0.51-0.56). Calculation results show that assemblage (E) Grt2 + Bt2 + St + Ilm + Pl + Qz, formed between 4.5-8.0 kbar and $<640\,^{\circ}$C (Fig. 4.8d).

Sample BN43 records a clockwise P-T path. Prograde burial and heating from amphibolite-facies conditions of about 9.0 kbar, $650\,^{\circ}$C across the solidus to transitional amphibolite–high-P granulite facies conditions of 10.0-11.0 kbar, $700\,^{\circ}$C is documented by the evolution from assemblage (A) to (B). Metamorphic conditions at peak P fit a 15-20 $^{\circ}$C/ km apparent geothermal gradient (calculated for an average density = 2750 kg m^{-3}). High-P (>10 kbar) melting is followed by near isothermal decompression to 5.0-8.0 kbar, into the stability field of assemblage (C). The rock then records heating to form assemblage D at the amphibolite Ű low-P granulite facies transition. Recorded peak T conditions of about $750\,^{\circ}$C fit a hot 30-35 $^{\circ}$C/ km apparent geotherm. Assemblage (E) testifies of a retrograde metamorphism in the lower amphibolite facies.

Sample BN47 (Garnet–kyanite - staurolite schist) Results of P-T pseudosection construction are presented in Fig. 4.9, with assemblages and reactions identified in 4.9d. Comparing modelled and measured garnet compositions provides constraints for a prograde evolution at the blueschist–amphibolite facies transition, with increasing T and decreasing P from the nucleation of garnet core (Grt1) at 11-14 kbar, 520-560 $^{\circ}$C to growth of garnet rim (Grt2) at 9.0-13.0 kbar, 570-600 $^{\circ}$C (Fig. 4.9b). The conditions of garnet1 formation correspond to the calculated stability field of the assemblage Chl + Ms + Cld + Pg + Grt1 + Rt. However, assemblage (A) is not fully characterised and only chlorite inclusions are preserved in garnet1. The absence of chloritoid and paragonite may be due to their complete consumption by prograde metamorphic reactions. Garnet2 is predicted to be in equilibrium with staurolite1 (#Mg = 0.15-0.17) at around 11.0 kbar, $600\,^{\circ}$C (Fig. 4.9c). These conditions correspond to the stability field of Grt + St + Chl + Ms + Pg + Rt, while assemblage (B) consists of Grt2 + St1 + Ilm + Qz. The discrepancies between the observed and calculated assemblage may be due to the complete consumption of chlorite and white micas, and to the retrogression of rutile to ilmenite during subsequent metamorphic evolution.

Further information on the shape of the P-T path may be drawn from the observation that garnet2 is in equilibrium contact with kyanite. Garnet composition and zoning patterns suggest that garnet mode did not increase between assemblage

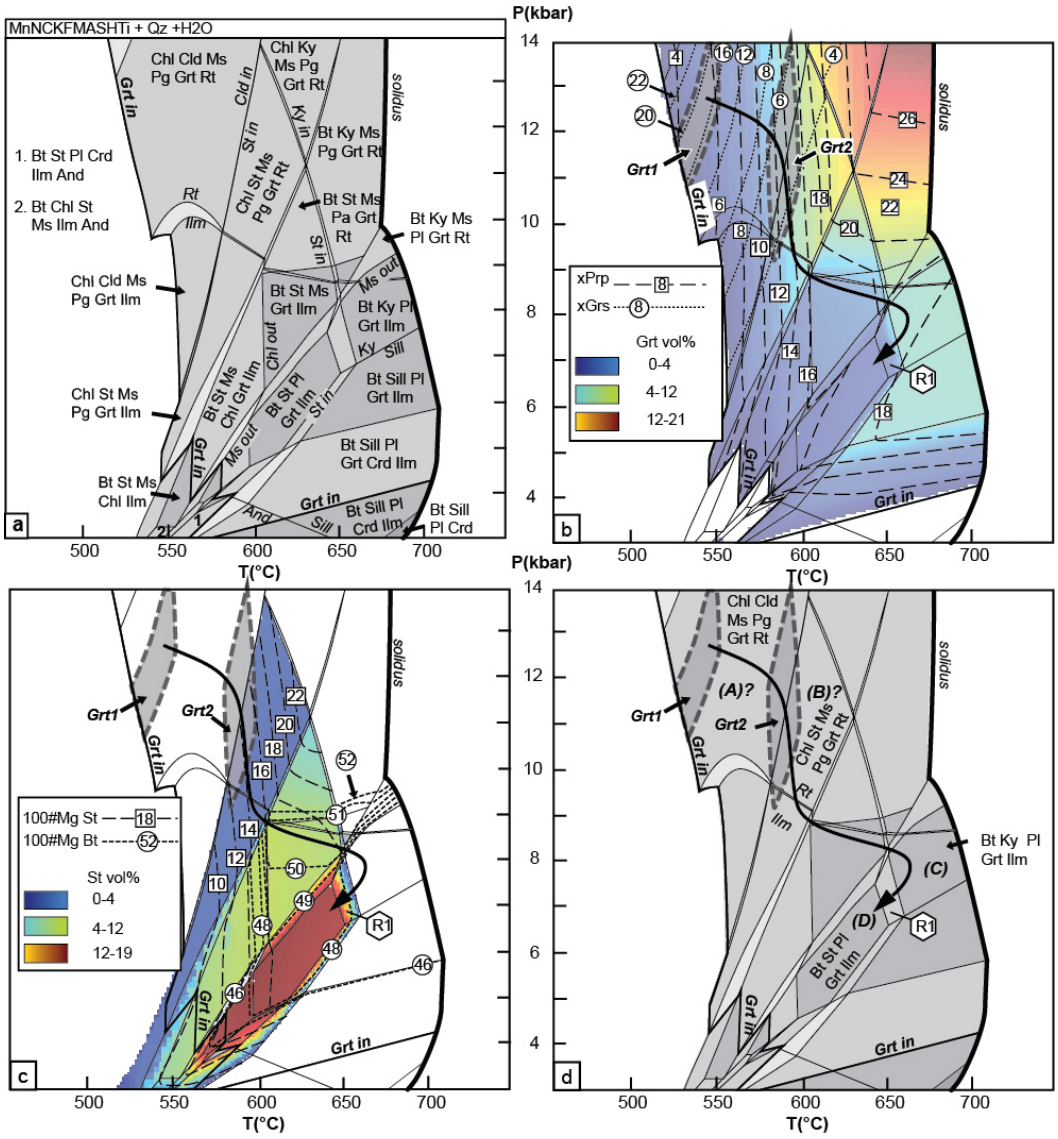

FIGURE 4.9: MnNCKFMASHTi P-T pseudosections illustrating phase equilbria for metagreywacke sample BN47. (**a**) Calculated stable assemblages. (**b**) Calculated garnet Prp and Grs content (black dashed lines, numbers in boxes and dotted lines, numbers in circles, respectively) and garnet mode. The shaded domain represents the P-T fields of garnet1 and garnet2 formation. (**c**) Calculated biotite and staurolite #Mg (dotted line, number in circles, and dashed line, number in boxes respectively) and staurolite modal proportion. (**d**) (A-D) and (R1) refer to metamorphic assemblages and reactions identified in the main text. A P-T path consistent with petrological relationships is drawn.

(B) and assemblage (C) Grt2 + Ky + Bt + Pl + Ilm + Qz ± Ms. Figure 4.9b shows that such an evolution first requires decompression without any temperature increase, down into the ilmenite stability field (in agreement with the observation of ilmenite in staurolite1), at P $<$ 9.5 kbar T$>$550 $^{\circ}$ C, followed by near isobaric heating to peak T of at least 650 $^{\circ}$ C at 8.0-9.0 kbar, in the amphibolite facies. Monazite is

interpreted to have crystallised close to peak temperature conditions. The rock then crossed reaction R1 and developed assemblage (D) : Grt2 + St2 + Bt + Pl + Ilm + Qz at 4.0-7.0 kbar, 600-650 ° C. The modal proportion of staurolite is expected to increase from 2-4 to 16-19 vol% between (B) and (D) (Fig. 4.9c), in agreement with observations. Results from P-T modelling reveal a clockwise P-T path for sample BN47. Garnet cores represent HP-LT metamorphic relics formed near to the transition between the blueschist facies and the epidote amphibolite sub-facies, along a cold ∼15 ° C/ km apparent geothermal gradient. Following near isothermal decompression and near isobaric heating, peak temperature was reached in the amphibolite-facies at conditions which reflect a moderate, ∼25 ° C/ km apparent geotherm.

Sample BN436 (Garnet–kyanite–gedrite granofels) Figure 4.10 presents results of P-T pseudosection construction. The coexistence of garnet in equilibrium with rutile and epidote (modelled here as zoisite in the absence of Fe^{3+}, Appendix 4.2.11.1) in assemblage (A) Grt1 + Chl1 + Ep + Rt1 + Qz, implies that the sample crossed the *Grt* in reaction at pressures above 7.0 kbar, ∼520 ° C (invariant point ***i***, Fig. 4.10b). The calculated assemblage Grt + Chl + Zo + Pg + Cld + Rt + Qz is the closest match to assemblage (A), but Cld was not observed, possibly due to complete consumption by prograde metamorphic reactions. The compositions of garnet1 and staurolite1 (Prp 17-20, Grs3-6 ; and #Mg< 0.10 respectively ; dark shaded areas in Fig. 4.10b) suggest that assemblage (B) : Grt1 + Chl1 + St1 + Pl1 + Pg1 + Ilm + Qz, formed at amphibolite-facies conditions of 4.0-6.5 kbar, 550-600 ° C. Petrological relationships and calculated isopleths therefore provide evidence for a prograde evolution from 7.0-8.0 kbar, ∼520 ° C to 4.0-6.5 kbar, 550-600 ° C.

Following the formation of assemblage (B), the rock crossed reaction (R1), out of the stability domain of ilmenite (light shaded area in Fig. 4.10b) into that of rutile. This requires a pressure increase above 7.0 kbar. The formation of plagioclase2 (An50) included in garnet outer cores (Fig. 4.10b) followed by that of the peak metamorphic assemblage (C) : Grt2 + Ged + Ky + Pl3 + Rt2 + Qz ± Bt (light shaded area, Fig. 4.10d) imply further burial and heating. Peak conditions of 6.5-8.5 kbar, 650-700 ° C in the upper-amphibolite facies are deduced from the comparison of calculated and measured compositions of garnet2, gedrite and plagioclase3 (Fig. 4.10c, d). The pseudosection provides a satisfactory explanation for the observed crystallisation sequence of Ti-phases : Rt1 > Ilm > Rt2. Monazite preserved in garnet porphyroblasts crystallised along the prograde path at T< 640 ° C, before the formation of assemblage (C). The absence of cordierite or sillimanite suggests that the rock underwent limited decompression during the retrograde metamorphic overprint. Cooling to <530 ° C is reflected by the crystallisation of minerals belonging to assemblage (D) Grt2 + Pg2 + Chl2 + St2 + Qz.

Sample BN436 records a complex metamorphic evolution. The early metamorphic assemblage (A) records lower-amphibolite-facies conditions that fit an apparent geotherm of ∼20 ° C/ km. The sample then followed a clockwise P-T path that includes a first decompression-heating segment between the stability fields of assemblages (A) and (B), followed by a second burial-heating segment into the field of assemblage (C). Peak P and T conditions are reached in the upper-amphibolite facies and correspond to a moderate to warm, ∼30 ° C/ km apparent geothermal

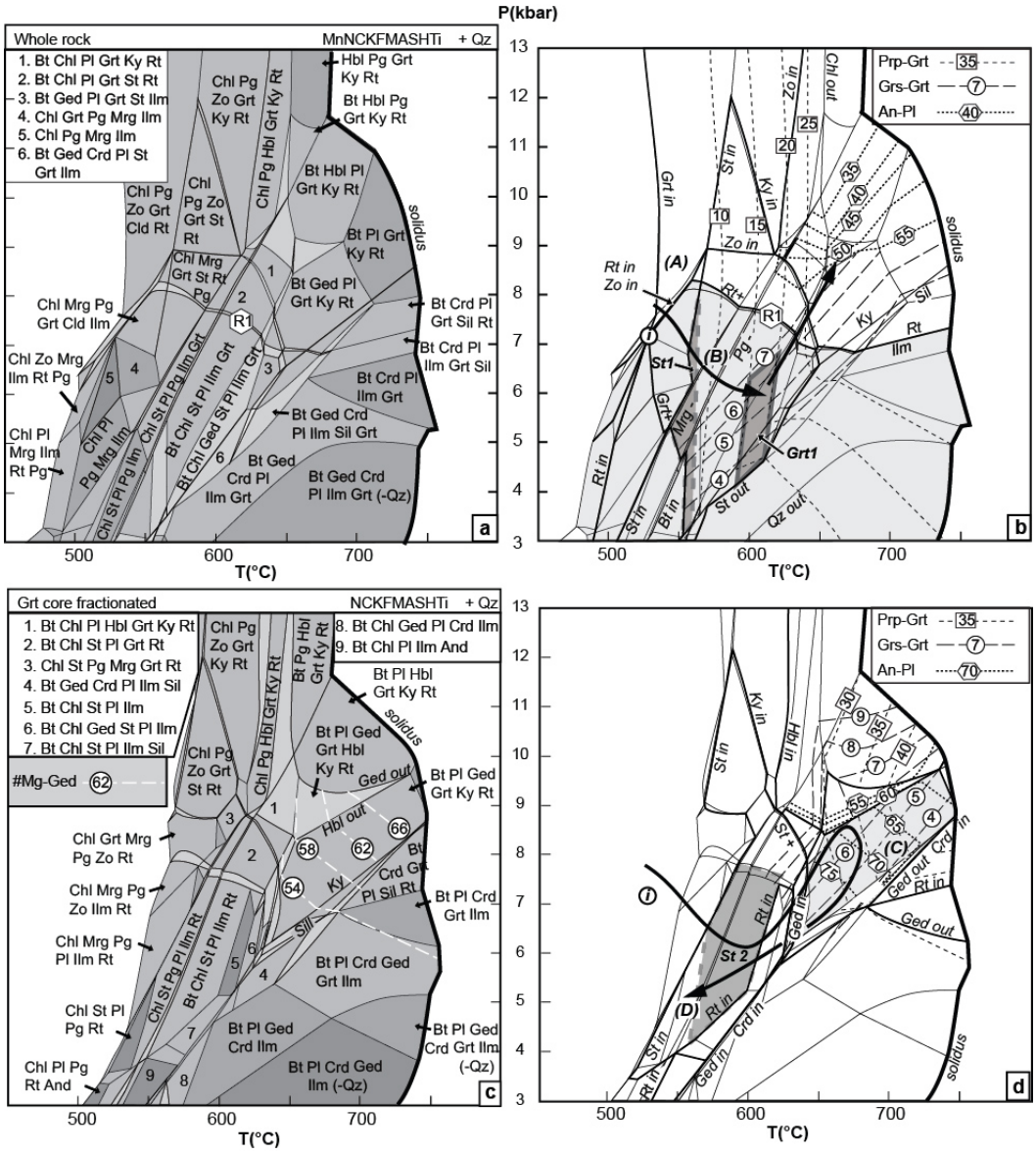

FIGURE 4.10: P-T pseudosections displaying phase equilibria for sample BN436. (**a-b**) : pseudosections showing metamorphic phase relationships suitable to determine the prograde metamorphic evolution of the sample in the MnNCKFMASHTi system. (**c-d**) pseudosections presenting phase relationships after garnet fractionation (Table 4.2, Appendix 4.2.11.1) in the NCKFMASHTi system, suitable for the peak and retrograde metamorphic evolution.

gradient. In the absence of post-peak decompression, a tight P-T loop is suggested.

Sample BN365 (migmatitic amphibolite gneiss) The P-T pseudosection for sample BN365 is built by using the whole rock composition. It reveals that assemblage (A) Grt + Hbl1 + Pl1 + Cpx + Rt + Qz + Bt + L is stable at >10.0 kbar, 700-800 ° C (Fig. 4.11a), at the transition between the amphibolite and the high-pressure granulite facies. Calculated compositions indicate that garnet grew

FIGURE 4.10: (**a**) Calculated stable assemblages. (**b**) Light shaded domain represents the ilmenite stability field. Dark shaded areas with dashed and full contours respectively show the conditions of staurolite1 and garnet1 formation. (**c**) Calculated stable assemblages. (**d**) Light shaded domain corresponding to the observed peak metamorphic assemblage. Dark shaded box with dashed contour shows formation conditions of staurolite2. Invariant point ***i*** represents a minimal P constraint for the coexistence of garnet with zoisite and rutile. Isopleths of garnet Prp and Grs content, and of plagioclase An content are shown, along with a possible P-T path consistent with observations. (A-D) and (R1) refer to metamorphic assemblages and reactions identified in the main text.

at 10.5-12.0 kbar, 720-750 ˚ C (Fig. 4.11b). These conditions overlap with the 10.0-11.0 kbar, 730-800 ˚ C conditions deduced from the compositions of clinopyroxene and plagioclase belonging to assemblage (B) (Fig. 4.11c). Increasing Ca/Na between hornblende1 to hornblende2 or 3 reveals decompression in the stability field of assemblage (B) and across reaction (R1) (Fig. 4.11b). The retrogression of rutile and ilmenite to titanite and the formation of assemblage (C) requires cooling in the amphibolite facies below 700 ˚ C at <9.0 kbar. Sample BN365 evolved along a clockwise P-T path. It records melting above 10.5 kbar, followed by a limited decompression to form metamorphic assemblage (B) at peak metamorphic temperatures of 730-800 ˚ C, at the transition between the high-pressure granulite- and amphibolite-facies, and finally records an amphibolite-facies overprint. Peak metamorphic conditions correspond to a moderate apparent geothermal gradient of 15-20 ˚ C/ km.

Sample BN534 (Garnet–kyanite-bearing migmatitic paragneiss) The pseudosection used to constrain the prograde and peak P-T conditions is identical to that used for sample BN43 (Fig. 4.8), which is built with the composition of an average paragneiss. Isopleths of retrograde biotite were calculated from a pseudosection using the sample whole-rock composition (Table 4.2). The stability field of assemblage (A) : Grt + Ky + Bt1 + Ms1 + Rt + Pl + Qz + L overlaps with the calculated conditions of garnet formation between 9.5-11.0 kbar, 680-730 ˚ C. This indicates the rock crossed the solidus at P> 9.5 kbar (Fig. 4.12a). The evolution from assemblage (A) to assemblage (B) : Grt + Ky + Bt1 + Pl + Qz + L requires heating to about 750 ˚ C and/or decompression, in agreement with measured garnet and biotite compositions (Fig. 4.12b). Calculated plagioclase compositions in assemblage (B) only partly match measured compositions, possibly due to local equilibria controlling plagioclase crystallisation from segregated melt in the leucosome. The crystallisation of retrograde sillimanite indicates that the rock crossed back below the solidus between 5.0 and 7.0 kbar. Assemblage (C) : Grt + Bt2 + St + Ms2 + Pl + Ilm + Qz formed at 4.0-7.0 kbar, below 650 ˚ C. Sample BN534 records a clockwise P-T path. It crossed over the solidus above 9.5kbar and reached peak conditions of 9.5-11.0kbar, 680-730 ˚ C, that fit a moderate apparent geothermal gradient of 15-20 ˚ C/ km, and that correspond to the transition between the amphibolite and high-P granulite facies. The rock then followed a decompression–cooling path back below the solidus and underwent a metamorphic overprint in the sub-solidus amphibolite facies.

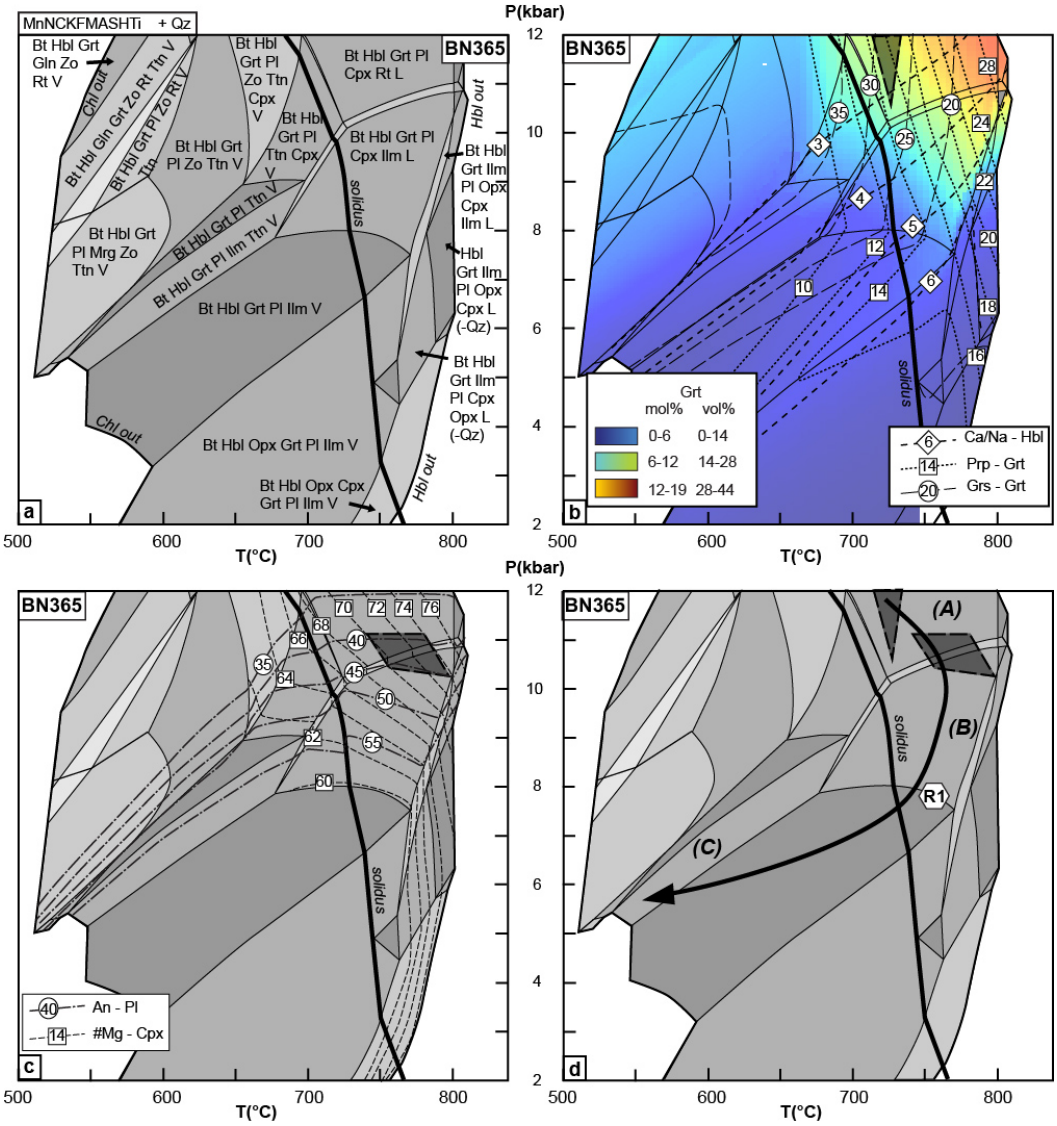

FIGURE 4.11: MnNCKFMASHTi P-T pseudosection illustrating phase equilbria for amphibolite sample BN365. (**a**) Calculated stable assemblages. (**b**) Calculated garnet Prp and Grs content, and Ca/Na ratio in hornblende (black dotted lines, numbers in boxes, dashed lines, numbers in circles, and bold dashed lines, numbers in diamonds respectively) and garnet mode. The shaded domain is defined by the intersection of calculated garnet isopleths fitting measured compositions. (**c**) Calculated plagioclase An composition and pyroxene #Mg (bold dashed and dotted line, numbers in circles ; and dashed line, numbers in boxes, respectively). The shaded domain represents the intersection of isopleths matching measured compositions. (**d**) (A-C) and (R1) refer to metamorphic assemblages identified in the main text. A P-T path consistent with observations is drawn.

Sample BN491 (Garnet–kyanite–staurolite-bearing paragneiss) The P-T pseudosection (Fig. 4.12c, d) for sample BN491 uses the whole rock composition (Table 4.1). Intersecting isopleths corresponding to measured garnet1 and garnet2

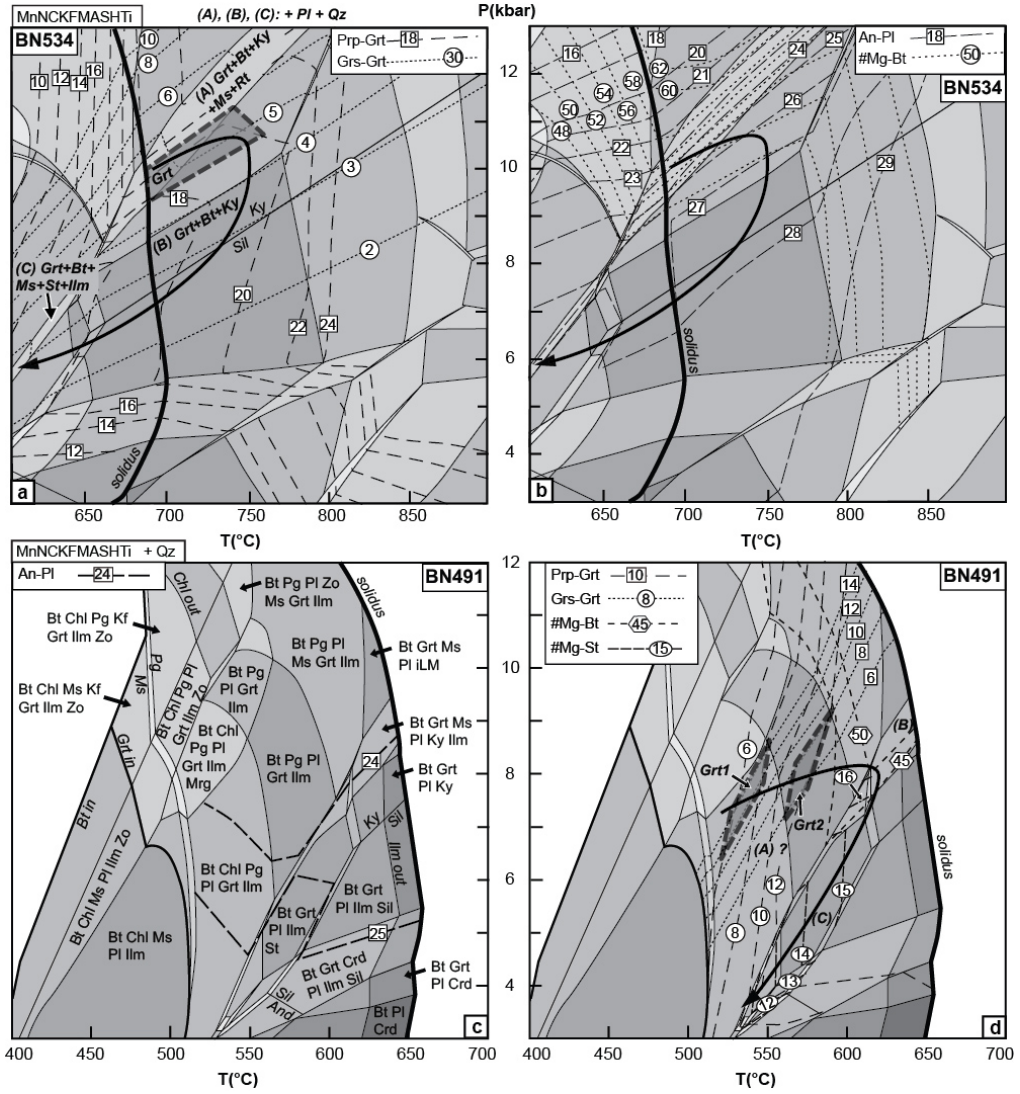

FIGURE 4.12: (**a, b**) MnNCKFMASHTi P-T pseudosection calculated using the average paragneiss composition (similar to Fig. 4.8) used to determine the metamorphic evolution of migmatite sample BN534. (**a**) Calculated garnet Prp and Grs content (black dashed lines, numbers in boxes and dotted lines, numbers in circles, respectively). The shaded area is defined by the intersection of isopleths matching measured compositions. (**b**) Calculated plagioclase An content (similar to Fig. 4.8, dashed lines, numbers in boxes), and biotite #Mg (using the whole rock composition of sample BN534, dotted lines, numbers in circles). (A-C) refer to assemblages identified in the text, and a possible P-T path is shown. (**c, d**) MnNCKFMASHTi P-T pseudosection illustrating phase equilbria for paragneiss sample BN491. (**c**) Calculated stable assemblage and plagioclase isopleths matching measured compositions. (**d**) Calculated garnet Prp (numbers in boxes) and Grs content (numbers in circles), along with the #Mg of biotite (numbers in diamonds) and staurolite (numbers in ellipses). (A-C) indicate the assemblages identified in the text, and a possible P-T path is shown.

compositions suggests a prograde evolution from 6.5-8.5 kbar, 520-550 ° C, to 7.0-9.0 kbar, 560-590 ° C (Fig. 4.12c). The crystallisation conditions of garnet1 correspond to the calculated stability field of assemblage Bt + Chl + Pg + Grt + Pl + Ilm + Qz. This assemblage is compared to the observed assemblage (A) Grt1 + Chl + Ilm + Qz. No other phases were found to be preserved as inclusions in garnet1. Assemblage (B) : Grt + Bt + Pl + Ky + Ms + Qz is predicted to form at 7.5-9.5 kbar, 610-650 ° C. Under these conditions, calculated plagioclase and biotite compositions show a good agreement with measured mineral compositions. The formation of assemblage (C) : Grt + St + Bt + Pl + Ilm + Qz, with staurolite #Mg varying from 16-18 to 8-10 from core to rim, requires that the rock follows a decompression-cooling path from about 7.0 kbar, 610 ° C to 4.0 kbar, 550 ° C (Fig. 4.12c). The P-T conditions determined from the successive assemblages describe a clockwise P-T path. Peak P and T conditions were reached synchronously in the amphibolite facies and match a ∼20 ° C/ km apparent geotherm.

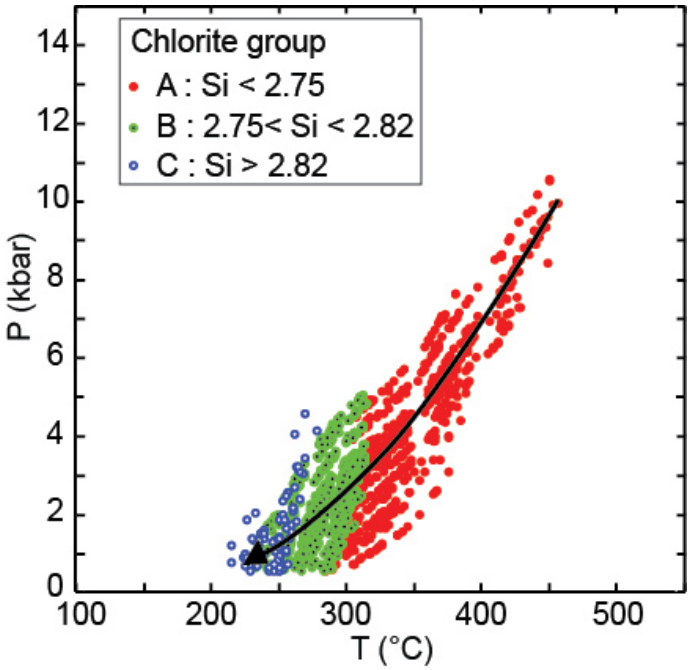

FIGURE 4.13: P-T diagram presenting the chemical composition of chlorite vs. P-T equilibrium conditions. The black arrow shows a P-T path consistent with multi-equilibria calculations. Each point on the P-T diagram represents equilibrium conditions for one chlorite composition, equilibrated with one white mica composition (Table 4) using the multi-equilibria method described in Appendix 4.2.11.1.

Sample BN185 (volcano-sedimentary rock) Table 4.5 shows compositions of white mica and chlorite pairs that formed together at equilibrium, and provides the corresponding equilibrium conditions determined by using the multi-equilibria calculation method presented in Appendix 4.2.11.2. Three compositionally different chlorite-phengite couples, equilibrated in different P-T ranges were identified. Low-Si (Si < 2.75 a.p.f.u) chlorite and low-K white mica (K < 0.80) equilibrated at

$> 300\,^{\circ}$C and up to 10 kbar (group A). Moderate-Si ($2.75 < Si < 2.82$) chlorite and moderate-K ($0.80 < 0.85$) white mica formed between 250 and $300\,^{\circ}$C, below 5 kbar (group B). High-Si ($Si > 2.82$) chlorite and high-K ($K > 0.85$) white mica equilibrated at $< 250\,^{\circ}$C, below 4 kbar (group C). They together define a near-continuous trend in P-T space from $\sim$ 10 kbar, $450\,^{\circ}$C, to 1 kbar, $220\,^{\circ}$C (Fig. 4.13). Peak metamorphic conditions correspond to an apperent geothermal gradient of$\sim 15\,^{\circ}$C/ km, at the transition between the greenschist and blueschist facies. The sample was then exhumed along a decompression-cooling path.

Sample BN246 (Micaschist) The overlap of P-T conditions obtained independently from the Chl-Qz-H_2O and Ph-Qz-H_2O equilibria provide conditions of possible equilibrium (Appendix 4.2.11.2). For sample BN246, they define an area in P-T space ranging from 310-380 $^{\circ}$C at 2.0 kbar to 420-480 $^{\circ}$C at 9.5 kbar. The results are presented in Figs. 4.15 and 4.16.

Pair	**1**		**2**		**3**		**4**		**5**		**6**		**7**		**8**		**9**		**10**		**11**		**12**	
Mineral	Chl	Wm	Chl	Wm	Chl	Wm	Chl	Wm	Chl	Wm	Chl	Wm	Chl	Wm	Chl	Wm	Chl	Wm	Chl	Wm	Chl	Wm	Chl	Wm
Si	2.85	3.33	2.86	3.36	2.81	3.26	2.78	3.21	2.77	3.24	2.77	3.31	2.75	3.30	2.74	3.21	2.73	3.30	2.71	3.25	2.69	3.21	2.68	3.25
Ti	0.01	-	0.03	-	0.01	0.01	-	0.01	-	0.01	0.01	0.01	0.00	0.01	-	0.01	-	0.01	-	-	0.02	0.01	-	-
Al^{IV}	1.15	0.67	1.14	0.64	1.19	0.74	1.22	0.79	1.23	0.76	1.23	0.69	1.25	0.70	1.26	0.79	1.27	0.70	1.29	0.75	1.31	0.79	1.32	0.75
Al^{VI}	1.37	1.67	1.32	1.65	1.35	1.68	1.35	1.59	1.30	1.65	1.27	1.66	1.34	1.67	1.34	1.60	1.34	1.67	1.42	1.63	1.35	1.60	1.40	1.63
Al	2.52	2.34	2.46	2.29	2.54	2.42	2.57	2.39	2.53	2.41	2.50	2.35	2.59	2.37	2.59	2.40	2.62	2.37	2.71	2.38	2.66	2.40	2.71	2.37
Fe^{2+}	2.42	0.14	2.36	0.13	2.25	0.15	2.32	0.25	2.37	0.18	2.37	0.17	2.34	0.18	2.36	0.26	2.34	0.18	2.34	0.23	2.32	0.26	2.36	0.24
Mn^{2+}	0.01	-	0.01	-	0.03	-	0.02	-	0.02	-	0.02	-	0.01	-	0.01	-	0.03	-	0.02	-	0.02	-	0.02	-
Mg	2.04	0.20	2.14	0.23	2.26	0.17	2.22	0.26	2.25	0.22	2.28	0.20	2.25	0.22	2.22	0.25	2.24	0.22	2.13	0.24	2.22	0.25	2.16	0.24
Na	-	0.01	-	0.02	-	0.03	-	0.01	-	0.01	-	0.02	-	0.04	-	0.04	-	0.04	-	0.04	-	0.04	-	0.01
Ca	0.01	-	0.01	-	0.01	0.01	-	-	0.01	-	-	-	-	-	-	-	-	-	0.01	0.00	-	-	-	-
K	0.01	0.90	0.01	0.89	-	0.89	-	0.88	-	0.86	-	0.85	-	0.79	-	0.81	-	0.79	-	0.84	-	0.81	-	0.82
Cr	-	0.01	0.01	0.01	0.01	0.02	-	0.02	-	0.03	0.01	0.02	0.01	-	0.01	0.02	0.01	-	0.01	0.01	0.01	0.02	0.01	0.03
X Am	0.17		0.16		0.22		0.25		0.25		0.24		0.26		0.13		0.30		0.32		0.32		0.34	
X Clin-Daph	0.71		0.74		0.69		0.69		0.71		0.73		0.69		0.34		0.66		0.61		0.64		0.61	
X Sud	0.12		0.11		0.09		0.07		0.04		0.03		0.05		0.02		0.04		0.07		0.04		0.04	
X Cel		0.26		0.29		0.22		0.13		0.16		0.21		0.16		0.08		0.16		0.14		0.08		0.11
X Ms		0.62		0.58		0.65		0.63		0.63		0.60		0.56		0.59		0.56		0.59		0.59		0.60
X Prl		0.09		0.08		0.06		0.10		0.11		0.12		0.16		0.14		0.16		0.12		0.14		0.16
Group	C	C	C	C	B	C	B	C	B	C	B	B	B	B	A	B	A	A	A	B	A	B	A	B
P (bar)	**915**		**1999**		**739**		**1136**		**2538**		**4195**		**4925**		**3357**		**6343**		**5789**		**8004**		**10636**	
T ($^\circ$C)	**222**		**228**		**243**		**266**		**287**		**294**		**310**		**311**		**354**		**381**		**423**		**449**	
dG (J)	1787.2		1867.9		1724.5		2247.4		1455.3		1342.3		1410.0		1621.5		1847.7		2262.2		2036.1		2266.0	

TABLE 4.5: Results of Quartz-Chlorite-Phengite-H_2O multi-equilibria calculations. Chemical compositions of representative white mica and chlorite mineral pairs which met equilibrium conditions are presented. Equilibrium is considered to be achieved for dG $<$ 2400 J (Appendix 4.2.11.2).

4.2.6.2 Geochronology

Sample BN43 (Garnet–kyanite-bearing migmatitic gneiss) A total of 22 U-Th-Pb LA-ICP-MS spot analyses were carried out on 12 monazite grains from sample BN43. This includes 8 analyses on 4 grains located in leucosomes, 9 analyses on 4 grains located in biotite selvedge, and 5 analyses on 3 grains enclosed in peritectic garnet (Tables 4.6 and 4.7). Some monazite grains are unzoned, while in other grains core zones have a slightly different luminescence (Fig. 4.14f). These patches were too small to be selectively targeted for ablation. Ten concordant analyses from grains in every textural setting yielded a U-Pb Concordia age of 2137.1±7.6 Ma ($MSWD_{C+E}$ = 0.25, $Probability_{C+E}$=0.99, C+E = concordance and equivalence ; Fig. 4.14a). This result is supported by 17 U-Th-Pb SHRIMP analyses performed on 10 monazite grains located in peritectic garnet2, in neosomes and in the matrix. Among them, 9 concordant analyses on 5 monazite grains situated in every textural setting provided an identical within errors Concordia age of 2141.2±6.4 Ma, ($MSWD_{C+E}$=1.3, $Prob._{C+E}$=0.19 ; Fig. 4.14b). However, three LA-ICP-MS spots performed on a single grain (grain n ° 1 ; table 4.6 ; Fig. 4.14a) reveal a significantly older imprecise upper intercept age of c. 2211±62 Ma (MSWD=0.65, Probability=0.42). The *ca.* 2140 Ma Concordia age is interpreted to date melting in sample BN43, during metamorphism at the amphibolite-granulite facies transition, prior to or during garnet2 growth. The *ca.* 2210 Ma age may reflect an inherited component in the volcano-sedimentary protolith of the rock.

Sample BN47 (Garnet–kyanite - staurolite schist) Seventeen U-Th-Pb LA-ICP-MS spot analyses were carried out on 4 unzoned monazite grains from sample BN47. Among them, 5 analyses were performed on a grain included in a staurolite porphyroblast, 9 on two grains elongated parallel to the metamorphic banding in the matrix (Fig. 4.14g), and 3 on a grain included in matrix biotite (Table 4.6). All LA-ICP-MS analyses but one yielded identical $^{207}Pb/^{206}Pb$ ages within errors of *ca.* 2130 Ma (weighted mean $^{207}Pb/^{206}Pb$ age = 2127±7 Ma ; MSWD=1.5, n=16), and eleven of them give a U-Pb Concordia age of 2127.0±7.4 Ma ($MSWD_{C+E}$=0.67, $Prob._{C+E}$=0.87 ; Fig. 4.14c). The Concordia age is identical to an upper intercept age of 2130.2±6.4 Ma (MSWD=1.3, Prob.=0.2) obtained by SHRIMP on 18 monazite grains (Fig. 4.14d) enclosed in kyanite porphyroblasts or found in the matrix. The *ca.* 2130 Ma age is interpreted to date the peak of the amphibolite-facies metamorphic overprint, which is reflected by assemblage (C) in sample BN47.

Sample BN436 (Garnet–kyanite–gedrite granofels) Twenty-one U-Th-Pb laser spot analyses were carried out on 11 monazite grains devoid of any chemical zoning and located in garnet porphyroblats of sample BN436. Eighteen of these analyses yielded a U-Pb Concordia age of 2131.0±6.4 Ma ($MSWD_{C+E}$ = 0.35, $Prob._{C+E}$=0.99, Fig. 4.14e). The presence of ilmenite inclusions in monazite suggests that monazite formed at the same time as assemblage (C) (Fig. 4.14h). This age is therefore interpreted to date prograde metamorphism in sample BN436.

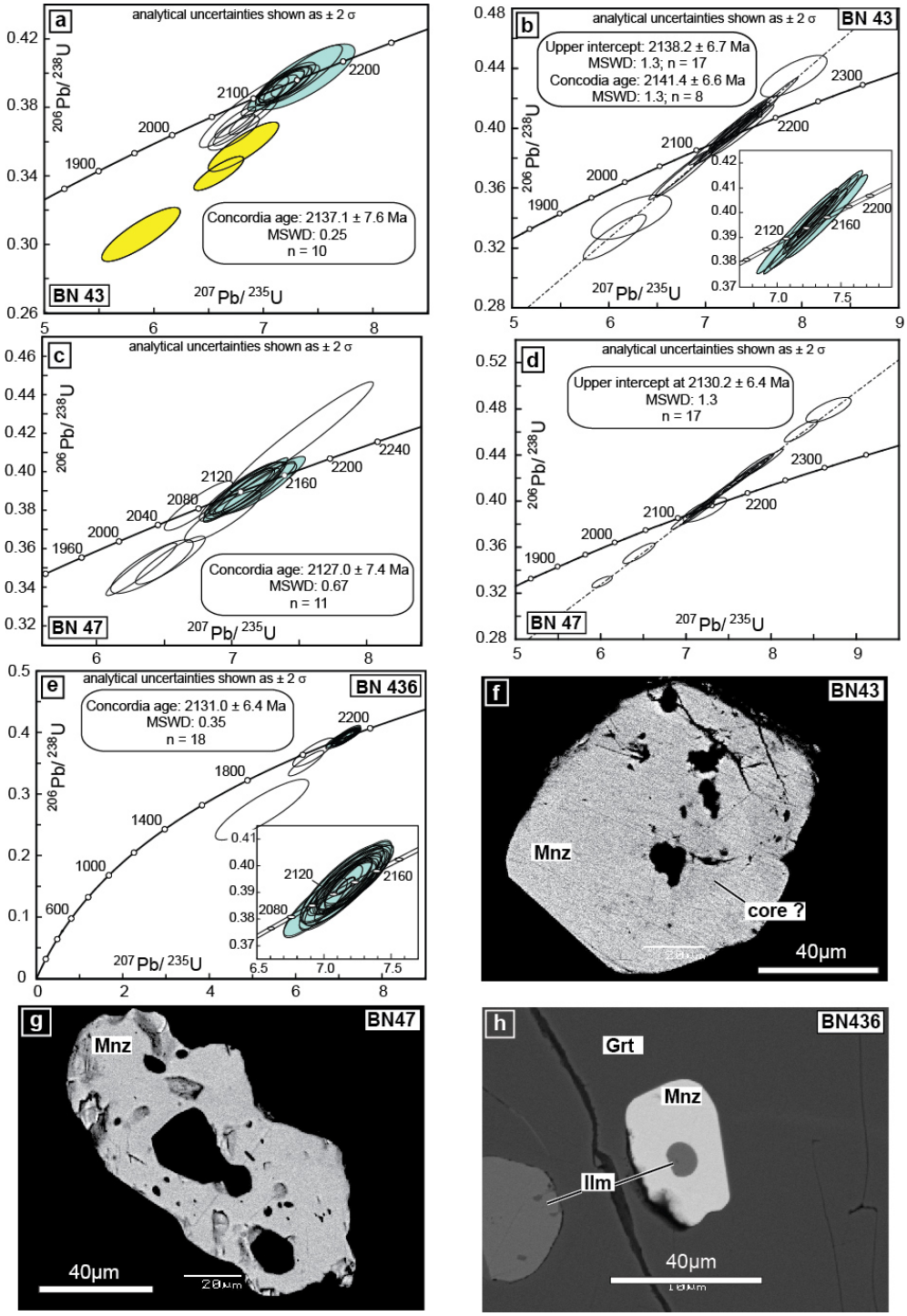

FIGURE 4.14: (**a-e**) : Results of U-Pb dating of monazite of samples BN43, BN47 and BN436, presented in Concordia diagrams. Errors include decay constant uncertainties.

FIGURE 4.14: (**b, d**) : Results of U-Pb dating by SHRIMP method. Shaded ellipses represent concordant analyses used for Concordia age calculation. Yellow ellipses in (**a**) show results of spot analyses from an inherited grain that yielded an older age. (**f-h**) : Back-scattered electron images. (**f**) Monazite grain in a neosome in sample BN43. It displays very slight luminescence variations between bright rims and a darker core zone. (**g**) Monazite grain devoid of zoning and containing quartz inclusions, elongated parallel to the fabric in the matrix of sample BN47. (**h**) Unzoned monazite grain included in garnet and containing an ilmenite inclusion in sample BN436.

4.2.7 Discussion

4.2.7.1 Metamorphic synthesis

Figure 4.15 presents a simplified spatial distribution of metamorphic facies, based on field mapping, along with P-T conditions and P-T paths of the studied samples. The variability of metamorphic conditions across the area are interpreted as documenting four distinct sets of conditions and P-T paths (Figs. 4.15 and 4.16).

1. An early metamorphic phase developed under a relatively cool (15 °C/ km) setting, close to the greenschist-blueschist facies boundary at 8.0-10.0 kbar and 400-500 °C (BN185 ; Fig. 4.15a) ; or (BN47 ; Fig. 4.15c) at 11.0-14.0 kbar, 520-560 °C at the transition between the blueschist facies and the epidote-amphibolite sub-facies.
2. Melting at the granulite-amphibolite facies transition is developed in the Bole Bulenga domain at 8.0-12.0 kbar, with peak temperatures of 700-800 °C reached close to the peak pressure (BN534, BN365 ; Fig. 4.15b,f), or following a period of isothermal decompression (BN43 ; Fig. 4.15d).
3. A regional scale amphibolite facies overprint in the Bole Bulenga and Abulembire domains of the older HP-LT relics and granulites. Coeval peak pressures and temperatures of 6.0-9.0 kbar and 550-680 °C were obtained under an apparent thermal gradient of 30 °C/ km (BN491 and BN436 ; Fig. 4.15e, h). This event followed an exhumation phase that is suggested by isothermal decompression paths in rocks metamorphosed at higher pressure (BN47 ; Fig. 4.15c).

   4. Greenschist facies developed in the Maluwe domain (BN246 ; Fig. 4.15g) reaching 2.0-9.5 kbar and 310-480 °C.

In high-grade metamorphic domains, the P-T paths of the samples merge at 5.0-8.0 kbar, 550-650 °C (Fig. 4.16), which corresponds to conditions of the amphibolite-facies metamorphic overprint. This evolution documents a change in the thermal regime of the crust. It may be interpreted as the result of thermal re-equilibration of the various high-grade units which were tectonically assembled in the lower crust (England and Thompson, 1984) along a ∼30 °C/ km apparent geotherm (Fig. 4.16). However, the amphibolite-facies regional metamorphic overprint is not documented in sample BN185. The overprint may have been spatially limited to the Bole-Bulenga and Abulembire domains, allowing the preservation of the early metamorphic evolution characterised by a cold apparent geotherm elsewhere. Alternatively, both cool and warm metamorphic settings may be coeval and represent distinct geodynamic

settings.

In any case, the metamorphic record of the Paleoproterozoic craton of north-western Ghana shows that low-grade and high-grade rocks are juxtaposed (Fig 4.15 and 4.16). The coexistence of diverse P-T paths and P-T conditions at regional scale implies that rock units forming the Eburnean crust witnessed evolutions in contrasting thermal environments before the final amalgamation and stabilisation of this part of the craton.

analysis	grain n°	location	U[b] (ppm)	Pb[b] (ppm)	$\frac{Th}{U}$[b]	$^{206}Pb^{c}$ (%)	$\frac{^{206}Pb}{^{238}U}$[d]	±2σ (%)	$\frac{^{207}Pb}{^{235}U}$[d]	±2σ (%)	$\frac{^{207}Pb}{^{206}Pb}$[d]	±2σ (%)	ρ[e]	$\frac{^{206}Pb}{^{238}U}$	±2σ (Ma)	$\frac{^{207}Pb}{^{235}U}$	±2σ (Ma)	$\frac{^{207}Pb}{^{206}Pb}$	±2σ (Ma)	conc.[f] (%)
sample BN47																				
a06	mnz1	matrix	7392	4100	1.49	b.d.l	0.35400	2.9	6.548	3.2	0.1342	1.4	0.89	1954	49	2052	29	2153	25	9
a07	mnz1		7430	4400	1.54	0.09	0.38980	3.2	7.07	3.6	0.1316	1.5	0.91	2122	59	2120	32 (Ma)	2119	26	100
a08	mnz1		7769	4800	1.71	0.04	0.39140	2.7	7.212	3.1	0.1336	1.4	0.88	2130	49	2138	28	2146	25	99
a09	mnz1	matrix	10224	5600	1.59	b.d.l.	0.34930	3.2	6.333	3.4	0.1315	1.1	0.95	1931	54	2023	30	2118	19	91
a10	mnz1		8445	5300	1.84	0.05	0.38880	2.8	7.082	3.2	0.1321	1.6	0.86	2117	50	2122	29	2126	29	100
a11	mnz2	in st	4994	4400	3.32	0.05	0.41810	5.6	7.518	5.8	0.1304	1.5	0.97	2252	107	2175	53	2104	26	107
a12	mnz2	in st	8531	6900	3.13	b.d.l	0.39150	2.9	7.2	3.1	0.1334	1.1	0.93	2130	52	2137	28	2143	20	99
a13	mnz2	in st	3554	3100	3.60	b.d.l	0.35070	3.3	6.412	3.9	0.1326	2.1	0.83	1938	55	2034	35	2133	38	91
a14	mnz2	in stn	7540	6400	3.52	0.02	0.37680	2.9	6.936	3.3	0.1335	1.6	0.88	2061	52	2103	30	2144	28	96
a15	mnz2	in st	5429	4900	3.99	0.18	0.39130	2.8	7.114	3.2	0.1318	1.5	0.88	2129	51	2126	29	2123	26	100
a16	mnz3	in matrix bt	7220	6700	4.13	0.03	0.39500	2.7	7.283	3.0	0.1337	1.3	0.91	2146	49	2147	27	2147	22	100
a17	mnz3	in matrix bt	6876	6400	4.31	0.10	0.38230	2.7	6.755	3.0	0.1281	1.3	0.90	2087	49	2080	27	2073	23	101
a18	mnz3	in matrix bt	6734	5700	3.66	0.07	0.39300	3.0	7.147	3.1	0.1319	0.9	0.96	2137	54	2130	28	2124	15	101
a19	mnz4	matrix	7490	6600	3.78	0.03	0.39070	2.9	7.063	3.1	0.1311	1.0	0.95	2126	53	2119	28	2113	17	101
a20	mnz4		7696	7100	4.12	0.05	0.39100	3.0	7.133	3.1	0.1323	1.0	0.95	2128	54	2128	28	2129	18	100
a22	mnz4	matrix	8009	7600	4.23	0.17	0.38740	2.9	7.055	3.1	0.1321	1.1	0.94	2111	52	2118	28	2126	18	99
a23	mnz4		7674	7000	4.10	0.05	0.38990	2.5	7.068	2.8	0.1315	1.1	0.92	2122	46	2120	25	2118	19	100
sample BN43																				
a08	mnz1	leucosome	4965	5500	6.24	0.02	0.35700	3.3	6.819	3.9	0.1385	2.0	0.86	1968	56	2088	35	2209	35	89
a09	mnz1	leucosome	6482	5800	4.73	0.01	0.34140	2.4	6.593	2.8	0.1401	1.5	0.84	1893	39	2058	25	2228	26	85
a10	mnz1	leucosome	5427	4800	4.59	0.03	0.30580	4.2	5.883	5.0	0.1395	2.6	0.85	1720	64	1959	44	2221	46	77
a11	mnz2	in bt selv.	2059	5800	20.25	0.04	0.39920	3.5	7.361	4.0	0.1338	1.9	0.88	2165	65	2156	36	2148	34	101
a12	mnz2	in bt selv.	5540	6500	6.67	0.01	0.37500	2.4	6.912	2.7	0.1337	1.2	0.90	2053	42	2100	24	2147	20	96
a13	mnz2	in bt selv.	1309	6100	34.97	0.13	0.36500	2.3	6.729	2.8	0.1337	1.7	0.79	2006	39	2076	25	2147	30	93
a14	mnz2	in bt selv.	2146	5200	18.03	b.d.	0.39320	2.2	7.186	2.6	0.1326	1.3	0.86	2137	41	2135	23	2132	23	100
a15	mnz3	in bt selv.	3467	3200	4.25	0.01	0.39460	2.4	7.216	3.0	0.1326	1.7	0.82	2144	44	2138	27	2133	30	101
a16	mnz4	in grt	1451	1700	6.16	0.02	0.39780	3.9	7.383	5.0	0.1346	3.1	0.79	2159	73	2159	46	2159	54	100
a17	mnz4	in grt	6722	7500	6.37	0.06	0.38410	1.9	6.987	2.2	0.1319	1.1	0.86	2095	34	2110	20	2124	20	99
a19	mnz5	leucosome	2849	3200	5.93	0.07	0.39150	2.2	7.151	2.6	0.1325	1.3	0.87	2130	40	2130	23	2131	23	100
a21	mnz6	in bt selv.	5627	6600	7.04	0.05	0.37130	2.0	6.743	2.3	0.1317	1.0	0.89	2036	35	2078	20	2121	18	96
a22	mnz6	in bt selv.	1580	4200	18.60	0.07	0.38840	2.2	7.085	2.6	0.1323	1.4	0.85	2115	40	2122	24	2129	24	99
a28	mnz7	in bt selv.	3767	6900	12.72	0.04	0.39210	1.9	7.168	2.3	0.1326	1.3	0.82	2133	35	2133	21	2133	23	100
a29	mnz7	in bt selv.	1700	3700	15.53	0.04	0.39550	1.9	7.292	2.5	0.1337	1.5	0.78	2148	35	2148	22	2147	27	100
a31	mnz8	in grt	5570	6900	7.96	0.02	0.36690	2.1	6.732	2.3	0.1331	1.1	0.89	2015	36	2077	21	2139	18	94
a32	mnz9	leucosome	3653	4000	6.31	b.d.	0.39480	2.7	7.253	3.4	0.1332	2.2	0.78	2145	49	2143	31	2141	38	100
a33	mnz9	leucosome	3379	3900	6.72	0.06	0.39480	2.1	7.24	2.5	0.133	1.5	0.82	2145	38	2141	23	2138	26	100
a34	mnz10	leucosome	1230	1300	5.65	0.17	0.39290	4.0	7.216	4.6	0.1332	2.2	0.87	2136	73	2138	42	2141	39	100
a38	mnz11	leucosome	3304	4000	6.79	0.06	0.39400	2.1	7.207	2.7	0.1327	1.8	0.76	2141	38	2137	25	2134	31	100
a39	mnz12	in grt	941	950	5.23	0.06	0.37730	4.5	6.824	4.9	0.1312	1.9	0.92	2064	80	2089	44	2114	34	98
a41	mnz12	in grt	2857	3400	7.18	0.04	0.39280	2.3	7.194	2.9	0.1328	1.8	0.79	2136	42	2136	26	2136	31	100
sample BN436		in grt																		
a44	mnz1		984	5600	41.63	0.02	0.39190	3.0	7.148	3.5	0.1323	1.9	0.84	2131	54	2130	32	2129	33	100
a49	mnz2		531	1200	15.01	b.d.l	0.27460	14.7	5.224	16.9	0.138	8.4	0.87	1564	207	1856	155	2202	146	71
a50	mnz3		2227	4400	13.44	0.03	0.39080	2.0	7.08	2.4	0.1314	1.3	0.83	2127	36	2122	22	2117	23	100
a51	mnz4		565	4700	64.15	b.d.l	0.39470	1.8	7.214	2.5	0.1325	1.6	0.75	2145	34	2138	22	2132	29	101
a52	mnz4		1030	4700	33.45	b.d.l	0.38420	2.4	6.936	2.8	0.1309	1.5	0.85	2096	43	2103	25	2111	26	99
a53	mnz4		716	5100	54.85	0.33	0.39100	2.8	7.14	3.2	0.1324	1.6	0.87	2127	51	2129	29	2131	28	100
a54	mnz5		745	4800	50.30	0.58	0.39180	2.0	7.166	2.5	0.1327	1.5	0.79	2131	36	2132	23	2133	27	100
a55	mnz5		745	4800	48.88	2.75	0.35000	4.8	6.244	5.4	0.1294	2.4	0.89	1935	81	2011	48	2089	42	93
a56	mnz5		648	4800	57.15	0.16	0.39240	2.2	7.183	2.5	0.1328	1.3	0.86	2134	39	2134	23	2135	22	100
a57	mnz5		684	4500	50.41	b.d.l	0.39240	2.2	7.124	2.7	0.1317	1.5	0.82	2134	40	2127	24	2120	27	101
a58	mnz5		1067	5200	37.07	b.d.l	0.39310	2.0	7.161	2.3	0.1321	1.1	0.89	2137	37	2132	21	2127	18	100
a59	mnz6		840	5000	44.35	0.11	0.39190	2.1	7.145	2.4	0.1322	1.3	0.85	2132	37	2130	22	2128	22	100
a60	mnz6		775	4200	41.68	0.01	0.39180	2.1	7.155	2.7	0.1325	1.6	0.79	2131	39	2131	24	2131	29	100
a61	mnz7		1021	3700	24.93	0.05	0.39240	3.5	7.16	3.9	0.1323	1.8	0.88	2134	63	2132	36	2129	32	100
a62	mnz7		1146	3100	18.80	b.d.	0.39220	2.8	7.2	3.1	0.1332	1.3	0.91	2133	51	2137	28	2140	23	100
a63	mnz8		980	1500	9.50	0.28	0.36770	5.2	6.416	6.1	0.1266	3.3	0.84	2018	90	2034	55	2051	59	98
a64	mnz9		1032	2600	18.41	b.d.l	0.39500	2.1	7.215	2.4	0.1325	1.2	0.87	2146	38	2138	22	2131	21	101
a65	mnz10		790	3000	26.46	b.d.l	0.39300	3.0	7.133	3.6	0.1316	1.9	0.85	2137	55	2128	32	2120	33	101
a66	mnz10		843	3300	28.02	b.d.l	0.39510	2.4	7.211	3.1	0.1324	2.0	0.76	2146	43	2138	28	2130	35	101
a67	mnz11		806	4600	41.54	0.11	0.39560	2.5	7.261	2.9	0.1331	1.5	0.86	2149	45	2144	26	2140	26	100
a68	mnz11		541	4600	62.79	0.06	0.39520	2.5	7.22	3.1	0.1325	1.9	0.80	2147	46	2139	28	2131	33	101

TABLE 4.6: U–Pb isotopic data obtained by LA–ICP(SF)–MS analyses at Goethe University Frankfurt, Germany.[a] Within run background-corrected mean 207Pb signal in cps (counts per second). [b] U and Pb content and Th/U ratio were calculated relative to GJ-1 reference zircon. [c] percentage of the common Pb on the ^{206}Pb. b.d.l. = below dectection limit. [d] corrected for background, within-run Pb/U fractionation (in case of $^{206}Pb/^{238}U$) and common Pb using Stacey and Kramers (1975) model Pb composition and subsequently normalised to GJ-1 (ID-TIMS value/measured value); $^{207}Pb/^{235}U$ calculated using $^{207}Pb/^{206}Pb/(^{238}U/^{206}Pb*1/137.88)$. [e] ρ is the $^{206}Pb/^{238}U/^{207}Pb/^{235}U$ error correlation coefficient. [f] degree of concordance = $^{206}Pb/^{238}U$ age / $^{207}Pb/^{206}Pb$ age x 100.

analysis	grain n°	location	U (ppm)	Th (ppm)	$\frac{Th}{U}$	$\frac{^{206}Pb^a}{^{238}U}$	$\pm 2\sigma$ (%)	$\frac{^{207}Pb^a}{^{235}U}$	$\pm 2\sigma$ (%)	$\frac{^{207}Pb^a}{^{206}Pb}$	$\pm 2\sigma$ (%)	ρ^b	$\frac{^{206}Pb^c}{^{238}U}$	$\pm 2\sigma$ (Ma)	$\frac{^{207}Pb}{^{235}U}$	$\pm 2\sigma$ (Ma)	$\frac{^{207}Pb}{^{206}Pb}$	$\pm 2\sigma$ (Ma)	conc.^{d} (%)
BN43																			
BN43D-4.1	4	leucosome	3429	22288	6.50	0.40	2.73	7.39	2.78	0.1334	0.52	0.98	2186	51	2159	25	2130	10	103
BN43D-5.1	5	bt selvedge	1750	28319	16.2	0.40	2.18	7.25	2.28	0.1331	0.67	0.95	2151	40	2142	20	2130	12	101
BN43D-6.1	6	leucosome	3350	11308	3.38	0.39	3.62	7.16	3.69	0.1325	0.74	0.98	2134	66	2131	32	2125	13	100
BN43D-6.2	6		4639	19138	4.13	0.40	2.82	7.33	2.85	0.1329	0.40	0.99	2169	52	2152	25	2132	7	102
BN43D-8A.1	8	leucosome	5299	23468	4.43	0.42	3.26	7.65	3.29	0.1337	0.41	0.99	2246	62	2191	29	2136	8	105
BN43D-8A.2	8	leucosome	7651	24518	3.20	0.43	2.61	7.92	3.56	0.1585	1.59	0.73	2326	51	2222	32	2124	42	110
BN43D-1.1	1		1666	26462	15.9	0.368	3.61	6.72	3.68	0.1333	0.67	0.98	2020	63	2076	32	2128	13	95
BN43D-1.2	1	elongated in matrix	1705	17983	10.5	0.340	3.58	6.24	5.43	0.1460	2.06	0.66	1887	59	2010	46	2135	71	88
BN43D-1.3	1		3327	17870	5.37	0.399	3.33	7.34	3.36	0.1334	0.46	0.99	2165	61	2154	30	2139	8	101
BN43D-10.1	10	bt selvedge	1255	39290	31.3	0.369	3.46	6.78	3.57	0.1336	0.86	0.97	2027	60	2083	31	2136	15	95
BN43D-22.1	22	bt selvedge	2679	11065	4.13	0.327	3.78	6.07	4.34	0.1383	1.60	0.87	1823	60	1986	37	2155	37	85
BN43D-26.1	26	matrix	1127	25646	22.8	0.398	3.47	7.39	3.57	0.1347	0.84	0.97	2162	64	2160	31	2154	15	100
BN43D-23.1	23	leucosome	3386	19158	5.66	0.402	3.33	7.34	3.37	0.1327	0.49	0.99	2178	62	2154	30	2127	9	102
BN43D-23.2	23	grt incl.	5193	21958	4.23	0.401	3.31	7.37	3.39	0.1333	0.74	0.98	2173	61	2157	30	2139	13	102
BN43D-23.3	23	grt incl.	2607	14741	5.66	0.393	3.38	7.25	3.46	0.1351	0.64	0.98	2139	62	2142	30	2142	13	100
BN43D-23.4	23	grt incl.	4025	16965	4.21	0.391	3.33	7.19	3.37	0.1339	0.48	0.99	2127	60	2135	30	2138	9	99
BN43D-11.1	11	bt selvedge	2324	27279	11.7	0.405	3.36	7.43	3.53	0.1336	1.06	0.95	2192	62	2164	31	2134	19	103
BN47																			
BN47-11.1	11	ky incl.	7568	29430	3.89	0.479	1.87	8.7	2.51	0.1337	0.84	0.75	2522	39	2304	23	2113	29	119
BN47-11.2	11	ky incl.	5358	27289	5.09	0.46	1.70	8.4	1.93	0.1329	0.86	0.88	2442	35	2270	17	2115	16	115
BN47-13.1	13	ky incl.	5225	19233	3.68	0.43	2.30	7.8	2.42	0.1321	0.74	0.95	2300	45	2208	22	2120	13	109
BN47-12.1	12	matrix	4399	21482	4.88	0.41	2.93	7.5	2.97	0.1320	0.44	0.99	2214	55	2167	26	2120	8	104
BN47-15.1	15	matrix	4923	24931	5.06	0.43	2.06	7.9	2.11	0.1340	0.42	0.97	2324	40	2224	19	2131	8	109
BN47-16.1	16	ky incl.	5479	20923	3.82	0.42	2.78	7.7	2.80	0.1325	0.38	0.99	2270	53	2197	25	2126	7	107
BN47-18.1	18	matrix	4969	22770	4.58	0.41	2.50	7.5	2.53	0.1325	0.40	0.99	2224	47	2175	22	2125	7	105
BN47-19.1	19	matrix	4635	22434	4.84	0.42	2.71	7.6	2.75	0.1326	0.42	0.99	2240	51	2182	24	2125	8	105
BN47-20.1	20	ky incl.	5733	27273	4.76	0.35	2.06	6.5	2.36	0.1369	0.71	0.87	1954	35	2040	21	2123	20	92
BN47-13.2	13	ky incl.	5036	20949	4.16	0.43	2.41	7.7	2.46	0.1330	0.44	0.98	2284	46	2202	22	2123	9	108
BN47-22.1	22	matrix bt	4603	22979	4.99	0.38	2.07	7.0	2.15	0.132	0.59	0.96	2098	37	2113	19	2124	10	99
BN47-24.1	24	matrix bt	3998	19788	4.95	0.389	2.13	7.1	2.16	0.133	0.38	0.98	2120	38	2130	19	2136	7	99
BN47-27.1	27	matrix bt	4504	21622	4.80	0.392	2.23	7.2	2.86	0.146	0.93	0.78	2132	40	2140	25	2143	31	99
BN47-29.1	29	matrix bt	4615	24236	5.25	0.392	1.49	7.2	1.53	0.132	0.38	0.97	2134	27	2133	14	2128	7	100
BN47-31.1	31	matrix	4976	26326	5.29	0.395	2.10	7.2	2.13	0.132	0.37	0.98	2147	38	2136	19	2121	7	101
BN47-26.1	26	matrix	2699	14999	5.56	0.329	1.18	6.0	1.60	0.135	0.96	0.74	1835	19	1979	14	2130	19	86
BN47-23.1	23	matrix	5589	28839	5.16	0.399	2.36	7.3	2.38	0.133	0.32	0.99	2164	43	2147	21	2127	6	102
BN47-28.1	28	matrix	6362	28692	4.51	0.396	1.55	7.2	1.59	0.132	0.31	0.98	2151	28	2139	14	2123	5	101

TABLE 4.7: U–Pb isotopic data obtained by SHRIMP II analyses at JLC, Perth, Australia.[a] Corrected for background. [b] ρ is the $^{206}Pb/^{238}U/^{207}Pb/^{235}U$ error correlation coefficient. [c] Common Pb corrected using measured ^{204}Pb. [d] degree of concordance = $^{206}Pb/^{238}U$ age / $^{207}Pb/^{206}Pb$ age x 100.

4.2.7.2 Regional evolution

Partial melting and metamorphism at the amphibolite-granulite facies transition or in the upper-amphibolite facies are recorded in gneisses of both the Abulembire and Bole-Bulenga domains, between 2145 and 2120 Ma. This suggests that they belonged to the same crustal slice at that time. It was not possible to date the early metamorphic phase that formed the HP-LT relics in a relatively cool (∼15 °C/km) environment. These rocks could have followed a continuous evolution from blueschist-facies to high-T amphibolite facies with increasing T and decreasing P during a single burial-exhumation cycle. Conversely, based on our data, we cannot exclude that HP-LT metamorphism and anatexis represent two diachronous events.

A crystallisation age of 2196±1 Ma was obtained from rhyolitic pyroclastites from the low-grade Maluwe domain by Duodu (2009). It is identical within errors to the crystallisation ages of orthogneisses intrusive the high-grade paragneisses of the Bole-Bulenga domain (De Kock et al., 2011). This constraint indicates that the rocks in both high-grade and low-grade domains formed prior to the orogenic cycle that generated high-grade metamorphism. We infer from this that the metamorphic breaks across the study area are the result of the tectonic juxtaposition of coeval units, which represent different slices of the same orogen. Furthermore, De Kock et al. (2011) obtained crystallisation ages of 2131±4 Ma from lapilli tuff interbedded with greywacke in the Maluwe domain, indicating synchronous volcanic activity and crustal anatexy. Consequently, we consider that the term "basin" is inadequate to qualify the Maluwe tectono-metamorphic domain, as there is no basin-basement relationship between the Maluwe and Bole-Bulenga rocks. The Maluwe domain rather represents a shallow crustal slice of the Eburnean orogen, which did not witness much burial. A similar conclusion could be drawn for the low-grade units of the Wa-Lawra belt, based on the maximal deposition ages of 2139±2 Ma obtained for volcano-sedimentary rocks located to the West of the Jirapa shear zone (Duodu, 2009). The 2145-2120 Ma age for high-grade, near-peak T metamorphism overlaps with the crystallisation age of intrusive TTGs and monzogranites in the Bole-Bulenga and Maluwe domains. The granitoids crystallised between 2120 and 2115 Ma are volumetrically significant (De Kock et al., 2011, 2009; Siegfried et al., 2009; Thomas et al., 2009), but no migmatites with similar metamorphic ages have been found. This suggests that partial melting possibly propagated in the lower crust after 2120 Ma, with the migmatite front migrating downwards from the current-day exposed surface.

Our results show that the study area displays different crustal levels, belonging to the same Paleoproterozoic orogenic crust, metamorphosed in a wide range of thermal environments ranging from the greenschist facies to the amphibolite-granulite facies transition, before being tectonically juxtaposed. These conclusions do not support the poly-cyclic orogenic model for this portion of the West African Craton. They are also at odds with the vast isobaric domains and high dT/dP thermal regimes reported from Precambrian accretionary belts (Percival and Skulski, 2000; Sandiford, 1989), which are considered to be typical of "hot" orogens (Cagnard et al., 2006; Gapais et al., 2009).

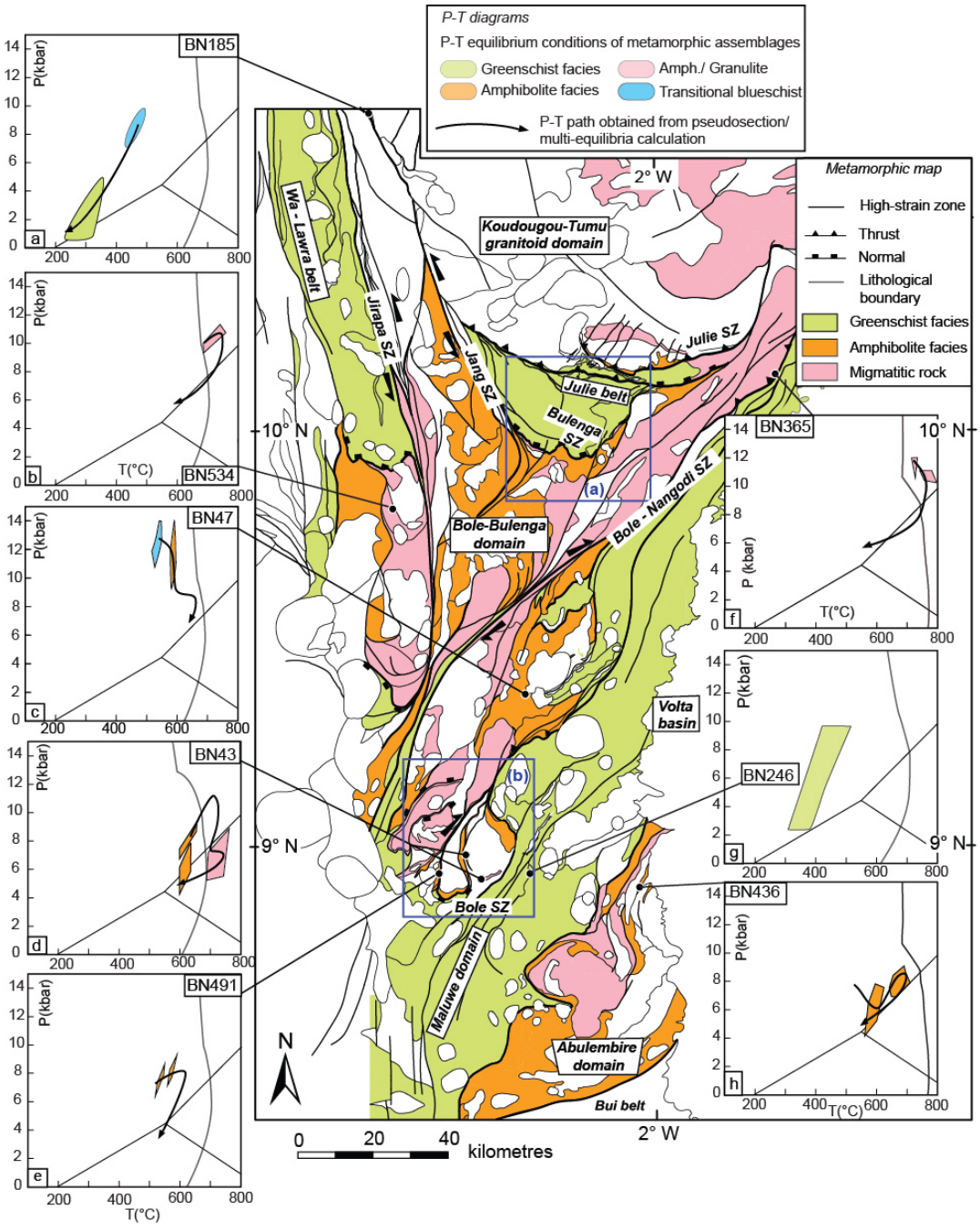

FIGURE 4.15: Metamorphic map of north-western Ghana showing the position of studied samples, the corresponding schematic P-T diagrams, and the spatial distribution of metamorphic facies. Blue boxes (a) and (b) refer to detailed maps in Fig. 4.17. Colored fields in P-T diagrams are deduced from P-T pseudosections or multi-equilibria calculations. They represent equilibrium conditions for the formation of specific minerals or assemblages which serve as constraints to P-T paths.

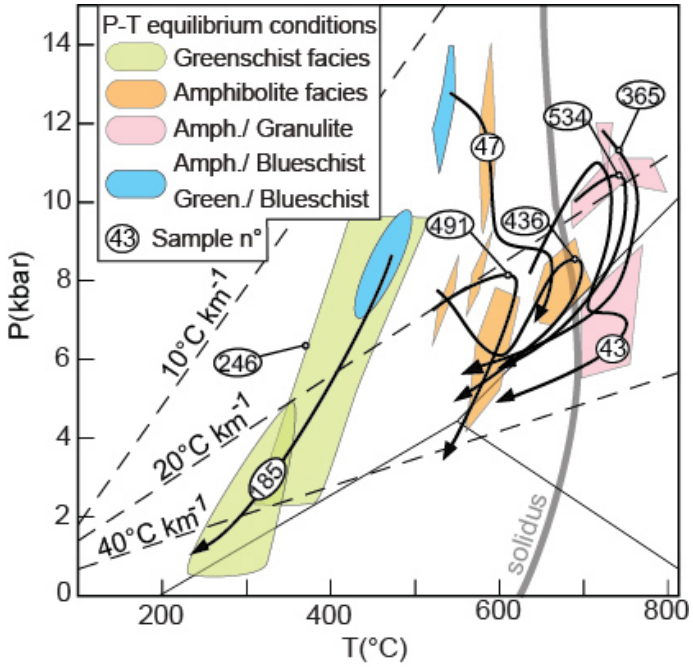

FIGURE 4.16: Synthesis of P-T conditions and P-T paths deduced from the investigated samples. Individual samples are labelled and are identified from Fig. 4.15. They reveal a wide range of metamorphic facies and apparent geothermal gradients.

4.2.7.3 Burial and exhumation

This study reveals that supracrustal rocks were buried in the lower crust, at up to 13.0 kbar, and along a ∼15 ° C/ km apparent geotherm. This pressure corresponds to a ∼45 km depth, which represents a minimum thickness for the crust at that time. In modern orogens, such thermal conditions are met in accretionary prisms and during the early stages of crustal thickening, before thermal relaxation of the thickened crust (e.g. Stöckhert and Gerya (2005); Yamato et al. (2007a)). Burial of rocks metamorphosed under these conditions is attributed to thrusting and crustal thickening, while exhumation is proposed to be driven by boundary tectonic forces and prism corner flow (e.g. Burov and Yamato (2008)). In north-western Ghana, early thrust zones (D1) brought in contact different metamorphic units and have some control on the present-day distribution of metamorphic grades (Fig. 4.15). We propose that D1 thrusting can account for the documented crustal thickening and burial of superficial rocks. Heterogeneous crustal thickening induced by thrusting is expected to cause localised uplift and erosion, which may significantly contribute to remove the overburden above lower-crustal rocks (e.g. England and Molnar (1990); Platt (1993). This is in agreement with the limited occurrence of syn-tectonic sedimentary basins containing immature polymictic sedimentary rocks, which suggests that erosion played a role in exhumation.

Following peak P conditions, clockwise P-T paths of the investigated high-grade metamorphic rocks frequently display alternating segments with a negative dP/dT, and segments of near-isothermal decompression. Increasing T during decompression requires a low exhumation rate relative to the thermal relaxation rate of the

thickened crust (England and Thompson, 1984). Contrastingly, near isothermal decompression reflects a deflection of isotherms towards the surface and rapid exhumation due to tectonically-driven removal of the overburden (e.g. DucheËĘne et al. (1997)). In modern orogenic belts, partially molten lower-crustal rocks are frequently exhumed in anatectic migmatite domes (Rey et al., 2001; Vanderhaeghe, 2009; Vanderhaeghe and Teyssier, 2001b; Whitney et al., 2004) where they record supra-solidus isothermal decompression (e.g. Rey et al. (2009)). These structures develop during the extensional gravitational collapse of overthickened orogens, and provide an efficient tectonic mechanism to remove the overburden on top of lower-crustal rocks.

In north-western Ghana, high-grade, partially molten rocks are bounded by the the Bole and Bulenga extensional shear zones (Fig. 4.17a, b). These structures are parallel to the trajectories of the early ubiquitous foliation S1 which, in the gneisses, carries high-grade mineral assemblages. The shear zones contain high strain rocks and form metamorphic breaks at the transition between migmatitic gneisses and low-grade metamorphic rocks (Fig. 4.17c). Such structures coeval with metamorphism localised deformation during N-S directed stretching (D2). They exhumed the lower crust against rock units metamorphosed at shallower depths. The P-T paths of samples BN43 and BN47 have segments which are consistent with tectonic exhumation during extension (Fig. 4.17d, highlighted segments). However, sample BN491 (Fig 4.17d), which is located across the Bole shear zone from samples BN43 and BN47, has a different P-T path. Peak pressure is followed by a decompression-cooling path. This suggests that exhumation dynamics may be variable. Extension is probably significant, but it is not the only process responsible for the exhumation of the lower crust.

The thrusts and the extensional shear zones are strongly overprinted by subsequent deformation (D3), consistent with east-west directed shortening (Fig. 4.17a, b). Pre-existent tectonic contacts, metamorphic gradients and isograds are folded and transposed into sub-vertical shear zones striking N to NE. Early fabrics (S1 and S2) are overprinted by a sub-vertical, penetrative schistose cleavage striking to the north (S3). Strong metamorphic gradients are observed across D3 shear zones and large (km-scale) folds. We argue that post-extension (D2) exhumation of high-grade rocks below 6 kbar occurred during D3, in a crust dominated by a compressional to transpressional deformation during E-W bulk shortening.

4.2.8 Implications for Precambrian accretionary orogens

The Paleoproterozoic craton of NW Ghana displays a close association of high-grade metamorphic domains, comprising rocks metamorphosed at the amphibolite-granulite facies transition, juxtaposed with coeval low-grade upper crustal slices. The variability of metamorphic conditions cannot be reconciled with a stable, steady-state, spatially and temporally homogeneous thermal regime. Furthermore, P-T paths displaying decompression at constant or increasing temperature cannot be interpreted as the result of homogeneous slow exhumation of vast units in a large and flat orogen (Gapais et al., 2009). The metamorphic record is more consistent with high exhumation rates, structurally-driven horizontal and vertical movements and differential exhumation in the crust, generating major lateral baric metamorphic gradients. Coupled metamorphic and structural data support the view that

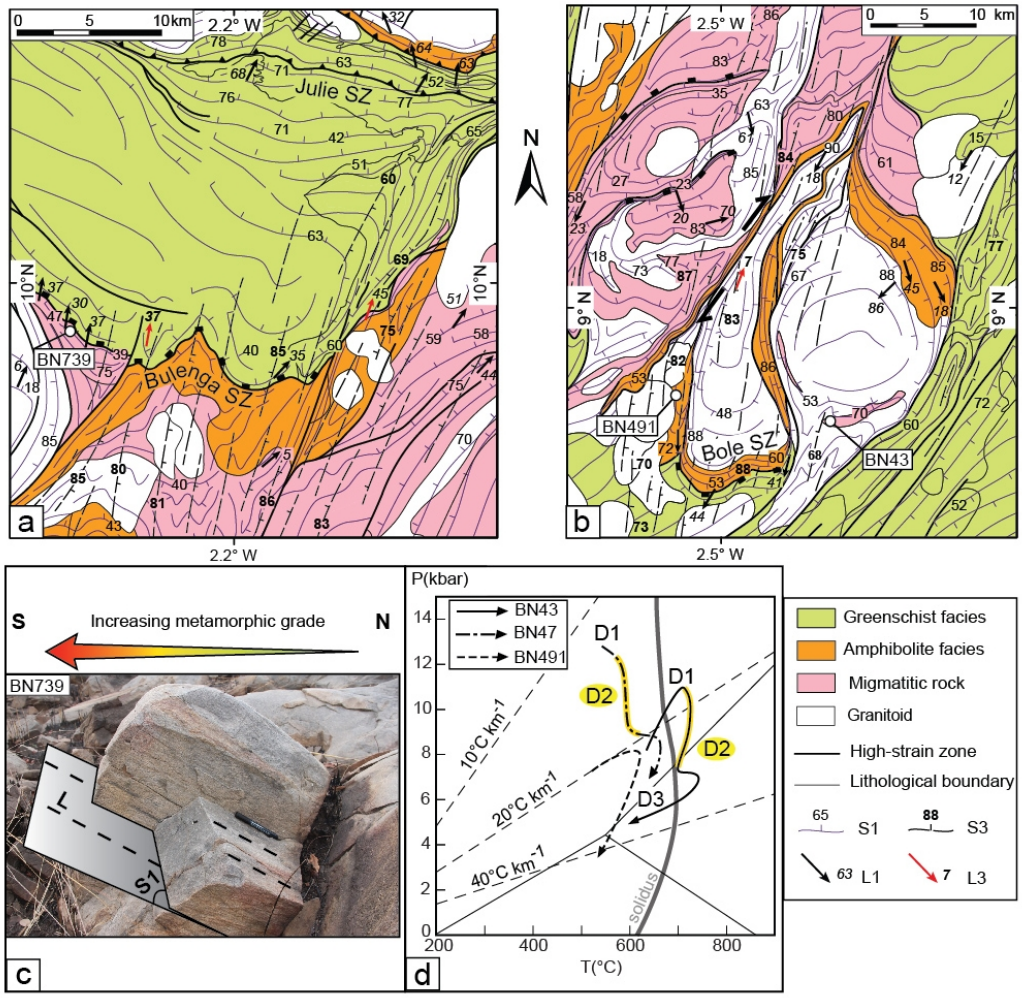

FIGURE 4.17: (**a, b**) Structural-metamorphic maps of the northern and southern terminations of the Bole-Bulenga domain, delimited by the Bulenga and Bole shear zones respectively (Fig. 12). Small spacing between S1 foliation trajectory lines illustrates high strain intensity. (**c**) Outcrop from the Bulenga extensional shear zone displaying a shallow-dipping high-strain fabric and down-dip mineral stretching lineations, plunging towards decreasing metamorphic grade. (**d**) P-T diagram illustrating various P-T paths obtained from rocks of the Bole-Bulenga domain. Segments attributed to exhumation during extensional deformation D2 are highlighted.

extensional detachments developed in a thickened, partially molten orogenic crust and contributed to the exhumation of high-grade rocks. Evidence for this crustal mechanical behaviour has not been reported from the Paleoproterozoic West African Craton so far, and evidence for extensional detachments are lacking in Precambrian accretionary orogens in general.

The coexistence of metamorphic terranes recording diverse geothermal gradients implies the existence of regional-scale heterogeneities in the thermal evolution of maturing crusts. Similar to modern orogens, the source of such thermo-mechanical

variations may lie in the large-scale architecture of the Eburnean orogen (Hyndman et al., 2005; Moresi et al., 2014), which remains an active research topic. The metamorphic diversity and heterogeneity of ancient orogens is increasingly recognised. Relics of high-P metamorphism are reported from the Minto Block, Canada, which was previously considered to be a very large and homogeneous high-T, low-P granulite province (Percival and Skulski, 2000). Eclogites - high-pressure granulites reported from various Paleoproterozoic orogenic belts (e.g. Anderson et al. (2012); Möller et al. (1995) reflect a broadening range of tectono-metamorphic environments at this period (Brown, 2007). Harley (1992) shows that the metamorphic record of Proterozoic granulites requires multiple geodynamic settings. It further demonstrates that significant variation in peak metamorphic pressure and in P-T paths are found within individual provinces. The complex metamorphic evolution of the Superior province has been interpreted as the result of the diachronous accretion of thermally heterogeneous crustal fragments (Easton, 2000). Similarly, the existence of non-unique settings for Archean crustal growth and craton-building has been proposed by various authors, based on structural-metamorphic constraints (e.g. in the Yilgarn craton, Goscombe et al. (2009)) or on geochemical and petrological arguments (e.g. Bédard et al. (2013); Moyen (2011). The secular change of the Earth's thermal regime is well documented by the metamorphic record. The coexistence of distinct thermal environments is proposed to reflect the onset of some kind of plate tectonics (Brown (2007, 2009)and references therein) during or after the Neoarchean. In this sense, we suggest that the metamorphic record of the West African Craton is representative of the geodynamic settings at work in a Paleoproterozoic "proto-plate tectonic regime".

4.2.9 Conclusion

We recognise contrasting metamorphic patterns from juxtaposed terranes in an interference zone between two craton-scale ductile shear zones, in the Paleoproterozoic West African craton, in NW Ghana. The range of metamorphic data illustrates heterogeneous thermal conditions in the juvenile crust at an early stage of its tectono-metamorphic evolution, prior to final accretion and thermal re-equilibration. Strong lateral metamorphic gradients are interpreted to result from the exhumation of the lower crust ; and from the tectonic assembly of distinct crustal slices, which underwent coeval evolutions at different depths. Extensional detachments localised deformation in a thickened, partially molten crust and contributed to the exhumation of high-grade rocks. The diversity of geothermal environments at the scale of the study area is consistent with the spatial variations in metamorphic conditions recorded across the southern West African Craton. The Paleoproterozoic craton in north-western Ghana provides an exceptionally clear window on the lower crust of the Eburnean orogen, and in this sense, it is key to the understanding of Eburnean geodynamics.

We interpret the metamorphic record of NW Ghana as being the product of a monocyclic orogenic evolution which brought in contact exhumed lower-crust with middle and upper crustal units. This view represents a working hypothesis which deserves testing in other regions of the West African Craton, in order to re-interpret the significance of metamorphism during the Eburnean orogeny. In any case, we emphasise that the "hot orogeny" model, proposed to account for homogeneous, near

isobaric metamorphic conditions across large domains recording low dP/dT apparent geothermal gradients, is not the only model for Paleoproterozoic accretionary orogens.

4.2.10 Acknowledgements

We gratefully acknowledge AMIRA International and the industry sponsors, including AusAid and the ARC Linkage Project LP110100667, for their support of the WAXI project (P934A). We acknowledge the facilities, and scientific and technical assistance of the Australian Microscopy & Microanalysis Research Facility at the Centre for Microscopy, Characterization & Analysis of UWA, a facility funded by the University, State and Commonwealth Governments. We thank Erwann Lebrun and the staff of the John De Laeter Centre for Isotope Research, hosted at Curtin University of Technology. Dominique Chardon is warmly thanked for sharing advice and constructive discussions which contributed to improve the quality of the manuscript. Allen Kennedy is thanked for providing expertise with regards to SHRIMP dating. We thank Philippe de Parseval and Sophie Gouy for their assistance for micro-analysis aquisition. We recognise the logistical support and datasets provided by the Geological Survey Department of Ghana, as well as the chauffeurs from the IRD in Ouagadougou (Salifou Yougbaré, Boukary Ouedraogo and Matthieu Kaboré) and from the GSD of Ghana (Kwasi Duah).

4.2.11 Appendix

4.2.11.1 Pseudosection calculation

Pseudosections were constructed using the Perple-X software (Connolly, 2005) updated in 2013 to version 6.6.8, and using the hp04 thermodynamic database of Holland and Powell (1998) updated in 2004. The solution models used for the pseudosection calculations are as follows : Bio(TCC) for biotite (Tajčmanová et al., 2009), Chl(HP) for chlorite (Holland et al., 1998), St(HP) for staurolite, Ctd(HP) for chloritoid (Holland and Powell, 1998), Amph(DPW) for hornblende (Dale et al., 2005), oAmph(DP) for gedrite (Diener et al., 2007), Gt(WPH) for garnet, Ilm(WPH) for ilmenite (White et al., 2000), hCrd for cordierite, Mica(CHA1) for titanium-bearing white mica (Auzanneau et al., 2010; Coggon and Holland, 2002), Mica(M) for white mica in the muscovite-paragonite-margarite system, Act(M) for actinolite (Massonne and Willner, 2008), melt(HP) (Holland et al., 1998; White et al., 2001), Pl(h) for plagioclase feldspar (Newton et al., 1980), Kf/San for low/highT potassic feldspar (Waldbaum and Thompson, 1969), Opx(HP) for orthopyroxene (Holland and Powell, 1998), Omph(GHP2) for clinopyroxene (Diener et al., 2007; Green et al., 2007). Pseudosections were built by using the whole rock composition obtained by XRF analysis for rocks displaying homogeneous mineralogy and modal compositions at sample scale. In the case of heterogeneous samples displaying large porphyroblasts or a compositional layering, whole rock compositions were recalculated based on average mineral compositions and modal proportions established by SEM mapping or image processing techniques. Ferric iron was approximated to 0 for all samples, based on results of T-XFe^{3+} pseudosections that failed to reproduce observed mineral assemblages for positive XFe^{3+} values. Ca concentration was

corrected for apatite and carbonates when they are present in significant amounts.

BN43 & BN534 Sample BN43 and BN534 are migmatites concerned by melt loss and open-system behaviour. Their metamorphic P-T evolutions were modelled by the complementary use of different pseudosections (Johnson et al., 2008; White and Powell, 2002). The prograde evolution was investigated by constructing a P-T pseudosection in the MnNCKFMASHTi system using the average of 21 whole rock chemical compositions of subsolidus metagreywacke samples from the study area obtained by XRF (e.g. Johnson and Brown (2004) ; Table 4.2). H_2O content was constrained so that saturation conditions were met on the wet solidus at 10 kbar, which corresponds to about 1.15 wt%. The peak and post-peak metamorphic evolutions were investigated by using pseudosections built with the whole rock composition of the migmatite sample. We suppose that the hand sample composition is valid to model phase relationships after hypothetical melt loss. Garnet core fractionation was ignored because it was found to have negligible effects, due to their minor modal proportion.

BN47 & BN491 P-T pseudosections were built in the MnNCKFMASHTi system. Because of the compositional layering inherited from the sedimentary protolith, large staurolite and kyanite porphyroblasts are distributed heterogeneously. The bulk rock chemistries used for modelling were recalculated to take into account local chemical heterogeneities, by evaluating modal compositions of a thin section. The isopleth intersect method was used to constrain the conditions of garnet growth, by comparing measured and calculated compositions. Chemically distinct cores represent small (max. 1 vol%) of the rock. Because of this low proportion, garnet fractionation was found to have insignificant effects.

BN436 Chemical fractionation due to large garnet porphyroblast growth was integrated to model the metamorphic evolution of sample BN436 (Evans, 2004; Marmo et al., 2002). A first pseudosection was built with the whole rock composition obtained by XRF to model prograde evolution in the MnNCKFMASHTi system. A second pseudosection, suitable to interpret peak and post-peak P-T conditions, was constructed in the NCKFMASHTi system by fractionating garnet core. Ferric iron content was set to 0 based on results of T-XFe^{3+} pseudosections : observed assemblages were successfully modelled for $XFe^{3+} = 0$. As a consequence, epidote group minerals are represented by zoisite (Zo) in the P-T pseudosections.

BN365 Leucosomes in sampe BN365 represent small volumes and are not connected, suggesting that the rock experienced limited melt loss. Consequently, the pseudosection was constructed using the whole rock composition of the sample and H2O was constrained to be saturated on the solidus at 10 kbar (i.e. 1.5 wt%).

4.2.11.2 Multi-equilibria calculations

Quartz-chlorite-phengite-H_2O thermobarometre Multi-equilibria calculations were performed with Matlabľ on the Chorite-Phengite-Quartz-H_2O assemblage, following a new procedure detailed in Ganne et al. (2012). Multi-equilibria calculations

were performed using the latest thermodynamic model for phengite (Dubacq et al., 2010), which takes into account the T-dependent interlayer water content of dioctahedral mica. Calculations were carried out using the thermodynamic data of five chlorite and six phengite end-members. These end-members are Fe amesite (FeAm : $Si_2Al_4(Fe)_4O_{10}(OH)_8$), Mg amesite (MgAm : $Si_2Al_4(Mg)_4O_{10}(OH)_8$), clinochlore (Clin : $Si_3Al_2Mg_5O_{10}(OH)_8$, daphnite (Daph : $Si_3Al_2Fe_5O_{10}(OH)_8$) and sudoite (Sud : $Si_3Al_4(Mg, Fe)_2O_{10}(OH)_8$) for chlorite ; and muscovite (Ms : $Si_3Al_3KO_{10}(OH)_2$), pyrophyllite (Prl : $Si_4Al_2O_{10}(OH)_2$), hydrated pyrophyllite (Prl.H : $Si_4Al_2O_{10}(OH)_2.H_2O$), Fe celadonite (FeCel : $Si_4Al(Fe)KO_{10}(OH)_2$), Mg celadonite (MgCel : $Si_4Al(Mg)KO_{10}(OH)_2$) and phlogopite (Phl : $Si_3AlMg_3KO_{10}(OH)_2$ for phengite. P-T equilibrium conditions, as well as the Fe^{3+} content in chlorite and phengite and the water content of phengite were calculated to minimize the sum of the Gibbs free energy $\Sigma\Delta G^2$ of the following seven independent reactions :

1. 1 Sud + 15 Qtz + 10 FeCel + 2 MgAm > 4 Prl + 10 MgCel + 2 Daph
2. 6 MgCel + 7 Qtz + 4 FeAm + 4 H2O > 6 FeCel + 3 Sud + 2 Daph
3. 5 MgAm + 4 Daph > 5 FeAm + 4 Clin
4. 14 Qtz + 5 FeAm + 3 MgAm + 8 H2O > 4 Daph + 6 Sud
5. 2 Sud + 4 Qtz + 4 Daph + 4 Ms > 2 Prl.H + 4 MgCel + 5 FeAm
6. 1 Prl + 1 H2O > 1 Prl.H
7. 11 Qtz + 2 Ms + 1 Phl + 2 H2O > 3 MgCel + 2 Prl

In theory, thermodynamic equilibrium is achieved if $\sqrt{(\Sigma\Delta G^2/nr)}$ is equal to 0 (nr = number of reactions considered). In practice, however, a deviation from 0 occurs because of analytical uncertainties. Equilibrium is considered to be achieved when $\sqrt{(\Sigma\Delta G^2/nr)} < 2400$ J. These values account for the analytical uncertainties and they were estimated after Monte Carlo simulations (Vidal et al., 2006).

Quartz-chlorite-H_2O and quartz-phengite-H_2O thermometres Multi-equilibria calculations were performed using the Chorite-Quartz-H_2O assemblage and assuming a water activity equal to unity. It was performed with Matlabl using a script built by Vincent de Andrade and the thermodynamic data of five chlorite end-members (Vidal et al., 2001) : Fe amesite (FeAm : $Si_2Al_4(Fe)_4O_{10}(OH)_8$), Mg amesite (MgAm : $Si_2Al_4(Mg)_4O_{10}(OH)_8$), clinochlore (Clin : $Si_3Al_2Mg_5O_{10}(OH)_8$), daphnite (Daph : $Si_3Al_2Fe_5O_{10}(OH)_8$ and sudoite (Sud : $Si_3Al_4(Mg,Fe)_2O_{10}(OH)_8$). With these end members, four independent equilibria are considered.

1. 2 Clin + 3 Sud > 4 MgAm + 7 Qtz + 4 $H_2$2O
2. 4 Clin + 5 FeAm > 4 Daph + 5 MgAm
3. 16 Daph + 15 Sud >20 FeAm + 6 Clin + 35 Qtz + 20 H_2O
4. 4 Daph + 6 Sud >5 FeAm + 3 MgAm + 14 Qtz + 8 H_2O

A minimum amount of Fe^{3+} in chlorite was estimated using the stoichiometric criteria given in Vidal et al. (2005), and Fe^{3+} content was iteratively modified to minimize $\Sigma\Delta G^2$ (Vidal et al., 2006). Parra et al. (2002) calibrated a model for the phengite-quartz equilibrium, calculated from activities of chosen end-members, taking into account the non-ideal term of activity coefficients.Dubacq et al. (2010)

extended this model to smectite, illite, interlayered smectite-illite and mica by considering the T-hydration relationship, pressure and the rock composition, using multi-equilibrium thermobarometry.

The model involves nine end-members : Muscovite (Ms : $Si_3Al_3KO_{10}(OH)_2$), Paragonite (Pg : $Na(Al_2)(Si_3Al)O_{10}(OH)_2$), Mg-celadonite (MgCel : $Si_4Al(Mg)KO_{10}(OH)_2$), Fe-celadonite (Fe-Cel : $Si_4Al(Mg)KO_{10}(OH)_2$), Phlogopite (Phl : $Si_3AlMg_3KO_{10}(OH)_2$), Annite (Ann : $K(Fe_3)(Si_2Al)O_{10}(OH)_2$), Pyrophyllite (Prl : $Si_4Al_2O_{10}(OH)_2$), hydrated Pyrophyllite (Prl.H_2O : $Si_4Al_2O_{10}(OH)_2.H_2O$) and Margarite (Mrg : $CaAl_2(Al_2Si_2)O_{10}(OH)_2$). Three independent equilibria - and their hydrated derivatives - can be written for the Phg-Qtz-water assemblage.

1. 3 MgCel.mH_2O + 2 Prl.(m+1)H_2O >2 Musc.mH_2O + Phl.mH_2O + 11Qtz + (2m+4)H_2O
2. 3 FeCel.mH_2O + 2 Prl.(m+1)H_2O > 2 Musc.mH_2O + Ann.mH_2O + 11Qz + (2m+4)H_2O
3. Prl.(m+1)H_2Onw > Prl.(m'+1)H_2O_{nw} + (m-m')H_2O

where (m+1) and (m'+1) are the maximum and minimum amount of water, with m and m' varying from 0 to 6 and 0 to 3 according to the water layers content (noted nw). Fe^{3+} is not taken into account by the model. The hydration state is modified iteratively to minimize $\Sigma\Delta G^2$. Calculations are carried out with Matlabl software using a script build by Benoit Dubacq. The Quartz-Chlorite-Phengite-H2O thermobarometre provided satisfactory results for sample BN185. 646 Œ 441 Ph/Chl microprobe point analyses were first filtered on the basis of the compositional criteria (Vidal and Parra, 2000). Calculations of P-T equilibrium conditions eventually involved 198 x 162 Ph/Chl analyses. Calculations for samples BN246 failed to fulfill strict equilibrium criteria by using the Quartz-Chlorite-Phengite-H_2O thermobarometre. P-T conditions were investigated independently by coupling the Quartz-Chlorite-H_2O and Quartz-Phengite-H_2O thermometres. Multi-equilibria calculations involved 19 chlorite analyses and 47 phengite analyses for sample BN246.

Analysis	SiO_2	TiO_2	Al_2O_3	FeO	MnO	MgO	CaO	Na2O	K_2O	Cr_2O_3	Total	Si	Al^{IV}	Al^{VI}	Al	Ti	Fe^{2+}	Mn^{2+}	Mg	Ca	Na	K	Cr
BN185	**Chlorite**																						
BN-185-C1-G1_1_4	37.6	0.08	25.4	18.2	0.00	4.26	0.14	0.09	4.87	0.00	90.7	7.25	0.75	5.03	5.78	0.01	2.93	0.00	1.23	0.03	0.04	1.20	0.00
BN-185-C1-G1_1_5	25.9	0.05	21.5	25.7	0.19	12.8	0.10	0.00	0.44	0.04	86.8	5.54	2.46	2.96	5.42	0.01	4.59	0.03	4.06	0.02	0.00	0.12	0.01
BN-185-C1-G1_10_3	38.6	0.13	25.2	12.8	0.12	7.36	0.07	0.06	5.83	0.00	90.2	7.32	0.68	4.95	5.63	0.02	2.04	0.02	2.08	0.01	0.02	1.41	0.00
BN-185-C1-G1_10_4	33.0	0.15	23.4	18.6	0.19	11.1	0.04	0.01	3.11	0.04	89.7	6.51	1.49	3.95	5.44	0.02	3.06	0.03	3.27	0.01	0.00	0.78	0.01
BN-185-C1-G1_12_1	31.3	0.00	18.6	8.4	0.12	2.76	16.87	0.20	5.50	0.02	83.8	6.82	1.18	3.59	4.77	0.00	1.54	0.02	0.90	3.94	0.08	1.53	0.00
BN-185-C1-G1_13_4	36.2	0.27	23.2	2.3	0.00	1.91	11.97	0.12	7.65	0.13	83.7	7.42	0.58	5.02	5.60	0.04	0.39	0.00	0.59	2.63	0.05	2.00	0.02
BN-185-C1-G1_15_5	27.9	0.02	20.4	24.4	0.28	13.5	0.15	0.09	0.32	0.07	87.0	5.86	2.14	2.92	5.06	0.00	4.29	0.05	4.23	0.03	0.04	0.09	0.01
BN-185-C1-G1_17_2	35.9	0.08	14.2	1.6	0.00	0.82	19.68	4.39	2.06	0.00	78.8	7.96	0.04	3.68	3.71	0.01	0.30	0.00	0.27	4.67	1.89	0.58	0.00
BN-185-C1-G1_18_3	33.8	0.13	25.1	18.9	0.15	8.71	0.10	0.00	3.64	0.08	90.6	6.59	1.41	4.36	5.78	0.02	3.08	0.02	2.53	0.02	0.00	0.90	0.01
BN-185-C1-G1_2_4	33.6	0.00	25.2	19.3	0.12	8.53	0.07	0.00	3.86	0.11	90.9	6.56	1.44	4.36	5.80	0.00	3.15	0.02	2.48	0.02	0.00	0.96	0.02
BN-185-C1-G1_2_5	26.7	0.27	15.6	1.6	0.00	0.85	29.22	0.13	6.08	0.04	80.5	6.26	1.74	2.58	4.32	0.05	0.31	0.00	0.30	7.35	0.06	1.82	0.01
BN-185-C1-G1_20_4	35.6	0.24	22.1	2.0	0.00	1.37	13.49	0.70	7.38	0.08	82.9	7.43	0.57	4.85	5.42	0.04	0.35	0.00	0.43	3.01	0.28	1.96	0.01
BN-185-C1-G1_22_4	30.2	0.08	13.0	1.3	0.00	0.67	26.52	2.40	3.52	0.00	77.7	7.14	0.86	2.75	3.61	0.01	0.25	0.00	0.24	6.71	1.10	1.06	0.00
BN-185-C1-G1_26_1	40.0	0.25	25.7	10.1	0.01	8.37	0.04	0.10	6.35	0.05	91.0	7.41	0.59	5.03	5.62	0.04	1.57	0.00	2.31	0.01	0.04	1.50	0.01
BN-185-C1-G1_27_3	38.8	0.23	26.0	7.4	0.04	3.21	0.11	0.12	7.31	0.00	83.1	7.77	0.23	5.91	6.13	0.03	1.23	0.01	0.96	0.02	0.05	1.87	0.00
BN-185-C1-G1_28_1	29.1	0.15	20.7	20.0	0.08	11.3	0.07	0.00	2.60	0.00	84.1	6.24	1.76	3.48	5.24	0.02	3.60	0.01	3.62	0.02	0.00	0.71	0.00
BN-185-C1-G1_28_2	36.5	0.17	23.4	19.5	0.11	9.57	0.06	0.00	3.13	0.00	92.5	6.93	1.07	4.18	5.25	0.02	3.10	0.02	2.71	0.01	0.00	0.76	0.00
BN-185-C1-G1_29_3	27.1	0.02	22.4	24.2	0.20	12.2	0.00	0.00	0.68	0.07	86.8	5.71	2.29	3.27	5.57	0.00	4.26	0.04	3.83	0.00	0.00	0.18	0.01
BN-185-C1-G1_29_5	25.6	0.00	21.3	25.8	0.26	13.4	0.04	0.00	0.19	0.00	86.6	5.48	2.52	2.85	5.37	0.00	4.63	0.05	4.28	0.01	0.00	0.05	0.00
BN-185-C1-G1_5_1	38.2	0.00	22.0	19.0	0.19	8.83	0.08	2.95	1.41	0.06	92.8	7.20	0.80	4.10	4.90	0.00	3.00	0.03	2.48	0.02	1.08	0.34	0.01
BN-185-C1-G1_6_3	38.5	0.17	26.1	11.4	0.12	4.80	0.10	0.08	5.67	0.02	86.9	7.48	0.52	5.47	5.99	0.02	1.85	0.02	1.39	0.02	0.03	1.41	0.00
BN-185-C1-G1_7_3	37.5	0.12	25.1	14.9	0.09	8.46	0.24	0.00	5.45	0.02	91.9	7.07	0.93	4.65	5.59	0.02	2.35	0.01	2.38	0.05	0.00	1.31	0.00
BN-185-C1-G1_8_5	30.1	0.05	23.0	23.8	0.21	13.1	0.08	0.00	1.32	0.02	91.6	5.96	2.04	3.31	5.36	0.01	3.94	0.04	3.88	0.02	0.00	0.33	0.00
BN-185-C2-G2_1_2	25.9	0.08	20.1	26.1	0.14	14.0	0.10	0.00	0.02	0.14	86.5	5.55	2.45	2.63	5.08	0.01	4.69	0.03	4.47	0.02	0.00	0.01	0.02
BN-185-C2-G2_11_1	26.0	0.12	21.1	26.5	0.22	14.1	0.06	0.00	0.00	0.16	88.3	5.46	2.54	2.70	5.24	0.02	4.67	0.04	4.41	0.01	0.00	0.00	0.03
BN-185-C2-G2_11_2	36.9	0.30	25.3	15.3	0.11	7.72	0.20	0.00	4.83	0.04	90.7	7.04	0.96	4.73	5.69	0.04	2.44	0.02	2.20	0.04	0.00	1.18	0.01
BN-185-C2-G2_11_3	25.7	0.00	19.9	26.3	0.22	14.0	0.07	0.00	0.01	0.04	86.3	5.55	2.45	2.61	5.06	0.00	4.74	0.04	4.51	0.02	0.00	0.00	0.01
BN-185-C2-G2_14_3	25.7	0.03	20.4	26.6	0.24	13.9	0.07	0.00	0.01	0.17	87.1	5.49	2.51	2.64	5.15	0.00	4.76	0.04	4.42	0.02	0.00	0.00	0.03
BN-185-C2-G2_16_2	26.2	0.10	19.3	25.6	0.32	14.6	0.02	0.00	0.00	0.25	86.4	5.62	2.38	2.51	4.89	0.02	4.59	0.06	4.68	0.00	0.00	0.00	0.04
BN-185-C2-G2_17_2	26.5	0.09	19.9	25.8	0.14	14.6	0.00	0.00	0.01	0.37	87.4	5.62	2.38	2.58	4.97	0.01	4.56	0.02	4.60	0.00	0.00	0.00	0.06
BN-185-C2-G2_17_3	25.6	0.08	19.9	26.8	0.25	13.9	0.06	0.00	0.01	0.06	86.5	5.52	2.48	2.57	5.05	0.01	4.83	0.05	4.45	0.01	0.00	0.00	0.01
BN-185-C2-G2_2_2	25.8	0.08	20.2	26.6	0.26	14.1	0.06	0.00	0.00	0.11	87.2	5.50	2.50	2.60	5.10	0.01	4.76	0.05	4.48	0.01	0.00	0.00	0.02
BN-185-C2-G2_3_1	26.5	0.00	20.9	26.5	0.28	13.9	0.08	0.00	0.01	0.13	88.2	5.57	2.43	2.74	5.17	0.00	4.66	0.05	4.35	0.02	0.00	0.00	0.02
BN-185-C2-G2_3_2	25.7	0.00	20.4	25.7	0.18	13.9	0.06	0.00	0.00	0.15	86.0	5.54	2.46	2.71	5.17	0.00	4.62	0.03	4.45	0.01	0.00	0.00	0.03
BN-185-C2-G2_4_1	25.9	0.04	20.5	26.0	0.20	14.1	0.02	0.00	0.03	0.04	86.8	5.53	2.47	2.69	5.16	0.01	4.64	0.04	4.50	0.01	0.00	0.01	0.01
BN-185-C2-G2_5_1	25.6	0.00	20.9	27.0	0.18	14.0	0.04	0.00	0.00	0.12	87.7	5.44	2.56	2.66	5.22	0.00	4.80	0.03	4.42	0.01	0.00	0.00	0.02
BN-185-C2-G2_6_1	25.9	0.00	20.7	26.3	0.09	14.2	0.03	0.00	0.00	0.11	87.3	5.50	2.50	2.68	5.18	0.00	4.68	0.02	4.49	0.01	0.00	0.00	0.02
BN-185-C2-G2_6_2	26.1	0.15	20.3	26.8	0.24	13.3	0.09	0.00	0.03	0.17	87.1	5.57	2.43	2.69	5.12	0.02	4.78	0.04	4.24	0.02	0.00	0.01	0.03
BN-185-C2-G2_7_1	25.6	0.02	21.0	26.3	0.23	14.3	0.02	0.00	0.01	0.07	87.7	5.43	2.57	2.69	5.26	0.00	4.67	0.04	4.52	0.00	0.00	0.00	0.01
BN-185-C2-G2_7_3	25.6	0.00	20.5	26.4	0.28	13.9	0.02	0.00	0.00	0.12	86.8	5.49	2.51	2.66	5.17	0.00	4.73	0.05	4.45	0.01	0.00	0.00	0.02
BN-185-C2-G2_8_2	26.3	0.07	18.7	25.6	0.29	15.0	0.02	0.00	0.00	0.33	86.4	5.66	2.34	2.41	4.75	0.01	4.60	0.05	4.80	0.00	0.00	0.00	0.06
BN-185-C2-G2_8_3	25.6	0.02	20.2	26.3	0.15	14.0	0.05	0.00	0.01	0.08	86.4	5.51	2.49	2.63	5.13	0.00	4.74	0.03	4.49	0.01	0.00	0.00	0.01
BN-185-C2-G2_9_2	26.2	0.06	19.0	25.6	0.27	14.4	0.06	0.00	0.02	0.18	85.8	5.67	2.33	2.50	4.84	0.01	4.63	0.05	4.65	0.01	0.00	0.01	0.03
BN-185-C3-10	39.0	0.30	26.1	14.3	0.12	8.32	0.11	0.09	5.07	0.04	93.4	7.16	0.84	4.80	5.64	0.04	2.20	0.02	2.28	0.02	0.03	1.19	0.01
BN-185-C3-101	25.8	0.06	20.9	25.7	0.23	13.7	0.10	0.03	0.02	0.08	86.6	5.52	2.48	2.78	5.26	0.01	4.59	0.04	4.38	0.02	0.01	0.01	0.01
BN-185-C3-103	27.8	0.00	21.4	25.7	0.19	13.4	0.05	0.00	0.39	0.05	89.1	5.75	2.25	2.96	5.21	0.00	4.44	0.03	4.14	0.01	0.00	0.10	0.01
BN-185-C3-104	26.2	0.08	20.1	25.2	0.28	14.1	0.07	0.00	0.03	0.09	86.2	5.61	2.39	2.70	5.08	0.01	4.52	0.05	4.50	0.02	0.00	0.01	0.01
BN-185-C3-14	25.7	0.00	21.4	25.8	0.23	13.0	0.02	0.00	0.24	0.03	86.4	5.51	2.49	2.91	5.40	0.00	4.63	0.04	4.15	0.00	0.00	0.07	0.01
BN-185-C3-15	27.3	0.15	20.8	24.3	0.27	12.6	0.12	0.00	0.97	0.03	86.6	5.81	2.19	3.03	5.22	0.02	4.31	0.05	3.98	0.03	0.00	0.26	0.01
BN-185-C3-16	38.1	0.53	26.8	13.6	0.04	5.55	0.05	0.13	5.72	0.01	90.5	7.21	0.79	5.20	5.98	0.07	2.15	0.01	1.57	0.01	0.05	1.38	0.00
BN-185-C3-18	25.7	0.04	20.7	25.8	0.26	13.5	0.06	0.00	0.06	0.02	86.1	5.53	2.47	2.79	5.26	0.01	4.64	0.05	4.33	0.01	0.00	0.02	0.00
BN-185-C3-29	29.8	0.22	22.4	21.9	0.19	11.1	0.06	0.00	2.07	0.06	87.7	6.14	1.86	3.57	5.44	0.03	3.77	0.03	3.40	0.01	0.00	0.54	0.01
BN-185-C3-45	32.7	0.04	21.2	26.2	0.10	13.2	0.03	0.00	0.14	0.03	93.8	6.32	1.68	3.15	4.83	0.01	4.24	0.02	3.81	0.01	0.00	0.04	0.01
BN-185-C3-46	38.1	0.26	27.7	14.4	0.12	6.82	0.10	0.06	4.99	0.02	92.6	7.05	0.95	5.10	6.05	0.04	2.23	0.02	1.88	0.02	0.02	1.18	0.00
BN-185-C3-52	26.0	0.01	20.9	25.8	0.16	13.9	0.10	0.00	0.01	0.02	86.8	5.53	2.47	2.78	5.25	0.00	4.60	0.03	4.41	0.02	0.00	0.00	0.00
BN-185-C3-54	29.8	0.19	22.1	25.2	0.19	12.4	0.05	0.02	1.22	0.01	91.1	5.98	2.02	3.20	5.23	0.03	4.23	0.03	3.71	0.01	0.01	0.31	0.00
BN-185-C3-58	25.8	0.15	21.2	26.7	0.22	13.6	0.05	0.00	0.05	0.00	87.7	5.47	2.53	2.76	5.29	0.02	4.73	0.04	4.29	0.01	0.00	0.01	0.00
BN-185-C3-60	29.8	0.08	23.2	24.4	0.10	12.0	0.10	0.00	1.06	0.05	90.8	5.97	2.03	3.44	5.47	0.01	4.08	0.02	3.57	0.02	0.00	0.27	0.01
BN-185-C3-61	38.7	0.11	27.3	11.9	0.09	5.70	0.04	0.14	7.13	0.00	91.1	7.27	0.73	5.31	6.03	0.02	1.88	0.01	1.60	0.01	0.05	1.71	0.00
BN-185-C3-63	25.7	0.06	20.9	25.9	0.18	13.9	0.07	0.00	0.03	0.05	86.8	5.48	2.52	2.75	5.26	0.01	4.62	0.03	4.44	0.02	0.00	0.01	0.01
BN-185-C3-66	32.5	0.31	23.9	19.4	0.18	9.63	0.09	0.04	3.02	0.11	89.1	6.47	1.53	4.08	5.61	0.05	3.23	0.03	2.86	0.02	0.01	0.77	0.02
BN-185-C3-67	25.9	0.10	21.2	26.2	0.27	14.1	0.08	0.00	0.00	0.00	87.8	5.47	2.53	2.74	5.28	0.02	4.63	0.05	4.43	0.02	0.00	0.00	0.00
BN-185-C3-68	25.7	0.06	20.6	25.6	0.08	13.9	0.05	0.00	0.03	0.05	86.0	5.53	2.47	2.75	5.22	0.01	4.60	0.01	4.44	0.01	0.00	0.01	0.01
BN-185-C3-71	35.7	0.30	26.1	15.3	0.13	7.06	0.05	0.11	4.48	0.02	89.2	6.91	1.09	4.89	5.97	0.04	2.48	0.02	2.04	0.01	0.04	1.11	0.00
BN-185-C3-72	30.0	0.00	22.3	24.1	0.14	12.6	0.09	0.45	0.89	0.02	90.6	6.01	1.99	3.28	5.27	0.00	4.04	0.02	3.77	0.02	0.18	0.23	0.00
BN-185-C3-73	38.9	0.33	27.8	13.0	0.07	4.26	0.08	0.14	6.28	0.00	90.9	7.31	0.69	5.48	6.17	0.05	2.04	0.01	1.19	0.02	0.05	1.51	0.00
BN-185-C3-8	27.0	0.00	21.7	24.2	0.09	12.6	0.08	0.00	1.33	0.06	87.2	5.71	2.29	3.11	5.41	0.00	4.28	0.02	3.97	0.02	0.00	0.36	0.01
BN-185-C3-9	30.4	0.21	22.7	22.1	0.15	9.99	0.08	0.00	2.18	0.05	87.9	6.24	1.76	3.74	5.50	0.03	3.80	0.03	3.06	0.02	0.00	0.57	0.01
BN-185-C3-90	26.0	0.30	20.8	26.7	0.27	12.8	0.06	0.00	0.13	0.05	87.0	5.55	2.45	2.78	5.23	0.05	4.77	0.05	4.09	0.01	0.00	0.04	0.01
BN-185-C3-91	28.8	1.44	18.4	27.3	0.02	11.6	0.13	0.00	0.51	0.10	88.3	6.06	1.94	2.62	4.56	0.23	4.81	0.00	3.64	0.03	0.00	0.14	0.02
BN-185-C3-92	26.7	0.19	21.9	26.2	0.24	14.1	0.09	0.00	0.01	0.09	89.6	5.51	2.49	2.84	5.33	0.03	4.52	0.04	4.32	0.02	0.00	0.00	0.01
BN-185-C3-97	39.5	0.34	26.6	12.0	0.08	6.39	0.03	0.13	6.61	0.01	91.7	7.34	0.66	5.18	5.84	0.05	1.86	0.01	1.77	0.01	0.05	1.57	0.00
BN-185-C4-10	26.1	0.00	20.4	26.2	0.24	13.6	0.09	0.00	0.04	0.00	86.6	5.60	2.40	2.74	5.14	0.00	4.69	0.04	4.33	0.02	0.00	0.01	0.00
BN-185-C4-101	26.1	0.04	21.3	25.8	0.26	14.1	0.01	0.00	0.12	0.09	87.8	5.49	2.51	2.79	5.30	0.01	4.55	0.05	4.42	0.00	0.00	0.03	0.01
BN-185-C4-102	28.1	0.00	20.9	25.0	0.18	13.7	0.07	0.00	0.41	0.12	88.5	5.82	2.18	2.93	5.10	0.00	4.33	0.03	4.24	0.02	0.00	0.11	0.02
BN-185-C4-103	36.9	0.35	26.2	11.9	0.06	6.13	0.06	0.04	6.03	0.17	87.9	7.18	0.82	5.18	6.00	0.05	1.94	0.01	1.78	0.01	0.02	1.50	0.03
BN-185-C4-104	34.8	0.22	25.7	17.8	0.15	8.06	0.04	0.02	4.06	0.10	90.9	6.72	1.28	4.56	5.84	0.03	2.87	0.02	2.32	0.01	0.01	1.00	0.02
BN-185-C4-106	26.1	0.09	20.9	26.5	0.31	13.5	0.10	0.00	0.03	0.09	87.6	5.53	2.47	2.76	5.23	0.01	4.70	0.06	4.26	0.02	0.00	0.01	0.02
BN-185-C4-107	39.3	0.36	26.1	14.4	0.11	4.46	0.16	0.04	5.01	0.15	90.1	7.45	0.55	5.29	5.84	0.05	2.28	0.02	1.26	0.03	0.01	1.21	0.02
BN-185-C4-11	25.7	0.10	20.3	26.4	0.25	13.8	0.08	0.00	0.05	0.02	86.7	5.52	2.48	2.66	5.13	0.02	4.73	0.05	4.41	0.02	0.00	0.01	0.00
BN-185-C4-113	28.1	0.15	22.0	24.4	0.20	13.0	0.06	0.00	1.18	0.12	89.2	5.78	2.22	3.11	5.32	0.02	4.20	0.03	3.97	0.01	0.00	0.31	0.02
BN-185-C4-114	27.1	0.14	20.9	25.8	0.22	13.0	0.05	0.00	0.78	0.08	88.1	5.70	2.30	2.88	5.18	0.02	4.54	0.04	4.07	0.01	0.00	0.21	0.01
BN-185-C4-116	27.1	0.00	20.7	26.5	0.21	14.2	0.03	0.00	0.07	0.12	88.8	5.65	2.35	2.72	5.07	0.00	4.61	0.04	4.40	0.01	0.00	0.02	0.02
BN-185-C4-117	25.9	0.06	20.8	26.6	0.14	14.0	0.02	0.00	0.02	0.13	87.7	5.48	2.52	2.67	5.19	0.01	4.72	0.03	4.44	0.00	0.00	0.01	0.02
BN-185-C4-118	27.0	0.00	20.1	25.9	0.29	14.1	0.06	0.00	0.02	0.09	87.6	5.70	2.30	2.70	5.00	0.00	4.58	0.05	4.43	0.01	0.00	0.01	0.02
BN-185-C4-119	31.9	0.28	23.4	22.0	0.24	7.67	0.13	0.00	1.93	0.06	87.6	6.51	1.49	4.15	5.64	0.04	3.76	0.04	2.34	0.03	0.00	0.50	0.01
BN-185-C4-12	25.7	0.00	21.2	26.3	0.18	14.0	0.08	0.00	0.05	0.04	87.5	5.46	2.54	2.75	5.29	0.00	4.66	0.03	4.42	0.02	0.00	0.01	0.01
BN-185-C4-121	27.6	0.24	20.2	25.7	0.20	13.0	0.11	0.00	0.32	0.10	87.6	5.82	2.18	2.85	5.03	0.04	4.52	0.03	4.10	0.03	0.00	0.08	0.02
BN-185-C4-122	27.0	0.12	20.7	25.8	0.29	14.5	0.09	0.00	0.03	0.08	88.6	5.62	2.38	2.70	5.08	0.02	4.50	0.05	4.51	0.02	0.00	0.01	0.01
BN-185-C4-123	27.8	0.00	21.6	25.0	0.18	11.8	0.09	0.00	0.69	0.13	87.4	5.85	2.15	3.20	5.35	0.00	4.40	0.03	3.71	0.02	0.00	0.19	0.02
BN-185-C4-124	26.0	0.07	20.1	26.8	0.19	13.9	0.07	0.00	0.03	0.01	87.2	5.55	2.45	2.62	5.07	0.01	4.78	0.04	4.43	0.02	0.00	0.01	0.00
BN-185-C4-125	33.6	0.00	22.4	19.3	0.09	11.8	0.14	0.00	3.06	0.03	90.5	6.59	1.41	3.77	5.18	0.00	3.17	0.01	3.45	0.03	0.00	0.76	0.00
BN-185-C4-127	26.4	0.00	20.7	25.9	0.24	14.5	0.06	0.00	0.04	0.09	87.9	5.55	2.45	2.68	5.14	0.00	4.55	0.04	4.56	0.01	0.00	0.01	0.01
BN-185-C4-128	26.5	0.00	20.9	26.3	0.25	13.4	0.03	0.00	0.13	0.11	87.6	5.60	2.40	2.81	5.20	0.00	4.65	0.05	4.24	0.01	0.00	0.04	0.02
BN-185-C4-129	27.2	0.07	20.7	26.0	0.17	13.7	0.02	0.00	0.50	0.14	88.5	5.69	2.31	2.79	5.10	0.01	4.55	0.03	4.26	0.00	0.00	0.13	0.02

TABLE 4.8: Chlorite and white mica compositions used for multi-equilibria calculations.

Analysis	SiO_2	TiO_2	Al_2O_3	FeO	MnO	MgO	CaO	Na2O	K_2O	Cr_2O_3	Total	Si	Al^{IV}	Al^{VI}	Al	Ti	Fe^{2+}	Mn^{2+}	Mg	Ca	Na	K	Cr
BN185	**Chlorite**																						
BN-185-C4-130	27.8	0.05	21.6	25.4	0.21	11.8	0.09	0.00	0.81	0.15	87.9	5.83	2.17	3.15	5.32	0.01	4.45	0.04	3.69	0.02	0.00	0.22	0.03
BN-185-C4-131	39.1	0.25	26.4	12.3	0.08	7.76	0.11	0.10	5.78	0.08	92.0	7.25	0.75	5.00	5.75	0.03	1.91	0.01	2.14	0.02	0.04	1.36	0.01
BN-185-C4-133	33.3	0.17	25.3	18.2	0.09	7.89	0.02	0.08	3.70	0.16	89.0	6.60	1.40	4.51	5.91	0.03	3.02	0.02	2.33	0.00	0.03	0.93	0.02
BN-185-C4-138	25.9	0.06	20.7	25.7	0.26	13.6	0.04	0.00	0.07	0.05	86.5	5.54	2.46	2.78	5.24	0.01	4.61	0.05	4.35	0.01	0.00	0.02	0.01
BN-185-C4-139	25.9	0.13	21.1	26.4	0.29	13.6	0.06	0.00	0.03	0.14	87.6	5.49	2.51	2.76	5.27	0.02	4.67	0.05	4.30	0.01	0.00	0.01	0.02
BN-185-C4-14	25.7	0.00	21.2	27.0	0.33	13.7	0.08	0.00	0.02	0.16	88.2	5.43	2.57	2.72	5.28	0.00	4.77	0.06	4.32	0.02	0.00	0.01	0.03
BN-185-C4-140	25.7	0.01	20.6	26.5	0.22	13.2	0.08	0.00	0.04	0.05	86.4	5.53	2.47	2.77	5.24	0.00	4.77	0.04	4.24	0.02	0.00	0.01	0.01
BN-185-C4-142	26.1	0.00	20.9	25.7	0.17	13.8	0.10	0.00	0.12	0.10	86.9	5.55	2.45	2.78	5.23	0.00	4.58	0.03	4.38	0.02	0.00	0.03	0.02
BN-185-C4-145	38.7	0.25	27.0	14.3	0.18	6.11	0.05	0.14	5.50	0.17	92.3	7.19	0.81	5.11	5.92	0.03	2.22	0.03	1.69	0.01	0.05	1.30	0.03
BN-185-C4-146	35.7	0.13	25.1	14.5	0.10	5.54	0.14	0.09	5.13	0.15	86.6	7.14	0.86	5.04	5.91	0.02	2.42	0.02	1.65	0.03	0.03	1.31	0.02
BN-185-C4-147	26.2	0.03	20.6	26.0	0.25	12.9	0.12	0.02	0.15	0.16	86.4	5.62	2.38	2.83	5.21	0.00	4.67	0.05	4.14	0.03	0.01	0.04	0.03
BN-185-C4-148	25.7	0.09	20.8	26.2	0.31	13.4	0.10	0.00	0.11	0.14	86.8	5.50	2.50	2.74	5.24	0.01	4.69	0.06	4.29	0.02	0.00	0.03	0.02
BN-185-C4-149	25.8	0.10	20.8	26.2	0.26	14.0	0.06	0.00	0.03	0.18	87.4	5.49	2.51	2.69	5.20	0.02	4.65	0.05	4.42	0.01	0.00	0.01	0.03
BN-185-C4-15	25.8	0.00	21.0	26.4	0.30	14.2	0.03	0.00	0.03	0.09	87.8	5.45	2.55	2.69	5.23	0.00	4.68	0.05	4.48	0.01	0.00	0.01	0.02
BN-185-C4-16	27.2	0.12	21.5	25.6	0.18	12.6	0.02	0.00	0.67	0.06	88.0	5.70	2.30	3.02	5.32	0.02	4.49	0.03	3.95	0.00	0.00	0.18	0.01
BN-185-C4-18	26.0	0.01	20.5	26.0	0.24	14.0	0.04	0.00	0.01	0.02	86.8	5.56	2.44	2.71	5.15	0.00	4.65	0.04	4.44	0.01	0.00	0.00	0.00
BN-185-C4-22	25.7	0.06	20.1	26.3	0.26	13.8	0.03	0.00	0.00	0.00	86.2	5.54	2.46	2.65	5.11	0.01	4.74	0.05	4.45	0.01	0.00	0.00	0.00
BN-185-C4-23	37.9	0.18	24.8	13.1	0.08	7.86	0.05	0.06	5.92	0.11	90.1	7.23	0.77	4.81	5.58	0.03	2.09	0.01	2.24	0.01	0.02	1.44	0.02
BN-185-C4-24	26.5	0.05	21.0	26.2	0.27	12.3	0.07	0.00	0.32	0.05	86.8	5.67	2.33	2.96	5.30	0.01	4.67	0.05	3.91	0.02	0.00	0.09	0.01
BN-185-C4-26	28.5	0.22	19.3	26.9	0.12	13.7	0.12	0.00	0.34	0.22	89.4	5.91	2.09	2.63	4.72	0.03	4.67	0.02	4.23	0.03	0.00	0.09	0.04
BN-185-C4-27	25.7	0.10	20.6	26.7	0.22	13.9	0.00	0.00	0.01	0.14	87.4	5.48	2.52	2.64	5.17	0.02	4.76	0.04	4.43	0.00	0.00	0.00	0.02
BN-185-C4-28	25.7	0.05	20.2	27.1	0.29	13.5	0.02	0.00	0.02	0.11	87.0	5.51	2.49	2.63	5.12	0.01	4.86	0.05	4.33	0.01	0.00	0.01	0.02
BN-185-C4-29	26.1	0.11	20.2	26.5	0.18	13.6	0.07	0.00	0.00	0.06	86.8	5.59	2.41	2.69	5.10	0.02	4.74	0.03	4.33	0.02	0.00	0.00	0.01
BN-185-C4-30	26.3	0.12	20.3	26.3	0.25	13.6	0.07	0.00	0.07	0.05	87.2	5.61	2.39	2.70	5.09	0.02	4.69	0.04	4.33	0.02	0.00	0.02	0.01
BN-185-C4-31	26.1	0.00	19.9	27.5	0.22	13.6	0.05	0.00	0.06	0.09	87.4	5.57	2.43	2.59	5.02	0.00	4.91	0.04	4.33	0.01	0.00	0.02	0.01
BN-185-C4-32	25.7	0.09	20.4	26.8	0.28	14.2	0.03	0.00	0.00	0.00	87.5	5.48	2.52	2.60	5.12	0.02	4.77	0.05	4.51	0.01	0.00	0.00	0.00
BN-185-C4-33	26.0	0.13	20.4	26.8	0.15	13.9	0.07	0.00	0.00	0.15	87.5	5.53	2.47	2.63	5.11	0.02	4.76	0.03	4.40	0.02	0.00	0.00	0.02
BN-185-C4-35	28.4	0.67	17.5	27.9	0.13	11.3	0.09	0.00	0.36	0.09	86.5	6.15	1.85	2.61	4.47	0.11	5.04	0.02	3.64	0.02	0.00	0.10	0.02
BN-185-C4-36	31.5	0.12	23.3	21.6	0.22	9.80	0.08	0.00	2.56	0.11	89.3	6.34	1.66	3.87	5.53	0.02	3.63	0.04	2.94	0.02	0.00	0.66	0.02
BN-185-C4-38	28.5	0.69	17.5	27.4	0.08	11.5	0.15	0.00	0.40	0.00	86.2	6.16	1.84	2.62	4.46	0.11	4.96	0.01	3.71	0.03	0.00	0.11	0.00
BN-185-C4-42	25.9	0.14	19.4	26.3	0.15	12.4	0.06	0.00	0.08	0.06	84.6	5.70	2.30	2.74	5.04	0.02	4.84	0.03	4.08	0.01	0.00	0.02	0.01
BN-185-C4-43	26.1	0.10	19.9	26.0	0.20	13.5	0.06	0.00	0.29	0.06	86.2	5.63	2.37	2.68	5.04	0.02	4.68	0.04	4.35	0.01	0.00	0.08	0.01
BN-185-C4-44	25.6	0.06	20.2	26.5	0.20	14.1	0.03	0.00	0.00	0.07	86.8	5.49	2.51	2.60	5.11	0.01	4.76	0.04	4.51	0.01	0.00	0.00	0.01
BN-185-C4-45	35.0	0.41	24.1	17.5	0.12	7.56	0.07	0.00	4.33	0.18	89.3	6.89	1.11	4.48	5.59	0.06	2.88	0.02	2.22	0.02	0.00	1.08	0.03
BN-185-C4-47	27.1	0.07	20.8	25.8	0.15	13.7	0.04	0.00	0.30	0.06	88.1	5.68	2.32	2.82	5.14	0.01	4.53	0.03	4.29	0.01	0.00	0.08	0.01
BN-185-C4-5	26.4	0.00	20.7	26.5	0.19	13.7	0.07	0.00	0.16	0.17	87.9	5.58	2.42	2.73	5.15	0.00	4.68	0.03	4.33	0.02	0.00	0.04	0.03
BN-185-C4-51	26.9	0.09	19.7	26.1	0.22	13.9	0.08	0.00	0.04	0.10	87.1	5.72	2.28	2.65	4.94	0.01	4.64	0.04	4.40	0.02	0.00	0.01	0.02
BN-185-C4-53	35.1	0.39	30.4	24.5	0.28	3.58	0.13	0.00	0.95	0.15	95.5	6.48	1.52	5.11	6.63	0.05	3.79	0.04	0.99	0.03	0.00	0.22	0.02
BN-185-C4-54	25.8	0.15	19.7	26.4	0.20	14.2	0.00	0.00	0.00	0.08	86.5	5.55	2.45	2.54	4.99	0.02	4.75	0.04	4.57	0.00	0.00	0.00	0.01
BN-185-C4-57	26.8	0.03	20.7	25.4	0.21	13.4	0.07	0.00	0.62	0.03	87.4	5.68	2.32	2.85	5.17	0.01	4.50	0.04	4.24	0.02	0.00	0.17	0.00
BN-185-C4-58	35.5	0.04	20.0	22.6	0.16	11.6	0.04	2.53	0.01	0.00	92.5	6.85	1.15	3.39	4.54	0.01	3.65	0.03	3.33	0.01	0.95	0.00	0.00
BN-185-C4-6	26.2	0.18	20.9	26.6	0.20	13.8	0.09	0.00	0.01	0.04	88.1	5.53	2.47	2.71	5.19	0.03	4.69	0.04	4.35	0.02	0.00	0.00	0.01
BN-185-C4-61	25.9	0.17	20.0	26.4	0.25	13.9	0.02	0.00	0.00	0.16	86.8	5.55	2.45	2.61	5.06	0.03	4.72	0.04	4.45	0.01	0.00	0.00	0.03
BN-185-C4-65	25.7	0.07	20.2	26.4	0.29	14.0	0.02	0.00	0.00	0.12	86.9	5.51	2.49	2.62	5.10	0.01	4.73	0.05	4.48	0.00	0.00	0.00	0.02
BN-185-C4-66	26.1	0.00	20.2	26.3	0.16	13.7	0.10	0.00	0.01	0.16	86.6	5.59	2.41	2.69	5.10	0.00	4.72	0.03	4.37	0.02	0.00	0.00	0.03
BN-185-C4-67	25.9	0.20	21.1	26.5	0.15	14.1	0.03	0.00	0.07	0.10	88.2	5.46	2.54	2.69	5.23	0.03	4.68	0.03	4.43	0.01	0.00	0.02	0.02
BN-185-C4-68	26.4	0.02	20.9	26.7	0.18	14.3	0.04	0.00	0.03	0.05	88.7	5.53	2.47	2.69	5.16	0.00	4.67	0.03	4.47	0.01	0.00	0.01	0.01
BN-185-C4-69	26.0	0.09	20.3	25.9	0.25	13.8	0.10	0.03	0.00	0.08	86.5	5.57	2.43	2.70	5.13	0.01	4.64	0.05	4.40	0.02	0.01	0.00	0.01
BN-185-C4-70	29.4	0.07	21.5	23.2	0.15	14.0	0.06	0.00	1.29	0.10	89.8	5.95	2.05	3.08	5.13	0.01	3.93	0.03	4.23	0.01	0.00	0.33	0.02
BN-185-C4-71	28.6	0.00	21.8	24.6	0.20	13.2	0.11	0.00	0.76	0.00	89.3	5.85	2.15	3.12	5.27	0.00	4.21	0.03	4.02	0.02	0.00	0.20	0.00
BN-185-C4-73	26.0	0.06	20.3	26.6	0.18	13.5	0.05	0.00	0.04	0.10	86.9	5.57	2.43	2.69	5.12	0.01	4.77	0.03	4.31	0.01	0.00	0.01	0.02
BN-185-C4-74	27.1	0.33	19.8	26.9	0.12	13.6	0.07	0.00	0.11	0.13	88.2	5.71	2.29	2.63	4.92	0.05	4.73	0.02	4.28	0.02	0.00	0.03	0.02
BN-185-C4-75	27.9	0.07	21.9	24.3	0.14	12.2	0.01	0.00	1.00	0.14	87.7	5.83	2.17	3.22	5.39	0.01	4.24	0.03	3.80	0.00	0.00	0.27	0.02
BN-185-C4-76	26.6	0.12	19.9	26.3	0.27	13.2	0.14	0.00	0.13	0.13	86.8	5.70	2.30	2.71	5.01	0.02	4.71	0.05	4.21	0.03	0.00	0.03	0.02
BN-185-C4-77	38.6	0.41	25.0	14.7	0.14	7.34	0.16	0.08	5.60	0.10	92.1	7.24	0.76	4.77	5.53	0.06	2.30	0.02	2.05	0.03	0.03	1.34	0.01
BN-185-C4-79	37.5	0.20	24.8	14.2	0.21	7.86	0.07	0.04	5.50	0.08	90.4	7.16	0.84	4.74	5.59	0.03	2.26	0.03	2.24	0.01	0.02	1.34	0.01
BN-185-C4-8	25.7	0.08	21.0	26.2	0.34	13.8	0.05	0.00	0.00	0.09	87.3	5.48	2.52	2.74	5.27	0.01	4.66	0.06	4.37	0.01	0.00	0.00	0.01
BN-185-C4-80	25.9	0.10	21.6	26.5	0.18	13.6	0.02	0.00	0.10	0.02	88.0	5.46	2.54	2.84	5.37	0.02	4.67	0.03	4.26	0.01	0.00	0.03	0.00
BN-185-C4-81	35.3	0.17	25.3	16.3	0.02	7.35	0.06	0.02	4.25	0.11	88.9	6.91	1.09	4.74	5.84	0.02	2.66	0.00	2.14	0.01	0.01	1.06	0.02
BN-185-C4-82	27.1	0.06	22.2	25.0	0.20	13.5	0.08	0.00	0.65	0.14	88.9	5.60	2.40	3.01	5.41	0.01	4.33	0.04	4.17	0.02	0.00	0.17	0.02
BN-185-C4-84	30.9	0.07	22.3	23.6	0.17	11.6	0.08	0.05	1.68	0.19	90.6	6.18	1.82	3.44	5.27	0.01	3.94	0.03	3.47	0.02	0.02	0.43	0.03
BN-185-C4-85	33.5	0.33	23.3	18.5	0.21	8.55	0.07	0.00	2.99	0.20	87.7	6.73	1.27	4.25	5.52	0.05	3.11	0.04	2.56	0.01	0.00	0.77	0.03
BN-185-C4-88	26.4	0.04	20.4	25.9	0.19	14.2	0.11	0.00	0.01	0.09	87.3	5.59	2.41	2.69	5.10	0.01	4.59	0.03	4.48	0.03	0.00	0.00	0.02
BN-185-C4-9	27.0	0.08	21.5	26.8	0.27	12.8	0.02	0.00	0.31	0.08	88.9	5.63	2.37	2.93	5.30	0.01	4.67	0.05	3.98	0.01	0.00	0.08	0.01
BN-185-C4-90	26.0	0.00	20.5	26.3	0.17	14.0	0.02	0.00	0.03	0.08	87.1	5.54	2.46	2.70	5.16	0.00	4.68	0.03	4.44	0.00	0.00	0.01	0.01
BN-185-C4-92	27.0	0.06	22.2	25.6	0.16	12.9	0.00	0.00	0.72	0.11	88.7	5.61	2.39	3.06	5.45	0.01	4.45	0.03	3.99	0.00	0.00	0.19	0.02
BN-185-C4-93	25.7	0.16	21.7	26.6	0.16	13.3	0.05	0.00	0.05	0.05	87.8	5.44	2.56	2.85	5.41	0.02	4.71	0.03	4.19	0.01	0.00	0.01	0.01
BN-185-C4-94	32.7	0.20	21.8	18.6	0.16	11.7	0.10	0.00	3.31	0.08	88.6	6.56	1.44	3.71	5.15	0.03	3.12	0.03	3.49	0.02	0.00	0.85	0.01
BN-185-C4-95	33.1	0.24	23.9	18.2	0.16	8.06	0.05	0.03	3.40	0.11	87.4	6.69	1.31	4.38	5.69	0.04	3.08	0.03	2.42	0.01	0.01	0.88	0.02
BN-185-C4-96	40.0	0.01	25.6	12.4	0.02	6.96	0.10	0.00	6.12	0.15	91.4	7.45	0.55	5.08	5.63	0.00	1.93	0.00	1.93	0.02	0.00	1.46	0.02
BN-185-C4-97	26.4	0.07	21.0	25.8	0.22	12.9	0.04	0.00	0.51	0.04	87.0	5.62	2.38	2.90	5.28	0.01	4.60	0.04	4.09	0.01	0.00	0.14	0.01
BN-185-C4-98	26.6	0.00	20.4	25.5	0.25	13.2	0.07	0.00	0.36	0.19	86.6	5.68	2.32	2.81	5.13	0.00	4.56	0.04	4.22	0.02	0.00	0.10	0.03
BN-185-C4-99	25.9	0.06	20.1	25.9	0.20	14.2	0.06	0.00	0.00	0.00	86.4	5.56	2.44	2.64	5.08	0.01	4.64	0.04	4.55	0.01	0.00	0.00	0.00
BN185-G1_1_12	38.0	0.33	26.7	13.9	0.09	6.67	0.14	0.00	5.49	0.11	91.4	7.14	0.86	5.04	5.90	0.05	2.18	0.01	1.87	0.03	0.00	1.32	0.02
BN185-G1_1_13	39.7	0.07	26.5	10.9	0.00	5.28	0.45	0.02	6.75	0.13	89.9	7.50	0.50	5.40	5.90	0.01	1.72	0.00	1.48	0.09	0.01	1.62	0.02
BN185-G1_1_14	39.6	0.45	25.6	9.6	0.01	4.64	1.66	0.09	6.79	0.11	88.5	7.57	0.43	5.35	5.78	0.06	1.53	0.00	1.32	0.34	0.03	1.66	0.02
BN185-G1_1_3	37.3	0.28	26.7	14.7	0.21	7.27	0.08	0.05	5.16	0.08	91.9	7.00	1.00	4.92	5.92	0.04	2.31	0.03	2.03	0.02	0.02	1.24	0.01
BN185-G1_1_4	35.0	0.08	25.5	16.9	0.30	8.41	0.11	0.00	4.20	0.09	90.6	6.76	1.24	4.56	5.80	0.01	2.72	0.05	2.42	0.02	0.00	1.03	0.01
BN185-G1_1_7	38.4	0.05	26.3	14.0	0.18	7.00	0.04	0.04	5.75	0.00	91.7	7.19	0.81	5.01	5.82	0.01	2.19	0.03	1.96	0.01	0.01	1.37	0.00
BN185-G1_2_10	33.4	0.12	23.4	17.2	0.12	8.79	0.16	0.03	3.59	0.06	86.9	6.75	1.25	4.33	5.58	0.02	2.91	0.02	2.65	0.03	0.01	0.93	0.01
BN185-G1_2_11	39.0	0.25	25.9	12.3	0.11	6.48	0.16	0.03	6.15	0.07	90.5	7.35	0.65	5.12	5.77	0.04	1.95	0.02	1.82	0.03	0.01	1.48	0.01
BN185-G1_2_12	38.1	0.32	24.8	10.4	0.01	6.06	0.24	0.05	6.65	0.16	86.9	7.46	0.54	5.18	5.72	0.05	1.71	0.00	1.77	0.05	0.02	1.66	0.03
BN185-G1_2_13	30.4	0.13	22.6	19.8	0.19	11.1	1.65	0.04	2.29	0.18	88.4	6.18	1.82	3.59	5.41	0.02	3.37	0.03	3.37	0.36	0.01	0.59	0.03
BN185-G1_2_14	34.9	0.44	25.2	17.5	0.08	8.46	0.79	0.00	3.48	0.08	90.9	6.72	1.28	4.43	5.71	0.06	2.81	0.01	2.43	0.16	0.00	0.85	0.01
BN185-G1_2_8	39.9	0.00	27.2	12.3	0.12	7.12	0.10	0.05	6.08	0.11	92.9	7.30	0.70	5.17	5.86	0.00	1.88	0.02	1.94	0.02	0.02	1.42	0.02
BN185-G1_2_9	27.6	0.22	21.6	23.4	0.11	11.6	0.09	0.01	1.27	0.11	86.0	5.87	2.13	3.27	5.41	0.03	4.16	0.02	3.69	0.02	0.00	0.34	0.02
BN185-G1_3_11	36.5	0.03	24.9	14.7	0.15	7.90	0.21	0.04	5.23	0.00	89.7	7.06	0.94	4.73	5.67	0.00	2.37	0.02	2.28	0.04	0.01	1.29	0.00
BN185-G1_3_12	34.2	0.22	23.8	17.1	0.15	8.56	0.10	0.00	3.93	0.12	88.1	6.81	1.19	4.38	5.57	0.03	2.85	0.02	2.54	0.02	0.00	1.00	0.02
BN185-G1_3_13	36.6	0.51	25.4	16.4	0.08	8.34	0.17	0.02	4.23	0.14	91.8	6.92	1.08	4.57	5.65	0.07	2.59	0.01	2.35	0.04	0.01	1.02	0.02
BN185-G1_3_15	37.6	0.22	25.0	13.6	0.00	6.77	0.14	0.05	5.63	0.07	89.1	7.26	0.74	4.95	5.69	0.03	2.19	0.00	1.95	0.03	0.02	1.39	0.01
BN185-G1_3_17	36.7	0.24	24.2	14.4	0.12	8.46	0.19	0.25	4.56	0.16	89.3	7.10	0.90	4.60	5.50	0.03	2.33	0.02	2.44	0.04	0.09	1.12	0.02
BN185-G1_3_18	33.0	0.00	22.8	20.8	0.20	11.11	0.17	0.63	1.96	0.16	90.8	6.48	1.52	3.75	5.27	0.00	3.41	0.03	3.25	0.03	0.24	0.49	0.02
BN185-G1_3_19	33.9	0.08	21.4	20.5	0.07	11.9	0.11	0.89	1.60	0.03	90.5	6.66	1.34	3.59	4.94	0.01	3.36	0.01	3.49	0.02	0.34	0.40	0.00
BN185-G1_3_20	29.3	0.13	20.4	25.9	0.11	12.7	0.13	0.44	0.13	0.00	89.2	6.02	1.98	2.98	4.95	0.02	4.45	0.02	3.89	0.03	0.17	0.03	0.00
BN185-G1_4_10	29.2	0.02	22.2	23.3	0.03	12.6	0.02	0.01	1.38	0.16	89.0	5.96	2.04	3.31	5.35	0.00	3.98	0.01	3.84	0.00	0.00	0.36	0.03
BN185-G1_4_11	26.4	0.16	20.7	25.1	0.32	14.3	0.09	0.00	0.14	0.05	87.2	5.58	2.42	2.74	5.16	0.03	4.44	0.06	4.50	0.02	0.00	0.04	0.01
BN185-G1_4_12	26.7	0.00	20.6	25.4	0.16	14.0	0.09	0.00	0.20	0.08	87.3	5.65	2.35	2.79	5.14	0.00	4.48	0.03	4.41	0.02	0.00	0.05	0.01
BN185-G1_4_13	28.2	0.16	21.3	23.5	0.30	13.6	0.09	0.00	0.69	0.19	88.0	5.84	2.16	3.04	5.20	0.02	4.07	0.05	4.19	0.02	0.00	0.18	0.03

Analysis	SiO_2	TiO_2	Al_2O_3	FeO	MnO	MgO	CaO	Na2O	K_2O	Cr_2O_3	Total	Si	Al^{IV}	Al^{VI}	Al	Ti	Fe^{2+}	Mn^{2+}	Mg	Ca	Na	K	Cr
BN185	**Chlorite**																						
BN185-G1_4_13	28.2	0.16	21.3	23.5	0.30	13.6	0.09	0.00	0.69	0.19	88.0	5.84	2.16	3.04	5.20	0.02	4.07	0.05	4.19	0.02	0.00	0.18	0.03
BN185-G1_4_14	29.0	0.06	22.0	24.4	0.17	13.7	0.13	0.00	0.84	0.10	90.4	5.84	2.16	3.07	5.23	0.01	4.13	0.03	4.13	0.03	0.00	0.22	0.02
BN185-G1_4_15	30.6	0.06	22.7	23.2	0.10	12.6	0.09	0.00	1.88	0.03	91.2	6.08	1.92	3.39	5.31	0.01	3.85	0.02	3.74	0.02	0.00	0.48	0.00
BN185-G1_4_16	30.5	0.20	22.6	23.1	0.15	12.6	0.05	0.02	1.60	0.19	90.9	6.06	1.94	3.36	5.29	0.03	3.84	0.02	3.74	0.01	0.01	0.41	0.03
BN185-G1_4_17	28.5	0.18	21.9	25.4	0.08	14.2	0.04	0.00	0.45	0.18	91.0	5.73	2.27	2.93	5.20	0.03	4.28	0.01	4.28	0.01	0.00	0.12	0.03
BN185-G1_4_18	27.5	0.11	21.6	25.3	0.14	14.3	0.05	0.00	0.14	0.14	89.3	5.65	2.35	2.88	5.24	0.02	4.34	0.02	4.39	0.01	0.00	0.04	0.02
BN185-G1_4_19	27.0	0.09	21.3	25.1	0.24	13.8	0.06	0.00	0.29	0.18	88.1	5.64	2.36	2.88	5.24	0.01	4.38	0.04	4.30	0.01	0.00	0.08	0.03
BN185-G1_4_20	26.5	0.04	21.0	26.0	0.17	13.5	0.06	0.00	0.05	0.11	87.3	5.60	2.40	2.84	5.24	0.01	4.60	0.03	4.25	0.01	0.00	0.01	0.02
BN185-G1_4_5	36.9	0.19	22.6	16.2	0.00	8.50	0.12	1.74	2.94	0.06	89.2	7.18	0.82	4.35	5.17	0.03	2.64	0.00	2.47	0.02	0.65	0.73	0.01
BN185-G1_4_9	37.5	0.22	25.1	14.3	0.00	7.53	0.07	0.01	5.19	0.13	90.0	7.17	0.83	4.82	5.65	0.03	2.29	0.00	2.15	0.01	0.00	1.27	0.02
BN185-G1_5_10	30.3	0.00	22.8	21.7	0.06	11.8	0.03	0.00	1.99	0.19	88.9	6.15	1.85	3.58	5.44	0.00	3.68	0.01	3.56	0.01	0.00	0.51	0.03
BN185-G1_5_11	26.0	0.14	21.2	25.9	0.09	13.7	0.07	0.00	0.05	0.10	87.2	5.52	2.48	2.80	5.29	0.02	4.59	0.02	4.34	0.02	0.00	0.01	0.02
BN185-G1_5_12	25.8	0.00	21.8	26.6	0.25	13.6	0.06	0.00	0.02	0.15	88.3	5.42	2.58	2.83	5.41	0.00	4.68	0.04	4.26	0.01	0.00	0.01	0.03
BN185-G1_5_13	25.9	0.14	21.7	25.7	0.24	14.0	0.07	0.01	0.01	0.15	88.0	5.45	2.55	2.82	5.37	0.02	4.52	0.04	4.38	0.02	0.00	0.00	0.03
BN185-G1_5_14	26.1	0.00	21.9	26.6	0.19	14.0	0.10	0.00	0.04	0.07	89.1	5.44	2.56	2.82	5.38	0.00	4.64	0.03	4.34	0.02	0.00	0.01	0.01
BN185-G1_5_15	26.4	0.16	21.4	25.8	0.30	14.3	0.08	0.00	0.04	0.01	88.6	5.51	2.49	2.77	5.26	0.02	4.50	0.05	4.45	0.02	0.00	0.01	0.00
BN185-G1_5_16	26.6	0.08	21.1	25.8	0.19	14.1	0.09	0.00	0.02	0.08	88.0	5.57	2.43	2.79	5.22	0.01	4.52	0.03	4.40	0.02	0.00	0.01	0.01
BN185-G1_5_17	27.4	0.14	21.2	25.7	0.07	14.3	0.10	0.00	0.07	0.08	89.0	5.66	2.34	2.83	5.17	0.02	4.43	0.01	4.39	0.02	0.00	0.02	0.01
BN185-G1_5_18	27.1	0.00	21.5	25.7	0.13	13.9	0.08	0.00	0.09	0.06	88.7	5.63	2.37	2.89	5.27	0.00	4.47	0.02	4.31	0.02	0.00	0.02	0.01
BN185-G1_5_19	26.2	0.00	21.6	26.6	0.33	14.2	0.05	0.00	0.05	0.09	89.1	5.45	2.55	2.76	5.31	0.00	4.63	0.06	4.41	0.01	0.00	0.01	0.02
BN185-G1_5_20	25.7	0.01	22.0	27.0	0.26	13.9	0.03	0.00	0.02	0.11	89.0	5.37	2.63	2.79	5.43	0.00	4.72	0.05	4.32	0.01	0.00	0.00	0.02
BN185-G1_5_6	38.1	0.30	25.0	13.2	0.16	7.48	0.11	0.06	5.50	0.05	90.0	7.26	0.74	4.88	5.61	0.04	2.11	0.03	2.12	0.02	0.02	1.34	0.01
BN185-G1_5_7	30.1	0.04	22.5	22.8	0.20	12.4	0.02	0.00	1.29	0.04	89.3	6.08	1.92	3.44	5.36	0.01	3.86	0.03	3.72	0.01	0.00	0.33	0.01
BN185-G1_5_8	35.8	0.00	25.3	16.6	0.19	8.86	0.04	0.04	3.88	0.22	91.0	6.84	1.16	4.55	5.71	0.00	2.66	0.03	2.52	0.01	0.02	0.95	0.03
BN185-G1_5_9	38.0	0.07	25.8	13.8	0.04	7.26	0.03	0.15	5.53	0.01	90.7	7.19	0.81	4.96	5.76	0.01	2.19	0.01	2.05	0.01	0.06	1.34	0.00
BN185-G1_6_10	26.9	0.00	21.4	24.9	0.23	13.2	0.03	0.00	0.67	0.12	87.5	5.67	2.33	2.98	5.31	0.00	4.38	0.04	4.14	0.01	0.00	0.18	0.02
BN185-G1_6_11	26.0	0.15	21.1	26.3	0.30	13.6	0.07	0.00	0.09	0.21	87.8	5.51	2.49	2.76	5.25	0.02	4.65	0.05	4.29	0.02	0.00	0.02	0.03
BN185-G1_6_12	26.7	0.10	20.7	25.8	0.22	13.7	0.00	0.00	0.03	0.18	87.4	5.64	2.36	2.80	5.16	0.02	4.55	0.04	4.31	0.00	0.00	0.01	0.03
BN185-G1_6_13	26.6	0.07	20.8	25.3	0.23	13.9	0.00	0.01	0.03	0.21	87.1	5.63	2.37	2.80	5.18	0.01	4.48	0.04	4.38	0.00	0.00	0.01	0.04
BN185-G1_6_14	26.6	0.15	21.5	26.0	0.24	14.0	0.05	0.00	0.09	0.23	88.9	5.54	2.46	2.81	5.27	0.02	4.51	0.04	4.33	0.01	0.00	0.02	0.04
BN185-G1_6_15	25.9	0.08	21.6	26.3	0.26	14.2	0.04	0.00	0.00	0.15	88.5	5.43	2.57	2.75	5.33	0.01	4.61	0.05	4.42	0.01	0.00	0.00	0.03
BN185-G1_6_16	26.8	0.13	21.1	26.6	0.24	13.8	0.08	0.00	0.06	0.21	89.0	5.58	2.42	2.76	5.18	0.02	4.62	0.04	4.29	0.02	0.00	0.02	0.03
BN185-G1_6_17	27.0	0.00	20.9	25.7	0.15	14.4	0.09	0.00	0.07	0.09	88.4	5.62	2.38	2.75	5.13	0.00	4.49	0.03	4.49	0.02	0.00	0.02	0.02
BN185-G1_6_18	26.6	0.00	21.5	26.3	0.17	14.1	0.02	0.00	0.01	0.18	88.9	5.53	2.47	2.79	5.26	0.00	4.58	0.03	4.39	0.00	0.00	0.00	0.03
BN185-G1_6_19	25.8	0.29	21.6	26.5	0.25	14.2	0.03	0.00	0.03	0.11	88.8	5.39	2.61	2.71	5.32	0.05	4.64	0.04	4.43	0.01	0.00	0.01	0.02
BN185-G1_6_20	26.4	0.05	21.3	26.5	0.06	14.5	0.05	0.00	0.00	0.07	89.0	5.50	2.50	2.73	5.23	0.01	4.61	0.01	4.49	0.01	0.00	0.00	0.01
BN185-G1_6_5	37.1	0.13	25.1	16.2	0.00	9.03	0.11	0.00	4.61	0.12	92.4	6.97	1.03	4.53	5.56	0.02	2.55	0.00	2.53	0.02	0.00	1.11	0.02
BN185-G1_6_6	29.6	0.00	22.4	23.4	0.15	12.4	0.02	0.01	1.39	0.14	89.5	6.01	1.99	3.36	5.35	0.00	3.96	0.03	3.75	0.00	0.00	0.36	0.02
BN185-G1_6_7	29.5	0.17	22.6	24.0	0.17	13.0	0.04	0.00	1.36	0.19	91.1	5.90	2.10	3.23	5.33	0.03	4.01	0.03	3.89	0.01	0.00	0.35	0.03
BN185-G1_6_8	32.5	0.05	23.9	20.6	0.18	11.5	0.03	0.00	2.54	0.11	91.4	6.33	1.67	3.83	5.50	0.01	3.35	0.03	3.35	0.01	0.00	0.63	0.02
BN185-G1_6_9	29.4	0.27	23.0	22.6	0.14	12.5	0.05	0.00	1.51	0.18	89.7	5.92	2.08	3.40	5.47	0.04	3.82	0.02	3.77	0.01	0.00	0.39	0.03
BN185-G2_1_5	33.7	0.17	24.5	17.2	0.18	9.87	0.10	0.00	3.72	0.09	89.6	6.61	1.39	4.27	5.66	0.02	2.81	0.03	2.88	0.02	0.00	0.93	0.01
BN185-G2_2_2	39.3	0.00	26.4	12.5	0.08	7.82	0.09	0.10	6.09	0.00	92.3	7.26	0.74	5.01	5.75	0.00	1.94	0.01	2.15	0.02	0.04	1.44	0.00
BN185-G2_2_4	39.1	0.34	27.0	11.8	0.19	6.18	0.13	0.13	6.16	0.09	91.2	7.29	0.71	5.24	5.95	0.05	1.85	0.03	1.72	0.03	0.05	1.47	0.01
BN185-G2_2_5	39.6	0.39	26.4	11.4	0.08	5.86	0.07	0.03	6.55	0.17	90.6	7.43	0.57	5.27	5.84	0.05	1.79	0.01	1.64	0.01	0.01	1.57	0.03
BN185-L1_4	38.5	0.00	26.5	12.9	0.02	6.76	0.09	0.02	5.75	0.16	90.8	7.25	0.75	5.13	5.88	0.00	2.03	0.00	1.89	0.02	0.01	1.38	0.02
BN185-L1_5	38.0	0.32	25.6	11.4	0.02	5.56	0.16	0.02	6.55	0.10	87.8	7.38	0.62	5.25	5.87	0.05	1.85	0.00	1.61	0.03	0.01	1.62	0.02
BN185-L1_7	35.3	0.47	25.4	16.2	0.07	8.94	0.02	0.04	4.24	0.06	90.7	6.77	1.23	4.51	5.75	0.07	2.60	0.01	2.56	0.00	0.02	1.04	0.01
BN185-L2_9	39.8	0.25	27.9	10.3	0.03	5.35	0.11	0.08	7.00	0.05	90.9	7.40	0.60	5.52	6.12	0.03	1.59	0.00	1.48	0.02	0.03	1.66	0.01
BN185-L3_1	37.4	0.48	26.4	3.0	0.05	1.33	9.45	0.16	7.85	0.13	86.2	7.37	0.63	5.50	6.12	0.07	0.49	0.01	0.39	1.99	0.06	1.97	0.02
BN185-L3_3	35.6	0.07	24.6	16.4	0.25	9.45	0.07	0.09	4.41	0.12	91.1	6.84	1.16	4.39	5.56	0.01	2.63	0.04	2.70	0.01	0.03	1.08	0.02
BN185-L3_4	39.1	0.24	27.6	12.8	0.00	5.85	0.11	0.01	5.94	0.11	91.7	7.26	0.74	5.30	6.04	0.03	1.99	0.00	1.62	0.02	0.00	1.41	0.02
BN185-L3_6	30.9	0.08	23.8	21.5	0.21	11.27	0.06	0.00	2.04	0.00	89.9	6.16	1.84	3.76	5.60	0.01	3.59	0.04	3.35	0.01	0.00	0.52	0.00
BN185-L4_1	38.4	0.31	26.5	14.2	0.11	7.18	0.09	0.02	5.14	0.11	92.0	7.16	0.84	4.97	5.81	0.04	2.21	0.02	2.00	0.02	0.01	1.22	0.02
BN185-L4_13	37.2	0.34	25.7	15.4	0.04	7.25	0.10	0.19	5.24	0.03	91.6	7.05	0.95	4.79	5.74	0.05	2.44	0.01	2.05	0.02	0.07	1.27	0.00
BN185-L4_7	28.9	0.00	22.2	23.9	0.19	12.60	0.07	b.d.l	1.07	0.10	89.0	5.91	2.09	3.26	5.35	0.00	4.09	0.03	3.85	0.01	0.00	0.28	0.02
BN185-L4_8	28.3	0.22	20.8	23.1	0.26	13.47	0.06	0.00	0.79	0.03	87.2	5.92	2.08	3.05	5.13	0.03	4.04	0.05	4.19	0.01	0.00	0.21	0.01
BN185-L4_9	39.0	0.06	26.7	13.0	0.02	6.30	0.09	0.18	5.48	0.00	90.9	7.31	0.69	5.21	5.90	0.01	2.05	0.00	1.76	0.02	0.07	1.31	0.00
BN246	**Chlorite**																						
BN-246-4	27.7	0.09	23.6	29.6	0.10	7.75	0.12	0.00	1.19	0.07	90.3	5.76	2.24	3.54	5.78	0.01	5.15	0.02	2.40	0.03	0.00	0.32	0.01
BN-246-18	24.9	0.01	21.8	32.0	0.13	8.58	0.15	0.00	0.00	0.04	87.6	5.44	2.56	3.05	5.61	0.00	5.84	0.02	2.79	0.03	0.00	0.00	0.01
BN-246-16	24.9	0.00	21.9	31.7	0.11	8.97	0.07	0.00	0.01	0.06	87.7	5.42	2.58	3.03	5.61	0.00	5.78	0.02	2.91	0.02	0.00	0.00	0.01
BN-246-10	24.8	0.09	21.3	31.4	0.21	9.43	0.12	0.00	0.00	0.07	87.4	5.42	2.58	2.91	5.49	0.01	5.73	0.04	3.07	0.03	0.00	0.00	0.01
BN-246-6	24.8	0.00	21.6	31.5	0.11	9.61	0.03	0.00	0.02	0.04	87.7	5.39	2.61	2.94	5.55	0.00	5.73	0.02	3.12	0.01	0.00	0.01	0.01
BN-246-	24.5	0.14	22.0	31.6	0.00	9.32	0.03	0.00	0.01	0.03	87.6	5.35	2.65	2.99	5.64	0.02	5.76	0.00	3.03	0.01	0.00	0.00	0.00
BN-246-31	24.5	0.00	21.5	31.0	0.10	8.91	0.06	0.00	0.08	0.07	86.2	5.42	2.58	3.03	5.61	0.00	5.74	0.02	2.94	0.01	0.00	0.02	0.01
BN-246-30	24.5	0.00	21.4	31.8	0.18	9.69	0.01	0.00	0.01	0.02	87.6	5.35	2.65	2.87	5.52	0.00	5.82	0.03	3.16	0.00	0.00	0.00	0.00
BN-246-2	24.4	0.08	21.5	31.0	0.10	9.46	0.07	0.00	0.00	0.04	86.7	5.36	2.64	2.95	5.59	0.01	5.71	0.02	3.11	0.02	0.00	0.00	0.01
BN-246-27	24.3	0.00	21.7	31.2	0.03	9.31	0.07	0.00	0.00	0.02	86.6	5.36	2.64	2.99	5.63	0.00	5.75	0.01	3.06	0.02	0.00	0.00	0.00
BN-246-23	24.2	0.02	21.9	33.2	0.10	8.02	0.07	0.00	0.01	0.02	87.6	5.33	2.67	3.02	5.69	0.00	6.12	0.02	2.63	0.02	0.00	0.00	0.00
BN-246-32	24.2	0.02	21.6	30.9	0.00	9.47	0.08	0.00	0.07	0.00	86.4	5.34	2.66	2.97	5.63	0.00	5.72	0.00	3.12	0.02	0.00	0.02	0.00
BN-246-1	24.1	0.00	22.0	32.7	0.04	8.96	0.08	0.00	0.00	0.12	87.9	5.27	2.73	2.94	5.67	0.00	5.98	0.01	2.92	0.02	0.00	0.00	0.02
BN-246-9	24.0	0.00	21.6	32.3	0.00	8.62	0.03	0.00	0.02	0.04	86.6	5.33	2.67	2.98	5.65	0.00	5.99	0.00	2.85	0.01	0.00	0.01	0.01
BN-246-8	23.9	0.09	21.8	32.4	0.15	8.89	0.02	0.00	0.04	0.01	87.4	5.27	2.73	2.93	5.65	0.01	5.98	0.03	2.92	0.01	0.00	0.01	0.00
BN-246-5	23.9	0.11	21.7	31.6	0.08	9.16	0.08	0.00	0.02	0.00	86.7	5.29	2.71	2.95	5.66	0.02	5.84	0.02	3.02	0.02	0.00	0.00	0.00
BN-246-33	23.9	0.09	21.2	31.1	0.12	9.11	0.07	0.00	0.01	0.03	85.7	5.34	2.66	2.93	5.59	0.01	5.82	0.02	3.04	0.02	0.00	0.00	0.01
BN-246-29	23.8	0.00	21.7	31.4	0.07	9.30	0.08	0.00	0.00	0.14	86.5	5.28	2.72	2.93	5.66	0.00	5.82	0.01	3.07	0.02	0.00	0.00	0.02
BN-246-28	23.8	0.05	21.5	31.4	0.07	8.83	0.07	0.01	0.00	0.07	85.9	5.32	2.68	2.98	5.66	0.01	5.86	0.01	2.94	0.02	0.00	0.00	0.01
BN185	**Mica**																						
BN-185-C1-G1_10_1	45.2	0.10	29.3	5.64	0.00	3.01	0.10	0.16	8.75	0.43	92.7	6.30	1.70	3.11	4.81	0.01	0.66	0.00	0.62	0.01	0.04	1.56	0.05
BN-185-C1-G1_10_2	48.8	0.18	28.5	2.58	0.05	1.64	0.00	0.06	9.39	0.22	91.4	6.74	1.26	3.38	4.64	0.02	0.30	0.01	0.34	0.00	0.02	1.66	0.02
BN-185-C1-G1_10_5	48.8	0.10	25.8	5.59	0.00	2.21	0.07	2.10	6.50	0.21	91.3	6.80	1.20	3.04	4.24	0.01	0.65	0.00	0.46	0.01	0.57	1.16	0.02
BN-185-C1-G1_11_1	46.2	0.14	26.4	6.64	0.07	3.07	0.06	1.48	6.88	0.16	91.1	6.54	1.46	2.93	4.39	0.02	0.79	0.01	0.65	0.01	0.41	1.24	0.02
BN-185-C1-G1_11_2	41.2	0.07	27.7	9.63	0.07	3.97	0.06	0.12	6.91	0.13	89.8	6.03	1.97	2.81	4.78	0.01	1.18	0.01	0.87	0.01	0.03	1.29	0.01
BN-185-C1-G1_11_3	47.3	0.09	30.1	2.79	0.00	1.88	0.08	0.22	10.3	0.46	93.2	6.48	1.52	3.35	4.87	0.01	0.32	0.00	0.38	0.01	0.06	1.80	0.05
BN-185-C1-G1_12_2	47.2	0.14	27.7	3.49	0.05	2.93	0.07	0.17	9.77	0.24	91.8	6.58	1.42	3.14	4.56	0.01	0.41	0.01	0.61	0.01	0.05	1.74	0.03
BN-185-C1-G1_12_3	51.5	0.16	25.8	2.41	0.00	1.42	0.03	2.79	7.58	0.17	91.9	7.04	0.96	3.21	4.17	0.02	0.28	0.00	0.29	0.00	0.74	1.32	0.02

Analysis	SiO_2	TiO_2	Al_2O_3	FeO	MnO	MgO	CaO	Na2O	K_2O	Cr_2O_3	Total	Si	Al^{IV}	Al^{VI}	Al	Ti	Fe^{2+}	Mn^{2+}	Mg	Ca	Na	K	Cr
BN185	**Mica**																						
BN-185-C1-G1_12_5	46.7	0.10	28.8	2.87	0.00	2.03	0.07	0.13	10.1	0.41	91.2	6.55	1.45	3.30	4.75	0.01	0.34	0.00	0.42	0.01	0.03	1.81	0.05
BN-185-C1-G1_13_1	44.5	0.16	27.9	6.04	0.00	3.45	0.06	0.56	8.68	0.21	91.6	6.31	1.69	2.97	4.67	0.02	0.72	0.00	0.73	0.01	0.16	1.57	0.02
BN-185-C1-G1_13_2	47.3	0.14	29.6	2.41	0.00	1.71	0.00	0.18	10.5	0.37	92.2	6.55	1.45	3.37	4.82	0.01	0.28	0.00	0.35	0.00	0.05	1.85	0.04
BN-185-C1-G1_13_3	42.2	0.10	27.6	8.67	0.11	5.23	0.03	0.13	7.23	0.08	91.4	6.05	1.95	2.72	4.67	0.01	1.04	0.01	1.12	0.00	0.04	1.32	0.01
BN-185-C1-G1_14_1	49.8	0.13	28.1	3.84	0.00	1.99	0.04	1.14	8.74	0.37	94.1	6.73	1.27	3.20	4.47	0.01	0.43	0.00	0.40	0.01	0.30	1.51	0.04
BN-185-C1-G1_14_2	45.9	0.08	27.2	5.06	0.05	2.87	0.00	0.93	8.46	0.18	90.7	6.51	1.49	3.06	4.55	0.01	0.60	0.01	0.61	0.00	0.26	1.53	0.02
BN-185-C1-G1_14_3	49.3	0.16	29.7	2.98	0.02	2.03	0.03	0.13	9.88	0.34	94.7	6.62	1.38	3.33	4.71	0.02	0.33	0.00	0.41	0.00	0.03	1.69	0.04
BN-185-C1-G1_14_4	42.8	0.12	29.3	9.37	0.15	4.17	0.05	0.04	7.64	0.29	93.9	6.00	2.00	2.83	4.83	0.01	1.10	0.02	0.87	0.01	0.01	1.37	0.03
BN-185-C1-G1_14_5	46.4	0.19	29.8	4.31	0.00	2.61	0.04	0.21	9.26	0.47	93.3	6.38	1.62	3.21	4.83	0.02	0.50	0.00	0.53	0.01	0.06	1.63	0.05
BN-185-C1-G1_15_1	45.1	0.14	27.8	7.00	0.00	4.11	0.05	0.09	8.34	0.17	92.8	6.31	1.69	2.90	4.59	0.01	0.82	0.00	0.86	0.01	0.02	1.49	0.02
BN-185-C1-G1_15_3	45.4	0.12	23.7	10.82	0.12	3.69	0.04	3.07	3.82	0.22	91.0	6.52	1.48	2.53	4.01	0.01	1.30	0.01	0.79	0.01	0.85	0.70	0.03
BN-185-C1-G1_15_4	48.2	0.11	29.3	2.42	0.03	1.97	0.06	0.56	10.1	0.21	93.0	6.60	1.40	3.33	4.73	0.01	0.28	0.00	0.40	0.01	0.15	1.77	0.02
BN-185-C1-G1_16_1	45.8	0.09	30.6	2.43	0.05	1.59	0.04	0.18	10.3	0.51	91.6	6.39	1.61	3.43	5.04	0.01	0.28	0.01	0.33	0.01	0.05	1.83	0.06
BN-185-C1-G1_16_2	52.9	0.22	28.7	2.12	0.00	1.18	0.05	1.02	8.67	0.27	95.1	6.95	1.05	3.41	4.45	0.02	0.23	0.00	0.23	0.01	0.26	1.45	0.03
BN-185-C1-G1_16_4	48.0	0.13	29.6	4.15	0.04	3.00	0.09	0.14	9.82	0.29	95.3	6.47	1.53	3.16	4.69	0.01	0.47	0.00	0.60	0.01	0.04	1.69	0.03
BN-185-C1-G1_16_5	47.3	0.21	29.8	2.35	0.00	1.78	0.03	0.22	10.1	0.42	92.2	6.53	1.47	3.37	4.84	0.02	0.27	0.00	0.37	0.01	0.06	1.78	0.05
BN-185-C1-G1_17_1	52.5	0.24	22.7	4.75	0.00	0.94	0.03	4.46	5.61	0.16	91.4	7.27	0.73	2.97	3.70	0.02	0.55	0.00	0.19	0.00	1.20	0.99	0.02
BN-185-C1-G1_17_4	43.8	0.13	29.3	8.37	0.11	5.16	0.05	0.15	7.43	0.22	94.8	6.04	1.96	2.80	4.76	0.01	0.96	0.01	1.06	0.01	0.04	1.31	0.02
BN-185-C1-G1_17_5	47.7	0.11	29.0	2.42	0.00	1.88	0.03	0.30	10.1	0.38	92.0	6.61	1.39	3.34	4.73	0.01	0.28	0.00	0.39	0.00	0.08	1.79	0.04
BN-185-C1-G1_18_2	47.4	0.21	30.0	2.70	0.00	1.68	0.15	0.24	10.1	0.43	92.9	6.51	1.49	3.36	4.85	0.02	0.31	0.00	0.34	0.02	0.06	1.77	0.05
BN-185-C1-G1_18_4	48.2	0.18	29.1	2.48	0.00	1.90	0.02	0.09	9.99	0.24	92.2	6.63	1.37	3.36	4.73	0.02	0.29	0.00	0.39	0.00	0.02	1.75	0.03
BN-185-C1-G1_18_5	47.0	0.20	29.6	3.20	0.08	2.14	0.04	0.08	9.78	0.47	92.6	6.49	1.51	3.30	4.81	0.02	0.37	0.01	0.44	0.01	0.02	1.72	0.05
BN-185-C1-G1_19_1	52.2	0.10	25.8	2.42	0.00	1.51	0.00	3.77	7.04	0.41	93.2	7.04	0.96	3.14	4.10	0.01	0.27	0.00	0.30	0.00	0.99	1.21	0.04
BN-185-C1-G1_19_3	48.2	0.12	29.9	3.00	0.00	1.95	0.04	0.32	9.90	0.28	93.7	6.56	1.44	3.34	4.78	0.01	0.34	0.00	0.40	0.01	0.09	1.72	0.03
BN-185-C1-G1_19_5	48.0	0.12	29.6	2.49	0.08	1.93	0.06	0.18	9.72	0.14	92.2	6.59	1.41	3.38	4.79	0.01	0.29	0.01	0.40	0.01	0.05	1.70	0.02
BN-185-C1-G1_20_2	46.4	5.15	24.1	1.10	0.06	0.97	0.06	4.99	4.31	0.09	87.2	6.66	1.34	2.73	4.07	0.56	0.13	0.01	0.21	0.01	1.39	0.79	0.01
BN-185-C1-G1_20_3	43.3	0.30	27.6	7.82	0.10	3.28	0.05	0.18	8.05	0.10	90.8	6.24	1.76	2.91	4.68	0.03	0.94	0.01	0.70	0.01	0.05	1.48	0.01
BN-185-C1-G1_20_5	48.6	0.13	29.1	2.35	0.03	1.77	0.11	0.63	9.71	0.00	92.5	6.67	1.33	3.37	4.70	0.01	0.27	0.00	0.36	0.02	0.17	1.70	0.00
BN-185-C1-G1_21_2	48.2	0.12	30.2	2.12	0.01	1.69	0.06	0.19	10.5	0.42	93.4	6.56	1.44	3.40	4.84	0.01	0.24	0.00	0.34	0.01	0.05	1.82	0.05
BN-185-C1-G1_21_4	48.1	0.17	29.2	2.68	0.00	1.81	0.06	0.63	9.92	0.41	93.0	6.59	1.41	3.31	4.72	0.02	0.31	0.00	0.37	0.01	0.17	1.73	0.04
BN-185-C1-G1_21_5	45.3	0.14	27.5	6.90	0.00	4.79	0.06	0.07	8.21	0.42	93.4	6.30	1.70	2.81	4.51	0.02	0.80	0.00	0.99	0.01	0.02	1.46	0.05
BN-185-C1-G1_22_3	41.8	4.97	19.4	3.61	0.00	1.64	0.00	3.37	4.28	0.14	79.2	6.72	1.28	2.38	3.67	0.60	0.49	0.00	0.39	0.00	1.05	0.88	0.02
BN-185-C1-G1_23_3	52.7	0.12	26.4	1.74	0.02	1.43	0.00	3.54	7.09	0.48	93.5	7.06	0.94	3.22	4.16	0.01	0.19	0.00	0.28	0.00	0.92	1.21	0.05
BN-185-C1-G1_23_4	49.5	0.13	27.6	3.80	0.07	2.07	0.01	1.35	8.72	0.35	93.6	6.74	1.26	3.17	4.43	0.01	0.43	0.01	0.42	0.00	0.36	1.51	0.04
BN-185-C1-G1_23_5	41.4	0.08	13.5	21.71	0.18	8.85	0.00	0.00	0.08	0.00	85.9	6.58	1.42	1.12	2.53	0.01	2.88	0.02	2.10	0.00	0.00	0.02	0.00
BN-185-C1-G1_24_1	47.8	0.09	31.4	2.39	0.01	1.46	0.02	0.21	10.0	0.34	93.7	6.48	1.52	3.48	5.01	0.01	0.27	0.00	0.29	0.00	0.05	1.73	0.04
BN-185-C1-G1_24_3	46.0	0.06	29.7	4.42	0.00	3.71	0.04	0.09	9.24	0.33	93.6	6.32	1.68	3.12	4.80	0.01	0.51	0.00	0.76	0.01	0.02	1.62	0.04
BN-185-C1-G1_24_4	49.6	0.07	30.5	2.76	0.06	2.24	0.00	0.15	10.4	0.16	96.0	6.58	1.42	3.35	4.77	0.01	0.31	0.01	0.44	0.00	0.04	1.76	0.02
BN-185-C1-G1_25_1	46.2	0.00	28.7	3.95	0.00	2.26	0.01	0.30	9.35	0.22	91.0	6.50	1.50	3.26	4.76	0.00	0.47	0.00	0.47	0.00	0.08	1.68	0.02
BN-185-C1-G1_25_2	41.5	0.01	16.4	21.47	0.21	8.56	0.00	0.00	0.73	0.03	88.9	6.37	1.63	1.33	2.96	0.00	2.75	0.03	1.96	0.00	0.00	0.14	0.00
BN-185-C1-G1_25_3	47.1	0.06	29.5	2.58	0.05	2.05	0.03	0.16	10.4	0.23	92.1	6.52	1.48	3.34	4.82	0.01	0.30	0.01	0.42	0.00	0.04	1.84	0.03
BN-185-C1-G1_25_4	47.6	0.09	30.6	2.06	0.00	1.68	0.02	0.23	10.4	0.39	93.0	6.51	1.49	3.43	4.93	0.01	0.24	0.00	0.34	0.00	0.06	1.81	0.04
BN-185-C1-G1_26_3	50.2	0.06	31.9	2.16	0.00	1.73	0.06	0.18	10.3	0.38	97.0	6.55	1.45	3.46	4.91	0.01	0.24	0.00	0.34	0.01	0.04	1.72	0.04
BN-185-C1-G1_27_1	48.0	0.13	31.1	2.63	0.00	2.07	0.00	0.16	10.2	0.28	94.6	6.46	1.54	3.40	4.93	0.01	0.30	0.00	0.42	0.00	0.04	1.74	0.03
BN-185-C1-G1_28_3	48.7	0.02	30.6	2.23	0.00	1.51	0.00	0.17	10.5	0.54	94.2	6.57	1.43	3.43	4.86	0.00	0.25	0.00	0.30	0.00	0.05	1.80	0.06
BN-185-C1-G1_28_4	48.7	0.12	31.7	3.02	0.02	1.62	0.00	0.18	9.87	0.22	95.5	6.48	1.52	3.45	4.97	0.01	0.34	0.00	0.32	0.00	0.05	1.68	0.02
BN-185-C1-G1_29_2	47.7	0.04	31.1	2.35	0.03	1.52	0.07	0.16	10.0	0.26	93.3	6.49	1.51	3.48	4.99	0.00	0.27	0.00	0.31	0.01	0.04	1.74	0.03
BN-185-C1-G1_3_1	45.1	0.12	28.9	6.49	0.02	3.78	0.10	0.10	8.51	0.18	93.3	6.27	1.73	2.99	4.72	0.01	0.75	0.00	0.78	0.01	0.03	1.51	0.02
BN-185-C1-G1_3_2	50.2	0.22	29.9	2.72	0.03	1.88	0.02	0.81	9.95	0.34	96.0	6.64	1.36	3.31	4.66	0.02	0.30	0.00	0.37	0.00	0.21	1.68	0.04
BN-185-C1-G1_3_3	45.7	0.05	28.5	6.31	0.00	5.21	0.18	0.08	8.63	0.00	94.7	6.25	1.75	2.86	4.60	0.01	0.72	0.00	1.06	0.03	0.02	1.51	0.00
BN-185-C1-G1_3_5	49.3	0.20	31.1	2.67	0.00	2.20	0.12	0.42	10.3	0.30	96.6	6.50	1.50	3.33	4.83	0.02	0.30	0.00	0.43	0.02	0.11	1.73	0.03
BN-185-C1-G1_30_2	44.7	0.04	27.5	5.68	0.01	4.58	0.02	0.06	9.34	0.25	92.2	6.31	1.69	2.88	4.57	0.00	0.67	0.00	0.96	0.00	0.02	1.68	0.03
BN-185-C1-G1_30_3	47.3	0.00	29.5	4.50	0.00	2.93	0.11	0.19	9.65	0.19	94.4	6.44	1.56	3.18	4.74	0.00	0.51	0.00	0.59	0.02	0.05	1.68	0.02
BN-185-C1-G1_30_5	47.5	0.14	33.1	2.11	0.05	1.01	0.00	0.31	10.2	0.50	94.8	6.36	1.64	3.57	5.22	0.01	0.24	0.01	0.20	0.00	0.08	1.74	0.05
BN-185-C1-G1_4_1	48.7	0.03	30.6	2.63	0.00	2.25	0.09	0.15	10.2	0.35	95.1	6.52	1.48	3.36	4.83	0.00	0.29	0.00	0.45	0.01	0.04	1.74	0.04
BN-185-C1-G1_4_4	46.8	0.10	30.8	2.37	0.00	1.68	0.06	0.21	10.3	0.46	92.7	6.44	1.56	3.42	4.98	0.01	0.27	0.00	0.34	0.01	0.05	1.80	0.05
BN-185-C1-G1_5_2	46.5	0.14	29.3	4.41	0.00	2.55	0.01	0.11	9.93	0.32	93.3	6.42	1.58	3.19	4.77	0.01	0.51	0.00	0.53	0.00	0.03	1.75	0.03
BN-185-C1-G1_5_3	44.9	0.01	31.0	3.67	0.06	2.04	0.05	0.28	9.38	0.32	91.7	6.27	1.73	3.38	5.10	0.00	0.43	0.01	0.43	0.01	0.08	1.67	0.04
BN-185-C1-G1_5_4	43.7	0.02	30.3	5.69	0.06	2.71	0.08	0.12	8.51	0.33	91.5	6.16	1.84	3.21	5.05	0.00	0.67	0.01	0.57	0.01	0.03	1.53	0.04
BN-185-C1-G1_6_1	47.9	0.05	31.8	2.03	0.01	1.51	0.02	0.29	10.3	0.47	94.5	6.45	1.55	3.49	5.04	0.00	0.23	0.00	0.30	0.00	0.07	1.77	0.05
BN-185-C1-G1_6_2	48.6	0.11	30.6	2.23	0.03	1.68	0.06	0.12	10.5	0.41	94.3	6.55	1.45	3.41	4.87	0.01	0.25	0.00	0.34	0.01	0.03	1.81	0.04
BN-185-C1-G1_6_4	47.3	0.10	32.3	1.90	0.00	1.04	0.10	0.23	10.4	0.40	93.7	6.41	1.59	3.56	5.15	0.01	0.22	0.00	0.21	0.01	0.06	1.79	0.04
BN-185-C1-G1_6_5	42.7	0.23	20.6	21.05	0.05	5.89	0.01	3.36	1.77	0.03	95.7	6.14	1.86	1.63	3.50	0.02	2.53	0.01	1.26	0.00	0.94	0.32	0.00
BN-185-C1-G1_7_1	47.2	0.06	31.1	2.04	0.00	1.40	0.07	0.18	10.4	0.38	92.8	6.46	1.54	3.49	5.03	0.01	0.23	0.00	0.29	0.01	0.05	1.81	0.04
BN-185-C1-G1_7_2	50.2	0.03	29.0	2.39	0.00	2.34	0.01	0.17	10.5	0.14	94.7	6.72	1.28	3.31	4.59	0.00	0.27	0.00	0.47	0.00	0.04	1.79	0.01
BN-185-C1-G1_7_4	47.3	0.08	32.9	1.58	0.04	0.85	0.00	0.29	10.3	0.49	93.8	6.39	1.61	3.62	5.24	0.01	0.18	0.00	0.17	0.00	0.07	1.77	0.05
BN-185-C1-G1_7_5	47.0	0.06	29.3	3.50	0.03	2.35	0.00	0.19	10.3	0.53	93.3	6.47	1.53	3.23	4.76	0.01	0.40	0.00	0.48	0.00	0.05	1.81	0.06
BN-185-C1-G1_8_1	46.8	0.10	28.8	3.98	0.01	2.03	0.00	0.12	9.75	0.19	91.8	6.53	1.47	3.27	4.74	0.01	0.46	0.00	0.42	0.00	0.03	1.74	0.02
BN-185-C1-G1_8_2	47.3	0.06	29.2	3.15	0.02	2.06	0.06	0.36	9.73	0.35	92.2	6.54	1.46	3.30	4.76	0.01	0.36	0.00	0.42	0.01	0.10	1.72	0.04
BN-185-C1-G1_8_3	51.0	0.10	26.1	3.85	0.00	2.25	0.06	2.95	7.31	0.15	93.8	6.90	1.10	3.06	4.16	0.01	0.44	0.00	0.45	0.01	0.77	1.26	0.02
BN-185-C1-G1_8_4	45.0	0.09	28.4	4.34	0.00	2.52	0.08	0.12	9.37	0.22	90.1	6.42	1.58	3.20	4.77	0.01	0.52	0.00	0.54	0.01	0.03	1.71	0.02
BN-185-C1-G1_9_1	43.1	0.12	28.7	10.85	0.01	2.71	0.07	0.10	7.52	0.29	93.4	6.10	1.90	2.88	4.78	0.01	1.28	0.00	0.57	0.01	0.03	1.36	0.03
BN-185-C1-G1_9_2	47.4	0.03	29.5	2.23	0.04	1.81	0.02	0.18	10.1	0.00	91.3	6.59	1.41	3.42	4.83	0.00	0.26	0.00	0.38	0.00	0.05	1.79	0.00
BN-185-C1-G1_9_4	43.1	0.00	28.6	8.11	0.03	3.72	0.02	0.05	7.77	0.16	91.5	6.14	1.86	2.95	4.80	0.00	0.97	0.00	0.79	0.00	0.02	1.41	0.02
BN-185-C1-G1_9_5	49.3	0.05	30.3	3.41	0.06	2.78	0.01	0.15	9.75	0.15	96.0	6.54	1.46	3.28	4.74	0.00	0.38	0.01	0.55	0.00	0.04	1.65	0.02
BN-185-C3-1	49.0	0.07	31.2	2.27	0.04	1.57	0.01	0.21	10.2	0.70	95.3	6.53	1.47	3.43	4.90	0.01	0.25	0.00	0.31	0.00	0.05	1.73	0.07
BN-185-C3-102	49.8	0.20	30.3	3.27	0.03	2.23	0.00	0.31	9.33	0.00	95.4	6.61	1.39	3.35	4.74	0.02	0.36	0.00	0.44	0.00	0.08	1.58	0.00
BN-185-C3-11	47.0	0.11	29.8	4.63	0.03	2.50	0.01	0.31	9.28	0.44	94.1	6.41	1.59	3.21	4.80	0.01	0.53	0.00	0.51	0.00	0.08	1.62	0.05
BN-185-C3-12	47.4	0.02	31.3	3.12	0.02	1.48	0.05	0.23	10.3	0.58	94.4	6.42	1.58	3.41	4.99	0.00	0.35	0.00	0.30	0.01	0.06	1.77	0.06
BN-185-C3-13	44.8	0.09	29.7	6.24	0.02	2.72	0.03	0.22	9.12	0.42	93.3	6.24	1.76	3.11	4.87	0.01	0.73	0.00	0.56	0.00	0.06	1.62	0.05
BN-185-C3-17	48.2	0.09	31.4	2.43	0.07	1.52	0.00	0.33	9.87	0.73	94.7	6.47	1.53	3.44	4.97	0.01	0.27	0.01	0.30	0.00	0.09	1.69	0.08
BN-185-C3-2	48.5	0.01	31.0	2.11	0.02	1.85	0.03	0.26	10.4	0.31	94.5	6.52	1.48	3.43	4.91	0.00	0.24	0.00	0.37	0.00	0.07	1.78	0.03
BN-185-C3-20	47.1	0.08	29.7	2.30	0.05	1.64	0.00	0.17	10.5	0.43	92.1	6.53	1.47	3.39	4.86	0.01	0.27	0.01	0.34	0.00	0.05	1.86	0.05
BN-185-C3-21	48.2	0.15	30.1	2.85	0.04	1.87	0.03	0.09	10.1	0.27	93.7	6.55	1.45	3.37	4.82	0.02	0.32	0.00	0.38	0.00	0.02	1.76	0.03
BN-185-C3-22	48.7	0.10	31.4	2.39	0.05	1.56	0.10	0.14	10.3	0.28	95.1	6.51	1.49	3.46	4.94	0.01	0.27	0.01	0.31	0.01	0.03	1.76	0.03
BN-185-C3-23	47.5	0.06	30.5	2.11	0.03	1.46	0.09	0.20	10.5	0.39	92.8	6.52	1.48	3.44	4.92	0.01	0.24	0.00	0.30	0.01	0.05	1.84	0.04
BN-185-C3-24	47.0	0.09	30.5	2.00	0.05	1.39	0.02	0.18	10.4	0.51	92.2	6.49	1.51	3.46	4.97	0.01	0.23	0.01	0.29	0.00	0.05	1.84	0.06
BN-185-C3-25	47.2	0.04	30.8	2.10	0.04	1.47	0.02	0.29	10.6	0.45	93.0	6.47	1.53	3.45	4.98	0.00	0.24	0.01	0.30	0.00	0.08	1.85	0.05
BN-185-C3-26	48.1	0.14	31.7	2.01	0.03	1.44	0.08	0.26	10.7	0.39	94.9	6.46	1.54	3.47	5.01	0.01	0.22	0.00	0.29	0.01	0.07	1.83	0.04
BN-185-C3-27	49.2	0.13	31.0	2.41	0.00	1.88	0.12	0.17	10.0	0.25	95.2	6.55	1.45	3.42	4.87	0.01	0.27	0.00	0.37	0.02	0.04	1.70	0.03
BN-185-C3-3	48.1	0.07	29.8	4.18	0.04	2.33	0.06	0.08	9.47	0.47	94.6	6.50	1.50	3.25	4.75	0.01	0.47	0.00	0.47	0.01	0.02	1.63	0.05
BN-185-C3-30	44.4	0.05	29.4	5.01	0.05	2.61	0.11	0.18	9.33	0.57	91.7	6.26	1.74	3.16	4.89	0.00	0.59	0.01	0.55	0.02	0.05	1.68	0.06
BN-185-C3-31	48.4	0.09	31.8	2.25	0.01	1.52	0.00	0.36	10.3	0.31	95.0	6.47	1.53	3.48	5.01	0.01	0.25	0.00	0.30	0.00	0.09	1.75	0.03
BN-185-C3-32	48.9	0.11	31.5	2.51	0.09	1.73	0.04	0.39	9.90	0.25	95.4	6.50	1.50	3.44	4.94	0.01	0.28	0.01	0.34	0.01	0.10	1.68	0.03
BN-185-C3-33	47.7	0.08	31.9	3.24	0.02	1.61	0.05	0.17	8.98	0.35	94.2	6.42	1.58	3.48	5.06	0.01	0.36	0.00	0.32	0.01	0.05	1.54	0.04
BN-185-C3-34	47.5	0.02	31.2	2.25	0.00	1.44	0.12	0.18	10.7	0.68	94.0	6.44	1.56	3.44	4.99	0.00	0.26	0.00	0.29	0.02	0.05	1.85	0.07
BN-185-C3-35	46.1	0.09	31.4	2.47	0.02	1.21	0.08	0.27	10.1	0.44	92.2	6.37	1.63	3.50	5.12	0.01	0.29	0.00	0.25	0.01	0.07	1.78	0.05
BN-185-C3-36	48.6	0.09	31.3	2.77	0.03	1.92	0.00	0.35	10.1	0.18	95.3	6.49	1.51	3.41	4.92	0.01	0.31	0.00	0.38	0.00	0.09	1.72	0.02

Analysis	SiO_2	TiO_2	Al_2O_3	FeO	MnO	MgO	CaO	Na2O	K_2O	Cr_2O_3	Total	Si	Al^{IV}	Al^{VI}	Al	Ti	Fe^{2+}	Mn^{2+}	Mg	Ca	Na	K	Cr
BN185	Mica																						
BN-185-C3-37	50.4	0.13	33.0	2.53	0.04	1.66	0.00	0.24	8.35	0.00	96.3	6.55	1.45	3.59	5.04	0.01	0.27	0.00	0.32	0.00	0.06	1.38	0.00
BN-185-C3-38	47.5	0.10	31.1	2.20	0.00	1.39	0.03	0.18	9.22	0.33	92.1	6.51	1.49	3.54	5.03	0.01	0.25	0.00	0.28	0.00	0.05	1.61	0.04
BN-185-C3-39	48.1	0.05	31.2	2.14	0.05	1.61	0.01	0.16	10.7	0.41	94.4	6.49	1.51	3.45	4.96	0.01	0.24	0.01	0.32	0.00	0.04	1.83	0.04
BN-185-C3-4	48.9	0.04	28.8	3.36	0.00	1.77	0.00	1.47	8.84	0.30	93.4	6.65	1.35	3.27	4.62	0.00	0.38	0.00	0.36	0.00	0.39	1.54	0.03
BN-185-C3-40	47.8	0.04	31.0	2.62	0.00	2.18	0.01	0.24	10.1	0.46	94.4	6.45	1.55	3.38	4.93	0.00	0.30	0.00	0.44	0.00	0.06	1.73	0.05
BN-185-C3-41	46.9	0.04	30.5	2.86	0.08	1.79	0.00	0.25	10.3	0.31	93.1	6.44	1.56	3.39	4.94	0.00	0.33	0.01	0.37	0.00	0.07	1.80	0.03
BN-185-C3-42	48.3	0.07	30.8	2.13	0.03	1.96	0.00	0.18	10.1	0.31	93.9	6.52	1.48	3.43	4.91	0.01	0.24	0.00	0.39	0.00	0.05	1.75	0.03
BN-185-C3-43	48.7	0.09	32.5	2.05	0.00	1.32	0.07	0.24	10.4	0.52	95.9	6.45	1.55	3.51	5.06	0.01	0.23	0.00	0.26	0.01	0.06	1.75	0.05
BN-185-C3-44	48.0	0.02	31.0	2.17	0.03	1.60	0.08	0.31	10.5	0.17	93.9	6.51	1.49	3.46	4.95	0.00	0.25	0.00	0.32	0.01	0.08	1.81	0.02
BN-185-C3-47	49.2	0.03	31.5	2.32	0.08	1.58	0.00	0.15	10.5	0.30	95.7	6.53	1.47	3.46	4.93	0.00	0.26	0.01	0.31	0.00	0.04	1.78	0.03
BN-185-C3-48	48.5	0.09	31.4	2.59	0.02	2.00	0.06	0.28	10.1	0.27	95.3	6.47	1.53	3.40	4.93	0.01	0.29	0.00	0.40	0.01	0.07	1.72	0.03
BN-185-C3-49	48.0	0.10	31.5	2.09	0.00	1.45	0.02	0.30	10.4	0.37	94.2	6.48	1.52	3.48	5.00	0.01	0.24	0.00	0.29	0.00	0.08	1.79	0.04
BN-185-C3-5	48.3	0.07	30.6	2.52	0.03	1.98	0.06	0.21	10.2	0.28	94.2	6.52	1.48	3.39	4.87	0.01	0.28	0.00	0.40	0.01	0.05	1.75	0.03
BN-185-C3-50	47.7	0.13	32.4	2.24	0.01	1.30	0.05	0.18	9.85	0.43	94.4	6.41	1.59	3.54	5.13	0.01	0.25	0.00	0.26	0.01	0.05	1.69	0.05
BN-185-C3-51	47.9	0.01	30.3	2.55	0.01	1.69	0.04	0.23	10.6	0.66	94.0	6.51	1.49	3.36	4.85	0.00	0.29	0.00	0.34	0.01	0.06	1.85	0.07
BN-185-C3-53	45.5	0.04	30.6	5.06	0.05	3.98	0.02	0.10	8.82	0.22	94.4	6.21	1.79	3.12	4.91	0.00	0.58	0.01	0.81	0.00	0.03	1.53	0.02
BN-185-C3-56	47.4	0.08	32.3	2.54	0.04	1.25	0.05	0.23	10.19	0.50	94.6	6.38	1.62	3.51	5.13	0.01	0.29	0.00	0.25	0.01	0.06	1.75	0.05
BN-185-C3-57	47.7	0.00	31.2	2.53	0.02	1.59	0.05	0.28	10.5	0.42	94.3	6.45	1.55	3.43	4.98	0.00	0.29	0.00	0.32	0.01	0.07	1.82	0.04
BN-185-C3-59	49.0	0.07	30.0	3.01	0.06	2.26	0.05	0.12	9.95	0.98	95.5	6.54	1.46	3.26	4.72	0.01	0.34	0.01	0.45	0.01	0.03	1.70	0.10
BN-185-C3-6	48.7	0.16	30.7	2.40	0.01	1.68	0.02	0.27	9.83	0.16	93.9	6.57	1.43	3.44	4.88	0.02	0.27	0.00	0.34	0.00	0.07	1.69	0.02
BN-185-C3-62	41.0	0.14	26.9	14.08	0.15	6.41	0.04	0.06	5.85	0.11	94.7	5.81	2.19	2.31	4.50	0.02	1.67	0.02	1.35	0.01	0.02	1.06	0.01
BN-185-C3-64	46.1	0.01	28.8	7.71	0.05	2.98	0.00	1.67	7.47	0.31	95.1	6.31	1.69	2.95	4.64	0.00	0.88	0.01	0.61	0.00	0.44	1.30	0.03
BN-185-C3-65	48.5	0.11	29.9	2.59	0.00	1.89	0.03	0.15	10.5	0.59	94.2	6.57	1.43	3.33	4.77	0.01	0.29	0.00	0.38	0.00	0.04	1.80	0.06
BN-185-C3-69	43.4	0.07	29.5	8.57	0.12	4.00	0.06	0.16	7.73	0.34	94.0	6.05	1.95	2.90	4.85	0.01	1.00	0.01	0.83	0.01	0.04	1.37	0.04
BN-185-C3-7	49.2	0.10	29.9	2.55	0.00	1.91	0.07	0.18	9.82	1.61	95.3	6.57	1.43	3.27	4.70	0.01	0.28	0.00	0.38	0.01	0.05	1.67	0.17
BN-185-C3-70	47.6	0.11	30.8	2.59	0.02	1.62	0.05	0.21	10.4	0.54	93.9	6.47	1.53	3.40	4.93	0.01	0.29	0.00	0.33	0.01	0.06	1.80	0.06
BN-185-C3-74	41.5	0.08	26.9	11.99	0.08	6.11	0.12	0.03	6.79	0.27	93.9	5.90	2.10	2.41	4.51	0.01	1.42	0.01	1.30	0.02	0.01	1.23	0.03
BN-185-C3-75	44.9	0.05	30.5	6.52	0.09	3.01	0.01	0.17	8.66	0.39	94.4	6.17	1.83	3.12	4.95	0.01	0.75	0.01	0.62	0.00	0.05	1.52	0.04
BN-185-C3-76	46.4	0.05	29.1	4.26	0.01	3.13	0.08	0.13	9.21	0.38	92.7	6.42	1.58	3.16	4.74	0.00	0.49	0.00	0.64	0.01	0.03	1.63	0.04
BN-185-C3-77	48.4	0.02	31.6	2.59	0.03	1.64	0.03	0.30	10.3	0.43	95.4	6.46	1.54	3.43	4.97	0.00	0.29	0.00	0.33	0.00	0.08	1.76	0.04
BN-185-C3-78	47.1	0.09	31.1	2.34	0.00	1.60	0.09	0.28	10.1	0.56	93.3	6.43	1.57	3.44	5.01	0.01	0.27	0.00	0.33	0.01	0.07	1.75	0.06
BN-185-C3-79	45.7	0.00	31.8	10.11	0.02	1.80	0.02	0.23	6.09	0.56	96.4	6.14	1.86	3.19	5.05	0.00	1.14	0.00	0.36	0.00	0.06	1.04	0.06
BN-185-C3-80	47.9	0.06	30.0	3.07	0.00	1.97	0.00	0.12	10.6	0.28	94.0	6.52	1.48	3.33	4.81	0.01	0.35	0.00	0.40	0.00	0.03	1.84	0.03
BN-185-C3-85	48.8	0.08	31.3	2.17	0.00	1.52	0.02	0.19	10.2	0.34	94.6	6.53	1.47	3.48	4.94	0.01	0.24	0.00	0.30	0.00	0.05	1.74	0.04
BN-185-C3-87	49.5	0.05	31.4	2.08	0.00	1.75	0.00	0.10	10.4	0.52	95.8	6.55	1.45	3.45	4.90	0.01	0.23	0.00	0.34	0.00	0.03	1.75	0.05
BN-185-C3-89	48.0	0.03	31.2	2.32	0.00	1.59	0.06	0.32	10.5	0.32	94.3	6.48	1.52	3.44	4.96	0.00	0.26	0.00	0.32	0.01	0.08	1.81	0.03
BN-185-C3-93	47.6	0.02	30.8	3.17	0.00	1.98	0.09	0.17	10.4	0.56	94.9	6.43	1.57	3.33	4.90	0.00	0.36	0.00	0.40	0.01	0.05	1.80	0.06
BN-185-C3-94	49.3	0.02	30.1	2.63	0.10	1.98	0.05	0.14	10.2	0.48	95.0	6.60	1.40	3.35	4.74	0.00	0.29	0.01	0.40	0.01	0.04	1.74	0.05
BN-185-C3-95	48.2	0.06	31.1	2.45	0.02	1.60	0.02	0.28	10.5	0.63	94.8	6.48	1.52	3.41	4.93	0.01	0.28	0.00	0.32	0.00	0.07	1.80	0.07
BN-185-C3-96	45.1	0.10	28.5	6.02	0.00	3.17	0.08	0.18	8.67	0.28	92.1	6.33	1.67	3.05	4.72	0.01	0.71	0.00	0.66	0.01	0.05	1.56	0.03
BN-185-C3-99	47.8	0.06	30.5	2.85	0.03	2.07	0.03	0.31	10.1	0.00	93.8	6.50	1.50	3.38	4.88	0.01	0.32	0.00	0.42	0.00	0.08	1.75	0.00
BN-185-C4-1	44.9	0.04	27.4	8.12	0.05	3.17	0.00	0.14	8.36	0.34	92.5	6.34	1.66	2.90	4.56	0.00	0.96	0.01	0.67	0.00	0.04	1.51	0.04
BN-185-C4-100	48.8	0.06	31.3	2.47	0.02	1.56	0.14	0.25	10.6	0.49	95.7	6.50	1.50	3.42	4.92	0.01	0.28	0.00	0.31	0.02	0.06	1.80	0.05
BN-185-C4-105	45.7	0.10	30.1	3.87	0.01	2.50	0.19	0.18	9.37	0.23	92.3	6.34	1.66	3.28	4.93	0.01	0.45	0.00	0.52	0.03	0.05	1.66	0.03
BN-185-C4-108	46.5	0.07	31.3	3.28	0.04	1.63	0.16	0.25	9.42	0.59	93.2	6.36	1.64	3.41	5.05	0.01	0.38	0.00	0.33	0.02	0.07	1.65	0.06
BN-185-C4-109	47.4	0.04	32.2	2.14	0.00	1.24	0.12	0.28	9.89	0.32	93.6	6.42	1.58	3.55	5.14	0.00	0.24	0.00	0.25	0.02	0.07	1.71	0.03
BN-185-C4-112	48.6	0.08	32.6	2.88	0.02	1.80	0.09	0.32	9.55	0.41	96.4	6.40	1.60	3.46	5.06	0.01	0.32	0.00	0.35	0.01	0.08	1.60	0.04
BN-185-C4-120	46.5	0.08	30.1	4.31	0.03	2.28	0.07	0.23	9.27	0.10	92.9	6.41	1.59	3.29	4.88	0.01	0.50	0.00	0.47	0.01	0.06	1.63	0.01
BN-185-C4-126	48.5	0.03	31.4	3.46	0.04	1.71	0.21	0.15	9.82	0.48	95.8	6.46	1.54	3.39	4.93	0.00	0.39	0.00	0.34	0.03	0.04	1.67	0.05
BN-185-C4-134	48.2	0.00	31.6	2.43	0.04	1.54	0.03	0.28	10.5	0.53	95.2	6.45	1.55	3.44	4.99	0.00	0.27	0.01	0.31	0.00	0.07	1.80	0.06
BN-185-C4-135	52.0	0.02	33.6	2.51	0.01	1.65	0.00	0.13	6.79	0.00	96.7	6.63	1.37	3.69	5.05	0.00	0.27	0.00	0.31	0.00	0.03	1.10	0.00
BN-185-C4-136	47.2	0.03	29.5	2.52	0.00	1.49	0.11	0.17	9.92	0.50	91.5	6.56	1.44	3.41	4.84	0.00	0.29	0.00	0.31	0.02	0.05	1.76	0.06
BN-185-C4-137	46.9	0.08	30.9	3.15	0.02	2.10	0.09	0.27	9.96	0.21	93.7	6.40	1.60	3.36	4.96	0.01	0.36	0.00	0.43	0.01	0.07	1.73	0.02
BN-185-C4-141	46.7	0.07	30.0	2.94	0.01	2.24	0.03	0.16	9.79	0.37	92.3	6.45	1.55	3.34	4.89	0.01	0.34	0.00	0.46	0.01	0.04	1.72	0.04
BN-185-C4-143	49.0	0.11	31.5	2.50	0.00	1.87	0.09	0.29	10.3	0.26	95.9	6.50	1.50	3.42	4.92	0.01	0.28	0.00	0.37	0.01	0.07	1.73	0.03
BN-185-C4-144	40.3	0.06	26.0	12.46	0.02	5.50	0.11	0.28	5.96	0.33	91.1	5.92	2.08	2.42	4.50	0.01	1.53	0.00	1.20	0.02	0.08	1.12	0.04
BN-185-C4-2	47.0	0.00	31.9	2.21	0.01	1.21	0.12	0.43	10.7	0.28	93.7	6.39	1.61	3.51	5.11	0.00	0.25	0.00	0.25	0.02	0.11	1.85	0.03
BN-185-C4-20	46.7	0.02	31.1	2.96	0.05	1.48	0.05	0.39	10.5	0.41	93.6	6.39	1.61	3.41	5.02	0.00	0.34	0.01	0.30	0.01	0.10	1.84	0.04
BN-185-C4-21	47.7	0.01	30.3	2.85	0.00	1.75	0.09	0.43	10.8	0.24	94.2	6.49	1.51	3.35	4.86	0.00	0.32	0.00	0.36	0.01	0.11	1.87	0.03
BN-185-C4-3	47.1	0.06	31.4	2.28	0.00	1.18	0.09	0.50	10.3	0.53	93.5	6.42	1.58	3.47	5.05	0.01	0.26	0.00	0.24	0.01	0.13	1.80	0.06
BN-185-C4-34	49.3	0.04	18.0	11.26	0.08	5.63	0.07	0.06	5.82	0.13	90.4	7.12	0.88	2.18	3.07	0.00	1.36	0.01	1.21	0.01	0.02	1.07	0.02
BN-185-C4-39	42.7	0.08	25.6	8.78	0.08	7.64	0.18	0.11	7.83	0.36	93.4	6.05	1.95	2.33	4.28	0.01	1.04	0.01	1.61	0.03	0.03	1.41	0.04
BN-185-C4-4	48.7	0.05	31.8	2.58	0.01	1.59	0.05	0.26	10.5	0.74	96.2	6.45	1.55	3.41	4.96	0.00	0.29	0.00	0.32	0.01	0.07	1.77	0.08
BN-185-C4-48	45.5	0.08	29.7	4.13	0.06	2.20	0.06	0.26	9.46	0.39	91.8	6.37	1.63	3.26	4.90	0.01	0.48	0.01	0.46	0.01	0.07	1.69	0.04
BN-185-C4-56	46.6	0.07	30.8	4.81	0.09	2.43	0.16	0.21	9.41	0.11	94.6	6.33	1.67	3.26	4.93	0.01	0.55	0.01	0.49	0.02	0.06	1.63	0.01
BN-185-C4-59	42.4	0.11	26.6	11.80	0.04	5.21	0.06	0.86	6.34	0.70	94.2	6.00	2.00	2.44	4.44	0.01	1.40	0.00	1.10	0.01	0.24	1.14	0.08
BN-185-C4-60	48.3	0.22	31.1	2.62	0.00	1.40	0.08	0.24	9.90	0.54	94.4	6.50	1.50	3.43	4.94	0.02	0.29	0.00	0.28	0.01	0.06	1.70	0.06
BN-185-C4-62	48.4	0.08	32.3	2.21	0.02	1.46	0.06	0.14	10.5	0.51	95.6	6.43	1.57	3.49	5.06	0.01	0.25	0.00	0.29	0.01	0.04	1.78	0.05
BN-185-C4-63	47.7	0.12	31.5	2.51	0.00	1.59	0.15	0.13	10.2	0.38	94.3	6.44	1.56	3.45	5.01	0.01	0.28	0.00	0.32	0.02	0.03	1.75	0.04
BN-185-C4-64	41.9	0.07	26.0	8.53	0.05	7.72	0.10	0.06	7.57	0.38	92.4	5.99	2.01	2.36	4.38	0.01	1.02	0.01	1.64	0.01	0.02	1.38	0.04
BN-185-C4-78	44.1	0.03	28.3	7.11	0.07	4.42	0.09	0.14	8.79	0.03	93.1	6.19	1.81	2.87	4.68	0.00	0.83	0.01	0.92	0.01	0.04	1.57	0.00
BN-185-C4-91	46.0	0.04	28.4	5.49	0.06	3.97	0.16	0.05	9.23	0.60	94.0	6.34	1.66	2.95	4.61	0.00	0.63	0.01	0.82	0.02	0.01	1.62	0.07
BN185-G1_1_1	41.7	0.04	27.8	9.43	0.10	4.75	0.00	0.06	7.52	0.47	91.9	5.99	2.01	2.70	4.71	0.00	1.13	0.01	1.02	0.00	0.02	1.38	0.05
BN185-G1_1_10	42.8	0.21	26.5	7.21	0.03	3.35	0.05	0.00	7.77	0.23	88.2	6.31	1.69	2.92	4.61	0.02	0.89	0.00	0.74	0.01	0.00	1.46	0.03
BN185-G1_1_11	40.3	0.09	27.8	11.47	0.00	5.90	0.09	0.05	6.46	0.24	92.4	5.80	2.20	2.52	4.72	0.01	1.38	0.00	1.26	0.01	0.01	1.19	0.03
BN185-G1_1_15	44.4	0.26	28.7	6.16	0.00	3.48	0.08	0.07	8.86	0.37	92.4	6.24	1.76	3.00	4.75	0.03	0.72	0.00	0.73	0.01	0.02	1.59	0.04
BN185-G1_1_16	46.2	0.19	29.6	4.71	0.00	2.76	0.15	0.27	9.42	0.31	93.6	6.36	1.64	3.16	4.80	0.02	0.54	0.00	0.57	0.02	0.07	1.65	0.03
BN185-G1_1_17	48.4	0.12	30.4	3.61	0.00	2.06	0.00	0.24	10.0	0.26	95.2	6.50	1.50	3.32	4.82	0.01	0.40	0.00	0.41	0.00	0.06	1.72	0.03
BN185-G1_1_18	47.8	0.12	31.0	3.14	0.00	1.94	0.08	0.31	10.2	0.19	94.8	6.45	1.55	3.37	4.92	0.01	0.35	0.00	0.39	0.01	0.08	1.75	0.02
BN185-G1_1_19	46.9	0.13	30.2	3.87	0.00	2.13	0.08	0.46	9.73	0.54	94.0	6.40	1.60	3.26	4.86	0.01	0.44	0.00	0.43	0.01	0.12	1.70	0.06
BN185-G1_1_2	45.0	0.19	29.7	5.34	0.05	3.35	0.06	0.21	8.91	0.40	93.2	6.24	1.76	3.09	4.86	0.02	0.62	0.01	0.69	0.01	0.06	1.57	0.04
BN185-G1_1_20	51.1	0.18	25.8	4.65	0.00	1.90	0.05	3.05	6.62	0.42	93.8	6.92	1.08	3.03	4.11	0.02	0.53	0.00	0.38	0.01	0.80	1.14	0.04
BN185-G1_1_5	44.3	0.14	28.5	6.73	0.08	3.68	0.14	0.12	8.63	0.25	92.6	6.23	1.77	2.95	4.72	0.01	0.79	0.01	0.77	0.02	0.03	1.55	0.03
BN185-G1_1_6	40.9	0.09	27.3	10.91	0.09	6.03	0.16	0.00	6.80	0.24	92.6	5.88	2.12	2.50	4.62	0.01	1.31	0.01	1.29	0.03	0.00	1.24	0.03
BN185-G1_1_8	42.2	0.15	28.4	9.88	0.08	5.05	0.02	0.12	7.27	0.43	93.5	5.95	2.05	2.67	4.72	0.02	1.17	0.01	1.06	0.00	0.03	1.31	0.05
BN185-G1_1_9	40.7	0.13	27.6	10.33	0.05	5.45	0.04	0.04	7.29	0.08	91.7	5.89	2.11	2.60	4.70	0.01	1.25	0.01	1.18	0.01	0.01	1.35	0.01
BN185-G1_2_1	48.1	0.14	31.1	3.35	0.00	1.65	0.03	0.18	10.1	0.51	95.1	6.46	1.54	3.38	4.92	0.01	0.38	0.00	0.33	0.00	0.05	1.72	0.05
BN185-G1_2_15	47.3	0.17	30.4	4.57	0.09	2.60	0.11	0.22	9.42	0.35	95.3	6.38	1.62	3.21	4.83	0.02	0.52	0.01	0.52	0.02	0.06	1.62	0.04
BN185-G1_2_16	50.4	0.09	30.0	2.58	0.00	2.06	0.00	0.08	10.6	0.22	96.1	6.67	1.33	3.34	4.68	0.01	0.29	0.00	0.41	0.00	0.02	1.79	0.02
BN185-G1_2_17	50.8	0.10	30.0	2.52	0.14	1.99	0.13	0.42	10.2	0.27	96.5	6.68	1.32	3.33	4.65	0.01	0.28	0.02	0.39	0.02	0.11	1.71	0.03
BN185-G1_2_2	48.3	0.11	31.5	2.57	0.00	1.63	0.05	0.27	10.5	0.30	95.2	6.46	1.54	3.43	4.97	0.01	0.29	0.00	0.32	0.01	0.07	1.80	0.03
BN185-G1_2_3	47.8	0.08	32.5	2.53	0.02	1.48	0.00	0.30	10.5	0.34	95.5	6.38	1.62	3.49	5.10	0.01	0.28	0.00	0.29	0.00	0.08	1.79	0.04
BN185-G1_2_4	47.2	0.09	31.7	2.53	0.00	1.41	0.09	0.20	10.5	0.62	94.3	6.39	1.61	3.45	5.05	0.01	0.29	0.00	0.28	0.01	0.05	1.82	0.07
BN185-G1_2_5	47.7	0.13	31.2	2.76	0.00	1.68	0.02	0.26	10.1	0.74	94.7	6.43	1.57	3.39	4.96	0.01	0.31	0.00	0.34	0.00	0.07	1.74	0.08
BN185-G1_2_6	42.3	0.20	27.3	10.12	0.04	5.20	0.08	0.14	7.16	0.41	92.9	6.01	1.99	2.59	4.58	0.02	1.20	0.00	1.10	0.01	0.04	1.30	0.05
BN185-G1_2_7	42.9	0.06	28.4	8.20	0.04	5.35	0.04	0.11	7.75	0.55	93.4	6.02	1.98	2.72	4.70	0.01	0.96	0.00	1.12	0.01	0.03	1.39	0.06
BN185-G1_3_1	46.9	0.12	31.1	2.44	0.05	1.39	0.12	0.39	10.3	0.26	93.1	6.42	1.58	3.45	5.03	0.01	0.28	0.01	0.29	0.02	0.10	1.80	0.03
BN185-G1_3_10	43.7	0.07	27.6	8.59	0.03	5.07	0.00	0.07	7.77	0.00	92.9	6.16	1.84	2.74	4.58	0.01	1.01	0.00	1.07	0.00	0.02	1.40	0.00

Analysis	SiO_2	TiO_2	Al_2O_3	FeO	MnO	MgO	CaO	Na2O	K_2O	Cr_2O_3	Total	Si	Al^{IV}	Al^{VI}	Al	Ti	Fe^{2+}	Mn^{2+}	Mg	Ca	Na	K	Cr
BN185	**Mica**																						
BN185-G1_3_14	43.1	0.10	28.1	8.71	0.09	5.28	0.12	0.07	7.67	0.39	93.7	6.05	1.95	2.69	4.65	0.01	1.02	0.01	1.10	0.02	0.02	1.37	0.04
BN185-G1_3_16	45.0	0.00	27.7	5.94	0.04	3.24	0.18	0.05	9.29	0.51	91.9	6.36	1.64	2.98	4.62	0.00	0.70	0.01	0.68	0.03	0.01	1.68	0.06
BN185-G1_3_2	49.3	0.12	30.5	2.55	0.00	1.98	0.06	0.12	10.4	0.08	95.1	6.58	1.42	3.39	4.81	0.01	0.28	0.00	0.39	0.01	0.03	1.77	0.01
BN185-G1_3_3	48.2	0.04	30.5	2.96	0.00	1.95	0.15	0.20	10.5	0.30	94.9	6.50	1.50	3.34	4.85	0.00	0.33	0.00	0.39	0.02	0.05	1.81	0.03
BN185-G1_3_4	47.5	0.09	29.2	3.18	0.00	1.76	0.07	0.81	9.92	0.34	92.9	6.55	1.45	3.29	4.74	0.01	0.37	0.00	0.36	0.01	0.22	1.74	0.04
BN185-G1_3_5	48.9	0.18	25.2	5.07	0.00	2.87	0.00	2.49	7.15	0.26	92.0	6.79	1.21	2.91	4.12	0.02	0.59	0.00	0.60	0.00	0.67	1.27	0.03
BN185-G1_3_6	45.3	0.26	24.1	8.51	0.01	4.38	0.00	1.85	5.58	0.00	90.0	6.53	1.47	2.62	4.09	0.03	1.03	0.00	0.94	0.00	0.52	1.03	0.00
BN185-G1_3_7	42.5	0.15	26.7	10.69	0.00	5.10	0.14	0.74	5.94	0.26	92.2	6.08	1.92	2.57	4.49	0.02	1.28	0.00	1.09	0.02	0.20	1.08	0.03
BN185-G1_3_8	43.3	0.10	28.6	8.72	0.00	4.54	0.06	0.20	7.49	0.20	93.2	6.08	1.92	2.81	4.73	0.01	1.02	0.00	0.95	0.01	0.06	1.34	0.02
BN185-G1_3_9	44.5	0.06	28.5	5.81	0.07	3.27	0.00	0.12	9.19	0.58	92.0	6.28	1.72	3.02	4.74	0.01	0.69	0.01	0.69	0.00	0.03	1.65	0.06
BN185-G1_4_1	47.5	0.06	33.0	2.12	0.05	0.97	0.20	0.34	10.4	0.63	95.3	6.35	1.65	3.54	5.19	0.01	0.24	0.01	0.19	0.03	0.09	1.77	0.07
BN185-G1_4_2	47.6	0.14	32.8	2.12	0.09	1.00	0.13	0.37	10.3	0.50	95.0	6.37	1.63	3.54	5.17	0.01	0.24	0.01	0.20	0.02	0.10	1.76	0.05
BN185-G1_4_3	47.9	0.09	32.1	2.49	0.00	1.35	0.21	0.27	10.1	0.41	94.9	6.42	1.58	3.49	5.07	0.01	0.28	0.00	0.27	0.03	0.07	1.72	0.04
BN185-G1_4_4	50.7	0.15	26.8	4.29	0.00	1.98	0.12	2.14	7.94	0.08	94.2	6.85	1.15	3.11	4.27	0.01	0.48	0.00	0.40	0.02	0.56	1.37	0.01
BN185-G1_4_6	41.7	0.13	27.8	9.49	0.00	5.29	0.04	0.10	7.27	0.28	92.1	5.97	2.03	2.66	4.68	0.01	1.14	0.00	1.13	0.01	0.03	1.33	0.03
BN185-G1_4_7	43.4	0.12	28.0	8.67	0.01	5.85	0.08	0.12	7.69	0.37	94.4	6.05	1.95	2.64	4.59	0.01	1.01	0.00	1.21	0.01	0.03	1.36	0.04
BN185-G1_4_8	41.3	0.03	27.1	10.76	0.08	6.64	0.00	0.06	7.04	0.08	93.0	5.89	2.11	2.45	4.55	0.00	1.29	0.01	1.41	0.00	0.02	1.28	0.01
BN185-G1_5_1	47.0	0.11	32.6	2.11	0.00	1.04	0.09	0.34	10.4	0.50	94.2	6.35	1.65	3.54	5.20	0.01	0.24	0.00	0.21	0.01	0.09	1.80	0.05
BN185-G1_5_2	47.5	0.06	32.7	2.13	0.00	1.28	0.15	0.34	10.4	0.44	95.0	6.36	1.64	3.53	5.16	0.01	0.24	0.00	0.26	0.02	0.09	1.78	0.05
BN185-G1_5_3	47.3	0.06	32.6	2.07	0.08	1.07	0.08	0.17	10.0	0.71	94.2	6.38	1.62	3.56	5.18	0.01	0.23	0.01	0.21	0.01	0.05	1.72	0.08
BN185-G1_5_4	47.3	0.13	30.3	2.80	0.09	1.81	0.05	0.17	10.5	0.26	93.4	6.47	1.53	3.37	4.89	0.01	0.32	0.01	0.37	0.01	0.04	1.83	0.03
BN185-G1_5_5	44.1	0.14	26.6	9.43	0.08	5.37	0.12	1.03	6.81	0.19	93.9	6.17	1.83	2.57	4.39	0.02	1.10	0.01	1.12	0.02	0.28	1.22	0.02
BN185-G1_6_1	47.8	0.04	32.8	2.20	0.05	1.30	0.00	0.30	10.2	0.48	95.2	6.38	1.62	3.54	5.16	0.00	0.25	0.01	0.26	0.00	0.08	1.73	0.05
BN185-G1_6_2	47.7	0.08	32.6	2.37	0.00	1.24	0.04	0.26	10.1	0.47	94.9	6.39	1.61	3.53	5.14	0.01	0.27	0.00	0.25	0.01	0.07	1.73	0.05
BN185-G1_6_3	47.8	0.07	32.1	2.59	0.00	1.29	0.08	0.21	10.2	0.21	94.5	6.43	1.57	3.52	5.09	0.01	0.29	0.00	0.26	0.01	0.05	1.74	0.02
BN185-G1_6_4	47.5	0.09	29.4	4.84	0.10	2.15	0.13	0.04	9.74	0.23	94.2	6.49	1.51	3.22	4.73	0.01	0.55	0.01	0.44	0.02	0.01	1.70	0.02
BN185-G2_1_1	48.0	0.11	30.8	2.46	0.00	1.59	0.16	0.19	10.4	0.39	94.1	6.50	1.50	3.41	4.91	0.01	0.28	0.00	0.32	0.02	0.05	1.79	0.04
BN185-G2_1_2	47.2	0.11	29.7	3.33	0.00	2.46	0.00	0.15	9.97	0.33	93.3	6.47	1.53	3.27	4.80	0.01	0.38	0.00	0.50	0.00	0.04	1.74	0.04
BN185-G2_1_3	48.4	0.09	28.9	3.41	0.05	2.66	0.14	0.12	9.85	0.23	93.9	6.59	1.41	3.22	4.63	0.01	0.39	0.01	0.54	0.02	0.03	1.71	0.02
BN185-G2_1_4	42.9	0.05	27.7	8.89	0.11	5.20	0.00	0.04	7.78	0.29	93.0	6.07	1.93	2.69	4.62	0.01	1.05	0.01	1.10	0.00	0.01	1.40	0.03
BN185-G2_2_1	41.0	0.03	25.7	11.59	0.08	6.29	0.11	0.00	6.36	0.00	91.1	5.99	2.01	2.40	4.41	0.00	1.41	0.01	1.37	0.02	0.00	1.18	0.00
BN185-G2_2_3	48.3	0.13	30.3	2.38	0.04	1.72	0.05	0.24	10.5	0.42	94.1	6.54	1.46	3.38	4.84	0.01	0.27	0.00	0.35	0.01	0.06	1.81	0.04
BN185-G3_1_1	47.6	0.00	30.3	3.02	0.04	1.81	0.04	0.24	10.6	0.12	93.8	6.50	1.50	3.37	4.87	0.00	0.34	0.00	0.37	0.01	0.06	1.84	0.01
BN185-G3_1_2	47.9	0.03	31.4	2.34	0.07	1.73	0.05	0.24	11.0	0.51	95.4	6.43	1.57	3.40	4.97	0.00	0.26	0.01	0.35	0.01	0.06	1.89	0.05
BN185-G3_1_3	47.9	0.07	31.8	1.96	0.00	1.44	0.03	0.26	10.8	0.52	94.8	6.44	1.56	3.47	5.03	0.01	0.22	0.00	0.29	0.00	0.07	1.85	0.06
BN185-G3_2_1	47.4	0.04	31.7	2.19	0.12	1.51	0.04	0.22	10.8	0.63	94.7	6.40	1.60	3.44	5.05	0.00	0.25	0.01	0.30	0.01	0.06	1.86	0.07
BN185-G3_2_2	47.8	0.02	31.9	2.45	0.04	1.50	0.05	0.24	10.8	0.28	95.2	6.42	1.58	3.47	5.05	0.00	0.28	0.00	0.30	0.01	0.06	1.85	0.03
BN185-G3_2_3	48.1	0.00	31.3	2.61	0.09	1.42	0.01	0.25	10.8	0.23	94.9	6.48	1.52	3.45	4.97	0.00	0.29	0.01	0.28	0.00	0.07	1.86	0.02
BN185-L1_1	42.1	0.08	27.1	10.08	0.13	5.72	0.00	0.09	7.21	0.08	92.6	6.01	1.99	2.57	4.56	0.01	1.20	0.02	1.22	0.00	0.02	1.31	0.01
BN185-L1_2	48.0	0.12	32.5	2.25	0.00	1.24	0.03	0.25	10.7	0.17	95.2	6.41	1.59	3.53	5.12	0.01	0.25	0.00	0.25	0.00	0.07	1.82	0.02
BN185-L1_3	47.8	0.11	30.1	3.48	0.11	2.31	0.14	0.17	9.89	0.24	94.3	6.48	1.52	3.28	4.81	0.01	0.39	0.01	0.47	0.02	0.05	1.71	0.03
BN185-L1_6	46.3	0.12	29.6	4.63	0.00	2.62	0.09	0.21	9.85	0.18	93.6	6.38	1.62	3.19	4.81	0.01	0.53	0.00	0.54	0.01	0.06	1.73	0.02
BN185-L1_8	44.8	0.14	29.7	5.98	0.03	2.99	0.03	0.17	9.09	0.35	93.3	6.23	1.77	3.10	4.86	0.01	0.70	0.00	0.62	0.00	0.04	1.61	0.04
BN185-L2_1	47.9	0.08	30.3	2.30	0.00	1.77	0.09	0.33	10.6	0.29	93.7	6.52	1.48	3.39	4.86	0.01	0.26	0.00	0.36	0.01	0.09	1.83	0.03
BN185-L2_10	47.7	0.14	30.4	4.58	0.05	1.95	0.07	0.18	9.65	0.47	95.2	6.43	1.57	3.27	4.84	0.01	0.52	0.01	0.39	0.01	0.05	1.66	0.05
BN185-L2_11	46.2	0.14	27.6	4.33	0.05	2.76	0.00	0.04	9.79	0.00	90.9	6.53	1.47	3.14	4.61	0.02	0.51	0.01	0.58	0.00	0.01	1.77	0.00
BN185-L2_2	47.9	0.14	27.7	3.48	0.07	2.26	0.00	0.09	10.1	0.00	91.8	6.67	1.33	3.23	4.55	0.01	0.41	0.01	0.47	0.00	0.02	1.80	0.00
BN185-L2_3	47.6	0.04	30.0	2.53	0.00	1.71	0.00	0.24	10.4	0.00	92.6	6.55	1.45	3.42	4.87	0.00	0.29	0.00	0.35	0.00	0.06	1.83	0.00
BN185-L2_4	47.5	0.06	30.3	3.72	0.00	2.40	0.00	0.24	9.90	0.00	94.1	6.45	1.55	3.31	4.86	0.01	0.42	0.00	0.49	0.00	0.06	1.72	0.00
BN185-L2_5	45.8	0.05	28.4	6.46	0.00	2.60	0.00	0.13	8.61	0.00	92.1	6.43	1.57	3.12	4.69	0.01	0.76	0.00	0.54	0.00	0.03	1.54	0.00
BN185-L2_6	47.0	0.11	28.5	4.79	0.04	2.66	0.00	0.15	9.57	0.00	92.8	6.51	1.49	3.17	4.66	0.01	0.55	0.00	0.55	0.00	0.04	1.69	0.00
BN246	**Mica**																						
BN-246-19	50.9	0.00	30.6	1.58	0.02	0.84	0.23	1.61	7.63	0.00	93.4	6.78	1.22	3.58	4.80	0.00	0.18	0.00	0.17	0.03	0.42	1.30	0.00
BN-246-42	50.7	0.05	19.2	1.62	0.00	0.13	0.38	2.82	7.49	0.00	82.4	7.70	0.30	3.13	3.43	0.01	0.21	0.00	0.03	0.06	0.83	1.45	0.00
BN-246-83	50.4	0.24	35.5	1.10	0.04	0.65	0.17	0.51	9.67	0.00	98.3	6.43	1.57	3.75	5.32	0.02	0.12	0.00	0.12	0.02	0.13	1.57	0.00
BN-246-73	49.9	0.14	33.0	1.19	0.03	0.59	0.11	1.41	9.14	0.00	95.5	6.55	1.45	3.66	5.11	0.01	0.13	0.00	0.11	0.01	0.36	1.53	0.00
BN-246-52	49.6	0.13	34.9	1.13	0.04	0.79	0.09	0.45	9.68	0.00	96.9	6.42	1.58	3.74	5.32	0.01	0.12	0.00	0.15	0.01	0.11	1.60	0.00
BN-246-53	49.5	0.01	28.9	1.21	0.02	0.48	0.27	2.08	8.26	0.00	90.7	6.83	1.17	3.53	4.70	0.00	0.14	0.00	0.10	0.04	0.56	1.45	0.00
BN-246-	49.5	0.51	34.0	1.20	0.00	0.84	0.16	0.33	9.51	0.00	96.1	6.45	1.55	3.68	5.23	0.05	0.13	0.00	0.16	0.02	0.08	1.58	0.00
BN-246-24	48.9	0.17	32.8	1.58	0.02	1.03	0.09	0.44	9.60	0.00	94.7	6.50	1.50	3.64	5.14	0.02	0.18	0.00	0.20	0.01	0.11	1.63	0.00
BN-246-78	48.6	0.17	33.8	1.28	0.03	0.56	0.16	0.50	9.66	0.00	94.8	6.44	1.56	3.72	5.28	0.02	0.14	0.00	0.11	0.02	0.13	1.63	0.00
BN-246-35	48.3	0.00	33.7	1.25	0.06	0.72	0.16	0.43	9.71	0.00	94.3	6.43	1.57	3.73	5.30	0.00	0.14	0.01	0.14	0.02	0.11	1.65	0.00
BN-246-43	48.0	0.28	31.9	2.38	0.05	0.97	0.19	0.42	8.30	0.00	92.5	6.51	1.49	3.61	5.10	0.03	0.27	0.01	0.20	0.03	0.11	1.44	0.00
BN-246-57	48.0	0.12	32.8	1.41	0.00	0.81	0.12	0.43	9.71	0.00	93.4	6.46	1.54	3.68	5.22	0.01	0.16	0.00	0.16	0.02	0.11	1.67	0.00
BN-246-84	47.9	0.33	33.1	1.24	0.00	0.75	0.13	0.48	9.83	0.00	93.7	6.43	1.57	3.67	5.24	0.03	0.14	0.00	0.15	0.02	0.12	1.68	0.00
BN-246-34	47.8	0.04	33.6	1.54	0.06	0.64	0.00	0.46	10.3	0.00	94.5	6.40	1.60	3.70	5.30	0.00	0.17	0.01	0.13	0.00	0.12	1.77	0.00
BN-246-72	47.8	0.13	33.3	1.31	0.00	0.72	0.09	0.46	9.91	0.00	93.7	6.42	1.58	3.70	5.28	0.01	0.15	0.00	0.14	0.01	0.12	1.70	0.00
BN-246-80	47.7	0.03	33.1	1.25	0.00	0.63	0.11	0.52	9.63	0.00	93.0	6.45	1.55	3.72	5.27	0.00	0.14	0.00	0.13	0.02	0.14	1.66	0.00
BN-246-37	47.7	0.00	31.2	2.00	0.05	0.94	0.45	0.35	8.82	0.00	91.5	6.55	1.45	3.61	5.05	0.00	0.23	0.01	0.19	0.07	0.09	1.55	0.00
BN-246-74	47.7	0.18	33.6	1.16	0.01	0.70	0.10	0.41	9.48	0.00	93.4	6.41	1.59	3.74	5.33	0.02	0.13	0.00	0.14	0.01	0.11	1.63	0.00
BN-246-54	47.6	0.06	33.2	1.47	0.00	0.63	0.17	0.40	9.59	0.00	93.1	6.43	1.57	3.71	5.28	0.01	0.17	0.00	0.13	0.03	0.11	1.65	0.00
BN-246-20	47.6	0.03	34.2	1.50	0.00	0.54	0.05	0.47	9.79	0.00	94.1	6.36	1.64	3.76	5.39	0.00	0.17	0.00	0.11	0.01	0.12	1.67	0.00
BN-246-77	47.4	0.11	32.5	1.31	0.05	0.71	0.11	0.42	9.45	0.00	92.1	6.47	1.53	3.70	5.23	0.01	0.15	0.01	0.14	0.02	0.11	1.64	0.00
BN-246-46	47.4	0.19	32.4	1.49	0.08	0.52	0.14	0.64	9.22	0.00	92.0	6.48	1.52	3.69	5.21	0.02	0.17	0.01	0.11	0.02	0.17	1.61	0.00
BN-246-36	47.4	0.03	30.8	1.88	0.03	0.86	0.49	0.30	7.21	0.00	88.9	6.62	1.38	3.68	5.07	0.00	0.22	0.00	0.18	0.07	0.08	1.28	0.00
BN-246-50	47.3	0.05	34.5	1.57	0.00	0.59	0.04	0.42	9.50	0.00	94.0	6.33	1.67	3.77	5.44	0.01	0.18	0.00	0.12	0.01	0.11	1.62	0.00
BN-246-70	47.1	0.23	33.7	1.20	0.07	0.68	0.03	0.47	9.80	0.00	93.3	6.36	1.64	3.72	5.36	0.02	0.14	0.01	0.14	0.00	0.12	1.69	0.00
BN-246-49	47.1	0.10	33.2	2.68	0.00	0.80	0.05	0.42	9.86	0.00	94.2	6.35	1.65	3.62	5.27	0.01	0.30	0.00	0.16	0.01	0.11	1.69	0.00
BN-246-59	46.9	0.02	31.5	1.29	0.00	0.65	0.11	0.49	10.0	0.00	91.0	6.51	1.49	3.66	5.15	0.00	0.15	0.00	0.13	0.02	0.13	1.78	0.00
BN-246-44	46.6	0.05	31.0	1.39	0.05	0.73	0.21	0.41	9.08	0.00	89.6	6.54	1.46	3.67	5.13	0.00	0.16	0.01	0.15	0.03	0.11	1.63	0.00
BN-246-	46.6	0.10	35.9	1.08	0.00	0.14	0.09	1.32	8.99	0.00	94.2	6.21	1.79	3.85	5.64	0.01	0.12	0.00	0.03	0.01	0.34	1.53	0.00
BN-246-85	46.6	0.36	33.2	1.27	0.02	0.56	0.01	0.48	9.73	0.00	92.2	6.37	1.63	3.71	5.34	0.04	0.14	0.00	0.11	0.00	0.13	1.70	0.00
BN-246-65	46.6	0.07	35.1	0.81	0.00	0.27	0.12	1.05	9.38	0.00	93.4	6.27	1.73	3.83	5.57	0.01	0.09	0.00	0.06	0.02	0.27	1.61	0.00
BN-246-76	46.5	0.13	33.3	1.20	0.05	0.59	0.17	0.41	9.60	0.00	92.0	6.37	1.63	3.74	5.37	0.01	0.14	0.01	0.12	0.02	0.11	1.67	0.00
BN-246-39	46.4	0.18	28.3	2.10	0.05	0.62	0.27	1.49	6.38	0.00	85.8	6.73	1.27	3.57	4.84	0.02	0.25	0.01	0.13	0.04	0.42	1.18	0.00
BN-246-75	45.4	0.00	29.4	1.50	0.05	0.82	0.16	0.29	8.62	0.00	86.2	6.60	1.40	3.64	5.04	0.00	0.18	0.01	0.18	0.03	0.08	1.60	0.00
BN-246-66	45.3	0.26	32.2	1.05	0.04	0.61	0.10	0.52	8.98	0.00	89.0	6.38	1.62	3.73	5.35	0.03	0.12	0.00	0.13	0.02	0.14	1.62	0.00
BN-246-86	45.3	0.17	30.0	1.45	0.00	0.68	0.23	0.35	8.71	0.00	86.8	6.55	1.45	3.65	5.11	0.02	0.18	0.00	0.15	0.04	0.10	1.61	0.00
BN-246-58	45.3	0.20	31.5	1.22	0.00	0.58	0.13	0.33	10.1	0.00	89.3	6.41	1.59	3.67	5.26	0.02	0.15	0.00	0.12	0.02	0.09	1.82	0.00
BN-246-61	45.1	0.15	32.2	1.31	0.06	0.57	0.12	0.56	9.99	0.00	90.1	6.35	1.65	3.68	5.33	0.02	0.15	0.01	0.12	0.02	0.15	1.79	0.00
BN-246-62	45.0	0.17	34.4	0.90	0.00	0.11	0.07	1.19	9.62	0.00	91.5	6.21	1.79	3.81	5.60	0.02	0.10	0.00	0.02	0.01	0.32	1.69	0.00
BN-246-71	44.9	0.00	30.7	1.25	0.00	0.64	0.14	0.44	9.34	0.00	87.5	6.47	1.53	3.69	5.22	0.00	0.15	0.00	0.14	0.02	0.12	1.72	0.00
BN-246-63	44.8	0.10	31.9	1.20	0.01	0.54	0.16	1.05	9.48	0.00	89.3	6.35	1.65	3.68	5.33	0.01	0.14	0.00	0.11	0.02	0.29	1.71	0.00
BN-246-82	44.7	0.15	31.6	1.46	0.04	0.67	0.03	0.36	10.2	0.00	89.3	6.36	1.64	3.66	5.30	0.02	0.17	0.01	0.14	0.00	0.10	1.86	0.00
BN-246-51	44.1	0.12	30.6	0.98	0.04	0.50	0.08	0.38	8.93	0.00	85.8	6.46	1.54	3.74	5.28	0.01	0.12	0.00	0.11	0.01	0.11	1.67	0.00
BN-246-64	44.0	0.00	28.6	1.51	0.02	1.11	0.15	0.32	9.99	0.00	85.7	6.52	1.48	3.53	5.00	0.00	0.19	0.00	0.25	0.02	0.09	1.89	0.00
BN-246-60	43.9	0.25	30.3	1.31	0.00	0.61	0.12	0.42	10.2	0.00	87.1	6.40	1.60	3.62	5.22	0.03	0.16	0.00	0.13	0.02	0.12	1.89	0.00
BN-246-68	43.3	0.34	34.7	1.15	0.00	0.07	0.15	1.00	7.90	0.00	88.6	6.12	1.88	3.90	5.78	0.04	0.14	0.00	0.02	0.02	0.27	1.42	0.00
BN-246-41	43.2	0.19	29.1	1.39	0.04	0.75	0.28	0.26	8.52	0.00	83.8	6.49	1.51	3.64	5.15	0.02	0.17	0.01	0.17	0.04	0.07	1.63	0.00

4.2.11.3 U-Pb dating

SHRIMP II analytical techniques Selected monazite crystals as small as 10 μm from samples BN43 and BN47 were dated using Sensitivity High Resolution Ion Microprobe (SHRIMP II). The selected crystals were cut it into 3 mm discs out from polished thin sections, and were later casted into an a 25mm epoxy disc and prepared for SHRIMP analysis as described by Rasmussen et al. (2010). Analytical conditions and procedures are described in Foster et al. (2000) and Rasmussen et al. (2001). Internal calibration was done using the standards GM3, IND and VK 1 (Fletcher et al., 2010; Kennedy and Kinny, 2004; Rasmussen et al., 2002; Ruschel et al., 2012; Schmitz et al., 2009; Wingate and Kirkland, 2010).

LA-ICP-MS analytical techniques Analytical techniques for the LA-ICP-MS analyses carried out at Goethe University Frankfurt are detailed in Chapter 3, in the Appendix 3.2.9.1.

Chapitre 5

Exhumation modes on the WAC : insights from numerical modeling

Introduction (en français)

Les chapitres 3 et 4 mettent en évidence l'exhumation de roches métamorphisées dans la croûte inférieure, à la faveur d'une interaction entre des contractions tectoniques et une extension induite par l'effondrement gravitaire de la croûte épaissie. L'extension dans la croûte constitue un mécanisme efficace pour dénuder les niveaux structuraux supérieurs et exhumer des portions de la croûte inférieure. Sur les cratons archéens, la grande majorité des déformations et des accidents structuraux est interprétée comme étant formés au cours d'une contraction. Peu de structures sont attribuées à des régimes tectoniques extensifs, et les orogènes archéens ne semblent pas présenter d'analogues des dômes anatectiques bordés par des détachements ("metamorphic core complexes") qui sont fréquemment décrits dans les orogènes protérozoïques ou phanérozoïques. Dans ce chapitre, un modèle numérique est développé pour étudier un autre méchanisme d'exhumation. Est-il possible d'exhumer la croûte inférieure partiellement fondue lors d'une contraction horizontale à l'échelle de la croûte ? Peut-on reproduire le registre métamorphique du Craton Ouest Africain en déformant la croûte dans un régime purement compressif ? Cette hypothèse est testée à l'aide d'un modèle numérique thermo-mécanique qui prend en compte les changements de phases induits par les réactions métamorphiques. Un modèle de lithosphère est raccourci à taux constant. Sous l'effet de la déformation, les conditions P-T de certaines roches changent, provoquant des changements de phases, une fusion partielle et des changements de densité, qui entraînent la mise en place de diapirs. Plusieurs scénarios sont modélisés. Les chemins P-T-t suivis par des particules de roches sont comparés aux données thermo-barométriques issues des études métamorphiques sur le craton. Ce chapitre constitue un article qui a été publié en 2014 dans la revue *Precambrian Research* (vol. 43, p 88-109).

Résumé

Cette étude porte sur le lien entre le registre métamorphique et l'évolution thermo-mécanique de l'orogenèse Éburnéenne (environ 2.10 Ga). Elle vise à identifier et à discuter les mécanismes d'enfouissement et d'exhumation ayant affecté les roches volcano-sédimentaires birimiennes (2.25-2.07 Ga) du Craton Ouest Africain, qui enregistrent des conditions métamorphiques de moyenne à haute pression (6-8 à >10 kbar). Des études métamorphiques effectuées sur des échantillons du Burkina Faso, du sud-ouest du Ghana, et du Sénégal oriental permettent de reconstituer un gradient géothermique apparent de 20-30 °C/km (M2a) pour la croûte paléoprotérozoïque. Un tel régime thermique correspond à un transfert de chaleur par conduction dans une croûte à l'équilibre thermique. L'orogenèse Éburnéenne a produit des assemblages métamorphiques équilibrés le long du gradient M2a dans les faciès amphibolite et schiste vert. Cet épisode métamorphique a lieu dans un contexte de raccourcissement horizontal synchrone de la mise en place de plutons de granitoïdes. Le métamorphisme associé au gradient M2a sur-imprime des roches métamorphiques plus anciennes, équilibrées entre les faciès schiste vert et schiste bleu. Cet épisode métamorphique antérieur témoigne d'un régime thermique précoce caractérisé par un géotherme apparent froid (M1 : <10-15 °C/km). M1 est attribué au régime thermique en vigueur dans les bassins volcano-sédimentaires

dans lesquels le protolithe des roches métamorphiques s'est déposé. Ce gradient froid pourrait reflèter soit un contexte de subduction, soit un enfouissement lié à une subsidence et une accumulation sédimentaire. Son origine n'est cependant pas débattue d'avantage dans cet article.

Une série de modèles thermo-mécaniques est construite pour étudier la déformation de la croûte soumise à un raccourcissement horizontal. Initiallement, la croûte comporte une couche supérieure constituée de roches basiques (modélisant un arc volcanique) et d'un bassin sédimentaire épais (15km). Elle repose sur une couche inférieure composée de Tonalites-Trondhjemites-Granodiorites (TTG). Les résultats des modèles suggèrent que l'épaississement crustal et l'enfouissement des roches de surface sont contrôlés par des plissements d'échelle crustale et par le développement simultané d'instabilités gravitaires dans la croûte. Les TTG atteignent les conditions P-T de la fusion paritelle à environ 25 km de profondeur. L'anatexie produit des magmas acides susceptibles de nourrir des plutons de granitoïdes. Les diapirs ascendants sont constitués de matériel partiellement fondu de faible viscosité, d'abord issu de la fusion partielle de TTG ou de sédiments, puis également de roches basiques à un stade de déformation plus avancé. Les diapirs remontent dans la croûte et intrudent les roches sédimentaires sus-jacentes. Ils entraînent dans la dynamique ascendante la croûte inférieure et des roches sédimentaires métamorphisées à leur contact. Ce scénario fournit une explication possible à la présence de lentilles de roches métamorphiques enregistrant des pressions élevées ($P > 8$ kbar) dans les auréoles thermiques de granitoïdes. Ceux-ci sont intrusifs dans des ceintures de roches vertes constituées de roches métamorphiques de bas grade ($P < 6$ kbar ; $T < 450$?C). La fusion partielle affecte la majorité de la croûte inférieure et cause le recyclage des TTG.

La modélisation permet de reproduire fidèlement les trajets P-T des roches métamorphiques du craton. Malgré des limites évidentes, telles que la contrainte d'un champ de déformation en 2 dimensions, le modèle suggère que l'exhumation dans un contexte compressif est viable pour un géotherme initialement "ordinaire". La possibilité d'appliquer aux orogènes anciens les mécanismes mis en évidence par les résultats de cette étude est discutée.

5.1 Introduction

Chapters 3 and 4 document the exhumation of lower-crustal, high-grade metamorphic rocks in a tectonic setting characterised by the interplay of bulk horizontal contraction and extensional gravitational collapse. The development of an extensional setting provides an efficient mechanisms to remove the over-burden and exhume rocks from the lower-crust. However, most fabrics and structures observed on Archean cratons are interpreted to be formed during contraction. The Archean rock record seems to lack large-scale extensional structures analogue to the detachments bounding the metamorphic core complexes found in Phanerozoic and Proterozoic orogenic belts, or at least they haven't they been recognised as such. In this chapter, we examine the viability of an alternative scenario : Is it mechanically possible to exhume partially molten lower-crustal rocks in a tectonic regime characterised by contractional deformation alone ? Can the metamorphic record of the West African Craton be accounted for in a strictly convergent setting ? To explore this possibility, a 2D thermo-mechanical model coupled with P-T thermodynamic modelling is proposed. A model lithospheric pile is submitted to shortening. Changing P-T conditions induce phase transitions, partial melting, density changes and doming. The P-T-t paths of rock particles obtained for different deformation scenarios are compared to P-T paths deduced from metamorphic studies. The chapter is an article that was published in 2014 in *Precambrian Research* journal (vol. 43, p 88-109).

5.2 Thermo-mechanical modeling of lower crust exhumation – Constraints from the metamorphic record of the Palaeoproterozoic Eburnean orogeny, West African Craton.

Precambrian Research 243 (2014) 88–109

Contents lists available at ScienceDirect

Precambrian Research

journal homepage: www.elsevier.com/locate/precamres

Thermo-mechanical modeling of lower crust exhumation—Constraints from the metamorphic record of the Palaeoproterozoic Eburnean orogeny, West African Craton

J. Ganne[a,*], M. Gerbault[b], S. Block[a]

[a] IRD, UR 234, GET, Université Toulouse III, 14 Avenue Edouard Belin, 31400 Toulouse, France
[b] Géoazur, UNSA, IRD, CNRS, OCA, (UMR 7329), 250 Albert Einstein, 06560 Valbonne, France

ARTICLE INFO

Article history:
Received 4 September 2013
Received in revised form
21 December 2013
Accepted 26 December 2013
Available online 15 January 2014

Keywords:
Palaeoproterozoic orogenies
High-pressure rocks
Exhumation
Thermo-mechanical model
West African Craton

ABSTRACT

The aim of this paper is to explore the link between the metamorphic record of a Palaeoproterozoic orogeny and its thermo-mechanical evolution, in order to discuss the burial and exhumation processes of moderate- to high-pressure volcano-sedimentary rocks (6–8 to >10 kbar) in the Birimian Province (2.2–2.0 Ga) of the West African Craton. Metamorphic data collected in Burkina Faso, southwest Ghana and eastern Senegal suggests a Palaeoproterozoic Birimian crust dominated by moderate apparent geothermal gradients of 20–30 °C/km (M2a), which fit a purely conductive thermal crustal regime. This produced greenschist- to amphibolite-facies metamorphic assemblages that developed during the Eburnean orogeny (~2.1 Ga), associated with regional shortening and granitoid intrusions. The M2a gradient is superimposed on an early thermal regime (M1: <10–15 °C/km) that produced high-*P* greenschist- to blueschist-facies metamorphic assemblages. M1 most likely recorded an earlier thermal history in the volcano-sedimentary basins where the protolith of the metamorphic terrains formed. Whether M1 is related to distributed burial associated with sediment accumulation or early subduction-related tectonics remains an open question, not directly addressed here.

Thermo-mechanical models were built based on the assumption of an initial crust made up of a succession of volcanic island arcs emplaced on top of a basement dominated by CaO-rich Tonalite–Trondhjemite–Granodiorite suites (TTGs), and tectonically paired with sedimentary basins. From the results of these thermo-mechanical models, we propose a mechanism of burial, heating and exhumation of meta-sediments through the Birimian crust controlled by simultaneous folding/shortening and gravitational instabilities in the juvenile crust. We postulated here the pre-existence of thick sedimentary basins (depth 15 km) in the Birimian orogenic crust to model the late-stage exhumation of meta-sediments, collected in the thermal aureole of CaO-poor granitoids, and which record elevated metamorphic pressures (P > 6–8 kbar). At around 25 km depth, TTGs reached appropriate *PT* conditions to start melting. The buoyant and low-viscosity partially molten material, comprising a fraction of CaO-poor melt and residual material, then ascended through the overlying sediments. It entrained upwards lower crustal material as well as the surrounding sediments. This scenario explains the important breaks in metamorphic conditions observed in the Birimian province between the thin slivers (<2 km thick) of high-pressure rocks (P > 8 kbar) preserved in the thermal aureoles of granites and the adjacent synforms of greenstones, which consist of low-grade metasediments (P < 6 kbar; T < 450 °C). This scenario is in agreement with a significant recycling of the TTGs in the genesis of CaO-poor granitoid melts. We discuss the implications of our results for the tectono-metamorphic and mechanical evolution of Palaeoproterozoic orogenies.

© 2014 Elsevier B.V. All rights reserved.

1. Introduction

Most Precambrian orogens differ from modern ones by exposing very broad regions, exceeding several hundred kilometers in width, of nearly isobaric metamorphism and lateral temperature gradients due to long-lived magmatism and repeated granitoid intrusions (Chardon et al., 2009, with references to Grambling et al., 1989; Bleeker, 1990; Collins and Vernon, 1991; Percival et al., 1992; Elhers et al., 1993; Percival and Skulski, 2000; Caby et al., 2000 or Cagnard et al., 2006, 2007). The apparent lack of pressure gradients across Precambrian provinces motivated several authors to suggest a moderate but widespread exhumation over their entire

* Corresponding author. Tel.: +33 05 61 33 26 55.
E-mail address: ganne@get.obs-mip.fr (J. Ganne).

0301-9268/$ – see front matter © 2014 Elsevier B.V. All rights reserved.
http://dx.doi.org/10.1016/j.precamres.2013.12.016

width (Galer and Mezger, 1998 or Gapais et al., 2009 and references therein).

In this paper we aim to unravel the link between the metamorphic record of a Palaeoproterozoic orogeny and its mechanical evolution in order to discuss the exhumation processes of moderate- to high-pressure rocks (6–8 to >10 kbar) identified by different authors (Junner and Harwood, 1928; John et al., 1999; Galipp et al., 2003; Castaing et al., 2003; Debat et al., 2003; Soumaïla and Garba, 2006; Ganne et al., 2012) in the Birimian Province (2.2–2.0 Ga) of the West African Craton (WAC). The Birimian Province of the WAC constitutes one of the largest and best exposed Palaeoproterozoic juvenile continental domain on Earth. The geodynamic setting of juvenile crust formation between 2.25 and 2.15 Ga is strongly debated ("oceanic plateau": Abouchami et al., 1990; Boher et al., 1992; "island arc": Sylvester and Attoh, 1992a,b; Ama Salah et al., 1996; Dia et al., 1997; Lüdtke et al., 1998). The tectonic styles driving subsequent crustal deformation until 2.0 Ga are equally controversial, as some authors interpret field observations as a result of "Archean type" gravitational tectonics (e.g. Vidal et al., 2009), while other claim they are produced by "modern type" thrusting and lateral accretion (Feybesse and Milési, 1994; Hirdes et al., 1996; Feybesse et al., 2006).

We first present the geological setting of the Birimian Province, and several lines of evidences that arise from petrological analysis, metamorphic modeling and structural observations (Sections 2 and 3). We then use these informations to constrain thermo-mechanical models which explore the conditions allowing for the exhumation of lower crust (i.e. 20–30 km depth) in a convergent regime. Modeling assumptions are first presented and argumented (Section 4), then our results are described along with a few parametric tests (Section 5). Acknowledging the lack of data that would allow to better demonstrate a specific scenario, the numerical results are discussed in terms of their contribution to our understanding of exhumation of partially molten material. Placed in a broader geodynamic scheme, this thermo-mechanical modeling study addresses the conditions by which the growth and stabilisation of the Birimian crust might have been achieved. Because of our multi-disciplinary approach, we chose to discuss the inferences and limits of our methods in each section, so that the final Section 6 is a conclusive discussion on the geodynamical implications of our study, rather than a summary of each approach.

2. Geological setting

The southern part of the WAC is dominated by Birimian terranes of Palaeoproterozoic age (ca. ~2.2–2.0 Ga, Castaing et al., 2003 and references therein) which extend to the east and the north of the Archaean cratonic nucleus centred on Liberia (Fig. 1A). The Birimian formations consist of linear or arcuate narrow volcanic belts (greenstones s.s.) often associated to narrow or large volcano-sedimentary basins (greenstones s.l.). They are intruded by several generations of granitoids (Hirdes et al., 1996; Doumbia et al., 1998; Gasquet et al., 2003; Dioh et al., 2006 and references therein). The Birimian series, referenced as greenstones (s.l.) in this paper, comprise a thick sequence of tholeiitic basalts, covered by a detrital sedimentary pile which includes inter-bedded calc-alkaline volcanic rocks (Baratoux et al., 2011 and references therein). The Birimian formations were accreted during the Eburnean orogeny (Bonhomme, 1962) around 2.1 Ga (Boher et al., 1992) when the volcanic and meta-sedimentary rocks underwent horizontal shortening and folding (Baratoux et al., 2011), associated to a greenschist to amphibolites-facies metamorphic overprint.

A few granitoid intrusions occurred contemporaneously with the Birimian volcanism at 2.20–2.18 Ga (Oberthür et al., 1998; De Kock et al., 2012) but the main plutonic activity took place later, during several protracted pulses between 2.15 and 2.07 Ga (e.g. Milési et al., 1992; Hirdes et al., 1996; Vidal et al., 1996, 2009; Feybesse et al., 2006; Hein, 2010). Although petrographic variability is large and classification of granitoid suites in the WAC is complex, at the regional scale a calc-alkaline evolution can be established with:

1) Na_2O- and CaO-rich Tonalite–Trondhjemite–Granodiorites (TTG) with amphibole as the major ferro-magnesian phase, mainly emplaced between 2.15 and 2.13 Ga (Hirdes et al., 1996; Doumbia et al., 1998; Gasquet et al., 2003; Tapsoba et al., 2013 and others). They commonly display a strong banded fabric viewed by some authors as a magmatic foliation reflecting segregation and aggregation of crystals in a magma (Pons et al., 1995), interpreted by others as a synmigmatitic foliation reflecting segregation of silicate melts in a partially molten rock (Lemoine, 1988) and/or as a gneissic foliation reflecting solid-state deformation (Ducellier, 1963; Hirdes et al., 1996; Lüdtke et al., 1998).
2) Granitoids with high K_2O content and moderate to low CaO content, with biotite as major ferro-magnesian phase mainly emplaced between 2.13 and 2.07 Ga (Doumbia et al., 1998; Egal et al., 2002; Hirdes and Davis, 2002).

The CaO-poor granitoids are often characterized by a depleted composition in heavy rare earth elements (Dioh et al., 2006), which is interpreted by some authors as reflecting the presence of stable garnet in the residual material (Martin et al., 2005; Moyen and Martin, 2012) after melting of older TTG, sedimentary and/or volcanic sources (Doumbia et al., 1998; Egal et al., 2002; Klein et al., 2012). Meta-sediments recording elevated pressures (>6–8 kbar) are commonly found in the thermal aureoles of CaO-poor granitoids (Fig. 2B) which cross-cut the early generation of Na_2O- and CaO-rich Tonalites–Trondhjemites–Granodiorites (TTGs)-like. A significant reworking of TTGs in the genesis of CaO-poor granitoid melts is thus expected (Tapsoba et al., 2013 and others).

In the South-Comoé area (Ivory Coast), Vidal et al. (1996, 2009) observed that greenstones (s.s.) were affected by two main deformation events during the Eburnean orogeny. The first deformation is linked to intrusions of CaO-rich granitoids and is characterized by vertical structures. The metamorphic foliation in the surrounding volcanic and sedimentary rocks wraps around the granitoid plutons, with down dip mineral/stretching lineations. These structural features are similar to those described by Pouclet et al. (2006) in the greenstones (s.l.) of the North-Comoé area (Ivory Coast) and are interpreted as deformation related to diapir emplacement. The second deformation event is marked by coeval diapir emplacement of CaO-poor granitoids and horizontal regional scale shortening accommodated by strain localization along strike-slip high-strain zones (Naba et al., 2004).

Different authors (Pons et al., 1992, 1995; Vidal et al., 2009 and references therein) have proposed that Birimian greenstones (s.l.) were dragged up by ascending buoyant, partially molten material in the thermal aureoles of ascending granitoids. This exhumation mechanism implies that the whole system was flowing with negligible viscosity contrast (e.g. less than one order of magnitude) between the partially molten granitoids and the crystalline country rock (Pons et al., 1995; Chardon et al., 2009 and references therein). Mass transfer and exhumation of lower crustal rocks resulting from gravitational instabilities initiating at the base of an orogenic crust has already been invoked and modeled numerically for a number of geodynamic contexts, including Palaeoproterozoic, Variscan, and Phanerozoic orogenies (e.g. Vanderhaeghe, 2012; Gerya et al., 2008; Maierová et al., 2013). In Sections 4 and 5, we discuss this literature together with our thermo-mechanical models to gain insight

on the conditions for such a scenario to have occurred in the Paleoproterozoic crust of the WAC.

A geothermal gradient for the Palaeoproterozoic Birimian crust is first estimated in Section 3 by using structural and metamorphic observations and *PT* calculations derived from meta-sediments sampled in the thermal aureoles of granitoids (Fig. 2A and B), in order to provide constraints for the thermo-mechanical study. The obtained thermal gradient is then used to explore the changes in physical properties of crustal rocks (melting temperature, fluid release, density increase, etc) with depth. These physical properties are also used as input constraints in the thermo-mechanical models of Section 4.

3. Petrological and structural constraints

3.1. Structural constraints

The thermal aureoles of Birimian granitoids yield a large variety of metamorphic assemblages, as attested by the occurrence of garnet, biotite, staurolite, kyanite, sillimanite and cordierite identified by Pons et al. (1995) in the Tera greenstone belt, at the border between Niger and Burkina Faso (Fig. 1B). The Tera greenstone belt is made up of an NE–SW trending synform comprising a thick sequence of volcanic rocks with bimodal tholeiitic and calc-alkaline affinities, as well as detrital sedimentary rocks. It is intruded by granodioritic plutons with moderate or low CaO concentrations which form the Tera batholith. The Tera greenstone belt is affected by a regional syn-kinematic greenschist-facies metamorphic overprint. Greenschist facies mineral assemblages are aligned parallel to a penetrative metamorphic cleavage which generally dips steeply to the NW or to the SE, and bears strongly plunging mineral lineations.

Small (<5 × 10 km) slivers, located in the vicinity granitoid plutons which intrude the belt bear mineral assemblages characterisitic of an amphibolite-facies metamorphic overprint (Pons et al., 1995; Soumaïla and Garba, 2006). Amphibolites and paragneisses (with locally evidences of migmatitic fabrics) from these higher-grade units commonly display shallow- to steep-dipping foliations bearing moderately plunging (<50 °C) mineral elongation lineations (Fig. 1D). Tight folds, locally isoclinal are also observed.

Fabrics in high-grade and low-grade units are consistent with a single deformation event corresponding to NW–SE directed regional shortening, which is equivalent to the deformation event termed D2 by Ganne et al. (2012). Therefore we interpret the metamorphic breaks between high-grade and low-grade units of the

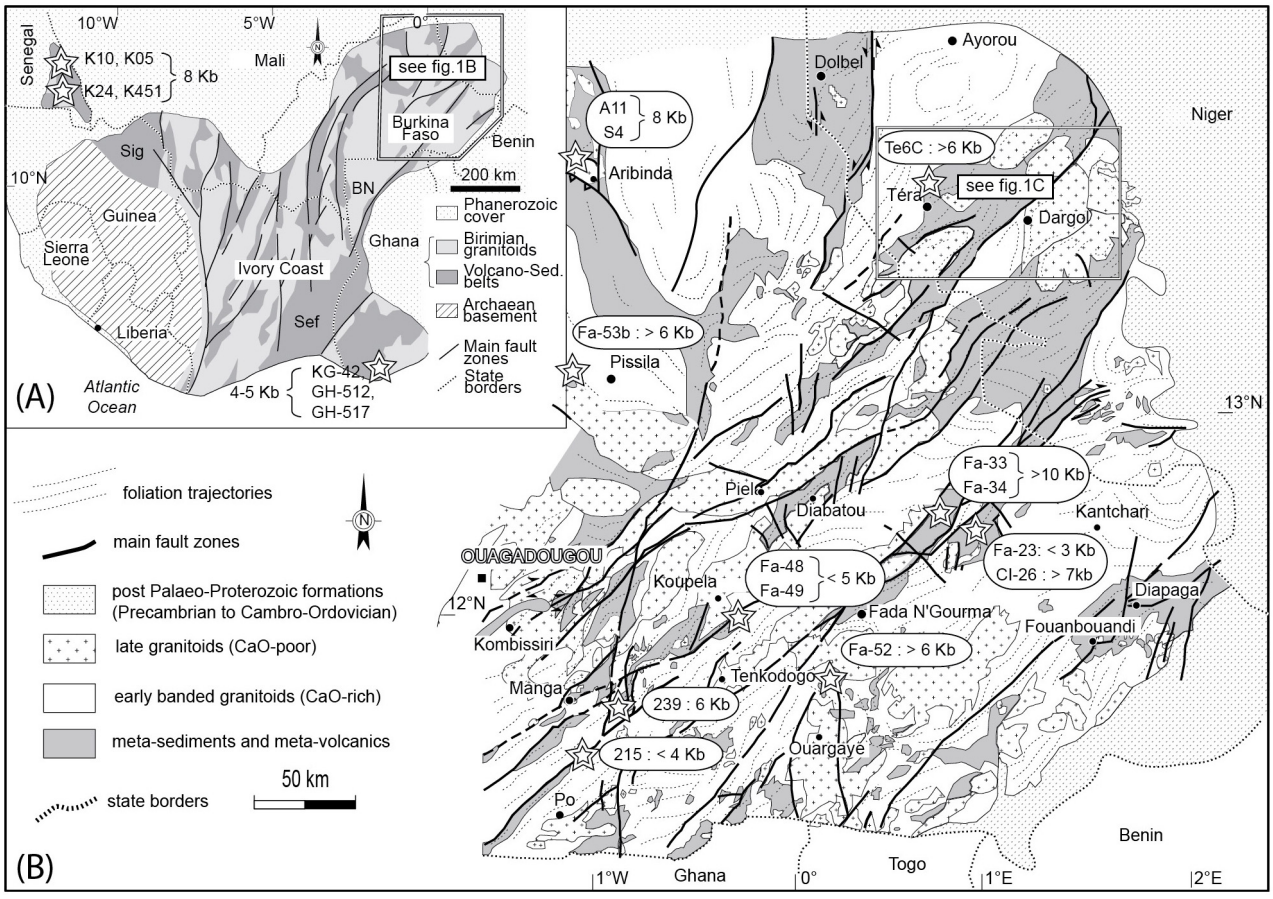

Fig. 1. Metamorphic record of meta-sediments sampled in the thermal aureoles of granitoids plutons. (A) Geological sketch map of the southern part of the West African Craton (WAC) showing the Archaean basement surrounded by the Palaeoproterozoic meta-volcanic and meta-sedimentary greenstone belts (dark grey) and granitoids (light grey). The position of the Siguiri (Sig) basin, Sefwi (Sef) and Bolé-Nangodi (BN) belts discussed in the text is given in (A). (B) Simplified geological map of the Birimian province cropping out in the eastern regions of the WAC (modified after Vegas et al., 2007). White stars correspond to the location of samples used for metamorphic modeling (reference numbers of samples are given in the adjacent boxes). (C and D) Geological setting of the Tera area in Niger (after Soumaïla and Garba, 2006; modified with our own metamorphic and structural informations). The Tera greenstone belt is mainly composed by volcano-sedimentary rocks defining a synform geometry, with a prevalence of mafic volcanites (tholeiitic affinity evolving to a calc-alkaline serie) located at the borders (bottom) of the belt. The low-grade metamorphic assemblages are mostly observed within the sedimentary-dominant core (top) of the belt, whereas the medium- to high-grade ones are restricted to the vicinity of the granodioritic plutons. The largest of those plutons, referred as the pluton of Tera (Pons et al., 1995), consists of banded TTGs that started to coalesce early at around 2.15 Ga (Cheilletz et al., 1994), in a large, NE–SW-elongated batholith. The meta-pelite (Te6C) sampled for metamorphic analysis crops out 5–6 km in the north of Tera village, within terrains of medium- to high-grade metamorphism (Soumaïla, 2000; Soumaïla and Garba, 2006). (For interpretation of colour in the artwork, the reader is referred to the web version of the article.)

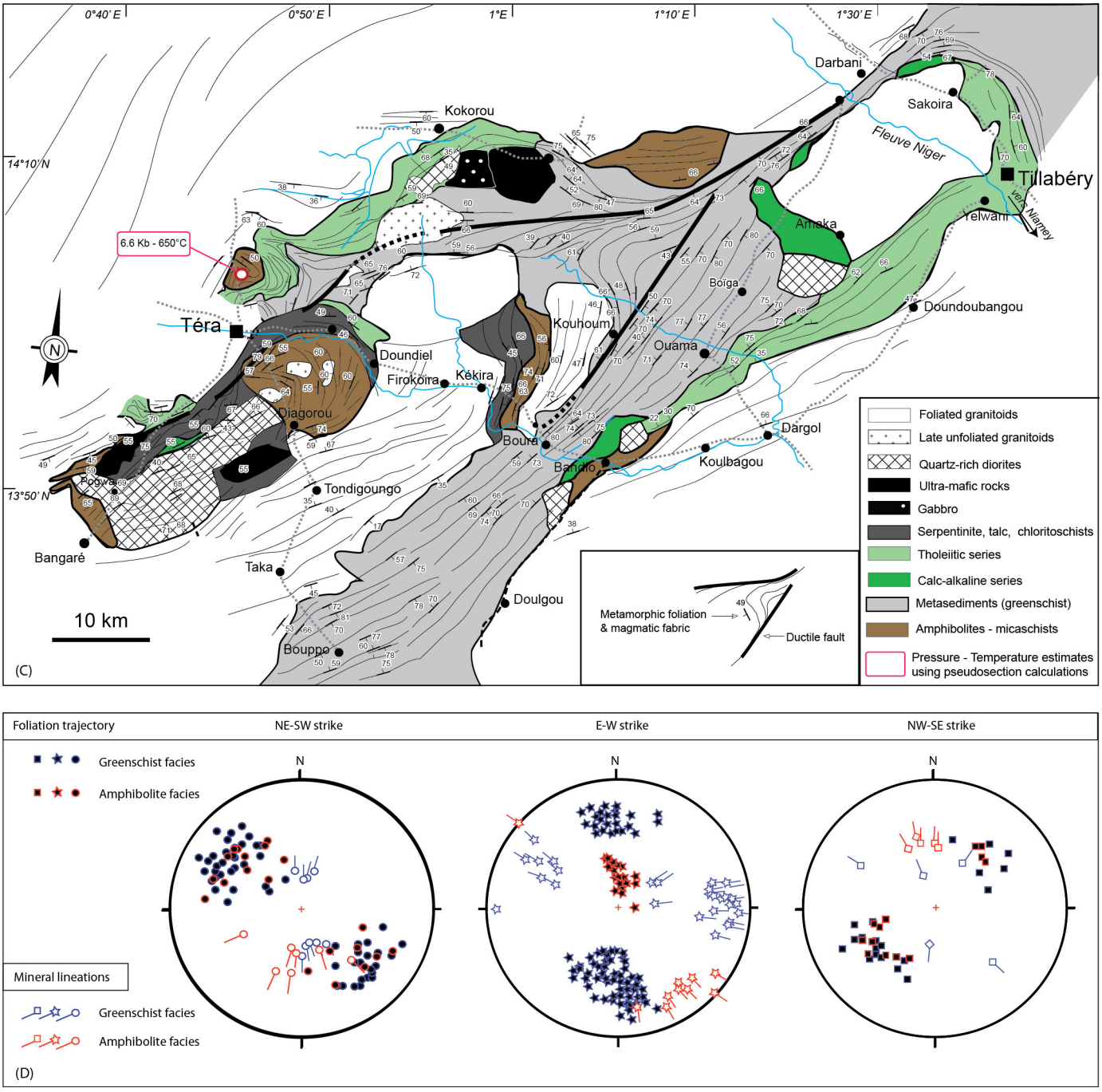

Fig. 1. (*Continued*)

Tera greenstone belt as being produced by strain localisation along narrow shear zones formed during D2.

The regional metamorphic foliation is locally transposed parallel to an E–W striking subvertical, greenschist-facies foliation which bears shallowly plunging mineral lineations along high-strain zones where deformation localised. Although they form prominent map features, these structures are representative of the latest stages of the ductile deformation affecting the area. The kinematics associated to late-stage shear zones indicate that they do not account for significant metamorphic breaks nor for important vertical or horizontal offsets.

There are no evidence for tensile structures, detachment zones or substractive contacts which could hint at regional extensional kinematics across the Tera greenstone belt.

3.2. Metamorphic constraints

Metamorphic studies carried out by Ganne et al. (2012) on meta-sediments reveal important variations in peak metamorphic pressure across the north-eastern region of Burkina Faso (Fig. 1B), with widespread greenschist-facies metamorphism along the margins of intrusive granitoid plutons. These meta-sediments underwent metamorphism along a 20–30 °C/km apparent metamorphic gradient at 3–6 kbar, 250–400 °C (e.g. sample Fa-23; Fig. 2A) and are found in a context termed low-temperature (low-*T*) aureoles by Ganne et al. (2012). As the maximum pressure recorded by our samples occurred coevally with peak temperature, it was assumed that the apparent metamorphic gradient could correspond to a geothermal gradient. Within these same low-*T*

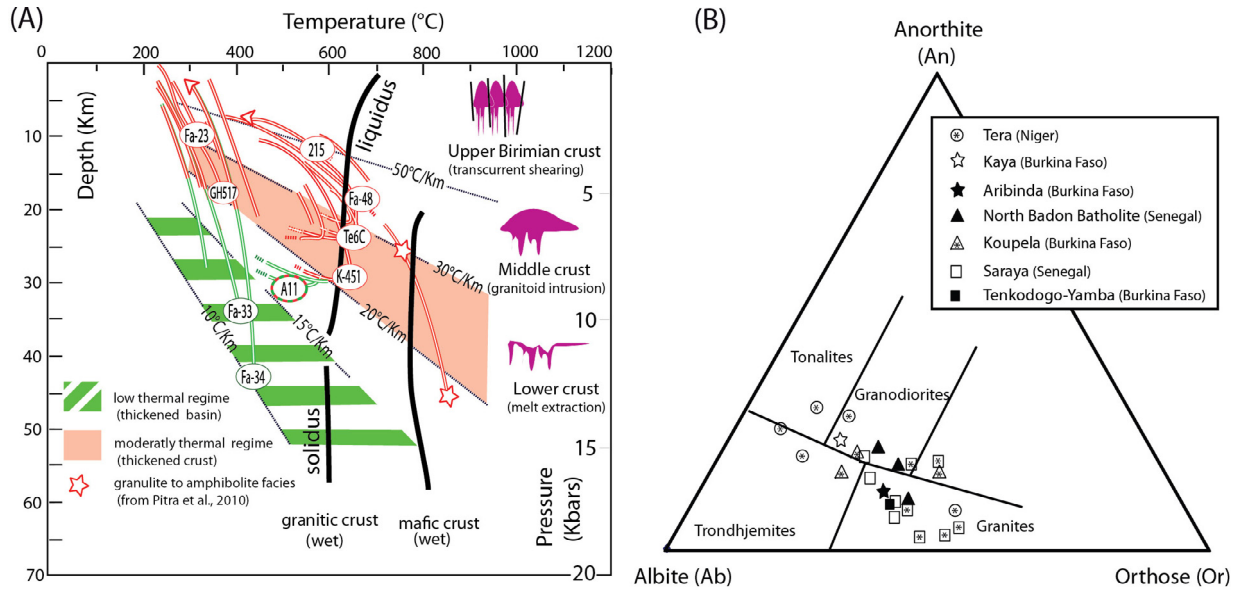

Fig. 2. Pressure and temperature (*P–T*) paths recorded by meta-sediments in the WAC (modified after Ganne et al., 2012 and new data from southwest Ghana). The black thick lines superimposed on the grid correspond to the solidus/liquidus thermal boundary of wet mafic (gabbro) and felsic (granitoids) materials. A lithostatic pressure of 3.5–3.6 kbar/km (Spear, 1993) was considered, accounting for the mafic and felsic composition of the Birimian crust. (B) Normative plots of Ab-An-Or (Barker, 1979) for the granitoids bordering the meta-sediments we investigated in this study. Note they are dominantly ranging in the CaO-poor granitoids fields (granites–granodiorites). The GPS coordinates of the samples used for the *PT* calculations and the chemical analyses of granitoids bordering the meta-sediments are given in a supplementary information (excel) file (Table 2 SI). (For interpretation of colour in the artwork, the reader is referred to the web version of the article.)

aureoles, two additional samples (Fa-33 and Fa-34; Fig. 2A) collected at granitoid margins in Burkina-Faso recorded particularly elevated peak pressure conditions of 10 and 12 kbar, along a low apparent geothermal gradient of 10–15 °C/km, which we refer to as M1 (Ganne et al., 2012).

Chlorite-rich meta-sediments collected by Perrouty (2012) in the Ashanti greenstone belt in southwest Ghana (e.g. Sample GH517; Fig. 2A) are characterised by pressures <5–6 kbar and peak temperatures of 370–450 °C.

Moderate-pressure (>6–8 kbar) meta-sediments were only observed in a context termed high-*T* aureoles by Ganne et al. (2012), near to granitoid plutons intrusive in thick sequences of sedimentary rocks (for example in the Diale-Dalema basin in Senegal). They commonly display peak metamorphic assemblages characterised by the occurrence of garnet-chloritoid (ex. sample A11, Fig. 2A), chloritoid-kyanite or garnet–staurolite–kyanite. Petrological relationships in these samples provide evidence for a prograde near-isobaric heating from 450 °C to 650 °C at pressures of 6–8 kbar, in the *P–T* field termed M2a by Ganne et al. (2012). The peak metamorphic conditions are followed by a post-peak-pressure retrograde overprint (near-isothermal decompression), consistent with open clockwise *P–T* loops, and associated with regional static (cordierite corona around kyanite, ex. sample Te6C; Fig. 2A) or dynamic (sigmoidal inclusion trails of quartz within staurolite, e.g. sample K451; Fig. 2A) parageneses. The retrograde evolution of these samples suggests a gradual cooling from 4 kbar, 550 °C to 2 kbar, 400 °C along the M2b geothermal gradient (30–50 °C/km, referred to as M2b; Ganne et al., 2012), illustrating a possible change in exhumation dynamics.

Some sporadically observed meta-sediments (ex. Sample 215; Fig. 2A) reached peak metamorphic conditions along the M2b apparent geothermal gradient at $P = 6$ kbar and $T = 650$ °C. Their peak *P–T* conditions range in a moderately high geothermal field of 30–50 °C/km. Their retrograde *PT* paths include a nearly isobaric segment which may reflect a rapid cooling of the meta-sediments after heating.

Except for rare migmatitic fabrics (samples Fa-48; Fig. 2A) in the thermal aureole of granitoids in the area of Koupela and Kouaré in Burkina Faso and Tera in Niger (Fig. 1B), no regional evidence of sediments melting is reported.

As a whole, metamorphic data collected in the thermal aureole of the greenstones (s.l.) belt suggests, a temperature evolution with depth dominated by moderate geothermal gradients of 20–30 °C/km (M2a) for the Palaeoproterozoic crust.

An evolution between the M1 and M2a fields is recorded by a few samples which underwent a prograde heating at rather constant but elevated pressures (6–10 kbar, samples K10, A11 and Te6 C; Fig. 2A). This indicates that some portions of the sediments were initially deeply buried (25–35 km) along a cold apparent geothermal gradient (M1) before heating up to M2. The *PT* evolution in the upper crust is less linear and reflects the competition between the dominant thickening-induced geothermal field (M2a, 20–30 °C/km) and irregular heat influx (M2b, 30–50 °C/km) induced by hot granitoid magmas entering the upper portions of the crust.

The M1 apparent geothermal gradient is recorded in a limited number of samples with a restricted spatial distribution. For most samples, it characterizes their early metamorphic evolution. As a consequence, we consider that it may record early thermal conditions in rock piles set in a specific geodynamic setting. We cannot assume that it is illustrative of the thermal regime in the Eburnean orogenic crust. Rather, we consider that a moderate geothermal gradient of 20–30 °C/km (M2a), as recorded in numerous metamorphic rocks, dominated the Paleoproterozoic crust.

The diversity of peak pressure conditions and the different apparent geothermal gradients recorded across the study area suggest that differential heating and exhumation took place. Although no regional melting is clearly recognised in the study area, abundant granitoid emplacement suggests that lower crustal layers were affected by significant melt production and extraction during the orogenic processes recorded in more superficial lithologies.

Periods of melt extraction in the deeper parts of the Birimian crust and magmatic intrusions in the middle and upper parts

Table 1
(A) Average values of major element compositions (wt%) for the Sefwi Group meta-gabbros, meta-basalts, meta-sediments and CaO-rich granitoids (from Perrouty, 2012). (B) Major element compositions for different lithology recognised in the Tera area. The Tonalite composition is given from Boher et al. (1992).

	Sefwi Group (South Ghana) (low-metamorphosed area)			
	Gabbro	Basalt	Granitoid	Sediment
SiO_2	50.05	49.655	66.725	65.8
TiO_2	0.12	0.695	0.405	0.6
Al_2O_3	12.9	14.038	14.525	14.35
Fe_2O_3	6.395	11.65	4.235	6.2
FeO[a]	5.7555	10.485	3.8115	5.58
MnO	0.13	0.178	0.073	0.07
MgO	14.25	7.878	1.625	1.99
CaO	12.8	8.868	3.268	1.12
Na_2O	0.68	2.365	4.158	1.72
K_2O	0.04	0.098	2.523	3.15
LOI	1.55	3.885	2.17	2.28
Fluid to saturation	3.2745	5.74	2.8865	5.62

[a] $FeO = Fe_2O_3 \times 0.9$.

(Fig. 2A) are likely to generate density contrasts and instabilities, as will be discussed below (Section 4.3). The thermo-mechanical modeling presented in Sections 4 and 5 aims at testing the implication of widespread melting on exhumation, under a continued shortening and thickening regime. It is therefore critical to precisely infer the depth of melting and melt production for mafic and felsic metamorphic rocks in the Birimian crust.

3.3. Metamorphic modeling

We aim to constrain the properties of a model crustal pile along a fixed geotherm through a pseudosection approach. In agreement with results of metamorphic studies, we chose a geothermal gradient of 25 °C/km. The density and mineralogy of different rock-types (i.e. sediment, basalt/gabbro, TTGs) is explored between 300 °C, 12 km and 1200 °C, 48 km; 1200 °C being the upper thermal limit before total melting of mafic rocks in the crust. A lithostatic pressure of 2.857 kbar/km (Spear, 1993) was considered, accounting for the mafic and felsic composition of this crust. Tectonic overpressure is neglected (e.g. Schmalholz and Podladchikov, 2013).

The impact of melt and fluid extraction on rock density and *P–T* conditions of metamorphic reactions is investigated by iteratively fractionating the modeled rock and recalculating a new pseudosection after each fractionation step (Fig. 3B, D–F), and by comparing the results with a 'no fractionation' scenario where melt and fluid stay in situ (Fig. 3A and C). Free-H_2O and/or free-melt in the rock is absent during fractionation modeling. A similar reasoning was followed in Vanderhaeghe (2009), who provided only an empirical estimation of the density evolution of partially molten rocks in absence of reliable data on the density of silicate melts at high *P* and *T*.

The *P–T* pseudosections were calculated for the Na_2O–CaO–K_2O–FeO–MgO–MnO–Al_2O_3–TiO_2–SiO_2–H_2O system, using bulk rock compositions obtained by XRF analysis and for subsolidus H_2O saturations conditions. However, note in Fig. 3A and C that the H_2O contents for the pelitic, granitic and mafic compositions were enhanced to allow the formation of a free hydrous fluid phase and melt on the wet solidus.

The original composition of samples was not modified (Table 1) to fit this 10-component system, except for ferric iron transformed into ferrous iron using the following equation:

$$M\,Fe_{total} = M\,FeO\,(wt\%) = 0.9 \times M\,Fe_2O_3\,(wt\%).$$

CaO content was corrected for apatite using measured P_2O_5.

Mineral chemical analyses within rocks were carried out at the GET at Université Toulouse III, France, using a Cameca SX 50 electron microprobe analyser. Operating conditions were 15 kV, 20 nA, 1–5 μm beam size and counting time of 10 s per element. CO_2 was neglected because no carbonates were observed in the meta-sedimentary rocks analysed. In the mafic lithologies (meta-basalt and meta-gabbro), the formation of Ca-carbonate can be related to late metamorphic events.

Pseudosections were constructed using the PerpleX software version 6.6.8 (Connolly and Kerrick, 1987; Connolly, 2005, 2009) and the thermodynamic database hp04 of Holland and Powell (1998, revised 2004). For solid solutions, we used the internally consistent thermodynamic dataset termed solution_model.dat (November 24, 2012; available at www.perplex.ethz.ch/). The solution models used for the pseudosections are as follows (Tables 2 and 3): Bio(TCC) for biotite (Tajčmanová et al., 2009), Chl(HP) for chlorite (Holland et al., 1998), St(HP) for staurolite (Powell et al., 1998), Ctd(SGH) for chloritoid (Smye et al., 2010), oAmph (DP2) and cAmph(DP2) for ortho- and clinoamphibole, respectively (Diener et al., 2007), Gt(WPPH) for garnet (White et al., 2005), Ilm(WPH) for ilmenite (White et al., 2000), hCrd for cordierite, mica(SGH) for white micas (Smye et al., 2010),melt(HP) (Holland and Powell, 2001), Pl(h) for plagioclase feldspar (Newton, 1990), Kf for potassic feldspar (Waldbaum and Thompson, 1968), Opx(HP) for orthopyroxene (Holland and Powell, 1996), Omph(GHP2) for clinopyroxene (Diener and Powell, 2012), O(HP) for olivine (Holland and Powell, 1998) and MF for magnesio-ferrite/magnetite.

A first set of models was produced using compositions of rocks originating from low-grade metamorphic terrains of SW Ghana. The results are presented in Fig. 3, we note the following features:

(1) Meta-granitoids are the rock type melting at lowest *T* in H_2O-saturated conditions (Fig. 3A). Melting in the crust occurs at about 25 km depth, and affects meta-granitoids, meta-sediments, meta-basalts and then meta-gabbros with increasing depth. At 48 km depth, melt is generated in much larger proportions (100 vol%) from meta-sediment and meta-granitoids than from the mafic material (80 and 50%, respectively).
(2) In a H_2O unsatured scenario (Fig. 3B) where fluid extraction is considered (free-H_2O is missing along the progade *PT* history of rocks), the depth of crustal melting for the meta-granitoids is rather similar to what observed in a hydrated system. The solidus of dehydrated meta-sediments and mafic rocks is slightly more elevated (from 10 to 20 °C, respectively). Note however that melt is generated in smaller proportions at the base of the crust compared to the hydrated system, down to 80 vol% for meta-sediment and meta-granitoids and

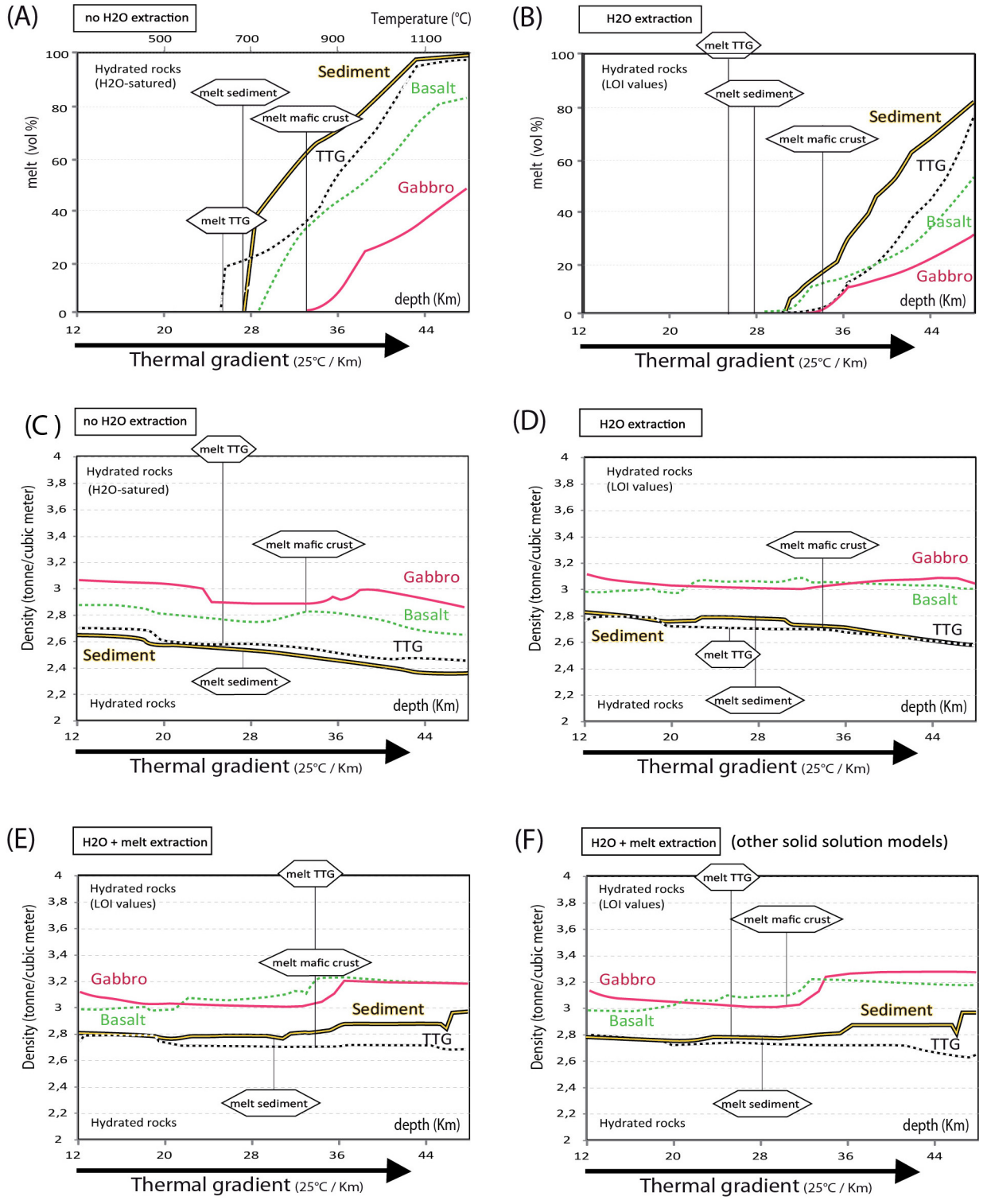

Fig. 3. Metamorphic modeling in low-grade metamorphic terrains. Pseudosections were computed on TTGs, meta-gabbro, meta-basalt and meta-sediments sampled in the southern Ashanti belt region (southwest Ghana) for a CaTiMnNKFMASH system and for bulk rock compositions obtained by ICP-MS analysis (analyses are given in Table 1). (A and B) Melt proportion (wt%) released from rocks was first depicted as a function of depth along a gradient of 25 °C/km and for varying H_2O contents (e.g. H_2O-saturated and dehydrated conditions). (C–E) Density evolution in rocks was also depicted as a function of H_2O and melt extraction and depending on chosen solid solution models (E versus F). (For interpretation of colour in the artwork, the reader is referred to the web version of the article.)

to 30–50 vol% for mafic material (meta-gabbro and meta-basalt, respectively).

(3) There is a rapid increase of the density of the meta-sediments once melt is extracted from the rock (Fig. 3E), unlike for meta-granitoids, that do not record important density changes during burial and melt extraction.

The reliability of our results was strengthened with other P(T)-X calculations performed with a different set of solid solution models proposed for metamorphic mineral as Ctd(HP) for chloritoid (Holland and Powell, 1998), GlTrTsPg for amphibole (White et al., 2003; Wei et al., 2003), Gt(HP) for garnet (Holland and Powell, 1998), Pheng(HP) for phengite (Holland and Powell, 1998), MuPa

Table 2
Endmembers used for Perple-X pseudosection calculation (see documentation in Perple_X 6.6.8 for references on solid solution models – http://www.perplex.ethz.ch).

Mineral	Solid solution model	Endmembers
Olivine	O(HP)	teph fo fa
Clinopyroxene	Omph(GHP)	di, jd, acm, hed
	Omph(GHP2)	
Orthopyroxene	Opx(HP)	mgts fets_d
		en fs
		mots feots
Amphibole	GlTrTsPg	tr, ts, Parg, gl
	oAmph(DP2)	tr ftr
		mpa2 fpa
		ged_dqf2 fged
		ogl_dqf fgl
		anth fanth_dq
		omrb_dqf frb
	cAmph(DP2)	tr ftr
		parg_dqf fparg
		ts_dqf fts
		gl_dqf fgl
		cumm grun
		mrb frb
Garnet	Gt(GCT)	spss, alm, p expndtw-5 y, gr
	Gt(WPPH)	spss alm py gr
		fmn_i fkho_i kho andr_i
Staurolite	St(HP)	mnst, fst, mst
Cordierite	hCrd	fcrd, crd, hcrd
Chloritoid	Ctd(HP)	mnctd, fctd, mctd
	Ctd(SGH)	octd mnctd fctd mctd
Chlorite	Chl(HP)	daph, ames, afchl, clin
Biotite	Bio(TCC)	mfbit ffbit fbit
		mtbit ftbit tbit
		mts sdph east
		mnbi ann phl
Micas	Mica(SGH)	mu pa ma_dqf cel fmu fcel
Phengite	Pheng(HP)	pa, cel, fcel, mu
Paragonite	MuPa	mu, pa
Plagioclase	Pl(h)	abh, an
K-feldspar	Kf	mic, ab
Ilmenite	Ilm(WPH)	pnt, geik, hem, oilm
		dilm
melt	melt(HP)	h2oL, fo8L, fa8L, abL
		sil8L, anL, kspL, q8L

for white micas (Chatterjee and Froese, 1975) or Omph(GHP) for clinopyroxene (Green et al., 2007). Results are given in Fig. 3F. Very small differences can be observed when comparing with Fig. 3E; in terms of either density changes or melts production along the M2a thermal gradient selected for Perple-X calculations.

P(T)-X results obtained on sediments, mafic materials (gabbro and basalt) and TTGs collected in the low-grade metamorphic terrains of SW Ghana are summarized in Table 4. Data is displayed according to general "Temperature" and "Depth" conditions for melting of these three different materials constituting the Birimian crust, so as to incorporate them in the thermo-mechanical modeling below.

Major implications of these results are:

- In both H_2O saturated and H_2O unsaturated scenario, melting in the crust occurs at about 25 km depth and first affects the meta-granitoids, then the meta-sediments (28 km). Fertile sediments deeply buried in the Birimian crust could have been in contact with partially molten granites and, ultimately, could have been incorporated as metamorphic enclaves within the pluton.
- In both H_2O satured and unsaturated scenario, an important increase of the density of the meta-sediments is calculated once melt is extracted from the rock, unlike for meta-granitoids, which do not record important changes in density during burial process and melt extraction.

The thermo-mechanical models proposed in Sections 4 and 5 were built with physical parameters (solidus, density and melt production versus depth) drawn from metamorphic modeling on rocks of SW Ghana, considering a fluid unsaturated scenario with H_2O extraction (see Section 4.4). Despite fluid transfers from depth promoting melting in the upper sections, it is unlikely that fluid saturation was maintained in the whole Birimian crust during the orogeny. Furthermore, because of difficulties to consider melt extraction in numerical models, we chose the scenario detailed in Fig. 3B and D (H_2O extraction but no melt fractionation) to constrain our density profiles and melt production (see Section 4.5).

4. Assumptions for a thermo-mechanical model

Let us recall that a priori we are not as much interested in reproducing the burial mechanisms at work during the Eburnean orogeny, for which field data is too sparse, as in the geometrical and kinematical conditions that triggered the exhumation of lower crustal rocks. However, we need to assess appropriate assumptions on a geometrical setting of the Eburnean orogeny after the achievement of a minimal crustal thickening, and from which a driving mechanism for exhumation may initiate. In this sense we proceed similarly to studies of post-orogenic evolution (such as for instance Rey et al., 2009; Vanderhaeghe, 2012; Maierová et al., 2012, 2013). We make the following first order considerations.

Table 3
Endmembers used for Perple-X pseudosection calculation on sediments, mafic materials (gabbro and basalt) and TTGs collected in the low-grade terrains of SW Ghana with different solid solution models.

Other solid soluation models	**Greenschist metamorphic facies (South Ghana):** **TTG** oAmph(DP2), cAmph(DP2), Ep(HP), Bio(HP), Chl(HP), Mica(SGH), Gt(WPPH), Pl(h), Ilm(WPH), Kf, melt(HP) **Sediment** oAmph(DP2), cAmph(DP2), Bio(TCC), Chl(HP), Omph(GHP2), Pheng(HP), Gt(WPPH), St(HP), Ctd(SGH), hCrd, Pl(h), Ilm(WPH), Kf, MF, melt(H expndtw1 P) **Basalt/Gabbro** O(HP), oAmph(DP2), cAmph(DP2), Bi expnd0o(TCC), Omph(GHP2), Opx(HP),Mica(SGH), Ctd(SGH), Gt(WPPH), Ep(HP), Chl(HP), Pl(h), Ilm(WPH), Kf, melt(HP)
	Greenschist metamorphic facies (South Ghana): **TTG** GlTrTsPg, Ep(HP), Bio(HP), Chl(HP), Pheng(HP), MuPa, Gt(HP), Pl(h), Ilm(WPH), Kf, melt(HP) **Sediment** Bio(TCC), Chl(HP), Omph(GHP), Pheng(HP), Gt(HP), St(HP), Ctd(HP), MuPa, hCrd, Pl(h), Ilm(WPH), Kf, MF, melt(HP) **Basalt/Gabbro** GlTrTsPg, O(HP), Cpx(HP), Opx(HP), Ep(HP), Bio(HP), Chl(HP), Pheng(HP), MuPa, Gt(HP), Pl(h), Ilm(W expnd0PH), Kf, melt(HP)

Table 4
Perple-X P(T)-X calculations along a geothermal gradient of 25 °C/km leading to infer in witch proportion and at witch depth metamorphic rocks of mafic and felsic composition will be transformed into melt in the Birimian crust. Rocks collected in the low-grade terrains of SW Ghana have been considered. Density of fertile material before and after melt extraction was specified in the table. Here, we have considered that melt extraction from rocks occurred at the time the ratio "molten" versus "infertile" material oversized the value 0.1 (10 vol%). Conversely, fluid extraction from rocks during burial and dehydratation was considered to be immediate and continuous along the M2a geothermal gradient.

Ghana (Greenschist facies; $T < 300$ °C and $P < 5$ kbar)										
			T solidus	Corresponding depth		10% of melt in the rock	Corresponding depth		Unfertile material	Corresponding depth
Sediments	300 °C	H_2O	690 °C	28 km	H_2O	800 °C	32 km	H_2O + melt	1200 °C	48 km
melt	0% (volume)	extraction	<1%		extraction	10%		extraction	80% of melting	
density of rock	2800		2770			2720			2960	
Gabbro	300 °C	H_2O	836 °C	33 km	H_2O	910 °C	36 km	H_2O + melt	1200 °C	48 km
melt	0% (volume)	extraction	<1%		extraction	10%		extraction	30% of melting	
density of rock	3110		3020			3050			3180	
Wet basalt	300 °C	H_2O	718 °C	28 km	H_2O	827 °C	33 km	H_2O + melt	1200 °C	48 km
melt	0% (volume)	extraction	<1%		extraction	10%		extraction	50% of melting	
density of rock	2980		3050			3050			3170	
TTG	300 °C	H_2O	636 °C	25 km	H_2O	900 °C	36 km	H_2O + melt	1200 °C	48 km
melt	0% (volume)	extraction	<1%		extraction	10%		extraction	80% of melting	
density of rock	2730		2700			2670			2670	

4.1. System initial geometry

Thick piles of volcano-sediments (~10 km) in the Birimian province (e.g. Diallé-Dalema Basin in eastern Senegal; Bassot, 1966) are consistently observed and are considered to have formed during the Eburnean orogeny. Deformation in the volcano-sedimentary piles is associated with regional metamorphism and is correlated across the extent of the craton (Bonhomme, 1962; Feybesse et al., 2006 and refs therein). These features are interpreted as a consequence of collisional tectonics.

However, 10–15 km thick sedimentary layers cannot alone explain the high pressures recorded by the Birimian rocks (Section 3.2), and therefore a mechanism of compressional tectonics is again required to explain the further burial of these rocks, over a distributed horizontal extent and in association with a rather uniform geothermal gradient of 20–30 °C/km (Section 3.2). Therefore our modeled "initial orogenic" geometry should consider a relatively wide domain of moderately deep sedimentary sequences, which will be submitted to compressional boundary conditions.

What simplest "initial" geometry could have prevailed at some point of the Eburnean orogeny, which would represent a suitable starting stage that further triggered the exhumation of buried material? Acknowledging that such an "initial orogenic" geometry could not remain in gravitational and thermal equilibrium, we first assume a model geometry in which the mafic crust had a doubled-thickness of 20–30 km, with respect to present day average oceanic crust thickness. Second, we assume that somewhere either above or adjacent to this thickened crust lied large sedimentary basins, equivalent to the deepest sedimentary basins reported today worldwide (Cobbold et al., 1993; Laske and Masters, 1997). We choose a crustal geometry that we think best corresponds to a remnant volcanic fore-arc to back-arc domain in an oceanic environment. At the center of the model, the mafic crust is replaced by a thick (15 km) and large (200 km) volcano-sedimentary basin and lies over a crustal melange. This melange is composed of basaltic oceanic crust and composite granulite representing the early TTGs emplaced at the bottom of the arc and back-arc system ("layered plutonic complex" in Senegal; Dioh et al., 2006).

4.2. Exhumation processes

Syntectonic granite emplacement is often interpreted as the result of melt migration along opportunistic mechanical weaknesses such as foliation planes or dilatant shearing channels (e.g. Clemens and Mawer, 1992; Weinberg, 1996 or Vanderhaeghe, 2001 and references therein). It has been proposed that weak buoyant rocks can rise within narrow and permeable fracture pathways (e.g. Pons et al., 1995; Foroozan et al., 2012; Mourgues et al., 2012). However, this mechanism as a driving force of exhumation does not win unanimous support for several reasons (e.g. Vigneresse and Clemens, 2000; de Saint Blanquat et al., 2011). Indeed, it cannot account for exhumation of source migmatites and does not explain regional-scale exhumation (e.g. the hundreds of km^2 areas of amphibolite facies reported by De Kock et al., 2012 and Block et al., 2012 in the Bolé-Nangodi belt area in north Ghana). Such large regions of exhumed lower crust advocate for a broad regional low viscosity of the entire medium, allowing buoyant material to ascend massively (e.g. pluton emplacement descriptions by Pons et al., 1992, 1995 or Vidal et al., 2009, for the Birimian crust. Analog and numerical modeling explored this mechanism (Cagnard et al., 2006, 2007, 2011) in Precambrian 'hot' orogens and (Lexa et al., 2011; Burg et al., 2004; Gerya et al., 2008) in Variscan domains.

The ability of partially molten lower crustal rock to ascend towards the surface by gravitational instability depends on viscosity and density contrasts with the surrounding country rock. If the latter is too competent, any buoyant rock remains stuck underneath a resistant cap (cf. known limitations on diapiric ascent of magmas, e.g. Vigneresse and Clemens, 2000). Numerical studies have shown that gravitational instabilities are indeed a plausible mechanism to exhume lower crustal rocks under a compressional regime, under the following conditions:

- First, melting of lower crustal rocks may occur over a time-scale of tens of millions of years, due to the accumulation of radiogenic heat (Thompson and Connolly, 1990; Vanderhaeghe et al., 2003; Gerya et al., 2008), or as the consequence of an astenospheric heat influx (e.g. slab delamination, Ueda et al., 2012).
- Second, gravitational instabilities may develop within low viscosity channelised flow when accounting for non-linear rheologies and asymetric surface processes (Vanderhaeghe et al., 2003; Maierová et al., 2012).

The viability of such an exhumation process for the Birimian crust depends on its composition, which was obviously dominated by a mafic composition. Yet, a dominantly mafic crustal composition produces relatively little radiogenic heat (despite Birimian times producing about 1.7 more heat than present day, e.g. Perry et al., 2006) and behaves competent (cf. extrapolation of an

equivalent viscosity from laboratory experiments showing that mafic compositions lie amongst the most competent rheologies after olivine, e.g. Kirby and Kronenberg, 1987; review in Bürgmann and Dresen, 2008). In contrast, wet granite has among the weakest rheologies estimated experimentally (e.g. Kohlstedt et al., 1995; Bürgmann and Dresen, 2008), thus it appears as an appropriate candidate to represent a dominant crustal composition that is weak enough to endorse the exhumation of significant volumes of sediments and melts. Hence, a spatially extended mechanism of either heating or hydration seems required in order to significantly weaken the originally mafic Birimian crust. Therefore, we need to define the hypothetic thermal conditions that would have acted at the base of the juvenile Birimian crust. One "easy" option is to bring heat from the base by assuming the opportunistic arrival of some sort of thermal plume (for instance due to mantle convection at depth or consequently to some slab breakoff, e.g. Burov et al., 2007; Ueda et al., 2012). Another option consists in supposing that at Birimian times, convection in the mantle was probably much more active, and that its boundary with top conductive plates was shallower than today. Details on how we implemented both these options are provided in the next section, when describing the technical aspects of our modeling approach.

Exhumation of orogenic crust driven by extensional kinematics is an alternative mechanism that has been advocated for modern orogens such as the Alps, the Aegean domains and the North American ranges. Field data has been compared with a number of numerical and analog approaches, aiming at explaining the *P–T–t* patterns accompanying the exhumation of gneiss domes and the development of metamorphic core complexes (e.g. Rey et al., 2009; Huet et al., 2011; Le Pourhiet et al., 2012; Tirel et al., 2013). Lineation orientations associated with lower crustal doming below thinning upper crust appear comparable to shortening-induced folding structures. In addition, *P–T–t* paths resemble those obtained for the Birimian rocks. However, the timing of exhumation is fast in an extensional setting (of the order of about 10 Myr: Huet et al., 2011; Tirel et al., 2013), in comparison to the ~50 Myr period during which crustal exhumation is assumed throughout the WAC region (i.e. exhumation of metasediments in the thermal aureole of the Saraya (Senegal) and Tera (Niger) plutons at 2.08 and 2.15 Ga, respectively). Furthermore, crustal boudinage wavelengths are typically similar to buckle-folding wavelengths (same relationship to characteristic layer thickness). However, the sparse field data (described in Section 3) impedes a precise structural and petrological analysis for the Birimian terranes, and lacks evidence for extensional structures both at local scale and at large scale. Yet, the lack of field evidence does not mean extension did not occur and this mechanism will be further mentioned in the conclusive discussion (Section 6).

The probable effects of transcurrent tectonics on exhumation dynamics cannot be handled with a two-dimensional approach. Section 6 also addresses some of the questions raised on the contribution of this tectonic regime to exhumation.

In the numerical study presented below, we intend to explore the possibility of exhumation on a regional scale, driven by density contrasts and viscosity changes induced by metamorphic reactions, upon shortening of a lithospheric pile as described in Section 3.2. Metamorphic *P–T–t* paths followed by particles in the numerical model will serve as a comparison with *P–T* paths obtained from metamorphic studies, and will form a basis to discuss the viability of the modeled exhumation mechanism.

4.3. Thermo-mecanical numerical method and setup

We use a version of the numerical code Parovoz (Poliakov et al., 1993), based on the FLAC method (Fast Lagragian Analysis of Continuum, Cundall and Board, 1988). This two-dimensional plane-strain, finite-differences method has been adapted to many geodynamical applications, at crustal and lithospheric scales, in collision and extensional settings (e.g. Burov and Poliakov, 2001; Burov et al., 2007; Yamato et al., 2007; Gerbault et al., 1999, 2009). The equations of motion are solved in a large-strain Lagrangian formulation and with an explicit time-marching scheme. The method is briefly recalled here, and detailed equations can be found for instance in Gerbault et al. (2009). At each time-step, Newton's equations (1) are used to calculate nodal velocities (v), which are in turn derived to calculate new elementary stresses (Lagrangian stress tensor σ) from the constitutive laws (2):

$$\rho \cdot \frac{Dv_{ij}}{Dt} = \frac{\partial \sigma_{ij}}{\partial x_j} + \rho \cdot g_i, \tag{1}$$

$$\frac{D\sigma_{ij}}{Dt} = F(\sigma, T, \dot{\varepsilon}, \ldots) \tag{2}$$

where ρ is density, t is time, g is gravity acceleration, σ is the Cauchy stress tensor and i, j refer to two-dimensional components. From the velocity components elementary strain-rates $\dot{\varepsilon}$ are then calculated and implemented into the temperature (T)-dependent visco-elasto-plastic constitutive laws (F) in order to deduce new elementary stresses. Nodal forces are integrated from the elementary stress components to compute new nodal velocities as an input for the next time-step.

Self-consistent visco-elasto-plastic rheology (F function) is accounted for, with the elementary total strain increment being the sum of elastic, viscous and plastic contributions. Elasto-plasticity is prescribed with a Mohr–Coulomb non-associative criterion (dilatancy is 0, see Tables 5 and 6 for friction and cohesion values). Maxwell visco-elasticity accounts for temperature via a dislocation creep power-law relationship deduced from laboratory rock experiments (e.g. Bürgmann and Dresen, 2008; Kohlstedt et al., 1995, and references therein). The minimum of the elasto-plastic and visco-elastic stress is retained at each time step within each element. The creep flow law and associated parameters for each rheological layer are given in Tables 5 and 6. The remeshing technique makes use of passive markers, which carry elementary material properties (stresses and temperature) from the old mesh to the new mesh (e.g. Gerbault et al., 2009, this technique was benchmarked with the tests presented in Gerya and Yuen, 2003, and Schmeling et al., 2008).

The modeled domain is initially 800 km wide and 60 km deep, and is meshed with 400 × 60 elements (horizontal resolution is 2 km, and vertical resolution is 1 km). The modeled crust is made of 15 km of mafic granulite (dark blue layer in Fig. 5), underlain down to 20 km by a layer of generally lighter granulite melange (assumed to contain the early TTGs, light blue layer). At the center of the model, the crust is replaced by a 16 km thick and wide sedimentary basin (equivalent to the present day deepest basins, turquoise and green layers), which lies over 8 km of a crustal melange. This melange is composed of 3 km of basaltic oceanic crust and 5 km of composite granulite representing the early TTGs. We have chosen a width of 280 km for this sedimentary basin, corresponding to indications of the width of the Siguiri Basin (>200 km) located in Upper Guinea – Southwest Mali (Fig. 1A). The bottom shape of this basin is described with a flexural thickness of 60 km, and it is isostatically compensated with a self-consistent topography (the initial top surface is calculated so that the weight of every 60 km thick elementary column is constant). A maximum residual stress of 40 MPa develops at the center of the basin due to this initial geometry (with no shortening applied; this represents about 10% of the maximum stresses developed when applying lateral motion). The low density TTG material that is inserted below the crust renders the model unstable gravitationally at the beginning of the model run, yet this layer is embedded in between resistant mafic crust

Table 5
Thermo-mechanical model parameters, Units and values. Dislocation creep power-law is $\eta_{eff} = 0.25 \cdot (3A/4)^{-1/n} \cdot \dot{\varepsilon}_{II}^{((1/n)-1)} \cdot \exp^{(E/nRT)}$, with parameters A, n, Q given for specific rock values in Table 6. Flexural equation is from Turcotte and Schubert (2002). Grey values are modifications from the reference model M0 for the alternative models A, B and C (see text).

Symbol	Description	Value-units
g	gravity	9.81 m²/s
ρ	density	kg/m³
G, λ	Lamé elastic constants	10 GPa
φ, S_o	Friction angle and cohesion for Coulomb failure	5-20°, 5-10 MPa
Vbc	Horizontal velocity (modified for model B)	5 - 20 mm/yr
k_{er}	Diffusion coefficient for surface processes	100 m²/yr
H_s,h_r	Radiogenic crustal source $H_s = H_o \exp(-y/h_r)$	2.10^{-10} W/kg,10km
A_q, H_q	Gaussian plume for alternative model (A)	8 km, 40 km
Q_l	Latent heat for melting material	3.10^5 J/kg
α_o	Reference thermal heat expansion	3.10^{-5} /K
β_o	Reference thermal compressibility	10^{-11} /K
Cp_o	Reference heat capacity	1000 J/kg/C
k	Thermal conductivity	W/m/°C
A	Dislocation creep power law pre-exponential factor	MPa^{-n} /s
n	Dislocation creep power law exponent	-
Q	Power law creep activation energy	kJ/mol
w_o, H_e	Flexural amplitude and thickness for Crustal thickness	8 km, 60 km
SS	Sedimentary basin maximum width and thickness (positioned laterally for model C)	280 km-15 km 100 km-10 km

and lithospheric mantle, therefore it remains mechanically stable if no boundary motion is applied.

Far-field convergence is then applied at a rate of 5 mm/yr for about 50 Myr, during which shortening concentrates in the relatively weak central pre-thickened domain (Figs. 4 and 5, stage 1). Alternative models in which a convergence of 2 cm/yr, and then extension at 5 mm/yr, were applied will be explored afterwards (Section 5, Fig. 6). At the base of the modeled domain, normal stress balances the overburden weight (Dirichlet stress condition), whereas the top surface is stress free and submitted to erosion and sedimentation processes, according to a standard diffusion equation (coefficient given in Table 5).

The thermal field is initially calculated according to a modified plate cooling model from Parsons and Sclater (1977), which depends on an effective thermo-tectonic age of the lithosphere (e.g. as in Yamato et al., 2007). An effective age of 200 Myr and a radiogenic source in the crust of 5×10^{-10} W/kg (were assumed. This radiogenic heat source is chosen equivalent to present day averages, considering that first, 2 Gyr ago it was about 1.7 times greater than present day, and second that our Birimian crust is dominantly mafic (e.g. Perry et al., 2006). These assumptions together with setting the 1300 °C isotherm at 70 km depth (H_l, Table 5) generate an initial geothermal gradient of about 24 °C/km, with the isotherm 600 °C lying at 25 km depth (M2a gradient described in Section 3). The conductive heat equation is then resolved iteratively in time, and accounts for radioactive heat sources and shear heating. The advective term is implicitly resolved by the displacements of the Lagrangian grid.

For the basal thermal condition, numerical models usually apply either a fixed temperature or a fixed heat flow at the model bottom boundary. However in Section 4.2, we identified the need to "bring" heat to the system, since preliminary tests showed that no exhumation occurs if such usual basal heat boundary conditions are applied. Therefore the following two options were tested:

- One option assumes active and shallow mantle convection, and is considered in our reference model M0. We choose to maintain the 1300 °C isotherm at the constant depth of 60 km, so that any material buried below this depth immediately gains this temperature (models M0, B and C).
- The other option mimics the arrival of a plume (e.g. Burov et al., 2007), and will be considered in alternative model A. Additional basal temperature is applied from 10 to 15 Myr of the model run time, with a central Gaussian geometry the 1300 °C isotherm approaching 45 km depth (model A, see Table 5 for numerical values).

Table 6
Rheological properties of modeled lithospheric layers (from Ranalli, 1995 and references therein). Parameters units in Table 5 Partially molten layers have an effective density, heat capacity, thermal expansion and viscosity controled by Eqs. (3)–(6), respectively, bounded by the reference molten density at the given maximum melt % at fusion temperature 1200 °C (deduced from calculations Fig. 3). Therefore *ρ_solid* is given in the first 4 lines for intact rocks, whereas *ρ_molten* are provided in the last two lines below. See text (Section 4.3) for critical temperatures for melting.

Layer	Rock type	ρ	k	A	n	Q
Upper (mafic) crust	Diabase	3050	2.9	2.0×10^{-4}	3.4	260
Lower crust TTG melange	Quartzodiorite	2700	2.9	1.3×10^{-3}	2.4	219
Mantle	Dry olivine	3250	3.3	7.0×10^{4}	3.0	520
Sediments	Wet quartzite	2800	2.5	3.2×10^{-4}	2.3	154
80% molten TTG and sediments	Wet granite	2600	2.5	–	–	–
30% molten mafic crust	Wet granite	3050	2.5	–	–	–

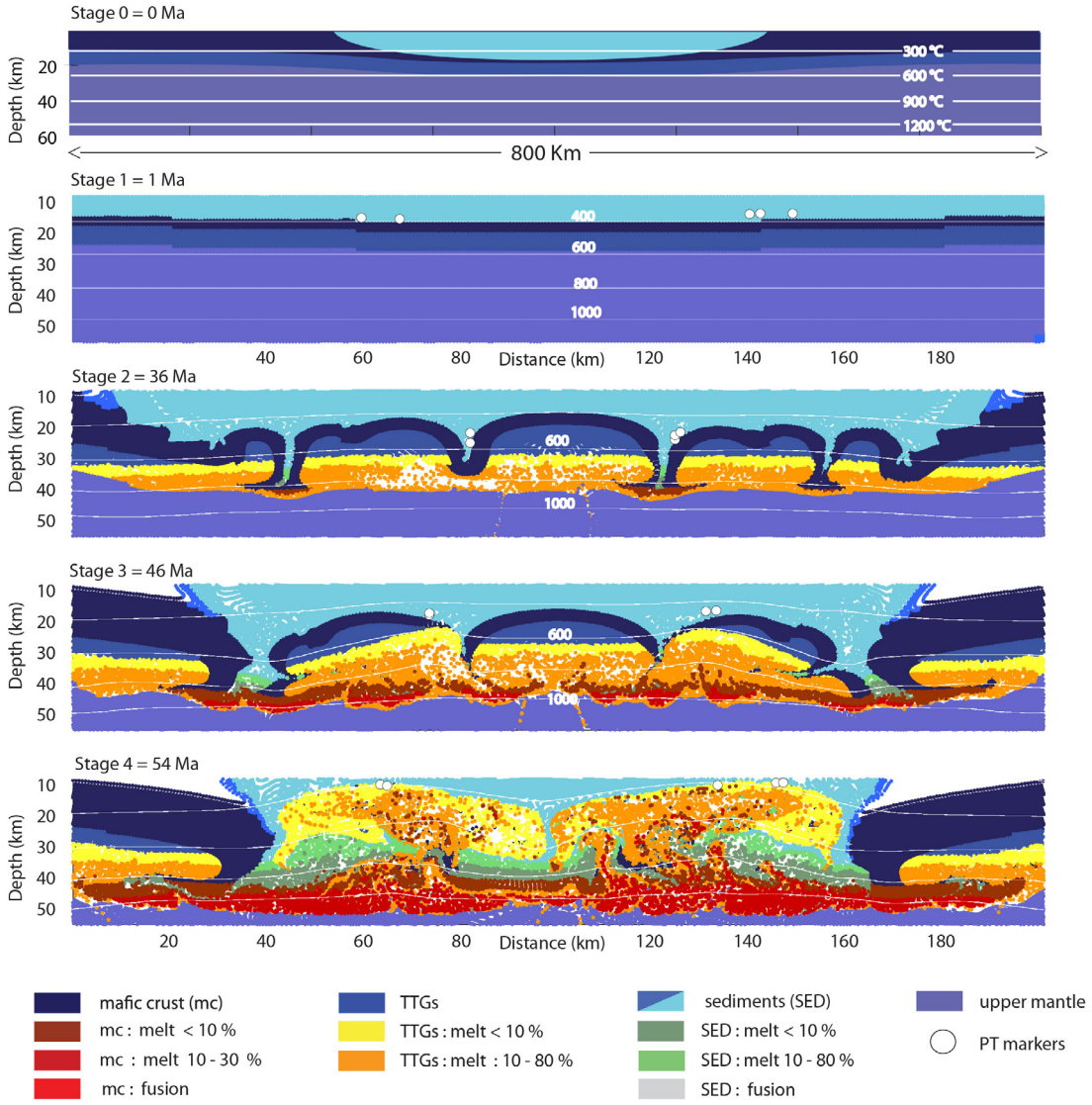

Fig. 4. Thermo-mechanical model of folding, melting and buoyant exhumation of TTGs. The figure displays the markers for the reference model (M0) defined with a 15 km thick sedimentary basin (turquoise layer) lying over 10 km of crustal melange (blue layers). The base of this crustal melange is made of early TTGs material (intermediate blue layer, stage 0 and 1; see Tables 5 and 6 for layers properties). The second image (stage 1) is a zoom of the central part of the domain at its initial stage. Under applied far-field convergence, the whole crust shortens and folds develop below the sedimentary basin (stage 2). As the deepest TTG elements located in fold hinges reach the prescribed melting conditions they switch to other material properties (orange colors for partially molten TTGs) with progressive changes in density and viscosity as described in the text. This buoyant and low viscosity material eventually breaks through the competent mafic layer and ascends through the weak sediments from 35 Ma on (stages 3–4). The white domains are filled with elements (not shown for clarity) on which the thermo-mechanical equations are computed. (For interpretation of colour in the artwork, the reader is referred to the web version of the article.)

4.4. Melting assumptions

In agreement with the constraints obtained from metamorphic modeling (Section 3), metamorphic reactions start with melting of the TTGs and continue with that of the sediments, respectively around 636 and 700 °C (wet solidus). We estimate that the newly formed melt loses about 5% (TTGs-derived) to 10% (sediments-derived) of its total mass (e.g. the density ratio between melt and un-molten rocks; see Fig. 3C). This information provides the evolving relationship between densities and partial melting. Whereas a number of numerical approaches deal with phase changes in rocks by coupling a thermo-mechanical code with a thermodynamical code (such as Parovoz with Theriak, Yamato et al., 2007), other approaches describe melting by assuming that the volumetric melt fraction increases linearly with temperature (Gerya and Yuen, 2003; Gerya et al., 2008). We adopt a similar approximation here, where (M) designates the volumetric melt fraction:

$$\begin{aligned} M &= 0, && \text{at } T = Tsol, \\ M &= \frac{(T - Tsol)}{(Tliq - Tsol)}, && \text{at } Tsol < T < Tliq \\ M &= 1, && \text{at } T \geq Tliq, \end{aligned} \tag{3}$$

and where $Tsol$ and $Tliq$ are the wet solidus and dry liquidus temperatures of the considered rock, respectively, drawn from Fig. 3B.

The effective density, ρ_eff, of partially molten rocks is calculated from the pressure- and temperature-dependent densities of solid and molten rock (respectively ρ_solid and ρ_molten):

$$\begin{aligned} \rho\_eff &= \rho\_solid - M(\rho\_solid - \rho\_molten), \\ \rho(P,T) &= \rho_0[1 - \alpha(T - T_0)][1 + \beta(P - P_0)] \end{aligned} \tag{4}$$

with ρ_0 the standard density at $P_0 = 0.1$ MPa and $T_0 = 298$ K; α and β are the thermal expansion and compressibility coefficients, respectively.

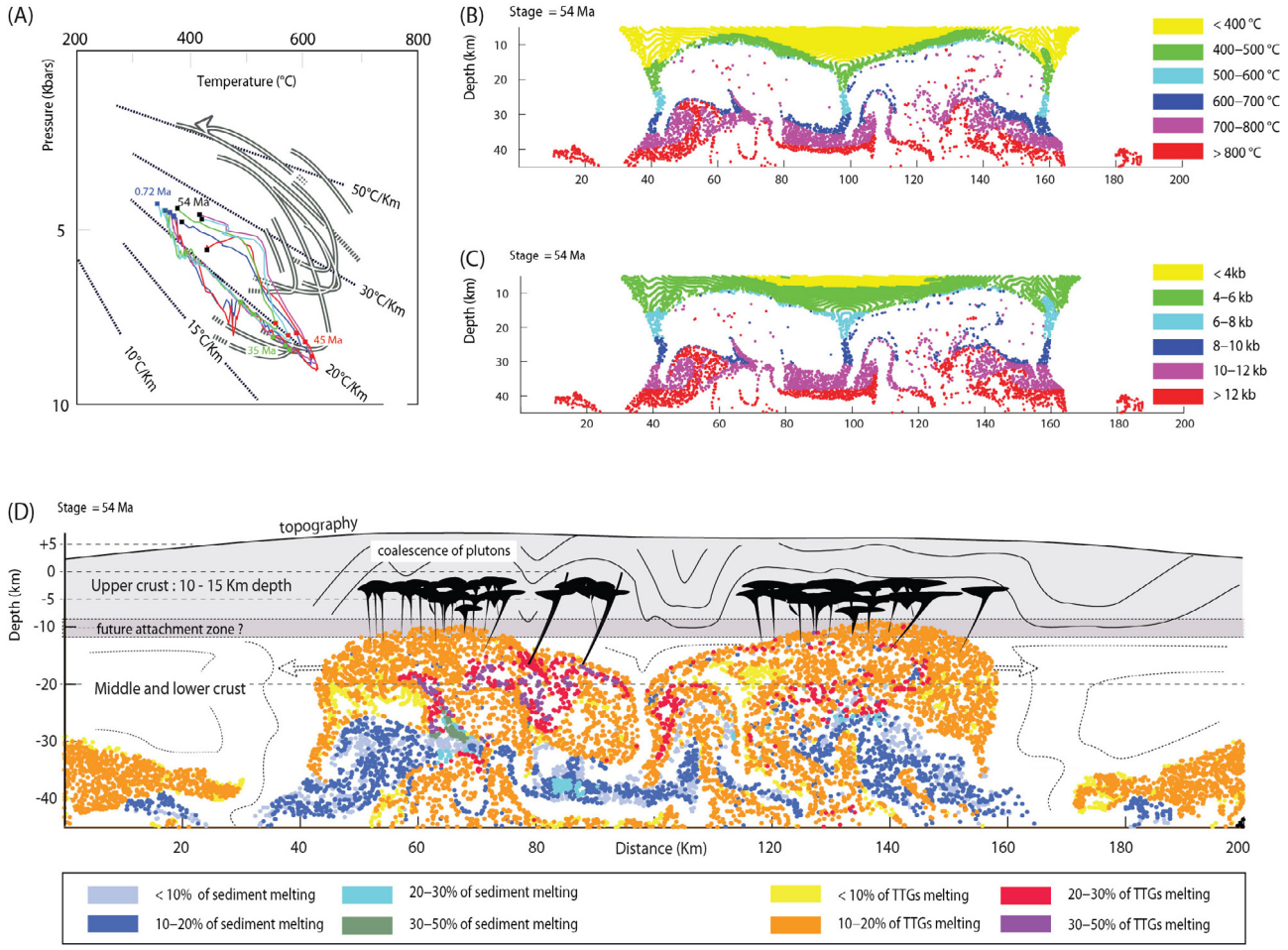

Fig. 5. Related pressure–temperature–time (*PTt*) paths in sediments. (A) Exhumation patterns are consistent with the general *PT* paths depicted from meta-sediments (Ganne et al., 2012) of the Birimian province (grey arrow). Sedimentary rocks reach a peak at ~6–8 kbar and ~500–600 °C, and return to 4 kbar and 450 °C. At the same time, TTGs-derived molten material achieves ~8–12 kbar and 600–800 °C, and return to ~5 kbar and ~500 °C. (B and C) The maximal temperature and pressure recorded by particles of sediments over the duration of the model and their distribution as discontinuous and thin packages around the granitic pluton. (D) Melting proportions throughout the model crust at stage 4. It shows the small proportion of particles that went through more than say 30–40% of partial melting, which corresponds to the potential threshold marking the transition from migmatites to heterogeneous granites (Vanderhaeghe et al., 2003; Rey et al., 2009). Note that most of the sediments and TTGs crossing their solidus during burial processes will not record more than 20% of melting. The mafic crust appears also weakly reworked by partial melting (<10%; not visible in the figure). (For interpretation of colour in the artwork, the reader is referred to the web version of the article.)

In a way similar to Gerya et al. (2008), the effects of latent heating during melting are accounted for with a modification of the effective heat capacity of partially molten rocks (Cp_{eff}), and of their thermal expansion coefficient (α_{eff}):

$$Cp_{eff} = Cp_0 + Q\_L\frac{M}{Tsol}, \quad \alpha_{eff} = \alpha_0 + Q\_L\rho\frac{M}{T}, \tag{5}$$

where Cp_0 and α_0 are the heat capacity and the thermal expansion coefficient of the initial rock assemblage, respectively, and Q_L is the latent heat of melting, fixed for all crustal rocks to 3×10^5 J/kg (Bittner and Schmeling, 1995).

Experimental data show that the strength of rocks decreases by 2–3 orders of magnitude if they contain a few % of silicate melts (Rosenberg and Handy, 2001). An exponential relationship function of the volumetric melt fraction M is obtained from experiments (e.g. Bittner and Schmeling, 1995). Here it is prescribed similarly to Gerya and Yuen (2003), for $M > 1\%$:

$$\mu_{eff} = 5 \times 10^{16} \exp\left(2.5 + (1-M)\left(\frac{(1-M)}{M}\right)^{0.48}\right). \tag{6}$$

During the model run, three layers are allowed to melt according to the procedure described above, at conditions corresponding to the results from metamorphic modeling (Section 3, Fig. 3, and Tables 3–6):

- The TTG material composing the lower crust (light blue layer) is prescribed to transform into a wet granite of lower density (2600 kg/m^3 when temperature reaches $Tsol = 636$ °C. Melt fraction ranges from 1% to 80% at 1200 °C (Fig. 3B), and density and viscosity evolve with (M) according to Eqs. (3)–(6).
- Sedimentary rocks (light blue layer) start melting at $Tsol = 700$ °C and reach 80% of melt at 1200 °C (Fig. 3B and D). They are assumed to transform progressively into an assemblage of density equal to 2600 kg/m^3.
- Mafic rocks (dark blue layer) display a lower rate of melt productivity. Melting starts at $Tsol = 836$ °C, and achieves 30% at 1200 °C (Fig. 3B). Metamorphic modeling indicates that their density does not evolve significantly with increasing (M) (Fig. 3D), and it is thus assumed to remain constant at 3050 kg/m^3.

5. Thermo-mechanical modeling results and discussion

Our reference model M0 is first described with Figs. 4 and 5, associated to the parameters detailed in Tables 5 and 6. Three other models are then presented to illustrate several first order

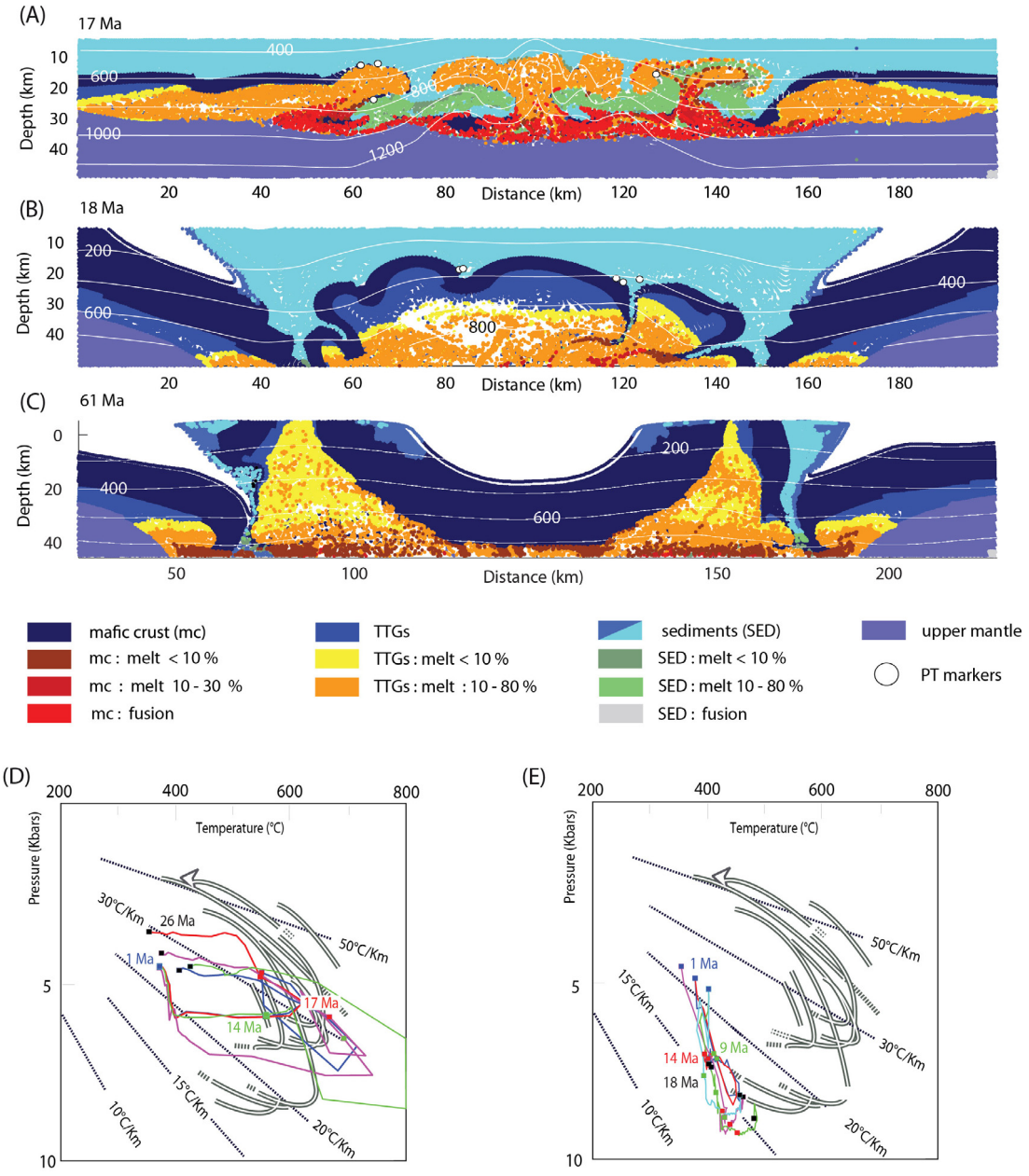

Fig. 6. Alternative models illustrating the range of applicability of the thermo-mechanical exhumation process. (A) In this model, in comparison to the main model M0, Fig. 4, a thermal plume is simulated with the application of a gaussian additional temperature at the center of the domain from 10 to 15 Myr (see text and Table 5 for details). With this enhanced basal heat, buoyant molten TTGs start piercing the competent mafic crust much faster, gravitational instabilities develop rapidly and are much more vigorous (stage 3, 17 Ma). Within 17 Mrs, the whole crust is involved into active mixing of molten sediments, TTGs and mafic crust. (B) In this model B, compression is applied at 2 cm/yr. Note the thickening of the sedimentary basin without exhumation of molten material. Folding and melting occur and form a huge flower structure, that remains buried below 20 km. (C) In this model C, the initial geometry is modified to simulate sedimentary basins 10 km thick aside a volcanic arc. With applied shortening, the TTGs start melting below the arc, and large thrusts develop at the margins of the basin. After 61 Myr, and despite the burial of sedimentary rocks along these shear zones, they remain stuck below the competent mafic crust (about 20 km depth), despite exhumation of molten TTGs. Unrealistic high temperatures (for these depths) would be required to trigger exhumation. (D) *P–T–t* peak and exhumation patterns, for model A with a heating plume assumption. They exceed the 30 °C/km geotherm. (E) *P–T–t* patterns for model B. They reach the cold geotherm of 15 °C/km, but particles never exhume. (For interpretation of colour in the artwork, the reader is referred to the web version of the article.)

parametric effects (alternative grey values in Table 6), and are displayed in Fig. 6.

5.1. Results of reference model scenario (M0)

Within the first 10 Myr of the model run, the weakest central domain of the basin thickens because of the applied convergence. During this stage, the competent crust below the sedimentary basin develops folds, and the buried TTGs start to melt, deepest areas first. At 20 Myr (not shown), the basal TTGs are molten over a distance of about 100 km laterally in the central domain and between ~30 and almost 40 km depth. Simultaneously, the overlying unmolten mafic crust continues to fold, with fold amplitudes greater than 5 km at about 20 km depth. The more compliant sediments above accommodate this deformation and thus also fold passively. At about 35 Myr, the amount of shortening in the model reaches 180 km (22.5%), and the base of the sedimentary basin has shortened to a width of about 160 km (almost 50%, Fig. 4, stage 2). Molten TTGs are widespread under the basin, and melting is still confined at 30–40 km depth. Unmolten mafic crust still separates the molten

TTGs from the sediments. The buckle folds tend to coalesce into three large folds under the basin, with a wavelength of about 40 km. This wavelength is proportional to 4–5 times the thickness of the rigid lower crust, and is controlled by the relative strength contrast between crustal layers (e.g. Lambeck, 1983; Gerbault et al., 1999; Schmalholz and Podladchikov, 1999; Burg and Podladchikov, 2000). As shortening continues, the amount of molten material increases and starts to rise within the buckle-folds.

At 45 Ma (Fig. 4 stage 3), gravitational instabilities become significant. The buoyant molten TTGs start to ascend through the mafic crust along the flanks of two of these buckle-folds (stage 3 in Fig. 4), and into sediments, owing to their low-density and low-viscosity. Once in the relatively soft sedimentary units, the head of the TTGs "diapirs" widens laterally and reaches depths of about 10 km at 54 Myr (stage 4, Fig. 4). Diapiric rises are separated by a wavelength of ~70 km which results from the combined mechanisms of buckle-folding and gravitational instabilities. Sediments entering in contact with this rising hot molten material start to melt and are displaced aside and downwards to compensate the ascent of lower-crustal material. Some deep-seated sediment particles are first entrained into the center of the diapirs before being exhumed. They record relatively high peak *P*–*T* metamorphic conditions.

The resulting *P*–*T*–*t* paths for sedimentary material are plotted in Fig. 5A. The maximum temperature (Fig. 5B) and maximum pressure (Fig. 5C) recorded by particles of sediments after 50 Myr are displayed. Relatively high values occur at the contact around the diapiric bulges and form metamorphic aureoles within the sedimentary bedrock, whereas highest *P*–*T* values are found in the core of the diapirs along their vertical head and spread around as circular domes. The proportion of melting achieved after 45 Myr by sedimentary, mafic and TTG layers are reported in Fig. 5D, and show that exception made of local pockets of greater TTG melts (red and brown markers achieving 30% of melt), overall molten material is lower than 20%. Important lateral breaks in metamorphic conditions are observed in the model between the high-pressure layers ($P > 8$ kbar) and the adjacent low-metamorphosed sediments ($P < 6$ kbar; $T < 450$ °C) filling the synforms between the bulges of partially molten material. In the final stages of the evolution of the model crust, rocks recording both cold and warm apparent geothermal gradients end up being adjacent, as the diapiric entities drive temperature upwards and entrain sedimentary piles, while more mafic material and cold sedimentary piles are driven downwards.

5.2. Discussion of results of model (M0)

The spatial and structural association of different rocks predicted by the model is in broad agreement with reported field observations. In particular, this model produced two 'diapiric' rises, separated by about 70 km, which is similar to the wavelength of the alternation between granitoid and greenstone terrains across the craton (e.g. Baratoux et al., 2011). Mechanisms of Buckling and folding had already been invoked to have occurred in the WAC at Birimian times (Pons et al., 1995; Pitra et al., 2010; Baratoux et al., 2011).

Here, this 70 km wavelength is generated by a combination of buckling and gravitational instabilities. It primarily depends on the initial wavelength of the buckle-folds which first develop at stage 2. Then, buoyant material takes advantage of low-stress zones induced by folding to flow upwards through one flank of the folds (where pressure and shear stress gradients are smallest, e.g. Lambeck, 1983; Schmalholz and Podladchikov, 1999; Gerbault et al., 1999). We understand that one fold over two is "intruded" because of the limited space available in between the folds. Alternatively, material ascent could perhaps flow upwards if channelised through tensile fault zones in the fold hinges, yet the quantification of this mechanism cannot be handled with the present numerical method as it requires a two-phase numerical approach (Keller et al., 2013).

Furthermore, the control of buckle-folding on the wavelength of diapiric ascent may be insignificant if ambiant viscosities were low. However from a theoretical point of view both gravitational and buckling instabilities tend to produce a similar dominant wavelength, that depends mostly on viscosity contrasts. Density constrasts in turn rather influence the growth rate of the diapirs. See Ismail-Zadeh et al. (2002) and Burg et al. (2004) for further details on the theoretical aspects of the predominance of either gravitational or buckling instabilities.

The similarity between the *P*–*T*–*t* paths obtained from numerical modeling and those deduced from metamorphic studies give confidence in the modeling assumptions and in the choice of the parameters. The model predicts the formation of thin layers of high-pressure meta-sediments (blue particles) in the vicinity of the partially molten material. However, we note that the ~50 °C/km apparent geothermal gradients recorded by the late-stage metamorphic evolution of rocks from the West African craton is never reproduced by the numerical model.

5.3. Model range of applicability, alternative parameters

Several parametric tests allow us to better understand the range of applicability of this exhumation scenario of sedimentary, granitic and migmatitic rocks. While the parametric space is large, main effects are described here and illustrated in Fig. 6:

- In case of a heat supply at the base of the model at around 15 Myr, corresponding to the second boundary thermal condition discussed in Section 4.3, then exhumation occurs within less than 18 Myr (model A, Fig. 6A–D), along geothermal gradients slightly warmer than 30 °C/km. This scenario is interesting to fit the prograde, nearly isobaric paths and retrograde heating reflected by *P*–*T* paths of rock samples presented Section 3.1 and Fig. 2A. However, high pressures (>8 kbar) are never obtained.
- In contrast, if the initial geothermal gradient is set deeper (e.g. 15 or 20 °C/km), or if the bottom temperature is fixed to follows the boundary of the Lagrangian grid, then melting is delayed and exhumation of partially molten rock does not occur because of the resistance of the overlying rocks.
- Faster convergence applied to the boundary of the model domain triggers greater thickening, which in turn impedes the ascent of buoyant material: Horizontal shortening prevails on gravitational instabilities. Model B, Fig. 6B, illustrates this case for an applied convergence rate of 2 cm/yr. *P*–*T*–*t* paths fit the 15 °C/km gradient at 9 kbar (Fig. 6E), but the transformed material remains stuck at depth. For a convergence rate of 1 cm/yr, exhumation occurs along the intermediate gradient of 25 °C/km (close to M0). If convergence is applied slower than 5 mm/yr, exhumation may occur over a proportionally longer time period (>50 Myr). Slower convergence also favors homogeneous shortening and homogeneous thermal conductive equilibrium, which reduces melting processes and the growth of gravitational instabilities.
- Zero convergence or an extensional setting cannot reproduce the burial of sediments at depths >15 km, as recorded by field metamorphic data (Appendix A2). One could then advocate to define a deeper initial sedimentary sequence, but then this would raise the issue of how such sediments could have been buried that deep over such broad spatial extents. One is faced with the inconsistency of supposing that subduction type shear zones could bury sedimentary layers over broad spatial scales, much broader than localised megathrust zones (subduction interfaces). However, such a tectonic regime successfully reproduces

exhumation of rocks along *P–T–t* patterns which fit a 50 °C/km gradient.

- Overall a less competent mafic crust also favors exhumation, as it reduces the buoyancy force required to overcome its resistance. This is why the presence of the thick sedimentary layer is found to be necessary in order to enable the ascent of buoyant and weak material. This point is illustrated in model C, Fig. 6C, in which we define a mafic middle crust at the center of the domain, and sedimentary basins lain on either side. Large crustal-scale shear zones develop at the limits of the basins as convergence goes on. However, field evidence for such structures are tenuous (Fig. 1C). Molten material below 20 km can hardly ascend because it is capped by the resistant mafic crust. This result is consistent with previous studies (e.g. Weinberg and Podladchikov, 1994; Vigneresse and Clemens, 2000; Petford and Clemens, 2000). The TTGs are finally exhumed after about 60 Myr, but they never enter in direct contact with the sediments, some of which are buried below 20 km depth, along a cold thermal gradient (Fig. 6D).
- Asymmetric initial geometries or surface (erosion/sedimentation) processes facilitate exhumation up to the surface (e.g. Maierová et al., 2012; Vanderhaeghe et al., 2003). Yet, final ascent of material through the upper crust could also occur through localised weak and permeable vertical fault zones activated during regional scale transcurrent motion. This complementary mode of exhumation was proposed by Jessell et al. (2012) for the Birimian province, and is further discussed in Section 6.
- Considering a crustal pile without significant density contrasts obviously prevents the development of gravitational instabilities (Appendix 2). In this case crustal thickening involves buckling instabilities of the TTG and mafic layer lower crustal melange, and the sedimentary layer deepens. But high-*P* sediments are never exhumed.

5.4. Modeling limitations and implications

We have presented above some of the effects of changing numerical assumptions, initial and boundary conditions, and rheological properties. The parametric space is wide and we intend to explore it in the near future, together with the addition of further field constraints. Yet, three main limitations appear:

a) The numerical modeling presented here accounted for specific initial conditions (a symmetrical and homogeneously pre-thickened flexural basin) that attempted to approximate the geometry of a typical transitional orogenic stage (for instance similar to the approach of Maierová et al., 2012). Our chosen geometry is of course debatable, and future investigation should attempt to add constraints on this. We have chosen on purpose symmetrical conditions in order to illustrate the "natural" asymmetry produced by a physical instability. We could have chosen a prism like geometry of the sedimentary basin, simulating for instance an orogenic fore-arc wedge. One other approach would be to model the whole history of the Eburnean orogeny, including the successive accretion of developing magmatic arcs. Yet these choices would also be questionable, because of the lack of constraints from data. Modeling successive orogenic stages is premature for the same reason.

b) The present numerical models also assumed relatively straightforward melting processes (as in Gerya et al., 2008), but which account for the main progressive evolution of density and thermal constraints provided by the metamorphic approach of Section 3. We believe that despite our approximations, we grasped first order features. Implementation of self-consistent petro-thermo-mechanical coupling is a fore-coming plan. One should also have in mind that the present models have a kilometer scale resolution. Additionally we could not handle material transfer via non-linear two-phases fluid–solid mechanisms (e.g. Keller et al., 2013). Therefore the modeled Pressure–Temperature pattern may not grasp peak local values.

c) The presence of large strike–slip shear zones throughout the Precambrian Provinces (Jessell et al., 2012 and references therein) has already been shown to have played an important role in the exhumation of deep crustal material (e.g. Martelat et al., 2000). However, field relationships do not seem to support this hypothesis in the Birimian context. Three-dimensional modeling remains necessary in order to quantify the respective contribution of each end-member mechanism (transcurrent motion, local extension, and body forces) to lower crust exhumation. Accommodation of horizontal shortening in the perpendicular direction reduces conversely accommodation by vertical thickening. In other words, it reduces the proportion of homogeneous thickening at given amount of shortening, and thus reduces the additional downward-directed force that works against the rise of gravitational instabilities. Therefore, one may anticipate that once melting conditions were achieved in the lower crust, transcurrent motion facilitated the rise of gravitational instabilities and crustal exhumation.

d) Another limitation of our models is that they do not explain the final emplacement in the upper crust of such thin slivers of high-pressure meta-sediments in the vicinity of granitic plutons, as it was observed in the greenstone of Tera (Niger) as well as the (apparent) absence or widespread occurrence of migmatite in these areas. Indeed, in our model molten material below 10–15 km can hardly ascend because it is capped by a resistant upper crust. A simple explanation could be found in a process of melt-segregation from the partially molten material stopped along this mechanical boundary, their temporary storage then brutal release, entraining some thin slivers of high-pressure rocks in the upper crust. It was shown from the analysis of migmatites and granites by Vanderhaeghe (2009) and then Toé et al. (2013) that a drastic change will occur in the structural record of former partially molten rocks (migmatites with a continuous gneissic foliation) when compared to former magmas (magmatic rocks with enclaves).

Even if our model was not specifically designed to distinguish the behavior of former partially molten rocks and of former magmas, we tried in Fig. 5D to identify the crustal layers forming the sources of granitic magmas. Our model predicts that the 10% melt threshold – above which melt is thought to segregate (e.g. Arzi, 1978; Sawyer, 1994; Brown et al., 1995) – is reached by large rock volumes stored at around 10–15 km depth (more than 10% of melt present in the rocks), that, potentially, will constitute a melt-reservoir for granite plutonism. A 30–40% melting rate, which corresponds to the theoretical threshold marking the transition from migmatites to heterogeneous granites, concerns much smaller rock volumes (red and brown markers in Fig. 5C).

e) Finally, this numerical study led us to consider the thermal conditions prevailing at the base of the lithosphere at Birimian times. Although the opportunistic arrival of a thermal plume is plausible, as it is invoked in some present day orogenic contexts (e.g. Burov et al., 2007, for the European lithosphere), it would have had to extend over several thousands of kilometers below the WAC without generating rifting. Therefore we prefer the assumption of a permanently hotter upper mantle than at present day, as suggested by some authors for the early Earth (Thompson, 1984; Richter, 1984; Nisbet et al., 1993; Labrosse and Jaupart, 2007; Brown, 2008 or Korenaga, 2013 and references therein).

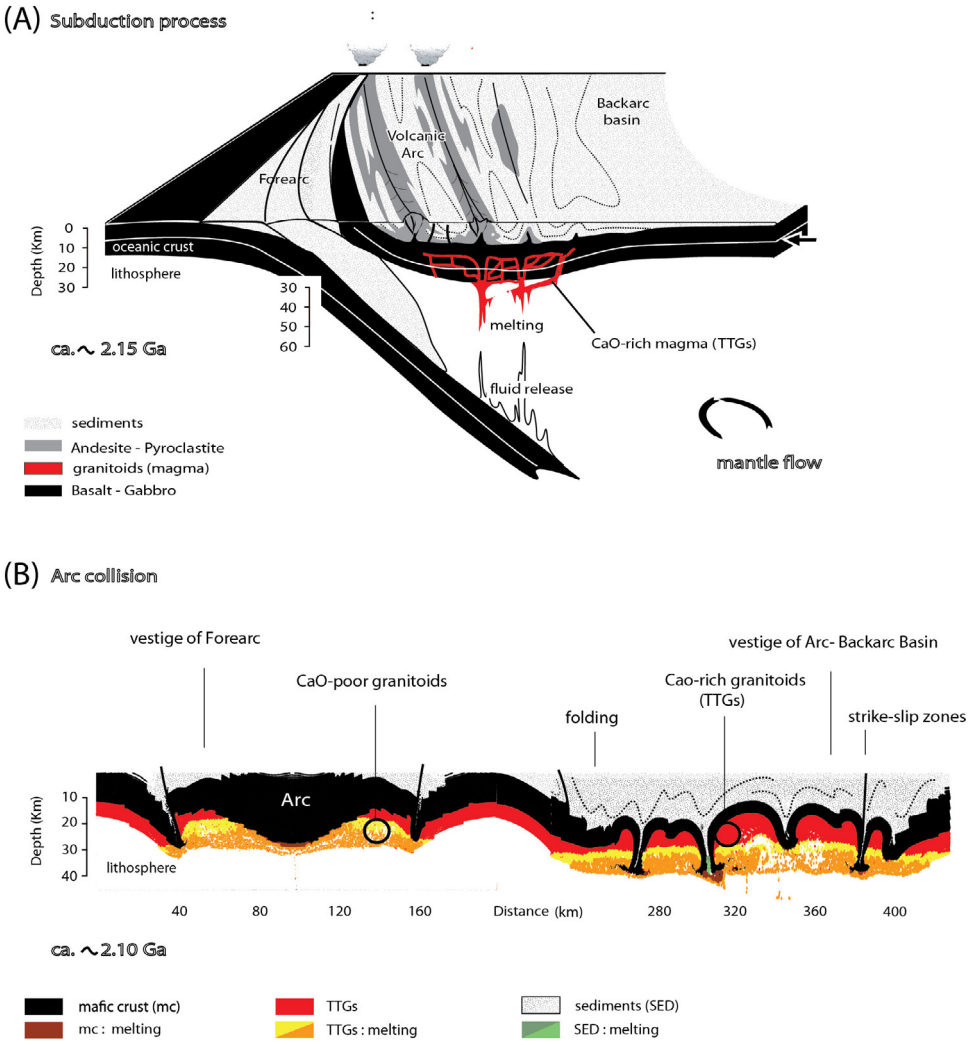

Fig. 7. Inferred geodynamic model for the tectonic evolution of the Palaeoproterozoic Birimian crust (2.2–2.0 Ga) in the WAC, from subduction processes (A) to arcs-collision (B), and the associated metamorphic evolution of middle- to high-pressure meta-sediments. Numbered rectangles (ex. 25 °C/km) show the thermal regime evolution in different portions of the juvenile crust. (For interpretation of colour in the artwork, the reader is referred to the web version of the article.)

6. Geodynamical considerations

In this last section, we propose a geodynamic scenario accounting for (1) thickening and reworking of the Birimian crust, constrained by our petrological data (Section 3), and (2) exhumation of portions of middle and lower crust, based on our numerical modeling results (Sections 4 and 5). We discuss the implications of our results for the tectono-metamorphic and mechanical evolution of Palaeoproterozoic orogenies.

6.1. Buildup and evolution of the Birimian crust

The TTGs emplaced between 2.20 and 2.15 Ga may be the product of melting of the base of a volcanic island arc which received hydrous fluids from slab dehydration and heat from the mantle wedge (Fig. 7A). Alternatively, the metasomatized mantle wedge may be the source for the TTGs (Martin, 1993; Moyen and Martin, 2012). In any case, TTG generation could have operated in a subduction-driven geodynamic setting. The medium to high *P*–low *T* environment (M1: 10–15 °C/km) identified by Ganne et al. (2012) was probably related to subduction zones associated with crustal growth in an accretionary orogeny (Cawood et al., 2009) during the early stages of the Eburnean orogeny (2.20–2.15 Ga).

The consumption of oceanic crust by repetitive subduction/megathrusting continued during the late stages of the Eburnean orogeny, between 2.15 and 2.10 Ga (Fig. 7B), and led to arc collision throughout the Birimian province. The regional thermal conditions were probably too warm for subducted oceanic crust to generate slab-pull driving forces as significant as in modern subduction zones (e.g. Van Hunen and Moyen, 2012). Therefore subducted sediments and thickened volcanic arcs would not have been able to subside deep into the mantle, and instead, they would have been accreted together and have remained stuck at lower crustal depths (similar to what is infered for Archean tectonics, e.g. Gray and Pysklywec, 2013). Transition from volcanic-arc dynamics to the subsequent arc-collision is likely to have occurred after 2.15 Ga, and culminated at around 2.1 Ga (Hirdes et al., 1996; Doumbia et al., 1998; Egal et al., 2002; de Kock et al., 2011 or Tapsoba et al., 2013). Therefore, the model presented in this study applies to the post-accretion late Eburnean collisional orogeny (2.15–2.1 Ga) (Zhao et al., 2002), and is associated with a progressive evolution of the thermal regime of the orogenic crust (Vanderhaeghe, 2012).

Pitra et al. (2010) suggested that collisional processes in the Birimian Province were mostly accommodated by a combination of transpressive shear zones, lateral crustal spreading and large-scale folding that assisted thickening of hot continental crust. In

accordance with the concept of intracrustal folding followed by vertical extrusion generalized by Schulmann et al. (2008), Baratoux et al. (2011) proposed that the transition, from an oceanic crust overlain by volcanic-arcs, to a 'normal' continental crust (~30 km thickness), was achieved through an interplay of long-wavelength amplitude buckling of rigid mafic units in conjunction with voluminous magma input.

Metamorphic data collected in the thermal aureole of low- to moderate-CaO magmatic plutons similar to the 2.15 Ga Tera batolith (Fig. 1C) indicate that the Birimian crust had a minimal thickness of 25 or 30 km by this time, and comprised para-derived rocks in the middle crust dominated by a 20–30 °C/km geothermal gradient. Geochemical data indicate that these granitoids may have resulted from re-melting of CaO-rich tonalitic bodies (TTGs), associated to the anatexy of meta-sedimentary, felsic and mafic rocks (Lüdtke et al., 1998; Hirdes et al., 1996; Doumbia et al., 1998 or Tapsoba et al., 2013). Re-melting of TTGs normally occurs at the base of a 25–30 km deep crust at around 700–750 °C under hydrated conditions, for a geothermal gradient of 20–30 °C/km. The thermal and magmatic evolution of the Birimian crust was most probably accompanied by a chemical differentiation in its deeper domains (>25–30 km), which were intensively re-worked (Fig. 5D). This reworking would have concentrated refractory mafic rocks in the lower crust, relative to intermediate levels (15–20 km) which were dominated by more felsic material. Ultimately, this process may have led to the formation of a layered Palaeoproterozoic crust, in a similar way to Paleozoic orogenic domains (see Vielzeuf et al., 1990; Wedepohl, 1995; McLennan and Taylor, 1996; Rudnick and Gao, 2003; Vanderhaeghe, 2009).

Our thermo-mechanical numerical modeling showed that exhumation of subsolidus and suprasolidus lower crustal rocks can occur in a moderately slow convergent setting (~5 mm/yr). Exhumation is driven by gravitational instabilities which are initiated as a consequence of crustal-scale buckle-folding. Folding causes burial and melting of some units. As melting rates increase, density contrasts become significant and diapiric ascent of partially molten rocks drives vertical advection in the orogenic crust, through the mechanical weaknesses generated by the buckle-folds. Subsolidus middle crustal units are driven up by diapiric ascent while superficial rocks are buried. Numerical results indicate that this mechanism is able to generate strong lateral metamorphic gradients on the margins of diapirs made of partially molten rocks. Exhumation is therefore heterogeneous and spatially localised. It produces a metamorphic pattern at 10–15 km depth which matches the observed diversity of the metamorphic rock record. We speculate that these metamorphic rocks at 10–15 km were further dragged up with melt through the upper crust along weak and permeable transform shear-zones (work in progress).

We suggest that this exhumation mechanism, accounting for some characteristics of the Eburnean orogeny of the West African craton, may have been active in Precambrian accretionary orogens in general.

6.2. Implications for Precambrian accretionary orogens

Some of the results gained in this study can be used to discuss the thermal evolution of Palaeoproterozoic crusts, and its control on the rheology and tectonic style of deformation at that time. Indeed, it is commonly accepted that warmer lithosphere is also "softer", promoting a style of deformation that differs from modern-style sheet-like thrusting features (e.g. Cagnard et al., 2006, 2007; Rey and Houseman, 2006; Chardon et al., 2009; Vidal et al., 2009).

In the Birimian Province of West Africa, we have identified only one tectonic style, very homogeneous across the studied areas and characterized by the widespread development of a distributed subvertical foliation, that is also axial-planar to elongated synforms and antiforms developed in greenstone lithologies. This deformation occurred in a regime of moderate regional convergence and involved vertical movements of material in the upper portions of the crust (down-dip mineral lineations) and localised strike-slip displacements (Vidal et al., 2009; Jessell et al., 2012). Such tectonic features are quite similar to those recognized in the supracrustal portions of the Archean crust (Chardon et al., 2009). The "weak type" orogenic model proposed by Vidal et al. (2009) for the Eburnean orogeny is rather well supported by the long-lived and important magmatic activity accompanying deformation. However, this model requires elevated temperatures in the middle portions of the crust (700–800 °C at 15 km depth, corresponding to the "Attachment zone" in Fig. 5D; Chardon et al., 2009) which is not supported by our metamorphic data.

The geodynamic evolution of the Birimian crust from an accretionary orogen to a collisional orogen between 2.2 and 2.0 Ga (Fig. 7) had profound implications on the tectonic regime This was observed by Cagnard et al. (2011) in the Palaeoproterozoic "Finnish Lapland Granulite Belt" and southern "Svecofennides belt", where the tectonic regime evolves under the competing effects of volume forces and boundary forces between 2.0 and 1.8 Ga.

Such a mechanical competition is also exemplified in the Palaeoproterozoic "Trans-North China Belt" (TNCB) that evolved from an accretionary orogeny with archaic-style structures to a modern collisional belt with exhumation of HP rocks, within a few tens of millions of years (Faure et al., 2007). This geodynamic evolution is interpreted by Trap et al. (2012 and references therein) as the result of closure of oceanic domains, collision of continental blocks and intra-lithospheric deformation, that propagated from the internal zones towards the forelands of the Palaeoproterozoic belt. The TNCB shows a development of all of the classic features of modern belts (e.g. thrust-induced thickening of the crust, exhumation processes, erosion and molasse deposition in foreland basins as well as detachment faulting) between 1.9 and 1.8 Ga (Brown, 2008) and therefore demonstrates that the Palaeoproterozoic lithosphere could have behaved like a modern lithosphere.

When considering the metamorphic data in Trap et al. (2012), it seems obvious that the TNCB formed in a rather cool thermal environment, with geothermal gradients of 20–30 °C/km (Zhao et al., 2000a,b; O'Brien et al., 2005; Trap et al., 2011, 2012) that are quite similar to those depicted in our study. However, Palaeoproterozoic eclogite-facies rocks (Collins et al., 2004) exhumed by large-scale thrusting or syn-collisional channel flow (Trap et al., 2011) are absent from the Eburnean orogeny. Such a difference raises the following question: Was the rheology of Precambrian crusts, and by extension the tectonic style recorded in these terrains, solely controlled (to a first order) by the thermal state of the Precambrian lithosphere?

Indeed, a weak lithosphere which preferentially develops "Archaic" tectonic patterns is classically linked to a hot geothermal gradient. As a corollary, it is often suggested that thrusts and large-scale detachment faults characterize a stiff and cold lithosphere. It is now well established from the Darwar craton in India, that (1) high-temperature metamorphism and widespread migmatisation occurred in the deepest portions of the crust along a moderate thermal gradient of 30 °C/km (Friend, 1984 or Moyen et al., 2003 and references therein); and (2) subsequent emplacement of granitic magmas in the middle and upper crust both efficiently contributed to the softening of the Neoarchaean continental crust and allowed the development of gravitational instabilities (Moyen et al., 2003; Chardon et al., 2009).

Although partial melting depends on a rise of temperature in the crust, it should be noted that hot lithospheres do not necessarily produce significant magmatism. Some Palaeoproterozoic belts such as the "Trans-Hudson Orogen" in the North American craton (2.1–1.8 Ga) and, more specifically, the "Thompson Belt", are

characterized by a crustal-scale tangential tectonic regime that took place in a high geothermal environment (Mareschal et al., 2005 or Perry et al., 2006) without widespread production of magma or partially molten rocks.

Both the lithological profile and the thermal evolution of these Palaeoproterozoic crusts could equally control magma production, which may in turn influence the tectonic style of orogenies. Therefore, it is likely that some segments of the Palaeoproterozoic crust derived from amalgamated island arcs were more exposed to melting compared to homogeneously thick and anydrous mafic oceanic plateaus. As suggested by different authors (Cagnard et al., 2006; Chardon et al., 2009; Vanderhaeghe, 2012 or Trap et al., 2012 and references therein), when partially molten material is missing or heterogeneously distributed in the crust (Perry et al., 2006), important thrusts may develop in a tangential tectonics regime and cause the exhumation of high-pressure material, even in abnormally warm lithospheres. Conversely, intensive production of viscous magma can occur along moderate geothermal gradients (20–30 °C/km) in fertile felsic material. Under a regional convergence regime, a more archaic-style of deformation take place, combining folding structures and partially molten material ascent that also efficiently contribute to the exhumation of high-pressure rocks as demonstrated in this study.

Acknowledgments

P. Debat is warmly thanked for fruitful discussions at different stages of the project. The paper benefits from helpful comments from D. Chardon, M. Jessell, L. Baratoux, S. Perrouty and J.-L. Bouchez. We thank reviewers L. Le Pourhiet and O. Vanderhaeghe for their very constructive comments. The project was supported by IRD and INSU-CNRS research funds.

Appendix A. Supplementary data

Supplementary data associated with this article can be found, in the online version, at http://dx.doi.org/10.1016/j.precamres.2013.12.016.

References

Abouchami, W., Boher, M., Michard, A., Albarede, F., 1990. A major 2.1 Ga event of mafic magmatism in West Africa; an early stage of crustal accretion. J. Geophys. Res. B: Solid Earth Planets 95, 17605–17629.

Ama Salah, I., Liegeois, J.-P., Pouclet, A., 1996. Evolution d'un arc insulaire océanique birimien précoce au Liptako nigérien (Sirba): géologie, géochronologie et géochimie. J. Afr. Earth Sci. 22, 235–254.

Arzi, A.A., 1978. Critical phenomena in the rheology of partially melted rocks. Tectonophysics 44 (1), 173–184.

Baratoux, L., Metelka, V., Naba, S., Jessell, M., Grégoire, M., Ganne, J., 2011. Juvenile Paleoproterozoic crust evolution during the Eburnean orogeny (~2.2–2.0 Ga), western Burkina Faso. Precam. Res. 191, 18–45.

Barker, F., 1979. Trondhjemites, Dacites, and Related Rocks. Elsevier, Amsterdam.

Bassot, J.P., 1966. Etude géologique du Sénégal oriental et de ses confins Guinéo-Maliens, vol. 40. Mém. B.R.G.M, 332 pp.

Bittner, D., Schmeling, H., 1995. Numerical modeling of melting processes and induced diapirism in the lower crust. Geophys. J. Int. 123, 59–70.

Bleeker, W., 1990. New structural-metamorphic constraints on Early Proterozoic oblique collision along the Thompson Nickel Belt, Manitoba. Geol. Assoc. Can. Spec. 37, 57–73.

Block, S., Baratoux, L., Bosse, V., Jessell, M., Ganne, J., Aillères, L., Sagna, R., Mensah, E., 2012. The paleoproterozoic craton of North-West Ghana: structural and metamorphic evidence for post-accretion collisional tectonics. In: 24th Colloquium of African Geology, 8 January 2013, Addis Abeba, Ethiopia.

Boher, M., Abouchami, W., Michard, A., Albarede, F., Arndt, N.T., 1992. Crustal growth in West Africa at 2.1 Ga. J. Geophys. Res. B: Solid Earth Planets 97, 345–369.

Bonhomme, M., 1962. Contribution à l'étude géochronologique de la plate-forme de l'Ouest Africain. In: Ann. Fac. Sci. Univ. Clermont-Ferrand, p. 5.

Brown, M.D., 2008. Characteristic thermal regimes of plate tectonics and their metamorphic imprint throughout Earth history: when did Earth first adopt a plate tectonics mode of behavior? In: Condie, K.C., Pease, V. (Eds.), When Did Plate Tectonics Begin on Planet Earth?, GSA special issue, vol. 440, pp. 97–128.

Brown, M., Averkin, Y.A., McLellan, E.L., Sawyer, E.W., 1995. Melt segregation in migmatites. J. Geophys. Res. 100, 655679.

Burg, J.-P., Podladchikov, Y., 2000. From buckling to asymmetric folding of the continental lithosphere: Numerical modeling and application to the Himalayan syntaxes. In: Khan, M.A., et al. (Eds.), Tectonics of the Western Himalayas and Karakoram, vol. 170. Geological Society [London] Special Publication, pp. 219–236.

Burg, J-P., Kaus, B.J.P., Podladchikov, Y.Y., 2004. Dome structures in collision orogens. Mechanical investigation of the gravity/compression interplay. In: Whitney, D.L., Teyssier, C., Siddoway, C.S. (Eds.), Gneiss Domes in Orogeny, vol. 380. Geological Society of America Special Paper, Boulder, Colorado, pp. 47–66.

Bürgmann, R., Dresen, G., 2008. Rheology of the lower crust and upper mantle: evidence from rock mechanics, geodesy, and field observations. Annu. Rev. Earth Planet.: Sci. 36, 531–567.

Burov, E.B., Poliakov, A., 2001. Erosion and rheology controls on synrift and postrift evolution: verifying old and new ideas using a fully coupled numerical model. J. Geophys. Res. 106, 16461–16481.

Burov, E., Guillou-Frottier, M., d'Accremont, E., Le Pourhiet, L., Cloetingh, S., 2007. Plume heat–lithosphere interaction near intra-continental plate boundaries. Tectonophysics 434, 15–38.

Caby, R., Delor, C., Agoh, O., 2000. Lithology, structure and metamorphism of the Birimian formations in the Odienne area (Ivory Coast): the major role played by plutonic diapirism and strike–slip faulting at the border of the Man Craton. J. Afr. Earth Sci. 30, 351–374.

Cagnard, F., Durrieu, N., Gapais, D., Brun, J.-P., Ehlers, C., 2006. Crustal thickening and lateral flow during compression of hot lithospheres, with particular reference to Precambr. times. Terra Nova 18, 72–78.

Cagnard, F., Gapais, D., Barbey, P., 2007. Collision tectonics involving juvenile crust: the example of the southern Finnish Svecofennides. Precam. Res. 154, 125–141.

Cagnard, F., Barbey, P., Gapais, D., 2011. Transition between Archaean-type and modern-type tectonics: insights from the Finnish Lapland Granulite Belt. Precam. Res. 187, 127–142.

Castaing, C., Billa, M., Milési, J.P., Thieblemont, D., Le Métour, J., Egal, E., Donzeau, M. (BRGM) (coordonnateurs) Guerrot, C., Cocherie, A., Chèvremont, P., Tegyey, M., Itard, Y. (BRGM), Zida, B., Ouédraogo, I., Koté, S., Kaboré, B.E., Ouédraogo, C. (BUMIGEB), Ki, J.C., Zunino, C. (ANTEA), 2003. Notice explicative de la carte géologique et minière du Burkina Faso à 1/1 000 000. BRGM, Orléans, France, 147.

Cawood, P.A., Kröner, A., Collins, W.J., Kusky, T.M., Mooney, W.D., Windley, B.F., 2009. Accretionary Orogens through Earth History, vol. 318. Geological Society Special Publications, London, pp. 1–36.

Chardon, D., Gapais, D., Cagnard, F., 2009. Flow of ultra-hot orogens: a view from the Precambrian, clues for the Phanezozoic: "Hot orogens" special issue. Tectonophysics 477, 105–118.

Chatterjee, N.D., Froese, E., 1975. A thermodynamic study of the pseudobinary join muscovite-paragonite in the system $KAlSi_3O_8$–$NaAlSi_3O_8$–Al_2O_3–SiO_2–H_2O. Am. Mineral. 60, 985–993.

Cheilletz, A., Barbey, P., Lama, C., Pons, J., Zimmermann, J.L., Dautel, D., 1994. Age de refroidissement de la croûte juvénile birimienne d'Afrique de l'Ouest. Données U–Pb, Rb–Sr et K–At sur les formations à 2.1 Ga du SW Niger. C. R. Acad. Sci. Paris 11, 319, 435–442.

Clemens, J.D., Mawer, C.K., 1992. Granitic magma transport by fracture propagation. Tectonophysics 204, 339–360.

Cobbold, P.R., Davy, P., Gapais, D., Rossello, E.A., Sadybakasov, E., Thomas, J.C., Tondji Biyo, J.J., de Urreiztieta, M., 1993. Sedimentary basins and crustalthickening. Sediment. Geol. 86, 77–89.

Collins, W.J., Vernon, R.H., 1991. Orogeny associated with anticlockwise *P*–*T*–*t* paths: evidence from low-*P*, high-*T* metamorphic terranes in the Arunta Inlier, central Australia. Geology 19, 835–838.

Collins, A.S., Reddy, S.M., Buchan, C., Mruma, A., 2004. Temporal constraints on Palaeoproterozoic eclogite formation and exhumation (Usagaran Orogen, Tanzania). Earth Planet. Sci. Lett. 224, 175–192.

Connolly, J.A.D., 2005. Computation of phase equilibria by linear programming. A tool for geodynamic modelling and its application to subduction zone decarbonation. Earth Planet. Sci. Lett. 236, 524–554.

Connolly, J.A.D., 2009. The geodynamic equation of state: what and how. Geochem. Geophys. Geosyst. 10, Q10014, 19 pp.

Connolly, J.A.D., Kerrick, D.M., 1987. An algorithm and computer program for calculating composition phase diagrams. CALPHAD 11, 1.

Cundall, P., Board, M., 1988. A microcomputer programme for modelling large-strain plasticity problems. Num. Meth. Geomech. 6, 2101–2108.

de Kock, G.S., Armstrong, R.A., Siegfried, H.P., Thomas, E., 2011. Geochronology of the Birim Supergroup of the West African craton in the Wa-Bolé region of west-central Ghana: implications for the stratigraphic framework. J. Afr. Earth Sci. 59, 1–40.

De Kock, G.S., Théveniaut, H., Botha, P.M.W., Gyapong, W., 2012. Timing the structural events in the Palaeoproterozoic Bolé-nangodi belt terrane and adjacent Maluwe basin, West African craton, in central-west Ghana. J. Afr. Earth Sci. 65, 1–24.

Debat, P., Nikiema, S., Mercier, A., Lompo, M., Beziat, D., Bourges, F., Roddaz, M., Salvi, S., Tollon, F., Wenmenga, U.A., 2003. New metamorphic constraint for the Eburnean orogeny from Paleoproterozoic formations of the Man shield (Aribinda and Tampelga countries, Burkina Faso). Precam. Res. 123, 47–65.

de Saint Blanquat, M., Horsman, E., Habert, G., Morgan, S., Vanderhaeghe, O., Law, R., Tikoff, B., 2011. Multiscale magmatic cyclicity, duration of pluton construction,

and the paradoxical relationship between tectonism and plutonism in continental arcs. Tectonophysics 500, 20–33.
Dia, A., Van Schmus, W.R., Kröner, A., 1997. Isotopic constraints on the age and formation of a Palaeoproterozoic volcanic arc complex in the Kedougou Inlier eastern Senegal, West Africa. J. Afr. Earth Sci. 24, 197–213.
Diener, J.F.A., Powell, R., 2012. Revised activity–composition models for clinopyroxene and amphibole. J. Metamorph. Geol. 30 (2), 131–142.
Diener, J.F.A., Powell, R., White, R.W., Holland, T.J.B., 2007. A new thermodynamic model for clino- and orthoamphiboles in the system Na_2O–CaO–FeO–MgO–Al_2O_3–SiO_2–H_2O–O. J. Metamorph. Geol. 25 (6), 631–656.
Dioh, E., Béziat, D., Debat, P., Grégoire, M., Ngom, M., 2006. Diversity of the Paleoproterozoic granitoids of the Kédougou inlier (eastern Sénégal): petrographical and geochemical constraints. J. Afr. Earth Sci. 44, 351–371.
Doumbia, S., Pouclet, A., Kouamelan, A., Peucat, J.J., Vidal, M., Delor, C., 1998. Petrogenesis of juvenile-type Birimian (Paleoproterozoic) granitoids in Central Cote-d'Ivoire, West Africa: geochemistry and geochronology. Precam. Res. 87, 33–63.
Ducellier, J., 1963. Contribution à l'étude des formations cristallines et métamorphiques du centre et du Nord de la Haute-Volta, vol. 10. Mém. B.R.G.M., Paris, 320 p.
Egal, E., Thiéblemont, D., Lahondère, D., Guerrot, C., Costea, C.A., Iliescu, D., Delor, C., Goujou, J.C., Lafon, J.M., Tegyey, M., Diaby, S., Kolié, P., 2002. Late Eburnean granitization and tectonics along the western and northwestern margin of the Archean Kénéma–Man domain (Guinea, West African Craton). Precam. Res. 117, 57–84.
Elhers, C., Lindroos, A., Selonen, O., 1993. The late-Svecofenian granite–migmatite zone of southern Finland – a belt of transpressive deformation and granite emplacement. Precam. Res. 64, 295–309.
Faure, M., Trap, P., Lin, W., Monié, P., 2007. Polyorogenic evolution of the Paleoproterozoic Trans-North China Belt, new insights from the Lüliangshan-Hengshan-Wutaishan and Fuping massifs. Episodes 30, 1–12.
Feybesse, J.L., Milési, J.P., 1994. The Archaean/Proterozoic contact zone in West Africa: a mountain belt of decollement thrusting and folding on a continental margin related to 2.1 Ga convergence of Archaean cratons? Precam. Res. 69, 199–227.
Feybesse, J.L., Billa, M., Guerrot, C., Duguey, E., Lescuyer, J.L., Milesi, J.-P., Bouchot, V., 2006. The Paleoproterozoic Ghanaian province: geodynamic model and ore controls, including regional stress modeling. Precam. Res. 149, 149–196.
Friend, C.R.L., 1984. The origin of the Closepet granites and the implications for the crustal evolution of Southern India. J. Geol. Soc. India 25, 73–84.
Foroozan, R., Elsworth, D., Flemings, P., Bilotti, F., Muhuri, S., 2012. The role of permeability evolution in fault zones on the structural and hydromechanical characteristics of shortening basins. Mar. Petrol. Geol. 29, 143–151.
Galer, S.J.G., Mezger, K., 1998. Metamorphism, denudation and sea level in the Archean and cooling of the Earth. Precam. Res. 92, 389–412.
Galipp, K., Klemd, R., Hirdes, W., 2003. Metamorphism and geochemistry of the Paleoproterozoic Birimian Sefwi volcanic belt (Ghana, West Africa). In: Geologisches Jahrbuch, no. D111., pp. 151–191.
Ganne, J., De Andrade, V., Weinberg, R., Dubacq, B., Vidal, O., Kagambega, N., Naba, S., Baratoux, L., Jessell, M., Allibon, J., 2012. Modern-style plate subduction preserved in the Palaeoproterozoic West African Craton. Nat. Geosci. 5, 60–65.
Gapais, D., Cagnard, F., Gueydan, F., Barbey, P., Ballèvre, M., 2009. Mountain building and exhumation processes through time: inferences from nature and models. Terra Nova 21, 188–194.
Gasquet, D., Barbey, P., Adou, M., Paquette, J.L., 2003. Structure, Sr–Nd isotope geochemistry and zircon U–Pb geochronology of the granitoids of the Dabakala area (Cote d'Ivoire): evidence for a 2.3 Ga crustal growth event in the Palaeoproterozoic of West Africa? Precam. Res. 127, 329–354.
Gerbault, M., Burov, E.B., Poliakov, A.N.B., Daignières, M., 1999. Do faults trigger folding in the lithosphere? Geophys. Res. Lett. 26, 271–274.
Gerbault, M., Cembrano, J., Mpodozis, C., Farias, M., Pardo, M., 2009. Continental margin deformation along the Andean subduction zone: thermo-mechanicalmodels. Phys. Earth Planet. Interiors 177 (34), 180–205, http://dx.doi.org/10.1016/j.pepi.2009.09.001.
Gerya, T., Yuen, D., 2003. Rayleigh-Taylor instabilities from hydration and melting propel 'cold plumes' at subduction zones. Earth Planet. Sci. Lett. 212, 47–62.
Gerya, T., Perchuk, L.L., Burg, J.-P., 2008. Transient hot channels: perpetrating and regurgitating ultrahigh-pressure, high-temperature crust–mantle associations in collision belts. Lithos 103, 236–256.
Grambling, J.A., Williams, M.L., Smith, R.F., Mawer, C.K., 1989. The role of crustal extension in the metamorphism of Proterozoic rocks in Northen New Mexico. Geol. Soc. Am. Spec. Pap. 235, 87–110.
Gray, R., Pysklywec, R.N., 2013. Influence of viscosity pressure dependence on deep lithospheric tectonics during continental collision. J. Geophys. Res. Solid Earth 118, 3264–3273, http://dx.doi.org/10.1002/jgrb.50220.
Green, E., Holland, T., Powell, R., 2007. An order-disorder model for omphacitic pyroxenes in the system jadeite-diopside-hedenbergite-acmite, with applications to eclogitic rocks. Am. Mineral. 92 (7), 1181–1189.
Hein, K.A.A., 2010. Succession of structural events in the Goren greenstone belt (Burkina Faso): implications for West African tectonics. J. Afr. Earth Sci. 56, 83–94.
Hirdes, W., Davis, D.W., 2002. U–Pb geochronology of paleoproterozoic rocks in the southern part of the Kedougou-Kéniéba Inlier, Senegal, West Africa: evidence for diachronous accretionary development of the Eburnean Province. Precam. Res. 118, 83–99.
Hirdes, W., Davis, D.W., Lüdtke, G., Konan, G., 1996. Two generations of Birimian Paleoproterozoic volcanic belts in northeastern Côte d'Ivoire West Africa: consequences for the Birimian controversy. Precam. Res. 80, 173–191.
Holland, T., Powell, R., 1996. Thermodynamics of order-disorder in minerals. 2. Symmetric formalism applied to solid solutions. Am. Mineral. 81, 1425–1437.
Holland, T.J.B., Powell, R., 1998. An internally consistent thermodynamic data set for phases of petrological interest. J. Metamorph. Geol. 16, 309–334.
Holland, T., Powell, R., 2001. Calculation of phase relations involving haplogranitic melts using an internally consistent thermodynamic dataset. J. Petrol. 42, 673–683.
Holland, T., Baker, J., Powell, R., 1998. Mixing properties and activity–composition relationships of chlorites in the system MgO–FeO–Al_2O_3–SiO_2–H_2O. Eur. J. Mineral. 10, 395–406.
Huet, B., Le Pourhiet, L., Labrousse, L., Burov, E.B., Jolivet, L., 2011. Post-orogenic extension and metamorphic core complexes in a heterogeneous crust: the role of crustal layering inherited from collision. Application to the cyclades (Aegean domain). Geophys. J. Int. 184, 611–625.
Ismail-Zadeh, A., Huppert, H.E., Lister, J.R., 2002. Gravitational and buckling instabilities of a rheologically layered structure: implications for salt diapirism. Geophys. J. Int. 148, http://dx.doi.org/10.1046/j.1365-246X.2002.01612.x.
Jessell, M.W., Amponsah, P.O., Baratoux, L., Asiedu, D.K., Loh, G.K., Ganne, J., 2012. Crustal-scale transcurrent shearing in the Paleoproterozoic Sefwi-Sunyani-Comoé region, West Africa. Precamb. Res. 212–213, 155–168.
John, T., Klemd, R., Hirdes, W., Loh, G., 1999. The metamorphic evolution of the Paleoproterozoic (Birimian) volcanic Ashanti belt (Ghana, West Africa). Precam. Res. 98, 11–30.
Junner, N.R., Harwood, H.F., 1928. Microscopical features and chemical analysis of certain representative igneous rocks from the gold coast, British West Africa. Gold Coast Geol. Surv. Bull. 4, 10–11.
Keller, T., May, D.A., Kaus, B.J., 2013. Numerical modeling of magma dynamics coupled to tectonic deformation of lithosphere and crust. Geophys. J. Int. 195, 1406–1442.
Kirby, S.H., Kronenberg, A.K., 1987. Rheology of the lithosphere: selected topics. Rev. Geophys. 25, 1219–1244.
Klein, E.L., Rodrigues, J.B., Lopes, Elem C.S., Soledade, G.L., 2012. Diversity of Rhyacian granitoids in the basement of the Neoproterozoic-Early Cambrian Gurupi Belt, northern Brazil: geochemistry, U–Pb zircon geochronology, and Nd isotope constraints on the Paleoproterozoic magmatic and crustal evolution. Precam. Res. 220–221, 192–216.
Kohlstedt, D.L., Evans, B., Mackwell, S.J., 1995. Strength of the lithosphere: constraints imposed by laboratory experiments. J. Geophys. Res. 100, 17587–17602.
Korenaga, J., 2013. In: Benn, K., Mareschal, J.-C., Condie, K.C. (Eds.), Archean Geodynamics and the Thermal Evolution of Earth, in Archean Geodynamics and Environments. American Geophysical Union, Washington, DC, http://dx.doi.org/10.1029/164GM03.
Labrosse, S., Jaupart, C., 2007. Thermal evolution of the Earth: secular changes and fluctuations of plate characteristics. Earth Planet. Sci. Lett. 260, 465–481.
Lambeck, K., 1983. Structure and evolution of the intracratonic basins of central Australia. Geophys. J. R. Astron. Soc. 74, 843–886.
Laske, G., Masters, G., 1997. A global digital map of sediment thickness. EOS Trans. AGU 78, F483.
Le Pourhiet, L., Huet, B., May, D.A., Labrousse, L., Jolivet, L., 2012. Kinematic interpretation of the 3D shapes of metamorphic core complexes. Geochem. Geophys. Geosyst. 13 (9), Q09002.
Lemoine, S., (Thèse ès Sciences) 1988. Evolution géologique de la région de Dabakala (NE de la Côted'Ivoire) au Protérozoïque. Possibilités d'extension au reste de la Côte-d'Ivoire et au Burkina Faso: similitudes et différences; les linéaments de Greenville-Ferkéssédougou et Grand-Cess-Niakaramandougou. Univ. Cl.-Ferrand, 388 p.
Lexa, O., Schulmann, K., Janousek, V., Stipska, P., Guy, A., Racek, M., 2011. Heat sources and trigger mechanisms of exhumation of HP granulites in Variscan orogenic root. J. Metamorph. Geol. 29, 79–102.
Lüdtke, G., Hirdes, W., Konan, G., Koné, Y., Yao, C., Diarra, S., Zamblé, Z., 1998. Géologie de la région Haute Comoé Nord—feuilles Kong (4b et 4d) et Téhini-Bouna (3a à 3d), Direction de la Géologie Abidjan Bulletin, 178 p.
Maierová, P., Čadek, O., Lexa, O., Schulmann, K., 2012. A numerical model of exhumation of the orogenic lower crust in the Bohemian Massif during the Variscan orogeny. Stud. Geophys. Geodaet. 56, 595–619.
Maierová, P., Lexa, O., Schulmann, K., Štípská, P., 2013. Contrasting tectono-metamorphic evolution of orogenic lower crust in the Bohemian Massif: a numerical model. Gondwana Res., http://dx.doi.org/10.1016/j.gr.2012.08.020.
Mareschal, J.-C., Jaupart, C., Rolandone, F., Gariepy, C., Fowler, C.M.R., Bienfait, G., Carbonne, C., Lapointe, R., 2005. Heat flow, thermal regime, and elastic thickness of the lithosphere in the Trans-Hudson Orogen. Can. J. Earth Sci. 42, 517–532.
Martelat, J.-M., Lardeaux, J.-M., Nicollet, C., Rakotondrazafy, R., 2000. Strain pattern and late Precambrian deformation history in southern Madagascar. Precam. Res. 102, 1–20.
Martin, H., 1993. The mechanisms of petrogenesis of the Archaean continental crust – comparison with modern processes. Lithos 30, 373–388.
Martin, H., Smithies, R.H., Rapp, R., Moyen, J.F., Champion, D.C., 2005. An overview of adakite, tonalite–trondhjemite–granodiorite (TTG), and sanukitoid: relationships and some implications for crustal evolution. Lithos 79, 1–24.
McLennan, S.M., Taylor, S.R., 1996. Heat flow and the chemical composition of continental crust. J. Geol. 104, 369–377.

Milési, J.P., Ledru, P., Feybesse, J.L., Dommanget, A., Marcoux, E., 1992. Early Proterozoic ore deposits and tectonics of the Birimian Orogenic Belt, West Africa. Precam. Res. 58, 305–344.
Mourgues, R., Bureau, D., Bodet, L., Gay, A., Gressier, J.B., 2012. Formation of conical fractures in sedimentary basins: experiments involving pore fluids and implications for sandstone intrusion mechanisms. Earth Planet. Sci. Lett. 313–314, 67–78.
Moyen, J.F., Martin, H., 2012. Forty years of TTG research. Lithos 148, 312–336.
Moyen, J.-F., Martin, H., Jayananda, M., Auvray, B., 2003. Late Archaean granites: a typology based on the Dharwar Craton (India). Precam. Res. 127, 103–123.
Naba, S., Lompo, M., Debat, P., Bouchez, J.L., Beziat, D., 2004. Structure and emplacement model for late-orogenic Paleoproterozoic granitoids: the Tenkodogo-Yamba elongate pluton (Eastern Burkina Faso). J. Afr. Earth Sci. 38, 41–57.
Newton, R.C., 1990. Fluids and melting in the Archaean deep crust of southern India. In: Ashworth, J.C., Brown, M. (Eds.), High-temperature Metamorphism and Crustal Anatexis. Unwin Hyman, pp. 149–179.
Nisbet, E.G., Cheadle, M.J., Ardnt, N.T., Bickle, M.J., 1993. Constraining the potential temperature of the Archaean mantle: a review of the evidence from komatiites. Lithos 30, 291–307.
Oberthür, T., Vetter, U., Davis, D.W., Amanor, J.A., 1998. Age constraints on gold mineralization and Paleoproterozoic crustal evolution in the Ashanti belt of southern Ghana. Precambrian Res. 89, 129–143.
O'Brien, P.J., Walte, N., Li, J.H., 2005. The petrology of two distinct granulite types in the Hengshan Mts, China, and tectonic implications. J. Asian Earth Sci. 24, 615–627.
Parsons, B., Sclater, T.G., 1977. An analysis of the variation of ocean floor bathymetry andheat flow with age. J. Geophys. Res. 82, 803–827.
Percival, J.A., Skulski, T., 2000. Tectonothermal Evolution of the Northern Minto Block, Superior Province, Quebec, vol. 38. The Canadian Mineralogist, Canada, pp. 345–378.
Percival, J.A., Mortensen, J.K., Stern, R.A., Card, K.D., Bégin, N.J., 1992. Giant granulite terranes of northeastern Superior Province: the Ashuanipi complex and Minto block. Can. J. Earth Sci. 29, 2287–2308.
Perrouty, S., (PhD thesis) 2012. Evolution Structurale de la Ceinture Minéralisée d'Ashanti, Sud-Ouest Ghana. Uinversité Paul Sabatier, Toulouse, France, 232 p.
Perry, H.K.C., Mareschal, J.-C., Jaupart, C., 2006. Variations of strength and localized deformation in cratons: the 1.9 Ga Kapuskasing uplift, Superior Province, Canada. Earth Planet. Sci. Lett. 249, 216–228.
Petford, N., Clemens, J.D., 2000. Granites are not diapiric! Geol. Today 16, 180–184.
Pitra, P., Kouamelan, A.N., Ballèvre, M., Peucat, J.-J., 2010. Palaeoproterozoic high-pressure granulite overprint of the Archean continental crust: evidence for homogeneous crustal thickening (Man Rise, Ivory Coast). J. Metamorph. Geol. 28, 41–58.
Poliakov, A.N., Cundall, P.A., Podladchikov, Y.Y., Lyakhovsky, V.A., 1993. An explicit inertial method for the simulation of viscoelastic flow: an evaluation of elastic effects on diapiric flow in two- and three-layer models. In: Stone, D.B., Runcorn, S.K. (Eds.), Flow and Creep in the Solar System: Observations, Modelling and Theory. Kluwer Academic Publishers, Dordrecht, pp. 175–195.
Pons, J., Oudin, C., Valero, J., 1992. Kinematics of large syn-orogenic intrusions: example of the Lower Proterozoic Saraya batholith (Eastern Senegal). Geologische Rundschau 81, 473–486.
Pons, J., Barbey, P., Dupuis, D., Léger, J.M., 1995. Mechanisms of pluton emplacement and structural evolution of a 2.1 Ga juvenile continental crust: the Birimian of southwestern Niger. Precam. Res. 70, 281–301.
Pouclet, A., Doumbia, S., Vidal, M., 2006. Geodynamic setting of the Birimian volcanism in central Ivory Coast (western Africa) and its place in the Palaeoproterozoic evolution of the Man Shield. Bulletin de la Société Géologique de France 177, 105–121.
Powell, R., Holland, T.J.B., Worley, B., 1998. Calculating phase diagrams involving solid solutions via non-linear equations, with examples using THERMOCALC. J. Metamorph. Geol. 16, 577–588.
Ranalli, G., 1995. Rheology of the Earth. Chapman & Hall, London, pp. 413.
Rey, P.F., Houseman, G., 2006. Lithospheric scale gravitational flow: the impact of body forces on orogenic processes from Archaean to Phanerozoic. Geol. Soc. Lond. Spec. Publ. 253, 153–167.
Rey, P.F., Teyssier, C., Whitney, D., 2009. Extension rates, crustal melting, and core complex dynamics. Geology 37, 394–397.
Richter, F.M., 1984. Regionalized models for thermal evolution of the earth. Earth Planet. Sci. Lett. 68, 471–484.
Rosenberg, C.L., Handy, M.R., 2001. Mechanisms and orientation of melt segregation paths during pure shearing of a partially molten rock analog (norcamphorbenzamide). Journal of Structural Geology 23 (12), 1917–1932.
Rudnick, R.L., Gao, S., 2003. The Composition of the Continental Crust, pp. 1–64. In: The Crust (Rudnick, R.L. (Ed.)), vol. 3, Treatise on Geochemistry (Holland, H.D., Turekian, K.K. (Eds.)), Elsevier-Pergamon, Oxford.
Sawyer, E.W., 1994. Melt segregation in the continental crust. Geology 22, 1019–1022.
Schmalholz, S.M., Podladchikov, Y.Y., 1999. Buckling versus folding: importance of viscoelasticity. Geophys. Res. Lett. 26, 2641–2644.
Schmalholz, S.M., Podladchikov, Y.Y., 2013. Tectonic overpressure in weak crustal-scale shear zones and implications for the exhumation of high-pressure rocks. Geophys. Res. Lett. 40, 1984–1988, http://dx.doi.org/10.1002/grl.50417.
Schmeling, H., Babeyko, A.Y., Enns, A., Faccenna, C., Funiciello, F., Gerya, T., Golabek, G.J., Grigull, S., Kaus, B.J.P., Morra, G., Schmalholz, S.M., van Hunen, J., 2008. A benchmark comparison of spontaneous subduction models—Towards a free surface. Phys. Earth Planet. Interiors 171, 198–223, http://dx.doi.org/10.1016/j.pepi.2008.06.028.
Schulmann, K., Lexa, O., Štípská, P., Racek, M., Tajčmanová, L., Konopásek, J., Edel, J.-B., Peschler, A., Lehmann, J., 2008. Vertical extrusion and horizontal channel flow of orogenic lower crust: key exhumation mechanisms in large hot orogens? J. Metamorph. Geol. 26, 273–297.
Smye, A.J., Greenwood, L.V., Holland, T.J.B., 2010. Garnet–chloritoid–kyanite assemblages: eclogite facies indicators of subduction constraints in orogenic belts. J. Metamorph. Geol. 28, 753–768.
Soumaïla, A., 2000. Étude structurale, pétrographique et géochimique de la ceinture-birimienne de Diagorou-Darbani, Liptako, Niger occidental (Afrique de l'Ouest). Ph.D. thesis. université de Franche - Comté, France, 253 p.
Soumaïla, A., Garba, Z., 2006. Le metamorphisme des formations de la ceinture de roches vertes birimienne (paléoproterozoïque) de Diagorou-Darbani (Liptako, Niger, Afrique de l'Ouest). Afr. Geosci. Rev. 13, 107–128.
Spear, F.S., 1993. Metamorphic Phase Equilibria and Pressure-Temperature-Time Paths. Mineralogical Society of America, Washington, D.C, 799 p.
Sylvester, P.J., Attoh, K., 1992a. Lithostratigraphy and composition of 2.1 Ga greenstone belts of the West African Craton and their bearing on crustal evolution and Archean-Proterozoïc boundary. J. Geol. 100, 377–393.
Sylvester, P.J., Attoh, K., 1992b. Lithostratigraphy and composition of 2.1 Ga greenstone belts of the West African Craton and their bearing on crustal evolution and the Archean-Proterozoic boundary. J. Geol. 100, 377–393.
Tajčmanová, L., Connolly, J.A.D., Cesare, B., 2009. A thermodynamic model for titanium and ferric iron solution in biotite. J. Metamorph. Geol. 27, 153–164.
Tapsoba, B., Lo, C.-H., Jahn, B.-M., Chung, S.-L., Wenmenga, U., Iizuka, Y., 2013. Chemical and Sr–Nd isotopic compositions and zircon U–Pb ages of the Birimian granitoids from NE Burkina Faso, West African Craton: implications on the geodynamic setting and crustal evolution. Precam. Res. 224, 364–396.
Thompson, A.B., 1984. Geothermal gradients through time. In: Holland, H.D., Trendall, A.F. (Eds.), Patterns of Change in Earth Evolution. Springer-Verlag, Berlin, pp. 345–355.
Thompson, A.B., Connolly, J.A.D., 1990. Metamorphic fluids and anomalous porosities in the lower crust. Tectonophysics 182, 47–55.
Tirel, C., Brun, J.P., Burov, E., Wortel, M.J.R., Lebedev, S., 2013. A plate tectonics oddity: caterpillar-walk exhumation of subducted continental crust:. Geology 41, 555–558.
Toé, W., Vanderhaeghe, O., André-Mayer, A.-S., Feybesse, J.-L., Milési, J.-P., 2013. From migmatites to granites in the Pan-African Damara orogenic belt, Namibia. J. Afr. Earth Sci. 85, 62–74.
Trap, P., Faure, M., Lin, W., Augier, R., Fouassier, A., 2011. Syn-collisional channel flow and exhumation of Paleoproterozoic high-pressure rocks in the Trans-North China Orogen: the critical role of partial-melting and orogenic bending. Gondwana Res. 20, 498–515.
Trap, P., Faure, M., Wei, L., Le Breton, N., Monié, P., 2012. Paleoproterozoic tectonic evolution of the Trans-North China Orogen: toward a comprehensive mode. Precam. Res. 222–223, 191–211.
Turcotte, D.L., Schubert, G., 2002. Geodynamics. Cambridge University Press, Cambridge, pp. 456.
Ueda, K., Gerya, T.V., Burg, J.-P., 2012. Delamination in collisional orogens: thermomechanical modeling. J. Geophys. Res. 117, http://dx.doi.org/10.1029/2012JB009144.
Van Hunen, J., Moyen, J.-F., 2012. Archean subduction: fact or fiction? Annu. Rev. Earth Planet. Sci. 40, 195–219.
Vanderhaeghe, O., 2001. Melt segregation, pervasive melt migration and magma mobility in the continental crust: the structural record from pores to orogens. Phys. Chem. Earth 26, 213–223.
Vanderhaeghe, O., 2009. Migmatites, granites and orogeny: flow modes of partially-molten rocks and magmas associated with melt/solid segregation in orogenic belts. Tectonophysics 477, 119–134.
Vanderhaeghe, O., 2012. The thermal–mechanical evolution of crustal orogenic belts at convergent plate boundaries: a reappraisal of the orogenic cycle. J. Geodyn. 56–57, 124–145.
Vanderhaeghe, O., Medvedev, S., Fullsack, P., Beaumont, C., Jamieson, R.A., 2003. Evolution of orogenic wedges and continental plateaux: insights from crustal thermal–mechanical models overlying subducting mantle lithosphere. Geophys. J. Int. 153, 27–51.
Vegas, N., Naba, S., Bouchez, J.L., Jessell, M., 2007. Structure and emplacement of granite plutons in the Paleoproterozoic crust of Eastern Burkina Faso: rheological implications. Int. J. Earth Sci. 97, 1165–1180.
Vidal, M., Delor, C., Pouclet, A., Simeon, Y., Alric, G., 1996. Evolution géodynamique de l'Afrique de l'Ouest entre 2,2 Ga et 2 Ga; le style archéen' des ceintures vertes et des ensembles sedimentaires birimiens du nord-est de la Côte-d'Ivoire. Bulletin de la Société géologique de France 167, 307–319.
Vidal, M., Gumiaux, C., Cagnard, F., Pouclet, A., Ouattara, G., Pichon, M., 2009. Evolution of a Paleoproterozoic weak type orogeny in the West African Craton (Ivory Coast). "Hot orogens" special issue. Tectonophysics 477, 145–159.
Vielzeuf, D., Clemens, J.D., Pin, C., Moinet, E., 1990. Granites, granulites and crustal differentiation. In: Vielzeuf, D., Vidal, P. (Eds.), Granulites and Crustal Evolution. Kluwer, Dordrecht, pp. 59–85.
Vigneresse, J.L., Clemens, J.D., 2000. Granitic magma ascent and emplacement: neither diapirism nor neutral buoyancy. In: Vendeville, B., Mar, Y., Vigneresse, J.L. (Eds.), Salt, Shale and Igneous Intrusions in and around Europe, vol. 174. Geol. Soc. London Spec. Publ., pp. 1–19.

Waldbaum, D.R., Thompson, J.B., 1968. Mixing properties of sanidine crystalline solutions. 2. Calculations based on volume data. Am. Mineral. 53.
Wedepohl, K.H., 1995. The composition of the continental crust. Geochim. Cosmochim. Acta 59, 1217–1232.
Wei, C.J., Powell, R., Zhang, L.F., 2003. Eclogites from the south Tianshan, NW China: petrological characteristic and calculated mineral equilibria in the Na_2O–CaO–FeO–MgO–Al_2O_3–SiO_2–H_2O system. J. Metamorph. Geol. 21, 163–180.
Weinberg, R.F., 1996. The ascent mechanism of felsic magmas: news and views. In: Third Hutton Symposium on Granites, Trans. R. Soc. Edinburgh, vol. 87, pp. 95–103.
Weinberg, R.F., Podladchikov, Y., 1994. Diapiric ascent of magmas through power law crust and mantle. J. Geophys. Res. 99, 9543.
White, R.W., Powell, R., Holland, T.J.B., Worley, B.A., 2000. The effect of TiO_2 and Fe_2O_3 on metapelitic assemblages at greenschist and amphibolites facies conditions: mineral equilibria calculations in the system K_2O–FeO–MgO–Al_2O_3–SiO_2–H_2O–TiO_2–Fe_2O_3. J. Metamorph. Geol. 18, 497–511.
White, R.W., Powell, R., Phillips, G.N., 2003. A mineral equilibria study of hydrothermal alteration in mafic greenschist facies rock at Kalgoorlie, Western Australia. J. Metamorph. Geol. 21, 455–468.
White, R.W., Pomroy, N.E., Powell, R., 2005. An in-situ metatexite-diatexite transition in upper amphibolite facies rocks from Broken Hill, Australia. J. Metamorph. Geol. 23, 579–602.
Yamato, P., Agard, P., Burov, E., Le Pourhiet, L., Jolivet, L., Tiberi, C., 2007. Burial and exhumation in a subduction wedge: mutual constraints from thermomechanical modeling and natural *P–T–t* data (Schistes Lustres, western Alps). J. Geophys. Res. 112, B07410, http://dx.doi.org/10.1029/2006JB004441.
Zhao, G.C., Cawood, P.A., Wilde, S.A., Lu, L.Z., 2000a. Metamorphism of basement rocks in the Central Zone of the North China Craton: implications for Paleoproterozoic tectonic evolution. Precambrian Res. 103, 55–88.
Zhao, G.-C., Wilde, S.A., Cawood, P.A., Lu, L.-Z., 2000b. Petrology and P–T–t path of the Fuping mafic granulites: implications for tectonic evolution of the central zone of the North China Craton. J. Metamorph. Geol. 18, 375–391.
Zhao, G., Cawood, P.A., Wilde, S.A., Sun, M., 2002. Review of global 2.1–1.8 Ga orogens: implications for a pre-Rodinia supercontinent. Earth Sci. Rev. 59, 125–162.

Chapitre 6

Crustal evolution in NW Ghana, implications for the WAC

Introduction (en français)

Les chapitres précédents portaient sur les processus géodynamiques contrôlant l'orogenèse Éburnéenne. Celui-ci s'intéresse aux processus magmatiques ayant pris part à la production et à l'évolution de la croûte continentale au nord du Ghana. Il présente les caractéristiques lithologiques, petrologiques et géochimiques du magmatisme dans la zone d'étude. Les compositions en éléments traces et majeurs des roches volcaniques et plutoniques permettent d'étudier les sources du magmatisme à l'origine de la croûte paléoprotérozoïque. Les analyses U–Pb et Lu–Hf sur zircon fournissent des contraintes chronologiques sur l'histoire de la croûte et de ses précurseurs.

Ce chapitre s'intéresse au magmatisme primitif qui initie la genèse du craton, ainsi qu'à l'évolution des processus pétrogénétiques dans le temps, avant et après l'orogenèse Éburnéenne au nord du Ghana. Il couvre également une aire géographique plus vaste, puisqu'une comparaison est effectuée entre l'histoire magmatique du nord du Ghana et celle des domaines avoisinants. Cette comparaison fournit une vision du magmatisme à grande échelle, et permet de discuter de la place du nord du Ghana dans l'évolution des régions orientales et méridionales du Craton Ouest Africain. Les différents jeux de données sont analysées afin de proposer un modèle d'évolution géodynamique de la région et de discuter des contextes de croissance crustale au Paléoprotérozoïque. Cette étude est destinée à être soumise à la revue *Precambrian Research* début 2015.

Résumé

La croûte paléoprotérozoïque du Craton Ouest African au nord du Ghana est essentiellement constituée de roches volcaniques et plutoniques issues des séries calco-alcaline ou des TTG. Les laves incluent des basaltes tholéiitiques, des andésites, des dacites et des rhyolites. Les roches plutoniques sont majoritairement des tonalites, des diorites, des granodiorites et des granites. Leurs charactéristiques géochimiques suggèrent que les magmas ont été produits par l'intéraction à divers degrés entre deux sources, un manteau enrichi en éléments incompatibles LILE et une croûte basique, et par leur fusion simultanée. La diversité lithologique et géochimique des roches magmatiques est relativement limitée, ce qui reflèterait des processus magmatiques et pétrogénétiques homogènes au cours de l'histoire géologique de la région, aussi bien avant qu'après l'orogenèse Éburnéenne. Cependant, la composition en éléments trace des tonalites mises en place le plus tardivement, après le paroxysme de l'orogenèse, suggère une fusion de leur source à des pressions plus élevées par rapport aux magmas précoces. Cette évolution est atypique et diffère de celle observée sur la plupart des cratons archéens, où le magmatisme tardif implique plutôt le recyclage de sources crustales ou peu profondes. De nouvelles datations U–Pb sur zircon confirment que l'activité magmatique était quasiment continue pendant près de 100 Ma, entre 2.21 et 2.11 Ga. Des cœurs de zircons hérités mettent en évidence le recyclage d'une croûte plus ancienne, formée entre 2.32 et 2.21 Ga. L'isotopie Lu-Hf des zircons révèle que la croûte est juvénile. Les roches magmatiques étudiées sont issues du recyclage intense d'une "proto-croûte" basique exraite du manteau entre 2.45 et 2.25 Ga. Les analyse ne font pas état d'un recyclage

de croûte continentale archéenne dans la source des magmas paléoprotérozoïques. Le protolithe juvénile de la croûte du Craton Ouest Africain se serait donc formé en milieu océanique, par exemple dans un plateau océanique, plutôt que le long d'une marge continentale active. L'analyse d'une synthèse des âges U–Pb publiés au nord du Ghana et dans les régions mitoyennes révèle l'existence de diachronismes dans l'activité magmatique entre différents domaines du craton. Le magmatisme semble démarrer simultanément sur l'ensemble de la zone considérée (qui correspond au sud-est du Craton Ouest Africain). Un pic d'activité est observé vers 2130 Ma au nord du Ghana et à l'est du Burkina Faso. Il coïncide avec le paroxysme métamorphique au nord-ouest du Ghana, et avec une période de faible activité dans les régions mitoyennes du sud du Ghana, du sud du Burkina Faso et de l'est de la Côte d'Ivoire. Cet épisode marque la fin de l'activité magmatique au nord du Ghana et à l'est du Burkina Faso, alors qu'un regain d'activité est observé jusqu'à 2080 Ma dans les domaines voisins. La distribution des âges magmatiques suggère l'existence de deux domaines différant par leurs histoires géologiques et leurs évolutions magmatiques. Ces sous-ensembles ont été amalgamés au cours d'une collision éburnéenne entre 2.14 et 2.12 Ga. La collision a sans doute joué un rôle déterminant dans la maturation et la stabilisation de la croûte, puisqu'elle annonce la fin de l'activité géodynamique dans un domaine cratonique, et constitue le terme d'une évolution de 300-400 Ma, depuis la genèse d'une croûte juvénile à la cratonisation.

6.1 Introduction

The previous chapters explored the geodynamic processes controlling the Eburnean orogeny in northern Ghana. The present chapter focuses on the magmatic processes that controlled the crustal growth and evolution in northern Ghana. It provides an overview of the lithology, petrology and geochemistry of igneous rocks in the study area. Major and trace element geochemical data are presented and analysed to investigate the possible magma sources that were mobilised to generate the Paleoproterozoic continental crust. Zircon U–Pb and Lu–Hf isotopy additionally provide constraints on the timing and duration of craton formation and stabilisation. This study has a wider scope than the previous chapters, because it is concerned with the early magmatism that initiated the formation of the craton crust, as well as with the petrogenesis of rocks formed during crustal recycling before, during and after the Eburnean orogeny. Furthermore, it considers a broader geographic area by comparing the geochronological development of magmatism in northern Ghana with the evolution of neighbouring provinces. This gives a regional-scale vision of magmatism and provides arguments to discuss the significance of the geology of northern Ghana on the evolution of the greater paleoproterozoic craton. The various datasets are interpreted in order to propose a model for the geodynamic evolution of (parts of) the West African Craton and to raise new questions on the geodynamic settings of crustal growth in the Paleoproterozoic. This study is intended to be submitted for publication to *Precambrian Research* early in 2015.

6.2 Juvenile crust formation and stabilisation in the south-eastern West African Craton. Insights into post-Archean craton building processes.

Sylvain Block[1], Lenka Baratoux[1,2], Armin Zeh[3], Oscar Laurent[3], 4, Olivier Bruguier[5], Delphine Bosch[5], Renaud Caby[5] Mark Jessell[6], Laurent Ailleres[6], Luis A Parra-Avila[6], Raymond Sagna[8], Suzelle Sigo[1]

[1] *Géosciences Environnement Toulouse, Observatoire Midi Pyrénées, 14 ave E. Belin, 31400, Toulouse, France*
[2] *IFAN, Cheikh Anta Diop, Dakar, Senegal* [3] *Institut für Geowissenschaften, Altenhöfer Allee 1, D-60438 Frankfurt am Main, Germany*
[4] *Unité de Pétrologie, Géochimie Endogène et Pétrophysique (PGEP), Université de Liège, Département de Géologie B20, Boulevard du Rectorat, 4000 Liège (Sart-Tilman), Belgium.*
[5] *Géosciences Montpellier, Université Montpellier 2-CNRS, cc 066, Place Eugène Bataillon,34095 Montpellier Cedex 5, France*
[6] *Center for Exploration Targeting, The University of Western Australia, 35 Stirling Highway, Crawley, Perth, Western Australia 6009*
[7] *Monash University, School of Geosciences, Wellington Road, Clayton, Vic 3800, Australia*
[8] *Direction des Mines et de la Géologie, 104 rue Carnot, Dakar.*

Abstract

The crust of the Paleoproterozoic West African Craton in northern Ghana is dominated by calc-alkaline and Tonalite-Trondjhemite-Granodiorite (TTG) plutonic suites and lavas. Their whole-rock geochemical signatures suggest that they are derived from variable degrees of interaction between a mafic crustal source and an LILE-rich mantle source, both of which melted simultaneously. The limited geochemical and lithological igneous rock diversity indicates that magmatic processes remained relatively unchanged during the whole maturation and stabilisation of the continental crust. However, a greater occurrence of high-pressure TTGs during the late-stage magmatic evolution of the craton is an unusual feature that contrasts with Archean cratons. Zircon U-Pb age data reveals that plutonic suites and lavas in northern Ghana were coeval and emplaced continuously between 2.21 and 2.12 Ga. Inherited cores in zircon grains provide evidence for the recycling of crustal material formed between 2.32 and 2.21 Ga. Zircon Lu-Hf isotope data indicate that the exposed crust is derived from the complete recycling of a juvenile proto-crust which was extracted from the depleted mantle after 2.50 Ga. Older Archean crustal sources did not contribute to magmatism in this portion of the craton. This is interpreted to reflect juvenile proto-crust formation at a distance from active continental margins, possibly in an oceanic plateau environment. A regional-scale

U-Pb crystallisation age database is used to discuss the geodynamic setting of post-2.20 Ga crustal evolution. The dataset reveals the existence of crustal blocks that witnessed different geological histories. It suggests that the Paleoproterozoic West African Craton comprises a minimum of two distinct fragments, with north-western Ghana lying at their interface. Horizontal tectonic forces led to the collision and to the assembly of these fragments at 2.14-2.12 Ga during the Eburnean orogeny. Collision played a major role in the stabilisation of the continental crust, and marks the final stages of a 300-400 Ma long period of juvenile continental crust production and stabilisation.

Keywords : Paleoproterozoic, Magmatism, Craton, Lu-Hf isotopy, Crustal evolution

6.2.1 Introduction

The plate tectonics theory postulates that the Earth's lithosphere is divided into independent rigid plates interacting at their margins. As a consequence, active plate margins are the sites of localised magmatic activity, accretion of juvenile crust, crustal recycling and reworking, and associated deformation and metamorphism. The widespread analysis of combined isotope systems allows us to investigate juvenile crust production and preservation events, mapping juvenile *vs* recycled crustal fragments, characterising magma sources and determining provenance sources of detrital sediments (Amelin et al., 2000, 1999; Condie et al., 2005; Hawkesworth and Kemp, 2006; Patchett et al., 1982; Rino et al., 2004; Stevenson and Patchett, 1990; Zeh et al., 2009, 2007). They are tools to explore the architecture and the evolution of continental crust (e.g. Cawood et al. (2013); Dhuime et al. (2012); Hawkesworth et al. (2010) Dhuime et al., 2012 ; Hawkesworth et al, 2010, 2013).

Many authors have emphasised the peculiarities of Archean cratons, including the occurrence of komatiites, typical alternations of granite-greenstone terranes bounded by craton-scale shear zones (Condie, 1981; De Wit and Ashwal, 1997), large volumes of TTG plutons and gneisses (e.g. Moyen and Martin (2012)), and occasional dome and basin strain patterns (e.g. Choukroune et al. (1995)). Conversely, the presence of blueschist and UHP metamorphism (Chopin, 1984; Ernst, 1972; Smith, 1984), unequivocal nappes, fold and thrust belts, extensional domes or ophiolites are common in Phanerozoic provinces. The Proterozoic rock record seems to represent a transitional phase between the archaic and modern Earth, as Proterozoic cratons and orogens display some of the features which characterise both Archean and Phanerozoic eons (Brown, 2009; Harley, 1992; Helmstaedt and Scott, 1992; Windley, 1992). This is interpreted to reflect changes in geodynamic processes through time, inferred to result from secular changes in the thermal regime of the Earth. The plate tectonics theory is built from constraints and observations drawn from the Phanerozoic rock record. Hence, its applicability to the early Earth, where geodynamic processes were apparently different, remains debated (Bédard et al., 2013; Condie and Kröner, 2008; de Wit, 1998; Ernst, 2009; Hamilton, 2003; Smithies et al., 2003; Stern, 2005; Windley, 1981, 1993).

The discovery of lateral model age gradients between crustal fragments within cratons demonstrates the existence of suture zones separating domains with different geological histories (Champion and Sheraton, 1997; Czarnota et al., 2010; Zeh et al., 2013). This evidence has been interpreted in favour of lateral growth mo-

dels of continental masses by accretion of juvenile crust onto the margins of stable cratonic nuclei. Such models are analogous to crustal formation models in modern accretionary orogens (Cawood et al., 2009). Therefore, isotopic studies provide a tool to investigate the applicability of plate-tectonic models through the Earth history. Complementary geochemical, petrologic and structural approaches allow us to explore the processes controlling crust production, recycling and accretion, which in turns may be used to calibrate geodynamic models for crustal evolution.

The Paleoproterozoic Sao Luis - West African Craton, formed between 2.25 and 2.07 Ga (Abouchami et al., 1990; Boher et al., 1992), is among the youngest large ($\sim 3.10^6$ km^2) provinces of juvenile crustal material on Earth. Global crustal evolution models suggest that it formed just before a major crustal growth period that culminated at ca. 2.00 Ga (Condie and Aster, 2010). The West African Craton formed and stabilised in a relatively short time interval, which implies high continental crust production and preservation rates. Furthermore, the contribution of older continental material to magmatism has been shown to be small or negligible (Boher et al., 1992). In the field, the West African Craton shares some lithological and architectural characteristics with Archean provinces. As a result of these unusual features, it potentially holds important information for the understanding of crustal growth and preservation mechanisms near to the Archean-Proterozoic transition. This paper aims at investigating the growth mechanisms and architecture of the eastern part of the Baoulé-Mossi domain of the West African Craton, based on data obtained from the Paleoproterozoic domains of northern Ghana. New U-Pb and Lu-Hf data on magmatic rocks are presented and interpreted in light of a craton-scale geochronological database. Complementary constraints on the tectono-metamorphic evolution of northern Ghana are used to propose a geodynamic evolution model for the eastern part of the Paleoproterozoic West African Craton.

6.2.2 Geological setting

The West African Craton is exposed in north-western Africa in the Reguibat rise, and in western equatorial Africa in the Leo-Man rise (Fig. 6.1a). It comprises a 3.60-2.60 Ga Archean nucleus to the west (Auvray et al., 1992; Potrel et al., 1998, 1996; Thiéblemont et al., 2001) and 2.25- 2.07 Ga Paleoproterozoic domains to the east. In the Leo-Man rise, the Archean Kénéma-Man domain is separated from the Paleoproterozoic Baoulé-Mossi domain by the Sassandra shear zone, while the El Mdena shear zone forms the boundary between both age domains in the Reguibat rise (Bessoles, 1977). The Paleoproterozoic part of the West African Craton is made of a succession of Birimian volcanic belts (Junner, 1940), volcano-sedimentary basins and Tarkwaian fluvio-deltaic basins granite-greenstone terranes (e.g. Baratoux et al. (2011); Gasquet et al. (2003)). They alternate with granite-gneiss domains that comprise Tonalite-Trondjhemite-Granodiorite (TTG) gneisses or plutons, diorites and granites, that form most of the exposed surface of the craton. Birimian greenstone belts comprise elongated sequences of volcano-sedimentary and volcanic rocks. The latter have tholeiitic to calc-alkaline affinities (e.g. Baratoux et al. (2011); Leube et al. (1990)). Basins are mostly made of volcano-sedimentary rocks, shales, greywackes, and occasional chemical sediments. Across the craton, the ages of inherited and detrital zircon grains reveal that magmatism started as early as

ca. 2.30 Ga (e.g.Gasquet et al. (2003)). Intense volcanic activity is recorded from greenstone belts between 2.25 and 2.19 Ga (Duodu (2009); Feybesse et al. (2006); Hirdes et al. (1996); Hirdes and Davis (1998), in Ghana ; Schwartz and Melcher (2003) in Burkina Faso ; Delor and d'Ivoire (1995) in Côte d'Ivoire ; Lahondère et al. (2002) in Guinea) ; and is coeval with the formation of early TTG suites (Dia et al. (1997); Gueye et al. (2008), in Senegal ; De Kock et al. (2011); Feybesse et al. (2006), in Ghana ; Tshibubudze et al. (2013), in Burkina Faso, Peucat et al. (2005), in Algeria). Magmatic activity is apparently uninterrupted until ca. 2.10 Ga (Davis et al., 1994; Doumbia et al., 1998; Kouamelan, 1996; Oberthür et al., 1998; Tapsoba et al., 2013). Younger granitoids and lavas, dated between 2.10 and 2.07 Ga are mostly restricted to the western portion of the Baoulé-Mossi domain, to the Reguibat rise and to the contact zone with the Archean craton (Egal et al., 2002; Hirdes and Davis, 2002; Liégeois et al., 1991; Peucat et al., 2005)

Geodynamic scenarios invoked for the formation of the Paleoproterozoic continental crust of the West African Craton range from magmatic accretion in an oceanic plateau setting (Abouchami et al., 1990; Boher et al., 1992; Lompo, 2009) to lateral accretion in volcanic island arcs (Attoh et al., 2006; Baratoux et al., 2011; Dampare et al., 2008; Ganne et al., 2012; Peucat et al., 2005; Pouclet et al., 2006; Sylvester and Attoh, 1992; Vidal and Alric, 1994). Previous work using the Sm-Nd isotopic system all report crustal residence ages of 2.50-2.20 Ga (Abouchami et al., 1990; Boher et al., 1992; Gasquet et al., 2003; Peucat et al., 2005). These results are in agreement with studies in the Sao Luis Craton of Brazil (Klein et al., 2005; Klein and Veloso Moura, 2001), which as a whole suggest a coeval evolution and a rapid stabilization for all the Paleoproterozoic domains of the Sao Luis - West African Craton. However, the geodynamic settings which prevailed during craton formation remain weakly constrained.

The structural trend of litho-tectonic units and the dominant fabrics on the West African Craton are attributed to contractional deformation during the Eburnean orogeny (Bonhomme, 1962; Eisenlohr and Hirdes, 1992; Milési et al., 1989, 1992). The Eburnean orogeny approximately occurred during a maximum time span of 2140-2070 Ma (e.g. Feybesse et al. (2006); Perrouty et al. (2012)). In most provinces of the craton, it consists of an early phase, dominated by contractional deformation, crustal thickening and medium- to high-grade metamorphism (Block et al., 2015; Caby et al., 2000; Debat et al., 2003; Galipp et al., 2003; Ganne et al., 2012; John et al., 1999; Klemd et al., 2002; Liégeois et al., 1991), followed by a 2100-2070 Ma phase of transcurrent tectonics and low-grade metamorphic overprint (e.g. (Feybesse et al., 2006; White et al., 2014)), except along craton margins where granulites were formed (Bendaoud et al., 2008; Kouamelan et al., 1997; Pitra et al., 2010; Schofield et al., 2006). In some parts of the craton, authors propose a polycyclic orogenic model with two discrete deformation stages separated by a period of basin opening in extensional settings (De Kock et al., 2012; Feybesse et al., 2006; Hein, 2010; Lemoine et al., 1990; Perrouty et al., 2012; Tempier, 1986; Tshibubudze et al., 2009; Vidal et al., 2009). However, other authors support alternative interpretations for specific provinces. They suggest that volcanic belts and sedimentary basins formed simultaneously, and that distinct tectono-metamorphic domains underwent a coeval evolution during progressive deformation (Block et al., 2015; Eisenlohr and Hirdes, 1992; Gasquet et al., 2003; Leube et al., 1990).

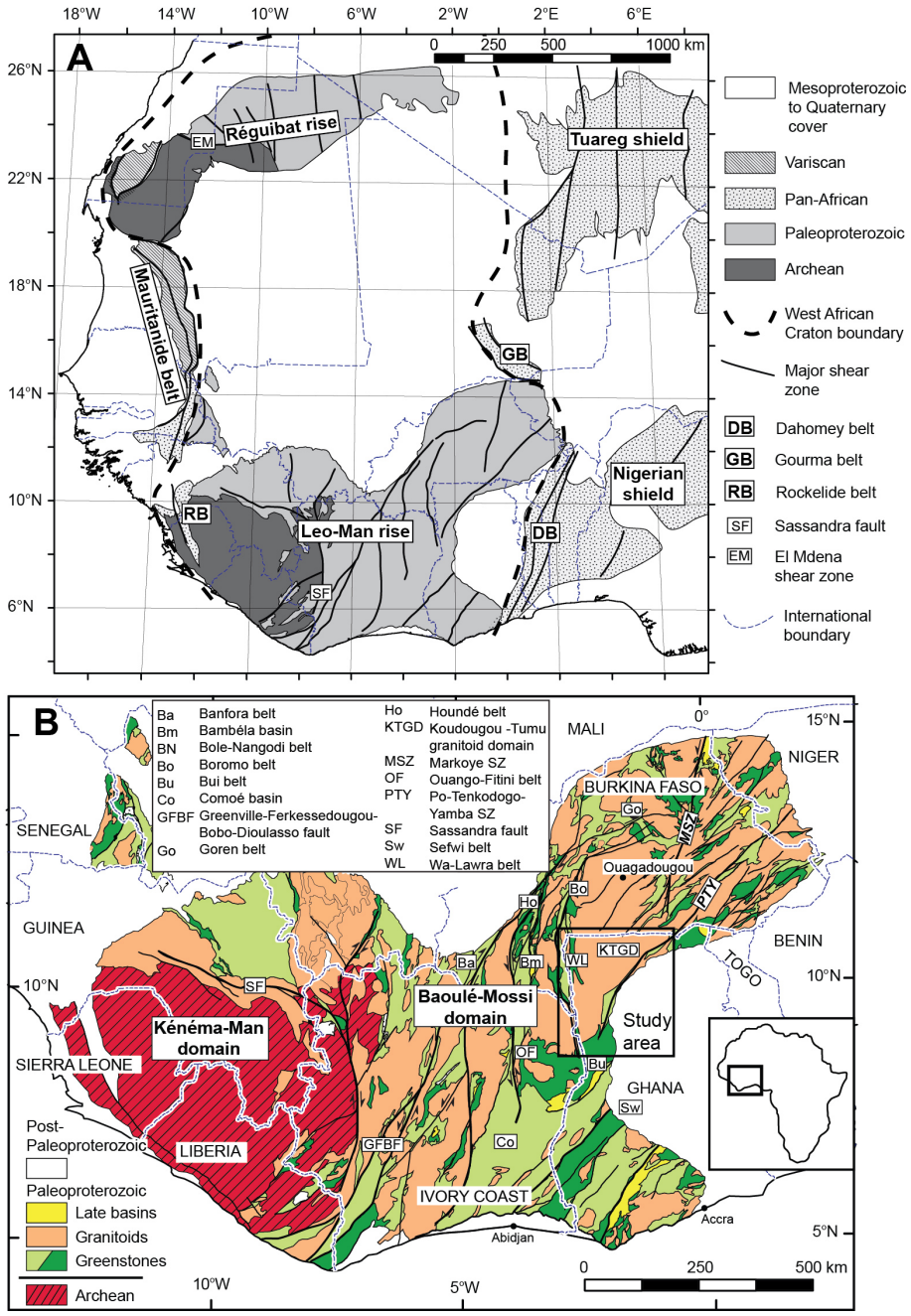

FIGURE 6.1: **A**. Simplified geological map of the Precambrian basement of western Africa. The thick dashed line represents inferred limits of the West African Craton (modified after Abdelsalam et al. (2002); Bessoles (1977); Bronner (1975); Caby et al. (2008); Liégeois et al. (2003); Roussel et al. (1984). **B**. Simplified geological map of the Leo-Man rise (modified after the BRGM SIGAfrique map, Milési et al. (2004)), indicating the study area. Light and dark green areas show intermediate to acidic volcano-sedimentary formations and mafic volcanics respectively. SZ = shear zone.

6.2.3 Northern Ghana

6.2.3.1 Crustal architecture

The architecture of the Baoulé-Mossi domain of the West African Craton is characterized by two major N-S and NE-SW structural trends. In the eastern part (in Niger, Ghana and eastern Burkina Faso), greenstone belts and major shear zones strike to the NE, while they strike N-S in its western part (in Mali, Côte d'Ivoire and south-western Burkina Faso). Both trends join in an interference zone exposed in north-western Ghana : The Jirapa and Jang shear zones (SZ, Fig. 2) belong to a N-S shear zone system and merge to the south with the NE-SW trending Bole-Nangodi SZ, which extends into Burkina Faso. These two major structures subdivide the study area into three crustal segments.

(1) To the west of the Jirapa SZ, the Wa-Lawra belt is the extension of the N-S trending Boromo greenstone belt, which is exposed in south-western Burkina Faso (Baratoux et al., 2011; Metelka et al., 2011). It is made of low-grade metamorphic rocks, including shales, volcano-sedimentary rocks and lavas such as dacites, andesites and basalts.

(2) Between the Jirapa and Bole-Nangodi shear zones, the Koudougou-Tumu granitoid domain (KTGD), extends north into Burkina Faso. It comprises felsic migmatitic orthogneisses, and small volumes of mafic orthogneisses and paragneisses. The protolith of some orthogneisses crystallised between 2163 and 2154 Ma (Duodu, 2009). The KTGD is bounded to the south by the E-W trending Julie belt (Fig. 6.2), which is formed of low-grade volcano-sedimentary rocks and lavas. It includes a unit of cross-bedded quartzites, interbedded with silicic volcano-sedimentary rocks, some of which crystallised at 2129 ± 7 Ma (BN110 ; Fig. 6.2 ; (Block et al., Subm)), which indicating that at least part of this belt formed at ca. 2130 Ma. In the interference zone, the Bole-Bulenga domain is formed of paragneisses and minor metabasites, which are frequently migmatitic. They are intruded by orthogneisses with crystallisation ages between 2195 and 2135 Ma.

(3) To the south of the Bole-Nangodi SZ, the Maluwe domain is a low-grade tectono-metamorphic terrane elongated SW-NE along ∼ 250 km. It is dominated by greywackes and shales intercalated with volcanoclastic rocks and lavas crystallised between 2197 and 2125 Ma (De Kock et al., 2009; Thomas et al., 2009). It also comprises chemical sediments and mafic intrusives, gabbros and pyroxenites. Along strike of the Maluwe domain, the Nangodi belt (Melcher and Stumpfl, 1994), in the north-eastern part of the study area (Fig. 6.2) is formed by a succession of shales, greywackes and Mn-rich cherts alternating with MORB-type basalts, overlain by calc-alkaline andesitic to rhyolitic lava flows. The Maluwe domain is in contact to the south with the Abulembire domain, which is essentially made of paragneisses, sometimes migmatitic, intruded by orthogneisses with crystallisation ages ranging from 2200 to 2125 Ma (De Kock et al., 2009; Duodu, 2009).

6.2.3.2 Tectono-metamorphic evolution

An early contractional deformation D1, consistent with N-S directed shortening, is distributed across the study area. The penetrative metamorphic foliation S1 is developed in both low and high-grade metamorphic terranes. In high-grade rocks,

the gneissic banding S1 carries amphibolite- to granulite-facies metamorphic assemblages. They locally overprint blueschist- to amphibolite-facies high-pressure, low temperature relics, inherited from an earlier pre-D1 tectonic event (D1-e ; (Block et al., Subm)). The D1 tectono-metamorphic event is linked to crustal thickening. Recent U-Pb dating of zircon and metamorphic monazite constrain D1 between 2145 and 2125 Ma (Block et al., Subm, 2015). N-S directed extension (D2) is shown by extensional shear zones along the northern and southern margins of the Bole-Bulenga domain, at the transition with lower-grade rocks. They are interpreted by Block et al. (Subm, 2015) to reflect extensional gravitational collapse of the partially-molten thickened crust after D1. However, De Kock et al. (2012) link extension to the deposition of volcano-sedimentary rocks and greywackes in the Maluwe domain, which they describe as a basin between the rifted Bole-Bulenga and Abulembire domains. After ca. 2130 Ma, D1 and D2 fabrics are overprinted by contractional deformation D3, consistent with E-W directed shortening. Leucosomes and monazite crystallised parallel to S3 fabrics in high-grade rocks have ages between 2123 and 2111 Ma (Block et al., Subm). D3 strain is most intense in the Wa-Lawra belt, the Maluwe and Bole-Bulenga domains. It is localized in NNW-striking, sinistral (D4, e.g. the Jirapa SZ) and NE-striking, dextral strike-slip shear zones (D5, e.g. the Bole-Nangodi SZ), which re-activated or transected older structures. Deformation was coeval with progressive exhumation and cooling, as shown by brittle fabrics (D6) formed later during E-W shortening. Late-stage E-W crenulations define a last brittle deformation event (D7).

6.2.4 Petrography of igneous rocks

6.2.4.1 Plutonic rocks

The investigated plutonic rocks can be separated into four distinct groups : (i) tonalites, trondhjemites ± granodiorites, (ii) quartz-diorites and monzodiorites, frequently associated with (iii) granodiorites and (iv) granites. The petrography of individual samples is summarised in a table in appendix 6.2.10.1

Orthogneisses have tonalitic, trondhjemitic, granodioritic (TTG) or granitic compositions and are leucocratic to mesocratic. They are relatively fine grained and display aligned biotite and hornblende (Fig. 6.3a). Rarely, hornblende is the only ferro-magnesian silicate. The gneisses are sometimes migmatitic and contain granodioritic or granitic melt segregates. Fine-grained leucocratic trondhjemite plutons intrude the gneisses. They contain subhedral to euhedral plagioclase feldspar. Biotite is the main ferro-magnesian silicate and hornblende is present in smaller proportions (Fig. 6.3b). Large (>10km) moderately deformed and composite plutons have dioritic, monzodioritic or granodioritic mineral assemblages. They are leucocratic to melanocratic, are characterised by a coarse (centimetric) grain size (Fig. 6.3c, d). Diorites and granodiorites form different terms of the same plutons. They have similar textures and grain sizes, but they differ by their quartz and potassic feldspar contents. Hornblende is the most abundant ferro-magnesian silicate and coexists with biotite. Epidote is often present (Fig. 6.3e). Microcline is absent or found in subordinate amounts, while magnetite, ilmenite and/or titanite are present in some facies.

Biotite-rich granite plutons are widespread and vary in size, mineralogy and

texture. Vast (>10km wide) porphyric granite plutons display non-oriented centimetric orthoclase crystals (Fig. 6.3f). They are mesocratic or pinkish. Late-stage granitic dikes with similar mineralogy cut across other lithologies. Leucocratic two-mica granites are less frequent (Fig. 6.3g, h). They form plutons of limited extents and are mostly non-deformed. The primary magmatic assemblages are transformed during metamorphism. The development of biotite-epidote rims around hornblende, and the replacement of biotite by chlorite provide evidence for a metamorphic overprint or a late-magmatic fluid-rock interaction. Furthermore, plagioclase is often partly replaced by sericite and secondary white mica recrystallised along schistosity planes.

6.2.4.2 Volcanic rocks

Volcanic rocks range from basalts to rhyolites. Mafic and intermediate lavas contain hornblende which is either magmatic or which replaces clinopyroxene. Metabasalts are mostly microlithic (Fig. 6.4a) except for a coarse grained sample (BN104) whose protolith may have been gabbroic. Andesites and meta-andesites frequently have porphyric textures with hornblende and plagioclase phenocrysts in a microlithic or glassy matrix (Fig. 6.4b). Magmatic hornblende is replaced by actinolite, leucoxene and/or chlorite. Secondary calcite is often present. Felsic lavas display euhedral phenocrysts of quartz and plagioclase surrounded by a microlithic or glassy matrix. Dacites and rhyolites are massive or display epiclastic textures, volcanic bombs and breccias (Fig. 6.4c). K-feldspar is rarely present. Plagioclase is often replaced by albite, epidote, zoisite and white mica. Accessory minerals include sphene, pyrite, allanite, and hematite. Some samples display a variably pronounced metamorphic foliation defined by white mica and biotite, and sometimes contain garnet.

6.2.5 Bulk-rock geochemistry

A total of 70 rocks were sampled for this study. They include 56 granitoids and 14 lavas sampled in all of the main litho-tectonic terranes of northern Ghana. Sampling aimed to provide an extensive geographical coverage of the study area and to investigate the diversity of rock-types. Analytical procedures are presented in Appendix 6.2.10.2. All geochemical data are presented in tables 6.1 and 6.2. Sample location is shown in Fig. 6.2. The data were plotted using the GCDkit software (Janoušek et al., 2006).

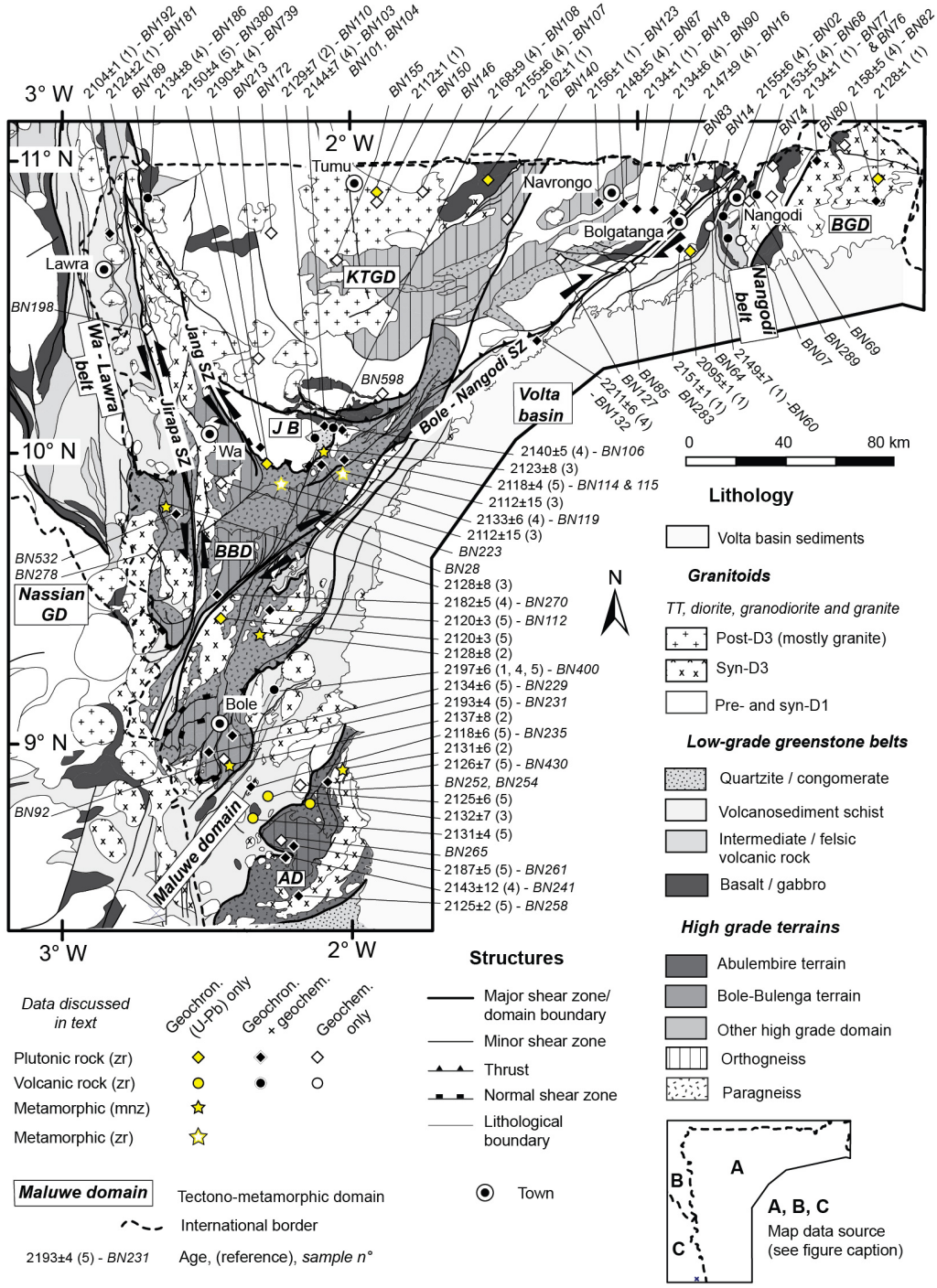

FIGURE 6.2: Litho-structural map of northern Ghana showing the location of samples that were dated and analysed in this study, along with other samples for which geochronological data is available. AD : Abulembire domain ; BBD : Bole-Bulenga domain ; BGD : Bawku granitoid domain ; JB : Julie Belt ; KTGD : Koudougou-Tumu granitoid domain, SZ = shear zone. Radiometric data : (1) : Duodu (2009) ; (2) : Block et al. (2015) ; (3) : Block et al. (Subm) ; (4) : This study ; (5) : De Kock et al. (2011). Map data compilation : A : Block et al. (Subm). B : Baratoux et al. (2011). C : Vidal et al. (2009).

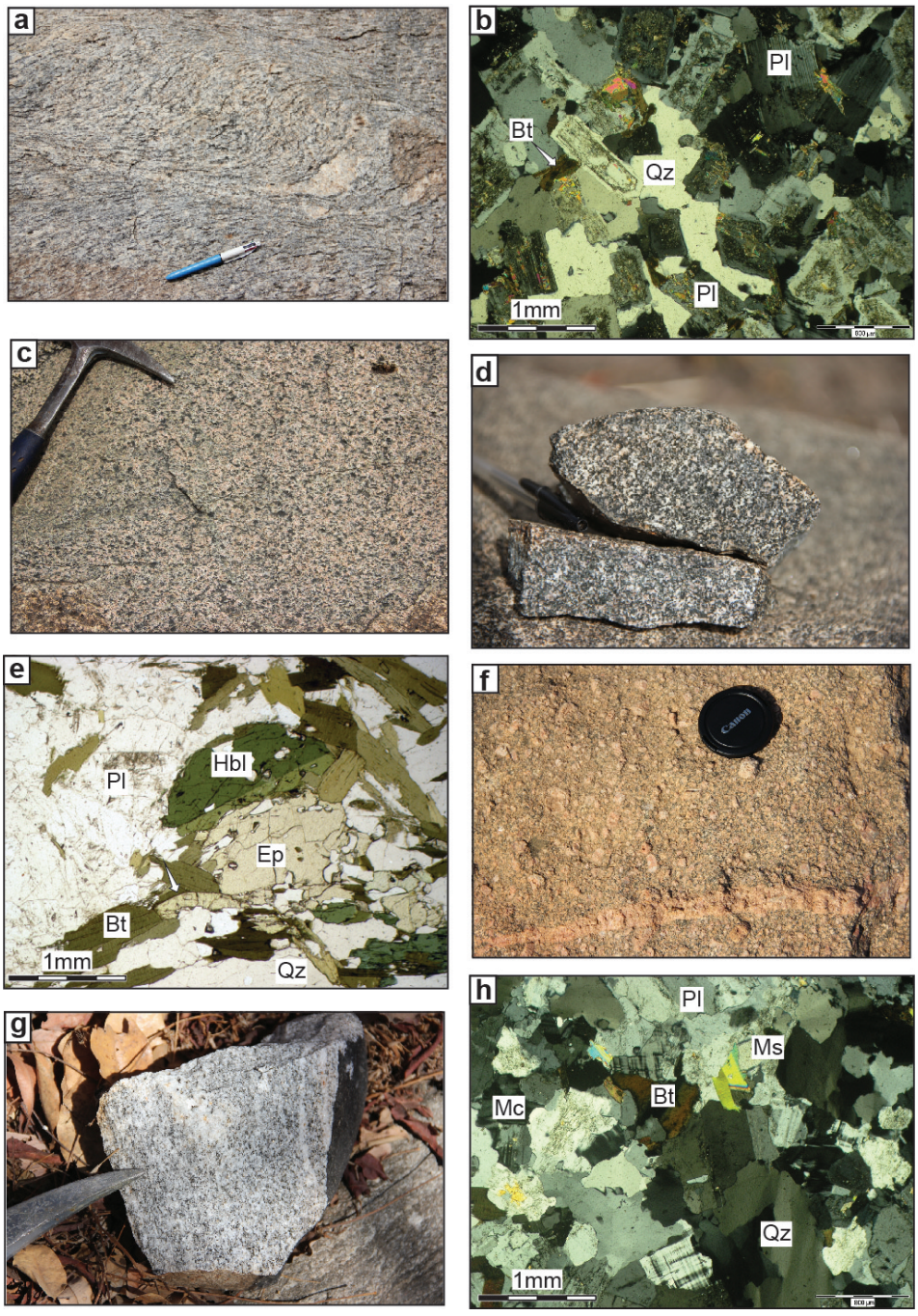

FIGURE 6.3: Rock textures and microphotographs of tonalites (**a-b**) granodiorites and diorites (**c-e**) and granites (**f-h**). (**a**) Sheared trondhjemitic hornblende-biotite-magnetite-bearing orthogneiss, locally migmatitic. (**b**) Fine-grained trondhjemitic rock. Euhedral plagioclase grains display a magmatic zoning and are surrounded by anhedral quartz. Biotite represents the only ferro-magnesian silicate. Secondary white mica develops after plagioclase.

FIGURE 6.3: (**c**) Mesocratic coarse-grained granodiorite, comprising centimetric hornblende-biotite-epidote aggregates in a quartz-plagioclase-alkali feldspar matrix. (**d**) Medium-grained melanocratic hornblende-rich quartz-diorite. (**e**) Hornblende-biotite-epidote aggregate in a coarse grained granodiorite. Epidote displays some euhedral grain boundaries (white arrow) and is probably magmatic. Diorites have similar textures with higher hornblende and lower quartz proportions. (**f**) Pinkish porphyric potassic granite containing quartz-plagioclase-orthoclase-rich segregates. (**g, h**) Fine-grained two-mica leucocratic granitic rock dominated by a quartz-plagioclase-microcline assemblage, with subordinate amounts of muscovite.

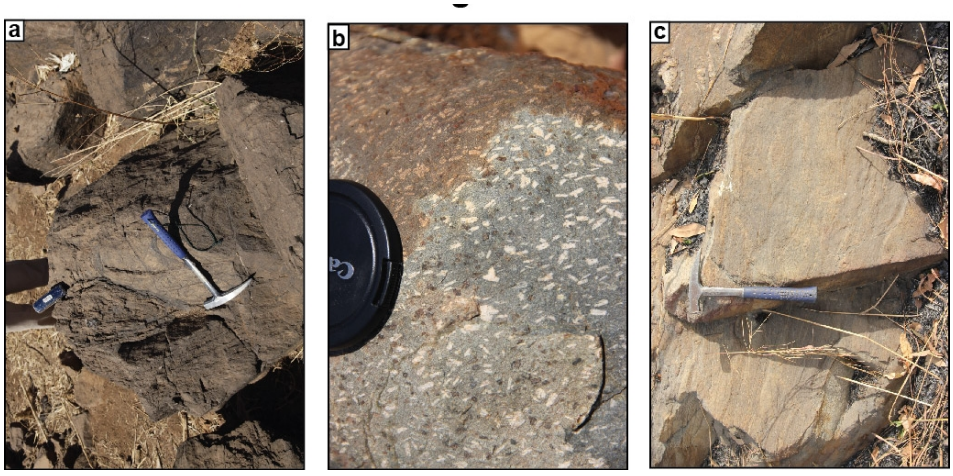

FIGURE 6.4: Petrography and geochemistry of volcanic rocks. (**a**) Fine grained metabasalt of the Nangodi belt. (**b**) Andesitic lava with plagioclase and hornblende phenocrysts, in the Nangodi belt. (**c**) Rhyolitic volcano-clastic rock containing volcanic bombs, in the Maluwe domain.

SAMPLE	BN123 B	BN132	BN231	BN90	BN119	BN115	BN181	BN14	BN83	BN85 B	BN92	BN114	BN140	BN146	BN198	BN223	BN265	BN28B	BN106	BN261	BN16	BN241B
Rock type	granite	granite	granite	granite	granite	granite	granite	granite	granite	granite	granite	granite	granite	granite	granite	granite	granite	granite	granite	tonal.	trondh.	trondh.
Lat (°)	10.8470	10.4013	8.9856	10.8226	9.9692	9.9695	10.7731	10.9234	10.8263	10.6317	8.9334	9.9728	10.8096	10.8864	10.4175	9.8981	8.6565	9.7507	10.0873	8.6428	10.8048	8.5818
Long (°)	-1.1040	-1.3319	-2.4985	-0.9413	-2.1148	-2.0327	-2.7293	-0.7175	-0.8381	-1.0316	-2.4363	-2.0199	-1.4463	-1.7445	-2.7212	-2.4580	-2.2486	-2.1162	-2.0363	-2.1952	-0.8846	-2.2238
Age	2156	2211	2193	2134	2133	2118	2124												2140	2187	2147	2143
Error	1	6	4	6	6	4	2												5	5	9	12
SiO2	75.6	71.7	73.8	68.5	69.3	72.3	69.3	70	69.4	69.3	65	72.1	66.4	69.6	69.4	74.2	76.6	74.6	71.8	72	66.1	71.3
TiO2	0.21	0.2	0.33	0.33	0.32	0.23	0.45	0.27	0.41	0.32	0.47	0.23	0.49	0.51	0.35	0.11	0.08	0.05	0.28	0.22	0.5	0.26
Al2O3	12.2	13.4	12.7	14.2	15.5	14.8	15.8	14.1	14.2	14.7	14.6	14.9	14.8	14.5	14.2	15.2	12.3	13.9	13.8	14.6	16.2	15.7
FeOt	2.15	2.37	2.47	2.87	2.55	1.59	2.69	2.47	2.54	2.82	4.49	1.84	3.55	2.47	1.89	1.41	1.22	1.16	1.74	2.38	3.72	2.20
MnO	0.03	0.07	0.05	0.04	0.06	0.03	0.03	0.04	0.04	0.05	0.07	0.01	0.07	0.03	0.02	0.04	0.06	0.02	0.04	0.05	0.04	0.03
MgO	0.46	0.55	0.69	0.96	0.8	0.3	0.74	0.63	0.8	0.98	2.35	0.53	1.2	0.61	0.51	0.45	0.14	0.11	0.74	0.72	1.28	0.63
CaO	1.25	2.1	2.13	2.08	2.25	1.42	2.58	2.31	1.77	2.59	3.93	1.81	3.28	1.49	1.89	1.58	1.02	0.63	1.52	3.25	3.18	2.05
Na2O	3.76	4.22	3.89	4.38	4.39	4.89	5.1	4.93	4.31	5.14	3.99	4.56	4.58	3.77	4.15	5.21	4.44	4.04	4.30	4.63	5.5	5.08
K2O	3.57	2.63	2.49	3.08	3.46	3.88	2.59	2.34	5.16	2.38	3.07	3.52	2.32	5.07	3.56	2.69	2.93	4.85	3.82	0.92	1.61	2.07
P2O5	0.04	0.05	0.07	0.11	0.14	0.07	0.15	0.08	0.23	0.11	0.14	0.04	0.14	0.12	0.09	0.08	0.03	0.09	0.13	0.06	0.17	0.1
LOI	0.83	0.76	0.69	0.98	0.99	0.86	0.71	2.54	0.82	1.16	1.49	0.83	1.09	1.04	2.38	0.63	0.92	0.46	0.66	0.45	1.01	1.31
Total	100.5	98.5	99.7	98.1	100.2	100.8	100.6	100.2	100.4	100.1	100.3	100.9	98.5	99.8	98.9	102.0	99.9	100.1	99.0	99.6	99.8	101.1
Mg#	27.6	29.3	33.2	37.4	35.9	25.1	32.9	31.2	36.0	38.3	48.3	34.0	37.6	30.6	32.5	36.2	16.9	14.5	43.3	35.0	38.0	33.8
V	21	28	33	39	39	17	38	40	40	53	102	24	60	26	20	17	<5	<5		45	64	30
Cr	210	300	150	240	40	220	120	390	70	330	230	80	120	120	150	150	30	230		120	160	190
Ni	6	6	3	6	7	2	2	6	7	9	24	<1	2	<1	1	3	<1	1		7	6	3
Rb	101.5	85.9	77.6	69.6	114.5	64.5	72.2	63.9	190	62.9	99.9	67.3	75.8	157	109.5	81.6	76.5	249	140.6	24	64.5	77
Sr	135.5	234	191.5	620	728	1055	991	754	1665	757	640	756	599	354	585	722	56	64.9	395.7	308	723	568
Y	11.1	11.4	15.4	3.1	7.1	6.2	4.4	4.6	12.7	5.6	14.4	2.7	11.1	6	3.1	7	20.6	6.9	7.79	4.3	6.6	6.4
Zr	130	110	190	120	150	130	180	110	280	130	170	210	130	400	180	60	70	40	143.3	50	250	120
Nb	4.5	7.6	6.2	3.4	6.7	3.3	4.4	3.3	6.3	3.5	6	2.5	6.3	8	3.9	2.9	8.6	8.8	7.65	3.5	6.9	3.4
Ba	879	709	704	1275	1265	1445	1030	635	2160	632	699	2280	748	1825	1290	1095	619	176.5	883.8	393	304	612
La	27.1	9.1	31	16.5	22.3	22.4	30.4	16.8	58.5	22.7	13.5	48.1	22.7	106.5	30.5	8.2	16.4	6.6	37.4	19.7	44.4	18.9
Ce	47.9	16.6	66.3	29.9	55.5	46.8	64.1	30.9	120	41.7	31.1	92.2	45	190	58.6	17.4	32.3	14.1	71.0	36.4	75.5	40.1
Pr	4.97	2.03	6.8	3.36	5.64	5.85	7.69	3.55	13.5	4.91	4.47	10.9	5.6	19.75	6.57	2.2	3.98	1.63	7.37	3.87	7.83	4.95
Nd	16.1	7.7	23.9	11.7	20.6	22.1	29	13	49.8	18.7	19.4	38.8	21.9	60.9	23.1	9	14.7	5.9	27.0	12.9	24.8	19.4
Sm	2.61	1.78	4.03	1.66	3.63	3.69	4.72	2.08	8.23	3.15	4.13	5.56	3.91	7.08	3.31	2.09	3.24	1.82	4.13	1.86	3.36	3.32
Eu	0.36	0.54	0.95	0.62	1.04	0.82	1.22	0.6	1.97	0.83	1.03	1.23	1.05	1.06	0.87	0.46	0.36	0.19	0.91	0.49	0.9	0.99
Gd	1.93	1.75	2.91	1.11	2.35	2.16	2.67	1.44	5.14	2.04	3.44	2.82	3.07	3.25	1.72	1.77	2.93	1.53		1.21	2.1	2.1
Tb	0.29	0.28	0.46	0.13	0.3	0.25	0.28	0.18	0.57	0.24	0.48	0.25	0.39	0.32	0.19	0.26	0.51	0.26	0.31	0.16	0.26	0.25
Dy	1.7	1.77	2.61	0.61	1.39	1.21	1.08	0.88	2.61	1.14	2.59	0.78	2.01	1.33	0.74	1.32	3.2	1.4	1.48	0.86	1.31	1.26
Ho	0.36	0.4	0.52	0.11	0.25	0.23	0.16	0.17	0.45	0.21	0.53	0.11	0.4	0.23	0.11	0.26	0.67	0.24	0.25	0.16	0.24	0.21
Er	1.09	1.21	1.57	0.27	0.6	0.58	0.34	0.43	1.05	0.49	1.44	0.21	1.07	0.54	0.25	0.65	1.92	0.6	0.69	0.4	0.65	0.51
Tm	0.19	0.21	0.25	0.05	0.1	0.09	0.06	0.08	0.15	0.09	0.22	0.04	0.17	0.09	0.04	0.09	0.31	0.08	0.10	0.06	0.11	0.07
Yb	1.2	1.41	1.66	0.28	0.6	0.48	0.25	0.41	0.84	0.46	1.43	0.19	1.07	0.5	0.22	0.64	2.1	0.53	0.65	0.35	0.6	0.46
Lu	0.21	0.23	0.29	0.04	0.1	0.07	0.04	0.07	0.14	0.08	0.23	0.03	0.17	0.08	0.03	0.11	0.35	0.08	0.10	0.06	0.1	0.07
Hf	3.9	3.2	5.1	3.5	3.9	3.6	4.5	3.2	7	3.5	4.7	5.7	3.8	9.8	4.5	1.8	2.9	1.9	4.06	1.4	5.9	3.1
Ta	0.6	1.1	0.4	0.1	0.4	0.2	0.3	0.2	0.5	0.2	0.4	0.1	0.6	0.3	0.2	0.2	1	1	0.74	0.3	0.4	0.3
Pb	14	8	4	10	21	24	13	11	29	11	10	16	11	15	16	16	5	21	19.4	5	8	13
Th	8.09	2.57	7.49	2.56	5.45	3.34	4.14	3.54	13.9	5.56	3.49	7.77	3.34	23.1	4.23	1.42	3.82	6.64	12.1	3.79	5.92	3.26
U	2.8	1.38	1.67	0.58	1.48	0.88	1.44	1.6	4.45	1.7	2.15	0.95	1.15	1.03	1.16	0.87	1.75	9.93	4.59	0.29	0.68	1.95

TABLE 6.1: Whole rock major (wt%) and trace element (ppm) composition of the investigated plutonic rocks of northern Ghana. [a] Total Fe as FeO. [b] Loss On Ignition. [c] Molar (Mg/(Mg+Fe^{II}).

SAMPLE	BN77	BN112A	BN430	BN69B	BN76C	BN82A	BN150B	BN155	BN172	BN189	BN213	BN112A	BN430	BN69B	BN76C	BN82A	BN150B	BN155	BN172	BN189	BN213	BN252
Rock type	trondh.	trondh.	trondh.	trondh.	trondh.	trondh.	trondh.	trondh.	trondh.	trondh.	trondh.	trondh.	trondh.	trondh.	trondh.	trondh.	trondh.	trondh.	trondh.	trondh.	trondh.	trondh.
Lat (°)	11.0021	9.4677	8.8420	10.8768	11.0022	10.8538	10.8674	10.6727	10.7596	10.9829	10.3125	9.4677	8.8420	10.8768	11.0022	10.8538	10.8674	10.6727	10.7596	10.9829	10.3125	8.8806
Long (°)	-0.3720	-2.2790	-2.0870	-0.5577	-0.3812	-0.1703	-1.9281	-2.0307	-2.2773	-2.7176	-2.3317	-2.2790	-2.0870	-0.5577	-0.3812	-0.1703	-1.9281	-2.0307	-2.2773	-2.7176	-2.3317	-2.1764
Age	2134	2120	2126									2120	2126									
Error	1	3	7									3	7									
SiO2	69.2	67	71.6	69.7	67.7	70.5	70.4	70.6	70.6	72	72.5	67	71.6	69.7	67.7	70.5	70.4	70.6	70.6	72	72.5	74.4
TiO2	0.37	0.56	0.26	0.27	0.32	0.23	0.35	0.37	0.27	0.36	0.29	0.56	0.26	0.27	0.32	0.23	0.35	0.37	0.27	0.36	0.29	0.26
Al2O3	15.7	16.4	15.3	15.2	15.1	14.8	14.8	14.9	15.4	11.9	14.3	16.4	15.3	15.2	15.1	14.8	14.8	14.9	15.4	11.9	14.3	13.5
FeOt	2.89	3.12	2.36	2.31	2.69	1.89	2.88	2.38	2.29	5.55	2.63	3.12	2.36	2.31	2.69	1.89	2.88	2.38	2.29	5.55	2.63	2.27
MnO	0.05	0.03	0.02	0.04	0.04	0.02	0.05	0.03	0.04	0.12	0.04	0.03	0.02	0.04	0.04	0.02	0.05	0.03	0.04	0.12	0.04	0.06
MgO	1	1.12	0.88	0.67	0.92	0.5	0.85	0.73	0.73	0.03	0.64	1.12	0.88	0.67	0.92	0.5	0.85	0.73	0.73	0.03	0.64	0.52
CaO	3.32	2.95	2.64	2.85	2.42	2.12	2.75	2.74	2.57	2.95	2.44	2.95	2.64	2.85	2.42	2.12	2.75	2.74	2.57	2.95	2.44	2.09
Na2O	5.27	5.28	5.33	5.54	5.34	5.28	4.95	5.01	5.97	4.37	4.84	5.28	5.33	5.54	5.34	5.28	4.95	5.01	5.97	4.37	4.84	5.01
K2O	1.91	2.03	1.12	1.17	1.46	2.27	1.38	1.72	1.24	1.07	1.71	2.03	1.12	1.17	1.46	2.27	1.38	1.72	1.24	1.07	1.71	1.31
P2O5	0.12	0.2	0.11	0.08	0.1	0.05	0.08	0.09	0.08	0.01	0.1	0.2	0.11	0.08	0.1	0.05	0.08	0.09	0.08	0.01	0.1	0.04
LOI	0.86	1.35	0.74	0.92	2.92	1.59	0.81	0.78	0.6	0.6	0.52	1.35	0.74	0.92	2.92	1.59	0.81	0.78	0.6	0.6	0.52	0.71
Total	101.2	100.6	100.8	99.1	99.5	99.6	99.7	99.8	100.3	99.7	100.6	100.6	100.8	99.1	99.5	99.6	99.7	99.8	100.3	99.7	100.6	100.5
Mg#	38.2	39.0	40.0	34.1	37.9	32.1	34.5	35.3	36.2	1.0	30.3	39.0	40.0	34.1	37.9	32.1	34.5	35.3	36.2	1.0	30.3	29.0
V	43	56	42	39	38	30	40	32	31	<5	24	56	42	39	38	30	40	32	31	<5	24	14
Cr	120	150	150	100	260	350	80	70	170	210	210	150	150	100	260	350	80	70	170	210	210	250
Ni	7	3	7	4	8	5	3	2	10	<1	2	3	7	4	8	5	3	2	10	<1	2	4
Rb	47.5	69.6	44.7	40.5	45.2	81.1	77.5	64.1	48.6	22.4	32.2	69.6	44.7	40.5	45.2	81.1	77.5	64.1	48.6	22.4	32.2	39.9
Sr	930	1010	753	683	810	568	439	712	1165	228	422	1010	753	683	810	568	439	712	1165	228	422	183
Y	7.1	3.9	2.8	6.3	5.7	2.6	7	3.3	7.6	80.8	5.9	3.9	2.8	6.3	5.7	2.6	7	3.3	7.6	80.8	5.9	14.9
Zr	130	290	110	130	120	130	150	210	130	710	200	290	110	130	120	130	150	210	130	710	200	170
Nb	4	2.7	1.8	3.3	3.6	2.3	8	4.2	4	16.8	2.8	2.7	1.8	3.3	3.6	2.3	8	4.2	4	16.8	2.8	5.9
Ba	867	891	436	307	628	663	211	613	360	333	1515	891	436	307	628	663	211	613	360	333	1515	356
La	20.8	63.8	18.5	18.1	20.2	18.3	22.3	29.6	15.9	25.3	32.9	63.8	18.5	18.1	20.2	18.3	22.3	29.6	15.9	25.3	32.9	17.6
Ce	42.3	117.5	38.3	34.8	39.3	32.6	44.3	48.6	28.6	67.3	58.4	117.5	38.3	34.8	39.3	32.6	44.3	48.6	28.6	67.3	58.4	35
Pr	5.26	13.25	4.64	4.2	4.62	3.59	4.65	5.02	3.73	9.34	6.16	13.25	4.64	4.2	4.62	3.59	4.65	5.02	3.73	9.34	6.16	4.13
Nd	20.2	45.7	18	15.6	17.1	12.6	16.1	16.3	14.4	43.3	21.5	45.7	18	15.6	17.1	12.6	16.1	16.3	14.4	43.3	21.5	15.6
Sm	3.46	6.17	2.95	2.88	2.66	2.07	2.8	1.98	2.63	12.05	3.24	6.17	2.95	2.88	2.66	2.07	2.8	1.98	2.63	12.05	3.24	2.97
Eu	0.94	1.44	0.85	0.8	0.77	0.57	0.65	0.82	0.64	3.61	1.03	1.44	0.85	0.8	0.77	0.57	0.65	0.82	0.64	3.61	1.03	0.74
Gd	2.23	2.81	1.66	2.12	1.73	1.3	1.99	1.08	2.01	14	2.06	2.81	1.66	2.12	1.73	1.3	1.99	1.08	2.01	14	2.06	2.41
Tb	0.28	0.24	0.17	0.28	0.21	0.14	0.27	0.12	0.27	2.37	0.25	0.24	0.17	0.28	0.21	0.14	0.27	0.12	0.27	2.37	0.25	0.4
Dy	1.35	0.98	0.7	1.31	1.06	0.58	1.42	0.54	1.45	14.65	1.26	0.98	0.7	1.31	1.06	0.58	1.42	0.54	1.45	14.65	1.26	2.47
Ho	0.25	0.15	0.11	0.24	0.2	0.1	0.26	0.11	0.29	3.17	0.24	0.15	0.11	0.24	0.2	0.1	0.26	0.11	0.29	3.17	0.24	0.52
Er	0.66	0.34	0.25	0.6	0.53	0.22	0.65	0.29	0.72	8.74	0.63	0.34	0.25	0.6	0.53	0.22	0.65	0.29	0.72	8.74	0.63	1.52
Tm	0.11	0.06	0.03	0.09	0.09	0.04	0.1	0.06	0.12	1.25	0.08	0.06	0.03	0.09	0.09	0.04	0.1	0.06	0.12	1.25	0.08	0.24
Yb	0.62	0.32	0.2	0.5	0.49	0.19	0.53	0.32	0.65	7.95	0.55	0.32	0.2	0.5	0.49	0.19	0.53	0.32	0.65	7.95	0.55	1.72
Lu	0.1	0.05	0.04	0.08	0.08	0.03	0.09	0.06	0.11	1.26	0.1	0.05	0.04	0.08	0.08	0.03	0.09	0.06	0.11	1.26	0.1	0.3
Hf	3.1	6.6	2.9	3.5	3.1	3.3	3.8	5.5	3.6	16.6	5.3	6.6	2.9	3.5	3.1	3.3	3.8	5.5	3.6	16.6	5.3	4.2
Ta	0.3	0.2	0.1	0.3	0.3	0.2	0.5	0.3	0.3	1.1	0.1	0.2	0.1	0.3	0.3	0.2	0.5	0.3	0.3	1.1	0.1	0.5
Pb	10	9	7	6	5	9	10	9	8	3	7	9	7	6	5	9	10	9	8	3	7	3
Th	2.45	12.85	2.46	2.98	2.79	4.63	5.51	5.7	2.23	2.75	4.76	12.85	2.46	2.98	2.79	4.63	5.51	5.7	2.23	2.75	4.76	2.55
U	0.78	1.55	0.5	0.52	0.85	1.97	0.75	0.65	0.62	0.78	0.45	1.55	0.5	0.52	0.85	1.97	0.75	0.65	0.62	0.78	0.45	0.71

SAMPLE	BN278	BN289	BN82B	BN87	BN98A	BN270	BN283	BN150 A	BN192	BN258	BN28A	BN74	BN80	BN127	BN598	BN103	BN380	BN532	BN229	BN235	BN18	BN254
Rock type	trondh.	trondh.	grano.	grano.	grano.	grano.	grano.	grano.	grano.	grano.	grano.	grano.	grano.	grano.	grano.	grano.	diorite	diorite	diorite	monzodio.	diorite	diorite
Lat (°)	9.6433	10.8549	10.8538	10.8302	9.7971	9.5075	10.6700	10.8674	10.7653	8.4819	9.7507	10.9867	11.0403	10.6530	10.1886	10.0939	9.9783	9.8070	9.0358	8.8597	10.8301	8.8408
Long (°)	-2.7001	-0.6102	-0.1703	-1.0719	-2.1650	-2.4655	-0.8620	-1.9281	-2.8434	-2.1834	-2.1162	-0.5300	-0.2785	-1.2717	-1.9013	-2.0927	-2.2965	-2.6130	-2.4367	-2.3393	-0.9921	-2.1431
Age			2158	2148	2149	2182	2151	2112	2104	2125						2144	2150	2147	2134	2118	2134	
Error			5	5.4	30	5	1	1	1	2						7	4	13	6	6	1	
SiO2	73.5	71.3	63	64.8	69.1	71	67.3	69.1	67.9	66.9	67.8	67	69.1	65.3	63.2	63.8	60.9	60.1	60.9	55.2	62.5	56.9
TiO2	0.14	0.24	0.56	0.5	0.41	0.39	0.47	0.37	0.38	0.44	0.39	0.48	0.39	0.52	0.61	0.42	0.68	0.63	0.57	0.42	0.67	0.66
Al2O3	15.1	15.1	16.3	15.6	15.4	15.2	14.6	15.2	14.5	14.8	14.9	15.2	15.3	15.7	15.5	13.5	15.7	14.7	16.2	13.4	16.5	15.2
FeOt	1.13	1.93	4.87	4.02	3.48	3.20	4.04	3.18	3.55	3.67	4.02	4.44	3.65	4.05	4.88	4.71	5.42	5.20	5.07	5.02	4.80	6.91
MnO	0.02	0.03	0.07	0.06	0.06	0.05	0.09	0.05	0.06	0.06	0.07	0.07	0.06	0.05	0.09	0.07	0.1	0.09	0.09	0.09	0.07	0.12
MgO	0.21	0.54	2.56	1.87	1.16	1.04	1.56	0.98	2.29	2.14	1.36	1.51	0.8	1.46	2.74	2.60	2.59	4.7	3.51	4.41	2.33	6.64
CaO	1.64	2.17	5.01	4.03	3.74	3.56	3.67	3.26	3.32	3.66	3.2	4.52	3.26	3.74	4.48	3.32	5.19	4.8	5.24	5.09	4.9	6.96
Na2O	5.52	5.71	4.82	4.79	4.31	4.45	3.84	4.91	3.74	4.22	4.03	4.33	5.07	4.97	4.4	4.31	4.43	4.05	4.58	3.1	5.33	4.25
K2O	2.22	1.51	1.36	1.33	1.46	1.57	3.45	1.27	3.18	2.42	1.69	1.5	1.33	1.55	2.1	1.50	1.48	1.94	1.49	2.35	0.96	0.96
P2O5	0.03	0.07	0.21	0.15	0.1	0.1	0.16	0.1	0.13	0.15	0.08	0.15	0.11	0.14	0.23	0.12	0.24	0.31	0.19	0.1	0.22	0.24
LOI	0.45	0.89	0.94	1.26	0.87	0.59	1.04	0.92	1.05	0.82	0.99	1.61	0.67	1.01	0.66	4.18	0.87	0.92	1.68	9.15	0.94	1.67
Total	100.3	99.8	100.5	99.0	100.5	101.6	100.8	99.8	100.7	99.9	99.1	101.5	100.2	99.1	99.6	99.1	98.4	98.3	100.3	99.0	100.0	101.5
Mg#	24.8	33.3	48.4	45.3	37.3	36.7	40.8	35.5	53.5	51.0	37.6	37.8	28.1	39.1	50.0	49.9	46.0	61.7	55.2	61.0	46.4	63.1
V	7	28	99	65	58	46	106	45	70	84	76	81	45	75	102		125	115	119	129	95	176
Cr	20	120	160	240	40	230	130	100	180	130	300	460	130	100	160		170	350	200	530	130	600
Ni	<1	3	28	22	8	8	1	7	26	18	16	18	4	14	25		32	100	50	82	20	122
Rb	51.1	44.6	49.6	37.4	52.9	37.5	98.7	78	99.4	93.8	115.5	45.9	54.6	64.6	59.9	38.4	37.4	59.1	38.4	74.9	23.2	26.5
Sr	833	855	1115	669	385	353	644	457	679	713	477	608	548	783	982	456.7	951	1025	885	490	1390	818
Y	2.6	3.8	6.9	7.1	8.2	10.2	15.4	9.3	9	10.4	5.4	11.5	16.3	10.7	10.9	22.4	14.2	13.8	14.1	8.5	7.7	12
Zr	90	130	120	150	160	150	140	150	130	140	100	150	190	190	150	132.9	170	200	140	70	140	120
Nb	1.8	2.5	2.9	3.9	4.4	5.7	4.5	6.1	4.3	5	3.1	5	9.5	6.6	4.2	6.59	4.5	5.1	3.5	2.3	2.7	3.3
Ba	921	429	503	571	361	345	646	243	1075	595	341	481	350	516	968	544.8	651	912	726	469	708	368
La	10.2	18.1	16.8	17	23	18.5	31.5	30	23.4	23.4	10.1	23	27.7	22.5	38.6	16.8	22.2	36.4	28.6	11.6	12.8	17.2
Ce	20.7	39.9	35.1	32.2	39.8	35	59.3	54.4	44.4	49.2	18.1	46.7	51.3	42.5	74.6	37.3	49.7	77.3	59.1	23.8	28.9	38.1
Pr	2.51	4.44	4.88	3.78	4.28	3.86	7.03	5.97	4.92	6.13	2.2	5.93	6.03	5.1	8.6	4.69	6.71	9.95	7.4	2.92	4.36	5.03
Nd	9.5	16.8	20.5	14	14.5	14.2	26.8	20	18.1	23.9	8.2	22.9	21.9	19.2	31.7	20.4	28.1	39.9	29.5	12	19.3	21.9
Sm	1.76	2.88	3.78	2.37	2.31	2.57	4.61	3.26	3.22	4.42	1.57	3.98	4.23	3.52	5.12	4.22	5.28	7.1	5.29	2.31	3.71	4.59
Eu	0.6	0.82	1.17	0.85	0.67	0.68	1.2	0.8	0.99	1.17	0.47	1.1	1.13	0.91	1.35	0.90	1.58	2.01	1.55	0.76	1.2	1.39
Gd	1.11	1.6	2.69	1.94	1.87	2.08	3.35	2.42	2.21	3.07	1.27	3.11	3.96	2.89	3.1		3.86	4.88	3.83	1.88	2.68	3.31
Tb	0.13	0.2	0.32	0.26	0.26	0.33	0.47	0.34	0.31	0.4	0.18	0.39	0.59	0.38	0.41	0.58	0.51	0.61	0.53	0.26	0.32	0.45
Dy	0.58	0.85	1.47	1.39	1.5	1.87	2.67	1.78	1.62	2	0.99	2.07	3.14	2.06	2.04	3.58	2.77	2.98	2.78	1.57	1.63	2.32
Ho	0.09	0.13	0.26	0.27	0.31	0.37	0.53	0.34	0.31	0.39	0.21	0.41	0.6	0.4	0.39	0.73	0.54	0.53	0.53	0.31	0.29	0.46
Er	0.2	0.33	0.6	0.7	0.84	0.99	1.49	0.87	0.84	1.01	0.59	1.11	1.56	1.04	1.03	2.14	1.38	1.29	1.36	0.92	0.77	1.16
Tm	0.03	0.04	0.1	0.11	0.13	0.14	0.23	0.13	0.13	0.14	0.11	0.17	0.22	0.16	0.14	0.35	0.2	0.2	0.2	0.13	0.11	0.17
Yb	0.19	0.29	0.51	0.66	0.82	0.92	1.58	0.77	0.87	0.92	0.64	1	1.26	0.99	0.9	2.40	1.29	1.1	1.28	0.84	0.63	1.05
Lu	0.03	0.05	0.08	0.11	0.13	0.14	0.28	0.12	0.14	0.16	0.1	0.16	0.17	0.15	0.15	0.38	0.21	0.17	0.21	0.14	0.1	0.16
Hf	2.8	3.4	2.9	3.7	4	3.4	4	3.7	3.3	3.8	2.6	3.8	4.8	5	3.7	4.03	4.2	4.8	3.5	1.9	3.2	3
Ta	0.2	0.2	0.2	0.2	0.4	0.6	0.4	0.8	0.4	0.4	0.2	0.5	1	0.5	0.2	0.70	0.2	0.3	0.2	0.2	0.1	0.2
Pb	15	10	10	8	6	4	9	9	15	10	7	7	7	9	12	7.28	8	12	6	8	7	5
Th	1.55	5.02	1.45	2.31	3.33	2.44	5.89	4.24	5.31	6.82	1.64	2.88	4.85	5.33	4.71	4.21	1.16	4.25	2.29	1.82	0.24	2.04
U	0.76	1.3	0.56	0.3	0.76	0.59	1.95	0.97	1.72	1.51	0.75	0.88	0.92	0.87	0.82	1.29	0.46	0.87	0.48	0.94	0.13	0.46

Sample	BN02B	BN07	BN60B	BN64D	BN67D	BN68D	BN88	BN101	BN104	BN107	BN108	BN110	BN186	BN400
Rock type	Andesite	Basaltic andesite	Dacite	Andesite	Basaltic andesite	Basaltic andesite	Rhyolite	Basalt	Basalt	Dacite	Rhyolite	Dacite	Rhyolite	Rhyolite
Lat (°)	10.8017	10.7133	10.7230	10.8291	10.8757	10.8783	10.8942	10.0950	10.0899	10.0955	10.0961	10.0675	10.8878	9.1692
Long (°)	-0.7087	-0.6805	-0.6882	-0.7332	-0.6159	-0.5922	-1.0810	-2.0961	-2.0364	-2.0369	-2.0409	-2.1197	-2.6951	-2.2817
Age (Ma)	2155		2149			2153				2155	2168	2129	2134	2197
Error (2s)	6		7			5				6	9	7	8	6
wt%														
SiO2	63.4	52.6	68.9	60.4	56.9	56.1	73.9	49.5	51.4	68.5	72.1	68.3	70.8	75.3
TiO2	0.48	0.66	0.34	0.55	0.47	0.68	0.25	0.93	0.28	0.32	0.23	0.33	0.20	0.28
Al2O3	15.0	13.8	15.1	15.1	11.9	16.7	12.6	14.2	16.9	14.5	14.1	16.0	14.2	12.8
FeOt	4.97	8.20	2.17	5.69	6.37	6.51	2.90	11.84	6.61	2.40	2.03	2.84	1.28	1.91
MnO	0.07	0.10	0.03	0.09	0.13	0.10	0.07	0.20	0.14	0.05	0.02	0.04	0.03	0.07
MgO	2.94	5.24	0.88	3.59	8.87	4.38	0.07	7.08	9.23	1.54	0.70	0.74	0.37	0.29
CaO	5.48	5.59	3.20	5.52	7.06	7.51	0.85	10.82	10.86	3.01	2.46	1.59	1.66	2.09
Na2O	4.73	3.59	5.81	4.01	2.28	3.51	3.94	2.33	2.05	5.02	4.72	3.88	4.74	4.43
K2O	0.51	0.73	0.66	1.42	2.23	1.27	3.87	0.14	0.50	1.77	1.39	3.40	3.22	0.79
P2O5	0.16	0.09	0.14	0.15	0.15	0.21	0.03	0.06	0.03	0.09	0.11	0.13	0.09	0.08
LOI	1.60	7.43	1.17	1.55	1.99	2.07	0.35	1.67	1.73	1.69	0.59	1.73	1.98	0.76
Total	99.3	98.1	98.4	98.1	98.3	99.1	98.8	98.7	99.7	99.0	98.5	98.9	98.5	98.8
Mg#	51.3	53.3	42.0	52.9	71.3	54.5	4.2	51.6	71.3	53.4	38.0	31.6	34.0	21.0
ppm														
Cs	0.384	0.706	0.78	0.869	1.092	0.905	1.448	0.184	10.23	3.876	2.075	4.108	0.967	1.013
Rb	12.21	18.95	12.53	28.07	60.78	31.48	87.31	1.766	34.61	49.83	40.5	92.8	82.85	29.46
Sr	496	212.3	911.1	479.1	473.4	597.7	84.7	131	284.4	474.4	620.5	446.8	551.6	231
Y	9.937	12.48	3.974	11.9	16.11	12.81	30.11	18.97	8.284	7.696	6.312	9.225	4.929	11.3
Zr	100.3	68.94	116.6	90.43	114.5	99.74	330.6	43.35	25.08	81.48	57.08	103.5	86.2	131.4
Nb	2.302	1.982	2.407	2.743	4.939	3.69	10.13	1.497	0.973	2.765	2.605	3.728	4.294	4.54
Ba	199.2	203.5	813	382.9	714.5	406.1	1008	24.64	98.06	408	434.6	1009	1086	281.6
La	16.04	9.662	18.12	15.17	21.33	18.3	35.01	2.536	4.283	17.64	21.4	27.39	17.6	22.1
Ce	33.31	19.35	37.59	30.71	40.37	37.7	68.42	6.519	8.409	34.46	38.66	46.44	33.44	43.35
Pr	3.914	2.324	4.439	3.593	4.734	4.46	7.778	0.968	1.009	3.863	4.159	5.191	3.663	4.581
Nd	16.43	10.12	18.49	15.07	19.34	18.8	30.36	5.164	4.248	15.37	15.71	19.54	14.23	17.1
Sm	3.161	2.287	3.295	3.044	3.807	3.557	5.893	1.742	0.994	2.726	2.502	3.167	2.465	2.951
Eu	0.908	0.777	0.882	0.925	0.955	1.085	1	0.747	0.392	0.826	0.803	0.934	0.675	0.73
Gd	2.401	2.186	1.978	2.593	3.265	2.826	4.936	2.461	1.127	1.959	1.717	2.193	1.645	2.298
Tb	0.326	0.343	0.213	0.367	0.479	0.394	0.787	0.444	0.193	0.257	0.22	0.275	0.196	0.331
Dy	1.804	2.069	0.887	2.066	2.694	2.23	4.848	3.035	1.282	1.346	1.15	1.407	0.979	1.845
Ho	0.332	0.424	0.128	0.398	0.526	0.434	0.996	0.664	0.28	0.25	0.198	0.255	0.157	0.356
Er	0.935	1.26	0.332	1.125	1.489	1.223	3.017	1.943	0.849	0.708	0.58	0.702	0.399	1.054
Tm	0.137	0.189	0.042	0.168	0.231	0.176	0.495	0.297	0.134	0.104	0.087	0.1	0.056	0.168
Yb	0.953	1.308	0.264	1.15	1.535	1.229	3.421	2.037	0.957	0.703	0.585	0.691	0.362	1.201
Lu	0.151	0.204	0.039	0.183	0.238	0.189	0.543	0.324	0.146	0.109	0.09	0.111	0.054	0.195
Hf	2.593	1.838	3.088	2.381	2.974	2.48	7.686	1.235	0.685	2.144	1.541	2.7	2.628	3.485
Ta	0.187	0.17	0.174	0.245	0.474	0.3	0.605	0.12	0.082	0.284	0.313	0.423	0.416	0.443
Pb	2.3111	2.1039	5.9841	3.9155	6.489	4.3583	12.4375		2.1369	7.6606	10.0397	7.665	15.3693	9.1161
Th	2.237	1.378	2.386	2.404	3.939	2.226	4.504	0.235	0.484	3.113	3.9	6.513	3.481	5.675
U	0.81	0.426	1.154	0.805	1.497	0.761	1.748	0.075	0.153	0.884	1.144	1.936	1.851	1.711

TABLE 6.2: Whole rock major (wt%) and trace element (ppm) composition of the investigated volcanic rocks of northern Ghana. [a] Total Fe as FeO. [b] Loss On Ignition. [c] Molar (Mg/(Mg+Fe^{II}).

6.2.5.1 Plutonic rocks

The 56 granitoid samples have mineral assemblages that correspond to tonalites-trondhjemites, quartz-diorites, granodiorites, and granites (see Section 4.1). They cover a wide range of silica contents, from 55-62 wt.% SiO_2 for diorites to 70-76 wt.% SiO2 for granites (Fig. 6.5). In the feldspar triangle (O'connor, 1965), the samples plot in the trondjhemite (n=16), granodiorite (n=18) and granite (n=19) fields, while three samples fall in the tonalite field (Fig. 6.5). In the Na-K-Ca ternary diagram, most samples plot parallel to the calc-alkaline differentiation trend, except for tonalites and trondhjemites that are enriched in Na and fall closer to the Archean TTG field. In the K_2O vs. SiO_2 diagram, tonalites and tronhjemites plot in the tholeiitic (TH) and calc-alkaline (CA) series, granodiorites and diorites plot in the CA to high-K calc-alkaline (HKCA) fields, and granites have HKCA to shoshonitic characters. In Harker diagrams, most data plot along roughly linear differentiation trends (except for the two most mafic diorites BN235 and BN254) of decreasing oxide content with increasing silica, except for Na_2O and K_2O that show strong scatter, particularly in silicic granitoids (SiO2> 65%).

The K_2O/Na_2O is <0.5 for tonalites-trondhjemites, >0.5 and up to 1.4 for granites, while granodiorites and quartz-diorites show intermediate values. The diorites are clearly metaluminous (A/CNK = 0.73-0.88 ; A/CNK : molar ratio l_2O_3/[CaO+Na_2O+K_2O] and A/NK = 1.68-1.89 ; A/NK : molar ratio Al_2O_3/ [Na_2O+K_2O]) while granodiorites are slightly metaluminous (A/CNK = 0.87-1.04 and A/NK = 1.45-1.77). Granites and trondhjemites are metaluminous to slightly peraluminous in composition (A/CNK is 0.87-1.09 and A/NK is 1.16-1.69). Diorites show elevated #Mg (0.46-0.63) and concentrations of mafic oxydes (FeO_T + MgO = 8.0-13.6 wt%) with respect to granodiorites (Mg# = 0.28-0.51, FeO_T + MgO = 4.2-7.6 wt%), tonalites-trondhjemites (Mg# = 0.25-0.40 and FeO_T + MgO = 1.3-5.6 wt%) and granites (Mg# = 0.14-0.48 and FeO_T+ MgO = 1.3-6.8 wt%). In Fig. 6.5, the granitoids were separated into three groups according to the age data : older than 2130 Ma, younger than 2130 Ma, and no available age data. The 2130 Ma threshold was chosen because it is the approximate age of peak metamorphism and marks a shift in the regional tectono-metamorphic evolution (Block et al., Subm, 2015). Representatives of all rock types occur in both age groups, regardless of their chemical composition. No significant major element trend is observed from the older to the younger intrusions in Harker diagrams. However, quartz-diorites only form a minor proportion of the younger age group compared to other rock-types.

The trace element geochemistry of the granitoid samples is presented in chondrite-normalised rare earth element (REE) spectra and in primitive mantle-normalised multi-element diagrams (Fig. 6.6). In spite of strong variations (up to one order of magnitude) in absolute concentrations for most elements, all rock types show fractionated multi-element patterns with negative HFSE (Nb, Ta, Ti) and P anomalies as well as positive Pb ones, typical of crustal material. The quartz-diorites and the granodiorites have similar moderately fractionated and broadly parallel REE spectra, which suggest that they reflect variable differentiation rates of magmas that share a common origin, as hinted by field relationships. They have moderate heavy REE (HREE) and Y contents (Yb_N = 2.4-11.5, average (avg.) = 4.9, standard deviation (std.) = 2.0) moderate to high light REE (LREE) contents (La_N =32.6-124.5, avg. = 72.8, std. = 25.2) and a low La_N/Yb_N between 5 and 29.

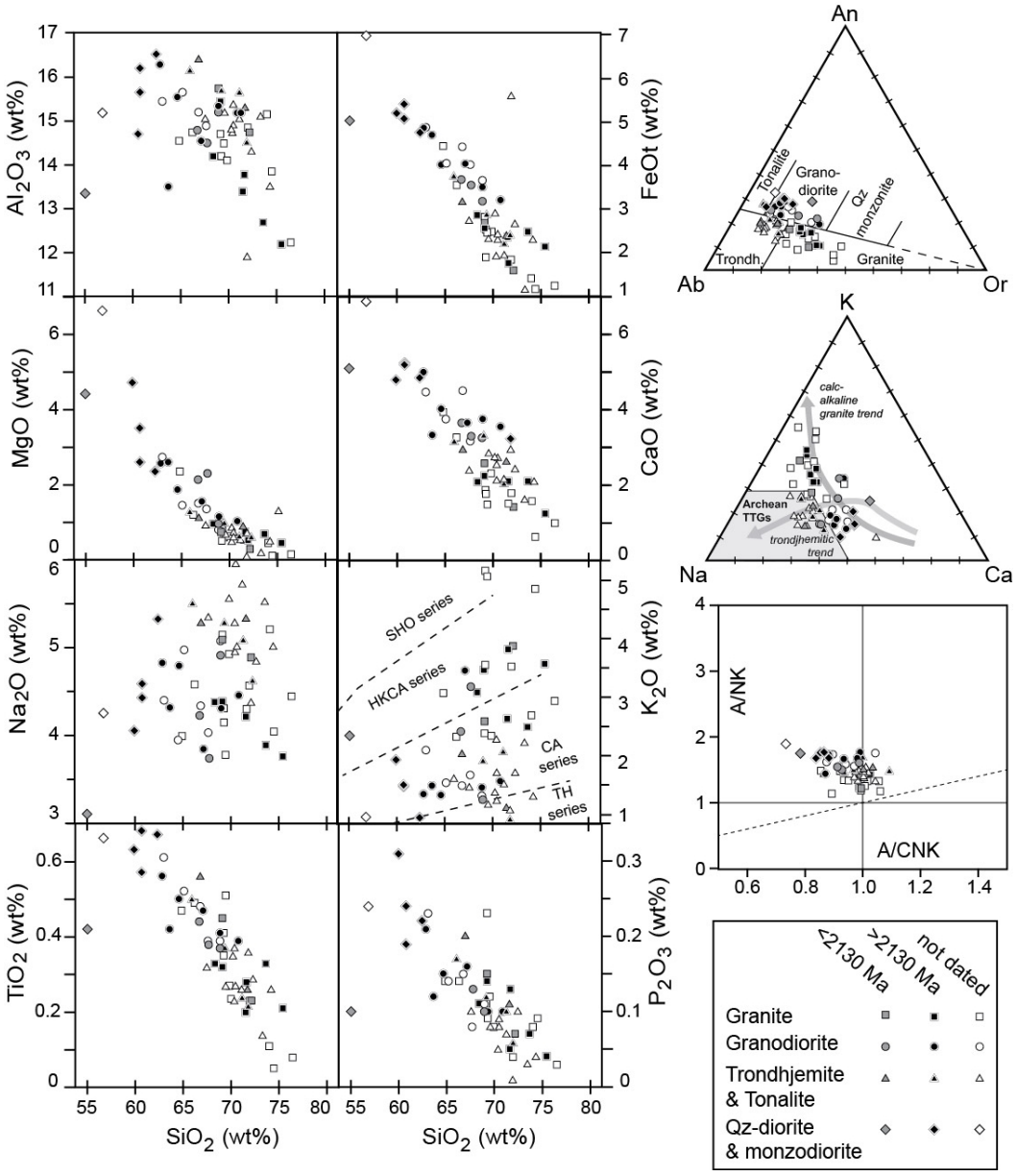

FIGURE 6.5: Major element geochemistry of plutonic rocks presented in Harker diagrams (right), and (left) in feldspar and molecular Na-K-Ca ternary diagrams, and in a A/NK vs A/CNK diagram. Symbols represent lithological groups based on the feldspar diagram (except for quartz diorites and monzodiorites identified by their mineralogy). Square : granite, circle : granodiorite, triangle : tonalite/trondhjemite, diamond : quartz diorite/monzodiorite. Full black symbols : crystallisation age >2130 Ma, full grey symbols : crystallisation age <2130 Ma, empty symbols : no available age data.

Some samples have slight positive or negative Eu anomalies (Eu/Eu* is 0.84-1.21, $Eu^* = [Sm_N + Gd_N]^{1/2}$), although most rocks cluster around Eu/Eu* = 1. They are enriched in large ion lithophile elements (LILE; Rb_N/La_N = 1.7-12.3, avg. = 3.2, std. = 2.5), including Sr (457-1390 ppm), and diorites show moderate positive

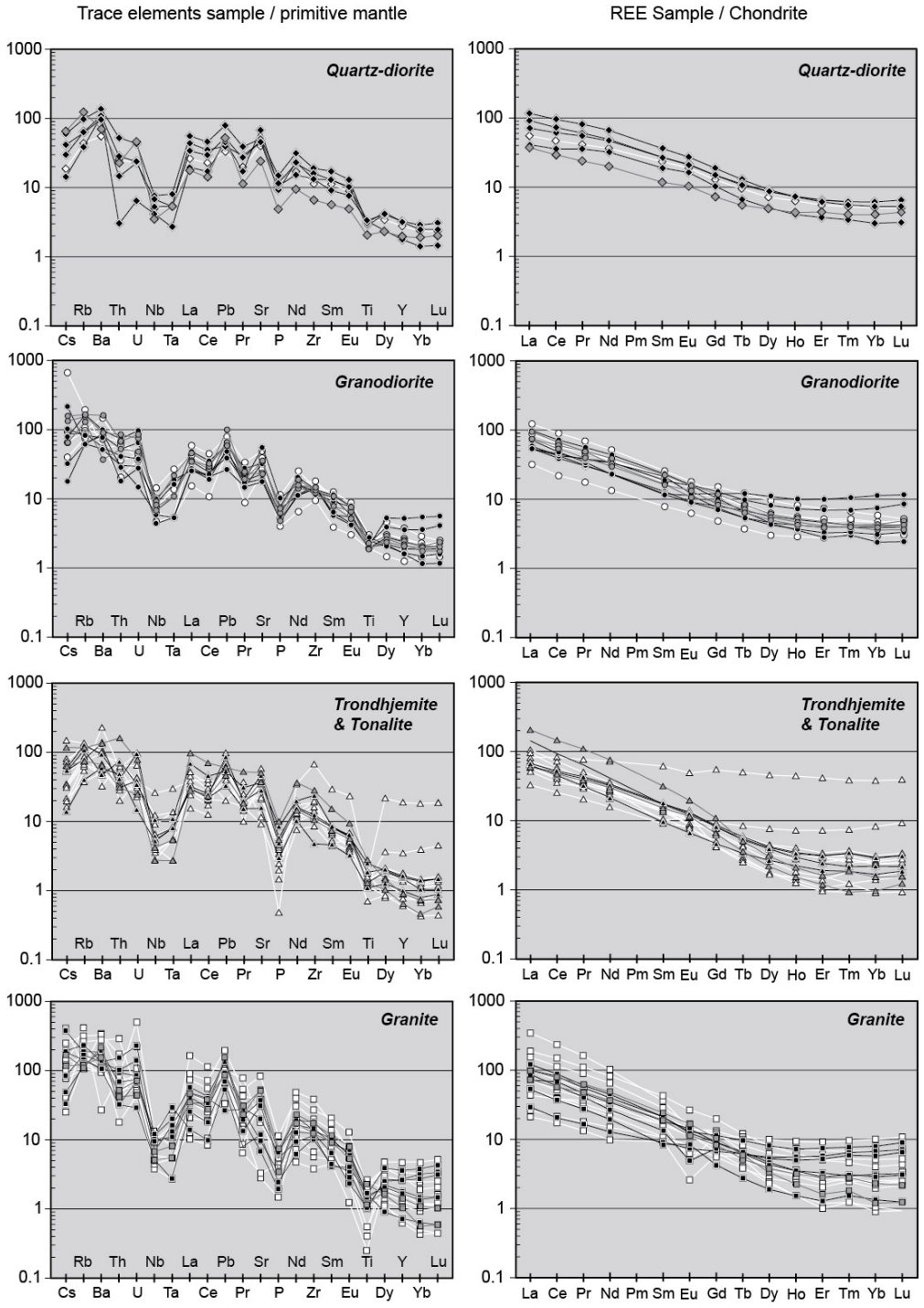

FIGURE 6.6: Primitive mantle-normalised trace element (McDonough and Sun, 1995) and chondrite normalised REE (Boynton, 1984) spidergrams of plutonic rocks of northern Ghana. Symbols are identical as in Fig. 6.5. Black lines link full black symbols (>2130 Ma rocks), grey lines : full grey symbols (<2130 Ma rocks) and white lines link empty symbols.

Ba, Rb and Pb anomalies in multi-element diagrams. These rocks display a small

negative Ti anomaly, strong negative P, Nb and Ta anomalies. Quartz-diorites are also characterized by moderate to strong Th and U negative anomalies, restricted to this particular rock type.

Tonalites and trondjhemites have higher LREE (La_N = 51.3-205.8, avg. = 79.9, std. = 43.6) and lower HREE - Y contents than diorites and granodiorites (Yb_N = 0.8-3.1, avg. = 2.0, std. = 0.8), resulting in more fractionated REE spectra and (La_N/Yb_N = 16.5-134.4), except for two samples, BN189 and BN252. The latter have flat or weakly fractionated REE spectra and relatively high HREE contents, which suggest that their petrogenesis is different. The rocks belonging to this lithological group do not display significant Eu anomalies (Eu/Eu* = 0.84-1.22) except for one sample (BN155, Eu/Eu* = 1.71) and they also show a moderate enrichment in LILE (e.g. Rb_N/La_N = 1.0-4.8, avg. = 2.65, std. = 1.3). Positive Pb anomalies and negative Ti, P, Nb and Ta anomalies are stronger than for the granodioritic and dioritic rocks, albeit showing some variations from one sample to another. Sr contents are variable (128-1165 ppm), but no anomaly is observed.

Granitic samples have more heterogeneous trace element geochemical signatures compared to other lithological groups. Some rocks display weakly fractionated REE spectra, characterised by relatively high HREE contents ($Yb_N > 3.0$), low LREE ($La_N < 40.0$) and low La_N/Yb_N between 4.0 and 15.0, similar to the diorites and granodiorites. Contrastingly, LREE are extremely fractionated respective to HREE in other rocks that have La_N/Yb_N greater than 100. Independently from these differences, some granites have marked negative Eu anomalies (Eu/Eu* < 0.50) while others do not. Among the different rock-types, granitic samples have the strongest enrichment in LILE (Rb_N/La_N = 1.6-40.7, avg. = 6.45, std. = 8.68). They have pronounced positive Pb, and negative Ti, P, Nb and Ta anomalies, varying strongly from one sample to the other. Their Sr content is extremely scattered (65-1665 ppm) and both positive and negative Sr anomalies are observed.

The major and trace element compositions of the granitoids crystallised before and after 2130 Ma broadly overlap, thus no clear systematic geochemical evolution can be established between the two age groups.

6.2.5.2 Volcanic rocks

In the TAS diagram of Le Bas et al. (1986), the samples taken from various volcanic units of northern Ghana range from picro-basalts to rhyolites. All of them plot in the sub-alkaline field (Fig. 6.7a). In the AFM diagram (Irvine and Baragar, 1971), the samples plot in the calc-alkaline field (Fig. 6.7b), except for two tholeiitic metabasalts/gabbros sampled in the Julie belt (BN101 and BN104). The concentration in incompatible elements and LREE/HREE fractionation increases with increasing SiO_2 content (Fig. 6.7c, d). Most rocks have incompatible trace element patterns characterized by enrichment in LILE such as Rb, Ba, Th and U. They display positive Pb and Sr and negative Ti, P, Nb and Ta anomalies. Except for sample BN67D with Eu/Eu* = 0.83, they do not display any Eu anomaly. The andesite trace element characteristics are similar to those of granodiorites and diorites. Basalts are enriched in REE by less than one order of magnitude relative to chondrite, and have nearly flat spectra. Similarly, they have low incompatible element contents compared to the primitive mantle, except for a strong enrichment in LILE (Cs, Rb, Ba), presumably of secondary origin. Andesites have homogeneous

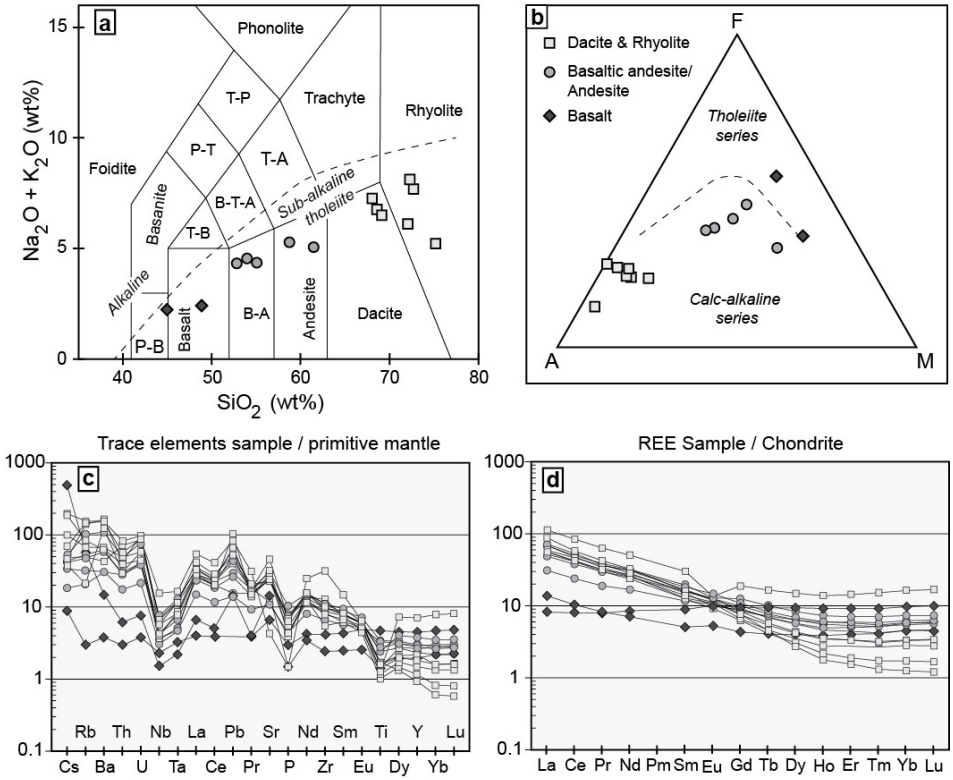

FIGURE 6.7: (**a**) TAS diagram (Le Bas et al., 1986) of the investigated rocks that range from basalts (diamonds) to andesites (circles) and sub-alkaline dacites and rhyolites (squares). P-B : picrobasalt, B-A : basaltic andesite, T-A : trachy-andesite, T-B : trachy-basalt, B-T-A : basaltic trachy-andesite, P-T : phono-tephrite, T-P : tephra-phonolite (**b**) AFM diagram (Irvine and Baragar, 1971) where F is FeO_T, A is Na_2O+K_2O and M is MgO. (**c**) Primitive mantle-normalised trace element (McDonough and Sun, 1995) and (**d**) chondrite normalised REE (Boynton, 1984) spidergrams.

trace element signatures. HREE content is low (Yb_N = 4.6-7.3), LREE content is moderate (La_N = 31.2-68.8) with La_N/Yb_N between 5.0 and 11.3. Felsic lavas are more heterogeneous. Rhyolite sample BN88 is strongly enriched in HREE (Yb_N = 16.4) and has a marked negative Eu anomaly (Eu/Eu* = 0.57). Both characteristics contrast with the geochemistry of other dacites and rhyolites, which have YbN = 1.3-5.8, Eu/Eu* = 0.86-1.18 and high La_N/Yb_N of 12.4-46.3. A similar duality in REE signatures characterises tonalitic and trondhjemitic plutons (see previous secton and Fig. 6.6. This suggests that the lavas represent the volcanic equivalents of some of the most silicic plutons.

6.2.6 Geochronology

6.2.6.1 Methodology

Thirteen samples representative of the different rock-types described in the previous sections, including 7 volcanic and 11 plutonic rocks, were selected for LA-ICP-

MS, U–Pb zircon dating at Géosciences Montpellier. Zircons from five additional samples of plutonic rocks were analyzed for both U-Pb and Lu-Hf isotopes by LA-(MC-)ICP-MS at Goethe University Frankfurt. See Appendix 6.2.10.3 and 6.2.10.4 for a detailed description of sample preparation and analytical procedures. The results of U–Pb dating is shown in tables 6.3 to 6.5, and Lu–Hf isotopic analyses are presented in table 6.6.

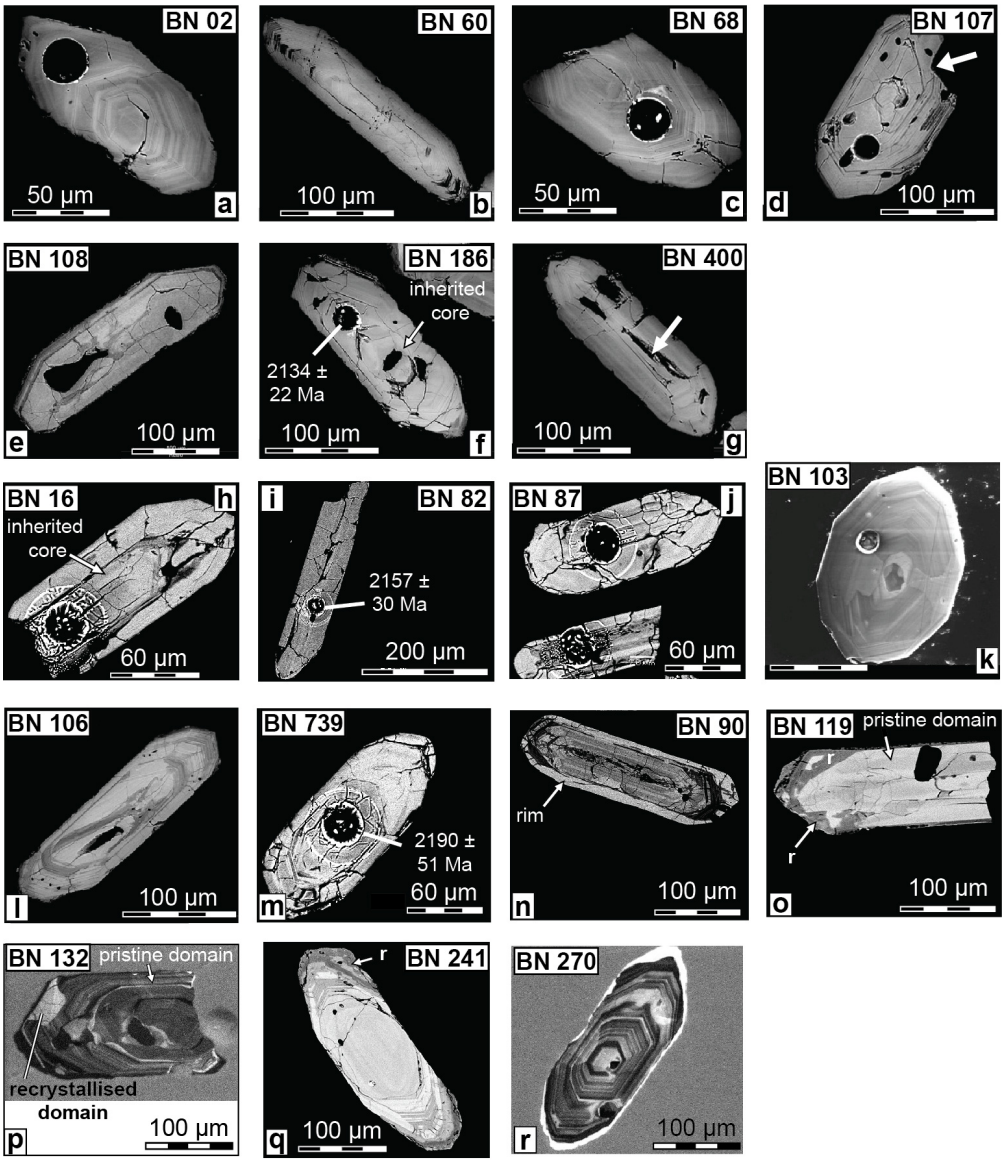

FIGURE 6.8: SEM and cathodoluminescence imaging of zircon grains from the investigated samples. r : recrystallized domains. Ages are given with 2σ errors.

6.2.6.2 Results of U–Pb and Lu–Hf isotope analyses

BN02 - Andesite - Nangodi belt. Zircon grains are translucent and colourless, have euhedral shapes and display oscillatory zoning, typical of magmatic zircons (Fig. 6.8a).). Twenty laser spots focused on cores and rims were performed on

nineteen grains and yield a single population (Fig. 6.9a). All analyses but one are concordant (98-102% concordance) but too scattered to calculate a Concordia age. A $^{207}Pb/^{206}Pb$ weighted average age of 2155 ± 6 Ma (2σ, MSWD = 0.90) was obtained from 19 spots. It is interpreted as dating the eruption and crystallisation of the andesitic magma.

BN60 - Dacite - Nangodi belt. Zircon grains from dacite sample BN60 are translucent and colourless to light brown. They have euhedral shapes, and a thin oscillatory zoning which indicates a magmatic origin (Fig. 6.8b). Twenty laser spot analyses were performed on as many grains . All analyses are concordant and are assumed to represent a single age population with a Concordia age of 2145 ± 5 Ma (2σ, $MSWD_{C+E} = 1.04$, $Probability_{C+E} = 0.40$, C+E : concordance + equivalence), which is interpreted as the age of the dacitic magma (Fig. 6.9b).

BN68 - Basaltic andesite - Nangodi belt Zircon grains from sample BN68 are elongated, translucent, colourless and have euhedral shapes. Observed under BSE imaging, grains display an oscillatory zoning (Fig. 6.8c). Out of twenty four spot analyses, 23 are concordant or sub-concordant (95-105% concordant), and 22 of them yield a weighted average $^{207}Pb/^{206}Pb$ age of 2153 ± 5 Ma (MSWD = 0.70), which is interpreted as the rock crystallisation age (Fig 6.9c). One analysis (#11-1, red shaded ellipse in Fig. 6.9) aimed at the core of a grain yields an older age of 2233 ± 26 Ma (2σ) and is interpreted as inherited.

BN107 - Dacite intercalated in volcano-sedimentary rocks - Juile belt Zircons from sample BN107 have euhedral shapes with angular terminations, that are not consistent with a long sedimentary transport. Additionally, the grains occasionally display irregular shapes, which we interpret as growth lack due to contact with other minerals, a feature typical of volcanic zircons (Fig. 6.8d, white arrow). Thirty one spot analyses were carried out on 29 grains. Twenty nine analyses are concordant or sub-concordant (less than 5% discordance) and define a weighted average $^{207}Pb/^{206}Pb$ age of 2155 ±6 Ma (MSWD = 0.60), interpreted to date the crystallisation of the volcanic rock and its sedimentary reworking. One concordant core analysis (#28-1, red shaded ellipse in Fig. 6.9d) has a higher U and Th contents, Th/U ratios and an older age of 2222 ± 23 (2σ) Ma, interpreted as reflecting inheritance from a 2.2 Ga-old crustal material.

BN108 - Rhyoacite epiclastite - Julie belt BSE imaging of zircons separated from this rock reveals euhedral grains with oscillatory zoning, consistent with with a magmatic origin (Fig. 6.8e). The 10 analyses obtained from as many grains reveal a single age population, and are concordant or sub-concordant (Fig. 6.8e). The calculated weighted average $^{207}Pb/^{206}Pb$ age of 2168 ± 9 Ma (MSWD = 0.20, n = 10) is interpreted to represent the crystallization age and to date the deposition of the volcanoclastic material.

BN186 - Metadacite - Wa-Lawra belt Zircon grains from sample BN186 are translucent colourless to light brown. They display an oscillatory zoning typical of a magmatic origin. Some grains have zoned cores overgrown by magmatic rims

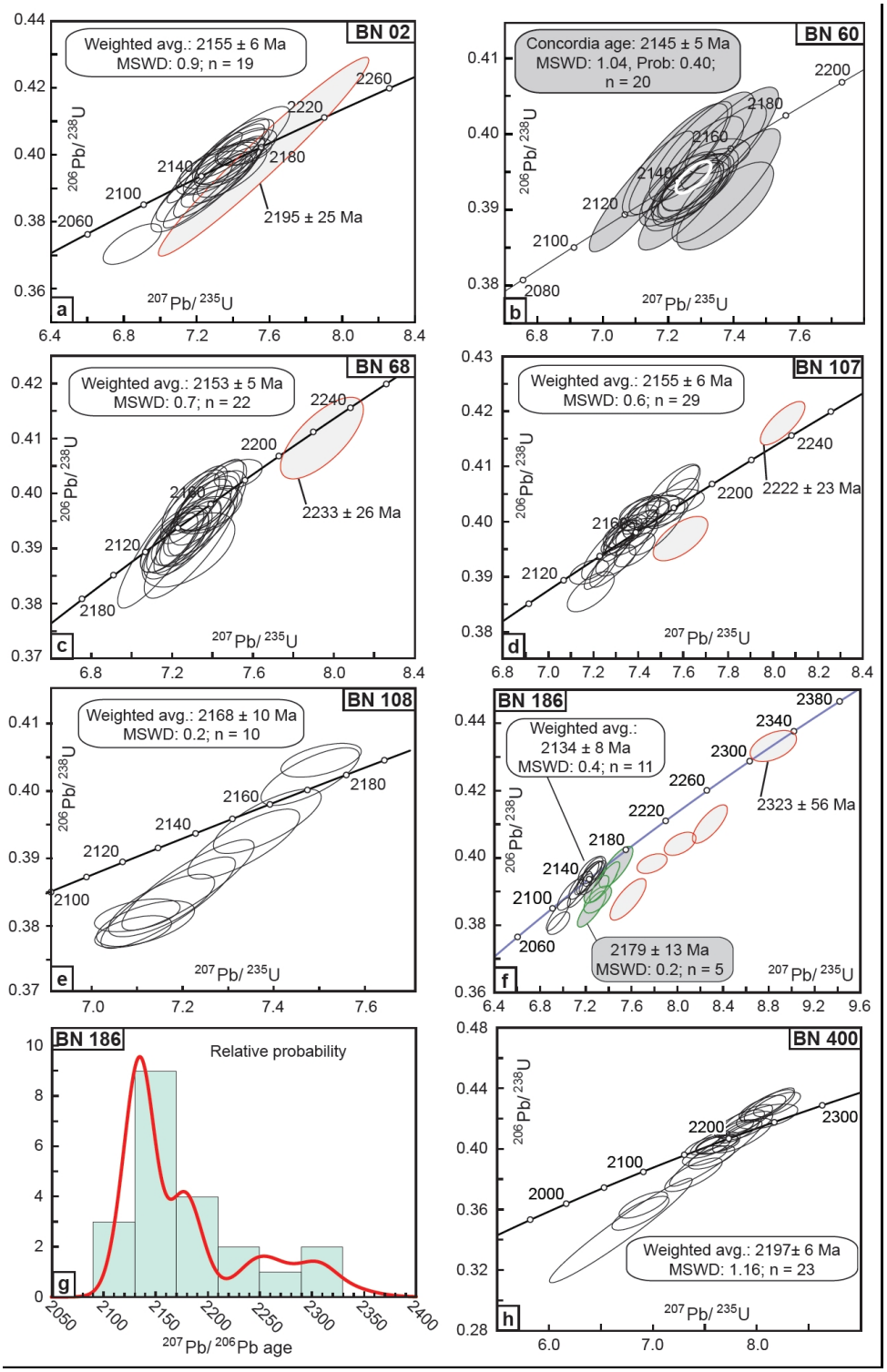

FIGURE 6.9: Concordia diagrams (**a-f, h**) and probability histogram (**g**) presenting results of U–Pb dating of zircons from andesites, dacites and rhyolites from the Paleoproterozoic greenstone belts of NW Ghana. Dark shaded ellipses are data points used to calculate Concordia ages.

(Fig. 6.8f). In a concordia diagram, the 21 analyses from 18 grains show a complex distribution, suggesting multiple age populations (Fig. 6.9f, g), consistently with the complex internal structures. Homogeneous euhedral grains or rims provided the youngest, most concordant ages (black empty ellipses, Fig. 6.9). with a weighted average $^{207}Pb/^{206}Pb$ age of 2134 ± 8 Ma (MSWD = 0.40; n = 11). We interpret this age as representing the crystallisation age of the dacitic magma. A second population was obtained from inherited cores. Among it, five analyses are concordant (98-102%) at *ca.* 2180 Ma (green shaded ellipses) and provide a weighted average $^{207}Pb/^{206}Pb$ age of 2179 ± 13 Ma (MSWD = 0.20) which we relate to the age of an inherited source component. Other analyses yield even older ages (red shaded ellipses), including a grain (#15.2) with a concordant 2323 ± 56 Ma (2σ) age, and a set of discordant analyses with ages between 2.18 and 2.32 Ga.

BN400 - Rhyolite - Maluwe domain Euhedral colourless zircons from sample BN400 display oscillatory magmatic zoning, and occasional tubular cavities (possibly ancient gas tube, white arrow, Fig. 6.8g). The twenty-three spot analyses carried out on 23 grains have discordant, yet consistent individual ages. The data points spread along a regression line and define a weighted average $^{207}Pb/^{206}Pb$ age of 2197 ± 6 Ma (MSWD = 1.16, Fig. 6.9h). It is interpreted as the crystallisation age of the rhyolite.

BN16 - Trondhjemitic gneiss - KTGD Euhedral zircon grains were separated from sample BN16. Inherited grain cores are overgrown by euhedral magmatic domains which display oscillatory zoning patterns, consistent with a magmatic origin (Fig 6.8h). Seventeen spot analyses carried out on thirteen zircon grains spread along a regression line and have consistent $^{207}Pb/^{206}Pb$ ages, with a weighted average of 2143 ± 13 Ma (MSWD = 1.02, Fig. 6.10a). Five concordant analyses (black shaded ellipses) allow calculating a Concordia age of 2147 ± 9 Ma ($MSWD_{C+E}$ = 1.60, $Prob._{C+E}$=0.10), which is interpreted as the crystallisation age.

BN82 - Trondhjemite - Bawku granitoid domain Sample BN82 contains translucent, subhedral zircons with oscillatory zoning that comprise inherited zoned cores (Fig. 6.8i). Fourteen analyses were carried out on 13 grains. Most analyses are concordant to sub-concordant and data point ellipses overlap on a Concordia diagram (black shaded ellipses, Fig 6.10b). Assuming that this distribution represents a single zircon crystallisation event, a weighted average $^{207}Pb/^{206}Pb$ age of 2153 ± 17 Ma (MSWD = 0.35, n=12) is interpreted as the rock crystallisation age. Two laser spots (#8.1 and #13.1, Table 6.5) focused on zircon cores yield concordant analyses with $^{207}Pb/^{206}Pb$ age of 2267 ± 47 Ma (2σ, red shaded ellipses) which are interpreted to represent the age of inherited material.

BN87 - Granodioritic gneiss - KTGD Zircon grains from sample BN87 are euhedral to subhedral. They generally comprise a magmatic core which is overgrown by another magmatic domain, characterized by an oscillatory zoning pattern (Fig. 6.8j). Twenty analyses were carried out on nineteen zircon grains. They reveal a complex age distribution (Fig. 6.10c). Concordant data points overlap between *ca.* 2200 and 2120 Ma. A population of five concordant analyses aimed at outer

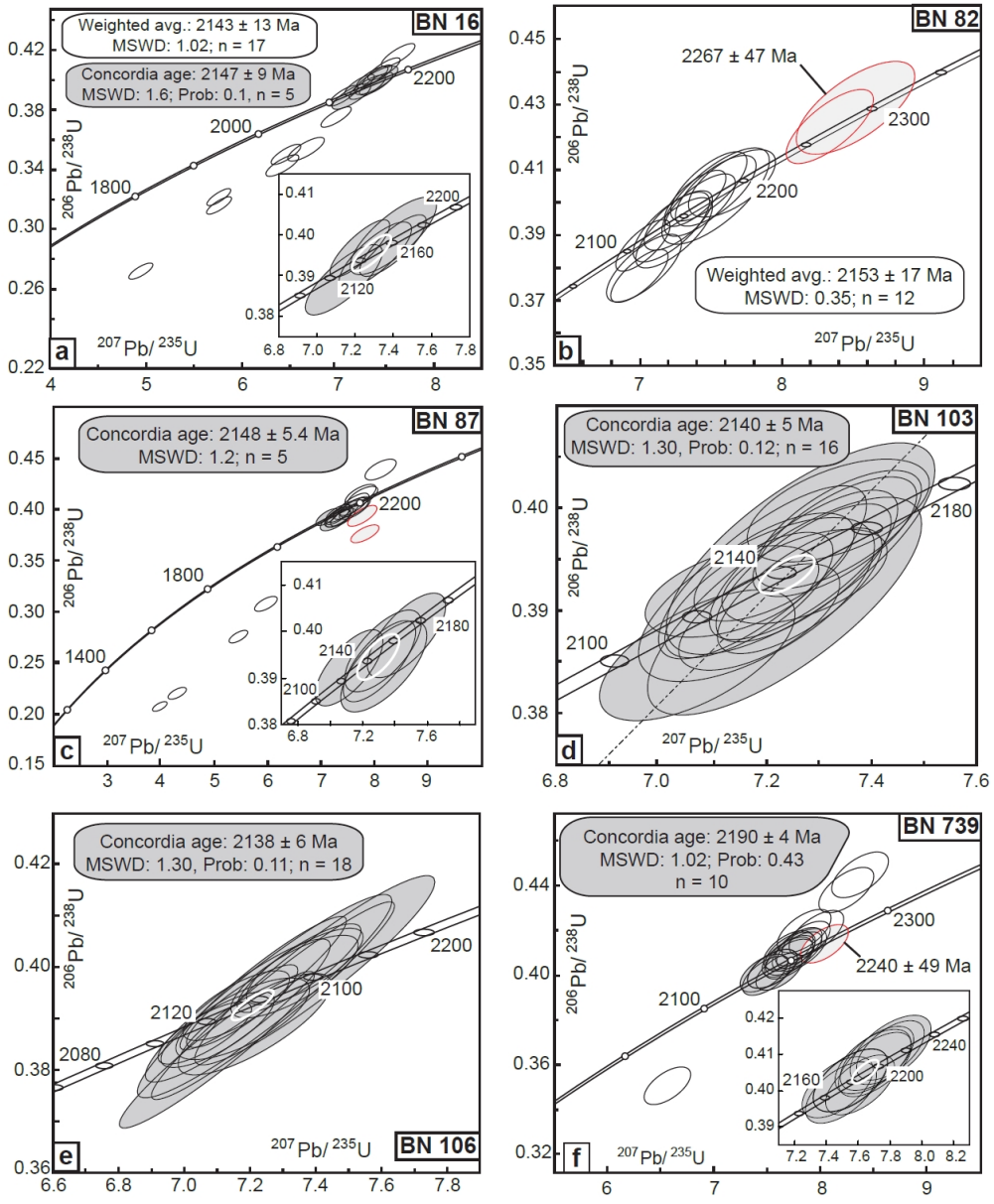

FIGURE 6.10: Concordia diagrams (**a-f**) presenting results of U–Pb dating of zircons from tonalite, granodiorite and granite gneisses or plutons from the Paleoproterozoic granitoid domains of NW Ghana. Dark shaded ellipses are data points used to calculate Concordia ages.

magmatic domains defines a Concordia age of 2148 ± 5 Ma ($MSWD_{C+E}$ = 1.20, $Prob._{C+E}$=0.29), interpreted as the granodiorite crystallisation age. Other concordant analyses have older ages which are interpreted to reflect zircons inherited from rocks formed between 2200 and 2170 Ma. Five discordant analyses yield $^{207}Pb/^{206}Pb$ ages between 2230 and 2350 Ma. They may represent inheritance from early crustal material which was not preserved in northern Ghana.

BN103 - Granodiorite - Julie belt Zircons separated from granodiorite BN103 are translucent, colourless and display euhedral shapes with angular terminations. SEM imaging reveals a thin oscillatory zoning, which is sometime overprinted by transgressive unzoned domains (Fig. 6.8k). Analyses focused on both zoned and unzoned domains do not show any significant differences neither in terms of U or Th contents, nor in terms of ages. All analyses are concordant (98-102%) and form a single age population (Fig. 6.10d). They define a Concordia age of 2140 ± 5 Ma ($MSWD_{C+E}$ = 1.30, $Prob._{C+E}$=0.12, n=16) that is interpreted as the crystallisation age of the granodiorite.

BN106 - Granite - Julie belt Zircon grains have euhedral shapes and have an oscillatory zoning, consistent with a magmatic origin (Fig 6.8l). Fifteen data points out of 18 are concordant and define a Concordia age of of 2138 ± 6 Ma ($MSWD_{C+E}$ = 1.30, $Prob._{C+E}$=0.11) which is interpreted to date the crystallisation of the granite (Fig. 6.10e).

BN739 - Orthogneiss - Bole-Bulenga terrain Zircons from orthogneiss BN739 are elongated, translucent and have euhedral shapes. They display a fine oscillatory magmatic zoning (Fig. 6.8m). Twenty analyses were performed on sixteen grains. Nineteen spots have consistent $^{207}Pb/^{206}Pb$ ages. Among these, ten concordant analyses from as many grains define a Concordia age of 2190 ± 4 Ma ($MSWD_{C+E}$ = 1.02, $Prob._{C+E}$=0.43), interpreted as the crystallisation age of the magmatic protolith (Fig. 6.10f).

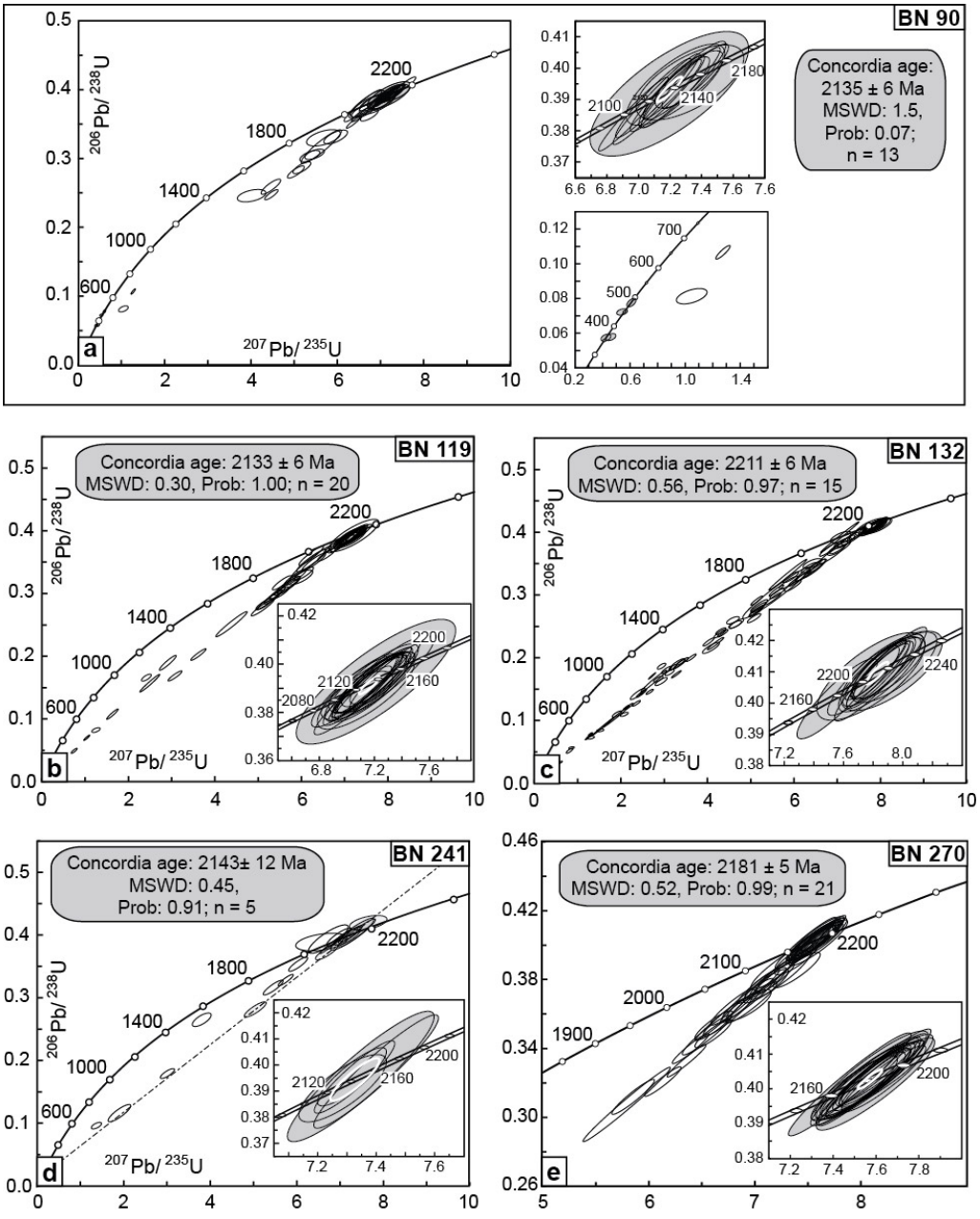

FIGURE 6.11: Concordia diagrams (**a-e**) presenting results of U-Pb dating of zircons from granodiorite gneisses or plutons from the Paleoproterozoic granitoid domains of NW Ghana. Dark shaded ellipses are data points used to calculate Concordia ages.

Sample Analysis	Pb[a] (ppm)	Th (ppm)	U (ppm)	$\frac{Th}{U}$	$\frac{^{208}Pb}{^{206}Pb}$	$\frac{^{207}Pb}{^{206}Pb}$	$\pm2\sigma$ (%)	$\frac{^{207}Pb}{^{235}U}$	$\pm2\sigma$ (%)	$\frac{^{206}Pb}{^{238}U}$	$\pm2\sigma$ (%)	ρ^b	$\frac{^{206}Pb^c}{^{238}U}$	$\pm2\sigma$ (Ma)	$\frac{^{207}Pb}{^{206}Pb}$	$\pm2\sigma$ (Ma)	conc.[d] (%)
BN02B																	
Andesite																	
#1-1	55.6	55.3	113.3	0.49	0.148	0.1326	1.2	7.2446	2.33	0.3961	2.2	0.93	2151.3	40	2133.1	20	100.9
#2-1	61.1	56.5	134.0	0.42	0.125	0.1350	1.4	7.4629	1.65	0.4009	0.8	0.51	2173.0	15	2164.3	25	100.4
#3-1	40.4	49.3	80.1	0.62	0.180	0.1337	1.8	7.2942	2.32	0.3956	1.6	0.67	2148.5	29	2147.7	32	100.0
#4-1	54.7	51.2	119.4	0.43	0.128	0.1342	1.2	7.4493	1.62	0.4025	1.1	0.69	2180.3	21	2154.2	20	101.2
#5-1	40.7	42.4	87.8	0.48	0.144	0.1348	1.4	7.4764	1.78	0.4022	1.1	0.61	2179.1	20	2161.8	24	100.8
#1-2	34.8	51.3	73.3	0.70	0.197	0.1358	1.4	7.3941	2.11	0.3949	1.6	0.75	2145.6	29	2174.2	24	98.7
#6-1	65.7	35.8	142.4	0.25	0.077	0.1350	1.4	7.2437	2.56	0.3893	2.3	0.91	2119.5	42	2163.5	24	98.0
#7-1	45.2	51.0	97.6	0.52	0.140	0.1351	1.3	7.3240	2.80	0.3931	2.5	0.88	2137.0	45	2165.8	23	98.7
#8-1	60.4	73.0	119.6	0.61	0.188	0.1374	1.5	7.5682	6.24	0.3994	6.1	0.97	2166.4	111	2195.0	25	98.7
#9-1	80.2	99.0	170.9	0.58	0.165	0.1340	1.3	7.4088	2.38	0.4009	2.0	0.83	2173.4	36	2151.3	23	101.0
#10-1	66.4	73.1	144.6	0.51	0.148	0.1340	1.9	7.3081	2.25	0.3955	1.2	0.52	2148.2	21	2151.3	33	99.9
#11-1	78.0	102.9	166.4	0.62	0.170	0.1345	1.7	7.2438	3.32	0.3907	2.9	0.87	2125.9	52	2157.4	29	98.5
#12-1	26.1	21.6	58.6	0.37	0.112	0.1342	1.6	7.4487	2.88	0.4025	2.4	0.84	2180.3	45	2154.1	27	101.2
#13-1	91.9	106.1	194.2	0.55	0.157	0.1335	1.3	7.4005	2.18	0.4021	1.8	0.82	2178.6	33	2144.4	22	101.6
#14-1	34.2	40.6	73.2	0.56	0.165	0.1344	1.6	7.3645	2.08	0.3974	1.3	0.62	2157.1	24	2156.3	28	100.0
#15-1	64.7	46.6	137.5	0.34	0.111	0.1356	1.3	7.3554	1.95	0.3933	1.6	0.82	2138.2	29	2172.1	22	98.4
#16-1	27.1	25.5	60.0	0.42	0.126	0.1349	1.5	7.3458	2.56	0.3950	2.2	0.86	2145.8	40	2162.6	26	99.2
#17-1	31.7	33.3	66.9	0.50	0.151	0.1338	1.6	7.1875	2.39	0.3895	2.0	0.83	2120.6	36	2148.8	27	98.7
#18-1	40.1	45.4	90.7	0.50	0.157	0.1337	1.3	7.3498	2.48	0.3988	2.1	0.86	2163.4	39	2146.8	22	100.8
#19-1	30.2	47.4	70.9	0.67	0.190	0.1330	1.4	6.8471	1.92	0.3733	1.3	0.69	2045.1	23	2138.1	24	95.6
BN60B																	
Dacite																	
#1-1	70.9	25.5	172.6	0.15	0.044	0.1321	1.6	7.2224	2.93	0.3967	2.5	0.84	2153.7	45	2125.5	28	101.3
#2-1	79.8	29.0	187.8	0.15	0.047	0.1323	1.5	7.2390	2.86	0.3969	2.5	0.86	2154.8	45	2128.5	27	101.2
#3-1	75.3	24.2	183.4	0.13	0.039	0.1330	1.6	7.3031	2.88	0.3984	2.4	0.83	2161.6	44	2137.4	28	101.1
#4-1	129.7	75.0	297.5	0.25	0.075	0.1316	1.5	7.1198	2.95	0.3925	2.7	0.91	2134.3	48	2119.0	26	100.7
#5-1	56.5	26.2	134.1	0.20	0.055	0.1341	1.7	7.3601	3.18	0.3981	2.7	0.85	2160.1	50	2152.4	29	100.4
#6-1	73.9	26.1	171.3	0.15	0.050	0.1361	1.8	7.3784	2.96	0.3933	2.5	0.85	2137.9	46	2177.9	31	98.2
#7-1	78.7	35.3	176.9	0.20	0.060	0.1335	1.6	7.2329	2.18	0.3928	1.6	0.75	2135.9	30	2145.1	28	99.6
#8-1	89.1	36.4	200.3	0.18	0.058	0.1345	1.6	7.2405	2.36	0.3905	1.9	0.83	2125.3	35	2157.1	27	98.5
#9-1	87.5	37.1	205.4	0.18	0.054	0.1340	1.6	7.2610	2.00	0.3929	1.3	0.66	2136.4	24	2151.3	27	99.3
#10-1	68.3	25.8	166.4	0.16	0.044	0.1336	1.6	7.2391	2.16	0.3931	1.4	0.67	2137.0	26	2145.5	28	99.6
#11-1	109.3	40.4	261.8	0.15	0.047	0.1334	1.6	7.3105	2.19	0.3975	1.6	0.74	2157.5	30	2143.1	27	100.7
#12-1	75.3	37.1	175.4	0.21	0.067	0.1341	1.6	7.2470	2.11	0.3918	1.5	0.72	2131.2	28	2152.9	27	99.0
#13-1	92.0	39.5	215.7	0.18	0.056	0.1344	1.7	7.2935	2.21	0.3935	1.6	0.71	2139.1	28	2156.6	29	99.2
#14-1	79.6	25.6	189.1	0.14	0.048	0.1370	1.9	7.3753	2.64	0.3906	2.0	0.74	2125.5	35	2189.0	33	97.1
#15-1	124.3	60.6	284.4	0.21	0.069	0.1342	1.6	7.3708	2.33	0.3983	1.9	0.80	2161.3	34	2153.7	27	100.4
#16-1	73.7	28.5	185.4	0.15	0.045	0.1342	1.6	7.2681	2.15	0.3929	1.5	0.71	2136.4	28	2153.0	27	99.2
#17-1	85.3	54.0	204.5	0.26	0.071	0.1344	1.6	7.2850	2.12	0.3931	1.5	0.70	2137.1	27	2156.5	27	99.1
#18-1	60.2	43.1	139.5	0.31	0.086	0.1344	1.6	7.2734	2.16	0.3926	1.6	0.74	2135.0	29	2155.7	27	99.0
#19-1	62.5	23.5	154.5	0.15	0.045	0.1343	1.6	7.3516	1.78	0.3971	0.8	0.43	2155.8	14	2154.4	28	100.1
#20-1	63.3	24.4	146.9	0.17	0.050	0.1343	1.6	7.2838	1.89	0.3932	1.1	0.59	2137.9	20	2155.4	28	99.2
BN68																	
Basaltic andesite																	
#1-1	68.5	77.0	151.2	0.51	0.154	0.1353	1.2	7.5276	1.29	0.4035	0.5	0.42	2185.2	10	2167.9	20	100.8
#2-1	18.9	14.5	43.3	0.33	0.099	0.1347	1.6	7.3797	1.85	0.3973	0.8	0.46	2156.7	15	2160.2	28	99.8
#3-1	61.0	64.2	122.3	0.52	0.165	0.1352	1.3	7.2929	2.59	0.3911	2.1	0.82	2128.1	38	2167.0	23	98.2
#4-1	61.6	66.0	133.8	0.49	0.152	0.1344	1.2	7.2818	1.82	0.3930	1.3	0.70	2136.5	23	2156.2	21	99.1
#5-1	64.4	65.2	142.4	0.46	0.138	0.1341	1.1	7.3607	1.51	0.3980	1.0	0.63	2159.7	17	2152.9	20	100.3
#6-1	65.8	59.5	147.2	0.40	0.122	0.1333	1.1	7.1854	1.61	0.3911	1.1	0.70	2127.8	21	2141.3	19	99.4
#7-1	37.4	35.1	83.9	0.42	0.123	0.1343	1.3	7.3807	1.72	0.3986	1.1	0.65	2162.7	21	2154.8	22	100.4
#8-1	64.3	67.3	135.8	0.50	0.151	0.1331	1.2	7.1823	2.86	0.3914	2.6	0.89	2129.3	46	2139.1	21	99.5
#9-1	61.4	80.8	128.5	0.63	0.181	0.1344	1.3	7.3574	1.88	0.3969	1.3	0.69	2154.7	24	2156.9	23	99.9
#10-1	53.4	38.3	121.3	0.32	0.096	0.1341	1.2	7.2207	1.82	0.3906	1.3	0.71	2125.8	23	2151.8	21	98.8
#11-1	44.8	40.3	97.8	0.41	0.135	0.1405	1.5	7.9423	2.11	0.4101	1.5	0.70	2215.2	28	2233.1	26	99.2
#12-1	77.4	55.5	174.6	0.32	0.101	0.1346	1.2	7.2754	1.86	0.3920	1.4	0.75	2131.9	25	2159.1	20	98.7
#13-1	33.4	29.1	70.3	0.41	0.139	0.1349	1.3	7.3724	2.14	0.3964	1.6	0.75	2152.4	29	2162.6	23	99.5
#14-1	93.5	114.6	201.7	0.57	0.169	0.1332	1.1	7.3076	1.85	0.3980	1.4	0.78	2159.6	27	2140.4	20	100.9
#15-1	251.5	957.6	554.2	1.73	0.486	0.1309	1.1	5.6565	6.36	0.3135	6.3	0.98	1757.7	96	2109.7	20	83.3
#16-1	95.9	126.6	212.6	0.60	0.171	0.1333	1.2	7.1993	1.78	0.3917	1.3	0.71	2130.6	23	2142.0	21	99.5
#17-1	38.7	46.8	86.4	0.54	0.156	0.1340	1.2	7.2480	1.70	0.3923	1.1	0.66	2133.6	20	2150.9	22	99.2
#18-1	73.5	82.1	164.4	0.50	0.142	0.1347	1.5	7.3580	1.67	0.3961	0.7	0.42	2150.8	13	2160.7	26	99.5
#19-1	33.8	33.9	72.4	0.47	0.147	0.1355	2.0	7.2807	2.58	0.3897	1.4	0.55	2121.6	26	2170.3	35	97.8
#20-1	43.4	35.9	96.3	0.37	0.116	0.1330	1.2	7.3077	1.75	0.3984	1.2	0.69	2161.7	22	2138.3	21	101.1
#21-1	68.7	83.3	149.0	0.56	0.168	0.1343	1.2	7.3564	2.21	0.3974	1.8	0.82	2157.1	33	2154.4	21	100.1
#22_1	101.8	39.1	248.2	0.16	0.046	0.1339	1.2	7.2267	1.73	0.3914	1.2	0.71	2129.4	22	2149.9	21	99.0
#23-1	49.9	42.0	117.0	0.36	0.103	0.1343	1.4	7.3971	1.90	0.3995	1.3	0.70	2166.6	25	2155.0	23	100.5
#24-1	65.1	72.4	150.0	0.48	0.142	0.1348	1.3	7.3154	1.97	0.3937	1.5	0.74	2140.0	27	2161.0	23	99.0
BN108																	
Rhyodacite																	
#1-1	70.3	105.2	158.1	0.67	0.180	0.1350	1.9	7.1002	2.17	0.3816	1.0	0.48	2083.6	19	2163.5	33	96.3
#2-1	72.4	107.2	168.3	0.64	0.167	0.1356	1.7	7.0912	1.95	0.3791	1.0	0.52	2072.2	18	2172.4	29	95.4
#3-1	28.5	33.9	65.7	0.52	0.151	0.1357	2.0	7.1185	2.47	0.3803	1.4	0.58	2077.9	26	2173.6	35	95.6
#4-1	46.2	64.1	104.6	0.61	0.166	0.1355	1.8	7.1536	2.67	0.3830	2.0	0.74	2090.4	35	2169.9	31	96.3
#5-1	85.0	101.1	192.0	0.53	0.144	0.1354	1.7	7.3860	2.62	0.3955	2.0	0.75	2148.3	36	2169.7	30	99.0
#6-1	77.1	160.1	255.3	0.63	0.195	0.1356	1.7	7.1681	3.37	0.3835	2.9	0.86	2092.4	52	2171.5	30	96.4
#7-1	57.0	72.8	138.1	0.53	0.166	0.1356	1.7	7.3343	2.74	0.3921	2.2	0.79	2132.8	39	2172.4	29	98.2
#8-1	115.0	144.6	243.1	0.59	0.175	0.1345	1.6	7.5043	1.92	0.4046	1.0	0.53	2190.0	19	2158.0	28	101.5
#9-1	117.0	169.2	240.7	0.70	0.200	0.1349	1.6	7.4801	2.36	0.4021	1.7	0.73	2178.9	32	2162.8	28	100.7
#10-1	161.4	270.7	353.4	0.77	0.219	0.1355	1.7	7.2118	3.29	0.3861	2.8	0.86	2104.5	51	2170.3	29	97.0

TABLE 6.3: U–Pb isotopic data obtained by LA-ICP-MS analyses at Géosciences Montpellier, France, from zircons from volcanic rocks of northern Ghana.[a] Corrected for background. [b]ρ is the $^{206}Pb/^{238}U/^{207}Pb/^{235}U$ error correlation coefficient. [c] Common Pb corrected using measured ^{204}Pb. [d] degree of concordance = $^{206}Pb/^{238}U$ age / $^{207}Pb/^{206}Pb$ age x 100.

Sample Analysis	Pb[a] (ppm)	Th (ppm)	U (ppm)	$\frac{Th}{U}$	$\frac{^{208}Pb}{^{206}Pb}$	$\frac{^{207}Pb}{^{206}Pb}$	$\pm2\sigma$ (%)	$\frac{^{207}Pb}{^{235}U}$	$\pm2\sigma$ (%)	$\frac{^{206}Pb}{^{238}U}$	$\pm2\sigma$ (%)	ρ[b]	$\frac{^{206}Pb^c}{^{238}U}$	$\pm2\sigma$ (Ma)	$\frac{^{207}Pb}{^{206}Pb}$	$\pm2\sigma$ (Ma)	conc.[d] (%)
BN107																	
Dacite																	
#1-1	40.2	67.8	83.5	0.81	0.227	0.1351	1.8	7.5543	2.62	0.4056	1.9	0.74	2194.8	36	2165.0	31	101.4
#2-1	78.7	101.2	171.5	0.59	0.177	0.1358	1.7	7.5518	2.52	0.4033	1.8	0.73	2184.1	34	2174.5	30	100.4
#3-1	52.4	63.8	115.1	0.55	0.160	0.1343	1.8	7.4440	1.99	0.4020	1.0	0.48	2178.1	18	2155.1	30	101.1
#4-1	49.5	64.4	112.1	0.57	0.160	0.1332	1.7	7.1811	1.98	0.3909	0.9	0.47	2126.9	17	2141.1	30	99.3
#5-1	222.0	286.3	468.7	0.61	0.180	0.1335	1.5	7.2650	2.65	0.3947	2.2	0.82	2144.6	39	2144.4	27	100.0
#6-1	42.1	48.9	97.5	0.50	0.144	0.1346	1.8	7.1884	2.38	0.3873	1.5	0.65	2110.3	28	2159.0	31	97.7
#7-1	52.7	65.1	115.2	0.57	0.168	0.1351	1.7	7.4864	2.09	0.4020	1.2	0.55	2178.0	21	2165.1	30	100.6
#8-1	69.3	124.2	151.5	0.82	0.211	0.1347	1.6	7.2996	1.99	0.3930	1.2	0.59	2136.6	21	2160.4	28	98.9
#9-1	77.5	94.4	171.9	0.55	0.154	0.1338	1.6	7.3462	2.05	0.3983	1.2	0.60	2161.0	22	2148.2	29	100.6
#9-2	63.2	78.9	140.5	0.56	0.163	0.1337	1.6	7.3313	1.94	0.3978	1.0	0.53	2158.8	19	2146.8	29	100.6
#10-1	34.9	45.9	76.7	0.60	0.169	0.1360	2.6	7.5676	2.73	0.4036	0.9	0.34	2185.6	17	2176.7	44	100.4
#11-1	34.2	36.3	75.2	0.48	0.136	0.1348	3.1	7.4689	3.32	0.4018	1.2	0.35	2177.3	22	2161.7	54	100.7
#12-1	36.4	37.7	81.3	0.46	0.127	0.1346	1.7	7.4444	2.02	0.4012	1.1	0.52	2174.5	19	2158.6	30	100.7
#13-1	112.1	136.6	246.6	0.55	0.157	0.1341	1.6	7.4068	1.85	0.4007	0.9	0.51	2172.2	17	2152.0	28	100.9
#14-1	59.4	94.3	121.7	0.77	0.214	0.1337	1.6	7.4036	2.02	0.4015	1.2	0.62	2176.2	23	2147.4	28	101.3
#15-1	99.7	128.9	199.0	0.65	0.192	0.1345	1.7	7.3776	2.40	0.3980	1.7	0.70	2159.6	31	2157.0	30	100.1
#16-1	99.9	142.5	223.4	0.64	0.174	0.1356	1.6	7.3831	2.01	0.3948	1.3	0.63	2145.3	23	2171.9	27	98.8
#17-1	33.4	37.5	74.7	0.50	0.140	0.1348	1.8	7.3936	2.09	0.3979	1.1	0.53	2159.3	20	2161.0	31	99.9
#17-2	99.2	155.1	205.7	0.75	0.212	0.1346	1.7	7.3347	3.35	0.3951	2.9	0.87	2146.5	53	2159.3	29	99.4
#18-1	41.1	59.5	89.1	0.67	0.180	0.1360	1.7	7.4831	2.71	0.3990	2.1	0.77	2164.6	38	2177.0	30	99.4
#19-1	182.7	248.7	396.1	0.63	0.170	0.1346	1.7	7.4354	2.28	0.4006	1.5	0.67	2172.0	28	2158.8	29	100.6
#20-1	72.0	97.7	155.4	0.63	0.166	0.1339	1.0	7.3506	1.45	0.3982	1.0	0.70	2160.9	19	2149.4	18	100.5
#21-1	59.8	84.5	127.3	0.66	0.163	0.1353	1.1	7.5978	1.55	0.4074	1.1	0.73	2202.8	21	2167.5	18	101.6
#22-1	28.1	33.1	61.8	0.54	0.150	0.1337	1.2	7.3015	1.51	0.3962	0.9	0.59	2151.6	16	2146.5	21	100.2
#23-1	95.5	143.4	196.9	0.73	0.211	0.1340	1.0	7.3198	1.74	0.3962	1.4	0.81	2151.6	26	2150.8	18	100.0
#24-1	47.8	55.2	104.5	0.53	0.143	0.1340	1.2	7.4134	1.90	0.4013	1.5	0.77	2175.0	27	2150.8	21	101.1
#25-1	73.0	117.3	150.5	0.78	0.221	0.1386	2.0	7.5879	2.61	0.3969	1.7	0.63	2154.9	30	2210.4	35	97.5
#26-1	47.1	47.4	104.8	0.45	0.123	0.1335	1.1	7.3145	1.55	0.3973	1.1	0.71	2156.8	20	2144.7	19	100.6
#27-1	115.8	123.7	255.7	0.48	0.135	0.1341	0.9	7.2327	1.67	0.3910	1.4	0.83	2127.6	25	2153.0	16	98.8
#28-1	165.7	314.3	296.5	1.06	0.303	0.1396	1.3	8.0424	2.02	0.4178	1.5	0.76	2250.6	29	2222.2	23	101.3
#29-1	54.5	64.3	120.7	0.53	0.143	0.1336	1.0	7.3170	1.66	0.3971	1.3	0.80	2155.5	24	2146.4	17	100.4
BN186																	
Dacite																	
#1-1	40.4	26.5	108.8	0.24	0.069	0.1317	1.3	6.9597	2.49	0.3833	2.1	0.85	2091.6	37	2120.7	23	98.6
#1-2	86.2	124.7	194.7	0.64	0.174	0.1363	1.9	7.4638	3.23	0.3973	2.5	0.79	2156.5	46	2180.2	33	98.9
#3-1	13.2	12.0	34.4	0.35	0.092	0.1326	1.8	6.9609	2.31	0.3806	1.4	0.63	2079.1	26	2133.3	31	97.5
#3-2	44.4	43.7	105.8	0.41	0.142	0.1416	2.5	7.7786	2.77	0.3983	1.2	0.43	2161.2	22	2247.4	43	96.2
#4-1	37.2	64.4	87.3	0.74	0.217	0.1367	1.6	7.2501	2.79	0.3848	2.3	0.81	2098.6	41	2185.3	28	96.0
#5-1	69.1	68.3	172.8	0.40	0.113	0.1327	1.3	7.2085	2.40	0.3940	2.0	0.84	2141.1	37	2134.1	22	100.3
#6-1	38.0	47.2	90.4	0.52	0.152	0.1336	1.7	7.2614	2.70	0.3941	2.1	0.77	2142.0	38	2146.1	29	99.8
#7-1	48.7	119.6	96.6	1.24	0.356	0.1360	1.5	7.3649	2.92	0.3929	2.5	0.85	2136.1	45	2176.4	25	98.2
#8-1	43.3	58.0	98.3	0.59	0.188	0.1440	2.5	8.0238	2.82	0.4042	1.4	0.49	2188.3	26	2275.6	42	96.2
#9-1	100.2	119.4	244.3	0.49	0.138	0.1328	1.4	7.2610	1.98	0.3967	1.4	0.72	2153.8	26	2134.7	24	100.9
#10-1	47.9	62.4	104.6	0.60	0.152	0.1327	2.0	7.2519	2.69	0.3964	1.7	0.63	2152.3	31	2133.9	35	100.9
#11-1	35.2	45.9	79.5	0.58	0.151	0.1366	2.1	7.3032	2.70	0.3876	1.7	0.63	2111.8	31	2185.1	36	96.6
#12-1	69.6	45.0	160.2	0.28	0.097	0.1416	2.2	7.5688	3.40	0.3877	2.6	0.76	2112.0	47	2246.9	38	94.0
#13-1	38.8	34.2	91.5	0.37	0.097	0.1354	1.7	7.2926	2.44	0.3907	1.7	0.71	2126.0	31	2169.0	30	98.0
#14-1	68.5	41.6	151.8	0.27	0.114	0.1465	2.0	8.2846	3.01	0.4101	2.3	0.75	2215.2	43	2305.8	34	96.1
#15-1	78.7	120.6	170.8	0.71	0.180	0.1330	1.4	7.2298	2.50	0.3942	2.0	0.81	2142.3	37	2138.1	25	100.2
#15-2	97.2	51.0	205.3	0.25	0.110	0.1480	3.3	8.8388	3.76	0.4332	1.7	0.46	2320.3	34	2322.6	56	99.9
#16-1	84.4	109.4	192.4	0.57	0.146	0.1334	1.4	7.2670	2.05	0.3952	1.5	0.73	2147.0	27	2142.7	24	100.2
#17-1	78.3	114.7	168.8	0.68	0.174	0.1329	1.3	7.1500	2.53	0.3903	2.1	0.83	2124.3	38	2136.0	23	99.5
#18-1	61.7	93.0	141.5	0.66	0.158	0.1324	1.6	7.1524	2.32	0.3918	1.7	0.74	2131.4	31	2129.8	27	100.1
BN400																	
Rhyolite																	
#1-1	35.6	53.3	69.6	0.77	0.254	0.1394	2.5	8.0997	2.99	0.4214	1.6	0.53	2266.8	30	2219.8	43	102.1
#2-1	30.9	35.6	70.1	0.51	0.136	0.1375	1.9	7.4983	2.33	0.3955	1.4	0.59	2148.3	25	2196.0	33	97.8
#3-1	54.0	97.4	111.9	0.87	0.231	0.1371	1.7	7.6161	2.14	0.4030	1.3	0.62	2182.8	25	2190.5	29	99.7
#4-1	15.0	18.1	33.5	0.54	0.148	0.1373	1.9	7.6253	2.25	0.4029	1.2	0.53	2182.3	22	2193.1	33	99.5
#5-1	13.1	13.2	29.6	0.45	0.124	0.1395	1.9	7.8595	2.96	0.4087	2.3	0.76	2209.1	42	2220.6	33	99.5
#6-1	26.0	29.6	59.5	0.50	0.136	0.1392	1.8	7.5664	2.41	0.3944	1.6	0.66	2143.0	29	2216.7	31	96.7
#7-1	27.7	43.6	68.5	0.64	0.155	0.1380	2.0	6.9085	2.77	0.3630	2.0	0.71	1996.4	34	2202.7	34	90.6
#8-1	61.8	70.5	130.7	0.54	0.150	0.1372	1.7	8.1040	2.64	0.4284	2.1	0.78	2298.3	40	2192.3	29	104.8
#9-1	57.7	65.1	125.3	0.52	0.148	0.1364	1.7	7.8350	2.52	0.4166	1.8	0.72	2244.9	34	2182.1	30	102.9
#10-1	79.4	119.6	167.3	0.71	0.207	0.1390	1.8	7.6071	4.79	0.3969	4.4	0.93	2154.6	81	2215.0	31	97.3
#11-1	32.5	50.7	73.7	0.69	0.203	0.1400	2.0	7.3915	3.07	0.3829	2.4	0.77	2089.7	42	2227.4	34	93.8
#12-1	13.9	16.7	31.7	0.53	0.141	0.1360	1.9	7.5266	2.43	0.4014	1.5	0.63	2175.3	28	2177.0	33	99.9
#13-1	42.4	55.0	94.7	0.58	0.156	0.1370	1.8	7.6263	2.31	0.4038	1.5	0.64	2186.4	27	2189.5	31	99.9
#14-1	58.7	71.5	123.9	0.58	0.160	0.1368	1.6	8.0558	2.29	0.4270	1.6	0.70	2292.1	31	2187.5	28	104.8
#15-1	33.9	46.6	84.3	0.55	0.161	0.1396	2.0	6.8811	3.27	0.3575	2.6	0.78	1970.4	43	2222.2	35	88.7
#16-1	72.9	97.5	153.8	0.63	0.181	0.1380	1.8	7.9019	2.62	0.4154	1.9	0.71	2239.4	35	2202.0	32	101.7
#17-1	137.8	239.0	287.2	0.83	0.214	0.1367	1.7	7.9086	2.53	0.4195	1.9	0.76	2258.0	36	2186.4	29	103.3
#18-1	65.1	86.4	133.7	0.65	0.183	0.1384	1.7	8.1961	2.26	0.4294	1.5	0.68	2302.9	30	2207.8	29	104.3
#19-1	32.2	31.1	69.9	0.45	0.130	0.1356	1.3	7.5520	2.06	0.4041	1.6	0.78	2187.7	30	2171.2	22	100.8
#20-1	116.1	199.5	272.6	0.73	0.303	0.1402	2.2	6.6923	8.41	0.3461	8.1	0.97	1916.0	134	2230.2	37	85.9
#21-1	67.3	67.8	141.4	0.48	0.139	0.1370	1.2	7.8048	1.74	0.4131	1.2	0.71	2228.8	23	2190.2	21	101.8
#22-1	50.0	50.8	100.2	0.51	0.150	0.1371	1.3	8.1213	2.43	0.4295	2.1	0.85	2303.3	40	2191.5	22	105.1
#23-1	60.8	55.3	129.7	0.43	0.121	0.1379	1.3	7.8292	2.01	0.4117	1.5	0.76	2222.5	29	2201.5	22	101.0
BN16																	
Trondhjemite																	
#1-1	80.7	100.6	192.7	0.52	0.117	0.1350	2.5	7.3988	1.93	0.3973	1.6	0.81	2156.8	28	2163.6	43	99.7
#1-2	98.2	100.2	289.3	0.35	0.094	0.1337	2.5	6.4579	1.97	0.3502	1.6	0.80	1935.4	26	2146.9	44	90.1
#2-1	95.6	114.1	253.2	0.45	0.110	0.1331	2.8	7.1409	2.31	0.3890	1.8	0.78	2118	33	2139.4	49	99.0
#3-1	196.0	186.9	476.8	0.39	0.110	0.1321	2.4	7.2248	1.77	0.3966	1.4	0.82	2153.5	27	2126	41	101.3
#3-2	143.5	236.0	581.4	0.41	0.067	0.1322	2.5	5.7606	1.86	0.3160	1.5	0.81	1770	23	2127.6	43	83.2
#4-1	223.4	129.5	506.8	0.26	0.067	0.1332	2.4	7.4805	1.85	0.4073	1.5	0.81	2202.5	28	2140.7	42	102.9
#5-1	154.7	25.0	468.8	0.05	0.013	0.1314	2.4	7.0561	1.77	0.3895	1.4	0.82	2120.3	26	2116.9	41	100.2
#6-1	166.8	168.7	483.5	0.35	0.090	0.1299	2.4	5.7582	1.78	0.3216	1.4	0.81	1797.3	23	2096.5	41	85.7
#6-2	449.5	697.5	1098.7	0.63	0.168	0.1334	2.3	7.4110	1.70	0.4031	1.4	0.82	2183.3	26	2142.9	40	101.9
#7-1	102.8	36.5	297.1	0.12	0.041	0.1329	2.4	7.3585	1.83	0.4018	1.5	0.81	2177.5	27	2136.1	42	101.9
#7-2	225.9	106.0	461.6	0.23	0.067	0.1329	2.5	7.6283	1.89	0.4165	1.5	0.80	2244.7	29	2136.3	43	105.1
#8-1	111.2	57.9	304.1	0.19	0.057	0.1342	2.7	7.3058	2.13	0.3950	1.7	0.79	2146	31	2153.6	46	99.6
#9-1	123.0	278.2	426.9	0.65	0.185	0.1368	2.9	6.6679	2.35	0.3536	1.8	0.78	1951.8	31	2187.5	50	89.2
#10-1	77.6	143.3	150.8	0.95	0.248	0.1344	3.0	7.3998	2.50	0.3997	1.9	0.78	2167.8	36	2155.6	52	100.6
#11-1	99.9	52.8	296.3	0.18	0.079	0.1360	2.7	6.4203	2.19	0.3427	1.7	0.78	1899.7	28	2176.4	47	87.3
#12-1	108.6	136.5	266.5	0.51	0.142	0.1351	2.4	6.9812	1.86	0.3751	1.5	0.80	2053.5	26	2164.8	42	94.9
#13-1	70.9	166.9	332.3	0.50	0.237	0.1319	2.7	4.9446	2.09	0.2720	1.6	0.78	1551.2	22	2123.7	46	73.0

Sample Analysis	Pb[a] (ppm)	Th (ppm)	U (ppm)	$\frac{Th}{U}$	$\frac{^{208}Pb}{^{206}Pb}$	$\frac{^{207}Pb}{^{206}Pb}$	$\pm 2\sigma$ (%)	$\frac{^{207}Pb}{^{235}U}$	$\pm 2\sigma$ (%)	$\frac{^{206}Pb}{^{238}U}$	$\pm 2\sigma$ (%)	ρ[b]	$\frac{^{206}Pb^c}{^{238}U}$	$\pm 2\sigma$ (Ma)	$\frac{^{207}Pb}{^{206}Pb}$	$\pm 2\sigma$ (Ma)	conc.[d] (%)
BN82																	
Trondhjemite																	
#1-1	100.4	171.0	223.2	0.77	0.209	0.1317	2.7	7.0213	2.22	0.3869	1.7	0.75	2108.3	30	2120.2	47	99.4
#2-1	68.8	100.2	158.0	0.63	0.175	0.1344	2.9	6.9968	2.36	0.3775	1.8	0.74	2064.8	31	2156.8	49	95.7
#3-1	27.3	30.2	63.9	0.47	0.117	0.1344	3.5	7.2408	3.05	0.3907	2.3	0.74	2126.3	41	2156.7	61	98.6
#4-1	55.3	71.8	131.7	0.55	0.139	0.1335	3.5	7.2215	3.03	0.3925	2.2	0.73	2134.5	40	2144.1	61	99.6
#5-1	99.5	114.4	219.9	0.52	0.134	0.1336	2.9	7.3889	2.39	0.4013	1.7	0.73	2175	32	2145.5	50	101.4
#6-1	53.3	95.4	114.4	0.83	0.182	0.1359	4.6	7.5324	4.10	0.4020	3.0	0.73	2178.2	55	2176	79	100.1
#6-2	32.7	31.1	71.1	0.44	0.121	0.1341	3.4	7.4845	2.94	0.4050	2.1	0.73	2191.8	40	2152.1	59	101.8
#7-1	38.7	48.4	86.7	0.56	0.147	0.1342	3.5	7.0292	3.07	0.3800	2.2	0.73	2076	40	2153.8	61	96.4
#8-1	43.2	34.9	88.3	0.40	0.113	0.1429	3.5	8.3359	3.00	0.4233	2.2	0.73	2275.5	42	2262.1	59	100.6
#9-1	65.0	73.1	141.8	0.52	0.136	0.1349	3.2	7.4221	2.74	0.3992	2.0	0.71	2165.5	36	2162.3	56	100.1
#10-1	47.9	78.5	98.3	0.80	0.214	0.1354	3.5	7.5340	3.07	0.4036	2.2	0.71	2185.7	41	2169.3	61	100.8
#11-1	65.4	98.1	139.6	0.70	0.174	0.1337	3.2	7.2706	2.70	0.3945	1.9	0.70	2143.8	34	2147	55	99.9
#12-1	104.2	88.3	222.9	0.40	0.102	0.1367	3.8	7.6481	3.27	0.4059	2.1	0.64	2196.1	39	2185.3	65	100.5
#13-1	40.0	47.6	72.4	0.66	0.174	0.1440	4.5	8.5175	4.00	0.4290	2.7	0.68	2301.3	52	2275.7	77	101.1
BN87																	
Granodiorite																	
#1-1	33.6	51.6	78.0	0.66	0.153	0.1346	3.0	7.3043	2.51	0.3937	1.8	0.72	2139.8	33	2158.8	52	99.1
#2-1	21.5	17.6	44.8	0.39	0.119	0.1370	3.0	7.4076	2.54	0.3923	1.8	0.72	2133.2	33	2189.5	52	97.4
#2-2	24.1	16.5	55.6	0.30	0.095	0.1433	3.4	7.7724	2.88	0.3935	2.1	0.73	2139.1	38	2267.2	57	94.3
#3-1	128.6	388.0	395.1	0.98	0.142	0.1316	2.9	7.1157	2.41	0.3923	1.7	0.70	2133.3	31	2119.4	51	100.7
#4-1	91.2	10.3	217.8	0.05	0.030	0.1365	3.5	7.6156	3.00	0.4048	2.2	0.73	2191.3	40	2182.8	60	100.4
#5-1	59.1	59.4	131.3	0.45	0.100	0.1358	3.1	7.4720	2.65	0.3992	1.9	0.70	2165.4	34	2174	54	99.6
#6-1	50.8	130.1	118.0	1.10	0.171	0.1380	3.6	7.6307	3.13	0.4012	2.2	0.72	2174.5	41	2201.9	62	98.8
#7-1	85.9	95.6	238.2	0.40	0.108	0.1435	3.1	5.4557	2.64	0.2758	1.8	0.69	1570.1	25	2269.8	54	69.2
#8-1	82.2	122.1	175.9	0.69	0.162	0.1342	3.1	7.3255	2.64	0.3959	1.8	0.68	2150	33	2154.1	54	99.8
#9-1	54.2	90.0	133.8	0.67	0.144	0.1359	3.2	7.3240	2.65	0.3910	1.8	0.68	2127.5	33	2175.2	54	97.8
#10-1	53.3	58.7	137.2	0.43	0.121	0.1509	3.2	7.8212	2.76	0.3761	1.9	0.68	2057.9	33	2355.8	55	87.4
#11-1	56.8	73.5	123.2	0.60	0.138	0.1355	3.5	7.3311	2.97	0.3925	2.0	0.68	2134.6	37	2170.1	60	98.4
#12-1	85.0	336.2	339.1	0.99	0.258	0.1392	3.3	3.9861	2.80	0.2078	1.9	0.66	1216.9	21	2217	57	54.9
#13-1	41.9	51.8	88.8	0.58	0.162	0.1354	3.6	7.2672	3.16	0.3894	2.2	0.69	2119.9	39	2169	63	97.7
#14-1	62.8	144.5	175.8	0.82	0.169	0.1407	3.4	5.9704	2.91	0.3077	1.9	0.67	1729.6	29	2236.2	58	77.3
#15-1	109.4	216.4	273.2	0.79	0.192	0.1375	3.4	7.6157	2.94	0.4018	1.9	0.66	2177.1	36	2196	59	99.1
#16-1	79.1	87.8	181.3	0.48	0.128	0.1368	3.5	7.7788	2.97	0.4125	1.9	0.65	2226.4	36	2186.9	59	101.8
#17-1	62.0	65.8	126.6	0.52	0.134	0.1356	3.6	7.7388	3.07	0.4140	2.0	0.66	2233.2	38	2171.6	61	102.8
#18-1	147.2	46.7	318.3	0.15	0.041	0.1342	3.4	8.1140	2.95	0.4387	1.9	0.64	2344.7	37	2153.2	59	108.9
#19-1	47.0	29.1	311.1	0.09	0.197	0.1418	3.8	4.3114	3.25	0.2206	2.1	0.66	1284.9	25	2249.2	64	57.1
BN103																	
Granite																	
#1-1	27.3	41.9	57.6	0.73	0.203	0.1337	1.3	7.2708	2.02	0.3945	1.5	0.75	2143.5	28	2146.9	23	99.8
#2-1	32.7	52.0	68.3	0.76	0.215	0.1327	1.3	7.2149	1.73	0.3943	1.1	0.63	2142.5	20	2134.3	23	100.4
#2-2	23.1	27.3	51.7	0.53	0.148	0.1325	1.4	7.1926	2.25	0.3937	1.8	0.78	2140.1	32	2131.2	25	100.4
#3-1	18.0	19.5	40.3	0.48	0.139	0.1320	1.7	7.1344	1.90	0.3919	0.9	0.49	2131.5	17	2125.3	29	100.3
#4-1	31.1	29.5	68.3	0.43	0.127	0.1331	1.6	7.3372	1.93	0.3998	1.0	0.53	2168.0	19	2139.4	29	101.3
#5-1	45.5	70.2	94.0	0.75	0.208	0.1328	1.3	7.1669	1.83	0.3915	1.3	0.70	2129.9	23	2134.8	23	99.8
#6-1	37.2	36.5	83.6	0.44	0.127	0.1337	1.3	7.3375	1.76	0.3979	1.2	0.67	2159.4	22	2147.6	23	100.5
#7-1	32.7	33.5	72.8	0.46	0.131	0.1344	1.2	7.2635	1.76	0.3919	1.3	0.72	2131.8	23	2156.4	21	98.9
#8-1	39.6	49.1	84.6	0.58	0.164	0.1340	1.3	7.2711	1.88	0.3937	1.4	0.74	2139.9	25	2150.5	22	99.5
#8-2	21.2	23.5	46.7	0.50	0.140	0.1339	1.4	7.1865	1.75	0.3894	1.1	0.62	2119.9	20	2149.2	24	98.6
#9-1	27.3	30.9	59.7	0.52	0.146	0.1341	1.5	7.2728	1.77	0.3933	1.0	0.54	2138.3	17	2152.4	26	99.3
#10-1	43.2	49.0	92.3	0.53	0.154	0.1338	1.3	7.3305	1.74	0.3972	1.2	0.69	2156.2	22	2149.1	22	100.3
#11-1	24.1	29.1	53.8	0.54	0.145	0.1329	1.7	7.0681	2.16	0.3856	1.4	0.63	2102.6	24	2137.0	29	98.4
#12-1	18.3	22.5	41.4	0.54	0.155	0.1330	1.9	7.2654	2.88	0.3960	2.1	0.74	2150.8	39	2138.6	34	100.6
#13-1	15.7	17.6	36.5	0.48	0.136	0.1344	1.9	7.2347	2.95	0.3904	2.2	0.75	2124.9	40	2156.1	34	98.6
#14-1	18.1	19.9	41.9	0.48	0.134	0.1332	1.9	7.1812	2.56	0.3911	1.7	0.65	2127.8	30	2140.3	34	99.4
BN106																	
Granodiorite																	
#1-1	220.9	415.9	514.5	0.81	0.180	0.1343	1.4	7.3969	4.04	0.3994	3.8	0.93	2166.1	69	2155.4	25	100.5
#2-1	181.6	180.1	536.1	0.34	0.096	0.1292	1.1	5.5445	2.92	0.3113	2.7	0.92	1746.9	41	2087.1	20	83.7
#3-1	271.8	740.1	483.1	1.53	0.442	0.1323	1.0	7.2399	2.86	0.3969	2.7	0.94	2154.6	49	2128.8	18	101.2
#4-1	81.5	269.5	634.4	0.42	0.126	0.1079	1.1	1.7299	2.39	0.1163	2.1	0.89	709.4	14	1763.6	19	40.2
#5-1	230.8	109.1	525.7	0.21	0.070	0.1333	1.1	7.3489	2.09	0.3998	1.8	0.84	2168.1	32	2142.1	20	101.2
#6-1	113.0	67.9	270.4	0.25	0.072	0.1326	1.0	7.1759	1.93	0.3924	1.7	0.87	2133.9	30	2133.1	17	100.0
#7-1	233.9	563.5	413.9	1.36	0.393	0.1323	1.0	7.0620	1.65	0.3872	1.3	0.78	2109.6	23	2128.7	18	99.1
#8-1	130.5	48.9	324.2	0.15	0.056	0.1341	1.1	7.0989	3.41	0.3839	3.2	0.95	2094.5	58	2152.5	19	97.3
#9-1	372.2	861.0	646.9	1.33	0.332	0.1332	1.5	7.2444	4.37	0.3943	4.1	0.94	2142.9	75	2141.1	26	100.1
#10-1	82.0	157.2	155.5	1.01	0.290	0.1327	1.4	7.1625	3.21	0.3915	2.9	0.91	2130.0	53	2133.6	24	99.8
#11-1	404.4	655.7	837.9	0.78	0.217	0.1323	1.2	7.1582	1.85	0.3925	1.4	0.77	2134.4	26	2128.3	21	100.3
#12-1	80.2	131.3	176.4	0.74	0.186	0.1335	1.6	7.1775	2.32	0.3899	1.7	0.72	2122.5	30	2144.6	28	99.0
#9-2	102.0	222.4	186.0	1.20	0.366	0.1345	1.6	7.2138	2.64	0.3889	2.1	0.79	2117.6	37	2158.0	28	98.1
#13-1	113.6	165.6	230.6	0.72	0.199	0.1336	1.4	7.3350	2.16	0.3981	1.7	0.77	2160.5	30	2146.0	24	100.7
#13-2	140.4	114.6	473.4	0.24	0.075	0.1301	1.2	4.9932	4.01	0.2783	3.8	0.95	1582.6	54	2100.0	21	75.4
#14-1	179.0	352.3	367.9	0.96	0.259	0.1335	1.2	7.3665	1.97	0.4001	1.5	0.77	2169.5	28	2144.9	22	101.1
#15-1	167.2	150.7	402.7	0.37	0.098	0.1328	1.2	7.1010	1.99	0.3878	1.6	0.78	2112.7	28	2135.3	22	98.9
#16-1	119.3	87.9	318.7	0.28	0.083	0.1340	1.2	7.2698	4.16	0.3935	4.0	0.96	2138.8	73	2151.1	20	99.4
BN739																	
Trondjhmeite																	
#1-1	69.7	116.5	184.5	0.63	0.163	0.1410	2.8	8.0391	2.28	0.4140	1.7	0.74	2233.2	32	2239.6	48	99.7
#1-2	62.5	62.8	130.1	0.48	0.125	0.1381	3.1	7.9644	2.63	0.4189	2.0	0.74	2255.3	37	2203.3	54	102.4
#2-1	101.4	87.3	220.2	0.40	0.105	0.1372	2.8	7.7982	2.31	0.4127	1.7	0.73	2227.2	32	2192.5	49	101.6
#3-1	112.3	90.0	252.9	0.36	0.111	0.1378	2.8	7.8033	2.23	0.4111	1.6	0.73	2220	31	2200.2	48	100.9
#4-1	68.7	87.6	136.4	0.64	0.173	0.1367	3.1	8.2444	2.55	0.4380	1.9	0.74	2341.6	37	2185.7	53	107.1
#4-2	119.3	131.2	250.2	0.52	0.142	0.1374	3.0	7.7068	2.44	0.4072	1.8	0.73	2202.2	33	2195	51	100.3
#5-1	157.5	150.5	318.2	0.47	0.134	0.1377	2.9	7.6130	2.33	0.4016	1.7	0.72	2176.3	31	2198	49	99.0
#6-1	110.0	102.4	242.2	0.42	0.115	0.1375	2.9	7.8680	2.34	0.4155	1.7	0.72	2239.9	32	2196.2	50	102.0
#7-1	133.7	199.4	270.6	0.74	0.189	0.1371	3.0	7.7189	2.45	0.4089	1.8	0.72	2209.9	33	2190.6	51	100.9
#8-1	104.0	167.3	201.0	0.83	0.223	0.1361	3.0	7.4955	2.47	0.3998	1.8	0.72	2168	33	2178.7	52	99.5
#8-2	113.8	142.9	311.2	0.46	0.139	0.1359	3.2	6.5659	2.71	0.3507	2.0	0.72	1937.9	33	2176.2	56	89.0
#9-1	91.0	95.4	179.1	0.53	0.147	0.1367	3.1	8.3743	2.60	0.4448	1.9	0.72	2371.9	37	2185.9	54	108.5
#10-1	114.3	120.0	227.1	0.53	0.144	0.1358	3.1	7.8491	2.62	0.4197	1.9	0.72	2259	36	2174.2	54	103.9
#11-1	112.6	127.0	233.9	0.54	0.171	0.1353	3.0	7.4709	2.44	0.4009	1.7	0.70	2173.3	32	2167.7	52	100.3
#12-1	113.5	122.6	237.5	0.52	0.139	0.1360	3.0	7.7000	2.47	0.4111	1.7	0.70	2220.1	33	2176.5	52	102.0
#13-1	75.9	66.7	165.7	0.40	0.095	0.1369	3.1	7.6936	2.53	0.4080	1.8	0.70	2205.9	33	2188.1	53	100.8
#14-1	79.3	101.5	157.4	0.64	0.174	0.1378	3.2	7.8045	2.67	0.4113	1.9	0.71	2220.7	36	2199.2	55	101.0
#15-1	127.8	115.3	265.7	0.43	0.120	0.1365	3.0	7.7184	2.49	0.4105	1.7	0.70	2217	32	2183.3	52	101.5
#15-2	124.5	161.9	247.9	0.65	0.186	0.1360	3.1	7.5504	2.53	0.4029	1.8	0.70	2182.4	33	2177.2	53	100.2
#16-1	121.8	335.3	256.1	1.31	0.186	0.1361	3.1	7.5527	2.54	0.4028	1.8	0.69	2181.8	33	2178.3	53	100.2

TABLE 6.4: U–Pb isotopic data obtained by LA-ICP-MS analyses at Géosciences Montpellier, France, on zircons from plutonic rocks of northern Ghana.[a] Corrected for background. [b]ρ is the $^{206}Pb/^{238}U/^{207}Pb/^{235}U$ error correlation coefficient. [c] Common Pb corrected using measured ^{204}Pb. [d] degree of concordance = $^{206}Pb/^{238}U$ age / $^{207}Pb/^{206}Pb$ age x 100.

Sample Analysis	Pb[a] (ppm)	Th[a] (ppm)	U[a] (ppm)	$\frac{Th}{U}$ [a]	$\frac{^{208}Pb}{^{206}Pb}$	$\frac{^{207}Pb}{^{206}Pb}$ [b]	±2σ (%)	$\frac{^{207}Pb}{^{235}U}$ [b]	±2σ (%)	$\frac{^{206}Pb}{^{238}U}$ [b]	±2σ (%)	ρ[c]	$\frac{^{206}Pb}{^{238}U}$ [c]	±2σ (Ma)	$\frac{^{207}Pb}{^{206}Pb}$	±2σ (Ma)	conc.[d] (%)
BN132																	
Granite																	
#1.1	75	84	219	0.38	0.23	0.1361	0.9	5.518	2.8	0.29410	2.7	0.95	1662	39	2178	15	76
#1.2	24	27	97	0.28	0.42	0.1372	2.1	4.083	3.9	0.21580	3.3	0.85	1259	38	2193	36	57
#2.1	120	117	265	0.44	0.41	0.1355	1.0	7.21	2.3	0.38600	2.0	0.89	2104	36	2170	18	97
#2.2	160	152	515	0.29	0.82	0.1331	1.3	5.194	3.1	0.28310	2.8	0.90	1607	39	2139	23	75
#3.1	99	352	5801	0.06	6.85	0.1007	4.8	0.1642	6.4	0.01182	4.2	0.66	76	3	1637	90	5
#3.2	290	193	1408	0.14	1.97	0.1143	1.8	2.94	2.7	0.18650	2.1	0.76	1102	21	1869	32	59
#4.1	110	68	250	0.27	0.26	0.1389	0.9	7.831	2.2	0.40900	2.0	0.92	2210	38	2213	15	100
#4.2	43	28	94	0.30	0.03	0.14	1.9	7.941	3.0	0.41140	2.2	0.76	2221	42	2227	34	100
#5.1	75	102	1320	0.08	2.44	0.114	4.4	0.8143	7.8	0.05182	6.5	0.83	326	21	1864	79	17
#6.1	93	148	680	0.22	0.64	0.1277	1.0	2.125	2.8	0.12070	2.6	0.93	735	18	2066	17	36
#7.1	160	179	391	0.46	0.71	0.1367	1.3	6.868	3.5	0.36430	3.3	0.92	2003	56	2186	23	92
#8.1	80	93	563	0.17	3.73	0.1257	2.8	1.911	4.7	0.11020	3.8	0.80	674	24	2039	50	33
#9.1	220	191	764	0.25	2.53	0.1282	1.9	4.59	2.6	0.25970	1.8	0.69	1488	24	2073	33	72
#9.2	88	67	294	0.23	2.02	0.1329	1.7	4.64	2.6	0.25320	1.9	0.74	1455	25	2137	31	68
#10.1	130	74	386	0.19	0.30	0.1359	0.9	6.071	2.7	0.32400	2.6	0.94	1809	41	2176	16	83
#10.2	160	144	529	0.27	0.36	0.1281	0.7	5.14	2.2	0.29110	2.0	0.94	1647	30	2072	13	80
#11.1	89	56	243	0.23	0.10	0.1362	1.5	6.383	4.5	0.33990	4.2	0.94	1886	69	2180	26	87
#11.2	71	51	158	0.32	b.d.	0.1392	1.2	7.901	2.4	0.41150	2.1	0.86	2222	39	2218	21	100
#12.1	120	121	370	0.33	0.30	0.1321	0.8	5.596	2.5	0.30730	2.4	0.95	1727	36	2126	13	81
#13.1	91	48	264	0.18	0.68	0.1279	0.8	5.859	6.1	0.33230	6.1	0.99	1850	99	2069	14	89
#14.1	89	67	198	0.34	b.d.	0.1391	1.1	7.89	2.8	0.41130	2.6	0.92	2221	49	2216	19	100
#14.2	100	69	402	0.17	0.31	0.129	1.3	4.31	2.2	0.24230	1.8	0.82	1399	23	2084	23	67
#15.1	100	86	258	0.33	1.34	0.1342	1.3	6.357	2.4	0.34360	2.0	0.83	1904	33	2154	23	88
#16.1	94	69	216	0.32	b.d.	0.1359	0.9	7.48	2.6	0.39920	2.5	0.95	2165	46	2175	15	100
#17.1	83	92	371	0.25	0.31	0.1314	1.0	3.624	2.6	0.19990	2.4	0.92	1175	26	2117	18	55
#17.2	91	68	222	0.31	0.22	0.136	1.1	7.041	2.4	0.37550	2.1	0.88	2055	38	2177	20	94
#18.1	160	172	1063	0.16	1.68	0.1217	2.5	2.387	5.8	0.14230	5.2	0.90	857	42	1981	45	43
#18.2	80	104	523	0.20	1.15	0.1343	1.4	2.359	3.2	0.12730	2.9	0.89	773	21	2155	25	36
#19.1	99	84	273	0.31	0.73	0.1309	1.2	5.93	2.4	0.32840	2.1	0.88	1831	34	2111	20	87
#20.1-r	23	14	52	0.27	0.76	0.1394	1.6	7.904	2.5	0.41120	1.9	0.76	2220	36	2220	28	100
#20.2-r	54	67	155	0.43	0.79	0.1346	1.2	5.61	2.4	0.30240	2.2	0.88	1703	32	2159	20	79
#21.1	140	148	564	0.26	1.14	0.1297	1.1	4.025	2.6	0.22510	2.3	0.91	1309	28	2094	19	62
#22.1	73	114	688	0.17	0.45	0.1275	1.2	1.589	13.5	0.09038	13.5	1.00	558	72	2064	21	27
#23.1	65	30	148	0.21	0.74	0.139	1.6	7.844	2.9	0.40920	2.4	0.83	2211	45	2215	28	100
#24.1	110	94	547	0.17	2.78	0.1312	2.1	2.931	3.9	0.16210	3.2	0.83	968	29	2114	38	46
#25.1-r	160	145	400	0.36	0.31	0.1324	1.0	6.806	2.6	0.37270	2.4	0.92	2042	42	2131	18	96
#26.1	90	57	202	0.28	0.82	0.1365	1.3	7.557	2.9	0.40140	2.6	0.89	2175	48	2184	23	100
#26.2	140	158	656	0.24	1.30	0.1273	1.2	3.39	2.3	0.19310	2.0	0.87	1138	21	2061	20	55
#27.1	69	60	150	0.40	0.03	0.1387	1.3	7.84	2.6	0.41000	2.2	0.86	2215	41	2211	23	100
#27.2	130	434	2302	0.19	8.73	0.1304	4.0	0.5999	6.3	0.03337	4.8	0.77	212	10	2103	70	10
#28.1	77	177	924	0.19	0.29	0.1235	1.3	1.263	5.8	0.07417	5.7	0.97	461	25	2007	23	23
#28.2	110	181	779	0.23	1.22	0.1295	1.3	2.192	3.5	0.12270	3.2	0.93	746	23	2092	22	36
#29.1	96	183	531	0.34	0.81	0.1229	1.6	2.761	8.8	0.16290	8.7	0.98	973	79	1999	29	49
#29.2	120	80	335	0.24	0.09	0.1366	0.9	6.213	2.3	0.32980	2.1	0.92	1838	34	2185	16	84
#30.1-r	80	67	195	0.34	0.22	0.1362	1.6	7.049	3.1	0.37530	2.6	0.85	2054	46	2180	29	94
#30.2-r	170	242	1463	0.17	13.16	0.1294	5.3	1.296	5.9	0.07261	2.7	0.45	452	12	2090	93	22
#31.1	43	39	143	0.27	0.65	0.14	1.2	5.08	2.5	0.26310	2.2	0.88	1506	30	2228	21	68
#31.2	180	257	1293	0.20	4.17	0.1373	2.6	2.078	3.6	0.10980	2.4	0.69	672	16	2193	45	31
#32.1	77	77	252	0.31	0.18	0.1353	1.0	5.141	2.8	0.27550	2.6	0.94	1569	36	2168	17	72
#32.2	140	144	734	0.20	1.00	0.1257	1.3	3.203	2.5	0.18480	2.1	0.86	1093	21	2039	22	54
#33.1	92	176	1088	0.16	1.58	0.1201	1.6	1.294	3.1	0.07815	2.7	0.86	485	13	1958	28	25
#33.2	59	41	132	0.31	0.18	0.1378	1.2	7.734	2.5	0.40720	2.2	0.88	2202	42	2199	21	100
#34.1	140	118	691	0.17	0.88	0.1282	1.3	3.387	4.0	0.19150	3.8	0.95	1130	40	2074	22	54
#34.2	120	105	783	0.13	0.81	0.1254	1.3	2.466	3.6	0.14260	3.4	0.93	860	27	2034	23	42
#35.1	23	36	158	0.23	0.94	0.1294	1.6	1.898	13.2	0.10640	13.1	0.99	652	81	2090	29	31
#35.2	180	47	2868	0.02	12.71	0.09088	7.1	0.3763	7.5	0.03003	2.6	0.34	191	5	1444	134	13
#36.1-r	400	120	1277	0.09	2.27	0.1337	2.9	5.595	11.4	0.30350	11.0	0.97	1709	168	2147	51	80
#37.1	59	48	169	0.28	0.26	0.1377	1.2	5.977	2.7	0.31490	2.4	0.89	1765	37	2198	21	80
#37.2	61	51	138	0.37	b.d.l	0.1391	1.1	7.805	2.8	0.40700	2.6	0.92	2201	48	2216	19	99
#38.1-r	14	10	31	0.33	0.33	0.1401	2.5	7.924	3.5	0.41030	2.5	0.72	2216	48	2228	42	99
#38.2-r	110	68	246	0.28	1.43	0.135	1.5	7.129	2.3	0.38290	1.8	0.78	2090	32	2165	26	97
#38.3-r	200	198	2151	0.09	12.82	0.1108	5.6	0.8609	6.1	0.05637	2.5	0.41	353	9	1812	102	20
#39.1	76	45	181	0.25	0.35	0.1361	1.2	7.323	2.4	0.39020	2.1	0.86	2124	38	2179	21	97
#39.2	110	102	529	0.19	2.36	0.1285	1.8	3.127	2.8	0.17650	2.2	0.78	1048	21	2078	31	50
#40.1	190	219	1545	0.14	8.78	0.131	4.0	1.522	4.5	0.08425	2.0	0.45	521	10	2112	71	25
#40.2	88	75	191	0.39	0.12	0.138	0.9	7.815	2.1	0.41080	2.0	0.91	2219	37	2202	15	101
#41.1	55	47	199	0.24	0.71	0.1333	1.6	4.672	2.9	0.25430	2.5	0.84	1460	32	2141	27	68
#42.1	86	95	281	0.34	0.37	0.1342	1.2	5.179	2.7	0.27980	2.5	0.90	1591	35	2154	21	74
#42.2	19	22	41	0.55	0.80	0.1382	2.6	7.785	3.8	0.40850	2.8	0.73	2208	53	2205	45	100
#43.1	130	75	383	0.20	0.28	0.1333	1.4	5.876	2.9	0.31960	2.6	0.88	1788	41	2142	25	83
#44.1	110	83	438	0.19	0.40	0.1321	1.0	4.355	2.3	0.23900	2.1	0.91	1382	26	2127	17	65
#45.1	150	154	664	0.23	3.47	0.1262	2.2	3.302	4.4	0.18970	3.8	0.86	1120	40	2046	40	55
#46.1	88	63	219	0.29	2.43	0.1331	2.0	6.426	2.7	0.35020	1.8	0.68	1936	31	2139	35	90
#47.1	96	111	444	0.25	2.00	0.1228	1.7	3.057	3.2	0.18050	2.7	0.84	1070	27	1998	30	54
#48.1	150	189	768	0.25	2.69	0.1253	2.0	2.864	3.1	0.16580	2.3	0.76	989	21	2032	35	49
#49.1	110	91	413	0.22	0.91	0.1304	1.2	4.288	2.7	0.23850	2.4	0.90	1379	30	2104	21	66
#50.1	83	56	186	0.30	0.21	0.1387	0.7	7.855	2.0	0.41060	1.9	0.93	2218	35	2211	13	100
#51.1	120	188	621	0.30	0.00	0.137	0.8	3.283	2.9	0.17370	2.7	0.96	1033	26	2190	14	47
#52.1	120	160	782	0.20	0.17	0.1327	1.2	2.667	2.6	0.14570	2.3	0.88	877	19	2134	21	41
#53.1-r	47	39	161	0.24	0.06	0.1361	1.0	5.112	2.4	0.27240	2.2	0.90	1553	31	2179	18	71
#53.2-r	110	85	299	0.28	0.13	0.138	0.8	6.444	2.8	0.33860	2.7	0.96	1880	44	2202	14	85
#53.3	120	110	795	0.14	0.19	0.1253	0.9	2.517	2.6	0.14560	2.5	0.93	876	20	2033	17	43
#54.1	130	121	290	0.42	b.d.l	0.1383	0.7	7.835	2.0	0.41080	1.8	0.93	2219	34	2206	13	101
#54.2	63	48	162	0.30	0.00	0.1367	1.2	6.519	2.9	0.34590	2.7	0.91	1915	44	2185	21	88
#55.1	76	69	306	0.23	0.00	0.1364	0.9	4.189	3.7	0.22260	3.6	0.97	1296	43	2183	16	59
#56.1	700	128	1766	0.07	b.d.l	0.1305	0.5	7.062	5.1	0.39240	5.1	1.00	2134	94	2105	9	101
BN90																	
Granite																	
#1.1	95	33	231	0.14	0.06	0.39740	2.1	7.359	2.3	0.1343	1.0	0.91	2157	39	2155	17	100
#1.2-r	85	40	197	0.21	3.37	0.37570	3.4	6.657	4.3	0.1285	2.6	0.79	2056	60	2078	47	99
#1.3	140	50	362	0.14	0.10	0.38670	2.3	7.087	2.4	0.1329	0.7	0.96	2107	42	2137	12	99
#1.4-r	130	41	361	0.11	4.74	0.30360	2.2	5.363	3.5	0.1281	2.8	0.62	1709	33	2072	49	82
#2.1	95	67	184	0.37	7.59	0.39180	4.1	7.195	5.7	0.1332	3.9	0.73	2131	76	2140	68	100
#2.2	310	631	4642	0.14	7.30	0.05746	2.9	0.4241	6.9	0.05353	6.2	0.42	360	10	351	141	103
#3.1	170	110	409	0.27	4.15	0.36880	2.1	6.597	3.3	0.1297	2.5	0.65	2024	37	2094	44	97
#3.2	68	26	176	0.15	0.70	0.36280	1.9	6.738	2.5	0.1347	1.6	0.76	1996	32	2160	28	92

TABLE 6.5: U–Pb isotopic data obtained by LA-ICP-MS analyses at Goethe Universität Frankfurt, Germany, on zircons from plutonic rocks of northern Ghana. Analyses on overgrowths or recrystallized domains are marked Ür. [a] U and Pb content and Th/U ratio were calculated relative to GJ-1 reference zircon. [b] corrected for background, within-run Pb/U fractionation (in case of $^{206}Pb/^{238}U$) and common Pb using Stacey and Kramers (1975) model Pb composition and subsequently normalised to GJ-1 (ID-TIMS value/measured value); $^{207}Pb/^{235}U$ calculated using $^{207}Pb/^{206}Pb/(^{238}U/^{206}Pb*1/137.88)$. [c] ρ is the $^{206}Pb/^{238}U/^{207}Pb/^{235}U$ error correlation coefficient. [d] degree of concordance = $^{206}Pb/^{238}U$ age / $^{207}Pb/^{206}Pb$ age x 100.

Sample Analysis	Pb[a] (ppm)	Th[a] (ppm)	U[a] (ppm)	$\frac{Th}{U}$ [a]	$\frac{^{208}Pb}{^{206}Pb}$	$\frac{^{207}Pb}{^{206}Pb}$ [b]	±2σ (%)	$\frac{^{207}Pb}{^{235}U}$ [b]	±2σ (%)	$\frac{^{206}Pb}{^{238}U}$ [b]	±2σ (%)	ρ[c]	$\frac{^{206}Pb}{^{238}U}$ [c]	±2σ (Ma)	$\frac{^{207}Pb}{^{206}Pb}$	±2σ (Ma)	conc.[d] (%)
BN90																	
Granite																	
#4.1	83	35	208	0.17	4.58	0.33120	2.5	5.961	3.8	0.1305	2.8	0.67	1844	40	2105	49	88
#4.2-r	420	55	884	0.06	12.41	0.33000	3.0	5.679	5.7	0.1248	4.8	0.52	1838	48	2026	85	91
#5.1-r	310	129	824	0.16	0.35	0.35290	2.1	6.381	2.2	0.1311	0.8	0.94	1948	35	2113	13	92
#5.2	160	226	454	0.50	3.18	0.28660	2.5	5.18	3.3	0.1311	2.1	0.75	1625	35	2112	38	77
#6.1	210	172	461	0.37	2.94	0.38020	2.4	6.78	3.3	0.1293	2.2	0.74	2077	43	2089	39	99
#6.2-r	520	462	4850	0.10	1.05	0.10660	3.0	1.275	3.3	0.08676	1.5	0.89	653	19	1355	29	48
#7.1	190	43	482	0.09	0.24	0.39330	2.0	7.217	2.1	0.1331	0.6	0.95	2138	36	2139	11	100
#7.2	97	63	235	0.27	0.40	0.37940	2.0	7.027	2.4	0.1343	1.3	0.85	2074	36	2155	22	96
#7.3	200	54	507	0.11	0.05	0.39190	2.5	7.183	2.7	0.1329	0.9	0.94	2132	46	2137	15	100
#8.1	96	77	212	0.36	1.39	0.39640	1.9	7.321	2.4	0.134	1.5	0.78	2153	35	2150	26	100
#8.2-r	440	824	5534	0.15	6.54	0.07226	2.0	0.5416	5.9	0.05436	5.5	0.34	450	9	386	124	116
#9.1-r	120	102	268	0.38	0.09	0.39480	2.8	7.278	3.1	0.1337	1.2	0.92	2145	52	2147	21	100
#9.2	90	39	218	0.18	0.09	0.39380	2.7	7.267	2.8	0.1338	0.9	0.95	2141	49	2149	16	100
#10.1	120	44	344	0.13	4.14	0.30610	2.0	5.472	3.4	0.1297	2.7	0.59	1722	30	2093	48	82
#10.2	110	46	256	0.18	0.73	0.39350	2.1	7.239	2.4	0.1334	1.1	0.88	2139	38	2143	20	100
#11.1	260	111	642	0.17	0.25	0.39040	2.6	7.095	2.8	0.1318	0.8	0.95	2125	48	2122	15	100
#11.2	300	61	760	0.08	0.05	0.38530	2.5	6.968	2.6	0.1312	0.7	0.97	2101	45	2114	12	99
#12.1	67	44	139	0.32	4.36	0.39540	2.5	7.326	3.8	0.1344	2.9	0.65	2148	45	2156	50	100
#12.2-r	86	39	195	0.20	3.55	0.38470	2.8	7.047	3.7	0.1328	2.4	0.75	2098	50	2136	43	98
#13.1	66	34	150	0.23	1.21	0.39470	2.7	7.235	3.5	0.133	2.3	0.76	2144	49	2137	40	100
#13.2	82	51	185	0.28	0.09	0.40770	2.2	7.591	2.4	0.135	1.0	0.91	2204	41	2164	18	102
#14.1-r	380	770	4699	0.16	2.73	0.07763	2.5	0.6095	4.4	0.05694	3.6	0.58	482	12	489	79	99
#14.2	62	27	138	0.19	5.10	0.38090	3.6	6.928	5.0	0.1319	3.5	0.72	2081	64	2123	61	98
#15.1	56	45	201	0.22	1.20	0.24730	2.4	4.472	2.8	0.1311	1.4	0.86	1425	31	2113	25	67
#15.2	240	75	601	0.12	0.05	0.39010	3.0	7.113	3.1	0.1322	0.8	0.97	2124	55	2128	14	100
#16.1	210	233	703	0.33	3.26	0.25900	3.5	4.461	4.1	0.1249	2.2	0.84	1485	46	2028	39	73
#17.1	150	49	360	0.14	2.08	0.37670	5.1	6.592	5.4	0.1269	1.9	0.94	2061	90	2056	33	100
#17.2-r	210	82	556	0.15	0.85	0.36320	2.2	6.526	2.4	0.1303	1.1	0.90	1997	38	2102	19	95
#18.1	290	22	807	0.03	17.49	0.24590	3.0	4.016	6.7	0.1184	6.0	0.44	1417	38	1933	108	73
#19.1	120	47	332	0.14	2.70	0.31730	6.3	5.627	6.8	0.1286	2.6	0.93	1776	98	2079	45	85
#19.2	140	54	341	0.16	0.54	0.37910	4.4	6.675	5.0	0.1277	2.4	0.87	2072	78	2066	43	100
#20.1	180	98	553	0.18	2.57	0.28030	2.6	5.039	3.1	0.1304	1.8	0.82	1593	36	2103	32	76
#20.2-r	280	474	4154	0.11	7.59	0.05779	2.8	0.4594	6.6	0.05765	6.0	0.42	362	10	517	131	70
#20.3-r	190	56	1648	0.03	17.29	0.08134	4.5	1.048	8.7	0.09342	7.4	0.51	504	22	1496	141	34
#21.1	670	104	3995	0.03	0.00	0.1155	0.5	2.722	2.5	0.17100	2.5	0.98	1017	23	1888	9	54
#21.2	100	48	233	0.21	2.23	0.131	2.0	7.084	2.8	0.39230	1.9	0.68	2133	35	2111	35	101
#22.1	97	54	233	0.23	0.02	0.38540	1.9	7.158	2.1	0.1347	0.9	0.90	2101	34	2160	16	97
#22.2	540	499	3592	0.14	0.04	0.14630	2.3	2.039	3.0	0.1011	1.9	0.76	880	19	1644	36	54
#23.1-r	400	180	1461	0.12	0.00	0.27150	4.2	4.416	4.4	0.1179	1.3	0.96	1549	58	1925	23	80
#24.1	100	30	510	0.06	0.10	0.18990	2.9	3.406	3.0	0.1301	0.9	0.96	1121	30	2100	15	53
#25.1	79	36	221	0.16	1.24	0.33350	2.1	6.006	2.6	0.1306	1.5	0.81	1855	34	2106	27	88
#26.1	120	96	304	0.32	0.89	0.34520	2.2	6.203	2.6	0.1303	1.4	0.84	1912	36	2102	25	91
#26.2	100	67	242	0.28	0.32	0.39260	2.1	7.188	2.4	0.1328	1.2	0.87	2135	38	2135	21	100
#27.1-r	470	332	2069	0.16	1.73	0.22230	2.4	3.437	3.3	0.1121	2.2	0.75	1294	29	1834	39	71
#28.1-r	180	57	491	0.12	0.17	0.36430	2.1	6.66	2.2	0.1326	0.8	0.94	2003	36	2132	13	94
#28.2-r	210	64	514	0.13	0.24	0.38740	3.2	6.752	3.4	0.1264	1.0	0.96	2111	58	2049	17	103
#29.1	280	53	833	0.06	0.01	0.32980	2.7	6.076	2.8	0.1336	0.8	0.96	1838	43	2146	14	86
#29.2-r	630	76	1673	0.05	0.04	0.37670	2.3	6.849	2.4	0.1319	0.6	0.97	2061	41	2123	10	97
#30.1	160	67	470	0.14	0.33	0.32990	2.5	6.047	2.6	0.1329	0.9	0.94	1838	40	2137	15	86
#31.1-r	290	188	1504	0.13	0.59	0.17580	2.8	3.276	3.1	0.1352	1.3	0.91	1044	27	2166	22	48
#32.1	260	210	971	0.22	3.26	0.23870	3.1	3.841	3.9	0.1167	2.5	0.78	1380	38	1906	44	72
#33.1	55	24	136	0.17	0.48	0.38030	2.3	7.055	2.6	0.1345	1.4	0.85	2078	40	2158	24	96
#33.2	69	34	163	0.21	b.d.	0.39720	2.5	7.298	2.7	0.1333	1.0	0.92	2156	45	2141	18	101
#34.1	200	165	448	0.37	0.78	0.39440	2.1	7.219	2.5	0.1327	1.3	0.85	2143	39	2135	23	100
#35.1	67	18	249	0.07	0.93	0.25510	3.5	4.634	3.8	0.1317	1.4	0.93	1465	46	2121	25	69
#36.1-r	450	60	2190	0.03	0.17	0.20800	3.5	3.191	3.6	0.1113	0.7	0.98	1218	39	1820	12	67
#36.2-r	360	178	1770	0.10	0.05	0.18910	3.4	3.486	3.5	0.1337	0.5	0.99	1116	35	2147	8	52
#37.1	380	63	966	0.07	0.03	0.39380	2.0	7.148	2.1	0.1316	0.7	0.94	2140	36	2120	13	101
#38.1	69	38	164	0.23	0.06	0.39490	2.2	7.278	2.5	0.1337	1.0	0.91	2145	41	2147	18	100
#38.2	270	31	744	0.04	0.42	0.36070	1.8	6.679	1.9	0.1343	0.6	0.95	1985	30	2155	10	92
#39.1	140	144	293	0.49	0.92	0.39480	2.1	7.255	2.4	0.1333	1.2	0.87	2145	38	2142	21	100
#39.2	180	60	591	0.10	0.15	0.28870	2.0	5.321	2.1	0.1337	0.6	0.95	1635	30	2147	11	76
#40.1	110	20	280	0.07	0.00	0.39270	1.9	7.104	2.0	0.1312	0.6	0.95	2135	35	2114	11	101
#41.1	400	144	1734	0.08	2.51	0.20550	3.2	3.718	3.6	0.1312	1.7	0.89	1205	35	2114	29	57
#42.1	100	89	239	0.37	0.28	0.38870	3.4	7.089	3.6	0.1323	1.3	0.93	2117	61	2128	23	99
#42.2-r	270	80	723	0.11	0.00	0.35850	2.3	6.48	2.4	0.1311	0.6	0.97	1975	40	2113	10	93
#43.1	110	87	238	0.36	0.26	0.39420	2.9	7.224	3.1	0.1329	1.1	0.93	2142	53	2137	20	100
#44.1	200	88	482	0.18	0.48	0.39140	2.1	7.166	2.3	0.1328	0.9	0.92	2129	38	2135	15	100
#44.2-r	970	368	3171	0.12	1.04	0.27090	4.3	4.727	4.5	0.1265	1.1	0.97	1546	60	2050	19	75
#45.1	40	15	97	0.16	0.02	0.39260	2.4	7.191	2.6	0.1329	1.1	0.91	2135	43	2136	19	100
#45.1-r	200	57	1701	0.03	0.70	0.11440	5.3	2.023	5.4	0.1283	1.2	0.98	698	35	2074	21	34
#46.1	120	62	301	0.21	6.71	0.32160	2.4	5.485	4.3	0.1237	3.5	0.56	1798	38	2010	63	89
#46.2	420	267	1895	0.14	0.00	0.21190	2.7	3.701	3.0	0.1267	1.3	0.91	1239	31	2052	22	60
#47.1	550	47	1445	0.03	0.03	0.38030	3.5	6.89	3.6	0.1314	0.8	0.97	2078	63	2117	15	98
#47.2	120	62	290	0.21	0.80	0.39280	1.9	7.215	2.3	0.1332	1.3	0.83	2136	35	2141	23	100
#48.1-r	110	24	264	0.09	0.12	0.39180	2.2	7.161	2.4	0.1326	1.0	0.91	2131	40	2132	17	100
#49.1	200	104	734	0.14	2.24	0.24530	3.7	4.425	4.2	0.1308	1.8	0.90	1414	47	2109	32	67
#49.2	120	126	272	0.46	1.34	0.37250	2.1	6.739	2.6	0.1312	1.4	0.83	2041	37	2114	25	97
#50.1	320	32	1033	0.03	0.02	0.31420	2.1	5.65	2.1	0.1304	0.5	0.97	1761	32	2103	9	84
#51.1	62	24	154	0.16	1.08	0.37240	2.0	6.82	2.8	0.1328	1.9	0.73	2041	35	2136	33	96
#52.1	150	83	1933	0.04	10.53	0.06001	2.8	0.6273	7.5	0.07581	7.0	0.37	376	10	1090	140	34
#53.1	86	53	201	0.26	0.11	0.39290	2.2	7.223	2.4	0.1333	1.1	0.90	2136	40	2142	19	100
BN241																	
Trondhjemite																	
#1.1	220	98	460	0.21	12.73	0.38310	2.9	6.582	7.4	0.1246	6.8	0.39	2091	52	2023	121	103
#2.1	460	73	2555	0.03	0.89	0.17750	3.5	3.017	4.4	0.1233	2.6	0.80	1053	34	2004	47	53
#3.1	56	36	127	0.28	0.32	0.39110	2.7	7.17	3.4	0.1329	2.1	0.79	2128	49	2137	37	100
#3.2	44	19	100	0.19	1.85	0.39560	5.2	7.294	5.6	0.1337	2.3	0.92	2149	95	2148	39	100
#4.1	31	28	66	0.42	0.60	0.39100	2.9	6.975	3.3	0.1294	1.6	0.88	2127	52	2090	28	102
#4.2	360	44	1011	0.04	1.36	0.34850	2.6	6.04	3.0	0.1257	1.5	0.87	1928	43	2039	26	95
#5.1	33	20	75	0.27	0.12	0.39750	4.5	7.4	4.7	0.135	1.5	0.95	2157	82	2164	27	100
#5.2-r	370	91	3279	0.03	9.49	0.09599	4.4	1.376	7.0	0.104	5.5	0.62	591	25	1696	101	35
#6.1-r	170	80	400	0.20	1.93	0.36740	2.7	6.702	3.2	0.1323	1.7	0.84	2017	47	2128	30	95
#6.2-r	280	16	753	0.02	0.05	0.37770	2.7	6.777	2.8	0.1301	0.7	0.97	2065	49	2100	12	98
#7.1	160	60	357	0.17	1.55	0.41330	2.3	7.659	4.6	0.1344	4.0	0.49	2230	43	2156	70	103
#7.2	380	60	1412	0.04	4.30	0.26160	3.3	3.811	4.7	0.1056	3.3	0.70	1498	44	1726	61	87
#8.1-r	730	27	2288	0.01	0.11	0.32370	2.2	5.754	2.5	0.1289	1.1	0.90	1808	36	2084	19	87
#9.1-r	180	57	1102	0.05	11.49	0.11560	9.5	1.908	11.2	0.1197	5.9	0.85	705	64	1952	105	36
#10.1	140	78	302	0.26	4.24	0.38780	4.7	6.735	5.6	0.126	3.0	0.84	2112	85	2043	54	103
#10.2-r	270	33	913	0.04	2.63	0.27780	3.5	5.049	4.1	0.1318	2.1	0.86	1580	50	2122	37	74
#11.1	110	63	252	0.25	0.20	0.39540	2.9	7.252	3.1	0.133	1.2	0.92	2148	53	2139	21	100
#11.2	49	32	110	0.29	0.35	0.39550	2.3	7.234	2.7	0.1327	1.3	0.86	2148	42	2133	24	101
#12.1	220	39	691	0.06	1.33	0.31200	3.0	5.461	3.4	0.1269	1.6	0.88	1751	46	2056	29	85

Sample Analysis	Pb^a (ppm)	Th^a (ppm)	U^a (ppm)	$\frac{Th}{U}^a$	$\frac{^{208}Pb}{^{206}Pb}$	$\frac{^{207}Pb}{^{206}Pb}^b$	$\pm 2\sigma$ (%)	$\frac{^{207}Pb}{^{235}U}^b$	$\pm 2\sigma$ (%)	$\frac{^{206}Pb}{^{238}U}^b$	$\pm 2\sigma$ (%)	ρ^c	$\frac{^{206}Pb^c}{^{238}U}$ (Ma)	$\pm 2\sigma$	$\frac{^{207}Pb}{^{206}Pb}$ (Ma)	$\pm 2\sigma$	conc.^{d} (%)
BN119																	
Granite#1.3	150	54	354	0.15	0.45	0.39240	3.3	7.179	3.9	0.1327	2.0	0.86	2134	61	2134	34	100
#2.1-r	160	48	389	0.12	b.d.l.	0.39260	3.8	7.182	4.0	0.1327	1.5	0.93	2135	69	2133	26	100
#2.2-r	260	66	743	0.09	0.20	0.35220	4.2	6.228	4.5	0.1283	1.7	0.93	1945	70	2074	29	94
#3.1	46	46	142	0.32	0.44	0.27760	4.0	5.105	4.3	0.1334	1.5	0.94	1579	56	2143	25	74
#3.2	310	82	967	0.08	0.80	0.31690	3.0	5.554	3.3	0.1271	1.4	0.90	1775	46	2058	26	86
#4.1	350	248	2037	0.12	1.02	0.15640	7.4	2.496	7.5	0.1157	1.6	0.98	937	65	1891	28	50
#5.1	130	203	314	0.64	0.38	0.32570	3.3	5.856	3.6	0.1304	1.4	0.92	1818	53	2103	25	86
#5.2	220	346	424	0.82	b.d.l.	0.39230	3.1	7.188	3.2	0.1329	0.8	0.97	2133	56	2137	14	100
#6.1	62	85	133	0.64	b.d.l.	0.38290	2.3	7.001	2.7	0.1326	1.4	0.86	2090	41	2133	24	98
#7.1	120	195	246	0.79	0.38	0.39220	2.6	7.175	2.9	0.1327	1.4	0.87	2133	47	2134	25	100
#7.2	230	77	637	0.12	3.76	0.32560	2.9	5.977	3.9	0.1331	2.6	0.75	1817	47	2140	45	85
#8.1	100	35	255	0.14	0.13	0.39230	3.1	7.185	3.3	0.1328	1.3	0.92	2133	56	2136	23	100
#8.2	160	33	373	0.09	0.02	0.39120	2.4	7.18	2.8	0.1331	1.5	0.86	2128	44	2140	25	99
#9.1	320	100	834	0.12	0.15	0.37810	3.1	6.773	3.2	0.1299	0.8	0.97	2067	54	2097	14	99
#10.1	560	1178	1046	1.13	0.05	0.37960	3.0	6.944	3.2	0.1327	1.1	0.94	2074	54	2134	19	97
#10.2	360	740	658	1.13	0.95	0.38910	3.2	7.053	3.6	0.1315	1.7	0.89	2119	58	2118	29	100
#11.1	120	171	247	0.69	0.14	0.38500	3.0	7.044	3.3	0.1327	1.2	0.93	2100	54	2134	22	98
#12.1	230	71	647	0.11	0.27	0.35040	3.3	6.288	3.5	0.1302	1.4	0.92	1936	55	2100	25	92
#12.2	250	501	527	0.95	1.18	0.33150	2.6	6.057	3.0	0.1325	1.5	0.86	1846	42	2132	27	87
#13.1-r	170	185	2131	0.09	1.55	0.06920	5.1	1.039	5.5	0.1089	1.9	0.94	431	21	1782	34	24
#13.2-r	340	242	2930	0.08	1.22	0.10690	6.4	1.631	6.7	0.1106	2.1	0.95	655	40	1809	38	36
#14.1	390	588	785	0.75	0.10	0.39550	3.1	7.323	3.4	0.1343	1.3	0.92	2148	57	2155	23	100
#14.2	260	363	581	0.62	0.17	0.36180	2.3	6.582	2.6	0.1319	1.2	0.88	1991	39	2124	21	94
#15.1	180	100	438	0.23	0.36	0.37530	2.3	6.829	2.6	0.132	1.3	0.88	2054	41	2124	22	97
#15.2-r	270	500	4643	0.11	6.00	0.04827	6.8	0.7461	7.7	0.1121	3.7	0.88	304	20	1834	67	17
#16.1-r	77	69	169	0.41	0.88	0.39200	2.5	7.156	3.3	0.1324	2.1	0.76	2132	46	2130	37	100
#16.2-r	400	108	1303	0.08	0.36	0.29010	4.4	5.273	4.6	0.1318	1.2	0.97	1642	64	2123	21	77
#17.1	43	59	187	0.32	0.76	0.16800	3.9	3.078	4.3	0.1329	1.7	0.92	1001	36	2136	29	47
#17.2-r	330	365	3234	0.11	10.13	0.08151	3.7	1.251	6.3	0.1113	5.1	0.59	505	18	1820	93	28
#18.1	80	61	180	0.34	0.09	0.39190	2.6	7.152	2.9	0.1324	1.3	0.90	2132	47	2129	22	100
#19.1	450	162	1708	0.09	0.30	0.25080	6.6	4.385	6.7	0.1268	1.6	0.97	1442	85	2054	28	70
#20.1	220	62	538	0.12	0.06	0.39050	3.0	7.137	3.1	0.1326	0.8	0.96	2125	55	2132	15	100
#21.1	220	42	557	0.07	0.19	0.39150	2.8	7.149	3.0	0.1324	1.1	0.94	2130	52	2131	18	100
#22.1	100	40	248	0.16	0.69	0.39270	5.4	7.211	6.6	0.1332	3.7	0.82	2135	99	2140	65	100
#23.1	160	105	462	0.23	0.37	0.31120	3.3	5.689	3.5	0.1326	1.3	0.93	1746	51	2133	23	82
#24.1	120	129	267	0.48	0.13	0.39050	3.0	7.195	3.4	0.1336	1.6	0.88	2125	55	2146	28	99
#24.2-r	700	578	4134	0.14	2.25	0.16530	2.7	2.416	3.8	0.106	2.6	0.73	986	25	1732	47	57
#25.1	250	527	562	0.94	b.d.l.	0.35090	5.8	6.229	6.0	0.1287	1.4	0.97	1939	98	2081	25	93
#26.1-r	100	52	303	0.17	1.17	0.30060	2.7	5.493	3.2	0.1326	1.8	0.84	1694	40	2132	31	79
#26.2-r	410	64	2145	0.03	1.22	0.18900	5.1	2.911	5.4	0.1117	1.9	0.94	1116	53	1827	34	61
#26.3	130	163	283	0.58	0.45	0.39430	2.2	7.255	2.6	0.1335	1.4	0.85	2143	41	2144	24	100
#27.1	97	158	264	0.60	0.26	0.29210	2.5	5.318	2.8	0.1321	1.3	0.89	1652	36	2126	23	78
#28.1	130	40	328	0.12	0.18	0.39150	2.5	7.15	2.6	0.1325	0.8	0.95	2130	45	2131	15	100
#29.1	250	182	638	0.28	0.30	0.36030	3.5	6.225	3.7	0.1253	1.3	0.94	1984	60	2033	23	98
#30.1	310	215	960	0.22	0.15	0.29830	3.4	5.397	3.6	0.1312	1.1	0.95	1683	50	2114	19	80
#30.2	110	48	491	0.10	0.62	0.20220	3.8	3.619	4.0	0.1298	1.3	0.94	1187	41	2095	23	57
#31.1	110	123	238	0.52	0.38	0.39380	2.4	7.212	2.8	0.1328	1.6	0.83	2140	43	2136	27	100
#32.1-r	410	66	1278	0.05	0.16	0.31520	3.2	5.731	3.5	0.1319	1.3	0.92	1766	50	2123	23	83
#32.2-r	58	19	194	0.10	0.70	0.28290	2.6	5.138	3.1	0.1317	1.5	0.87	1606	38	2121	27	76
#33.1	47	41	103	0.40	0.11	0.38830	3.2	7.139	4.0	0.1333	2.4	0.80	2115	58	2142	43	99
BN270																	
Granodiorite																	
#1.1	40	24	96	0.25	0.07	0.39210	1.9	7.39	2.3	0.1367	1.2	0.85	2133	35	2186	21	98
#1.2	56	37	142	0.26	0.13	0.36450	2.5	6.802	2.6	0.1353	0.9	0.93	2004	43	2168	17	92
#2.1	130	78	302	0.26	b.d.l.	0.40360	2.0	7.601	2.2	0.1366	0.9	0.92	2185	37	2185	15	100
#3.1	240	235	532	0.44	0.02	0.40270	1.9	7.549	1.9	0.136	0.6	0.96	2181	35	2177	10	100
#4.1	58	38	152	0.25	0.11	0.35330	1.9	6.612	2.2	0.1357	1.0	0.88	1950	33	2173	18	90
#5.1	150	55	360	0.15	0.05	0.40110	2.4	7.529	2.5	0.1362	0.9	0.94	2174	44	2179	15	100
#6.1	100	62	281	0.22	0.00	0.33280	2.3	6.355	2.4	0.1385	0.6	0.97	1852	37	2208	10	84
#6.2	65	42	149	0.28	0.00	0.40340	1.7	7.587	1.9	0.1364	0.8	0.89	2185	31	2182	15	100
#7.1	67	50	171	0.29	0.07	0.34860	1.9	6.607	2.1	0.1375	1.0	0.90	1928	32	2196	17	88
#7.2	180	141	458	0.31	0.01	0.35690	2.8	6.675	2.9	0.1356	0.6	0.98	1968	48	2172	10	91
#8.1	160	40	401	0.10	b.d.l.	0.38350	1.7	7.2	1.8	0.1362	0.7	0.93	2093	31	2179	11	96
#9.1	62	38	141	0.27	0.00	0.40670	2.1	7.648	2.2	0.1364	0.8	0.94	2200	39	2182	13	101
#9.2	61	78	170	0.46	0.06	0.31190	2.7	5.852	2.8	0.1361	0.9	0.95	1750	41	2178	16	80
#10.1	86	36	269	0.13	0.50	0.30750	5.7	5.791	5.8	0.1366	0.9	0.99	1729	88	2184	17	79
#11.1	120	62	287	0.22	0.01	0.40040	2.2	7.548	2.3	0.1367	0.7	0.96	2171	42	2186	12	99
#12.1	75	52	180	0.29	0.05	0.38080	1.9	7.186	2.1	0.1369	0.9	0.91	2080	34	2188	15	95
#12.2	94	50	274	0.18	0.03	0.32080	2.2	6.131	2.3	0.1386	0.8	0.95	1794	34	2210	13	81
#13.1	89	56	204	0.27	0.03	0.40410	1.9	7.632	2.1	0.137	0.8	0.93	2188	36	2189	13	100
#14.1	69	138	166	0.83	0.02	0.36670	2.7	6.97	2.8	0.1378	0.9	0.94	2014	46	2200	16	92
#15.1	63	32	148	0.22	0.00	0.40280	2.3	7.596	2.5	0.1368	0.9	0.93	2182	42	2187	16	100
#15.2	56	40	125	0.32	0.04	0.40530	2.1	7.648	2.3	0.1369	1.1	0.89	2193	39	2188	18	100
#16.1	90	57	209	0.27	0.03	0.40130	3.0	7.478	3.1	0.1351	0.9	0.96	2175	56	2166	15	100
#16.2	51	28	133	0.21	0.06	0.35850	2.6	6.741	2.8	0.1364	1.0	0.94	1975	44	2182	17	91
#17.1	150	114	380	0.30	0.12	0.36420	2.1	6.859	2.2	0.1366	0.7	0.95	2002	36	2184	12	92
#17.2	81	52	184	0.28	0.00	0.40360	2.3	7.578	2.5	0.1362	1.0	0.92	2185	43	2179	17	100
#18.1	44	21	102	0.21	0.10	0.40090	2.0	7.53	2.3	0.1362	1.1	0.88	2173	37	2180	19	100
#18.2	190	90	478	0.19	0.00	0.38110	2.2	7.173	2.2	0.1365	0.5	0.97	2081	39	2184	9	95
#19.1	21	14	48	0.29	b.d.l.	0.40140	2.7	7.598	3.0	0.1373	1.3	0.91	2175	50	2193	22	99
#19.2	64	66	147	0.45	b.d.l.	0.37810	1.9	7.102	2.2	0.1362	1.1	0.87	2068	35	2180	19	95
#20.1	52	41	129	0.32	b.d.l.	0.36520	2.0	6.944	2.5	0.1379	1.4	0.82	2007	35	2201	25	91
#20.2	100	42	252	0.17	0.16	0.38260	3.0	7.237	3.3	0.1372	1.4	0.91	2089	54	2192	23	95
#21.1	25	19	54	0.36	0.04	0.40400	2.6	7.58	2.8	0.1361	1.3	0.90	2187	48	2178	22	100
#21.2	89	66	218	0.30	0.00	0.37620	2.1	7.103	2.4	0.1369	1.2	0.87	2058	38	2189	21	94
#22.1	47	59	113	0.52	0.04	0.34780	2.7	6.545	2.9	0.1365	0.9	0.94	1924	45	2183	16	88
#23.1	220	197	477	0.41	0.00	0.40500	1.9	7.612	2.0	0.1363	0.5	0.96	2192	36	2181	9	101
#23.2	41	32	94	0.33	0.08	0.38550	2.2	7.395	2.4	0.1391	1.1	0.88	2102	39	2216	20	95
#24.1	110	47	270	0.18	0.13	0.40280	2.7	7.578	2.8	0.1365	0.8	0.95	2182	49	2183	15	100
#25.1	53	34	121	0.29	0.00	0.40270	2.1	7.561	2.4	0.1362	1.1	0.89	2181	40	2179	19	100
#26.1	120	74	308	0.24	0.00	0.37620	2.2	7.035	2.3	0.1356	0.7	0.95	2058	39	2172	13	95
#27.1	65	89	140	0.63	0.20	0.38590	2.5	7.204	2.8	0.1354	1.2	0.90	2104	45	2169	21	97
#27.2	78	73	188	0.39	0.06	0.36850	2.7	6.933	2.9	0.1365	1.0	0.94	2022	47	2183	17	93
#28.1	150	170	329	0.52	0.16	0.40170	2.1	7.503	2.2	0.1354	0.7	0.95	2177	40	2170	12	100
#28.2	110	60	295	0.20	0.03	0.33990	2.1	6.393	2.2	0.1364	0.7	0.95	1886	34	2182	12	86
#28.3	83	37	195	0.19	b.d.l.	0.40290	1.9	7.636	2.1	0.1375	0.8	0.92	2182	36	2196	15	99
#29.1	59	26	138	0.19	0.06	0.40020	1.9	7.499	2.2	0.1359	1.1	0.88	2170	35	2176	18	100
#29.2	55	23	131	0.17	0.02	0.40180	2.0	7.566	2.2	0.1366	0.8	0.93	2177	37	2184	14	100

Sample / Analysis	$^{176}Yb/^{177}Hf^{a}$	$\pm 2\sigma$ (10^{-4}))	$^{176}Lu/^{177}Hf^{a}$	$\pm 2\sigma$ (10^{-4}))	$^{178}Hf/^{177}Hf$	$^{180}Hf/^{177}Hf$	Sig^{b}_{Hf} (V)	$^{176}Hf/^{177}Hf$	$\pm 2\sigma^{c}$	$^{176}Hf/^{177}Hf_{(t)}$	$\varepsilon Hf^{d}_{(t)}$	$\pm 2\sigma^{c}$	T^{e}_{DM} (Ga)	Age^{e} (Ma)	$\pm 2\sigma$	conc.	$\varepsilon Hf_{(Int)}$
BN132																	**2210 Ma**
#4.2	0.0590	60	0.00236	25	1.46720	1.88670	8	0.281646	32	0.281546	6.7	1.1	2.38	2227	34	100	6.3
#10.2	0.1478	46	0.00386	14	1.46710	1.88659	11	0.281673	40	0.281521	2.2	1.4	2.51	2072	13	80	5.0
#11.2	0.0372	53	0.00147	17	1.46718	1.88654	11	0.281567	38	0.281505	5.0	1.4	2.47	2218	21	100	4.8
#14.1	0.1184	253	0.00360	63	1.46718	1.88661	8	0.281664	35	0.281512	5.2	1.3	2.45	2216	19	100	5.1
#14.2	0.0830	48	0.00258	14	1.46718	1.88661	11	0.281623	30	0.281520	2.4	1.1	2.50	2084	23	67	5.1
#16.1	0.0555	40	0.00222	16	1.46714	1.88658	5	0.281619	43	0.281527	4.8	1.5	2.45	2175	15	100	5.5
#17.2	0.1028	86	0.00291	20	1.46713	1.88656	6	0.281601	28	0.281480	3.2	1.0	2.54	2177	20	94	3.9
#20.1-r	0.1332	233	0.00356	60	1.46716	1.88651	10	0.281645	34	0.281495	4.7	1.2	2.49	2220	28	100	4.5
#26.1	0.0430	29	0.00163	10	1.46715	1.88662	10	0.281593	29	0.281525	4.9	1.0	2.44	2184	23	100	5.5
#26.2	0.0713	129	0.00236	36	1.46716	1.88668	11	0.281611	33	0.281518	1.8	1.2	2.52	2061	20	55	5.0
#27.1	0.0732	80	0.00200	21	1.46720	1.88668	14	0.281575	27	0.281491	4.3	0.9	2.50	2211	23	100	4.3
#32.2	0.0985	115	0.00307	31	1.46714	1.88654	10	0.281634	36	0.281515	1.2	1.3	2.54	2039	22	54	4.8
#33.1	0.1599	267	0.00441	73	1.46715	1.88665	12	0.281674	37	0.281510	-0.8	1.3	2.59	1958	28	25	4.2
#33.2	0.0549	83	0.00174	20	1.46721	1.88656	11	0.281564	32	0.281490	4.0	1.2	2.50	2199	21	100	4.3
#34.2	0.0929	63	0.00283	18	1.46719	1.88674	7	0.281607	37	0.281498	0.5	1.3	2.57	2034	23	42	4.2
#35.1	0.0733	49	0.00226	14	1.46718	1.88656	12	0.281608	34	0.281518	2.5	1.2	2.51	2090	29	31	5.1
#38.1-r	0.0121	2	0.00056	1	1.46715	1.88655	9	0.281499	29	0.281475	4.2	1.0	2.52	2228	42	99	3.7
#38.2-r	0.0118	3	0.00051	1	1.46720	1.88669	10	0.281497	27	0.281476	2.7	1.0	2.55	2165	26	97	3.8
#38.3-r	0.0755	297	0.00193	70	1.46716	1.88661	16	0.281588	29	0.281521	-3.8	1.0	2.63	1812	102	20	4.9
#39.2	0.0416	15	0.00148	3	1.46712	1.88651	11	0.281579	39	0.281520	2.3	1.4	2.51	2078	31	50	5.2
#40.2	0.0423	25	0.00159	6	1.46718	1.88663	11	0.281579	39	0.281512	4.9	1.4	2.46	2202	15	101	5.1
#45.1	0.1279	146	0.00395	35	1.46718	1.88667	9	0.281655	37	0.281501	0.9	1.3	2.56	2046	40	55	4.2
#50.1	0.0941	116	0.00284	31	1.46720	1.88659	12	0.281643	37	0.281524	5.5	1.3	2.43	2211	13	100	5.5
#53.2-r	0.0686	33	0.00246	9	1.46711	1.88665	10	0.281572	34	0.281469	3.4	1.2	2.54	2202	14	85	3.5
#53.1-r	0.0517	74	0.00182	25	1.46711	1.88669	10	0.281544	34	0.281469	2.8	1.2	2.56	2179	18	71	3.5
#54.1	0.0811	43	0.00285	16	1.46711	1.88667	10	0.281606	35	0.281486	4.0	1.2	2.51	2206	13	101	4.1
										0.281505							**4.7**
										± 0.000041							**± 1.4**
BN90																	**2135 Ma**
#1.1	0.0241	7	0.00095	2	1.46721	1.88647	8	0.281592	33	0.281553	5.3	1.2	2.40	2155	17	100	4.8
#1.2-r	0.0250	18	0.00087	7	1.46721	1.88655	12	0.281581	30	0.281547	3.2	1.1	2.45	2078	47	99	4.5
#2.1	0.0381	12	0.00130	4	1.46712	1.88662	7	0.281590	37	0.281537	4.3	1.3	2.44	2140	68	100	4.2
#2.2	0.0424	9	0.00123	2	1.46713	1.88678	12	0.281561	29	0.281553	-35.8	1.0	3.20	351	141	103	3.3
#4.1	0.0451	18	0.00176	4	1.46718	1.88670	14	0.281584	27	0.281513	2.7	1.0	2.51	2105	49	88	3.3
#4.2-r	0.0282	8	0.00095	2	1.46715	1.88683	10	0.281544	30	0.281507	0.6	1.1	2.56	2026	85	91	3.1
#6.1	0.0400	28	0.00131	10	1.46716	1.88644	10	0.281586	29	0.281534	3.0	1.0	2.48	2089	39	99	4.0
#6.2-r	0.0387	21	0.00120	5	1.46717	1.88675	16	0.281546	30	0.281515	-14.5	1.1	2.86	1355	29	48	2.8
#7.1	0.0295	4	0.00108	3	1.46722	1.88662	12	0.281564	36	0.281520	3.7	1.3	2.48	2139	11	100	3.6
#7.2	0.0234	16	0.00093	6	1.46716	1.88655	9	0.281556	33	0.281518	4.0	1.2	2.47	2155	22	96	3.6
#8.1	0.0271	19	0.00097	3	1.46719	1.88666	10	0.281544	26	0.281504	3.4	0.9	2.50	2150	26	100	3.0
#8.2-r	0.0405	14	0.00128	2	1.46714	1.88657	15	0.281573	30	0.281563	-34.6	1.1	3.17	386	124	116	3.6
#9.1-r	0.0390	6	0.00136	2	1.46713	1.88685	10	0.281556	31	0.281501	3.2	1.1	2.51	2147	21	100	2.9
#9.2	0.0248	8	0.00094	2	1.46718	1.88672	9	0.281552	31	0.281513	3.7	1.1	2.49	2149	16	100	3.4
#11.1	0.0307	10	0.00112	4	1.46722	1.88664	11	0.281556	31	0.281511	3.0	1.1	2.50	2122	15	100	3.3
#11.2	0.0122	5	0.00048	2	1.46714	1.88660	14	0.281527	35	0.281508	2.7	1.2	2.51	2114	12	99	3.2
#14.1-r	0.0406	16	0.00126	5	1.46714	1.88677	14	0.281566	25	0.281555	-32.6	0.9	3.15	489	79	99	3.4
#14.2	0.0263	15	0.00083	4	1.46719	1.88659	11	0.281560	28	0.281526	3.6	1.0	2.47	2123	61	98	3.8
#15.1	0.0345	22	0.00138	7	1.46722	1.88665	20	0.281561	30	0.281505	2.6	1.1	2.52	2113	25	67	3.1
#15.2	0.0091	2	0.00040	1	1.46718	1.88650	27	0.281502	38	0.281486	2.2	1.4	2.55	2128	14	100	2.4
#20.1	0.0170	10	0.00056	3	1.46715	1.88664	8	0.281531	35	0.281509	2.5	1.2	2.52	2103	32	76	3.2
#20.2-r	0.0323	10	0.00108	2	1.46716	1.88688	11	0.281537	30	0.281527	-33.0	1.1	3.19	517	131	70	2.6
#20.3-r	0.0454	24	0.00133	4	1.46717	1.88667	13	0.281568	30	0.281531	-10.7	1.1	2.76	1496	141	34	3.4
#21.2	0.0098	12	0.00038	5	1.46724	1.88658	10	0.281531	27	0.281518	-2.2	1.0	2.61	1888	9	54	3.5
#21.1	0.0197	9	0.00076	4	1.46724	1.88682	7	0.281541	35	0.281510	2.7	1.3	2.51	2111	35	101	3.2
#22.1	0.0215	11	0.00086	4	1.46722	1.88676	10	0.281542	28	0.281506	3.7	1.0	2.49	2160	16	97	3.1
#23.1-r	0.0286	27	0.00097	9	1.46716	1.88664	14	0.281526	29	0.281491	-2.3	1.0	2.64	1925	23	80	2.4
#25.1	0.0227	7	0.00086	3	1.46718	1.88659	14	0.281575	33	0.281540	3.7	1.2	2.45	2106	27	88	4.3
#32.1	0.0260	15	0.00094	4	1.46713	1.88670	12	0.281565	30	0.281531	-1.3	1.1	2.57	1906	44	72	3.8
#33.2	0.0301	37	0.00096	12	1.46718	1.88645	17	0.281609	28	0.281569	5.5	1.0	2.38	2141	18	101	5.4
#34.1	0.0321	34	0.00117	13	1.46711	1.88660	12	0.281573	30	0.281526	3.8	1.1	2.47	2135	23	100	3.8
#36.1-r	0.0316	16	0.00116	4	1.46714	1.88656	20	0.281565	27	0.281525	-3.5	0.9	2.62	1820	12	67	3.5
#36.2-r	0.0211	6	0.00079	2	1.46713	1.88671	23	0.281496	27	0.281463	1.9	0.9	2.58	2147	8	52	1.6
#39.1	0.0284	28	0.00105	10	1.46717	1.88662	10	0.281573	30	0.281530	4.1	1.1	2.46	2142	21	100	4.0
#40.1	0.0213	20	0.00080	9	1.46724	1.88660	18	0.281545	31	0.281512	2.8	1.1	2.50	2114	11	101	3.3
#42.1	0.0203	29	0.00077	10	1.46719	1.88663	10	0.281552	33	0.281521	3.5	1.2	2.48	2128	23	99	3.6
#42.2-r	0.0408	17	0.00133	8	1.46715	1.88678	15	0.281547	27	0.281493	2.1	1.0	2.54	2113	10	93	2.6
#43.1	0.0318	52	0.00114	17	1.46714	1.88672	12	0.281545	30	0.281498	2.9	1.1	2.52	2137	20	100	2.8
#44.1	0.0193	15	0.00074	6	1.46716	1.88664	15	0.281530	29	0.281499	2.9	1.0	2.52	2135	15	100	2.9
#44.2-r	0.0274	20	0.00107	7	1.46717	1.88657	21	0.281562	31	0.281521	1.7	1.1	2.52	2050	19	75	3.6
#45.1	0.0199	33	0.00076	11	1.46721	1.88662	13	0.281568	34	0.281538	4.3	1.2	2.44	2136	19	100	4.2
#47.1	0.0232	11	0.00086	3	1.46718	1.88669	17	0.281534	26	0.281499	2.4	0.9	2.53	2117	15	98	2.8
#47.2	0.0389	40	0.00135	12	1.46718	1.88663	17	0.281586	30	0.281531	4.1	1.1	2.45	2141	23	100	4.0
#48.1-r	0.0258	8	0.00094	2	1.46720	1.88653	16	0.281588	26	0.281550	4.6	0.9	2.42	2132	17	100	4.7
#51.1	0.0206	8	0.00076	2	1.46714	1.88656	12	0.281546	32	0.281515	3.4	1.1	2.49	2136	33	96	3.4
#52.1-r	0.0435	25	0.00144	6	1.46721	1.88663	19	0.281592	29	0.281563	-18.8	1.0	2.88	1090	140	34	4.1
#53.1	0.0247	4	0.00084	1	1.46714	1.88650	17	0.281577	27	0.281542	4.6	1.0	2.43	2142	19	100	4.4
										0.281522							**3.5**
										± 0.000044							**± 1.2**

TABLE 6.6: Lu-Hf isotopic data of zircons from plutonic rocks of northern Ghana, obtained by LA–ICP(SF)–MS analyses at Goethe University Frankfurt, Germany. Analyses on overgrowths or recrystallized domains are indicated as Ür. [a] : $^{176}Yb/^{177}Hf = {}^{176}Yb/^{173}Yb_{true}$ x $^{173}Yb/^{177}Hf_{meas}$ x $(M_{173}(Yb)/M_{177}(Hf))b(Hf)$, $b(Hf) = \ln[(^{179}Hf/^{177}Hf_{true})/(^{179}Hf/^{177}Hf_{meas})]/\ln[M_{179}(Hf)/M_{177}(Hf)]$. [b] Mean Hf signal in Volt. [c] Uncertainties are quadratic additions of the within-run precision and the daily reproducibility of the zircon GJ-1. Uncertainties for GJ-1 is 2 standard deviation. [d] Initial $^{176}Hf/^{177}Hf$ and εHf calculated using the age in column ([e]), and the CHUR parameters : $^{176}Lu/^{177}Hf = 0.0336$, and $^{176}Hf/^{177}Hf = 0.282785$ (Bouvier et al., 2008). [e] two stage model age in billion years using the measured $^{176}Lu/^{177}Lu$ (first stage), a value of 0.0113 for the average continental crust (second stage), and a depleted mantle $^{176}Lu/^{177}Hf$ and $^{176}Hf/^{177}Hf$ of 0.03933 and 0.283294 (Blichert-Toft and Puchtel, 2010).

Sample Analysis	$\frac{^{176}Yb}{^{177}Hf}$[a]	$\pm 2\sigma$ (10^{-4}))	$\frac{^{176}Lu}{^{177}Hf}$[a]	$\pm 2\sigma$ (10^{-4}))	$\frac{^{178}Hf}{^{177}Hf}$	$\frac{^{180}Hf}{^{177}Hf}$	Sig^{b}_{Hf} (V)	$\frac{^{176}Hf}{^{177}Hf}$	$\pm 2\sigma$[c]	$\frac{^{176}Hf}{^{177}Hf}_{(t)}$	$\varepsilon Hf^{d}_{(t)}$	$\pm 2\sigma$[c]	T^{e}_{DM} (Ga)	Age[e] (Ma)	$\pm 2\sigma$	conc.	$\varepsilon Hf_{(Int)}$
BN119																	**2135 Ma**
#1.1	0.0254	19	0.00089	6	1.46717	1.88666	17	0.281563	28	0.281527	3.8	1.0	2.47	2132	37	99	3.9
#1.2	0.0326	14	0.00119	6	1.46716	1.88657	16	0.281589	29	0.281541	4.1	1.0	2.44	2124	32	82	4.3
#2.2-r	0.0221	13	0.00077	5	1.46719	1.88665	10	0.281575	31	0.281545	3.1	1.1	2.46	2074	29	94	4.5
#5.1	0.0660	9	0.00239	3	1.46719	1.88683	9	0.281640	29	0.281544	3.7	1.0	2.45	2103	25	86	4.4
#5.2	0.0527	28	0.00197	10	1.46717	1.88674	10	0.281649	30	0.281569	5.4	1.1	2.38	2137	14	100	5.3
#8.1	0.0159	20	0.00057	6	1.46720	1.88680	18	0.281541	31	0.281518	3.5	1.1	2.48	2136	23	100	3.5
#8.2	0.0351	58	0.00116	18	1.46711	1.88692	11	0.281580	42	0.281533	4.2	1.5	2.45	2140	25	99	4.1
#12.1	0.0510	22	0.00160	7	1.46714	1.88671	17	0.281601	28	0.281537	3.4	1.0	2.46	2100	25	92	4.2
#12.2	0.0171	2	0.00066	1	1.46720	1.88665	12	0.281528	26	0.281501	2.9	0.9	2.52	2132	27	87	2.9
#14.1	0.0480	123	0.00144	36	1.46712	1.88669	13	0.281602	35	0.281543	4.9	1.3	2.42	2155	23	100	4.4
#14.2	0.0508	71	0.00148	20	1.46723	1.88648	14	0.281624	35	0.281565	4.9	1.2	2.40	2124	21	94	5.2
#16.1-r	0.0268	15	0.00108	7	1.46719	1.88656	11	0.281561	30	0.281517	3.4	1.1	2.49	2130	37	100	3.5
#16.2-r	0.0347	25	0.00115	9	1.46721	1.88666	15	0.281577	29	0.281531	3.7	1.0	2.46	2123	21	77	4.0
#18.1	0.0330	15	0.00115	5	1.46718	1.88672	18	0.281564	27	0.281517	3.4	1.0	2.49	2129	22	100	3.5
#21.1	0.0350	44	0.00119	13	1.46717	1.88667	22	0.281581	31	0.281532	3.9	1.1	2.46	2131	18	100	4.0
#26.1-r	0.0361	42	0.00111	13	1.46718	1.88664	17	0.281578	29	0.281533	4.0	1.0	2.46	2132	31	79	4.1
#26.2-r	0.0507	13	0.00167	3	1.46717	1.88680	21	0.281586	31	0.281528	-3.2	1.1	2.61	1827	34	61	3.5
#26.3	0.0189	22	0.00063	8	1.46719	1.88655	13	0.281563	29	0.281537	4.4	1.0	2.44	2144	24	100	4.2
#28.1	0.0174	6	0.00062	2	1.46717	1.88653	16	0.281563	32	0.281538	4.2	1.1	2.45	2131	15	100	4.2
#30.1	0.0379	32	0.00126	12	1.46717	1.88661	13	0.281574	33	0.281523	3.2	1.2	2.48	2114	19	80	3.7
#30.2	0.0278	20	0.00100	8	1.46721	1.88668	13	0.281584	30	0.281544	3.5	1.1	2.45	2095	23	57	4.4
#33.1	0.0463	35	0.00160	9	1.46719	1.88672	17	0.281643	26	0.281577	5.8	0.9	2.36	2142	43	99	5.6
										0.281585							**4.2**
										± 0.000035							**± 1.3**
BN270																	**2180 Ma**
#1.1	0.0160	15	0.00068	6	1.46715	1.88683	9	0.281497	31	0.281468	2.9	1.1	2.56	2186	21	98	2.8
#1.2	0.0231	7	0.00095	2	1.46712	1.88674	10	0.281497	32	0.281458	2.2	1.2	2.58	2168	17	92	2.4
#2.1	0.0262	12	0.00111	5	1.46722	1.88679	11	0.281543	32	0.281497	3.9	1.1	2.50	2185	15	100	3.8
#3.1	0.0175	24	0.00076	9	1.46719	1.88674	15	0.281489	28	0.281458	2.4	1.0	2.58	2177	10	100	2.4
#7.1	0.0225	15	0.00096	6	1.46722	1.88666	11	0.281529	32	0.281489	3.9	1.2	2.51	2196	17	88	3.6
#8.1	0.0270	14	0.00145	7	1.46715	1.88669	22	0.281520	27	0.281460	2.5	1.0	2.57	2179	11	96	2.5
#9.1	0.0243	13	0.00100	4	1.46714	1.88656	10	0.281534	36	0.281493	3.7	1.3	2.51	2182	13	101	3.7
#9.2	0.0391	16	0.00148	5	1.46710	1.88674	12	0.281546	28	0.281484	3.3	1.0	2.53	2178	16	80	3.4
#12.1	0.0247	7	0.00102	2	1.46718	1.88666	11	0.281536	32	0.281494	3.9	1.1	2.50	2188	15	95	3.7
#12.2	0.0198	17	0.00076	6	1.46714	1.88662	15	0.281529	34	0.281497	4.5	1.2	2.49	2210	13	81	3.8
#13.1	0.0195	16	0.00081	6	1.46718	1.88663	14	0.281520	29	0.281486	3.7	1.0	2.52	2189	13	100	3.5
#14.1	0.0289	74	0.00093	20	1.46719	1.88645	13	0.281538	29	0.281499	4.4	1.0	2.49	2200	16	92	3.9
#15.1	0.0187	12	0.00078	4	1.46712	1.88679	14	0.281489	31	0.281456	2.5	1.1	2.58	2187	16	100	2.4
#15.2	0.0168	11	0.00068	4	1.46717	1.88666	13	0.281498	30	0.281469	3.0	1.1	2.55	2188	18	100	2.9
#17.1	0.0190	10	0.00076	4	1.46717	1.88657	14	0.281503	27	0.281471	3.0	1.0	2.55	2184	12	92	2.9
#17.2	0.0258	13	0.00103	4	1.46717	1.88671	13	0.281504	30	0.281461	2.5	1.1	2.57	2179	17	100	2.5
#18.1	0.0217	14	0.00092	5	1.46719	1.88667	8	0.281508	32	0.281470	2.8	1.1	2.56	2180	19	100	2.9
#18.2	0.0264	15	0.00105	5	1.46719	1.88680	15	0.281501	33	0.281457	2.5	1.2	2.58	2184	9	95	2.4
#23.1	0.0177	6	0.00078	4	1.46719	1.88660	12	0.281503	27	0.281471	2.9	1.0	2.55	2181	9	101	2.9
#23.2	0.0100	6	0.00041	2	1.46713	1.88670	21	0.281460	27	0.281443	2.7	1.0	2.59	2216	20	95	1.9
#28.1	0.0229	16	0.00100	6	1.46721	1.88669	8	0.281518	33	0.281476	2.9	1.2	2.55	2170	12	100	3.1
#28.2	0.0099	15	0.00042	6	1.46714	1.88679	16	0.281465	32	0.281447	2.1	1.1	2.60	2182	12	86	2.1
#29.1	0.0197	7	0.00083	3	1.46717	1.88664	12	0.281535	27	0.281501	3.9	1.0	2.50	2176	18	100	4.0
#29.2	0.0474	45	0.00170	13	1.46714	1.88672	12	0.281557	28	0.281486	3.5	1.0	2.52	2184	14	100	3.5
										0.281475							**3.2**
										± 0.000035							**± 1.2**
BN241																	**2145 Ma**
#1.1	0.0419	34	0.00150	10	1.46723	1.88645	15	0.281623	39	0.281565	2.6	1.4	2.45	2023	121	103	5.3
#2.1	0.0413	15	0.00142	6	1.46719	1.88655	17	0.281629	29	0.281575	2.5	1.0	2.44	2004	47	53	5.6
#3.1	0.0359	29	0.00109	8	1.46717	1.88649	14	0.281621	30	0.281577	5.7	1.1	2.37	2137	37	100	5.8
#3.2	0.0355	34	0.00112	10	1.46719	1.88651	16	0.281629	32	0.281583	6.1	1.1	2.35	2148	39	100	6.1
#4.1	0.0262	18	0.00097	7	1.46722	1.88661	11	0.281575	31	0.281536	3.1	1.1	2.47	2090	28	102	4.4
#4.2	0.0201	26	0.00061	7	1.46715	1.88669	14	0.281544	37	0.281520	1.4	1.3	2.53	2039	26	95	3.8
#5.1	0.0311	15	0.00097	5	1.46719	1.88660	15	0.281580	30	0.281540	5.0	1.1	2.42	2164	27	100	4.6
#5.2-r	0.0192	14	0.00061	4	1.46717	1.88658	16	0.281544	28	0.281524	-6.4	1.0	2.68	1696	101	35	3.8
#6.1-r	0.0330	39	0.00092	8	1.46719	1.88658	14	0.281599	28	0.281562	4.9	1.0	2.40	2128	30	95	5.3
#6.2-r	0.0184	21	0.00066	7	1.46718	1.88658	20	0.281580	28	0.281554	4.0	1.0	2.43	2100	12	98	5.0
#7.1	0.0279	30	0.00111	17	1.46717	1.88658	16	0.281584	32	0.281539	4.8	1.1	2.43	2156	70	103	4.5
#7.2	0.0402	12	0.00129	4	1.46713	1.88677	16	0.281578	31	0.281536	-5.3	1.1	2.65	1726	61	87	4.0
#8.1-r	0.0336	12	0.00155	5	1.46711	1.88674	21	0.281570	26	0.281509	2.0	0.9	2.53	2084	19	87	3.4
#9.1-r	0.0349	9	0.00147	4	1.46713	1.88663	14	0.281595	28	0.281540	0.1	1.0	2.53	1952	105	36	4.4
#10.1	0.0573	20	0.00260	15	1.46719	1.88661	15	0.281652	29	0.281551	2.6	1.0	2.46	2043	54	103	4.7
#10.2-r	0.0409	26	0.00123	6	1.46712	1.88666	16	0.281586	30	0.281537	3.9	1.1	2.45	2122	37	74	4.4
#11.1	0.0303	22	0.00105	7	1.46715	1.88669	15	0.281580	30	0.281537	4.3	1.1	2.44	2139	21	100	4.4
#11.2	0.0315	14	0.00093	4	1.46718	1.88653	17	0.281598	29	0.281560	5.0	1.0	2.40	2133	24	101	5.3
#12.1	0.0673	37	0.00264	17	1.46714	1.88669	17	0.281663	31	0.281560	3.2	1.1	2.44	2056	29	85	5.1
										0.281548							**4.7**
										± 0.000040							**± 1.5**

BN90 - Granite - KTGD BSE and CL imaging reveal subhedral zircons with cores displaying oscillatory zoning patterns. The magmatic zoning is frequently interrupted by transgressive unzoned domains and overgrown by highly luminescent rims (Fig. 6.8n). Analyses were focused at the different textural domains of 53 grains. Thirteen concordant analyses of magmatic domains yield a Concordia age of 2135 ± 6 Ma ($MSWD_{C+E}$ = 1.50, $Prob_{C+E}$=0.07) which dates the crystallisation of the granite (Fig. 6.11a). Other analyses are concordant at *ca.* 2070-2080 Ma, which suggests lead loss at about 2070 (e.g. #1.2, 6.1, 19.2, Table 6.5), possibly due to alteration during later deformation. A few analyses of recrystallised domains devoid of zoning are concordant or sub-concordant at *ca.* 400 - 500 Ma (#2.2, 8.2, 20.2, Table 6.5), and have large uncertainties. Forty-seven Lu–Hf isotope analyses were carried out on 31 zircon grains, on top of selected concordant and discordant U-Pb analyses in the different textural domains. The measured $^{176}Hf/^{177}Hf(t)$ values form a single population (Fig. 6.12a), defined by a range of overlapping data points between 0.281463 ± 0.000027 and 0.281569 ± 0.000028, with an average $^{176}Hf/^{177}Hf(t)$ of 0.281522 ± 0.000044 (n = 47/47, 2 s.d. ext.). The homogeneity in $^{176}Hf/^{177}Hf(t)$ values suggests that all zircons formed simultaneously during the crystallisation of the granodiorite at *ca.* 2135 Ma, and no subsequent zircon growth occurred. It indicates that the concordant spots at 400-500 Ma as well as the discordant analyses may reflect Proterozoic and early Phanerozoic thermal events which caused resetting of U-Pb system in zircon and intra-grain recrystallisation. This interpretation is also supported by the spread along the zircon Pb-loss trend of analyses which yield younger Pb-Pb ages (Fig. 6.12a). Applying the intrusion age to all zircons, the initial εHf(2135 Ma) is supra-chondritic and varies between +4.7 and +2.3, which corresponds to T_{DM}^{Hf} between 2.40 and 2.60 Ga (Table 6.6).

BN119 - Granite - Bole-Bulenga domain Zircon grains from sample BN119 have euhedral shapes and angular terminations, and they display a thin oscillatory zoning. Grain tips are occasionally recrystallized, as shown by the resorption of magmatic textures (Fig. 6.8o). Most analyses are concordant or sub-concordant and have consistent $^{207}Pb/^{206}Pb$ ages. Twenty analyses yield a Concordia age of 2133 ± 6 Ma ($MSWD_{C+E}$ = 0.30, $Prob_{C+E}$=1.00), which represents the crystallisation age of the granite (Fig. 6.11b). The $^{176}Hf/^{177}Hf(t)$ values measured from all domains on 12 zircon grains vary between 0.281528 ± 0.000026 and 0.281649 ± 0.000030, with an average $^{176}Hf/^{177}Hf(t)$ of 0.281536 ± 0.000035 (n = 22/22, 2 s.d. ext.). Most data points have similar apparent Pb–Pb ages that are consistent with the *ca.* 2135 Ma crystallisation age of the granodiorite, and $^{176}Hf/^{177}Hf(t)$ does not vary with decreasing apparent Pb–Pb ages (Fig. 6.12b). Therefore, we interpret the zircon grains to have formed during a single magmatic event. However, similarly to sample BN90, there is a small variation of $^{176}Hf/^{177}Hf(t)$ within the population, which suggests a slightly heterogeneous magma source. The initial εHf(2135 Ma) has a supra-chondritic value of 4.2 ± 1.3 (2 s.d.), which corresponds to T_{DM}^{Hf} initial between 2.35 and 2.55 Ga (Table 6.6).

BN132 - Granitic gneiss - KTGD Zircon grains separated from sample BN132 are euhedral and display an oscillatory zoning pattern, consistent with a magmatic origin. CL imaging reveals that some grains are partially recrystallized, as shown

by transgressive unzoned domains of patchy luminescence overprinting magmatic zoning, or by weakly luminescent rims around magmatic cores (Fig. 6.8p). Eighty eight spot analyses were obtained on 56 grains. A population of 15 concordant points on pristine magmatic domains yields a Concordia age of 2211 ± 6 Ma ($MSWD_{C+E}$ = 0.56, $Prob._{C+E}$=0.97), interpreted as the crystallisation age of the granite (Fig. 6.11c). Concordant analyses with ages of 2175 ± 15 and 2105 ± 9 Ma (#16.1 and 56.1, 2σ, Table 6.5) do not seem to correlate with recrystallized domains, suggesting that these younger ages reflect lead loss rather than secondary crystallisation. Twenty-six Lu–Hf analyses were performed on different textural domains of 20 grains. The $^{176}Hf/^{177}Hf(t)$ of all analyses defines a single zircon population with overlapping values between 0.281469 ± 0.000034 and 0.281546 ± 0.000032, and a weighted average $^{176}Hf/^{177}Hf(t)$ of 0.281505 ± 0.000041 (n = 26/26, 2 s.d. ext.). Analyses with younger apparent Pb–Pb ages do not show a distinct Hf signature. This suggests zircon formation during a single magmatic event at *ca.* 2210 Ma (Fig. 6.12c). The εHf(2210 Ma) is supra-chondritic (4.7 ± 1.4, 2 S.D.), corresponding to T_{DM}^{Hf} initial between 2.40 and 2.55 Ga (Table 6.6). Again, a significant variation of εHf by almost 3 units from one analysis to the other is consistent with slightly heterogeneous magma sources.

BN241 - Trondhjemite - Abulembire domain Sample BN241 contains subhedral zircon grains, which display oscillatory zoning patterns, although many grains are metamict or partially recrystallized (Fig. 6.8q). Nineteen laser ablation spots were focused on pristine magmatic domains. Data points spread along a Discordia which defines an upper-intercept age of 2142 ± 13 Ma (MSWD = 0.66, n=7), consistent with a Concordia age of 2143 ± 12 Ma ($MSWD_{C+E}$ = 0.45, $Prob._{C+E}$=0.91) (Fig. 6.11d), calculated from the 5 most concordant analyses. This age is interpreted as the crystallisation age. Nineteen Lu–Hf analyses performed on 13 grains reveal homogeneous $^{176}Hf/^{177}Hf(t)$ values ranging from 0.281509 ± 0.000026 to 0.281583 ± 0.000030, with an average of 0.281548 ± 0.000040 (n = 19/19, 2 s.d.). Individual $^{176}Hf/^{177}Hf(t)$ and apparent Pb–Pb ages are not correlated, which suggests that young Pb–Pb ages are due to multiple lead loss rather than to secondary zircon growth (Fig. 6.12d). The initial εHf at the time of magma crystallisation (*ca.* 2145 Ma) is suprachondritic, ranges from 3.4 to 6.1, and corresponds to a crustal residence time T_{DM}^{Hf} between 2.35 and 2.55 Ga.

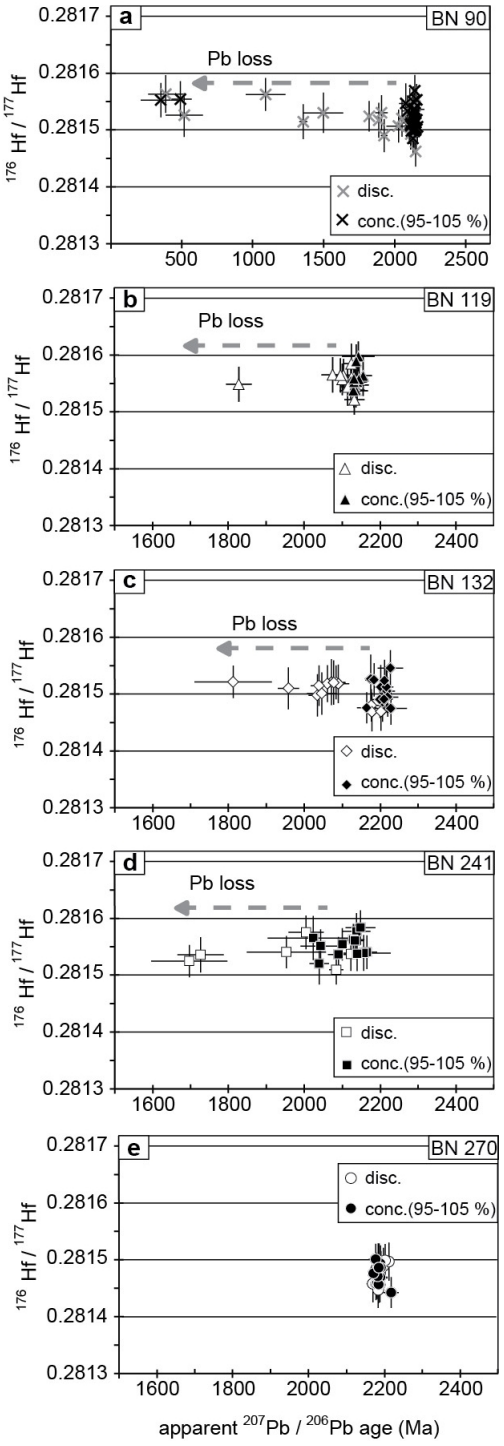

FIGURE 6.12: Results of combined Hf and U-Pb zircon spot analyses of samples from north-western Ghana, presented as $^{176}Hf/^{177}Hf(t)$ *vs* apparent $^{207}Pb/^{206}Pb$ age. $^{176}Hf/^{177}Hf(t)$ is the ratio calculated at the time t, t being the apparent $^{207}Pb/^{206}Pb$ age. Dashed arrow : zircon Pb-loss trend with decreasing apparent $^{207}Pb/^{206}Pb$ age at constant $^{176}Hf/^{177}Hf(t)$.

BN270 - Granodiorite gneiss - Bole-Bulenga terrain Zircons separated from sample BN270 are translucent and euhedral. CL imaging reveals oscillatory zoning, consistent with zircon crystallisation from a magma, rimmed by a very luminescent overgrowth (Fig. 6.8r). The overgrowth, although too thin to be analysed, may have formed during partial melting of the rock. Forty six analyses aimed at magmatic domains have consistent $^{207}Pb/^{206}Pb$ ages, suggesting a single magmatic episode. Twenty one concordant analyses yield a Concordia age of 2181 ± 5 Ma ($MSWD_{C+E}$ = 0.52, $Prob._{C+E}$=0.99), interpreted as the crystallisation age of the granodiorite pluton (Fig. 6.11e). Twenty four Lu–Hf analyses on 16 zircon grains show $^{176}Hf/^{177}Hf(t)$ varying between 0.281443 ± 0.000027 and 0.281501 ± 0.000027 (Fig. 6.12e), with an average of 0.281475 ± 0.000035 (n = 24/24, 2 s.d. ext.). The zircons are interpreted to have formed at the time of emplacement of the magmatic protolith, at ca. 2180 Ma. They display a εHf(2180 Ma) of 3.0 ± 1.2 (2 s.d.), consistent with a magma source extracted from the depleted mantle between 2.50 and 2.60 Ga.

6.2.7 Discussion

6.2.7.1 Magmatogenesis in northern Ghana

Since the Paleoproterozoic basement of NW Ghana shares many geological characteristics with Archean cratons, we assessed the origin of magmatic rocks investigated here by comparing them with Archean granitoids. The latter can be separated in four groups : (i) TTGs, characterized by internal diversity reflecting different conditions of formation (Moyen, 2011; Moyen and Martin, 2012), (ii) sanukitoids and related rocks, (iii) crust-derived biotite- and two-mica granites and (iv) hybrid granitoids, showing intermediate compositions between the first three groups (Laurent et al., 2014). When plotted in the ternary diagrams of Fig. 12a and b, proposed by Laurent et al. (2014) to discriminate between those granitoid types, major element compositions of samples from northern Ghana reveal a more restricted compositional range than late-Archean granitoids.

A majority of our samples, including tonalites, trondhjemites as well as most granodiorites and felsic volcanics (dacites, rhyolites) all overlap in composition with Archean TTGs and clearly point to sources dominated by low-K mafic rocks. This is consistent with their richness in plagioclase, high Na_2O/K_2O ratios (>2) as well as elevated Al_2O_3 and SiO_2 contents. Moyen (2011) demonstrated that most Archean TTGs derive essentially from the same low-K, hydrous mafic source, but that their minor and trace element systematics strongly depend on melting conditions. Garnet is a major repository for Y and HREE, while Nb and Ta are compatible in rocks containing rutile. On the other hand, the Na, Sr, Eu and Al contents of the melt are largely controlled by the stability of plagioclase feldspar in the residuum. Since garnet and rutile are stable residual phases during high-pressure (>2 GPa) melting of mafic rocks, whereas plagioclase only remains in the residue at low pressures (<1.5 GPa), the HREE, Y, Nb, Ta, Eu, Sr, Na and Al contents of TTG magmas are good proxies for melting pressure (Halla et al., 2009; Moyen, 2011; Moyen and Martin, 2012; Moyen and Stevens, 2006).

As shown in Fig. 6.13c-f, most of the sampled trondhjemites and tonalites (as well as the dacites and rhyolites) have high Sr/Y ratios (and high LREE/HREE, see Fig. 6.6), high Sr content, low Nb and Y contents, and no significant Eu anomaly (Eu/Gd is close to 0.5). Therefore, the trondhjemites and tonalites have signatures identical to high- and medium-pressure Archean TTGs (Moyen, 2011) (Fig. 6.13), and likely formed by similar petrogenetic processes, i.e. the partial melting of hydrous metabasalts at depth > 45km, at garnet-amphibolite (1.5-2.0 GPa)- to eclogite-facies (>2 GPa) conditions (Moyen and Stevens, 2006; Rapp et al., 1991). However, the geochemical signatures of the diorites, some granodiorites and granites (and of intermediate lavas) do not match those of the TTG suite. They broadly define a calc-alkaline differentiation trend, with the most differentiated terms being enriched in K_2O (pointing to high-K calc-alkaline to shoshonitic affinities ; see Fig. 6.5). The most felsic rocks, in particular granites with SiO_2 >70 wt.%, have lower Sr contents and Eu/Gd ratios, higher K_2O/Na_2O together with, on average, greater concentrations in Y and HREE and less fractionated REE patterns than tonalites and trondhjemites (Fig. 6.13c-f ; see also Fig. 6.6). Their compositions are thus consistent with a lower pressure origin, in the plagioclase stability field and without significant proportions of residual garnet. Fig. 6.13c-f shows that they are akin to

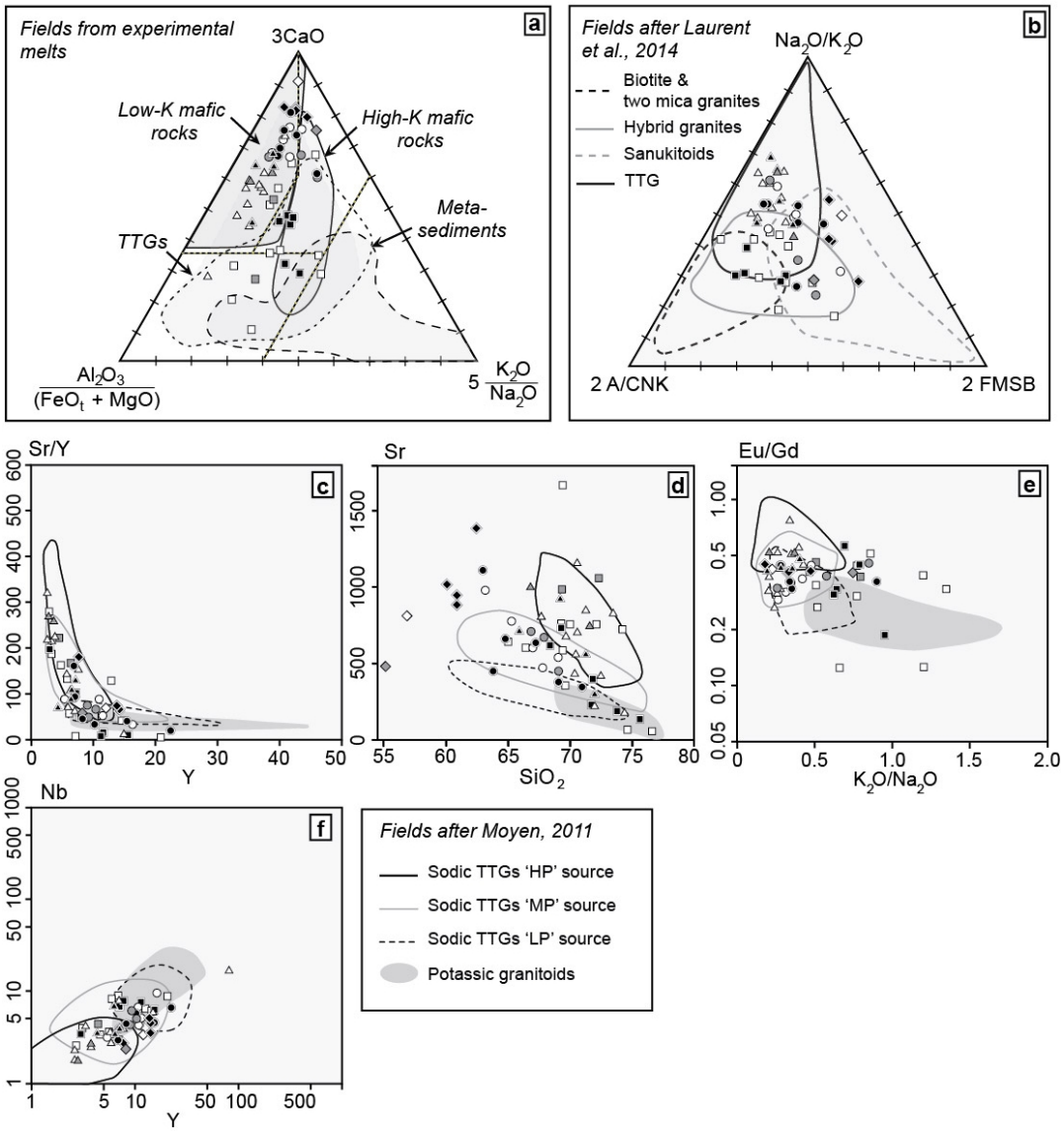

FIGURE 6.13: Binary and ternary diagrams showing the major and trace element characteristics of the plutonic rock sample set. The symbols used are similar to Figs. 6.5 and 6.6. Ternary diagrams (**a, b**) are after Laurent et al. (2014) and are used to discriminate between potential source rocks for the granitoids (see text). Binary diagrams (**c-g**) show proxies for a mantle contribution to the source (**c**) and for the melting pressure of an inferred mafic source rock (**c-f**, fields after Moyen (2011)). Compositions of experimental melts in (**b**) are from Beard and Lofgren (1991); Coldwell et al. (2011); Douce and Johnston (1991); Patino-Douce and Beard (1996); Patiño Douce and Harris (1998); Singh and Johannes (1996); Sisson et al. (2005); Tatsumi and Suzuki (2009); Vielzeuf and Holloway (1988); Watkins et al. (2007); Wolf and Wyllie (1994)

the "potassic granitoids" subgroup of (Moyen, 2011) that result from partial melting of sodic TTG and/or metasedimentary lithologies at shallow crustal pressures (<1.5 GPa). The compositions of these samples also match that of experimental melts derived from TTG analogues (Fig. 6.13a). Such granites could therefore re-

flect reworking of pre-existing felsic rocks such as TTGs, which is in line with the abundance of partially molten gneisses on the field.

Other samples show lower SiO_2 contents that are inconsistent with melting of pre-existing felsic rocks. Among them, diorites, intermediate and mafic lavas have characteristics that point to the possible involvement of mantle sources (low SiO_2, high FeO_T + MgO and Mg#). In particular, diorites plot in the field of sanukitoids in Fig. 6.13a, but only marginally, owing to lower concentrations in both LILE (and other incompatible elements such as LREE and HFSE) and FeO_T + MgO compared to the "classical" sanukitoids (Laurent et al., 2014; Martin et al., 2009) (Bédard, 1996; Heilimo et al., 2010; Laurent et al., 2014; Martin et al., 2009, 2005; Shirey and Hanson, 1984; Smithies, 2000; Stern and Hanson, 1991; Stevenson et al., 1999) (see also Fig. 6.6). Yet, their greater enrichment in LILE relative to REE and HFSE implies that their geochemistry is rather similar to that of Phanerozoic arc magmas (e.g. Arculus (1994); Tatsumi and Eggins (1995) and references therein). Thus, the geochemistry of the diorites (and the compositionally equivalent intermediate lavas) implies the involvement of LILE-rich mantle sources, albeit less metasomatized than in the case of sanukitoids. Furthermore, the flat or weakly fractionated REE spectra of the diorites point to magma production at pressures lower than the garnet stability range. We therefore suggest that diorites of northern Ghana were generated by the shallow differentiation (through melting or crystallization) of mafic material derived from a LILE-enriched mantle source. Such material is presumably represented by mafic and intermediate lavas that show variously LILE-enriched trace element patterns (Fig. 6.5). It must be noted that several samples show intermediate or ambiguous chemical characteristics with respect to those different groups, and accordingly plot in the field of "hybrid" granitoids in the ternary diagram of Fig. 6.13a. This emphasizes that igneous rocks from northern Ghana were likely derived from the involvement and interplay of the different sources and petrogenetic mechanisms mentioned above. Among them, melting of low-K, hydrous mafic rocks played a prominent role. The differentiation of felsic crustal lithologies also took place, as well as the implication of LILE-enriched mantle sources that produced mafic to intermediate rocks and their differentiation products.

There is no clear temporal evolution of granitoid sources and petrogenesis in northern Ghana. Indeed, granitoids from both age groups (that is, older and younger than 2130 Ma) largely overlap in composition (Figs. 6.5, 6.6, 6.13). This first-order observation suggests that petrogenetic processes did not change much through time. However, a more detailed investigation reveals that the geochemical variability of younger rocks is more restricted compared to older rocks. Most of the younger samples have compositions consistent with melting of low-K mafic sources at relatively higher pressure, and are compositionally close to the TTG suite. Contrastingly, samples emplaced during the early stages are more scattered in composition. For instance, mafic rocks are almost exclusively restricted to ages <2130 Ma. This, along with the limited magmatic rock diversity, is in contrast with the magmatic record of many Archean cratons, especially their late evolution between 3.00 and 2.50 Ga ago. Late-Archean magmatism is characterised by a specific evolution, starting with a long period of TTG magmatism, immediately followed by rapid emplacement of potassic, peraluminous biotite- or two-mica granites, plutons belonging to the sanukitoid suite, and all intermediates thereof (Laurent et al., 2014). TTGs would result

from the high-pressure melting of basalts, granites are products of felsic crust recycling, while sanukitoids reflect the involvement of mantle metasomatised by crustal components. This peculiar evolution is interpreted (Laurent et al., 2014) to reflect the succession of subduction-related processes (producing TTGs and building up large volumes of continental crust) followed by continental collision (crustal anatexis and involvement of mantle lithosphere modified during previous subduction events). Contrastingly, magmatism on the Paleoproterozoic West African Craton is less diversified, and analogues of Archean TTGs rather emplaced during the late stages of the geological evolution, which is not consistent with the sequence depicted above. Its magmatic record therefore suggests an evolution that differs from typical Archean geodynamics, and that may not be compatible with a classical orogenic sequence of subduction and continental collision.

6.2.7.2 Timing of crust production and recycling in northern Ghana

Results of U-Pb dating of zircons from magmatic rocks from northern Ghana demonstrate that magmatism was continuous between *ca.* 2210 and 2120 Ma. The oldest dated rock has a crystallisation age of 2211 ± 6 Ma, and old inherited zircon cores formed between 2320 and 2200 Ma. Lava and pluton emplacement seem to be coeval. These findings are in agreement with data collected in the same region by De Kock et al. (2011) and Duodu (2009), who report a magmatic activity spanning a 2200-2115 Ma period. The data is also consistent with inherited zircon and crystallisation ages from surrounding provinces (e.g. Gasquet et al. (2003); Hirdes et al. (1996); Oberthür et al. (1998)).

All the zircons from the analysed samples show positive (super-chondritic) εHf values between + 1.6 and + 6.3 at the time of magma crystallisation. These results suggest that (i) magmatic rocks of northern Ghana belong to a juvenile crust extracted from a depleted mantle source and (ii) reworking of Archean crustal components did not play a significant role. They confirm the findings of previous studies that the Paleoproterozoic crust of the Sao Luis and West African cratons is juvenile (Abouchami et al., 1990; Boher et al., 1992; Gasquet et al., 2003; Klein and Veloso Moura, 2001; Peucat et al., 2005). In Fig. 6.14a, individual concordant and discordant zircon grains define a linear trend of decreasing εHf with decreasing apparent Pb–Pb age. This trend can be modelled by a $^{176}Lu/^{177}Hf = 0.0010$, consistent with the evolution of zircon which experienced multiple lead loss without changing significantly the $^{176}Hf/^{177}Hf$ ratio (e.g. Gerdes and Zeh (2009); Zeh et al. (2009)). Such a distribution rules out any later recycling of the crust following magma emplacement, or metamorphic zircon growth.

The Hf signature of the studied samples is compatible with the recycling of a crustal component that was extracted from a depleted mantle source between 2.60 and 2.30 Ga (Fig. 6.14a, light grey array and white stars) ; i.e. at most 300 Ma before the crystallisation of *ca.* 2.30 Ga inherited zircon cores. In every investigated sample, individual zircon grains show slight yet significant variations in Hf isotope compositions up to 3 εHf units. Furthermore, the data do not define any clear trend of εHf with time : 2145-2130 Ma samples have within errors identical Hf isotope signatures to 2210-2180 Ma samples. This is not consistent with the evolution a homogeneous magma source, which is expected to produce a linear trend of decreasing εHf towards younger ages (Kemp et al., 2006; Zeh et al., 2009). It

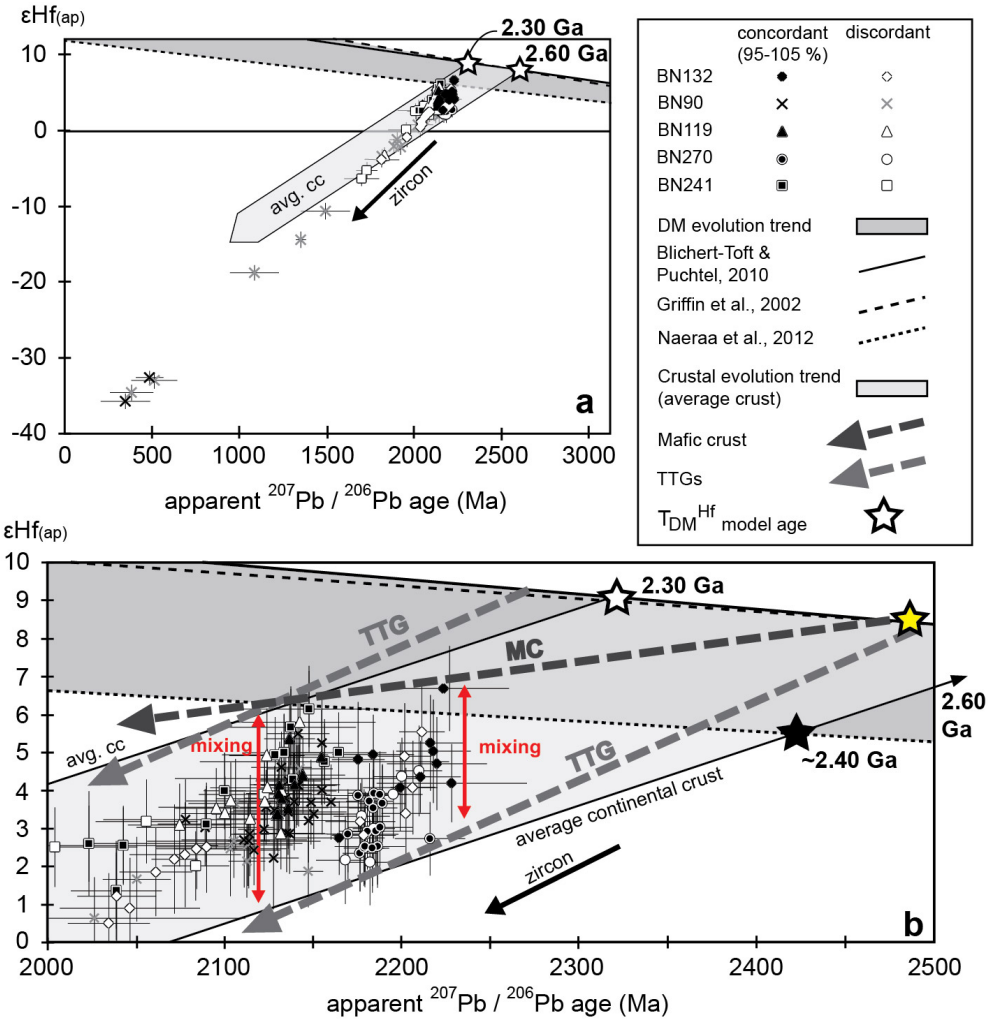

FIGURE 6.14: εHf versus Pb–Pb age diagram showing the data obtained from magmatic zircon grains from granitoids of northern Ghana. Arrows marked "zircon" show the isotopic evolution trend of zircon witnessing multiple lead loss. This is expected to produce a linear evolution trend with time calculated for $^{176}Lu/^{177}Hf$ = 0.0010.The dark shaded array is the evolution trend of the depleted mantle defined by compositions proposed by different authors (Blichert-Toft and Puchtel, 2010; Griffin et al., 2002; Næraa et al., 2012). The light shaded array represents the average continental crust (avg. cc) evolution. The evolution trend of a hypothetical mafic protocrust (MC) is calculated for an average $^{176}Lu/^{177}Hf = 0.0210$ (Kramers, 2007), while recycling of TTGs is modelled with $^{176}Lu/^{177}Hf = 0.0050$ (Condie et al., 2005; Kamber et al., 2002). Stars at the intersection of depleted mantle and crustal evolution trends represent Hafnium model ages.

rather suggests a repeated contribution of a highly-radiogenic source to produce the granitoids emplaced between 2210 and 2130 Ma (Fig. 6.14b, red arrows). Two end-member models may be considered. Firstly, the variability in εHf values at a given age may be interpreted as the result of magma production from the melting of crustal sources with different Hf isotopic compositions. The εHf array may be

produced by the combined contribution of a radiogenic mafic crust (Fig. 6.14b, MC, dark grey dashed arrow) and a much less radiogenic TTG-dominated upper crust (light grey dashed arrow), or a sedimentary component, belonging to a juvenile proto-crust extracted from the mantle at 2.50-2.40 Ga (yellow star) and recycled at 2.20-2.10 Ga. The second hypothesis is a crustal rejuvenation model. In this setting, juvenile magma is extracted from the depleted mantle between 2.20 and 2.10 Ga and is added to a pre-existing average crust, thus producing an array of εHf values (red vertical arrows). This protracted mantle contribution is supported by the geochemistry of the granitoids and lavas.

At the scale of the Baoulé-Mossi domain, there is very limited evidence for geological activity before ca. 2.40 Ga (Table 6.7). The oldest age for an inherited zircon is ca. 2390 Ma (Siegfried et al., 2009), and the oldest known rock has a crystallisation age of 2253 Ma (Tshibubudze et al., 2013). This lack of old material may have different explanations : (i) the 2.30-2.60 Ga proto-crust of the craton was totally recycled, as the geodynamic setting of proto-crust formation may not have been favorable to crust preservation ; or (ii) it is a bias resulting from the particular DM model used for Hf model age calculation. Næraa et al. (2012) propose a different, less depleted compositions for the Archean depleted mantle ($^{176}Lu/^{177}Hf = 0.03750$ and $^{176}Hf/^{177}Hf = 0.283120$) than those of Blichert-Toft and Puchtel (2010) and Griffin et al. (2002). Using intermediate values between the former and those of Blichert-Toft and Puchtel (2010) to model the depleted mantle evolution provides younger T_{DM}Hf model ages, with a maximum of 2.40 Ga more consistent with the geological record (Fig. 6.14b, dark grey array, black star). We therefore consider that this second hypothesis is more likely, and that the less depleted mantle model of Næraa et al. (2012) appears to be more suitable. It yields younger Hf model ages and conversely shorter crustal residence times, and it implies a crustal evolution not exceeding 300 Ma from juvenile crust extraction to its final stabilisation.

6.2.7.3 Geological evolution of the south-eastern West African Craton

The geological evolution of northern Ghana is compared to other provinces of the West African Craton. Table 6.7 presents available U–Pb age data from the eastern part of the Baoulé-Mossi domain. The data is subset into four cratonic domains, defined on the basis of craton architecture and strike of major litho-tectonic units. These subsets are : (a) northern Ghana ; (b) northern and eastern Burkina Faso and Niger, where E-W trending greenstone belts are overprinted by NE-striking structures ; (c) southern Ghana ; dominated by alternations of NE-SW striking greenstone belts, Birimian and Tarkwaian basins ; (d) south-western Burkina Faso and Côte dŠIvoire, characterised by a dominant N-S structural trend. Probability density distribution plots and age histograms (bin width = 10 Ma) were constructed using the software Agedisplay (Sircombe, 2004) and are shown in Fig. 6.15 for each of these subsets. Domains (a) and (b) show similar evolution trends, with continuous magmatic activity recorded between 2.18 and 2.10 Ga. Magmatism culminates between 2.14 and 2.12 Ga, which corresponds to the timing of high-grade metamorphism in north-western Ghana. Magmatism wanes out shortly afterwards, between 2.10 and 2.09 Ga. Lavas and granitoids emplaced between 2.20 and 2.18 Ga in northern Ghana have no equivalents in northern and eastern Burkina Faso and Niger, while 2.23-2.26 Ga rocks are preserved in both areas. These differences may be due to sampling bias,

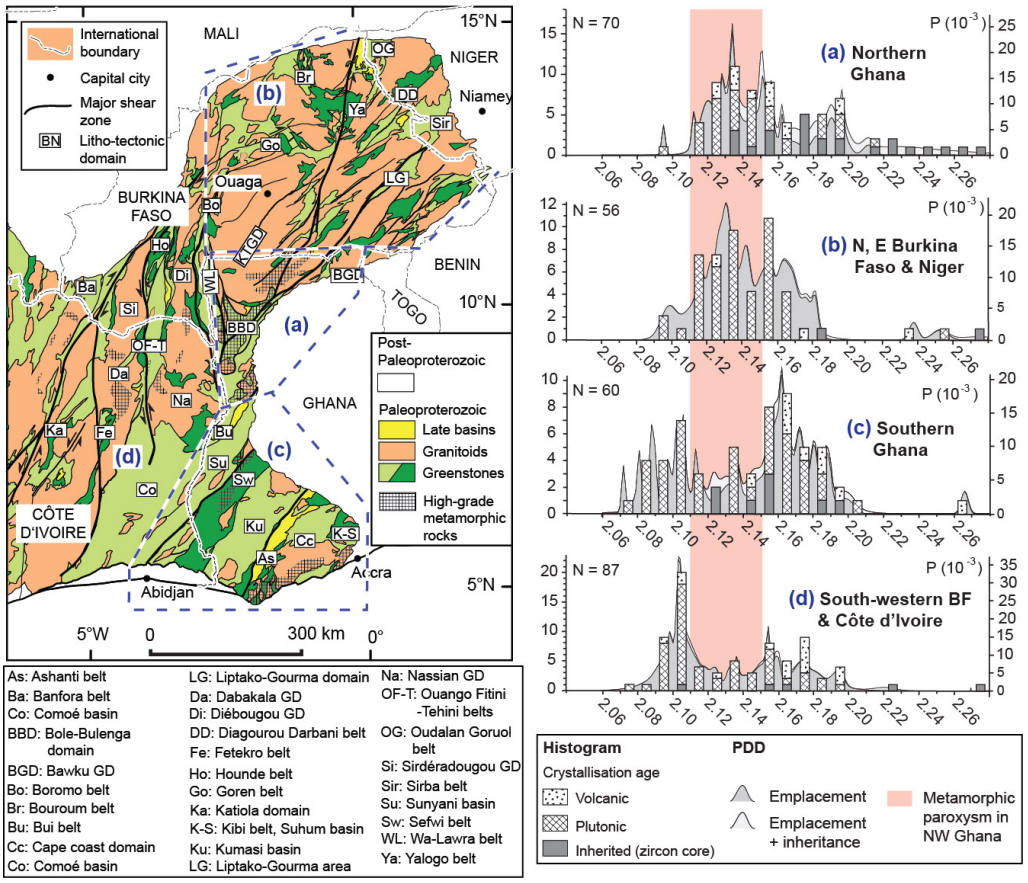

FIGURE 6.15: Left : simplified geological map of the eastern Paleoproterozoic Baoulé-Mossi domain subset into four blocks (a-d) defined by distinct litho-structural features. Right : age histograms and probability density distribution (PDD) diagrams displaying the crystallisation ages of lavas, granitoids and inherited zircon cores for each of the blocks (a-d). The database is presented in Table 6.7.

and ancient (2.20-2.30 Ga) inherited zircon cores have been dated in both provinces. The age distributions in domains (c) and (d) also provide evidence for continuous magmatism between 2.20 and 2.12 Ga. In contrast, they illustrate a lull in magmatic activity in this part of the craton, at the time of metamorphic and magmatic paroxysm in north-western Ghana (i.e. 2.12-2.14 Ga, Fig. 6.15). This period of less activity in (c-d) is followed by intense volcanism and plutonism between 2.10 and 2.07 Ga, which has no equivalent in (a-b). The results additionally show evidence that magmatism older than 2.20 Ga is distributed across the four domains (a-d). No old Paleoproterozoic nucleus can be identified based on the available data 6.7. To summarise, the south-eastern part of the West African Craton comprises various coeval crustal domains which have distinctive histories and architectural features, despite many lithological and geochronological similarities. They were stabilised sequentially. This conclusion implies that care is needed when correlating lithologies and tectono-metamorphic features across the craton.

Age (Ma)	1σ	Lat	Lon	Ref	Country	Domain	Technique	Mineral	Sample	Litho	Interp	Area
N. Ghana												
Inherited												
2386	42	9.0839	-2.4892	Siegfried et al., 2009	Ghana	BBD	U-Pb SHRIMP	Zr	SC 1011		I	A
2269	20	10.8538	-0.1703	This study	Ghana	KTGD	U-Pb ICPMS	Zr	BN82		I	A
2258	19	9.0839	-2.4892	Siegfried et al., 2009	Ghana	BBD	U-Pb SHRIMP	Zr	SC 1011		I	A
2240	24	9.9744	-2.3092	This study	Ghana	BBD	U-Pb ICPMS	Zr	BN739		I	A
2233	16	10.8783	-0.5922	This study	Ghana	NB	U-Pb ICPMS	Zr	BN068		I	A
2227	13	8.5650	-2.0583	de Kock et al., 2009	Ghana	AD	U-Pb SHRIMP	Zr	GD 3080		I	A
2222	23	10.0955	-2.0369	This study	Ghana	JB	U-Pb ICPMS	Zr	BN107		I	A
2217	20	8.7862	-2.1573	Block et al., 2014b	Ghana	AD	U-Pb ICPMS	Zr	BN446		I	A
2197	7	9.6194	-2.0711	Thomas et al., 2009	Ghana	BBD	U-Pb SHRIMP	Zr	EA 1300		I	A
2189	11	9.4567	-2.2462	Siegfried et al., 2009	Ghana	BBD	U-Pb SHRIMP	Zr	SB 3183		I	A
2186	26	9.4333	-2.4352	Siegfried et al., 2009	Ghana	BBD	U-Pb SHRIMP	Zr	SA 1154A		I	A
2178	13	8.8467	-2.0911	de Kock et al., 2009	Ghana	AD	U-Pb SHRIMP	Zr	GB 1291		I	A
2179	9	9.6575	-2.2934	Thomas et al., 2009	Ghana	BBD	U-Pb SHRIMP	Zr	EC 3020		I	A
2174	24	9.9509	-2.0399	Block et al., 2014b	Ghana	BBD	U-Pb ICPMS	Zr	BN377		I	A
2174	13	8.8602	-2.3400	de Kock et al., 2009	Ghana	MD	U-Pb SHRIMP	Zr	GA 1070		I	A
2170	11	8.8290	-2.2994	de Kock et al., 2009	Ghana	MD	U-Pb SHRIMP	Zr	GA 2070		I	A
2159	14	8.8467	-2.0911	de Kock et al., 2009	Ghana	AD	U-Pb SHRIMP	Zr	GB 1291		I	A
2157	24	9.9694	-2.0338	Thomas et al., 2009	Ghana	BBD	U-Pb SHRIMP	Zr	EA 1180A		I	A
2150	1	9.4333	-2.4352	Thomas et al., 2009	Ghana	BBD	U-Pb SHRIMP	Zr	SA 1154A		I	A
2141	10	9.4333	-2.4352	Siegfried et al., 2009	Ghana	BBD	U-Pb SHRIMP	Zr	SA1154B		I	A
2139	5	9.9694	-2.0338	Thomas et al., 2009	Ghana	BBD	U-Pb SHRIMP	Zr	EA 1180A		I	A
2139	12	8.5903	-2.1042	de Kock et al., 2009	Ghana	AD	U-Pb SHRIMP	Zr	GD 2165A		I	A
2136	11	8.5650	-2.0583	de Kock et al., 2009	Ghana	AD	U-Pb SHRIMP	Zr	GD 3080		I	A
2195	25	10.8017	-0.7087	This study	Ghana	NB	U-Pb ICPMS	Zr	BN002		I	A
Intrusive												
2211	3	10.4013	-1.3319	This study	Ghana	MD	U-Pb ICPMS	Zr	BN132	Granite	C	A
2195	4	9.0839	-2.4892	Siegfried et al., 2009	Ghana	BBD	U-Pb SHRIMP	Zr	SC 1011	Granite	C	A
2190	1.9	9.9744	-2.3092	This study	Ghana	BBD	U-Pb ICPMS	Zr	BN739	Granodiorite	C	A
2193	4	8.9841	-2.4972	de Kock et al., 2009	Ghana	BBD	U-Pb SHRIMP	Zr	GA 1009	Granite	C	A
2187	3	9.6261	-2.3800	de Kock et al., 2009	Ghana	BBD	U-Pb SHRIMP	Zr	EA 1074A	Granite	C	A
2187	5	8.6428	-2.1952	de Kock et al., 2009	Ghana	AD	U-Pb SHRIMP	Zr	GD 4187	Granite	C	A
2181	2.5	9.5075	-2.4655	This study	Ghana	BBD	U-Pb ICPMS	Zr	BN270	Granodiorite	C	A
2168	7	10.9414	-0.4801	Duodu et al., 2009	Ghana	BGD	U-Pb	Zr		Trondhjemite	C	A
2162	1	10.9316	-1.5491	Duodu et al., 2009	Ghana	KTGD	U-Pb	Zr		Granodiorite	C	A
2156	1	10.8470	-1.1040	Duodu et al., 2009	Ghana	KTGD	U-Pb	Zr	BN123	Granite	C	A
2151	1	10.6700	-0.8620	Duodu et al., 2009	Ghana	KTGD	U-Pb	Zr	BN283	Granodiorite	C	A
2150	4	9.9743	-2.3027	Siegfried et al., 2009	Ghana	KTGD	U-Pb SHRIMP	Zr	EA 1161	Qz Diorite	C	A
2148	12	9.6575	-2.2934	Thomas et al., 2009	Ghana	BBD	U-Pb SHRIMP	Zr	EC 3020	Granodiorite	C	A
2147	4.5	10.8048	-0.8846	This study	Ghana	KTGD	U-Pb ICPMS	Zr	BN016	Trondhjemite	C	A
2145	6	10.8538	-0.1703	This study	Ghana	KTGD	U-Pb ICPMS	Zr	BN082	Granodiorite	C	A
2144	7	10.0939	-2.0927	This study	Ghana	JB	Pb-Pb ICPMS	Zr	BN103	Granite	C	A
2143	6	8.5818	-2.2238	This study	Ghana	AD	U-Pb ICPMS	Zr	BN241	Trondhjemite	C	A
2140	5	10.0873	-2.0363	This study	Ghana	JB	Pb-Pb ICPMS	Zr	BN106	Granodiorite	C	A
2135	3	10.8226	-0.9413	This study	Ghana	KTGD	U-Pb ICPMS	Zr	BN90	Granite	C	A
2134	1	10.8301	-0.9921	Duodu et al., 2009	Ghana	KTGD	U-Pb SHRIMP	Zr	BN18	Qz Diorite	C	A
2134	6	9.0374	-2.4114	Siegfried et al., 2009	Ghana	BBD	U-Pb SHRIMP	Zr	SC 3028	Qz Diorite	C	A
2134	1	10.9991	-0.3697	Duodu et al., 2009	Ghana	BGD	U-Pb	Zr	BN77	Trondhjemite	C	A
2133	3	9.9692	-2.1148	This study	Ghana	BBD	Pb-Pb ICPMS	Zr	BN119	Granite	C	A
2128	1	10.9156	-0.1942	Duodu et al., 2009	Ghana	BGD	U-Pb	Zr		Trondhjemite	C	A
2128	20	9.4333	-2.4352	Siegfried et al., 2009	Ghana	BBD	U-Pb SHRIMP	Zr	SA 1154A	Granite	C	A
2126	7	8.8467	-2.0911	de Kock et al., 2009	Ghana	AD	U-Pb SHRIMP	Zr	GB 1291	Granite	C	A
2122	6	8.5903	-2.1042	de Kock et al., 2009	Ghana	AD	U-Pb SHRIMP	Zr	GD 2165A	Granite	C	A
2121	4	9.6194	-2.0711	de Kock et al., 2009	Ghana	BBD	U-Pb SHRIMP	Zr	EA 1300	Granite	C	A
2121	8	8.5650	-2.0583	Thomas et al., 2009	Ghana	AD	U-Pb SHRIMP	Zr	GD 3080	Granodiorite	C	A
2120	3	9.8375	-2.3603	Siegfried et al., 2009	Ghana	BBD	U-Pb SHRIMP	Zr	EA 3137	Granite	C	A
2119	4	8.6743	-2.0494	de Kock et al., 2009	Ghana	AD	U-Pb SHRIMP	Zr	GD 1236	Granite	C	A
2118	5	8.8602	-2.3400	de Kock et al., 2009	Ghana	MD	U-Pb SHRIMP	Zr	GA 1070	Granite	C	A
2118	4	9.9694	-2.0338	Thomas et al., 2009	Ghana	BBD	U-Pb SHRIMP	Zr	EA 1180A	Granite	C	A
2112	1	10.8674	-1.9281	Duodu et al., 2009	Ghana	KTGD	U-Pb	Zr	BN150A	Granodiorite	C	A
2095	1	10.6965	-0.8189	Hirdes et al., 1992	Ghana	NB	Pb-Pb (dissolution)	Zr	Bolga	Granite	C	A
Effusive												
2197	3	9.1692	-2.2817	This study	Ghana	MD	Pb-Pb ICPMS	Zr	BN400	Rhyolite	C	A
2196	1	9.2324	-2.2511	Duodu et al., 2009	Ghana	MD	U-Pb	Zr		Rhyolite	C	A
2168	4.5	10.0961	-2.0409	This study	Ghana	JB	Pb-Pb ICPMS	Zr	BN108	Epiclastite	C	A
2166	16	10.1143	-2.0333	This study	Ghana	JB	Pb-Pb ICPMS	Zr	BN109	Volcanosediment	C	A
2155	3	10.8017	-0.7087	This study	Ghana	NB	Pb-Pb ICPMS	Zr	BN002	Andesite	C	A
2155	3	10.0955	-2.0369	This study	Ghana	NB	Pb-Pb ICPMS	Zr	BN107	Tuff	C	A
2153	2.5	10.8783	-0.5922	This study	Ghana	NB	Pb-Pb ICPMS	Zr	BN068	Andesite	C	A
2149	3.5	10.7230	-0.6882	This study	Ghana	NB	Pb-Pb ICPMS	Zr	BN060	Dacite	C	A
2134	4	10.8878	-2.6951	This study	Ghana	Bo - W-L	U-Pb ICPMS	Zr	BN186	Dacite	C	A
2132	3.5	8.7862	-2.1573	Block et al., 2014b	Ghana	AD	U-Pb ICPMS	Zr	BN446	Paragneiss	C	A
2131	4	8.8290	-2.2994	de Kock et al., 2009	Ghana	MD	U-Pb SHRIMP	Zr	GA 2070	Rhyodacite	C	A
2129	3.5	10.0675	-2.1197	Block et al., 2014b	Ghana	JB	U-Pb ICPMS	Zr	BN110	Rhyolite	C	A
2125	6	8.7447	-2.3446	de Kock et al., 2009	Ghana	MD	U-Pb SHRIMP	Zr	GC 1123	Rhyodacite	C	A
Metamorphic												
2136	6	9.8231	-2.6960	Block et al., unpubl.	Ghana	BBD	U-Pb ICPMS	Mnz	BN520	Paragneiss	M	A
2137	4	8.9289	-2.4320	Block et al., 2014a	Ghana	BBD	U-Pb ICPMS	Mnz	BN43	Paragneiss	M	A
2134	5	9.8346	-2.6865	Block et al., unpubl.	Ghana	BBD	U-Pb ICPMS	Mnz	BN518	Paragneiss	M	A
2131	3	8.9090	-2.0391	Block et al., 2014a	Ghana	AD	U-Pb ICPMS	Mnz	BN436	Paragneiss	M	A
2130	4.5	9.8135	-2.6371	Block et al., unpubl.	Ghana	BBD	U-Pb ICPMS	Mnz	BN533	Paragneiss	M	A
2128	4	9.3733	-2.3180	Block et al., 2014a	Ghana	BBD	U-Pb ICPMS	Mnz	BN047	Paragneiss	M	A
2128	4	9.8166	-2.6401	Block et al., 2014b	Ghana	BBD	U-Pb ICPMS	Mnz	BN534	Paragneiss	M	A
2125	2	8.4875	-2.1995	Zitsmann et al., 1997	Ghana	AD	U-Pb	Zr		Paragneiss	M	A
2123	4	9.9694	-2.1074	Block et al., 2014b	Ghana	BBD	U-Pb ICPMS	Mnz	BN118	Paragneiss	M	A
2112	7	9.9509	-2.0399	Block et al., 2014b	Ghana	BBD	U-Pb ICPMS	Zr	BN377	Orthogneiss	M	A
2111	3.5	9.8755	-2.2366	Block et al., 2014b	Ghana	BBD	U-Pb ICPMS	Zr	BN753	Paragneiss	M	A
2105	10	8.5650	-2.0583	de Kock et al., 2009	Ghana	AD	U-Pb SHRIMP	Zr	GD 3080	Granodiorite	M	A
2104	31	9.6575	-2.2934	Thomas et al., 2009	Ghana	BBD	U-Pb SHRIMP	Zr	EC 3020	Granodiorite	M	A
2098	2	9.6194	-2.0711	Thomas et al., 2009	Ghana	BBD	U-Pb SHRIMP	Zr	EA 1300	Granite	M	A
Detrital grain												
2139	2	10.5978	-2.8880	Duodu et al., 2009	Ghana	Bo - W-L	U-Pb	2141	Lawra belt sediments		S	A

TABLE 6.7: Published U-Pb data on zircon, monazite and titanite from the central and eastern portions of the Baoulé-Mossi domain, West African craton. Column "Domain" refers to the lithological and tectonic units displayed on maps in Figs. 6.2 and 6.15. Interp : I : crystallisation age of inherited grain extracted from an igneous rock. C : rock crystallisation age. M : age interpreted as dating metamorphism. S : crystallisation age of detrital grain extracted from a sedimentary rock. Column "Geographical area" refers to the subsets shown in Fig. **??** (see text for explanation).

Age (Ma)	1σ	Lat	Lon	Ref	Country	Domain	Technique	Mineral	Sample	Litho	Interp	Area
NE Burkina Faso												
Inherited												
2275	13			Tapsoba et al 2013	Burkina Faso	Ya	U-Pb ICPMS	Zr	EF09		I	B
2181	11			Tapsoba et al 2013	Burkina Faso	Ya	U-Pb ICPMS	Zr	EF09		I	B
2155	6	14.3300	-1.0324	Parra et al. in prep.	Burkina Faso	Br	U-Pb SHRIMP	Zr	BE5		I	B
2151		12.3736	-2.5999	Parra	Burkina Faso	Bo - W-L	U-Pb SHRIMP	Zr	HO640C		I	B
Intrusive												
2255	26			Tshibubudze etal 2013	Burkina Faso	OG	U-Pb SHRIMP	Zr	BF 1147	Granite	C	B
2253	9			Tshibubudze etal 2013	Burkina Faso	OG	U-Pb SHRIMP	Zr	BF 1144	Granodiorite	C	B
2182	1.5	13.2067	-1.0291	Castaing et al., 2003	Burkina Faso	Go	Pb-Pb (evaporation)	Zr	EE0456	Granite	C	B
2178	4	13.4818	-0.0747	Tapsoba et al 2013	Burkina Faso	Ya	U-Pb ICPMS	Zr	AB14	Granodiorite	C	B
2176	6	13.3533	-0.4783	Tapsoba et al 2013	Burkina Faso	Ya	U-Pb ICPMS	Zr	RGE04	Qz diorite	C	B
2170	3	12.1427	-0.0610	Castaing et al., 2003	Burkina Faso	KTGD	Pb-Pb (evaporation)	Zr	MD0004	Qz diorite	C	B
2170	9			Ama Salah 1996	Niger	Si	U-Pb	Zr	AS1093	Granodiorite	C	B
2169	2.5	12.2130	-0.5232	Castaing et al., 2003	Burkina Faso	KTGD	Pb-Pb (evaporation)	Zr	MD0016	Qz diorite	C	B
2169	4	14.3420	-1.3706	Parra et al. in prep.	Burkina Faso	Br	U-Pb SHRIMP	Zr	BE13	Granitoid	C	B
2165	3	13.7670	0.1960	Castaing et al., 2003	Burkina Faso	LG	Pb-Pb (evaporation)	Zr	PC0042A	Granite	C	B
2164	2.5	13.3610	-0.4800	Castaing et al., 2003	Burkina Faso	Br	Pb-Pb (evaporation)	Zr	PC0004	Tonalite	C	B
2162	3	13.0070	-0.1540	Castaing et al., 2003	Burkina Faso	LG	Pb-Pb (evaporation)	Zr	PC0022	Tonalite	C	B
2162	4.5	13.7670	0.1960	Castaing et al., 2003	Burkina Faso	LG	Pb-Pb (evaporation)	Zr	PC0042B	Tonalite	C	B
2158	9			Cheilletz et al 1994	Niger	DD	Pb-Pb (dissolution)	Zr	Tera	Granodiorite	C	B
2158	4.5	12.9550	-1.3481	Tapsoba et al 2013	Burkina Faso	Go	U-Pb ICPMS	Zr	KK07	Granodiorite	C	B
2156	1.5	13.7740	-1.0070	Castaing et al., 2003	Burkina Faso	Br	Pb-Pb (evaporation)	Zr	CC0769	Tonalite	C	B
2154	9	13.1436	1.5839	PPML-1997	Niger	Si	U-Pb	Zr				B
2153	3.5	12.7804	-1.2581	Castaing et al., 2003	Burkina Faso	Go	Pb-Pb (evaporation)	Zr	EE0152	Trondhjemite	C	B
2152	7.5	13.2431	-0.1231	Tapsoba et al 2013	Burkina Faso	LG	U-Pb ICPMS	Zr	TW02	Qz diorite	C	B
2152	4.5			Tapsoba et al 2013	Burkina Faso	LG	U-Pb ICPMS	Zr	TW12	Granodiorite	C	B
2152	4.5			Tapsoba et al 2013	Burkina Faso	Br	U-Pb ICPMS	Zr	GAG05	Orthogneiss	C	B
2150	6.5	13.4872	-0.0876	Tapsoba et al 2013	Burkina Faso	Ya	U-Pb ICPMS	Zr	AB03	Qz diorite	C	B
2150	5	13.3551	-0.0654	Tapsoba et al 2013	Burkina Faso	LG	U-Pb ICPMS	Zr	IJ10	Granite	C	B
2143	2	11.0814	0.5829	Castaing et al., 2003	Burkina Faso	LG	Pb-Pb (evaporation)	Zr	MD0072	Granite	C	B
2143	2.5	12.6410	-0.9487	Castaing et al., 2003	Burkina Faso	Go	Pb-Pb (evaporation)	Zr	MD0030	Qz diorite	C	B
2142	2.5	14.4356	-1.0070	Parra et al. in prep.	Burkina Faso	Br	U-Pb SHRIMP	Zr	BE3A	Gabbro	C	B
2140	3	12.1440	-1.7042	Castaing et al., 2003	Burkina Faso	KTGD	Pb-Pb (evaporation)	Zr	PC0652	Tonalite	C	B
2136	4.5	11.4743	-1.1843	Castaing et al., 2003	Burkina Faso	KTGD	Pb-Pb (evaporation)	Zr	CC2125	Granite	C	B
2135	11	13.1203	1.3611	PPML 1997	Niger	Si	U-Pb	Zr				B
2135	3	12.7419	-1.4739	Tapsoba et al 2013	Burkina Faso	Go	U-Pb ICPMS	Zr	SMT01	Granodiorite	C	B
2135	6	14.3300	-1.0324	Parra et al. in prep.	Burkina Faso	Br	U-Pb SHRIMP	Zr	BE5	Granitoid	C	B
2134	4	12.9022	-0.9686	Tapsoba et al 2013	Burkina Faso	Go	U-Pb ICPMS	Mnz	ANT03	Granodiorite	C	B
2133	3	14.2876	-0.9517	Parra et al. in prep.	Burkina Faso	Br	U-Pb SHRIMP	Zr	BE2	Granitoid	C	B
2132	3	11.1684	-2.0786	Castaing et al., 2003	Burkina Faso	KTGD	Pb-Pb (evaporation)	Zr	OK0014	Granite	C	B
2132	2	14.3009	-1.0540	Castaing et al., 2003	Burkina Faso	Br	Pb-Pb (evaporation)	Zr	MD1699	Granite	C	B
2131	1.5	13.7650	0.2690	Castaing et al., 2003	Burkina Faso	DD	Pb-Pb (evaporation)	Zr	MD0130	Granodiorite	C	B
2129	11	13.1289	1.3136	PPML 1997	Niger	Si	U-Pb	Zr				B
2128	2	11.9148	0.2947	Castaing et al., 2003	Burkina Faso	LG	Pb-Pb (evaporation)	Zr	MD0042	Tonalite	C	B
2127	3	13.0990	-0.9970	Castaing et al., 2003	Burkina Faso	Go	Pb-Pb (evaporation)	Zr	PC0001	Qz diorite	C	B
2126	6	12.8183	1.6783	PPML 1997	Niger	Si	U-Pb	Zr				B
2125	2.5	14.3414	-1.0446	Parra et al. in prep.	Burkina Faso	Br	U-Pb SHRIMP	Zr	BE6	Granitoid	C	B
2122	1.5	14.4284	-1.5400	Castaing et al., 2003	Burkina Faso	Br	Pb-Pb (evaporation)	Zr	PC0994	Granodiorite	C	B
2122	7.5	13.3548	-0.1626	Tapsoba et al 2013	Burkina Faso	Ya	U-Pb ICPMS	Zr	KL02	Granodiorite	C	B
2118	10	13.2511	1.4878	PPML 1997	Niger	Si	U-Pb	Zr				B
2117	2	11.4495	-0.8337	Castaing et al., 2003	Burkina Faso	KTGD	Pb-Pb (evaporation)	Zr	NK0036	Granite	C	B
2117	3	11.7719	-0.3368	Castaing et al., 2003	Burkina Faso	KTGD	Pb-Pb (evaporation)	Zr	NK0004	Leucogranite	C	B
2115	5			Cheilletz et al 1994	Niger	Si	Pb-Pb (dissolution)	Zr	Torodi	Granite	C	B
2112	12	13.1903	1.1297	PPML 1997	Niger	Si	U-Pb	Zr				B
2110	4	11.5758	-1.2083	Castaing et al., 2003	Burkina Faso	KTGD	Pb-Pb (evaporation)	Zr	CC2122	Granite	C	B
2100	4	11.5281	-1.7764	Castaing et al., 2003	Burkina Faso	KTGD	Pb-Pb (evaporation)	Zr	CC2138	Granodiorite	C	B
2099	5	12.7690	-2.1150	Castaing et al., 2003	Burkina Faso	Bo - W-L	Pb-Pb (evaporation)	Zr	PC0408	Granite	C	B
2097	4	12.7142	-0.3242	Castaing et al., 2003	Burkina Faso	KTGD	Pb-Pb (evaporation)	Zr	MD0017		C	B
2172		12.3527	-2.5841	Parra	Burkina Faso	Bo - W-L	U-Pb SHRIMP	Zr	HO479A	Gabbro	C	B
2165		12.3580	-2.5810	Parra	Burkina Faso	Bo - W-L	U-Pb SHRIMP	Zr	HO480	Granitoid	C	B
2169		12.3736	-2.5999	Parra	Burkina Faso	Bo - W-L	U-Pb SHRIMP	Zr	HO640A	Granitoid	C	B
2114		12.3736	-2.5999	Parra	Burkina Faso	Bo - W-L	U-Pb SHRIMP	Zr	HO640C	Granitoid	C	B
Effusive												
2238	2.5	13.2726	-1.3063	Castaing et al., 2003	Burkina Faso	Go	Pb-Pb Zr evap	Zr	MD1264	Rhyolite	C	B
2177	2.5	12.9371	-1.0592	Castaing et al., 2003	Burkina Faso	Go	Pb-Pb Zr evap	Zr	EE0243	Dacite tuff	C	B
2127	2	11.3456	0.8366	Castaing et al., 2003	Burkina Faso	LG	Pb-Pb Zr evap	Zr	MD0066	Rhyolite	C	B
S. Ghana												
2197	10	6.477	-1.133	Oberthür et al.. 1998	Ghana	As	Pb-Pb (dissolution)	Zr	GH390		I	C
2156	8	6.477	-1.133	Oberthür et al.. 1998	Ghana	As	Pb-Pb (dissolution)	Zr	GH390		I	C
2128	4	6.477	-1.133	Oberthür et al.. 1998	Ghana	As	Pb-Pb (dissolution)	Zr	GH390		I	C
2156	3	6.263	-1.6069	Oberthür et al.. 1998	Ghana	As	Pb-Pb (dissolution)	Zr	GH388		I	C
2123	2	6.263	-1.6069	Oberthür et al.. 1998	Ghana	As	Pb-Pb (dissolution)	Zr	GH388		I	C
2144	3	6.263	-1.6069	Oberthür et al.. 1998	Ghana	As	Pb-Pb (dissolution)	Zr	GH1014		I	C
2159	12	6.263	-1.6069	Oberthür et al.. 1998	Ghana	As	Pb-Pb (dissolution)	Zr	GH789		I	C
2187	11	6.263	-1.6069	Oberthür et al.. 1998	Ghana	As	Pb-Pb (dissolution)	Zr	GH1014		I	C
Intrusive												
2200	4	5.98	-0.5233	Feybesse et al.. 2006	Ghana	K-S	Pb-Pb (evaporation)	Zr	G113B	Granodiorite	C	C
2187	1	5.11315	-1.51348	Loh et al., 1999	Ghana	Cc	Pb-Pb	Zr		Gneiss	C	C
2182	2	5.49974	-2.98864	Duodu et al., 2009	Cote d'Ivoire	Su	U-Pb TIMS	Zr			C	C
2179	2	6.130124	-2.551952	Hirdes et al., 1992	Ghana	Sw	Pb-Pb (dissolution)	Zr	6668	Granitoid	C	C
2174	2	4.9555	-1.6629	Oberthür et al.. 1998	Ghana	Cc	Pb-Pb (dissolution)	Zr	GH852	Granitoid	C	C
2172	2	4.79161	-1.94793	Opare Addo, 1992	Ghana	Cc	U-Pb	Zr	Dixcove	Gneiss	C	C
2172	2	4.834242	-1.908986	Hirdes et al., 1992	Ghana	Cc	Pb-Pb (dissolution)	Zr	6427	Granitoid	C	C
2165	9	5.39542	-0.58077	Opare Addo, 1992	Ghana	K-S	U-Pb	Zr		Gneiss	C	C
2164	8	5.475	-1.865	White et al. 2014	Ghana	As	U-Pb SIMS	Zr	AWADi	Diorite	C	C
2162	1	5.840333	-3.202833	Hirdes et al., 2007	Cote d'Ivoire	Sw	Pb-Pb (dissolution)	Zr	GB2293	Qz diorite	C	C
2161	7	5.403	-3.128	Feybesse et al.. 2006	Ghana	Sw	Pb-Pb (evaporation)	Zr	Sefwi 227	Monzonite	C	C
2161	4	5.583	-3.426	Feybesse et al.. 2006	Ghana	Sw	Pb-Pb (evaporation)	Zr	Sefwi 238	Monzonite	C	C
2161	7			Feybesse et al.. 2006	Ghana	Sw	Pb-Pb (evaporation)	Zr	Sefwi 225	Diorite	C	C
2159	4	4.83	-2.16	Attoh et al.. 2006	Ghana	As	U-Pb TIMS	Zr	BPD61	Granodiorite	C	C
2159	4	7.093	-2.4098	Feybesse et al.. 2006	Ghana	Sw	Pb-Pb (evaporation)	Zr	Sefwi D14	Granitoid	C	C
2159	4	5.43224	-2.7751	Duodu et al., 2009	Cote d'Ivoire	Ku	U-Pb TIMS	Zr			C	C
2158	8	5.166667	-1.9	Parra et al. in prep.	Ghana	As	U-Pb SHRIMP	Zr			C	C
2158	5	5.517	-0.445	Feybesse et al.. 2006	Ghana	K-S	Pb-Pb (evaporation)	Zr	G1d	Monzonite	C	C
2148	3	5.7655	-3.184833	Hirdes et al., 2007	Cote d'Ivoire	Sw	Pb-Pb (dissolution)	Zr	GB2165	Granite	C	C
2137	2	5.7695	-3.157833	Hirdes et al., 2007	Cote d'Ivoire	Sw	Pb-Pb (dissolution)	Zr	GB2145	Qz monzonite	C	C
2136	9	5.980056	-2.444778	Adadey et al.. 2009	Ghana	Ku	U-Pb SHRIMP	Zr	AK2091	Granite	C	C
2136	11	6.7055	-2.7672	Amponsah, P. MSc 2011	Ghana	Sw	U-Pb	Zr	ASU002	Granitoid	C	C

2135	9	6.6847	-2.7688	Amponsah, P. MSc 2011	Ghana	Sw	U-Pb	Zr	NF002	Granitoid	C	C
2132	4	5.6384	-0.6213	Duodu et al., 2009	Ghana	K-S	U-Pb	Zr		Gneiss	C	C
2116	2	6.4871	-2.2162	Hirdes et al., 1992	Ghana	Ku	Pb-Pb (dissolution)	Zr	6899A	Granitoid	C	C
2113	1	5.3353	-0.6237	Duodu et al., 2009	Ghana	K-S	U-Pb	Zr		Granite	C	C
2112	19	5.9815	-2.1788	Adadey et al.. 2009	Ghana	Ku	U-Pb SHRIMP	Zr	AK5216	Granite	C	C
2108	18	5.6525	-2.5011	Adadey et al.. 2009	Ghana	Ku	U-Pb SHRIMP	Zr	AK4018	Granite	C	C
2106	3	6.2630	-1.6069	Oberthür et al.. 1998	Ghana	As	Pb-Pb (dissolution)	Mnz	GH789, GH1014	Granite	C	C
2106	1	5.5758	-0.4249	Duodu et al., 2009	Ghana	K-S	U-Pb	Zr		Granodiorite	C	C
2105	3	5.9160	-1.9020	Oberthür et al.. 1998	Ghana	Ku	Pb-Pb (dissolution)	Mnz	GH794	Granite	C	C
2104	2	6.2630	-1.6069	Oberthür et al.. 1998	Ghana	As	Pb-Pb (dissolution)	Mnz/Ttn	GH1017, GH388	Granitoid	C	C
2102	13	5.5266	-1.9992	Adadey et al.. 2009	Ghana	As	U-Pb SHRIMP	Zr	AK1334	Diorite	C	C
2102	1	5.7550	-1.3073	Duodu et al., 2009	Ghana	Cc	U-Pb	Zr		Granite	C	C
2097	2	6.4770	-1.1330	Oberthür et al.. 1998	Ghana	As	Pb-Pb (dissolution)	Ttn	GH390	Granodiorite	C	C
2090	44	5.6724	-2.2203	Adadey et al., 2009	Ghana		U-Pb SHRIMP	Zr	AK1249	Granite	C	C
2090	1	5.1458	-1.3466	Davis et al., 1994	Ghana	As	Pb-Pb (evaporation)	Zr	HCP1-3	Monzonite	C	C
2088	1	7.0682	-2.6548	Duodu et al., 2009	Ghana	Su	U-Pb	Zr		Granite	C	C
2088	1	7.0950	-2.5364	Hirdes et al., 1992	Ghana	Su	Pb-Pb (dissolution)	Zr	8909A	Granitoid	C	C
2081	1	5.9655	-3.1812	Hirdes et al., 2007	Cote d'Ivoire	Su	Pb-Pb (dissolution)	Zr/Mnz	GB2324	Granite	C	C
2080	3	5.4850	-0.9698	Duodu et al., 2009	Ghana	Cc	U-Pb	Zr		Pegmatite	C	C
2072	1	5.1537	-1.1613	Duodu et al., 2009	Ghana	Cc	U-Pb	Zr		Pegmatite	C	C
Effusive												
2266	2			Loh et al., 1999	Ghana	As	Pb-Pb	Zr		Volcanic	C	C
2193	5	5.4606	-1.7435	Parra et al. in prep.	Ghana	As	U-Pb SHRIMP	Zr			C	C
2189	1	6.9075	-2.0306	Hirdes et al., 1998	Ghana	Sw	Pb-Pb (dissolution)	Zr	H285	Rhyolite	C	C
2180	2	5.6722	-3.0323	Hirdes et al., 2007	Cote d'Ivoire	Sw	Pb-Pb (dissolution)	Zr		Volcanoclastite	C	C
2178	9	5.4750	-1.8650	White et al. 2014	Ghana	As	U-Pb SIMS	Zr	AWABv	Volcanoclastite	C	C
2166	2	5.6218	-3.2005	Hirdes et al., 2007	Cote d'Ivoire	Sw	Pb-Pb (evaporation)	Zr		Volcanic	C	C
2164	7	5.5805	-3.1152	Delor et al., 1992.	Cote d'Ivoire	Sw	U-Pb monozircon	Zr		Rhyolite	C	C
2162	6			Loh et al., 1999	Ghana	As	Pb-Pb	Zr		Volcanic	C	C
2142	24	5.5871	-2.4471	Adadey et al., 2009	Ghana	Ku	U-Pb SHRIMP	Zr	AK4124	Andesite		
Metam.												
2144	3			Hirdes et al., 2007	Cote d'Ivoire	Sw	Pb-Pb (dissolution)	Ttn	GB2293	Qz diorite	M	C
2098	7	6.263	-1.6069	Oberthür et al.. 1998	Ghana	As	Pb-Pb (dissolution)	Rt	GH789	Granite	M	C
2092	3	4.9555	-1.6629	Oberthür et al.. 1998	Ghana	Cc	Pb-Pb (dissolution)	Ttn	GH852	Granitoid	M	C
Detrital												C
2245	4.0	5.29751	-1.99152	Davis et al., 1994	Ghana	As	Pb-Pb (dissolution)	Zr	TK013		S	C
2194	3.0	5.35814	-1.94285	Davis et al., 1994	Ghana	As	Pb-Pb (dissolution)	Zr	sample 2069		S	C
2189	2.0			Hirdes et al., 2007	Cote d'Ivoire	Sw	Pb-Pb (dissolution)	Zr	GB0027		S	C
2185	2.0	5.34279	-1.98735	Davis et al., 1994	Ghana	As	Pb-Pb (dissolution)	Zr	TK001		S	C
2184	3.0	5.81708	-2.01644	Davis et al., 1994	Ghana	Kumasi basin	Pb-Pb (dissolution)	Zr	HUN1-3		S	C
2184	3.0	5.83065	-2.00652	Davis et al., 1994	Ghana	Kumasi basin	Pb-Pb (dissolution)	Zr	HUN1-3		S	C
2183	3.0	5.34279	-1.98735	Davis et al., 1994	Ghana	As	Pb-Pb (dissolution)	Zr	TK001		S	C
2180	4.0	5.29751	-1.99152	Davis et al., 1994	Ghana	As	Pb-Pb (dissolution)	Zr	TK013		S	C
2179	3.0	5.34279	-1.98735	Davis et al., 1994	Ghana	As	Pb-Pb (dissolution)	Zr	TK001		S	C
2174	5.0	5.34279	-1.98735	Davis et al., 1994	Ghana	As	Pb-Pb (dissolution)	Zr	TK001		S	C
2173	4.0	5.35814	-1.94285	Davis et al., 1994	Ghana	As	Pb-Pb (dissolution)	Zr	sample 2069		S	C
2172	4.0	5.29751	-1.99152	Davis et al., 1994	Ghana	As	Pb-Pb (dissolution)	Zr	TK013		S	C
2172	5.0	5.29764	-1.99074	Davis et al., 1994	Ghana	As	Pb-Pb (dissolution)	Zr	Wta34		S	C
2170	15.0	5.34279	-1.98735	Davis et al., 1994	Ghana	As	Pb-Pb (dissolution)	Zr	TK001		S	C
2169	11.0	5.29751	-1.99152	Davis et al., 1994	Ghana	As	Pb-Pb (dissolution)	Zr	TK013		S	C
2168	4.0	5.29751	-1.99152	Davis et al., 1994	Ghana	As	Pb-Pb (dissolution)	Zr	TK013		S	C
2168	3.0	5.83065	-2.00652	Davis et al., 1994	Ghana	Kumasi basin	Pb-Pb (dissolution)	Zr	HUN1-3		S	C
2167	3.0	5.29764	-1.99074	Davis et al., 1994	Ghana	As	Pb-Pb (dissolution)	Zr	Wta34		S	C
2167	3.0	5.83065	-2.00652	Davis et al., 1994	Ghana	Kumasi basin	Pb-Pb (dissolution)	Zr	HUN1-3		S	C
2164	7.0	5.29764	-1.99074	Davis et al., 1994	Ghana	As	Pb-Pb (dissolution)	Zr	Wta34		S	C
2163	31.0	5.35814	-1.94285	Davis et al., 1994	Ghana	As	Pb-Pb (dissolution)	Zr	sample 2069		S	C
2161	3.0	5.29764	-1.99074	Davis et al., 1994	Ghana	As	Pb-Pb (dissolution)	Zr	Wta34		S	C
2161	2.0			Hirdes et al., 2007	Cote d'Ivoire		Pb-Pb (dissolution)	Zr	GB0024		S	C
2159	4.0	5.29751	-1.99152	Davis et al., 1994	Ghana	As	Pb-Pb (dissolution)	Zr	TK013		S	C
2158	3.0	5.34279	-1.98735	Davis et al., 1994	Ghana	As	Pb-Pb (dissolution)	Zr	TK001		S	C
2155	5.0	5.35814	-1.94285	Davis et al., 1994	Ghana	As	Pb-Pb (dissolution)	Zr	sample 2069		S	C
2155	5.0	5.83065	-2.00652	Davis et al., 1994	Ghana	Kumasi basin	Pb-Pb (dissolution)	Zr	HUN1-3		S	C
2152.5	19.5	5.29764	-1.99074	Davis et al., 1994	Ghana	As	Pb-Pb (dissolution)	Zr	Wta34		S	C
2135	5.0	5.81708	-2.01644	Davis et al., 1994	Ghana	Kumasi basin	Pb-Pb (dissolution)	Zr	HUN1-3		S	C
2135	5.0	5.81708	-2.01644	Davis et al., 1994	Ghana	Kumasi basin	Pb-Pb (dissolution)	Zr	HUN1-3		S	C
2135	5.0	5.83065	-2.00652	Davis et al., 1994	Ghana	Kumasi basin	Pb-Pb (dissolution)	Zr	HUN1-3		S	C
2133	3.0	5.29764	-1.99074	Davis et al., 1994	Ghana	As	Pb-Pb (dissolution)	Zr	Wta34		S	C
2132	3.0	5.35814	-1.94285	Davis et al., 1994	Ghana	As	Pb-Pb (dissolution)	Zr	sample 2069		S	C
2129	2.0			Hirdes et al., 2007	Cote d'Ivoire		Pb-Pb (dissolution)	Zr	GB0024		S	C
2129	2.0			Hirdes et al., 2007	Cote d'Ivoire		Pb-Pb (dissolution)	Zr	GB0027		S	C
2132	2.8	5.337	-1.998	Hirdes and Nunoo., 1994	Ghana	As	U-Pb	Zr			S	C
2132.6	3.4	5.337	-1.998	Hirdes and Nunoo., 1994	Ghana	As	U-Pb	Zr			S	C
2155.0	4.5	5.337	-1.998	Hirdes and Nunoo., 1994	Ghana	As	U-Pb	Zr			S	C
2158.0	4.2	5.337	-1.998	Hirdes and Nunoo., 1994	Ghana	As	U-Pb	Zr			S	C
2158.2	3.1	5.337	-1.998	Hirdes and Nunoo., 1994	Ghana	As	U-Pb	Zr			S	C
2158.5	4.0	5.337	-1.998	Hirdes and Nunoo., 1994	Ghana	As	U-Pb	Zr			S	C
2160.5	3.4	5.337	-1.998	Hirdes and Nunoo., 1994	Ghana	As	U-Pb	Zr			S	C
2164.0	7.1	5.337	-1.998	Hirdes and Nunoo., 1994	Ghana	As	U-Pb	Zr			S	C
2167.1	2.8	5.337	-1.998	Hirdes and Nunoo., 1994	Ghana	As	U-Pb	Zr			S	C
2168.1	3.7	5.337	-1.998	Hirdes and Nunoo., 1994	Ghana	As	U-Pb	Zr			S	C
2171.5	5.1	5.337	-1.998	Hirdes and Nunoo., 1994	Ghana	As	U-Pb	Zr			S	C
2172.0	3.5	5.337	-1.998	Hirdes and Nunoo., 1994	Ghana	As	U-Pb	Zr			S	C
2173.5	3.8	5.337	-1.998	Hirdes and Nunoo., 1994	Ghana	As	U-Pb	Zr			S	C
2174.1	5.8	5.337	-1.998	Hirdes and Nunoo., 1994	Ghana	As	U-Pb	Zr			S	C
2179.0	2.8	5.337	-1.998	Hirdes and Nunoo., 1994	Ghana	As	U-Pb	Zr			S	C
2180.0	4.2	5.337	-1.998	Hirdes and Nunoo., 1994	Ghana	As	U-Pb	Zr			S	C
2184.4	3.2	5.337	-1.998	Hirdes and Nunoo., 1994	Ghana	As	U-Pb	Zr			S	C
2184.5	2.4	5.337	-1.998	Hirdes and Nunoo., 1994	Ghana	As	U-Pb	Zr			S	C
2194.2	2.9	5.337	-1.998	Hirdes and Nunoo., 1994	Ghana	As	U-Pb	Zr			S	C
2244.6	3.5	4.761	-2.030	Hirdes and Nunoo., 1994	Ghana	As	U-Pb	Zr			S	C
2152.6	4.8	4.761	-2.030	Loh et al., 1999	Ghana	As	Pb-Pb	Zr			S	C
2161.9	3.1	4.761	-2.030	Loh et al., 1999	Ghana	As	Pb-Pb	Zr			S	C
2166.6	2.2	4.761	-2.030	Loh et al., 1999	Ghana	As	Pb-Pb	Zr			S	C
2166.7	2.0	4.761	-2.030	Loh et al., 1999	Ghana	As	Pb-Pb	Zr			S	C
2168.2	3.1	4.761	-2.030	Loh et al., 1999	Ghana	As	Pb-Pb	Zr			S	C
2182.3	1.5	4.761	-2.030	Loh et al., 1999	Ghana	As	Pb-Pb	Zr			S	C
2256.7	1.4	4.761	-2.030	Loh et al., 1999	Ghana	As	Pb-Pb	Zr			S	C
2262.1	3.8	4.761	-2.030	Loh et al., 1999	Ghana	As	Pb-Pb	Zr			S	C
2264.2	7.3	4.761	-2.030	Loh et al., 1999	Ghana	As	Pb-Pb	Zr			S	C
2265.5	1.1	4.761	-2.030	Loh et al., 1999	Ghana	As	Pb-Pb	Zr			S	C
2090	17	5.517	-1.862	Pigois et al., 2003	Ghana	As	U-Pb SHRIMP	Zr			S	C
2095	17	5.517	-1.862	Pigois et al., 2003	Ghana	As	U-Pb SHRIMP	Zr			S	C

Age (Ma)	1σ	Lat	Lon	Ref	Country	Domain	Technique	Mineral	Sample	Litho	Interp	Area
2100	26	5.517	-1.862	Pigois et al., 2003	Ghana	As	U-Pb SHRIMP	Zr			S	C
2103	19	5.517	-1.862	Pigois et al., 2003	Ghana	As	U-Pb SHRIMP	Zr			S	C
2104	16	5.517	-1.862	Pigois et al., 2003	Ghana	As	U-Pb SHRIMP	Zr			S	C
2104	61	5.517	-1.862	Pigois et al., 2003	Ghana	As	U-Pb SHRIMP	Zr			S	C
2105	76	5.517	-1.862	Pigois et al., 2003	Ghana	As	U-Pb SHRIMP	Zr			S	C
2109	10	5.517	-1.862	Pigois et al., 2003	Ghana	As	U-Pb SHRIMP	Zr			S	C
2109	19	5.517	-1.862	Pigois et al., 2003	Ghana	As	U-Pb SHRIMP	Zr			S	C
2109	18	5.517	-1.862	Pigois et al., 2003	Ghana	As	U-Pb SHRIMP	Zr			S	C
2111	30	5.517	-1.862	Pigois et al., 2003	Ghana	As	U-Pb SHRIMP	Zr			S	C
2111	22	5.517	-1.862	Pigois et al., 2003	Ghana	As	U-Pb SHRIMP	Zr			S	C
2113	27	5.517	-1.862	Pigois et al., 2003	Ghana	As	U-Pb SHRIMP	Zr			S	C
2113	36	5.517	-1.862	Pigois et al., 2003	Ghana	As	U-Pb SHRIMP	Zr			S	C
2114	15	5.517	-1.862	Pigois et al., 2003	Ghana	As	U-Pb SHRIMP	Zr			S	C
2114	29	5.517	-1.862	Pigois et al., 2003	Ghana	As	U-Pb SHRIMP	Zr			S	C
2115	22	5.517	-1.862	Pigois et al., 2003	Ghana	As	U-Pb SHRIMP	Zr			S	C
2116	16	5.517	-1.862	Pigois et al., 2003	Ghana	As	U-Pb SHRIMP	Zr			S	C
2116	14	5.517	-1.862	Pigois et al., 2003	Ghana	As	U-Pb SHRIMP	Zr			S	C
2118	11	5.517	-1.862	Pigois et al., 2003	Ghana	As	U-Pb SHRIMP	Zr			S	C
2119	27	5.517	-1.862	Pigois et al., 2003	Ghana	As	U-Pb SHRIMP	Zr			S	C
2119	12	5.517	-1.862	Pigois et al., 2003	Ghana	As	U-Pb SHRIMP	Zr			S	C
2119	24	5.517	-1.862	Pigois et al., 2003	Ghana	As	U-Pb SHRIMP	Zr			S	C
2119	16	5.517	-1.862	Pigois et al., 2003	Ghana	As	U-Pb SHRIMP	Zr			S	C
2122	18	5.517	-1.862	Pigois et al., 2003	Ghana	As	U-Pb SHRIMP	Zr			S	C
2122	9	5.517	-1.862	Pigois et al., 2003	Ghana	As	U-Pb SHRIMP	Zr			S	C
2122	15	5.517	-1.862	Pigois et al., 2003	Ghana	As	U-Pb SHRIMP	Zr			S	C
2123	18	5.517	-1.862	Pigois et al., 2003	Ghana	As	U-Pb SHRIMP	Zr			S	C
2123	17	5.517	-1.862	Pigois et al., 2003	Ghana	As	U-Pb SHRIMP	Zr			S	C
2123	16	5.517	-1.862	Pigois et al., 2003	Ghana	As	U-Pb SHRIMP	Zr			S	C
2124	16	5.517	-1.862	Pigois et al., 2003	Ghana	As	U-Pb SHRIMP	Zr			S	C
2124	14	5.517	-1.862	Pigois et al., 2003	Ghana	As	U-Pb SHRIMP	Zr			S	C
2124	11	5.517	-1.862	Pigois et al., 2003	Ghana	As	U-Pb SHRIMP	Zr			S	C
2125	23	5.517	-1.862	Pigois et al., 2003	Ghana	As	U-Pb SHRIMP	Zr			S	C
2126	12	5.517	-1.862	Pigois et al., 2003	Ghana	As	U-Pb SHRIMP	Zr			S	C
2128	17	5.517	-1.862	Pigois et al., 2003	Ghana	As	U-Pb SHRIMP	Zr			S	C
2131	14	5.517	-1.862	Pigois et al., 2003	Ghana	As	U-Pb SHRIMP	Zr			S	C
2131	18	5.517	-1.862	Pigois et al., 2003	Ghana	As	U-Pb SHRIMP	Zr			S	C
2131	18	5.517	-1.862	Pigois et al., 2003	Ghana	As	U-Pb SHRIMP	Zr			S	C
2133	11	5.517	-1.862	Pigois et al., 2003	Ghana	As	U-Pb SHRIMP	Zr			S	C
2134	15	5.517	-1.862	Pigois et al., 2003	Ghana	As	U-Pb SHRIMP	Zr			S	C
2134	9	5.517	-1.862	Pigois et al., 2003	Ghana	As	U-Pb SHRIMP	Zr			S	C
2135	12	5.517	-1.862	Pigois et al., 2003	Ghana	As	U-Pb SHRIMP	Zr			S	C
2135	32	5.517	-1.862	Pigois et al., 2003	Ghana	As	U-Pb SHRIMP	Zr			S	C
2136	19	5.517	-1.862	Pigois et al., 2003	Ghana	As	U-Pb SHRIMP	Zr			S	C
2140	30	5.517	-1.862	Pigois et al., 2003	Ghana	As	U-Pb SHRIMP	Zr			S	C
2142	13	5.517	-1.862	Pigois et al., 2003	Ghana	As	U-Pb SHRIMP	Zr			S	C
2142	16	5.517	-1.862	Pigois et al., 2003	Ghana	As	U-Pb SHRIMP	Zr			S	C
2142	13	5.517	-1.862	Pigois et al., 2003	Ghana	As	U-Pb SHRIMP	Zr			S	C
2142	19	5.517	-1.862	Pigois et al., 2003	Ghana	As	U-Pb SHRIMP	Zr			S	C
2143	16	5.517	-1.862	Pigois et al., 2003	Ghana	As	U-Pb SHRIMP	Zr			S	C
2143	16	5.517	-1.862	Pigois et al., 2003	Ghana	As	U-Pb SHRIMP	Zr			S	C
2143	23	5.517	-1.862	Pigois et al., 2003	Ghana	As	U-Pb SHRIMP	Zr			S	C
2144	13	5.517	-1.862	Pigois et al., 2003	Ghana	As	U-Pb SHRIMP	Zr			S	C
2144	21	5.517	-1.862	Pigois et al., 2003	Ghana	As	U-Pb SHRIMP	Zr			S	C
2145	8	5.517	-1.862	Pigois et al., 2003	Ghana	As	U-Pb SHRIMP	Zr			S	C
2145	17	5.517	-1.862	Pigois et al., 2003	Ghana	As	U-Pb SHRIMP	Zr			S	C
2146	52	5.517	-1.862	Pigois et al., 2003	Ghana	As	U-Pb SHRIMP	Zr			S	C
2146	23	5.517	-1.862	Pigois et al., 2003	Ghana	As	U-Pb SHRIMP	Zr			S	C
2146	19	5.517	-1.862	Pigois et al., 2003	Ghana	As	U-Pb SHRIMP	Zr			S	C
2147	23	5.517	-1.862	Pigois et al., 2003	Ghana	As	U-Pb SHRIMP	Zr			S	C
2148	16	5.517	-1.862	Pigois et al., 2003	Ghana	As	U-Pb SHRIMP	Zr			S	C
2149	11	5.517	-1.862	Pigois et al., 2003	Ghana	As	U-Pb SHRIMP	Zr			S	C
2151	14	5.517	-1.862	Pigois et al., 2003	Ghana	As	U-Pb SHRIMP	Zr			S	C
2153	19	5.517	-1.862	Pigois et al., 2003	Ghana	As	U-Pb SHRIMP	Zr			S	C
2155	10	5.517	-1.862	Pigois et al., 2003	Ghana	As	U-Pb SHRIMP	Zr			S	C
2155	22	5.517	-1.862	Pigois et al., 2003	Ghana	As	U-Pb SHRIMP	Zr			S	C
2155	24	5.517	-1.862	Pigois et al., 2003	Ghana	As	U-Pb SHRIMP	Zr			S	C
2156	21	5.517	-1.862	Pigois et al., 2003	Ghana	As	U-Pb SHRIMP	Zr			S	C
2156	17	5.517	-1.862	Pigois et al., 2003	Ghana	As	U-Pb SHRIMP	Zr			S	C
2158	9	5.517	-1.862	Pigois et al., 2003	Ghana	As	U-Pb SHRIMP	Zr			S	C
2159	31	5.517	-1.862	Pigois et al., 2003	Ghana	As	U-Pb SHRIMP	Zr			S	C
2159	28	5.517	-1.862	Pigois et al., 2003	Ghana	As	U-Pb SHRIMP	Zr			S	C
2159	22	5.517	-1.862	Pigois et al., 2003	Ghana	As	U-Pb SHRIMP	Zr			S	C
2162	25	5.517	-1.862	Pigois et al., 2003	Ghana	As	U-Pb SHRIMP	Zr			S	C
2163	23	5.517	-1.862	Pigois et al., 2003	Ghana	As	U-Pb SHRIMP	Zr			S	C
2163	19	5.517	-1.862	Pigois et al., 2003	Ghana	As	U-Pb SHRIMP	Zr			S	C
2164	21	5.517	-1.862	Pigois et al., 2003	Ghana	As	U-Pb SHRIMP	Zr			S	C
2164	24	5.517	-1.862	Pigois et al., 2003	Ghana	As	U-Pb SHRIMP	Zr			S	C
2165	18	5.517	-1.862	Pigois et al., 2003	Ghana	As	U-Pb SHRIMP	Zr			S	C
2165	14	5.517	-1.862	Pigois et al., 2003	Ghana	As	U-Pb SHRIMP	Zr			S	C
2168	12	5.517	-1.862	Pigois et al., 2003	Ghana	As	U-Pb SHRIMP	Zr			S	C
2168	20	5.517	-1.862	Pigois et al., 2003	Ghana	As	U-Pb SHRIMP	Zr			S	C
2169	19	5.517	-1.862	Pigois et al., 2003	Ghana	As	U-Pb SHRIMP	Zr			S	C
2173	14	5.517	-1.862	Pigois et al., 2003	Ghana	As	U-Pb SHRIMP	Zr			S	C
2174	23	5.517	-1.862	Pigois et al., 2003	Ghana	As	U-Pb SHRIMP	Zr			S	C
2174	19	5.517	-1.862	Pigois et al., 2003	Ghana	As	U-Pb SHRIMP	Zr			S	C
2176	20	5.517	-1.862	Pigois et al., 2003	Ghana	As	U-Pb SHRIMP	Zr			S	C
2176	31	5.517	-1.862	Pigois et al., 2003	Ghana	As	U-Pb SHRIMP	Zr			S	C
2179	21	5.517	-1.862	Pigois et al., 2003	Ghana	As	U-Pb SHRIMP	Zr			S	C
2180	44	5.517	-1.862	Pigois et al., 2003	Ghana	As	U-Pb SHRIMP	Zr			S	C
2180	20	5.517	-1.862	Pigois et al., 2003	Ghana	As	U-Pb SHRIMP	Zr			S	C
2180	22	5.517	-1.862	Pigois et al., 2003	Ghana	As	U-Pb SHRIMP	Zr			S	C
2182	17	5.517	-1.862	Pigois et al., 2003	Ghana	As	U-Pb SHRIMP	Zr			S	C
2182	14	5.517	-1.862	Pigois et al., 2003	Ghana	As	U-Pb SHRIMP	Zr			S	C
2184	12	5.517	-1.862	Pigois et al., 2003	Ghana	As	U-Pb SHRIMP	Zr			S	C
2186	17	5.517	-1.862	Pigois et al., 2003	Ghana	As	U-Pb SHRIMP	Zr			S	C
2187	12	5.517	-1.862	Pigois et al., 2003	Ghana	As	U-Pb SHRIMP	Zr			S	C
2188	10	5.517	-1.862	Pigois et al., 2003	Ghana	As	U-Pb SHRIMP	Zr			S	C
2188	23	5.517	-1.862	Pigois et al., 2003	Ghana	As	U-Pb SHRIMP	Zr			S	C
2191	11	5.517	-1.862	Pigois et al., 2003	Ghana	As	U-Pb SHRIMP	Zr			S	C
2198	22	5.517	-1.862	Pigois et al., 2003	Ghana	As	U-Pb SHRIMP	Zr			S	C
2198	23	5.517	-1.862	Pigois et al., 2003	Ghana	As	U-Pb SHRIMP	Zr			S	C
2200	19	5.517	-1.862	Pigois et al., 2003	Ghana	As	U-Pb SHRIMP	Zr			S	C
2205	24	5.517	-1.862	Pigois et al., 2003	Ghana	As	U-Pb SHRIMP	Zr			S	C

Age (Ma)	1σ	Lat	Lon	Ref	Country	Domain	Technique	Mineral	Sample	Litho	Interp	Area
2211	14	5.517	-1.862	Pigois et al., 2003	Ghana	As	U-Pb SHRIMP	Zr			S	C
2222	25	5.517	-1.862	Pigois et al., 2003	Ghana	As	U-Pb SHRIMP	Zr			S	C
2223	15	5.517	-1.862	Pigois et al., 2003	Ghana	As	U-Pb SHRIMP	Zr			S	C
2236	19	5.517	-1.862	Pigois et al., 2003	Ghana	As	U-Pb SHRIMP	Zr			S	C
2242	29	5.517	-1.862	Pigois et al., 2003	Ghana	As	U-Pb SHRIMP	Zr			S	C
2257	21	5.517	-1.862	Pigois et al., 2003	Ghana	As	U-Pb SHRIMP	Zr			S	C
Côte d'Ivoire & W Burkina												
Inherited												
2312	17	8.5858	-4.3853	Gasquet et al., 2003	Côte-d'Ivoire.	Si - Da	U-Pb IMS & TIMS	Zr	s8-32	Tonalite	I	D
2220	6	8.2053	-5.0449	Kouamelan, 1996	Ivory Coast	Ka	Pb-Pb (evaporation)	Zr	TD61b	Granodiorite	I	D
2163	5	8.6102	-4.0838	Lüdtke et al., 1999	Côte-d'Ivoire.	Ho - O-F - T	Pb-Pb (dissolution)	Zr	DK3118	Granodiorite	I	D
2154	5.5	11.1270	-3.5208	Bruguier, unpubl	Burkina Faso	Ho - O-F - T	U-Pb ICPMS	Zr	HO076B	Rhyolite	I	D
2143	3			Kouamelan 96	Côte-d'Ivoire.		Pb-Pb (evaporation)	Zr	SEN-1	Orthogneiss	I	D
2135	3			Kouamelan 96	Côte-d'Ivoire.		Pb-Pb (evaporation)	Zr	SOK-1a	Tonalite	I	D
2108	4	8.7468	-4.1637	Lüdtke et al., 1999	Côte-d'Ivoire.	Ho - O-F - T	Pb-Pb (dissolution)	Zr	DK3118	Granodiorite	I	D
Intrusive												
2195	3	10.2465	-3.2696	Bruguier, unpubl	Burkina Faso	Di - Na	U-Pb ICPMS	Zr	HO261A	Trondhjemite	C	D
2183	3.5	11.7376	-3.2820	Bruguier, unpubl	Burkina Faso	Ho - O-F - T	U-Pb ICPMS	Zr	HO22	Trondhjemite	C	D
2181	13	10.2716	-3.0886	Parra et al. in prep.	Burkina Faso	Bo - W-L	U-Pb SHRIMP	Zr	HO631B	Granitoid	C	D
2178.5	5.8	10.3167	-3.2193	Parra et al. in prep.	Burkina Faso	Bo - W-L	U-Pb SHRIMP	Zr	HO253	Granitoid	C	D
2175	1			Scwhartz, Melcher, 2003	Burkina Faso	Ho - O-F - T	U-Pb	Zr	Perkoa	Qz-diorite	C	D
2170	19	8.5858	-4.3853	Gasquet et al.. 2003	Ivory Coast	Si - Da	U-Pb IMS & TIMS	Zr	s8-32	Tonalite	C	D
2162	32	8.5194	-4.6692	Gasquet et al.. 2003	Ivory Coast	Si - Da	U-Pb IMS & TIMS	Zr	s8-27	leucogranite	C	D
2154	1	8.5858	-4.3853	Gasquet et al.,2003	Côte-d'Ivoire.	Si - Da	U-Pb IMS & TIMS	Zr	s8-32	Tonalite	C	D
2154	1	8.7271	-4.0851	Lüdtke et al., 1999	Côte-d'Ivoire.	Ho - O-F - T	Pb-Pb (dissolution)	Zr	DK2069	Granodiorite	C	D
2153		10.4715	-5.2160	Parra et al. in prep.	Burkina Faso	Ba	U-Pb SHRIMP	Zr	BNF561	Granitoid	C	D
2152	4	9.5977	-4.2832	Hirdes et al.. 1996	Ivory Coast	Si - Da	Pb-Pb (dissolution)	Zr	KN5000	Granodiorite	C	D
2152	3	9.6192	-3.6708	Hirdes et al., 1996	Côte-d'Ivoire.	Ho - O-F - T	Pb-Pb (dissolution)	Zr/Ttn	TH4374	Granodiorite	C	D
2151	5	8.8843	-3.7209	Delor et al 95	Côte-d'Ivoire.	Di - Na	U-Pb monozircon	Zr		Tonalite	C	D
2150	4	8.3276	-3.4327	Kouamelan 96	Côte-d'Ivoire.	Di - Na	Pb-Pb (evaporation)	Zr	NAD109	Orthogneiss	C	D
2149.1	6.9	10.2683	-3.0892	Parra et al. in prep.	Burkina Faso	Bo - W-L	U-Pb SHRIMP	Zr	HO631A	Granodiorite	C	D
2144	6	8.3538	-4.3471	Lemoine 88	Côte-d'Ivoire.	Si - Da	U-Pb	Zr		Orthogneiss	C	D
2143	8	7.5575	-6.6395	Kouamelan 96	Côte-d'Ivoire.		Pb-Pb (evaporation)	Zr	VAA-1	Orthogneiss	C	D
2143		10.4426	-5.4569	Parra	Burkina Faso	Ba	U-Pb SHRIMP	Zr	BNF559	Granitoid	C	D
2142.8	5.1	10.2683	-3.0892	Parra et al. in prep.	Burkina Faso	Bo - W-L	U-Pb SHRIMP	Zr	HO631B	Aplite	C	D
2137	7	9.5823	-4.1613	Hirdes et al. 1996	Ivory Coast	Si - Da	Pb-Pb (dissolution)	Zr	KN1065	Granodiorite	C	D
2136	1	8.4903	-4.2823	Lüdtke et al., 1999	Côte-d'Ivoire.	Si - Da	Pb-Pb (dissolution)	Zr	DK2123	Orthogneiss	C	D
2135.8	4	10.3012	-3.2307	Parra et al. in prep.	Burkina Faso	Bo - W-L	U-Pb SHRIMP	Zr	HO257	Granitoid	C	D
2132	1.5	10.1741	-3.4951	Bruguier, unpubl	Burkina Faso	Ho - O-F - T	U-Pb ICPMS	Zr	HO585	Granite	C	D
2126		10.3339	-5.2756	Parra et al. in prep.	Burkina Faso	Ba	U-Pb SHRIMP	Zr	BNF562	Granitoid	C	D
2124	2	10.7731	-2.7293	Duodu et al. 2009	Ghana	Bo - W-L	U-Pb	Zr	BN181	Granodiorite	C	D
2121	4	9.9825	-3.8391	Bruguier, unpubl	Burkina Faso	Ho - O-F - T	U-Pb ICPMS	Zr	HO621	Granite	C	D
2120		10.4715	-5.2160	Parra et al. in prep.	Burkina Faso	Ba	U-Pb SHRIMP	Zr	BNF561	Granitoid	C	D
2118	2	8.1528	-5.0228	Gasquet et al.. 2003	Ivory Coast	Si - Da	U-Pb IMS & TIMS	Zr	s8-45	Trondhjemite	C	D
2118		10.6494	-4.7971	Parra et al. in prep.	Burkina Faso	Ba	U-Pb SHRIMP	Zr	BF12-01	Granitoid	C	D
2114	3	11.6975	-3.1979	Bruguier, unpubl	Burkina Faso	Ho - O-F - T	U-Pb ICPMS	Zr	HO13	granite	C	D
2113	2	8.8450	-4.1441	Lüdtke et al., 1999	Côte-d'Ivoire.	Ho - O-F - T	Pb-Pb (dissolution)	Zr	DK4000	Monzodiorite	C	D
2110	6	9.7758	-3.9267	Hirdes et al., 1996	Côte-d'Ivoire.	Ho - O-F - T	Pb-Pb (dissolution)	Zr	TH2153	Granodiorite	C	D
2109	3	8.2817	-4.1965	Lemoine 88	Côte-d'Ivoire.	Ho - O-F - T	U-Pb	Zr	118 LS	Granodiorite	C	D
2109	2	11.7810	-2.9460	Castaing et al., 2003	Burkina Faso	Di - Na	Pb-Pb (evaporation)	Zr	PC0170	Qz diorite	C	D
2108	13	8.2290	-5.0787	Doumbia et al.. 1998	Ivory Coast	Ka	Pb-Pb (evaporation)	Zr	KTD71	lamprophyre	C	D
2108	12	8.3365	-5.1030	Doumbia et al.. 1998	Ivory Coast	Ka	Pb-Pb (evaporation)	Zr	KTD61a	Diorite	C	D
2108	3	12.3090	-2.7820	Castaing et al., 2003	Burkina Faso	Bo - W-L	Pb-Pb (evaporation)	Zr	PC0443	Granitoid	C	D
2107	4			Kouamelan 96	Côte-d'Ivoire.		Pb-Pb (evaporation)	Zr	SOK-1a	Tonalite	C	D
2107	3	10.9894	-4.0214	Bruguier, unpubl	Burkina Faso	Si - Da	U-Pb ICPMS	Zr	HO425B	Granodiorite	C	D
2106	2	8.9760	-4.1113	Lüdtke et al., 1999	Côte-d'Ivoire.	Ho - O-F - T	Pb-Pb (dissolution)	Zr	DK2090	Orthogneiss	C	D
2106	7	11.2600	-3.6780	Castaing et al., 2003	Burkina Faso	Ho - O-F - T	Pb-Pb (evaporation)	Zr	PC0190	Granitoid	C	D
2104	1	10.7659	-2.8451	Duodu et al. 2009	Ghana	Bo - W-L	U-Pb	Zr	BN192	Granodiorite	C	D
2104	2	9.8350	-3.9712	Hirdes et al.. 1996	Ivory Coast	Ho - O-F - T	Pb-Pb (dissolution)	Zr	TH2173	Qz diorite	C	D
2103	1	8.1686	-4.4289	Gasquet et al.. 2003	Ivory Coast	Si - Da	U-Pb IMS & TIMS	Zr	s8-43	Granodiorite	C	D
2103	1	9.5753	-4.0942	Hirdes et al.. 1996	Ivory Coast	Ho - O-F - T	Pb-Pb (dissolution)	Zr/Ttn	KN1081	Monzodiorite	C	D
2103	1	8.1945	-4.1985	Lüdtke et al., 1999	Côte-d'Ivoire.	Ho - O-F - T	Pb-Pb (dissolution)	Zr	DK1097	Tonalite	C	D
2102	11	8.6389	-4.4522	Gasquet et al.. 2003	Ivory Coast	Si - Da	U-Pb IMS & TIMS	Zr	s8-33	Granodiorite	C	D
2102	2	8.7468	-4.1637	Lüdtke et al., 1999	Côte-d'Ivoire.	Ho - O-F - T	Pb-Pb (dissolution)	Zr	DK3118	Granodiorite	C	D
2101	3	11.1561	-4.1931	Bruguier, unpubl	Burkina Faso	Si - Da	U-Pb ICPMS	Zr	HO37A	Granodiorite	C	D
2101	3.5	11.7630	-2.9920	Bruguier, unpubl	Burkina Faso	Di - Na	U-Pb ICPMS	Zr	HO491	Granite	C	D
2100	6	9.3293	-5.6635	Kouamelan 96	Côte-d'Ivoire.		Pb-Pb (evaporation)	Zr	KG-32-33	Orthogneiss	C	D
2098	1	8.8843	-4.0655	Lüdtke et al., 1999	Côte-d'Ivoire.	Ho - O-F - T	Pb-Pb (dissolution)	Zr	DK2098	Granodiorite	C	D
2097	17	8.0090	-5.5024	Doumbia et al.. 1998	Ivory Coast	Ka	Pb-Pb (evaporation)	Zr	KTD73	Granitoid	C	D
2097	3	8.1773	-5.0886	Doumbia et al.. 1998	Ivory Coast	Ka	Pb-Pb (evaporation)	Zr	KT147	Trondjhemite	C	D
2097	3	9.6225	-3.7695	Hirdes et al.. 1996	Ivory Coast	Ho - O-F - T	Pb-Pb (dissolution)	Zr/Ttn	TH2079	granodiorite	C	D
2097	10	11.7810	-2.9460	Castaing et al., 2003	Burkina Faso	Di - Na	Pb-Pb (evaporation)	Zr	PC0170	Granite	C	D
2095	10	6.3588	-4.1709	Delor et al 95	Côte-d'Ivoire.	Comoé	U-Pb monozircon	Zr			C	D
2094	6	8.4930	-5.3780	Doumbia et al.. 1998	Ivory Coast	Ka	Pb-Pb (evaporation)	Mnz	KT116	Leucogranite	C	D
2092	3	8.1979	-5.0485	Kouamelan 96	Côte-d'Ivoire.	Ka	Pb-Pb (evaporation)	Zr	KTD61b	Granodiorite	C	D
2091	8			Kouamelan 96	Côte-d'Ivoire.		Pb-Pb (evaporation)	Zr	SEN-1	Orthogneiss	C	D
2087	6	6.6249	-4.8296	Delor et al 95	Côte-d'Ivoire.	Co	U-Pb monozircon	Zr			C	D
2085	7			Kouamelan 96	Côte-d'Ivoire.		Pb-Pb (evaporation)	Zr	BEZ-1	Orthogneiss	C	D
2079	11	6.7565	-4.7981	Delor et al 95	Côte-d'Ivoire.	Co	U-Pb monozircon	Zr			C	D
Effusive												
2195	10	8.7599	-3.4262	Delor et al 95	Côte-d'Ivoire.	Di - Na	U-Pb monozircon	Zr		Metarhyolite	C	D
2195	2			Scwhartz, Melcher, 2003	Burkina Faso	Ho - O-F - T	U-Pb	Zr	Poura	Rhyolite	C	D
2191	2.5	10.1189	-3.4954	Bruguier, unpubl	Burkina Faso	Ho - O-F - T	U-Pb ICPMS	Zr	HO270	Rhyolite	C	D
2178	7	7.8221	-4.8314	Kouamelan 96	Côte-d'Ivoire.	Fe	Pb-Pb (evaporation)	Zr	MB2	Volcanite	C	D
2176	4	11.2560	-3.6530	Castaing et al., 2003	Burkina Faso	Ho - O-F - T	Pb-Pb (evaporation)	Zr	PC0198	Rhyolite	C	D
2173	7	8.4520	-4.0812	Kouamelan 1996	Côte-d'Ivoire.	Ho - O-F - T	Pb-Pb (evaporation)	Zr	DB331	Volcanite	C	D
2172	2.5	11.2151	-3.7415	Bruguier, unpubl	Burkina Faso	Ho - O-F - T	U-Pb ICPMS	Zr	HO124B	Andesite	C	D
2171	7	11.0405	-3.2636	Castaing et al., 2003	Burkina Faso	Bo - W-L	U-Pb IMS	Zr	MD0207	Rhyolite	C	D
2170	5	8.5896	-4.0419	Lüdtke et al., 1999	Côte-d'Ivoire.	Ho - O-F - T	Pb-Pb (dissolution)	Zr	DK3114	Felsic tuf	C	D
2163	4	8.0794	-4.6092	Kouamelan 96	Côte-d'Ivoire.	Ho - O-F - T	Pb-Pb (evaporation)	Zr	DB26	Volcanite	C	D

Age (Ma)	1σ	Lat	Lon	Ref	Country	Domain	Technique	Mineral	Sample	Litho	Interp	Area
2176	18.2	10.2564	-3.0548	Parra et al. in prep.	Burkina Faso	Bo - W-L	U-Pb SHRIMP	Zr	HO298	Volcanosediment	C	D
2160	1			Lüdtke et al., 1998	Côte-d'Ivoire.	Ho - O-F - T	Pb-Pb (dissolution)	Zr	TH5600	volcanoclastite	C	D
2158	1	8.6485	-4.1572	Lüdtke et al., 1999	Côte-d'Ivoire.	Ho - O-F - T	Pb-Pb (dissolution)	Zr	DK4335	rhyolite	C	D
2123	3	8.2780	-5.2500	Doumbia et al.. 1998	Ivory Coast	Ka	Pb-Pb	Zr	KT304	rhyodacite	C	D
2105	1	8.0749	-4.7202	Leake 92	Côte-d'Ivoire.	Fe	U-Pb	Zr	Fetekro	rhyolite	C	D
2104	2	9.6862	-4.1052	Hirdes et al.. 1996	Ivory Coast	Ho - O-F - T	Pb-Pb (dissolution)	Zr	KN1395	rhyolite	C	D
2095	4.5	11.1270	-3.5208	Bruguier, unpubl	Burkina Faso	Ho - O-F - T	U-Pb ICPMS	Zr	HO076B	Rhyolite	C	D
Metam.												
2100	3	9.5977	-4.2832	Hirdes et al.. 1996	Côte-d'Ivoire.	Si - Da	Pb-Pb (dissolution)	Ttn	KN5000	Granodiorite	M	D
2090	42	8.7271	-4.0851	Lüdtke et al., 1999	Côte-d'Ivoire.	Ho - O-F - T	Pb-Pb (dissolution)	Ttn	DK2069	Granodiorite	M	D
2080	10			Kouamelan 96	Côte-d'Ivoire.		Pb-Pb (evaporation)	Mnz/Ttn	SEN-1	Orthogneiss	Melting	D
2144	3	10.2465	-3.2696	Bruguier, unpubl	Burkina Faso	Di - Na	U-Pb ICPMS	Zr	HO261B	Trondjhemite	M	D
2137	7	9.5823	-4.1613	Hirdes et al. 1996	Ivory Coast	Si - Da	Pb-Pb (dissolution)	Zr	KN1065	Granodiorite	Melting	D
Detrital												
2101	7	8.1656	-5.3464	Doumbia et al.. 1998	Côte-d'Ivoire.	Ka	Pb-Pb (evaporation)	Zr	KTD45a		S	D
2133	3	8.1648	-5.3456	Doumbia et al., 1998	Côte-d'Ivoire.	Ka	Pb-Pb (evaporation)	Zr	KTD45a		S	D
2131	6			Lüdtke et al., 1999	Côte-d'Ivoire.	Ho - O-F - T	Pb-Pb (dissolution)	Zr	TH3136	Conglomerate	S	D
2134	1			Lüdtke et al., 1999	Côte-d'Ivoire.	Ho - O-F - T	Pb-Pb (dissolution)	Zr	TH3136	Conglomerate	S	D
2143	2			Lüdtke et al., 1999	Côte-d'Ivoire.	Ho - O-F - T	Pb-Pb (dissolution)	Zr	TH3136	Conglomerate	S	D
2145	2			Lüdtke et al., 1999	Côte-d'Ivoire.	Ho - O-F - T	Pb-Pb (dissolution)	Zr	TH3136	Conglomerate	S	D
2155	2			Lüdtke et al., 1999	Côte-d'Ivoire.	Ho - O-F - T	Pb-Pb (dissolution)	Zr	TH3136	Conglomerate	S	D
2164	3			Lüdtke et al., 1999	Côte-d'Ivoire.	Ho - O-F - T	Pb-Pb (dissolution)	Zr	TH3136	Conglomerate	S	D
2170	3			Lüdtke et al., 1999	Côte-d'Ivoire.	Ho - O-F - T	Pb-Pb (dissolution)	Zr	TH3136	Conglomerate	S	D
2126	1	8.23783	-4.003	Lüdtke et al., 1998	Côte-d'Ivoire.	Ho - O-F - T	Pb-Pb (dissolution)	Zr	DK1046	Sandstone	S	D
2146	2	8.23783	-4.003	Lüdtke et al., 1998	Côte-d'Ivoire.	Ho - O-F - T	Pb-Pb (dissolution)	Zr	DK1046	Sandstone	S	D
2150	2	8.23783	-4.003	Lüdtke et al., 1998	Côte-d'Ivoire.	Ho - O-F - T	Pb-Pb (dissolution)	Zr	DK1046	Sandstone	S	D
2151	2	8.23783	-4.003	Lüdtke et al., 1998	Côte-d'Ivoire.	Ho - O-F - T	Pb-Pb (dissolution)	Zr	DK1046	Sandstone	S	D
2179	2	8.23783	-4.003	Lüdtke et al., 1998	Côte-d'Ivoire.	Ho - O-F - T	Pb-Pb (dissolution)	Zr	DK1046	Sandstone	S	D
2181	2	8.23783	-4.003	Lüdtke et al., 1998	Côte-d'Ivoire.	Ho - O-F - T	Pb-Pb (dissolution)	Zr	DK1046	Sandstone	S	D
2115	2	8.21983	-4.10233	Lüdtke et al., 1998	Côte-d'Ivoire.	Ho - O-F - T	Pb-Pb (dissolution)	Zr	DK1069	Arkose	S	D
2139	3	8.21983	-4.10233	Lüdtke et al., 1998	Côte-d'Ivoire.	Ho - O-F - T	Pb-Pb (dissolution)	Zr	DK1069	Arkose	S	D
2141	1	8.21983	-4.10233	Lüdtke et al., 1998	Côte-d'Ivoire.	Ho - O-F - T	Pb-Pb (dissolution)	Zr	DK1069	Arkose	S	D
2163	2	8.21983	-4.10233	Lüdtke et al., 1998	Côte-d'Ivoire.	Ho - O-F - T	Pb-Pb (dissolution)	Zr	DK1069	Arkose	S	D
2177	1	8.21983	-4.10233	Lüdtke et al., 1998	Côte-d'Ivoire.	Ho - O-F - T	Pb-Pb (dissolution)	Zr	DK1069	Arkose	S	D
2179	8			Delor et al 95	Côte-d'Ivoire.	Ho - O-F - T	U-Pb monozircon	Zr		sediment	S	D
2126	4			Delor et al 95	Côte-d'Ivoire.	Ho - O-F - T	U-Pb monozircon	Zr		sediment	S	D
2148	4	10.889	-3.545	Bossière et al. 1996	Burkina Faso	Ho - O-F - T	Pb-Pb (evaporation)	Zr	91-49	Conglomerate	S	D
2140	17	11.33	-3.47	Bossière et al. 1996	Burkina Faso	Ho - O-F - T	Pb-Pb (evaporation)	Zr		Conglomerate	S	D
2145	8	11.33	-3.47	Bossière et al. 1996	Burkina Faso	Ho - O-F - T	Pb-Pb (evaporation)	Zr	91-23	Conglomerate	S	D
2147	11	11.33	-3.47	Bossière et al. 1996	Burkina Faso	Ho - O-F - T	Pb-Pb (evaporation)	Zr	91-23	Conglomerate	S	D
2158	12	11.33	-3.47	Bossière et al. 1996	Burkina Faso	Ho - O-F - T	Pb-Pb (evaporation)	Zr	91-23	Conglomerate	S	D
2124	9			Bossière et al. 1996	Burkina Faso	Ho - O-F - T	Pb-Pb (evaporation)	Zr	91-15	Conglomerate	S	D
2171	7			Bossière et al. 1996	Burkina Faso	Ho - O-F - T	Pb-Pb (evaporation)	Zr	91-15	Conglomerate	S	D

6.2.7.4 A geodynamic evolution model for the south-eastern West African Craton.

The available data from northern Ghana and neighbouring domains documents a three-stage evolution and a rapid stabilisation for the south-eastern part of the Paleoproterozoic West African Craton. The first step corresponds to a major magmatic episode after the Archean-Paleoproterozoic transition, at about 2.40 Ga. It formed a juvenile proto-crust, dominantly mafic, which represented a major component of the protolith of the modern-day exposed crust. The absence of older reworked crust points to its generation away from active continental margins. However, the geodynamic setting of the juvenile proto-crust formation is speculative. It has to account for (i) the production of a low-K mafic proto-crust across areas of >1000 km radius, and (ii) the formation and mobilisation of LILE-enriched mantle sources, which requires the geometric association of hydrous crustal rocks and mantle rocks. An oceanic plateau environment is compatible with the production of a mafic crust on a large scale, and accretion of oceanic plateaus has been proposed to be a key mechanism of crustal growth on the early Earth (Albarède, 1998; Benn and Moyen, 2008; Desrochers et al., 1993; Puchtel et al., 1998). However, the genesis of a mafic crust on such an extensive scale in analogues of modern island arcs would probably require a few coeval arcs, because the juvenile crust production in modern subduction zones is focused in linear belts rather than across vast areas in the oceanic realm. Mantle enrichment in LILE implies that the mantle is metasomatised by hydrous fluids. The subduction of hydrated oceanic crustal rocks provides a mechanism to enrich the mantle in LILE, and is consistent with an arc setting for juvenile crust production. The delamination of sub-solidus eclogite at the base of thickened oceanic plateau fragments may also provide a mechanism to transfer hydrous fluids to the mantle, thus forming LILE-enriched sources below the proto-crust (Bédard, 2006; Bédard et al., 2013).

The dominance of felsic magmatic rocks over mafic rocks on the West African Craton, as in other Archean and Paleoproterozoic cratons, implies that in a second phase starting at ca. 2.25 Ga, the older mafic proto-crust is recycled. In agreement with Hf isotopic signatures, pulses of mantle-derived calc-alkaline magmas are added to the crust, which undergoes melting and differentiation to form TTG magmas. Mantle derived magmas are produced more abundantly in the early stages of crust maturation, while crustal magmas such as TTGs gradually predominate. Therefore, the geodynamic evolution during this period has to account for a near synchronous melting of both mantle and crustal sources, with a shift in their relative contributions from a predominance of mantle melting to that of crust recycling. This evolution may reflect that of a maturing magmatic arc in a subduction setting. Calc-alkaline magmas are emplaced above a subducted mafic crust which dehydrates. As the arc gradually thickens, the shallow differentiation of mantle-derived magmas generates a range of lavas (basalts and andesites) and plutons (diorites and granodiorites). This scenario is at odds with the proposed production of TTGs by the partial melting of the slab in "hot" subduction zones (Drummond and Defant, 1990; Foley et al., 2002; Martin, 1986; Martin and Moyen, 2002; Smithies et al., 2003), because the subducting crust (oceanic lithosphere, plateau fragments, etc) dehydrates before melting. The source of TTGs may rather be the dominantly mafic crust, which undergoes sufficient tectonic thickening to melt at its base (Atherton

and Petford, 1993; Bédard, 2006; Bédard et al., 2013; Smithies, 2000; Zegers and van Keken, 2001). The combined contribution of mantle and crustal sources may be a consequence of rapidly alternating (and possibly diachronous) phases of contraction and extension, the latter allowing for the development of volcano-sedimentary and clastic sedimentary basins documented in northern Ghana and neighbouring provinces (Block et al., Subm; De Kock et al., 2012; Feybesse et al., 2006; Perrouty et al., 2012; Pouclet et al., 2006; Vidal and Alric, 1994). The composition of the Paleoproterozoic crust of northern Ghana is not strictly similar to that of modern accretionary orogens. This may be due to differences in the lithological and thermo-mechanical state of the craton crust, which might imply alternative geodynamic settings. Early metamorphism in northern Ghana records cold geothermal gradients of 15 $^{\circ}$ C/km (Block et al., 2015). Under such thermal conditions, the base of a tectonically thickened basaltic oceanic plateau would be transformed to negatively buoyant fertile eclogite. In a hotter Paleoproterozoic mantle (e.g. Herzberg et al. (2010); Nisbet et al. (1993)), the crustal keel may form dense negative diapirs which could delaminate. The delaminated crust would further melt, react, metasomatise and fertilise the underlying mantle (Bédard, 2006; Van Thienen et al., 2004a,b). Crust delamination would be compensated by mantle upwelling, transferring heat to shallower levels in the crust and driving crustal recycling. Alternating cycles of crustal thickening, delamination and thermal relaxation may equally account for the combined crustal and mantle-derived magmatism, as well as for the alternations between contractional and extensional tectonic phases. Such a mechanism would remain viable until the crust becomes dominantly felsic, hot and buoyant. Both scenarios mentioned above have contrasting implications in terms of craton architecture. Modern subduction zones are asymmetric structures, which form lithological and metamorphic zoning and lateral age gradients. The internal recycling of an oceanic plateau implies distributed magma sources, as long as tectonic forces can cause its distributed thickening. Ancient >2.20 Ga lavas or plutons are distributed across the whole craton. This suggests that recycling of the proto-crust was spatially distributed and involved magma sources which spread over 1000 km width. Hence, the locus of crustal growth and recycling does not seem to be restricted to an accretionary front. This constraint is more consistent with the second scenario, i.e. distributed internal recycling of the oceanic plateau, than with a modern subduction setting, unless multiple magmatic arcs were formed and accreted in a limited time range. Investigating architectural constraints may require further detailed geochronological and metamorphic studies at the scale of the craton.

The third stage of the craton evolution corresponds to the tectonic assembly of the cratonic domains during the Eburnean orogeny, between 2.14 and 2.07 Ga. Magmatic accretion formed coeval but potentially separate crustal fragments, all of which are presently characterised by terrane-scale strain and structures which imply bulk horizontal contraction. These observations recall the structural patterns of many Archean provinces (e.g. Chardon et al. (2011); Kusky and Polat (1999); Li and Kusky (2007); Windley and Garde (2009)). They suggest that convergence and orogeny played a fundamental role in stabilising juvenile continental masses and in shaping the final craton architecture. Across the West African Craton, the orogeny is marked by coeval plutonism. The geochronological record of the north-eastern domains (a-b) of the Baoulé-Mossi domain (Fig. 6.15) supports a continuous, 80-

100 Ma long magmatic activity which terminates with a 2.14-2.11 Ga orogenic cycle (Block et al., Subm). Although magma sources seem unchanged in this period, the geochemical signature of some of the youngest TTG plutons suggests an increase in melting pressure with time. This may reflect a progressive thickening of the crust, the development of local "cold" geotherms and mechanically stronger crustal fragments, which were buried deeper before reaching the solidus, in agreement with the progressive waning of volcanism in this period. Contrastingly, the bimodal distribution of crystallisation ages of magmatic rocks in south-central provinces (c-d) may be consistent with a polycyclic orogenic model for the Eburnean orogeny. The second orogenic cycle starts at *ca.* 2.12 Ga and is about 40 Ma long. It directly follows peak metamorphism and anatexis in NW Ghana, and develops while tectono-magmatic activity terminates in provinces (a-b). Based on these constraints, we suggest that the metamorphic paroxysm in NW Ghana is the result of a collision between the north-eastern (a-b) and south-western (c-d) Baoulé-Mossi domain (Block et al., Subm). The collision marks the final stabilisation of compartment (a-b), while tectono-magmatic activity propagated further in a "mobile belt" (c-d) to the south, and along the contact with the Archean craton to the west. The high-grade interference zone in NW Ghana is at the transition between the two cratonic domains, and therefore it may represent a Paleoproterozoic suture zone. Eburnean tectono-magmatic re-activation and metamorphic overprinting of the Archean craton is dated between 2.12 and 2.05 Ga (Egal et al., 2002; Kouamelan et al., 1997; Schofield et al., 2006). This suggests that the collision with the Archean block took place during the final stages of the evolution of the adjacent Paleoproterozoic domain, and precludes that the Archean craton played a major role in the 2.20-2.12 Ga orogenic evolution of the Paleoproterozoic crust, consistently with Lu-Hf isotope data.

Following an uniformitarian approach, numerous authors propose that the forces driving bulk horizontal contraction on cratons were the result of subduction (e.g. Cawood et al. (2009, 2006); de Wit (1998); Komiya et al. (1999); Kusky (1989); Pease et al. (2008)). However, other authors insist that horizontal contraction does not necessarily require subduction (e.g. Bédard et al. (2013); Rey et al. (2001)) and argue that alternative geodynamic settings can account for the observed geology (Hamilton, 1998, 2003; Smithies et al., 2003, 2005). This point has extra significance in light of results of numerical modelling, which suggest different subduction dynamics (sluggish or intermittent subduction) on the early Earth (Korenaga, 2006; van Hunen and van den Berg, 2008). The applicability of the subduction model for the Paleoproterozoic West African Craton is not unambiguously demonstrated, and the inferred suture zone in north-western Ghana cannot be considered as a strict analogue of a subduction-related oceanic suture found in modern orogens. It lacks characteristic features such as Ultra-High-Pressure metamorphism (e.g. Chopin (1984); Smith (1984)) or ophiolites (Helmstaedt and Scott, 1992; Moores, 1982). It does however show evidence for amalgamation of terranes with different geological histories, tectonically driven exhumation of lower-crustal rocks, and low-temperature, high-pressure metamorphic rocks paired with amphibolite- to granulite-facies metamorphic rocks (Block et al., Subm, 2015), all of which could be considered to result from some sort of plate tectonics.

6.2.8 Conclusion

The Paleoproterozoic West African Craton evolved from a proto-crust which was extracted from the depleted mantle after 2.40 Ga. The proto-crust was intensely recycled until 2.25-2.20 Ga. By that time, TTG and calc-alkaline suites formed continental fragments which escaped recycling. Although mobilized in different tectonic settings, magmatic systems remained relatively unchanged between 2.21 and 2.12 Ga, and were dominated by low-K, hydrous mafic rocks and, to a lesser extent, a LILE-rich mantle source. Crustal maturation through melting of pre-existing felsic rocks (TTG) played a minor role. The Paleoproterozoic juvenile crustal blocks were subject to horizontal tectonic forces which caused alternating horizontal contraction and extension. Based on architectural and geochronological arguments, we claim that the north-eastern and south-western portions of the modern day eastern Baoulé-Mossi domain represent two distinct crustal blocks which were originally separated. Both fragments collided together at ca. 2.13 Ga, causing localized crustal thickening and anatexis. Following collision, tectono-magmatic activity stopped in the north-eastern portion of the craton, and propagated further south and west. Younger geodynamic activity was localized until ca. 2.05 Ga in mobile belts along the margins of the Archean craton, and in modern-day southern Ghana. We suggest that the juvenile protolith of the actual Paleoproterozoic crust formed away from active continental margins, in an oceanic plateau or in multiple coeval island arcs. The TTG suites and volcanic rocks which presently constitute the continental crust are derived from the tectono-magmatic reworking of the proto-crust by orogenic processes. Although its architecture resembles that of Archean crust, the magmatic evolution of the West African Craton differs from that of late-Archean domains, while its metamorphic record shows some similarities with modern orogenic belts. The forces driving lateral tectonic accretion of the various Paleoproterozoic domains and the Archean nucleus remain unclear, particularly because of the lack of evidence for modern-day subduction analogues. Subduction may have played a role in driving lateral terrane accretion, but it did not produce the markers classically attributed to Phanerozoic accretionary orogens. The Paleoproterozoic geodynamics may therefore be interpreted as an intermediate thermal regime in the secular evolution of the Earth.

6.2.9 Acknowledgements

We wish to gratefully acknowledge AMIRA International and the industry sponsors, including AusAid and the ARC Linkage Project LP110100667, for their support of the WAXI project (P934A). We thank Philippe de Parseval, Sophie Gouy and Thierry Aigouy for their assistance for micro-analysis and imagery aquisition. We recognise the logistical support and datasets provided by the Geological Survey Department of Ghana, as well as the chauffeurs from the IRD in Ouagadougou (Salifou Yougbaré, Boukary Ouedraogo and Matthieu Kaboré) and from the GSD of Ghana (Kwasi Duah).

6.2.10 Appendix

6.2.10.1 Synthesis of sample petrography

Sample	Lat	Long	Age	Error	Qz	Pl	Kf	Amp	Bt	Ep_met	Ep_mag	Ttn	Opaque	Chl	Ms
BN014	10.92339	-0.71749			xxxx	xxx	xx	o	x	x	o	x	x	o	o
BN018	10.83008	-0.99215	2134	1	xxxx	xxx	o	xxx	xx	x	o	o	xx	o	o
BN028A	9.750725	-2.11622			xxxx	xxx	o	o	xxx	x	o	o	o	o	o
BN028B	9.750725	-2.11622			xxxx	xx	xxx	o	x	o	xx	o	o	x	o
BN069B	10.8768	-0.55773			xxxx	xxx	xx	o	xx	o	x	x	o	o	o
BN074	10.98672	-0.53			xxxx	xx	xxx	x	o	xx	o	x	o	x	o
BN077	11.0021	-0.37198	2134	1	xxxx	xxx	xx	x	xx	x	o	o	o	x	o
BN080	11.04035	-0.27845			xxxx	xxx	x	o	xx	o	o	o	x	o	o
BN082A	10.85383	-0.17034			xxxx	xxx	x	o	o	o	o	o	o	o	o
BN082B	10.85383	-0.17034			xxxx	xxx	xx	xx	xx	x	o	o	o	o	o
BN083	10.82629	-0.83814			xxxx	xxx	xx	x	xx	o	o	o	o	o	o
BN087	10.83016	-1.07189			xxxx	xxx	o	xx	xx	x	o	o	o	o	o
BN090	10.82261	-0.94131	2134	6	xxxx	xxx	xx	o	x	x	x	o	o	o	x
BN112	9.467688	-2.27897	2120	3	xxxx	xxx	xx	o	xx	o	xx	o	o	o	o
BN114	9.97276	-2.01986			xxxx	xxx	x	o	xx	o	o	o	o	o	o
BN115	9.969464	-2.03272	2118	4	xxxx	xxx	xxx	o	xx	x	o	o	xx	x	o
BN119	9.969197	-2.11479	2133	6	xxxx	xxx	xxx	o	x	x	o	o	o	o	o
BN123B	10.847	-1.104	2156	1	xxxx	xxx	xx	o	xx	x	o	o	x	o	o
BN127	10.65298	-1.27168			xxxx	xx	o	o	xxx	xx	o	x	o	x	o
BN146	10.88645	-1.74452			xxxx	xxx	xxx	o	xx	x	o	o	x	o	o
BN155	10.67273	-2.03074			xxxx	x	xx	o	xxx	xx	o	o	o	o	o
BN181	10.77311	-2.72933	2124	2	xxxx	x	xx	o	xx	o	o	o	x	o	o
BN189	10.98288	-2.71763			xxxx	xxx	x	o	xxx	o	o	o	o	o	o
BN192	10.76531	-2.84338	2104	1	xxxx	xxx	xx	x	xx	o	x	o	o	x	o
BN198	10.41746	-2.72118			xxxx	xxx	x	o	xx	xx	o	o	o	o	x
BN213	10.31252	-2.33172			xxxx	x	xx	o	x	o	x	o	o	o	o
BN223	9.898058	-2.45798			xxxx	xxx	xx	o	xx	o	x	o	o	o	o
BN229	9.035799	-2.43675	2134	6	xxxx	xxx	o	xxx	o	o	xx	o	o	o	o
BN231	8.985552	-2.49849	2193	4	xxxx	xxx	x	x	xx	x	o	o	x	o	o
BN235	8.859711	-2.33931	2118	6	xxxx	xxx	o	o	x	xxx	o	o	x	o	xxx
BN252	8.880621	-2.17644			xxxx	xx	xx	o	x	x	o	o	o	o	o
BN254	8.840761	-2.14315			xxx	x	o	xxx	o	x	o	o	o	o	o
BN258	8.481899	-2.18339	2125	2	xxxx	xxx	x	xxx	xxx	x	o	o	o	o	o
BN261	8.642792	-2.19517	2187	5	xxxx	xx	xxx	xx	xx	o	o	x	o	o	o
BN261B	8.642792	-2.19517	2187	5	xxxx	xxx	xx	o	xx	o	x	o	o	xx	o
BN265	8.656513	-2.24863			xxxx	xxx	o	x	x	o	x	o	o	o	o
BN278	9.643339	-2.70015			xxxx	xxx	xx	o	xx	o	x	o	o	x	o
BN283	10.67003	-0.862	2151	1	xxxx	xx	xxx	o	xxx	x	o	o	x	x	o
BN289	10.85494	-0.61019			xxxx	xxx	xxx	o	xx	xx	o	x	o	o	o
BN380	9.97831	-2.29645	2150	4	xxxx	xxx	o	xx	x	x	o	o	o	o	o
BN430	8.841989	-2.08698	2126	7	xxxx	xxx	xxx	o	xx	x	o	o	o	o	o
BN532	9.806999	-2.61299			xxxx	xxxx	xxx	xx	xxx	x	o	o	o	o	o
BN598	10.18862	-1.90132			xxxx	xxx	xxx	xx	xx	o	x	x	o	o	o
BN76C	11.00216	-0.38124			xxxx	xxx	o	o	xx	o	o	o	o	o	o
BN85B	10.63174	-1.03162			xxxx	xxx	x	xx	xx	x	o	x	x	o	o

TABLE 6.8: Petrography of granitoid samples. The abundance of mineral phases is given by symbols and ranges from absent (o) to very abundant (xxxx).

6.2.10.2 Whole-rock geochemistry analytical procedures

At ALS Global, whole rock measurements were performed using ICPAES for major elements (ME-ICP06 and OA- GRA05 methods, ALS Minerals, 2006a) and base metal (ME-4ACD81, ALS Minerals, 2009) ; trace elements including Rare Earth Elements composition were measured by ICP-MS (ME-MS81 and ME-MS42 methods, ALS Minerals, 2009, 2006b). At Géosciences Montpellier, trace element analyses were performed by conventional nebulisation ICP-MS using an Agilent 7700x mass spectrometer. Sample digestion procedure was achieved on batches of 100 mg. The samples were dissolved twice on a hot plate at 130 ° C with a mixture of 48% HF/HNO3 for 48 hours in closed teflon beakers. After evaporation all samples were subjected to three steps of evaporation with decreasing HNO3 quantities and at increasing temperatures up to 150 ° C to remove fluorides. Samples were then dissolved in 2% HNO_3 and diluted shortly before analysis to a final dilution factor of *ca.* 5 000. Dilution factor were kept high to avoid detector saturation, and to minimize drift which was corrected for by addition of doping elements, namely In and Bi, at a concentration level of 1 ppb. Element concentrations were determined by external calibrations except for Nb and Ta which were measured by surrogate calibration using Zr and Hf respectively following the method outlined by Jochum et al. (1990) for Spark Source Mass Spectrometry and applied to ICP-MS in this study. Reproducibility and accuracy were checked by carrying out replicate analyses of both certified reference materials (BEN and UBN) and samples. Polyatomic interferences were controlled by running the machine at an oxyde production level $<$ 1.5% and corrected for by running batches of synthetic solutions containing interfering elements.

6.2.10.3 U–Pb dating

A classic mineral separation procedure has been applied to concentrate zircon grains using the facilities available at Géosciences Environnement Toulouse. Rocks were crushed and only the powder fraction with a diameter $<$ 250 ţm was kept. Heavy minerals were successively concentrated by Wilfley table and heavy liquids. Magnetic minerals were then removed with an isodynamic Frantz separator. Zircon grains were handpicked under a binocular microscope and embedded in epoxy mounts. The grains were then hand-grounded and polished on a lap wheel with a 6 μm and 1 μm diamond suspension successively. The internal structure of zircon grains were characterised by raster electron microscopy (REM) at Geosciences Environnement Toulouse using a JEOL SM-6360 OLV Scanning Electron Microscope, at Université de Montpellier II using an Environmental Scanning Electron Microscope FEI model, and back-scattered electron (BSE) imaging using a ThermoScientific Element 2 sector field ICP-MS coupled to a Resolution M-50 (Resonetics) 193 nm ArF excimer laser (ComPexPro 102F, Coherent) system.

The laser system at Université de Montpellier II is a Compex 102 (Lambda Physiks) 193nm excimer laser, coupled to Element XR sector field ICP-MS (for details on the analytical technique see Bosch et al. (2011)). U-Th-Pb analyses were performed under helium, in a 15 cm^3 circular shaped cell using an energy density of 12J/cm^2 at a frequency of 4Hz. Laser spot sizes was 26 μm. Analyses were calibrated against the zircon standard G91500 (Wiedenbeck et al., 1995) which was used to

correct the collected data for mass discrimination and inter-element fractionation. The ^{202}Hg was used to monitor the ^{204}Hg interference on ^{204}Pb, but common Pb correction was not performed as this often resulted in over-correction, the 204 mass being largely dominated by ^{204}Hg. Data presented in this study thus only report analyses for which no common Pb was detected.

Five additional samples were analysed for U-Pb and Lu-Hf using laser ablation - inductively coupled plasma - sector field - mass spectrometry (LA-ICP(SF)-MS) at Goethe University Frankfurt.

Data was process using ISOPLOT macro (Ludwig, 2001).

6.2.10.4 Lu–Hf analysis

Laser spots for Lu–Hf were placed directly "on-top" of the U–Pb laser spots , or within the same zone characterised by CL and SEM imaging.

Calculation of initial^{176}Hf/^{177}Hf ratios were performed using the individual ^{176}Lu/^{177}Hf ratio of each measurement, a decay constant of $\lambda^{176}\text{Lu} = 1.867 \text{ x } 10^{-11}$ (Söderlund et al., 2004) and the ^{207}Pb/^{206}Pb age of the corresponding spot. For the calculation of ε Hf(t), parameters of the chondritic uniform reservoir (CHUR) recommended by Bouvier et al. (2008) were used (^{176}Lu/^{177}Hf = 0.0336 ; ^{176}Hf/^{177}Hf = 0.282785). Depleted mantle model ages (T_{DM}Hf) given in Table 6.6 are calculated using a ^{176}Lu/^{177}Hf ratio of 0.0113 for the crustal source (Taylor and McLennan, 1985; Wedepohl, 1995) and the DM model of Blichert-Toft and Puchtel (2010), i.e. characterized by linear regression from present-day MORB (^{176}Lu/^{177}Hf = 0.03933 and ^{176}Hf/^{177}Hf = 0.283294). Næraa et al. (2012) proposed an alternative (less depleted) DM model based on the analysis of Archean samples from western Greenland (^{176}Lu/^{177}Hf = 0.03750 and ^{176}Hf/^{177}Hf = 0.283120), that was also considered in this study.

Chapitre 7

General discussion / Conclusion générale

7.1 Résultats et perspectives

7.1.1 Controverses sur l'évolution du Craton Ouest Africain

7.1.1.1 Evolution tectonique et métamorphique

Cette thèse constitue la première étude métamorphique portant sur les domaines paléoprotérozoïques du Craton Ouest Africain qui associe des données pétrologiques avec la datation de phases métamorphiques, et qui présente des chemins P-T permettant de contraindre le régime thermique de la croûte pendant l'orogenèse Éburnéenne. Les gradients géothermiques apparents enregistrés par les roches métamorphiques du nord du Ghana sont variables dans le temps et dans l'espace. Ils ne sont pas particulièrement élevés, ce qui suggère que les modèles de croûte "chaude" proposés pour les orogènes anciens ne sont pas applicables à l'ensemble de l'histoire géologique du Craton Ouest Africain. Le registre métamorphique du nord du Ghana suggère plutôt que différents régimes thermiques ont pu co-exister dans le temps, ou que la thermicité de la croûte a changé au cours de l'évolution géologique.

Cette étude offre également une représentation de la distribution cartographique des roches et des faciès métamorphiques. Elle révèle qu'un domaine de gneisses migmatitiques est cerné de ceintures de roches vertes de bas grade. Les protolithes de ces deux types de domaines métamorphiques (gneisses et ceintures de roches vertes) comprennent des roches volcaniques et plutoniques dont les âges de crystallisation sont compris entre 2.21 et 2.13 Ga. Ces roches sont pour la plupart plus anciennes que l'épisode métamorphique de haut grade (en faciès amphibolite à granulite) qui est daté de 2.14-2.13 Ga. Ce résultat permet de ré-interpréter la relation entre les ceintures de roches vertes et les domaines gneissiques au nord du Ghana. Il implique que les différentes unités ont toutes subi le même épisode orogénique à l'origine du métamorphisme. Les contrastes de conditions métamorphiques entre gneisses et ceintures de roches vertes ne peuvent donc pas être attribuées à un dépôt en discordance des formations volcano-sédimentaires des ceintures sur un socle gneissique plus ancien. Elles sont plutôt dues à la mise en contact tectonique de différentes écailles crustales métamorphisées simultanément, à des profondeurs variées pendant l'orogenèse. Les ceintures de roches vertes pourraient donc représenter des équivalents superficiels de certains paragneisses de haut grade. Les données géochronologiques et structurales obtenues sont compatibles avec un unique cycle orogénique relativement bref (2.14-2.11 Ga). Il s'accompagne de la formation syn-tectonique de bassins détritiques dans lesquels les roches volcano-sédimentaires sont remaniées. La formation d'un dôme anatectique, au sein duquel des migmatites sont exhumées, est imputée à une extension syn-orogénique lors de l'effondrement gravitaire de l'orogène. L'exhumation des migmatites dans le dôme constitue une explication possible de la disposition des gneisses au centre de plusieurs domaines de plus faible degré métamorphique.

La juxtaposition de domaines métamorphiques contrastés implique que des roches mises en place en surface ont été enfouies dans la croûte inférieure, puis exhumées et mises en contact tectonique avec des unités plus superficielles. Ces résultats indiquent que la lithosphère était suffisament résistante pour pouvoir s'épaissir au point d'enfouir des sédiments en profondeur pendant l'orogenèse Éburnéenne. Les changements des contraites tectoniques, du régime thermique et des proprié-

tés rhéologiques de la croûte ont ensuite entraîné l'effondrement gravitaire de la croûte sur-épaissie. Cette évolution requiert une rhéologie initiale correspondant à une croûte relativement froide, contrairement à ce qui est généralement suggéré pour les orogènes chauds des cratons datant de l'Archéen.

La compréhension de l'évolution géologique du nord du Ghana pose de nouvelles questions sur les autres provinces du Craton Ouest Africain. Les ceintures de roches vertes représentent-elles toutes des équivalents faiblement métamorphiques des gneisses exhumés depuis la croûte inférieure ? Les migmatites distribuées sur le craton ont été relativement peu étudiées jusqu'à présent, bien qu'elles puissent fournir des informations majeures sur les processus tectoniques contrôlant l'orogenèse Éburnéenne. D'autres études sont souhaitables pour quantifier les conditions métamorphiques, dater les roches métamorphiques et contraindre leurs environnements tectoniques en diverses zones du craton. Elles permettraient d'évaluer les relations entre les différents domaines tectono-métamorphiques à la lumière de données nouvelles. De plus, le déroulement de l'orogenèse Éburnéenne à l'échelle du craton demeure sujet à débat. L'orogenèse s'est elle manifestée de façon synchrone d'une extrémité à l'autre du craton ? Ou bien y a-t-il eu une migration de la déformation et du métamorphisme à mesure qu'un front d'accrétion se propageait ? D'avantage de contraintes sur l'âge du métamorphisme permettraient d'éclaircir ce point.

7.1.1.2 Croissance crustale

La croûte continentale paléoprotérozoique est essentiellement issue de la différenciation précoce d'une croûte basique juvénile, extraite du manteau au maximum 350 Ma avant la stabilisation du craton. Cette période entre le début de la formation du craton et la fin de l'activité géodynamique est relativement courte comparée à l'histoire des autres cratons. Le caractère juvénile de la croûte continentale suggère que son protolithe basique s'est formé loin de continents plus anciens, sans impliquer le recyclage de matériel crustal pré-existant. Ainsi, des événements magmatiques majeurs ont contribué à la croissance crustale au Paléoprotérozoique, loin des marges continentales actives. La croûte continentale au nord du Ghana est constituée de roches analogues aux TTG archéens, mises en place en même temps que des roches calco-alcalines d'arc. Leurs caractéristiques géochimiques suggèrent la fusion d'une source hybride comprenant un manteau métasomatisé et une croûte basique. D'avantage de contraintes sur l'évolution crustale pourraient être tirées de l'étude des roches magmatiques basiques, qui n'a pas été entreprise lors de cette thèse. Elle pourrait fournir des informations supplémentaires sur les sources du magmatisme. L'isotopie Lu-Hf et U-Pb sur des zircons de roches magmatiques basiques permettrait d'affiner l'évolution précoce du craton et de contraindre la nature de la "proto-croûte" juvénile, qui représente une composante de la source des magmas différenciés.

L'étude géochimique des roches du nord du Ghana démontre que les sources du magmatisme et les processus pétrogénétiques sont demeurés relativement constants au cours de l'évolution du craton. Ils ont produit une gamme limitée de roches. Ce registre magmatique contraste avec celui qui caractérise l'évolution tardive des cratons archéens. Ce dernier comprend des roches présentant une plus grande diversité géochimique, qui reflète des processus pétrogénétiques variés et changeants, conséquence d'une évolution des contextes géodynamiques dans lesquels les magmas sont

produits à la fin de l'Archéen. De plus, l'évolution géodynamique tardive au nord du Ghana est marquée par la mise en place de TTG issus d'une fusion à grande profondeur. Ceci est inhabituel, car le magmatisme tardi-Archéen implique plutôt le recyclage de sources crustales peu profondes.

7.1.1.3 Architecture crustale - La subduction est elle nécessaire ?

Le Craton Ouest Africain est constitué de domaines continentaux qui sont distincts par leur architecture crustale et leur histoire géologique. En particulier, les accidents structuraux et les ceintures de roches vertes au nord et à l'est du Burkina Faso et au nord du Ghana ont des orientations distinctes des grands traits structuraux du sud-ouest du Burkina Faso et de la Côte d'Ivoire. Ces domaines cratoniques diffèrent par leurs évolutions tectoniques et magmatiques. Les gneisses de haut grade au nord-ouest du Ghana se trouvent à l'interface de ces deux domaines d'architecture crustale contrastée. L'histoire géologique, métamorphique et tectonique du nord du Ghana suggère qu'une zone de collision s'y est formée lorsque les deux domaines cratoniques ont été amalgamés, au cours de l'orogenèse Eburnéenne. Le nord du Ghana pourrait donc représenter une suture entre deux compartiments du craton.

La nature des forces motrices à l'origine de la collision et du raccourcissement horizontal demeure hypothétique. La subduction est un candidat de choix pour expliquer ces forces tectoniques, car le fonctionnement de la Terre moderne nous apprend qu'elle fournit les forces à l'origine de la tectonique des plaques. Cependant, les mouvements des plaques lithosphériques sur la Terre moderne ne sont pas tous *directement* induits par la traction d'une plaque en subduction (le déplacement du continent nord Américain vers l'ouest n'est pas lié à la traction d'un slab). Sur le Craton Ouest Africain, de nombreux objets géologiques sont interprétés dans la littérature comme étant produits dans un contexte géologique dominé par une zone de subduction. C'est le cas des roches magmatiques appartenant à la série calco-alcaline, des unités géologiques présentant des similarités avec les turbidites ou les ophiolites modernes, des minéralisations de sulfures massifs et de porphyres de cuivre, dont on considère qu'ils sont produits dans des arcs magmatiques, au dessus d'une lithosphère plongeante. Par contre, certains marqueurs qui caractérisent les subductions modernes, tels qu'un zonage métamorphique incluant des unités de schistes bleus ou de UPH, sont absents du craton. De plus, les zones de subduction modernes sont associées à une activité magmatique localisée dans des arcs magmatiques linéaires, et aboutissent à la mise en contact de domaines d'âge et d'origine distincts. Aucun de ces aspects n'a été rapporté sur le Craton Ouest Africain. L'activité magmatique semble démarrer simultanément sur l'ensemble du craton. Des laves anciennes, mises en places vers 2.20 Ga, constituent la base de la séquence stratigraphique de nombreuses ceintures de roches vertes distribuées dans tous les domaines paléoprotérozoïques. Cette donnée indique que le magmatisme était distribué plutôt que géométriquement localisé, tel que c'est le cas dans les zones de subduction modernes.

Par contre, la géologie du Craton Ouest Africain démontre que des fragments de croûte ont été enfouis, sans doute jusqu'au manteau. Les reliques métamorphiques de HP-BT décrites dans cette thèse constituent une observation importante. Elles reflètent un géotherme apparent relativement faible, et elles sont spatialement asso-

ciées à des roches de haute température, voire sur-imprimées par un métamorphisme MP-MT. Ceci démontre l'existance d'hétérogénéités thermiques dans la croûte, ce qui est compatible avec un modèle de subduction, sans que celle-ci ne soit forcément strictement équivalente aux subductions modernes. Cependant, la distribution des roches métamorphiques HP-BT à l'échelle du craton est méconnue, et leur origine est peu comprise. Il serait utile de chercher d'autres occurrences de roches métamorphiques HP-BT et de mieux contraindre leur contexte tectonique, afin d'apporter de nouveaux arguments à la controverse portant sur la présence ou non d'une zone de subduction au Paléoprotérozoïque. Tant que l'existence de celle-ci n'est pas démontrée avec confiance, il parait souhaitable de considérer et de tester des modèles géodynamiques alternatifs, compatibles avec le registre géologique observé.

7.1.2 Conséquences sur l'évolution séculaire de la Terre

Le registre magmatique paléoprotérozoïque du nord du Ghana conjugue des éléments caractéristiques du magmatisme archéen et des arcs magmatiques modernes. Il pourrait être le reflet d'un système magmatique hybride mis en place dans un contexte géodynamique "transitionnel", entre ceux de l'Archéen d'une part, et du Protérozoïque ou du Phanérozoïque d'autre part. L'association de roches métamorphiques enregistrant des conditions de HP-BT avec des roches métamorphisées à la limite entre les faciès amphibolite et granulite HP se démarque du registre métamorphique "ordinaire" qui caractérise l'Archéen. Le registre métamorphique du Ghana semble constituer un des exemples précoces de la diversité des régimes thermiques qui sont enregistrés dans les orogènes post-archéens. Enfin, l'exhumation de roches de haut grade et leur mise en contact tectonique avec des unités contrastées indique que le comportement rhéologique de la lithosphère était similaire à celui des orogènes modernes. La partie paléoprotérozoïque du Craton Ouest Africain partage donc des similitudes aussi bien avec le registre géologique de l'Archéen qu'avec celui du Protérozoïque ou du Phanérozoïque. Par contre, certaines lithologies décrites dans d'autres orogènes du même âge, telles que les éclogites, ne sont pas connues sur le craton. L'ensemble de ces caractéristiques définit un registre géologique unique, qui pourrait refléter des processus géodynamiques transitionnels.

L'interprétation selon laquelle la partie paléoprotérozoïque du Craton Ouest Africain s'est formée au terme d'un cycle de subduction-collision, analogue à ceux se déroulant sur la Terre moderne, est sujet à débat, puisque certains des processus intervenant dans sa mise en place ne correspondent pas à ceux en vigueur sur la Terre moderne. La formation du Craton Ouest Africain au Paléoprotérozoïque représente un épisode discret de croissance continentale entre 2.30 et 2.10 Ga, qui témoigne de l'extraction massive de croûte juvénile à partir du manteau. La chronologie de cet épisode le place entre deux periodes marquées par une forte croissance du volume de croûte continentale, et qui correspondraient à la genèse cyclique de "super-continents" à 2.70-2.50 et 2.10-1.80 Ga. Ces cycles sont interprétés comme une manifestation d'une sorte de tectonique des plaques. Le diachronisme entre la formation du Craton Ouest Africain et les pics globaux de croissance crustale illustre la mise en place d'un autre type de configuration géodynamique, également favorable à la préservation de croûte continentale juvénile. Il suggère que des événements magmatiques majeurs, peut-être liés à la formation ponctuelle de panaches mantelliques, ont pu contribuer à la croissance des continents au Paléoprotérozoïque.

Depuis quelques décennies, un courant de pensée en sciences de la Terre affirme que la tectonique des plaques s'est initiée au Néoarchéen, peut être dès 3.00 Ga. La période comprise entre 3.00 et 2.50 Ga est décrite comme une phase de transition globale, au cours de laquelle la tectonique des plaques s'est progressivement généralisée. La mutation de la géodynamique terrestre à cette époque est interprétée comme la conséquence du refroidissement séculaire de la Terre. Le changement du registre géologique reflète une modification du régime thermique de la Terre et de ses effets dans la lithosphère. Cette modification pourrait faire suite au franchissement d'un seuil par des paramètres qui contrôlent le mode de convection de la Terre, tels que la température du manteau. De nombreuses études montrent cependant que les changements géodynamiques ont été diachrones d'un craton à un autre. Des contextes géodynamiques différents ont pu coexister dans différentes provinces du même âge. De plus, des particularités locales, propres à chaque craton, ont peut-être eu des impacts déterminants sur les processus géologiques et sur la chronologie de la mise en place d'une géodynamique moderne. Par conséquent, le registre géologique à une époque donnée est le double reflet d'une configuration géodynamique unique à l'échelle régionale, et de l'état thermique de la Terre à l'échelle globale.

La coexistence d'une tectonique "moderne" avec une tectonique "archaïque" sur Terre a donc peut-être duré jusqu'à environ 2.00 Ga. Cette conclusion impose de discuter le sens d'une "transition" dans l'évolution séculaire de la Terre. En effet, la transition Archéen-Protérozoïque représenterait alors une longue période (3.00-2.00 Ga) de transformations progressives et continues, et une conversion lente de l'ensemble de la planète à la tectonique des plaques, plutôt qu'une mutation abrupte du mode de fonctionnement de la Terre. Mais la tectonique des plaques néoarchéenne ou paléoprotérozoïque aurait pu fonctionner par intermittence, ou se mettre en place localement avant de se généraliser. Il est donc envisageable que le Paléoprotérozoïque ait connu une alternance entre des contextes s'apparentant à la tectonique des plaques, et d'autres sans équivalent moderne, par exemple entre les périodes de formation des super-continents.

7.2 Main results and perspectives

7.2.1 Controversies on the evolution of the West African Craton

7.2.1.1 Tectonic and metamorphic evolution

This thesis provided the opportunity to produce the first complete metamorphic study on a part of the Paleoproterozoic West African Craton, that combines petrological data with texturally-controlled dating of metamorphic phases, yielding P-T paths which can be used to constrain the thermal regime of the crust during the Eburnean orogeny in northern Ghana. The main results indicate that geothermal gradients varied both spatially and temporally. In general, metamorphic conditions do not record particularly hot geotherms. The results cast doubts on the suitability and applicability of "hot orogen" models for the whole Paleoproterozoic history of the West African Craton, and rather support the idea that different thermal environments coexisted.

This work also provides a view of the regional distribution of metamorphic rocks and facies. Low-grade greenstone belts circumscribe a vast migmatitic gneissic domain. The protolith of both low- and high-grade metamorphic domains comprises volcanic and plutonic rocks with crystallisation ages between 2.21 and 2.13 Ga. Most of these rocks are older than the 2.14-2.13 Ga high-grade (amphibolite to granulite facies) regional metamorphism. This result allows us to re-assess the relationship between greenstone belts and granite-gneiss terranes (at least as far as northern Ghana is concerned). It implies that all of the metamorphic domains witnessed the same orogenic event which is associated with metamorphism. Therefore, the contrasting metamorphic conditions between gneisses and greenstone belts cannot be due to the deposition of discordant volcano-sedimentary rocks in belts emplaced on an older gneissic basement. The metamorphic breaks rather originate from the tectonic juxtaposition of different crustal-scale slices that underwent synchronous metamorphism at different crustal depths. The greenstone belts may well represent supracrustal equivalents of some of the high-grade paragneisses. The structural and geochronological data obtained are consistent with a short and monocyclic orogenic evolution, characterised by the development of syn-orogenic basins where volcano-sedimentary rocks are reworked. An anatectic migmatite dome formed due to local, syn-orogenic extentional tectonics during gravitational collapse of the orogen. The exhumation of migmatites in the dome provides a possible explanation for the location of a gneissic domain in between lower-grade units.

The spatial association of terranes with contrasting metamorphic histories requires that rocks were buried in the lower crust, and that subsequently they were tectonically exhumed and brought in contact with more superficial rock-units. These results have important implications on the rheological and mechanical evolution of the craton lithosphere. They imply that the crust was initially strong enough to be tectonically thickened so that supracrustal rocks were buried in the lower crust, and show that a changing thermal regime, rheology, and/or stress field led to the gravitational collapse of the over-thickened Eburnean crust. Both conclusions suggest that the lithosphere was rheologically stronger (and cooler) than which is generally considered for hot orogens on the early Earth.

The understanding of the geological evolution of northern Ghana raises new

questions regarding other provinces on the craton. Do greenstone-belts represent supracrustal equivalents of gneisses exhumed from the lower crust in other provinces of the craton ? High-grade metamorphic rocks have received comparatively little attention so far, while they hold the potential to provide key information on the geodynamic processes controlling the Eburnean orogeny. Other studies aimed at quantifying metamorphic conditions, dating metamorphic rocks, and constraining their tectonic evolution could lead to a re-interpretation of the relationships between greenstone belts and granite-gneiss domains. Furthermore, it remains unclear whether the Eburnean orogeny represents a single orogenic cycle that affects simultaneously the whole craton. Were deformation and metamorphism synchronous in all provinces, or did they migrate or propagate from one region to the other ? Additional constraints on the timing of metamorphic events are necessary to these hypotheses.

7.2.1.2 Crustal growth

The Paleoproterozoic continental crust is essentially derived from the differenciation of a mafic juvenile crust that was extracted from the mantle less than 350 Ma before the complete stabilisation of the craton. This time period is relatively brief compared to the evolution of other cratons. These findings confirm that the formation of "proto-continents" away from active continental margins was a viable crustal growh mechanism in the Paleoproterozoic. The results of geochemical studies point to the coeval production of Archean TTG analogues and of modern "arc-like" calc-alkaline rocks. It implies the contribution of a hybrid source composed of a mantle component and a mafic crustal component. Further detail could be obtained on the crustal evolution history by carrying out similar investigations on mafic igneous rocks. They could provide a more direct information on the sources of magmatism. Lu-Hf and U-Pb isotope data on zircon from mafic magmas may also allow to refine the early magmatic evolution of the craton and to investigate the nature of the "proto-crust", i.e. the mafic source rock of the felsic magmas forming most of the crust.

The investigation carried out in northern Ghana shows that the geochemical characteristics, inferred source rocks and petrogenetic processes controlling Paleoproterozoic crustal magmatism differ from those found in Archean cratons. They remained broadly unchanged through time and produced a relatively limited rock diversity. Contrastingly the late-stage evolution of Archean cratons shows a greater rock diversity, implying more varied and changing petrogenetic processes. Furthermore, TTGs with geochemical characteristics consistent with high-P melting crystallised at the end of the geodynamic evolution in northern Ghana. This magmatic evolution is unusual because late-Archean magmatism generally shows the involvement of shallow crustal sources.

7.2.1.3 Crustal architecture - is subduction needed ?

The West African Craton is made of different continental domains which can be distinguished based on their crustal architecture and on their geological histories. The major shear zones and greenstone belts of northern and eastern Burkina Faso and of northern Ghana have orientations that contrast with the structural trend of

south-western Burkina Faso and Côte d'Ivoire. Both cratonic domains record differences in their tectonic and magmatic evolutions. The high-grade gneisses found in north-western Ghana lay at the interface of the two crustal domains. The geological, metamorphic and tectonic history of northern Ghana is consistent with the development of a collision zone during the Eburnean orogeny, when both cratonic domains were amalgamated. Hence this region may represent a suture-zone between two "sub-cratons".

The driving forces of collision, which are responsible for bulk horizontal shortening, remain speculative. Subduction is an obvious candidate because the modern Earth shows us that it provides the driving force of modern plate tectonics. Nevertheless, plate motion on the modern Earth is not necessarily *directly* driven by a subducting crust (the westwards drift of northern America is not related to a slab pull). In the West African Craton, the occurrence of calc-alkaline magmatic suites, rock formations similar to ophiolites or to turbidites, VMS and porphyry copper deposits have all previously been considered to have formed in volcanic arcs, and hence to testify of subduction. However, the craton lacks typical subduction features such as a thermal/metamorphic zoning or asymmetry, with UHP or blueschist-facies metamorphic units and accretionary prisms associated to HT-LP metamorphic units derived from arc or back-arc settings. Modern subduction also creates age zoning between genetically distinct terranes, and focuses magmatism into linear island arc systems. None of these features have been reported from the craton so far. Magmatic activity apparently started simultaneously across the whole extent of the craton. Ancient lavas emplaced at ca. 2.20 Ga form the base of the stratigraphic sequence of many greenstone belts and are not geographically localised. This suggests that magmatism was distributed rather than tectonically focussed, and does not support the initial existence of a magmatic front.

However, the geology of the West African Craton does provide evidence for the burial of crustal material, possibly at mantle depths. In northern Ghana, the HP-LT metamorphic relics represent an important observation. They reflect cold apparent geothermal gradients, and they are spatially juxtaposed to or overprinted by higher T metamorphism. This demostrates the existence of thermal heterogeneities in the craton crust. This piece of evidence is consistent with some sort of subduction zone. However, the spatial distribution of such relics is not well known, and their significance is not well understood. Future work focussing on HP-LT metamorphism on the craton, on its geological setting and on its regional distrubution could bring new arguments to this controversy. For now, in the absence of unambiguous evidence in favour of modern subduction, alternative geodynamic scenarios that may equally account for the observed geological record (e.g. underthrusting, crustal delamination, etc) cannot be ruled out and deserve to be considered.

7.2.2 Implications of the secular evolution of the Earth

The magmatic record of the Paleoproterozoic continental crust combines features that are typical of both Archean and modern arc magmatism. It may therefore be interpreted to reflect a hybrid magmatic system that developed in a "transitional" geodynamic setting, between Archean and Proterozoic or Phanerozoic eons. The spatial association of HP-LT metamorphic relics and of rocks metamorphosed at the transition between the amphibolite- and high-pressure granulite facies

contrasts with the "ordinary" metamorphic conditions that characterise the Archean eon. This metamorphic record represents an early example of the diversification of thermal regimes which characterises post-Archean orogens. Finally, the exhumation of high-grade rocks and their tectonic juxtaposition against contrasting rock-units indicates that the lithosphere of the craton locally met thermo-mechanical conditions that are widespread in modern orogenic belts. The Paleorpoterozoic West African Craton shares some characteristics with Archean and Proterozoic or Phanerozoic rock-records. Furthermore, some of the rock-types that are frequent in other Paleoproterozoic provinces, (e.g. eclogites) are unreported here. Altogether, these characteristics define a unique combination of geological features which may reflect specific, transitional geodynamic processes.

The interpretation that the Paleoproterozoic West African Craton was assembled during a subduction-collision cycle similar to those at work on the modern Earth remains debated, because some of the geological processes involved in its evolution are not similar to those observed on the modern Earth. The formation of the Paleoproterozoic West African Craton represents a discrete episode of continental growth between 2.30 and 2.10 Ga, when juvenile crust was extracted massively from the mantle. It does not appear to be chronologically linked to any of the inferred ancient super-continent formation events at 2.70-2.50 and 2.10-1.80 Ga. These episodes, which show net crustal growth and high crust preservation rates, are interpreted to result from a plate tectonics geodynamic setting. The diachronism between peaks of continental crust growth and the formation of the West African Craton reflect the development of geodynamic settings favourable to crust preservation, independently from super-continent cycles. It also suggests that major magmatic events, possibly linked to mantle plumes, contributed to crustal growth in the Paleoproterozoic.

In the last decades, many Earth scientists have argued that plate tectonics started in some areas of the Earth during the Neoarchean, possibly as early as 3.00 Ga. Consequently, the time period between 3.00 and 2.50 Ga is seen as a global transition that saw the onset and the progressive generalisation of plate tectonics. This global geodynamic shift is interpreted as a consequence of the secular cooling of the Earth. It could reflect the crossing of a threshold by the parameters controlling the Earth thermal regime (e.g. mantle temperature), which triggered major transformations of its lithospheric expression. There is increasing evidence that geodynamic changes were diachronous from one craton to another, and that contrasting settings may have existed in different coeval provinces. Local phenomena may also have controlled the onset of modern geodynamics at the scale of a province. Therefore, the observed rock record is determined both by the uniqueness of each geodynamic configuration, and by the global parameters of the Earth's thermal regime.

The coexistence of "modern" and "archaic" tectonics on Earth may therefore have lasted until 2.00 Ga. This conclusion has implications for the significance of a "transitions" in the secular evolution of the Earth. It would imply that the Archean-Proterozoic transition represents a long period of smooth and gradual diachronous transformations that produced a wide diversity of geological records, rather than a short period marking abrupt geodynamic changes. Furthermore, Neoarchean or Paleoproterozoic plate tectonics may have been local or intermittent before beco-

ming dominant. Theerefore, “plate-like” geodynamics would have alternated with processes that do not have any modern equivalent, for example between periods of super-continent assembly.

Liste des tableaux

Liste des figures

Annexe A

Appendix

Livret-guide du stage de terrain - Field training course guidebook

Livret guide : Géologie du nord-ouest du Ghana.

Sylvain Block

10-16 Février 2014

Table des matières

Introduction

Il est probable que nombre de participants à cette formation de terrain disposent déjà de connaissances sur la géologie du craton Ouest Africain. Le craton, d'âge Paléoproterozoique, est en particulier connu pour les importants gisements d'or situés dans les ceintures de roches vertes birimiennes et les bassins tarkwaiens. Ceci étant dit, ces ressources ne représentent qu'un des aspects de la géologie du craton Ouest Africain. Comprendre les processus géologiques nécessite de considérer les multiples interactions entre la pétrologie, la géologie structurale, la géologie métamorphique, la métallogénie, la géochimie, etc. En d'autres termes, la compréhension globale de l'histoire géologique d'une région requiert une approche d'ensemble.

La géologie du nord-ouest du Ghana présente cependant un caractère atypique par rapport au reste du craton. On y trouve de vastes unités de roches métamorphiques de haut grade tels que des gneiss et des migmatites. Ces roches sont relativement peu abondantes ailleurs sur le craton et ne représentent nulle part des surfaces aussi étendues. La région comprend également les lithologies plus classiques rencontrées dans les ceintures de roches vertes et les domaines de granitoïdes ailleurs sur le craton. La diversité des roches à l'affleurement permet d'observer les processus géologiques ayant dominé l'orogenèse Eburnéenne à la fois dans la croûte profonde et dans les niveaux plus superficiels. Enfin, les bonnes qualités d'affleurement en font une zone d'étude privilégiée.

Le nord-ouest du Ghana est donc une région permettant de s'intéresser à l'évolution du craton Ouest Africain en alliant plusieurs approches complémentaires. Nous espérons que cette formation suscite des discussions stimulantes et satisfasse votre curiosité.

1 Programme

Jour	Date	Activité	Hébergement
0	Dimanche 9 Février	Arrivée à Wa, présentation des participants et du programme de la formation, point logistique.	Wa, Tiegber Guest House.
1	Lundi 10 Février	Coupe géologique à travers la ceinture de Wa-Lawra afin d'observer les lithologies caractéristiques de la ceinture. Reconnaissance des faciès métamorphiques représentés dans la ceintures, et des indicateurs cinématiques dans les zones de forte déformation.	Wa, Tiegber Guest House.
2	Mardi 11 Février	Matinée : Observations de carottes de forage au camp de la société Azumah Resources. Les carottes proviennent de roches minéralisées en or dans la zone d'étude et fournissent une occasion de discuter des contextes structuraux et métamorphiques de la minéralisation. Après-midi : Étude des zones de cisaillement de la ceinture de Wa-Lawra.	Wa, Tiegber Guest House.
3	Mercredi 12 Février	Coupe nord-sud depuis l'unité de Julie jusqu'au domaine de Bolé-Bulenga afin d'illustrer les changement de conditions métamorphiques à travers des structures localisant la déformation. Aperçu de la nature des déformations précoces.	Wa, Tiegber Guest House.
4	Jeudi 13 Février	Étude de la fusion partielle de la croûte dans le domaine de Bolé-Bulenga, caractérisé par un métamorphisme de haut grade. Observation des interactions entre fusion partielle et déformation.	Wa, Tiegber Guest House.
5	Vendredi 14 Février	Mise en évidence de la diversité des conditions métamorphiques dans le domaine de Bolé-Bulenga, ainsi que de la chronologie relative des événements déformation en lien avec l'évolution métamorphique. A la fin de la journée, nous nous dirigerons vers Bolé.	Bole, Guest House.
6	Samedi 15 Février	La journée est consacrée à l'étude des contacts entre les unités dont les conditions métamorphiques sont contrastées, au métamorphisme rétrograde et à la déformation tardive.	Bolé, Guest House.
7	Dimanche 16 Février	Coupe N-S à travers le bassin de Maluwe et dans le domaine d'Abulembire afin de se rendre compte de la distribution spatiale régionale des roches de bas degré et de haut degré métamorphique. Ceci permet de discuter des implications géodynamiques du métamorphisme, et de placer dans un contexte régional les observations effectuées durant la formation.	Bolé, Guest House.
8	Lundi 17 Février	Départ	

2 Contexte géologique

2.1 Géologie régionale

La formation de terrain a lieu au nord-ouest du Ghana, dans la partie orientale du domaine de Baoulé-Mossi, sur le craton Ouest Africain d'âge Paléoprotérozoique. Le craton est constitué d'une succession de ceintures de roches vertes et de terrains granito-gneissiques. Les ceintures de roches vertes contiennent des roches volcaniques, volcano-sédimentaires et sédimentaires birimiennes. Les terrains granito-gneissiques sont formés de séries de Tonalite - Trondjheimite - Granodiorite (TTG) et de granites. Leurs âges de mise en place varient entre 2.25 et 2.10 Ga. Une intense activité magmatique a permis la formation de la croûte continentale entre 2.25 et 2.15 Ga. Celle-ci a par la suite subi un remaniement intense et a été affectée par d'autres épisodes magmatiques au cours de l'orogenèse Eburnéenne, entre 2.15 et 2.10 Ga.
A l'échelle régionale, la zone d'étude où se déroule la formation de terrain se situe à l'interface entre deux sous-ensembles du craton. Ceux-ci se distinguent par l'orientation générale des unités litho-tectoniques. Les ceintures de roches vertes et les failles d'échelle crustale ont une orientation NE-SO dans la partie orientale de la zone, au Ghana et à l'est du Burkina Faso, alors qu'elles sont orientées N-S dans la partie occidentale, en Côte d'Ivoire et au sud du Burkina Faso (Fig. 1). Ces deux familles de structures tendent à se rejoindre au nord-ouest du Ghana.

La géologie du nord-ouest du Ghana est marquée par deux grands ensemble litho-structuraux d'orientation différente (Fig. 2).

- La ceinture de Wa-Lawra est allongée parallèlement à une direction N-S. Elle représente la partie ghanéenne de la ceinture de Boromo, au Burkina Faso (Baratoux et al., 2011 ; Metelka et al., 2011). La ceinture de Wa-Lawra est limitée à l'est par un cisaillement ductile nommé la faille de Jang.

- La ceinture de Bolé-Nangodi désigne l'alignement des unités géologiques selon une direction NE-SO, le long de la zone de cisaillement de Bolé-Nangodi (Fig. 2). Cette zone de cisaillement s'étend sur environ 300 km, y compris à l'est du Burkina Faso, où elle porte le nom de structure de Po-Tenkodogo-Yamba (Naba et al., 2004).

2.2 La ceinture de Wa-Lawra

La ceinture de Wa-Lawra est l'équivalent ghanéen de la ceinture de roches vertes de Boromo. La ceinture de Boromo est orientée N-S sur environ 250 km depuis le centre du Burkina Faso jusqu'à la frontière entre la Côte d'Ivoire et le Ghana. D'ouest en est, elle est constituée de trois grands ensembles. A l'ouest, au Burkina Faso, se trouvent essentiellement des roches volcaniques et volcano-sédimentaires de faible degré métamorphique, dont les figures primaires, sédimentaires ou volcaniques, sont souvent préservés du fait d'une déformation peu intense. Dans sa partie centrale, de part et d'autre de la frontière avec le Ghana, les roches sédimentaires et volcano-sédimentaires sont dominantes. Il s'agit d'argilites, de greywacke et de volcanoclastites ainsi que de laves peu abondantes. L'ensemble est métamorphisé dans le faciès schiste vert (Fig. 56). Enfin, la partie orientale de la ceinture est essentiellement constituée de granitoides et de quelques formations volcaniques. Les plutons de granitoïdes sont généralement des granites syn-tectoniques à biotite, contenant des enclaves de paragneiss, et dont les âges de formation sont compris entre 2134 and 2118 Ma (Agyei Duoudu, 2009 ; De Kock et al., 2011). Ils appartiennent à la série plutonique dite de Tanina (G4 dans les figures 2 ; 3).

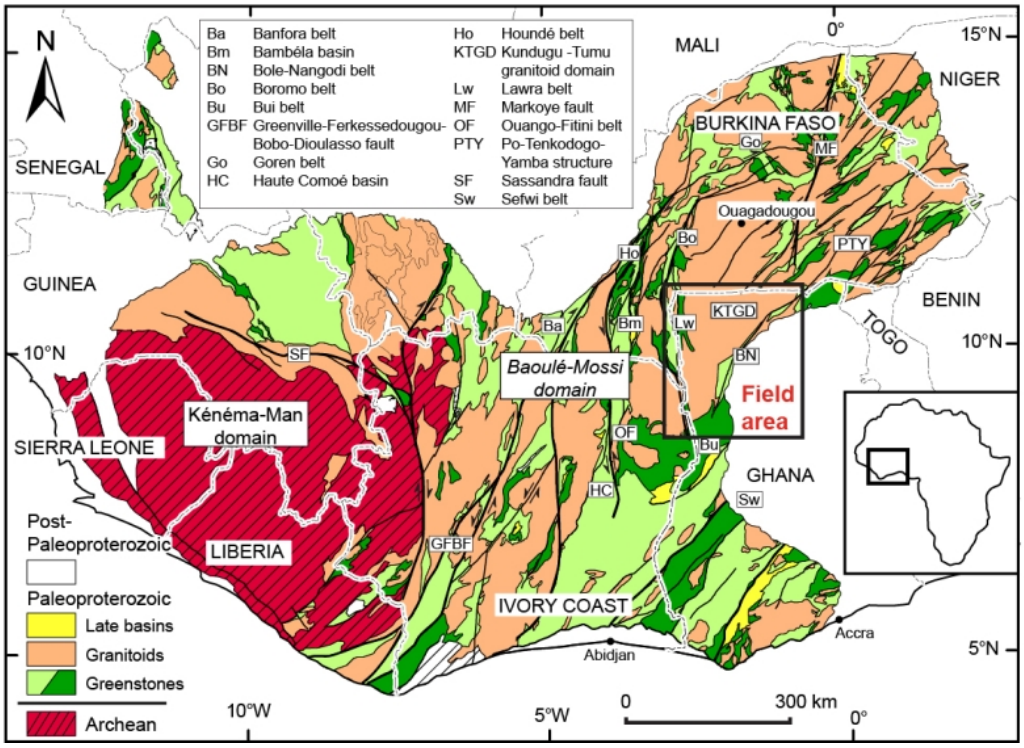

FIGURE 1 – Carte géologique simplifiée du craton de Leo-Man, modifiée d'après la carte du BRGM SIGAfrique, de Milési et al. (2004). La zone concernée par la formation est indiquée par le cadre. Le vert clair et le vert foncé désignent respectivement les roches volcano-sédimentaires et volcaniques acides ou basiques.

Les trois domaines décrits ci-dessus sont séparés par des zones de cisaillement ductiles senestres d'orientation NNO-SSE. Dans la ceinture de Wa-Lawra, on observe une schistosité plus ou moins bien marquée, sub-verticale et orientée approximativement N-S. Celle-ci est parfois décalée par des bandes de cisaillement à l'échelle de l'affleurement. L'ensemble de ces structures peut s'expliquer par un raccourcissement dans la direction E-O.

Les conditions métamorphiques sont variables dans la ceinture. Le degré métamorphique augmente d'ouest en est à travers les zones de cisaillement, et augmente également du nord vers le sud au sein des unités géologiques. Les foliations d'orientation N-S s'atténuent progressivement au voisinage de la terminaison sud de la ceinture de Boromo, et laissent la place à une foliation gneissique d'azimut ouest ou nord-ouest. Les orthogneiss du domaine de Nassian, au NE de la Côte d'Ivoire, constituent la limite sud de la ceinture.

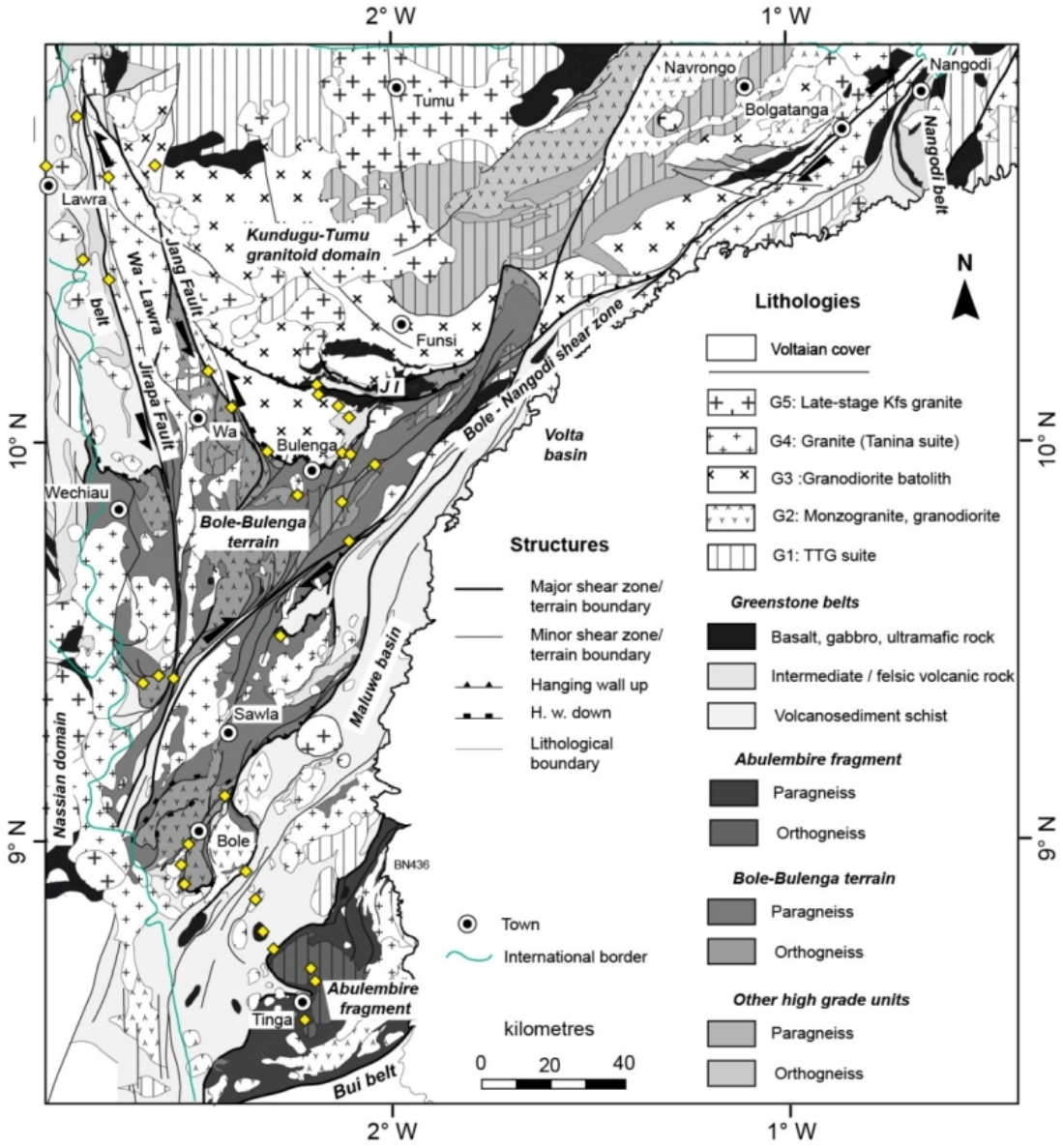

FIGURE 2 – Carte présentant les principales lithologies et structures de la zone d'étude. JL : Unité de Julie. La cinématique des failles est représentée lorsqu'elle est sans ambiguïté. Les losanges jaune montrent l'emplacement des affleurements vus pendant la formation.

2.3 La ceinture de Bolé-Nangodi

La ceinture de Bolé-Nangodi est l'ensemble des lithologies étirées parallèlement à une direction NE-SO, le long de la zone de cisaillement du même nom, qui est clairement mise en évidence par les données géophysiques (Fig. 5). Il ne s'agit cependant pas d'un domaine litho-structural distinct. Cette structure est une zone de localisation de la déformation dans laquelle les contacts lithologiques sont transposés parallèlement à la zone de cisaillement. La déformation est très importante le long de structures d'azimut N0-N20, où l'aplatissement semble être dominant. Ces structures forment un système de failles en "queue de cheval" en se raccordant à une zone de cisaillement ductile dextre : la zone de cisaillement de Bolé-Nangodi.

Au sud du domaine de Bolé-Bulenga, la déformation régionale se localise graduellement

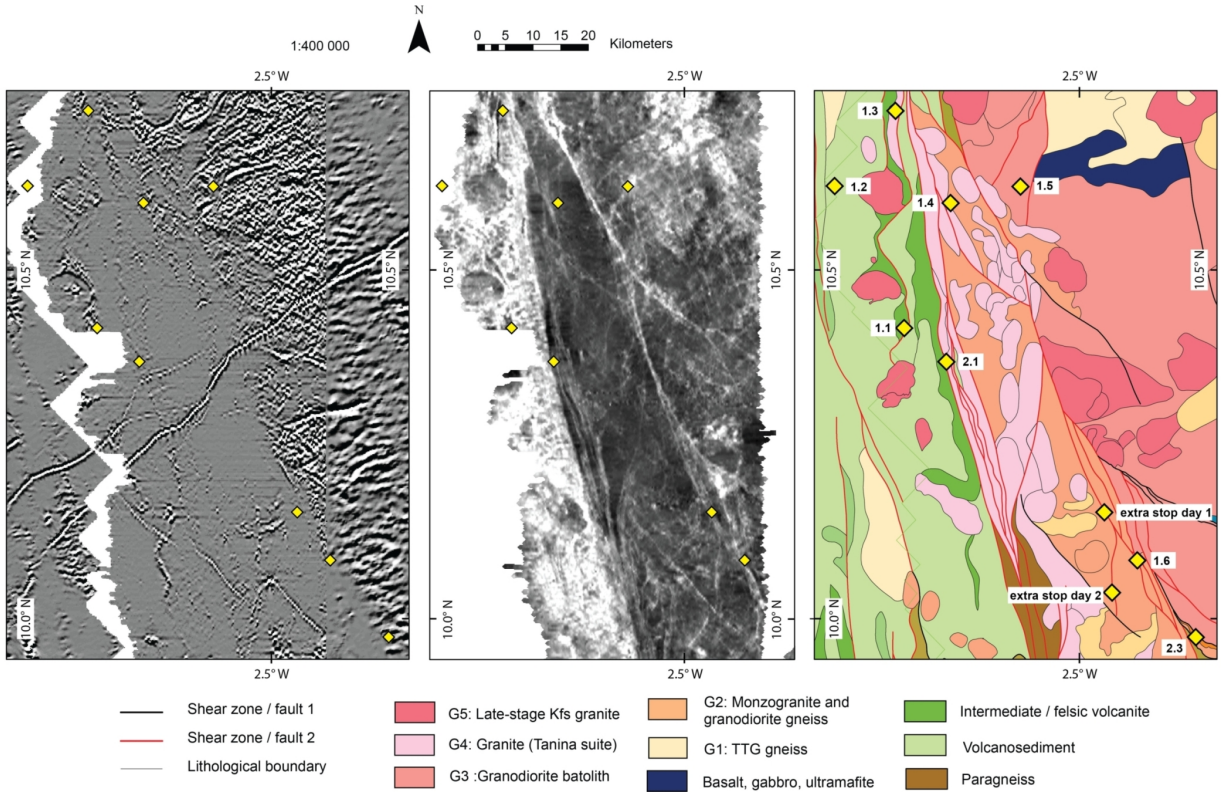

FIGURE 3 – Ceinture de Wa-Lawra. De gauche à droite : Première dérivée verticale (1VD) de la susceptibilité magnétique, données électromagnétiques, carte géologique simplifiée. Les losanges jaunes donnent la position des affleurements vus lors de la formation.

pour constituer la zone de cisaillement de Bolé-Nangodi. Les roches dans la zone de cisaillement sont migmatitiques, ce qui suggère que l'accident tectonique s'enracine dans la croûte partiellement fondue. Le contact entre le domaine de Bolé-Bulenga, de haut degré métamorphique ; et celui de Maluwe, de faible degré métamorphique, est réactivé et entraîné dans la zone de cisaillement dextre de Bolé-Nangodi (Fig. 2).

Au nord-est du Ghana, la ceinture de Nangodi (Melcher et Stumpfl, 1994) forme un petit domaine litho-structural affleurant sur une cinquantaine de km selon une direction N-S. Il contient des roches volcaniques, volcano-sédimentaires, sédimentaires, et des quartzites manganésifères. Il est également défléchi au nord dans la zone de cisaillement de Bolé-Nangodi, et mis en contact avec les gneiss et granitoides du domaine de Tumu-Koudougou (KTGD).

2.4 Le domaine de Bolé-Bulenga

Le domaine de Bolé-Bulenga s'étend sur 150 par 20 à 80 km, selon une direction NNE. il est constitué de roches de haut degré métamorphique. Il s'agit essentiellement de paragneiss (nommés Buki gneiss par De Kock et al., 2011), d'orthogneiss et de métabasites mineures. Les paragneiss sont dérivés de pélites, de greywacke et de roches volcano-sédimentaires. Ils sont intrudés par des orthogneiss issus de TTG et par des plutons de monzogranite (respectivement G1 et G2, Fig. 2 ; 5), dont les âges d'intrusion varient entre 2195 et 2135 Ma. Les roches du domaine de Bolé-Bulenga enregistrent un métamorphisme dans le faciès amphibolite, souvent au delà du solidus, et jusqu'à la transition avec le faciès des granulites de haute pression (Fig. 56). Certaines roches préservent enfin des reliques d'un métamorphisme dans le faciès éclogite.

(a) Plis serrés et roches fortement déformées dans la zone de cisaillement de Bolé-Nangodi.

(b) Déformation intense et forte réduction d'épaisseur de marqueurs dans un gneiss contenant des xénolithes de pyroxénites. La déformation finie a une composante dextre.

FIGURE 4 – Déformation dans la zone de cisaillement de Bolé-Nangodi.

Les structures de grande échelle orientées N-S dans la ceinture de Wa-Lawra, et NE-SO le long de la zone de cisaillement de Bolé-Nangodi, se rejoignent dans le domaine de Bolé-Bulenga pour former une zone d'interférence. Les structures précoces y sont plissées et transposées parallèlement à des structures tardives orientées NNE. Le domaine de Bolé-Bulenga est intrudé par des granites à biotite entre 2134 et 2118 Ma (série de Tanina, G4, Fig. 2 ; 5). Sur sa bordure SE, les roches de haut grade sont en contact avec le bassin de Maluwé. La zone de transition présente des roches fortement déformées ayant subi un important métamorphisme rétrograde. Cet interface est également plissé et transposé parallèlement à des structures tardives NNE.

2.5 Le bassin de Maluwe

Le bassin de Maluwe est un vaste domaine litho-tectonique formé de laves, de roches volcano-sédimentaires et sédimentaires. Il est pincé à son extrémité NE le long de la zone de cisaillement de Bolé-Nangodi, et semble se rouvrir pour former une continuité avec la ceinture de Bolé-Nangodi. Il communique au sud-ouest avec le bassin de la Comoé dans l'est de la Côte d'Ivoire, bien que les relations tectoniques ou stratigraphiques entre les deux unités ne soient pas connues. Le bassin de Maluwe contient des basaltes de type MORB, des roches volcaniques intermédiaires et acides calco-alcalines, des greywacke et argilites, ainsi que des quartzites manganésifères. Les roches volcaniques ont des âges de cristallisation allant de 2197 à 2125 Ma (De Kock et al., 2009 ; Thomas et al., 2009).Le bassin comporte également des plutons étirés de granodiorites. L'ensemble de ces roches enregistre un métamorphisme de faciès schiste vert. Les roches les plus compétentes ne présentent que peu de structures, bien qu'elles soient alignées parallèlement aux principales directions structurales (Fig. 5). Les lithologies incompétentes portent une schistosité pénétrative de pendage faible, recoupée par et transposé parallèlement à une seconde schistosité sub-verticale d'azimut N-NNE. Le bassin de Maluwe est intrudé par des plutons de granite à biotite et de syénite tardifs (G4 et G5, Fig. 2 ; voir partie 8.2).

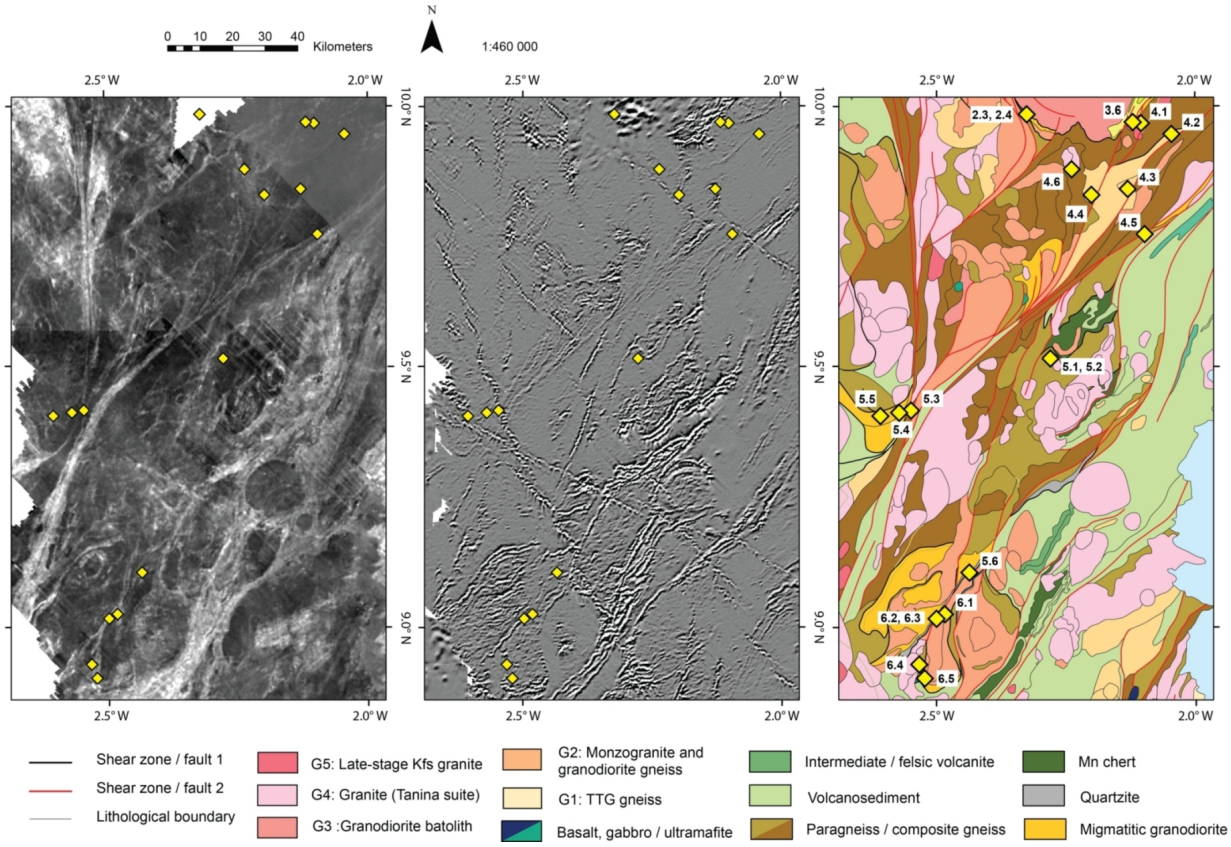

FIGURE 5 – Le domaine de Bolé-Bulenga. De gauche à droite, relevé électromagnétique, première dérivée verticale de la susceptibilité magnétique, carte géologique simplifiée. Les losanges jaunes désignent les affleurements vus lors de l'excursion.

(a) Rhyolite métamorphisée contenant des bombes volcaniques aplaties.

(b) Chloritoschiste pyriteux.

FIGURE 6 – Lithologies du bassin de Maluwe.

2.6 Le domaine d'Abulembire

Le domaine litho-structural d'Abulembire (De Kock et al., 2012), qui se situe au sud du bassin de Maluwe, est constitué d'orthogneiss et de paragneiss ayant subi un métamorphisme de faciès amphibolite. Ces lithologies sont fréquemment migmatitiques, et sont similaires aux roches du domaine de Bolé-Bulenga par leurs nature, leurs faciès métamorphique et leurs

âges. Les deux domaines sont interprétés comme étant deux fragments équivalents issus de la croûte moyenne à inférieure. Les granitoïdes rencontrés dans le domaine d'Abulembire ont des âges de mise en place allant de 2200 à 2120 Ma (De Kock et al., 2009 ; Agyei Duodu et al., 2009). Ce domaine présente les mêmes relations de chronologie relative que celles identifiées par ailleurs. A grande échelle, le domaine d'Abulembire est structuré par des zones de cisaillement orientées NNE. Elles sont parallèles à une schistosité imprimée par dessus une foliation gneissique précoce. Cette foliation homogène dans tout le domaine est caractérisée par une orientation O-E ou NO-SE. La transition entre le bassin de Maluwe et le domaine d'Abulembire représente un gradient métamorphique important.

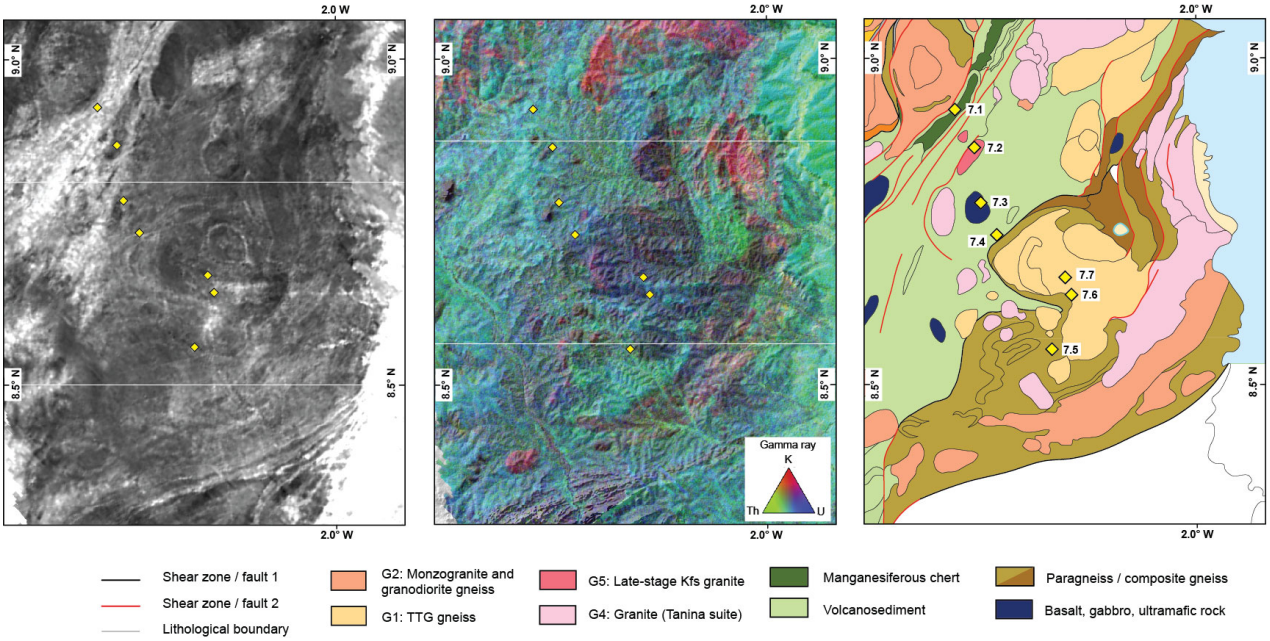

FIGURE 7 – Domaine d'Abulembire. De gauche à droite : relevé électromagnétique, signal radiométrique calquée sur un modèle numérique de terrain (SRTM), carte géologique simplifiée. Les losanges jaunes désignent les affleurements vus lors de l'excursion.

2.7 Le domaine de granitoïdes de Koudougou-Tumu et l'unité de Julie.

Le domaine de granitoïdes de Koudougou-Tumu (KTGD) se situe au nord du domaine de Bolé-Bulenga. Il est borné par la faille de Jang sur sa marge occidentale, et par la zone de cisaillement de Bolé-Nangodi le long de sa bordure sud-est. Il se prolonge au nord dans la partie orientale du Burkina Faso. Ce domaine litho-structural est constitué d'orthogneiss migmatitiques issus de TTG, d'un batholithe granodioritique (G3 in Fig. 2), et de quelques massifs de gabbro. Les orthogneiss ont des âges de formation compris entre 2165 et 2135 Ma (Agyei Duodu et al., 2009). L'ensemble est intrudé par de volumineux granites porphyroïdes (G5, Fig. 1) dont les âges varient de 2128 à 2086 (Taylor et al., 1992 ; Agyei Duodu et al., 2009).

L'unité de Julie se trouve sur la marge méridionale du domaine de Koudougou-Tumu. Il s'agit d'un ensemble de roches alignées le long d'une direction E-O comportant des laves, des roches sédimentaires et volcano-sédimentaires. Les basaltes sont abondamment représentés, et on note la présence de roches détritiques et de volcano-sédiments acides (quartzites et arkoses) ressemblant aux sédiments du Tarkwaien retrouvés ailleurs sur le craton Ouest Africain. L'unité de Julie présente une répétition des séquences lithologiques qui s'explique par un plissement à l'échelle kilométrique. Les surfaces axiales de ces plis sont orientées selon une direction E-O. La géométrie de ces plis est mise en évidence par les relevés de données géophysiques (Fig. 9). La déformation plicative est associée à un métamorphisme de faciès schiste-vert. Les structures E-O sont recoupées par des plans de schistosité d'azimut N0 et des failles N30.

(a) Granite porphyroïde tardif à feldspath potassique.

(b) Orthogneiss migmatitique issu d'une granodiorite.

FIGURE 8 – Lithologies du domaine de granitoïdes de Koudougou-Tumu.

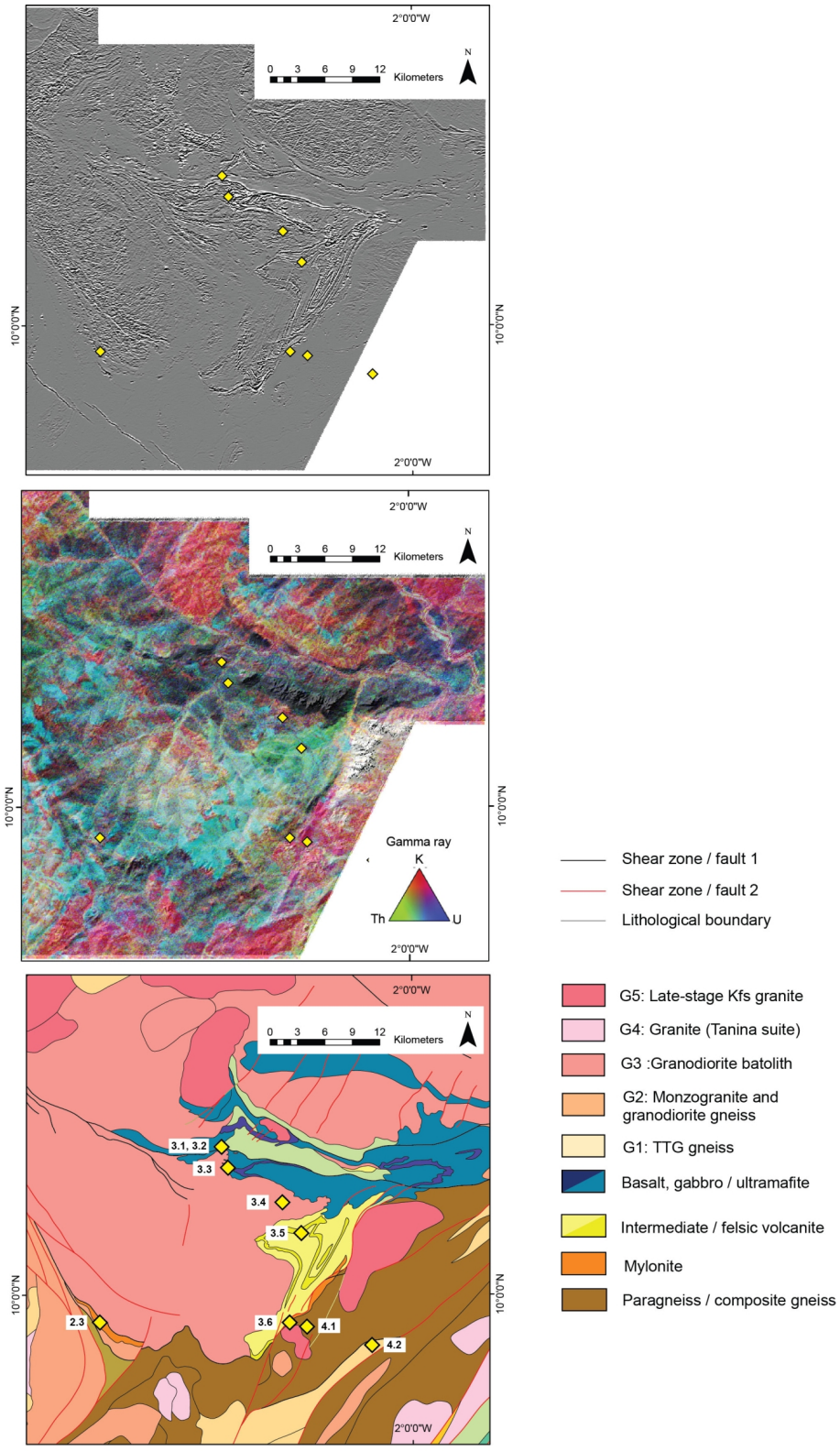

FIGURE 9 – Unité de Julie. De haut en bas : Première dérivée verticale avec amplitude normalisée (AGC) de la susceptibilité magnétique, signal radiométrique calqué sur un modèle numérique de terrain (SRTM), carte géologique simplifiée. Les losanges jaunes désignent les affleurements vus lors de l'excursion.

3 Evolution tectonique

3.1 D1 : raccourcissement N-S et chevauchements.

Dans la zone d'étude, les structures précoces sont préservées à distance des cisaillements ductiles tardifs qui structurent les deux ceintures. Par exemple, l'unité de Julie constitue un domaine de faible degré métamorphique organisé le long de structures orientées est-ouest. Celles-ci ne sont que modérément affectées par les déformations postérieures. Les trajectoires de foliation dans les gneiss du domaine de Koudougou-Tumu dessinent un arc entre les deux ceintures, et les contacts tectoniques y sont obliques par rapport aux ceintures (Fig. 11). Les trajectoires de foliation et les contacts tectoniques dans les laves métamorphiques et les gneiss à l'ouest de la faille de Jirapa, dans la partie méridionale de la ceinture de Wa-Lawra, sont orientés NO-SE. On y observe une transposition progressive des structures précoces au voisinage de la zone de cisaillement sénestre. De même, une foliation précoce est identifiable dans le domaine de Bolé-Bulenga. Elle est plus ou moins intensément transposée parallèlement aux structures tardives. L'ensemble des domaines litho-structuraux de la région présente donc des structures précoces étant incompatibles avec les épisodes de déformation à l'origine des zones de cisaillement majeurs. La déformation aillant généré ces structures est D1.

Dans l'unité de Julie, D1 forme des plans de cisaillement à pendage nord, portant une linéation à pitch élevé et indiquant une cinématique inverse, du nord vers le sud. S1 a un pendage modéré ou élevé qui correspond aux surfaces axiales de plis isoclinaux F1. Dans les roches de haut degré métamorphique, la schistosité S1 a un pendage faible à modéré, bien qu'elle soit fréquemment transposée selon une orientation verticale. Le pitch des lignes L1 est généralement élevé. S1 représente la surface axiale de plis recombants ou isoclinaux. Les roches migmatitiques contiennent des leucosomes orientés parallèlement à S1, et les métapélites contiennent du grenat et du disthène dont les grains sont orientés dans les plans de foliation parallèlement à L1.

Compte tenu de ces observations, la déformation D1 est interprétée comme un raccourcissement N-S. Dans le domaine de granitoïdes de Koudougou-Tumu, des chevauchements associés à D1 forment de forts gradients de conditions métamorphiques. D1 est à l'origine d'un important épaississement crustal ayant causé la fusion partielle de la croûte à l'échelle de la zone d'étude.

3.2 D2 : extension N-S

Les contacts tectoniques entre roches de haut grade et de bas grade conservent leurs géométries d'origine à distance des deux ceintures de Wa-Lawra et Bolé-Nangodi, hors de la zone d'interférence où les ceintures se joignent. La zone de transition entre le nord du domaine de Bolé-Bulenga et le sud de l'unité de Julie sépare des gneiss migmatitiques de volcano-sédiments et de granitoïdes de faible degré métamorphique. Le contact est matérialisé par un orthogneiss fortement déformé, ayant une foliation de pendage modéré (40-50°) vers le nord. Elle porte une linéation plongeant vers le nord. On observe une relation similaire à l'interface entre le sud du domaine de Bolé-Bulenga et le bassin de Maluwe. Des orthogneiss et des quartzites y présentent un pendage modéré vers le sud et une ligne plongeant vers le sud.

Les roches de haut degré métamorphique constituent donc le mur de ces failles, et celles de faible degré métamorphique constituent le toit. La distribution des faciès métamorphiques de part et d'autre suggère qu'il s'agit de failles normales ductiles, formées dans un contexte extensif. S2 représente la foliation gneissique développée dans ces zones de cisaillement.

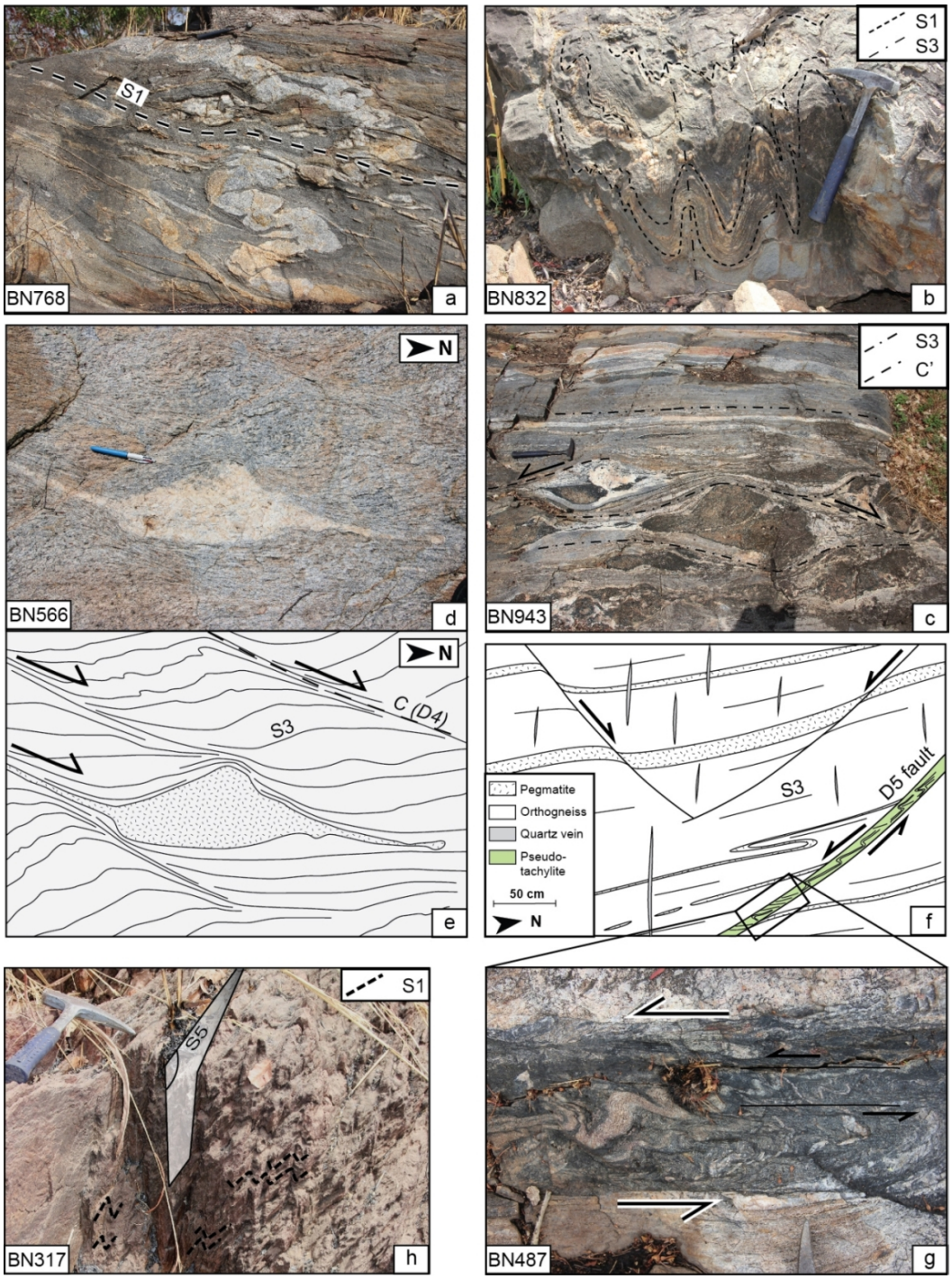

FIGURE 10 – Présentation des différents types de structures reliés aux événements de déformation successifs.

3.3 D3 : Raccourcissement E-W

La foliation S1 est recoupée par des structures formées lors d'un raccourcissement E-O nommé D3. La déformation D3 génère une schistosité fortement marquée, orientée N-S. Celle-ci correspond, dans les roches de haut degré métamorphique, aux plans axiaux de plis isoclinaux ou ptigmatiques F3 (Fig. 10.b) affectant la foliation S1. La déformation induite par D3 présente de forts gradients d'intensité. Elle est très intense le long de structures planaires

localisant la déformation (Fig. 10.c).

Dans les orthogneiss et les paragneiss des domaines de Bolé-Bulenga et d'Abulembire, S1 et S3 ont des aspects comparables et portent les mêmes assemblages de minéraux. Dans les migmatites, les leucosomes sont tantôt disposés parallèlement à S1 ou à S3. Ces observations suggèrent que la croûte était partiellement fondue aussi bien pendant D1 que D3. Les conditions de la fusion partielle sont donc réunies à la transition entre D1 et D3.

3.4 D4 : Raccourcissement NO-SE et décrochements senestres.

Les structures correspondant à D1-D3 sont recoupées par des décrochements ductiles tardifs senestres, dont l'orientation indique un raccourcissement orienté nord ouest - sud est (D4). Ces zones de cisaillement, qui peuvent réactiver des accidents pré-existants, forment les contacts litho-structuraux principaux de la ceinture de Wa-Lawra, à savoir les failles de Jirapa et de Jang. A petite échelle, des bandes de cisaillement senestres affectent les plis F3.

3.5 D5 : Raccourcissement O-E et décrochements dextres.

Les décrochements ductiles dextres sont postérieurs aux décrochements senestres D4, et correspondent donc à une déformation D5. Des accidents tectoniques précoces, tels que la zone de cisaillement de Bolé-Nangodi, sont réactivés en cisaillement dextre durant D5. Cette déformation tardive génère des décalages entre unités géologiques de part et d'autre des zones de cisaillement. A l'échelle de l'affleurement, D5 se manifeste par des bandes de cisaillement recoupant les structures antérieures (Fig. 10.e).

L'évolution de D3 à D5 se caractérise par la transition d'une déformation homogène et distribuée, à une déformation de plus en plus localisée le long de zones de cisaillement décrochantes.

3.6 D6 : Raccourcissement O-E, structures à la limite ductile-cassant.

D6 représente une déformation des roches dans des conditions à la limite ductile-cassant, et dans un contexte de raccourcissement O-E. Ces structures incluent des fentes de tension orientées O-E remplies de quartz, accompagnées de failles décrochantes conjuguées. Les plans de faille contiennent généralement de la chlorite, du mica blanc ou de l'épidote. Les figures 10.f, g illustrent la nature des structures liées à D6.

L'épisode de déformation le plus tardif enregistré dans la région, D7, forme des crénulations dont les plans sont orientés NO-SE, essentiellement développés dans les roches incompétentes telles que les argilites (Fig. 10.h).

3.7 Une interprétation possible de l'histoire tectonique.

Les observations structurales et métamorphiques permettent de suggérer que la région a connu une évolution tectonique continue de D1 à D3, au sein d'un champ de déformation régional changeant. En effet, la présence de leucosomes alignés parallèlement à S1 et à S3, suggère que les conditions métamorphiques des roches n'ont pas fondamentalement changé entre D1 et D3. Cette hypothèse est renforcée par l'observation d'assemblages métamorphiques similaires alignés parallèlement à S1 et S3. Les chemins P-T-t déterminés à l'appui de pseudosections (cf. partie suivante, fig. 57 indiquent que la fusion partielle de la croûte est associée à une décompression. Ceci suggère un contexte extensif synchrone de la fusion partielle. Remarquons enfin que l'extension dans une direction N-S est compatible avec un raccourcissement dans une direction E-0. Sans s'avancer sur le contexte géodynamique de la transition de D1 à D3, il semble que celle-ci soit continue, et accompagnée d'un changement de style tectonique.

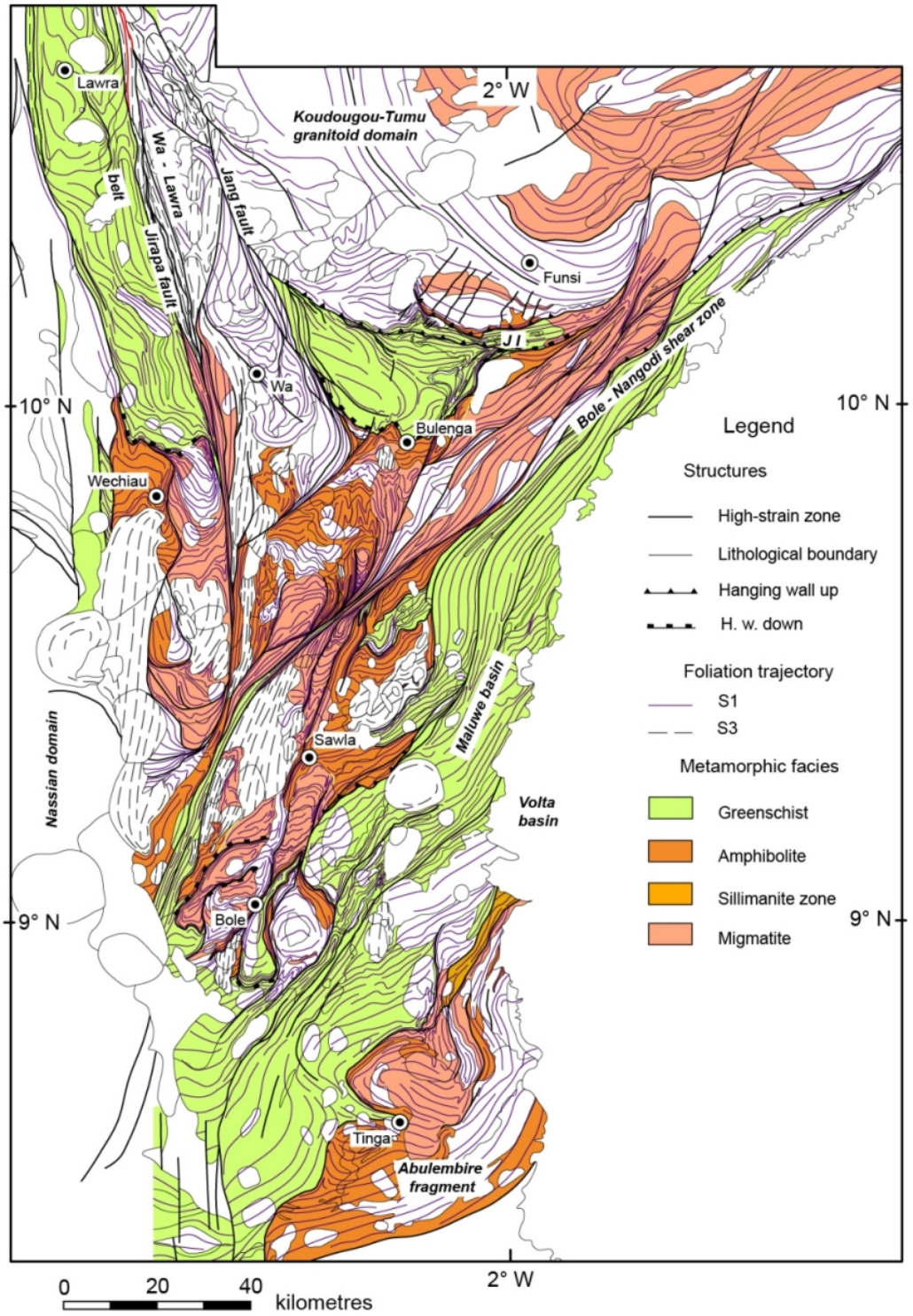

FIGURE 11 – Carte représentant les faciès métamorphiques et les trajectoires de foliation dans la zone d'étude.

La figure 11 présente la trajectoire de la foliation S1 à l'échelle régionale. S1 est parallèle à des contacts tectoniques représentant d'importants sauts de métamorphisme. A distance des ceintures, S1 peut être fortement oblique aux structures tardives telles que les zones de cisaillement. S1 est plissée par des plis de surface axiale N-S, et est transposé parallèlement aux zones de forte déformation formées de D3 à D5.

4 Histoire métamorphique.

Dans les paragneiss de fort degré métamorphique, la foliation métamorphique S1 est définie par une alternance de lits riche en quartz et en biotite, contenant fréquemment du grenat et du disthène. L'estimation des conditions métamorphiques a été effectuée en construisant des pseudosections P-T à l'aide du logiciel Perplex. Les résultats indiquent des conditions de pression P = 9-11 kbar, et de température T = 600-700°C pour les roches n'ayant pas franchi le solidus, et P = 5-10 kbar, T = 650-800°C pour les migmatites. Il s'agit donc de roches métamorphisées dans la coûte profonde. Les données de terrain indiquent que le métamorphisme de haut grade a lieu durant D1 et a atteint des condition de fusion partielle de la croûte. De rares reliques témoignant d'un métamorphisme en faciès éclogite sont préservées dans certaines roches de haut degré métamorphique (Fig. 12), sous la forme de cœurs de grenats zonés. Les conditions métamorphiques correspondantes sont de P = 10-13 kbar, T = 550-620 °C. Ceci correspond à un épisode métamorphique intervenant précocement pendant D1.

Dans les roches de plus faible degré métamorphique, la foliation S1 contient des assemblages minéraux incluant la chlorite, quartz-chlorite-mica blanc, quartz-albite-actinote, etc. Ce métamorphisme de faciès schiste vert est synchrone de D1.

Les relations entre les structures et les assemblages métamorphiques qu'elles contiennent permettent de suggérer que l'ensemble des domaines litho-structuraux de la région ont subi un métamorphisme pendant D1, qu'il soit de haut degré ou de bas degré. Ceci implique que les différents domaines ont été métamorphisés simultanément à des profondeurs crustales différentes. Les datations U-Pb sur monazite appartenant aux assemblages métamorphiques de haut grade permettent de contraindre l'âge du métamorphisme. La fusion partielle de paragneiss provenant du sud du domaine de Bolé-Bulenga est daté à 2136 ± 8 Ma. Le métamorphisme de faciès amphibolite observé dans les domaines de Bolé-Bulenga et d'Abulembire est daté à 2130 ± 6 Ma et 2131 ± 6 Ma respectivement (données non publiées).

La distribution géographique des faciès métamorphiques n'est pas directement liée à la géométrie des grandes zones de cisaillement tardifs activés à partir de D3. Dans certaines unités du domaine de Bolé-Bulenga, les leucosomes parallèles à S1 sont connectés à des leucosomes parallèles à S3, qui peuvent être interprétés comme des structures drainant le magma. Ceci indique que la fusion partielle a lieu aussi bien pendant D1 que D3. Des zircons provenant de leucosomes parallèles à S3 donnent un âge de cristallisation de 2111 ± 7 Ma (données non publiées).

Des grains de staurotide sub-automorphe recoupent S3 dans les paragneiss du domaine de Bolé-Bulenga, indiquant un métamorphisme rétrograde dans le champ de stabilité de ce minéral. La datation de monazites alignées parallèlement à S3 dans un schiste à staurotide provenant d'une zone de cisaillement donne un âge U-Pb de 2123 ± 8 Ma. Cette contrainte représente un âge maximal pour le métamorphisme rétrograde.

L'évolution rétrograde plus tardive se manifeste par des veines et fractures remplies de quartz ou d'épidote, ainsi que par la formation de chlorite et de mica blanc sur des plans de cisaillement associés à D4.

La variabilité des conditions métamorphiques à l'échelle régionale est illustrée par la figure 12. Elle présente les chemins P-T déduits de l'étude pétrologique d'échantillons de roches

métamorphiques de la zone d'étude. Les échantillons peuvent être identifiés et localisés sur la figure 57 de l'annexe 8.1.

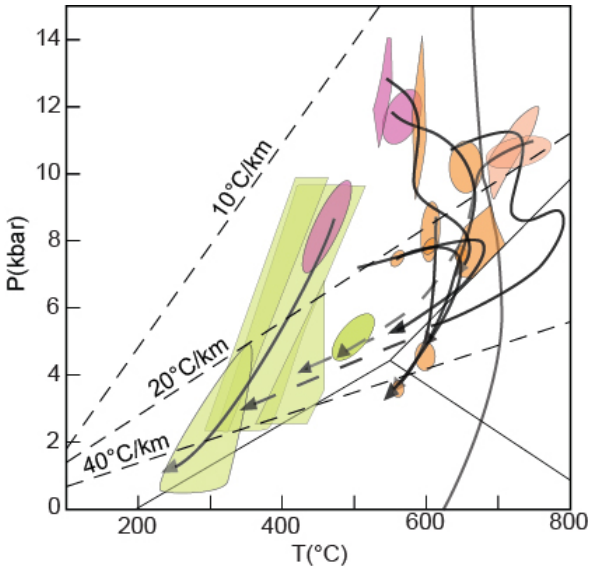

FIGURE 12 – Diagramme P-T synthétique représentant les chemins P-T déduits de l'étude de roches métamorphiques de la zone d'étude. Plages vertes : assemblages métamorphiques formés dans le faciès schiste vert, brun : faciès amphibolite, violet : faciès éclogite, rouge : conditions supra-solidus.

Un rappel sur les faciès métamorphiques et les gradients géothermiques est présenté dans l'annexe 8.1 (Fig. 56).

Quelques mots sur les données métamorphiques présentées dans ce document. Les conditions métamorphiques évoquées dans ce livret ont été déterminées par l'utilisation de pseudosections. Une pseudosection est un diagramme thermodynamique (P-T par exemple) construit en contraignant la composition chimique de la roche, c'est à dire qu'il est valable pour une composition donnée. La méthode consiste à utiliser un logiciel qui calcule, en utilisant des modèles thermodynamiques, les assemblages minéraux stables en chaque point du champ P-T. Le calcul détermine également la composition et la proportion des phases stables en chaque point. Une pseudosection est donc un modèle.

L'évolution métamorphique d'un échantillon est ensuite évaluée en comparant le diagramme modèle (la pseudosection) avec les observations pétrographiques, les relations entre minéraux et la chimie des minéraux. Des contraintes de chronologie relative sont tirées de l'observation des textures et des relations entre minéraux. Il s'agit en effet d'identifier les *paragenèses* successives, qui puissent illustrer des changements de condition P-T. Les zonations chimiques des minéraux traduisent également une variation des conditions P-T. Ces données permettent de reconstituer des chemins P-T lorsqu'elles sont confrontées à la pseudosection.

Les diagrammes P-T présentés ici montrent des résultats de l'utilisation de cette méthode. Les zones de couleur désignent les champs P-T d'équilibration des paragenèses observées et modélisées par la pseudosection. Une convention de couleur est employée. Vert : faciès schiste vert, brun : faciès amphibolite, violet : faciès éclogite, rouge : conditions supra-solidus (voir Fig. 56).

5 Géochronologie U-Pb et stratigraphie

Les roches magmatiques constitutives du craton au nord-ouest du Ghana contiennent parfois des zircons dont les cœurs hérités remontent à 2.30 Ga, voire 2.50 Ga. Cet âge représenterait un âge maximal de matériel continental primitif recyclé dans les terrains birrimiens. La roche la plus ancienne ayant été datée dans la région est un granitoïde formé il y a 2211 ± 6 **Ma** (données non publiées). Des orthogneiss âgés de **ca. 2195 Ma** (De Kock et al., 2011) forment d'importantes parties des domaines de Bolé-Bulenga et d'Abulembire. Ils sont intrusifs dans les paragneiss de "Buki" et les métabasites de ces deux domaines. La formation des roches basiques, de volcanoclastites et de roches volcano-sédimentaires remonte donc au minimum à environ 2.20 Ga. Le plutonisme est synchrone de la mise en place de laves, comment l'atteste l'âge de 2197 ± 6 **Ma** pour la mise en place d'une lave acide dans le bassin de Maluwe.

La formation de TTG se poursuit entre **2180 et 2140 Ma** dans les domaines d'Abulembire, de Bolé-Bulenga et de Tumu-Koudougou. On trouve également des andésites et des dacites d'âges compris entre **2180 and 2130 Ma**, qui représentent peut être les équivalents extrusifs des plutons.

L'épisode métamorphique de haut degré enregistré dans les domaines d'Abulembire et de Bolé-Bulenga a eu lieu entre **2144 et 2123 Ma.**. La fusion partielle qui en résulte a dû produire des magmas granitiques, or on observe une correspondance entre l'âge de cette fusion et la mise en place de plutons dans toute la région. Des monzodiorites et des granites agés entre **2150 et 2130 Ma** sont intrusifs dans les domaines de haut grade, et la série granitique de Tanina se met en place entre **2130 et 2118 Ma.** Les laves les plus jeunes ayant été datées jusqu'à présent ont un âge de 2129 ± 7 **Ma**. Elles sont intercalées dans des quartzites et des arkoses au sein d'un bassin détritique. Des granites potassiques et des syénites se mettent en place dans toute la région entre **2120 et 2095 Ma**. De Kock et al. (2011) décrit des sur-croissances métamorphiques autour de zircons magmatiques. Ces bordures ont un âge aux alentours de **2105 Ma.**

Les sédiments du bassin de la Volta, d'âge Néoprotérozoique, recouvrent en discordance les terrains du Paléoprotérozoique.

Les dykes doléritiques ont trois orientations principales dans la région. 1) NO-SE, 2) NE-SO et 3) O-E. Certains dykes sont associés à l'ouverture de l'océan Atlantique au Jurassique.

Age (Ma)	age error (±)	Lithology	Terrain / Unit	Rocktype	Dating technique	Age interp	Reference
2196	1	Rhyolite	Maluwe Basin	Eff		C	Agyei Duodu et al., 2009
2195	4	Orthogneiss	Bole-Bulenga terrain	Int	Zr SHRIMP	C	Siegfried et al., 2009
2193	4	Orthogneiss	Bole-Bulenga terrain	Int	Zr SHRIMP	C	de Kock et al. 2009
2187	5	Orthogneiss	Abulembire fragment	Int	Zr SHRIMP	C	de Kock et al. 2009
2168	7	Granite	Nangodi belt	Int		C	Agyei Duodu et al., 2009
2162	1	Granitoid	KTGD	Int		C	Davis and Dewaele, 2008
2156	1	Granodiorite	KTGD	Int		C	Davis and Dewaele, 2008
2151	1	Orthogneiss	Nangodi belt	Int		C	Davis and Dewaele, 2008
2150	4	Monzogranite	KTGD	Int	Zr SHRIMP	C	Siegfried et al., 2009
2148	12	Monzogranite	Bole-Bulenga terrain	Int	Zr SHRIMP	C	Thomas et al. 2009
2134	6	Monzodiorite	Bole-Bulenga terrain	Int	Zr SHRIMP	C	Siegfried et al., 2009
2134	1	Granodiorite	KTGD	Int		C	Davis and Dewaele, 2008
2134	1	Granite	Nangodi belt	Int		C	Agyei Duodu et al., 2009
2131	4	Volcanoclastic rock	Maluwe Basin	Eff	Zr SHRIMP	C	de Kock et al. 2009
2128	1	Granite	Nangodi belt	Int		C	Davis and Dewaele, 2008
2128	20	Granite	Bole-Bulenga terrain	Int	Zr SHRIMP	C	Siegfried et al., 2009
2126	7	Granite	Abulembire fragment	Int	Zr SHRIMP	C	de Kock et al. 2009
2125	6	Volcanoclastic rock	Maluwe Basin	Eff	Zr SHRIMP	C	de Kock et al. 2009
2124	2	Granite	Wa-Lawra belt	Int		C	Davis and Dewaele, 2008
2122	6	Monzodiorite	Abulembire fragment	Int	Zr SHRIMP	C	de Kock et al. 2009
2121	4	Monzogranite	Bole-Bulenga terrain	Int	Zr SHRIMP	C	de Kock et al. 2009
2121	8	Granodiorite	Maluwe Basin	Int	Zr SHRIMP	C	Thomas et al. 2009
2120	3	Granite	Bole-Bulenga terrain	Int	Zr SHRIMP	C	Siegfried et al., 2009
2120	3	Granite	Bole-Bulenga terrain	Int		C	Agyei Duodu et al., 2009
2119	4	Granite	Abulembire fragment	Int	Zr SHRIMP	C	de Kock et al. 2009
2118	5	Syenite	Maluwe Basin	Int	Zr SHRIMP	C	de Kock et al. 2009
2118	4	Granite	Bole-Bulenga terrain	Int	Zr SHRIMP	C	Thomas et al. 2009
2112	1	Granite	KTGD	Int		C	Davis and Dewaele, 2008
2104	1	Granite	Wa-Lawra belt	Int		C	Agyei Duodu et al., 2009
2095	1	Granite	Nangodi belt	Int		C	Agyei Duodu et al., 2009
2125	2	Paragneiss	Abulembire fragment	Sed	Zr U-Pb	M	Zitsmann et al. 1997
2105	10	Granodiorite	Abulembire fragment	Int	Zr SHRIMP	M	de Kock et al. 2009
2104	31	Monzogranite	Bole-Bulenga terrain	Int	Zr SHRIMP	M	Thomas et al. 2009
2098	4	Granite	Bole-Bulenga terrain	Int	Zr SHRIMP	M	Thomas et al. 2009
2139	2	Volcano-sedimentary rock	Wa-Lawra belt	Sed		Minimal deposition	Agyei Duodu et al., 2009

FIGURE 13 – Le tableau ci-dessus présente l'ensemble des âges U-Pb publiés dans la zone d'étude. KTGD = Koudougou-Tumu granitoid domain. Rocktype : Int = intrusive, Eff = effusive, Sed = sedimentaire. Interpretation : C = âge de formation, M = âge métamorphique.

6 Données géophysiques

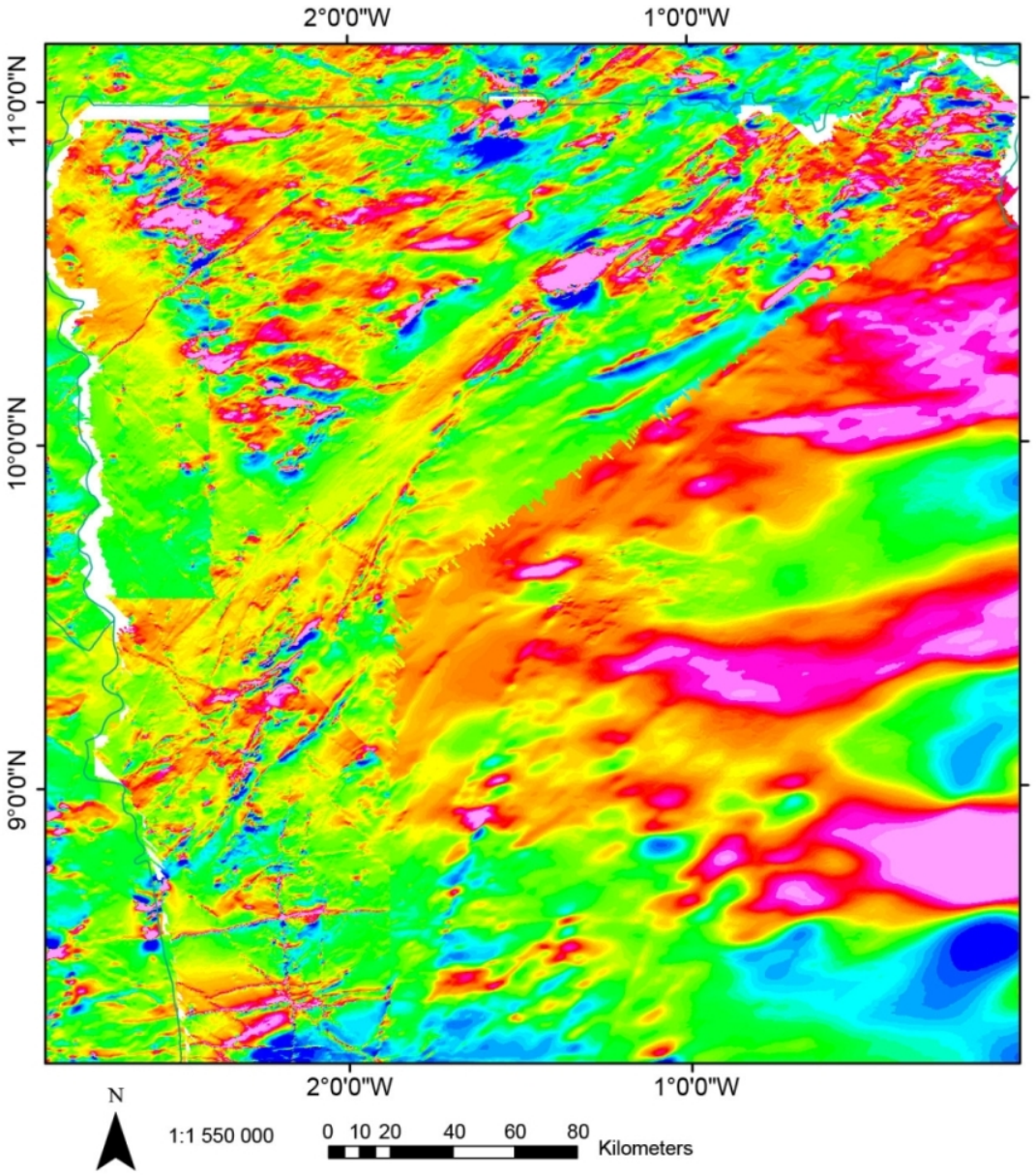

FIGURE 14 – Données magnétiques aéroportées (1-données réduites à l'équateur). Les tons rouges et roses correspondent aux susceptibilités magnétiques élevées, le bleu aux susceptibilités faibles.

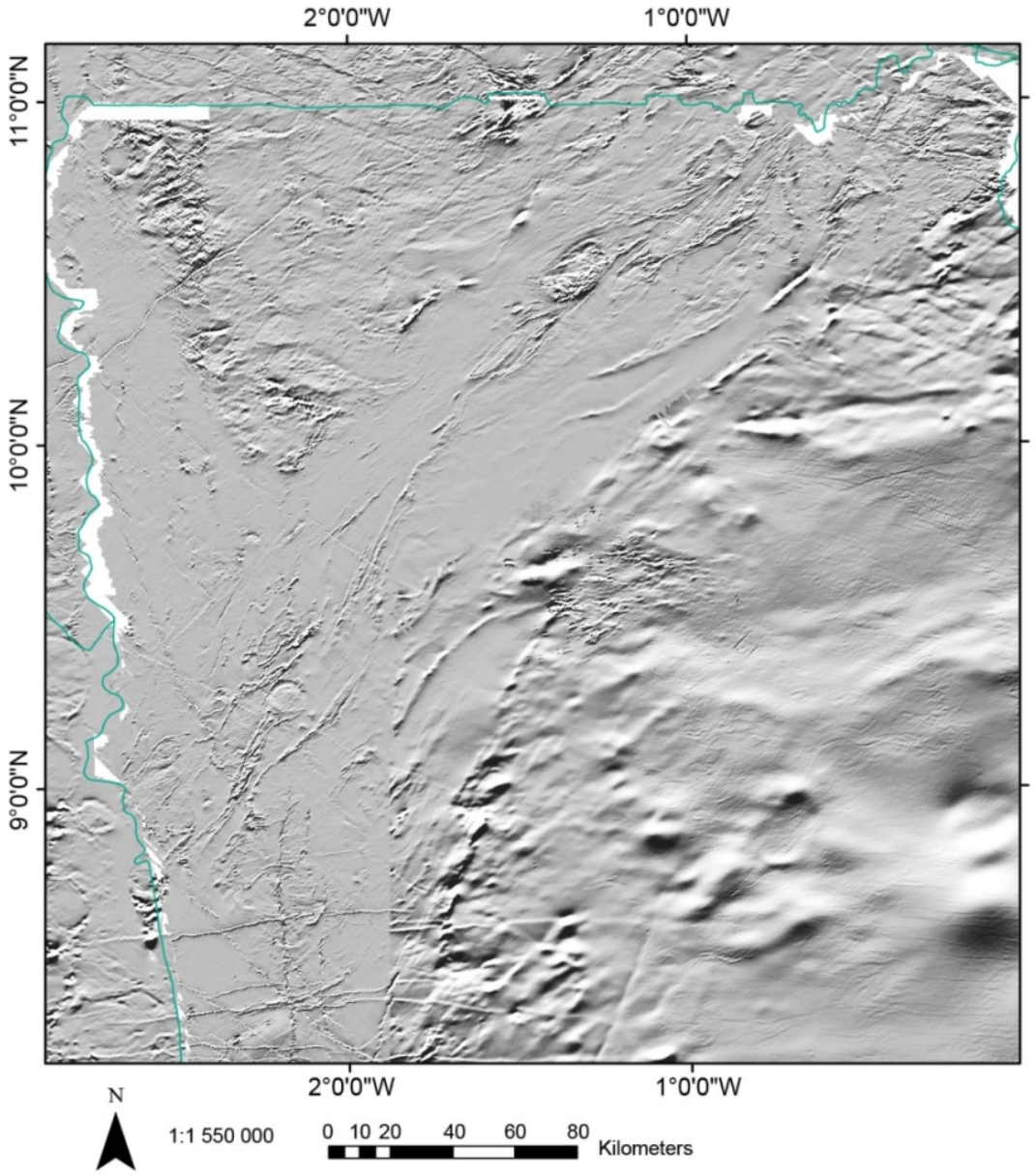

FIGURE 15 – Première dérivée verticale (1VD) des données magnétiques réduites, mettant en évidence les gradients de susceptibilité magnétique.

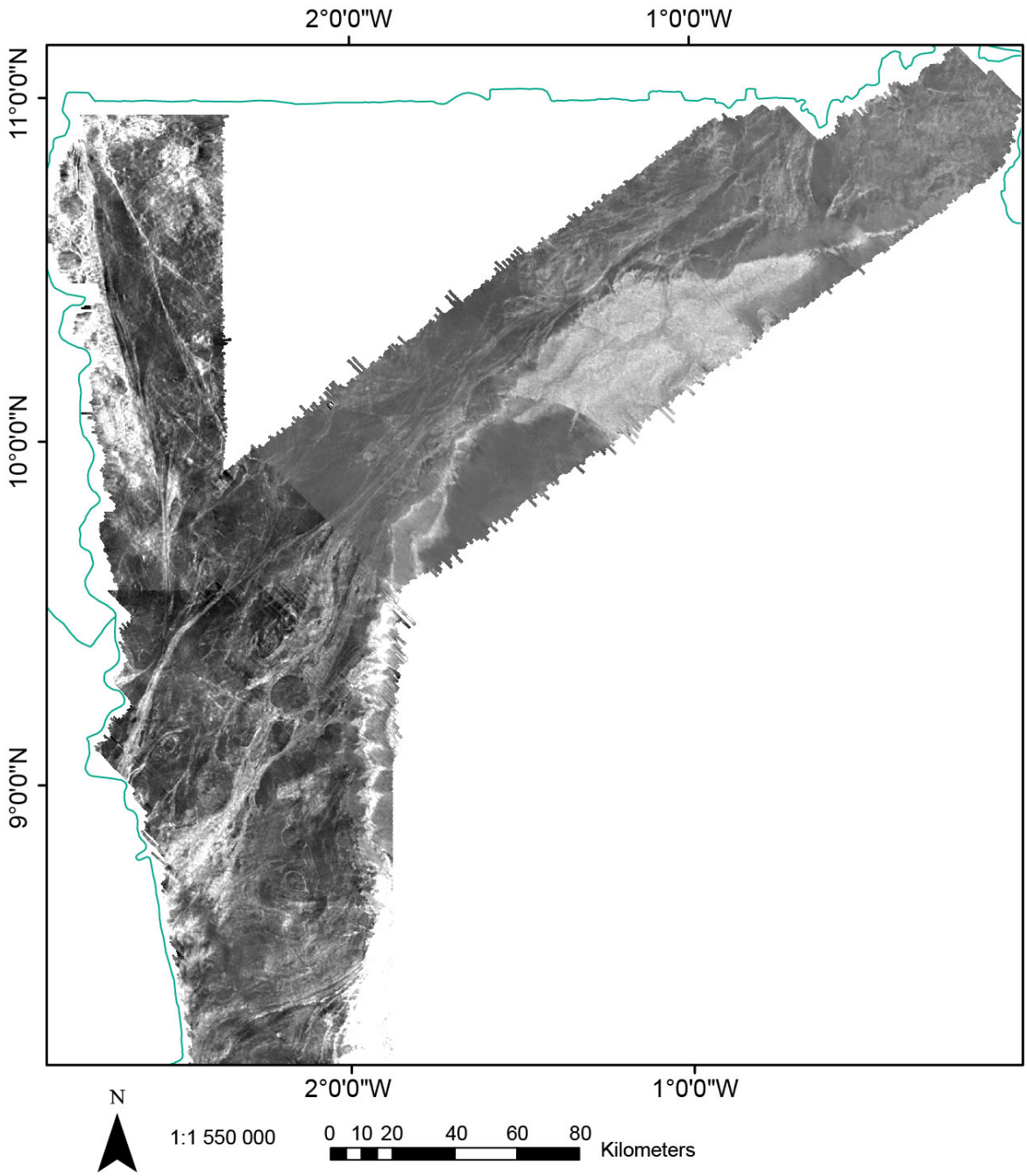

FIGURE 16 – Données électromagnétiques. Le gris clair et le blanc indiquent des roches dont la résistivité électrique est faible. Des roches riches en sulfures ou en graphite ont par exemple cette propriété.

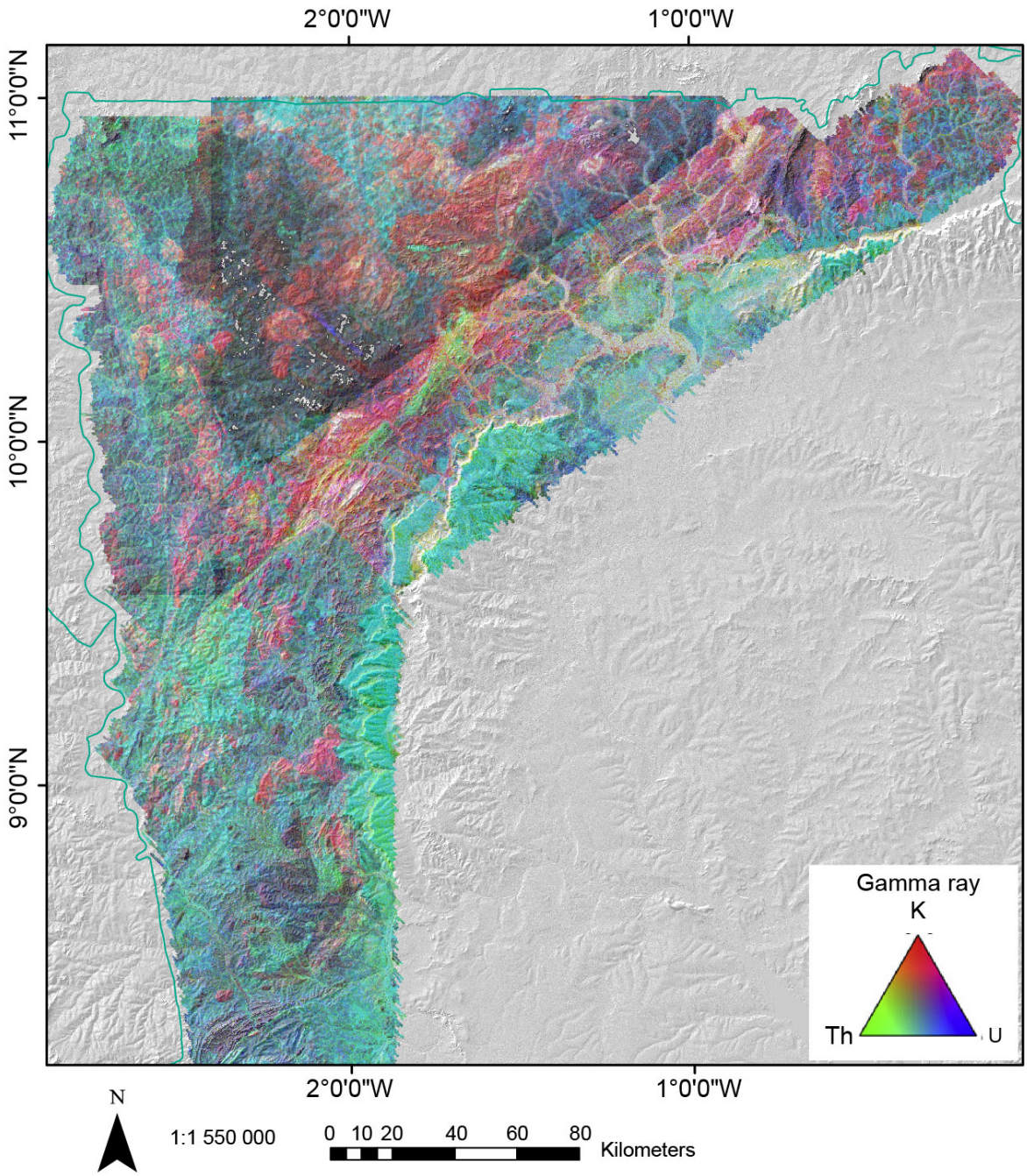

FIGURE 17 – Signal radiométrique calqué sur le modèle numérique de terrain SRTM.

7 Excursion de terrain

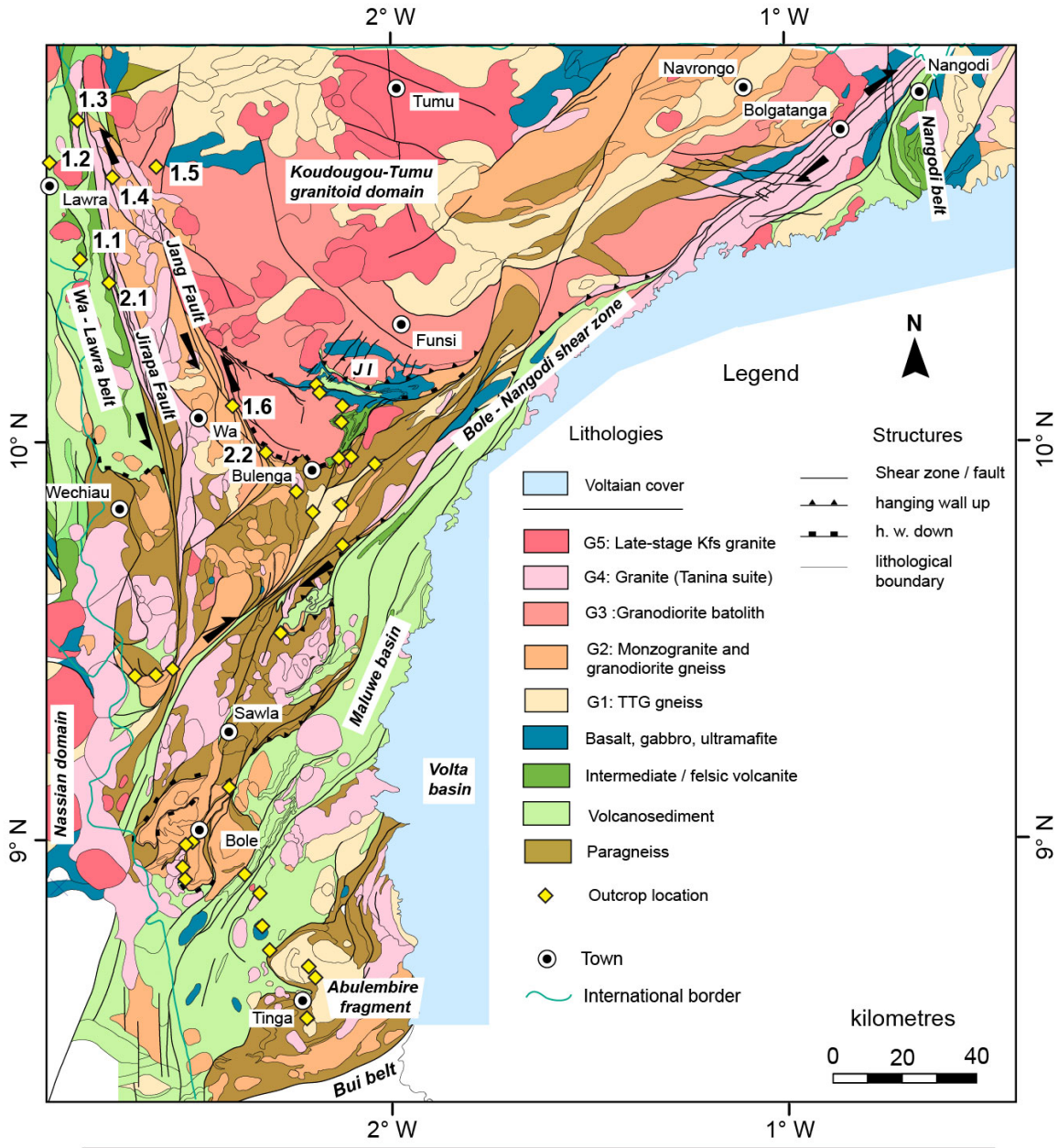

Simplified geological map of the Paleoproterozoic of northern Ghana. Refer to small scale maps for outcrop numbering.
Carte géologique simplifiée du Paléoprotérozoique du nord du Ghana. Se référer aux cartes de plus petite échelle pour les numéros des affleurements.

FIGURE 18 – Carte géologique simplifiée et localisation des affleurements.

Précisions sur les affleurements et les conventions utilisées.

Affleurements Les affleurements dont le numéro est précédé du symbole $*$ sont des affleurements facultatifs dont la visite dépendra du temps disponible. Les coordonnées géographiques des affleurements sont donnés en Lat/Long (degrés décimaux) et l'ellipsoïde est WGS84.

Convention de lecture des mesures structurales. Des mesures structurales sont parfois données dans le texte. Les conventions de mesure utilisées sont les suivantes :

1. Un plan est mesuré par sa *direction de pendage/pendage*, ex : 236/78 est un plan dont le pendage est de 78° dans la direction de l'azimut 236, soit vers le sud-ouest.
2. Une linéation sur un plan de pendage fort est mesurée par son pitch. Le pitch est l'angle entre l'axe horizontal et la linéation dans le plan vertical contenant ces deux lignes. On approxime donc le plan de foliation comme étant vertical. Une mesure de pitch donne le *pendage de la ligne* dans le plan et sa direction. Par exemple, sur un plan orienté 236/78 ; une ligne pourrait avoir un pitch de 13° NE.
3. Une linéation sur un plan faiblement penté est mesurée par son plongement. Le plongement mesure la *direction de pendage/pendage*. Par exemple, une linéation sur un plan faiblement penté vers le nord peut avoir un plongement de 335/28, c'est à dire qu'elle plonge de 28° vers le nord-ouest (azimut 335).

Jour 1 : Ceinture de Wa-Lawra

Le premier jour est dédié à la réalisation d'une coupe à travers la ceinture de Wa-Lawra. Ceci permet d'avoir un aperçu des lithologies constituant la ceinture, de qualifier les conditions métamorphiques qu'elles ont subi, et d'observer les contacts tectoniques afin d'avoir une vision de l'organisation générale de la ceinture.

Arrêt 1.1 (BN 197) : Métabasaltes métamorphisés dans le faciès schiste vert

Route de Nadowli à Lawra, N 10,4719 ; E -2.7792

Les roches volcano-sédimentaires à l'ouest de la faille de Jirapa alternent avec quelques laves massives. Des métabasaltes forment une unité de quelques centaines de mètres de large allongée sur des dizaines de km parallèlement à cette faille. Cette roche génère une légère topographie dans le paysage. La schistosité est grossière plutôt que pénétrative, le plan de débit principal a une orientation de 315/75 et porte une linéation d'étirement avec un pitch de 63°SO. De rares indicateurs cinématiques suggèrent un mouvement inverse du NO vers le SE.

FIGURE 19 – Arrêt 1.1 (BN 197). Métabasaltes métamorphisés en faciès schiste vert développant une schistosité grossière.

Arrêt 1.2 (BN 193) : Sédiments pélitiques et psammitiques

Route de Lawra à Nandom, N 10,6878 ; E -2.8930

Les roches sédimentaires et volcano-sédimentaires à l'ouest de la faille de Jirapa sont essentiellement des pélites, des psammites ou des greywacke tels que ceux à l'affleurement. La présence de chlorite atteste d'un métamorphisme dans le faciès schiste vert. La foliation, orientée environ 100/50, est pénétrative et est parallèle aux horizons sédimentaires (i.e. les strates). Elle est bien plus développée que dans les basaltes vus à l'arrêt précédent, du fait de la compétence bien plus importante de ces derniers. La schistosité est pliée par des crénulations de petite longueur d'onde, aux surfaces axiales orientées 180/85. L'intersection entre ces deux plans forme une linéation d'intersection.

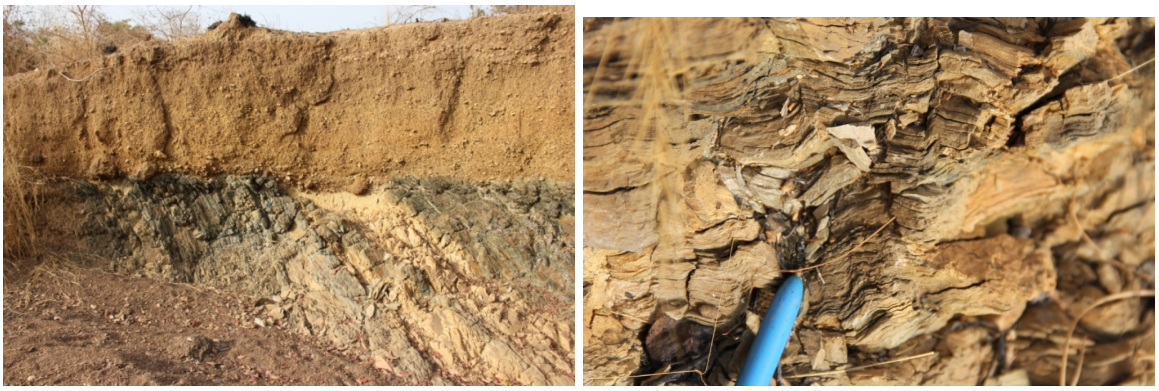

(a) Métapélites et métagreywacke de bas grade recouverts par des alluvions récentes.

(b) Schistosité principale crénulée

FIGURE 20 – Arrêt 1.2 (BN 193)

*Arrêt 1.3 (BN 191) : Granite potassique porphyroïde proche de la faille de Jirapa

Route de Lawra à Nandom, N 10,8062 ; E -2.7978

Le compartiment à l'ouest de la faille de Jirapa est essentiellement constitué de granites. Il s'agit ici d'un granite potassique à orthose porphyrique. Les porphyres ont subi une déformation ductile. Ils forment des objets asymétriques qui semblent indiquer que la déformation possède une une composante décrochante senestre.

FIGURE 21 – Arrêt 1.3 (BN 191). Granite à orthose porphyrique ayant subi une déformation ductile.

Arrêt 1.4 (BN 179) : Granite à biotite contenant des enclaves de paragneiss.

Route de Lawra à Hain, N 10,6469 ; E -2.7392

Cet affleurement se situe à quelques km à l'ouest de la ceinture de Wa-Lawra. La lithologie principale est un granite à biotite folié. Il contient des bandes de cisaillement orientées environ 270/80 qui portent une linéation d'étirement minéral de pitch 14°N. des feldspaths asymétriques indiquent un cisaillement senestre. Les bandes de cisaillement son parfois anastomosées plutôt que distribuées de façon homogène dans la roche. Elles contiennent de la chlorite, ce qui révèle que la déformation a eu lieu sous des conditions métamorphiques du faciès schiste vert.

On observe également des enclaves métriques de paragneiss. Il s'agit de roches de haut grade, dont le protolithe est équivalent aux roche de bas grade vues à l'arrêt précédent. Ces métasédiments contiennent du disthène et du staurotide, révélateurs de conditions métamorphiques relativement élevées. On observe donc une augmentation significative du degré de métamorphisme de part et d'autre de la faille de Jirapa. Ceci nécessite que la faille ait accommodé des déplacements verticaux importants à un certain stade de son activité.

Un granite similaire à celui-ci est daté non loin à 2124±2 Ma, prouvant que la déformation a dû avoir lieu après cette date.

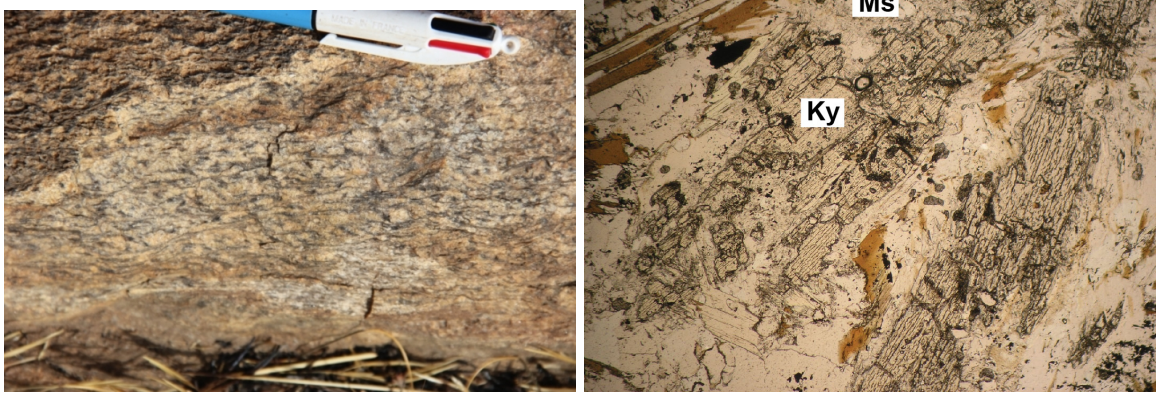

(a) Structures C-S dans le granite.

(b) Photographie de lame mince de l'enclave de paragneiss dans le granite. On y trouve des porphyroblastes de disthène (Ky) partiellement rétromorphosés en muscovite (Ms).

FIGURE 22 – Arrêt 1.4 (BN 179)

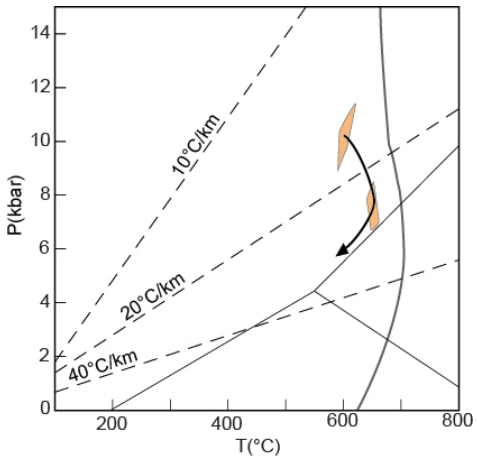

FIGURE 23 – Diagramme P-T schématique présentant le chemin P-T suivi par le paragneiss (échantillon 179). Il enregistre des conditions métamorphiques dans le faciès amphibolite, à environ 600°C, 10kbar. Il a ensuite subi une décompression jusqu'à 7kbar, 630°C, et a donc suivi un chemin P-T horaire (données non publiées).

Arrêt 1.5 (BN 176) : Granodiorite à grain grossier du domaine de Koudougou-Tumu.

Route de Lawra à Hain, N 10,6842 ; E -2.6021

L'affleurement se situe à l'est de la faille de Jang, qui forme la limite orientale de la ceinture de Wa-Lawra. La roche est une granodiorite à grain grossier. La hornblende est parfois centimétrique. La foliation principale est une foliation de haute température orientée 100/60, approximativement parallèle aux structures de la ceinture.

(a) Arrêt 1.5 (BN 176). Granodiorite à grain grossier foliée.

(b) Arrêt 1.6 (BN 222). Gneiss sombre migmatitique contenant des leucosomes parallèles à la foliation, et développant des structures C-C' correspondant à un cisaillement sénestre.

FIGURE 24 –

7.0.1 Arrêt 1.6 (BN 222) : Faille de Jang

Au nord de Wa, N 10,1209 E -2.4243

La faille de Jang est un cisaillement ductile senestre. Les conditions métamorphiques augmentent du nord au sud le long de cet accident, et cet affleurement se situe le long de sa partie sud. Les roches sont partiellement fondues, comme l'atteste la présence de "leucosomes", riches en quartz et feldspaths, dans le gneiss autrement sombre. Ces leucosomes sont interprétés comme étant des reliques de magma granitique formé in-situ. Ils sont déformés et alignés parallèlement à la foliation, ce qui indique que la fusion partielle de la roche a lieu avant ou pendant la déformation. Dans les roches subissant un fort raccourcissement, on observe souvent des bandes de cisaillement en réponse à la déformation. Ces bandes dites " C' " indiquent une accommodation de la déformation par une extension conjuguée au raccourcissement. Leur symétrie constitue un critère de sens. Dans le cas présent, il s'agit d'un cisaillement à composante senestre.

Remarques et conclusion

Les affleurements vus montrent l'existence d'importants gradients de déformation et de métamorphisme dans la ceinture de Wa-Lawra. La déformation est en particulier localisée le long de zones de cisaillement étroites, qui forment des discontinuités dans les conditions métamorphiques. Celles-ci augmentent d'ouest en est. Un granite intrusif dans les métasédiments de la ceinture est âgé de 2104 ± 1 Ma. Cette contrainte représente un âge minimal de la déformation.

Jour 2 : Contexte de la mise en place de la minéralisation, contacts tectoniques majeurs.

Ce jour est consacré à l'observation de carottes de forage provenant de zones minéralisées dans la zone d'étude. L'intérêt est également porté sur des contacts tectoniques fortement déformés dans la ceinture de Wa Lawra et au sud du domaine de Koudougou-Tumu.

Arrêt 2.1 : Observation de carottes de forage, camp de la compagnie Azumah Resources.

De nombreux indices d'or sont connus de mineurs artisanaux et de compagnies minières dans le nord du Ghana. Les contextes structuraux et la période de mise en place de ces gisements au cours de l'histoire géologique régionale sont variés. La minéralisation en or est parfois associée à la déformation D1 dans l'unité de Julie. Elle peut être localisée dans des zones de cisaillement ou dans des veines de quartz formées pendant D3, y compris le long de contacts lithologiques cisaillés. Enfin, certaines veines de quartz d'orientation E-O recoupant les structures ductiles et les contacts lithologiques sont parfois minéralisées. Il s'agit de structures tardives cassantes associées à D4. La minéralogie accompagnant la minéralisation est tout aussi variable.

(a) Veines de quartz déformées et arsénopyrite (b) Or visible à l'œil nu dans un schiste noir syn-cinématique associée à la minéralisation riche en graphite.
en or dans la ceinture de Wa-Lawra.

FIGURE 25 –

Arrêt 2.2 (BN 198) : Granite folié

Route de Nadowli à Lawra, N 10,4175 ; E -2.7212

Cet affleurement est situé le long de la faille de Jirapa, qui sépare des roches volcano-sédimentaires à l'ouest des granitoïdes à l'est.

La roche est fortement déformée et a un débit caractéristique en "pierre tombale". La foliation est orientée 90/75. Elle porte une linéation peu pentée (pitch 10°N) définie par la chlorite. Une linéation antérieure définie par la biotite est également visible. La roche témoigne donc de deux générations de structures.

Arrêt 2.3 (BN739) : Granodiorite gneissique, un contact tectonique de pendage faible

Route de Wa à Bulenga, N 9,9744 E -2.3092

Cette roche est un orthogneiss à grain fin, ce qui suggère qu'il a subi une déformation très intense. Il pourrait être qualifié de mylonite. La foliation gneissique est faiblement pentée vers le NE (35/47) et porte une linéation minérale plongeant vers le N (355/27). On trouve par endroits des leucosomes contenant des grains de hornblende plus grossiers. Ceci indique que la roche a été métamorphisée dans des conditions au delà du solidus. A plus grande échelle, cet affleurement se trouve dans une zone de transition entre un domaine de faible degré métamorphique au nord (l'unité de Julie), et un domaine de degré métamorphique élevé au sud (le domaine de Bolé-Bulenga). On peut donc suggérer que ce contact tectonique représente une faille normale ductile. Cette structure est rattachée la déformation D2.

(a) Arrêt 2.2 (BN 198). Granitoïde folié dans la faille de Jirapa.

(b) Arrêt 2.3 (BN739). Foliation fortement marquée à pendage faible dans une granodiorite gneissique située dans une faille normale ductile.

FIGURE 26 –

Jour 3 : Coupe N-S depuis l'unité de Julie vers le domaine de Bolé-Bulenga.

Le jour 3 est destiné à l'étude des roches formant l'unité de Julie. Il s'agit d'une séquence plissée de roches de faible degré métamorphique. Les relations chronologiques entre les différents épisodes de déformation sont illustrées.

Arrêt 3.1 (BN317) : Crête de roches sédimentaires métamorphiques

Kjersti, N 10.1446 E -2.1866

Cet affleurement de roches sédimentaires appartient à l'unité de Julie, qui est orientée E-O. Il s'agit d'une roche à grain fin, riche en quartz et en micas, dont le protolithe est sans doute une argilite. La chlorite et les micas sont caractéristiques d'un métamorphisme de faciès schiste-vert. Une première schistosité est parallèle à l'orientation générale de la roche, qui correspond sans doute à une ancienne stratification. Cette structure S0-1 a une orientation 05/75. Elle est recoupée par une seconde schistosité, plus grossière, S2 : 355/80. Cette dernière pourrait être liée aux plis de grande échelle visibles dans les données géophysiques (Fig. 9). On observe enfin une crénulation orientée 165/90, qui recoupe l'ensemble.

(a) Vue de la crête formée par les métasédiments.

(b) Deux familles de schistosités sont identifiables.

FIGURE 27 – Arrêt 3.1 (BN317)

Arrêt 3.2 (BN316) : Granodiorite déformée

Kjersti, N 10.1396 E -2.1846

Cette granodiorite contient de la biotite, de la hornblende et du quartz bleuté. Elle est intrusive dans la séquence de roches volcaniques et sédimentaires qui constitue l'unité de Julie, et elle en forme la limite sud. Elle porte une foliation parfois fortement marquée, définie par l'orientation préférentielle des minéraux. Cette anisotropie est recoupée par des bandes de cisaillement formées à la limite ductile-cassant contenant de la chlorite. On observe également qu'elle est affectée par des plis de longueur d'onde métrique, parfois serrés. Le plissement d'un pluton de granitoïde compétent nécessite de développer au préalable une forte anisotropie. Les axes des plis plongent vers l'est ou le sud-est.

Arrêt 3.3 (BN314) : Basaltes de faible degré métamorphique intrudés par une granodiorite.

Kjersti, N 10.1234 E -2.1824

Des basaltes forment le cœur d'un synforme orienté E-O dans l'unité de Julie. Cette structure est clairement mise en évidence par les données magnétiques, du fait du signal magnétique intense des basaltes (Fig. 9). Le métamorphisme est de faible degré. La déformation peut être importante aux limites lithologiques, mais elle est faible au sein des basaltes. On observe à l'affleurement des basaltes intrudés par une granodiorite altérée.

(a) Arrêt 3.2 (BN314). Basaltes dans l'unité de Julie.

(b) Arrêt 3.3 (BN316). Échantillon de la granodiorite à biotite et hornblende.

FIGURE 28 –

***Arrêt 3.4 (BN340) : Pli recombant dans une granodiorite foliée.**

Route de Kjersti à Bulenga, N 10.0928 E -2.1341

La granodiorite présente une foliation (348/42) correspondant aux surfaces axiales de plis recombants. Ces structures peuvent être interprétées comme indiquant un épaississement de la pile de roches dû à un raccourcissement. L'orientation des linéations d'étirement et les critères cinématiques suggèrent un mouvement inverse à vergence sud.

Arrêt 3.5 (BN110) : Sédiments détritiques siliceux à grain grossier, ressemblant aux sédiments tarkwaiens.

Route de Kjersti à Bulenga, N 10.1234 E -2.1824

Cette unité est constituée de roches volcanoclastiques remaniées et déposées sous forme de sédiments, ainsi que d'arkoses grossières. Elle constitue la partie sud de l'unité de Julie et forme un antiforme orienté est-ouest, dont les flancs sont sub-verticaux. Ce pli E-O, attribué à D1, est replissé à l'est le long d'une faille orientée N20, qui est attribuée à D3. La structure d'interférence de plis est clairement mise en évidence par les données aéromagnétiques (Fig. 9). A l'échelle de l'affleurement, on observe des figures de stratification entrecroisée.

FIGURE 29 – *Arrêt 3.4 (BN340). Foliation pénétrative peu pentée associée à des plis recombants dans la granodiorite.

(a) Roche volcano-sédimentaire acide ou arkose métamorphisée.

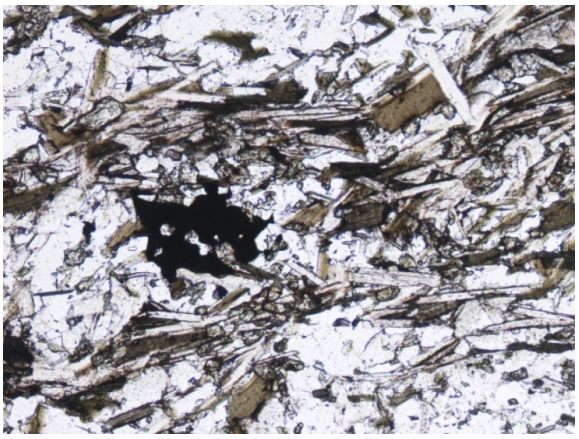

(b) Photographie de lame mince de roche volcano-sédimentaire métamorphique contenant du quartz, du feldspath, de la biotite, du mica blanc, de l'épidote et des minéraux opaques.

FIGURE 30 – Arrêt 3.5 (BN110)

Arrêt 3.6 (BN351) : Zone de contact entre les quartzites "'tarkwaiennes" et le domaine de haut grade de Bolé-Bulenga.

Route de Bulenga à Funsi, N 9.9738 E -2.1196

Le domaine qui comprend l'unité de Julié, la granodiorite foliée vue précédemment et les sédiments de type tarkwaien constituent un ensemble de faible degré métamorphique. Il est en contact sur son flanc sud avec le domaine de Bolé-Bulenga, qui sera étudié dans les jours à venir. L'affleurement vu à l'arrêt 2.3 est un affleurement situé dans la zone de transition entre les deux domaines.

Les structures observées ici sont différentes de celles vues à l'arrêt 2.3. Au nord et à l'ouest, se trouvent des sédiments de type tarkwaien et des métabasaltes métamorphisés en faciès schiste vert. Ces roches sont en contact avec un paragneiss qui a subi un cisaillement intense. Le paragneiss contient une paragenèse incluant grenat et biotite. I présente des

plans de foliation orientés 308/76, portant une linéation de pitch 5° SO. Les structures C-S et les boudins de quartz asymétriques indiquent un cisaillement dextre. Par endroits, une granodiorite intrusive dans le paragneiss a un aspect mylonitique et contient des leucosomes.

(a) Structures SC-C'. Elles indiquent un cisaillement dextre dans les paragneiss.

(b) Leucosome contenant de la hornblende péritectique dans une granodiorite au sein de la zone de contact.

FIGURE 31 – Arrêt 3.6 (BN351)

Remarques et conclusion

L'unité de Julie appartient à un domaine qui a subi un métamorphisme en faciès schiste-vert au cours d'un épisode de déformation consistant en un raccourcissement N-S (D1). Cet ensemble est en contact avec le domaine de Bolé-Bulenga au sud. La zone de contact est constituée de roches fortement déformées, dont des orthogneiss et des paragneiss. Une granodiorite mylonitique à pendage nord forme le segment occidental du contact. La disposition spatiale des faciès métamorphiques suggère qu'il s'agit d'un contact soustractif (une faille normale). Plus à l'est, la transition entre les deux domaines correspond à une zone de cisaillement dextre orientée NNE. La structure d'origine est transposée parallèlement à un plan vertical. La formation de cette structure plus récente doit corresponde à un changement du champ de déformation à l'échelle régionale. Ceci concorde avec les observations d'une schistosité correspondant à un raccourcissement E-O (D3) recoupant les structures plus anciennes.

Jour 4 : Fusion partielle dans le domaine de Bolé-Bulenga.

Le jour 4 a pour objet les processus de fusion partielle que l'on observe dans le domaine de Bolé-Bulenga. Les structures et textures liées à la fusion partielle sont étudiées, ainsi que les interactions entre fusion et déformation. La fusion est enfin abordée par son volet métamorphique et pétrologique.

Arrêt 4.1 (BN118) : Paragneiss à staurotide enregistrant deux épisodes de déformation.

Route de Bulenga à Funsi, N 9.9738 E -2.1196

Des paragneiss à grenat se trouvent dans le domaine de Bolé-Bulenga, au voisinage du contact avec l'unité de Julie. On y observe une schistosité S1 parallèle au litage sédimentaire. S1 est recoupée par la schistosité S3 (84/72) qui correspond à la surface axiale de plis serrés. Le staurotide est présent dans certains horizons stratigraphiques de composition favorable, et est aligné parallèlement à S3. Les conditions métamorphiques durant D3 sont donc dans le champ de stabilité du staurotide. L'orientation de S3 est compatible avec l'orientation de la zone de cisaillement dextre orientée N30 -N40 vue à l'arrêt 3.6. La datation U-Pb de monazites étirées parallèlement à S3 donne un âge de 2123 ± 8 Ma (non publié). Cet âge peut être interprété comme un âge maximal de la déformation D3.

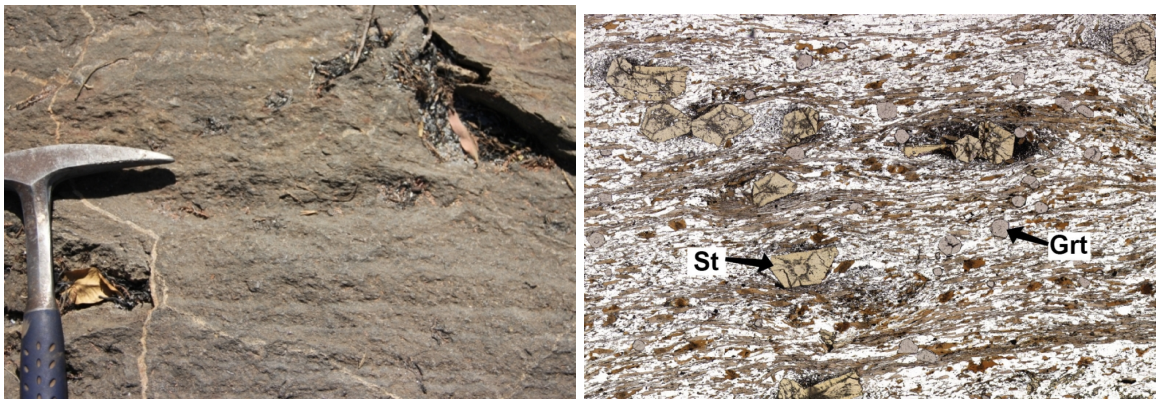

(a) Paragneiss contenant des porphyroblastes syn-cinématiques alignés parallèlement à un plan de schistosité S3 d'orientation N-S.

(b) Lame mince dans le paragneiss montrant des grains sub-automorphes de staurotide (St) orientés parallèlement à S3. Ils sont faiblement déformés, voire non déformés, ce qui indique qu'ils ont crû à une phase tardive de la déformation.

FIGURE 32 – Arrêt 4.1 (BN118)

Arrêt 4.2 (BN377/BN542) : "Gneiss composite" migmatitique.

Route de Bulenga à Funsi, N 9.9470 E -2.0390

L'isograde de la fusion partielle se trouve au sud et à l'est de l'arrêt 4.1. Les orthogneiss et paragneiss possèdent une foliation métamorphique définie par l'alternance de **néosomes** et de **paléosomes.** Lorsque cette alternance forme un fort contraste de couleur, on peut parler de **leucosome** et de **melanosome** respectivement pour les niveaux clairs et sombres. Les leucosomes sont interprétés comme représentant un résidu de magma. La proportion de

leucosomes dans la roche augmente progressivement vers le sud de l'affleuremeent, ce qui indique une croissance du taux de fusion.

Les leucosomes sont parallèles à la foliation S1, qui est grossièrement orientée E-O (347/56). S1 correspond aux surfaces axiales de plis isoclinaux dont les axes sont orientés 240/20. Le magma granitique produit par la fusion s'accumule dans des bandes de cisaillement qui recoupent S1. Ces structures ont des azimuts compris entre N0 et N20, et sont compatibles avec un raccourcissement approximativement orienté E-O, correspondant à D3.

Cet affleurement permet d'observer en détail certaines caractéristiques des roches migmatitiques. Parmi elles, on compte,

1. Des roches contenant une phase solide et une phase liquide (le magma),
2. Une ségrégation et une migration du magma,
3. Des contrastes rhéologiques entre les deux phases,
4. Des réactions métamorphiques impliquant le magma comme produit ou comme réactif,
5. Des phases minérales péritectiques caractéristiques des réactions de déshydratation.

(a) Gneiss migmatitique contenant des leucosomes foliés parallèlement à S1. Une bande de cisaillement oblique par rapport à S1 est remplie de magma granitique qui s'y est accumulé. On observe des liserés de biotite à l'interface entre le leucosome et le mélanosome.

(b) Leucosomes parallèles à la foliation drainés dans un dyke granitique sécant. La géométrie de la foliation, qui semble se resserrer au voisinage du dyke, illustre une perte de volume de la roche par extraction de magma.

FIGURE 33 – Arrêt 4.2 (BN377/BN542)

***Arrêt 4.3 (BN551) : Orthogneiss migmatitique.**

Route de Bulenga à Ducie, N 9.8538 E -2.1216

Cet orthogneiss est fortement marqué par la déformation D3. La foliation S1 est affectée par des plis F3, dont les surfaces axiales sont orientées N20. Alors que certains leucosomes sont orientés parallèlement à S1, d'autres recoupent cette foliation. Ceci indique que la transition de D1 a D3 dans cette roche s'est produite sous des conditions de fusion partielle.

Arrêt 4.4 (BN566) : Orthogneiss migmatitique et phases péritectiques.

Route de Tuasa à Jeyiri, N 9.8360 E -2.2005

On observe à cet arrêt un orthogneiss dont la foliation est sub-verticale et orientée approximativement N0 (83/74). Les dykes granitiques qu'il contient sont plissés de nombreuses

fois, indiquant un cisaillement intense et un fort raccourcissement. Les plis symétriques sont en faveur d'un raccourcissement dominé par l'aplatissement. Des bandes de cisaillement régulièrement espacées sont conjuguées au raccourcissement. Elles sont essentiellement dextres et orientées N30. La direction d'extension qui en résulte (l'axe X de l'ellipsoïde de la déformation finie) est approximativement à angle droit de la direction de raccourcissement. Les relations entre les leucosomes et les bandes de cisaillement suggèrent que cette déformation a eu lieu dans des conditions de fusion partielle.

(a) Dyke granitique dans un orthogneiss illustrant un intense raccourcissement, peut être essentiellement accommodé par de l'aplatissement, en réponse au raccourcissement E-O (D3).

(b) Bandes de cisaillement dextres accommodant le raccourcissement par un fluage latéral conjugué.

FIGURE 34 – Arrêt 4.4 (BN566)

Arrêt 4.5 (BN28) : Zone de cisaillement de Bolé-Nangodi.

Chasia, N 9.7507 E -2.1162

Le contact entre le domaine de Bolé-Bulenga et le bassin de Maluwe est matérialisée par une zone de cisaillement ductile. Elle contient des orthogneiss et des paragneiss partiellement fondus, ainsi que des granites et des dykes pegmatitiques. Les relations de terrain suggèrent que le granite pourrait représenter le produit de fusion partielle des migmatites environnantes dans le domaine de Bolé-Bulenga. Des structures SC-C' sont fortement développées. Les plans C sont orientés 140/80 et portent une linéation d'étirement 4° SO. La foliation correspond aux surfaces axiales de plis isoclinaux. Les plans C' sont orientés environ 170/90, et les structures dans leur ensemble indiquent un cisaillement dextre.

Arrêt 4.6 (BN753) : Relations entre D1, D3 et la fusion partielle.

Non loin de la route de Chasia à Wa, N 9.8755 E -2.2366

Cet affleurement est formé de paragneiss partiellement fondu. Le paragneiss est une roche sombre, micacée, contenant grenat et silicate d'alumine. Les leucosomes sont constitués de lentilles et de veines de granite rosé. On distingue une foliation précoce parallèle à un litage sédimentaire S0-1, orientée 160/40. Cette première structure est plissée. Les surfaces axiales des plis correspondent à un second plan de schistosité S3, orienté 82/88, et formé lors d'un raccourcissement E-O. On observe des lentilles de magma transposées parallèlement à S3, montrant que le magma s'est accumulé dans les charnières de plis F3. Cette ségrégation du

(a) Roches fortement déformées dans la zone de cisaillement de Bolé-Nangodi.

(b) Structures SC-C' autour de porphyroclastes d'orthose dans un filon de granite pegmatitique.

FIGURE 35 – Arrêt 4.5 (BN28)

magma est permise par sa faible viscosité : il se déforme plus facilement que la phase solide. Les leucosomes sont parfois connectés à des veines de granites parallèles à S3 et étirées selon la linéation d'étirement, qui plonge vers 170/35. On en déduit deux interprétations.

1. Le magma est présent dans la roche durant D3, les leucosomes sont parallèles à S3. Nous avons vu par ailleurs des leucosomes parallèles à S1. Le magma est présent dans les structures liées à D1 et D3. Les conditions métamorphiques n'ont pas changé entre D1 et D3, qui doivent donc être continues.
2. Le raccourcissement E-O est accommodé par un plissement et un étirement N-S.

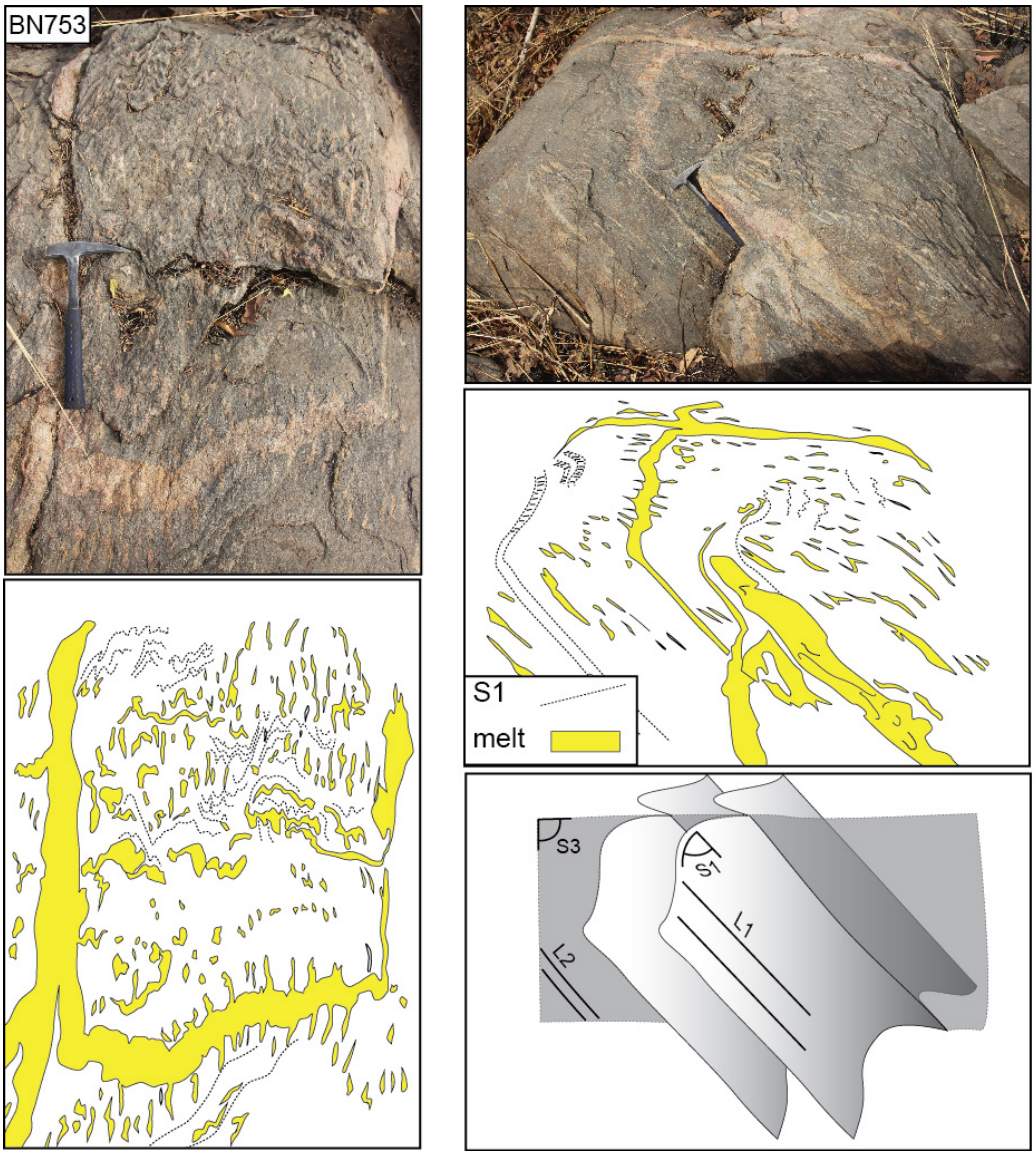

FIGURE 36 – Arrêt 4.6 (BN753). Interprétation des structures de la migmatite.

Remarques et conclusion.

Cette journée permet d'illustrer la transition de roches non fondues aux gneiss migmatitiques, et finalement aux granites issus de la migration et de l'accumulation du magma. Les affleurements mettent en évidence les structures qui assurent l'extraction et la migration de magma depuis la roche source partiellement fondue vers le pluton. Ce gradient vu sur le terrain correspondrait à une augmentation progressive de la profondeur à laquelle résidait la croûte à l'affleurement lors du métamorphisme. Les réactions de fusion peuvent être abordées comme n'importe quelle réaction métamorphique. Il s'agit de réactions de déshydratation dont la particularité est de produire une phase liquide. A l'échelle crustale, la fusion partielle produit du magma dont la migration entraîne des transferts de matière, de chaleur et d'eau. C'est un moteur de la différenciation de la croûte.

Jour 5 : Gradients métamorphiques et gradients de déformation dans le domaine de Bolé-Bulenga.

Cette journée permet de constater l'existence de gradients métamorphiques et de gradients de déformation entre les différentes unités du domaine de Bolé-Bulenga, et de discuter de leur signification.

Arrêt 5.1 (BN539) : Paragneiss à grenat et staurotide enregistrant deux épisodes de déformation.

Poyentanga, N 9.8738 E -2.4583

L'affleurement est constitué d'un paragneiss intrudé par un leucogranite. L'orientation générale des horizons stratigraphiques est approximativement N80. Cet horizon est parallèle à une schistosité fine S0-1, qui correspond à la surface axiale de plis isoclinaux. Ces structures sont associées à D1. Les dykes intrusifs de granite sont essentiellement parallèles à S0-1, bien qu'ils puissent parfois la recouper. L'ensemble est affecté par une seconde schistosité pénétrative (S3 : 80/85), qui correspond à la surface axiale de plis serrés. Son orientation constante correspond au raccourcissement E-O rattaché à D3. Les minéraux orientés dans S0-1 et S3 sont les mêmes, indiquant que les deux déformations ont eu lieu dans des conditions métamorphiques similaires. La transition de D1 à D3 est donc sans doute continue.

Arrêt 5.2 (BN053) : Paragneiss à grenat, staurotide, disthène.

Aux environs de Kong, N 9.5002 E -2.2936

L'affleurement est situé non loin de la limite orientale du domaine de Bolé-Bulenga. Il est constitué de métagreywacke et de métapélites orientées approximativement E-O. Quelques km à l'ouest, les métadédiments sont intrudés par un granite à biotite peu ou non déformé. Le contact entre ces métasédiments de haut degré métamorphiques et les roches du bassin, de faible degré métamorphique, est dissimulé par les plutons granitiques.

A l'échelle de l'affleurement, le paragneiss ne montre aucun signe de fusion partielle. On observe une stratification marquée par l'alternance de bancs gréseux et pélitiques. Les bancs pélitiques sont caractérisés par l'abondance de minéraux alumineux, tels que le grenat, le staurotide et les silicates d'alumine. Cette stratification est parallèle à une schistosité S0-1, de pendage modéré vers le sud (180/55). S0-1 est recoupée par une foliation plus tardive (S3) orientée 100/80. S3 correspond aux surfaces axiales de plis sérrés de faible longueur d'onde, et S0-1 est par endroits transposée parallèlement à S3. Les plis P3 ont des axes plongeant environ 60°S. Le staurotide est sub-automorphe et contient des inclusions de grenat. Il représente donc un minéral formé tardivement durant l'évolution métamorphique.

Conditions métamorphiques.

Les microstructures et les relations texturales entre phases observées en lame mince dans les affleurements étudiés fournissent les informations suivantes :

1. Il existe deux générations de schistosités dans les roches du domaine de Bolé-Bulenga.
2. La première schistosité (S0-1) est parallèle à la stratification des métasédiments.
3. S0-1 est plissée lors d'un raccourcissement E-O (D3) et est recoupée par S3.
4. Les minéraux du métamorphisme (grenat, biotite et silicates d'alumine) sont alignés tantôt selon S0-1, tantôt selon S3. Le staurotide est souvent automorphe, aligné dans S3 ou bien la recoupant.

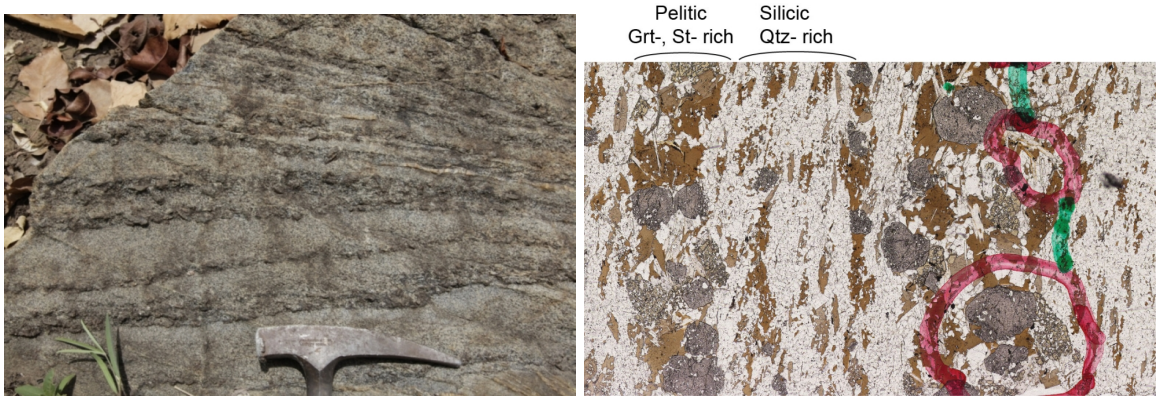

(a) Horizons stratigraphiques contrôlant la proportion des minéraux métamorphiques.

(b) Photographie de lame mince du paragneiss. Le grenat (Grt), la biotite (Bt) et le staurotide (St) sont concentrés dans des lits fins de composition pélitique.

FIGURE 37 – Arrêt 5.2 (BN053)

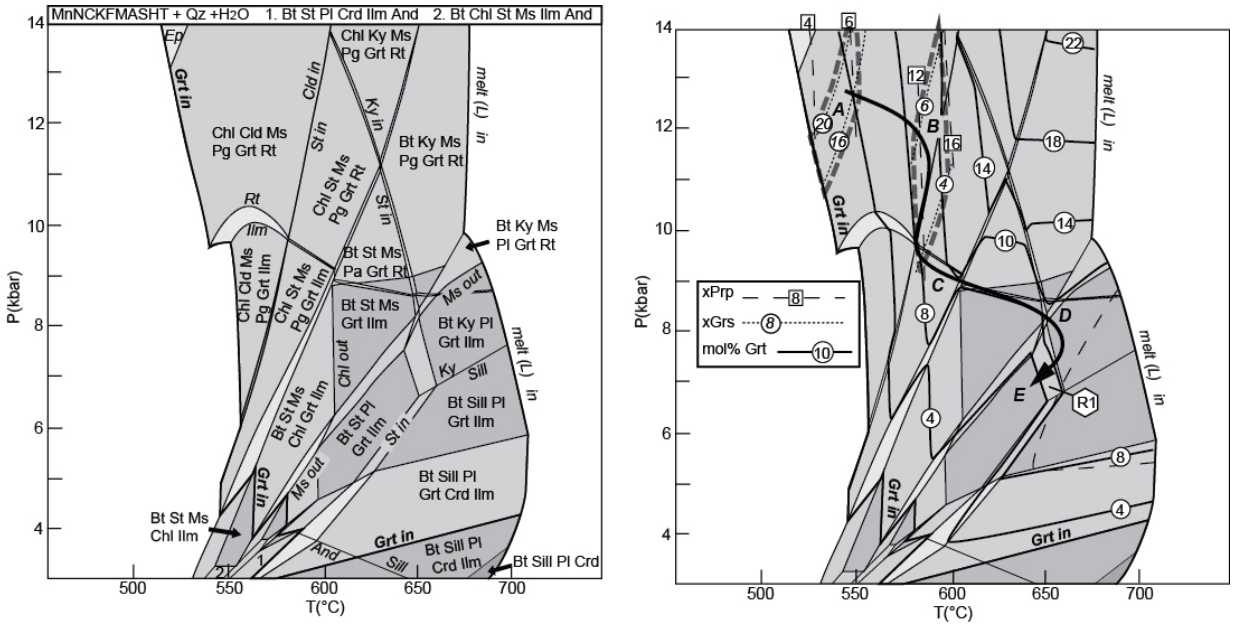

FIGURE 38 – **Gauche** : Pseudosection P-T d'une métapélite (BN047)issue de la partie orientale du domaine de Bolé-Bulenga, présentant les domaines de stabilité de différentes paragenèses. **Droite** : Chemin P-T de l'échantillon déterminé par comparaison des paragenèses observées avec les paragenèses modélisées.

Les pseudosections P-T sont construites pour contraindre les conditions métamorphiques, sur la base des observations pétrologiques et de la chimie des minéraux. Elles fournissent les observations suivantes :

1. Le grenat s'est formé à pression relativement élevée, à P> 11 kbar, T 550°C, dans le faciès des éclogites (Fig. 56). Cette empreinte métamorphique précoce correspondrait à D1.
2. La roche a ensuite subi une décompression accompagnée d'une hausse de température, pour atteindre le champ de stabilité du disthène, à 650-700°C, 7-10 kbar, dans le faciès amphibolite. Un tel trajet illustre une exhumation qui peut être favorisée par l'exten-

sion, pendant D2.

3. Le staurotide est une phase minérale rétrograde formée lors du refroidissement de la roche, à T<650°C, P< 8 kbar. Sa formation intervient tardivement pendant D3.

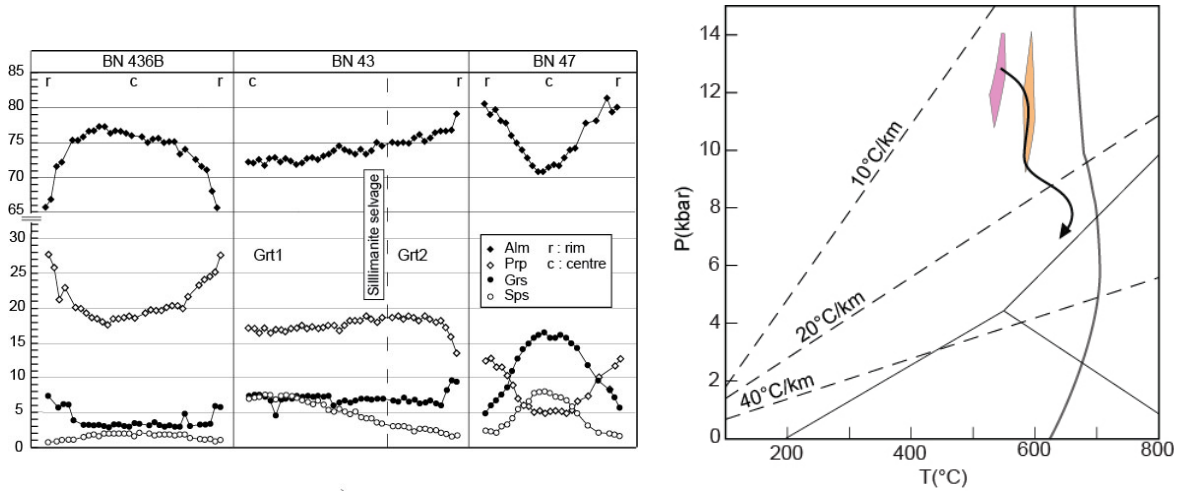

(a) Profil radial de composition chimique à travers les porphyroblastes de grenat dans quelques échantillons provenant des domaines de degré métamorphique élevé. Les zonations sont la manifestration de conditions P-T changeantes lors de la croissance du minéral. Les échantillons BN047, BN053 et BN056 sont issus de la même unité géologique.

(b) Diagramme P-T schématique présentant le chemin P-T suivi par l'échantillon BN047. Violet : faciès éclogite, marron : faciès amphibolite (Fig. 56).

FIGURE 39 –

*Arrêt 5.3 (BN511) : Mylonite dans l'extrémité sud de la faille de Jirapa.

A l'est de Nakwabi, N 9.4125 E -2.5511

Les trois affleurements qui suivent dessinent une coupe est-ouest à travers la terminaison sud de la faille de Jirapa et la partie occidentale du domaine de Bolé-Bulenga (Fig. 5).

Le degré métamorphique le long de la faille de Jirapa semble être maximal au sud, dans la zone d'interférence avec la zone de cisaillement de Bolé-Nangodi. La déformation, distribuée de façon homogène dans les gneiss alentours, tend à se localiser pour constituer la faille de Jirapa. Il en résulte un important gradient de déformation, dont l'intensité culmine dans la zone de cisaillement sénestre. A échelle kilométrique, la foliation régionale est déviée et entraînée dans la zone de cisaillement.

Le premier arrêt se situe dans la zone de cisaillement, orientée N-S. On y trouve un granitoïde fortement déformé. La foliation est orientée 280/85 et porte une linéation d'étirement minérale dont le pitch est 15°S. Les indicateurs cinématiques montrent un cisaillement senestre.

*Arrêt 5.4 (BN509) : Granodiorite migmatitique et structures transposées.

A l'est de Nakwabi, N 9.4155 E -2.5725

L'affleurement est constitué d'un orthogneiss basique contenant essentiellement de la hornblende, du plagioclase et du quartz. La roche comporte des agrégats de minéraux étirés et des dykes granitiques plissés, qui témoignent d'une déformation très intense. Les plans de foliation ont une orientation d'environ 310/85, soit à 30° de l'orientation de la foliation à l'arrêt précédent. La présence de néosomes aplatis indique une fusion antérieure à la déformation. La foliation est décalée par des bandes C' symétriques, ce qui pourrait indiquer une déformation principalement coaxiale.

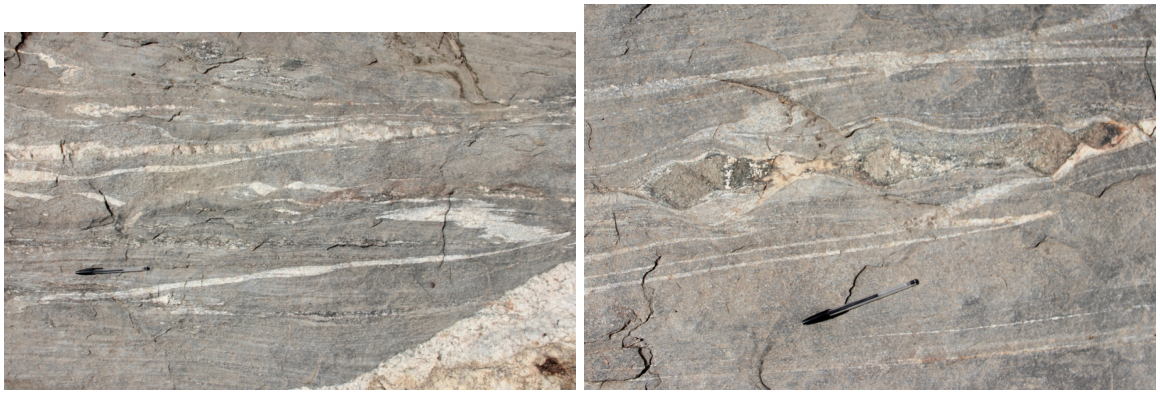

(a) Plis et bandes de cisaillement dans les gneiss fortement déformés.

(b) Néosomes et agrégats de minéraux formant des boudins symétriques.

FIGURE 40 – Arrêt 5.4 (BN509)

***Arrêt 5.5 (BN506) : Granodiorite migmatitique, déformation peu intense et structures non transposées.**

A l'est de Nakwabi, N 9.4102 E -2.6040

La roche à l'affleurement est équivalente à celle vue à l'affleurement précédent. Elle n'a cependant pas subi de déformation d'intensité comparable, comme l'indique la taille plus importante des grains. Les leucosomes sont fins et orientés parallèlement à la foliation. Ils contiennent des grains grossiers de hornblende recristallisée, et parfois des grenats péritectiques. La foliation est orientée 42/61 et porte une linéation plongeant de 60° vers le NO. Il s'agit de la foliation précoce S1, qui n'a pas été transposée dans les structures tardives de la déformation D3. Elle est orientée à 70° de la foliation de l'affleurement précédent.

(a) L'orthogneiss migmatitique contient des leucosomes fins orientés parallèlement à la foliation.

(b) Agrégats d'amphibole et de grenat péritectique dans un leucosome.

FIGURE 41 – Arrêt 5.5 (BN506)

Les conditions P-T de cristallisation des amphiboles magmatiques (péritectiques) sont effectuées en utilisant la calibration expérimentale de Ridolfi et Renzulli (2012). Ce thermobaromètre est basé sur la teneur en Al des amphiboles calciques. Il permet d'obtenir des conditions de formation des amphiboles de 750-800°C, 4-7 kbar, ce qui est grossièrement en accord avec les conditions de fusion déduites de l'étude de migmatites ailleurs dans le domaine de Bolé-Bulega.

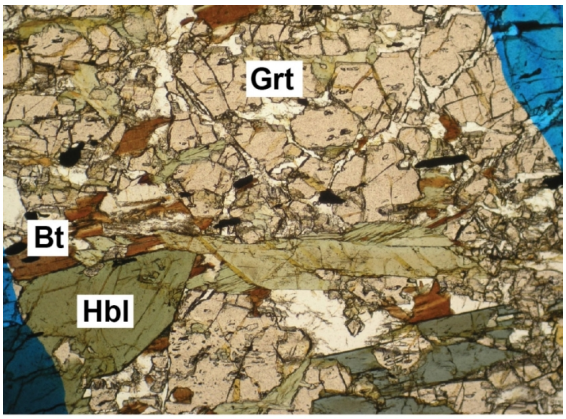

(a) Photographie de lame mince dans un néosome de l'échantillon BN506 contenant de la biotite, de l'ilmenite, du quartz, du plagioclase, ainsi que de la hornblende et du grenat péritectique.

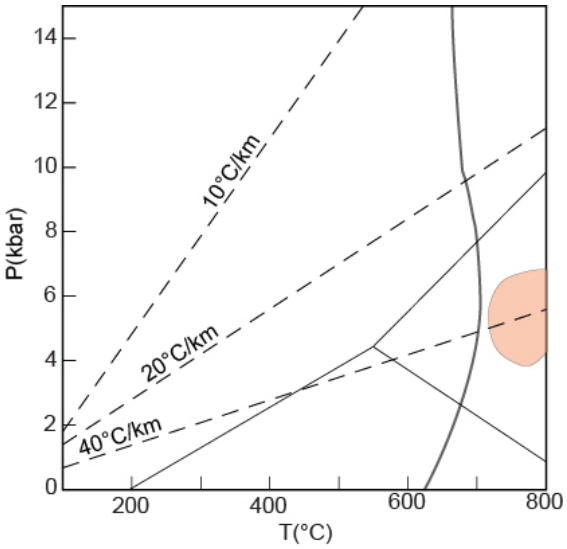

(b) Domaine P-T d'équilibration des hornblendes, déterminé à l'aide du thermobaromètre de Ridolfi et Renzulli (2012).

FIGURE 42 –

Arrêt 5.6 (BN858) : Quartzite à disthène dans la zone de contact entre domaines de haut grade et de bas grade.

Non loin de la route entre Sawla et Bolé, N 9.1098 E -2.4302

Dans la partie sud du domaine de Bolé-Bulenga, le contact avec les roches de bas grade du bassin de Maluwe est fréquemment caractérisé par la présence d'une roche siliceuse fortement déformée. Le protolithe de cette roche est incertain car elle a subi une altération importante. Elle ressemble à une quartzite qui contient une proportion variable, mais parfois élevée, de disthène. Il est possible de suivre cette lithologie sur plusieurs km le long de zones de cisaillement et dans les flancs de plis d'échelle kilomètrique.

(a) Quartzite à disthène dans une zone de contact représentant une importante discontinuité de conditions métamorphiques.

(b) Granite altéré et recoupé par des veines de quartz, au contact de la quartzite à disthène.

FIGURE 43 – Arrêt 5.6 (BN858)

Jour 6 : Métamorphisme rétrograde et déformations tardives.

L'objectif est d'étudier le métamorphisme rétrograde et les facteurs qui le contrôlent. Les observations montrent que le métamorphisme rétrograde est souvent associé dans l'espace à des structures localisantes tardives. Lorsque la température diminue, la rhéologie des roches change et la déformation tend à se localiser dans des zones de cisaillement étroites.

Arrêt 6.1 (BN232) : Orthogneiss affecté par un cisaillement ductile tardif.

Au sud de Bolé, N 9.0129 E -2.4948

La partie sud du domaine de Bolé-Bulenga présente une alternance de domaine de haut degré et de bas degré métamorphiques. Elle pourrait être le résultat d'une succession de synformes et d'antiformes orientés parallèlement à une direction NNE, formés pendant le raccourcissement E-O (D3). Les contacts entre les unités géologiques sont plissés et transposés dans des zones de cisaillement ductiles orientées N0-N40. Ces structures sont formées ou réactivées tardivement. Le métamorphisme rétrograde est particulièrement développé dans ces zones localisant la déformation.

On observe à l'affleurement un orthogneiss cisaillé présentant des structures C-S dextres. Les plans S sont orientés 126/86, les plans C 149/85 et la linéation sur les plans C a un pitch de 11° NE. La linéation est définie par la chlorite, indiquant un cisaillement dans le faciès schiste vert.

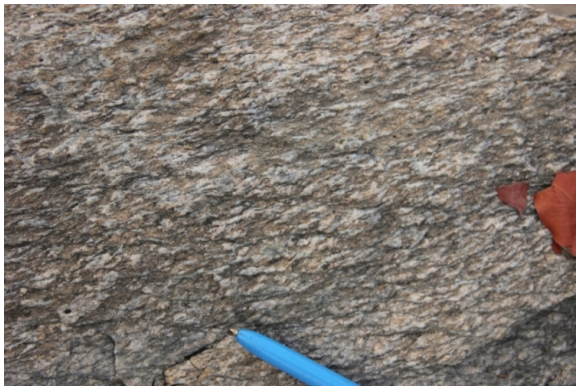

(a) Structures C-S dextres dans un orthogneiss.

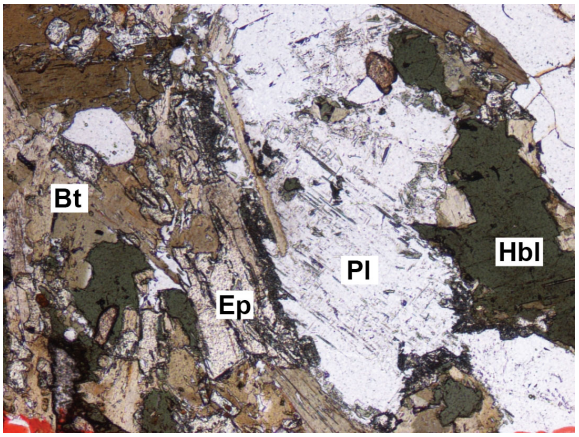

(b) Photographie de lame mince de l'orthogneiss. Les minéraux métamorphiques (biotite et épidote) remplacent partiellement la hornblende magmatique.

FIGURE 44 – Arrêt 6.1 (BN232).

Arrêt 6.2 (BN487) : Orthogneiss déformé sous des conditions de température variables.

Au sud de Bolé, N 9.0082 E -2.4984

L'orthogneiss est similaire à celui observé à l'arrêt 6.1. On y voit une foliation gneissique de haute température (110/80). Des niveaux mélanocrates, sans doute des enclaves à l'origine, sont étirés parallèlement à la foliation. Celle-ci est décalée par des bandes de cisaillement ou des failles cassantes conjuguées dextres et senestres. La déformation se localise donc dans des

structures étroites plutôt que de se distribuer dans le volume de la roche. A quelques pas à l'ouest, la roche est altérée et contient de nombreuses veines de quartz, qui représentent des fentes de tension sub-verticales, orientées E-O (azimut N100).

Les structures cassantes sont compatibles avec un raccourcissement E-O (D6), comme le sont les structures ductiles et la foliation gneissique. On peut donc interpréter ces structures successives comme étant formées pendant un refroidissement progressif de la roche dans un champ de déformation relativement stable.

(a) Faille décrochante senestre contenant des fragments plissés de l'encaissant, et peut-être remplies de pseudotachylites. La déformation est associée à une métamorphisme de bas degré et à une altération.

(b) Fentes de tensions emplies de quartz associées aux failles cassantes. Ces structures sont compatibles avec la même direction de raccourcissement.

FIGURE 45 – Arrêt 6.2 (BN487)

Arrêt 6.3 (BN488) : Quartzite à disthène.

Au sud de Bolé, N 9.0123 E -2.5104

L'affleurement précédent se situe sur la marge d'une zone de cisaillement clairement mise en évidence par le relevé de données électromagnétiques (Fig. 5). De l'autre côté de la zone de cisaillement se trouve une colline de quartzite contenant du disthène, et parfois du mica blanc. Cette unité marqueur, similaire à celle vue à l'arrêt 5.6, peut être suivie sur plusieurs dizaines de km du nord au sud. Elle matérialise généralement des zones de transition entre domaines métamorphiques différents. Il est possible que l'abondance de quartz, qui est un minéral rhéologiquement faible, ait permis de localiser la déformation dans cette roche.

On observe une foliation fortement marquée, orientée 135/70. Le disthène et les micas sont orientés préférentiellement le long de lignes de pitch 18°SO.

Arrêt 6.4 (BN491) : Paragneiss intrudé par un granite.

South of Bole, N 8.9275 E -2.5326

On trouve à l'affleurement un paragneiss intrudé par un granite à biotite. Le paragneiss est fortement déformé, et la foliation métamorphique est orientée 90/80. Elle porte une linéation d'étirement minérale de pitch 85°N. Le grenat est dans la foliation, il est anté- ou syn-cinématique. Des grains de staurotide automorphe recoupent la foliation et poussent par dessus le grenat. Ils sont post-cinématiques. Le granite à biotite intrusif est faiblement déformé, ne présentant qu'une légère orientation minérale, possiblement d'origine magmatique.

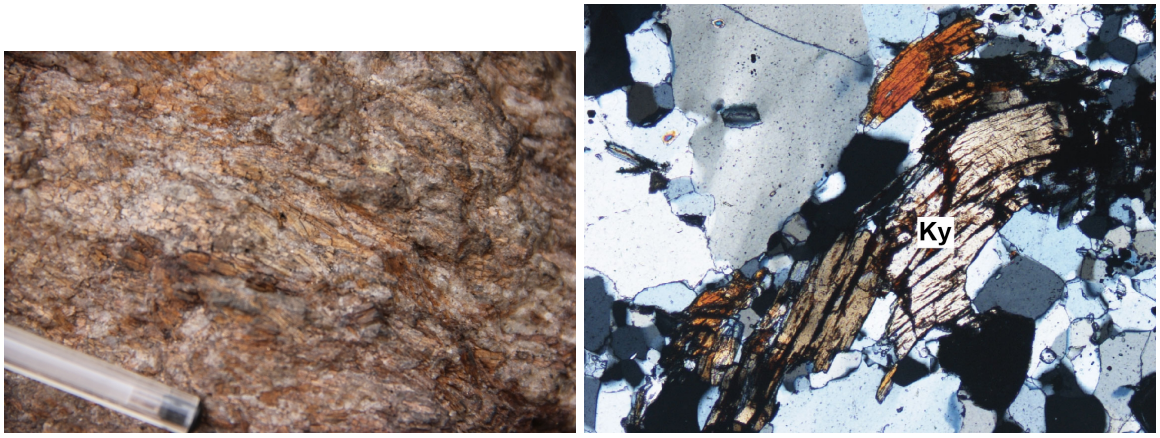

(a) Grains de disthène (brun) allongés dans une quartzite.

(b) Photo de lame mince de la quartzite à disthène. Les grains de disthène sont plissés.

FIGURE 46 – Arrêt 6.3 (BN488)

(a) Staurotide automorphe recoupant la foliation et croissant sur le grenat, qui se retrouve en inclusion.

(b) Leucogranite intrusif dans les paragneiss sombres.

FIGURE 47 – Arrêt 6.4 (BN491)

Le paragneiss a subi un métamorphisme dans le faciès amphibolite. Il pourrait être issu d'un niveau crustal plus superficiel que les roches migmatitiques vues par ailleurs, qui représentent la partie profonde de la croûte orogènique. En effet, le paragneiss se situe au niveau de la croûte dans lequel les granites se mettent en place, alors que les migmatites sont la source du magma.

L'étude métamorphique et les pseudosections P-T confirment cette hypothèse. L'échantillon a suivi un chemin P-T horaire et a atteint des conditions de pic de métamorphisme d'environ de 7 kbar, 600°C. Il s'agit de conditions plus basses que celles enregistrées par les migmatites voisines, comme illustré dans la figure 48.

Arrêt 6.5 (BN721) : Granodiorite mylonitique à hornblende, dans une zone de contact.

Au sud de Bolé, N 8.9075 E -2.5246

Cet affleurement se situe à la limite entre les roches de faciès amphibolite à l'ouest, et un granite déformé à basse température à l'est. Les roches volcano-sédimentaires du bassin de

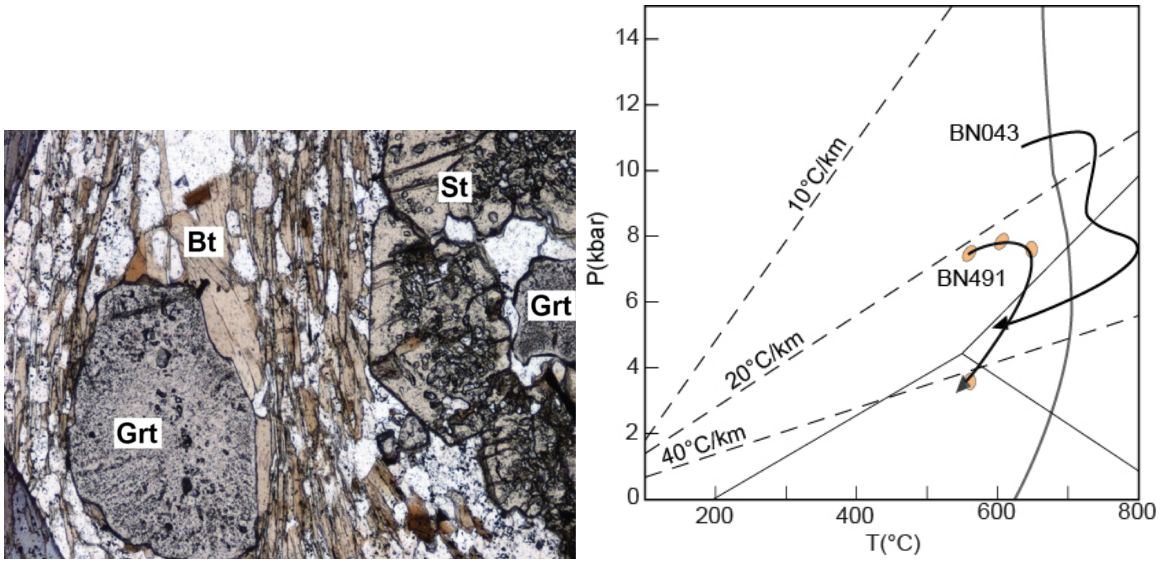

(a) Photographie de lame mince du paragneiss.

(b) Diagramme P-T montrant le chemin P-T suivi par le paragneiss (BN491) et par le gneiss migmatitique situé à quelques km à l'est (BN 043).

FIGURE 48 – Arrêt 6.4 (BN491)

Maluwe se situent à quelques km plus au sud.

La roche à l'affleurement est fortement affectée par un métamorphisme rétrograde, et les minéraux d'origine sont presque entièrement remplacés par des micas. On observe des veines de quartz. Quelques portions de l'affleurement sont préservées du métamorphisme rétrograde, et on y observe une paragenèse à quartz, plagioclase et hornblende. Il s'agit donc d'un granitoïde plutôt basique. Des plages leucocrates contenant des minéraux plus grossiers pourraient représenter des leucosomes antérieurs à l'altération rétrograde. La foliation mylonitique est orientée 100/85, elle porte une linéation d'étirement avec un pitch de 20°S.

(a) Affleurement de roche mylonitique rétromorphosée.

(b) La minéralogie d'origine (de haut degré métamorphique) est préservée localement. Les veines de quartz sécantes sont tardives.

FIGURE 49 – Arrêt 6.5 (BN721)

Selon le temps disponible, il est possible de recouper cette roche mylonitique en plusieurs points dans la région.

Remarques et conclusions pour les jours 5 et 6.

Les roches du domaine de haut grade de Bolé-Bulenga enregistrent des conditions métamorphiques et des chemins P-T variables. Ces différences suggèrent que les roches constitutives de ce domaine ont été métamorphisées dans des contextes légèrement différents, à des profondeurs variables, et peut être le long de gradients géothermiques distincts. Les roches de haut degré métamorphique ont été exhumées et mises en contact avec des roches de bas degré métamorphique. Les contacts entre ces roches sont matérialisés par des zones fortement déformées, parfois mylonitiques. Le métamorphisme rétrograde est intense dans ces zones de transition, et les assemblages du pic de métamorphisme sont parfois totalement détruits. Ces résultats on plusieurs implications :

1. Les zones de contact mylonitiques ont dû localiser la déformation au cours de l'évolution tectonique puisqu'elles ont mis en contact les différents domaines tectono-métamorphiques.
2. Le métamorphisme rétrograde est catalysé par la déformation, et donc en particulier dans les zones de cisaillement tardives.

En lame mince, le métamorphisme rétrograde est identifiable par les textures illustrant un remplacement des minéraux de haut degré métamorphique (grenat, disthène, etc.), par des minéraux de faible degré métamorphique (chlorite, épidote, mica blanc, etc.). Les photos suivantes présentent quelques exemples.

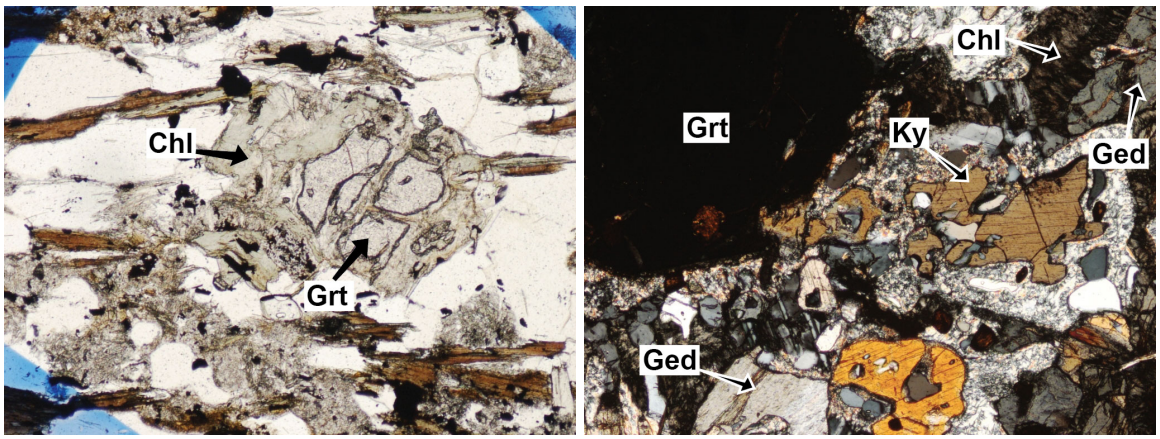

(a) Grenat (Grt) partiellement remplacé par la chlorite (Chl) dans un paragneiss.

(b) Disthène (Ky) et gèdrite (ortho-amphibole, Ged) corrodés et remplacés par le mica blanc et la chlorite dans une métabasite.

FIGURE 50 – Textures liées au métamorphisme rétrograde.

Jour 7 : Bassin de Maluwe et domaine d'Abulembire.

Cette journée permet d'apprécier la distribution des faciès métamorphiques à l'échelle régionale. Une coupe N-S est effectuée à travers le bassin de Maluwe et le domaine d'Abulembire. Le premier est un domaine métamorphisé dans la partie superficielle de l'orogenèse Eburnéenne, le second correspond à la croûte plus profonde. Ce schéma métamorphique régional a des implications en terme de mécanismes d'exhumation et d'évolution géodynamique du craton pendant l'orogenèse Eburnéenne.

Arrêt 7.1 (BN245) : Sédiments siliceux (cherts) manganésifères sur la marge du bassin de Maluwe.

Route de Bolé à Kaledo, N 8.9238 E -2.3665

L'affleurement se situe à quelques km de la zone de contact entre le bassin de Maluwe et le domaine de Bolé-Bulenga. Des sédiments siliceux manganésifères se trouvent fréquemment à cet interface. Il s'agit de sédiments sombres, stratifiés, contenant essentiellement du quartz, ainsi que des minéraux à Mn. La stratification a une orientation générale 300/80 et est plissée.

*Arrêt 7.2 (BN235) : Granitoïde métamorphisé, intrusif dans le bassin de Maluwe.

Route entre Bolé et Maluwe, N 8.8597 E -2.3393

Les roches volcaniques et sédimentaires du bassin de Maluwe sont intrudées par des granitoïdes généralement faiblement déformés. Ce n'est qu'au voisinage de zones de cisaillement que la déformation est intense. Des plutons de granitoides sont étirés le long de telles structures. Ils sont métamorphisés dans les conditions du faciès schiste vert.

On observe à l'affleurement un granitoïde étiré selon une direction NE-SO. La roche a une couleur verte provenant du remplacement de minéraux ferro-magnésiens abondants par des minéraux caractéristiques du faciès schiste vert (chlorite, amphibole verte). Elle contient une schistosité marquée orientée approximativement 130/40. Le granitoïde a un âge de cristallisation de 2118 ± 5 Ma, contraignant l'âge maximal de la déformation.

(a) Arrêt 7.1 (BN245). Horizons sédimentaires plissés dans un échantillon de sédiment manganésifère.

(b) Arrêt 7.2 (BN235). Veine de quartz et grains de pyrite dans un granitoïde intrusif dans le bassin de Maluwe.

FIGURE 51 –

Arrêt 7.3 (BN602) : Complexe basique intrusif, Mt Wakawka, bassin de Maluwe.

Route entre Bolé et Maluwe, N 8.7700 E -2.3222

Le bassin de Maluwe contient quelques complexes basiques intrusifs de forme elliptique, atteignant 5 à 10 km de long. Ils sont essentiellement constitués de gabbronorites et de pyroxenites mineures (voir paragraphe 8.3). Les contacts lithologiques dans ces complexes sont de nature magmatique. On observe une foliation magmatique sur-imprimée par une schistosité. Celle-ci, définie par l'alignement des minéraux et des enclaves, est orientée approximativement 300/80. Dans les pyroxènites, on observe des couronnes de plagioclase autour de phénocristaux de pyroxène. Il pourrait s'agir d'une texture liée à la fusion partielle de la roche.

(a) Contact magmatique entre une gabbronorite sombre, parfois pegmatitique, avec une roche plus leucocrate et riche en plagioclase (gabbro anorthosique ?). On distingue une orientation préférentielle des minéraux dans la roche leucocrate.

(b) Couronne de plagioclase autour d'un grain de pyroxène, qui pourrait indiquer une réaction de fusion partielle.

FIGURE 52 – Arrêt 7.3 (BN602)

Arrêt 7.4 (BN238) : Laves intermédiaires métamorphisées dans le faciès schiste vert.

Route entre Bolé et Maluwe, N 8.7700 E -2.3222

L'affleurement est constitué de roches volcaniques intermédiaires et de schistes dérivés de roches volcano-sédimentaires. Des clastes et des bombes volcaniques sont identifiables dans les roches volcaniques, et les sédiments présentent une stratification. Celle-ci est transposée parallèlement à une schistosité orientée 90/60. La schistosité correspond à la surface axiale de plis serrés, et porte une linéation dont le pitch est 20°S.

En lame mince, les roches volcano-sédimentaires contiennent une paragenèse qui comporte le quartz, la chlorite, le mica blanc et l'épidote, caractéristiques du faciès schiste vert. On y trouve également des grains de pyrite automorphe.

Arrêt 7.5 (BN938) : Métasédiments de haut degré métamorphique, domaine d'Abulembire.

Au sud de Tinga, N 8.5551 E -2.2271

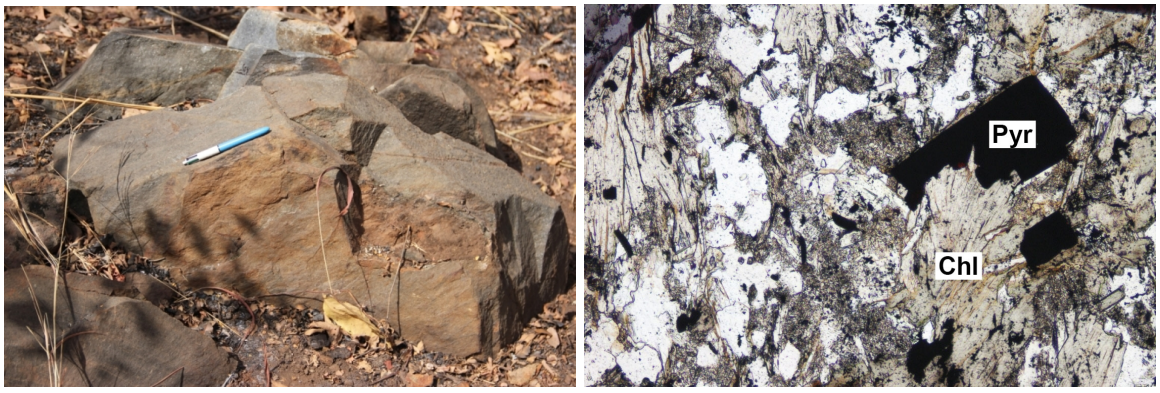

(a) Laves de faible degré métamorphique (faciès schiste vert).

(b) La lave contient de la chlorite et du mica blanc orientés parallèlement à la schistosité, qui alternent avec des lits riches en quartz et épidote. La pyrite recoupe la schistosité.

FIGURE 53 – Arrêt 7.4 (BN238)

Nous avons traversé le bassin de Maluwe du nord au sud pour atteindre le domaine d'Abulembire. Celui-ci contient en son cœur un orthogneiss daté à 2187±5 Ma. En périphérie de l'orthogneiss se trouvent des paragneiss, parfois migmatitiques, similaires aux paragneiss du domaine de Bolé-Bulenga. Les conditions métamorphiques diminuent sous le solidus, dans le faciès amphibolite, vers le sud du domaine d'Abulembire. La transition avec le bassin de Maluwe est abrupte sur le flanc nord du domaine d'Abulembire, mais elle est plus progressive à l'ouest et au sud-ouest.

Dans la partie sud du domaine d'Abulembire, les structures liées au raccourcissement est-ouest (D3) s'atténuent fortement. La déformation manifeste dans la ceinture de Wa-Lawra et le domaine de Bolé-Bulenga n'a pas affecté cet ensemble. Les structures observées, généralement orientées ONO-ESE, sont attribuées à D1.

Cet affleurement est constitué de paragneiss à grenat et disthène, caractéristiques d'un métamorphisme en faciès amphibolite. On trouve parfois du staurotide qui croît par dessus la foliation. Un litage sédimentaire se démarque et est orienté 240/75. Il est recoupé par une schistosité orientée 216/55 qui porte une linéation d'étirement sub-horizontale.

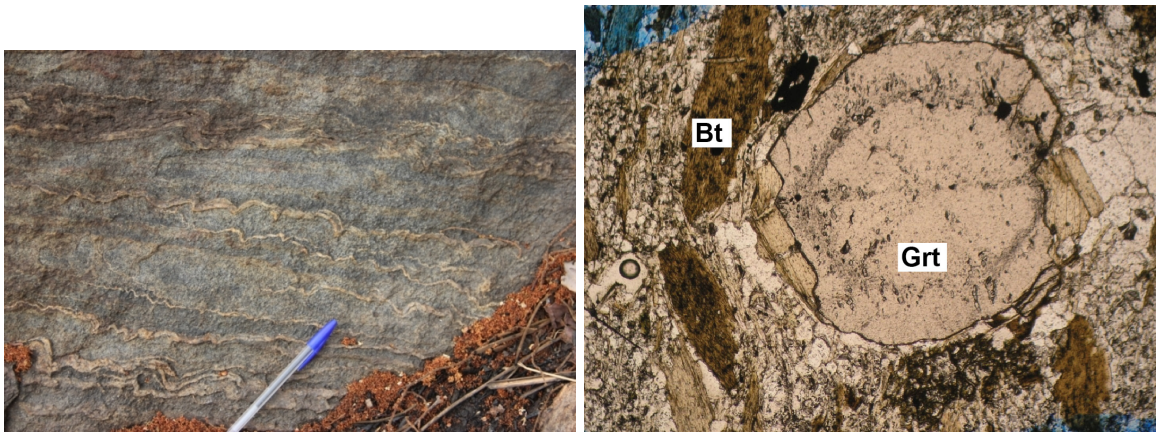

(a) Strates plissées et recoupées par une schistosité dans des paragneiss du domaine d'Abulembire.

(b) Porphyroblaste de grenat contenant une cerne d'inclusions, qui illustre la croissance en deux étapes du minéral.

FIGURE 54 – Arrêt 7.5 (BN938)

***Arrêt 7.6 (BN261) : Orthogneiss, coeur du domaine d'Abulembire.**

Au nord-est de Tinga, N 8.6428 E -2.1952

Cet orthogneiss a un aspect similaire à ceux observés dans le domaine de Bolé-Bulenga, et est daté à 2187 ± 5 Ma. Il constitue la croûte ancienne de la zone d'étude. La foliation gneissique est orientée 290/70 et porte une linéation d'étirement de pitch 22 NO.

Arrêt 7.7 (BN262) : Pyroxenite intrudée par un orthogneiss.

Au nord-est de Tinga, N 8.6428 E -2.1952

L'orthogneiss constituant le cœur du domaine d'Abulembire est intrusif dans une pyroxénite. Celle-ci contient des agrégats caractéristiques de pyroxènes centimétriques dans une matrice sombre. Des couronnes de plagioclase autour des pyroxènes pourraient être liées à la fusion de la roche. L'orthogneiss intrusif dans la pyroxénite, daté à 2187 ± 5 Ma, est parmi les plus vieux dans la région. La pyroxènite représenterait donc une roche relativement primitive.

(a) Stop 7.6 (BN261). Orthogneiss tonalitique constituant le matériel crustal ancien dans la zone d'étude.

(b) Pyroxénite à grain grossier intrudée par l'orthogneiss.

FIGURE 55 –

8 Annexes

8.1 Faciès métamorphiques et synthèse régionale.

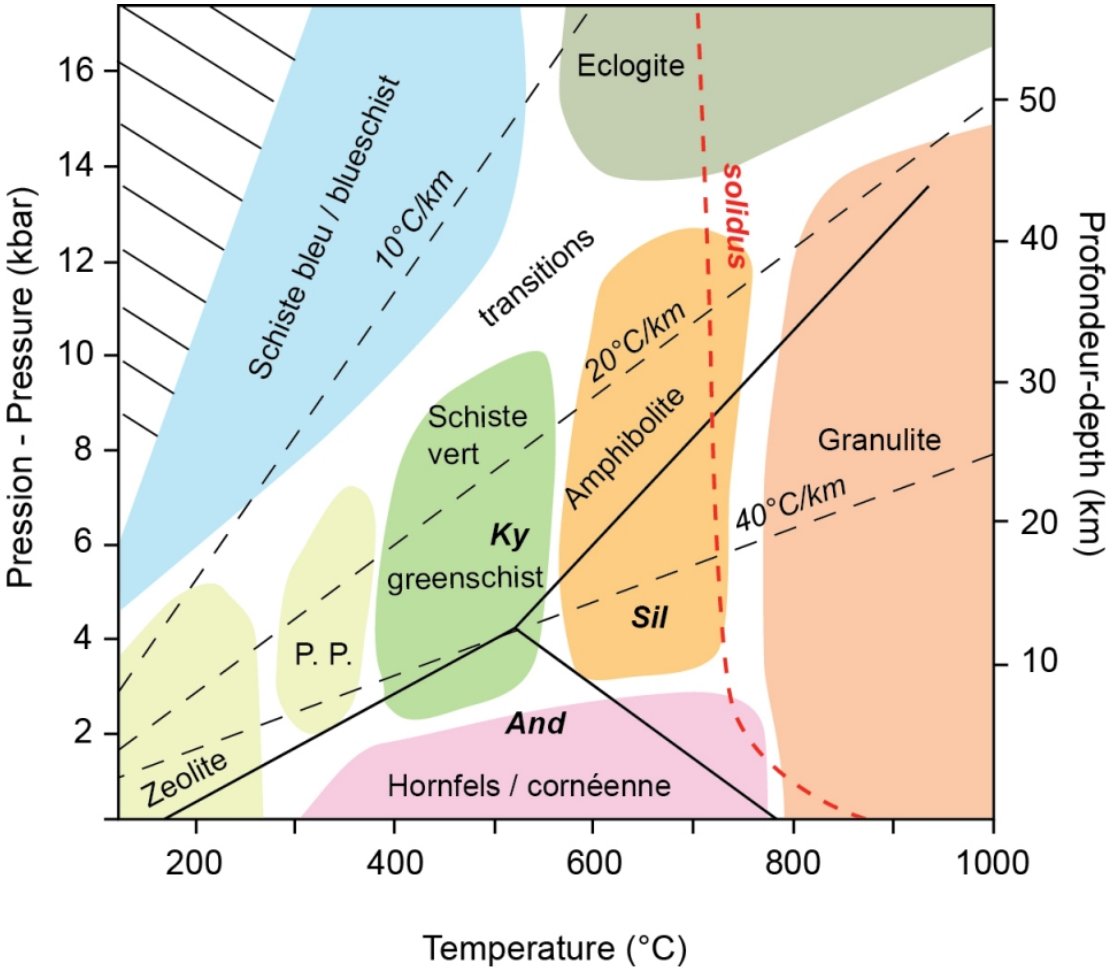

FIGURE 56 – Diagramme P-T présentant la position des faciès métamorphiques dans le champ P-T et des gradients géothermiques.

8.2 Diagramme de Strekeisen

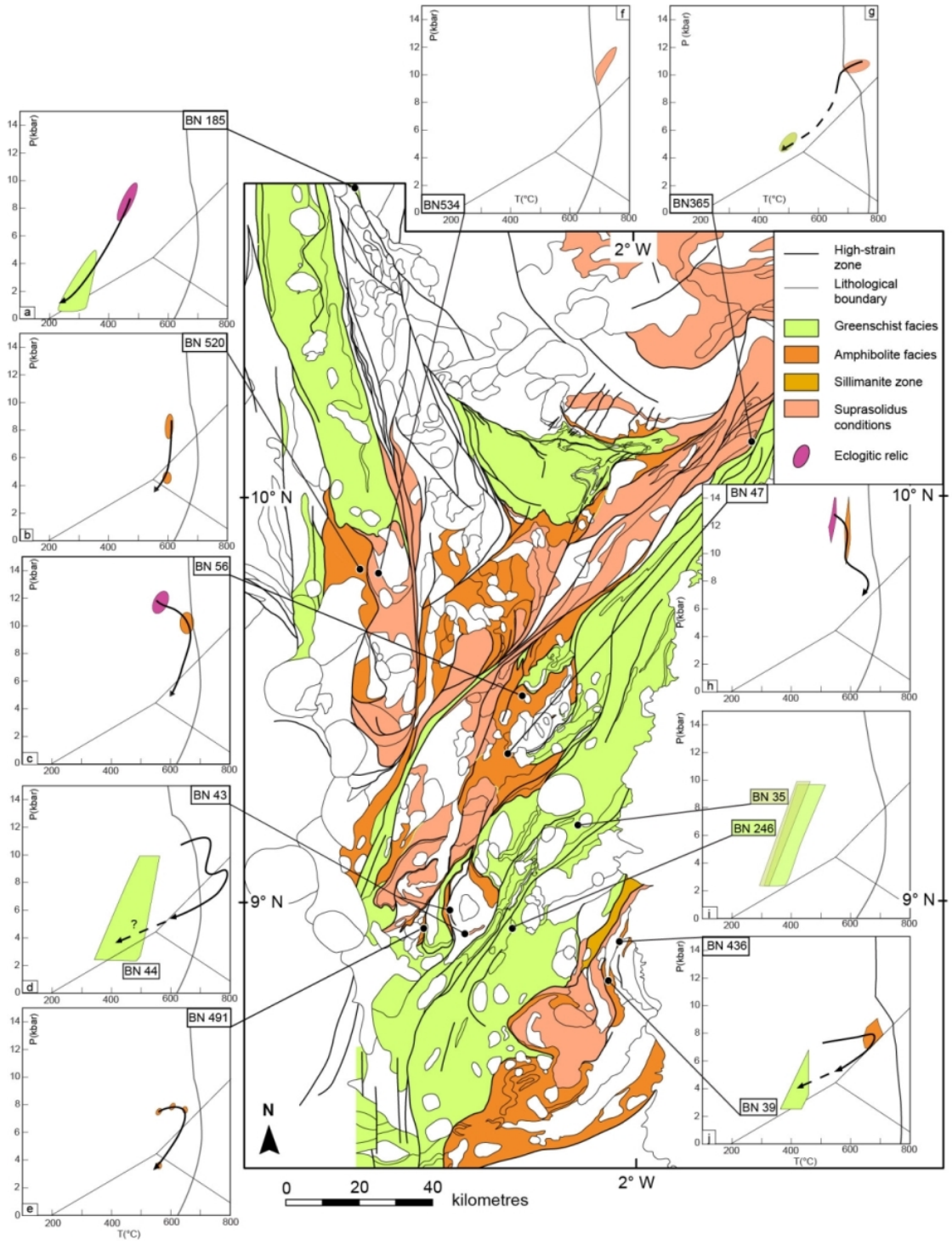

FIGURE 57 – Synthèse métamorphique régionale : position des échantillons utilisés pour reconstituer des chemins P-T dans la zone d'étude, projetés sur la carte métamorphique régionale.

8.3 Roches basiques

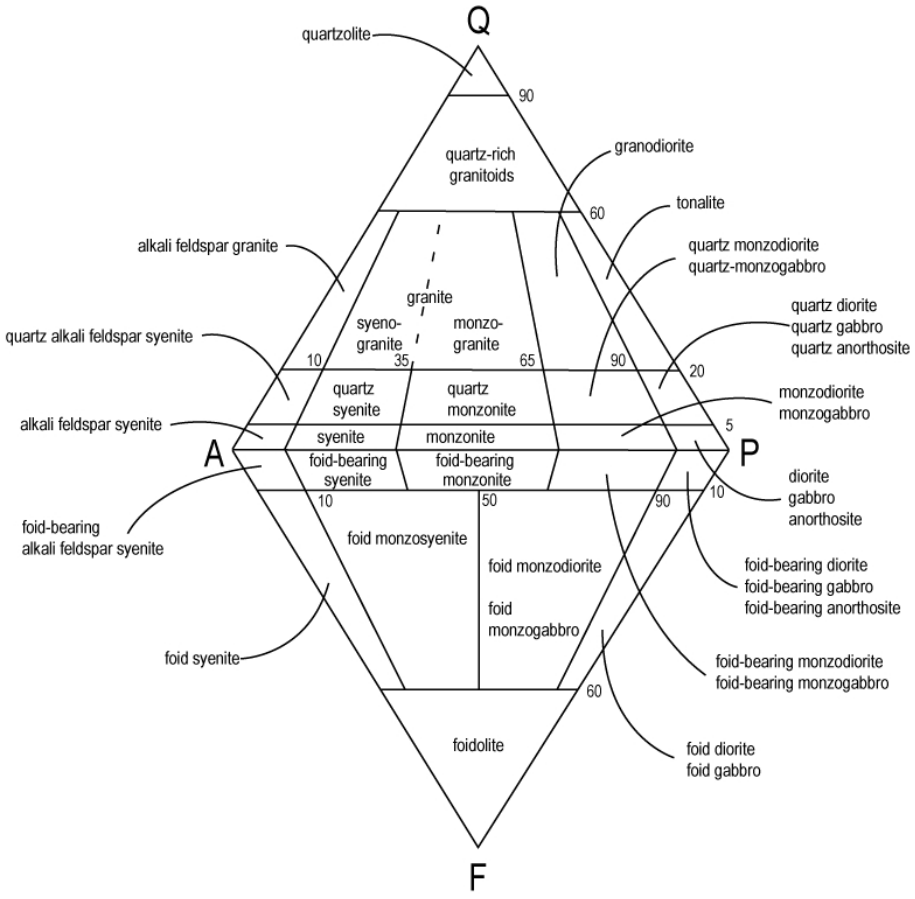

FIGURE 58 – Diagramme de Strekeisen pour les roches plutoniques

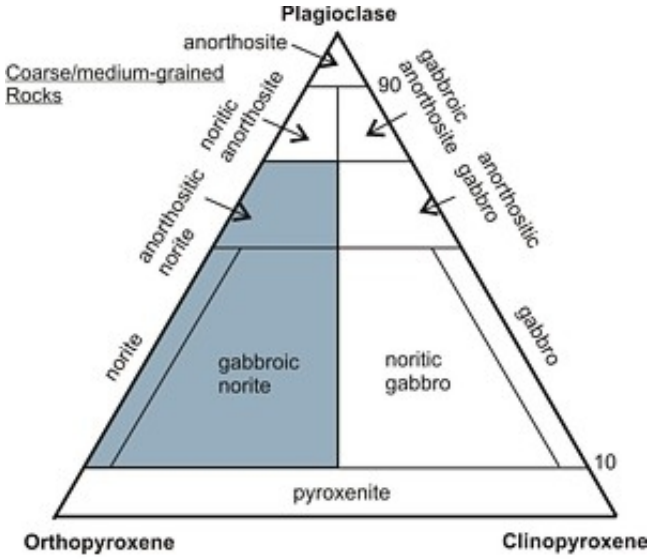

FIGURE 59 – Classification des roches basiques plutoniques.

Références

[1] Baratoux, L., Metelka, V., Naba, S., Jessell, W.M., Gregoire, M., Ganne, J., 2011. *Juvenile paleoproterozoic crust evolution during the Eburnean orogeny (2.2-2.0 Ga), western Burkina Faso.* Precambrian Research, 191, 18–45 .

[2] De Kock, G.S. Theveniaut, H., Botha, P.W., Gyapong, W., 2012. *Timing the structural events in the Palaeoproterozoic Bolé–Nangodi belt terrane and adjacent Maluwe basin, West African craton, in central-west Ghana.* Journal of African Earth Sciences, 65, 1–24.

[3] De Kock, G.S., Armstrong, R.A., Siegfried, H.P., Thomas, E., 2011 *Geochronology of the Birim Supergroup of the West African craton in the Wa-Bolé region of central-west Ghana : implications for the stratigraphic framework.* Journal of African Earth Sciences, 59, 1–40.

[4] Melcher, F., 1995. *Genesis of chemical sediments in Birimian greenstone belts : evidence from gondites and related manganese-bearing rocks from northern Ghana.* Mineralogical Magazine, 59, 229-251.

[5] Melcher, F. and Stumpfl, E.F., 1994. *Palaeoproterozoic Exhalite Formation in Northern Ghana ; Source of Epigenetic Gold-Quartz Vein Mineralization ?* Geologisches Jahrbuch, 100, 201-246.

[6] Metelka, V., Baratoux, L., Naba, S., Jessell, W.M., 2011. *A geophysically constrained litho-structural analysis of the Eburnean greenstone belts and associated granitoid domains, western Burkina Faso.* Precambrian Research, 190, 48–69.

[7] Milési, J.P., Feybesse, J.L., Pinna, P., Deschamps, Y., Kampunzu, H., Muhongo, S., Lescuyer, J.L., Le Goff, E., Delor, C., Billa, M., Ralay, F., Heinry, C., 2004. *Geological map of Africa 1 :10,000,000, SIGAfrique project.* In : 20th Conference of African Geology, BRGM, Orleans, France, 2–7 June, http ://www.sigafrique.net.

[8] Naba, S., Lompo, M., Debat, P., Bouchez, J.L., Beziat, D., 2004. *Structure and emplacement model for late-orogenic Paleoproterozoic granitoids : the Tenkodogo-Yamba elongated pluton (Eastern Burkina Faso).* Journal of African Earth Sciences, 38, 41–57.

[9] Ridolfi, F. and Renzulli, A. 2012. *Calcic amphiboles in calc-alkaline and alkaline magmas : thermobarometric and chemometric empirical equations valid up to 1,130°C and 2.2 GPa.* Contributions to Mineralogy and Petrology, 163 :877–895.

[10] Thomas, E., De Kock, G.S., Baglow, N., Viljoen, J., Siaka, Z., 2009. *Geological map explanation—map sheet 0903D (1 :100,000).* CGS/BRGM/Geoman. Geological Survey Department of Ghana (GSD).

Bibliographie

Abati, J., Aghzer, A. M., Gerdes, A., and Ennih, N. (2010). Detrital zircon ages of neoproterozoic sequences of the moroccan anti-atlas belt. *Precambrian Research*, 181(1) :115–128. (Cité pp. 73.)

Abbott, D., Burgess, L., Longhi, J., and Smith, W. H. (1994). An empirical thermal history of the earth's upper mantle. *Journal of Geophysical Research : Solid Earth (1978–2012)*, 99(B7) :13835–13850. (Cité pp. 18.)

Abbott, D. and Menke, W. (1990). Length of the global plate boundary at 2.4 ga. *Geology*, 18(1) :58–61. (Cité pp. 19.)

Abbott, D. and Mooney, W. (1995). The structural and geochemical evolution of the continental crust : support for the oceanic plateau model of continental growth. *Reviews of Geophysics*, 33(S1) :231–242. (Cité pp. 28.)

Abbott, D. H., Drury, R., and Mooney, W. D. (1997). Continents as lithological icebergs : the importance of buoyant lithospheric roots. *Earth and Planetary Science Letters*, 149(1) :15–27. (Cité pp. 28.)

Abdelsalam, M. G., Liégeois, J.-P., and Stern, R. J. (2002). The saharan metacraton. *Journal of African Earth Sciences*, 34(3) :119–136. (Cité pp. 225.)

Abouchami, W., Boher, M., Michard, A., and Albarede, F. (1990). A major 2.1 ga event of mafic magmatism in west africa : an early stage of crustal accretion. *Journal of Geophysical Research : Solid Earth (1978–2012)*, 95(B11) :17605–17629. (Cité pp. 28, 58, 68, 73, 79, 86, 87, 133, 134, 223, 224 et 262.)

Affaton, P., Sougy, J., Trompette, R., et al. (1980). The tectono-stratigraphic relationships between the upper precambrian and lower paleozoic volta basin and the pan-african dahomeyide orogenic belt (west africa). *American Journal of Science*, 280(3) :224–248. (Cité pp. 97 et 137.)

Airy, G. B. (1855). On the computation of the effect of the attraction of mountain-masses, as disturbing the apparent astronomical latitude of stations in geodetic surveys. *Philosophical Transactions of the Royal Society of London*, pages 101–104. (Cité pp. 14.)

Albarède, F. (1998). The growth of continental crust. *Tectonophysics*, 296(1) :1–14. (Cité pp. 28, 39, 86 et 272.)

Allègre, C. J. and Rousseau, D. (1984). The growth of the continent through geological time studied by nd isotope analysis of shales. *Earth and Planetary Science Letters*, 67(1) :19–34. (Cité pp. 25.)

Allibone, A., McCuaig, T., Harris, D., Etheridge, M., Munroe, S., Byrne, D., Amanor, J., and Gyapong, W. (2002). Structural controls on gold mineralization at the ashanti deposit, obuasi, ghana. *Special Publication-Society of Economic Geologists*, 9 :65–94. (Cité pp. 88 et 133.)

Almeida, F. F. M. d., Brito Neves, B. B. d., and Dal Ré Carneiro, C. (2000). The origin and evolution of the south american platform. *Earth-Science Reviews*, 50(1) :77–111. (Cité pp. 70.)

Almeida, J. d. A. C., Dall'Agnol, R., Dias, S. B., and Althoff, F. J. (2010). Origin of the archean leucogranodiorite–granite suites : evidence from the rio maria terrane and implications for granite magmatism in the archean. *Lithos*, 120(3) :235–257. (Cité pp. 37.)

Ama Salah, I., Liegeois, J.-P., and Pouclet, A. (1996). Evolution d'un arc insulaire océanique birimien précoce au liptako nigérien (sirba) : géologie, géochronologie et géochimie. *Journal of African Earth Sciences*, 22(3) :235–254. (Cité pp. 79.)

Amelin, Y., Lee, D.-C., and Halliday, A. (2000). Early-middle archaean crustal evolution deduced from lu-hf and u-pb isotopic studies of single zircon grains. *Geochimica et Cosmochimica Acta*, 64(24) :4205–4225. (Cité pp. 222.)

Amelin, Y., Lee, D.-C., Halliday, A. N., and Pidgeon, R. T. (1999). Nature of the earth's earliest crust from hafnium isotopes in single detrital zircons. *Nature*, 399(6733) :252–255. (Cité pp. 222.)

Andersen, T. B. (1998). Extensional tectonics in the caledonides of southern norway, an overview. *Tectonophysics*, 285(3) :333–351. (Cité pp. 54.)

Anderson, J. R., Payne, J. L., Kelsey, D. E., Hand, M., Collins, A. S., and Santosh, M. (2012). High-pressure granulites at the dawn of the proterozoic. *Geology*, 40(5) :431–434. (Cité pp. 177.)

Anhaeusser, C. R. (2014). Archaean greenstone belts and associated granitic rocks–a review. *Journal of African Earth Sciences*. (Cité pp. 30.)

Anhaeusser, C. R., Mason, R., Viljoen, M. J., and Viljoen, R. P. (1969). A reappraisal of some aspects of precambrian shield geology. *Geological Society of America Bulletin*, 80(11) :2175–2200. (Cité pp. 60.)

Arculus, R. (1994). Aspects of magma genesis in arcs. *Lithos*, 33(1) :189–208. (Cité pp. 28 et 261.)

Arndt, N., Lesher, M. C., Barnes, S. J., et al. (2008). Komatiite. (Cité pp. 34.)

Arnould, M. (1961). *Étude géologique des migmatites et des granites précambriens du Nord-Est de la Côte d'Ivoire et de la Haute-Volta méridionale : cadre géologique, classification, principaux types. Marcel Arnould.* Éditions Technip (Clermont-Ferrand, impr. G. de Bussace). (Cité pp. 76, 77, 88, 134 et 135.)

Artemieva, I. M. and Mooney, W. D. (2001). Thermal thickness and evolution of precambrian lithosphere : A global study. *Journal of Geophysical Research : Solid Earth (1978–2012)*, 106(B8) :16387–16414. (Cité pp. 64.)

Arzi, A. A. (1978). Critical phenomena in the rheology of partially melted rocks. *Tectonophysics*, 44(1) :173–184. (Cité pp. 56, 114 et 156.)

Atherton, M. P. and Petford, N. (1993). Generation of sodium-rich magmas from newly underplated basaltic crust. (Cité pp. 34, 39 et 272.)

Attoh, K. and Ekwueme, B. (1997). The west african shield. *Oxford Monographs on Geology and Geophysics*, 35 :517–528. (Cité pp. 73 et 79.)

Attoh, K., Evans, M. J., and Bickford, M. (2006). Geochemistry of an ultramafic-rodingite rock association in the paleoproterozoic dixcove greenstone belt, southwestern ghana. *Journal of African Earth Sciences*, 45(3) :333–346. (Cité pp. 79, 134 et 224.)

Auvray, B., Peucat, J.-J., Potrel, A., Burg, J.-P., Caruba, C., Dars, R., and Lo, K. (1992). Données géochronologiques nouvelles sur l'archéen de l'amsaga (dorsale réguibat, mauritanie). *Comptes rendus de l'Académie des sciences. Série 2, Mécanique, Physique, Chimie, Sciences de l'univers, Sciences de la Terre*, 315(1) :63–70. (Cité pp. 72 et 223.)

Auzanneau, E., Schmidt, M., Vielzeuf, D., and Connolly, J. D. (2010). Titanium in phengite : a geobarometer for high temperature eclogites. *Contributions to Mineralogy and Petrology*, 159(1) :1–24. (Cité pp. 178.)

Ballevre, M., Lagabrielle, Y., and Merle, O. (1990). Tertiary ductile normal faulting as a consequence of lithospheric stacking in the western alps. *Mémoires de la Société géologique de France*, 156 :227–236. (Cité pp. 54.)

Ballevre, M., Pitra, P., and Bohn, M. (2003). Lawsonite growth in the epidote blueschists from the ile de groix (armorican massif, france) : a potential geobarometer. *Journal of metamorphic Geology*, 21(7) :723–735. (Cité pp. 59.)

Baratoux, L., Metelka, V., Naba, S., Jessell, M. W., Grégoire, M., and Ganne, J. (2011). Juvenile paleoproterozoic crust evolution during the eburnean orogeny (2.2–2.0 ga), western burkina faso. *Precambrian Research*, 191(1) :18–45. (Cité pp. 73, 74, 76, 79, 88, 89, 92, 93, 119, 133, 135, 137, 223, 224, 226 et 229.)

Barbarin, B. (1999). A review of the relationships between granitoid types, their origins and their geodynamic environments. *Lithos*, 46(3) :605–626. (Cité pp. 37.)

Barbey, P. (1975). The adam talha epizonal sequence (north mauritania) and a general scheme for the eburnean orogenic belt of west africa. *Precambrian Research*, 2(3) :255–262. (Cité pp. 76.)

Bard, J.-P. and Lemoine, S. (1976). Phases tectoniques superposées dans les métasédiments précambriens du domaine côtier occidental de la côte d'ivoire. *Precambrian Research*, 3(3) :209–229. (Cité pp. 76 et 135.)

Barrell, J. (1915). The strength of the earth's crust. *The Journal of Geology*, pages 27–44. (Cité pp. 14.)

Barrere, J. (1967). *Le Groupe précambrien de l'Amsaga entre Atar et Akjoujt : Mauritanie, étude d'un métamorphisme profond et de ses relations avec la migmatisation. Jean Barrère*. Éditions BRGM. (Cité pp. 72.)

Barrow, G. (1893). On an intrusion of muscovite-biotite gneiss in the south-eastern highlands of scotland, and its accompanying metamorphism. *Quarterly Journal of the Geological Society*, 49(1-4) :330–358. (Cité pp. 55.)

Beard, J. S. and Lofgren, G. E. (1991). Dehydration melting and water-saturated melting of basaltic and andesitic greenstones and amphibolites at 1, 3, and 6. 9 kb. *Journal of Petrology*, 32(2) :365–401. (Cité pp. 260.)

Beaumont, C., Jamieson, R., and Nguyen, M. (2010). Models of large, hot orogens containing a collage of reworked and accreted terranes. *Canadian Journal of Earth Sciences*, 47(4) :485–515. (Cité pp. 63.)

Beaumont, C., Jamieson, R. A., Nguyen, M., and Lee, B. (2001). Himalayan tectonics explained by extrusion of a low-viscosity crustal channel coupled to focused surface denudation. *Nature*, 414(6865) :738–742. (Cité pp. 57.)

Bédard, J. H. (2003). Evidence for regional-scale, pluton-driven, high-grade metamorphism in the archaean minto block, northern superior province, canada. *The Journal of geology*, 111(2) :183–205. (Cité pp. 40 et 61.)

Bédard, J. H. (2006). A catalytic delamination-driven model for coupled genesis of archaean crust and sub-continental lithospheric mantle. *Geochimica et Cosmochimica Acta*, 70(5) :1188–1214. (Cité pp. 39, 86, 272 et 273.)

Bédard, J. H., Brouillette, P., Madore, L., and Berclaz, A. (2003). Archaean cratonization and deformation in the northern superior province, canada : an evaluation of plate tectonic versus vertical tectonic models. *Precambrian Research*, 127(1) :61–87. (Cité pp. 40, 59 et 60.)

Bédard, J. H., Harris, L. B., and Thurston, P. C. (2013). The hunting of the snarc. *Precambrian Research*, 229 :20–48. (Cité pp. 29, 31, 39, 59, 60, 86, 177, 222, 272, 273 et 274.)

Bédard, L. P. (1996). Archean high-mg quartz-monzodiorite suite : A re-evaluation of the parental magma and differentiation. *The Journal of Geology*, pages 713–728. (Cité pp. 261.)

Belousova, E., Kostitsyn, Y., Griffin, W., Begg, G., O'reilly, S., and Pearson, N. (2010). The growth of the continental crust : constraints from zircon hf-isotope data. *Lithos*, 119(3) :457–466. (Cité pp. 26 et 27.)

Ben-Avraham, Z., Nur, A., Jones, D., and Cox, A. (1981). Continental accretion : from oceanic plateaus to allochthonous terranes. *Science*, 213(4503) :47–54. (Cité pp. 28.)

Bendaoud, A., Ouzegane, K., Godard, G., Liégeois, J.-P., Kienast, J.-R., Bruguier, O., and Drareni, A. (2008). Geochronology and metamorphic ptx evolution of the eburnean granulite-facies metapelites of tidjenouine (central hoggar, algeria) : witness of the latea metacratonic evolution. *Geological Society, London, Special Publications*, 297(1) :111–146. (Cité pp. 75 et 224.)

Benn, K. and Moyen, J.-F. (2008). The late archean abitibi-opatica terrane, superior province : a modified oceanic plateau. *Geological Society of America Special Papers*, 440 :173–197. (Cité pp. 272.)

Berger, J., Féménias, O., Ohnenstetter, D., Bruguier, O., Plissart, G., Mercier, J.-C. C., and Demaiffe, D. (2010). New occurrence of uhp eclogites in limousin (french massif central) : age, tectonic setting and fluid–rock interactions. *Lithos*, 118(3) :365–382. (Cité pp. 59.)

Berman, R. G. (1991). Thermobarometry using multi-equilibrium calculations : a new technique, with petrological applications. *Canadian Mineralogist*, 29(4) :833–855. (Cité pp. 154.)

Bertrand, J. and Caby, R. (1978). Geodynamic evolution of the pan-african orogenic belt : a new interpretation of the hoggar shield (algerian sahara). *Geologische Rundschau*, 67(2) :357–388. (Cité pp. 75.)

Bertrand, J. M. and Jardim de Sá, E. F. (1990). Where are the eburnian-transamazonian collisional belts ? *Canadian Journal of Earth Sciences*, 27(10) :1382–1393. (Cité pp. 75.)

Bertrand, M. A. (1892). *Sur la déformation de l'écorce terrestre*. Gauthier-Villars. (Cité pp. 14.)

Bessoles, B. (1977). *Géologie de l'Afrique : le craton Ouest African*. Ed. du BRGM. (Cité pp. 71, 72, 73, 76, 77, 88, 223 et 225.)

Béziat, D., Bourges, F., Debat, P., Lompo, M., Martin, F., and Tollon, F. (2000). A paleoproterozoic ultramafic-mafic assemblage and associated volcanic rocks of the boromo greenstone belt : fractionates originating from island-arc volcanic activity in the west african craton. *Precambrian Research*, 101(1) :25–47. (Cité pp. 79.)

Béziat, D., Dubois, M., Debat, P., Nikiéma, S., Salvi, S., and Tollon, F. (2008). Gold metallogeny in the birimian craton of burkina faso (west africa). *Journal of African Earth Sciences*, 50(2) :215–233. (Cité pp. 75.)

Bickle, M., Nisbet, E., and Martin, A. (1994). Archean greenstone belts are not oceanic crust. *The Journal of Geology*, pages 121–137. (Cité pp. 31.)

Billa, M., Feybesse, J.-L., Bronner, G., Lerouge, C., Milési, J.-P., Traoré, S., and Diaby, S. (1999). Les formations à quartzites rubanés ferrugineux des monts nimba et du simandou : des unités empilées tectoniquement, sur un «soubassementplutonique archéen (craton de kénéma-man), lors de l'orogène éburnéen. *Comptes Rendus de l'Académie des Sciences-Series IIA-Earth and Planetary Science*, 329(4) :287–294. (Cité pp. 78 et 89.)

Bleeker, W. (2003). The late archean record : a puzzle in ca. 35 pieces. *Lithos*, 71(2) :99–134. (Cité pp. 25 et 69.)

Blichert-Toft, J. and Puchtel, I. S. (2010). Depleted mantle sources through time : evidence from lu–hf and sm–nd isotope systematics of archean komatiites. *Earth and Planetary Science Letters*, 297(3) :598–606. (Cité pp. 254, 263, 264 et 278.)

Block, S., Baratoux, L., Jessell, M., Ailleres, L., Bruguier, O., bosch, D., Caby, R., Zeh, A., , Ganne, J., and Mensah, E. (Subm). Lower crust exhumation during paleoproterozoic (eburnean) orogeny, nw ghana, west african craton : interplay of coeval contractional deformation and extensional gravitational collapse. *Precambrian Research*. (Cité pp. 226, 227, 229, 236, 273 et 274.)

Block, S., Ganne, J., Baratoux, L., Zeh, A., Parra, L. A., Jessell, M., Ailleres, L., and Siebenaller, L. (2015). Petrological and geochronological constraints on lower crust exhumation during paleoproterozoic (eburnean) orogeny, nw ghana, west african craton. *Journal of Metamorphic Geology*. (Cité pp. 88, 102, 103, 105, 113, 115, 116, 224, 227, 229, 236, 273 et 274.)

Block, S., Moyen, J.-F., Zeh, A., Poujol, M., Jaguin, J., and Paquette, J.-L. (2013). The murchison greenstone belt, south africa : accreted slivers with contrasting metamorphic conditions. *Precambrian Research*, 227 :77–98. (Cité pp. 61 et 132.)

Boher, M., Abouchami, W., Michard, A., Albarede, F., and Arndt, N. T. (1992). Crustal growth in west africa at 2.1 ga. *Journal of Geophysical Research : Solid Earth (1978–2012)*, 97(B1) :345–369. (Cité pp. 73, 77, 79, 87, 133, 134, 135, 223, 224 et 262.)

Bohlen, S. R. and Liotta, J. J. (1986). A barometer for garnet amphibolites and garnet granulites. *Journal of Petrology*, 27(5) :1025–1034. (Cité pp. 145.)

Bonhomme, M. (1962). *Contribution à l'étude géochronologique de la plate-forme de l'Quest africain*. PhD thesis. (Cité pp. 74, 88, 133 et 224.)

Bonin, B. (2004). Do coeval mafic and felsic magmas in post-collisional to within-plate regimes necessarily imply two contrasting, mantle and crustal, sources ? a review. *Lithos*, 78(1) :1–24. (Cité pp. 37.)

Bosch, D., Garrido, C. J., Bruguier, O., Dhuime, B., Bodinier, J.-L., Padròn-Navarta, J. A., and Galland, B. (2011). Building an island-arc crustal section : Time constraints from a la-icp-ms zircon study. *Earth and Planetary Science Letters*, 309(3) :268–279. (Cité pp. 120 et 277.)

Bosse, V., Ballèvre, M., Féraud, G., and Peucat, J. (2000). Petrological and geochronological constraints in the ile de groix blueschists (armorican massif, france). *Variscan–Appalachian Dynamics : the Building of the Upper Palaeozoic Basement. Basement Tectonics, Coruña, Spain, Program and Abstracts*, 15 :63–66. (Cité pp. 59.)

Bossière, G., Bonkoungou, I., Peucat, J.-J., and Pupin, J.-P. (1996). Origin and age of paleoproterozoic conglomerates and sandstones of the tarkwaian group in burkina faso, west africa. *Precambrian Research*, 80(3) :153–172. (Cité pp. 73.)

Bouguer, P. (1749). *La figure de la terre, determinee par les observations de messieurs Bouguer, & de La Condamine, de l'Academie Royale des Sciences, envoyes par ordre du roy au Perou, pour observer aux environs de l'equateur. Avec une relation abregee de ce voyage, qui contient la description du pays dans lequel les operations ont ete faites. Par M. Bouguer*. quai des Augustins, chez

Charles-Antoine Jombert, libraire du Roy pour l'Artillerie & le Génie, à l'Image Notre-Dame. (Cité pp. 14.)

Bouhallier, H., Chardon, D., and Choukroune, P. (1995). Strain patterns in archaean dome-and-basin structures : The dharwar craton (karnataka, south india). *Earth and Planetary Science Letters*, 135(1) :57–75. (Cité pp. 60, 62 et 119.)

Bouhallier, H., Choukroune, P., and Ballèvre, M. (1993). Diapirism, bulk homogeneous shortening and transcurrent shearing in the archaean dharwar craton : the holenarsipur area, southern india. *Precambrian Research*, 63(1) :43–58. (Cité pp. 60.)

Bouvier, A., Vervoort, J. D., and Patchett, P. J. (2008). The lu–hf and sm–nd isotopic composition of chur : constraints from unequilibrated chondrites and implications for the bulk composition of terrestrial planets. *Earth and Planetary Science Letters*, 273(1) :48–57. (Cité pp. 254 et 278.)

Bowring, S. A. and Williams, I. S. (1999). Priscoan (4.00–4.03 ga) orthogneisses from northwestern canada. *Contributions to Mineralogy and Petrology*, 134(1) :3–16. (Cité pp. 25.)

Boynton, W. V. (1984). Cosmochemistry of the rare earth elements : meteorite studies. In *Rare earth element geochemistry*. (Cité pp. 238 et 240.)

Bronner, G. (1975). Le précambrien du tiris, région de fort-gouraud. *Notice de la carte géologique de la République Islamique de Mauritanie à*, 1(1000000) :103–108. (Cité pp. 225.)

Brown, M. (2002). Retrograde processes in migmatites and granulites revisited. *Journal of Metamorphic Geology*, 20(1) :25–40. (Cité pp. 141 et 142.)

Brown, M. (2006). Duality of thermal regimes is the distinctive characteristic of plate tectonics since the neoarchean. *Geology*, 34(11) :961–964. (Cité pp. 52.)

Brown, M. (2007). Metamorphic conditions in orogenic belts : a record of secular change. *International Geology Review*, 49(3) :193–234. (Cité pp. 62, 63, 64, 68, 86, 120, 132, 133 et 177.)

Brown, M. (2009). Metamorphic patterns in orogenic systems and the geological record. *Geological Society, London, Special Publications*, 318(1) :37–74. (Cité pp. 86, 87, 120, 132, 133, 177 et 222.)

Brown, M., Averkin, Y. A., McLellan, E. L., and Sawyer, E. W. (1995). Melt segregation in migmatites. *Journal of Geophysical Research : Solid Earth (1978–2012)*, 100(B8) :15655–15679. (Cité pp. 156.)

Brown, M. and Dallmeyer, R. D. (1996). Rapid variscan exhumation and the role of magma in core complex formation : southern brittany metamorphic belt, france. *Journal of Metamorphic Geology*, 14(3) :361–379. (Cité pp. 59.)

Brown, M. and Solar, G. S. (1998a). Granite ascent and emplacement during contractional deformation in convergent orogens. *Journal of Structural Geology*, 20(9) :1365–1393. (Cité pp. 117.)

Brown, M. and Solar, G. S. (1998b). Shear-zone systems and melts : feedback relations and self-organization in orogenic belts. *Journal of Structural Geology*, 20(2) :211–227. (Cité pp. 117.)

Brun, J.-P. and Faccenna, C. (2008). Exhumation of high-pressure rocks driven by slab rollback. *Earth and Planetary Science Letters*, 272(1) :1–7. (Cité pp. 54.)

Bull, A. (1927). Some aspects of the mountain building problem : Presidential address. *Proceedings of the Geologists' Association*, 38(2) :145–156. (Cité pp. 15.)

Burchfiel, B. C., Zhiliang, C., Hodges, K. V., Yuping, L., Royden, L. H., Changrong, D., and Jiene, X. (1992). The south tibetan detachment system, himalayan orogen : Extension contemporaneous with and parallel to shortening in a collisional mountain belt. *Geological Society of America Special Papers*, 269 :1–41. (Cité pp. 114.)

Burov, E., Jolivet, L., Le Pourhiet, L., and Poliakov, A. (2001). A thermomechanical model of exhumation of high pressure (hp) and ultra-high pressure (uhp) metamorphic rocks in alpine-type collision belts. *Tectonophysics*, 342(1) :113–136. (Cité pp. 53 et 54.)

Burov, E., Watts, A., et al. (2006). The long-term strength of continental lithosphere :"jelly sandwich" or "crème brûlée" ? *GSA today*, 16(1) :4. (Cité pp. 44 et 56.)

Burov, E. and Yamato, P. (2008). Continental plate collision, p–t–t–z conditions and unstable vs. stable plate dynamics : Insights from thermo-mechanical modelling. *Lithos*, 103(1) :178–204. (Cité pp. 174.)

Byerlee, J. (1978). Friction of rocks. *Pure and applied Geophysics*, 116(4-5) :615–626. (Cité pp. 42.)

Caby, R., Buscail, F., Dembélé, D., Diakité, S., Sacko, S., and Bal, M. (2008). Neoproterozoic garnet-glaucophanites and eclogites : new insights for subduction metamorphism of the gourma fold and thrust belt (eastern mali). *Geological Society, London, Special Publications*, 297(1) :203–216. (Cité pp. 225.)

Caby, R., Delor, C., and Agoh, O. (2000). Lithologie, structure et métamorphisme des formations birimiennes dans la région d'odienné (côte d'ivoire) : rôle majeur du diapirisme des plutons et des décrochements en bordure du craton de man. *Journal of African Earth Sciences*, 30(2) :351–374. (Cité pp. 75, 78, 88, 89, 135 et 224.)

Cagnard, F., Barbey, P., and Gapais, D. (2011). Transition between "archaean-type" and "modern-type" tectonics : Insights from the finnish lapland granulite belt. *Precambrian Research*, 187(1) :127–142. (Cité pp. 70 et 120.)

Cagnard, F., Durrieu, N., Gapais, D., Brun, J.-P., and Ehlers, C. (2006). Crustal thickening and lateral flow during compression of hot lithospheres, with particular reference to precambrian times. *Terra Nova*, 18(1) :72–78. (Cité pp. 62, 87, 132 et 172.)

Cagnard, F., Gapais, D., and Barbey, P. (2007). Collision tectonics involving juvenile crust : the example of the southern finnish svecofennides. *Precambrian Research*, 154(1) :125–141. (Cité pp. 60, 63, 70 et 132.)

Calvert, A., Sawyer, E., Davis, W., and Ludden, J. (1995). Archaean subduction inferred from seismic images of a mantle suture in the superior province. (Cité pp. 59.)

Calvert, A. J., Cruden, A. R., and Hynes, A. (2004). Seismic evidence for preservation of the archean uchi granite–greenstone belt by crustal-scale extension. *Tectonophysics*, 388(1) :135–143. (Cité pp. 60.)

Camil, J. (1984). Pétrographie, chronologie, des ensembles granulitiques archéens et formations associées de la région de man (côte dâĂŹivoire). implication pour l'histoire géologique du craton ouest-africain. *These dÕEtat, Universite Abidjan.* (Cité pp. 72.)

Carrington, D. and Watt, G. (1995). A geochemical and experimental study of the role of k-feldspar during water-undersaturated melting of metapelites. *Chemical Geology*, 122(1) :59–76. (Cité pp. 141.)

Castaing, C., Billa, M., Milési, J., Thiéblemont, D., Le Metour, J., Egal, E., Donzeau, M., Guerrot, C., Cocherie, A., Chevremont, P., et al. (2003). Notice explicative de la carte géologique et minière du burkina faso à 1/1000 000. *Ministère des Mines, des Carrières et de l'Energie, Ouagadougou.* (Cité pp. 78 et 88.)

Cawood, P. A., Hawkesworth, C., and Dhuime, B. (2013). The continental record and the generation of continental crust. *Geological Society of America Bulletin*, 125(1-2) :14–32. (Cité pp. 26, 68 et 222.)

Cawood, P. A., Kröner, A., Collins, W. J., Kusky, T. M., Mooney, W. D., and Windley, B. F. (2009). Accretionary orogens through earth history. *Geological Society, London, Special Publications*, 318(1) :1–36. (Cité pp. 26, 28, 31, 58, 86, 132, 223 et 274.)

Cawood, P. A., Kroner, A., and Pisarevsky, S. (2006). Precambrian plate tectonics : criteria and evidence. *GSA TODAY*, 16(7) :4. (Cité pp. 58, 86 et 274.)

Champion, D. and Sheraton, J. (1997). Geochemistry and nd isotope systematics of archaean granites of the eastern goldfields, yilgarn craton, australia : implications for crustal growth processes. *Precambrian Research*, 83(1) :109–132. (Cité pp. 222.)

Chardon, D. (1996). *Les déformations continentales archéennes : exemples naturels et modélisation thermomécanique.* PhD thesis, Université Rennes 1. (Cité pp. 72.)

Chardon, D., Choukroune, P., and Jayananda, M. (1998). Sinking of the dharwar basin (south india) : implications for archaean tectonics. *Precambrian Research*, 91(1) :15–39. (Cité pp. 59.)

Chardon, D., Gapais, D., and Cagnard, F. (2009). Flow of ultra-hot orogens : a view from the precambrian, clues for the phanerozoic. *Tectonophysics*, 477(3) :105–118. (Cité pp. 60, 62, 87, 120 et 132.)

Chardon, D. and Jayananda, M. (2008). Three-dimensional field perspective on deformation, flow, and growth of the lower continental crust (dharwar craton, india). *Tectonics*, 27(1). (Cité pp. 132.)

Chardon, D., Jayananda, M., Chetty, T. R., and Peucat, J.-J. (2008). Precambrian continental strain and shear zone patterns : South indian case. *Journal of Geophysical Research : Solid Earth (1978–2012)*, 113(B8). (Cité pp. 60.)

Chardon, D., Jayananda, M., and Peucat, J.-J. (2011). Lateral constrictional flow of hot orogenic crust : insights from the neoarchean of south india, geological and geophysical implications for orogenic plateaux. *Geochemistry, Geophysics, Geosystems*, 12(2). (Cité pp. 50, 63, 132 et 273.)

Chardon, D., Peucat, J.-J., Jayananda, M., Choukroune, P., and Fanning, C. M. (2002). Archean granite-greenstone tectonics at kolar (south india) : Interplay of diapirism and bulk inhomogeneous contraction during juvenile magmatic accretion. *Tectonics*, 21(3) :7–1. (Cité pp. 60.)

Chavagnac, V. and Jahn, B.-m. (1996). Coesite-bearing eclogites from the bixiling complex, dabie mountains, china : SmîŮÿ nd ages, geochemical characteristics and tectonic implications. *Chemical Geology*, 133(1) :29–51. (Cité pp. 53.)

Chemenda, A. I., Mattauer, M., and Bokun, A. N. (1996). Continental subduction and a mechanism for exhumation of high-pressure metamorphic rocks : new modelling and field data from oman. *Earth and Planetary Science Letters*, 143(1) :173–182. (Cité pp. 53.)

Chen, L., Booker, J. R., Jones, A. G., Wu, N., Unsworth, M. J., Wei, W., and Tan, H. (1996). Electrically conductive crust in southern tibet from indepth magnetotelluric surveying. *Science*, 274(5293) :1694–1696. (Cité pp. 56.)

Chen, S. F., Libby, J. W., Greenfield, J. E., Wyche, S., and Riganti, A. (2001). Geometry and kinematics of large arcuate structures formed by impingement of rigid granitoids into greenstone belts during progressive shortening. *Geology*, 29(3) :283–286. (Cité pp. 60.)

Chopin, C. (1984). Coesite and pure pyrope in high-grade blueschists of the western alps : a first record and some consequences. *Contributions to Mineralogy and Petrology*, 86(2) :107–118. (Cité pp. 53, 222 et 274.)

Chopin, C. (2003). Ultrahigh-pressure metamorphism : tracing continental crust into the mantle. *Earth and Planetary Science Letters*, 212(1) :1–14. (Cité pp. 86.)

Choukroune, P., Bouhallier, H., and Arndt, N. (1995). Soft lithosphere during periods of archaean crustal growth or crustal reworking. *Geological Society, London, Special Publications*, 95(1) :67–86. (Cité pp. 119 et 222.)

Choukroune, P., Roure, F., and Pinet, B. (1990). Main results of the ecors pyrenees profile. *Tectonophysics*, 173(1) :411–423. (Cité pp. 53.)

Clark, M. K. and Royden, L. H. (2000). Topographic ooze : Building the eastern margin of tibet by lower crustal flow. *Geology*, 28(8) :703–706. (Cité pp. 57 et 63.)

Clift, P. and Vannucchi, P. (2004). Controls on tectonic accretion versus erosion in subduction zones : Implications for the origin and recycling of the continental crust. *Reviews of Geophysics*, 42(2). (Cité pp. 27 et 29.)

Coffin, M. F. and Eldholm, O. (1994). Large igneous provinces : crustal structure, dimensions, and external consequences. *Reviews of Geophysics*, 32(1) :1–36. (Cité pp. 28.)

Coggon, R. and Holland, T. (2002). Mixing properties of phengitic micas and revised garnet-phengite thermobarometers. *Journal of Metamorphic Geology*, 20(7) :683–696. (Cité pp. 178.)

Coldwell, B., Clemens, J., and Petford, N. (2011). Deep crustal melting in the peruvian andes : felsic magma generation during delamination and uplift. *Lithos*, 125(1) :272–286. (Cité pp. 260.)

Collins, A. S., Reddy, S. M., Buchan, C., and Mruma, A. (2004). Temporal constraints on palaeoproterozoic eclogite formation and exhumation (usagaran orogen, tanzania). *Earth and Planetary Science Letters*, 224(1) :175–192. (Cité pp. 70 et 113.)

Collins, W., Van Kranendonk, M., and Teyssier, C. (1998). Partial convective overturn of archaean crust in the east pilbara craton, western australia : driving mechanisms and tectonic implications. *Journal of Structural Geology*, 20(9) :1405–1424. (Cité pp. 59, 61 et 119.)

Condie, K. C. (1981). *Archean greenstone belts*. Elsevier. (Cité pp. 29, 30 et 222.)

Condie, K. C. (1984). Archean geotherms and supracrustal assemblages. *Tectonophysics*, 105(1) :29–41. (Cité pp. 30.)

Condie, K. C. (1989). Geochemical changes in baslts and andesites across the archean-proterozoic boundary : identification and significance. *Lithos*, 23(1) :1–18. (Cité pp. 34 et 37.)

Condie, K. C. (1998). Episodic continental growth and supercontinents : a mantle avalanche connection ? *Earth and Planetary Science Letters*, 163(1) :97–108. (Cité pp. 25, 26, 69 et 132.)

Condie, K. C. (2004). Supercontinents and superplume events : distinguishing signals in the geologic record. *Physics of the Earth and Planetary Interiors*, 146(1) :319–332. (Cité pp. 24.)

Condie, K. C. and Aster, R. C. (2010). Episodic zircon age spectra of orogenic granitoids : the supercontinent connection and continental growth. *Precambrian Research*, 180(3) :227–236. (Cité pp. 223.)

Condie, K. C., Belousova, E., Griffin, W., and Sircombe, K. N. (2009). Granitoid events in space and time : constraints from igneous and detrital zircon age spectra. *Gondwana Research*, 15(3) :228–242. (Cité pp. 25.)

Condie, K. C. and Benn, K. (2006). Archean geodynamics : Similar to or different from modern geodynamics ? *Geophysical Monograph Series*, 164 :47–59. (Cité pp. 58 et 86.)

Condie, K. C., Beyer, E., Belousova, E., Griffin, W., and O'Reilly, S. Y. (2005). U–pb isotopic ages and hf isotopic composition of single zircons : the search for juvenile precambrian continental crust. *Precambrian Research*, 139(1) :42–100. (Cité pp. 25, 69, 222 et 263.)

Condie, K. C. and Kröner, A. (2008). When did plate tectonics begin ? evidence from the geologic record. *When did plate tectonics begin on planet Earth*, 440 :281–294. (Cité pp. 58, 86 et 222.)

Connolly, J. (2005). Computation of phase equilibria by linear programming : a tool for geodynamic modeling and its application to subduction zone decarbonation. *Earth and Planetary Science Letters*, 236(1) :524–541. (Cité pp. 153 et 178.)

Connolly, J. and Petrini, K. (2002). An automated strategy for calculation of phase diagram sections and retrieval of rock properties as a function of physical conditions. *Journal of Metamorphic Geology*, 20(7) :697–708. (Cité pp. 153.)

Cordani, U. G. and Sato, K. (1999). Crustal evolution of the south american platform, based on nd isotopic systematics on granitoid rocks. *Episodes-Newsmagazine of the International Union of Geological Sciences*, 22(3) :167–173. (Cité pp. 70.)

Coward, M. (1982). Surge zones in the moine thrust zone of nw scotland. *Journal of Structural Geology*, 4(3) :247–256. (Cité pp. 54.)

Czarnota, K., Champion, D., Goscombe, B., Blewett, R., Cassidy, K., Henson, P., and Groenewald, P. (2010). Geodynamics of the eastern yilgarn craton. *Precambrian Research*, 183(2) :175–202. (Cité pp. 29, 31 et 222.)

Dale, J., Powell, R., White, R., Elmer, F., and Holland, T. (2005). A thermodynamic model for ca–na clinoamphiboles in na2o–cao–feo–mgo–al2o3–sio2–h2o–o for petrological calculations. *Journal of Metamorphic Geology*, 23(8) :771–791. (Cité pp. 178.)

Dampare, S., Shibata, T., Asiedu, D., Osae, S., and Banoeng-Yakubo, B. (2008). Geochemistry of paleoproterozoic metavolcanic rocks from the southern ashanti volcanic belt, ghana : petrogenetic and tectonic setting implications. *Precambrian Research*, 162(3) :403–423. (Cité pp. 79, 134 et 224.)

Davies, G. F. (1992). On the emergence of plate tectonics. *Geology*, 20(11) :963–966. (Cité pp. 22.)

Davis, D., Hirdes, W., Schaltegger, U., and Nunoo, E. (1994). U-pb age constraints on deposition and provenance of birimian and gold-bearing tarkwaian sediments in ghana, west africa. *Precambrian Research*, 67(1) :89–107. (Cité pp. 74, 88, 97, 134 et 224.)

de Capitani, C. and Brown, T. H. (1987). The computation of chemical equilibrium in complex systems containing non-ideal solutions. *Geochimica et Cosmochimica Acta*, 51(10) :2639–2652. (Cité pp. 153.)

De Kock, G., Armstrong, R., Siegfried, H., and Thomas, E. (2011). Geochronology of the birim supergroup of the west african craton in the wa-bolé region of west-central ghana : Implications for the stratigraphic framework. *Journal of African Earth Sciences*, 59(1) :1–40. (Cité pp. 73, 74, 76, 77, 88, 91, 113, 115, 117, 135, 137, 172, 224, 229 et 262.)

De Kock, G., Botha, P., Théveniaut, H., and Gyapong, W. (2009). Geological map explanation–map sheet 0803b (1 : 100 000) : Ed. *Ghana Geological Survey Department*. (Cité pp. 89, 90, 92, 136, 172 et 226.)

De Kock, G., Théveniaut, H., Botha, P., and Gyapong, W. (2012). Timing the structural events in the palaeoproterozoic bolé–nangodi belt terrane and adjacent maluwe basin, west african craton, in central-west ghana. *Journal of African Earth Sciences*, 65 :1–24. (Cité pp. 76, 88, 117, 135, 224, 227 et 273.)

De Wit, M. and Tinker, J. (2004). Crustal structures across the central kaapvaal craton from deep-seismic reflection data. *South African Journal of Geology*, 107(1-2) :185–206. (Cité pp. 59 et 60.)

de Wit, M. J. (1998). On archean granites, greenstones, cratons and tectonics : does the evidence demand a verdict ? *Precambrian research*, 91(1) :181–226. (Cité pp. 58, 86, 222 et 274.)

de Wit, M. J. (2004). Archean greenstone belts do contain fragments of ophiolites. *Developments in Precambrian Geology*, 13 :599–614. (Cité pp. 31 et 86.)

De Wit, M. J. and Ashwal, L. D. (1997). *Greenstone belts*. Oxford University Press, USA. (Cité pp. 58, 86 et 222.)

Debat, P., Nikiéma, S., Mercier, A., Lompo, M., Béziat, D., Bourges, F., Roddaz, M., Salvi, S., Tollon, F., and Wenmenga, U. (2003). A new metamorphic constraint for the eburnean orogeny from paleoproterozoic formations of the man shield (aribinda and tampelga countries, burkina faso). *Precambrian Research*, 123(1) :47–65. (Cité pp. 75, 77, 132, 135 et 224.)

DeCelles, P. G. and Giles, K. A. (1996). Foreland basin systems. *Basin Research*, 8(2) :105–123. (Cité pp. 53.)

Delor, C. and d'Ivoire, C. (1995). *Carte géologique de la Côte d'Ivoire à 1/200 000 : feuille Nassian*. Direction des mines et de la géologie de Côte d'Ivoire. (Cité pp. 73, 88, 91 et 224.)

DePaolo, D. J. (1980). Crustal growth and mantle evolution : inferences from models of element transport and nd and sr isotopes. *Geochimica et Cosmochimica Acta*, 44(8) :1185–1196. (Cité pp. 32.)

Desrochers, J.-P., Hubert, C., Ludden, J. N., and Pilote, P. (1993). Accretion of archean oceanic plateau fragments in the abitibi, greenstone belt, canada. *Geology*, 21(5) :451–454. (Cité pp. 272.)

Dewey, J. F. (1988). Extensional collapse of orogens. *Tectonics*, 7(6) :1123–1139. (Cité pp. 57, 86 et 114.)

Dhuime, B., Hawkesworth, C. J., Cawood, P. A., and Storey, C. D. (2012). A change in the geodynamics of continental growth 3 billion years ago. *Science*, 335(6074) :1334–1336. (Cité pp. 26, 27, 120 et 222.)

Dia, A., Van Schmus, W., and Kröner, A. (1997). Isotopic constraints on the age and formation of a palaeoproterozoic volcanic arc complex in the kedougou inlier, eastern senegal, west africa. *Journal of African Earth Sciences*, 24(3) :197–213. (Cité pp. 73 et 224.)

Diener, J., Powell, R., White, R., and Holland, T. (2007). A new thermodynamic model for clino-and orthoamphiboles in the system na2o–cao–feo–mgo–al2o3–sio2–h2o–o. *Journal of Metamorphic Geology*, 25(6) :631–656. (Cité pp. 178.)

Dioh, E., Béziat, D., Debat, P., Grégoire, M., and Ngom, P. M. (2006). Diversity of the palaeoproterozoic granitoids of the kédougou inlier (eastern sénégal) : petrographical and geochemical constraints. *Journal of African Earth Sciences*, 44(3) :351–371. (Cité pp. 75.)

Dobrzhinetskaya, L. F., Eide, E. A., Larsen, R. B., Sturt, B. A., Trønnes, R. G., Smith, D. C., Taylor, W. R., and Posukhova, T. V. (1995). Microdiamond in high-grade metamorphic rocks of the western gneiss region, norway. *Geology*, 23(7) :597–600. (Cité pp. 53.)

Douce, A. E. P. and Johnston, A. D. (1991). Phase equilibria and melt productivity in the pelitic system : implications for the origin of peraluminous granitoids and aluminous granulites. *Contributions to Mineralogy and Petrology*, 107(2) :202–218. (Cité pp. 260.)

Doumbia, S., Pouclet, A., Kouamelan, A., Peucat, J., Vidal, M., and Delor, C. (1998). Petrogenesis of juvenile-type birimian (paleoproterozoic) granitoids in central côte-d'ivoire, west africa : geochemistry and geochronology. *Precambrian Research*, 87(1) :33–63. (Cité pp. 73, 74, 75, 88, 133 et 224.)

Drummond, M. S. and Defant, M. J. (1990). A model for trondhjemite-tonalite-dacite genesis and crustal growth via slab melting : Archean to modern comparisons. *Journal of Geophysical Research : Solid Earth (1978–2012)*, 95(B13) :21503–21521. (Cité pp. 39 et 272.)

Dubacq, B., Vidal, O., and De Andrade, V. (2010). Dehydration of dioctahedral aluminous phyllosilicates : thermodynamic modelling and implications for thermobarometric estimates. *Contributions to Mineralogy and Petrology*, 159(2) :159–174. (Cité pp. 180.)

Duchêne, S., Aissa, R., and Vanderhaeghe, O. (2006). Pressure-temperature-time evolution of metamorphic rocks from naxos (cyclades, greece) : Constraints from thermobarometry and rb/sr dating. *Geodinamica Acta*, 19(5) :301–321. (Cité pp. 57 et 115.)

DucheËĘne, S., Lardeaux, J.-M., and Albarède, F. (1997). Exhumation of eclogites : insights from depth-time path analysis. *Tectonophysics*, 280(1) :125–140. (Cité pp. 175.)

Duodu, J. A. (2009). *Geological Map of Ghana 1 : 1 000 000*. Geological Survey Department. (Cité pp. 6, 73, 74, 90, 91, 113, 114, 115, 137, 172, 224, 226, 229 et 262.)

Easton, R. M. (2000). Metamorphism of the canadian shield, ontario, canada. i. the superior province. *The Canadian Mineralogist*, 38(2) :287–317. (Cité pp. 177.)

Egal, E., Thiéblemont, D., Lahondère, D., Guerrot, C., Costea, C. A., Iliescu, D., Delor, C., Goujou, J.-C., Lafon, J. M., Tegyey, M., et al. (2002). Late eburnean granitization and tectonics along the western and northwestern margin of the archean kénéma–man domain (guinea, west african craton). *Precambrian Research*, 117(1) :57–84. (Cité pp. 74, 75, 79, 88, 134, 224 et 274.)

Eisenlohr, B. and Hirdes, W. (1992). The structural development of the early proterozoic birimian and tarkwaian rocks of southwest ghana, west africa. *Journal of African Earth Sciences (and the Middle East)*, 14(3) :313–325. (Cité pp. 74, 76, 88, 135 et 224.)

England, P. and McKenzie, D. (1982). A thin viscous sheet model for continental deformation. *Geophysical Journal of the Royal Astronomical Society*, 70(2) :295–321. (Cité pp. 48.)

England, P. and Molnar, P. (1990). Surface uplift, uplift of rocks, and exhumation of rocks. *Geology*, 18(12) :1173–1177. (Cité pp. 174.)

England, P. C. and Thompson, A. B. (1984). Pressure–temperature–time paths of regional metamorphism i. heat transfer during the evolution of regions of thickened continental crust. *Journal of Petrology*, 25(4) :894–928. (Cité pp. 55, 56, 113, 168 et 175.)

Ernst, R. E., Buchan, K. L., and Campbell, I. H. (2005). Frontiers in large igneous province research. *Lithos*, 79(3) :271–297. (Cité pp. 28.)

Ernst, W. (1972). Occurrence and mineralogic evolution of blueschist belts with time. *American Journal of Science*, 272(7) :657–668. (Cité pp. 222.)

Ernst, W. (2009). Archean plate tectonics, rise of proterozoic supercontinentality and onset of regional, episodic stagnant-lid behavior. *Gondwana Research*, 15(3) :243–253. (Cité pp. 30, 32, 58 et 222.)

Ernst, W., Maruyama, S., and Wallis, S. (1997). Buoyancy-driven, rapid exhumation of ultrahigh-pressure metamorphosed continental crust. *Proceedings of the National Academy of Sciences*, 94(18) :9532–9537. (Cité pp. 53.)

Eskola, P. (1915). On the relations between the chemical and mineralogical composition in the metamorphic rocks of the orijarvi region. *Bull. comm. géol. Finlande*, 44 :109–143. (Cité pp. 50.)

Evans, T. (2004). A method for calculating effective bulk composition modification due to crystal fractionation in garnet-bearing schist : implications for isopleth thermobarometry. *Journal of Metamorphic Geology*, 22(6) :547–557. (Cité pp. 179.)

Faure, M., Bé Mézème, E., Cocherie, A., Rossi, P., Chemenda, A., and Boutelier, D. (2008). Devonian geodynamic evolution of the variscan belt, insights from the french massif central and massif armoricain. *Tectonics*, 27(2). (Cité pp. 59.)

Feybesse, J.-L., Billa, M., Guerrot, C., Duguey, E., Lescuyer, J.-L., Milesi, J.-P., and Bouchot, V. (2006). The paleoproterozoic ghanaian province : Geodynamic model and ore controls, including regional stress modeling. *Precambrian Research*, 149(3) :149–196. (Cité pp. 73, 74, 77, 78, 88, 89, 133, 134, 136, 224 et 273.)

Feybesse, J.-L. and Milési, J.-P. (1994). The archaean/proterozoic contact zone in west africa : a mountain belt of décollement thrusting and folding on a continental margin related to 2.1 ga convergence of archaean cratons ? *Precambrian Research*, 69(1) :199–227. (Cité pp. 78.)

Feybesse, J.-L., Milési, J.-P., Ouedraogo, M., and Prost, A. (1990). La« ceinture» protérozoïque inférieur de boromo-goren (burkina faso) : un exemple d'interférence entre deux phases transcurrentes éburnéennes. *Comptes rendus de l'Académie des sciences. Série 2, Mécanique, Physique, Chimie, Sciences de l'univers, Sciences de la Terre*, 310(10) :1353–1360. (Cité pp. 76, 88, 89, 133 et 135.)

Flament, N., Coltice, N., and Rey, P. F. (2008). A case for late-archaean continental emergence from thermal evolution models and hypsometry. *Earth and Planetary Science Letters*, 275(3) :326–336. (Cité pp. 62.)

Fleitout, L. and Froidevaux, C. (1982). Tectonics and topography for a lithosphere containing density heterogeneities. *Tectonics*, 1(1) :21–56. (Cité pp. 46.)

Fletcher, I. R., McNaughton, N. J., Davis, W. J., and Rasmussen, B. (2010). Matrix effects and calibration limitations in ion probe u–pb and th–pb dating of monazite. *Chemical Geology*, 270(1) :31–44. (Cité pp. 188.)

Foley, S., Tiepolo, M., and Vannucci, R. (2002). Growth of early continental crust controlled by melting of amphibolite in subduction zones. *Nature*, 417(6891) :837–840. (Cité pp. 39 et 272.)

Fonarev, V., Pilugin, S., Savko, K., and Novikova, M. (2006). Exsolution textures of orthopyroxene and clinopyroxene in high-grade bif of the voronezh crystalline massif : evidence of ultrahigh-temperature metamorphism. *Journal of Metamorphic Geology*, 24(2) :135–151. (Cité pp. 62.)

Foster, G., Kinny, P., Vance, D., Prince, C., and Harris, N. (2000). The significance of monazite u–th–pb age data in metamorphic assemblages ; a combined study of monazite and garnet chronometry. *Earth and Planetary Science Letters*, 181(3) :327–340. (Cité pp. 188.)

Friend, C. R. and Nutman, A. P. (2010). Eoarchean ophiolites ? new evidence for the debate on the isua supracrustal belt, southern west greenland. *American Journal of Science*, 310(9) :826–861. (Cité pp. 31.)

Frost, B. R., Barnes, C. G., Collins, W. J., Arculus, R. J., Ellis, D. J., and Frost, C. D. (2001). A geochemical classification for granitic rocks. *Journal of Petrology*, 42(11) :2033–2048. (Cité pp. 37.)

Frost, C. D., Frost, B. R., Kirkwood, R., and Chamberlain, K. R. (2006). The tonalite-trondhjemite-granodiorite (ttg) to granodiorite-granite (gg) transition in the late archean plutonic rocks of the central wyoming province. *Canadian Journal of Earth Sciences*, 43(10) :1419–1444. (Cité pp. 37.)

Galipp, K., Klemd, R., and Hirdes, W. (2003). Metamorphism and geochemistry of the paleoproterozoic birimian sefwi volcanic belt (ghana, west africa). *Geol Jahrb D*, 111 :141–175. (Cité pp. 75, 77, 88, 135 et 224.)

Ganne, J., De Andrade, V., Weinberg, R., Vidal, O., Dubacq, B., Kagambega, N., Naba, S., Baratoux, L., Jessell, M., and Allibon, J. (2012). Modern-style plate subduction preserved in the palaeoproterozoic west african craton. *Nature geoscience*, 5(1) :60–65. (Cité pp. 75, 77, 79, 91, 118, 132, 135, 154, 179 et 224.)

Ganne, J., Gerbault, M., and Block, S. (2014). Thermo-mechanical modeling of lower crust exhumation - constraints from the metamorphic record of the palaeoproterozoic eburnean orogeny, west african craton. *Precambrian Research*, 243 :88–109. (Cité pp. 117.)

Gapais, D., Cagnard, F., Gueydan, F., Barbey, P., and Ballevre, M. (2009). Mountain building and exhumation processes through time : inferences from nature and models. *Terra Nova*, 21(3) :188–194. (Cité pp. 60, 62, 120, 132, 172 et 175.)

Gapais, D., Pelletier, A., Ménot, R.-P., and Peucat, J.-J. (2008). Paleoproterozoic tectonics in the terre adélie craton (east antarctica). *Precambrian Research*, 162(3) :531–539. (Cité pp. 132.)

Gasquet, D., Barbey, P., Adou, M., and Paquette, J. (2003). Structure, sr–nd isotope geochemistry and zircon u–pb geochronology of the granitoids of the dabakala area (côte d'ivoire) : evidence for a 2.3 ga crustal growth event in the palaeoproterozoic of west africa ? *Precambrian Research*, 127(4) :329–354. (Cité pp. 73, 74, 76, 77, 78, 87, 88, 119, 133, 135, 223, 224 et 262.)

Gasquet, D., Bertrand, J.-M., Paquette, J.-L., Lehmann, J., Ratzov, G., Guedes, R. D. A., Tiepolo, M., Boullier, A.-M., Scaillet, S., and Nomade, S. (2010). Miocene to messinian deformation and hydrothermal activity in a pre-alpine basement massif of the french western alps : new u-th-pb and argon ages from the lauzière massif. *Bulletin de la Société Géologique de France*, 181(3) :227–241. (Cité pp. 121 et 122.)

Gastil, R. G. (1960). The distribution of mineral dates in time and space. *American Journal of Science*, 258(1) :1–35. (Cité pp. 25 et 29.)

Gautier, P., Brun, J.-P., and Jolivet, L. (1993). Structure and kinematics of upper cenozoic extensional detachment on naxos and paros (cyclades islands, greece). *Tectonics*, 12(5) :1180–1194. (Cité pp. 58.)

Gebauer, D., Schertl, H.-P., Brix, M., and Schreyer, W. (1997). 35 ma old ultrahigh-pressure metamorphism and evidence for very rapid exhumation in the dora maira massif, western alps. *Lithos*, 41(1) :5–24. (Cité pp. 53.)

Gerdes, A. and Zeh, A. (2006). Combined u–pb and hf isotope la-(mc-) icp-ms analyses of detrital zircons : comparison with shrimp and new constraints for the provenance and age of an armorican metasediment in central germany. *Earth and Planetary Science Letters*, 249(1) :47–61. (Cité pp. 121.)

Gerdes, A. and Zeh, A. (2009). Zircon formation versus zircon alterationâĂŤnew insights from combined u–pb and lu–hf in-situ la-icp-ms analyses, and consequences for the interpretation of archean zircon from the central zone of the limpopo belt. *Chemical Geology*, 261(3) :230–243. (Cité pp. 121, 122 et 262.)

Gerya, T. V., Stöckhert, B., and Perchuk, A. L. (2002). Exhumation of high-pressure metamorphic rocks in a subduction channel : A numerical simulation. *Tectonics*, 21(6) :6–1. (Cité pp. 53.)

Goguel, J. (1965). Traité de tectonique. (Cité pp. 15.)

Goleby, B., Blewett, R., Korsch, R., Champion, D., Cassidy, K., Jones, L., Groenewald, P., and Henson, P. (2004). Deep seismic reflection profiling in the archaean northeastern yilgarn craton, western australia : implications for crustal architecture and mineral potential. *Tectonophysics*, 388(1) :119–133. (Cité pp. 59.)

Gorbatschev, R. and Bogdanova, S. (1993). Frontiers in the baltic shield. *Precambrian Research*, 64(1) :3–21. (Cité pp. 70.)

Goscombe, B., Blewett, R., Czarnota, K., Groenewald, P., and Maas, R. (2009). *Metamorphic evolution and integrated terrane analysis of the eastern Yilgarn Craton : rationale, methods, outcomes and interpretation*. Geoscience Australia. (Cité pp. 60 et 177.)

Green, D. (1975). Genesis of archean peridotitic magmas and constraints on archean geothermal gradients and tectonics. *Geology*, 3(1) :15–18. (Cité pp. 21.)

Green, E., Holland, T., and Powell, R. (2007). An order-disorder model for omphacitic pyroxenes in the system jadeite-diopside-hedenbergite-acmite, with applications to eclogitic rocks. *American Mineralogist*, 92(7) :1181–1189. (Cité pp. 178.)

Grégoire, M., Cottin, J. Y., Giret, A., Mattielli, N., and Weis, D. (1998). The meta-igneous granulite xenoliths from kerguelen archipelago : evidence of a continent nucleation in an oceanic setting. *Contributions to Mineralogy and Petrology*, 133(3) :259–283. (Cité pp. 28.)

Griffin, W., Doyle, B., Ryan, C., Pearson, N., Suzanne, Y., Davies, R., Kivi, K., Van Achterbergh, E., and Natapov, L. (1999a). Layered mantle lithosphere in the lac de gras area, slave craton : composition, structure and origin. *Journal of Petrology*, 40(5) :705–727. (Cité pp. 33.)

Griffin, W., O'Reilly, S., Abe, N., Aulbach, S., Davies, R., Pearson, N., Doyle, B., and Kivi, K. (2003). The origin and evolution of archean lithospheric mantle. *Precambrian Research*, 127(1) :19–41. (Cité pp. 32 et 33.)

Griffin, W., O'Reilly, S., and Ryan, C. (1999b). The composition and origin of subcontinental lithospheric mantle. *Mantle Petrology : Field Observations and High-Pressure Experimentation : A Tribute to Francis R.(Joe) Boyd : In : Ber1tka, CM (Ed.), The Geochemical Society Special Publication, Houston*, pages 13–45. (Cité pp. 32.)

Griffin, W., O'Reilly, S. Y., Ryan, C., Gaul, O., and Ionov, D. (1998). Secular variation in the composition of subcontinental lithospheric mantle : geophysical and geodynamic implications. *Geodynamics Series*, 26 :1–26. (Cité pp. 48.)

Griffin, W., Wang, X., Jackson, S., Pearson, N., O'Reilly, S. Y., Xu, X., and Zhou, X. (2002). Zircon chemistry and magma mixing, se china : in-situ analysis of hf isotopes, tonglu and pingtan igneous complexes. *Lithos*, 61(3) :237–269. (Cité pp. 263 et 264.)

Griggs, D. T. (1939). A theory of mountain-building. *American Journal of Science*, 237(9) :611–650. (Cité pp. 15.)

Gueye, M., Ngom, P. M., Diène, M., Thiam, Y., Siegesmund, S., Wemmer, K., and Pawlig, S. (2008). Intrusive rocks and tectono-metamorphic evolution of the mako paleoproterozoic belt (eastern senegal, west africa). *Journal of African Earth Sciences*, 50(2) :88–110. (Cité pp. 73 et 224.)

Halla, J. (2005). Late archean high-mg granitoids (sanukitoids) in the southern karelian domain, eastern finland : Pb and nd isotopic constraints on crust- mantle interactions. *Lithos*, 79(1) :161–178. (Cité pp. 39.)

Halla, J., van Hunen, J., Heilimo, E., and Hölttä, P. (2009). Geochemical and numerical constraints on neoarchean plate tectonics. *Precambrian Research*, 174(1) :155–162. (Cité pp. 24, 39 et 259.)

Hamilton, W. B. (1998). Archean tectonics and magmatism. *International Geology Review*, 40(1) :1–39. (Cité pp. 58, 86 et 274.)

Hamilton, W. B. (2003). An alternative earth. *GSA TODAY*, 13(11) :4–12. (Cité pp. 58, 86, 222 et 274.)

Hargraves, R. (1986). Faster spreading or greater ridge length in the archean ? *Geology*, 14(9) :750–752. (Cité pp. 19.)

Harley, S. (1989). The origins of granulites : a metamorphic perspective. *Geological Magazine*, 126(03) :215–247. (Cité pp. 60.)

Harley, S. (1992). Proterozoic granulite terranes. *Developments in Precambrian Geology*, 10 :301–359. (Cité pp. 177 et 222.)

Harris, L. B. and Bédard, J. H. (2014). Crustal evolution and deformation in a non-plate-tectonic archaean earth : comparisons with venus. In *Evolution of Archean Crust and Early Life*, pages 215–291. Springer. (Cité pp. 86.)

Harris, N. (2007). Channel flow and the himalayan–tibetan orogen : a critical review. *Journal of the Geological Society*, 164(3) :511–523. (Cité pp. 57.)

Harris, N. B., Pearce, J. A., and Tindle, A. G. (1986). Geochemical characteristics of collision-zone magmatism. *Geological Society, London, Special Publications*, 19(1) :67–81. (Cité pp. 37.)

Harrison, T. M. (2009). The hadean crust : evidence from> 4 ga zircons. *Annual Review of Earth and Planetary Sciences*, 37 :479–505. (Cité pp. 25.)

Haug, E. (1900). *Les géosynclinaux et les aires continentales : contribution à l'étude des transgressions et des régressions marines*. Au siège de la Société géologique de France. (Cité pp. 14.)

Hawkesworth, C., Dhuime, B., Pietranik, A., Cawood, P., Kemp, A., and Storey, C. (2010). The generation and evolution of the continental crust. *Journal of the Geological Society*, 167(2) :229–248. (Cité pp. 25, 26 et 222.)

Hawkesworth, C. and Kemp, A. (2006). Using hafnium and oxygen isotopes in zircons to unravel the record of crustal evolution. *Chemical Geology*, 226(3) :144–162. (Cité pp. 222.)

Heilimo, E., Halla, J., and Hölttä, P. (2010). Discrimination and origin of the sanukitoid series : geochemical constraints from the neoarchean western karelian province (finland). *Lithos*, 115(1) :27–39. (Cité pp. 36, 37 et 261.)

Heilimo, E., Halla, J., and Huhma, H. (2011). Single-grain zircon u–pb age constraints of the western and eastern sanukitoid zones in the finnish part of the karelian province. *Lithos*, 121(1) :87–99. (Cité pp. 36.)

Hein, K. A. (2010). Succession of structural events in the goren greenstone belt (burkina faso) : implications for west african tectonics. *Journal of African Earth Sciences*, 56(2) :83–94. (Cité pp. 76, 88, 118, 135 et 224.)

Hein, K. A., Morel, V., Kagoné, O., Kiemde, F., and Mayes, K. (2004). Birimian lithological succession and structural evolution in the goren segment of the boromo–goren greenstone belt, burkina faso. *Journal of African Earth Sciences*, 39(1) :1–23. (Cité pp. 97.)

Helmstaedt, H. and Scott, D. (1992). The proterozoic ophiolite problem. *Developments in Precambrian Geology*, 10 :55–95. (Cité pp. 31, 222 et 274.)

Herzberg, C. (1999). Phase equilibrium constraints on the formation of cratonic mantle. *Mantle Petrology : Field Observations and High Pressure Experimentation : a Tribute to Francis R.(Joe) Boyd. Geochemical Society, Special Publications*, 6 :241–257. (Cité pp. 33.)

Herzberg, C., Asimow, P. D., Arndt, N., Niu, Y., Lesher, C., Fitton, J., Cheadle, M., and Saunders, A. (2007). Temperatures in ambient mantle and plumes : Constraints from basalts, picrites, and komatiites. *Geochemistry, Geophysics, Geosystems*, 8(2). (Cité pp. 22.)

Herzberg, C., Condie, K., and Korenaga, J. (2010). Thermal history of the earth and its petrological expression. *Earth and Planetary Science Letters*, 292(1) :79–88. (Cité pp. 21, 22 et 273.)

Hess, H. H. (1962). History of ocean basins. *Petrologic studies*, 4 :599–620. (Cité pp. 15.)

Hirdes, W. and Davis, D. (2002). U–pb geochronology of paleoproterozoic rocks in the southern part of the kedougou-kenieba inlier, senegal, west africa : evidence for diachronous accretionary development of the eburnean province. *Precambrian Research*, 118(1) :83–99. (Cité pp. 79 et 224.)

Hirdes, W., Davis, D., and Eisenlohr, B. (1992). Reassessment of proterozoic granitoid ages in ghana on the basis of u/pb zircon and monazite dating. *Precambrian Research*, 56(1) :89–96. (Cité pp. 74, 88 et 89.)

Hirdes, W., Davis, D., Lüdtke, G., and Konan, G. (1996). Two generations of birimian (paleoproterozoic) volcanic belts in northeastern côte d'ivoire (west africa) : consequences for the âĂŸbirimian controversyâĂŹ. *Precambrian Research*, 80(3) :173–191. (Cité pp. 73, 74, 76, 77, 79, 88, 133, 135, 136, 224 et 262.)

Hirdes, W. and Davis, D. W. (1998). First u-pb zircon age of extrusive volcanism in the birimian supergroup of ghana/west africa. *Journal of African Earth Sciences*, 27(2) :291–294. (Cité pp. 73 et 224.)

Hirdes, W., Senger, R., Adjei, J., Efa, E., Loh, G., and Tettey, A. (1993). *Explanatory Notes for the Geological Map of Southwest Ghana 1 : 100,000 : Sheets Wiawso (0603D), Asafo (0603C), Kukuom (0603B), Goaso (0603A), Sunyani (0703D) and Berekum (0703C)*. Schweizerbart. (Cité pp. 78.)

Hirth, G. and Kohlstedt, D. (2003). Rheology of the upper mantle and the mantle wedge : A view from the experimentalists. *Geophysical Monograph Series*, 138 :83–105. (Cité pp. 42.)

Hodges, K., Parrish, R., Housh, T., Lux, D., Burchfiel, B., Royden, L., and Chen, Z. (1992). Simultaneous miocene extension and shortening in the himalayan orogen. *Science*, 258(5087) :1466–1470. (Cité pp. 114.)

Hoffman, P. F. (1988). United plates of america, the birth of a craton-early proterozoic assembly and growth of laurentia. *Annual Review of Earth and Planetary Sciences*, 16 :543–603. (Cité pp. 29.)

Hofmann, A. W. and White, W. M. (1982). Mantle plumes from ancient oceanic crust. *Earth and Planetary Science Letters*, 57(2) :421–436. (Cité pp. 32.)

Holbrook, W. S., Lizarralde, D., McGeary, S., Bangs, N., and Diebold, J. (1999). Structure and composition of the aleutian island arc and implications for continental crustal growth. *Geology*, 27(1) :31–34. (Cité pp. 28.)

Holland, T., Baker, J., and Powell, R. (1998). Mixing properties and activity-composition and relationships of chlorites in the system mgo-feo-al 2 o 3-sio 2-h 2 o. *European Journal of Mineralogy*, 10(3) :395–406. (Cité pp. 178.)

Holland, T. and Powell, R. (1998). An internally consistent thermodynamic data set for phases of petrological interest. *Journal of metamorphic Geology*, 16(3) :309–343. (Cité pp. 178.)

Holmes, A. (1931). Radioactivity and earth movements. *Nature*, 128 :496. (Cité pp. 15.)

Horstwood, M. S., Foster, G. L., Parrish, R. R., Noble, S. R., and Nowell, G. M. (2003). Common-pb corrected in situ u–pb accessory mineral geochronology by la-mc-icp-ms. *Journal of Analytical Atomic Spectrometry*, 18(8) :837–846. (Cité pp. 121 et 122.)

Hurley, P., Hughes, H., Faure, G., Fairbairn, H., and Pinson, W. (1962). Radiogenic strontium-87 model of continent formation. *Journal of Geophysical Research*, 67(13) :5315–5334. (Cité pp. 29.)

Hurley, P. M. and Rand, J. R. (1969). Pre-drift continental nuclei. *Science*, 164(3885) :1229–1242. (Cité pp. 25 et 26.)

Hyndman, R. D., Currie, C. A., and Mazzotti, S. P. (2005). Subduction zone backarcs, mobile belts, and orogenic heat. *GSA Today*, 15(2) :4–10. (Cité pp. 51, 52, 79 et 177.)

Iizuka, T., Horie, K., Komiya, T., Maruyama, S., Hirata, T., Hidaka, H., and Windley, B. F. (2006). 4.2 ga zircon xenocryst in an acasta gneiss from northwestern canada : Evidence for early continental crust. *Geology*, 34(4) :245–248. (Cité pp. 25.)

Irvine, T. and Baragar, W. (1971). A guide to the chemical classification of the common volcanic rocks. *Canadian journal of earth sciences*, 8(5) :523–548. (Cité pp. 239.)

Jackson, S. E., Pearson, N. J., Griffin, W. L., and Belousova, E. A. (2004). The application of laser ablation-inductively coupled plasma-mass spectrometry to in situ u–pb zircon geochronology. *Chemical Geology*, 211(1) :47–69. (Cité pp. 121.)

Jahn, B., Auvray, B., Shen, Q., Liu, D., Zhang, Z., Dong, Y., Ye, X., Zhang, Q., Cornichet, J., and Mace, J. (1988). Archean crustal evolution in china : the taishan complex, and evidence for juvenile crustal addition from long-term depleted mantle. *Precambrian Research*, 38(4) :381–403. (Cité pp. 36.)

Jahn, B.-M., Glikson, A., Peucat, J., and Hickman, A. (1981). Ree geochemistry and isotopic data of archean silicic volcanics and granitoids from the pilbara block, western australia : implications for the early crustal evolution. *Geochimica et Cosmochimica Acta*, 45(9) :1633–1652. (Cité pp. 34.)

James, H. L. (1978). Subdivision of the precambrian - a brief review and a report on recent decisions by the subcommission on precambrian stratigraphy. *Precambrian Research*, 7(3) :193–204. (Cité pp. 68.)

Jamieson, R. A. and Beaumont, C. (2011). Coeval thrusting and extension during lower crustal ductile flow–implications for exhumation of high-grade metamorphic rocks. *Journal of Metamorphic Geology*, 29(1) :33–51. (Cité pp. 114.)

Jamieson, R. A., Unsworth, M. J., Harris, N. B., Rosenberg, C. L., and Schulmann, K. (2011). Crustal melting and the flow of mountains. *Elements*, 7(4) :253–260. (Cité pp. 114.)

Janoušek, V., Farrow, C., and Erban, V. (2006). Interpretation of whole-rock geochemical data in igneous geochemistry : introducing geochemical data toolkit (gcdkit). *Journal of Petrology*, 47(6) :1255–1259. (Cité pp. 228.)

Jeffreys, H. (1926). The earth. its origin, history and physical constitution. *The earth. Its origin, history and physical constitution., by Jeffreys, H.. 6th edition (1976). Cambridge (UK) : Cambridge University Press, 12+ 574 p.*, 1. (Cité pp. 15.)

Jessell, M. W., Amponsah, P. O., Baratoux, L., Asiedu, D. K., Loh, G. K., and Ganne, J. (2012). Crustal-scale transcurrent shearing in the paleoproterozoic sefwi-sunyani-comoé region, west africa. *Precambrian Research*, 212 :155–168. (Cité pp. 75 et 89.)

Jochum, K., Seufert, H., and Thirlwall, M. (1990). High-sensitivity nb analysis by spark-source mass spectrometry (ssms) and calibration of xrf nb and zr. *Chemical Geology*, 81(1) :1–16. (Cité pp. 277.)

John, T., Klemd, R., Hirdes, W., and Loh, G. (1999). The metamorphic evolution of the paleoproterozoic (birimian) volcanic ashanti belt (ghana, west africa). *Precambrian Research*, 98(1) :11–30. (Cité pp. 77, 88, 135 et 224.)

Johnson, M. and Strachan, R. (2006). A discussion of possible heat sources during nappe stacking : the origin of barrovian metamorphism within the caledonian thrust sheets of nw scotland. *Journal of the Geological Society*, 163(4) :579–582. (Cité pp. 51.)

Johnson, T. and Brown, M. (2004). Quantitative constraints on metamorphism in the variscides of southern brittany - a complementary pseudosection approach. *Journal of Petrology*, 45(6) :1237–1259. (Cité pp. 59 et 179.)

Johnson, T., White, R., and Powell, R. (2008). Partial melting of metagreywacke : a calculated mineral equilibria study. *Journal of Metamorphic Geology*, 26(8) :837–853. (Cité pp. 153 et 179.)

Johnson, T. E., Brown, M., Kaus, B. J., and VanTongeren, J. A. (2013). Delamination and recycling of archaean crust caused by gravitational instabilities. *Nature Geoscience*. (Cité pp. 39.)

Junner, N. (1940). *Geology of the Gold Coast and Western Togoland with revised geological map*. Published under the authority of His Excellency Sir Arnold Hodson, Governor of the Gold Coast. (Cité pp. 73, 76, 87, 133 et 223.)

Kamber, B. S., Ewart, A., Collerson, K. D., Bruce, M. C., and McDonald, G. D. (2002). Fluid-mobile trace element constraints on the role of slab melting and implications for archaean crustal growth models. *Contributions to Mineralogy and Petrology*, 144(1) :38–56. (Cité pp. 263.)

Karlstrom, K. E., Åhäll, K.-I., Harlan, S. S., Williams, M. L., McLelland, J., and Geissman, J. W. (2001). Long-lived (1.8–1.0 ga) convergent orogen in southern laurentia, its extensions to australia and baltica, and implications for refining rodinia. *Precambrian Research*, 111(1) :5–30. (Cité pp. 132.)

Kazimoto, E. O., Schenk, V., and Berndt, J. (2014). Neoarchean and paleoproterozoic crust formation in the ubendian belt of tanzania : Insights from zircon geochronology and geochemistry. *Precambrian Research*, 252 :119–144. (Cité pp. 70.)

Keller, C. B. and Schoene, B. (2012). Statistical geochemistry reveals disruption in secular lithospheric evolution about 2.5 gyr ago. *Nature*, 485(7399) :490–493. (Cité pp. 29, 34, 35, 37 et 39.)

Kemp, A., Hawkesworth, C., Paterson, B., and Kinny, P. (2006). Episodic growth of the gondwana supercontinent from hafnium and oxygen isotopes in zircon. *Nature*, 439(7076) :580–583. (Cité pp. 262.)

Kennedy, A. and Kinny, P. (2004). Identifying inter-and intra-laboratory sims monazite standards. In *SHRIMP workshop, Hiroshima, Japan*, pages 11–14. (Cité pp. 188.)

Kerrich, R. and Xie, Q. (2002). Compositional recycling structure of an archean super-plume : Nb–th–u–lree systematics of archean komatiites and basalts revisited. *Contributions to Mineralogy and Petrology*, 142(4) :476–484. (Cité pp. 34.)

Key, R., Loughlin, S., Gillespie, M., Del Rio, M., Horstwood, M., Crowley, Q. G., Darbyshire, D., Pitfield, P., and Henney, P. (2008). Two mesoarchaean terranes in the reguibat shield of nw mauritania. *Geological Society, London, Special Publications*, 297(1) :33–52. (Cité pp. 72.)

King, E. M., Valley, J. W., Davis, D. W., and Edwards, G. R. (1998). Oxygen isotope ratios of archean plutonic zircons from granite–greenstone belts of the superior province : indicator of magmatic source. *Precambrian Research*, 92(4) :365–387. (Cité pp. 39.)

Kirby, S. H. (1983). Rheology of the lithosphere. *Reviews of Geophysics*, 21(6) :1458–1487. (Cité pp. 44.)

Kisters, A. F., Stevens, G., Dziggel, A., and Armstrong, R. A. (2003). Extensional detachment faulting and core-complex formation in the southern barberton granite–greenstone terrain, south africa : evidence for a 3.2 ga orogenic collapse. *Precambrian Research*, 127(4) :355–378. (Cité pp. 120.)

Kitson, A. E. (1928). *Provisional Geological Map of the Gold Coast and Western Togoland with Brief Descriptive Notes Thereon 19 Plates : By Sir Albert E. Kitson.* Benham & Company. (Cité pp. 73, 88 et 133.)

Klein, E. and Moura, C. (2008). São luís craton and gurupi belt (brazil) : possible links with the west african craton and surrounding pan-african belts. *Geological Society, London, Special Publications*, 294(1) :137–151. (Cité pp. 72.)

Klein, E. L., Moura, C. A., and Pinheiro, B. L. (2005). Paleoproterozoic crustal evolution of the são luís craton, brazil : evidence from zircon geochronology and sm-nd isotopes. *Gondwana Research*, 8(2) :177–186. (Cité pp. 73 et 224.)

Klein, E. L. and Veloso Moura, C. A. (2001). Age constraints on granitoids and metavolcanic rocks of the são luís craton and gurupi belt, northern brazil : implications for lithostratigraphy and geological evolution. *International Geology Review*, 43(3) :237–253. (Cité pp. 73, 224 et 262.)

Klemd, R., Hünken, U., and Olesch, M. (2002). Metamorphism of the country rocks hosting gold–sulfide-bearing quartz veins in the paleoproterozoic southern kibi-winneba belt (se-ghana). *Journal of African Earth Sciences*, 35(2) :199–211. (Cité pp. 77, 88, 135 et 224.)

Kohlstedt, D., Evans, B., and Mackwell, S. (1995). Strength of the lithosphere : Constraints imposed by laboratory experiments. *Journal of Geophysical Research : Solid Earth (1978–2012)*, 100(B9) :17587–17602. (Cité pp. 42.)

Komiya, T., Hayashi, M., Maruyama, S., and Yurimoto, H. (2002). Intermediate-p/t type archean metamorphism of the isua supracrustal belt : implications for secular change of geothermal gradients at subduction zones and for archean plate tectonics. *American Journal of Science*, 302(9) :806–826. (Cité pp. 60, 64 et 133.)

Komiya, T., Maruyama, S., Masuda, T., Nohda, S., Hayashi, M., and Okamoto, K. (1999). Plate tectonics at 3.8–3.7 ga : field evidence from the isua accretionary complex, southern west greenland. *The Journal of geology*, 107(5) :515–554. (Cité pp. 32, 86 et 274.)

Korenaga, J. (2006). Archean geodynamics and the thermal evolution of earth. *Geophysical Monograph Series*, 164 :7–32. (Cité pp. 19, 20, 21, 86 et 274.)

Korenaga, J. (2008). Urey ratio and the structure and evolution of earth's mantle. *Reviews of Geophysics*, 46(2). (Cité pp. 22.)

Kouamelan, A.-N. (1996). *Géochronologie et Géochimie des Formations Archéennes et Protérozoïques de la Dorsale de Man en Côte d'Ivoire. Implications pour la Transition Archéen-Protéozoïque*. PhD thesis, Université Rennes 1. (Cité pp. 74, 88, 133, 136 et 224.)

Kouamelan, A. N., Delor, C., and Peucat, J.-J. (1997). Geochronological evidence for reworking of archean terrains during the early proterozoic (2.1 ga) in the western cote d'ivoire (man rise-west african craton). *Precambrian Research*, 86(3) :177–199. (Cité pp. 72, 74, 77, 78, 135, 136, 224 et 274.)

Kramers, J. D. (2007). Hierarchical earth accretion and the hadean eon. *Journal of the Geological Society*, 164(1) :3–17. (Cité pp. 263.)

Kříbek, B., Sỳkorová, I., Machovič, V., and Laufek, F. (2008). Graphitization of organic matter and fluid-deposited graphite in palaeoproterozoic (birimian) black shales of the kaya-goren greenstone belt (burkina faso, west africa). *Journal of Metamorphic Geology*, 26(9) :937–958. (Cité pp. 77 et 135.)

Kröner, A. (1981). Precambrian plate tectonics. *Developments in Precambrian Geology*, 4 :57–90. (Cité pp. 31.)

Kushiro, I. (2001). Partial melting experiments on peridotite and origin of mid-ocean ridge basalt. *Annual Review of Earth and Planetary Sciences*, 29(1) :71–107. (Cité pp. 33.)

Kusky, T. (1989). Accretion of the archean slave province. *Geology*, 17(1) :63–67. (Cité pp. 32 et 274.)

Kusky, T. M. (2004). *Precambrian ophiolites and related rocks*, volume 13. Elsevier. (Cité pp. 31.)

Kusky, T. M. and Li, J. (2003). Paleoproterozoic tectonic evolution of the north china craton. *Journal of Asian Earth Sciences*, 22(4) :383–397. (Cité pp. 31 et 70.)

Kusky, T. M., Li, J.-H., and Tucker, R. D. (2001). The archean dongwanzi ophiolite complex, north china craton : 2.505-billion-year-old oceanic crust and mantle. *Science*, 292(5519) :1142–1145. (Cité pp. 86.)

Kusky, T. M. and Polat, A. (1999). Growth of granite–greenstone terranes at convergent margins, and stabilization of archean cratons. *Tectonophysics*, 305(1) :43–73. (Cité pp. 50, 86 et 273.)

Labrosse, S. and Jaupart, C. (2007). Thermal evolution of the earth : Secular changes and fluctuations of plate characteristics. *Earth and Planetary Science Letters*, 260(3) :465–481. (Cité pp. 18, 21 et 22.)

Lahondère, D., Thiéblemont, D., Tegyey, M., Guerrot, C., and Diabate, B. (2002). First evidence of early birimian (2.21 ga) volcanic activity in upper guinea : the volcanics and associated rocks of the niani suite. *Journal of African Earth Sciences*, 35(3) :417–431. (Cité pp. 73, 88 et 224.)

Lambert, R. S. J. (1976). Archean thermal regimes, crustal and upper mantle temperatures, and a progressive evolutionary model for the earth. In *The Early History of the Earth*, volume 1, pages 363–373. (Cité pp. 19.)

Lana, C., Kisters, A., and Stevens, G. (2010). Exhumation of mesoarchean ttg gneisses from the middle crust : Insights from the steynsdorp core complex, barberton granitoid-greenstone terrain, south africa. *Geological Society of America Bulletin*, 122(1-2) :183–197. (Cité pp. 120.)

Laurent, O. (2012). *Les changements géodynamiques à la transition Archéen-Protérozoïque : étude des granitoïdes de la marge Nord du craton du Kaapvaal (Afrique du Sud)*. PhD thesis, Université Blaise Pascal-Clermont-Ferrand II. (Cité pp. 32.)

Laurent, O., Martin, H., Doucelance, R., Moyen, J.-F., and Paquette, J.-L. (2011). Geochemistry and petrogenesis of high-k "sanukitoids" from the bulai pluton, central limpopo belt, south africa : Implications for geodynamic changes at the archaean–proterozoic boundary. *Lithos*, 123(1) :73–91. (Cité pp. 37, 39 et 132.)

Laurent, O., Martin, H., Moyen, J.-F., and Doucelance, R. (2014). The diversity and evolution of late-archean granitoids : Evidence for the onset of "modern-style" plate tectonics between 3.0 and 2.5 ga. *Lithos*, 205 :208–235. (Cité pp. 36, 37, 38, 39, 40, 68, 120, 132, 259, 260, 261 et 262.)

Laurent, O., Paquette, J.-L., Martin, H., Doucelance, R., and Moyen, J.-F. (2013). La-icp-ms dating of zircons from meso-and neoarchean granitoids of the pietersburg block (south africa) : Crustal evolution at the northern margin of the kaapvaal craton. *Precambrian Research*, 230 :209–226. (Cité pp. 36.)

Le Bas, M., Le Maitre, R., Streckeisen, A., Zanettin, B., et al. (1986). A chemical classification of volcanic rocks based on the total alkali-silica diagram. *Journal of petrology*, 27(3) :745–750. (Cité pp. 239 et 240.)

Le Breton, N. and Thompson, A. B. (1988). Fluid-absent (dehydration) melting of biotite in metapelites in the early stages of crustal anatexis. *Contributions to Mineralogy and Petrology*, 99(2) :226–237. (Cité pp. 141.)

Le Gall, B. (1992). The deep structure of the ardennes variscan thrust belt from structural and ecors seismic data. *Journal of structural geology*, 14(5) :531–546. (Cité pp. 53.)

Le Pichon, X., Fournier, M., and Jolivet, L. (1992). Kinematics, topography, shortening, and extrusion in the india-eurasia collision. *Tectonics*, 11(6) :1085–1098. (Cité pp. 56.)

Ledru, P., Courrioux, G., Dallain, C., Lardeaux, J., Montel, J., Vanderhaeghe, O., and Vitel, G. (2001). The velay dome (french massif central) : melt generation and granite emplacement during orogenic evolution. *Tectonophysics*, 342(3) :207–237. (Cité pp. 57 et 114.)

Ledru, P., Johan, V., Milési, J. P., and Tegyey, M. (1994). Markers of the last stages of the palaeoproterozoic collision : evidence for a 2 ga continent involving circum-south atlantic provinces. *Precambrian Research*, 69(1) :169–191. (Cité pp. 72, 73 et 75.)

Ledru, P., Pons, J., Milési, J., Feybesse, J., and Johan, V. (1991). Transcurrent tectonics and polycyclic evolution in the lower proterozoic of senegal-mali. *Precambrian Research*, 50(3) :337–354. (Cité pp. 75, 76, 88, 89, 133 et 135.)

Lemoine, S., Tempier, P., Bassot, J., Caen-Vachette, M., Vialette, Y., Toure, S., and Wenmenga, U. (1990). The burkinian orogenic cycle, precursor of the eburnian orogeny in west africa. *Geological Journal*, 25(2) :171–188. (Cité pp. 76, 88, 135 et 224.)

Lenoir, J., Liégeois, J.-P., Theunissen, K., and Klerkx, J. (1994). The palaeoproterozoic ubendian shear belt in tanzania : geochronology and structure. *Journal of African Earth Sciences*, 19(3) :169–184. (Cité pp. 70.)

Leube, A., Hirdes, W., Mauer, R., and Kesse, G. O. (1990). The early proterozoic birimian supergroup of ghana and some aspects of its associated gold mineralization. *Precambrian Research*, 46(1) :139–165. (Cité pp. 73, 76, 79, 88, 133, 135, 223 et 224.)

Lewry, J., Hajnal, Z., Green, A., Lucas, S., White, D., Stauffer, M., Ashton, K., Weber, W., and Clowes, R. (1994). Structure of a paleoproterozoic continent-continent collision zone : a lithoprobe seismic reflection profile across the trans-hudson orogen, canada. *Tectonophysics*, 232(1) :143–160. (Cité pp. 70.)

Li, J. and Kusky, T. (2007). A late archean foreland fold and thrust belt in the north china craton : implications for early collisional tectonics. *Gondwana Research*, 12(1) :47–66. (Cité pp. 273.)

Li, Q., Li, S., Zheng, Y.-F., Li, H., Massonne, H. J., and Wang, Q. (2003). A high precision u–pb age of metamorphic rutile in coesite-bearing eclogite from the dabie mountains in central china : a new constraint on the cooling history. *Chemical Geology*, 200(3) :255–265. (Cité pp. 53.)

Li, Z.-X., Bogdanova, S., Collins, A. S., Davidson, A., De Waele, B., Ernst, R., Fitzsimons, I. C., Fuck, R., Gladkochub, D., Jacobs, J., et al. (2008). Assembly, configuration, and break-up history of rodinia : a synthesis. *Precambrian research*, 160(1) :179–210. (Cité pp. 70.)

Liégeois, J.-P., Claessens, W., Camara, D., and Klerkx, J. (1991). Short-lived eburnian orogeny in southern mali. geology, tectonics, u-pb and rb-sr geochronology. *Precambrian Research*, 50(1) :111–136. (Cité pp. 75, 135 et 224.)

Liégeois, J. P., Latouche, L., Boughrara, M., Navez, J., and Guiraud, M. (2003). The latea metacraton (central hoggar, tuareg shield, algeria) : behaviour of an old passive margin during the pan-african orogeny. *Journal of African Earth Sciences*, 37(3) :161–190. (Cité pp. 225.)

Liégeois, J.-P., Navez, J., Hertogen, J., and Black, R. (1998). Contrasting origin of post-collisional high-k calc-alkaline and shoshonitic versus alkaline and peralkaline granitoids. the use of sliding normalization. *Lithos*, 45(1) :1–28. (Cité pp. 37.)

Lompo, M. (2009). Geodynamic evolution of the 2.25-2.0 ga palaeoproterozoic magmatic rocks in the man-leo shield of the west african craton. a model of subsidence of an oceanic plateau. *Geological Society, London, Special Publications*, 323(1) :231–254. (Cité pp. 73, 74, 75, 78, 79, 88, 89, 134 et 224.)

Ludwig, K. (2001). Isoplot/ex, a geochronological toolkit for microsoft excel, special publication, 1a. *Berkeley Geochronological Center, Berkeley, CA*. (Cité pp. 122 et 278.)

Malavieille, J., Guihot, P., Costa, S., Lardeaux, J., and Gardien, V. (1990). Collapse of the thickened variscan crust in the french massif central : Mont pilat extensional shear zone and st. etienne late carboniferous basin. *Tectonophysics*, 177(1) :139–149. (Cité pp. 57 et 114.)

Marmo, B., Clarke, G., and Powell, R. (2002). Fractionation of bulk rock composition due to porphyroblast growth : effects on eclogite facies mineral equilibria, pam peninsula, new caledonia. *Journal of Metamorphic Geology*, 20(1) :151–165. (Cité pp. 179.)

Marshak, S. (1999). Deformation style way back when : thoughts on the contrasts between archean/paleoproterozoic and contemporary orogens. *Journal of Structural Geology*, 21(8) :1175–1182. (Cité pp. 60.)

Martin, H. (1986). Effect of steeper archean geothermal gradient on geochemistry of subduction-zone magmas. *Geology*, 14(9) :753–756. (Cité pp. 39 et 272.)

Martin, H. and Moyen, J.-F. (2002). Secular changes in tonalite-trondhjemite-granodiorite composition as markers of the progressive cooling of earth. *Geology*, 30(4) :319–322. (Cité pp. 36 et 272.)

Martin, H., Moyen, J.-F., Guitreau, M., Blichert-Toft, J., and Pennec, J.-L. L. (2014). Why archaean {TTG} cannot be generated by {MORB} melting in subduction zones. *Lithos*, 198-199(0) :1 – 13. (Cité pp. 35 et 40.)

Martin, H., Moyen, J.-F., and Rapp, R. (2009). The sanukitoid series : magmatism at the archaean–proterozoic transition. *Earth and Environmental Science Transactions of the Royal Society of Edinburgh*, 100(1-2) :15–33. (Cité pp. 36 et 261.)

Martin, H. and Querré, G. (1984). A 2.5 ga reworked sialic crust : Rb-sr ages and isotopic geochemistry of late archaean volcanic and plutonic rocks from e. finland. *Contributions to Mineralogy and Petrology*, 85(3) :292–299. (Cité pp. 36.)

Martin, H., Smithies, R., Rapp, R., Moyen, J.-F., and Champion, D. (2005). An overview of adakite, tonalite–trondhjemite–granodiorite (ttg), and sanukitoid : relationships and some implications for crustal evolution. *Lithos*, 79(1) :1–24. (Cité pp. 36, 132 et 261.)

Maruyama, S. and Liou, J. (1998). Initiation of ultrahigh-pressure metamorphism and its significance on the proterozoic–phanerozoic boundary. *Island Arc*, 7(1-2) :6–35. (Cité pp. 62.)

Maruyama, S., Liou, J., and Terabayashi, M. (1996). Blueschists and eclogites of the world and their exhumation. *International geology review*, 38(6) :485–594. (Cité pp. 62.)

Massonne, H.-J. and Willner, A. P. (2008). Phase relations and dehydration behaviour of psammopelite and mid-ocean ridge basalt at very-low-grade to low-grade metamorphic conditions. *European Journal of Mineralogy*, 20(5) :867–879. (Cité pp. 178.)

Matte, P. and Burg, J. (1981). Sutures, thrusts and nappes in the variscan arc of western europe : plate tectonic implications. *Geological Society, London, Special Publications*, 9(1) :353–358. (Cité pp. 53.)

McDonough, W. F. and Sun, S.-S. (1995). The composition of the earth. *Chemical geology*, 120(3) :223–253. (Cité pp. 238 et 240.)

Melcher, F. (1995). Genesis of chemical sediments in birimian greenstone belts : evidence from gondites and related manganese-bearing rocks from northern ghana. *Mineralogical Magazine*, 59(395) :229–252. (Cité pp. 73.)

Melcher, F. and Stumpfl, E. (1994). Palaeoproterozoic exhalite formation in northern ghana : Source of epigenetic gold-quartz vein mineralization. *Geologisches Jahrbuch*, 100 :201–246. (Cité pp. 89, 137 et 226.)

Metelka, V., Baratoux, L., Naba, S., and Jessell, M. W. (2011). A geophysically constrained litho-structural analysis of the eburnean greenstone belts and associated granitoid domains, burkina faso, west africa. *Precambrian Research*, 190(1) :48–69. (Cité pp. 89, 92, 93, 137 et 226.)

Milési, J., Feybesse, J., Pinna, P., Deschamps, Y., Kampunzu, H., Muhongo, S., Lescuyer, J., Le Goff, E., Delor, C., Billa, M., et al. (2004). Geological map of africa 1 : 10,000,000, sigafrique project. In *20th Conference of African Geology, BRGM, Orléans, France*, pages 2–7. (Cité pp. 87, 134 et 225.)

Milési, J., Ledru, P., Ankrah, P., Johan, V., Marcoux, E., and Vinchon, C. (1991). The metallogenic relationship between birimian and tarkwaian gold deposits in ghana. *Mineralium Deposita*, 26(3) :228–238. (Cité pp. 75.)

Milési, J.-P., Heinry, C., and Sylvain, J.-P. (1989). *Minéralisations aurifères de l'Afrique de l'ouest leurs relations avec l'évolution lithostructurale au Proterozoique inférieur*. Bureau de recherches géologiques et minières. (Cité pp. 74, 75, 76, 78, 88, 89, 133, 134, 135 et 224.)

Milési, J.-P., Ledru, P., Feybesse, J.-L., Dommanget, A., and Marcoux, E. (1992). Early proterozoic ore deposits and tectonics of the birimian orogenic belt, west africa. *Precambrian Research*, 58(1) :305–344. (Cité pp. 72, 74, 75, 78, 88, 89, 133, 134 et 224.)

Millonig, L., Zeh, A., Gerdes, A., Klemd, R., and Barton, J. M. (2010). Decompressional heating of the mahalapye complex (limpopo belt, botswana) : a response to palaeoproterozoic magmatic underplating ? *Journal of Petrology*, page egp097. (Cité pp. 113 et 153.)

Miyashiro, A. (1961). Evolution of metamorphic belts. *Journal of Petrology*, 2(3) :277–311. (Cité pp. 86.)

Möller, A., Appel, P., Mezger, K., and Schenk, V. (1995). Evidence for a 2 ga subduction zone : Eclogites in the usagaran belt of tanzania. *Geology*, 23(12) :1067–1070. (Cité pp. 177.)

Molnar, P., England, P., and Martinod, J. (1993). Mantle dynamics, uplift of the tibetan plateau, and the indian monsoon. *Reviews of Geophysics*, 31(4) :357–396. (Cité pp. 57 et 114.)

Molnar, P. and Lyon-Caen, H. (1988). Some simple physical aspects of the support, structure, and evolution of mountain belts. *Spec. Pap. Geol. Soc. Am*, 218 :179–207. (Cité pp. 46.)

Montel, J.-M., Weber, C., Barbey, P., and Pichavant, M. (1986). Thermo-barométrie du domaine anatectique du velay (massif central, france) et conditions de genèse des granites tardi-migmatitiques. *Comptes rendus de l'Académie des sciences.*

Série 2, Mécanique, Physique, Chimie, Sciences de l'univers, Sciences de la Terre, 302(9) :647–652. (Cité pp. 59.)

Montero, P., Haissen, F., El Archi, A., Rjimati, E., and Bea, F. (2014). Timing of archean crust formation and cratonization in the awsard-tichla zone of the nw reguibat rise, west african craton : A shrimp, nd–sr isotopes, and geochemical reconnaissance study. *Precambrian Research*, 242 :112–137. (Cité pp. 72.)

Moores, E. (1982). Origin and emplacement of ophiolites. *Reviews of Geophysics*, 20(4) :735–760. (Cité pp. 31 et 274.)

Moresi, L., Betts, P., Miller, M., and Cayley, R. (2014). Dynamics of continental accretion. *Nature*, 508(7495) :245–248. (Cité pp. 29 et 177.)

Moresi, L. and Solomatov, V. (1998). Mantle convection with a brittle lithosphere : thoughts on the global tectonic styles of the earth and venus. *Geophysical Journal International*, 133(3) :669–682. (Cité pp. 24.)

Mougeot, R., Respaut, J.-P., Ledru, P., and Marignac, C. (1997). U-pb chronology on accessory minerals of the velay anatectic dome (french massif central). *European Journal of Mineralogy*, 9(1) :141–156. (Cité pp. 59.)

Moyen, J.-F. (2011). The composite archaean grey gneisses : petrological significance, and evidence for a non-unique tectonic setting for archaean crustal growth. *Lithos*, 123(1) :21–36. (Cité pp. 34, 37, 38, 39, 40, 177, 259 et 260.)

Moyen, J.-F. and Martin, H. (2012). Forty years of ttg research. *Lithos*, 148 :312–336. (Cité pp. 34, 36, 38, 222 et 259.)

Moyen, J.-F., Martin, H., Jayananda, M., and Auvray, B. (2003). Late archaean granites : a typology based on the dharwar craton (india). *Precambrian Research*, 127(1) :103–123. (Cité pp. 36 et 37.)

Moyen, J.-F. and Stevens, G. (2006). Experimental constraints on ttg petrogenesis : implications for archean geodynamics. *Geophysical Monograph Series*, 164 :149–175. (Cité pp. 35 et 259.)

Moyen, J.-F. and Van Hunen, J. (2012). Short-term episodicity of archaean plate tectonics. *Geology*, 40(5) :451–454. (Cité pp. 24 et 40.)

Naba, S., Lompo, M., Debat, P., Bouchez, J. L., and Béziat, D. (2004). Structure and emplacement model for late-orogenic paleoproterozoic granitoids : the tenkodogo–yamba elongate pluton (eastern burkina faso). *Journal of African Earth Sciences*, 38(1) :41–57. (Cité pp. 75, 91 et 138.)

Næraa, T., Scherstén, A., Rosing, M. T., Kemp, A., Hoffmann, J., Kokfelt, T., and Whitehouse, M. (2012). Hafnium isotope evidence for a transition in the dynamics of continental growth 3.2 [thinsp] gyr ago. *Nature*, 485(7400) :627–630. (Cité pp. 263, 264 et 278.)

Ndiaye, P., Dia, A., Vialette, Y., Diallo, D., Ngom, P., Sylla, M., Wade, S., and Dioh, E. (1997). Données pétrographiques, geochimiques et géochronologiques nouvelles

sur les granitoïdes du paléoprotérozoïque du supergroupe de dialé-daléma (sen ; égal oriental) : Implications pétrogénétiques et géodynamiques. *Journal of African Earth Sciences*, 25(2) :193–208. (Cité pp. 79.)

Ndiaye, P., Robineau, B., and Moreau, C. (1989). Deformation et metamorphisme des formations birrimiennes en relation avec la mise en place du granite eburneen de saraya (senegal oriental). *Bulletin de la Societe Geologique de France*, (3) :619–625. (Cité pp. 77 et 135.)

Nelson, K. D., Zhao, W., Brown, L., Kuo, J., Che, J., Liu, X., Klemperer, S., Makovsky, Y., Meissner, R., Mechie, J., et al. (1996). Partially molten middle crust beneath southern tibet : Synthesis of project indepth results. *Science*, 274(5293) :1684–1688. (Cité pp. 56.)

Newton, R., Charlu, T., and Kleppa, O. (1980). Thermochemistry of the high structural state plagioclases. *Geochimica et Cosmochimica Acta*, 44(7) :933–941. (Cité pp. 178.)

Nikiéma, S., Benkhelil, J., Corsini, M., Bourges, F., ABDOULAYE, D., and Maurin, J.-C. (1993). Tectonique transcurrente éburnéenne au sein du craton ouest-africain : exemple du sillon de djibo (burkina faso). *Comptes rendus de l'Académie des sciences. Série 2, Mécanique, Physique, Chimie, Sciences de l'univers, Sciences de la Terre*, 316(5) :661–668. (Cité pp. 89.)

Nironen, M. (1997). The svecofennian orogen : a tectonic model. *Precambrian Research*, 86(1) :21–44. (Cité pp. 70.)

Nisbet, E., Cheadle, M., Arndt, N., and Bickle, M. (1993). Constraining the potential temperature of the archaean mantle : a review of the evidence from komatiites. *Lithos*, 30(3) :291–307. (Cité pp. 21 et 273.)

Nisbet, E. G. and Fowler, C. (1983). Model for archean plate tectonics. *Geology*, 11(7) :376–379. (Cité pp. 19.)

Norlander, B. H., Whitney, D. L., Teyssier, C., and Vanderhaeghe, O. (2002). Partial melting and decompression of the thor-odin dome, shuswap metamorphic core complex, canadian cordillera. *Lithos*, 61(3) :103–125. (Cité pp. 57 et 114.)

Norton, M. (1986). Late caledonide extension in western norway : A response to extreme crustal thickening. *Tectonics*, 5(2) :195–204. (Cité pp. 114.)

Oberthür, T., Vetter, U., Davis, D. W., and Amanor, J. A. (1998). Age constraints on gold mineralization and paleoproterozoic crustal evolution in the ashanti belt of southern ghana. *Precambrian Research*, 89(3) :129–143. (Cité pp. 74, 75, 77, 136, 224 et 262.)

O'connor, J. (1965). A classification for quartz-rich igneous rocks based on feldspar ratios. *US Geol. Surv. Prof. Pap*, 525 :79–84. (Cité pp. 236.)

of Canada, G.-A., Lewry, J., and Stauffer, M. (1990). The early proterozoic trans-hudson orogen of north america. Geological Association of Canada. (Cité pp. 70.)

O'Neill, C., Lenardic, A., Moresi, L., Torsvik, T., and Lee, C.-T. (2007). Episodic precambrian subduction. *Earth and Planetary Science Letters*, 262(3) :552–562. (Cité pp. 24.)

Opare-Addo, E., Browning, P., and John, B. (1993). Pressure-temperature constraints on the evolution of an early proterozoic plutonic suite in southern ghana, west africa. *Journal of African Earth Sciences (and the Middle East)*, 17(1) :13–22. (Cité pp. 77, 88 et 134.)

Parra, T., Vidal, O., and Agard, P. (2002). A thermodynamic model for fe–mg dioctahedral k white micas using data from phase-equilibrium experiments and natural pelitic assemblages. *Contributions to Mineralogy and Petrology*, 143(6) :706–732. (Cité pp. 154 et 180.)

Patchett, P. J., Kouvo, O., Hedge, C. E., and Tatsumoto, M. (1982). Evolution of continental crust and mantle heterogeneity : evidence from hf isotopes. *Contributions to Mineralogy and Petrology*, 78(3) :279–297. (Cité pp. 222.)

Patchett, P. J., Todt, W., and Gorbatschev, R. (1987). Origin of continental crust of 1.9-1.7 ga age : Nd isotopes in the svecofennian orogenic terrains of sweden. *Precambrian Research*, 35 :145–160. (Cité pp. 70.)

Patiño Douce, A. and Beard, J. (1995). Dehydration-melting of biotite gneiss and quartz amphibolite from 3 to 15 kbar. *Journal of Petrology*, 36(3) :707–738. (Cité pp. 141.)

Patino-Douce, A. and Beard, J. (1996). Effects of p, f (o2) and mg/fe ratio on dehydration melting of model metagreywackes. *Journal of Petrology*, 37(5) :999–1024. (Cité pp. 260.)

Patiño Douce, A. E. and Harris, N. (1998). Experimental constraints on himalayan anatexis. *Journal of Petrology*, 39(4) :689–710. (Cité pp. 139 et 260.)

Pease, V., Percival, J., Smithies, H., Stevens, G., and Van Kranendonk, M. (2008). When did plate tectonics begin ? evidence from the orogenic record. *When did plate tectonics begin on planet Earth*, pages 199–228. (Cité pp. 58, 86 et 274.)

Pehrsson, S. J., Berman, R. G., Eglington, B., and Rainbird, R. (2013). Two neoarchean supercontinents revisited : the case for a rae family of cratons. *Precambrian Research*, 232 :27–43. (Cité pp. 69 et 70.)

Pehrsson, S. J., Buchan, K. L., Eglington, B. M., Berman, R. M., and Rainbird, R. H. (2014). Did plate tectonics shutdown in the palaeoproterozoic ? a view from the siderian geologic record. *Gondwana Research*. (Cité pp. 69.)

Percival, J., Mortensen, J., Stern, R., Card, K., and Bégin, N. (1992). Giant granulite terranes of northeastern superior province : the ashuanipi complex and minto block. *Canadian Journal of Earth Sciences*, 29(10) :2287–2308. (Cité pp. 132.)

Percival, J., Sanborn-Barrie, M., Skulski, T., Stott, G., Helmstaedt, H., and White, D. (2006). Tectonic evolution of the western superior province from natmap and lithoprobe studies. *Canadian Journal of Earth Sciences*, 43(7) :1085–1117. (Cité pp. 29.)

Percival, J. A. (1991). Granulite-facies metamorphism and crustal magmatism in the ashuanipi complex, quebecâĂŤlabrador, canada. *Journal of Petrology*, 32(6) :1261–1297. (Cité pp. 60.)

Percival, J. A. and Skulski, T. (2000). Tectonothermal evolution of the northern minto block, superior province, quebec, canada. *The Canadian Mineralogist*, 38(2) :345–378. (Cité pp. 60, 119, 132, 172 et 177.)

Perrouty, S., Aillères, L., Jessell, M. W., Baratoux, L., Bourassa, Y., and Crawford, B. (2012). Revised eburnean geodynamic evolution of the gold-rich southern ashanti belt, ghana, with new field and geophysical evidence of pre-tarkwaian deformations. *Precambrian Research*, 204 :12–39. (Cité pp. 73, 74, 75, 76, 88, 97, 118, 119, 134, 135, 224 et 273.)

Peucat, J.-J., Capdevila, R., Drareni, A., Mahdjoub, Y., and Kahoui, M. (2005). The eglab massif in the west african craton (algeria), an original segment of the eburnean orogenic belt : petrology, geochemistry and geochronology. *Precambrian Research*, 136(3) :309–352. (Cité pp. 73, 74, 79, 133, 224 et 262.)

Pigois, J.-P., Groves, D. I., Fletcher, I. R., McNaughton, N. J., and Snee, L. W. (2003). Age constraints on tarkwaian palaeoplacer and lode-gold formation in the tarkwa-damang district, sw ghana. *Mineralium Deposita*, 38(6) :695–714. (Cité pp. 75.)

Pitra, P., Kouamelan, A., Ballevre, M., and Peucat, J.-J. (2010). Palaeoproterozoic high-pressure granulite overprint of the archean continental crust : evidence for homogeneous crustal thickening (man rise, ivory coast). *Journal of Metamorphic Geology*, 28(1) :41–58. (Cité pp. 75, 78, 88, 132, 135 et 224.)

Platt, J. (1993). Exhumation of high-pressure rocks : A review of concepts and processes. *Terra nova*, 5(2) :119–133. (Cité pp. 174.)

Plumb, K. A. and James, H. L. (1986). Subdivision of precambrian time : recommendations and suggestions by the subcommission on precambrian stratigraphy. *Precambrian Research*, 32(1) :65–92. (Cité pp. 68.)

Pons, J., Barbey, P., Dupuis, D., and Léger, J. (1995). Mechanisms of pluton emplacement and structural evolution of a 2.1 ga juvenile continental crust : the birimian of southwestern niger. *Precambrian Research*, 70(3) :281–301. (Cité pp. 77, 78, 89, 134 et 135.)

Potrel, A., Peucat, J., and Fanning, C. (1998). Archean crustal evolution of the west african craton : example of the amsaga area (reguibat rise). u-pb and sm-nd evidence for crustal growth and recycling. *Precambrian Research*, 90(3) :107–117. (Cité pp. 72 et 223.)

Potrel, A., Peucat, J. J., Fanning, C. M., Auvray, B., Burg, J. P., and Caruba, C. (1996). 3.5 ga old terranes in the west african craton, mauritania. *Journal of the Geological Society*, 153(4) :507–510. (Cité pp. 72 et 223.)

Pouclet, A., Doumbia, S., and Vidal, M. (2006). Geodynamic setting of the birimian volcanism in central ivory coast (western africa) and its place in the palaeoproterozoic evolution of the man shield. *Bulletin de la Societe Geologique de France*, 177(2) :105–121. (Cité pp. 73, 78, 79, 88, 89, 133, 224 et 273.)

Pouclet, A., Vidal, M., Delor, C., Simeon, Y., and Alric, G. (1996). Le volcanisme birimien du nord-est de la cote-d'ivoire, mise en evidence de deux phases volcanotectoniques distinctes dans l'evolution geodynamique du paleoproterozoique. *Bulletin de la Société géologique de France*, 167(4) :529–541. (Cité pp. 134 et 135.)

Powell, R. and Holland, T. (2010). Using equilibrium thermodynamics to understand metamorphism and metamorphic rocks. *Elements*, 6(5) :309–314. (Cité pp. 153.)

Powell, R., Holland, T., and Worley, B. (1998). Calculating phase diagrams involving solid solutions via non-linear equations, with examples using thermocalc. *Journal of Metamorphic Geology*, 16(4) :577–588. (Cité pp. 153.)

Puchtel, I., Hofmann, A., Mezger, K., Jochum, K., Shchipansky, A., and Samsonov, A. (1998). Oceanic plateau model for continental crustal growth in the archaean : a case study from the kostomuksha greenstone belt, nw baltic shield. *Earth and Planetary Science Letters*, 155(1) :57–74. (Cité pp. 28 et 272.)

Raase, P., Raith, M., Ackermand, D., and Lal, R. (1986). Progressive metamorphism of mafic rocks from greenschist to granulite facies in the dharwar craton of south india. *The Journal of Geology*, pages 261–282. (Cité pp. 60.)

Ranall, G. (1995). *Rheology of the Earth*. Springer. (Cité pp. 44.)

Ranalli, G. and Murphy, D. C. (1987). Rheological stratification of the lithosphere. *Tectonophysics*, 132(4) :281–295. (Cité pp. 43, 44 et 45.)

Rapp, R. P., Shimizu, N., and Norman, M. D. (2003). Growth of early continental crust by partial melting of eclogite. *Nature*, 425(6958) :605–609. (Cité pp. 39.)

Rapp, R. P., Watson, E. B., and Miller, C. F. (1991). Partial melting of amphibolite/eclogite and the origin of archean trondhjemites and tonalites. *Precambrian Research*, 51(1) :1–25. (Cité pp. 35 et 259.)

Rasmussen, B., Bengtson, S., Fletcher, I. R., and McNaughton, N. J. (2002). Discoidal impressions and trace-like fossils more than 1200 million years old. *Science*, 296(5570) :1112–1115. (Cité pp. 188.)

Rasmussen, B., Fletcher, I. R., and McNaughton, N. J. (2001). Dating low-grade metamorphic events by shrimp u-pb analysis of monazite in shales. *Geology*, 29(10) :963–966. (Cité pp. 188.)

Rasmussen, B., Fletcher, I. R., Muhling, J. R., and Wilde, S. A. (2010). In situ u–th–pb geochronology of monazite and xenotime from the jack hills belt : Implications for the age of deposition and metamorphism of hadean zircons. *Precambrian Research*, 180(1) :26–46. (Cité pp. 188.)

Reddy, S. M. and Evans, D. (2009). Palaeoproterozoic supercontinents and global evolution : correlations from core to atmosphere. *Geological Society, London, Special Publications*, 323(1) :1–26. (Cité pp. 68.)

Rey, P., Teyssier, C., and Whitney, D. (2009). Extension rates, crustal melting, and core complex dynamics. *Geology*, 37(5) :391–394. (Cité pp. 57, 114 et 175.)

Rey, P., Vanderhaeghe, O., and Teyssier, C. (2001). Gravitational collapse of the continental crust : definition, regimes and modes. *Tectonophysics*, 342(3) :435–449. (Cité pp. 57, 114, 175 et 274.)

Rey, P. F. and Houseman, G. (2006). Lithospheric scale gravitational flow : the impact of body forces on orogenic processes from archaean to phanerozoic. *Geological Society, London, Special Publications*, 253(1) :153–167. (Cité pp. 46, 47, 49, 62, 86 et 120.)

Richter, F. M. (1985). Models for the archean thermal regime. *Earth and Planetary Science Letters*, 73(2) :350–360. (Cité pp. 18.)

Rino, S., Komiya, T., Windley, B. F., Katayama, I., Motoki, A., and Hirata, T. (2004). Major episodic increases of continental crustal growth determined from zircon ages of river sands ; implications for mantle overturns in the early precambrian. *Physics of the Earth and Planetary Interiors*, 146(1) :369–394. (Cité pp. 222.)

Rocci, G., Bronner, G., and Deschamps, M. (1991). Crystalline basement of the west african craton. In *The West African orogens and circum-Atlantic correlatives*, pages 31–61. Springer. (Cité pp. 71.)

Rogers, J. J. and Santosh, M. (2002). Configuration of columbia, a mesoproterozoic supercontinent. *Gondwana Research*, 5(1) :5–22. (Cité pp. 70.)

Roques, M. (1948). Le précambrien de l'afrique occidentale française. *Bull. Soc. Géol. France*, 18 :589–628. (Cité pp. 76, 88 et 134.)

Rosen, O. (2002). Siberian craton - sa fragment of a paleoproterozoic supercontinent. *Russian Journal of Earth Sciences*, 4(2) :103–119. (Cité pp. 70.)

Roussel, J., Lecorche, J.-P., Ponsard, J., Sougy, J., and Villeneuve, M. (1984). Panafrican to hercynian deformations in the mauritanides and tectonic significance of gravity anomalies. *Tectonophysics*, 109(1) :41–59. (Cité pp. 225.)

Royden, L. H., Burchfiel, B. C., King, R. W., Wang, E., Chen, Z., Shen, F., and Liu, Y. (1997). Surface deformation and lower crustal flow in eastern tibet. *science*, 276(5313) :788–790. (Cité pp. 57 et 63.)

Rubatto, D. and Hermann, J. (2001). Exhumation as fast as subduction ? *Geology*, 29(1) :3–6. (Cité pp. 113.)

Ruschel, K., Nasdala, L., Kronz, A., Hanchar, J. M., Többens, D. M., Škoda, R., Finger, F., and Möller, A. (2012). A raman spectroscopic study on the structural disorder of monazite–(ce). *Mineralogy and Petrology*, 105(1-2) :41–55. (Cité pp. 188.)

Sagatzky, J. (1954). *La Géologie et les ressources minières de la Haute-Volta méridionale : par J. Sagatzky,...* Grande Impr. africaine. (Cité pp. 76, 88 et 135.)

Sandiford, M. (1989). Horizontal structures in granulite terrains : A record of mountain building or mountain collapse ? *Geology*, 17(5) :449–452. (Cité pp. 172.)

Santosh, M. (2010). Assembling north china craton within the columbia supercontinent : the role of double-sided subduction. *Precambrian Research*, 178(1) :149–167. (Cité pp. 60 et 70.)

Sato, K. and Siga Junior, O. (2002). Rapid growth of continental crust between 2.2 to 1.8 ga in the south american platform : integrated australian, european, north american and sw usa crustal evolution study. *Gondwana Research*, 5(1) :165–173. (Cité pp. 70.)

Sawyer, E. (1994). Melt segregation in the continental crust. *Geology*, 22(11) :1019–1022. (Cité pp. 156.)

Schmitz, S., Möller, A., Wilke, M., Malzer, W., Kanngiesser, B., Bousquet, R., Berger, A., and Schefer, S. (2009). Chemical u-th-pb dating of monazite by 3d-micro x-ray fluorescence analysis with synchrotron radiation. *European Journal of Mineralogy*, 21(5) :927–945. (Cité pp. 188.)

Schofield, D. and Gillespie, M. (2007). A tectonic interpretation of âĂIJeburnean terraneâĂİ outliers in the reguibat shield, mauritania. *Journal of African Earth Sciences*, 49(4) :179–186. (Cité pp. 75 et 78.)

Schofield, D., Horstwood, M., Pitfield, P., Crowley, Q., Wilkinson, A., and Sidaty, H. C. O. (2006). Timing and kinematics of eburnean tectonics in the central reguibat shield, mauritania. *Journal of the Geological Society*, 163(3) :549–560. (Cité pp. 74, 79, 224 et 274.)

Schofield, D., Horstwood, M., Pitfield, P., Gillespie, M., Darbyshire, F., OâĂŹConnor, E., and Abdouloye, T. (2012). U–pb dating and sm–nd isotopic analysis of granitic rocks from the tiris complex : New constaints on key events in the evolution of the reguibat shield, mauritania. *Precambrian Research*, 204 :1–11. (Cité pp. 72.)

Schubert, G., Stevenson, D., and Cassen, P. (1980). Whole planet cooling and the radiogenic heat source contents of the earth and moon. *Journal of Geophysical Research : Solid Earth (1978–2012)*, 85(B5) :2531–2538. (Cité pp. 18.)

Schulmann, K., Lexa, O., Štípská, P., Racek, M., Tajčmanová, L., Konopásek, J., EDEL, J.-B., Peschler, A., and Lehmann, J. (2008). Vertical extrusion and horizontal channel flow of orogenic lower crust : key exhumation mechanisms in large hot orogens ? *Journal of Metamorphic Geology*, 26(2) :273–297. (Cité pp. 64 et 117.)

Schwartz, M. and Melcher, F. (2003). The perkoa zinc deposit, burkina faso. *Economic Geology*, 98(7) :1463–1485. (Cité pp. 73 et 224.)

Schwartz, M. and Melcher, F. (2004). The falémé iron district, senegal. *Economic Geology*, 99(5) :917–939. (Cité pp. 73.)

Seixas, L. A. R., David, J., and Stevenson, R. (2012). Geochemistry, nd isotopes and u–pb geochronology of a 2350ma ttg suite, minas gerais, brazil : Implications for the crustal evolution of the southern são francisco craton. *Precambrian Research*, 196 :61–80. (Cité pp. 69.)

Selverstone, J. (1988). Evidence for east-west crustal extension in the eastern alps : Implications for the unroofing history of the tauern window. *Tectonics*, 7(1) :87–105. (Cité pp. 54.)

Semikhatov, M., Shurkin, K., Aksenov, Y. M., Bekker, Y. R., Bibikova, Y. V., Duk, V., Yesipchuk, K. Y., Karsakov, L., Kiselev, V., Kozlov, V., et al. (1991). A new stratigraphic scale for the precambrian of the ussr. *International Geology Review*, 33(5) :413–422. (Cité pp. 68.)

Shatsky, V., Jagoutz, E., Sobolev, N., Kozmenko, O., Parkhomenko, V., and Troesch, M. (1999). Geochemistry and age of ultrahigh pressure metamorphic rocks from the kokchetav massif (northern kazakhstan). *Contributions to Mineralogy and Petrology*, 137(3) :185–205. (Cité pp. 53.)

Shirey, S. B. and Hanson, G. N. (1984). Mantle-derived archaean monozodiorites and trachyandesites. (Cité pp. 36 et 261.)

Shutong, X., Okay, A., Shouyuan, J., Sengor, A., Wen, S., Yican, L., and Laili, J. (1992). Diamond from the dabie shan metamorphic rocks and its implication for tectonic setting. *Science*, 256(5053) :80–82. (Cité pp. 53.)

Sibson, R. H. (1974). Frictional constraints on thrust, wrench and normal faults. (Cité pp. 42 et 43.)

Siegfried, P., De Kock, G., Clarke, B., Agenbacht, A., Delor, C., and Van Rooyen, R. (2009). Geological map explanation–map sheet 0903d (1 : 100 000). *Mining Sector Support Programme. CGS, BRGM, Geoman, GSD, Accra.* (Cité pp. 92, 136, 172 et 264.)

Singh, J. and Johannes, W. (1996). Dehydration melting of tonalites. part ii. composition of melts and solids. *Contributions to Mineralogy and Petrology*, 125(1) :26–44. (Cité pp. 260.)

Sircombe, K. N. (2004). Agedisplay : an excel workbook to evaluate and display univariate geochronological data using binned frequency histograms and probability density distributions. *Computers & Geosciences*, 30(1) :21–31. (Cité pp. 264.)

Sisson, T., Ratajeski, K., Hankins, W., and Glazner, A. (2005). Voluminous granitic magmas from common basaltic sources. *Contributions to Mineralogy and Petrology*, 148(6) :635–661. (Cité pp. 260.)

Sizova, E., Gerya, T., and Brown, M. (2014). Contrasting styles of phanerozoic and precambrian continental collision. *Gondwana Research*, 25(2) :522–545. (Cité pp. 86.)

Sizova, E., Gerya, T., Brown, M., and Perchuk, L. (2010). Subduction styles in the precambrian : Insight from numerical experiments. *Lithos*, 116(3) :209–229. (Cité pp. 22.)

Sleep, N. H. (1979). Thermal history and degassing of the earth : Some simple calculations. *The Journal of Geology*, pages 671–686. (Cité pp. 21.)

Smith, D. C. (1984). Coesite in clinopyroxene in the caledonides and its implications for geodynamics. (Cité pp. 53, 222 et 274.)

Smithies, R. (2000). The archaean tonalite–trondhjemite–granodiorite (ttg) series is not an analogue of cenozoic adakite. *Earth and Planetary Science Letters*, 182(1) :115–125. (Cité pp. 39, 261 et 273.)

Smithies, R., Champion, D., and Cassidy, K. (2003). Formation of earth's early archaean continental crust. *Precambrian Research*, 127(1) :89–101. (Cité pp. 39, 59, 222, 272 et 274.)

Smithies, R., Van Kranendonk, M., and Champion, D. (2005). It started with a plume–early archaean basaltic proto-continental crust. *Earth and Planetary Science Letters*, 238(3) :284–297. (Cité pp. 58, 86 et 274.)

Snyder, D. (2002). Lithospheric growth at margins of cratons. *Tectonophysics*, 355(1) :7–22. (Cité pp. 29.)

Sobolev, N. and Shatsky, V. (1990). Diamond inclusions in garnets from metamorphic rocks : a new environment for diamond formation. *Nature*, 343(6260) :742–746. (Cité pp. 53.)

Söderlund, U., Patchett, P. J., Vervoort, J. D., and Isachsen, C. E. (2004). The 176lu decay constant determined by lu–hf and u–pb isotope systematics of precambrian mafic intrusions. *Earth and Planetary Science Letters*, 219(3) :311–324. (Cité pp. 278.)

Soumaila, A. and Garba, Z. (2006). Le metamorphisme des formations de la ceinture de roches vertes birrimienne (paleoproterozoique) de diagorou-darbani (liptako, niger, afrique de l'ouest). *Africa Geoscience Review*, 13(1/2) :107. (Cité pp. 77, 78, 89 et 135.)

Srivastava, P. and Mitra, G. (1994). Thrust geometries and deep structure of the outer and lesser himalaya, kumaon and garhwal (india) : Implications for evolution of the himalayan fold-and-thrust belt. *Tectonics*, 13(1) :89–109. (Cité pp. 53.)

Stacey, J. t. and Kramers, J. (1975). Approximation of terrestrial lead isotope evolution by a two-stage model. *Earth and Planetary Science Letters*, 26(2) :207–221. (Cité pp. 121, 170 et 251.)

Stein, M. and Hofmann, A. (1994). Mantle plumes and episodic crustal growth. *Nature*, 372(6501) :63–68. (Cité pp. 28.)

Stern, R. A. and Hanson, G. N. (1991). Archean high-mg granodiorite : a derivative of light rare earth element-enriched monzodiorite of mantle origin. *Journal of Petrology*, 32(1) :201–238. (Cité pp. 261.)

Stern, R. A., Hanson, G. N., and Shirey, S. B. (1989). Petrogenesis of mantle-derived, lile-enriched archean monzodiorites and trachyandesites (sanukitoids) in southwestern superior province. *Canadian Journal of Earth Sciences*, 26(9) :1688–1712. (Cité pp. 36 et 37.)

Stern, R. J. (2005). Evidence from ophiolites, blueschists, and ultrahigh-pressure metamorphic terranes that the modern episode of subduction tectonics began in neoproterozoic time. *Geology*, 33(7) :557–560. (Cité pp. 58, 62, 86 et 222.)

Stevens, G. and Moyen, J.-F. (2007). Metamorphism in the barberton granite greenstone terrain : a record of paleoarchean accretion. *Earth's Oldest Rocks. Developments in Precambrian Geology*, 15 :669–698. (Cité pp. 61 et 132.)

Stevenson, R., Henry, P., and Gariépy, C. (1999). Assimilation–fractional crystallization origin of archean sanukitoid suites : Western superior province, canada. *Precambrian Research*, 96(1) :83–99. (Cité pp. 261.)

Stevenson, R. K. and Patchett, P. J. (1990). Implications for the evolution of continental crust from hf isotope systematics of archean detrital zircons. *Geochimica et Cosmochimica Acta*, 54(6) :1683–1697. (Cité pp. 222.)

Stocker, R. and Ashby, M. (1973). On the rheology of the upper mantle. *Reviews of Geophysics*, 11(2) :391–426. (Cité pp. 44.)

Stöckhert, B. and Gerya, T. V. (2005). Pre-collisional high pressure metamorphism and nappe tectonics at active continental margins : a numerical simulation. *Terra Nova*, 17(2) :102–110. (Cité pp. 174.)

Suzuki, T. and Akaogi, M. (1995). Element partitioning between olivine and silicate melt under high pressure. *Physics and Chemistry of Minerals*, 22(7) :411–418. (Cité pp. 33.)

Sylvester, P. J. (1994). Archean granite plutons. *Archean Crustal Evolution*, 11 :261–314. (Cité pp. 36 et 37.)

Sylvester, P. J. and Attoh, K. (1992). Lithostratigraphy and composition of 2.1 ga greenstone belts of the west african craton and their bearing on crustal evolution and the archean-proterozoic boundary. *The Journal of Geology*, pages 377–393. (Cité pp. 73, 79 et 224.)

Syracuse, E. M., van Keken, P. E., and Abers, G. A. (2010). The global range of subduction zone thermal models. *Physics of the Earth and Planetary Interiors*, 183(1) :73–90. (Cité pp. 39.)

Tagini, B. (1971). Esquisse structural de la cote d'lvoire. *Essai de geotectonique regionale : SODEMI, Abidjan.* (Cité pp. 74, 76, 88 et 133.)

Tajčmanová, L., Connolly, J., and Cesare, B. (2009). A thermodynamic model for titanium and ferric iron solution in biotite. *Journal of Metamorphic Geology*, 27(2) :153–165. (Cité pp. 178.)

Tapsoba, B., Lo, C.-H., Jahn, B.-M., Chung, S.-L., Wenmenga, U., and Iizuka, Y. (2013). Chemical and sr–nd isotopic compositions and zircon u–pb ages of the birimian granitoids from ne burkina faso, west african craton : Implications on the geodynamic setting and crustal evolution. *Precambrian Research*, 224 :364–396. (Cité pp. 73, 74, 89 et 224.)

Tatsumi, Y. and Eggins, S. (1995). *Subduction zone magmatism*, volume 1. Blackwell Science Cambridge. (Cité pp. 261.)

Tatsumi, Y. and Suzuki, T. (2009). Tholeiitic vs calc-alkalic differentiation and evolution of arc crust : constraints from melting experiments on a basalt from the izu–bonin–mariana arc. *Journal of Petrology*, 50(8) :1575–1603. (Cité pp. 260.)

Taylor, P. N., Moorbath, S., Leube, A., and Hirdes, W. (1992). Early proterozoic crustal evolution in the birimian of ghana : constraints from geochronology and isotope geochemistry. *Precambrian Research*, 56(1) :97–111. (Cité pp. 91 et 137.)

Taylor, S. R. (1967). The origin and growth of continents. *Tectonophysics*, 4(1) :17–34. (Cité pp. 28.)

Taylor, S. R. and McLennan, S. M. (1985). The continental crust : its composition and evolution. (Cité pp. 28, 37 et 278.)

Tempier, P. (1986). Le burkinien, cycle orogénique majeur du protérozoïque inférieur en afrique de l'ouest. *Publication CIFEG*, 10(1986) :17–23. (Cité pp. 76, 88, 135 et 224.)

Teyssier, C. and Whitney, D. L. (2002). Gneiss domes and orogeny. *Geology*, 30(12) :1139–1142. (Cité pp. 57.)

Théveniaut, H., Ndiaye, P., Buscail, F., Couëffé, R., Delor, C., Fullgraf, T., and Goujou, J. (2010). Notice explicative de la carte géologique du sénégal oriental à 1/500000. *Ministère des Mines, de l'Industrie, de l'Agro-Industrie et des PME, Direction des Mines et de la Géologie, Dakar*. (Cité pp. 89.)

Thiéblemont, D., Delor, C., Cocherie, A., Lafon, J. M., Goujou, J. C., Baldé, A., Bah, M., Sané, H., and Mark Fanning, C. (2001). A 3.5 ga granite–gneiss basement in guinea : further evidence for early archean accretion within the west african craton. *Precambrian Research*, 108(3) :179–194. (Cité pp. 72 et 223.)

Thiéblemont, D., Goujou, J. C., Egal, E., Cocherie, A., Delor, C., Lafon, J. M., and Fanning, C. M. (2004). Archean evolution of the leo rise and its eburnean reworking. *Journal of African Earth Sciences*, 39(3) :97–104. (Cité pp. 72 et 74.)

Thomas, E., De Kock, G., Baglow, N., Viljoen, J., and Siaka, Z. (2009). Geological map explanation–map sheet 0903b (1 : 100 000). *Mining Sector Support Programme. CGS, BRGM, Geoman, GSD, Accra*. (Cité pp. 89, 92, 136, 137, 172 et 226.)

Trap, P., Faure, M., Lin, W., Bruguier, O., and Monié, P. (2008). Contrasted tectonic styles for the paleoproterozoic evolution of the north china craton. evidence for a 2.1 ga thermal and tectonic event in the fuping massif. *Journal of Structural Geology*, 30(9) :1109–1125. (Cité pp. 60, 70 et 119.)

Trap, P., Faure, M., Lin, W., Le Breton, N., and Monié, P. (2012). Paleoproterozoic tectonic evolution of the trans-north china orogen : Toward a comprehensive model. *Precambrian Research*, 222 :191–211. (Cité pp. 70.)

Triboulet, C. and Feybesse, J. (1998). The birrimian and archean metabasic rocks of toulepleu-ity (ivory coast) : rocks subjected to 8 kbar (24 km) and 14 kbar (42 km) during palaeoproterozoic. *Comptes Rendus de l'Academie des Sciences Series IIA Earth and Planetary Science*, 327(1) :61–66. (Cité pp. 78, 88 et 135.)

Tshibubudze, A., Hein, K., Peters, L., Woolfe, A., and McCUAIG, T. (2013). Oldest u-pb crystallisation age for the west african craton from the oudalan-gorouol belt of burkina faso. *South African Journal of Geology*, 116(1) :169–181. (Cité pp. 73, 224 et 264.)

Tshibubudze, A., Hein, K. A., and Marquis, P. (2009). The markoye shear zone in ne burkina faso. *Journal of African Earth Sciences*, 55(5) :245–256. (Cité pp. 76, 88, 118, 135 et 224.)

Tsujimori, T., Sisson, V. B., Liou, J. G., Harlow, G. E., and Sorensen, S. S. (2006). Very-low-temperature record of the subduction process : a review of worldwide lawsonite eclogites. *Lithos*, 92(3) :609–624. (Cité pp. 62.)

Tunks, A. J., Selley, D., Rogers, J. R., and Brabham, G. (2004). Vein mineralization at the damang gold mine, ghana : controls on mineralization. *Journal of structural geology*, 26(6) :1257–1273. (Cité pp. 75.)

Turcotte, D. (1980). On the thermal evolution of the earth. *Earth and Planetary Science Letters*, 48(1) :53–58. (Cité pp. 18.)

Turner, S., Sandiford, M., and Foden, J. (1992). Some geodynamic and compositional constraints on" postorogenic" magmatism. *Geology*, 20(10) :931–934. (Cité pp. 29 et 37.)

Unsworth, M., Jones, A. G., Wei, W., Marquis, G., Gokarn, S., Spratt, J., Bedrosian, P., Booker, J., Leshou, C., Clarke, G., et al. (2005). Crustal rheology of the himalaya and southern tibet inferred from magnetotelluric data. *Nature*, 438(7064) :78–81. (Cité pp. 56.)

Väisänen, M., Mänttäri, I., and Hölttä, P. (2002). Svecofennian magmatic and metamorphic evolution in southwestern finland as revealed by u-pb zircon sims geochronology. *Precambrian research*, 116(1) :111–127. (Cité pp. 132.)

Valley, J., Lackey, J., Cavosie, A., Clechenko, C., Spicuzza, M., Basei, M., Bindeman, I., Ferreira, V., Sial, A., King, E., et al. (2005). 4.4 billion years of crustal maturation : oxygen isotope ratios of magmatic zircon. *Contributions to Mineralogy and Petrology*, 150(6) :561–580. (Cité pp. 25 et 27.)

Van der Molen, I. and Paterson, M. (1979). Experimental deformation of partially-melted granite. *Contributions to Mineralogy and Petrology*, 70(3) :299–318. (Cité pp. 56.)

van Hunen, J. and van den Berg, A. P. (2008). Plate tectonics on the early earth : limitations imposed by strength and buoyancy of subducted lithosphere. *Lithos*, 103(1) :217–235. (Cité pp. 21, 23, 86 et 274.)

van Hunen, J., van Keken, P. E., Hynes, A., and Davies, G. F. (2008). Tectonics of early earth : Some geodynamic considerations. *When did plate tectonics begin on planet Earth*, pages 157–171. (Cité pp. 24.)

Van Kranendonk, M. J., Collins, W., Hickman, A., and Pawley, M. J. (2004). Critical tests of vertical vs. horizontal tectonic models for the archaean east pilbara granite–greenstone terrane, pilbara craton, western australia. *Precambrian Research*, 131(3) :173–211. (Cité pp. 59 et 86.)

Van Kranendonk, M. J., Hugh Smithies, R., Hickman, A. H., and Champion, D. (2007). Review : secular tectonic evolution of archean continental crust : interplay between horizontal and vertical processes in the formation of the pilbara craton, australia. *Terra Nova*, 19(1) :1–38. (Cité pp. 59, 60 et 86.)

Van Thienen, P., Van den Berg, A., and Vlaar, N. (2004a). On the formation of continental silicic melts in thermochemical mantle convection models : implications for early earth. *Tectonophysics*, 394(1) :111–124. (Cité pp. 39, 41 et 273.)

Van Thienen, P., Van den Berg, A., and Vlaar, N. (2004b). Production and recycling of oceanic crust in the early earth. *Tectonophysics*, 386(1) :41–65. (Cité pp. 24 et 273.)

Vanderhaeghe, O. (2009). Migmatites, granites and orogeny : flow modes of partially-molten rocks and magmas associated with melt/solid segregation in orogenic belts. *Tectonophysics*, 477(3) :119–134. (Cité pp. 117 et 175.)

Vanderhaeghe, O., Ledru, P., Thiéblemont, D., Egal, E., Cocherie, A., Tegyey, M., and Milési, J.-P. (1998). Contrasting mechanism of crustal growth : Geodynamic evolution of the paleoproterozoic granite–greenstone belts of french guiana. *Precambrian Research*, 92(2) :165–193. (Cité pp. 72 et 132.)

Vanderhaeghe, O. and Teyssier, C. (2001a). Crustal-scale rheological transitions during late-orogenic collapse. *Tectonophysics*, 335(1) :211–228. (Cité pp. 46, 55, 56 et 114.)

Vanderhaeghe, O. and Teyssier, C. (2001b). Partial melting and flow of orogens. *Tectonophysics*, 342(3) :451–472. (Cité pp. 56, 57, 64, 114 et 175.)

Veizer, J. and Mackenzie, F. (2003). Evolution of sedimentary rocks. *Treatise on geochemistry*, 7 :369–407. (Cité pp. 30 et 32.)

Vernon, R. and Paterson, S. (2001). Axial-surface leucosomes in anatectic migmatites. *Tectonophysics*, 335(1) :183–192. (Cité pp. 103.)

Vidal, M. and Alric, G. (1994). The palaeoproterozoic (birimian) of haute-comoé in the west african craton, ivory coast : a transtensional back-arc basin. *Precambrian research*, 65(1) :207–229. (Cité pp. 77, 134, 135, 224 et 273.)

Vidal, M., Gumiaux, C., Cagnard, F., Pouclet, A., Ouattara, G., and Pichon, M. (2009). Evolution of a paleoproterozoic "weak type" orogeny in the west african craton (ivory coast). *Tectonophysics*, 477(3) :145–159. (Cité pp. 60, 63, 70, 74, 78, 87, 88, 89, 91, 119, 132, 133, 134, 224 et 229.)

Vidal, M., Prost, A., Alric, G., and Lemoine, S. (1992). Présence d'un socle antérieur à une suture océanique du birimien inférieur en côte-d'ivoire (afrique de l'ouest). *Comptes rendus de l'Académie des sciences. Série 2, Mécanique, Physique, Chimie, Sciences de l'univers, Sciences de la Terre*, 315(2) :193–200. (Cité pp. 76 et 135.)

Vidal, O., De Andrade, V., Lewin, E., Munoz, M., Parra, T., and Pascarelli, S. (2006). P–t-deformation-fe3+/fe2+ mapping at the thin section scale and comparison with xanes mapping : application to a garnet-bearing metapelite from the sambagawa metamorphic belt (japan). *Journal of Metamorphic Geology*, 24(7) :669–683. (Cité pp. 154 et 180.)

Vidal, O. and Parra, T. (2000). Exhumation paths of high-pressure metapelites obtained from local equilibria for chlorite–phengite assemblages. *Geological Journal*, 35(3-4) :139–161. (Cité pp. 181.)

Vidal, O., Parra, T., and Trotet, F. (2001). A thermodynamic model for fe-mg aluminous chlorite using data from phase equilibrium experiments and natural pelitic assemblages in the 100 to 600 c, 1 to 25 kb range. *American journal of Science*, 301(6) :557–592. (Cité pp. 154 et 180.)

Vidal, O., Parra, T., and Vieillard, P. (2005). Thermodynamic properties of the tschermak solid solution in fe-chlorite : Application to natural examples and possible role of oxidation. *American Mineralogist*, 90(2-3) :347–358. (Cité pp. 180.)

Vielzeuf, D. and Holloway, J. R. (1988). Experimental determination of the fluid-absent melting relations in the pelitic system. *Contributions to Mineralogy and Petrology*, 98(3) :257–276. (Cité pp. 260.)

Volodichev, O., Slabunov, A., Bibikova, E., Konilov, A., and Kuzenko, T. (2004). Archean eclogites in the belomorian mobile belt, baltic shield. *Petrology*, 12(6) :540–560. (Cité pp. 62.)

Waldbaum, D. and Thompson, J. (1969). Mixing properties of sanidine crystalline solutions. *American Mineralogist*, 54(9-10) :1274. (Cité pp. 178.)

Wang, X., Liou, J., and Mao, H. (1989). Coesite-bearing eclogite from the dabie mountains in central china. *Geology*, 17(12) :1085–1088. (Cité pp. 53.)

Watkins, J., Clemens, J., and Treloar, P. (2007). Archaean ttgs as sources of younger granitic magmas : melting of sodic metatonalites at 0.6–1.2 gpa. *Contributions to Mineralogy and Petrology*, 154(1) :91–110. (Cité pp. 260.)

Watts, A. and Burov, E. (2003). Lithospheric strength and its relationship to the elastic and seismogenic layer thickness. *Earth and Planetary Science Letters*, 213(1) :113–131. (Cité pp. 53.)

Wedepohl, H. K. (1995). The composition of the continental crust. *Geochimica et cosmochimica Acta*, 59(7) :1217–1232. (Cité pp. 278.)

Wegener, A. (1912). Die entstehung der kontinente. *Geologische Rundschau*, 3(4) :276–292. (Cité pp. 14.)

Wegener, A. (2012). *The origin of continents and oceans*. Courier Dover Publications. (Cité pp. 14.)

White, A., Burgess, R., Charnley, N., Selby, D., Whitehouse, M., Robb, L., and Waters, D. (2014). Constraints on the timing of late-eburnean metamorphism, gold mineralisation and regional exhumation at damang mine, ghana. *Precambrian Research*, 243 :18–38. (Cité pp. 75 et 224.)

White, R. and Powell, R. (2002). Melt loss and the preservation of granulite facies mineral assemblages. *Journal of Metamorphic Geology*, 20(7) :621–632. (Cité pp. 179.)

White, R., Powell, R., and Holland, T. (2001). Calculation of partial melting equilibria in the system na2o–cao–k2o–feo–mgo–al2o3–sio2–h2o (nckfmash). *Journal of Metamorphic Geology*, 19(2) :139–153. (Cité pp. 178.)

White, R., Powell, R., Holland, T., and Worley, B. (2000). The effect of tio˜ 2 and fe˜ 2o˜ 3 on metapelitic assemblages at greenschist and amphibolite facies conditions : mineral equilibria calculations in the system k˜ 2o-feo-mgo-al˜ 2o˜ 3-sio˜ 2-h˜ 2o-tio˜ 2-fe˜ 2o˜ 3. *Journal of Metamorphic Geology*, 18(5) :497–512. (Cité pp. 178.)

Whitney, D. L. and Evans, B. W. (2010). Abbreviations for names of rock-forming minerals. *American mineralogist*, 95(1) :185. (Cité pp. 102 et 138.)

Whitney, D. L., Teyssier, C., and Vanderhaeghe, O. (2004). Gneiss domes and crustalflow. *Gneiss domes in orogeny*, 380 :15. (Cité pp. 57, 114 et 175.)

Wiedenbeck, M., Alle, P., Corfu, F., Griffin, W., Meier, M., Oberli, F., Quadt, A. v., Roddick, J., and Spiegel, W. (1995). Three natural zircon standards for u-th-pb, lu-hf, trace element and ree analyses. *Geostandards newsletter*, 19(1) :1–23. (Cité pp. 121 et 277.)

Wilde, S. A., Valley, J. W., Peck, W. H., and Graham, C. M. (2001). Evidence from detrital zircons for the existence of continental crust and oceans on the earth 4.4 gyr ago. *Nature*, 409(6817) :175–178. (Cité pp. 25.)

Willett, S. D. and Brandon, M. T. (2002). On steady states in mountain belts. *Geology*, 30(2) :175–178. (Cité pp. 113.)

Windley, B. (1992). Proterozoic collisional and accretionary orogens. *Developments in Precambrian Geology*, 10 :419–446. (Cité pp. 28, 58, 86 et 222.)

Windley, B. F. (1981). Precambrian rocks in the light of the plate-tectonic concept. *Developments in Precambrian Geology*, 4 :1–20. (Cité pp. 58 et 222.)

Windley, B. F. (1984). The archaean-proterozoic boundary. *Tectonophysics*, 105(1) :43–53. (Cité pp. 68.)

Windley, B. F. (1993). Uniformitarianism today : plate tectonics is the key to the past. *Journal of the Geological Society*, 150(1) :7–19. (Cité pp. 16, 24 et 222.)

Windley, B. F. and Garde, A. A. (2009). Arc-generated blocks with crustal sections in the north atlantic craton of west greenland : crustal growth in the archean with modern analogues. *Earth-Science Reviews*, 93(1) :1–30. (Cité pp. 50 et 273.)

Wingate, M. and Kirkland, C. (2010). Introduction to geochronology information released in 2014. *age (Ma)*, 207 :206Pb. (Cité pp. 188.)

Wolf, M. B. and Wyllie, P. J. (1994). Dehydration-melting of amphibolite at 10 kbar : the effects of temperature and time. *Contributions to Mineralogy and Petrology*, 115(4) :369–383. (Cité pp. 260.)

Wyman, D., Kerrich, R., and Polat, A. (2002). Assembly of archean cratonic mantle lithosphere and crust : plume–arc interaction in the abitibi–wawa subduction–accretion complex. *Precambrian Research*, 115(1) :37–62. (Cité pp. 40.)

Wyman, D. A. and Kerrich, R. (2002). Formation of archean continental lithospheric roots : the role of mantle plumes. *Geology*, 30(6) :543–546. (Cité pp. 34.)

Yamato, P., Agard, P., Burov, E., Le Pourhiet, L., Jolivet, L., and Tiberi, C. (2007a). Burial and exhumation in a subduction wedge : Mutual constraints from thermomechanical modeling and natural p-t-t data (schistes lustrés, western alps). *Journal of Geophysical Research : Solid Earth (1978–2012)*, 112(B7). (Cité pp. 174.)

Yamato, P., Agard, P., Goffé, B., De Andrade, V., Vidal, O., and Jolivet, L. (2007b). New, high-precision p–t estimates for oman blueschists : implications for obduction, nappe stacking and exhumation processes. *Journal of Metamorphic Geology*, 25(6) :657–682. (Cité pp. 154.)

Zegers, T. E. and van Keken, P. E. (2001). Middle archean continent formation by crustal delamination. *Geology*, 29(12) :1083–1086. (Cité pp. 39 et 273.)

Zeh, A. (2001). Inference of a detailed p–t path from p–t pseudosections using metapelitic rocks of variable composition from a single outcrop, shackleton range, antarctica. *Journal of Metamorphic Geology*, 19(4) :329–350. (Cité pp. 153.)

Zeh, A. and Gerdes, A. (2012). U–pb and hf isotope record of detrital zircons from gold-bearing sediments of the pietersburg greenstone belt (south africa) - is there a common provenance with the witwatersrand basin ? *Precambrian Research*, 204 :46–56. (Cité pp. 121.)

Zeh, A., Gerdes, A., and Barton, J. M. (2009). Archean accretion and crustal evolution of the kalahari craton - the zircon age and hf isotope record of granitic rocks from barberton/swaziland to the francistown arc. *Journal of Petrology*, page egp027. (Cité pp. 29, 36, 222 et 262.)

Zeh, A., Gerdes, A., Klemd, R., and Barton, J. M. (2007). Archaean to proterozoic crustal evolution in the central zone of the limpopo belt (south africa–botswana) : constraints from combined u–pb and lu–hf isotope analyses of zircon. *Journal of Petrology*, 48(8) :1605–1639. (Cité pp. 222.)

Zeh, A., Jaguin, J., Poujol, M., Boulvais, P., Block, S., and Paquette, J.-L. (2013). Juvenile crust formation in the northeastern kaapvaal craton at 2.97 ga - implications for archean terrane accretion, and the source of the pietersburg gold. *Precambrian Research*, 233 :20–43. (Cité pp. 132 et 222.)

Zeh, A., Klemd, R., Buhlmann, S., and Barton, J. (2004). Pro-and retrograde p–t evolution of granulites of the beit bridge complex (limpopo belt, south africa) : constraints from quantitative phase diagrams and geotectonic implications. *Journal of Metamorphic Geology*, 22(2) :79–95. (Cité pp. 153.)

Zhao, G., Cawood, P. A., Wilde, S. A., and Sun, M. (2002). Review of global 2.1–1.8 ga orogens : implications for a pre-rodinia supercontinent. *Earth-Science Reviews*, 59(1) :125–162. (Cité pp. 69, 70 et 133.)

Zhao, G., Sun, M., Wilde, S. A., and Sanzhong, L. (2005). Late archean to paleoproterozoic evolution of the north china craton : key issues revisited. *Precambrian Research*, 136(2) :177–202. (Cité pp. 70.)

Zhao, G., Wilde, S. A., Cawood, P. A., and Lu, L. (1998). Thermal evolution of archean basement rocks from the eastern part of the north china craton and its bearing on tectonic setting. *International Geology Review*, 40(8) :706–721. (Cité pp. 60 et 70.)

Zitsmann, A., Kiessling, R., Ostwald, J., and Treder, H.-W. (1997). Geological, geophysical and geochemical investigations in the bui belt area in ghana. *Geologisches Jahrbuch*, 88 :269. (Cité pp. 90 et 137.)